

High-Luminosity Large Hadron Collider (HL-LHC)

Technical Design Report V. 0.1

Editors: Apollinari G.
Béjar Alonso I. (Executive Editor)
Brüning O.
Fessia P.
Lamont M.
Rossi L.
Tavian L.




CERN Yellow Reports: Monographs
Published by CERN, CH-1211 Geneva 23, Switzerland

ISBN 978-92-9083-470-0 (paperback)
ISBN 978-92-9083-471-7 (PDF)
ISSN 2519-8068 (Print)
ISSN 2519-8076 (Online)
DOI <https://doi.org/10.23731/CYRM-2017-004>

Accepted for publication by the CERN Report Editorial Board (CREB) on 18 September 2017
Available online at <https://e-publishing.cern.ch/> and <https://cds.cern.ch/>

Copyright © CERN, 2017, unless otherwise specified

 Creative Commons Attribution 4.0

Knowledge transfer is an integral part of CERN's mission.
CERN publishes this volume Open Access under the Creative Commons Attribution 4.0 license (<http://creativecommons.org/licenses/by/4.0/>) in order to permit its wide dissemination and use.
The submission of a contribution to a CERN Yellow Reports series shall be deemed to constitute the contributor's agreement to this copyright and license statement. Contributors are requested to obtain any clearances that may be necessary for this purpose.

This volume is indexed in: CERN Document Server (CDS), INSPIRE.

This report should be cited as:

High-Luminosity Large Hadron Collider (HL-LHC). Technical Design Report V. 0.1,
edited by G. Apollinari, I. Béjar Alonso, O. Brüning, P. Fessia, M. Lamont, L. Rossi, L. Taviani, CERN Yellow
Reports: Monographs, Vol. 4/2017, CERN-2017-007-M (CERN, Geneva, 2017).
<https://doi.org/10.23731/CYRM-2017-004>

Preface

The High Luminosity LHC (HL-LHC) Project was setup in 2010 by the CERN Director for Accelerators and Technology, Dr. Steve Myers, following a change of strategy and subsequent merging of the LHC upgrade Phase I and Phase II into one unique project. To this end, CERN in consortium with 15 European Institutions applied in November 2010 to the call for European funding under the 7th Framework Programme Design Study category: the application was approved with full budget in 2011 with the name FP7 High Luminosity Large Hadron Collider Design Study (also known as HiLumi LHC, Grant n. 284404).

The new European Strategy for Particle Physics, adopted by the special CERN Council of Brussels on 30 May 2013, placed HL-LHC as a first priority project for the next decade. Consequently, CERN management inserted the project in the Medium Term Plan (5-year plan) and a kick off meeting of HL-LHC as a construction project was organized in Daresbury on 11 November 2013. The HL-LHC project is accompanied by upgrade projects of all LHC Experiments and by the LHC Injector Upgrade Project (LIU). The Experiment upgrade projects are dealt with by their International Collaborations. The LIU project has a separate management, project structure and budget line and plans for a complete implementation during Long Shutdown 2 (LS2), by the end of 2020. The Experiments upgrade and LIU projects are not covered by this TDR.

A Cost and Schedule Review series, reviewing both the HL-LHC and LIU projects and reporting to the CERN Director of Accelerators and Technology, Dr. Frédéric Bordry, started in March 2015, with C&SR-I. Following the very positive results of the review, the CERN management endorsed the cost and planning. In September 2015 the CERN Council approved the MTP 2016-2020, containing the funding for the project for that period and envisaging the full Cost-to-Completion (CtC) of the project by 2026. Finally in June 2016, the CERN management had the High Luminosity LHC project, i.e. the upgrade of the collider and its infrastructure, formally approved by the CERN Council, with full financing till 2026. The approved CtC is 950 MCHF of material budget in CERN accounting.

In August 2016, a re-baselining of the HL-LHC project was approved by CERN management (and endorsed by the C&SR-II of October 2016) in order to keep the CtC ceiling while accommodating extra cost in the technical infrastructure (mainly in the civil engineering). The present TDR reflects the design of the project at the time of approval by the CERN council, June 2016, with the modifications introduced in the re-baselining exercise in summer 2016.

The project leadership is particularly grateful to the CERN management for its continuous support and encouragement and in particular to the CERN Director of Accelerators and Technology, Dr. Frédéric Bordry for his continuous support and guidance from the beginning of the project, to former Director-General Dr. Rolf Heuer for his engagement in having the project initiated and started the funding during his mandate, as well as to the present Director-General Dr. Fabiola Gianotti, for having pursued and obtained the full approval of the entire HL-LHC project by the Council in June 2016, the first CERN project with such status after the LHC.

CERN, 31 July 2017

Lucio Rossi, HL-LHC Project Leader
Oliver Brüning, HL-LHC Deputy Project Leader

Abstract

The Large Hadron Collider (LHC) is one of the largest scientific instruments ever built. Since opening up a new energy frontier for exploration in 2010, it has gathered a global user community of about 7,000 scientists working in fundamental particle physics and the physics of hadronic matter at extreme temperature and density. To sustain and extend its discovery potential, the LHC will need a major upgrade in the 2020s. This will increase its instantaneous luminosity (rate of collisions) by a factor of five beyond the original design value and the integrated luminosity (total collisions created) by a factor ten. The LHC is already a highly complex and exquisitely optimised machine so this upgrade must be carefully conceived and will require about ten years to implement. The new configuration, known as High Luminosity LHC (HL-LHC), relies on a number of key innovations that push accelerator technology beyond its present limits. Among these are cutting-edge 11-12 tesla superconducting magnets, compact superconducting cavities for beam rotation with ultra-precise phase control, new technology and physical processes for beam collimation and 100 metre-long high-power superconducting links with negligible energy dissipation. The present document describes the technologies and components that will be used to realise the project and is intended to serve as the basis for the detailed engineering design of HL-LHC.

Table of contents

TABLE OF CONTENTS	VII
TABLE OF FIGURES.....	XVI
TABLE OF TABLES.....	XXX
CONTRIBUTOR LIST	XXXIV
1 HIGH LUMINOSITY LARGE HADRON COLLIDER HL-LHC.....	1
1.1 INTRODUCTION.....	1
1.2 HL-LHC IN A NUTSHELL	2
1.2.1 Luminosity	5
1.2.2 Present luminosity limitations and hardware constraints	5
1.2.3 Luminosity levelling and availability.....	6
1.2.4 HL-LHC parameters and main systems for the upgrade	7
1.2.5 Re-baselining of June 2016.....	11
1.2.6 Performance	11
1.2.7 Main milestones	12
1.2.8 Cost.....	13
1.3 THE COLLABORATION	14
1.3.1 FP7-Hilumi LHC	15
1.3.2 LHC Accelerator R&D Program (LARP) and HL-LHC Accelerator Upgrade Project.....	17
1.3.3 KEK.....	19
1.3.4 Other collaborations.....	20
1.4 GOVERNANCE AND PROJECT STRUCTURE.....	21
1.4.1 Present project governance and structure.	21
1.4.2 New Project Governance and MoU	23
1.5 REFERENCES	23
2 MACHINE LAYOUT AND PERFORMANCE.....	25
2.1 PERFORMANCE GOALS (NOMINAL SCHEME).....	25
2.1.1 Parameter space and basic parameter choices.....	26
2.2 PROPOSED SYSTEMS UPGRADES AND IMPROVEMENTS	30
2.2.1 Insertion region magnets.....	30
2.2.2 Collision debris absorbers (TAXS/TAXN)	31
2.2.3 Crab cavities	31
2.2.4 Collimation	32
2.2.5 New cold powering.....	32
2.2.6 Enhanced machine protection and remote handling.....	33
2.2.7 New cryogenics plants and distribution.....	33
2.2.8 Enhanced beam instrumentation	34
2.2.9 Beam transfer and kickers.....	34
2.3 BASELINE OPTICS AND LAYOUT	35
2.3.1 Basic optics and layout choices for the High Luminosity insertions.....	35
2.3.2 Circuit specifications.....	42
2.3.3 Target field quality and dynamic aperture	45
2.4 PERFORMANCE.....	52
2.4.1 Beam stability.....	52
2.4.2 Beam-beam effects.....	59
2.4.3 Beam-induced heat load.....	62
2.4.4 Luminosity performance.....	67

2.5	VARIANTS AND OPTIONS.....	69
2.5.1	<i>Flat optics</i>	69
2.5.2	<i>8b+4e alternative filling scheme</i>	69
2.5.3	<i>Sub-harmonic RF system 200 MHz</i>	72
2.5.4	<i>Flat optics without crab cavities</i>	74
2.5.5	<i>80 bunch filling scheme</i>	76
2.5.6	<i>Pile-up density control</i>	76
2.6	THE HL-LHC AS A NUCLEUS–NUCLEUS COLLIDER.....	77
2.7	ACKNOWLEDGEMENTS.....	79
2.8	REFERENCES	80
3	INSERTION MAGNETS.....	95
3.1	OVERVIEW	95
3.2	LOW- β QUADRUPOLES	97
3.3	ORBIT CORRECTORS.....	102
3.4	HIGH-ORDER CORRECTORS.....	103
3.5	SEPARATION DIPOLE D1	106
3.6	RECOMBINATION DIPOLE D2.....	107
3.7	D2 CORRECTORS.....	109
3.8	Q4, Q5 AND Q6	110
3.9	OTHER INTERVENTIONS: SEXTUPOLE (MS) IN Q10 AND Q5 IN IR6	111
3.10	RESISTIVE MAGNETS	111
3.11	POWERING	111
3.12	COOLING.....	112
3.13	INSTRUMENTATION	112
3.14	TEST.....	113
3.15	SUMMARY OF BASELINE MODIFICATIONS WITH RESPECT TO THE PREVIOUS VERSION OF THE DESIGN REPORT	113
3.16	REFERENCES	114
4	RF SYSTEMS	117
4.1	INTRODUCTION.....	117
4.2	CRAB CAVITIES	117
4.2.1	<i>Beam and RF system parameters</i>	118
4.2.2	<i>RF cavity design</i>	119
4.2.3	<i>Beam loading and RF power</i>	120
4.2.4	<i>RF power coupler</i>	121
4.2.5	<i>Coupled bunch instabilities, Fundamental Mode</i>	122
4.2.6	<i>Impedance budget, Higher Order Modes</i>	123
4.2.7	<i>Higher order mode couplers</i>	123
4.2.8	<i>RF multipoles</i>	124
4.2.9	<i>Lorentz force detuning and multipacting</i>	125
4.2.10	<i>Cryomodule and integration</i>	125
4.2.11	<i>RF powering and control architecture</i>	135
4.2.12	<i>Low level RF architecture and operational scenarios</i>	136
4.2.13	<i>Cavity failure scenarios</i>	137
4.2.14	<i>Failure scenario mitigation</i>	138
4.2.15	<i>Heat loads and cryogenics</i>	139
4.2.16	<i>Vacuum system</i>	139
4.2.17	<i>Interlocks for machine protection</i>	140
4.2.18	<i>SM18 and SPS beam tests</i>	140
4.3	HARMONIC SYSTEMS	143

4.4	TRANSVERSE DAMPER (ADT) UPGRADE.....	144
4.5	REFERENCES	145
5	COLLIMATION SYSTEM	149
5.1	LHC MULTI-STAGE COLLIMATION SYSTEM	149
5.1.1	<i>Motivation</i>	149
5.1.2	<i>Collimation system inherited from the LHC</i>	150
5.2	BASELINE AND OPTION UPGRADES TO THE LHC COLLIMATION SYSTEM	154
5.2.1	Upgrades for cleaning improvement	154
5.2.2	<i>Upgrades for impedance improvement</i>	164
5.2.3	<i>Upgrades to the collimation of the incoming beam in the experimental IRs</i>	166
5.3	ADVANCED COLLIMATION CONCEPTS.....	168
5.3.1	<i>Halo diffusion control techniques</i>	168
5.3.2	<i>Crystal collimation</i>	172
5.3.3	<i>Improved optics scenarios for collimation insertions</i>	172
5.3.4	<i>Rotatory collimator design</i>	173
5.4	OTHER COLLIMATORS FROM THE PRESENT SYSTEM REQUIRED IN THE HL-LHC.....	173
5.4.1	<i>IR3 and IR7 primary collimators (target collimator primary and TCP with pick-up)</i>	173
5.4.2	<i>IR3 and IR7 secondary collimators (target collimator secondary graphite)</i>	174
5.4.3	<i>IR3 and IR7 active shower absorbers collimators (target collimator long absorber)</i>	174
5.4.4	<i>IR6 secondary collimators with pick-up (target collimator secondary with pick-up)</i>	175
5.4.5	<i>Passive absorbers in IR3 and IR7 (TCAPA, TCAPB, TCAPC, TCAPD)</i>	175
5.4.6	<i>Tertiary collimators with pick-up in the experimental regions (target collimator tertiary with pick-up)</i> .	176
5.4.7	<i>Physics debris collimators in the experimental regions (Target Collimators Long (TCL))</i>	176
5.5	REFERENCES	176
6A.	COLD POWERING OF THE SUPERCONDUCTING CIRCUITS.....	181
6A.1	OVERVIEW	181
6A.1.1	<i>Cold Powering Systems</i>	182
6A.1.2	<i>Superconducting Link basic design and R&D</i>	183
6A.2	COLD POWERING SYSTEM DESIGN	185
6A.2.1	<i>Cryostat for the superconducting link</i>	185
6A.3	INTERFACES TO THE SUPERCONDUCTING LINK.....	186
6A.3.1	<i>Electrical interface between the superconducting link and the current leads</i>	186
6A.3.2	<i>Cryogenic interface between the superconducting link and the current leads</i>	186
6A.3.3	<i>Control</i>	187
6A.4	INTERFACE TO THE LHC MACHINE	187
6A.4.1	<i>General</i>	187
6A.4.2	<i>Interface cryostat for the HL-LHC Insertions</i>	187
6A.4.3	<i>Interface cryostat for the Matching Sections</i>	188
6A.5	INTEGRATION OF THE COLD POWERING SYSTEMS AT LHC P1 AND P5.....	188
6A.6	REFERENCE.....	189
6B	POWER CONVERTERS FOR THE NEW SUPERCONDUCTING MAGNETS	191
6B.1	OVERVIEW	191
6B.2	SUPERCONDUCTING MAGNETS.....	191
6B.2.1	<i>Insertion region layout</i>	191
6B.2.2	<i>Integration and new civil engineering infrastructure</i>	192
6B.3	CIRCUIT LAYOUT	193
6B.3.1	<i>Inner Triplet circuit</i>	193
6B.3.2	<i>Inner Triplet orbit correctors</i>	195

6B.3.3	Inner Triplet high order correctors	195
6B.3.4	Separation dipole D1.....	196
6B.3.5	Recombination dipole D2	196
6B.3.6	D2 orbit correctors	197
6B.3.7	Individual powered quadrupole Q4, Q5 and Q6.....	197
6B.3.8	Q4, Q5 and Q6 orbit correctors	198
6B.4	POWER CONVERTERS	198
6B.4.1	Power converter lists	199
6B.4.2	Present LHC power converters	199
6B.4.3	R&D program	200
6B.5	POWER CONVERTER CONTROL AND PERFORMANCES	202
6B.5.1	Impact on the beam quality – Requirements from beam physics	202
6B.5.2	Control electronics: FGC4	204
6B.5.3	High precision measurement and regulation	206
6B.6	OTHERS PERFORMANCE IMPROVEMENTS	209
6B.6.1	Radiation-tolerant power converters	209
6B.6.2	Power converters and LHC machine availability	210
6B.7	REFERENCES	210
7	MACHINE PROTECTION, INTERLOCKS AND AVAILABILITY	213
7.1	MACHINE PROTECTION WITH A 700 MJ BEAM	213
7.2	PROTECTION AGAINST UNCONTROLLED BEAM LOSSES	214
7.2.1	Beam interlock system.....	217
7.2.2	Fast magnet current change monitor.....	217
7.3	MAGNET POWERING PROTECTION	218
7.3.1	Circuit layout and protection concept of the new HL-LHC triplet circuits in IP1 and IP5	219
7.3.2	Quench detection system (QDS)	222
7.3.3	CLIQ	224
7.3.4	Energy extraction system	225
7.3.5	Powering interlock system.....	226
7.4	AVAILABILITY REQUIREMENTS TO ACHIEVE HL-LHC GOALS FOR INTEGRATED LUMINOSITY.....	226
7.5	REFERENCES	229
8	INTERFACE WITH EXPERIMENTS	231
8.1	INTRODUCTION.....	231
8.2	BEAM DESIGN	233
8.3	BEAM OPERATIONS	233
8.4	EQUIPMENT.....	234
8.4.1	The experimental beam pipes.....	234
8.5	THE PASSIVE FORWARD ABSORBERS	236
8.5.1	The charged particle passive absorber - TAXS	237
8.5.2	The neutral particle passive absorber – TAXN	247
8.6	REFERENCES	251
9	CRYOGENICS FOR THE HL-LHC	253
9.1	INTRODUCTION.....	253
9.2	LHC MACHINE UPGRADES.....	254
9.2.1	Upgraded beam parameters and constraints.....	254
9.3	TEMPERATURE LEVEL AND HEAT LOADS	255
9.4	IMPACT ON EXISTING SECTOR CRYOGENIC PLANTS	257
9.5	NEW CRYOGENICS FOR POINT 4 INSERTION	258

9.6	NEW CRYOGENICS FOR HIGH LUMINOSITY INSERTIONS AT POINT 1 AND POINT 5	259
9.7	BUILDING AND GENERAL SERVICE REQUIREMENT	260
9.8	CONCLUSIONS	261
9.9	REFERENCES	261
10	ENERGY DEPOSITION AND RADIATION TO ELECTRONICS	263
10.1	CHARACTERIZATION OF THE RADIATION SOURCE	263
10.2	POWER AND DOSE EVALUATIONS CONCERNING THE TRIPLET-D1 REGION	264
10.2.1	<i>FLUKA–MARS modeling</i>	264
10.2.2	<i>Operational radiation loads</i>	266
10.2.3	<i>Lifetime radiation loads</i>	266
10.3	UPDATE TO HL-LHCv1.2	268
10.4	IMPACT ON THE MATCHING SECTION AND PROTECTION STRATEGY	271
10.5	EXPOSURE OF THE SUPERCONDUCTING LINKS	274
10.6	RADIATION TO ELECTRONICS	275
10.7	REFERENCES	280
11	11 T DIPOLE AND NEW CONNECTION CRYOSTAT FOR THE DISPERSION SUPPRESSOR COLLIMATORS	283
11.1	INTRODUCTION	283
11.2	THE 11 T DIPOLE FULL ASSEMBLY	283
11.2.1	<i>Description</i>	283
11.2.2	<i>Equipment parameters</i>	285
11.3	THE 11 T DIPOLE	285
11.3.1	<i>Description</i>	287
11.3.2	<i>Instrumentation</i>	289
11.3.3	<i>Equipment parameters</i>	291
11.3.4	<i>Quench performance</i>	294
11.3.5	<i>Protection</i>	299
11.3.6	<i>Powering</i>	299
11.3.7	<i>Radiation</i>	304
11.3.8	<i>Installation and dismantling</i>	305
11.3.9	<i>Cryogenics</i>	305
11.4	CONNECTION CRYOSTATS FOR INTEGRATION OF DISPERSION SUPPRESSOR COLLIMATORS IN IR2	305
11.4.1	<i>Description</i>	306
11.4.2	<i>Equipment parameters</i>	307
11.4.3	<i>Installation and dismantling</i>	307
11.5	INVENTORY OF UNITS TO BE INSTALLED AND SPARE POLICY	308
11.6	QUALITY ASSURANCE	308
11.7	REFERENCES	308
12	VACUUM SYSTEM	311
12.1	OVERVIEW	311
12.2	BEAM VACUUM REQUIREMENTS	311
12.3	VACUUM LAYOUT REQUIREMENTS	312
12.3.1	<i>Room temperature vacuum system requirements</i>	313
12.3.2	<i>Cryogenic temperature beam vacuum system requirements</i>	314
12.4	INSULATION VACUUM REQUIREMENTS	314
12.5	EXPERIMENTAL VACUUM SYSTEM REQUIREMENTS	315
12.5.1	<i>High luminosity experiments: ATLAS and CMS</i>	316
12.5.2	<i>ALICE and LHCb experiments</i>	317
12.6	BEAM SCREEN REQUIREMENTS	318

12.6.1	<i>Shielded beam screen</i>	320
12.6.2	<i>Non-shielded beam screen</i>	323
12.6.3	<i>Vacuum beam line interconnection</i>	324
12.7	REFERENCES	324
13	BEAM INSTRUMENTATION AND LONG-RANGE BEAM-BEAM COMPENSATION	327
13.1	INTRODUCTION.....	327
13.2	BEAM LOSS MEASUREMENT	327
13.2.1	<i>Beam loss monitors for the HL-LHC triplet magnets</i>	328
13.2.2	<i>A radiation-tolerant application-specific integrated circuit for the HL-LHC beam loss monitoring system</i> 329	
13.3	BEAM POSITION MONITORING	330
13.3.1	<i>Current performance and limitations</i>	330
13.3.2	<i>A high resolution orbit measurement system for the HL-LHC</i>	331
13.3.3	<i>High directivity strip-line pick-ups for the HL-LHC insertion regions</i>	332
13.3.4	<i>Button Electrode Beam Position Monitors for the HL-LHC insertion regions</i>	332
13.3.5	<i>Collimator beam position monitors</i>	333
13.4	BEAM PROFILE MEASUREMENTS.....	333
13.4.1	<i>A beam gas vertex profile monitor (BGV)</i>	333
13.4.2	<i>Gas Jet Monitoring</i>	334
13.5	DIAGNOSTICS FOR CRAB CAVITIES	335
13.5.1	<i>Bunch shape monitoring using electromagnetic pick-ups</i>	336
13.5.2	<i>Bunch shape monitoring using streak cameras</i>	336
13.6	HALO DIAGNOSTICS	337
13.7	LUMINOSITY MEASUREMENT	338
13.8	LONG-RANGE BEAM-BEAM COMPENSATION	338
13.8.1	<i>Long-range beam-beam demonstrator</i>	339
13.9	REFERENCES	340
14	INJECTION AND DUMPING SYSTEMS	343
14.1	INJECTION AND DUMPING SYSTEMS OVERVIEW.....	343
14.2	INJECTION SYSTEMS.....	343
14.2.1	<i>Upgrade of the primary injection absorbers (TDIS)</i>	344
14.2.1	<i>Supplementary shielding of D1 coils</i>	345
14.2.2	<i>Injection protection devices retained from the LHC</i>	346
14.2.3	<i>Injection kicker magnet (MKI)</i>	347
14.3	BEAM DUMPING SYSTEM	349
14.3.1	<i>Beam dump (TDE)</i>	349
14.3.2	<i>Beam dumping system absorbers (TCDQ and TCDS)</i>	350
14.3.3	<i>Extraction kicker generator and control system</i>	352
14.4	REFERENCES	353
15	INTEGRATION, (DE-)INSTALLATION AND ALIGNMENT	355
15.1	GEOGRAPHICAL DISTRIBUTION OF HL-LHC UPGRADE INTERVENTIONS	355
15.2	POINT 4.....	355
15.2.1	<i>Cryogenic system upgrade</i>	355
15.2.2	<i>New beam line elements</i>	356
15.3	POINT 6.....	357
15.4	POINT 7	357
15.5	POINT 2.....	358
15.6	POINT 1 AND POINT 5	358

15.6.1	<i>LHC machine tunnel</i>	358
15.6.2	<i>Existing LHC tunnel service areas</i>	359
15.6.3	<i>New HL-LHC tunnel service areas</i>	359
15.6.4	<i>New surface installation</i>	363
15.6.5	<i>Activity sequence considerations</i>	365
15.7	ALIGNMENT AND INTERNAL METROLOGY	365
15.7.1	<i>General objectives, requirements and constraints</i>	365
15.7.2	<i>Internal metrology</i>	367
15.7.3	<i>Monitoring of cold mass and crab cavities</i>	367
15.7.4	<i>Standard alignment</i>	369
15.7.5	<i>Alignment sensors and actuators</i>	369
15.8	REFERENCES	371
16	OPERATION, COMMISSIONING AND IT STRING	373
16.1	OPERATION DEFINITIONS AND PARAMETERS	373
16.1.1	<i>The nominal cycle</i>	373
16.1.2	<i>Availability and operational efficiency</i>	375
16.1.3	<i>Discussion</i>	377
16.2	HARDWARE COMMISSIONING	378
16.2.1	<i>Commissioning of the superconducting circuits</i>	378
16.2.2	<i>Hardware commissioning of the HL collimation system</i>	380
16.2.3	<i>Commissioning of the cryogenic systems</i>	381
16.2.4	<i>Commissioning of the crab cavities</i>	381
16.3	COMMISSIONING WITH BEAM	382
16.4	OPERATION WITH HEAVY IONS	383
16.4.1	<i>Pb–Pb operation</i>	383
16.4.2	<i>p–Pb operation</i>	384
16.4.3	<i>Other species</i>	384
16.5	HL-LHC IT STRING	385
16.5.1	<i>Introduction and goal of the HL-LHC IT String</i>	385
16.5.2	<i>Description of the IT String</i>	385
16.5.3	<i>Location of the IT String test stand</i>	386
16.5.4	<i>Time scale of the IT String test stand</i>	386
16.5.5	<i>Technical infrastructure for the IT String test stand</i>	387
16.5.6	<i>Preliminary Test program for the IT String</i>	390
16.6	REFERENCES	392
17	THE HL-LHC TECHNICAL INFRASTRUCTURE	393
17.1	CIVIL ENGINEERING	393
17.1.1	<i>Introduction</i>	393
17.1.2	<i>Underground Works</i>	394
17.1.3	<i>Surface Works</i>	396
17.1.4	<i>Requirements and constraints</i>	400
17.2	ELECTRICITY	403
17.2.1	<i>Introduction</i>	403
17.2.2	<i>Requirements and constraints</i>	403
17.2.3	<i>Technical description of the work</i>	405
17.3	COOLING	424
17.3.1	<i>General statements for CV installations</i>	424
17.3.2	<i>Primary water cooling</i>	424
17.3.3	<i>UW secondary water cooling</i>	424

17.3.4	<i>Chilled and cold water</i>	425
17.3.5	<i>Firefighting network</i>	425
17.3.6	<i>Compressed air</i>	425
17.3.7	<i>Clean and waste water</i>	425
17.3.8	<i>Underground air handling units</i>	425
17.3.9	<i>Fresh air distribution</i>	427
17.3.10	<i>Pressurization of staircase and lift shaft</i>	427
17.3.11	<i>HVAC for surface buildings</i>	427
17.3.12	<i>Smoke extraction</i>	429
17.4	ACCESS & ALARM SYSTEMS.....	429
17.4.1	<i>Introduction</i>	429
17.4.2	<i>Requirements and constraints</i>	429
17.4.3	<i>Technical description of the work</i>	430
17.5	MONITORING AND OPERATION OF GENERAL SERVICES.....	434
17.5.1	<i>Introduction</i>	434
17.5.2	<i>Technical description of the work</i>	435
17.6	TRANSPORT.....	435
17.6.1	<i>Introduction</i>	435
17.6.2	<i>Requirements and constraints</i>	436
17.6.3	<i>Technical description of the work</i>	436
17.7	LOGISTICS AND STORAGE.....	442
17.7.1	<i>Introduction</i>	442
17.7.2	<i>Requirements and constraints</i>	442
17.7.3	<i>Technical description of the work</i>	442
17.8	REFERENCES.....	443
18	CONTROLS	445
18.1	INTRODUCTION.....	445
18.2	CONTROL AREAS REQUIRING NEW DEVELOPMENTS FOR THE HL-LHC ERA.....	445
18.2.1	<i>Data Logging</i>	445
18.2.2	<i>New Distributed I/O Tier</i>	446
18.2.3	<i>A new High-speed Radiation-tolerant Fieldbus</i>	447
19	SAFETY	449
19.1	RADIATION PROTECTION.....	449
19.1.1	<i>Design constraints</i>	449
19.1.2	<i>The As Low As Reasonably Achievable (ALARA) principle</i>	449
19.1.3	<i>The FLUKA Monte Carlo code for radiation protection studies</i>	449
19.1.4	<i>Residual dose rate predictions for the Long Straight Sections in Point 1 and 5</i>	450
19.1.5	<i>Radiological risk assessments for the new underground infrastructures in Point 1 and 5</i>	453
19.2	GENERAL SAFETY.....	458
19.2.1	<i>Introduction</i>	458
19.2.2	<i>Project Safety at CERN</i>	458
19.2.3	<i>Safety File</i>	459
19.2.4	<i>Conformity with Safety Standards</i>	459
19.2.5	<i>HL-LHC Workplace Safety</i>	460
19.2.6	<i>An example - Superconducting magnets</i>	461
19.3	REFERENCES.....	462
A.	LIST OF MACHINE AND BEAM PARAMETERS	465
A.1.	MAIN MACHINE PARAMETERS.....	465

A.2.	PROTON BEAM PARAMETERS IN COLLISION	467
A.3.	PROTON BEAM PARAMETERS AT LHC INJECTION (AFTER CAPTURE)	468
A.4.	REQUIRED PROTON BEAM PARAMETERS AT SPS EXTRACTION	468
A.5.	ION BEAM PARAMETERS IN COLLISION	469
A.6.	MAIN INSERTION REGION MAGNET PARAMETERS.....	469
A.7.	FIELD ERROR TARGET FOR THE NEW INSERTION REGION MAGNETS.....	471
A.8.	REFERENCES	475
B.	CIRCUIT LAYOUT AND POWERING	479
B.1	HL-LHC CIRCUITS UPGRADE.....	479
B.2	INNER TRIplet AND TRIMS.....	480
B.3	TRIPLET ORBIT CORRECTORS	481
B.4	INNER TRIplet HIGH ORDER CORRECTORS	481
B.5	SEPERATION DIPOLE D1.....	482
B.6	RECOMBINATION DIPOLE D2	483
B.7	D2 ORBIT CORRECTORS	483
B.8	INDIVIDUALLY POWERED QUADRUPOLES Q4, Q5 AND Q6	484
B.9	Q4, Q5 AND Q6 ORBIT CORRECTORS.....	484
B.10	11T	485
C.	VOLTAGE WITHSTAND LEVELS.....	486
D.	HL-LHC ACRONYMS	489
E.	GLOSSARY AND DEFINITIONS	497
INDEX	511

Table of figures

FIGURE 1-1: LHC BASELINE PLAN FOR THE NEXT DECADE AND BEYOND SHOWING THE ENERGY OF THE COLLISIONS (UPPER RED LINE) AND LUMINOSITY (LOWER GREEN LINES). THE FIRST LONG SHUTDOWN (LS1) IN 2013–2014 SHOULD ALLOW THE DESIGN PARAMETERS OF BEAM ENERGY AND LUMINOSITY TO BE REACHED. THE SECOND LONG SHUTDOWN (LS2), 2019–2020, WILL CONSOLIDATE LUMINOSITY PRODUCTION AND RELIABILITY AS WELL AS UPGRADE THE LHC INJECTORS. AFTER LS3, 2024–2026, THE MACHINE WILL BE IN THE HIGH LUMINOSITY CONFIGURATION (HL-LHC).....	2
FIGURE 1-2: LHC LUMINOSITY PLAN UNTIL LS3 : BOTH PEAK (RED DOTS) AND INTEGRATED (BLUE LINE) LUMINOSITIES ARE INDICATED. MAIN SHUTDOWN PERIODS ARE ALSO SHOWN.....	3
FIGURE 1-3: (A) LUMINOSITY PROFILE FOR A SINGLE LONG FILL: STARTING AT NOMINAL PEAK LUMINOSITY (BLACK LINE), WITH UPGRADE AND WITHOUT LEVELLING (RED LINE), WITH LEVELLING (BLUE LINE). (B) LUMINOSITY PROFILE WITH OPTIMIZED RUN TIME, WITHOUT AND WITH LEVELLING (BLUE AND RED DASHED LINES), AND AVERAGE LUMINOSITY IN BOTH CASES (SOLID LINES).	7
FIGURE 1-4: LUMINOSITY CYCLE FOR HL-LHC WITH LEVELLING AND A SHORT DECAY (OPTIMIZED FOR INTEGRATED LUMINOSITY).	7
FIGURE 1-5: BEHAVIOUR OF GEOMETRICAL LUMINOSITY REDUCTION FACTOR VS. β^* FOR A CONSTANT NORMALIZED BEAM SEPARATION WITH THE INDICATION OF TWO OPERATIONAL POINTS: NOMINAL LHC AND HL-LHC WITH NO CRAB CAVITIES (CC). THE INSERT ILLUSTRATES THE BUNCH CROSSING OVERLAP REDUCTION EFFECT.	10
FIGURE 1-6: GEOMETRICAL REDUCTION FACTOR R VS β^* SHOWING THE INCREASED PERFORMANCE IN HL-LHC DUE TO CRAB CAVITIES (CC), BOTH IN THE PREVIOUS CONFIGURATION (FULL CC, SCALED TO β^* OF 20 CM) AND THE PRESENT ONE (HALF CC). THE CRAB CAVITY BEAM MANIPULATION IS DEPICTED THE PICTURE AT RIGHT (THE SMALL ARROWS INDICATE THE TORQUE ON THE BUNCH GENERATED BY THE TRANSVERSE RF FIELD).	10
FIGURE 1-7: FORECAST FOR PEAK LUMINOSITY (RED DOTS) AND INTEGRATED LUMINOSITY (BLUE LINE) IN THE HL-LHC ERA, ACCORDING TO THE NOMINAL HL-LHC PARAMETERS.	12
FIGURE 1-8: FORECAST FOR PEAK LUMINOSITY (RED DOTS) AND INTEGRATED LUMINOSITY (BLUE LINE) IN THE HL-LHC ERA, FOR THE CASE OF ULTIMATE HL-LHC PARAMETERS.	12
FIGURE 1-9: SCHEMATIC REPRESENTATION OF THE HL-LHC TIMELINE.	13
FIGURE 1-10: THE HL-LHC CONSTRUCTION PROJECT BUDGET ALLOCATION AS A FUNCTION OF TIME OVER 2015–2026, AS PER CERN MEDIUM-TERM PLAN 2017-2021 WITH THE FULL CtC.	14
FIGURE 1-11: TIMELINE OF THE VARIOUS COLLABORATION BRANCHES, CONVERGING TOWARD THE LHC LUMINOSITY UPGRADE.....	15
FIGURE 1-12: (A) TOTAL ESTIMATION OF THE COST OF THE DESIGN STUDY, SUBDIVIDED BY THE US AND JAPAN, EU INSTITUTES AND CERN. (B) TOTAL COST WITH THE US AND JAPAN REMOVED (I.E. ONLY COSTS THAT ARE ELIGIBLE FOR FUNDING BY THE EC). (C) EFFECT OF CERN WAIVING THE COST FOR TECHNICAL WORKS (RECOGNIZING THAT THE HL-LHC IS PART OF THE CORE CERN PROGRAMME FINANCED VIA THE NORMAL BUDGET), WHILE KEEPING THE EXTRA COST GENERATED BY THE MANAGEMENT AND COORDINATION OF THE PROJECT. THIS IS THE TOTAL COST DECLARED TO THE EC. (D) COST CLAIMED FROM THE EC: 50% OF THE DECLARED COST (ELIGIBLE COST REDUCED BY CERN WAIVING ACTION).	16
FIGURE 1-13: (A) TABLE SHOWING THE 15 MEMBERS ('BENEFICIARIES') OF THE FP7 HiLUMI LHC DESIGN STUDY AND (B) THE FIVE LARP LABORATORIES THAT ARE ASSOCIATED WITH THE PROJECT.	17
FIGURE 1-14: LEFT: IMPROVEMENT IN J_c (CURRENT DENSITY) IN Nb ₃ Sn SUPERCONDUCTOR DURING THE LAST THREE DECADES COMPARED WITH Nb-Ti J_c PERFORMANCE.	18
FIGURE 1-15: (LEFT) QUENCH PERFORMANCE OF THE LONG QUADRUPOLE (LQ), THE FIRST QUADRUPOLE DEMONSTRATING THE SCALE-UP OF Nb ₃ Sn TECHNOLOGY TO LENGTHS OF INTEREST FOR LHC APPLICATIONS (~3 M), (RIGHT) QUENCH PERFORMANCE OF MQXFS1 (150 MM APERTURE) DURING THE FIRST COLD TEST IN FEBRUARY 2016, SHOWING GOOD QUENCH PERFORMANCE AND MEMORY AFTER WARM-UP AND COOL-DOWN CYCLES.	18
FIGURE 1-16: THE GENERAL GOVERNANCE SCHEME OF FP-7 HiLUMI LHC, USED FOR THE WHOLE HL-LHC PROJECT.....	22
FIGURE 1-17: HL-LHC PROJECT STRUCTURE, WITH FP7 PART INDICATED IN DARK GREEN. THE ORANGE BOX REFERS TO THE HIGH-FIELD MAGNETS WORK PACKAGE, WHICH WAS STARTED BEFORE THE HL-LHC IN THE FRAMEWORK OF GENERIC R&D FOR THE LHC UPGRADE.....	22
FIGURE 1-18. THE HL-LHC ORGANIZATION IN THE GLOBAL CERN ACCELERATOR & TECHNOLOGY SECTOR STRUCTURE FOR THE CONSTRUCTION PHASE.	23
FIGURE 2-1: (A) EXPECTED ANNUAL INTEGRATED LUMINOSITY; (B) OPTIMUM FILL LENGTH AS A FUNCTION OF THE 'VIRTUAL' PEAK LUMINOSITY FOR THREE DIFFERENT VALUES OF THE LUMINOSITY AT WHICH LEVELLING IS PERFORMED. A CIRCULATING CURRENT OF 1.1 A	

(CORRESPONDING TO $N_{\text{BEAM}} = 6.1 \times 10^{14}$ p), A MINIMUM TURNAROUND TIME OF 3 HOURS AND A PERFORMANCE EFFICIENCY η OF 50% HAVE BEEN ASSUMED. ONLY BURN-OFF FOR A TOTAL HADRON CROSS-SECTION OF 111 MB HAS BEEN CONSIDERED FOR THE ESTIMATE OF THE BEAM POPULATION AND VIRTUAL LUMINOSITY EVOLUTION. TWO HIGH-LUMINOSITY INTERACTION POINTS HAVE BEEN ASSUMED... 26

FIGURE 2-2: PARAMETER $R\Sigma_z/B^*$ VS. B^* FOR DIFFERENT BUNCH LENGTHS FOR A ROUND OPTICS AND CONSTANT NORMALIZED LONG-RANGE BEAM-BEAM SEPARATION D_{BB} (A) WITHOUT CRAB CAVITIES AND (B) WITH CRAB CAVITIES. THE SMALL EFFECT OF RF CURVATURE IN THE CRAB CAVITIES IS NOT INCLUDED. 28

FIGURE 2-3: OVERALL LAYOUT OF THE INSERTION REGION BETWEEN THE IP AND Q4. THE DARK BLUE AND RED AREAS REPRESENT THE 2σ BEAM ENVELOPE FOR THE $B^*=20$ CM ROUND OPTICS. THE LIGHT REGIONS CORRESPOND TO A 12σ VALUE OF THE BEAM ENVELOPE FOR A NORMALIZED EMITTANCE OF 3.5 MM WITH A TOLERANCE OF 20% FOR BETA-BEATING, 2 MM OF RADIAL CLOSED ORBIT DISTORTION [67] AND ± 2 MM TO ALLOW IP TRANSVERSE POSITION ADJUSTMENTS BASED ON RUN 1 AND RUN 2 OPERATIONAL EXPERIENCE. THE SHADED GREY AREAS IN THE TRIPLET REGION REPRESENT THE LOCATIONS OF THE PARASITIC BEAM-BEAM ENCOUNTERS IN WHICH THE BPM (IN BLUE) SHOULD NOT BE INSTALLED. ADDITIONAL APERTURE MARGINS ARE NEEDED IN THE MATCHING SECTION TO BE COMPATIBLE WITH FLAT OPTICS OPERATIONS. 37

FIGURE 2-4: OPTICAL FUNCTIONS AT INJECTION (UPPER - $B^*=6$ M), COLLISION (MIDDLE - $B^*=0.2$ M) AND FOR THE CONFIGURATION REQUIRED FOR VAN DER MEER SCANS (LOWER - $B^*=30$ M) WITH NOMINAL ROUND OPTICS IN IR1 AND IR5 FOR BEAM 1. 41

FIGURE 2-5: POSSIBLE LAYOUTS FOR THE IT POWERING. 42

FIGURE 2-6: MAXIMUM TUNE-RIPPLE AMPLITUDE, RESULTING FROM NOISE ON POWER CONVERTERS AT TYPICAL FREQUENCIES (SEE TABLE 2-9) THE YELLOW CURVE REPRESENTS THE MAXIMUM TUNE-RIPPLE AMPLITUDE, INCLUDING THE WHOLE FREQUENCY SPECTRUM, COMPATIBLE WITH A NEGLIGIBLE IMPACT ON DA (THE POWER CONVERTER NOISE SPECTRUM HAS BEEN ASSUMED TO SCALE LINEARLY WITH RESPECT TO THAT DESCRIBED IN TABLE 2-9). IN CASE OF TUNE RIPPLE AT A SINGLE FREQUENCY, THE MAXIMUM TOLERABLE AMPLITUDE IS REPRESENTED BY THE BLUE BARS (THE HORIZONTAL SIZE IS ONLY FOR BETTER VISIBILITY). THE IMPACT ON DA HAS BEEN EVALUATED BY TAKING THE WORST CASE AMONG SEVERAL CONFIGURATIONS INCLUDING BEAM-BEAM AND CRAB CROSSING. THE DA SIMULATIONS HAVE BEEN PERFORMED FOR SLHCV3.1B AND ROUND COLLISION OPTICS ($B^*=0.15$ M). FOR THE SAKE OF COMPARISON, THE AMPLITUDE OF THE RIPPLE FOR DIFFERENT POWERING SCENARIOS IS ALSO SHOWN USING, HOWEVER, THE HLLHCV1.1 LAYOUT AND ROUND COLLISION OPTICS WITH $B^*=0.15$ M. IN THE VOLTAGE CONTROL REGIME ALL RIPPLE FREQUENCIES ARE IN PHASE, WHILE IN THE CURRENT CONTROL REGIME THE TUNE MODULATION IS RANDOM AND THE MAXIMUM TUNE-RIPPLE AMPLITUDE IS SHOWN IN THIS CASE [93-95]. 44

FIGURE 2-7: BEAM 1 DA AS A FUNCTION OF HORIZONTAL AND VERTICAL IP1-5 PHASE ADVANCE AT INJECTION ENERGY. BOTH THE MINIMUM (LEFT) AND THE AVERAGE VALUE (RIGHT) ARE GIVEN. 47

FIGURE 2-8: DA AT INJECTION AND COLLISION FOR BEAM 1 AND BEAM 2. THE DIFFERENT FAMILIES OF HL-LHC MAGNETS ARE INCLUDED ONE BY ONE IN THE SIMULATIONS. THE MARKERS REFER TO THE AVERAGE DA OVER SEEDS AND PHASE SPACE ANGLES, WHILE THE ERROR BARS REPRESENT THE DA DISTRIBUTION FOR THE VARIOUS SEEDS. 48

FIGURE 2-9: DA FOR BEAM 1 IN COLLISION (ROUND OPTICS) FOR VARIOUS CONFIGURATIONS OF THE MCBXF FIELD QUALITY. 49

FIGURE 2-10: DEPENDENCE OF THE BEAM 1 DYNAMIC APERTURE ON B^* DURING THE ATS SQUEEZE. THE MARKERS REFER TO THE AVERAGE DA, WHILE THE ERROR BARS REFER TO THE MINIMUM AND MAXIMUM DA OVER THE SEEDS. FLAT OPTICS CONFIGURATIONS HAVE ALSO BEEN CONSIDERED. 50

FIGURE 2-11: DEPENDENCE OF THE BEAM 1 DYNAMIC APERTURE ON LINEAR CHROMATICITY AT THE END OF THE ATS SQUEEZE. FLAT OPTICS CONFIGURATIONS HAVE ALSO BEEN CONSIDERED. 50

FIGURE 2-12: BEAM 1 DA AS A FUNCTION OF HORIZONTAL AND VERTICAL IP1-5 PHASE ADVANCE AT COLLISION ENERGY FOR ROUND OPTICS. BOTH THE MINIMUM (LEFT) AND THE AVERAGE VALUE (RIGHT) ARE GIVEN. 51

FIGURE 2-13: OVERVIEW OF SINGLE-BUNCH MEASUREMENTS OF THE INSTABILITY THRESHOLD (IN LANDAU OCTUPOLES CURRENT VS. CHROMATICITY) PERFORMED IN 2015, PLOTTED ALONGSIDE DELPHI [132] PREDICTIONS FOR DIFFERENT DAMPING TIMES. NOT SHOWN ARE THREE TRUNCATED POINTS FOR $Q' \approx 0$ THAT ARE SLIGHTLY BELOW 800A (SEE DISCUSSION BELOW). FT STANDS FOR FLAT TOP AND EOS STANDS FOR END OF SQUEEZE. 52

FIGURE 2-14: CONTRIBUTIONS TO THE REAL (LEFT) AND IMAGINARY (RIGHT) PARTS OF THE (UPPER) HORIZONTAL DIPOLAR, AND (LOWER) LONGITUDINAL IMPEDANCES IN HL-LHC FOR BEAM 1 WITHOUT CONSIDERING THE CRAB CAVITIES (FOR THE CASE OF $\beta^* = 15$ CM). THE VERTICAL DIPOLAR IMPEDANCE IS VERY SIMILAR TO THE HORIZONTAL ONE. A SIMILAR RESULT IS OBTAINED FOR BEAM 2. 53

FIGURE 2-15: RELATIVE VARIATION OF THE REAL (CONTINUOUS LINE) AND IMAGINARY (DASHED LINE) VERTICAL DIPOLAR IMPEDANCE BY REPLACING THE SECONDARY (TCSG) CFC COLLIMATORS WITH MO-COATED ($5 \mu\text{m}$) MO-GR COLLIMATORS IN LSS7 ONLY (BLUE) OR IN BOTH LSS7 AND LSS3 (BLACK). 54

FIGURE 2-16: STABILITY LIMITS OBTAINED BY SCALING FROM 2012 DATA (WITHOUT CRAB CAVITIES) FOR A CHROMATICITY Q' OF +15 UNITS, FOR A DAMPING TIME OF THE TRANSVERSE DAMPER OF 50 TURNS AND FOR THE MAXIMUM CURRENT OF THE LANDAU OCTUPOLES (USING

THE NEGATIVE POLARITY, I.E. -570 A). THE NUMBER OF PROTONS PER BUNCH IS PLOTTED IN THE VERTICAL AXIS, WHILE THE TRANSVERSE R.M.S. NORMALIZED EMITTANCE IS PLOTTED IN THE HORIZONTAL ONE. STABILITY IS ACHIEVED FOR THE BUNCH PARAMETERS FOR WHICH THE CORRESPONDING POINTS LIE BELOW THE PLOTTED CURVES.	54
FIGURE 2-17: REQUIRED ADDITIONAL CURRENT IN THE LANDAU OCTUPOLES TO DAMP (LEFT) THE SINGLE-BUNCH AND (RIGHT) MULTI-BUNCH INSTABILITIES. THIS PARTICULAR STUDY WAS PERFORMED FOR A CHROMATICITY OF + 5 UNITS, FOR A β^* OF 15 CM AND FOR A SINGLE CRAB CAVITY. THE EFFECT OF AN IDEAL TRANSVERSE DAMPER IS ALSO INCLUDED WITH A DAMPING TIME OF 50 TURNS.	55
FIGURE 2-18: OPTIMIZATION OF THE WORKING POINT AT INJECTION TO ACCOMMODATE THE LARGE TUNE SPREAD CREATED BY THE HIGH CHROMATICITY AND LANDAU OCTUPOLE VALUES NEEDED TO STABILIZE THE BEAM AGAINST ELECTRON CLOUD.	56
FIGURE 2-19: COMPARISON BETWEEN LONGITUDINAL INSTABILITY MEASUREMENTS AND PREDICTIONS OF THE LOSS OF LONGITUDINAL LANDAU DAMPING.	57
FIGURE 2-20: EVOLUTION OF THE STABILITY DIAGRAM IN THE PRESENCE OF LANDAU OCTUPOLES AND BEAM-BEAM LONG-RANGE AS A FUNCTION OF β^* (IN MM) DURING THE BETATRON SQUEEZE. THE CURVE « NEGATIVE LOF » (BELOW THE CURVE CORRESPONDING TO $\beta^* = 6$ M) REFERS TO THE STABILITY DIAGRAM WITH LANDAU OCTUPOLES ONLY (NEGATIVE CURRENT OF -570 A IN THE FOCUSING OCTUPOLES). THE MAXIMUM REDUCTION OF THE STABILITY DIAGRAM AT $\beta^* \sim 40$ CM (LEFT) CAN BE COMPENSATED BY 8% LARGER β FUNCTION IN THE LANDAU OCTUPOLES IN THE ARCS (RIGHT).	58
FIGURE 2-21: (LEFT) ESTIMATED ELECTRON CLOUD DENSITY IN THE DIPOLES AND QUADRUPOLES AS A FUNCTION OF SEY AND (RIGHT) ASSOCIATED TUNE FOOTPRINT AT THE END OF THE SCRUBBING (ASSUMING SEY CLOSE TO 1.3, SEE CROSS IN THE LEFT PLOT) STARTING FROM AN INITIAL UNIFORM ELECTRON CLOUD DISTRIBUTION.	59
FIGURE 2-22: MINIMUM DA DURING LUMINOSITY LEVELLING SIMULATED FOR THE BASELINE SCENARIO (ROUND OPTICS, CONSTANT CROSSING ANGLE 590 MRAD, FULL CROSSING ANGLE COMPENSATION BY CRAB CAVITIES) AS A FUNCTION OF THE BETA-FUNCTION AT THE IP, SIMULATED WITH SIXTRACK BEAM-BEAM CODE. DASHED HORIZONTAL LINE DEPICTS THE TARGET MINIMUM DA OF 6σ . SOLID LINES SHOW THE RESULTS FOR MACHINE WITH NO MULTIPOLE ERRORS, DASHED LINES – WITH MULTIPOLE ERRORS. DIAMONDS INDICATE THE EFFECT OF COLLISIONS AT IP2 AND 8 ACCORDING TO THE HL-LHC OPERATIONAL SCENARIOS DESCRIBED IN [136]. THE STUDIES WERE PERFORMED WITH HL-LHC OPTICS V1.0.	61
FIGURE 2-23: SIMULATED HEAT LOAD FROM ELECTRON CLOUD IN THE ARC MAIN MAGNETS AS A FUNCTION OF BUNCH INTENSITY AND SEY. .	64
FIGURE 2-24: HEAT LOAD MEASURED IN THE LHC ARCS DURING A PHYSICS FILL WITH BEAMS CONSISTING OF 2040 BUNCHES DISTRIBUTED IN TRAINS OF 72 BUNCHES IN 2016. THE HEAT LOAD VALUES ARE IN WATTS PER HALF-CELL. THE DASHED LINE SHOWS THE HEAT LOAD EXPECTED FROM IMPEDANCE AND SYNCHROTRON RADIATION.	65
FIGURE 2-25: SIMULATED HEAT LOAD FROM THE ELECTRON CLOUD ALONG THE TRIPLET AND D1 MAGNET ASSEMBLIES WITH HL-LHC BEAM PARAMETERS. THE VERTICAL DASHED LINES INDICATE THE LOCATIONS OF THE LONG-RANGE ENCOUNTERS.	66
FIGURE 2-26: SIMULATED TOTAL HEAT LOAD FROM THE ELECTRON CLOUD FOR THE TRIPLET AND D1 MAGNET ASSEMBLIES WITH HL-LHC BEAM PARAMETERS.	66
FIGURE 2-27: SIMULATED TOTAL HEAT LOAD ON THE BEAM SCREEN OF THE TWIN-BORE COLD MAGNETS FOR ALL THE IRs. BOTH IMPEDANCE AND E-CLOUD EFFECTS ARE INCLUDED.	67
FIGURE 2-28: EVOLUTION OF THE MAIN MACHINE AND BEAM PARAMETERS THE NOMINAL SCENARIO.	68
FIGURE 2-29: EVOLUTION OF THE MAIN PARAMETERS FOR TWO SCENARIOS: BASELINE (ROUND OPTICS) WITH $\beta^*=20$ CM (RED) AND FLAT OPTICS ($\beta^*=40$ CM/15 CM BLUE) WITH THE CRAB CAVITY VOLTAGE OF 6.8 MV PER IP SIDE AND PER BEAM.	70
FIGURE 2-30: PERFORMANCE COMPARISON OF THE HL-LHC BASELINE (RED) TO THE ALTERNATIVE 8B+4E FILLING SCHEME (BLUE). A REDUCTION ON THE INTEGRATED LUMINOSITY OF ABOUT 25% IS OBSERVED IN THE 8B+4E SCENARIO.	71
FIGURE 2-31: HEAT LOAD PER HALF-CELL AND PER APERTURE AT INJECTION INDUCED BY ELECTRON CLOUD IN DIPOLES VERSUS SEY FOR 4 DIFFERENT BUNCH LENGTHS: 7.5, 11.2, 15 AND 19 CM (CORRESPONDING TO A 4σ BUNCH DURATION OF 1, 1.5, 2 AND 2.5 NS). A VERY LOW HEAT LOAD IS ACHIEVED ALREADY FOR AN SEY OF 1.4 AND A BUNCH LENGTH 15 CM.	73
FIGURE 2-32: PERFORMANCE COMPARISON OF THE HL-LHC BASELINE (RED) TO THE ALTERNATIVE OF 200 MHz (BLUE) IN ORDER TO SUPPRESS THE ELECTRONS CLOUD EFFECTS. A BUNCH LENGTH OF 15 CM IS ASSUMED AT THE START OF THE FILL AND THEN REDUCED TO MAXIMIZE LUMINOSITY.	74
FIGURE 2-33: PERFORMANCE COMPARISON OF TWO ALTERNATIVES WITHOUT CRAB CAVITIES USING FLAT OPTICS WITH BEAM-BEAM LONG-RANGE COMPENSATION (BLUE) AND WITHOUT (RED).	75
FIGURE 2-34: SUMMARY CHART SHOWING PILE-UP (TOP) AND INTEGRATED LUMINOSITY PER YEAR (BOTTOM) VERSUS PEAK PILE-UP DENSITY FOR THE VARIOUS SCENARIOS CONSIDERED SECTION.	76
FIGURE 2-35: INITIAL LUMINOSITY FOR EACH COLLIDING BUNCH PAIR ALONG THE FULL TRAIN IN THE LHC.	78

FIGURE 2-36: (A) TOTAL LUMINOSITY (RED) AND INTEGRATED LUMINOSITY (BLUE) DURING A FILL STARTING WITH THE BUNCH-PAIR LUMINOSITIES SHOWN IN FIGURE 2-35. (B) AVERAGE LUMINOSITY PER DAY AS A FUNCTION OF TURNAROUND TIME (DUMP TO NEXT STABLE BEAMS) WHEN FILL LENGTHS ARE OPTIMIZED, WITH LENGTHS VARYING BETWEEN 3 H AND 6 H, WITH THE LUMINOSITY DEPENDENCE SHOWN IN THE LEFT PLOT.	78
FIGURE 3-1: SCHEMATIC LAYOUT OF THE IR REGION OF HL-LHC. THICK BOXES ARE MAGNETS, THIN BOXES ARE CRYOSTATS.	96
FIGURE 3-2: SCHEMATIC LAYOUT OF THE CURRENT IR REGION OF THE LHC. THICK BOXES ARE MAGNETS, THIN BOXES ARE CRYOSTATS.	96
FIGURE 3-3: BEAM SCREEN (GREY) WITH TUNGSTEN SHIELDING (DARK BROWN) AND COOLING TUBES IN Q1 (LEFTHAND SIDE) AND IN Q2-D1 (RIGHTHAND SIDE).	97
FIGURE 3-4: SKETCH OF TRIPLET QUADRUPOLE MAGNET CROSS-SECTION.	99
FIGURE 3-5: 200 MM SLICE OF MQXF USED TO TEST ASSEMBLY PROCEDURES AND VALIDATE MECHANICAL STRUCTURE.	100
FIGURE 3-6: QUENCH HEATERS FOR THE OUTER LAYER (LEFT); A DESIGN FOR THE INNER LAYER (RIGHT). STAINLESS STEEL (SS) IN GREY AND COPPER CLADDING IN RED. A ~300 MM LONG PORTION, OUT OF THE 4/7 M LONG STRIP, IS SHOWN.	101
FIGURE 3-7: CROSS-SECTION OF THE CRYOSTAT.	102
FIGURE 3-8: SKETCH OF ORBIT CORRECTOR CROSS-SECTION (SHORT VERSION MCBXFB, IN THE COLD MASS OF THE TRIPLET MAGNETS Q2A AND Q2B).	103
FIGURE 3-9: LAYOUT OF THE CORRECTOR REGION.	104
FIGURE 3-10: CROSS-SECTION OF THE SKEW QUADRUPOLE (LEFT, WITH OBSOLETE POSITION OF COOLING HOLES AT 90°) AND 3D VIEW OF A SEXTUPOLE (RIGHT).	104
FIGURE 3-11: SKETCH OF NONLINEAR CORRECTOR CROSS-SECTIONS OF (A) NORMAL SEXTUPOLE; (B) NORMAL OCTUPOLE; (C) NORMAL DECAPOLE; (D) NORMAL DODECAPOLE CORRECTORS.	104
FIGURE 3-12: SKETCH OF SEPARATION DIPOLE CROSS-SECTION (LEFT) AND YOKING TEST (RIGHT).	106
FIGURE 3-13: SKETCH OF RECOMBINATION DIPOLE CROSS-SECTION. ASYMMETRIC COIL (LEFT) AND MAGNET CROSS-SECTION (RIGHT). NOTE THE ELLIPTICAL SHAPE OF THE YOKE.	109
FIGURE 3-14: CROSS-SECTION OF D2 ORBIT CORRECTOR (LEFT) AND 3D VIEW OF THE SHORT MODEL COIL (RIGHT).	110
FIGURE 3-15: MQYY 90 MM APERTURE CROSS-SECTION.	110
FIGURE 3-16: BASELINE FOR TRIPLET POWERING.	111
FIGURE 3-17: SKETCH OF THE COOLING SYSTEM.	112
FIGURE 4-1: BUNCHES COLLIDING WITH A CROSSING ANGLE WITHOUT CRAB CROSSING (LEFT); WITH THE CRAB CROSSING (RIGHT).	118
FIGURE 4-2: SCHEMATIC LAYOUT OF THE CRAB CAVITIES IN THE LHC POINT 1 AND 5 W.R.T THE INTERACTION POINT.	118
FIGURE 4-3: COMPACT CAVITIES. (A): DOUBLE QUARTER WAVE CAVITY (DQW), BROOKHAVEN NATIONAL LAB. (B) RF DIPOLE CAVITY (RFD), OLD DOMINION UNIVERSITY. (C) FOUR-ROD CAVITY, LANCASTER UNIVERSITY.	120
FIGURE 4-4: FORWARD POWER VS. CAVITY Q _L FOR CENTRED (RED), 1 MM OFFSET (GREEN), AND 2 MM OFFSET (BLUE) BEAMS. ASSUMED RTQ = 400 Ω, 3.4 MV RF, 1.1 A DC.	121
FIGURE 4-5: (LEFT) INPUT COUPLER ASSEMBLY; (RIGHT) TEST BOX FOR RF CONDITIONING.	122
FIGURE 4-6: (LEFT) REAL PART OF THE DEFLECTING MODE IMPEDANCE WITH A DETUNING OF 1.5 kHz FROM 400 MHz. THE VERTICAL LINES REPRESENT THE DIFFERENCE IN R{Z} EVALUATED AT ±0.3 FREV FOR THE COMPUTATION OF DAMPING RATE (MODE L = -64). (RIGHT) MODULUS OF THE CAVITY IMPEDANCE SEEN BY THE BEAM WITH THE RF FEEDBACK ON (RED) AND OFF (BLUE) NORMALIZED TO THE CAVITY IMPEDANCE AT THE FUNDAMENTAL MODE.	123
FIGURE 4-7: HOM FILTER FOR THE RFD (LEFT) AND THE DQW (RIGHT).	124
FIGURE 4-8: SCHEMATIC VIEW OF THE CAVITY WITH INTERFACES (LEFT) DQW; (RIGHT) RFD.	125
FIGURE 4-9: DIMENSIONAL PLOT WITH TOLERANCES OF THE DQW CAVITY.	126
FIGURE 4-10: DIMENSIONAL PLOT WITH TOLERANCES OF THE RFD CAVITY.	126
FIGURE 4-11: SCHEMATIC OF THE HELIUM VESSEL ASSEMBLY OF THE BOLTED DESIGN (LEFT). MECHANICAL STRESS INDUCED BY MAXIMUM PRESSURE ON THE DQW CAVITY INSIDE ITS HELIUM TANK (RIGHT). RED INDICATES REGIONS WITH HIGHEST STRESS, WHICH CAN BE TOLERATED IF CONFINED TO SMALL AREAS.	127
FIGURE 4-12: (LEFT) THE DQW CAVITY INSIDE ITS HELIUM TANK WITH THE FIELD PROBE PORT (FRONT), BEAM PORT (RIGHT) AND TUNER FRAME AROUND. (RIGHT) SECTIONAL VIEW OF THE DQW CAVITY INSIDE ITS HELIUM TANK WITH THE POWER COUPLER (TOP RIGHT, ORANGE), HOM COUPLER (LEFT, TOP AND BOTTOM), AND TUNER (CENTRE, TOP, AND BOTTOM).	128
FIGURE 4-13: (LEFT) THE RFD CAVITY INSIDE ITS HELIUM TANK WITH THE FIELD PROBE PORT (CENTRE LEFT), BEAM PORT (CENTRE RIGHT), TUNER FRAME AROUND HELIUM VESSEL AND TUNER ACTUATION (TOP CENTRE). (RIGHT) SCHEMATIC SECTIONAL VIEW OF THE RFD CAVITY INSIDE ITS HELIUM TANK WITH THE POWER COUPLER (ORANGE) AND HOM COUPLER (VIOLET).	128

FIGURE 4-14: (A) ACTUATION SYSTEM OF THE PROTOTYPE TUNING SYSTEM FOR DQW AND RFD CAVITIES. (B) CROSS-SECTION. (C) THE PROTOTYPE TUNING SYSTEM MANUFACTURED FOR THE TEST IN SM18 VERTICAL TEST.	129
FIGURE 4-15: FORWARD POWER REQUIRED AS A FUNCTION OF Q_{EXT} FOR DIFFERENT FREQUENCY DETUNING OF THE CAVITY FROM ITS NOMINAL VALUE. THE CROSS-HATCHED AREA INDICATES THE NOMINAL RANGE OF Q_{EXT}	129
FIGURE 4-16: CRYOMODULE LAYOUT FOR ONE SIDE OF THE INTERACTION REGION IN THE LHC.	130
FIGURE 4-17: CRYOMODULES FOR (LEFT) DQW CAVITY; (RIGHT) RFD CAVITY.	130
FIGURE 4-18: (LEFT): COLD MAGNETIC SHIELDING INSIDE THE HELIUM VESSEL; (RIGHT): MAGNETIC FIELD AMPLITUDE INSIDE THE TWO-CAVITY CM WITHOUT THE SECOND INTERNAL COLD MAGNETIC SHIELD, SCALE 0 TO 1 mT. AN EXTERNAL FIELD OF 60 mT IN THE DIRECTION PARALLEL TO X (LONGITUDINAL) IS USED.	132
FIGURE 4-19: CRAB-CAVITIES ALIGNMENT TOLERANCES INSIDE THE CRYOSTAT.	132
FIGURE 4-20: (LEFT) ALIGNMENT PLATE IN BLUE WITH THE SUPPORTS USED FOR ATTITUDE AND POSITION ACTUATION. (RIGHT) FREQUENCY SCANNING INTERFEROMETRY (FSI) SYSTEM FOR ALIGNMENT MONITORING.	133
FIGURE 4-21: A SECTION LAYOUT IN THE LHC FOR BEAM 1 AND BEAM 2 WITH A TWO-CAVITY CRYOMODULE (LEFT). MAXIMUM VERTICAL ENVELOPE FOR THE CRYOMODULES INCLUDING THE RF AND CRYOGENIC SERVICES WITH INTERFACES ON THE TOP.	134
FIGURE 4-22: THE DESIGN OF THE VACUUM VESSEL FOR THE SPS TESTS WITH LATERAL PLATES IN ALUMINIUM FOR MAXIMUM ACCESS TO THE CAVITY COMPONENTS DURING ASSEMBLY AND MAINTENANCE (LEFT); ASSEMBLY CONCEPT OF THE DRESSED CAVITY STRING ON THE TOP PLATE OF THE VACUUM VESSEL (RIGHT).	134
FIGURE 4-23: SCHEMATIC OF THE RF SYSTEM LAYOUT (FOUR PER IP SIDE) IN THE UNDERGROUND CAVERN ABOVE THE LHC TUNNEL LATERAL VIEW (TOP); AND TOP VIEW (BOTTOM); NOTE THAT THESE ARE ONLY ESTIMATED VALUES OF SPACE REQUIREMENTS.	135
FIGURE 4-24: PRELIMINARY SKETCH OF A HIGH-POWER RF, CONTROLS AND LLRF LAYOUT IN THE UNDERGROUND RF CAVERN.	136
FIGURE 4-25: PROPOSED LLRF ARCHITECTURE FOR ONE RING AT ONE IP FOR OPERATION WITH A FINAL INSTALLATION OF EIGHT CAVITIES. THE SAME ARCHITECTURE IS USED FOR THE INITIAL STAGE OF FOUR CAVITIES PER IP.	137
FIGURE 4-26: VOLTAGE RESPONSE WITH STRONGLY COUPLED CAVITIES ACROSS THE IP AS A FUNCTION OF TIME [MS]. AT 50 MS, ONE CAVITY TRIPS (RED TRACE) AND THE OTHER ONE IS FORCED BY THE RF CONTROLLER TO FOLLOW (BLUE TRACE).	138
FIGURE 4-27: TOP VIEW OF THE INTEGRATION OF THE CRYOMODULE, RF ASSEMBLY, AND THE CRYOGENICS IN THE SPS-LSS6 REGION. THE ZONE MARKED IN RED AND GREEN ARE STAY CLEAR ZONES FOR TRANSPORT AND CABLING RESPECTIVELY.	141
FIGURE 4-28: (LEFT) CRYOMODULE AND RF SYSTEM LAYOUT; (RIGHT) A MODIFIED SPS-IOT AT 400 MHz UNDER TEST.	141
FIGURE 5-1: SCHEMATIC ILLUSTRATION OF MULTI-STAGE COLLIMATION CLEANING AT THE LHC. PRIMARY AND SECONDARY COLLIMATORS (DARKEST GREY) ARE THE DEVICES CLOSEST TO THE CIRCULATING BEAM AND ARE MADE OF ROBUST CARBON-FIBRE COMPOSITES. SHOWER ABSORBERS AND TERTIARY COLLIMATORS (LIGHTER GREY) SIT AT LARGER APERTURES AND ARE MADE OF A TUNGSTEN ALLOY TO IMPROVE ABSORPTION. COLLIMATORS OF DIFFERENT FAMILIES ARE ORDERED IN A PRE-DEFINED COLLIMATION HIERARCHY THAT MUST BE RESPECTED TO ENSURE THE REQUIRED SYSTEM FUNCTIONALITIES. THE COLLIMATOR HIERARCHY IS ENSURED BY DEFINING COLLIMATOR SETTINGS IN UNITS OF LOCAL BEAM SIZE AT THE COLLIMATOR LOCATION.	151
FIGURE 5-2: (A) HORIZONTAL LHC COLLIMATOR; (B) SKEW LHC COLLIMATOR. THE LATTER HAS THE VACUUM TANK OPEN TO SHOW THE TWO MOVABLE CFC JAWS.	152
FIGURE 5-3: PHOTOGRAPH OF THE ACTIVE ABSORBER TCLA.B6R7.B1 AS INSTALLED IN THE BETATRON CLEANING INSERTION.	152
FIGURE 5-4: NEW CFC COLLIMATOR JAW WITH INTEGRATED BPMs AT EACH EXTREMITY ('BUTTONS') TO BE INSTALLED AS THE SECONDARY COLLIMATOR IN THE DUMP INSERTION IR6. A DETAIL OF THE BPM IS GIVEN ON THE LEFT-HAND SIDE. A VARIANT OF THIS DESIGN, MADE WITH A GLIDCOP SUPPORT AND TUNGSTEN INSERTS ON THE ACTIVE JAW PART, WILL BE USED FOR THE TERTIARY COLLIMATORS IN ALL IRs.	153
FIGURE 5-5: BLOCK CHART WITH BASELINE (WHITE BACKGROUND BOXES) AND OPTION (GREY) COLLIMATION UPGRADE ITEMS. THE LHC COLLIMATORS THAT WILL CONTINUE TO BE PART OF THE HL-LHC COLLIMATION SYSTEM, WHICH AT THIS STAGE ARE CONSIDERED TO BE ADEQUATE FOR THE HL-LHC BEAM PARAMETERS, ARE ALSO SHOWN (BROWN).	155
FIGURE 5-6: DIAGRAM AS THAT OF FIG. 5.5 WHERE EQUIPMENT CODES ARE USED – WHEN ALREADY AVAILABLE – AS LABELS INSTEAD THAN THE EQUIPMENT FUNCTIONALITY.	155
FIGURE 5-7: (A–B) SCHEMATIC VIEW OF THE ASSEMBLY OF TWO SHORTER 11 T DIPOLES WITH A COLLIMATOR IN BETWEEN, WHICH CAN REPLACE ONE STANDARD MAIN DIPOLE. (C) 3D MODEL OF A TCLD ASSEMBLY SHOWING THE COLLIMATOR (IN GREY, AT THE CENTRE), THE TWO SHORT DIPOLE CRYOSTATS AND THE CONNECTION CRYOSTAT. NOTE THE VERY TIGHT SPACE AVAILABLE FOR THE COLLIMATOR UNIT.	156
FIGURE 5-8: SCHEMATIC LAYOUT IN THE P7 DS WITHOUT TCLDs (TOP), WITH 1 TCLD IN CELL 8 (MIDDLE) AND WITH 2 TCLDs IN CELLS 8 AND 10 (BOTTOM).	157

FIGURE 5-9: ILLUSTRATIVE SCHEME WITH POWER DEPOSITION PROFILES IN THE HORIZONTAL PLANE OF THE P7 DISPERSION SUPPRESSOR (B1). THE MAP MAKES A COMPARISON BETWEEN THE PRESENT LAYOUT WITHOUT TCLD COLLIMATORS (TOP) AND A LAYOUT WITH TWO TCLDS (BOTTOM). RESULTS CORRESPOND TO RELAXED COLLIMATOR SETTINGS. BEAM DIRECTION IS FROM THE RIGHT TO THE LEFT. FROM REF. [19].	157
FIGURE 5-10: PROTON ENERGY DEPOSITION PROFILES IN DS DOWNSTREAM OF IR7 SIMULATED WITH FLUKA, FOR THE CASES OF NO TCLDS (TOP), 1 TCLD (MIDDLE) AND 2 TCLDS (BOTTOM). NOMINAL LHC BEAM PARAMETERS ARE ASSUMED AND ABOUT A FACTOR 2 HIGHER NUMBERS SHOULD BE EXPECTED FOR HL-LHC. [69].....	158
FIGURE 5-11: DETAIL OF ONE EXTREMITY OF THE TCLD COLLIMATOR TO BE INSTALLED IN THE DS BETWEEN TWO NEW 11 T DIPOLES. THE PRESENT DESIGN FORESEES A 60 CM-LONG JAW MADE OF TUNGSTEN HEAVY ALLOY (THE FIRST OF THREE 20 CM INERMET 180 BLOCKS IS SHOWN) AND WILL HAVE TWO JAWS. THE LONGITUDINAL RF CONTACTS, BASED ON COPPER-BERYLLIUM CONTACTS AND FINGERS, ARE ALSO SHOWN.	160
FIGURE 5-12: A SCHEMATIC OF THE TRANSVERSE CROSS SECTION OF THE TCL DESIGN, AS IMPLEMENTED IN FLUKA (TOP), TOGETHER WITH A FIRST GUESS ON THE TCLX DESIGN (BOTTOM), INCLUDING THICKER JAWS, WHERE THE JAW MATERIAL SHOULD BE CHANGED FROM COPPER TO TUNGSTEN HEAVY ALLOY. FIGURE FROM REF. [55].....	161
FIGURE 5-13: DESIGN OF NEW TWO-IN-ONE COLLIMATOR WITH A COMMON VACUUM TANK HOUSING BOTH THE MOVABLE JAWS (LEFT PART) AND THE VACUUM CHAMBER OF THE OPPOSING BEAM. THIS NEW DESIGN IS REQUIRED FOR THE HORIZONTAL COLLIMATORS TO BE INSTALLED IN THE REGIONS OF IR1/5 BETWEEN D2 AND TAXN, WHERE TRANSVERSE INTEGRATION CONSTRAINTS PREVENT INSTALLING THE STANDARD SINGLE-BEAM COLLIMATORS.	162
FIGURE 5-15: 1σ ENVELOPE OF THE MAIN Pb^{82+} BEAM (VIOLET) TOGETHER WITH THE DISPERSIVE TRAJECTORIES OF IONS UNDERGOING BFPP1 (RED) AND EMD1 (BROWN), COMING OUT OF THE ALICE EXPERIMENT (IP2). THE DS COLLIMATOR JAWS APPEAR AS A BLACK LINES. THE GREEN LINE INDICATES THE SHIFTED BFPP1 ORBIT USING A CLOSED ORBIT BUMP, WHICH IS NECESSARY TO INTERCEPT THE BEAM WITH THE COLLIMATOR. THE EMD1 BEAM CAN BE INTERCEPTED WITH THE OTHER JAW.	163
FIGURE 5-16: (A) MOGR COMPONENTS FOR A JAW PROTOTYPE. LEFT: JAW EXTREMITY, DIMENSIONS: $147 \times 88 \times 25 \text{ mm}^3$; RIGHT: JAW ABSORBING BLOCK, DIMENSIONS: $125 \times 45 \times 25 \text{ mm}^3$. A JAW ASSEMBLY INCLUDES 2 JAW EXTREMITIES (TAPERINGS) AND 8 BLOCKS. (B) DETAIL OF THE MICROSTRUCTURE, WHERE THE GRAPHITE MATRIX IS VISIBLE TOGETHER WITH MOLYBDENUM CARBIDE GRAINS OF ABOUT 5 MM.	165
FIGURE 5-17: LHC MACHINE IMPEDANCE VERSUS FREQUENCY: IMPEDANCE RATIO WITH RESPECT TO PRESENT CFC JAW OF BULK MOGR (BLACK) AND $5 \mu\text{m}$ MO-COATED MOGR (BLUE) FOR THE REAL (SOLID) AND IMAGINARY (DOTTED) PARTS [35]. THE IMPEDANCE IS INCREASED BELOW $\sim 1 \text{ MHz}$, BUT THIS NOT EXPECTED TO BE A PROBLEM BECAUSE THIS FREQUENCY RANGE IS WELL WITHIN THE TRANSVERSE DAMPER BANDWIDTH OF 20 MHz.	165
FIGURE 5-18: DESIGN OF THE TCSMP JAW (A) AND OF ITS CROSS-SECTION (B). THE JAW ASSEMBLY FEATURES 8 MOGR BLOCKS. ALSO NOTE THAT THE JAW TAPERING IS LENGTHENED, FURTHER REDUCING ITS CONTRIBUTION TO HOM RF INSTABILITIES IN THE GEOMETRICAL TRANSITION ZONES.....	166
FIGURE 5-19: ILLUSTRATIVE VIEW (LEFT) OF THE COLLIMATION SYSTEM WITH INTEGRATED HOLLOW E-LENS OR EQUIVALENT HALO DIFFUSION MECHANISM; (RIGHT) AN IDEAL CRYSTAL-BASED COLLIMATION. A SIMPLIFIED COLLIMATOR LAYOUT TO THAT IN FIGURE 5-1 IS ADOPTED TO SHOW THE BETATRON CLEANING FUNCTIONALITY ONLY (ONE SIDE ONLY). HALO CONTROL TECHNIQUES ARE USED TO GLOBALLY CHANGE THE DIFFUSION SPEED OF HALO PARTICLES, AND RELY ON THE FULL COLLIMATION SYSTEM REMAINING IN PLACE. CRYSTALS ENTAIL A CHANGE OF CONCEPT WHERE THE WHOLE BEAM LOSSES ARE CONCENTRATED, IDEALLY, IN ONE SINGLE BEAM ABSORBER PER PLANE.	169
FIGURE 5-20: 3D DESIGN OF THE LHC HOLLOW E-LENS. AN 'S' SHAPE IS PROPOSED INSTEAD THAN THE MORE CONVENTIONAL 'U' SHAPE USED AT THE TEVATRON IN ORDER TO COMPENSATE THE CONTRIBUTION TO THE EMITTANCE GROWTH FROM THE ASYMMETRY OF THE ELECTRON BEAMS AT ENTRY AND EXIT OF THE PROTON BEAM. COURTESY OF D. PERINI.....	170
FIGURE 5-21: PHOTOGRAPH OF THE SLAC ROTATORY COLLIMATOR PROTOTYPE JAWS BEFORE ASSEMBLY IN THE VACUUM TANK.....	173
FIGURE 6-1: SUPERCONDUCTING LINKS AT LHC P1 AND P5.	184
FIGURE 6-2: CABLE ASSEMBLIES FOR SUPERCONDUCTING LINKS AT LHC P1 AND P5. FROM LEFT: A) SUB-UNIT OF THE 18 kA CABLE, $\Phi \sim 6.5 \text{ mm}$, RATED FOR 6 (??) kA; B) COMPLETE 18 kA CABLE, $\Phi \sim 19.5 \text{ mm}$; C) CONCENTRIC $2 \times 3 \text{ kA}$ CABLE, $\Phi \sim 8.5 \text{ mm}$; D) 0.4 kA CABLE (TOP) AND 0.12 kA CABLE (BOTTOM), $\Phi < 3 \text{ mm}$; E) 165 kA CABLE ASSEMBLY FOR LHC P1 AND P5 ($6 \times 20 \text{ kA}$, $7 \times 2 \times 3 \text{ kA}$, $4 \times 0.4 \text{ kA}$, $18 \times 0.12 \text{ kA}$), $\Phi \sim 65 \text{ mm}$. THE CABLES ARE MADE OF COPPER STABILIZER (RED) AND MgB_2 WIRE (GREEN).	184
FIGURE 6-3: CABLE ASSEMBLY FOR SUPERCONDUCTING LINKS AT LHC P1 AND P5 (SYSTEM POWERING THE HL-LHC INSERTIONS). FROM LEFT: CABLE ASSEMBLY; CABLE ASSEMBLY INSIDE THE SEMI-FLEXIBLE CRYOSTAT. THE EXTERNAL DIAMETER OF THE CRYOSTAT (VACUUM WALL), WHICH INCLUDES AN ACTIVE THERMAL SHIELD, IS $\sim 220 \text{ mm}$. THE WEIGHT OF THE CRYOSTAT WITH THE $ 150 \text{ kA}$ CABLE ASSEMBLY INSIDE IS $\sim 20 \text{ kg/m}$	184

FIGURE 6-4: TEST STATION DESIGNED AND OPERATED AT CERN FOR THE TEST OF 20 M LONG SUPERCONDUCTING LINKS. THE CABLES ARE COOLED BY FORCED FLOW OF HELIUM GAS OPERATING AT ANY TEMPERATURE FROM ABOUT 5 K TO 35 K. TEMPERATURES OF UP TO 70 K CAN BE ACHIEVED, ENABLING APPRAISAL OF CABLES MADE FROM DIFFERENT TYPES OF CONDUCTOR.	185
FIGURE 6-5: VIEW OF THE LHC UNDERGROUND AREA AT P1: SERVICE TUNNEL, PARALLEL TO THE LHC MAIN RING, WHERE POWER CONVERTERS AND CURRENT LEADS WILL BE LOCATED (HL-LHC BASELINE).....	188
FIGURE 6-6: SCHEMATIC VIEW OF THE LHC UNDERGROUND AT P1 WITH THE TWO SUPERCONDUCTING LINKS (RED LINES) ROUTED FROM TO THE LHC MAIN TUNNEL TO NEW LHC SERVICE TUNNEL (HL-LHC BASELINE), WHERE THE POWER CONVERTERS AND THE CURRENT LEADS WILL BE LOCATED.	189
FIGURE 6-7: SCHEMATIC VIEW OF THE LHC UNDERGROUND WITH THE TWO SUPERCONDUCTING LINKS ROUTED FROM TO THE LHC MAIN TUNNEL TO NEW LHC SERVICE TUNNEL (HL-LHC BASELINE). THE VERTICAL PATH OF THE LINKS COVERS A DIFFERENCE IN HEIGHT OF ABOUT 8 M.	189
FIGURE 6B-1: NEW HL-LHC UNDERGROUND INFRASTRUCTURE AT POINT 1, TOP VIEW.	192
FIGURE 6B-2: POWER CONVERTERS INSTALLED IN UR GALLERY.	193
FIGURE 6B-3: PRESENT LHC MAGNET LAYOUT	193
FIGURE 6B-4: NEW HL-LHC MAGNET LAYOUT (CRAB CAVITIES NOT SHOWN).	193
FIGURE 6B-5: POWERING LAYOUT OF THE PRESENT LHC INNER TRIPLETS.....	194
FIGURE 6B-6: CIRCUIT LAYOUT OF THE HL-LHC INNER TRIPLET (MQXFA, MQXFB).	194
FIGURE 6B-7: CONNECTIONS BETWEEN THE INNER TRIPLET POWER CONVERTERS AND THE ELECTRICAL FEED-BOXES.	195
FIGURE 6B-8: CIRCUIT LAYOUT OF EACH INNER TRIPLET CORRECTOR CIRCUIT (MCBXF).	195
FIGURE 6B-9: HIGH ORDER CORRECTORS CIRCUIT LAYOUT (MCS, MCO, MCD, MCT, AND MQSXF).....	196
FIGURE 6B-10: D1 MAGNET CIRCUIT LAYOUT (MBXF).	196
FIGURE 6B-11: D2 MAGNET CIRCUIT LAYOUT (MBRD).....	197
FIGURE 6B-12: D2 ORBIT CORRECTORS CIRCUIT LAYOUT (MCBRD).	197
FIGURE 6B-13: Q4, Q5 AND Q6 CIRCUIT LAYOUT (NO CHANGE WITH RESPECT TO THE PRESENT LHC LAYOUT).	198
FIGURE 6B-14: Q4, Q5 AND Q6 ORBIT CORRECTOR CIRCUIT LAYOUT.	198
FIGURE 6B-15: THE POWER CONVERTER TYPE DEPENDS UPON THE OPERATING CYCLE.....	200
FIGURE 6B-16: PROPOSED LAYOUT OF THE NEW POWER CONVERTER TOPOLOGY.	201
FIGURE 6B-17: TOPOLOGY OF NEW 600 A R2E POWER CONVERTER.	201
FIGURE 6B-18: FGC2 (LEFT) AND FGC3 (RIGHT) CONTROL UNITS.....	205
FIGURE 6B-19: LHC FGC2 NETWORK INFRASTRUCTURE (LEFT), FGC3 NETWORK INFRASTRUCTURE (RIGHT).	205
FIGURE 6B-20: SCHEMATIC REPRESENTATION OF THE FULL CURRENT MEASUREMENT FOR THE POWER CONVERTERS EQUIPPING THE MAIN CIRCUITS OF LHC (ACCURACY CLASS 1) INCLUDING THE REMOTE CALIBRATION SYSTEM.	207
FIGURE 6B-21: WORKING PRINCIPLE OF THE CERN DS22 DELTA-SIGMA ADC.	208
FIGURE 6B-22: LHC 20kA DCCT CALIBRATION TEST STATION.	208
FIGURE 6B-23: DECOUPLING LOOP FOR THE LHC INNER TRIPLETS CURRENT CONTROL.	209
FIGURE 7-1: STORED BEAM ENERGY AS A FUNCTION OF BEAM MOMENTUM FOR VARIOUS PARTICLE ACCELERATORS. THE BEAM ENERGY OF ABOUT 700 MJ OF EACH OF THE HL-LHC BEAMS IS SHOWN IN RED.	213
FIGURE 7-2: SOME FAILURE DETECTION TIMES AT THE LHC. THE SHORTEST FAILURE DETECTION TIME IS CURRENTLY ASSURED BY THE BLM SYSTEM, WITH THE FASTEST INTEGRATION TIME OF 40 MS, WHICH IS EQUIVALENT TO HALF AN LHC TURN. VERY FAST BEAM LOSS DETECTORS BASED ON DIAMOND DETECTORS CAN ACHIEVE NS RISE TIMES. FOR THE MOMENT THESE DETECTORS ARE ONLY USED FOR DIAGNOSTIC PURPOSES AND NOT INTERLOCKED. THIS MAY CHANGE IN THE HL-LHC ERA.	214
FIGURE 7-3: CURRENT MPS RESPONSE TIME FROM FAILURE DETECTION TO COMPLETION OF BEAM DUMP.....	215
FIGURE 7-4: SCHEMATIC OVERVIEW OF CRAB CAVITY FAILURE CATEGORIES [5].	216
FIGURE 7-5: SCHEMATIC OF THE INNER TRIPLET (IP1/5) POWERING AND PROTECTION LAYOUT.	220
FIGURE 7-6: SIMULATED TYPICAL CURRENTS DURING A QUENCH, WHEN TRIGGERING OUTER-LAYER QUENCH HEATERS AND CLIQ. THE CURRENT IN THE CIRCUIT BEFORE THE QUENCH IS 16.5 kA. THE CURRENTS IN THE TRIM CIRCUITS ARE ALL ZERO. D1, D2 AND D4 ARE THE CURRENTS THROUGH THE CROW-BAR OF THE TRIM CIRCUITS FOR Q1, Q2A AND Q3. D3 IS THE CURRENT THROUGH THE PARALLEL DIODES OF Q2B. NOTE: Q1=Q3, Q2A=Q2B AND $I_{D1}=I_{D4}$, AND $I_{D2}=I_{D3}$	221
FIGURE 7-7: INSTRUMENTATION SCHEME TO PROTECT A MAGNET ASSEMBLY CONSISTING OF EIGHT SUPERCONDUCTING COILS AGAINST SINGLE- AND MULTIPLE COIL QUENCHES. U1 – U8 ARE THE VOLTAGES MEASURED OVER THE DIFFERENT 8 SUPERCONDUCTING COILS. I_{CIRC} IS THE CIRCUIT CURRENT AND DI/DT THE FIRST TIME DERIVATIVE OF THE CIRCUIT CURRENT.....	222

FIGURE 7-8: BLOCK DIAGRAM OF THE UNIVERSAL QUENCH DETECTION SYSTEM (UQDS) UNIT.	223
FIGURE 7-9: BLOCK DIAGRAM OF A POLYVALENT ANALOGUE INPUT CHANNEL DESIGN UNDER EVALUATION.....	224
FIGURE 7-10: SCHEMATIC OF A CLIQ UNIT CONNECTED TO A MAGNET FOR ITS PROTECTION [12].	224
FIGURE 7-11: SENSITIVITY ANALYSIS OF INTEGRATED LUMINOSITY OVER 160 DAYS OF OPERATION TO THE MACHINE FAILURE RATE AND AVERAGE FAULT TIME. THE STARS INDICATE THE ACHIEVABLE YEARLY INTEGRATED LUMINOSITY BASED ON THE AVAILABILITY FIGURES OF THE 2016 REFERENCE PERIOD AND THE GOALS FOR NOMINAL (250 B^{-1}) AND ULTIMATE (320 FB^{-1}) HL-LHC PERFORMANCE.	228
FIGURE 8-1: GRAPH SHOWING THE FORESEEN LHC AND HL-LHC OPERATION PLANS FOR THE FOUR EXPERIMENTS. THE KEY ACTIVITIES PER EXPERIMENT ARE INDICATED, AS WELL AS THE EXPECTED INTEGRATED LUMINOSITIES. THE PERIODS IN RED INDICATE THE LONG-SHUTDOWNS OF THE LHC ACCELERATOR, WITH THE ONES FOLLOWING LS3 CONSIDERED AS TENTATIVE ONLY. THE HL-LHC PROGRAM STARTS AFTER LS3 IN 2026.	232
FIGURE 8-2: THE UPDATED ATLAS CENTRAL VACUUM CHAMBER AND THE NEW INNER DETECTOR.....	235
FIGURE 8-3: THE UPDATED CMS CENTRAL VACUUM CHAMBER AND THE NEW CONFIGURATION OF THE INNER DETECTOR PIXEL LAYERS.....	235
FIGURE 8-4: THE FULL CMS VACUUM CHAMBER LAYOUT (SINGLE SIDE) FROM THE IP TO THE TAS. THE PRESENT AND FUTURE POSITION OF THE PROXIMITY PUMPING STATION IS INDICATED.	236
FIGURE 8-5: ENERGY DEPOSITION IN THE TAXS FROM FLUKA SIMULATIONS. AN APERTURE OF 54MM IS CONSIDERED IN THESE SIMULATIONS.	238
FIGURE 8-6: 3-D VIEW OF THE TAXS REGION FROM Q1 (MACHINE SIDE, ON THE RIGHT) TO ATLAS TOROID (IN GREY). THE LAYOUT CORRESPONDS TO THE RUN CONFIGURATION. Q1 IS SHOWN ON THE LEFT (IN BLUE/RED), FOLLOWED BY THE TAXS ABSORBER (IN ORANGE), AND THE VACUUM ASSEMBLY MODULE. THE FORESEEN MODIFICATIONS REQUIRED TO HOST IT IN THE EXPERIMENTAL AREA CONCERN THE JFC (UPPER SHOWN IN WHITE, LOWER BRIDGE SHOWN IN ORANGE) AND JTT (IN GREY), AS DESCRIBED IN THE TEXT. ON THE RIGHT OF THE TAXS, THE FORWARD SHIELDING ELEMENTS SURROUND THE VAX AND THE BEAM PIPE BEFORE THE TOROID. INSIDE THE TOROID, (IN GREY) THE JTT SHIELDING RINGS. IN THE FIGURE, VAX IS RELOCATED AS FORESEEN FOR HL-LHC. NOTE THAT Q1-TAXS REGION, INSIDE THE TX1S (BLUE AREA), IS THE AREA WITH THE MOST DIFFICULT ACCESS OF THE WHOLE MACHINE. THE GATE VALVES AND CURRENT VAX MODULE WILL BE MOVED TO THE EXPERIMENTAL CAVERNS.	239
FIGURE 8-7: RIGHT- ZOOM INTO THE IP1 Q1-TAXS REGION AS FORESEEN FOR HL-LHC. TAXS (ORANGE) IS SHOWN INSIDE ITS CRADLE SHIELDING (DARK BLUE). BPM (YELLOW) WILL BE PLACED INSIDE Q1 SECONDARY VACUUM AND QUICK CONNECTOR, DOUBLE PUMP WHICH REQUIRES NO ACCESS AND THE HE TIGHTNESS DOME WILL REMAIN IN THE VERY LIMITED REGION (GREY ELEMENTS). THE GATE VALVES AND CURRENT VAX MODULE WILL BE MOVED TO THE EXPERIMENTAL CAVERNS. LEFT ZOOM ON IP5 Q1-TAXS REGION AS FORESEEN FOR HL-LHC.	239
FIGURE 8-8: 3D VIEW OF THE FORWARD SHIELDING REGION WITH THE RELOCATED VAXS AND SERVICES. THE LAYOUT CORRESPONDS TO A PHASE IN THE DETECTOR ACCESS PROCEDURE WHERE THE OCTAGONAL AND PART OF THE JFC SHIELDINGS ARE REMOVED. THE PASSAGE OF THE SERVICES FOR THE VACUUM EQUIPMENT MODULE (CABLING AND GAS INJECTION/EXTRACTION PIPES) IS SHOWN IN GREY.	240
FIGURE 8-9: RIGHT- VACUUM MODULE ASSEMBLY INSTALLED ON THE IP SIDE OF THE TAXS WITH ALL-METAL GATE VALVES. THE VALVES ARE CLOSED IN CASE OF REMOTE EXCHANGE OF THE VACUUM PUMP MODULE (LEFT). NOTE THAT THE CANTILEVER SUPPORT STRUCTURE IS NOT SHOWN IN THE PICTURE.	241
FIGURE 8-10: DETAIL CUT VIEW OF ATLAS FORWARD SHIELDING STRUCTURES THAT NEED TO BE MODIFIED. THE SHIELDING CONSISTS OF TWO PARTS: THE CYLINDRICAL CORE AND THE OCTAGONAL BACK. THREE PIECES CALLED JFC1 ("THE BRIDGE, IN ORANGE"), JFC2 (WHITE) AND JFC3 (WHITE) ARE USED FOR THE CORE AND TWO PIECES CALLED "JFS3 UPPER" AND "JFS3 LOWER" (ON THE LEFT, SURROUNDING THE BLUE NOSE MONOBLOC) ARE USED FOR THE OCTAGONAL BACK.	241
FIGURE 8-11: 3D VIEW OF THE ATLAS TOROID SHIELDING PLUG (JTT, IN GREY). ONLY THE FIRST OF THE FOUR DISKS IS SHOWN. FOR PRESENT LHC CONFIGURATION (LEFT) THE DISK IS A SINGLE BLOCK, WHILE FOR HL-LHC (RIGHT) WILL BE MODIFIED AND SHIELDING WILL BE DONE TWO PARTS: AN OUTER CYLINDER WITH A TAILORED BORE, AND AN INTERNAL BLOCK ATTACHED TO THE JFC2 MODULE (FIGURE 8-12). POLYETHYLENE LAYER (YELLOW) IS SHOWN AROUND THE HL-LHC JTT.	242
FIGURE 8-12: 3D VIEW OF THE ATLAS JFC2 MODULE. PRESENTLY THE MODULE IS A CYLINDRICAL SHAPED BLOCK, WHILE FOR HL-LHC AN "EXTRA NOSE" SHIELDING WILL BE ADDED TO FILL THE GAP REQUIRED IN JTT FOR THE DETECTOR OPENING WITHOUT REMOVING VAX.	242
FIGURE 8-13: RATIO OF $H^*(10)$ (AMBIENT DOSE) IN LS6 (ATLAS) SHOWING THE INCREASE IN DOSE RATE WITH VAX AFTER 1 MONTH COOLING. THE CALCULATION IS CONSERVATIVE, AS IT ASSUMES PEAK LUMINOSITY OF $7.5 \times 10^{34} \text{ CM}^{-2}\text{S}^{-1}$ (LEVELLING), INTEGRATED LUMI OF 300/FB PER YEAR IN HL-LHC, 7+7 TeV PP-COLLISIONS, 80 MB INELASTIC CROSS SECTION AND 3 YEARS OPERATION-1 YEAR SHUTDOWN X 3 PERIODS UNTIL LS6. RESULTS FOR LS4 AND LS5 ARE SIMILAR [11]. THE ATLAS FORWARD SHIELDING REMAINS OPEN	

DURING ACCESS AND THE ROUTINE OPERATIONS AT THE DETECTOR ARE NOT AFFECTED. RIGHT PICTURE ZOOMS IN THE RATIO AROUND THE VAX REGION.	243
FIGURE 8-14: RATIO OF $H^*(10)$ IN LS6 (AMBIENT DOSE IN ATLAS) ZOOMING AROUND THE VAX REGION. . THE CALCULATION IS CONSERVATIVE, ASSUMING PEAK LUMINOSITY OF $7.5 \times 10^{34} \text{ cm}^{-2}\text{s}^{-1}$ (LEVELLING), INTEGRATED LUMINOSITY OF 300/FB PER YEAR IN HL-LHC, 7+7 TeV PP-COLLISIONS, 80 MB INELASTIC CROSS SECTION AND 3 YEARS OPERATION-1 YEAR SHUTDOWN X 3 PERIODS UNTIL LS6. RESULTS FOR LS4 AND LS5 ARE SIMILAR [11]. THE INCREASE IN DOSE RATE WITH VAX AFTER 1-MONTH COOLING IS SHOWN. THE ATLAS FORWARD SHIELDING REMAINS OPEN DURING ACCESS AND THE ROUTINE OPERATIONS AT THE DETECTOR ARE NOT AFFECTED.	243
FIGURE 8-15: 3D VIEW OF THE CMS FORWARD SHIELDING REGION WITH THE TAXS AND VACUUM MODULE. THE LAYOUT CORRESPONDS TO THE RUN CONFIGURATION. THE TAXS ABSORBER IS ON THE LEFT INSIDE THE FIN (GREEN) AND THE SURROUNDING ROTATING SHIELDING (ORANGE). THE VACUUM ASSEMBLY MODULE ON THE IP SIDE IS SHOWN INSIDE THE BASEPLATE SUPPORT (TRANSPARENT YELLOW)...	244
FIGURE 8-16: RIGH-3D VIEW OF THE CURRENT CMS BEAM PIPE SUPPORT (YELLOW) IN FRONT OF TAS. THE LAYOUT CORRESPONDS TO THE OPEN DETECTOR CONFIGURATION. LEFT- THE NEW SUPPORT STRUCTURE (GREY) WHICH SUPPORTS THE RELOCATED VAX EQUIPMENT (BLUE).....	245
FIGURE 8-17: CUT OF THE CMS FORWARD SHIELDING SHOWING THE RELOCATED VAX INSIDE THE YELLOW BEAM PIPE SUPPORT MODULE. END OF TAXS IS SHOWN AT THE RIGHT END. THE REQUIRED MODIFICATIONS IN THE FORWARD SHIELDING (ORANGE) AND FIXED IRON NOSE (GREEN) ARE INSIDE THE RED BOXES. THE YELLOW BEAM PIPE SUPPORT MODULE. DETAILS OF THE BEAM PIPE SUPPORT AND THE CABLE TRAY TO BE MODIFIED ARE SHOWN ON THE LEFT.....	245
FIGURE 8-18: PHOTOS SHOWING THE CMS FORWARD SHIELDING DURING ACCESS. THE SMALL ROTATING SHIELDING IS OPEN SHOWING THE YELLOW BEAM PIPE SUPPORT MODULE. DETAILS OF THE BEAM PIPE SUPPORT AND THE CABLE TRAY TO BE MODIFIED ARE SHOWN ON THE LEFT.	245
FIGURE 8-19: RATIO OF $H^*(10)$ IN LS6 (AMBIENT DOSE IN CMS) SHOWING THE INCREASE IN DOSE RATE WITH VAX AFTER 1 MONTH COOLING. THE CALCULATION IS CONSERVATIVE, ASSUMING PEAK LUMINOSITY OF $7.5 \times 10^{34} \text{ cm}^{-2}\text{s}^{-1}$ (LEVELLING), INTEGRATED LUMI OF 300/FB PER YEAR IN HL-LHC, 7+7 TeV PP-COLLISIONS, 80 MB INELASTIC CROSS SECTION AND 3 YEARS OPERATION-1 YEAR SHUTDOWN X 3 PERIODS UNTIL LS6. RESULTS FOR LS4 AND LS5 ARE SIMILAR [11]. THE CMS FORWARD SHIELDING REMAINS OPEN DURING ACCESS, AND THE ROUTINE OPERATIONS AT THE DETECTOR ARE NOT AFFECTED.	246
FIGURE 8-20: RATIO OF $H^*(10)$ IN LS6 (AMBIENT DOSE IN CMS) ZOOMING AROUND THE VAX REGION. THE INCREASE IN DOSE RATE WITH VAX AFTER 1-MONTH COOLING IS SHOWN. THE CALCULATION IS CONSERVATIVE, ASSUMING PEAK LUMINOSITY OF $7.5 \times 10^{34} \text{ cm}^{-2}\text{s}^{-1}$ (LEVELLING), INTEGRATED LUMINOSITY OF 300/FB PER YEAR IN HL-LHC, 7+7 TeV PP-COLLISIONS, 80 MB INELASTIC CROSS SECTION AND 3 YEARS OPERATION-1 YEAR SHUTDOWN X 3 PERIODS UNTIL LS6. RESULTS FOR LS4 AND LS5 ARE SIMILAR [11]. THE CMS FORWARD SHIELDING REMAINS OPEN DURING ACCESS, AND THE ROUTINE OPERATIONS AT THE DETECTOR ARE NOT AFFECTED.....	246
FIGURE 8-21: RESULTS FROM FLUKA ENERGY DEPOSITION STUDIES FOR THE TAXN AT P1,P5. LEFT: THE ENERGY DEPOSITION LONGITUDINAL PROFILE, RIGHT: THE TRANSVERSE ENERGY DISTRIBUTION AT THE PEAK LOCATION.	248
FIGURE 8-22: TAXN GEOMETRY USING DIFFERENT MATERIAL FOR THE CORE ABSORBER: CU (LEFT), INERMET180 (RIGHT). MAINTAINING THE SAME EFFICIENCY (APPROX. 22-25 λ_{INT}) A GAIN IN LENGTH OF 1.5M CAN BE OBTAINED.	249
FIGURE 8-23. PEAK POWER DENSITY (LEFT PICTURE) AND PEAK DOSE (RIGHT PICTURE) IN THE IP8 D2 COILS.	249
FIGURE 8-24: 2D LAYOUT (TOP VIEW) OF THE D2 REGION AS CONSIDERED FOR THE FLUKA ANALYSIS. THE NEW TAXN (DARK BLUE) IS SITUATED BETWEEN D2 (WHITE) AND THE TCTPH COLLIMATOR Y-CHAMBER IS SHOWN ON THE LEFT OF THE PICTURE.	250
FIGURE 8-25: ENERGY DEPOSITION IN THE D2 FRONT FACE, IN THE LAYOUT INCLUDING THE 500 MM INERMET180 TAXN. A LOAD INCREASE OF 6 W IN D2 RESPECT TO LHC, 60% OF WHICH ARE ABSORBED IN THE FIRST METER.	250
FIGURE 8-26: 3D CONCEPTUAL DRAWING OF A MINI-TAXN TO BE INSTALLED IN LSS8 CURRENTLY UNDER CONSIDERATION. INNER PART IS MADE OF INERMET 180, WHILE THE SURROUNDING BOX PROVIDES BAKING CAPABILITIES. SUPPORT, SURVEY & ALIGNMENT STRUCTURES NOT SHOWN.....	251
FIGURE 9-1: OVERALL LHC CRYOGENIC LAYOUT, INCLUDING THE UPGRADED INFRASTRUCTURE.	253
FIGURE 9-2: UPGRADED LAYOUT OF THE CONTINUOUS CRYOSTAT AT P2 (AS WELL AT P1, P5, AND P7).	255
FIGURE 9-3: POSSIBLE UPGRADED LAYOUT OF THE P4 INSERTION REGION.	255
FIGURE 9-4: UPGRADED LAYOUT OF THE P1/P5 INSERTION REGION (HALF INSERTION).	255
FIGURE 9-5: COOLING CAPACITY REQUIREMENT OF SECTOR CRYOGENIC PLANTS. (A) COLD MASS; (B) CURRENT LEADS; (C) THERMAL SHIELDS; (D) BEAM SCREEN (DIPOLE OFF); (E) BEAM SCREEN (DIPOLE ON).....	258
FIGURE 9-6: UPGRADED CRYOGENIC ARCHITECTURE AT P4.....	259
FIGURE 9-7: UPGRADED CRYOGENIC ARCHITECTURE AT P1 AND P5.	259

FIGURE 10-1: BREAKDOWN OF THE DEBRIS PARTICLES PER SINGLE PROTON–PROTON INELASTIC INTERACTION AT 5 MM FROM THE INTERACTION POINT (BLACK) AND AT THE EXIT OF EACH 60 MM TAS APERTURE (RED).	264
FIGURE 10-2: HL-LHC INNER TRIPLET WITH MCBX/CP CORRECTORS AND D1 DIPOLE.	265
FIGURE 10-3: DETAILS OF THE FLUKA–MARS MODEL IN THE INNERMOST REGIONS OF (LEFT) THE Q2–Q3 QUADRUPOLES; (RIGHT) MCBX ORBIT CORRECTORS. A MORE ADVANCED IMPLEMENTATION IS DOCUMENTED IN SECTION 10.3.	265
FIGURE 10-4: (LEFT) POWER DENSITY ISOCONTOURS AT THE IP END OF Q2A CALCULATED BY MARS; (RIGHT) COMPARISON OF THE LONGITUDINAL PEAK POWER DENSITY PROFILE ON THE INNER COILS OF THE TRIPLET MAGNETS FOR THE MARS AND FLUKA CODES... ..	266
FIGURE 10-5: LONGITUDINAL DISTRIBUTIONS OF (LEFT) PEAK DOSE ON INNER COILS AND NEARBY INSULATORS; (RIGHT) PEAK DPA ON INNER COILS.	267
FIGURE 10-6: CROSS-SECTIONS OF TRIPLET QUADRUPOLES AND ORBIT CORRECTORS: (A) Q1; (B) Q2; (C) MCBX. THE EXTENSION OF THE INERMET ABSORBERS AROUND THE HELIUM CHANNEL AT 45°, IMPLEMENTED FROM Q2 ONWARDS IN ALTERNATION WITH PUMPING SLOT GAPS, CAN BE NOTED.	268
FIGURE 10-7: FLUKA MODEL OF TRIPLET INTERCONNECTS, INCLUDING A CIRCULAR BPM WITH ITS ELECTRODE STRIPS (IN BROWN).	269
FIGURE 10-8: PEAK POWER DENSITY PROFILE IN THE MAGNET INNER COILS (RADIALLY AVERAGED OVER THE CABLE WIDTH), FOR VERTICAL (RED) AND HORIZONTAL (BLUE) BEAM CROSSING. ERROR BARS INDICATE STATISTICAL UNCERTAINTIES. $L = 5 \times 10^{34} \text{ cm}^{-2} \text{ s}^{-1}$	270
FIGURE 10-9: PEAK DOSE PROFILE IN THE MAGNET INNER COILS (RADIALLY AVERAGED OVER THE INNERMOST LAYER, $\leq 3\text{mm}$), FOR VERTICAL (RED) AND HORIZONTAL (BLUE) BEAM CROSSING. ERROR BARS INDICATE STATISTICAL UNCERTAINTIES. $L_{\text{INT}} = 3000 \text{ fb}^{-1}$	270
FIGURE 10-10: DOSE TWO-DIMENSIONAL DISTRIBUTION OVER THE COIL RADIAL RANGE, CORRESPONDING TO THE Q2B MAXIMUM AS IN FIGURE 10-9, FOR VERTICAL (LEFT) AND HORIZONTAL (TIGHT) BEAM CROSSING.	271
FIGURE 10-11: DEBRIS PARTICLE DISTRIBUTION AT THE EXIT OF THE OUTGOING BEAM PIPE OF THE TA(X)N, (LEFT) FOR THE LHC; (RIGHT) FOR THE HL-LHC. RED POINTS INDICATE PROTONS WITH MAGNETIC RIGIDITY WITHIN 5% WITH RESPECT TO BEAM PROTONS AND GREEN POINTS INDICATE PROTONS WITH LOWER MAGNETIC RIGIDITY. BLUE POINTS INDICATE NEUTRAL PARTICLES (PHOTONS AND NEUTRONS). THE SAME NUMBER OF COLLISION IS SIMULATED IN BOTH CASES. THE BLACK ELLIPSE SHOWS THE 10σ OUTGOING BEAM ENVELOPE FOR ROUND BEAM OPTICS.	272
FIGURE 10-12: PEAK POWER DENSITY PROFILE IN THE MAGNET COILS AROUND THE OUTGOING BEAM BORE (RADIALLY AVERAGED OVER THE CABLE WIDTH), FOR VERTICAL (RED) AND HORIZONTAL (BLUE) BEAM CROSSING, ALONG THE MATCHING SECTION CRYOSTATS: (A) D2; (B) Q4 (NOTE THE DIFFERENT VERTICAL SCALE); (C) Q5 AND Q6; (D) Q7. THE POSITION OF THE Q5 AND Q6 CORRECTORS (THREE AND ONE, RESPECTIVELY) VARIES BETWEEN P1 (RED, VERTICAL CROSSING) AND P5 (BLUE, HORIZONTAL CROSSING). THE THREE TCL(X) OPENING IS ASSUMED TO BE 12σ (HALF GAP). ERROR BARS INDICATE STATISTICAL UNCERTAINTIES. $L = 5 \times 10^{34} \text{ cm}^{-2} \text{ s}^{-1}$	273
FIGURE 10-13: COOLING SCHEME OF THE COLD POWERING SYSTEM. LEFT-HAND SIDE: LOW TEMPERATURE (LT) SIDE, WHERE THERE ARE THE CONNECTIONS WITH THE SC MAGNET CABLE. RIGHT-HAND SIDE: CONNECTION WITH THE CURRENT LEADS (CL).	274
FIGURE 10-14: (A) 18 kA MgB_2 CABLE, $\varnothing = 19.5 \text{ mm}$; (B) TWO MgB_2 CONCENTRIC CABLES FOR 3 kA TOTAL CURRENT, $\varnothing = 8.5 \text{ mm}$; (C) 165 kA CABLE ASSEMBLY FOR LHC P1 AND P5 ($6 \times 20 \text{ kA}$, $7 \times 2 \times 3 \text{ kA}$, $4 \times 0.4 \text{ kA}$, $18 \times 0.12 \text{ kA}$), $\varnothing = 65 \text{ mm}$. THE CABLES ARE MADE OF COPPER STABILIZER (RED) AND MgB_2 WIRE (GREEN).	274
FIGURE 10-15: MAPS OF DOSE RELEASED IN THE SC LINK IN THE P1 SHUFFLING MODULE. (LEFT) SUPERCONDUCTING HORIZONTAL CABLE SHUFFLE MODULE DOSE; (RIGHT) SUPERCONDUCTING VERTICAL CABLE SHUFFLE MODULE DOSE. VALUES (IN MGy) ARE NORMALIZED TO 3000 fb^{-1}	275
FIGURE 10-16: LHC BEAM DUMPS DUE TO SINGLE EVENT EFFECTS AGAINST BEAM LUMINOSITY. DOTS (2011 AND 2012) REFER TO MEASUREMENTS, WHEREAS LINES SHOW ANNUAL AVERAGES FOR BOTH PAST AND FUTURE OPERATIONS.	276
FIGURE 10-17: ANNUAL RADIATION LEVELS IN THE LSS AND IN THE ADJACENT UJ, UL AND RR AREAS AT P1 DURING THE HL-LHC ERA (PER 250 fb^{-1}), CALCULATED WITH THE HL-LHCv1.2 ROUND OPTICS: (A) HEH FLUENCE; (B) 1 MeV NEUTRON EQUIVALENT FLUENCE; (C) ABSORBED DOSE. THE THREE TCL(X) COLLIMATORS ARE SET AT 12σ HALF GAP.	279
FIGURE 11-1: SIDE VIEW OF THE 11 T DIPOLE FULL ASSEMBLY SHOWING THE COLLIMATOR INSTALLED BETWEEN COLD-TO-WARM TRANSITIONS.	284
FIGURE 11-2: CROSS-SECTION OF THE BYPASS CRYOSTAT AND COLLIMATOR. THE THREE MAIN BUSBAR LINES HAVE BEEN MOVED AWAY FROM THE BEAM LINES RADIALLY IN ORDER TO CREATE SPACE FOR THE COLLIMATOR AND THE BEAM VACUUM SECTOR VALVES.	284
FIGURE 11-3: VIEW OF THE ENLARGED COLD MASS END COVER AND INTERCONNECT TO THE BYPASS CRYOSTAT	284
FIGURE 11-4-A: LONGITUDINAL SECTION OF THE COLD MASS ASSEMBLY LMBHA, RETRIEVED FROM DRAWING LHCLMBH_0001.	286
FIGURE 11-5: TOP AND SIDE VIEWS OF THE COIL, RETRIEVED FROM DRAWING Nb. LHCMBH_C0005.	287
FIGURE 11-6: CROSS-SECTION THROUGH (LEFT) THE 11 T DIPOLE COLLARED COIL; (RIGHT) THE COLD MASS ASSEMBLY.	288
FIGURE 11-7: POWERING SCHEME OF A PAIR OF MBH INSIDE THE COLD MASS ASSEMBLY.	288

FIGURE 11-8: THE BLUE LINE SHOWS THE DIFFERENCE IN INTEGRATED FIELD BETWEEN A PAIR OF MBHS AND AN MB, BOTH DELIVERING 119 T·M AT 11.85 KA. THE RED LINE SHOWS THE TRIM CURRENT NEEDED TO CORRECT THE DIFFERENCE AT CURRENTS BELOW 11.85 KA.	289
FIGURE 11-9: INSTRUMENTATION SCHEME IN THE MAIN/TRIM CIRCUITS OF THE 11 T DIPOLE FULL ASSEMBLY SUBSTITUTING A STANDARD MB_L.	290
FIGURE 11-10: INSTRUMENTATION SCHEME FOR THE TEMPERATURE SENSOR, CRYO-HEATER, SPOOL PIECES, AND QUENCH HEATERS IN THE 11 T DIPOLE FULL ASSEMBLY SUBSTITUTING A STANDARD MBA.	290
FIGURE 11-11: PERSISTENT CURRENT EFFECT ON B_z , IN DC CONDITIONS AS FUNCTION OF THE EXCITATION CURRENT, FOR THE TWO APERTURES OF MBHDP101, COMPARED TO CALCULATIONS. AN ARTIFICIAL OFFSET IS ADDED ON PURPOSE TO THE CURVE FOR THE 2D CALCULATIONS TO FACILITATE THE COMPARISON. THE REFERENCE RADIUS IS 17 MM.	292
FIGURE 11-12: MEASURED AND MODELLED TRANSFER FUNCTION AS A FUNCTION OF THE EXCITATION CURRENT IN DC CONDITIONS.	293
FIGURE 11-13: QUENCH PERFORMANCE OF SINGLE APERTURE MODEL MBHSP01.	294
FIGURE 11-14: QUENCH PERFORMANCE OF SINGLE APERTURE MODEL MBHSP02.	295
FIGURE 11-15: QUENCH PERFORMANCE OF SINGLE APERTURE MODEL MBHSP03.	295
FIGURE 11-16: QUENCH PERFORMANCE OF THE TWO-IN-ONE MODEL MBHDP01 DURING THE ORIGINAL TRAINING CARRIED OUT IN THE BEGINNING OF 2015.	295
FIGURE 11-17: QUENCH PERFORMANCE OF THE TWO-IN-ONE MODEL MBHDP01 DURING THE SECOND TEST CAMPAIGN CARRIED OUT IN JUNE-JULY 2016.	296
FIGURE 11-18: QUENCH PERFORMANCE OF THE SINGLE APERTURE MODEL MBHSP101.	297
FIGURE 11-19: QUENCH PERFORMANCE OF THE SINGLE APERTURE MODEL MBHSP102.	297
FIGURE 11-20: QUENCH PERFORMANCE OF THE SINGLE APERTURE MODEL MBHSP103.	298
FIGURE 11-21: QUENCH PERFORMANCE OF THE SINGLE APERTURE MODEL MBHSP104, COMPARED TO THE MODELS MBHSP102 AND MBHSP103 ON THE RIGHT.	298
FIGURE 11-22: QUENCH PERFORMANCE OF THE TWO-IN-ONE MODEL MBHDP101.	298
FIGURE 11-23: SCHEMATIC OF THE QUENCH HEATER CIRCUITS FOR ONE APERTURE OF AN MBH (LEFT), AND QUENCH HEATER GEOMETRY (RIGHT).	299
FIGURE 11-24: TRANSFER FUNCTION DIFFERENCE BETWEEN THE 11 T DIPOLE FULL ASSEMBLY AND THE MB, AND REQUIRED TRIM CURRENT (IN RED) TO COMPENSATE FOR THE DIFFERENCE.	300
FIGURE 11-25: MAIN DIPOLE CIRCUIT (RB.A67) CONFIGURATION FOR THE HL-LHC WITH THE 11T TRIM POWER CONVERTER.	300
FIGURE 11-26: MAIN DIPOLE CIRCUIT (RB.A78) CONFIGURATION FOR THE HL-LHC WITH THE 11 T TRIM POWER CONVERTER.	300
FIGURE 11-27: 11T TRIM CURRENTS FOR THREE LHC ENERGY LEVELS (RUN2, NOMINAL AND ULTIMATE).	301
FIGURE 11-28: CIRCUIT REPRESENTATION OF THE RB CIRCUIT WITH THE 11T MAGNETS AND THE POWER CONVERTER (CROWBAR INCLUDED).	302
FIGURE 11-29: TRIM PC CURRENT-VOLTAGE LOCUS FOR NOMINAL OPERATION AND OPERATION EXTREMUMS.	302
FIGURE 11-30: CROSS-SECTION OF THE CCC.	306
FIGURE 11-31: CCC COLD MASS (MBS SIDE)	307
FIGURE 11-32: CCC COLD MASS (QEN SIDE)	307
FIGURE 12-1: SCHEMATIC OF HL-LHC HIGH LUMINOSITY EXPERIMENTS INSTRUMENTATION AREAS. LEFT, CONNECTION BETWEEN Q1 AND TAXS. RIGHT, BUFFER ZONE BETWEEN SECTOR VALVES.	316
FIGURE 12-2: MEASURED ELECTRICAL RESISTIVITY OF INERMET 180 AS A FUNCTION OF TEMPERATURE. BATCH 1 CORRESPONDS TO REFERENCE NUMBER 8017006 AND BATCH 2 TO REFERENCE 802482. THE SAMPLE DIMENSIONS OF BATCH 1 AND 2 HAVE BEEN 2 MM X 2 MM X 73 MM.	320
FIGURE 12-3: (LEFT) TYPICAL INERMET 180 MAGNETIC PERMEABILITY AS A FUNCTION OF TEMPERATURE. VALUES OBTAINED FROM MEASUREMENT AT H=7162 KA/M. (RIGHT) TYPICAL INERMET 180 MAGNETIC PERMEABILITY AS A FUNCTION OF MAGNETIC FIELD. VALUES AT ROOM TEMPERATURE AND 4.2K.	321
FIGURE 12-4: GRAPH OF THE INERMET 180 THERMAL CONDUCTIVITY AS A FUNCTION OF TEMPERATURE. THE THERMAL CONDUCTIVITY OF ONE SAMPLE (802482) HAS BEEN MEASURED UP TO 70 K, WHILE FOR THE OTHER (8017006) THE TEMPERATURE RANGE HAS BEEN EXTENDED UP TO ROOM TEMPERATURE.	321
FIGURE 12-5: MECHANICAL DESIGN OF THE BEAM SCREEN WITH SHIELDING.	322
FIGURE 12-6: DEFORMATION OF THE BEAM SCREEN DURING A MAGNET QUENCH.	322
FIGURE 12-7: VON MISES STRESS FIELD IN THE BEAM SCREEN AND COLD BORE DURING A MAGNET QUENCH.	322
FIGURE 12-8: MODEL OF THE THERMAL LINK BETWEEN THE TUNGSTEN ABSORBER AND THE COOLING TUBE.	323

FIGURE 12-9: TEMPERATURE PROFILE OF THE HEAT TRANSFER FROM THE TUNGSTEN ABSORBER TO THE COOLING TUBES.	323
FIGURE 12-10: INFLUENCE OF THE NUMBER AND WIDTH OF THE THERMAL LINKS (0.5 MM THICK) ON THE TEMPERATURE DIFFERENCE BETWEEN THE COOLING HE GAS AND THE W ABSORBERS.....	323
FIGURE 13-1: CHARGE COLLECTION EFFICIENCY FOR SILICON AND DIAMOND DETECTORS WITH INCREASING RADIATION FLUENCE IN A CRYOGENIC ENVIRONMENT.	329
FIGURE 13-2: SCHEMATIC REPRESENTATION OF THE ASIC IMPLEMENTATION CURRENTLY UNDER DEVELOPMENT.	329
FIGURE 13-3: COMPARISON OF THE NEW LHC ORBIT SYSTEM ELECTRONICS WITH THE EXISTING SYSTEM DURING A VAN DER MEER SCAN. ...	331
FIGURE 13-4: A SKETCH DEMONSTRATING THE BEAM GAS VERTEX MEASUREMENT CONCEPT.	334
FIGURE 13-5: THE DEMONSTRATOR BEAM GAS VERTEX DETECTOR INSTALLED IN THE LHC DURING LS1.....	334
FIGURE 13-6: GAS JET PROFILE MONITORING SET-UP.	335
FIGURE 13-7: ILLUSTRATION OF THE COMPENSATION PRINCIPLE [12]. HERE LR.L5 AND LR.R5 INDICATE SCHEMATICALLY THE POTENTIAL POSITION OF COMPENSATING WIRES.	338
FIGURE 13-8: SKETCH OF AN ELECTRON COOLER TYPE LAYOUT FOR LONG-RANGE BEAM-BEAM COMPENSATION.	339
FIGURE 13-9: TECHNICAL DRAWING OF THE WIRE-IN-JAW COLLIMATOR DESIGN.	340
FIGURE 14-1: OVERVIEW OF THE PRESENT INJECTION SYSTEM INTO THE LHC AND THE ASSOCIATED PROTECTION DEVICES (BEAM 1, IR2). THE BEAM IS INJECTED FROM THE LEFT HAND SIDE.	343
FIGURE 14-2: PRELIMINARY DESIGN OF THE THREE TDIS TANKS, SUPPORTS AND VACUUM TRANSITION CHAMBERS.	344
FIGURE 14-3: ENERGY DEPOSITION IN A TDIS CONSISTING OF THREE MODULES (GRAPHITE, GRAPHITE AND ALUMINIUM - COPPER) FOR GRAZING BEAM IMPACT AND SHOWING THE EFFECT OF A 1 Σ ALIGNMENT DIFFERENCE BETWEEN THE FIRST AND SECOND MODULE.....	345
FIGURE 14-4: POSSIBLE SHIELDING INSIDE THE D1 CRYOSTAT.	346
FIGURE 14-5: FRACTION OF 5 Σ SINGLE PARTICLE EMITTANCE ABSORBED BY THE DIFFERENT INJECTION PROTECTION ABSORBERS TDIS, TCLIA, OR TCLIB FOR DIFFERENT INJECTION KICKER AMPLITUDES.	347
FIGURE 14-6: VIEW OF THE CAPACITIVELY COUPLED EXTREMITY OF THE MKI BEAM SCREEN SUPPORTING THE 24 SCREEN CONDUCTORS AND THE CONDUCTOR OVERLAP.	348
FIGURE 14-7: SWEEP PATH OF 25 NS SPACING LHC BEAM ON TDE DUMP BLOCK IN CASE OF A REGULAR DUMP AND IN CASE 2 HORIZONTAL DILUTION KICKERS WOULD NOT BE FIRING.	349
FIGURE 14-8: TRANSVERSE ENERGY DENSITY DISTRIBUTION IN THE TDE CORE FOR A REGULAR DUMP OF HL-LHC BEAMS, AND LONGITUDINAL ENERGY DENSITY DISTRIBUTION ALONG THE CORE FOR A REGULAR DUMP AND FOR A CASE WHERE 2 HORIZONTAL DILUTION KICKERS ARE NOT FIRING. THE FIGURE ON THE RIGHT SHOWS RESULTS BOTH FOR STANDARD HL-LHC BEAMS WITH 2.3×10^{11} PROTONS PER BUNCH AND AN EMITTANCE OF 2.1 MM RAD, AND FOR BCMS BEAMS WITH 2.0×10^{11} PROTONS PER BUNCH AND AN EMITTANCE OF 1.37 MM RAD.	350
FIGURE 14-9: SCHEMATIC LAYOUT OF THE BEAM DUMP AREA RIGHT OF P6 AS USED DURING LHC RUN 1, SHOWING THE EXTRACTION ABSORBER ELEMENT TCDS ON BEAM 2 AND THE TCDQ ON BEAM 1.....	350
FIGURE 14-10: PARTICLE DENSITY AT THE TCDQ IN CASE OF TYPE 1 AND Typ2 MKD ERRATICS.	351
FIGURE 14-11: ENERGY DENSITY DISTRIBUTION ALONG THE PRESENT TCDQ ABSORBER IN CASE OF A TYPE 2 MKD ERRATIC FOR STANDARD HL-LHC, BCMS AND LHC BEAMS.	351
FIGURE 14-12: ENERGY DENSITY DISTRIBUTION ALONG THE PRESENT TCDS ABSORBER IN CASE OF A TYPE 2 MKD ERRATIC FOR STANDARD HL-LHC, BCMS AND LHC BEAMS.	352
FIGURE 15-1: VOLUME RESERVED FOR THE INSTALLATION OF THE NEW COLD BOX UNIT DEDICATED TO RF SYSTEM COOLING (LIGHT BLUE). .	356
FIGURE 15-2: VIEW OF THE LHC CIVIL WORKS AT P4.	356
FIGURE 15-3: INTEGRATION 3D MODEL OF THE HL-LHC MACHINE. FROM LEFT TO RIGHT: Q1, Q2,Q3, D1, CORRECTOR PACKAGE, DFX, DFM, LBBR COMPENSATORS, TAXN, D2, 4 CRAB CAVITIES CRYO MODULES, Q4.....	359
FIGURE 15-4: ASSONOMETRIC VIEW OF THE HL-LHC UNDERGROUND CIVIL ENGINEERING INFRASTRUCTURES AS IT WOULD APPEAR IN IP1.	360
FIGURE 15-5: TOP VIEW OF THE HL-LHC UNDERGROUND CIVIL ENGINEERING INFRASTRUCTURES AS IT WOULD APPEAR IN IP1.....	361
FIGURE 15-6: THE CAVERN (US) HOSTING THE COLD BOX WITH OTHER TECHNICAL SERVICES.	361
FIGURE 15-7: INSTALLATION OF THE DFX IN THE UR AND ROUTING OF THE SC LINK TO THE TOP OF THE LHC MACHINE TUNNEL VIA THE UL GALLERY. TOP VIEW.	362
FIGURE 15-8: THE UL GALLERY WITH THE CRYOGENIC AND SUPERCONDUCTING LINK ROUTING AND THEIR VERTICAL CONNECTION TO THE LHC MACHINE TUNNEL.	362
FIGURE 15-9: THE AXONOMETRIC VIEW THE UA WITH THE WAVEGUIDE PROVIDING RF POWERING TO THE CRAB CAVITY INSTALLED IN THE LHC AND THE TETRODES INSTALLED ALONG THE UA.	363

FIGURE 15-11: THE LHC POINT 5 WITH THE NEW HL-LHC SURFACE BUILDING.....	364
FIGURE 15-10: THE LHC POINT 1 WITH THE NEW HL-LHC SURFACE BUILDING.....	365
FIGURE 15-12: CONFIGURATION OF FSI CHANNELS PER CRAB CAVITY.	368
FIGURE 15-13: FSI SYSTEM CONFIGURATION TO MONITOR THE CRAB CAVITIES.....	368
FIGURE 15-14: REQUIREMENTS CONCERNING THE MECHANICAL AXES OF THE MAGNETS.....	369
FIGURE 15-15: CONFIGURATION OF SENSORS ON THE INNER TRIPLET.....	370
FIGURE 15-16: RADIAL CONFIGURATION OF SENSORS AROUND IP.....	370
FIGURE 15-17: VERTICAL CONFIGURATION OF SENSORS AROUND IP.....	370
FIGURE 16-1: SCHEMATIC VIEW OF THE IT STRING.	385
FIGURE 16-2: INTEGRATION OF THE HL-LHC IT STRING IN SM18.....	386
FIGURE 16-3: DELIVERY SCHEDULE OF THE CRYO-MAGNET ASSEMBLIES FOR THE IT STRING.....	386
FIGURE 16-4: CRYOGENIC COOLING SYSTEM CAPACITY: ESTIMATE OF CONSUMPTION. THE UPPER PART SHOWS THE ESTIMATED LIQUID HE PRODUCTION NEEDS. THE LOWER PART SHOWS THE ESTIMATED PUMPING CAPACITY NEEDS.	388
FIGURE 16-5: DEMINERALISED WATER CONSUMPTION IN THE SM18 FROM 2016 TILL 2023.	388
FIGURE 16-6 SM18 POWER CONVERTERS AND THEIR CONNECTIONS TO THE ELECTRICAL NETWORK.	389
FIGURE 17-1: OVERALL INDICATIVE AXONOMETRY OF THE UNDERGROUND CIVIL INFRASTRUCTURES (HL-LHC IN BLUE).....	393
FIGURE 17-2: P1 INDICATIVE UNDERGROUND AXONOMETRY.	395
FIGURE 17-3: P5 INDICATIVE UNDERGROUND AXONOMETRY.	395
FIGURE 17-4: P1 INDICATIVE SURFACE AXONOMETRY.	398
FIGURE 17-5: P1 SURFACE LAYOUT.	398
FIGURE 17-6: P5 INDICATIVE SURFACE AXONOMETRY.	399
FIGURE 17-7: P5 SURFACE LAYOUT.	399
FIGURE 17-8: EXCAVATOR WITH HYDRAULIC CUTTING HEADS.	401
FIGURE 17-9: ROADHEADER TYPE MACHINE.	401
FIGURE 17-10: LINKING UP CYLINDERS OF ICE TO CONSTRUCT A TEMPORARY WALL.	402
FIGURE 17-11: HYDRAULIC HAMMER METHOD OF EXCAVATION.	402
FIGURE 17-12: TYPICAL ROCK SUPPORT STRATEGY DETAIL.....	403
FIGURE 17-13: GEOGRAPHICAL OVERVIEW OF CERN'S EXISTING ELECTRICAL NETWORK.	405
FIGURE 17-14: SINGLE LINE DIAGRAM OF THE ACTUAL CERN TRANSMISSION NETWORK (LHC1 AND LHC5 IN BOLD).....	406
FIGURE 17-15: LOCATION OF THE NEW 400 kV SUBSTATION BE2.	407
FIGURE 17-16: SINGLE LINE DIAGRAM OF THE CERN TRANSMISSION NETWORK AT THE END OF 2018, WITH BE2.	408
FIGURE 17-17: SINGLE LINE DIAGRAM OF THE TRANSMISSION NETWORK SUPPLYING LHC1.	410
FIGURE 17-18: SINGLE LINE DIAGRAM OF THE TRANSMISSION NETWORK SUPPLYING LHC6 AND LHC5.....	413
FIGURE 17-19: SINGLE LINE DIAGRAM OF THE HIGH VOLTAGE DISTRIBUTION NETWORK IN LHC1.	414
FIGURE 17-20: SINGLE LINE DIAGRAM OF THE HIGH VOLTAGE DISTRIBUTION NETWORK IN LHC5.	415
FIGURE 17-21: SINGLE LINE DIAGRAM OF THE 3.3 kV DISTRIBUTION IN SU4 – LHC4.	416
FIGURE 17-22: LOW VOLTAGE DISTRIBUTION LHC1.	417
FIGURE 17-23: ENS SYSTEM ARCHITECTURE.	419
FIGURE 17-24: BENDING RADIUS OF THE DC CABLES.....	420
FIGURE 17-25 – WATER COOLED CABLE TECHNOLOGY AND WATER COOLED CABLES USED IN LHC.....	420
FIGURE 17-26 – ASSIGNMENT OF CABLE LADDERS IN UR.....	423
FIGURE 17-27: PRELIMINARY UNDERGROUND ACCESS ZONING AND ACCESS ELEMENTS OF SITE 1. ZONING OF SITE 5 WILL BE SIMILAR AS APPLICABLE WITH THE EXCEPTION OF EXISTING ACCESS POINT AND SERVICE TUNNEL LOCATIONS.....	432
FIGURE 17-28: SD BUILDING LIFT MACHINERY.....	437
FIGURE 17-29: UW CAVERN EOT CRANES.	438
FIGURE 17-30: MOT CRANE IN UA GALLERY.	439
FIGURE 17-31: MOT CRANE IN UL GALLERY.....	439
FIGURE 17-32: DRAWBRIDGE IN US CAVERN.	441
FIGURE 17-33: MOBILE SHIELDING DOOR.....	441
FIGURE 18-1: STORAGE EVOLUTION.	446
FIGURE 18-2: PROPOSED CONTROLS ARCHITECTURE.....	446

FIGURE 19-1: RESIDUAL DOSE RATES IN UNITS OF $\mu\text{Sv}/\text{h}$ AROUND THE LOW-BETA TRIPLET QUADRUPOLE AND D1 MAGNETS FOR THE NOMINAL SCENARIO AFTER ONE MONTH OF COOLING TIME. DOSES ARE SHOWN FOR A HORIZONTAL SECTION AT THE LEVEL OF THE BEAM LINE. THE ORIGIN OF THE COORDINATE FRAME IS AT THE INTERACTION POINT.	451
FIGURE 19-2: RESIDUAL DOSE RATE PROFILES FOR THE NOMINAL SCENARIO IN THE AISLE AT 40 CM DISTANCE FROM THE CRYOSTAT AT FOUR DIFFERENT COOLING TIMES: 1 WEEK (BLUE), 1 MONTH (RED), 4 MONTHS (GREEN) AND 1 YEAR (VIOLET).	452
FIGURE 19-3: RESIDUAL DOSE RATES IN UNITS OF $\mu\text{Sv}/\text{h}$ AROUND THE LOW-BETA TRIPLET QUADRUPOLE AND D1 MAGNETS FOR THE ULTIMATE SCENARIO AFTER ONE MONTH OF COOLING TIME. DOSES ARE SHOWN FOR A HORIZONTAL SECTION AT THE LEVEL OF THE BEAM LINE. THE ORIGIN OF THE COORDINATE FRAME IS AT THE INTERACTION POINT.	452
FIGURE 19-4: RESIDUAL DOSE RATE PROFILES FOR THE ULTIMATE SCENARIO IN THE AISLE AT 40 CM FROM THE CRYOSTAT AT FOUR DIFFERENT COOLING TIMES: 1 WEEK (BLUE), 1 MONTH (RED), 4 MONTHS (GREEN) AND 1 YEAR (VIOLET).	452
FIGURE 19-5: RESIDUAL DOSE RATE PROFILES FOR THE NOMINAL (LIGHT-BLUE) AND ULTIMATE SCENARIOS (PINK) ALONG THE AISLE AT 40 CM DISTANCE TO THE CRYOSTAT AFTER ONE MONTH COOLING TIME.	453
FIGURE 19-6: DIFFERENT CROSS-SECTIONAL VIEWS OF THE FLUKA GEOMETRY OF THE UA GALLERY AND ELBOW INCLUDING THE EMERGENCY EXIT TOWARD LHC TUNNEL.	454
FIGURE 19-7: EFFECTIVE DOSE MAP IN THE UA ELBOW AND IN THE UA GALLERY, DUE TO THE FULL LOSS OF ONE BEAM IN FRONT OF THE EMERGENCY EXIT CONNECTION TO THE LHC TUNNEL.	454
FIGURE 19-8: EFFECTIVE DOSE PROFILE IN THE UA GALLERY, DUE TO THE FULL LOSS OF ONE BEAM IN FRONT OF THE CLOSEST CORE TO THE UA.	455
FIGURE 19-9: DIFFERENT SECTION VIEWS OF THE UL GALLERY GEOMETRY MODEL.	455
FIGURE 19-10: EFFECTIVE DOSE MAP (BOTTOM) AND THE DOSE PROFILE (TOP) ALONG THE UL GALLERY, DUE TO THE FULL LOSS OF ONE BEAM ON A BULKY OBJECT IN FRONT OF ONE OF THE CONNECTIONS CORES TO THE LHC TUNNEL.	456
FIGURE 19-11: EFFECTIVE DOSE MAP (BOTTOM) AND THE DOSE PROFILE (TOP) ALONG THE UL GALLERY WITH THE ADDITION OF AN IRON SHIELDING WALL 40 CM THICK, DUE TO THE FULL LOSS OF ONE BEAM ON A BULKY OBJECT IN FRONT OF ONE OF THE CONNECTIONS CORES TO THE LHC TUNNEL.	457
FIGURE 19-12: ON TOP, AMBIENT DOSE EQUIVALENT RATE MAP DUE TO STRAY RADIATION FOR MACHINE OPERATING AT ULTIMATE LUMINOSITY ($7.5 \times 10^{34} \text{ cm}^{-2} \text{ s}^{-1}$); ON THE BOTTOM, AMBIENT DOSE EQUIVALENT RATE PROFILE ALONG THE MACHINE.	458
FIGURE B-1: MAGNET REPRESENTATION FOR THE LHC INSERTION REGION.	479
FIGURE B-2: MAGNET REPRESENTATION FOR THE HL-LHC INSERTION REGION AT POINT 1 AND POINT 5.	479
FIGURE B-3: 11T CRYO-ASSEMBLY REPLACEMENT OF AN MB MAGNET FOR CIRCUIT RB.A67.	479
FIGURE B-4: 11T CRYO-ASSEMBLY REPLACEMENT OF AN MB MAGNET FOR CIRCUIT RB.A78.	479
FIGURE B-5: CIRCUIT LAYOUT OF THE HL-LHC INNER TRIPLET.	480
FIGURE B-6: CONNECTIONS TO COLD POWERING OF THE INNER TRIPLET POWER CONVERTERS.	481
FIGURE B-7: CIRCUIT LAYOUT OF EACH INNER TRIPLET CORRECTOR CIRCUIT (MCBXF).	481
FIGURE B-8: SUPERFERRIC, HIGH ORDER CORRECTORS' CIRCUIT LAYOUT.	482
FIGURE B-9: D1 MAGNET CIRCUIT LAYOUT.	483
FIGURE B-10: D2 MAGNET CIRCUIT LAYOUT.	483
FIGURE B-11: D2 CORRECTORS' CIRCUIT LAYOUT.	484
FIGURE B-12: Q4, Q5 AND Q6 CIRCUIT LAYOUT (NO CHANGE WITH RESPECT TO THE PRESENT LHC LAYOUT).	484
FIGURE B-13: CIRCUIT LAYOUT OF EACH OF THE 16 CORRECTOR CIRCUITS FOR Q4, Q5 AND Q6.	485
FIGURE B-14 – CIRCUIT LAYOUT OF THE 11T TRIM CIRCUIT.	485

Table of tables

TABLE 1-1: HIGH LUMINOSITY LHC MAIN PARAMETERS FOR PROTON COLLISIONS (RE-BASELINING SUMMER 2016).....	8
TABLE 1-2: HIGH LUMINOSITY LHC PARAMETERS FOR ION COLLISIONS.	8
TABLE 2-1: HL-LHC NOMINAL PARAMETERS FOR 25 NS OPERATION [22] FOR TWO PRODUCTION MODES OF THE LHC BEAM IN THE INJECTORS DESCRIBED IN REF. [8].....	29
TABLE 2-2: MAIN HL-LHC OPTICS VARIANTS CURRENTLY UNDER STUDY. THE BASELINE COLLISION OPTICS CORRESPONDS TO $B^* = 20$ CM IN BOTH TRANSVERSE PLANES (ROUND OPTICS) WITH A FULL CROSSING ANGLE OF 510 MRAD. OTHER COLLISION OPTICS ARE AVAILABLE, ROUND OR FLAT, FOR DEDICATED STUDIES. THE VALUES OF B^* REFER TO IP1 AND 5 AND THOSE REPORTED IN PARENTHESES REFER TO SOLUTIONS AVAILABLE FOR STUDIES.....	36
TABLE 2-3: NEW OR REFURBISHED QUADRUPOLES FOR HL-LHC, ALL OPERATING AT 1.9 K, APART FROM Q6.	38
TABLE 2-4: SEPARATION AND CORRECTOR DIPOLE MAGNETS FOR HL-LHC, ALL OPERATING AT 1.9 K. THE ORBIT CORRECTORS CAN BE NESTED OR CONSECUTIVE AS INDICATED. THE ORDER OF THE CORRECTORS REFERS TO IP5 RIGHT OF BEAM 1 STARTING FROM THE IP5.	38
TABLE 2-5: NEW MULTIPOLAR SUPERFERRIC CORRECTORS FOR HL-LHC, ALL OPERATING AT 1.9 K.	39
TABLE 2-6: NEW ABSORBERS FOR HL-LHC, ALL OPERATING AT ROOM TEMPERATURE.....	40
TABLE 2-7: AVAILABLE OPTICAL CONFIGURATIONS FOR THE BASELINE LAYOUT. IR3 AND IR7 ARE NOT INCLUDED AS THEY HAVE STATIC OPTICS FROM INJECTION TO COLLISION AND DO NOT TAKE PART IN THE ATS SCHEME. IR4 AND IR6 TAKE PART IN THE ATS AND THIS IS HIGHLIGHTED HERE, WHERE THE “NO ATS” CONFIGURATION CORRESPONDS TO AN INJECTION-COMPATIBLE OPTICS KEPT CONSTANT UP TO TOP ENERGY. THE TELESCOPIC SQUEEZE FACTORS ARE INDICATED IN PARENTHESIS. SOME ALTERNATIVE CONFIGURATIONS ARE ALSO SHOWN. THE PRE-SQUEEZE UP TO 70 CM COULD BE IMPLEMENTED DURING THE RAMP. IN ALTERNATIVE ALSO PART OF THE ATS SQUEEZE COULD BE ANTICIPATED DURING OR AFTER THE RAMP IF ENHANCED OCTUPOLES EFFECT IS NEEDED.	40
TABLE 2-8: NOMINAL CURRENT OF MAIN AND TRIM POWER SUPPLIES FOR THE DIFFERENT POWERING SCHEMES ASSUMING A MAXIMUM TRIPLET GRADIENT OF 132.6 T/M, A MAGNET INDUCTANCE OF 8.21 MH/M, AND THE HLLHV1.3 LAYOUT [92][93]. THE POWER CONVERTER AND THE CIRCUITS ARE RATED FOR EQUAL OR HIGHER CURRENT (SEE CHAPTER 6B, TABLE 6B-3 AND 6B-4).	43
TABLE 2-9: TOLERANCES ON THE CURRENT MODULATION ACHIEVABLE WITH CLASS 1 AND CLASS 2 POWER CONVERTERS IN THE CURRENT- AND VOLTAGE-CONTROL REGIME, RESPECTIVELY. FOR THE VOLTAGE-CONTROL REGIME, THE VALUES ARE GIVEN AS 1σ R.M.S. VALUES, WHILE FOR THE CURRENT-CONTROL REGIME THE UNITS PPM ARE USED, MEANING THAT $DI \text{ PPM} = I_{\text{NOISE,PCA}}/I_{\text{MAX,PC}}[A]$	43
TABLE 2-10: TUNE SHIFT INDUCED BY UNIFORMLY DISTRIBUTED RANDOM CURRENT ERROR OF ± 1 PPM FOR DIFFERENT POWERING SCHEMES, ASSUMING $I_{\text{MAX}}=17.4$ kA AND NOMINAL FIELD GRADIENT OF 140 T/M FOR ALL IT MAGNETS. THE SIMULATIONS HAVE BEEN PERFORMED FOR HLLHCV1.0, WITH ROUND OPTICS AND $B^*=0.15$ M, AND, FOR THE SAKE OF COMPARISON, ALSO FOR LHC V6.503, WITH ROUND OPTICS AND $B^*=0.55$ M. THE RESULTS CAN BE APPROXIMATELY EXTRAPOLATED TO HLLHCV1.3 BY SCALING WITH THE RATIO OF THE MAXIMUM CURRENT, NAMELY 16.5/17.4.	44
TABLE 2-11: PRELIMINARY CIRCUIT SPECIFICATION FOR HL-LHC SEPARATION AND CORRECTOR DIPOLES.....	45
TABLE 2-12: PARAMETERS OF SIMULATION CASES FOR EVALUATION OF BEAM-BEAM EFFECTS DURING LUMINOSITY LEVELLING, FOR THE SCHEME WITH FOUR CRAB CAVITIES (FULL CRABBING).	61
TABLE 2-13: SUMMARY OF THE IMPEDANCE-INDUCED HEAT LOAD COMPUTATIONS FOR SEVERAL KEY SYSTEMS.....	63
TABLE 2-14: IMPEDANCE-INDUCED HEAT LOADS FOR THE DIFFERENT TYPES OF BEAM SCREENS (INCLUDING THE EFFECTS OF THE LONGITUDINAL WELD, TWO COUNTER-ROTATING BEAMS, AND THE MAGNETO-RESISTANCE) VS. TEMPERATURE: VALUES ARE GIVEN FOR THE 25 NS BEAM.	65
TABLE 2-15: INTEGRATED PERFORMANCE ESTIMATE FOR THE NOMINAL SCENARIO.	69
TABLE 2-16: PARAMETERS ASSUMED FOR HL-LHC PERFORMANCE ESTIMATE.	69
TABLE 2-17: PARAMETERS OF THE HL-LHC BASELINE SCENARIOS AND MAIN ALTERNATIVES.	72
TABLE 2-18: AVERAGE VALUES OF PRINCIPAL BEAM PARAMETERS AT THE START OF PHYSICS [233][238].....	79
TABLE 3-1: OVERVIEW OF THE MAIN PARAMETERS OF THE INSERTION MAGNETS – SEE THE TEXT FOR DEFINITIONS OF FOOTNOTES.....	98
TABLE 3-2: EXPECTED FIELD QUALITY IN THE TRIPLET, MULTIPOLES IN UNITS AT 50 MM REFERENCE RADIUS.....	101
TABLE 3-3: OVERVIEW OF THE MAIN PARAMETERS OF THE TRIPLET CORRECTOR MAGNETS.	105
TABLE 3-4: EXPECTED FIELD QUALITY OF D1, MULTIPOLES GIVEN IN UNITS AT 50 MM REFERENCE RADIUS. STRAIGHT PART.	107
TABLE 3-5: EXPECTED FIELD QUALITY OF D2, MULTIPOLES GIVEN IN UNITS AT 35 MM REFERENCE RADIUS.	108
TABLE 4-1: RELEVANT RF PARAMETERS FOR HL-LHC CRAB CAVITIES.	119

TABLE 4-2: OVERVIEW OF CRAB CAVITY PLANNING FROM R&D TO INSTALLATION IN THE LHC.....	120
TABLE 4-3: CRYOMODULE ENVELOPE DIMENSIONS.	141
TABLE 4-4: DETUNING RANGES FOR THE LHC AND SPS.	142
TABLE 4-5: RELEVANT RF PARAMETERS FOR 800MHZ RF CAVITIES.....	144
TABLE 4-6: RELEVANT RF PARAMETERS FOR 200 MHz RF CAVITIES.	144
TABLE 5-1: COLLIMATORS FOR THE LHC RUN 2, STARTING IN 2015. FOR EACH TYPE, ACRONYMS, ROTATION PLANE (HORIZONTAL, VERTICAL OR SKEW), MATERIAL AND NUMBER OF DEVICES, SUMMED OVER THE TWO BEAMS, ARE GIVEN. FOR COMPLETENESS, MOVABLE INJECTION AND DUMP PROTECTION DEVICES ARE ALSO LISTED. IN ADDITION, THE COLLIMATION SYSTEM COMPRISES 10 FIXED-APERTURE ABSORBERS IN IR3 AND IR7 TO REDUCE TOTAL DOSES TO WORM MAGNETS OF THE CLEANING INSERTIONS.	151
TABLE 5-2: KEY PARAMETERS OF TCLD COLLIMATORS.....	160
TABLE 5-3: PARAMETERS OF TCSMP COLLIMATORS.	166
TABLE 5-4: EQUIPMENT PARAMETERS OF THE TCTPM.....	168
TABLE 5-5: HOLLOW ELECTRON BEAM EQUIPMENT PARAMETERS.....	171
TABLE 6B-1: SUPERCONDUCTING MAGNETS POWERED FROM THE RR GALLERIES.	191
TABLE 6B-2: SUPERCONDUCTING MAGNETS POWERED FROM THE UR GALLERIES.....	192
TABLE 6B-3: MAGNETS AT EACH SIDE OF LHC P1 AND P5.	199
TABLE 6B-4: LIST OF NEW POWER CONVERTERS FOR INNER TRIPLET AND MATCHING SECTION MAGNETS.	199
TABLE 6B-5: SUMMARY OF PRECISION REQUIREMENTS PER MAGNET.....	204
TABLE 6B-6: LHC ACCURACY CLASSES DEFINITION.	206
TABLE 7-1: CIRCUITS PARAMETERS.	219
TABLE 7-2: HOT SPOT TEMPERATURE IN THE TRIPLET MAGNETS IN CASE OF A QUENCH USING OUTER-LAYER QUENCH HEATERS (O-QH), OUTER- AND INNER-LAYER QUENCH HEATERS (O-QH+I-QH) AND OUTER-LAYER QUENCH HEATERS AND CLIQ (O-QH+CLIQ). THE RANGE INDICATES THE SPREAD OF THE SIMULATION RESULTS DEPENDING ON THE QUENCH LOCATION AND THE VARIATION OF CABLE PARAMETERS WITHIN THEIR SPECIFICATION.	221
TABLE 7-3: PEAK VOLTAGE TO GROUND IN THE TRIPLET MAGNETS IN CASE OF A QUENCH USING OUTER LAYER QUENCH HEATERS (O-QH), OUTER AND INNER LAYER QUENCH HEATERS (O-QH+I-QH), OUTER LAYER QUENCH HEATERS AND CLIQ (O-QH + CLIQ). THE RANGE INDICATES THE SPREAD OF THE SIMULATION RESULTS DEPENDING ON THE VARIATION OF CABLE PARAMETERS WITHIN THEIR SPECIFICATION.	221
TABLE 7-4: HOT SPOT TEMPERATURE IN THE TRIPLET MAGNETS IN CASE OF A QUENCH, WHEN ONE (F1) OR TWO (F2) QUENCH HEATER CIRCUITS DO NOT FUNCTION, USING OUTER-LAYER QUENCH HEATERS (O-QH), OUTER- AND INNER-LAYER QUENCH HEATERS (O-QH+I-QH) AND OUTER-LAYER QUENCH HEATERS AND CLIQ (O-QH + CLIQ). THE RANGE INDICATES THE SPREAD OF THE SIMULATION RESULTS DUE TO THE INITIAL LOCATION OF THE QUENCH.	222
TABLE 8-1: NOMINAL DESIGN LUMINOSITIES FOR P-P OPERATION FOR THE HL-LHC. IN PARENTHESIS THE VALUE ENVISAGED AS "ULTIMATE". THE LUMINOSITIES FOR THE LHC RUN-2 ARE ALSO INCLUDED FOR COMPARISON. TOTAL TARGETED INTEGRATED LUMINOSITY IN CMS AND ATLAS IS 3000 FB ⁻¹ ABOUT 12 YEARS AFTER UPGRADE.....	231
TABLE 8-2: ORIGINAL AND REDUCED INNER BEAM PIPE RADII LOCATED AT THE IPs VICINITY.	234
TABLE 8-3: TAXS DESIGN PARAMETERS FROM REF. [14].	237
TABLE 8-4: TAXS OPERATION PARAMETERS FROM REF. [15].....	238
TABLE 8-5: KEY DESIGN PARAMETERS FOR THE TAXN OF P1 AND P5.....	247
TABLE 8-6: TAXN OPERATIONAL PARAMETERS.	248
TABLE 9-1: LHC UPGRADED BEAM PARAMETERS FOR 25NS BUNCH SPACING.	254
TABLE 9-2: STATIC HEAT IN-LEAKS OF HL-LHC MACHINE (WITHOUT CONTINGENCY).	256
TABLE 9-3: DYNAMIC HEAT LOADS ON HL-LHC MACHINE (WITHOUT CONTINGENCY).	256
TABLE 9-4: INSTALLED CAPACITY REQUIREMENTS OF THE NEW CRYOGENIC PLANT AT P4.....	259
TABLE 9-5: INSTALLED CAPACITY REQUIREMENTS OF THE NEW CRYOGENIC PLANTS AT P1 AND P5.....	260
TABLE 9-6: BUILDING AND GENERAL SERVICE REQUIREMENT.....	260
TABLE 10-1: HEAT LOADS AT $5 \times 10^{34} \text{ cm}^{-2} \text{ s}^{-1}$ FOR DIFFERENT CROSSING SCHEMES AND ABSORBER IMPLEMENTATIONS.	269
TABLE 10-2: PREDICTED AND MEASURED ANNUAL HEH FLUENCE IN CRITICAL SHIELDED AREAS FOR A CUMULATED ATLAS/CMS LUMINOSITY OF 15 FB ⁻¹ DURING 2012 OPERATION, THEN EXTRAPOLATED BASED ON THE MEASUREMENT TO THE EXPECTED NOMINAL AND HL-LHC PERFORMANCE (50 FB ⁻¹ /Y FOR NOMINAL AND 250 FB ⁻¹ /Y FOR HL-LHC PERFORMANCE, EXCEPT FOR P8 WHERE 2012 CAN ALREADY BE	

CONSIDERED AS ALMOST NOMINAL AND HL-LHC REFERS TO A FIVE-FOLD INCREASE). FOR THE HL-LHC AN ESTIMATE FOR CORRESPONDING ANNUAL TID LEVELS IS ALSO GIVEN.	277
TABLE 11-1: MAIN PARAMETERS OF THE 11 T DIPOLE FULL ASSEMBLY.	285
TABLE 11-2: FIELD ERRORS – $R_{REF} = 17$ MM.	291
TABLE 11-3: MODELLED AND MEASURED GEOMETRIC MULTIPOLES. THE REFERENCE RADIUS IS 17 MM.	292
TABLE 11-4: MAIN PARAMETERS OF THE MBH.	293
TABLE 11-5: RB CIRCUIT CHARACTERISTICS IN THE CURRENT LHC CONFIGURATION AND AFTER THE INTRODUCTION OF 11 T DIPOLE FULL ASSEMBLY FOR CIRCUITS RB.A67 AND RB.A78.	301
TABLE 11-6: POWER CONVERTER MAIN PERFORMANCE REQUIREMENTS.	303
TABLE 11-7: INTERLOCK SYSTEMS.	303
TABLE 11-8: POWER CONVERTER ELECTRICAL PROTECTION.	303
TABLE 11-9: POWER CONVERTER INTERFACES.	304
TABLE 11-10: POWER CONVERTER RACK SPACE REQUIREMENTS.	304
TABLE 11-11: MAIN PARAMETERS OF THE CCC.	307
TABLE 12-1: SINGLE GAS SPECIES MOLECULAR GAS DENSITY (M^{-3}) TO SATISFY 100 H VACUUM LIFETIME IN THE LHC AND THE HL-LHC ASSUMING A SINGLE CIRCULATING BEAM [2].	312
TABLE 13-1: CHARACTERISTICS OF THE PROTOTYPE HL-LHC BLM SYSTEM ASIC.	330
TABLE 16-1: POTENTIAL BREAKDOWN OF A STANDARD HL-LHC YEAR UNTIL END RUN 4.	376
TABLE 16-2: BREAKDOWN OF TURNAROUND AND ESTIMATED MINIMUM TIME FOR EACH PHASE.	377
TABLE 16-3: OUTLINE OF INITIAL COMMISSIONING FOLLOWING LS3.	382
TABLE 16-4: CRYOGENIC COOLING NEEDS OF THE IT STRING.	387
TABLE 16-5 POWER CONVERTERS OF THE HL-LHC IT STRING.	389
TABLE 16-6: LENGTH AND ESTIMATED WEIGHT OF THE HEAVIEST CRYO-MAGNET ASSEMBLIES TO BE INSTALLED IN THE IT STRING.	390
TABLE 17-1: P1 UNDERGROUND STRUCTURES.	396
TABLE 17-2: P5 UNDERGROUND STRUCTURES.	396
TABLE 17-3: P1 SURFACE BUILDINGS.	398
TABLE 17-4: P5 SURFACE BUILDINGS.	399
TABLE 17-5: LOAD FORECAST MADE IN 2012, WITH THE HORIZON 2025 [5].	406
TABLE 17-6: HL-LHC LOADS IN P1.	409
TABLE 17-7: TOTAL POWER CONSUMPTION LHC1.	409
TABLE 17-8: HL-LHC LOADS IN LHC4.	411
TABLE 17-9: POWER CONSUMPTION LHC4.	411
TABLE 17-10: HL-LHC LOADS IN LHC5.	412
TABLE 17-11: POWER CONSUMPTION LHC5.	412
TABLE 17-12: POWER CONSUMPTION POINT 6.	413
TABLE 17-13: LOAD FORECAST FOR THE DIESEL GENERATORS IN LHC5.	417
TABLE 17-14: LOAD FORECAST FOR THE UPS IN LHC1 AND LHC5.	418
TABLE 17-15: INTENSITY REQUESTED AND CROSS-SECTION OF THE CABLES.	420
TABLE 17-16: ESTIMATED LENGTH OF THE DC CABLES.	421
TABLE 17-17: SUMMARY OF CABLE LOSSES.	421
TABLE 17-18: LIST OF SYSTEMS AND SUB-SYSTEMS AND ESTIMATED CABLE QUANTITIES.	423
TABLE 17-19: OVERALL COOLING POWER REQUIREMENTS AT P1.	424
TABLE 17-20: SYNTHESIS OF THE PRINCIPAL SAFETY, ACCESS, AND ALARM EQUIPMENT BY SYSTEM.	434
TABLE 17-21: MAIN LIFTS.	437
TABLE 17-22: MAIN OVERHEAD TRAVELLING CRANES.	437
TABLE 17-23: CRANES FOR RF INSTALLATION IN UA GALLERIES.	438
TABLE 17-24: CRANES FOR RF INSTALLATION IN UA GALLERIES.	439
TABLE 17-25: HOIST FOR THE LIFTING PUMPS OF THE WATER SUMPS.	440
TABLE 17-26: HOIST FOR MAINTENANCE OF UW CAVERN EQUIPMENT'S.	440
TABLE 17-27: HOIST FOR THE SHM BUILDINGS.	440
TABLE 17-28: DRAWBRIDGES.	440

TABLE 17-29: MOBILE SHIELDING DOORS.....	441
TABLE 19-1: LHC OPERATIONAL PARAMETERS. THE THIRD AND FOURTH COLUMNS REFER TO THE SO-CALLED ‘NOMINAL SCENARIO’, WHICH WILL LEAD TO A TOTAL INTEGRATED LUMINOSITY OF 3060 FB ⁻¹ . THE FIFTH AND SIXTH COLUMNS REFER TO THE SO-CALLED ‘ULTIMATE SCENARIO’. THIS SCENARIO WILL LEAD TO A TOTAL INTEGRATED LUMINOSITY OF 3910 FB ⁻¹ . THESE VALUES FOR THE TOTAL INTEGRATED LUMINOSITIES INCLUDE 310 FB ⁻¹ COLLECTED DURING THE OPERATIONAL PERIOD BEFORE LS3.....	450
TABLE C-1: TEST VALUES AT WARM AND COLD FOR A QXF COLD MASS.	486

Contributor list

O. Aberle	CERN, Accelerator & Technology Sector, CH-1211, Geneva, Switzerland
C. Adorisio	CERN, Accelerator & Technology Sector, CH-1211, Geneva, Switzerland
A. Adraktas	CERN, Accelerator & Technology Sector, CH-1211, Geneva, Switzerland
J. Albertone	CERN, Accelerator & Technology Sector, CH-1211, Geneva, Switzerland
L. Alberty	CERN, Accelerator & Technology Sector, CH-1211, Geneva, Switzerland
M. Alcaide Leon	CERN, Accelerator & Technology Sector, CH-1211, Geneva, Switzerland
D. Alesini	INFN-LNF, Via E. Fermi 40, 00044 Frascati, Rome, Italy
P. Alvarez Lopez	CERN, Accelerator & Technology Sector, CH-1211, Geneva, Switzerland
G. Ambrosio	Fermi National Accelerator Laboratory, Batavia, P.O. Box 500, IL, USA
M. Anerella	BNL, Brookhaven National Laboratory, Upton, NY 11973, USA
D. Angal-Kalinin	ASTeC, STFC, Daresbury Laboratory, Warrington WA4 4AD, UK
G. Apollinari	Fermi National Accelerator Laboratory, Batavia, P.O. Box 500, IL, USA
A. Apollonio	CERN, Accelerator & Technology Sector, CH-1211, Geneva, Switzerland
R.B. Appleby	UMAN, The University of Manchester, and the Cockcroft Institute, UK
G. Arduini	CERN, Accelerator & Technology Sector, CH-1211, Geneva, Switzerland
K. Artoos	CERN, Accelerator & Technology Sector, CH-1211, Geneva, Switzerland
S. Atieh	CERN, Accelerator & Technology Sector, CH-1211, Geneva, Switzerland
B. Auchmann	CERN, Accelerator & Technology Sector, CH-1211, Geneva, Switzerland
T. Baer	CERN, Accelerator & Technology Sector, CH-1211, Geneva, Switzerland
V. Baglin	CERN, Accelerator & Technology Sector, CH-1211, Geneva, Switzerland
M. Bajko	CERN, Accelerator & Technology Sector, CH-1211, Geneva, Switzerland
A. Ball	CERN, Physics & IT Sector, CH-1211, Geneva, Switzerland
A. Ballarino	CERN, Accelerator & Technology Sector, CH-1211, Geneva, Switzerland
S. Bally	CERN, Physics & IT Sector, CH-1211, Geneva, Switzerland
D. Banfi	EPFL, Lausanne, Switzerland
R. Barlow	UHUD, University of Huddersfield, Huddersfield, UK
M. Barnes	CERN, Accelerator & Technology Sector, CH-1211, Geneva, Switzerland
J. Barranco	EPFL, Lausanne, Switzerland
L. Barthelemy	CERN, Finance and Human Resources sector, CH-1211, Geneva, Switzerland
W. Bartmann	CERN, Accelerator & Technology Sector, CH-1211, Geneva, Switzerland
H. Bartosik	CERN, Accelerator & Technology Sector, CH-1211, Geneva, Switzerland
E. Barzi	Fermi National Accelerator Laboratory, Batavia, P.O. Box 500, IL, USA
M. Battistin	CERN, Accelerator & Technology Sector, CH-1211, Geneva, Switzerland
P. Baudrenghien	CERN, Accelerator & Technology Sector, CH-1211, Geneva, Switzerland
I. Bejar Alonso	CERN, Accelerator & Technology Sector, CH-1211, Geneva, Switzerland
S. Belomestnykh	BNL, Brookhaven National Laboratory, Upton, NY 11973, USA
A. Benoit	CERN, Accelerator & Technology Sector, CH-1211, Geneva, Switzerland
I. Ben-Zvi	BNL, Brookhaven National Laboratory, Upton, NY 11973, USA
A. Bertarelli	CERN, Accelerator & Technology Sector, CH-1211, Geneva, Switzerland
S. Bertolasi	CERN, Accelerator & Technology Sector, CH-1211, Geneva, Switzerland
C. Bertone	CERN, Accelerator & Technology Sector, CH-1211, Geneva, Switzerland

N. Biancacci CERN, Accelerator & Technology Sector, CH-1211, Geneva, Switzerland
 A. Bignami INFN-LASA, Milan, Italy
 N. Bliss STFC, Daresbury Laboratory, Warrington WA4 4AD, UK
 C. Boccard CERN, Accelerator & Technology Sector, CH-1211, Geneva, Switzerland
 J. Borburgh CERN, Accelerator & Technology Sector, CH-1211, Geneva, Switzerland
 B. Bordini CERN, Accelerator & Technology Sector, CH-1211, Geneva, Switzerland
 F. Borralho CERN, Accelerator & Technology Sector, CH-1211, Geneva, Switzerland
 R. Bossert Fermi National Accelerator Laboratory, Batavia, P.O. Box 500, IL, USA
 L. Bottura CERN, Accelerator & Technology Sector, CH-1211, Geneva, Switzerland
 A. Boucherie CERN, Accelerator & Technology Sector, CH-1211, Geneva, Switzerland
 C. Bracco CERN, Accelerator & Technology Sector, CH-1211, Geneva, Switzerland
 E. Bravin CERN, Accelerator & Technology Sector, CH-1211, Geneva, Switzerland
 G. Bregliozzi CERN, Accelerator & Technology Sector, CH-1211, Geneva, Switzerland
 D. Brett The University of Manchester and the Cockcroft Institute, UK
 K. Brodzinski CERN, Accelerator & Technology Sector, CH-1211, Geneva, Switzerland
 F. Broggi INFN-LASA, Milan, Italy
 R. Bruce CERN, Accelerator & Technology Sector, CH-1211, Geneva, Switzerland
 M. Brugger CERN, Accelerator & Technology Sector, CH-1211, Geneva, Switzerland
 O. Brüning CERN, Accelerator & Technology Sector, CH-1211, Geneva, Switzerland
 X. Buffat CERN, Accelerator & Technology Sector, CH-1211, Geneva, Switzerland
 H. Burkhardt CERN, Accelerator & Technology Sector, CH-1211, Geneva, Switzerland
 J.P. Burnet CERN, Accelerator & Technology Sector, CH-1211, Geneva, Switzerland
 A. Burov Fermi National Accelerator Laboratory, Batavia, P.O. Box 500, IL, USA
 G. Burt University of Lancaster, Lancaster, UK and Cockcroft Institute Sci-Tech
 Daresbury, Warrington UK
 Y. Cai SLAC National Accelerator Laboratory, 2575 Sand Hill Road, Menlo Park
 California 94025 USA
 R. Calaga CERN, Accelerator & Technology Sector, CH-1211, Geneva, Switzerland
 S. Calatroni CERN, Accelerator & Technology Sector, CH-1211, Geneva, Switzerland
 O. Capatina CERN, Accelerator & Technology Sector, CH-1211, Geneva, Switzerland
 T. Capelli CERN, Accelerator & Technology Sector, CH-1211, Geneva, Switzerland
 E. Carlier CERN, Accelerator & Technology Sector, CH-1211, Geneva, Switzerland
 F. Carra CERN, Accelerator & Technology Sector, CH-1211, Geneva, Switzerland
 F. Caspers CERN, Accelerator & Technology Sector, CH-1211, Geneva, Switzerland
 F. Cerutti CERN, Accelerator & Technology Sector, CH-1211, Geneva, Switzerland
 A. Chancé CEA/SACLAY, DSM/Irfu/SACM – 91191 Gif-sur-Yvette – France
 S. Chemli CERN, Accelerator & Technology Sector, CH-1211, Geneva, Switzerland
 D. Cheng LBNL, Lawrence Berkeley National Laboratory, Berkeley, CA 94720, USA
 P. Chiggiato CERN, Accelerator & Technology Sector, CH-1211, Geneva, Switzerland
 G. Chlachidze Fermi National Accelerator Laboratory, Batavia, P.O. Box 500, IL, USA
 S. Claudet CERN, Accelerator & Technology Sector, CH-1211, Geneva, Switzerland
 JM. Coello De Portugal CERN, Accelerator & Technology Sector, CH-1211, Geneva, Switzerland
 C. Collazos CERN, Accelerator & Technology Sector, CH-1211, Geneva, Switzerland
 J.P. Corso CERN, Accelerator & Technology Sector, CH-1211, Geneva, Switzerland
 P. Costa Pinto CERN, Accelerator & Technology Sector, CH-1211, Geneva, Switzerland

M. Crouch	The University of Manchester and the Cockcroft Institute, UK
P. Cruikshank	CERN, Accelerator & Technology Sector, CH-1211, Geneva, Switzerland
M. Czech	CERN, Accelerator & Technology Sector, CH-1211, Geneva, Switzerland
K. Dahlerup-Petersen	CERN, Accelerator & Technology Sector, CH-1211, Geneva, Switzerland
B. Dalena	CEA/SACLAY, DSM/Irfu/SACM – 91191 Gif-sur-Yvette – France
S. Danzeca	CERN, Accelerator & Technology Sector, CH-1211, Geneva, Switzerland
H. Day	CERN, Accelerator & Technology Sector, CH-1211, Geneva, Switzerland
J.P. De Carvalho Saraiva	CERN, Accelerator & Technology Sector, CH-1211, Geneva, Switzerland
B. Dehning	CERN, Accelerator & Technology Sector, CH-1211, Geneva, Switzerland
J. Delayen	Old Dominion University, 5115 Hampton Boulevard, Norfolk, VA 23529, USA
B. Delille	CERN, Accelerator & Technology Sector, CH-1211, Geneva, Switzerland
F. Delsaux	CERN, Accelerator & Technology Sector, CH-1211, Geneva, Switzerland
R. De Maria	CERN, Accelerator & Technology Sector, CH-1211, Geneva, Switzerland
R. Denz	CERN, Accelerator & Technology Sector, CH-1211, Geneva, Switzerland
G. De Rijk	CERN, Accelerator & Technology Sector, CH-1211, Geneva, Switzerland
S. De Silva	Old Dominion University, 5115 Hampton Boulevard, Norfolk, VA 23529, USA
A. Dexter	University of Lancaster, Lancaster, UK and Cockcroft Institute Sci-Tech Daresbury, Warrington UK
D. Dietderich	LBNL, Lawrence Berkeley National Laboratory, Berkeley, CA 94720, USA
B. Di Girolamo	CERN, Physics & IT Sector, CH-1211, Geneva, Switzerland
A. Doherty	University of Lancaster, Lancaster, UK and Cockcroft Institute Sci-Tech Daresbury, Warrington UK
N. Dos Santos	CERN, Accelerator & Technology Sector, CH-1211, Geneva, Switzerland
A. Drago	INFN-LNF, Via E. Fermi 40, 00044 Frascati, Rome, Italy
D. Drskovic	CERN, Accelerator & Technology Sector, CH-1211, Geneva, Switzerland
D. Duarte Ramos	CERN, Accelerator & Technology Sector, CH-1211, Geneva, Switzerland
L. Ducimetière	CERN, Accelerator & Technology Sector, CH-1211, Geneva, Switzerland
I. Efthymiopoulos	CERN, Accelerator & Technology Sector, CH-1211, Geneva, Switzerland
K. Einsweiler	CERN, Accelerator & Technology Sector, CH-1211, Geneva, Switzerland
L. Esposito	CERN, Accelerator & Technology Sector, CH-1211, Geneva, Switzerland
J. Esteban Muller	CERN, Accelerator & Technology Sector, CH-1211, Geneva, Switzerland
S. Evrard	CERN, Accelerator & Technology Sector, CH-1211, Geneva, Switzerland
P. Fabbricatore	INFN, Sezione di Genova, I-16146 Genova, Italy
S. Farinon	INFN, Sezione di Genova, I-16146 Genova, Italy
S. Fartoukh	CERN, Accelerator & Technology Sector, CH-1211, Geneva, Switzerland
A. Faus-Golfe	IFIC, Instituto de Fisica Corpuscular, CSIC,E-46071 Valencia, Spain
G. Favre	CERN, Accelerator & Technology Sector, CH-1211, Geneva, Switzerland
H. Felice	LBNL, Lawrence Berkeley National Laboratory, Berkeley, CA 94720, USA
B. Feral	CERN, Accelerator & Technology Sector, CH-1211, Geneva, Switzerland
G. Ferlin	CERN, Accelerator & Technology Sector, CH-1211, Geneva, Switzerland
P. Ferracin	CERN, Accelerator & Technology Sector, CH-1211, Geneva, Switzerland
A. Ferrari	CERN, Accelerator & Technology Sector, CH-1211, Geneva, Switzerland
L. Ferreira	CERN, Accelerator & Technology Sector, CH-1211, Geneva, Switzerland
P. Fessia	CERN, Accelerator & Technology Sector, CH-1211, Geneva, Switzerland
L. Ficcadenti	CERN, Accelerator & Technology Sector, CH-1211, Geneva, Switzerland

L. Fiscarelli	CERN, Accelerator & Technology Sector, CH-1211, Geneva, Switzerland
M. Fitterer	CERN, Accelerator & Technology Sector, CH-1211, Geneva, Switzerland
R. Folch	CERN, Accelerator & Technology Sector, CH-1211, Geneva, Switzerland
G. Foffano	CERN, Accelerator & Technology Sector, CH-1211, Geneva, Switzerland
K. Foraz	CERN, Accelerator & Technology Sector, CH-1211, Geneva, Switzerland
M. Frankl	CERN, Accelerator & Technology Sector, CH-1211, Geneva, Switzerland
O. Frasciello	INFN-LNF, Via E. Fermi 40, 00044 Frascati, Rome, Italy
M. Fraser	CERN, Accelerator & Technology Sector, CH-1211, Geneva, Switzerland
P. Freijedo Menendez	CERN, Accelerator & Technology Sector, CH-1211, Geneva, Switzerland
M. Gallilee	CERN, Accelerator & Technology Sector, CH-1211, Geneva, Switzerland
A. Gaddi	CERN, Accelerator & Technology Sector, CH-1211, Geneva, Switzerland
A. Gallo	INFN-LNF, Via E. Fermi 40, 00044 Frascati, Rome, Italy
R. Garcia Alia	CERN, Accelerator & Technology Sector, CH-1211, Geneva, Switzerland
H. Garcia Gavela	CERN, Accelerator & Technology Sector, CH-1211, Geneva, Switzerland
J. Garcia Matos	CIEMAT, Madrid, Spain
H. Garcia Morales	URHL, Royal Holloway, London, UK
A. Garcia-Tabares	
Valdivieso	CERN, Accelerator & Technology Sector, CH-1211, Geneva, Switzerland
C. Garion	CERN, Accelerator & Technology Sector, CH-1211, Geneva, Switzerland
J.C. Gascon	CERN, Accelerator & Technology Sector, CH-1211, Geneva, Switzerland
Ch. Gasnier	CERN, Finance and Human Resources sector, CH-1211, Geneva, Switzerland
L. Gentini	CERN, Accelerator & Technology Sector, CH-1211, Geneva, Switzerland
A. Ghosh	BNL, Brookhaven National Laboratory, Upton, NY 11973, USA
K. Gibran Hernandez	CERN, Accelerator & Technology Sector, CH-1211, Geneva, Switzerland
S.M. Gibson	URHL, Royal Holloway, London, UK
C. Ginburg	Fermi National Accelerator Laboratory, Batavia, P.O. Box 500, IL, USA
M. Giovannozzi	CERN, Accelerator & Technology Sector, CH-1211, Geneva, Switzerland
B. Goddard	CERN, Accelerator & Technology Sector, CH-1211, Geneva, Switzerland
P. Gomes	CERN, Accelerator & Technology Sector, CH-1211, Geneva, Switzerland
P. Goudket	ASTeC, STFC, Daresbury Laboratory, Warrington WA4 4AD, UK
P. Gradassi	CERN, Accelerator & Technology Sector, CH-1211, Geneva, Switzerland
L. Grand-Clément	CERN, Accelerator & Technology Sector, CH-1211, Geneva, Switzerland
JC. Guillaume	CERN, Accelerator & Technology Sector, CH-1211, Geneva, Switzerland
M. Guinchard	CERN, Accelerator & Technology Sector, CH-1211, Geneva, Switzerland
P. Hagen	CERN, Accelerator & Technology Sector, CH-1211, Geneva, Switzerland
B. Hall	University of Lancaster, Lancaster, UK and Cockcroft Institute Sci-Tech Daresbury, Warrington UK
T. Hakulinen	CERN, Accelerator & Technology Sector, CH-1211, Geneva, Switzerland
W. Herr	CERN, Accelerator & Technology Sector, CH-1211, Geneva, Switzerland
C. Hill	STFC, Daresbury Laboratory, Warrington WA4 4AD, UK
W. Höfle	CERN, Accelerator & Technology Sector, CH-1211, Geneva, Switzerland
B. Holzer	CERN, Accelerator & Technology Sector, CH-1211, Geneva, Switzerland
J. Hrivnak	CERN, Accelerator & Technology Sector, CH-1211, Geneva, Switzerland
G. Iadarola	CERN, Accelerator & Technology Sector, CH-1211, Geneva, Switzerland
S. Izquierdo Bermudez	CERN, Accelerator & Technology Sector, CH-1211, Geneva, Switzerland

S. Jakobsen	CERN, Accelerator & Technology Sector, CH-1211, Geneva, Switzerland
E. Jensen	CERN, Accelerator & Technology Sector, CH-1211, Geneva, Switzerland
R. Jones	CERN, Accelerator & Technology Sector, CH-1211, Geneva, Switzerland
T. Jones	STFC, Daresbury Laboratory, Warrington WA4 4AD, UK
J.M. Jowett	CERN, Accelerator & Technology Sector, CH-1211, Geneva, Switzerland
M. Juchno	CERN, Accelerator & Technology Sector, CH-1211, Geneva, Switzerland
C. Julie	CERN, Accelerator & Technology Sector, CH-1211, Geneva, Switzerland
T. Junginger	CERN, Accelerator & Technology Sector, CH-1211, Geneva, Switzerland
V. Kain	CERN, Accelerator & Technology Sector, CH-1211, Geneva, Switzerland
D. Kaltchev	TRIUMF, Accelerator Physics Group, Vancouver, B.C., Canada
P. Kardasopoulos	CERN, Accelerator & Technology Sector, CH-1211, Geneva, Switzerland
M. Karppinen	CERN, Accelerator & Technology Sector, CH-1211, Geneva, Switzerland
R. Kersevan	CERN, Accelerator & Technology Sector, CH-1211, Geneva, Switzerland
F. Killing	CERN, Accelerator & Technology Sector, CH-1211, Geneva, Switzerland
G. Kirby	CERN, Accelerator & Technology Sector, CH-1211, Geneva, Switzerland
O.S. Kononenko	SLAC National Accelerator Laboratory, 2575 Sand Hill Road, Menlo Park California 94025 USA
M. Korostelev	University of Liverpool, Liverpool L69 7ZE, UK
N. Kos	CERN, Accelerator & Technology Sector, CH-1211, Geneva, Switzerland
S. Krave	Fermi National Accelerator Laboratory, Batavia, P.O. Box 500, IL, USA
L.P. Krzempek	CERN, Accelerator & Technology Sector, CH-1211, Geneva, Switzerland
N. Kuder	CERN, Accelerator & Technology Sector, CH-1211, Geneva, Switzerland
R. Kwee-Hinzmann	URHL, Royal Holloway, London, UK
F. Lackner	CERN, Accelerator & Technology Sector, CH-1211, Geneva, Switzerland
M. Lamont	CERN, Accelerator & Technology Sector, CH-1211, Geneva, Switzerland
L. Lari	IFIC, Instituto de Fisica Corpuscular, CSIC,E-46071 Valencia, Spain (now at European Spallation Source)
M. Lazzaroni	CERN, Accelerator & Technology Sector, CH-1211, Geneva, Switzerland
A. Lechner	CERN, Accelerator & Technology Sector, CH-1211, Geneva, Switzerland
T. Lefevre	CERN, Accelerator & Technology Sector, CH-1211, Geneva, Switzerland
R. Leuxe	CERN, Accelerator & Technology Sector, CH-1211, Geneva, Switzerland
K. Li	CERN, Accelerator & Technology Sector, CH-1211, Geneva, Switzerland
Z. Li	SLAC National Accelerator Laboratory, 2575 Sand Hill Road, Menlo Park California 94025 USA
R. Lindner	CERN, Physics & IT Sector, CH-1211, Geneva, Switzerland
C. Lingwood	University of Lancaster, Lancaster, UK and Cockcroft Institute Sci-Tech Daresbury, Warrington UK
C. Löffler	CERN, Accelerator & Technology Sector, CH-1211, Geneva, Switzerland
LA. Lopez-Hernandez	CERN, Finance and Human Resources sector, CH-1211, Geneva, Switzerland
F.L. Maciariello	CERN, Accelerator & Technology Sector, CH-1211, Geneva, Switzerland
P. Mattelaer	CERN, Finance and Human Resources sector, CH-1211, Geneva, Switzerland
L.E. Medina Medrano	CERN, Accelerator & Technology Sector, CH-1211, Geneva, Switzerland
R. Losito	CERN, Accelerator & Technology Sector, CH-1211, Geneva, Switzerland
P. Macintosh	ASTeC, STFC, Daresbury Laboratory, Warrington WA4 4AD, UK
A. Macpherson	CERN, Accelerator & Technology Sector, CH-1211, Geneva, Switzerland

P. Maesen	CERN, Accelerator & Technology Sector, CH-1211, Geneva, Switzerland
C. Magnier	CERN, Accelerator & Technology Sector, CH-1211, Geneva, Switzerland
H. Mainaud Durand	CERN, Accelerator & Technology Sector, CH-1211, Geneva, Switzerland
M. Manfredi	CERN, Finance and Human Resources sector, CH-1211, Geneva, Switzerland
F. Marcellini	INFN-LNF, Via E. Fermi 40, 00044 Frascati, Rome, Italy
M. Marchevsky	LBNL, Lawrence Berkeley National Laboratory, Berkeley, CA 94720, USA
S. Maridor	CERN, Accelerator & Technology Sector, CH-1211, Geneva, Switzerland
K. Marinov	ASTeC, STFC, Daresbury Laboratory, Warrington WA4 4AD, UK
T. Markiewicz	SLAC National Accelerator Laboratory, 2575 Sand Hill Road, Menlo Park California 94025 USA
A. Marsili	CERN, Accelerator & Technology Sector, CH-1211, Geneva, Switzerland
A. Masi	CERN, Accelerator & Technology Sector, CH-1211, Geneva, Switzerland
T. Mastoridis	California Polytechnic State University, San Luis Obispo, USA
P. Mattelaer	CERN, Finance and Human Resources sector, CH-1211, Geneva, Switzerland
A. May	ASTeC, STFC, Daresbury Laboratory, Warrington WA4 4AD, UK
J. Mazet	CERN, Accelerator & Technology Sector, CH-1211, Geneva, Switzerland
E. McIntosh	CERN, Accelerator & Technology Sector, CH-1211, Geneva, Switzerland
S. McIlwraith	CERN, Finance and Human Resources sector, CH-1211, Geneva, Switzerland
P. Menendez	CERN, Accelerator & Technology Sector, CH-1211, Geneva, Switzerland
M. Mensi	CERN, Accelerator & Technology Sector, CH-1211, Geneva, Switzerland
A. Mereghetti	CERN, Accelerator & Technology Sector, CH-1211, Geneva, Switzerland
D. Mergelkuhl	CERN, Accelerator & Technology Sector, CH-1211, Geneva, Switzerland
T. Mertens	CERN, Accelerator & Technology Sector, CH-1211, Geneva, Switzerland
E. Métral	CERN, Accelerator & Technology Sector, CH-1211, Geneva, Switzerland
M. Migliorati	University of Rome “La Sapienza”, Rome, Italy
T. Mitsuhashi	KEK, Oho, Tsukuba, 305-0801, Japan
P. Minginette	CERN, Accelerator & Technology Sector, CH-1211, Geneva, Switzerland
N.V. Mokhov	Fermi National Accelerator Laboratory, Batavia, P.O. Box 500, IL, USA
J. Molson	UMAN, The University of Manchester and the Cockcroft Institute, UK
E. Montesinos	CERN, Accelerator & Technology Sector, CH-1211, Geneva, Switzerland
R. Moron-Ballester	CERN, Accelerator & Technology Sector, CH-1211, Geneva, Switzerland
M. Morrone	CERN, Accelerator & Technology Sector, CH-1211, Geneva, Switzerland
A. Mostacci	University of Rome “La Sapienza”, Rome, Italy
N. Mounet	CERN, Accelerator & Technology Sector, CH-1211, Geneva, Switzerland
P. Muffat	CERN, Accelerator & Technology Sector, CH-1211, Geneva, Switzerland
B. Muratori	ASTeC, STFC, Daresbury Laboratory, Warrington WA4 4AD, UK
Y. Muttoni	CERN, Accelerator & Technology Sector, CH-1211, Geneva, Switzerland
M. Navarro-Tapia	CERN, Accelerator & Technology Sector, CH-1211, Geneva, Switzerland
T. Nakamoto	KEK, Oho, Tsukuba, 305-0801, Japan
H. Neupert	CERN, Accelerator & Technology Sector, CH-1211, Geneva, Switzerland
L.J. Nevay	URHL, Royal Holloway, London, UK
T. Nicol	Fermi National Accelerator Laboratory, Batavia, P.O. Box 500, IL, USA
E. Nilsson	CERN, Accelerator & Technology Sector, CH-1211, Geneva, Switzerland
P. Ninin	CERN, Accelerator & Technology Sector, CH-1211, Geneva, Switzerland
A. Nobrega	Fermi National Accelerator Laboratory, Batavia, P.O. Box 500, IL, USA

C. Noels	CERN, Accelerator & Technology Sector, CH-1211, Geneva, Switzerland
E. Nolan	STFC, Daresbury Laboratory, Warrington WA4 4AD, UK
Y. Nosochkov	SLAC National Accelerator Laboratory, 2575 Sand Hill Road, Menlo Park California 94025 USA
L. Oberli	CERN, Accelerator & Technology Sector, CH-1211, Geneva, Switzerland
T. Ogitsu	KEK, Oho, Tsukuba, 305-0801, Japan
K. Ohmi	KEK, Oho, Tsukuba, 305-0801, Japan
R. Olave	Old Dominion University, 5115 Hampton Boulevard, Norfolk, VA 23529, USA
Ph. Orlandi	CERN, Accelerator & Technology Sector, CH-1211, Geneva, Switzerland
P. Ortega	CERN, Finance and Human Resources sector, CH-1211, Geneva, Switzerland
J. Osborne	CERN, Finance and Human Resources sector, CH-1211, Geneva, Switzerland
T. Otto	CERN, Accelerator & Technology Sector, CH-1211, Geneva, Switzerland
L. Palumbo	University of Rome “La Sapienza”, Rome, Italy
Y. Papaphilippou	CERN, Accelerator & Technology Sector, CH-1211, Geneva, Switzerland
A. Patapenka	CERN, Accelerator & Technology Sector, CH-1211, Geneva, Switzerland
C. Parente	CERN, Accelerator & Technology Sector, CH-1211, Geneva, Switzerland
S. Paret	LBNL, Lawrence Berkeley National Laboratory, Berkeley, CA 94720, USA
H. Park	Old Dominion University, 5115 Hampton Boulevard, Norfolk, VA 23529, USA
S. Pattalwar	ASTeC, STFC, Daresbury Laboratory, Warrington WA4 4AD, UK
J. Payet	CEA/SACLAY, DSM/Irfu/SACM – 91191 Gif-sur-Yvette – France
G. Pechaud	CERN, Accelerator & Technology Sector, CH-1211, Geneva, Switzerland
P. Pepinster	CERN, Accelerator & Technology Sector, CH-1211, Geneva, Switzerland
J.C. Perez	CERN, Accelerator & Technology Sector, CH-1211, Geneva, Switzerland
J. Perez Espinos	CERN, Accelerator & Technology Sector, CH-1211, Geneva, Switzerland
A. Perillo Marcone	CERN, Accelerator & Technology Sector, CH-1211, Geneva, Switzerland
P. Perini	CERN, Accelerator & Technology Sector, CH-1211, Geneva, Switzerland
T. Peterson	Fermi National Accelerator Laboratory, Batavia, P.O. Box 500, IL, USA
T. Pieloni	CERN, Accelerator & Technology Sector, CH-1211, Geneva, Switzerland
M. Pojer	CERN, Accelerator & Technology Sector, CH-1211, Geneva, Switzerland
L. Pontecorvo	CERN, Physics & IT Sector, CH-1211, Geneva, Switzerland
H. Prin	CERN, Accelerator & Technology Sector, CH-1211, Geneva, Switzerland
R. Principe	CERN, Accelerator & Technology Sector, CH-1211, Geneva, Switzerland
J. Qiang	LBNL, Lawrence Berkeley National Laboratory, Berkeley, CA 94720, USA
E. Quaranta	CERN, Accelerator & Technology Sector, CH-1211, Geneva, Switzerland
H. Rafique	UHUD, University of Huddersfield, Huddersfield, UK
I.L. Rakhno	Fermi National Accelerator Laboratory, Batavia, P.O. Box 500, IL, USA
D. Ramos Duarte	CERN, Accelerator & Technology Sector, CH-1211, Geneva, Switzerland
A. Ratti	Fermi National Accelerator Laboratory, Batavia, P.O. Box 500, IL, USA
E. Ravaioli	CERN, Accelerator & Technology Sector, CH-1211, Geneva, Switzerland
M. Raymond	CERN, Physics & IT Sector, CH-1211, Geneva, Switzerland
S. Redaelli	CERN, Accelerator & Technology Sector, CH-1211, Geneva, Switzerland
T. Renaglia	CERN, Accelerator & Technology Sector, CH-1211, Geneva, Switzerland
D. Ricci	CERN, Accelerator & Technology Sector, CH-1211, Geneva, Switzerland
J.M. Rifflet	CEA/SACLAY, DSM/Irfu/SACM – 91191 Gif-sur-Yvette – France
T. Rijoff	CERN, Accelerator & Technology Sector, CH-1211, Geneva, Switzerland

R. Rinaldesi	CERN, Accelerator & Technology Sector, CH-1211, Geneva, Switzerland
L. Rivkin	EPFL, Lausanne, Switzerland
F. Rodriguez Mateos	CERN, Accelerator & Technology Sector, CH-1211, Geneva, Switzerland
S. Roesler	CERN, Accelerator & Technology Sector, CH-1211, Geneva, Switzerland
I. Romera Ramirez	CERN, Accelerator & Technology Sector, CH-1211, Geneva, Switzerland
A. Rossi	CERN, Accelerator & Technology Sector, CH-1211, Geneva, Switzerland
L. Rossi	CERN, Accelerator & Technology Sector, CH-1211, Geneva, Switzerland
G. Rumolo	CERN, Accelerator & Technology Sector, CH-1211, Geneva, Switzerland
G.L. Sabbi	LBNL, Lawrence Berkeley National Laboratory, Berkeley, CA 94720, USA
T. Sahnner	CERN, Accelerator & Technology Sector, CH-1211, Geneva, Switzerland
B. Salvant	CERN, Accelerator & Technology Sector, CH-1211, Geneva, Switzerland
F. Sanchez Galan	CERN, Accelerator & Technology Sector, CH-1211, Geneva, Switzerland
A. Santamaria Garcia	CERN, Accelerator & Technology Sector, CH-1211, Geneva, Switzerland
I. Santillana	CERN, Accelerator & Technology Sector, CH-1211, Geneva, Switzerland
C. Santini	Politecnico of Milan, Italy
P. Santos Diaz	CERN, Accelerator & Technology Sector, CH-1211, Geneva, Switzerland
K. Sasaki	KEK, Oho, Tsukuba, 305-0801, Japan
F. Savary	CERN, Accelerator & Technology Sector, CH-1211, Geneva, Switzerland
A. Sbrizzi	CERN, Accelerator & Technology Sector, CH-1211, Geneva, Switzerland
M. Schaumann	CERN, Accelerator & Technology Sector, CH-1211, Geneva, Switzerland
J. Schmalzle	BNL, Brookhaven National Laboratory, Upton, NY 11973, USA
H. Schmickler	CERN, Accelerator & Technology Sector, CH-1211, Geneva, Switzerland
R. Schmidt	CERN, Accelerator & Technology Sector, CH-1211, Geneva, Switzerland
M. Segreti	CEA/SACLAY, DSM/Irfu/SACM – 91191 Gif-sur-Yvette – France
M. Serluca	UMAN, The University of Manchester and the Cockcroft Institute, UK
E. Shaposhnikova	CERN, Accelerator & Technology Sector, CH-1211, Geneva, Switzerland
D. Shatilov	BINP, Novosibirsk, Russia
A. Siemko	CERN, Accelerator & Technology Sector, CH-1211, Geneva, Switzerland
J. Skarita	BNL, Brookhaven National Laboratory, Upton, NY 11973, USA
E. Skordis	CERN, Accelerator & Technology Sector, CH-1211, Geneva, Switzerland
D. Smekens	CERN, Accelerator & Technology Sector, CH-1211, Geneva, Switzerland
Z. Sobiech	CERN, Accelerator & Technology Sector, CH-1211, Geneva, Switzerland
M. Sosin	CERN, Accelerator & Technology Sector, CH-1211, Geneva, Switzerland
B. Spataro	INFN-LNF, Via E. Fermi 40, 00044 Frascati, Rome, Italy
G. Spiezia	CERN, Accelerator & Technology Sector, CH-1211, Geneva, Switzerland
G. Stancari	Fermi National Accelerator Laboratory, Batavia, P.O. Box 500, IL, USA
J. Steckert	CERN, Accelerator & Technology Sector, CH-1211, Geneva, Switzerland
G. Steele	CERN, Accelerator & Technology Sector, CH-1211, Geneva, Switzerland
M. Sugano	KEK, Oho, Tsukuba, 305-0801, Japan
A. Szeberenyi	CERN, Accelerator & Technology Sector, CH-1211, Geneva, Switzerland
M. Taborelli	CERN, Accelerator & Technology Sector, CH-1211, Geneva, Switzerland
C. Tambasco	CERN, Accelerator & Technology Sector, CH-1211, Geneva, Switzerland
L. Tavian	CERN, Accelerator & Technology Sector, CH-1211, Geneva, Switzerland
B. Teissandier	CERN, Accelerator & Technology Sector, CH-1211, Geneva, Switzerland

N. Templeton STFC, Daresbury Laboratory, Warrington WA4 4AD, UK

M. Therasse CERN, Accelerator & Technology Sector, CH-1211, Geneva, Switzerland

H. Thiesen CERN, Accelerator & Technology Sector, CH-1211, Geneva, Switzerland

E. Thomas CERN, Physics & IT Sector, CH-1211, Geneva, Switzerland

A. Toader UHUD, University of Huddersfield, Huddersfield, UK

E. Todesco CERN, Accelerator & Technology Sector, CH-1211, Geneva, Switzerland

R. Tomás CERN, Accelerator & Technology Sector, CH-1211, Geneva, Switzerland

F. Toral CIEMAT, Madrid, Spain

R. Torres-Sanchez CERN, Accelerator & Technology Sector, CH-1211, Geneva, Switzerland

G. Trad CERN, Accelerator & Technology Sector, CH-1211, Geneva, Switzerland

I.S. Tropin Fermi National Accelerator Laboratory, Batavia, P.O. Box 500, IL, USA

A. Tsinganis CERN, Accelerator & Technology Sector, CH-1211, Geneva, Switzerland

J. Tuckamantel CERN, Accelerator & Technology Sector, CH-1211, Geneva, Switzerland

J. Uythoven CERN, Accelerator & Technology Sector, CH-1211, Geneva, Switzerland

A. Valishev INFN-LNF, Via E. Fermi 40, 00044 Frascati, Rome, Italy

F. Van Der Veken CERN, Accelerator & Technology Sector, CH-1211, Geneva, Switzerland

E. Van Weelderens CERN, Accelerator & Technology Sector, CH-1211, Geneva, Switzerland

A. Vande Craen CERN, Accelerator & Technology Sector, CH-1211, Geneva, Switzerland

B. Vazquez De Prada CERN, Accelerator & Technology Sector, CH-1211, Geneva, Switzerland

F. Velotti CERN, Accelerator & Technology Sector, CH-1211, Geneva, Switzerland

S. Verdu Andres BNL, Brookhaven National Laboratory, Upton, NY 11973, USA

A. Verweij CERN, Accelerator & Technology Sector, CH-1211, Geneva, Switzerland

N. Vittal Shetty CERN, Accelerator & Technology Sector, CH-1211, Geneva, Switzerland

V. Vlachoudis CERN, Accelerator & Technology Sector, CH-1211, Geneva, Switzerland

G. Volpini INFN-LASA, Milan, Italy

U. Wagner CERN, Accelerator & Technology Sector, CH-1211, Geneva, Switzerland

P. Wanderer BNL, Brookhaven National Laboratory, Upton, NY 11973, USA

M.H. Wang SLAC National Accelerator Laboratory, 2575 Sand Hill Road, Menlo Park California 94025 USA

X. Wang LBNL, Lawrence Berkeley National Laboratory, Berkeley, CA 94720, USA

R. Wanzenberg Deutsches Elektronen-Synchrotron Notkestr. 85, 2000 Hamburg 52, Germany

R.V. Weelderens CERN, Accelerator & Technology Sector, CH-1211, Geneva, Switzerland

S. Weisz CERN, Accelerator & Technology Sector, CH-1211, Geneva, Switzerland

C. Welsch University of Liverpool, Liverpool L69 7ZE, UK

J. Wenninger CERN, Accelerator & Technology Sector, CH-1211, Geneva, Switzerland

M. Wendt CERN, Accelerator & Technology Sector, CH-1211, Geneva, Switzerland

W. Weterings CERN, Accelerator & Technology Sector, CH-1211, Geneva, Switzerland

S. White CERN, Accelerator & Technology Sector, CH-1211, Geneva, Switzerland

G. Willering CERN, Accelerator & Technology Sector, CH-1211, Geneva, Switzerland

D. Wollmann CERN, Accelerator & Technology Sector, CH-1211, Geneva, Switzerland

A. Wolski University of Liverpool, Liverpool L69 7ZE, UK

Q. Wu BNL, Brookhaven National Laboratory, Upton, NY 11973, USA

B. Xiao BNL, Brookhaven National Laboratory, Upton, NY 11973, USA

L. Xiao SLAC National Accelerator Laboratory, 2575 Sand Hill Road, Menlo Park California 94025 USA

Q. Xu	KEK, Oho, Tsukuba, 305-0801, Japan
Y. Yakovlev	Fermi National Accelerator Laboratory, Batavia, P.O. Box 500, IL, USA
Y. Yang	University of Southampton, Southampton SO17 1BJ, UK
S. Yammine	CERN, Accelerator & Technology Sector, CH-1211, Geneva, Switzerland
M. Yu	Fermi National Accelerator Laboratory, Batavia, P.O. Box 500, IL, USA
I. Zacharov	EPFL, Lausanne, Switzerland
O. Zagorodnova	Deutsches Elektronen-Synchrotron Notkestr. 85, 2000 Hamburg 52, Germany
C. Zannini	CERN, Accelerator & Technology Sector, CH-1211, Geneva, Switzerland
C. Zaroni	CERN, Accelerator & Technology Sector, CH-1211, Geneva, Switzerland
M. Zerlauth	CERN, Accelerator & Technology Sector, CH-1211, Geneva, Switzerland
F. Zimmermann	CERN, Accelerator & Technology Sector, CH-1211, Geneva, Switzerland
A. Zlobin	Fermi National Accelerator Laboratory, Batavia, P.O. Box 500, IL, USA
M. Zobov	INFN-LNF, Via E. Fermi 40, 00044 Frascati, Rome, Italy
I. Zurbano Fernandez	CERN, Accelerator & Technology Sector, CH-1211, Geneva, Switzerland

Chapter 1

High Luminosity Large Hadron Collider HL-LHC

1 High Luminosity Large Hadron Collider HL-LHC

1.1 Introduction

The Large Hadron Collider (LHC) was successfully commissioned in 2010 for proton–proton collisions with a 7 TeV centre-of-mass energy. It delivered 8 TeV centre-of-mass proton collisions from April 2012 until the end of Run 1 in 2013. Following a long technical stop in 2013–2014, it operated with 13 TeV centre-of-mass proton collisions during Run 2 from 2015 onwards.

It is a remarkable era for cosmology, astrophysics and high energy physics (HEP) and the LHC is at the forefront of attempts to understand the fundamental nature of the universe. The discovery of the Higgs boson in 2012 is undoubtedly a major milestone in the history of science. Beyond this, the LHC has the potential to go on and help answer some of the key questions of the age: the existence, or not, of supersymmetry; the nature of dark matter; the existence of extra dimensions. It is also important to continue to study the properties of the Higgs – here the LHC is well placed to do this in exquisite detail.

Thanks to the LHC, Europe has decisively regained world leadership in high energy physics, a key sector of knowledge and technology development. The LHC can continue to act as catalyst for a global effort unrivalled by any other branch of science: out of the 11 000 CERN users, more than 7000 are scientists and engineers using the LHC, half of which are from countries outside the EU.

The LHC will remain the most powerful accelerator in the world for at least the next two decades. Its full exploitation is the highest priority of the European Strategy for particle physics. This strategy has been adopted by the CERN Council, and is a reference point for the Particle Physics Strategy of the US and, to a certain extent, Japan. To extend its discovery potential, the LHC will need a major upgrade in the 2020s to extend its operability by another decade and to increase its luminosity (and thus collision rate) by a factor of five beyond its design value. The integrated luminosity design goal is an increase by a factor of ten. As a highly complex machine, such an upgrade must be carefully studied. The necessary developments require about 10 years to prototype, test and realize new equipment. The novel machine configuration, the High Luminosity LHC (HL-LHC), will rely on a number of key innovative technologies representing exceptional technological challenges. These include among others: cutting-edge 11–12 T superconducting magnets; very compact superconducting cavities for beam rotation with ultra-precise phase control; new technology for beam collimation; and high-power superconducting links with almost zero energy dissipation.

HL-LHC federates the efforts and R&D of a large international community towards the ambitious HL-LHC objectives and contributes to establishing the European Research Area (ERA) as a focal point of global research cooperation and leadership in frontier knowledge and technologies. HL-LHC relies on strong participation from various partners, in particular from leading US and Japanese laboratories. This participation will be required for the execution of the construction phase as a global project. In particular, the US LHC Accelerator R&D Program (LARP) has developed some of the key technologies for the HL-LHC, such as the large-aperture niobium–tin (Nb_3Sn) quadrupoles and the crab cavities. The proposed governance model is being modified and is now tailored to support the construction phase that starts at the end of the Design Study.

1.2 HL-LHC in a nutshell

The new LHC baseline programme, defined in June 2015, is shown schematically in Figure 1-1. After the consolidation of the electrical splices between the superconducting magnets (and many other consolidation actions) in the Long Shutdown 1 (LS1), the LHC has operated in Run 2 at 13 TeV centre-of-mass energy from 3 June 2015 and has progressively increased the luminosity attaining the nominal design luminosity of $1 \times 10^{34} \text{ cm}^{-2} \text{ s}^{-1}$ on 26 June 2016. Despite a reduced number of bunches (about 2200 cf. 2800 nominal) a peak luminosity up to 1.2×10^{34} has been routinely obtained in 2016. This peak is largely thanks to reduced emittance from the injectors and a β^* value of 40 cm (cf. 55 cm nominal value) at the high luminosity interaction points. This excellent performance, together with an availability that is considerably higher than in previous years, should give a total integrated luminosity of about 35 fb^{-1} for the year. In the period 2017–2023 the LHC will hopefully further increase the peak luminosity. Margins in the design of the nominal LHC are expected to allow about two times the nominal design performance. The baseline programme for the next ten years is depicted in Figure 1-1, while Figure 1-2 shows the possible evolution of peak and integrated luminosity.

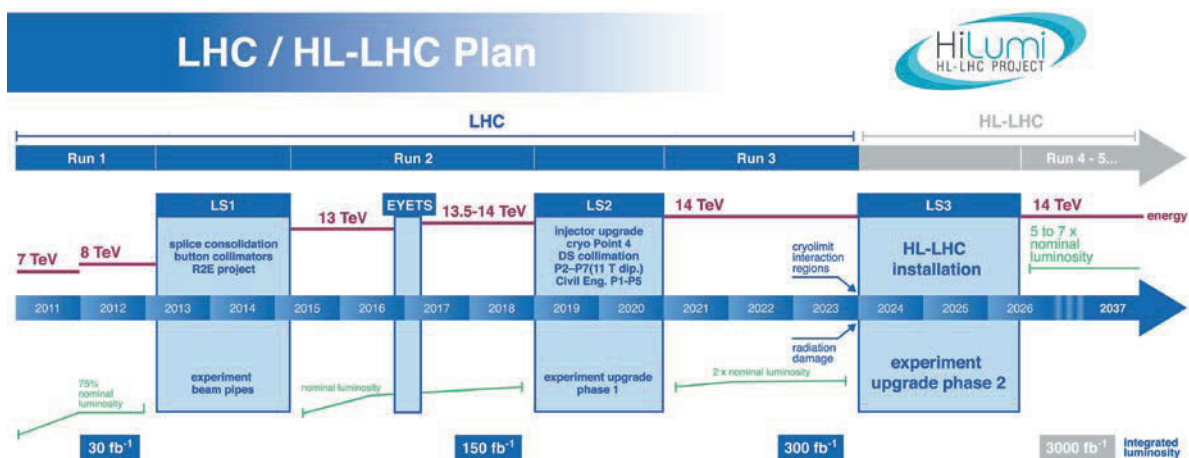


Figure 1-1: LHC baseline plan for the next decade and beyond showing the energy of the collisions (upper red line) and luminosity (lower green lines). The first long shutdown (LS1) in 2013–2014 should allow the design parameters of beam energy and luminosity to be reached. The second long shutdown (LS2), 2019–2020, will consolidate luminosity production and reliability as well as upgrade the LHC injectors. After LS3, 2024–2026, the machine will be in the High Luminosity configuration (HL-LHC).

After Run 3 (see Figure 1-1) the statistical gain in running the accelerator without a significant luminosity increase beyond its design and ultimate values will become marginal. The running time necessary to halve the statistical error of a given measurement after 2020 will be more than ten years. Therefore, to maintain scientific progress and to exploit its full capacity, the LHC will need to have a decisive increase of its luminosity after 2020. This is why, when the CERN Council adopted the European Strategy for particle physics in 2006 [1], its first priority was agreed to be ‘to fully exploit the physics potential of the LHC. A subsequent major luminosity upgrade, motivated by physics results and operation experience, will be enabled by focused R&D. The European Strategy for particle physics has been integrated into the European Strategy Forum on Research Infrastructures (ESFRI) Roadmap of 2006, as has the update of 2008 [2]. The priority to fully exploit the potential of the LHC has been recently confirmed as the *first priority* among the ‘High priority large-scale scientific activities’ in the new European Strategy for particle physics – Update 2013 [3]. This update was approved in Brussels on 30 May 2013 with the following wording: ‘Europe’s top priority should be the exploitation of the full potential of the LHC, including the high luminosity upgrade of the machine and detectors with a view to collecting ten times more data than in the initial design, by around 2030’.

The importance of the LHC luminosity upgrade for the future of high energy physics has also been reaffirmed in the May 2014 recommendation by the Particle Physics Project Prioritization Panel (P5) to the High Energy Physics Advisory Panel (HEPAP), which in turn advises the US Department of Energy (DOE) [4]. The

recommendation, a critical step in the updating of the US strategy for HEP, states the following: ‘Recommendation 10: The LHC upgrades constitute our highest-priority near-term large project’.

In Japan, the 2012 report of a subcommittee in the HEP community concluded that an e^+e^- linear collider and a large-scale neutrino detector would be the core projects in Japan, with the assumption that the LHC and its upgrade are pursued de facto. The updated KEK roadmap in 2013 states that ‘The main agenda at LHC/ATLAS is to continually participate in the experiment and to take a proactive initiative in upgrade programmes within the international collaboration at both the accelerator and detector facilities’. Following this support, the ATLAS-Japan group has undertaken intensive R&D on the detector upgrades and the KEK Cryogenic Science Center has started the R&D for the HL-LHC separation dipole magnets (D1).

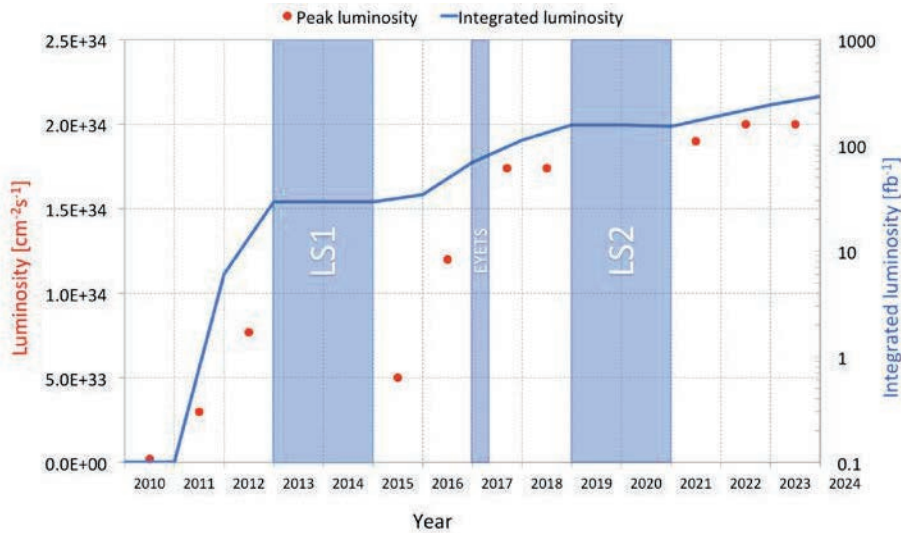


Figure 1-2: LHC luminosity plan until LS3 : both peak (red dots) and integrated (blue line) luminosities are indicated. Main shutdown periods are also shown.

In this context, CERN created the High Luminosity LHC (HL-LHC) project at the end of 2010 [5]. Started as a design study, and after the approval of the CERN Council on 30 May 2013 and the insertion of a consistent part of the HL-LHC budget in the CERN Medium Term Plan (MTP) approved by Council in June 2014, the HL-LHC has become CERN’s major construction project for the next decade. The writing of the Conceptual technical specifications and the Preliminary Design Report [6] are key deliverables of the FP7-HiLumi LHC Design Study. Further steps have been taken in 2015 to get a complete approval of the HL-LHC:

- Cost & Schedule Review (international panel of experts, composed by the CERN Machine Advisory Committee complemented by additional experts). First meeting in March 9-11 2015. The very positive report is available upon request (some information is confidential).
- Modification of the layout for civil engineering, more suitable to the actual needs and conditions;
- Insertion into CERN’s MTP of 2015 of the whole budget for the years 2016-2020 (the 5-year covered by MTP approved in 2015), with indication of the total CtC (Cost-to-Completion) of the project until full installation in 2026. The material cost is around 950 MCHF, without including the initial Design Study and prototype phases.

Thanks to the above-mentioned initiatives, the project and its budget for construction were approved for the period of the MTP by the Council at its 16 September 2015 Session.

In spring 2016 the CERN management submitted to Council the proposal for a global approval of the HL-LHC, describing the goals of the upgrade, the physics case for the HL-LHC, and the technology challenges. The proposal, [7], covers all the project period including installation and commissioning in 2026, and gives a total material cost for the HL-LHC of 950 MCHF. It is to be noted that this figure covers the High Luminosity LHC, i.e. the materials for collider with its infrastructure, while it does not include the cost of the detector

upgrade. The document was approved in the 181th session of the CERN Council on 16-17 June 2016. It is remarkable that HL-LHC has become the first project formally approved by the CERN Council since the final approval of the LHC in 1996.

The main objective of the High Luminosity LHC design study was to determine a set of beam parameters and the hardware configuration that will enable the LHC to reach the following targets:

- a peak luminosity of $5 \times 10^{34} \text{ cm}^{-2} \text{ s}^{-1}$ with levelling, allowing:
- an integrated luminosity of 250 fb^{-1} per year with the goal of 3000 fb^{-1} in about a dozen years after the upgrade. This integrated luminosity is about ten times the expected luminosity reach of the first twelve years of the LHC lifetime.

The overarching goals are the installation of the main hardware for the HL-LHC during LS3, scheduled for 2024–2026, finishing the hardware commissioning at machine re-start in 2026 while taking all actions to assure a high efficiency in operation until 2035-2040.

Since all equipment is being designed with a 50% margin with respect to the instantaneous heat deposition and the integrated radiation dose, the concept of *ultimate performance* has been defined, wherein all margins are used for performance increase. By using these margins, it should be possible to push the machine peak levelled luminosity to about $7\text{--}7.5 \times 10^{34} \text{ cm}^{-2} \text{ s}^{-1}$ increasing the average pile-up, i.e. the number of events per bunch crossing, in the detectors up to around 200. This luminosity level should enable the collection of up to $300\text{--}350 \text{ fb}^{-1}/\text{year}$ provided the experiments can digest this pile-up level. In terms of total integrated luminosity, the *ultimate performance* corresponds to a value of about 4000 fb^{-1} .

Similarly, all magnetic circuits have been designed with a 10% margin with respect to the powering at nominal beam energy of 7TeV. By using these margins, one could hope to operate the LHC from the magnet circuit point of view at a beam energy of 7.5TeV. However, such an increase in the beam energy implies additional challenges for many other systems (e.g. the machine protection and powering systems and the collimation and beam dump systems) and can therefore not be taken for granted at this stage. Even though the HL-LHC project baseline is 'only' for 7.0 TeV and does not include this 'ultimate beam energy' in its specification, the possibility of a potential separate energy increase to 7.5 TeV should be explicitly considered in the ongoing HL-LHC upgrades. If significant extra efforts and upgrades are needed for this energy, which are not possible in easy synergy within the HL-LHC resource envelope, then at least the limitations and required additional upgrades should be identified.

All of the hadron colliders in the world before the LHC have produced a combined total integrated luminosity of about 10 fb^{-1} . The LHC delivered nearly 30 fb^{-1} by the end of 2012 and should reach 300 fb^{-1} in its first 13–15 years of operation. The High Luminosity LHC is a major, extremely challenging, upgrade. For its successful realization, a number of key novel technologies have to be developed, validated, and integrated. The work was initiated early: ideas were circulating at the beginning of LHC construction [8] and this continued throughout construction [9]. From 2003 onwards, LARP (see Section 1.3.2) has been the main and continuous motor for technological development devoted to the LHC upgrade, matched in Europe by a study effort coordinated by the EC-FP6-CARE program (HHH and AMT networks and NED program). After a period during which the upgrade was conceived in two phases, the first one via established Nb-Ti technology (support by the FP7-SLHC-PP program) and the second based on novel Nb₃Sn technology, and following the suppression of the Phase-I upgrade project, all studies were concentrated in 2010 under the newly formed High Luminosity LHC Project. The first step consisted in launching a Design Study under the auspices of FP7 with the working title 'HiLumi LHC'. Following approval by the European Commission (EC) in 2011, FP7-HiLumi LHC has been instrumental in initiating a new global collaboration for the LHC, matching the spirit of the worldwide user community of the LHC experiments.

The High Luminosity LHC project is also working in close collaboration with the CERN project for the LHC Injector complex Upgrade (LIU) [10], the companion ATLAS and CMS upgrade projects of 2019–2020 and 2024–2026 and the upgrade foreseen in 2019–2020 for both LHCb and ALICE.

1.2.1 Luminosity

The (instantaneous) luminosity L can be expressed as:

$$L = \gamma \frac{n_b N^2 f_{\text{rev}}}{4\pi \beta^* \varepsilon_n} R; \quad R = 1 / \sqrt{1 + \frac{\theta_c \sigma_z}{2\sigma}} \quad (1-1)$$

where γ is the relativistic gamma factor; n_b is the number of bunches per beam colliding at the IP; N is the bunch population; f_{rev} is the revolution frequency; β^* is the beam beta function (focal length) at the collision point; ε_n is the transverse normalized emittance; R is a luminosity geometrical reduction factor from the crossing angle not including the Hourglass effect; θ_c is the full crossing angle between colliding beam; and σ , σ_z are the transverse and longitudinal r.m.s. sizes, respectively.

With the nominal parameter values shown in Table 2-1, a luminosity of $1 \times 10^{34} \text{ cm}^{-2} \text{ s}^{-1}$ is obtained, with an average pile-up (number of events in the same bunch crossing) of $\mu = 27$ (note $\mu = 19$ was the original forecast at LHC approval due to uncertainties in the total proton cross-section at higher energies).

1.2.2 Present luminosity limitations and hardware constraints

Before discussing the new configuration, it is useful to recall the systems that will need to be changed, and possibly improved, because they become vulnerable to breakdown and accelerated aging, or because they may become a bottleneck for operation in a higher radiation environment. This goes well beyond the ongoing basic consolidation.

- **Inner triplet magnets** (see chapter 3). After about 300 fb^{-1} some components of the inner triplet quadrupoles and their corrector magnets will have received a dose of 30 MGy, entering into the region of possible radiation damage. The quadrupoles may withstand a maximum of 400 fb^{-1} to 700 fb^{-1} , but some corrector magnets of nested type could fail already at 300 fb^{-1} . Actual damage must be anticipated because the most likely failure mode is through sudden electric breakdown, entailing serious and long repairs. Thus the replacement of the triplet magnets must be envisaged before damage occurs. Replacement of the low- β triplet is a long intervention, requiring a one to two year shutdown, at least, and must be coupled with the major detector upgrades (which also are required at around 300 fb^{-1}).
- **Cryogenics** (see chapter 9). To increase intervention flexibility and machine availability it is planned to “sectorize” the cooling of the superconducting RF (SRF) and the cooling of the magnets in the arc. Thanks to this, a mobile helium liquefier (procured for the Crab Cavity test in the SPS) could be used to cool down SRF cavities during a shutdown of the main refrigerators. The cooling of the inner triplets and matching section magnets must also be separated from the arc magnets. This would avoid the need to warm-up an entire arc in the case of intervention in the straight sections near the triplet magnets.
- **Collimation** (see chapter 5). The collimation system has been designed for the first operation phase of the LHC. The present system was optimized for robustness and will need an upgrade that takes into account the need for the lower impedance required for the planned increased beam intensities. A new configuration will also be required to protect the new triplets in IR1 and IR5.
- **The dispersion suppressor (DS) regions** (see chapter 11) also require special attention, where a leakage of off-momentum particles into the first and second main superconducting dipoles has already been identified as a possible LHC performance limitation. The issue is serious in P2 for ion collisions and in P7 (betatron cleaning) for both ion and proton beams. For P2 a solution has been found by modifying optics and placing collimators in a suitably modified connection cryostat. For P7 the solution is more elaborate due to the missing free space for collimators: an LHC main dipole will be substituted by dipoles of equal bending strength ($\sim 120 \text{ T}\cdot\text{m}$) obtained by a higher field (11 T) and shorter length (11 m) than those of the LHC dipoles (8.3 T and 14.2 m). The space gained is sufficient for the installation of additional DS collimators.

- **Radiation to electronics (R2R)** (see chapter 10) and **superconducting (SC) links** (see chapter 6A) for the remote powering of cold circuits. Considerable effort is being made to study how to replace the radiation-sensitive electronic boards of the power converter system with radiation-hard cards. A complementary solution is also being pursued for the high luminosity regions: the removal from the LHC tunnel of the power converters and associated electrical feedboxes (the DFBs - delicate equipment presently in line with the continuous cryostat) of the magnetic elements from Q1 to D2. While a removal to the surface was initially considered, this equipment will now be installed in a new underground gallery following a global optimization study. Displacement of power converters to distant locations favour the use of a novel technology: superconducting links (SCLs) made out of MgB₂ superconductors.

Other systems will potentially become problematic with the aging of the machine and the increased radiation level that comes with higher performance levels of 40 fb⁻¹ to 60 fb⁻¹ per year. Their replacement in the frame of the HL-LHC project gives the opportunity of improving their performance. A non-exhaustive list includes the following.

- The Quench Protection System (QPS) of the superconducting magnets is based on a design that is now almost 20 years old.
- Machine protection: improved robustness to mis-injected beams, kicker breakdown and asynchronous beam dumps will be required. The extraction system is, along with collimation and the injection protection devices, the main defence against severe beam-induced damage. These systems will need renovation after 2020, if not earlier.
- Remote manipulation: the level of activation from 2020 onwards, and perhaps even earlier, requires careful study and the development of special equipment to allow the repair and/or quick replacement of collimators, magnets, vacuum components, etc., according to the ‘as low as reasonably achievable’ (ALARA) principle. While full robotics is difficult to implement given the conditions on the ground, remote manipulation, enhanced reality and supervision are the key to minimizing the radiation doses sustained during interventions.

1.2.3 Luminosity levelling and availability

Both the consideration of energy deposition by collision debris in the interaction region magnets, and the necessity to limit the peak pile-up in the experimental detector, impose an a priori limitation upon peak luminosity. The consequence is that HL-LHC operation will have to rely on luminosity levelling. As shown in Figure 1-3 (a), the luminosity profile without levelling quickly decreases from the initial peak value due to ‘luminosity burn-off’ (protons consumed in the collisions). With luminosity levelling the collider is designed to operate with a constant luminosity at a value below the virtual maximum luminosity. The average luminosity achieved is almost the same as that without levelling see Figure 1-3 (b) in an ideal running configuration without premature fill aborts. The advantage, however, is that the maximum peak luminosity and energy deposition are lower. Among the various methods of levelling, the present favoured one is dynamic variation of β^* during the run. However, variation of crab cavity voltage and/or variation of beam separation are also being considered.

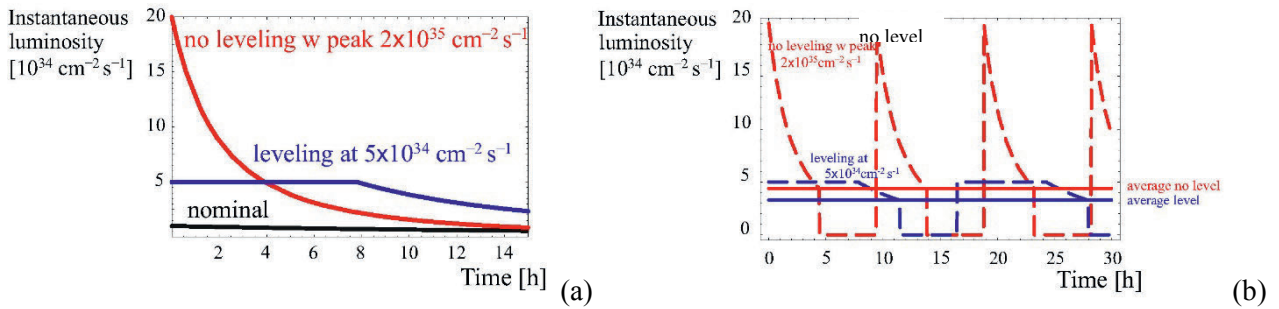


Figure 1-3: (a) luminosity profile for a single long fill: starting at nominal peak luminosity (black line), with upgrade and without levelling (red line), with levelling (blue line). (b) Luminosity profile with optimized run time, without and with levelling (blue and red dashed lines), and average luminosity in both cases (solid lines).

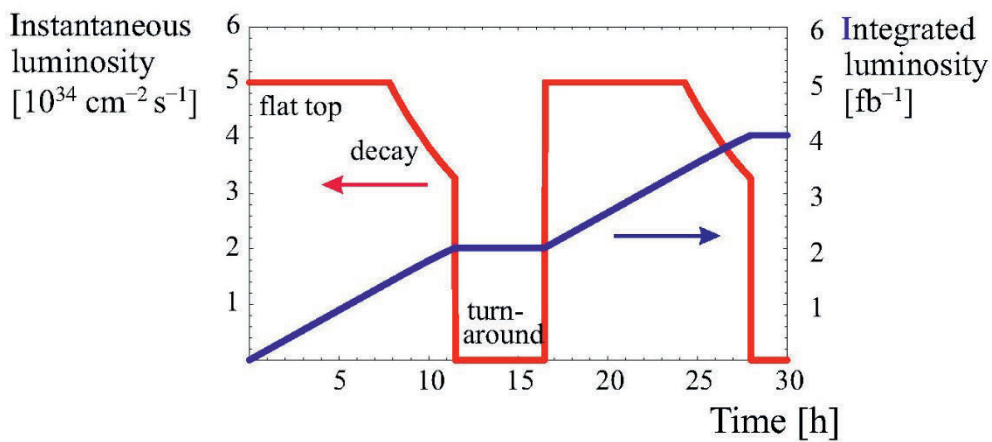


Figure 1-4: Luminosity cycle for HL-LHC with levelling and a short decay (optimized for integrated luminosity).

Assuming 160 days of physics operation per year, the HL-LHC needs a physics efficiency of about 50%. The overall LHC efficiency during the 2012 run, without luminosity levelling, was around 37%, while in 2016 physics efficiency over periods of weeks was up to around 60 to 70%. The requirement of an efficiency around 50% with a (levelled) luminosity five times that of nominal and stored beam energies about 5 times larger than during the 2012 run will be a challenge. However, in view of the most recent LHC results this seems a reasonable target. The project must foresee a vigorous consolidation for the high intensity and high luminosity regime: the High Luminosity LHC must also be a high availability LHC.

1.2.4 HL-LHC parameters and main systems for the upgrade

Table 1-1 lists the main parameters foreseen for high luminosity operation (the table includes already the few changes due to re-baselining of June 2016). The 25 ns bunch spacing is the baseline operation mode; however, another scheme where each eight bunches with beams are followed by four “empty bunches”, so-called 8b4e, is kept as a possible alternative in case the e-cloud or other unforeseen effects undermine 25 ns performance. This 8b4e scheme replaces the previous alternative of 50 ns space bunching that is punitive from the point of view of pile up. A slightly different parameter set at 25 ns (batch compression, bunch merging and splitting scheme (BCMS)) with very small transverse beam emittance might be interesting for HL-LHC operation in case operation with high beam intensities results in unforeseen emittance blow-up.

Table 1-1: High Luminosity LHC main parameters for proton collisions (re-baselining summer 2016).

Parameter	Nominal LHC (design report)	HL-LHC 25 ns (standard)	HL-LHC 25 ns (BCMS) ³	HL-LHC 8b+4e ⁴
Beam energy in collision [TeV]	7	7	7	7
N_b [10^{11}]	1.15	2.2	2.2	2.3
n_b	2808	2748	2604	1968
Beam current [A]	0.58	1.09	1.03	0.82
Minimum β^* [m]	0.55	0.2	0.2	0.2
ϵ_n [μm]	3.75	2.50	2.50	2.20
ϵ_L [eVs]	2.50	2.50	2.50	2.50
Total reduction factor R_0 without crab cavities at min. β^*	0.836	0.369	0.369	0.369
Total reduction factor R_0 without crab cavities at min. β^{*5}	(0.981)	0.715	0.715	0.740
Peak luminosity with crab cavities $L_{\text{peak}} \times R_1/R_0$ [$10^{34} \text{ cm}^{-2} \text{ s}^{-1}$] ⁵	(1.18)	12.6	11.9	11.6
Levelled luminosity for $\mu = 140$ [$10^{34} \text{ cm}^{-2} \text{ s}^{-1}$]	-	5.32 ¹	5.02	5.03
Events/crossing μ (with levelling and crab cavities) ²	27	140	140	140
Maximum line density of pile-up events during fill [events/mm] ⁵	0.21	1.3	1.3	1.3

The provisional set of parameters of ion beams for the high luminosity regime of ion collision has also been established (see Table 1-2). The parameters should be able to satisfy the ion integrated luminosity requirements of the ALICE experiment [11]. However, it must be underlined that the beam parameters are being discussed with the LIU project to assess feasibility and optimization. In addition a discussion with the management of the LHC experiments, arbitrated by CERN management, should also provide clarification on the best sharing of ions collisions between the various experiments.

Table 1-2: High Luminosity LHC parameters for ion collisions.

Parameter	Nominal LHC (design report)	HL-LHC (projected)	HL-LHC (LIU baseline)	HL-LHC (required)
Beam energy in collision [TeV]	574	574	574	574
Beam energy per nucleon in collision [TeV]	2.76	2.76	2.76	2.76
Particles per bunch, N [10^7]	7	10.4	14	19
Number of bunches per beam	592	1170	820	1170
N_{tot} [10^9]	41.4	121.7	115	222.3
Beam current [mA]	6.12	18.0	17.0	32.8
Minimum β^* [m]	0.5	0.5	0.5	0.5
ϵ_n [μm]	1.5	1.6	1.6	1.5
ϵ_L [eVs/charge]	2.50	2.50	2.50	2.50
r.m.s. energy spread [0.0001]	1.10	1.10	1.10	1.10
r.m.s. bunch length [cm]	7.94	7.94	7.94	7.94
IBS horizontal [h]	7.7	4.5	3.3	2.2
IBS longitudinal [h]	13	7.5	5.6	3.7
Half-crossing angle at IP2 [μrad]	60	100	100	100
Peak luminosity [$10^{27} \text{ cm}^{-2} \text{ s}^{-1}$]	1.00	4.5	4.5	8
Levelled luminosity [$10^{27} \text{ cm}^{-2} \text{ s}^{-1}$]	-	-	-	6-7
Levelling time [h]	-	-	-	1
Maximum number of bunches per injection	54	48	48	48

¹ For the design of the HL-LHC systems (collimators, triplet magnets,...), a design margin of 50% on the stated peak luminosity was agreed upon.

² The total number of events/crossing is calculated with an inelastic cross-section of 85 mb (also for nominal), while 111 mb is still assumed for calculating the proton burn off and the resulting levelling time

³ BCMS parameters are only considered for injection and as a backup parameter set in case one encounters larger than expected emittance growth in the HL-LHC during injection, ramp and squeeze

⁴ The 8b+4e variant represents a back-up scenario for the baseline 25ns operation in case of e-cloud limitations. The parameters are still evolving but are stated for the sake of performance reach comparison.

⁵ The current baseline foresees installation of ½ crab-cavity modules in LS3 and an option for ½ in LS4, having an initial impact on parameters like β^* , crossing angle, virtual luminosity reach and levelling time. The current HL-LHC baseline foresees the installation of 16 cavities of maximum voltage of 3.4 MV. Space will be reserved to optionally install the second half at a later stage after LS3

The upgrade should provide the potential for good performance over a wide range of parameters. The machine and experiments will find the best practical set of parameters in actual operation. The following items are the key variables targeted for luminosity performance by the upgrade:

- **Beam current:** the total beam current may be a hard limit in the LHC since many systems are affected by this parameter: RF power system and RF cavities; collimation; cryogenics; kickers; vacuum; beam diagnostics; QPS; etc. Radiation effects aside, all existing systems have been designed, in principle, for $I_{\text{beam}} = 0.86$ A, the so-called ‘ultimate’ beam current. However the ability to go to the ultimate limit is still to be experimentally demonstrated and the HL-LHC will need to go 30% beyond ultimate with 25 ns bunch spacing.
- **Beam Brightness:** The beam brightness, the ratio of the bunch intensity to its transverse emittance, is a beam characteristic that must be maximized at the beginning of beam generation and then preserved throughout the entire injector chain and in LHC itself. The LIU project has as its primary objective increasing the number of protons per bunch by a factor of two above the nominal design value while keeping emittance at the present low value.
- **β^* and cancelling of the reduction factor R.** A classical route for a luminosity upgrade with head-on collisions is to reduce β^* by means of stronger and larger aperture low- β triplet quadrupoles. This reduces the transverse size of the luminous region resulting in the gain in peak luminosity. There is a concomitant increase in beam sizes in the triplet magnets. For operation with a crossing angle a reduction in β^* values also implies an increase in the crossing angle when respecting the requirement for a constant normalized beam separation over the common part of the insertion. The increased crossing angle in turn requires a further increase in the triplet magnet aperture, a larger aperture D1 (first separation dipole), and further modifications to the matching section.
- **Stronger chromatic aberrations** coming from the larger β -functions inside the triplet magnets may furthermore exceed the strength of the existing correction circuits. The peak β -function is also limited by the possibility to match the optics to the regular beta functions of the arcs. A previous study has shown that the practical limit for β^* in the nominal LHC is around 30 cm cf. the nominal 55 cm (the LHC operated in 2016 with $\beta^*=40$ cm at 6.5 TeV beam energy). However, a novel scheme called Achromatic Telescopic Squeeze (ATS) [12] uses the adjacent arcs as enhanced matching sections. The increase of the beta-functions in these arcs can boost, at constant strength, the efficiency of the arc correction circuits. In this way a β^* value of 15-20 cm can be envisaged, and flat optics with a β^* as low as 10 cm in the plane perpendicular to the crossing plane could be realized. For such a β^* reduction the triplet quadrupoles need to double their aperture, and require a peak field 50% above those in the present LHC. This implies the use of new, advanced, superconducting technology based on Nb₃Sn. Also the magnets in the matching section (D2-Q4,Q5,Q6) must have a larger aperture than those in the present LHC, in order to accommodate the larger β -functions coming from the lower β^* . Indeed, in the HL-LHC the aperture of the Q5 quadrupole and its corrector will be increased to 70 mm (from the present 56 mm). The Q4 quadrupole, and associated correctors, initially designed for 90 mm aperture, will be kept at 70 mm aperture (present LHC), limiting the minimum β^* to 20 cm. However it is foreseen to eventually revert to a 90 mm wide Q4 (by installing a new quadrupole type (MQYY)) in a second phase as consolidation of the HL machine. This should allow a β^* of 10 cm to be attained by using flat beams, or a β^* of 15 cm for round beam operation.

The drawback of very small β^* is that it requires a larger crossing angle θ_c . This causes a severe reduction of the geometrical luminosity reduction factor R. In Figure 1-5 the reduction factor is plotted vs. β^* values.

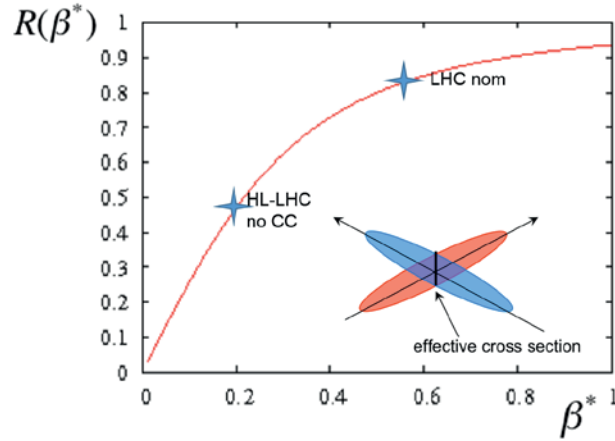


Figure 1-5: Behaviour of geometrical luminosity reduction factor vs. β^* for a constant normalized beam separation with the indication of two operational points: nominal LHC and HL-LHC with no crab cavities (CC). The insert illustrates the bunch crossing overlap reduction effect.

Various methods can be employed to at least partially counteract this effect. The most efficient and elegant solution for compensating the geometric reduction factor is the use of special superconducting RF crab cavities (CC), capable of generating transverse electric fields that rotate each bunch longitudinally by $\theta_c/2$, such that they effectively collide head on, overlapping perfectly at the collision points, as illustrated in Figure 1-6, see bottom right insert. Crab cavities allow access to the full performance of the small β^* values offered by the ATS scheme and the larger triplet quadrupole magnets, restoring the reduction value R to that of the present LHC despite the much larger θ_c . While the crab cavities boost the virtual peak luminosity, β^* variation during the fill – the so-called dynamic β^* squeeze – could be used as levelling mechanism. This would allow optimization of the size of the luminous region and thus the pile-up density throughout the whole fill.

The crab cavities can also be used to tilt the bunches in a direction perpendicular to the plane of crossing. Together with an additional higher harmonic RF system for bunch shaping, such a scheme could provide longitudinal pile-up density control and provide an additional handle for luminosity levelling through the so-called ‘crab-kissing’ scheme (see chapter 4). However, in the re-baselining exercise carried out in June 2016 to cope with the increased cost of the technical infrastructure, it has been decided to adopt in the baseline the installation of only two crab cavities per beam on each side of the relevant IPs, rather than the four crab cavities previously foreseen. As shown in Fig. 1-6 the new baseline (half CC system) brings the reduction factor R for the HL-LHC with $\beta^* = 20$ cm to the same level as LHC in 2016 operating at $\beta^* = 40$ cm.

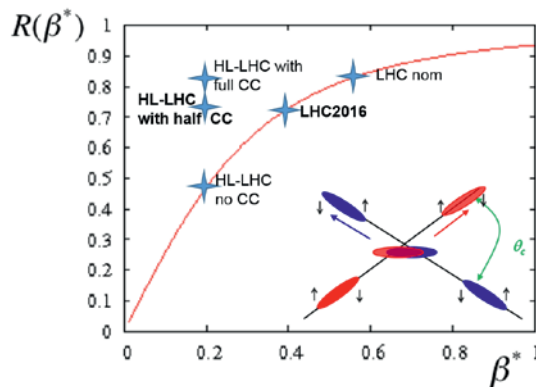


Figure 1-6: Geometrical reduction factor R vs β^* showing the increased performance in HL-LHC due to crab cavities (CC), both in the previous configuration (full CC, scaled to β^* of 20 cm) and the present one (half CC). The crab cavity beam manipulation is depicted the picture at right (the small arrows indicate the torque on the bunch generated by the transverse RF field).

1.2.5 Re-baselining of June 2016

To cope with an increase of the amount of required civil engineering (CE) and the estimated cost increase of the technical infrastructure, partly due to increase of underground volume and building surface, the project underwent a new optimization process aiming at a consistent cost saving. The cost saving breakdown is about 10% on the technological part of the project and 30% on the CE and technical infrastructure. A clear aim is to minimize the impact on luminosity performance. The main outcome is the following list of modifications. Included in the list are also a few modifications that were already in the pipeline before the June 2016 re-baselining – as such this list is the comprehensive list of changes with respect the previous edition TDRV0 [13].

- Powering the triplet with one main circuit per side (plus trims); previously, there were two main powering circuits.
- Operating temperature of Q6 quadrupole (in P1 and P6) at 4.2 K rather than 1.9 K.
- Avoiding doubling of the Q5 MQY magnet in P6 by operating it at 1.9 K instead of 4.2 K.
- Powering of the matching section quadrupoles (Q4-Q5-Q6) in P1 and P5, and their correctors, from RRs (rather than from the new UR service gallery).
- Shortening of the SC links following the choice of June 2015 to position the magnet power converters in the underground service gallery.
- Suppressing the 11 T dipole magnets in P2, by instead integrating the dispersion suppressor collimator (TCLD) in a new connection cryostat.
- Reduction of 11 T and TCLD requirements in P7: only one 11 T unit per side (left and right of P7) is to be installed in LS2. The second 11 T/TCLD unit per side to be installed in LS3 has been cancelled.
- Reduction of TCTPM (new tertiary collimators) collimators to be installed from 16 to 8.
- Reduction of the crab cavity system to two cavities per beam and per side (half CC system); 16 cavities (8 cryo-modules) are now foreseen to be installed. 8 of double quarter wave type (in P5) and 8 of RF dipole type (in P1).
- New integration layout of the mini-TAN into the D2 cold-mass.
- Scope reduction for the TCDD (that now is an absorber incorporated in D1 for P2 and P8, injection points); upgrade of the TCDS with one model rather than two.
- Insertion of the IT string test at SM18 into the HL-LHC Cost-to-Completion.

Other hardware changes that do not impact the tunnel layout include:

- a more extensive use of the quench heaters thereby eliminating many switches and energy extraction systems;
- reduction in the redundancy of discharge units of the protection system;
- a new layout of the cold box of the new refrigerators, with a separate distribution box;
- use of laminations for MQXF (triplet quadrupole);
- optimization of the vacuum layout.

All these changes are described in more detail in the relevant chapters.

1.2.6 Performance

The projected luminosity performance along the whole life of LHC/HL-LHC machine is shown in Figure 1-7, where some “luminosity learning” due to operational experience and staging of some components is included.

If the performance of the HL-LHC can go beyond the design levelled luminosity value of $L_{\text{peak}} = 5 \times 10^{34} \text{ cm}^{-2} \text{ s}^{-1}$, and if the upgraded detectors will accept a higher pile-up, up to 200 in average, then the performance could eventually reach $7.5 \times 10^{34} \text{ cm}^{-2} \text{ s}^{-1}$ with levelling. With such parameters a performance of more than 300 $\text{fb}^{-1}/\text{year}$ is possible if the days of proton physics per year can be increased after LS4 and LS5. Here one foresees the end of the ALICE ion program after LS4 and a reduced need for machine development time after LS5. This would allow up to 4000 fb^{-1} to be obtained before 2040, as shown in Figure 1-8. The graphs already include the small performance change due to the re-baseline exercise of June 2016, with an efficiency in luminosity production of 50%. A more detailed discussion of performance, and of impact on it due to June 2016 re-baseline exercise, can be found in Chapter 2.

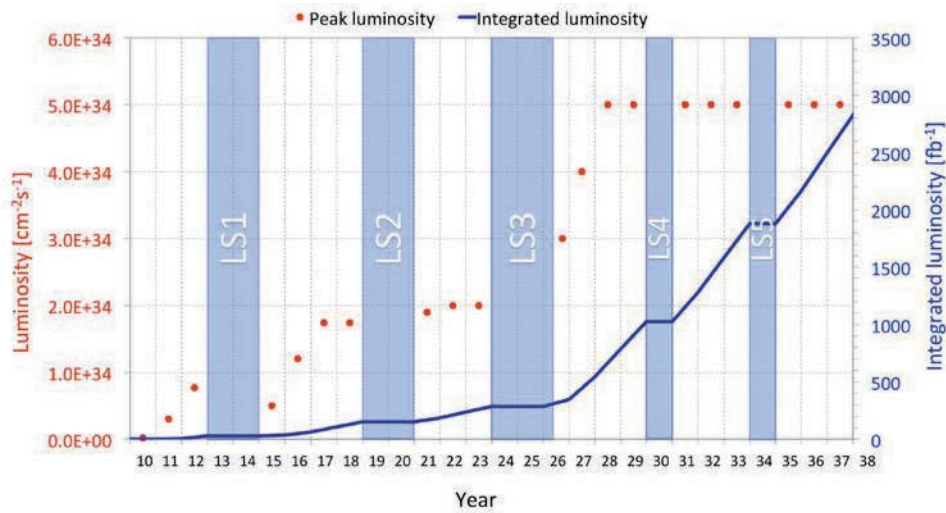


Figure 1-7: Forecast for peak luminosity (red dots) and integrated luminosity (blue line) in the HL-LHC era, according to the nominal HL-LHC parameters.

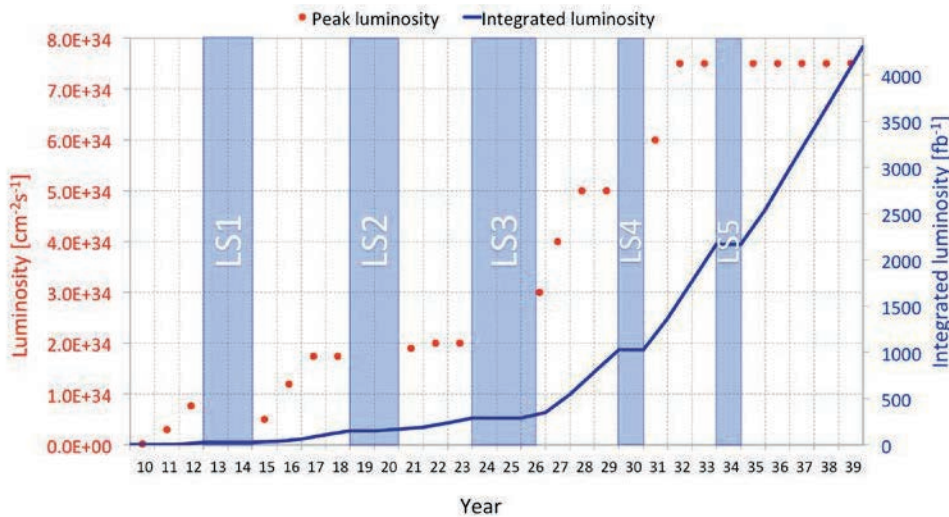


Figure 1-8: Forecast for peak luminosity (red dots) and integrated luminosity (blue line) in the HL-LHC era, for the case of ultimate HL-LHC parameters.

1.2.7 Main milestones

The HL-LHC schedule aims at the installation of the main HL-LHC hardware during LS3, together with the final upgrade of the experimental detectors (the so-called Phase II upgrade). However, a few items such as the new cryogenic lay-out for P4; new DS collimators integrated in the connection cryostat in P2 for ions; the 11 T

dipole magnets for DS collimation in P7 for both ion and proton beams, will be installed during LS2 or possibly during extended technical stops.

The HL-LHC schedule is based on the following milestones, summarized in Figure 1-9:

- 2014: Preliminary Design Report (PDR) (achieved);
- 2015: First Cost & Schedule Review (C&SR-1); end of design phase, release of Technical Design Report (TDR_v0) (achieved);
- 2016: Validation of main hardware components (short models or prototypes); TDR_v1 and C&SR-2 (achieved);
- 2017-2018: Testing of full prototypes (including crab cavity test in SPS) and release of final TDR;
- 2018–2023: Construction and test of long-lead hardware components (e.g. magnets, crab cavities, SC links, collimators);
- 2018–2020: Start heavy excavation works;
- 2019–2020: LS2 – New cryogenics lay-out in P4; DS collimators in connection cryostat in P2 and DS collimators with 11 T in P7; preparation of infrastructure in the tunnel and new service galleries;
- 2021–2023: String test of inner triplet;
- 2024–2026: LS3 – Main installation (new magnets, crab cavities, cryo-plants, collimators, SC Links, ancillary equipment, absorbers) and hardware commissioning.



Figure 1-9: Schematic representation of the HL-LHC timeline.

1.2.8 Cost

The HL-LHC project, as approved by the CERN Council of June 2016 with a cost ceiling of **950 MCHF** (Material budget), will end construction in 2026 with the installation and commissioning of the main equipment [7]. However, during its exploitation, the HL-LHC machine will continue to evolve and improve, thanks to an ongoing consolidation program, similar to that of the present LHC. The main hardware that one can foresee as an option for further improving performance are:

- Installation of wider aperture Q4: 90 mm aperture MQYY replacing the 70 mm MQY (beneficial for flat beams);
- Completion of CC system by installing further 16 cavities (for a total of 4 CC/beam/IP side);
- Hollow electron lens for halo cleaning;
- Wires or electron beams to compensate long range beam-beam (LRBB) effects;
- An additional SRF accelerating cavity system, operating at either 200 or 800 MHz;
- Wide band feedback system to fight intra-bunch instabilities such as those due to electron cloud.

The Cost-to-Completion (CtC) of the full HL-LHC project construction, as scrutinized and endorsed by the C&SR I in March 2015, amounts to about 950 MCHF for materials (including the cost for associate personnel, but excluding some items that are accounted for by the Consolidation project). In the C&SR-1, the bottom-up evaluation of staff personnel requirements amounts to more than 1600 fulltime equivalent (FTE) years. This CtC does not include any of the above listed options. It does include the civil engineering work for the underground caverns and galleries (both for IP1 and IP5).

At the time of the C&SR I the cost evaluation for WP17- Infrastructure, Logistics and Civil Engineering was presented with a budgetary envelope of 170 MCHF: 100 MCHF for Civil Engineering and 70 MCHF for all the remaining items of WP17. It is worth noting that 10 MCHF had been transferred as a contribution to the upgrade of the magnet test facility (the SM18 upgrade project managed by TE department). The budget profile approved by the CERN Council of June 2016, is shown in Figure 1-10.

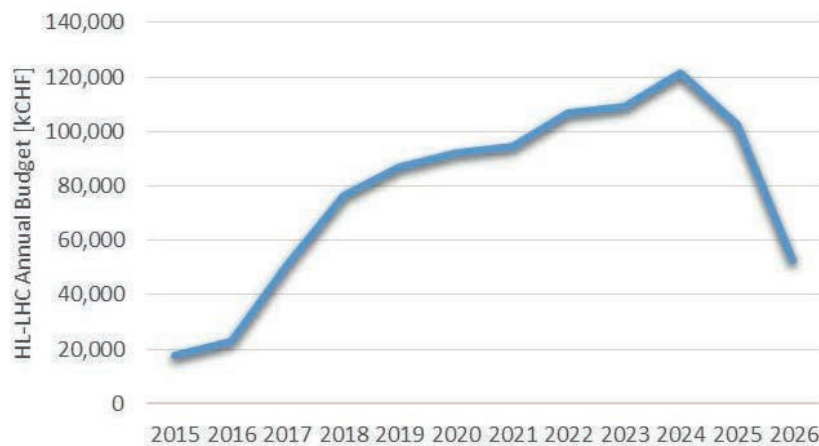


Figure 1-10: The HL-LHC construction project budget allocation as a function of time over 2015–2026, as per CERN Medium-Term Plan 2017-2021 with the full CtC.

The effect of the re-baselining exercise has not yet been taken into account in detail. However, the re-baseline as approved by the CERN executive committee of 3 August 2016 foresees the same amount of material budget: 950 MCHF. If needed, a re-profiling within the envelope could be implemented by CERN.

1.3 The collaboration

The LHC Luminosity Upgrade was envisioned from the beginning as being an international project. Indeed, US laboratories started to work on it with considerable resources well before CERN. In 2002–2003 collaboration between the US laboratories and CERN established a first road map for a LHC upgrade [9]. The LARP programme was then set up and approved by the US Department of Energy (DOE). In the meantime, CERN was totally engaged in LHC construction and commissioning: it could only participate in Coordinated Accelerator Research in Europe (CARE), an EC-FP6 programme, in 2004–2008. CARE contained a modest programme for the LHC upgrade. Then two FP7 programmes (SLH-PP and EuCARD) helped to reinforce the design and R&D work for the LHC upgrade in Europe, although still at a modest level. KEK in Japan, in the framework of the permanent CERN-KEK collaboration, also engaged from 2008 in activities for the LHC upgrade. LARP remained, until 2011, the main R&D activity in the world for the LHC upgrade.

Finally, with the approval of the FP7 Design Study *HiLumi LHC* in 2011, and the maturing of the main project lines considered in Section 1, the HL-LHC collaboration took its present form. It is worth noticing that FP7-HiLumi LHC covers only the design of a few systems, given the limited funding available to the programme. However, it has allowed the formation and structuring of a European participation in the LHC Upgrade from the very beginning of the project. Since 2013 efforts have been launched to establish a collaboration framework for the HL-LHC project that continues beyond the EC funded FP7 Design Study and to address not only system designs but also the contribution of actual hardware systems. The cornerstones in

these efforts are the transformation of the US LARP program to a construction project and the agreement with Japan for the deliverable of superconducting dipole magnets. In addition to these efforts with the USA and Japan, CEA (Saclay, France), INFN (Milan and Genova, Italy) and CIEMAT (Madrid, Spain) have signed further collaboration agreements in 2014 to carry out design, engineering and prototyping work for HL-LHC magnets in addition to the FP7-HiLumi LHC commitment. Furthermore, several CERN member states (e.g. UK, Sweden, Poland etc.) are in the process of setting up collaborations with CERN beyond FP7-HiLumi LHC. In all cases for member state agencies, the CERN funding for the activities is approximately 50%, with the balance being provided by the collaborating institutes. In Figure 1-11 a schematic indicating the various collaborating branches is shown.

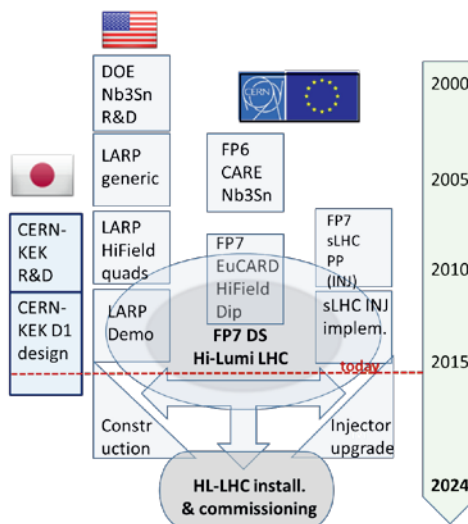


Figure 1-11: Timeline of the various collaboration branches, converging toward the LHC luminosity upgrade.

1.3.1 FP7-Hilumi LHC

The “FP7 High Luminosity Large Hadron Collider Design Study” (HiLumi LHC) proposal was submitted in November 2010 to the EC Seventh Framework Programme (FP7). Approved with a full score of 15/15 it has been fully funded by the EC. The contract was signed by the fifteen partners (beneficiaries). KEK is a partner without EC funding – all of their funding is internal. The US laboratories were part of the proposal, without EC funding, but then for various reasons (mainly related to Intellectual Property issues) they could not sign the FP7-HiLumi LHC Consortium Agreement, thus they are external associates with no formal obligations. In practice LARP is excellently coordinated with FP7-Hilumi and the project heavily relies on LARP to reach the project goals.

The rules of FP7 were such that each of the thirteen European institutions that were members of HiLumi LHC have to match the EC contribution with their own funding. In the case of FP7-HiLumi the matching funds equal the EC funds: each EU Institute received 50% of the total cost (including overheads). The exception was CERN, which received only 17% of its total costs, mainly for management and coordination. In Figure 1-12 the funding mechanism is explained. Given the success of the evaluation, see above, the project was ranked first in its category and was fully financed, with a EU contribution of M€4.9 against a request of M€4.97.

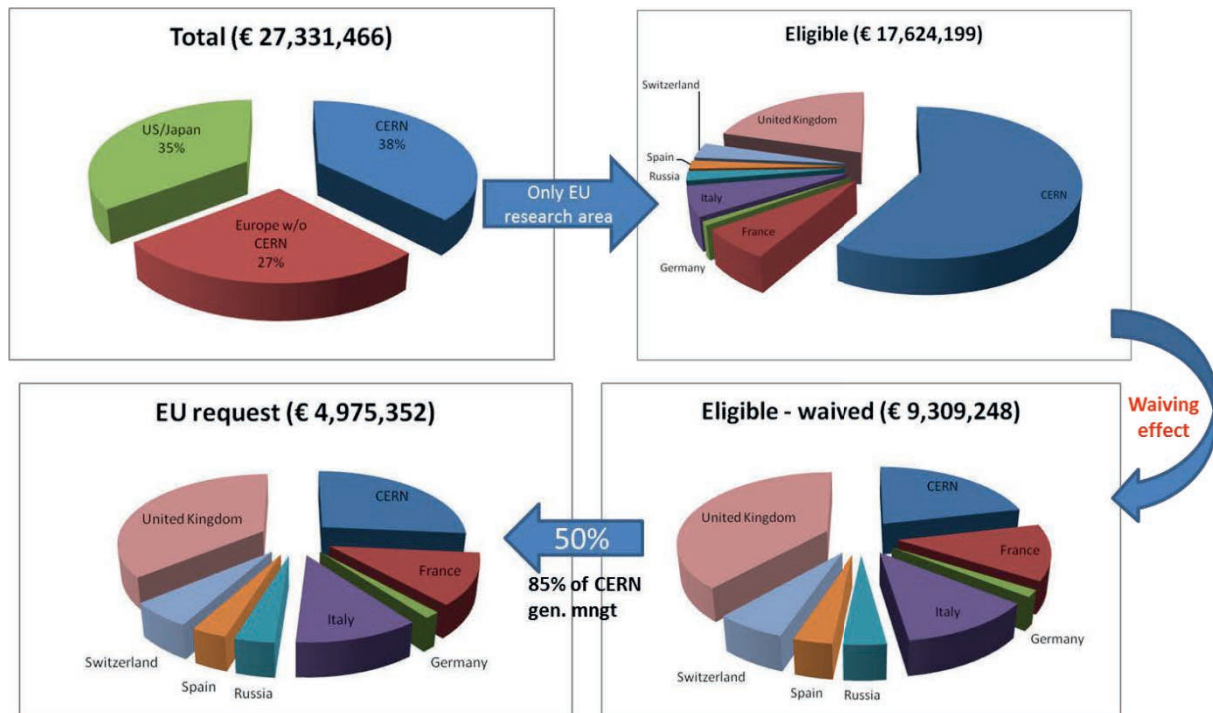




















Figure 1-12: (a) Total estimation of the cost of the design study, subdivided by the US and Japan, EU institutes and CERN. (b) Total cost with the US and Japan removed (i.e. only costs that are eligible for funding by the EC). (c) Effect of CERN waiving the cost for technical works (recognizing that the HL-LHC is part of the core CERN programme financed via the normal budget), while keeping the extra cost generated by the management and coordination of the project. This is the total cost declared to the EC. (d) Cost claimed from the EC: 50% of the declared cost (eligible cost reduced by CERN waiving action).

In Figure 1-13 a list of the 15 FP7-HiLumi institutions is given, followed by a list of the five US collaborating institutes. FP7-HiLumi LHC has closed its activity by delivering the last of the required reports, the most important being the TDR-V0 [13]. FP7-HiLumi LHC design study ended formally on 31 October 2015 (however last deliverable report was issued in January 2016) and the consortium dissolved. A new type of framework, based on a MoU is being set up to form the new collaboration, including partners beyond FP7-HiLumi. The first meeting of this new HL-LHC Collaboration Board will take place at the annual HL-LHC meeting in November 2016.

HIGH LUMINOSITY LARGE HADRON COLLIDER HL-LHC

Short Name	Country	Logo	Short Name	Country	Logo
CERN	Geneva Switzerland		STFC*	Daresbury United Kingdom	
CEA	Saclay France		ULANC*	Lancaster United Kingdom	
DESY	Hamburg Germany		UNILIV*	Liverpool United Kingdom	
INFN	Frascati Italy		UNIMAN*	Manchester United Kingdom	
CSIC	Madrid Spain		HUD	Huddersfield United Kingdom	
EPFL	Lausanne Switzerland		KEK	Tsukuba Japan	
SOTON	Southampton United Kingdom		BINP	Novosibirsk Russia	
RHUL	London United Kingdom		*Members of Cockcroft Institute		

(a)

Short Name	Country	Logo	
BNL	Upton, NY USA		
FNAL	Batavia, IL USA		
LBNL	Berkeley, CA USA		
SLAC	Menlo Park, CA USA		
ODU	Norfolk, VA USA		

(b)

Figure 1-13: (a) Table showing the 15 members (‘beneficiaries’) of the FP7 HiLumi LHC design study and (b) the five LARP laboratories that are associated with the project.

1.3.2 LHC Accelerator R&D Program (LARP) and HL-LHC Accelerator Upgrade Project

The LARP programme was initiated by the US Department of Energy (DOE) in 2003 to participate in the commissioning of the US-built interaction region triplets by bringing together and coordinating resources from the four US HEP laboratories (BNL, FNAL, LBNL and SLAC) with the inclusion of some universities as the programme evolved. In addition the Program supported the involvement of the US accelerator community in beam physics studies and beam instrumentation contributions aimed at answering fundamental beam physics questions, improving the LHC performance and maximizing the physics output of the HEP experiment at the LHC.

By 2003 it was already recognized, based on the Tevatron experience, that an increase in LHC luminosity would become necessary after a decade of LHC operation to reduce the ‘halving time’, i.e. the time needed to reduce statistical errors by a factor of two. Consequently, the programme focused – from the very beginning – on the design of improved focusing quadrupoles for the LHC low- β insertion regions, finding a synergy with the various DOE high-field magnet (HFM) R&D programmes at the participating laboratories. The conductor of choice for this R&D programme was selected to be Nb₃Sn and therefore LARP became synergetic with another DOE programme, the Conductor Development Program (CDP), initiated in 1998 with

the goal of improving the performance of Nb₃Sn. The LARP, CDP, and other US laboratories' HFM activities interacted in an extremely constructive way, achieving a substantial increase in the critical current performance of Nb₃Sn superconductors (Figure 1-14) and defining the assembly technique for accelerator quality high-field Nb₃Sn magnets in different kinds of configuration and with different apertures.

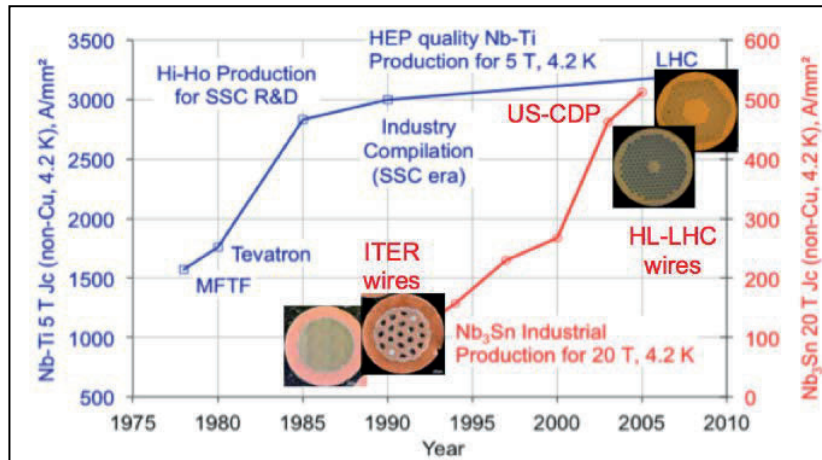


Figure 1-14: Left: Improvement in J_c (current density) in Nb₃Sn superconductor during the last three decades compared with Nb-Ti J_c performance.

The LARP effort was funded at approximately \$12–13 million/year, with 50% of the funding going directly to magnet development. Several magnets developed by LARP reached and surpassed the design field as shown in Figure 1-15(b) for one of the latest models (MQXFS1, the first 150 mm aperture quadrupole assembled and tested in 2016 with US and CERN coils). Additionally, LARP has demonstrated the scale-up of the Nb₃Sn technology (i.e. the performance of the technology for magnets as long as 3 m) as shown in Figure 1-15(a) for the 90-mm aperture long quadrupole (LQ). The achievements of the US programmes, in particular LARP, but also of the general R&D high-field magnet programme, have led to the adoption of the Nb₃Sn superconductor solution as the baseline for the HL-LHC's new focusing system and 11 T magnets.

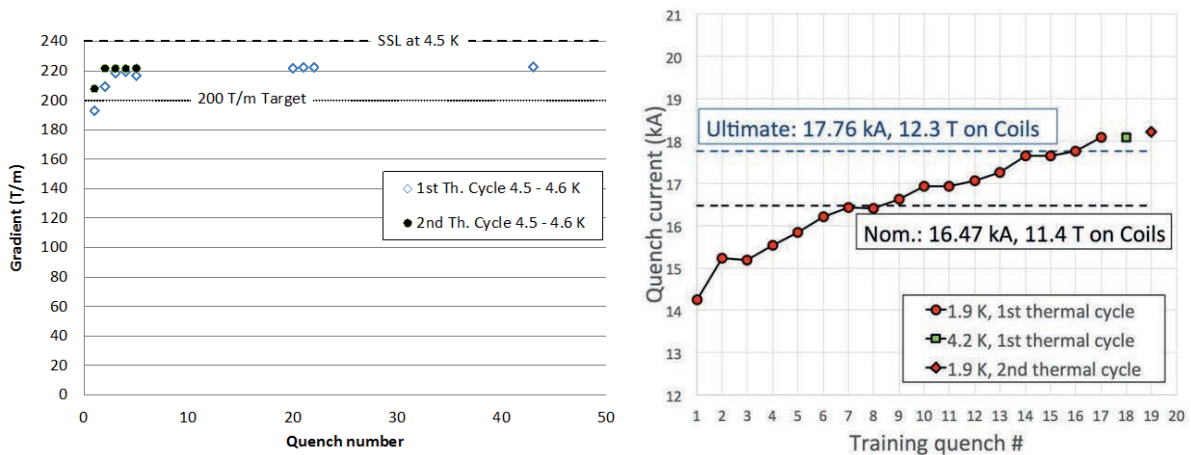


Figure 1-15: (left) Quench performance of the long quadrupole (LQ), the first quadrupole demonstrating the scale-up of Nb₃Sn technology to lengths of interest for LHC applications (~3 m), (right) quench performance of MQXFS1 (150 mm aperture) during the first cold test in February 2016, showing good quench performance and memory after warm-up and cool-down cycles.

In addition to contributions to LHC commissioning and magnet development-related activities, LARP was also tasked with the support and promotion of accelerator physics R&D activities at the LHC. One of the most fundamental contributions was the initial development of solutions to the scheme based on crab cavities (Chapter 4) to increase the instantaneous luminosity through a compensation of the geometric reduction factor

by allowing the bunches to collide effectively head-on through the application of transverse RF electric fields. By 2013-2014, LARP demonstrated the basic idea in “Proof Of Principle” cavities and subsequently completed the RF electromagnetic design for the crab cavities presently considered for the HL-LHC baseline. Other contributions from LARP included a scheme for rotatable collimators (with a prototype developed and built at SLAC and subsequently tested at CERN), a Wide Band Feedback System to control lateral instabilities in the LHC Injector chain and, possibly, in HL-LHC and presently being tested at the SPS, and several studies on e-cloud and mitigation of beam halo by use of e-lens collimators.

An additional, important aspect of LARP commitment was the institution of the Toohig Fellowship (<http://www.interactions.org/toohig/>) to support young accelerator physicists and engineers wishing to pursue research at the LHC in the early years of their career.

In 2016, DOE recognized the need for the HL-LHC upgrade by providing CD-0 (Critical Decision-0, Mission Need Statement) on April 13th 2016 and establishing the US “HL-LHC Accelerator Upgrade Project” (HL-LHC AUP). The HL-LHC AUP, with a funding guideline of approximately 200M\$ (US Accounting), will be executed between 2016 and 2024 to provide US in-kind contributions to HL-LHC. DOE and CERN will negotiate deliverables from the US in the coming year, with obvious candidates being the focusing magnets crab cavities and, in second priority, hollow e-lens and feedback systems.

In the CY16–CY17 period, LARP will concentrate on prototyping the elements needed by the HL-LHC project in which US national laboratories and universities have demonstrated excellent capabilities. In particular LARP has built and successfully tested one short triplet quadrupole QXF (1m) model and plans – subject to funding availability – to build a second short model in the near future. One (out of 3 planned) long (4 m) QXF magnet model is under construction as well and will be tested by the beginning of CY17. In addition, LARP contributed to the delivery of a wide band feedback system prototype for tests in the SPS (ongoing) and plans to deliver four fully-dressed SCRF crab cavities. This phase is expected to continue until the start of construction in the period 2018-2024.

1.3.3 KEK

Within the framework of the CERN-KEK collaboration, KEK has conducted Nb₃Al superconductor R&D for the high-field magnets aimed at the future LHC upgrade from the early 2000s in collaboration with the National Institute of Materials Science (NIMS) in Japan. The Nb₃Al superconductors are made by the rapid-heating, quenching transformation (RHQT) process, which was invented by NIMS. These superconductors have shown better critical current density and less strain dependence, and have been considered to be one of the promising candidates for high-field accelerator magnet applications. Nevertheless, KEK and NIMS faced technical difficulties in long wire production and it was judged in 2011 that the Nb₃Al superconductor was unfortunately not ready for industrialization for the HL-LHC upgrade anticipated in around 2022.

KEK has officially participated in the FP7 HiLumi LHC design study since 2011 in the context of enhancing the Japanese contribution to the physics outcome from the ATLAS experiment. Following the suppression of research activities on the development of the Nb₃Al superconductor, the main effort was redirected to the conceptual design study for the beam separation dipole magnet, D1, situated immediately after the low-beta insertion quadrupoles in the HL-LHC machine. While the conceptual design study has been pursued dominantly by KEK, close collaboration with CERN and other partners has strengthened the success of the design study. The D1 magnet is based on the mature Nb-Ti technology. Design challenges are the tight control of the field quality with the large iron saturation, and the accommodation of the heat load and the radiation dose. The research engagement includes development of the 2 m long model magnet and testing at 1.9 K. KEK has also contributed to the HiLumi LHC design study through beam dynamics studies and cooperative work associated with the crab cavity design.

Aside from the HiLumi LHC, KEK has also participated in the LHC Injectors Upgrade (LIU) project. The main collaboration items have been consolidation and upgrade of PS Booster RF systems using Finemet-FT3L technology and development of the longitudinal damper system.

1.3.4 Other collaborations

In 2014, CEA (Saclay, France), INFN (Milan and Genova, Italy), and CIEMAT (Madrid, Spain), have each signed a further collaboration agreement to carry out design, engineering, and prototype work for HL-LHC magnets in addition to their FP7 commitments. STFC and a collaboration of UK universities and UPPSALA University are in the process of signing new collaboration agreements in 2016. Further negotiations are ongoing with Russia, Canada, Poland and Georgia. In all cases, the CERN funding is about 50%, the rest being charged to the collaborating institutes.

1.3.4.1 CEA

The CEA agreement concerns ‘Research and Development for future LHC Superconducting Magnets’. It has six technical work packages, covering R&D for the HL-LHC and for post-LHC magnets. Among them, the following are of HL-LHC interest.

- Design and construction of a single aperture, 1 m long, full-size coil model magnet for the first quadrupole of the matching section, Q4. The magnet is based on classical Nb-Ti technology but has a very large aperture (90 mm) in a two-in-one cold mass, and thus presents a number of design challenges.
- Completion of the 13 T, large-aperture dipole Fresca2 (a technological HL-LHC work package that has served to promote Nb₃Sn at CERN).
- Studies on Nb₃Sn thermal properties and a finite element model of Nb₃Sn cabling.

1.3.4.2 INFN (Milan and Genova)

The INFN agreement is also related to R&D on superconducting magnets for the HL-LHC and concerns two main items:

- Design and construction of a prototype of each of the six high-order corrector magnets for the inner triplet, all with a single aperture of 150 mm. The work is based on Nb-Ti superferric technology and is carried out at INFN-LASA in Milano. An option based on the MgB₂ superconductor is also being considered by INFN.
- Engineering Design of the superconducting recombination dipole magnet, D2, the first Two-in-One magnet, at the end of the common beam pipe. The work is based on Nb-Ti technology, with design challenges coming from the large aperture and the relatively high fields that have a parallel direction in both apertures. The work is being carried out at INFN-Genova. The collaboration has been recently extended to include the construction by INFN via industrial procurement, of a short model (1.5 m long) and of a full length prototype (about 8 m long).

1.3.4.3 CIEMAT (Madrid)

The CIEMAT agreement concerns the design and construction of a 1 m long prototype of the 150 mm aperture nested orbit corrector dipole for the inner triplet. It features two dipoles coils, rotated by 90° for simultaneous horizontal and vertical beam steering, in the same aperture. The main challenges are the mechanical structures to withstand the large torque, and the unusual force distribution arising when both field directions are needed.

1.3.4.4 UK Universities and STFC

An agreement is in place between CERN and University of Manchester, with the latter representing other six British Institutes: ASTEC/STFC, Royal Holloway and Bedford New College, Lancaster University, University of Liverpool, University of Southampton and University of Huddersfield. The agreement concerns modelling and equipment construction for various WPs: crab cavities (various studies, construction of one pre-series cryo-module, participation in the test program); collimation system (studies, code development and one low impedance prototype); cold powering (study and design and construction of one component of the feed-box); beam diagnostics (studies and design of electro-optic beam position monitor (EO-BPM) and gas-jet based

beam profile monitor with prototype construction of the EO-BPM). The agreement is foreseen over four years: 2016-2019.

1.3.4.5 UPPSALA University

Uppsala university will upgrade the FREIA facility (being used for testing SRF cryomodules for ESS) to carry out power test at cryogenic conditions for Hilumi corrector magnets (namely the nested orbit corrector of the CIEMAT collaboration) and the SRF crab cavity prototypes.

1.3.4.6 Other agreements

Further agreements are under discussion. At this stage of the negotiations, the following agreements are worth mentioning¹:

- Finland: Lapland University has prepared a 3D visualization and virtual tour of the HL-LHC installation (underground and surface <http://hilumilhc.web.cern.ch/hilumi3d>). The underground visualization is particularly useful for integration purposes and, eventually, may be used as an outreach tool since visits will not be permitted.
- Russia: proposal to contribute to the design of cavity power coupler, new higher harmonic 800 MHz RF system, design and production of electron lenses and halo monitors.
- Canada: proposal to contribute to the refurbishment and production of new spares of warm quadrupole magnets for the LHC cleaning insertions and the study of beam-beam effects.
- Poland: proposal to contribute with manpower to the magnet measurement and installation campaigns.
- Georgia: proposal to contribute to the support feet and jacks for the new triplet and D1 and D2 magnets.

1.4 Governance and project structure

Given the fact that the application for the FP7 HiLumi LHC Design Study marked the start of the project in its present form, the structure and terminology are borrowed from the typical FP7 style. To avoid any duplication, the governance of the whole HL-LHC project has been conceived as an extension of the governance that was in place for the governance of the FP7-HiLumi LHC. The end of the Design Study at end of October 2015 is the opportunity to change the governance, better adapting it to the needs of the project in the construction phase. Here the present structure is briefly recalled and the new one introduced.

1.4.1 Present project governance and structure.

As noted above, the FP7-HiLumi LHC covered only a few work packages (WPs), recognizing that they make up the backbone of the upgrade. The WP structure, with tasks arranged in a tree-like structure, is the basic set-up of the project. LARP is a parallel structure, independently funded, associated with FP7 with connections both at project management level as well as at WP/task level to maximize synergy. KEK is a direct member of FP7-HiLumi. It is worth noting that HiLumi LHC is the term indicating the part of the HL-LHC that was covered by FP7 funds, even if in practice it has become a popular name for the whole project. In Figure 1-16 the general governance of the project during the FP7 funding period is shown. Each body contained the FP7 part and the part that was not covered by FP7. The Steering Committee was the main managing body: it met regularly every two months and all WPs were represented there, along with the participation of the LARP representatives. It oversees the progress of the technical work and planning, approving the milestones and deliverables for the HiLumi design study. The Steering Committee usually met in its 'enlarged' form, including the WPs not covered by FP7 and including the LARP leadership. The Collaboration Board was the highest-level governance body with representation from each institute.

¹ This is work in progress and reflects the state of negotiations as of end of August 2016.



Figure 1-16: The general governance scheme of FP-7 HiLumi LHC, used for the whole HL-LHC project.

In the case of approval of formal FP7 acts, only the FP7-WP coordinators and FP7 Institutes could vote. It is worth noting that the collaboration was based on a consortium agreement, signed by the 15 members (in FP7 terminology, beneficiaries) of FP7-HiLumi LHC. The US laboratories were not members of FP7-HiLumi LHC, however representatives of each US laboratory, including the LARP director, were co-opted onto the enlarged Collaboration Board. The formal link with the US laboratories was assured by the CERN-DOE Protocol II concerning the LHC and its upgrades. Given the fact that CERN is responsible for the LHC machine, the CERN director general, through his representative in the Collaboration Board, the project coordinator, had the right of veto.

The Parameter and Layout Committee and the Technical Committee had mainly technical functions inside the project. The Coordination group, chaired by the HL-LHC, LIU and Detector Management.

In Figure 1-17 the project structure, with all WPs and their coordinators, as well as the main collaborators, is shown. Typically, each WP is assigned three to six tasks. The tasks are the core of the technical work.

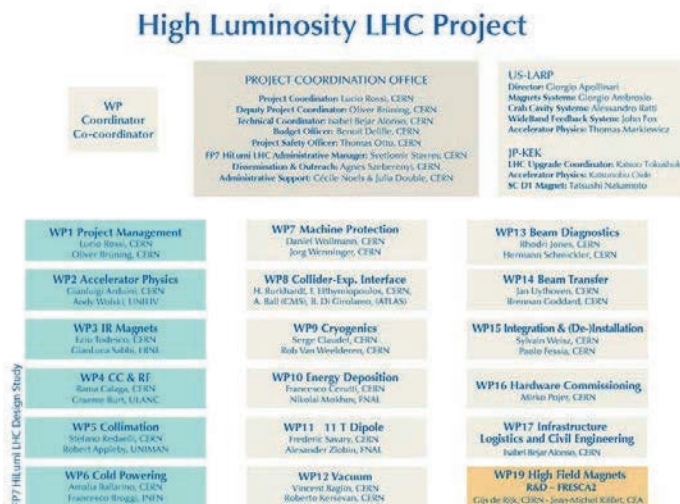


Figure 1-17: HL-LHC project structure, with FP7 part indicated in dark green. The orange box refers to the high-field magnets work package, which was started before the HL-LHC in the framework of generic R&D for the LHC upgrade.

1.4.2 New Project Governance and MoU

The transition from Design Study to a construction project requires modification of the project and committee structures. On the one hand, the transition requires a closer integration with the CERN equipment groups that control the manpower resources for the HL-LHC project and to establish a new Collaboration Board that recognizes the value and importance of the new collaboration partners with concrete hardware contributions and facilitates the coordination and information flow between the partners. On the other hand, the transition also implies the need to finish the design process, to freeze the key parameters, and to follow closely the hardware development. This second shift in the project needs requires a re-organization of the central HL-LHC committees. In particular, the HL-LHC project merged the HL-LHC Parameter & Layout Committee (PLC) and HL-LHC Technical Committee (HL-TC) in order to create one central HL-LHC Technical Coordination Committee (HL TCC) that follows up on the hardware developments and prototype testing. Figure 1-18 shows the present project structure that is in place since 2016.

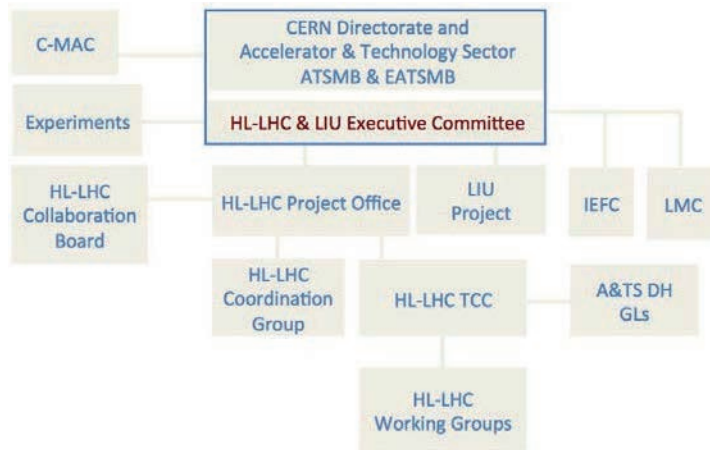


Figure 1-18. The HL-LHC organization in the global CERN Accelerator & Technology Sector structure for the construction phase.

The Steering Committee has been suppressed in this new structure as a committee for formal approval of the HiLumi deliverables. The part of technical follow up done in the Steering Committee has been taken up by the new Technical Coordination Committee, while its primary functions as managing body has been absorbed by the Project Office, with suitable participation of the WP leaders when necessary.

In addition to the above changes, the CERN management has introduced a new Executive Committee that looks after decisions that will affect both the LIU and HL-LHC projects. The change in the LHC schedule and shift of the LS2 technical stop are examples of decisions discussed at the new Executive Board. The HL-LHC Coordination Group has been reviewed in function and composition to avoid any overlap with the new Executive Committee.

1.5 References

- [1] The European Strategy for Particle Physics, adopted by the CERN Council at a special session at ministerial level in Lisbon in 2006, CERN (2006). <http://cern.ch/council/en/EuropeanStrategy/ESParticlePhysics.html>
- [2] European Strategy Forum for Research Infrastructures, ESFRI (2014). <http://ec.europa.eu/research/esfri>
- [3] The European Strategy for Particle Physics Update 2013, CERN-Council-S/106, adopted at a special session in Brussels on 30 May 2013, CERN (2013). <http://cern.ch/council/en/EuropeanStrategy/ESParticlePhysics.html>
- [4] Building for Discovery: Strategic Plan for U.S. Particle Physics in the Global Context, US DOE (2014). <http://science.energy.gov/hep/hepap/reports/>

- [5] L. Rossi, LHC Upgrade Plans: Options and Strategy, 2nd International Particle Accelerator Conference, San Sebastian, Spain, 4 - 9 Sep 2011, pp.TUYA02, p. 908. [CERN-ATS-2011-257](#)
- [6] G. Apollinari, I. Béjar Alonso, O. Brüning, M. Lamont, L. Rossi, High-Luminosity Large Hadron Collider (HL-LHC) : Preliminary Design Report, CERN-2015-005, DOI: [10.5170/CERN-2015-005](#)
- [7] The High-Luminosity LHC Project (Director-General) 298th Meeting of Scientific Policy Committee; [CERN/SPC/1068](#) ; CERN/FC/6014 ; CERN/3255, CERN (2016)
- [8] O. Brüning, R. Cappi, R. Garoby, O. Grobner, W. Herr, T. Linnekar, R. Ostojic, K. Potter, L. Rossi, F. Ruggiero (editor), K. Schindl, G. Stevenson, L. Taviani, T. Taylor, E. Tsesmelis, E. Weisse and F. Zimmermann, LHC Luminosity and Energy Upgrade: A Feasibility Study. [CERN-LHC-Project-Report-626](#), CERN (2002).
- [9] J. Strait, M. Lamm, P. Limon, N.V. Mokhov, T. Sen, A.V. Zlobin, O. Brüning, R. Ostojic, L. Rossi, F. Ruggiero, T. Taylor, H. ten Kate, A. Devred, R. Gupta, M. Harrison, S. Peggs, F. Pilat, S. Caspi, S. Gourlay and G. Sabbi, Towards a New LHC Interaction Region Design for a Luminosity Upgrade 20th IEEE Particle Accelerator Conference, Portland, OR, USA, 12 - 16 May 2003, pp.42-4, [CERN-LHC-Project-Report-643](#) (2003).
- [10] R. Garoby, S. Gilardoni, B. Goddard, K. Hanke, M. Meddahi, M. Vretenar, Plans for the upgrade of the LHC injectors. 2nd International Particle Accelerator Conference, San Sebastian, Spain, 4 - 9 Sep 2011, pp.[WEPS017](#) (2011)
- [11] J. Jowett, HL-LHC Heavy-Ion Beam Parameters at LHC Injection, CERN (2015) EDMS [1525065](#)
- [12] S. Fartoukh, Achromatic telescopic squeezing scheme and application to the LHC and its luminosity upgrade, Phys. Rev. Spec. Top. Accel. Beams 16 (2013) 111002; CERN-ACC-2013-0289 (2013). DOI: [10.1103/PhysRevSTAB.16.111002](#)
- [13] G. Apollinari, I. Béjar Alonso, O. Brüning, M. Lamont, L. Rossi, D1.10 - Annex 1 - Technical Design Report V0; EDMS: [1558149](#)

Chapter 2

Machine Layout and Performance

2 Machine layout and performance

2.1 Performance goals (nominal scheme)

The goal of the High Luminosity upgrade of the LHC is to deliver an integrated luminosity of the order of 250 fb⁻¹ per year in each of the two high-luminosity general-purpose detectors, ATLAS and CMS, located at the interaction points (IP) 1 and 5, respectively. The other two experiments, ALICE and LHCb with detectors located at IP2 and IP8 respectively, are expecting to collect integrated luminosities of 100 pb⁻¹ per year (of proton–proton data) and 5 fb⁻¹ to 10 fb⁻¹ per year, respectively [1-4]. No operation for forward physics experiments is expected after the upgrade.

The ATLAS and CMS detectors will be upgraded to handle an average number of pile-up events per bunch crossing of at least 140, corresponding to an instantaneous luminosity of approximately 5×10^{34} cm⁻² s⁻¹ for operation with 25 ns beams at 7 TeV, for a visible cross-section $\sigma_{vis} = 81$ mb [5]. The detectors are also expected to handle a line density of pile-up events of 1.3 events per mm per bunch crossing. ALICE and LHCb will be upgraded to operate at instantaneous luminosities of up to 2×10^{31} cm⁻² s⁻¹ and 2×10^{33} cm⁻² s⁻¹, respectively.

The HL-LHC upgrade project aims to achieve a ‘virtual’ peak luminosity that is considerably higher than the maximum imposed by the acceptable event pile-up rate, and to control the instantaneous luminosity during the physics fill (‘luminosity levelling’) so that the luminosity production can be sustained over longer periods to maximize the integrated luminosity.

A simplified model of the luminosity evolution has been developed [6] taking into account the beam population N_{beam} reduction due to the collisions (the so called ‘burn-off’) in n_{IP} collision points with instantaneous luminosity L_{inst} ,

$$\frac{dN_{beam}}{dt} = -n_{IP}\sigma_{tot}L_{inst}, \quad (2-1)$$

where we have considered pessimistically the total cross-section σ_{tot} (here assumed to be 111 mb [7]) for the estimate of the ‘burn-off lifetime’. No other sources of intensity reduction or emittance blow-up are considered in this model. Figure 2-1 shows the expected yearly-integrated luminosity as a function of the ‘virtual’ peak luminosity for three different values of the luminosity at which levelling is performed. In this figure, the corresponding optimum fill length T_{fill} (i.e. the length of time for each fill that will maximize the average luminosity production rate) is also shown. The annual integrated luminosity is determined for a minimum turnaround time ($T_{turnaround}$) of 3 hours (see Chapter 16), a scheduled physics time ($T_{physics}$) for luminosity production of 160 days per year, with N_{fills} successful physics fills of duration T_{fill} . A performance efficiency η of 50% (this was 53.5% in 2012 and it is 60.1% for 2016 at the time of writing¹) is assumed where [8]:

$$\eta = N_{fills} \frac{T_{turnaround} + T_{fill}}{T_{physics}} \times 100\% \quad (2-2)$$

¹ 24/09/2016 – The performance efficiency has been calculated for the period up to the start of MD3.

In order to reach the goal of integrating 250 fb⁻¹/year levelling must be performed at luminosities equal or larger than $5 \times 10^{34} \text{ cm}^{-2} \text{ s}^{-1}$ and peak virtual luminosities above $10^{35} \text{ cm}^{-2} \text{ s}^{-1}$. Furthermore, the performance efficiency must be at least 50% and the typical fill length must be comparable with the estimated optimum fill length (for comparison the average fill length during the 2012 run was 6.1 hours while it reached 15 hours in July 2016 [9]). In this respect, levelling to higher luminosities will be beneficial because it would make it easier to reach and even exceed the integrated luminosity goal, with comfortably short fill lengths. For that reason, the design aims at allowing an ultimate levelled luminosity of $7.5 \times 10^{34} \text{ cm}^{-2} \text{ s}^{-1}$ and all the systems will be designed to achieve such value but with no additional margin [10].

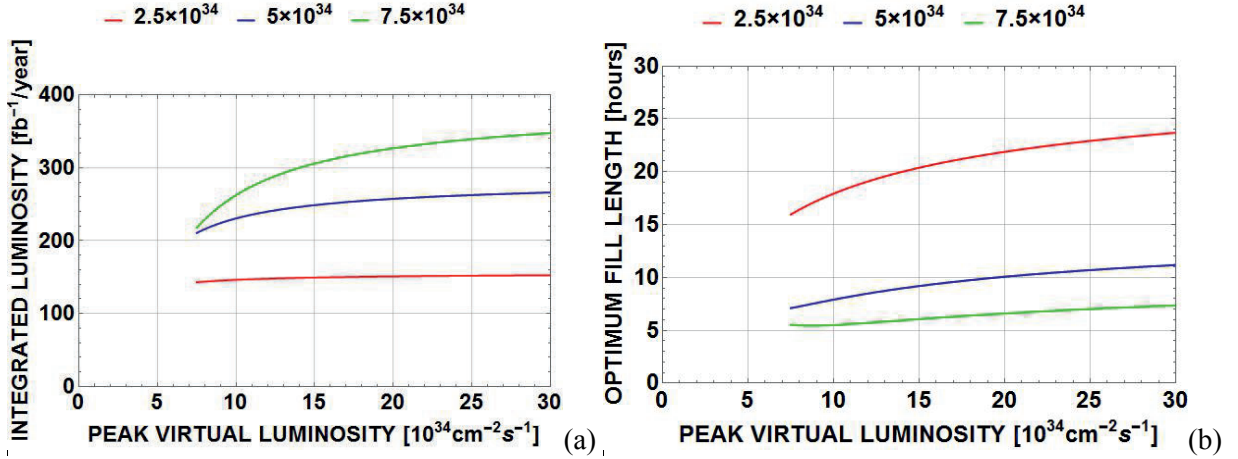


Figure 2-1: (a) Expected annual integrated luminosity; (b) optimum fill length as a function of the ‘virtual’ peak luminosity for three different values of the luminosity at which levelling is performed. A circulating current of 1.1 A (corresponding to $N_{\text{beam}} = 6.1 \times 10^{14}$ p), a minimum turnaround time of 3 hours and a performance efficiency η of 50% have been assumed. Only burn-off for a total hadron cross-section of 111 mb has been considered for the estimate of the beam population and virtual luminosity evolution. Two high-luminosity interaction points have been assumed.

2.1.1 Parameter space and basic parameter choices

The instantaneous luminosity L is given by

$$L = \frac{n_b N^2 f_{\text{rev}} \gamma}{4\pi \beta^* \varepsilon_n} R(\beta^*, \sigma_z, d_{\text{bb}}) \quad (2-3)$$

The R.M.S. normalized emittance ε_n in collision is assumed here to be equal for the two beams and for the horizontal and vertical planes. The Twiss beta function β^* in collision at the IP determines, together with the normalized emittance, the rams. beam size $\sigma^* = \sqrt{\varepsilon_n \beta^* / \gamma}$ at the IP (assuming that the contribution to the beam size due to the dispersion and the momentum spread of the beam can be neglected). Here and below it is assumed that the relativistic factor $\beta = 1$.

A crossing angle is needed to separate bunches immediately upstream and downstream of the collision point. This leads to a reduced geometric overlap between the colliding beams, and hence to a reduction in luminosity. The crossing angle needs to be increased when reducing the β^* in order to maintain a sufficiently large normalized long-range beam–beam separation d_{bb} . The luminosity is also reduced by the ‘hourglass effect’ that arises from the increase of the beta function upstream and downstream of the interaction point along the bunch longitudinal distribution. The hourglass effect is enhanced by a reduction in β^* and by an increase in bunch length σ_z . The luminosity reduction factor R in equation (2-3) takes both the crossing angle and the hourglass effect into account.

Equation (2-3) shows the parameters that can be varied to maximize the instantaneous luminosity. The considerations that constrain their values are briefly discussed below [11][12]:

- The maximum number of bunches n_b is limited by the minimum time interval between bunch crossings at the IP that can be handled by the detectors: this is limited to 25 ns. The maximum number of bunches that can be injected in the LHC is also limited by the following.
 - o The maximum number of bunches that can be transferred safely from the SPS to the LHC due to the maximum energy and transverse energy density that can be deposited on the injection protection absorber (TDI) in case of a mis-fire of a LHC injection kicker. The present limitation for the TDI is a maximum of 288 bunches per SPS extraction with ultimate LHC bunch population (1.7×10^{11} ppb) and with the nominal LHC beam normalized emittance at SPS extraction ($3.5 \mu\text{m}$) [13].
 - o The rise-time of the injection kickers in the SPS and LHC, extraction kickers in the PS and SPS, and abort gap kicker in the LHC.
 - o The need to inject one train consisting of a few bunches (typically 12 nominal bunches for 25 ns spacing) before injecting one nominal batch for machine protection considerations [14]. The last batch must have the maximum number of bunches to effectively use the space near the abort gap.
 - o The constraints imposed by the experiments: the need for non-colliding bunches for background evaluation, and a sufficient number of collisions for the lower luminosity experiments [1].
- The maximum bunch population N is limited in the LHC by the onset of the single bunch Transverse Mode Coupling Instability (TMCI), expected to occur at 3.5×10^{11} p/bunch [15].
- The total current of the beam circulating in the LHC, $I_{\text{beam}} = en_b N f_{\text{rev}}$ (where e is the proton charge), is expected to be limited to 1.1 A by the cryogenic power available to cool the beam screen. This assumes that a secondary electron yield (SEY) as low as 1.3 can be reached in the beam screen to limit the heat load due to the electron cloud in the arcs, and additional cryogenic plants are installed in Points 1 and 5 while the cryogenic plant in Point 4 is upgraded [10][11][16].
- The beam brightness $B \equiv N/\varepsilon_n$ is limited by the following considerations [11].
 - o The total head-on beam–beam tune shift $\Delta Q_{\text{bbho}} \propto N/\varepsilon_n$ is expected to be limited to 0.02–0.03 based on experience gained (from operations and dedicated experiments) during LHC Run 1. Its value is reduced in a similar fashion to the luminosity in the presence of a crossing angle.
 - o Intra-beam scattering induces transverse and longitudinal emittance blow-up, particularly at injection (low energy) but also in the acceleration, squeeze, and collision phases. The evolution of the beam emittances can be described by the equations:

$$\frac{1}{\tau_H} = \frac{1}{\varepsilon_{nH}} \frac{d\varepsilon_{nH}}{dt} \text{ and } \frac{1}{\tau_L} = \frac{1}{\varepsilon_L} \frac{d\varepsilon_L}{dt} \text{ with } \frac{1}{\tau_d} \propto \frac{N}{\gamma \varepsilon_{nH} \varepsilon_{nV} \varepsilon_L} \text{ and } d = H, L \quad (2-4)$$

where $\varepsilon_{nH,V}$ are the R.M.S. normalized horizontal and vertical emittances. Here it is assumed that vertical dispersion and coupling are negligible so that the vertical emittance blow-up can be neglected.

The minimum β^* is limited by the following items as already reported in [12]:

- The aperture at the triplet, taking into account that the maximum β function β_{max} at the triplet increases in inverse proportion to β^* , and that the crossing angle θ_c required to maintain a sufficiently large normalized long-range beam–beam separation d_{bb} to minimize the long-range beam–beam tune spread ΔQ_{bbLR} is $\theta_c = d_{\text{bb}} \sqrt{\varepsilon_n / \gamma \beta^*}$;
- The maximum β function at the triplet that can be matched to the regular optics of the arcs within the distance available in the matching section between the triplets and the arcs;
- The strengths of the arc sextupoles available to correct the chromaticity generated by the triplets (proportional to β_{max}) and, in general, the nonlinear chromaticities and off-momentum beta beating.

For a round optics (i.e. with equal β^* in the horizontal and vertical planes) in the presence of a crossing angle and at constant normalized long-range beam–beam separation d_{bb} , the increase in luminosity saturates for values of $\beta^* < \sigma_z$, as shown in Figure 2-2, because of the corresponding decrease of the luminosity reduction factor R . The effect of the geometric reduction due to the crossing angle can be counteracted by means of crab cavities operated at the LHC main RF frequency [17]. The comparison of the two plots of Figure 2-2 also shows that the effect of crab cavities (assuming full compensation of the crossing angle) in enhancing the peak virtual luminosity becomes less and less important for β^* greater than 30–40 cm.

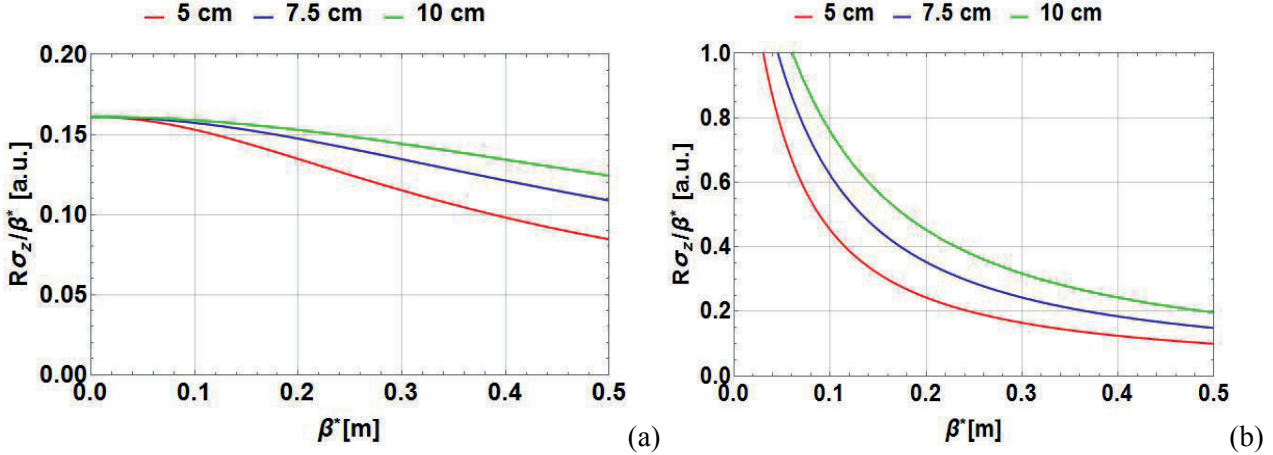


Figure 2-2: Parameter $R\sigma_z/\beta^*$ vs. β^* for different bunch lengths for a round optics and constant normalized long-range beam–beam separation d_{bb} (a) without crab cavities and (b) with crab cavities. The small effect of RF curvature in the crab cavities is not included.

Even after their planned upgrades [18], the injectors will also constrain the parameters of the beam that can be expected in the LHC in collision. The available power for the main 200 MHz SPS RF system will still limit the maximum bunch population to $N_{SPS} = 2.4 \times 10^{11}$ particles per bunch at SPS extraction for 288 bunches. To avoid longitudinal instabilities in the SPS, a controlled longitudinal emittance blow-up needs to be applied for high bunch population, which would lead to bunches that are longer than acceptable for clean capture in the LHC with the main 400 MHz RF system (even with the maximum 200 MHz RF voltage available in the SPS after upgrade at extraction). The identification of the elements contributing to the longitudinal impedance in the SPS and the reduction of their impedance, now planned for LS2, should be targeted to achieve longitudinal stability within the required longitudinal emittance for a clean SPS to LHC transfer for bunch populations up to $N_{SPS} = 2.4 \times 10^{11}$ particles per bunch [19-20]. This assumes that the pre-injectors can reliably supply the SPS with at least 2.6×10^{11} particles per bunch and losses in the SPS remain acceptable for this high intensity [19-20]. Furthermore, the brightness of the LHC beam in the injectors is expected to be limited by space charge effects at injection in the PSB, PS, and SPS. From present experience, it is expected that the maximum brightness of the LHC beams in the SPS after the full injector upgrade will be $B_{SPS} \sim 1.5 \times 10^{11}$ p/ μm [21] for the BCMS beam.

Table 2-1 shows the beam parameters at collision, selected on the basis of the above considerations [8][22]. These have been updated [23] taking into account the modifications to the baseline following a process of optimization, the result of internal and external reviews [24-27] and taking into account the latest information on mechanical tolerances for the construction of the triplet magnets and of the associated cold bore and beam screens [28].

Table 2-1: HL-LHC nominal parameters for 25 ns operation [22] for two production modes of the LHC beam in the injectors described in Ref. [8].

Parameter	Nominal LHC (design report)	HL-LHC (standard)	HL-LHC (BCMS)#
Beam energy in collision [TeV]	7	7	7
Particles per bunch, N [10^{11}]	1.15	2.2	2.2
Number of bunches per beam	2808	2748	2604
Number of collisions in IP1 and IP5*	2808	2736	2592
N_{tot} [10^{14}]	3.2	6.0	5.7
Beam current [A]	0.58	1.09	1.03
Crossing angle in IP1 and IP5 [μrad]	285	510	510
Minimum normalized long-range beam–beam separation [σ]	9.4	12.5	12.5
Minimum β^* [m]	0.55	0.2	0.2
ε_n [μm]	3.75	2.50	2.50
ε_L [eVs]	2.50	2.50	2.50
R.M.S. energy spread [0.0001]	1.13	1.08	1.08
R.M.S. bunch length [cm]	7.55	8.1	8.1
IBS horizontal in collision [h]	80→106	18.8	18.8
IBS longitudinal in collision [h]	61→60	20.6	20.6
Piwinski parameter	0.65	2.5	2.5
Total reduction factor R_0 without crab cavities at min. β^*	0.836	0.369	0.369
Total reduction factor R_1 with crab cavities at min. β^*	(0.981)	0.715	0.715
Beam–beam tune shift/IP	0.0031	0.01	0.01
Peak luminosity without crab cavities L_{peak} [$10^{34} \text{ cm}^{-2} \text{ s}^{-1}$]	1.00	6.52	6.18
Peak luminosity with crab cavities $L_{\text{peak}} \times R_1/R_0$ [$10^{34} \text{ cm}^{-2} \text{ s}^{-1}$]	(1.18)	12.6	11.9
Events/crossing without levelling and without crab cavities	27	172	172
Levelled luminosity for $\mu = 140$ [$10^{34} \text{ cm}^{-2} \text{ s}^{-1}$]	-	5.32 [†]	5.02 [†]
Events/crossing μ (with levelling and crab cavities) [‡]	27	140	140
Maximum line density of pile-up events during fill [events/mm]	0.21	1.3	1.3
Levelling time [h] (assuming no emittance growth) [‡]	-	5.23	5.23
Number of collisions in IP2/IP8	2808	2452/2524 ^{**}	2288/2396 ^{**}
N at injection [10^{11}] ^{††}	1.20	2.30	2.30
Maximum number of bunches per injection	288	288	288
N_{tot} /injection [10^{13}]	3.46	6.62	6.62
ε_n at SPS extraction [μm] ^{**†}	3.50	2.00	<2.00 ^{***}

#BCMS parameters are only considered for injection and as a backup parameter set in case one encounters larger than expected emittance growth in the HL-LHC during injection, ramp and squeeze

*Assuming one less batch from the PS for machine protection (pilot injection, transfer line steering with 12 nominal bunches) and non-colliding bunches for experiments (background studies, etc.). Note that due to RF beam loading the abort gap length must not exceed the 3 μs design value.

[†]For the design of the HL-LHC systems (collimators, triplet magnets, etc.), a margin of 50% on the peak luminosity (corresponding to the ultimate levelled luminosity of approximately $7.5 \times 10^{34} \text{ cm}^{-2} \text{ s}^{-1}$ and to a pile-up $\mu=200$) has been agreed.

[‡]The total number of events/crossing is calculated with an inelastic cross-section of 81 mb, while 111 mb is assumed as a pessimistic value for calculating the proton burn off and the resulting levelling time [5, 7].

^{**}The lower number of collisions in IR2/8 compared to the general-purpose detectors is a result of the agreed filling scheme, aiming as much as possible at an equal sharing of collisions between the experiments.

^{††}An intensity loss of 5% distributed along the cycle is assumed from SPS extraction to collisions in the LHC.

^{**†}A transverse emittance blow-up of 10–15% on the average H/V emittance in addition to that expected from intra-beam scattering (IBS) is assumed (to reach 2.5 μm of emittance in collision for 25 ns operation).

^{***}For the BCMS scheme, emittances down to 1.7 μm have already been achieved at LHC injection, which might be used to mitigate excessive emittance blow-up in the LHC during injection and ramp.

2.2 Proposed systems upgrades and improvements

The high luminosity configuration requires upgrades of numerous systems. In some cases, existing systems would not be able to face the increasingly harsh conditions that the highest luminosity performance will generate. Accelerated wear and radiation damage are serious concerns. Many changes will be necessary just in order to allow the machine to continue to run in a regime of nominal or ultimate luminosity. For certain systems, replacements could be made with equipment achieving better performance, rather than with spares of the same specification. This performance ‘improvement’ goes well beyond the basic consolidation that is already planned for the LHC.

For other systems, replacement, although triggered by technical reasons, is the chance to carry out a complete change of layout or performance and may be considered to be a real upgrade. The most striking example is the replacement of the inner triplet magnets with new magnets of different technology based on the Nb₃Sn superconductor. This will constitute the backbone of the upgrade. Another case is the replacement of a good part of the present collimation system with an improved design with lower impedance jaws.

In other cases, new equipment not included in the present LHC layout will be installed in order to increase performance, in terms of either peak luminosity or availability. The most important example is the superconducting RF crab cavities, which are of a compact design as required for the HL-LHC, comprising a completely new development installed for the first time on a proton collider. A further example is the installation of a collimation system in the continuous cryostat in the dispersion suppressors.

In this section, we compile a list of the systems that will require an upgrade or at least a serious improvement in performance, to meet the ambitious challenge of the High Luminosity LHC.

2.2.1 Insertion region magnets

It is expected that the LHC will reach an integrated luminosity of approximately 300 fb⁻¹ by about 2023, resulting in doses of up to 30 MGy to some components in the high luminosity interaction regions. The inner triplet quadrupoles should withstand the radiation resulting from 400 fb⁻¹ to 700 fb⁻¹, but some nested-type corrector magnets could fail at around 300 fb⁻¹. The most likely failure mode is sudden electric breakdown, entailing serious and long repairs. Replacement of the triplet must be anticipated before radiation damage reaches the level where serious failure is a significant possibility.

The replacement can be coupled with an increase in the quadrupole aperture to allow room for an increase in the luminosity via a lower β^* . However, larger aperture triplet quadrupoles and the increased luminosity, with consequent higher radiation levels, imply the redesign of the whole interaction region (IR) zone. This redesign includes larger D1 and D2 dipoles, a new electrical feedbox (DFB), and much better access to various components for maintenance. In addition, a redesign of the collimation system in the high luminosity insertions will be required. The initially foreseen replacement of the Q4 magnets with new, larger (90 mm) aperture, quadrupoles (MQYY) will be staged to after the HL-LHC Project implementation during LS3 (i.e. in LS4), if needed, and the present 70 mm MQY modified for operation at 1.9 K will be maintained.

To maximize the benefit of such a long shutdown, this work must be complemented by a series of improvements and upgrades for other systems, and must be coupled with a major upgrade of the experimental detectors. Both the machine and the detectors must be partially redesigned in order to withstand the expected level of integrated luminosity. The upgrade should allow the delivery of 3000 fb⁻¹, i.e. one order of magnitude greater than the nominal LHC design goal.

It is clear that the change of the triplets in the high luminosity insertions is the cornerstone of the LHC upgrade. The decision for the HL-LHC has been to rely on the success of the advanced Nb₃Sn technology, which provides access to magnetic fields well beyond 9 T, allowing the maximization of the aperture of the triplet quadrupoles. A 15-year-long study led by the DOE in the US under the auspices of the US LARP programme (see Chapter 1, Section 1.3.2), and more recently by other EU programmes, has shown the feasibility of Nb₃Sn accelerator magnets. For the HL-LHC, 24 Nb₃Sn quadrupoles are needed for the triplet

assemblies: they all feature a 150 mm aperture and a maximum operating gradient of 133 T/m, which entails about 12 T peak field on the coils. The Q1 and Q3 quadrupoles each consist of a pair of 4.2 m long magnets assembled in a single cold mass, while Q2a and Q2b each consist of a single magnet/cold mass 7.15 m long (see Chapter 3). The same Nb₃Sn technology will be used to provide collimation in the DS around P7, which will be achieved by replacing two main dipoles, each one with two shorter 11 T Nb₃Sn dipoles (see Chapter 11). A TCLD collimator will be installed in between the shorter dipoles, on the top of a special cold-warm-cold bypass unit (see, for example, Ref. [29] and references therein). In addition to the triplet quadrupoles, there are four new D1/D2 separation/recombination dipole pairs, a number of matching section (MS) quadrupoles, not only in IR1 and 5 (see Table 2-3 and Table 2-4), but also in IR6 (See section 3.9), and a smaller number of lattice sextupoles that can be made using well-known Nb-Ti technology. These magnets will feature a larger aperture and will be exposed to higher radiation doses if not properly protected, and thus will be more challenging than the present LHC equivalents (see Chapter 3).

The corrector packages in the IRs need to be significantly upgraded to increase aperture and (where needed) strength. Some 70 corrector magnets of various orders (from dipole for orbit correction to dodecapole skew correctors) and typology (from superferric to nested) have to be installed with the new larger IR magnets (see Table 2-4 and Table 2-5).

2.2.2 Collision debris absorbers (TAXS/TAXN)

The change of the IT aperture will require replacement of the TAS, the first absorber on either side of the high luminosity interaction points. The TAS protects the downstream magnets from collision debris. Its aperture roughly scales with the triplet aperture. The new absorber, named TAXS, will have an aperture of 60 mm (compared with 30 mm in the present TAS), and will have to withstand a flux of particles five times larger than in the present nominal design. In the current LHC, the TAS is probably the most highly activated component of the whole machine. The baseline choice at present is to replace the TAS with the TAXS during LS3 (see Chapter 8).

Given the fact that the experimental detectors have reduced the size of their vacuum chambers by nearly 50% (from 55 mm down to about 35 mm), it is clear that all challenges at the machine-detector interface are increased. This includes keeping background radiation in the detectors at acceptable levels.

2.2.3 Crab cavities

Superconducting (SC) RF crab cavities (CC) in the HL-LHC are needed in order to compensate, at least partially, for the geometric reduction factor, thus making the very low β^* fully useful for luminosity. HL-LHC crab cavities are beyond the state-of-the-art in terms of their unconventional, compact design, which cannot be achieved with the well-known geometry of an elliptical cavity. They also demand a very precise control of the phase and voltage amplitude of the RF (to better than 0.001° and 100 V, respectively [30][31]) so that the beam rotation given before collision is exactly cancelled on the other side of the interaction point (IP). The crab cavities will also pose new challenges for machine protection. Compact crab cavities will be installed on both sides of IP1 and IP5 without additional magnetic doglegs (as in IP4 for the accelerating cavities). Each cavity is designed to provide a transverse kick voltage of 3.4 MV. There are two crab cavities per beam on each side of the IP1/5. They will be assembled in cryo-modules, each containing two cavities. The installation of a second cryo-module per beam and IP side is not anymore in the project baseline; however, it is possible with a HiLumi consolidation program. A single cryomodule (two cavities) can be used for crossing angle compensation while a second cryomodule could provide a deflection in the orthogonal plane, enabling the so-called crab-kissing scheme for reducing the pile-up density [32]. The second cryomodule could also allow alternating the crossing angle plane to reduce the radiation in the triplet quadrupoles.

The first-generation, proof-of-principle, compact crab cavities have recently been tested successfully (see Chapter 4). However, a second generation with machine-oriented characteristics is now under construction by LARP, CERN, and UK institutions (Lancaster University, STFC, and the Cockcroft Institute). A full cryomodule will be tested in the SPS before LS2 to investigate experimentally the effect on a proton beam and

to gain necessary experience in view of HL-LHC operation and in time before launching the crab cavities' series production.

2.2.4 Collimation

The existing collimation system has been designed for the first phase of LHC operation. During Run 1 and Run 2 the collimation system has operated according to design up to an energy of 6.5 TeV. Possible limitations from collimation cleaning and impedance might be revealed by operation at higher energy and intensity. In particular, the collimator impedance poses serious concerns at high energy when the collimators have the minimum gap opening. The present impedance model, which has been validated by measurements performed during Run 1 and Run 2, indicates that the collimator impedance must be reduced significantly to operate with HL-LHC beams. A number of secondary collimators in LSS7, the main source of impedance, are planned to be replaced with low impedance collimators equipped with molybdenum-coated jaws made out of Mo-Graphite composite.

Safe handling of a beam of 1 A or more, with beta functions when colliding well beyond the LHC nominal design values, will constitute new territory. The triplet must remain protected during the large change of the optics during the squeeze (β^* transition from 6 m to 20 cm). This will be one of the most critical phases of HL-LHC operation: the beam halo itself could generate losses beyond the damage limit. An upgrade of the collimation system is thus required. The main additional needs associated with the upgrade are a better precision in alignment and materials capable of withstanding higher losses. Because of the larger peak luminosity, collimation of the luminosity debris around the high-luminosity points also requires an upgrade to adequately protect the matching sections.

Another area that will require special attention in connection with the collimation system is the dispersion suppressor (DS), where leakage of off-momentum particles into the first and second cells of the DS has already been identified as a possible LHC performance limitation. The most promising concept is to substitute an LHC main dipole with dipoles of equal bending strength ($120 \text{ T} \times \text{m}$) obtained by a higher field (11 T) and shorter magnetic length (11 m) than those of the LHC dipoles (8.3 T and 14.2 m). The space gained is sufficient for the installation of a special collimator. The baseline is to have two 15 m long units installed in the DS around P7 (one unit per side acting only on one beam) before end of LS2. A unit is composed of a 5.5 m long 11 T dipole, a 4 m long 2K-300K-2K bypass where a collimator operates at room temperature, and a second 5.5 m long 11 T dipole. Quench tests in 2015 in the LHC showed that a second unit per side of P7, initially foreseen, is actually not needed (see Chapter 5). Around P2, the ions debris losses hitting the DS dipoles are shifted in the connection cryostat zone by means of an orbit bump. The TCLD to intercept these losses will be then located in a newly designed connection cryostat, thus avoiding installing 11 T dipoles in P2 (a further change with respect to the previous baseline). In IP1 and IP5, the installation of dedicated collimators is not necessary because the peak loss can be moved at the location of the connection cryostat with dedicated orbit bumps (see Chapter 5).

2.2.5 New cold powering

While a considerable effort is under way to study how to replace the radiation-sensitive electronics boards with radiation-hard versions, another solution is also being pursued for IR1 and IR5 where we have new underground tunnels and or wherever possible: removal of the power converters, electrical feedboxes (DFBs) and delicate equipment associated with the continuous cryostat out of the tunnel. Besides improving LHC availability (fewer interruptions, faster interventions without the need for tunnel access), radiation dose to personnel would be reduced as well.

Removal of power converters and DFBs to locations far from the beam line, in a lateral tunnel along the insertion region of IP1 and IP5 is now the project baseline. It is possible, and advantageous from power consumption point of view, using a novel technology: superconducting links made out of high-temperature superconductors (YBCO or Bi-2223) and mainly of MgB_2 superconductors. The regions where this radical solution will be needed because of the high radiation load on electronics, and/or the 'as low as reasonably

achievable' principle (ALARA), are the high luminosity insertion regions IR1 and IR5, where many more higher current cables (carrying about 100 kA in total) are needed for the triplet magnets as compared to the LHC. Concerning the matching section magnets, the D2 dipole will be powered via an SC link from the lateral service gallery (UR). Another change that was decided in the June 2016 re-baselining exercise is that the individually powered quadrupoles, Q4-Q5-Q6, and their associated correctors, will be powered by power converters placed in the RRs (tunnel enlargements), re-using the present infrastructure as much as possible. The access to equipment in the lateral serviced gallery should be possible even during LHC operation, making maintenance easier, thus reducing the machine downtime.

2.2.6 Enhanced machine protection and remote handling

Various systems will become a bottleneck with aging of the machine and higher performance beyond the 40 fb⁻¹ to 60 fb⁻¹ per year envisaged in the original LHC design. One such system is the quench protection system (QPS) of the superconducting magnets. The new HL-LHC QPS, including that for the new Nb₃Sn magnets, should:

- become fully redundant in case of power loss;
- allow low energy discharge on quench heaters and easy adaption of the detection thresholds;
- provide an interlock for the quench heater discharge based on a sensor for quench heater integrity.

In general, the QPS will need an extensive renovation after 2020. Use of the new lateral gallery is also envisaged for certain QPS equipment around IP1 and IP5.

Machine protection will have to be improved, and not just because of the higher beam energy and energy density: it will have to cope with very fast events generated, for example, by crab cavities and by a possible increase of the events generated by falling particles (Unidentified Falling Objects - UFOs).

The LHC has not been designed specifically for remote handling. However, the level of activation from 2020, and even earlier, requires careful study and development of special equipment to allow replacement of collimators, magnets, vacuum components, etc. according to the ALARA principle. While full robotics are difficult to implement given the conditions, remote manipulation, enhanced reality, and supervision are the key to minimizing the radiation dose to personnel.

2.2.7 New cryogenics plants and distribution

To increase the flexibility for intervention and to maximise availability it was foreseen to install a new cryogenics plant in P4 for a full separation between superconducting RF and magnet cooling. This was planned for LS2 to avoid a possible weakness during Run 3. In the previous baseline [2] a new 6 kW (@ 4.2K) cryo-plant was foreseen. A detailed assessment of the requirements has arrived at a new, less expensive baseline, which comprises:

- The upgrade of the present 18 kW (@4.2K) cryo-plant to 20.5 kW. This is sufficient for all possible additional requests for cryo-power for the region around P4 (including non-baseline options i.e. a new SCRF harmonic system and the hollow e-lens for halo control, which requires a superconducting solenoid).
- The purchase of a small (700 W) mobile cryo-plant that can be used in P4 to cool down the RF cavities when the main plant is unavailable (this happens, for example, when the arc magnets are warm). When not in use at P4, which would be most of the time, this mobile unit could be used for other equipment: for example for the cold test with beam of the crab cavities in the BA6 zone of SPS.

Further consolidation that is deemed necessary in the long term is the separation between the cooling of the triplet and the few stand-alone superconducting magnets in the MS in IR1 and IR5 from the magnets of the neighbouring arcs. The present coupling of IR and arc magnets means that an intervention in the triplet region requires warm-up of the entire sector (an operation of three months that is not without risk).

New large power plants will be needed to cope with higher heat deposition from the high luminosity points. In particular, given the luminosity-driven heat load in the 1.9 K magnets and the cooling of superconducting crab cavities at 2 K, the power at 1.9 K of the new cryo-plant in IP1 and IP5 will be 2.4 kW (as for the present LHC cryo-plants). The 4.2 K cryo-power will also remain in the 18 kW range, as at present. The cooling scheme includes separation, with possible interconnection, between arc and IR cryogenics to gain in flexibility.

2.2.8 Enhanced beam instrumentation

Improving beam instrumentation is a continuous process during routine operation of an accelerator. The HL-LHC will require improved or new equipment to monitor and act on proton beams with more challenging parameters than those of the LHC. A short illustrative list includes the following (full details are provided in Chapter 13):

- New beam loss monitors for the IT quadrupoles.
- A radiation-tolerant Application-Specific Integrated Circuit (ASIC) for the beam loss monitoring system.
- A new beam position monitoring system, including a high-resolution orbit measurement system, and high-directivity strip-line pick-ups for the insertion regions.
- Emittance measurement: while improving the present system, a new concept-based Beam Gas Vertex (BGV) emittance monitor is envisaged for the HL-LHC.
- Halo diagnostics to control the halo in order to minimize losses (and especially loss peaks) in the presence of a beam with a stored energy close to 0.7 GJ. Synchrotron radiation imaging, and possibly wire scanners, appear to be the only candidates for halo monitoring in the HL-LHC.
- Diagnostics for crab cavities: electromagnetic pick-ups and streak cameras are being studied for beam shape monitoring.
- Luminosity measurements with new radiation-hard devices (located in the new TAXN) capable of withstanding the ten times higher radiation level.

2.2.9 Beam transfer and kickers

The higher beam current significantly increases the beam-induced power deposited in many elements, including the injection kicker magnets in the LHC ring. New designs for several components in the dump system devices will probably be needed because of the increased energy deposition in the case of direct impact, and because of an increased radiation background, which could affect the reliability of this key machine protection system. In certain cases, the improvements need to be anticipated in LS2 since in Run 3, after the LIU installation, there could already be a higher bunch population and/or brightness.

A non-exhaustive list of the elements that could need an improvement or a more radical upgrade (based on the experience from Run 2) is given below.

- Injector kicker magnets (better cooling of the magnets to cope with beam-induced heating, different type of ferrites with higher critical temperature, coating of ceramic tubes to reduce SEY and thus suppress e-cloud effects).
- Beam dump block (TDE) with its N₂ overpressure system and window VDWB: if these are not compatible with HL-LHC intensities, extension of the dilution pattern may be the only practical and safe solution, implying the installation of additional dilution kicker systems MKB (up to 50%).
- Injection absorber (TDI), auxiliary protection collimators, protection masks.
- Beam dump absorber system.

2.3 Baseline optics and layout

2.3.1 Basic optics and layout choices for the High Luminosity insertions

The current baseline optics design (HLLHCV1.3), presently being finalized after the June 2016 re-baselining, has evolved from the previous LHC Upgrade Phase I project [33-35]. A realistic, cost-efficient and robust (achromatic) implementation of low β^* collision optics requires the deployment of the Achromatic Telescopic Squeeze (ATS) scheme, together with the installation of insertion magnets of larger aperture [36-40]. Successful validation tests of the ATS with beam were achieved in 2011–2012 [41-45] in very specific conditions (low intensity, no crossing angle to save aperture, etc.). Additional machine studies are being carried out for validating this optics for potential implementation in operation during Run 2. The corresponding number, type, and specifications of the new magnets to reach low β^* [36][37] were then endorsed by the project (see, for example, [83] and references therein).

The historical development of the optics design is summarized in Ref. [47]; here, the most recent layouts are mentioned, namely SLHCV3.1b [48], HLLHCV1.0 [49], HLLHCV1.1-1.2-1.3 [50-53]. SLHCV3.1b uses ATS optics based on 150 T/m Nb₃Sn triplets and displacement of D2 for crab cavity integration [48]. HLLHCV1.0 is similar to SLHCV3.1b with a new triplet layout based on 140 T/m Nb₃Sn triplets [49]. HLLHCV1.1 is based on HLLHCV1.0, but with some modifications to take into account the results of design studies for D2, energy deposition studies for the passive protection of the superconducting elements, hardware integration studies, and updated naming conventions [54][55], and corresponding optical configurations. HLLHCV1.2, builds up on HLLHCV1.1, but with a new triplet layout based on longer 132.6 T/m Nb₃Sn triplets [51], which implied a rearrangement of the area from the triplet up to Q4. The correctors' layout and strength have been updated [56] and the masks in front of D2 and, tentatively, Q4 have been removed, thanks to thicker jaws of the newer TCLX collimator [57]. Necessary layout and naming convention modifications have been applied following a detailed integration study [58].

HLLHCV1.3 features a further rearrangement in the triplet area of IR1 and IR5, including a small reduction of L^* , new integration solutions to maintain all the triplet Beam Position Monitors (BPMs) far enough from long-range encounters to allow their operation with nominal bunch spacing [59-61]. In the matching section of IR1 and IR5 the layout has been updated to include the new baseline modifications following the project re-scoping in summer 2016, namely:

- the MQYY+2×MCBYY assembly for Q4 is replaced by with an MQY+4×MCBY assembly operated at 1.9 K based on MQY spares and a new production of MCBY magnets. The reduction of the aperture of Q4 might imply the installation of an additional protection mask on the IP side of this quadrupole. This has been included in the present layout.
- the Q6 (MQML) magnet is operated at 4.5 K as no request for high beta operation has been made [62][63]
- the number of crab cavities is reduced from 4 to 2 per IP, side and beam while the space for installing 4 cavities is maintained [27]

The layout of IR6 has been modified and a solution with a single MQY, modified for operation at 1.9 K, per IR side has been retained for the Q6 quadrupole instead of the previous solution consisting of two MQY quadrupoles operated at 4.5 K per IR side [64].

Table 2-2 presents an overview of the main features of the layouts SLHCV3.1b to HLLHCV1.3 and of the corresponding optical configurations. The modifications to the baseline and the updated values of the mechanical tolerances for the construction and installation of the cold bore and shielded beam screens lead to a reduction of the β^* reach for both the round and flat optics. The minimum β^* achievable for the round optics is limited by the triplet aperture while the minimum β^* achievable for the flat optics is limited by the aperture of the Q4 magnet [23][24][27][28][53].

Table 2-2: Main HL-LHC optics variants currently under study. The baseline collision optics corresponds to $\beta^* = 20$ cm in both transverse planes (round optics) with a full crossing angle of $510 \mu\text{rad}$. Other collision optics are available, round or flat, for dedicated studies. The values of β^* refer to IP1 and 5 and those reported in parentheses refer to solutions available for studies.

	SLHCV3.1b	HLLHCV1.0	HLLHCV1.1	HLLHCV1.2	HLLHCV1.3 (Baseline)
Collision β^*	Round: 15 cm, (10 cm, 33 cm, 40 cm). Flat: 30/7.5cm, (20/5 cm) with HV, VH crossing.	Round: 15 cm, (10 cm). Flat: 30/7.5cm, (20/5 cm) with HV, VH crossing.		Round: 15 cm Flat: (30/7.5) cm with HV, VH crossing.	Round: 20 cm (15 cm). Flat: 40/15 cm (30/7.5 cm) with HV, VH crossing.
Pre-squeeze β^*	40 cm, (2 m)	44 cm		48 cm	50 cm
Injection β^*	5.5 m (11 m)	6 m (15m)		6 m	6 m
Maximum operating triplet gradient	150 T/m	140 T/m		132.6 T/m	
Triplet magnetic length	Q1–Q3: 7.685 m Q2: 6.577 m	Q1–Q3: 4.002 m \times 2 Q2: 6.792 m	Q1–Q3: 4.0 m \times 2 Q2: 6.8 m	Q1–Q3: 4.20 m \times 2 Q2: 7.15 m	
Triplet corrector package	Nested nonlinear corrector package with additional a_5 , b_5 , a_6 corrector coils	Superferric, non-nested nonlinear corrector package with additional a_5 , b_5 , a_6 corrector coils			
Insertion region dipoles	D2 moved towards the IP by 15 m.				
	The magnetic length of D1 [55] and D2 has been reduced.				
Insertion region quadrupoles	MQYY type for Q4 in IR1, IR5. Q5 moved towards arc by 11 m. Additional MS in Q10 of IR1 and IR5.			IR1, IR5: Q4, Q5: MQY @ 1.9 K Q6: MQML @ 4.5 K Q4 and Q5 moved towards arc by 10 m and 11 m respectively Additional MS in Q10 of IR1 and IR5	
	MQYL type for Q5 in IR1, IR5, IR6.	Q4 moved towards arc by 8 m. MQY @ 1.9 K type for Q5 in IR1, IR5. IR6: Double MQY @ 4.5 K for Q5		IR6: Single MQY @ 1.9 K for Q5	
Crab cavities	3	4		2	

The current baseline layout incorporates various optimizations, and has been made compatible with the latest hardware parameters and constraints. The magnetic elements in the region between the IP and Q5 (Figure 2-3) have been positioned to optimize the strength requirements for the magnets and for ancillary equipment. For instance, moving the Q4 quadrupole changes the value of the beta functions at the location of the crab cavities, thus improving their efficiency.

In the triplet region (between 20 m to 80 m in Figure 2-3) the Q1 and Q3 magnets are split in two and the dipole corrector magnets (used to create the crossing and separation schemes) are implemented in a nested configuration for both planes. The corrector package close to Q3 consists of superferric magnets. The specifications and performance of the non-linear correctors (used to compensate the field quality effects of the triplets and D1 separation dipoles on both sides of the IP) are reported in Refs. [65][66]. Detailed numerical simulations indicate that additional corrector types are needed to cope with the pushed performance of the HL-LHC, so the layout of the correctors will not be a simple carbon copy of the existing layout.

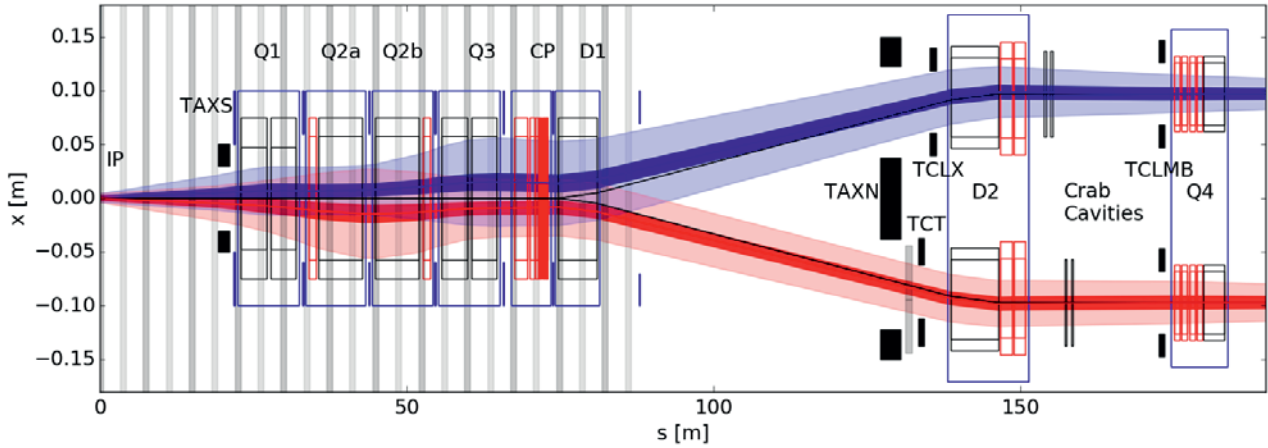


Figure 2-3: Overall layout of the insertion region between the IP and Q4. The dark blue and red areas represent the 2σ beam envelope for the $\beta^*=20$ cm round optics. The light regions correspond to a 12σ value of the beam envelope for a normalized emittance of $3.5\ \mu\text{m}$ with a tolerance of 20% for beta-beating, 2 mm of radial closed orbit distortion [67] and ± 2 mm to allow IP transverse position adjustments based on Run 1 and Run 2 operational experience. The shaded grey areas in the triplet region represent the locations of the parasitic beam-beam encounters in which the BPM (in blue) should not be installed. Additional aperture margins are needed in the matching section to be compatible with flat optics operations.

The block of two separation dipoles has been changed with respect to the nominal LHC layout, decreasing their separation. The D2 area is particularly delicate for several reasons. First, there are space constraints because of the need for protection devices such as the absorber for neutral debris from the collisions. Second, the transverse separation is not yet the nominal one (see Table 2-4), leading to a reduction in the amount of iron between the two apertures of the D2, as well as to reduced beam and mechanical apertures, because of the large values of the beta functions at this point. Downstream of D2, the situation is not much easier, as the crab cavities impose tight constraints on the space between D2 and Q4, as well as on the values of the beta functions.

Detailed work has been performed to specify the strengths of dipole orbit correctors in the triplets and the D2 and Q4 magnets [68-69]. Initially, significantly stronger dipole correctors were required in D2 as compared to those in Q4 to close the crossing bumps at the D2 dipole and avoid a non-zero closed orbit at the location of the crab cavities. The review of the RF and alignment aspects for the crab cavities [70] has led to a correction scheme requiring a reduced integrated strength, closing the orbit bumps further downstream from the D2 separation dipoles. In the current layout, the orbit strength required is obtained by two MCBY dipole correctors per plane of the Q4 quadrupole operated at 1.9 K. Both Q4 and Q5 quadrupoles will consist of MQY-type quadrupoles modified to be operated at 1.9 K (see Table 2-3 and Table 2-4).

The implementation of the ATS scheme requires hardware changes in other parts of the LHC ring. In particular, an additional lattice sextupole (MS) magnet should be installed in Q10 in IR1 and IR5. Moreover, Q5 in IR6 must be upgraded. The current baseline envisages the operation of the MQY-type quadrupole Q5 at 1.9 K after the formal proposal of a double MQY was proven not to be as cost effective as anticipated [64,71].

Table 2-3 lists the key parameters of the quadrupoles (new or refurbished) to be installed in IR1 and IR5, while Table 2-4 gives the corresponding parameters for the separation dipoles and orbit correctors. Table 2-5 gives the parameters for the multipolar correctors. The shape and inner size of the beam screens for the new magnets, which defines the region available for the beam, is based on preliminary design [72]. These have been updated recently [28] and the estimated mechanical tolerances will have to be refined following the development of hardware prototypes. The minimum β^* reach has been assessed based on the available mechanical aperture of the beam screens (including the mechanical tolerances) and taking into account optics and orbit errors based on the experience gained with LHC operation so far [67]. It has been also assumed that

the collimation system can protect an aperture of 12σ (for a normalized emittance of $3.5 \mu\text{m}$) for elements protected by tertiary collimators (TCTs) and 17σ for the rest of the machine [73]. For the computations reported in here, mechanical, alignment and beam tolerances are added linearly and accounts for about 13% of the triplet aperture. A reduction of these tolerances during the design, construction and operational phases could allow a further reduction of β^* [74]. Recent experience in the LHC has also shown that it is possible to protect a smaller aperture by reducing the phase advance between the beam dump kicker and the horizontal TCTs and therefore reducing the required retraction of the TCTs with respect to the TCDQ absorber [75][76]. Optics solutions have been worked out for the nominal LHC optics and proposed and implemented for the ATS optics [77]. This solution could allow extending the β^* reach.

The description of the shapes is made by providing the dimensions corresponding to the horizontal(H)/vertical(V) and 45° cuts for octagons; diameter (d) and gap (g) for rectellipses [78]; radius for circles. The values represent the inner dimensions of the beam screen including mechanical tolerances. This is different to what is done in, e.g., Ref. [79], where the nominal sizes of the beam screens are reported. The orientation of the rectellipse cross section depends on the IP side and beam type and it has been chosen to optimise the beam aperture in collision. The alignment tolerances are represented as a racetrack shape of radius (R), and horizontal (H), vertical (V) extent, respectively. The values provided include ground motion and fiducialization tolerances [80].

Table 2-3: New or refurbished quadrupoles for HL-LHC, all operating at 1.9 K, apart from Q6.

	Inner triplet (single aperture)			Matching section (two-in-one)		
Magnet	Q1	Q2	Q3	Q4	Q5	Q6
Number per side per insertion	2			1		
Type	MQXFA	MQXFB	MQXFA	MQY		MQML
Magnetic length [m]	4.2	7.15	4.2	3.4		4.8
Maximum Gradient [T/m]	132.6			200		160
Coil aperture [mm]	150			70		56
Aperture separation [mm]	NA			194		
Beam screen shape	Octagon			Rectellipse		
Beam screen aperture [mm]	95.0(H/V)/ 95.0(45°)	115.0(H/V)/ 106.0(45°)		57.8(d) / 48.0 (g)		45.1(d)/35.3(g)
Alignment tolerances (R/H/V) [mm]	0.6/1.0/1.0			0.84/1.36/0.6		As built

Table 2-4: Separation and corrector dipole magnets for HL-LHC, all operating at 1.9 K. The orbit correctors can be nested or consecutive as indicated. The order of the correctors refers to IP5 right of Beam 1 starting from the IP5.

	Separation/recombination dipoles		Orbit correctors				
Assembly	D1	D2	Corrector Package	Q2	D2	Q4	Q5
Number per side per insertion	1	1	1	2	2	4	3
Configuration			HV nested	HV nested	HV consecutive	VHVH consecutive	HVH consecutive
Type	MBXF	MBRD	MCBXFA	MCBXFB	MCBRD	MCBY	MCBY
Magnetic length [m]	6.27	7.78	2.2	1.2	1.89	0.9	0.9

MACHINE LAYOUT AND PERFORMANCE

Integrated field [Tm]	35	35	4.5	2.5	5.0	2.7	2.7
Coil aperture [mm]	150	105	150	150	100	70	70
Aperture separation [mm]	NA	188	NA	NA	194	194	194
Beam screen shape	Octagon	Octagon	Octagon	Octagon	Octagon	Rectellipse	Rectellipse
Beam screen aperture [mm]	115.0(H/V) 106.0(45°)	83.0(H/V) 74.0(45°)	115.0(H/V) 106.0(45°)	115.0(H/V) 106.0(45°)	83.0(H/V) 74.0(45°)	57.8(d) 48.0 (g)	57.8(d) 48.0 (g)
Alignment tolerances (R/H/V) [mm]	0.6/1.0/1.0	0.84/1.36/0.6	0.6/1.0/1.0	0.6/1.0/1.0	As built		

Table 2-5: New multipolar superferric correctors for HL-LHC, all operating at 1.9 K.

Number	1	1	1	1	1	1	1	1	1
Number of poles	4	12	12	10	10	8	8	6	6
Normal/skew	Skew	Normal	Skew	Normal	Skew	Normal	Skew	Normal	Skew
Type	MQSXF	MCTXF	MCTSXF	MCDXF	MCDSXF	MCOXF	M COSXF	MCSXF	MCSSXF
Magnetic length [m]	0.807	0.43	0.089	0.095	0.095	0.087	0.087	0.111	0.111
Integrated field [mT m] at 50 mm	1000	86	17	25	25	46	46	63	63
Coil aperture [mm]	150								
Beam screen shape	Octagon								
Beam screen aperture (H/V) [mm]	115.0/106.0								
Alignment tolerances (R/H/V) [mm]	0.6/1.0/1.0								

As already mentioned, protection devices are required for the new layout of the IR1 and IR5 regions. The current LHC layout has only a TAS in front of Q1, to protect this magnet from collision debris, and a TAN to protect D2 from the neutrals produced at the IP. For the HL-LHC, these two devices will have to be upgraded to withstand much larger luminosities. Furthermore, additional masks are envisaged to protect other magnets in the matching section. A summary with the characteristics of these devices can be found in Table 2-6.

Table 2-6: New absorbers for HL-LHC, all operating at room temperature.

Function	Inner triplet (single aperture)	Matching section (two-in-one)			
	Main secondary absorber	Main neutral absorber	Mask Q4	Mask Q5	Mask Q6
Aperture	1	2	2	2	2
Type	TAXS	TAXN	TCLMB	TCLMB	TCLMC
L [m]	1.8	3.5	1.0		
Aperture separation [mm]	NA	149–159	194		
Aperture shape	Circle	Circle	Rectellipse		
Aperture [mm]	60.0 (d)	85.0 (d)	57.8(d) / 48.0 (g)	57.8(d) / 48.0 (g)	45.1(d) / 35.3 (g)
Alignment tolerances (R/H/V) [mm]	2.0/0.5/0.5	0.6/1/1	0.6/1/1		

Figure 2-4 shows example optics configurations for injection and collision. Several configurations have been provided in addition to the nominal (i.e. round) optics.

Table 2-7 gives the main sets of β^* values (including the optical parameters corresponding to the ion runs). Since IR2 and IR8 are running with increased strength of the triplets at injection, a so-called pre-squeeze has to be applied at top energy to reduce the strength of the triplets at constant value of beta function at the IP. It is also planned to perform part of the pre-squeeze of the high luminosity IR optics during the ramp to minimize the turn-around time.

Table 2-7: Available optical configurations for the baseline layout. IR3 and IR7 are not included as they have static optics from injection to collision and do not take part in the ATS scheme. IR4 and IR6 take part in the ATS and this is highlighted here, where the “No ATS” configuration corresponds to an injection-compatible optics kept constant up to top energy. The telescopic squeeze factors are indicated in parenthesis. Some alternative configurations are also shown. The pre-squeeze up to 70 cm could be implemented during the ramp. In alternative also part of the ATS squeeze could be anticipated during or after the ramp if enhanced octupoles effect is needed.

Optics	IR1	IR5	IR2	IR8	IR4	IR6
Injection	$\beta^* = 6$ m	$\beta^* = 6$ m	$\beta^* = 10$ m	$\beta^* = 10$ m	No ATS	No ATS
End of ramp	$\beta^* = 6$ m	$\beta^* = 6$ m	$\beta^* = 10$ m	$\beta^* = 10$ m	No ATS	No ATS
Pre-squeeze	$\beta^* = 50$ cm	$\beta^* = 50$ cm	$\beta^* = 10$ m	$\beta^* = 3$ m	No ATS	No ATS
Collision round	$\beta^*_{ATS} = 20$ cm	$\beta^*_{ATS} = 20$ cm	$\beta^* = 10$ m, ATS (2.5 \times , 2.5 \times)	$\beta^* = 3$ m, ATS (2.5 \times , 2.5 \times)	ATS (2.5 \times , 2.5 \times)	ATS (2.5 \times , 2.5 \times)
Collision ions	$\beta^* = 50$ cm	$\beta^* = 50$ cm	$\beta^* = 50$ cm	$\beta^* = 50$ cm	No ATS	No ATS
Collision VDM	$\beta^* = 30$ m	$\beta^* = 30$ m	$\beta^* = 30$ m	$\beta^* = 30$ m	No ATS	No ATS
Alternative configurations						
Collision Flat	$\beta^*_{ATS} =$ 15/40 cm	$\beta^*_{ATS} =$ 40/15 cm	$\beta^* = 10$ m, ATS (3.33 \times , 1.25 \times)	$\beta^* = 3$ m, ATS (3.33 \times , 1.25 \times)	ATS (1.25 \times , 3.33 \times)	ATS (1.25 \times , 3.33 \times)
Collision FlatHV	$\beta^*_{ATS} =$ 40/15 cm	$\beta^*_{ATS} =$ 15/40 cm	$\beta^* = 10$ m, ATS (1.25 \times , 3.33 \times)	$\beta^* = 3$ m, ATS (1.25 \times , 3.33 \times)	ATS (3.33 \times , 1.25 \times)	ATS (3.33 \times , 1.25 \times)

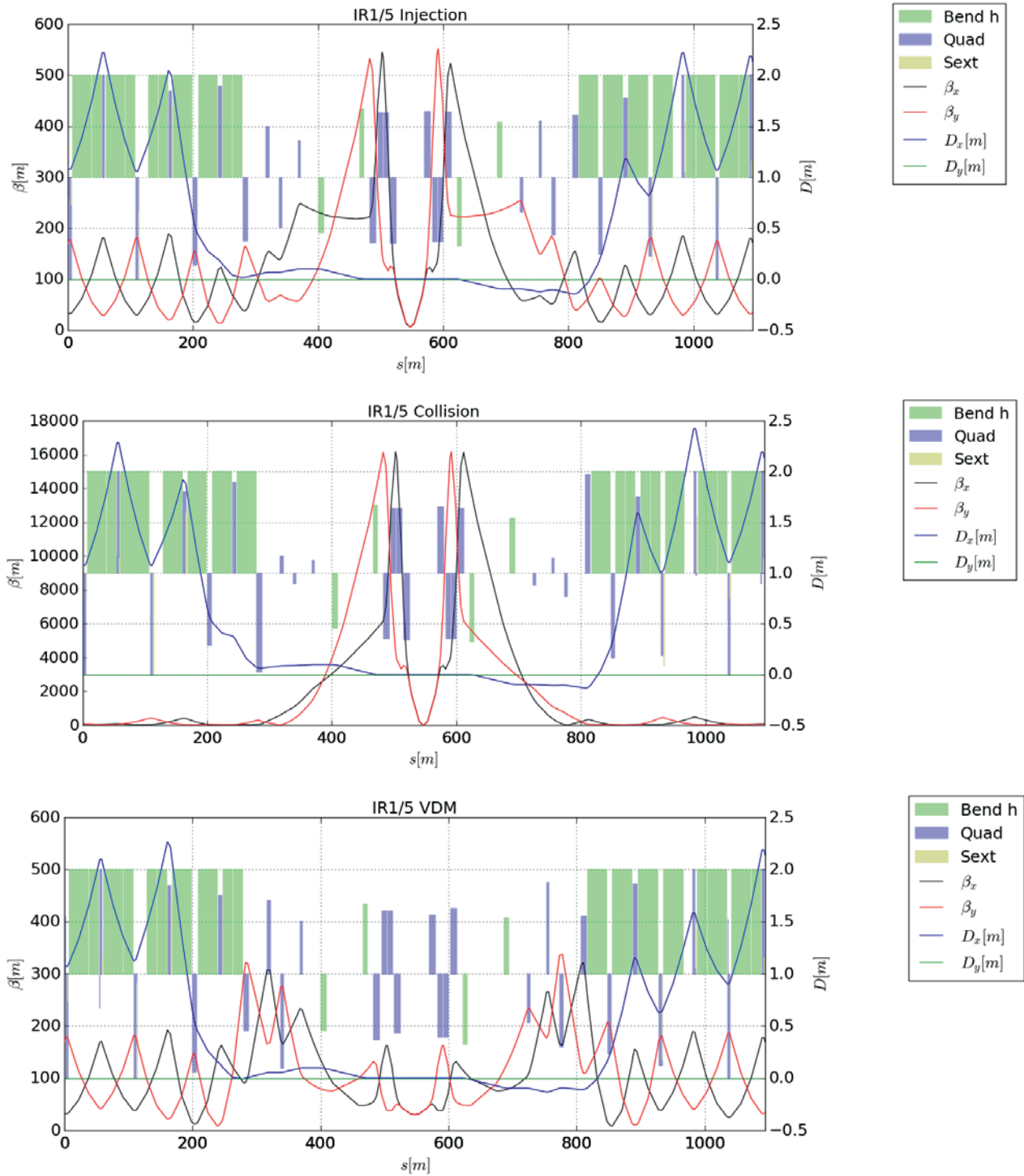


Figure 2-4: Optical functions at injection (upper - $\beta^*=6$ m), collision (middle - $\beta^*=0.2$ m) and for the configuration required for Van der Meer scans (lower - $\beta^*=30$ m) with nominal round optics in IR1 and IR5 for Beam 1.

Finally, it is worth mentioning additional studies that have looked at alternative layouts. Options have been studied based on triplets using 120 T/m and 170 T/m gradients [81][82], and an additional Q7 for crab cavity kick enhancements [83] without upgrading the matching section layout [84]. The latest results can be found in Ref. [85].

There are numerous constraints on the layout of components, arising from various considerations. The constraints and the associated issues are described in Chapter 15.

2.3.2 Circuit specifications

Performance and beam dynamics considerations guide some aspects of the selection of topology, power converter type, quench protection requirements for the new circuits, in particular:

- time required to perform a machine cycle, in particular squeeze, ramp-down or pre-cycle to optimize the turn-around time;
- time required to perform orbit corrections (operator adjustment or continuous feedback);
- time required to vary beam parameters (e.g. the time to reduce the separation between the two beams);
- reproducibility of the beam parameters between fills and during the year (e.g. to avoid additional optics correction campaigns);
- stability of the beam parameters during the cycle to limit emittance growth and luminosity losses;
- Precision and resolution in the adjustment of the beam (e.g. to perform optics measurement via k-modulation).

The transition between the various optical configurations has been studied in detail [86-88]. The sequence of gradients during the squeeze is available for HLLHCV1.0 and HLLHCV1.2 (limited to low-beta optics) and it has been used to perform first estimates of the hysteresis effects. Moreover, the time required to accomplish the squeeze has been estimated and compared with existing LHC circuits [89][90]. The results indicate that Q5 discharge dominates the squeeze duration for IR1 and IR5, while the triplets' discharge dominates the ramp down time. Several hardware solutions to reduce the duration, which has a direct impact on the turn-around time and therefore integrated luminosity, have been proposed and are currently under study [91]. The above estimates are being reviewed HLLHCV1.3 for which the squeeze sequence is being produced.

As far as the triplet is concerned, the ramp down time depends on the powering layout, where three different schemes have been considered (see Figure 2-5):

- Q1-Q3 and Q2a-Q2b in series;
- all triplet magnets in series (Q1-Q2-Q3);
- Q1-Q2a and Q2b-Q3 in series (Q1-Q2a Q2b-Q3).

The current rating for the different schemes is summarized in Table 2-8. Recently the second scheme has been endorsed as new baseline [26] together with 2-quadrant power converter to reduce the ramp-down time (see Chapter 6B).

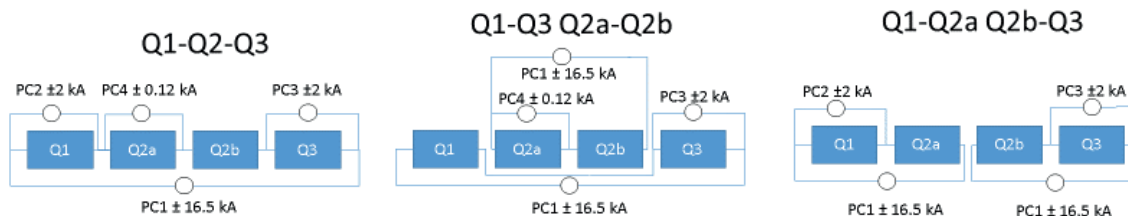


Figure 2-5: Possible layouts for the IT powering.

The tolerances on the current modulation have been specified based on what can be achieved with the LHC class 1 Power Converters (PC), whose performance is summarized in Table 2-9, and on the different powering schemes proposed in Table 2-8 [92-95]. Two regimes are distinguished: a low frequency regime (<0.1 Hz), where the current is directly controlled (current-control regime) and a high frequency regime (>0.1

Hz), in which the voltage is directly controlled (voltage-control regime) [96-97]. Those estimates are being reviewed thanks to new measurements [98].

Table 2-8: Nominal current of main and trim power supplies for the different powering schemes assuming a maximum triplet gradient of 132.6 T/m, a magnet inductance of 8.21 mH/m, and the HLLHV1.3 layout [92][93]. The power converter and the circuits are rated for equal or higher current (see Chapter 6B, Table 6B-3 and 6B-4).

	PC1	PC2	PC3	PC4
Q1-Q3 Q2a-Q2b	16.5 kA circuit: Q1-Q3 inductance: 138 mH	16.5 kA circuit: Q2a-Q2b inductance: 117 mH	±2.0 kA circuit: Q3 inductance: 69 mH	±0.12 kA circuit: Q2b inductance: 59 mH
Q1-Q2-Q3 (Baseline)	16.5 kA circuit: Q1-Q2-Q3 inductance: 255 mH	±2.0 kA circuit: Q1 inductance: 69 mH	±2.0 kA circuit: Q3 inductance: 69 mH	±0.12 kA circuit: Q2b inductance: 59 mH
Q1-Q2a Q2b-Q3	16.5 kA circuit: Q1-Q2a inductance: 128 mH	16.5 kA circuit: Q2b-Q3 inductance: 128 mH	±2.0 kA circuit: Q1 inductance: 69 mH	±2.0 kA circuit: Q3 inductance: 69 mH

As model for converting the PC output modulation to a modulation of the magnetic field experienced by the beam, the following has been assumed in the case of voltage-control regime

$$dB(f) = T_{Vacuum}(f) \times T_{ItoB}(f) \times T_{VtoI,load}(f) \times dV(f), \quad (2-5)$$

where $dV(f)$ is the voltage modulation, $T_{VtoI,load}(f)$ the transfer function of the load (circuit) seen by the power converter, modelled by a RL circuit, and $T_{Vacuum}(f)$ the transfer function of the cold bore, absorber, beam screen etc., with $T_{Vacuum}(f) < 1$. In the current-control regime the above equation reduces to

$$dB(f) = T_{Vacuum}(f) \times T_{ItoB}(f) \times dI(f), \quad (2-6)$$

$dI(f)$ being the amplitude of the current modulation.

Table 2-9: Tolerances on the current modulation achievable with Class 1 and Class 2 power converters in the current- and voltage-control regime, respectively. For the voltage-control regime, the values are given as 1 σ R.M.S. values, while for the current-control regime the units ppm are used, meaning that dI [ppm] = $I_{noise,PC}[A]/I_{max,PC}[A]$.

	Frequency range	Frequency	Class 1 PC	Class 2 PC
Current-control regime	<0.1 Hz.	random, Gaussian	±1 ppm	±10 ppm
Voltage-control regime	>0.1 Hz	50 Hz	3.2 mV	
		300 Hz, 20 kHz	10.0 mV	
		600 Hz, 40 kHz	2.5 mV	
		10 MHz	1.0 mV	
		all other frequencies	0.5 mV	

In the current control regime the tolerances are defined by the required tune stability, where the highest stability is needed for β^* -measurements performed with K-modulation [99]. As a first estimate, a stability of approximately $\Delta Q = 10^{-5}$ is needed [100][101]. With the current class 1 PCs, a tune shift $\Delta Q > 5 \times 10^{-5}$ can be achieved (see Table 2-10), where the smaller tune shifts can be obtained for the baseline and alternative powering scheme Q1-Q2a Q2b-Q3.

Table 2-10: Tune shift induced by uniformly distributed random current error of ± 1 ppm for different powering schemes, assuming $I_{\max}=17.4$ kA and nominal field gradient of 140 T/m for all IT magnets. The simulations have been performed for HLLHCV1.0, with round optics and $\beta^*=0.15$ m, and, for the sake of comparison, also for LHC V6.503, with round optics and $\beta^*=0.55$ m. The results can be approximately extrapolated to HLLHCV1.3 by scaling with the ratio of the maximum current, namely 16.5/17.4.

Powering Scheme	Nominal LHC	Q1-Q3 Q2a-Q2b	Q1-Q2-Q3	Q1-Q2a Q2b-Q3
R.M.S.($Q_{x/y}-Q_{x0/y0}$) [10^{-4}]	0.25	1.37	0.67	0.54

In the voltage-control regime, the tolerances are defined by beam quality, with the requirement that the tune modulation due to the triplet magnet and matching section quadrupoles PCs should not lead to its degradation. The beam stability can be assessed in terms of dynamic aperture (DA) described in more detail in Sec. 2.3.3. To determine the tolerance on the power supply ripple, particles have been tracked for 10^6 turns and different configurations, namely with and without beam-beam, with and without crab crossing, with beam-beam and crab crossing [93-95]. For the numerical simulation, the SLHCV3.1b layout has been used, assuming round collision optics and $\beta^*=0.15$ m. The effect of the power supply ripple can be quantified in terms of the amplitude of the induced tune ripple, which is depicted in Figure 2-6, calculated for the different frequencies using the tolerances listed in Table 2-9 the powering schemes with parameters from Table 2-8, and an inductance of about 2.9 mH for Q4.

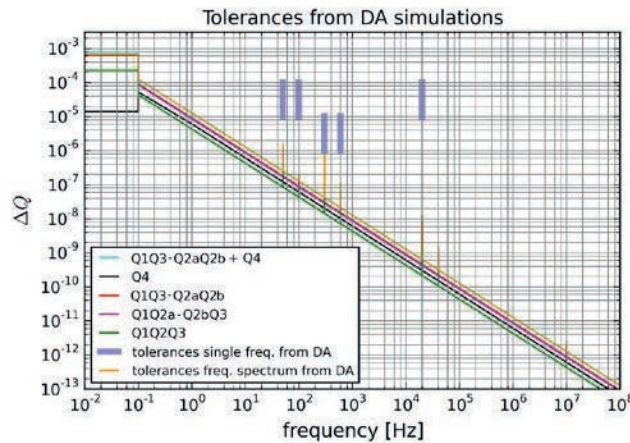


Figure 2-6: Maximum tune-ripple amplitude, resulting from noise on power converters at typical frequencies (see Table 2-9) The yellow curve represents the maximum tune-ripple amplitude, including the whole frequency spectrum, compatible with a negligible impact on DA (the power converter noise spectrum has been assumed to scale linearly with respect to that described in Table 2-9). In case of tune ripple at a single frequency, the maximum tolerable amplitude is represented by the blue bars (the horizontal size is only for better visibility). The impact on DA has been evaluated by taking the worst case among several configurations including beam-beam and crab crossing. The DA simulations have been performed for SLHCV3.1b and round collision optics ($\beta^*=0.15$ m). For the sake of comparison, the amplitude of the ripple for different powering scenarios is also shown using, however, the HLLHCV1.1 layout and round collision optics with $\beta^*=0.15$ m. In the voltage control regime all ripple frequencies are in phase, while in the current control regime the tune modulation is random and the maximum tune-ripple amplitude is shown in this case [93-95].

As simulation input for the ripple amplitude either the frequency spectrum given in Table 2-9 scaled by a factor 1 to 100 (yellow line in Figure 2-6) has been used, from which the tolerance on the voltage spectrum can be derived, or only a single frequency used and the ripple amplitude adjusted to yield a tune shift of 10^{-6} to 10^{-3} , from which a tolerance for the individual frequencies can be attained (blue bars in Figure 2-6). Moreover, all ripple frequencies are in phase in the voltage-control regime, while in the current-control regime the tune modulation is random. In the DA simulations, only the frequencies in the voltage-control regime have

been taken into account. All powering schemes lie below the limit obtained for the voltage spectrum, whereas the limit from the individual frequencies indicates that for 300 Hz the tune shift lies close to the obtained limit and a reduction by a factor 10 of the frequency is suggested. Comparing the different powering schemes, the baseline features the lowest tune shift. In the previous baseline, the power supply ripple from Q4 induced comparable tune ripple as that generated by the whole triplet because of the low inductance (2.9 mH) of the MQYY design based on a single-layer coil. The present baseline with the MQY type magnet should offer superior performance provided that a Class 1 PC is used.

In summary, the baseline triplet powering scheme achieves overall the best performance meeting the tolerances requirements for the voltage-control regime, whereas a reduction of the amplitude of the 300 Hz component is recommended. In the current-control regime the ripple performance of class 1 PCs is marginal and it is being reviewed with the power converter experts taking into account that tune ripple could have a detrimental effect on luminosity lifetime in particular in presence of large beam-beam tune spreads. More realistic models of the transfer function of the complex cold-bore/beam screen are required for a more precise assessment of the ripple effects.

The trim in Q2a will be needed to compensate for transfer function difference from MQXB magnet and in particular for k-modulation in Q2 for increasing the accuracy of the optics measurements. This will require an acceleration of $\sim 1A/s^2$.

In order to ensure sufficient orbit stability Class 1 PC should be used for D1/D2/MCBX/MCBRD dipoles. The MCBX, MCBRD and MCBY corrector circuits should allow large enough acceleration to be compatible with the orbit feedback. A preliminary summary of the target specifications for the dipole circuits are given in Table 2-11. Ramp rates and acceleration rates for the orbit correctors are calculated by matching the performance in terms of deflection ramp and acceleration rates of the MCBY correctors to be compatible with the operation as part of the orbit feedback. In addition, the specifications of the MCBX and MCBY circuits are also compatible with the requirement of reducing the beam separation from 2σ to 0 in less than 3 seconds as specified for beam-beam effects [102][103]. Ramp rate and acceleration rate for MBRD and MBXF are given to be similar to MBX and MBRC.

Table 2-11: Preliminary circuit specification for HL-LHC separation and corrector dipoles.

	MCBXFA	MCBXFB	MCBRD	MBRD	MBXF
Integrated field [T m]	4.5	2.5	5.0	35.0	35.0
Nom. Current [A]	1600	1600	430	12000	12000
Max. Ramp rate [A/s]	15.0	15.0	2.0	20.0	20.0
Field Rate [mTm/sec]	42	23	23	58	58
Angle Rate [μ rad/sec@7TeV]	1.8	1.0	1.0	2.5	2.5
Ramp Acc. [A/s^2]	5.0	5.0	1.0	2.0	2.0
Field Acc. [mTm/s ²]	14.1	7.8	11.6	5.8	5.8
Angle Acc. [μ rad/s ² @7TeV]	0.60	0.33	0.50	0.25	0.25
Time to max. ramp rate [sec]	3.0	3.0	2.0	10.0	10.0

2.3.3 Target field quality and dynamic aperture

The DA specifies the minimum stable amplitude in terms of R.M.S. beam size over a given number of turns in the machine. It has been used since the initial steps of the design of the LHC [78] to determine the required field quality of the various magnet classes. For computation of the DA in the HL-LHC, particles are tracked over 10^6 or 10^5 turns, depending on whether beam-beam effects are included or neglected, respectively. The initial momentum co-ordinate is set to two-thirds of the bucket height (2.7×10^{-4} and 7.5×10^{-4} for collision and injection energy, respectively). Sixty implementations of the random components in the magnets, corresponding to sixty realizations of the LHC lattice, are considered in the numerical simulations. Eleven phase space angles have routinely been used (although for special studies up to 59 values have been probed),

while thirty particle-pairs per 2σ amplitude step have been used. All these parameters have been specified during the design stage of the LHC. Since then, the amount of available computing power has increased, thanks to the increased CPU power of the CERN batch system and because of the use of volunteer-based computing resources [104]: this has enabled an increase of the number of directions considered in the studies, making the DA estimate more accurate. Note that the number of turns and random seeds affects the accuracy of the DA calculation, which is at least $\pm 0.1\sigma$ in this case.

For reference, the multipole expansion used to describe the magnetic field is given as in [78]:

$$B_y + iB_x = B_{\text{ref}} \sum_{n=1}^{\infty} (b_n + ia_n) \left(\frac{x+iy}{r_0} \right)^{n-1}, \quad (2-7)$$

where B_x , B_y , and B_{ref} are the transverse magnetic field components and the reference field, respectively. The coefficients a_n , b_n are the skew and normal field components, and r_0 is the reference radius. In the framework of the LHC studies, the magnetic errors are split into three components, namely systematic (S), uncertainty (U), and random (R), such that a given multipole is obtained by:

$$b_n = b_{n_S} + \frac{\xi_U}{1.5} b_{n_U} + \xi_R b_{n_R}, \quad (2-8)$$

where ξ_U , ξ_R are Gaussian-distributed random variables cut at 1.5σ and 3σ , respectively. The ξ_U variable is the same for all magnets of a given class, but changes from seed to seed and for the different multipoles. On the other hand, ξ_R also changes from magnet to magnet.

The target value of the DA differs between injection and collision energies. At injection, where the beam–beam effects can be neglected, the focus is on the impact of magnetic field quality. For the LHC design [78], a target value of 12σ (for a normalized emittance of $3.75\mu\text{m}$) was assumed. The best model of the LHC, including the measured field quality of the magnets and the sorting of magnets, provides a DA slightly lower than 11σ [105]. No signs of issues due to DA limitations have been observed during operation or dedicated studies in Run 1 and Run 2.

At top energy, beam–beam effects cannot be neglected and the DA has to be evaluated, including both magnetic field imperfections and head-on and long-range beam–beam phenomena (see Section 2.4.2). Hence, the approach taken consists of probing the impact on DA of the field quality of the new triplet magnets and asking that all the other new magnets have an impact on the DA that is in the shadow of the triplet quadrupoles. Eventually, the beam–beam effects are also included, providing the final DA value.

Studies for the field quality of the new magnets started from the top energy configuration and with an earlier version of the layout, SLHCV3.1b [48]. This allowed first estimates of the required field quality to be derived, which were then improved by including consideration of the injection energy, where the beam size reaches its maximum and the field quality is worse, due to the persistent current effect. The newer layout HLLHCV1.0 [49] has been extensively used following its release and it is the reference for the DA studies. It is worth stressing that given the CPU-time required by these studies, it is not always possible to keep them synchronised with the development and evolution of the layout. Moreover, in some cases the differences between the various layout versions are sometimes not relevant in terms of impact on DA.

In the numerical simulations consideration is made of the machine as built, i.e. the best knowledge of the measured magnetic errors is assigned to the magnets as installed, while, for the magnets that will be replaced according to the upgrade plans, the expected error table, with statistical assignment of errors, is used. This is the baseline configuration of the LHC ring to which magnetic field errors of other classes of magnets can be selectively added.

In these studies the acceptable minimum DA was set to 10σ (for a normalized emittance of $3.5\mu\text{m}$) at top energy, based on experience from the LHC (for which the design DA was set to 10σ [78]). The DA calculation was performed using long-term tracking in SixTrack [106][107], neglecting beam–beam effects and the impact of large chromaticity and large detuning with amplitude resulting from Landau Octupoles.

Determination of the required field quality based on DA computations is intrinsically a non-linear problem. The field quality obtained from electromagnetic simulations is used as an initial guess. Then, optimization of the field quality essentially involves determining the Jacobian of the DA as a function of the multipoles around the initial value of field quality. For this reason, it is of paramount importance to have a reliable estimate of the expected field quality from detailed electromagnetic simulations and measurements (see Chapter 3). The resulting error tables can be found in the official optics repositories [108][109] and are collected in Ref. [110] as well as in Annex A.4.

The previous triplet specifications at 7 TeV [111] were updated to take into account the additional triplet correctors for a_5 , b_5 , a_6 errors. These specifications will be referred to as IT_errortable_v66. An estimate of the D1 field quality is based on magnet design and referred to as D1_errortable_v1 [112]. Due to the evolution of the D2 dipole design, three versions of the D2 field quality were used in the study: these are referred to as D2_errortable_v3, _v4 [113], and _v5 [114]. Estimates for the Q4 and Q5 magnets are based on a scaling of the measured field of the existing MQY quadrupole and referred to as Q4_errortable_v1 and Q5_errortable_v0, respectively.

The systematic studies of the impact of the IR magnets field quality on the DA started using SLHCV3.1b layout and round collision optics, first. Then, injection energy was considered and as soon as the layout HLLHCV1.0 was made available, the studies were resumed using this layout. The field quality estimates also evolved based on the results of the numerical simulations of DA.

The main result is that the expected field quality is compatible with the request of having a minimum dynamic aperture over the sixty realisations of the field errors around 10σ (without beam-beam) [115].

The DA at injection energy, however, is about 1σ smaller than the DA of the nominal LHC as-built. Since the IR magnets do not limit it and since in the design of the ATS optics the phase advances between IP1 and 5 were not specified based on any optimisation criterion (currently the values are $\mu_x/2\pi=31.195$ and $\mu_y/2\pi=30.368$) possible optimizations have been studied. Tune scans indicate an effect of the 7th order horizontal resonance close to the current tune (62.28, 60.31). Reducing the horizontal and vertical tunes by about 0.01 would increase the DA by about 0.5σ . These results are being complemented by refined scans of the phase advance between IP1 and 5. A rather weak dependence on the vertical phase advance is found, while DA is more sensitive to the horizontal value of the phase advance. Figure 2-7 shows the behaviour of the minimum (left) and average (right) DA as a function of the horizontal and vertical IP1-5 phase advance [116].

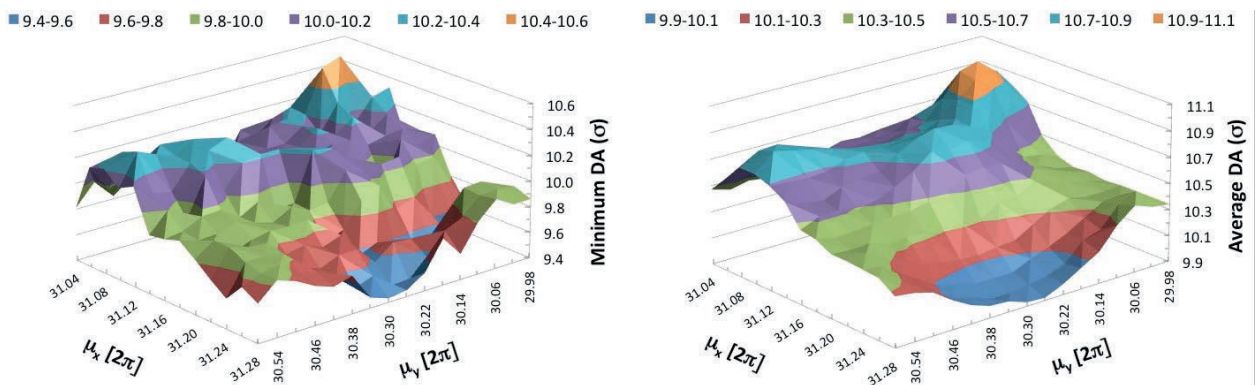


Figure 2-7: Beam 1 DA as a function of horizontal and vertical IP1-5 phase advance at injection energy. Both the minimum (left) and the average value (right) are given.

The optimised phase advance, corresponding to $\mu_x/2\pi=31.08$ and $\mu_y/2\pi=30.06$, can increase the minimum DA from 9.73σ to 10.65σ and the average value from 10.36σ to 11.06σ , which represent an interesting and cost-free gain.

The situation in collision energy is radically different [115]. The field quality of the new triplets has been scrutinised, by means of detailed dynamic aperture simulations, performed without the inclusion of beam-

beam effects. The latest estimates of the field quality as provided by WP3 have been probed. The harmful impact of the increased multipole components b_{10} and b_{14} has been clearly observed, with the minimum dynamic aperture approaching 9σ . Note that measured magnetic field errors are known up to a_{15} and b_{15} and these are the highest-order multipoles included in tracking simulations as the accuracy of even higher-order multipoles from measurements are not deemed precise enough. The field quality of the latest cross section of the triplet magnets has partly addressed the above issues and new simulations will be performed with the most recent data. These will be completed by the analysis of the impact of the field quality in the presence of beam-beam effects in order to assess the needs of a revision of the field quality specifications.

The quadrupolar component of fringe fields of triplet quadrupoles has already been considered and found non-problematic in Ref. [117]. Preliminary analytical results [118] indicate that, albeit small, the detuning with amplitude induced by the fringe fields is not completely negligible, thus calling for a second level of study. This should include long-term numerical simulations to study the non-linear effects generated. This opens the wide field of symplectic integrators, as, in the presence of 3D magnetic fields, the standard approach based on multipoles cannot be applied anymore. Work is underway to study the best integration schemes and their implementation [119][120], before starting the real numerical work.

In the meantime, estimates of the field quality for the heads of the triplet magnets have been provided [121] and models to perform tracking studies using this new information have been developed. At injection, the impact of the new models is negligible, while at collision energy, the situation is different and while the round optics is less sensitive to the addition of the effect of the triplet magnets' heads, the flat one is more affected [122]. All subsequent tracking campaigns have included the effects of the heads and the following results will be based on these new models. Additionally, the possibility of simulating the dynamics of Beam 2 has been opened also for HL-LHC, based on extended versions of the routines used to generate the error distributions of magnet families. Therefore, the impact of the field quality of the orbit correctors in the triplet region as well as the sensitivity of DA on the field quality of individual magnets' classes has been assessed using these two new features, i.e., triplet magnet head effects and Beam 2 DA.

The comparison of the dynamic aperture for Beam 1 and Beam 2 has been performed by adding one by one the HL-LHC magnet families, at injection and collision energies. The results of these simulations are summarised in Figure 2-8.

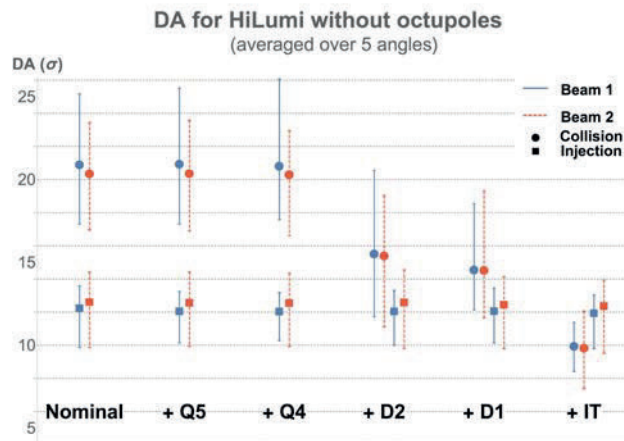


Figure 2-8: DA at injection and collision for Beam 1 and Beam 2. The different families of HL-LHC magnets are included one by one in the simulations. The markers refer to the average DA over seeds and phase space angles, while the error bars represent the DA distribution for the various seeds.

The behaviour of Beam 1 and Beam 2 remains very similar and no systematic difference between the two beams is found both at injection and in collision.

The impact of the magnet classes is clearly visible, with a large drop when adding magnetic errors to the D2 separation dipoles for the case with zero-strength Landau octupoles although the field quality of the D2

separation dipole has been significantly improved. Studies are currently on going to find the dominant contribution to this drop and whether the non-linear correctors in the corrector package could correct the D2 field quality. A second drop in DA is observed when adding magnetic field errors to the triplets.

Another campaign of DA simulations has been performed to investigate the effect of the inclusion of the MCBXF field quality to the dynamic aperture. The MCBXF error tables used can be found in [123], which so far only contains systematic errors. The results of these studies are shown in Figure 2-9.

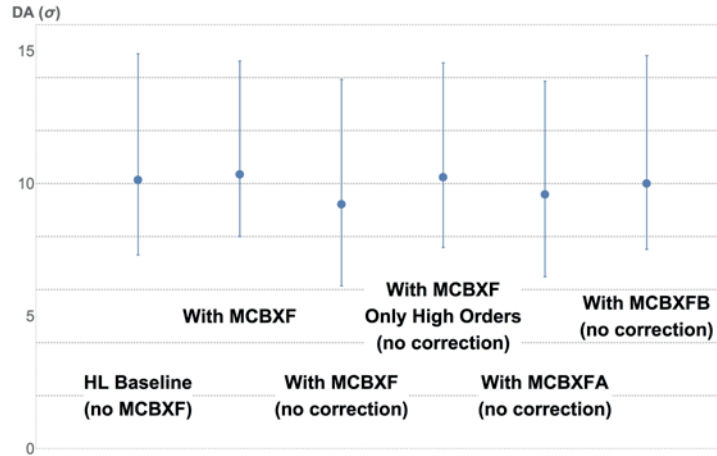


Figure 2-9: DA for Beam 1 in collision (round optics) for various configurations of the MCBXF field quality.

At a first glance, the impact of the MCBXF seems perfectly under control, as there is even a small increase of DA due to some internal compensation between the magnetic field errors of the various magnet classes. However, this result is obtained allowing the magnets in the corrector package to compensate for the MCBXF field quality. This is an overly optimistic situation, as in the simulations the correction algorithm has all exact information on the magnet field qualities, which is not the case in reality. For this reason, it was deemed useful to perform simulations without correcting the MCBXF field errors, which results in a reduction of the DA of 0.91 σ . Further investigations have resulted in two important conclusions on the nature of this drop in DA. First, the drop is fully dominated by the a_3 and b_3 multipole components as it can be seen in Figure 2-9, where different configurations are compared. The field quality of the MCBXF magnets has no harmful impact on DA, provided the non-linear corrector package is used to compensate their field quality (second configuration from the left), while if such a correction is not performed, then a sizeable reduction in DA is visible (third configuration). If only uncorrected, high-order magnetic multipoles are used, then the DA is almost unaffected (fourth configuration), indicating that the low-order multipoles are the harmful ones. The last two configurations indicate that MCBXFA is the magnet family with the largest impact on DA. Second, of the two magnet classes that make up the MCBXF magnets, the MCBXFA gives the dominant contribution to the DA drop (see Figure 2-9).

With the detailed specification of the operational conditions, it has been possible to launch the study of the evolution of the dynamic aperture during the squeeze and for various running conditions, mainly chromaticity and octupole settings [115]. The dependence of the dynamic aperture without beam-beam effects on the value of β^* is shown in Figure 2-10. A linear behaviour is clearly observed. Flat optics configurations have been studied too and the corresponding dynamic aperture value is very close to that of the round β^* configuration corresponding to $\sqrt{\beta_x^* \beta_y^*}$.

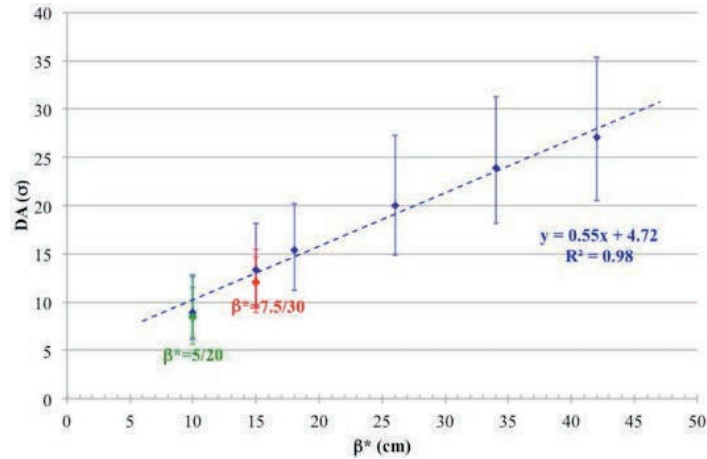


Figure 2-10: Dependence of the Beam 1 dynamic aperture on β^* during the ATS squeeze. The markers refer to the average DA, while the error bars refer to the minimum and maximum DA over the seeds. Flat optics configurations have also been considered.

The dependence of the dynamic aperture at top energy on the linear chromaticity is shown in Figure 2-11. Also in this case a linear behaviour is found, showing that high chromaticity values are detrimental for the single-particle beam stability. In the same plot both round nominal and flat optics configurations are shown.

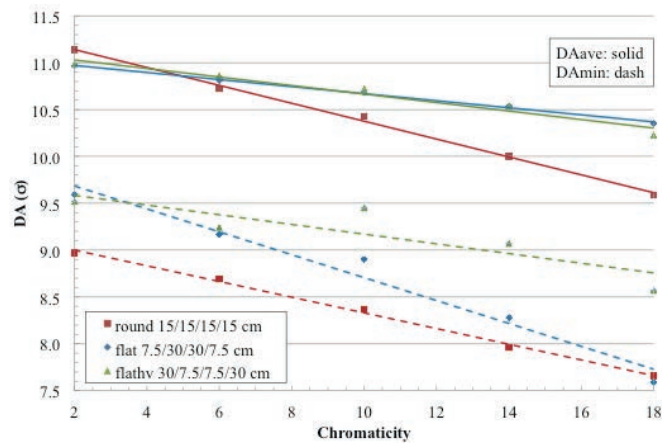


Figure 2-11: Dependence of the Beam 1 dynamic aperture on linear chromaticity at the end of the ATS squeeze. Flat optics configurations have also been considered.

The impact of the Landau octupoles on the DA has been also checked with numerical simulations. It turned out that the minimum DA of the round optics is modestly reduced, about 0.6σ , by full strength, negative octupoles; however, it falls below 8σ . The average DA reaches 9σ , with a much larger reduction (2σ) indicating a smaller DA spread among different seeds. The impact of the octupoles is stronger on flat optics for which the minimum and average DA are below 7σ and 8σ , respectively. These values are obtained for a chromaticity $Q' = +3$. In case a larger value ($Q' = +18$) is used, then the DA is further reduced just below 7σ . Another interesting feature to mention is that the presence of the strong octupoles makes the DA, both average and minimum, a nonlinear function of β^* . The above observations are clearly favouring a working point with lower chromaticity and low octupoles' strength in particular for the smaller values of β^* . A strong dependence of the DA on the sign of the octupoles (the positive sign being the worst case), at least for the nominal β^* value of the round optics configuration has been observed.

The non-linear correctors are key ingredients to maintain an acceptable dynamic aperture at the minimum β^* [66]. So far, their strength was set in numerical simulations based on the knowledge of the field quality of the other IR magnets in the area between D1 left and D1 right. In reality, the knowledge of the field

quality of these magnets and the transfer functions of the non-linear correctors will be limited and it may not allow a straightforward determination of the required strength of these special correctors. For this reason, a series of numerical simulations has been performed in which the strength of the non-linear correctors is varied in the interval 0.7-1.3 around the nominal strength. These miss-powering effects have been simulated assuming uniform distributions and the various correctors, both normal and skew, have been varied independently from each other. Overall, the impact on the average DA is modest, smaller than 0.3σ , while that on the minimum DA ranges from -0.7σ to $+0.3 \sigma$ [116].

Also at collision energy, a gain in DA can be achieved by optimising the phase advance between IP1 and 5, which is set to $\mu_x/2\pi=31.210$ and $\mu_y/2\pi=30.373$. A massive campaign of numerical simulations for the round optics configuration has been performed (no octupoles powered). In this case, the DA features a stronger dependence on the vertical phase advance than on the horizontal one and the situation is shown in Figure 2-12.

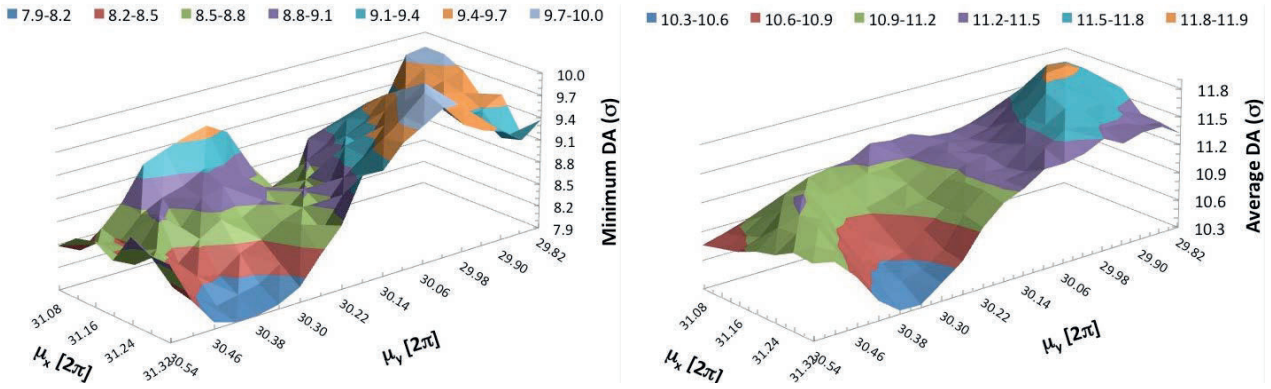


Figure 2-12: Beam 1 DA as a function of horizontal and vertical IP1-5 phase advance at collision energy for round optics. Both the minimum (left) and the average value (right) are given.

Optimisation can be carried out by using as figure of merit either the minimum or the average DA and slightly different results are obtained. In both cases, the minimum DA can be increased above 10σ although for slightly different values of the phase advance. The gain in DA due to the special phase advance is of the order of 0.4σ if the Landau octupoles are included in the numerical simulations and are set to their maximum value of -570 A . This indicates that the DA is dominated by the effect of the octupoles, in this case. The optimised phase advance determined for the round optics has only a limited impact, at the level of few tens of sigma, on the minimum DA (while the average remains mostly unaffected) for the flat optics configuration. This suggests that the phase advance optimisation should be performed also for the flat option [116].

Additional field quality and dynamic aperture studies are in progress and will be pursued in future studies along several lines, including:

- Dedicated studies to assess the impact of field quality of triplet quadrupole magnets, D1, D2, Q4 and Q5 on linear optics, knowing that the distortion of the optical parameters can stem from both the b_2 component and the feed-down from b_3 and a_3 via the crossing scheme bumps.
- Dedicated studies to assess the impact of transfer function errors for the non-linear triplet correctors and how they should be set during the physics cycle.
- Specification of crab cavity field quality: preliminary results [124-127] seem to indicate that the estimated field quality should be good enough to prevent any impact on DA.

Finally, it is important to stress that as soon as magnet prototypes will be built and field quality measurements will be carried out, studies should be launched to establish the impact of the measured field quality on DA (including beam-beam effects), possibly with the aim of providing feedback to the magnet designers and builders.

2.4 Performance

2.4.1 Beam stability

Transverse instabilities have been observed in the LHC during Run 1 with 50 ns beams and during Run 2 with 25 ns beams [128-130]. These have implied operating the machine with high chromaticity ($Q' \sim +15$) and high Landau octupole strength (close to the maximum current achievable by these circuits at top energy, i.e. +570 A in the LOF octupoles), and with maximum gain and bandwidth of the transverse feedback (50 turns and 20 MHz). The observations have evidenced that in several cases the observed instabilities are occurring as a result of the interplay of various mechanisms and it is important to take all of them into account. For that reason, on one side a significant effort has been spent in studying experimentally and by simulations cases in which some of these effects can be neglected and, on the other side, the models and the simulation codes are being gradually upgraded to take into account an increasing level of complexity. The effects of beam coupling impedance, electron cloud, head-on and long-range beam-beam forces, realistic transverse feedback and machine optical parameters like tunes, linear coupling, linear and non-linear chromaticity, Landau octupole strength and other non-linearities are gradually being included.

During 2015 and 2016 systematic measurements have been performed with single bunches (see Figure 2-13) to characterize the present LHC impedance model. These show a good agreement between the expected current of the Landau octupoles required to stabilize the beam and the measured values as a function of the chromaticity over values at which it is planned to operate HL-LHC ($Q' > +2$ units). The same agreement between measurements and simulations has been obtained with a bunch train consisting of 72 bunches after a period of operation with 25 ns beams that has led to a reduction of the SEY [130][131].

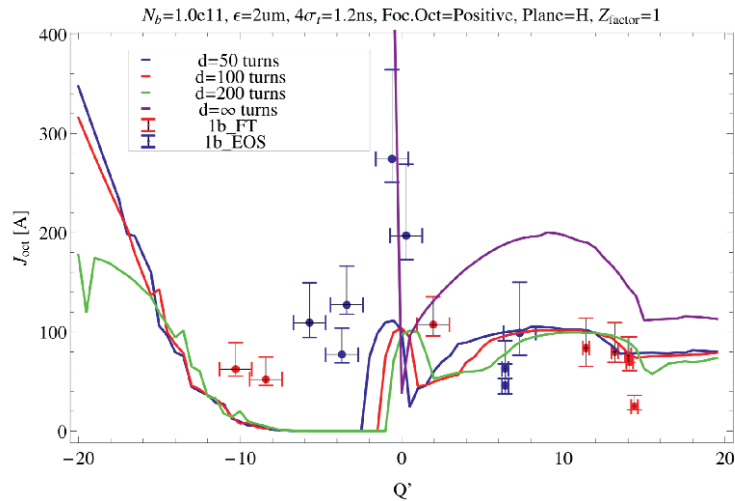


Figure 2-13: Overview of single-bunch measurements of the instability threshold (in Landau octupoles current vs. chromaticity) performed in 2015, plotted alongside DELPHI [132] predictions for different damping times. Not shown are three truncated points for $Q' \approx 0$ that are slightly below 800A (see discussion below). FT stands for Flat Top and EOS stands for End Of Squeeze.

The effective impedance of HL-LHC without considering the crab cavities and in the absence of impedance reduction measures would not be dramatically higher than that of the LHC [133], and the Carbon-Fibre-Carbon (CFC) collimators would represent the highest contributors to the HL-LHC impedance over a wide range of frequencies. Given the higher bunch population and brightness of the beams required for HL-LHC and the fact that almost the maximum values in chromaticity and Landau octupoles current have been used since 2012, we cannot afford to increase the transverse impedance of the machine and indeed we have to reduce it to achieve better conditions for beam stability. Among the CFC collimators, the secondary collimators (TCSGs) are the main contributors to the transverse impedance. New jaw materials for these collimators have been therefore explored, for example: Molybdenum (Mo), Molybdenum graphite (Mo-Gr, also written

sometimes MoC), Titanium nitride (TiN), and Titanium di-boride (TiB2). The HL-LHC baseline includes the installation of new Mo-Gr collimators with a 5 μm Mo coating in LSS7 only as the contribution from LSS3 is marginal due to the larger gaps at which these collimators are operated. The current HL-LHC impedance relative contributions for the horizontal and longitudinal planes are depicted in Figure 2-14 [134]; the vertical dipolar impedance is very similar to the horizontal one. It can be seen that for the transverse planes the collimator resistive wall impedance is still the first contribution (for both real and imaginary parts) and the beam screen is important mostly at low frequency and for the real part of the impedance. The relative variation of the vertical dipolar impedance vs. frequency is depicted in Figure 2-15, where it can be seen that above few MHz the impedance is significantly reduced. The horizontal impedance is similar to the vertical one within $\pm 10\text{-}20\%$ depending on the frequency. The fact that at low frequency the real part of the impedance is higher is due to the fact that a good conductor keeps the induced current closer to the beam, and the gain in conductivity is lower than the loss in distance to the beam [135]. This is however not worrying as the transverse damper can easily cope with this small decrease in instability rise-time, in particular at low frequency as the first unstable betatron line is around 8 kHz.

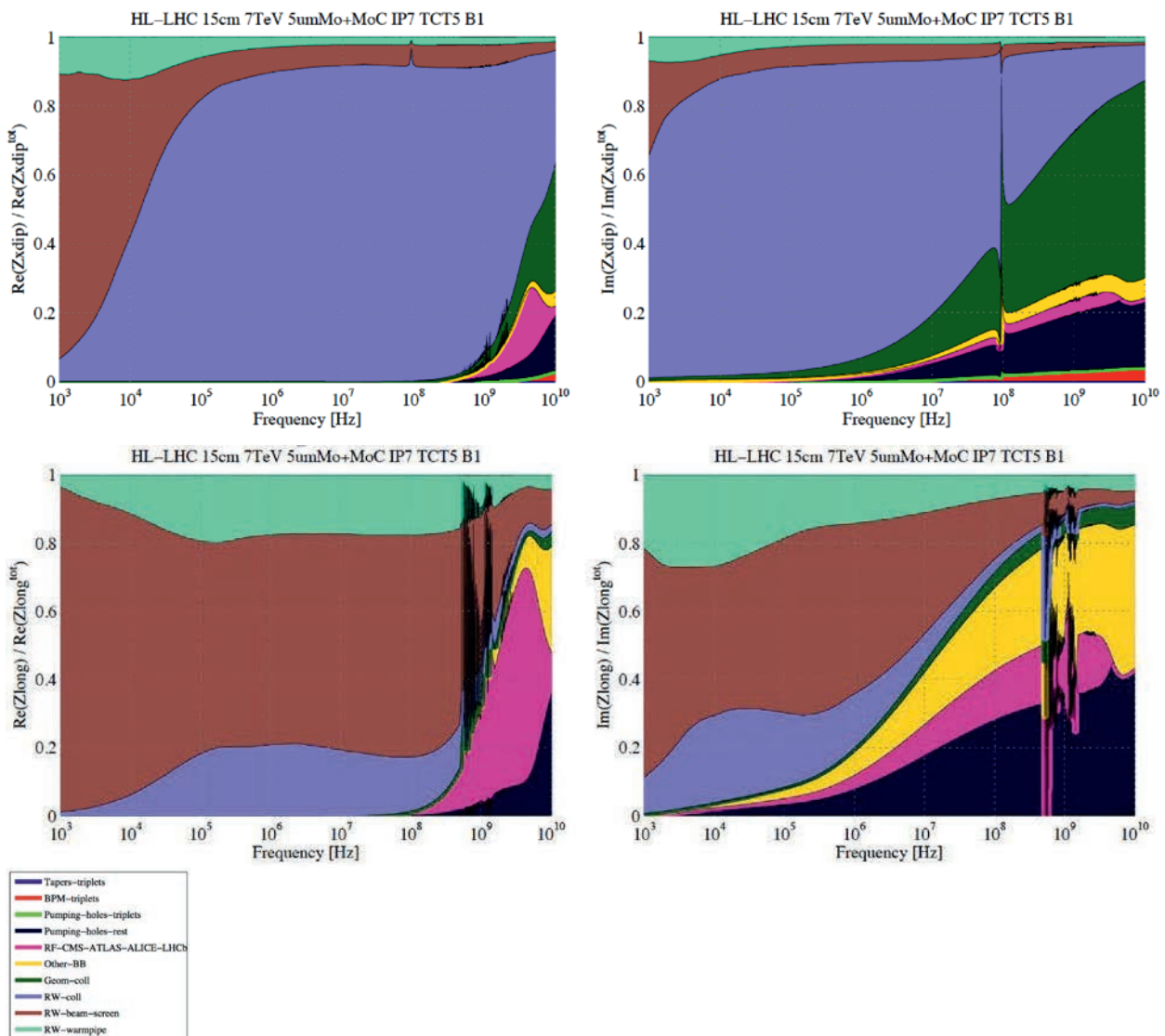


Figure 2-14: Contributions to the real (left) and imaginary (right) parts of the (upper) horizontal dipolar, and (lower) longitudinal impedances in HL-LHC for Beam 1 without considering the crab cavities (for the case of $\beta^* = 15\text{ cm}$). The vertical dipolar impedance is very similar to the horizontal one. A similar result is obtained for Beam 2.

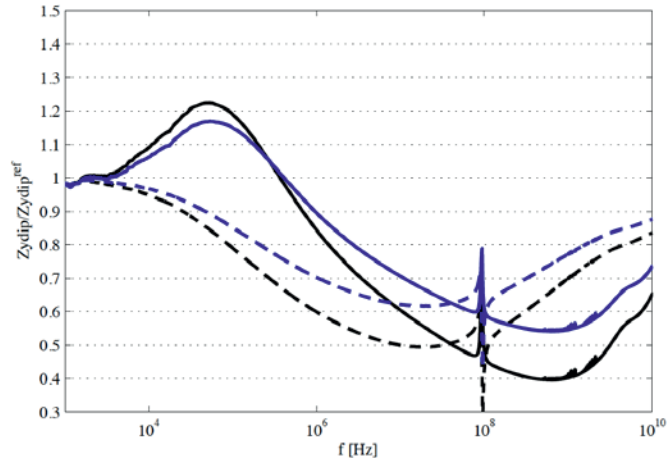


Figure 2-15: Relative variation of the real (continuous line) and imaginary (dashed line) vertical dipolar impedance by replacing the secondary (TCSG) CFC collimators with Mo-coated ($5 \mu\text{m}$) Mo-Gr collimators in LSS7 only (blue) or in both LSS7 and LSS3 (black).

The corresponding stability limit obtained by conservatively scaling from 2012 data is plotted in Figure 2-16 for a scenario without crab cavities, a chromaticity Q' of +15 units; a damping time of the transverse damper of 50 turns and for the maximum current of the Landau octupoles (using the negative polarity, i.e. -570 A in the focusing octupoles). The stability limit without and with Mo-Gr collimators is shown. The negative current in the Landau octupoles (which provides more stability for the impedance induced single-beam instabilities) was chosen after analysis of the interplay between octupoles and beam-beam long-range during the squeeze, as discussed below. As can be seen from Figure 2-16, it is necessary to replace the CFC collimators in LSS7 to reach beam stability for the beam parameters considered for HL-LHC (standard 25 ns, BCMS and 8b+4e – see Table 2-1 and Table 2-17).

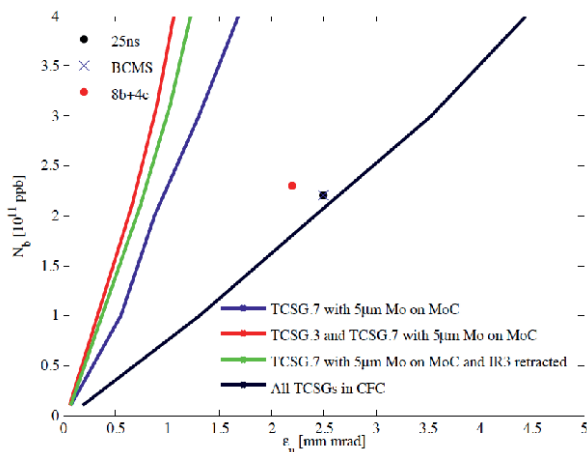


Figure 2-16: Stability limits obtained by scaling from 2012 data (without crab cavities) for a chromaticity Q' of +15 units, for a damping time of the transverse damper of 50 turns and for the maximum current of the Landau octupoles (using the negative polarity, i.e. -570 A). The number of protons per bunch is plotted in the vertical axis, while the transverse R.M.S. normalized emittance is plotted in the horizontal one. Stability is achieved for the bunch parameters for which the corresponding points lie below the plotted curves.

Special attention should be paid to the impedance of devices in high β regions such as the crab cavities and unshielded elements. In the present HL-LHC operational scenarios [136] chromaticity is close to +3 units to provide the largest stability margin based on the present impedance model and assuming no interplay with other mechanisms such as electron cloud, which can lead to both coherent and incoherent effects. This scenario is being reviewed taking into account the experience gained in 2015-16 showing that dedicated scrubbing runs

at injection are not sufficient to suppress electron cloud in the dipoles and additional scrubbing during physics is necessary. Operation for physics with an increasing number of bunches at nominal bunch population in the presence of electron cloud in the dipoles can be achieved compatibly with the available cryogenics power if the machine is operated at high chromaticity and by powering the Landau octupoles [137]. Furthermore, the feasibility of controlling the chromaticity along the cycle within few units (1 to 2) remains to be demonstrated in operation. For that reason, an operational scenario with high chromaticity must be foreseen at least for the ramp-up phase where conditioning of the dipole beam screen is required. Crab cavities have a visible impact on beam stability due to their significant contribution to transverse impedance, their number (4 per acting in the horizontal plane and 4 acting in the vertical plane on each of the two beams [10]) and because of the very large β functions achieved during the squeeze at their location [138][139]. The impedance effect is proportional to the β function and the number of crab cavities (which leads to a symmetric effect between the horizontal and vertical planes), while the crab angle is proportional to the square root of the β function at the crab cavities for a given β^* , the maximum voltage per cavity and the number of cavities (assuming that all cavities have the same design). Therefore, if we are limited by impedance, an optimum β function and number of cavities can be found for a given maximum voltage provided by each cavity. Of course increasing the maximum voltage would be an advantage. If we are not limited by impedance, we have all the interest to increase the β function. The instability growth rates (and similarly the instability limit) have been estimated [140][141] for the latest impedance models of the DQW and RFD crab cavities [138][139]. The results of the analysis, considering only one crab cavity, are represented in Figure 2-17 for both the single-bunch and multi-bunch instabilities, for both DQW and RFD crab cavity types, computing the required increase of the Landau octupoles current required to stabilize all the High Order Modes (HOMs) individually. It can be seen that an increase of less than ~ 10 A in the octupole current is sufficient to stabilize all modes, except one HOM at 920 MHz for the DQW crab cavities. The effect of this HOM has been also confirmed performing statistical simulations including random frequency spread of 3 MHz for the HOMs of different cavities. In order to ensure stability it is therefore recommended to reduce the impedance of this HOM in particular if the option of allowing collisions at minimum β^* and nominal intensity is maintained (e.g. if levelling by parallel separation is implemented as an alternative to β^* levelling).

As for the crab cavities the impedance of all the pieces of equipment being installed in regions with high β functions (e.g. beam screens, beam position monitors, RF fingers) are being carefully scrutinized and followed-up with the designers together with modifications foreseen in the experiments and interaction regions [142].

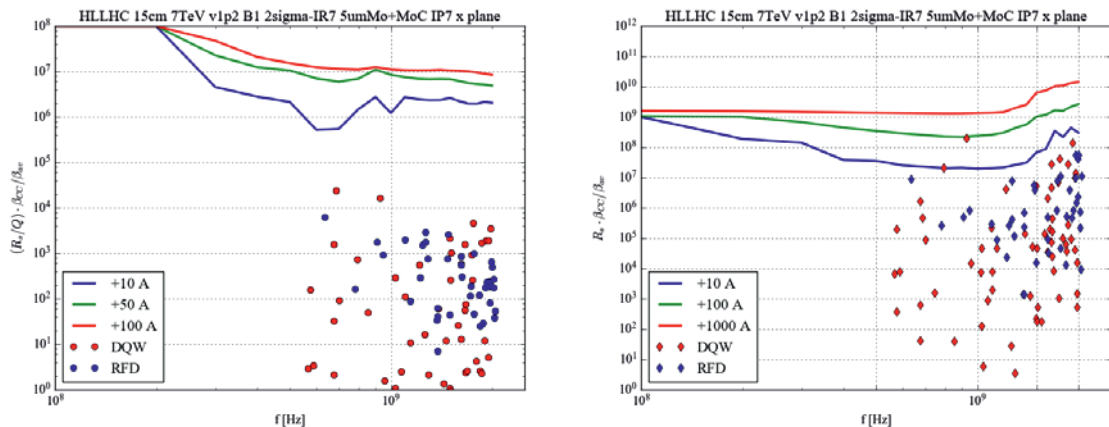


Figure 2-17: Required additional current in the Landau octupoles to damp (left) the single-bunch and (right) multi-bunch instabilities. This particular study was performed for a chromaticity of + 5 units, for a β^* of 15 cm and for a single crab cavity. The effect of an ideal transverse damper is also included with a damping time of 50 turns.

As a result of the experience gained in 2015 and 2016 and the experiments and studies conducted, the definition of the working point for HL-LHC has further progressed:

- It is proposed to operate HL-LHC at injection with the horizontal and vertical fractional tunes 0.27/0.295 instead of 0.28/0.31 and to compensate automatically the Laslett tune shifts during the injection process. This will allow accommodating the large tune spread created by the high chromaticity and Landau octupoles values needed to stabilize the beam against electron cloud (see Figure 2-18).
- The ratio between the tune separation and the closest tune approach should be larger than 2 as coupling can lead to instabilities due to a loss of transverse Landau damping [143]. Two measurements performed at 6.5 TeV confirmed predictions from simulations [130] that an increase by a factor 4 to 5 of the Landau octupoles current is required to stabilize the beam if linear coupling is not sufficiently well corrected.

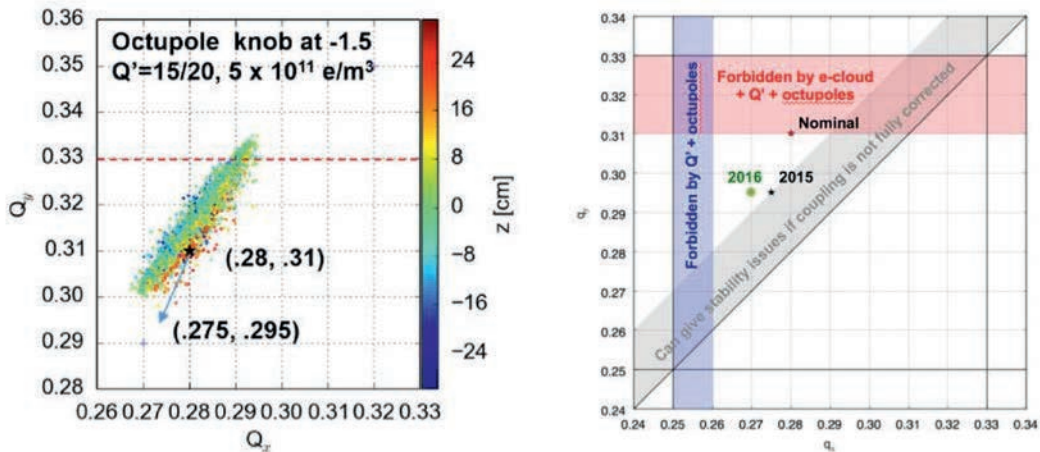


Figure 2-18: Optimization of the working point at injection to accommodate the large tune spread created by the high chromaticity and Landau octupole values needed to stabilize the beam against electron cloud.

A high harmonic (800 MHz) RF system [144-150] in Bunch Shortening Mode (BSM) could provide an additional margin for longitudinal stability. It could also reduce intra-beam scattering (IBS) emittance growth rates, beam-induced heating and pile-up density in Bunch Lengthening Mode (BLM), by flattening the bunch profile. More recently, it has been demonstrated that flattening of the bunch profile could be obtained also in BSM [151]. A preliminary cavity design for the 800 MHz RF system exists [152] but the proposed installation is dimensioned for operation in BSM. The installation for BLM operation would require a scaled-up version of the system. Longitudinal instabilities are not expected to be an issue in the HL-LHC [129] for the nominal bunch parameters, however, it is being considered to consider 1.2 ns as nominal average bunch length to guarantee stability even in the presence of bunch-to-bunch parameter variations (intensity and bunch length). These variations are observed already in the beams delivered by the injectors and they persist after controlled emittance blow-up during the ramp in the LHC. Single bunch measurements in the LHC at 4 TeV showed an intensity threshold at 1×10^{11} p/b, for an RF voltage of 12 MV and a longitudinal emittance of 1 eVs (4σ bunch length of 0.8 ns, scaled from the measurement of the full width at half maximum). Scaling to HL-LHC parameters (16 MV, 2.5 eVs) leads to an intensity threshold of 3.4×10^{11} p/b. A comparison between recent measurements and predictions of the loss of longitudinal Landau damping reveals a good agreement (see Figure 2-19), therefore a sufficient margin should exist for the HL-LHC beam parameters and the expected longitudinal impedance.

The effect of a double (800 MHz) RF system on the single-bunch transverse stability limit has been studied through HEADTAIL simulations, considering the HL-LHC impedance model without crab cavities [153][154]. The effects of chromaticity, Landau octupoles, (bunch-by-bunch) transverse damper and a phase error between the two RF systems (of ± 5 degrees) were considered. An increase of the single bunch transverse stability threshold by about a factor 4 can be obtained in BLM if combined with operation with $Q' = 15$,

+ 550 A in the octupoles and a damping time of the transverse damper of 50 turns. In BSM, the impact of the 800 MHz system on the single bunch transverse stability threshold is marginal and it can even lead to a slight reduction of the threshold according to the chromaticity settings [154].

From the above considerations, an 800 MHz RF system is not expected to be needed from beam stability considerations in the transverse or longitudinal plane.

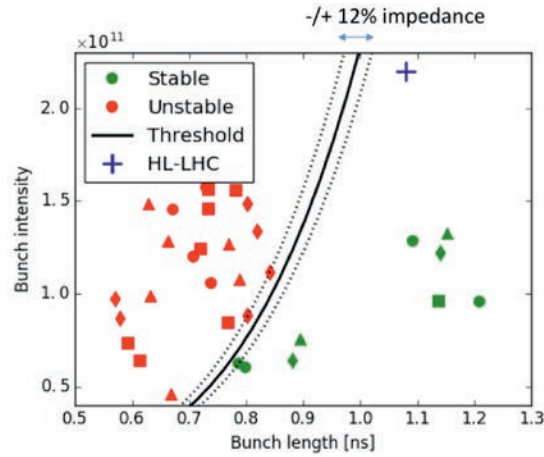


Figure 2-19: Comparison between longitudinal instability measurements and predictions of the loss of longitudinal Landau damping.

The use of a low harmonic RF system in the LHC (200 MHz) as the fundamental RF system has been suggested [155] since:

- it could help to reduce IBS, beam-induced heating, and electron cloud effects;
- together with the existing 400 MHz RF system, it could be used for luminosity and pile-up levelling;
- it also has a beneficial effect for ions and the momentum slip-stacking scheme in the SPS [156].

A new design has been proposed for a compact superconducting cavity [155] and the potential benefits have been studied showing that this option could allow operating the machine within the available cryogenics power if $SEY < 1.4$ cannot be obtained by scrubbing in the main dipoles [157]. Finally, the expected benefits of a double RF system should be weighed against the impedance increase and the possible reduced reliability.

Based on the experience from LHC Run 1, the interplay between impedance, Landau octupoles, and beam-beam is expected to play an important role in defining the stability limits during the betatron squeeze [128][158]. A detailed analysis of the evolution of the stability diagram in the presence of Landau octupoles and beam-beam long-range during the betatron squeeze has been done [159]. The result for the negative sign for the Landau octupoles, preferred for single beam stability, is shown in Figure 2-20. It can be seen that the maximum reduction of the stability diagram during the betatron squeeze (compared to the case without beam-beam) is reached for a β^* of approximately 40 cm and that below this value, the stability diagram increases due to the telescopic squeeze increasing the β functions in the arcs. It was also found that the maximum reduction of the stability diagram during the betatron squeeze can be compensated by 8% larger β at the Landau octupoles at $\beta^*=40$ cm.

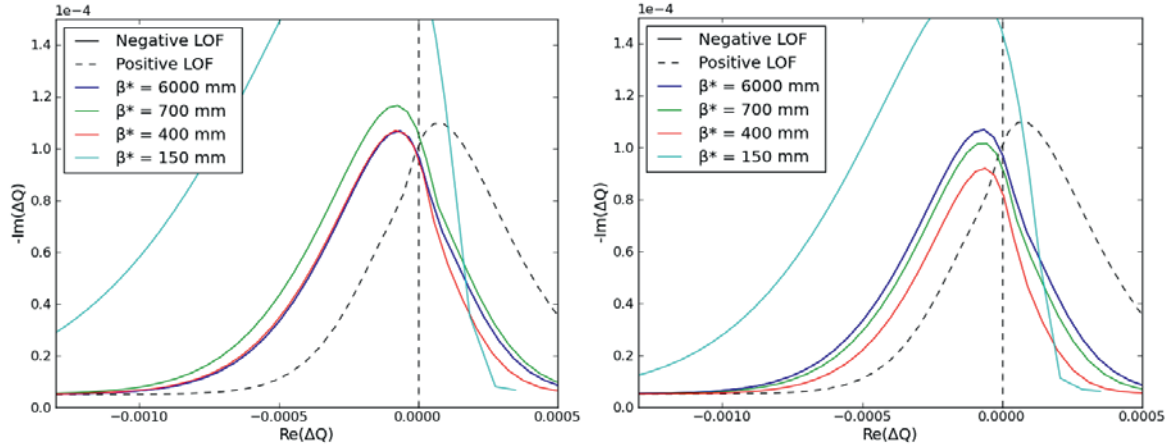


Figure 2-20: Evolution of the stability diagram in the presence of Landau octupoles and beam-beam long-range as a function of β^* (in mm) during the betatron squeeze. The curve « Negative LOF » (below the curve corresponding to $\beta^* = 6$ m) refers to the stability diagram with Landau octupoles only (negative current of -570 A in the focussing octupoles). The maximum reduction of the stability diagram at $\beta^* \sim 40$ cm (left) can be compensated by 8% larger β function in the Landau octupoles in the arcs (right).

The study of the stability diagrams during the collapse of the separation bump when going in collision has identified two minima, at a full separation of $\sim 6.5 \sigma$ and at $\sim 1.5 \sigma$. It was recommended to cross the most critical minimum, at $\sim 1.5 \sigma$, faster than the predicted instability rise-time, i.e. faster than 1 s therefore providing the specifications for the ramp and acceleration rates for the dipole correctors determining the separation bump (see Section 2.3.2) [103][130]. No instability has been observed so far at the minimum of the stability diagram during the regular operational fills, as expected from the rate at which the separation bump is presently reduced in the LHC and due to the fact that even at minima of stability diagrams, sufficient Landau damping exists in the presence of the transverse damper.

The operation with 25 ns beam (for both LHC and HL-LHC) relies heavily on beam-induced scrubbing: the LHC experience in 2015 and 2016 is thus of paramount importance to quantify how effectively scrubbing can mitigate electron cloud effects. The multipacting thresholds and heat loads have been already estimated and the induced heat loads from the electron cloud are discussed in Section 2.4.3 [160]. The detailed study of the impact of the shielding of the pumping holes (“baffles”) has been performed and the conclusion is that the electrons impacting on the cold bore (without baffle plates) contribute significantly to the multipacting inside the chamber. The resulting additional heat load on the cold bore would be non-negligible and therefore the recommendation was made to include shielding baffles behind the pumping slots in the design of the beam vacuum system for the HL-LHC triplet magnets [161]. The full electron cloud suppression should be possible for the arc dipoles, but it still needs to be confirmed, whereas it seems very unlikely for the quadrupoles. The expected heat load on the beam screen corresponding to that situation is estimated within the cryogenic cooling capacity while the impact on beam quality/stability is being assessed. First results revealed that after the reduction of the SEY through beam-induced scrubbing below 1.3, the electron cloud should not drive the beam unstable but the interplay between the electron cloud induced tune spread and the other sources of tune spreads and impedance/beam-beam effects still needs to be studied in depth. The tune spread due to electron cloud in the quadrupoles is shown in Figure 2-21, for the estimated SEY after scrubbing (SEY close to 1.3, see cross in Figure 2-21 left): an important tune spread of ~ 0.01 is expected, starting from an initial uniform e-cloud distribution. First tests performed with the electron cloud distribution from build-up simulations revealed significant changes with respect to the corresponding cases with uniform initial distribution and therefore, the instability thresholds and tune footprints are being updated with self-consistent distributions [162].

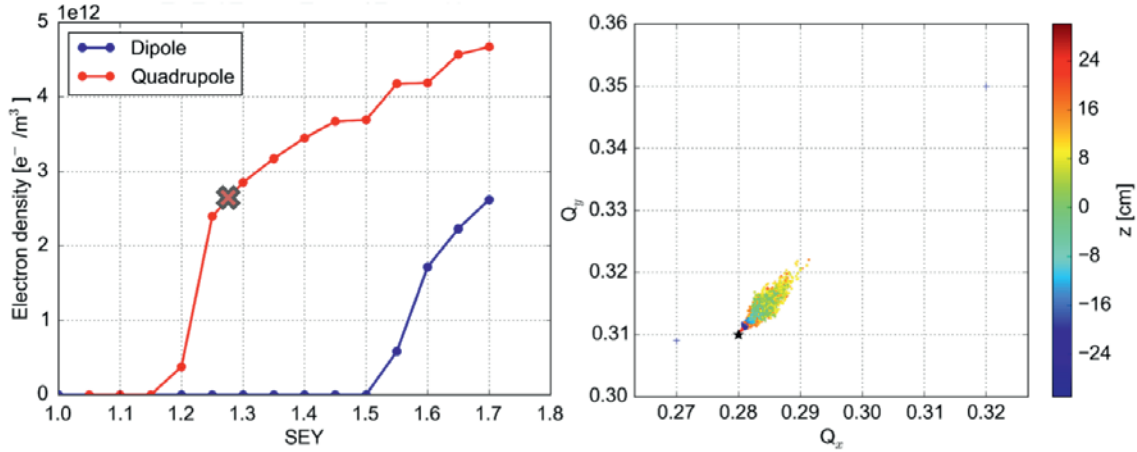


Figure 2-21: (Left) estimated electron cloud density in the dipoles and quadrupoles as a function of SEY and (right) associated tune footprint at the end of the scrubbing (assuming SEY close to 1.3, see cross in the left plot) starting from an initial uniform electron cloud distribution.

As foreseen, electron cloud effects have determined the pace of the intensity ramp-up both from the heat load (see Section 2.4.3) and beam stability point of view [163][164], in particular in 2015 after LS1 when most of the machine beam screens and vacuum chambers were vented to air for interventions. Coherent beam instabilities are observed at injection in the presence of electron cloud. These require to use high values of chromaticity ($Q' \sim +15$ units) in both planes, high transverse damper gain (damping times of ~ 10 turns) and high Landau octupole strength (corresponding to a current of +40 A in the LOF octupoles) with the presently available BCMS beams. These beams have emittances comparable to the nominal HL-LHC beam at injection but half the bunch population [165]. Considering only the effect of the impedance, a few Amps in the Landau octupoles should be enough to stabilize the beam. Simulation studies including electron cloud effects are currently being performed to see if only electron cloud is responsible for this effect or if some interplay between different mechanisms is involved. It is necessary to check first the scaling of the instability properties with bunch population to predict the behaviour of the HL-LHC beams.

A vertical instability (so called “pop-corn instability”) affecting the tail of the 72 bunches trains delivered by the injectors has been observed after a few hours in collision for beams consisting of more than 600 bunches [166]. A mechanism involving electron cloud effects has been proposed to explain this observation [164][167][168] and the simulations have allowed identifying chromaticity as a means to control the instability, as already tested at injection [169]. A detailed analysis of this mechanism is still under study.

In case of issues with transverse instabilities in the future, other remedies exist such as the introduction of a larger transverse tune spread (for Landau damping) using the second order chromaticity (Q'') or an additional RFQ [170], or the suppression of the intra-bunch motion by a wide-band feedback system [171]. In particular, the latter could be of interest in case of instabilities resulting from electron clouds. Note that the last two mitigation methods require new hardware and they are not part of the baseline and they are still in a study phase.

2.4.2 Beam–beam effects

The beam–beam interaction is known to be an important factor limiting the performance reach of present particle colliders. Two of the most significant effects of beam–beam interactions are: i) the induced particle losses due to crossing of excited resonances, enhanced by the large beam-beam tune-spread. These particle losses decrease the beam lifetime, create a high background load for physics experiments, and elevated heat and radiation load on the collimation system; and ii) the degradation of beam quality manifesting itself through the beam size blow-up, most commonly driven by noise effects, that decreases the luminosity delivered to particle physics experiments.

Owing to the broad theoretical and simulation campaign during the design of the LHC collider, the beam–beam effects in the present machine are extensively studied [172]. In addition, the present LHC has surpassed the beam-beam tune-shift thought to be the limit based on experience with past colliders [172]. However, the HL-LHC represents a quantitative as well as a qualitative leap into unknown territory with respect to beam–beam effects. The baseline configuration makes use of some novel concepts that have not been used to their full extent in hadron colliders so far and thus require careful evaluation. The concepts related to beam–beam effects are: i) luminosity levelling by variation of the beta function at the IPs; ii) tilting bunches in the main IPs with the use of RF crab cavities; iii) significantly higher value of the head-on beam–beam tune shift.

Hence, the expected impact of beam–beam interactions on HL-LHC machine performance has been evaluated in order to provide an insight into possible limitations. The studies were mostly performed with the use of the weak–strong approximation (i.e. assume that single particles representing the "weak" beam are affected by the electromagnetic field of the "strong" beam) and employed the SixTrack and Lifetrac codes, which have been successfully used for the design and optimization of past and existing colliders [173][174]. Both codes are capable of calculating the area of stable motion in phase space (the dynamic aperture), and hence a direct comparison of the results is possible. Additionally, the evolution of macroscopic beam parameters including intensity, emittance and luminosity lifetime were simulated with Lifetrac. The performance reach for weak–strong codes is a few million turns, which is equivalent to a few minutes of machine time. Where necessary (i.e. for evaluating coherent effects and the influence of noise), strong–strong simulations with BeamBeam3D, COMBI and a code by K. Ohmi [30,175-187] were carried out.

In the evaluation of the HL-LHC, the criteria used for establishing satisfactory beam dynamics behaviour were similar to those in the LHC design study. In particular, the target value for the one-million turn DA was 6σ (for the nominal HL-LHC emittance of $2.5\ \mu\text{m}$) or more for a particle with relative momentum deviation of 2.7×10^{-4} . The motivation for the choice of such a margin is explained in Ref. [173] and it has been validated with experiments in the LHC [177]. In short, the beam–beam driven diffusion at small amplitudes is quite slow, and the 10^6 turns of tracking typically does not represent the real long-term stability boundary. In the majority of studies, the 6σ DA corresponds to a true stability boundary of about 4σ with the appearance of chaotic motion [173]. The DA limit considerations are currently under scrutiny, based on the observed behaviour of the LHC during Run 1 and Run 2 [188] and in particular the ability to operate with lower crossing angle than the one anticipated. There is finally an effort to complement the calculations of DA with multi-particle simulations of bunch parameters, which are appreciably slower but produce directly measurable quantities [189].

In the baseline HL-LHC scenario (25 ns spacing) presented in the previous version of the Technical Design Report (TDR) [3], bunches begin colliding with 2.2×10^{11} p/b and transverse normalized emittance of $2.5\ \mu\text{m}$. The bunches are tilted by four crab cavities per beam and per side at each of the two main IPs to ensure head-on collisions despite the trajectories crossing at an angle. The luminosity is levelled at the constant value of $5 \times 10^{34}\ \text{cm}^{-2}\ \text{s}^{-1}$ by varying the beta function from $\sim 69\ \text{cm}$ at the beginning of the fill to $15\ \text{cm}$ at the end, in the case of constant crossing angle of $590\ \mu\text{rad}$. Assuming negligible transverse emittance growth, the separation of beams at parasitic crossings thus varies from 26σ at the beginning of the fill to 12.5σ at the end. The levelling process was evaluated from the point of view of beam–beam effects at several stages along the fill for the baseline luminosity of $5 \times 10^{34}\ \text{cm}^{-2}\ \text{s}^{-1}$ as well as the ‘ultimate’ luminosity of $7.5 \times 10^{34}\ \text{cm}^{-2}\ \text{s}^{-1}$. The parameters of these stages are presented in Table 2-12. The simulations for the updated baseline scenario presented in this TDR are ongoing.

Table 2-12: Parameters of simulation cases for evaluation of beam-beam effects during luminosity levelling, for the scheme with four crab cavities (full crabbing).

β^* [cm]	N [10^{11}]	Separation [σ]	Total head-on tune shift
Baseline luminosity $5 \times 10^{34} \text{ cm}^{-2} \text{ s}^{-1}$			
69	2.2	26	0.021
40	1.7	20	0.017
33	1.55	18	0.016
15	1.1	12.5	0.011
10	0.95	10.5	0.009
Ultimate luminosity $7.5 \times 10^{34} \text{ cm}^{-2} \text{ s}^{-1}$			
33	2.0	18	0.02
15	1.35	12.5	0.013
10	1.2	10.5	0.011

For the 4-crab cavities scenario, all simulations were performed with lattice version HLLHCV1.0. Figure 2-22 summarises the minimum DA values attained during the luminosity levelling. Apparently, operation at the constant crossing angle of $590 \mu\text{rad}$ provides substantial margin in terms of minimum DA during the entire levelling process down to $\beta^*=15 \text{ cm}$. This may open several possibilities for improvements: i) increasing the value of levelled luminosity up to the ‘ultimate’ $7.5 \times 10^{34} \text{ cm}^{-2} \text{ s}^{-1}$; ii) reducing the crossing angle down to $450 \mu\text{rad}$ and consequently, the crab cavity voltage; iii) operating at a larger value of chromaticity if so demanded by the coherent beam stability (preliminary evaluation suggests that it can be raised by 2-4 units [190]). The inclusion of multipolar lattice errors does not significantly affect the dynamics [191], as well as the collisions with a finite angle and separation at IP2 and IP8 [190].

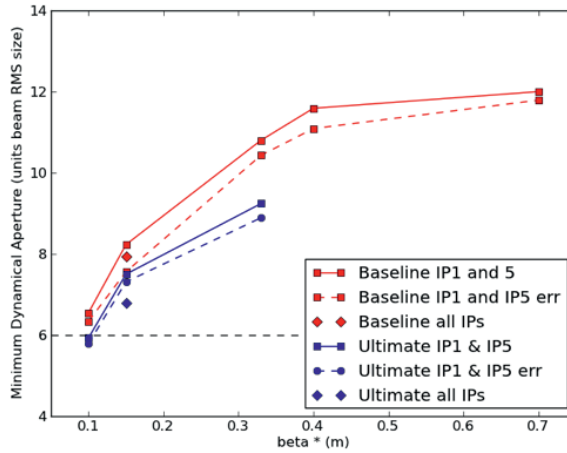


Figure 2-22: Minimum DA during luminosity levelling simulated for the baseline scenario (round optics, constant crossing angle $590 \mu\text{rad}$, full crossing angle compensation by crab cavities) as a function of the beta-function at the IP, simulated with SixTrack beam-beam code. Dashed horizontal line depicts the target minimum DA of 6σ . Solid lines show the results for machine with no multipole errors, dashed lines – with multipole errors. Diamonds indicate the effect of collisions at IP2 and 8 according to the HL-LHC Operational Scenarios described in [136]. The studies were performed with HL-LHC optics V1.0.

For the new baseline proposed in mid-2016 (see Table 2-1), the minimum DA (for HLLHCV1.2 without errors but with all IPs) with $\beta^* = 20 \text{ cm}$ and 1.3×10^{11} particles is still comfortable at around 6.2σ . In that case, the crossing angle is $510 \mu\text{rad}$. This gives confidence that for the new nominal, but also for the ultimate, scenario there is adequate margin, either for reducing the crossing angle or for accommodating the impact of non-linearities, such as multipole errors, high chromaticity and Landau octupoles. A global exploration of the impact to the DA of all the related parameters including possible compensation of the long-range beam-beam

effects for alternative scenarios [192] are under study for refining the various operational scenarios and optimizing the projected HL-LHC performance.

PACMAN effects [183][185][186] have been evaluated and shown not to have a significant impact on DA and luminosity. The PACMAN effects are expected to be strongest at the end of the fill ($\beta^* = 20$ cm), and will be weaker than the nominal LHC case due to a larger normalized long-range beam–beam separation (12.5σ compared to 9.5σ). With an intensity of $N = 1.1 \times 10^{11}$ p/b and a normalized long-range beam–beam separation of 12.5σ one expects a maximum orbit offset at IP1 and IP5 of about 0.3σ and it is only slightly increased (0.4σ) for the new baseline. The long-range variations at IP1 and IP5 result in a very small asymmetry in the tune footprint thanks to the passive compensation of the long-range effects via the alternating crossing [185], and no impact on long-term tracking has been noticed [181].

Beam–beam effects can induce beam emittance growth and related luminosity lifetime degradation via a variety of mechanisms. Weak–strong simulations of multi-particle bunches were used to evaluate the emittance growth due to beam–beam related betatron resonances. The results predict that the luminosity lifetime due to beam–beam effects will be more than 80 h even in the worst case [186][189]. A more significant mechanism of emittance degradation can be related to the interplay between the nonlinearity of the beam–beam interaction and various sources of noise. In particular, the phase errors of crab cavities and the ripple of dipole magnet power supplies lead to fluctuations in normalized long-range beam–beam separation. Strong–strong beam–beam simulations have been carried out for the HL-LHC parameters with a large crossing angle and crab cavity compensation [30][187]. A detailed damper model was included in the simulations. Both β^* levelling and crab cavity levelling were simulated including crab cavity noise and dipole power supply ripple [187]. For white random phase and relative voltage amplitude noise in the crab cavities, simulations suggest that the R.M.S. noise amplitudes should be kept around the level of 10^{-5} rad and 10^{-5} , respectively, in order to maintain a luminosity degradation rate below 1% / hour in the presence of a transverse feedback with a damping time of 20 turns. This tolerance limit might over-estimate the crab cavity phase noise level since the real phase error will have some spectral distribution different from white noise. For the present studies, the spectrum was sampled at a number of frequencies near the betatron frequency. Simulations suggest that strong emittance growth would occur with noise frequencies near the fractional tune of 0.30 and 0.31. The phase errors with those frequencies should be kept as small as possible. The 600 Hz dipole noise was found to have negligible effect on the beam emittance. These studies have to be re-evaluated for the new baseline, although the lower number of cavities is expected to relax the mentioned tolerances.

2.4.3 Beam-induced heat load

The circulating beam can deposit a significant amount of power on the structures exposed to it mainly through three different mechanisms: synchrotron radiation, impedances and electron cloud [129]. The impedance-induced heat loads with the HL-LHC beam parameters [22] for several key systems are summarized in Table 2-13. In the analysis, it is assumed that no forward physics detectors (e.g. ALFA and TOTEM) will be installed during the HL-LHC era.

In the superconducting arcs an important contribution to the heat load on the beam screens is given by synchrotron radiation, which amounts to 0.66 W/m/beam for HL-LHC beam parameters, whereas the longitudinal impedance of the beam screen introduces a further contribution of 0.47 W/m/beam.

Table 2-13: Summary of the impedance-induced heat load computations for several key systems.

Element	Expected heat load [W]	Conclusion/comment
Equipment with RF fingers [193]	Negligible for conforming RF fingers.	Robust mechanical and quality control required during the installation phase.
Experimental beam pipes (resonant modes) [194-199]	ATLAS: none expected. ALICE: potentially* ~ 2 kW. CMS: potentially* ~ 700 W. LHCb: potentially* ~ 500 W.	The temperature of the existing large-diameter regions of the ALICE vacuum chambers (where the HOM are localized) is being monitored to benchmark the simulations and allow extrapolations to the HL-LHC parameters. These did not reveal any issue so far. The design is being followed-up with the experiments to assess the impact of these expected heat loads on hardware integrity and outgassing. Particular attention requires the new VELO design.
Triplet beam screens ([200] and Table 2-14).	See Table 2-14 where the power losses have been computed vs. temperature (between 20 K and 70 K). An option with two welds is also considered. The impact of the carbon coating is negligible.	The effects of the beam screen longitudinal weld, the two counter-rotating beams, and the magneto-resistance have been taken into account. Decoupling of the cryogenics for the IR elements and the RF will provide more margin for acceptable heat load in the arcs.
Triplet beam position monitors [201]	~ 45 W for a stripline of 63 mm diameter (worst case), which would be mostly dissipated through the elements connected to the stripline.	This assumes no interferences between the two beams' electromagnetic fields (worst case) and copper coating.
New collimators with integrated BPMs and ferrites [202]	~100 W (of which ~5 W would be dissipated in the ferrites and 4 W in the RF fingers).	Experience so far has shown no heating issue for these new collimators.
Injection kickers (MKIs) [203][204]	Between ~125 W/m and ~191 W/m (based on measurements of 9 MKIs upgraded to have the full complement of 24 screen conductors and hence averaged over the length of an MKI). For comparison, most of the MKIs before LS1 had an average power deposition of ~ 70 W/m (which did not limit LHC operation). Simulations indicate that the power deposition is highly non-uniform and ~500 W/m are predicted to be deposited in the upstream cell.	Based on simulations and experience, following long physics fills, the upstream ferrites would exceed their Curie temperature (120°C) – by up to 100°C – and would require significant time to cool down. For the HL-LHC, we are looking at: (i) further reducing the power deposition in the upstream ferrite cells; (ii) improving the cooling; (iii) using high Curie temperature ferrites.
Crab cavities [205]	Potentially* multi kW range.	The design should allow detuning the longitudinal modes from multiples of 20 MHz by ~0.5 MHz.
Injection protection dump (TDI) [197]	The devices installed in Run 1 and in 2015 suffered from beam-induced heating (in the kW range for the injection settings) with nominal LHC parameters, due to inefficient cooling and material non-conformity.	The present TDI installed in the 2015-16 YETS with copper-coated graphite absorbers shows much lower beam induced heating. A new absorber (TDIS) is presently being designed for installation in LS2, with a significantly improved cooling efficiency.
Synchrotron radiation monitor (BSRT) [206]	The power deposited in the ferrite absorbers (heated at ~ 250°C to 350°C according to simulations and 2012 measurements) could not be efficiently transferred, leading to damage.	A new design has been installed during LS1 for operation with nominal LHC beams. The validity of this design for HL-LHC is being assessed after Run 2.

*If the longitudinal modes overlap with beam harmonic frequencies.

The remaining contribution from electron cloud effects will depend on the Secondary Electron Yield (SEY) of the beam screen surface that can be achieved through beam induced scrubbing. Figure 2-23 shows the heat load from the electron cloud simulations as a function of the bunch intensity for both an arc dipole and an arc quadrupole, for different SEY values (where the multipacting process is modelled as described in [207]). An SEY of 1.3 is sufficient to suppress the electron cloud in the dipoles, while much lower values are needed for the quadrupoles, hardly achievable by beam induced scrubbing. During Run 2, the LHC is being operated with 25 ns bunch spacing, accumulating a significant electron dose on the beam screen surfaces. Nevertheless, to this date a significant heat load from electron cloud can still be measured on the arc beam screens as shown in Figure 2-24. The figure also shows a significant difference in the conditioning state of the different sectors of the machine, the origin of which is presently not understood.

In the case in which a sufficiently low SEY cannot be achieved, e-cloud effects can be mitigated by using specially conceived filling patterns. The underlying idea is to use the flexibility of the injector complex to build bunch trains with long enough gaps interspersed, to prevent the build-up of electron cloud along the beam. An alternative scenario (referred to as 8b+4e [208]) based on very short trains with 25 ns spacing has been conceived to reduce the electron cloud effects in the HL-LHC and has been considered as part of the HL-LHC operational scenarios [8]. The effectiveness of the 8b+4e scheme for electron cloud suppression has been proven experimentally in the LHC in 2015 [209]. Moreover, operation with a 200 MHz main RF system would allow for significantly longer bunches in the LHC with a significant reduction of the heat load from impedance and electron cloud [155][157][210]. The performance for both these schemes is presented in Section 2.5.

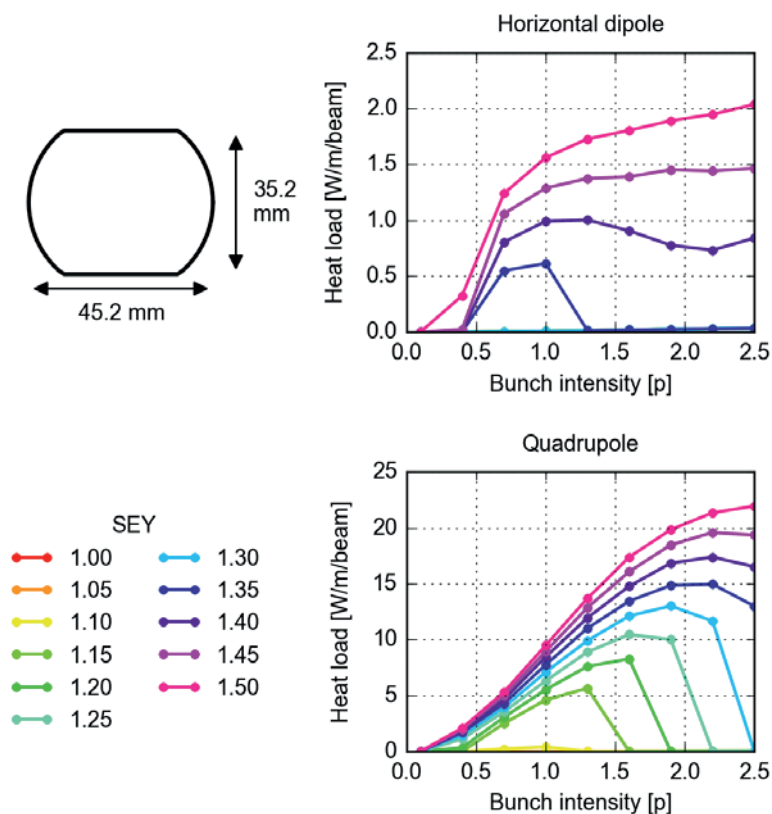


Figure 2-23: Simulated heat load from electron cloud in the arc main magnets as a function of bunch intensity and SEY.

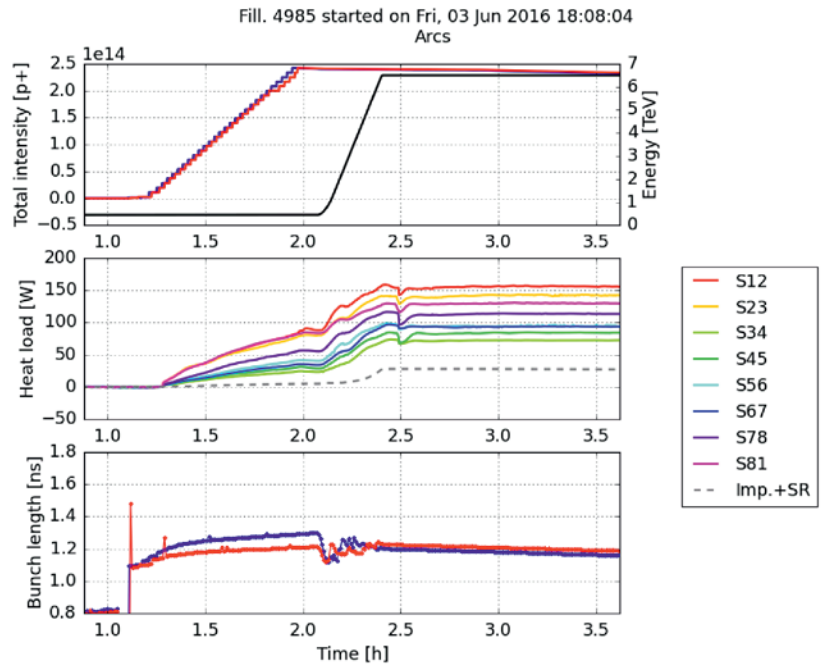


Figure 2-24: Heat load measured in the LHC arcs during a physics fill with beams consisting of 2040 bunches distributed in trains of 72 bunches in 2016. The heat load values are in Watts per half-cell. The dashed line shows the heat load expected from impedance and synchrotron radiation.

In the insertion regions, the synchrotron radiation contribution to the heat load is found to be negligible [211-213] while the impedance contribution is strongly dependent on the beam screen operating temperature as illustrated by Table 2-14.

Figure 2-25 shows the heat load expected from electron cloud along the triplet assemblies at the experimental IPs. It can be noticed that the least efficient multipacting (lower heat load) occurs at the locations of the long-range encounters (vertical dashed lines) and that the heat load values in the D1 dipole are comparable to the values in the quadrupoles. Figure 2-26 shows the total heat load expected per triplet assembly.

Table 2-14: Impedance-induced heat loads for the different types of beam screens (including the effects of the longitudinal weld, two counter-rotating beams, and the magneto-resistance) vs. temperature: values are given for the 25 ns beam.

Power loss [W/m]	20 K	30 K	40 K	50 K	60 K	70 K
Q1 (49 mm, 6.9 T)	0.23	0.24	0.28	0.34	0.40	0.47
Q2-Q3 (59 mm, 8.3 T)	0.19	0.20	0.23	0.28	0.33	0.38
D1 (59 mm, 5.6 T)	0.17	0.19	0.22	0.27	0.32	0.38
D2 (42 mm, 4.5 T)	0.25	0.27	0.32	0.39	0.47	0.54
Q4 (32 mm, 3.7 T)	0.34	0.37	0.44	0.54	0.64	0.74
Q5 (22 mm, 4.4 T)	0.59	0.63	0.72	0.86	1.01	1.16
Q6 (17.7 mm, 3.5 T)	0.79	0.84	0.96	1.14	1.32	1.51
Q7 (17.2 mm, 3.4 T)	0.82	0.87	1.00	1.18	1.37	1.56

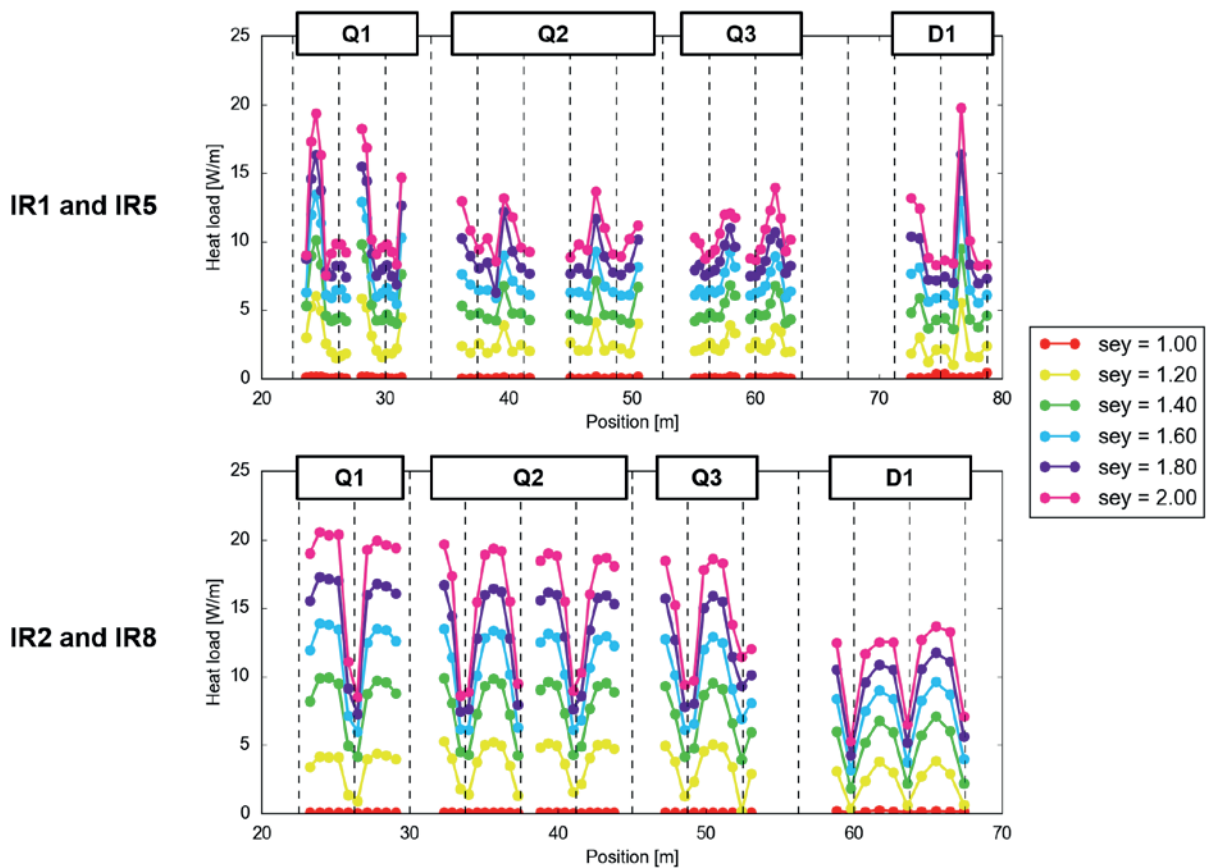


Figure 2-25: Simulated heat load from the electron cloud along the triplet and D1 magnet assemblies with HL-LHC beam parameters. The vertical dashed lines indicate the locations of the long-range encounters.

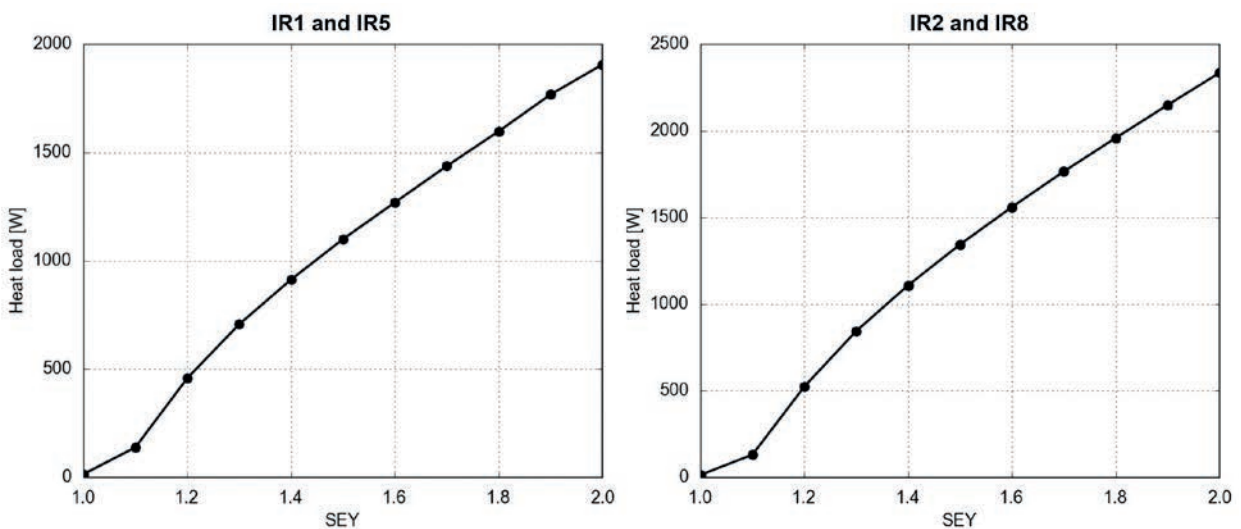


Figure 2-26: Simulated total heat load from the electron cloud for the triplet and D1 magnet assemblies with HL-LHC beam parameters.

Surface treatments (e.g. amorphous carbon coating) are foreseen on the beam screens of the triplet and D1 magnet assemblies for IP1/2/5/8 in order to achieve SEY of 1.1 or lower (these technologies are presently being validated at the COLDEX experiment at the SPS). This condition will lead to heat loads from e-cloud of the order of approximately 150 to 200 W per triplet or lower.

The heating mechanisms for the beam screens of the twin-bore cold magnets have been studied in detail and the estimated heat loads for all the insertion regions are reported in [214]. Figure 2-27 shows the total expected heat load on the beam screens of the twin-bore cold magnets for all the IRs. The red and blue bars show the values obtained assuming SEY=1.3, which could be obtained through beam induced scrubbing, and SEY=1.1, which would be provided by a low SEY treatment of the beam screen surface. The present baseline includes the surface treatment of the beam screens of the elements that will be installed in the matching section of the high luminosity IPs (D2, Q4 and Q5 and associated correctors). The need of coating additional elements in the IP2 and IP8 matching sections (D2, Q4, Q5 and associated correctors) are being assessed taking into account the heat load estimates and the available cryogenics power during the HL-LHC era.

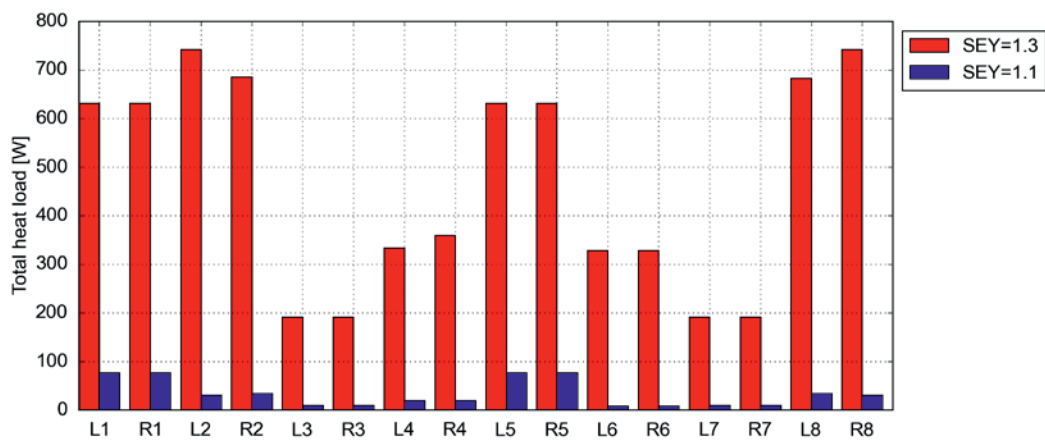


Figure 2-27: Simulated total heat load on the beam screen of the twin-bore cold magnets for all the IRs. Both impedance and e-cloud effects are included.

The above estimates rely strongly on the dependence of the SEY on the electron energy [207] that determines, among others, the scaling of the heat load on the bunch population. The validation of these simulations with measurements at bunch populations close to the nominal HL-LHC one will be carried out after LS2, when these beams will be available from the injectors. This is vital for the validation of the HL-LHC performance [215].

2.4.4 Luminosity performance

The peak performance at 7 TeV has been estimated in Table 2-1. The estimate of the integrated luminosity requires determining the luminosity evolution during a fill. The beam intensity evolution has been evaluated taking into account burn-off due to luminosity considering a total cross-section of 111 mb [5,7,216-218].

The emittance evolution has been determined including: intra-beam scattering (IBS) (based on Run 1 experience, no coupling has been assumed), radiation damping and an additional (unknown) source of vertical emittance blow-up with a lifetime of 40 h (based on observations during Run 1). A finite difference method in steps of 5 min has been implemented to model the intensity evolution and the evolution of the IBS lifetime as a function of the bunch population. Figure 2-28 shows the evolution of the main parameters for the nominal scenario for the standard filling scheme with parameters listed in Table 2-1. As a result of the reduction of the number of crab cavities, the line-density of pile-up events has increased for the nominal HL-LHC levelled luminosity as compared to the scenario presented in [3] and levelling on the pile-up density has to be applied in order not to exceed the maximum value acceptable by the experiments (1.3 events/mm/crossing). This implies a slightly lower levelled luminosity than $5.3 \cdot 10^{34} \text{ cm}^{-2} \text{ s}^{-1}$ in the last hour of the levelling process. The

crossing angle is assumed to be constant during the fill. β^* levelling has been considered as levelling mechanism and it has been applied when the pile-up deviates by more than 2% from the target value [219]. It is also assumed that longitudinal blow-up is applied to keep the longitudinal emittance and bunch length constant throughout the fill.

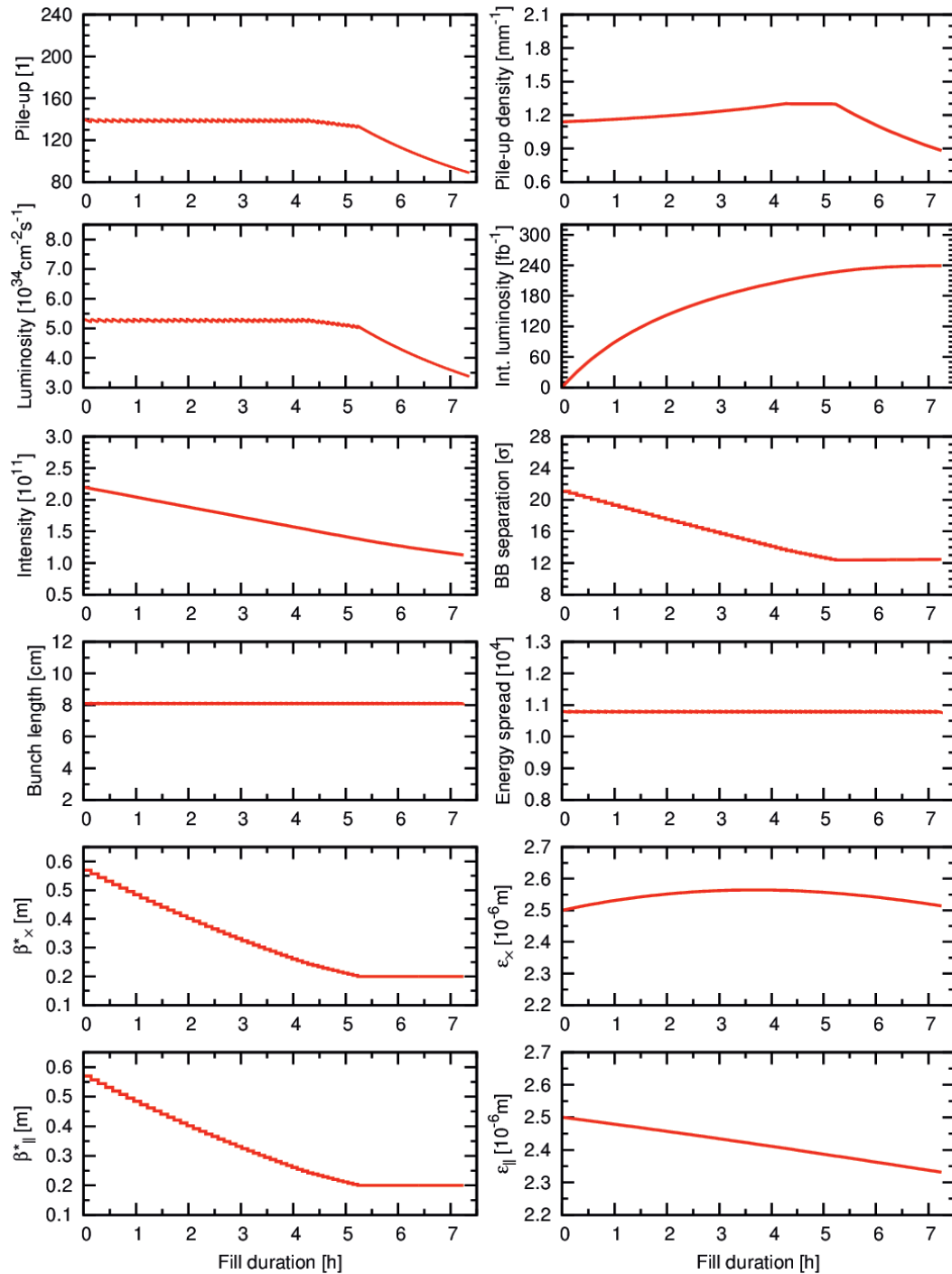


Figure 2-28: Evolution of the main machine and beam parameters the nominal scenario.

Alternative (or complementary) luminosity levelling scenarios include:

- crossing angle variation to increase the geometric reduction factor at the beginning of the fill;

- crab cavity RF voltage variation to have a partial crossing angle compensation at the beginning of the fill;
- dynamic bunch length reduction;
- controlled variation of the transverse separation of the two colliding beams.

The first two options have the disadvantage of increasing the line pile-up density at the start of the fill.

Table 2-15: Integrated performance estimate for the nominal scenario.

Levelling time [h]	Optimum fill length [h]	Integrated Lumi [fb^{-1}/y] for $\eta = 50\%$, optimum fill length IP1/IP5	Maximum mean pile-up density [events/mm/ crossing] in IP1/IP5	Maximum mean pile-up [events/ crossing] in IP1/IP5
5.2	7.2	239	1.3	140

The performance estimates for the nominal scenario is presented in Table 2-15. The parameters used for the estimates of the HL-LHC integrated performance are listed in Table 2-16.

Table 2-16: Parameters assumed for HL-LHC performance estimate.

Scheduled physics time for p–p luminosity production/year (T_{phys}) [days]	160
Minimum turnaround time [h]	3
Performance efficiency – goal [%]	50
Pile-up limit IP1/IP5 [events/crossing]	140/200
Pile-up limit IP8 [events/crossing]	4.5
Pile-up density limit – IP1/IP5 [events/mm/crossing]	1.3
Visible cross-section IP1/IP5 [mb]	81

2.5 Variants and options

The HL-LHC project includes the study of various alternatives to the present baseline configuration with the aim either of improving the potential performance of the machine or of providing options for addressing possible limitations or changes in parameters. These are briefly described in the following sections.

2.5.1 Flat optics

To improve the performance a flat optics might be used with IP β functions of 15 cm and 40 cm (limited by the aperture of the Q4 MQY-type magnet) in the separation and crossing planes, respectively. A crossing angle of 11.9σ could be reached at the end of the fill for bunch populations of 1.1×10^{11} p/bunch as shown in DA studies including beam-beam effects (but only in IP1 and IP5 and in the absence of magnetic errors, with no crab cavities and without working point optimization) [220-222]. The operation at ultimate luminosity might not be possible unless beam-beam long-range compensation schemes are implemented. The performance for this configuration is shown in Figure 2-29 and it approaches the HL-LHC nominal performance in terms of integrated luminosity but with lower peak pile-up density.

2.5.2 8b+4e alternative filling scheme

The 8b+4e filling scheme provides larger bunch charge with about 30% fewer bunches (see Table 2-17) [208]. The 4 empty buckets are expected to highly suppress the formation of the electron cloud [155]. The 8b+4e filling scheme consists of PS trains of 56 bunches with 2.3×10^{11} p/bunch and an emittance of $2.2 \mu\text{m}$. The lower number of bunches of the 8b+4e scheme implies a lower peak luminosity at the same number of pile-up events per crossing μ . The peak pile-up density reaches 1.30 events/mm, the same than the baseline. Thanks to the larger bunch population and lower emittances, the yearly-integrated luminosity is only reduced by about 25% as shown in Figure 2-30.

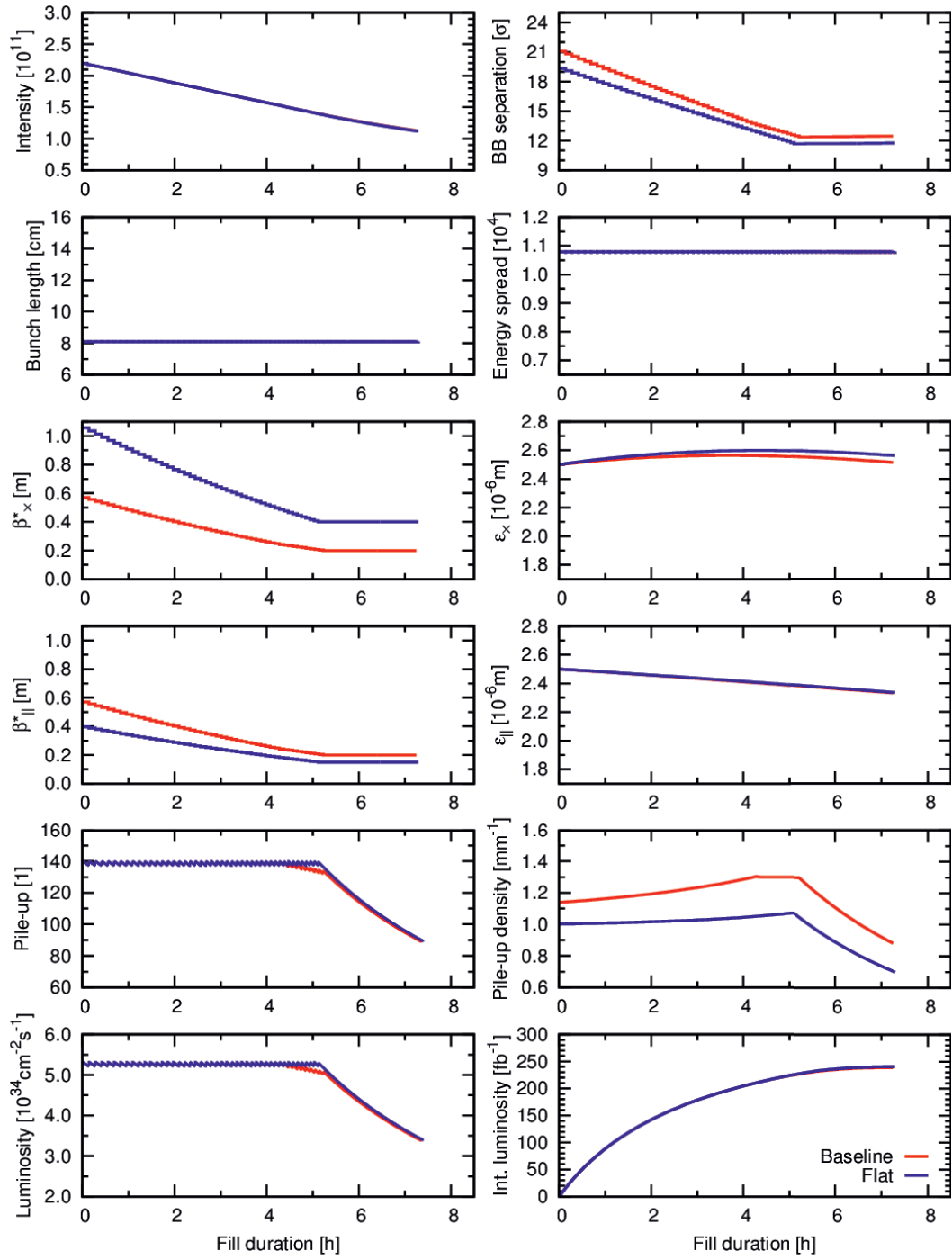


Figure 2-29: Evolution of the main parameters for two scenarios: baseline (round optics) with $\beta^*=20$ cm (red) and flat optics ($\beta^*=40$ cm/15 cm blue) with the crab cavity voltage of 6.8 MV per IP side and per beam.

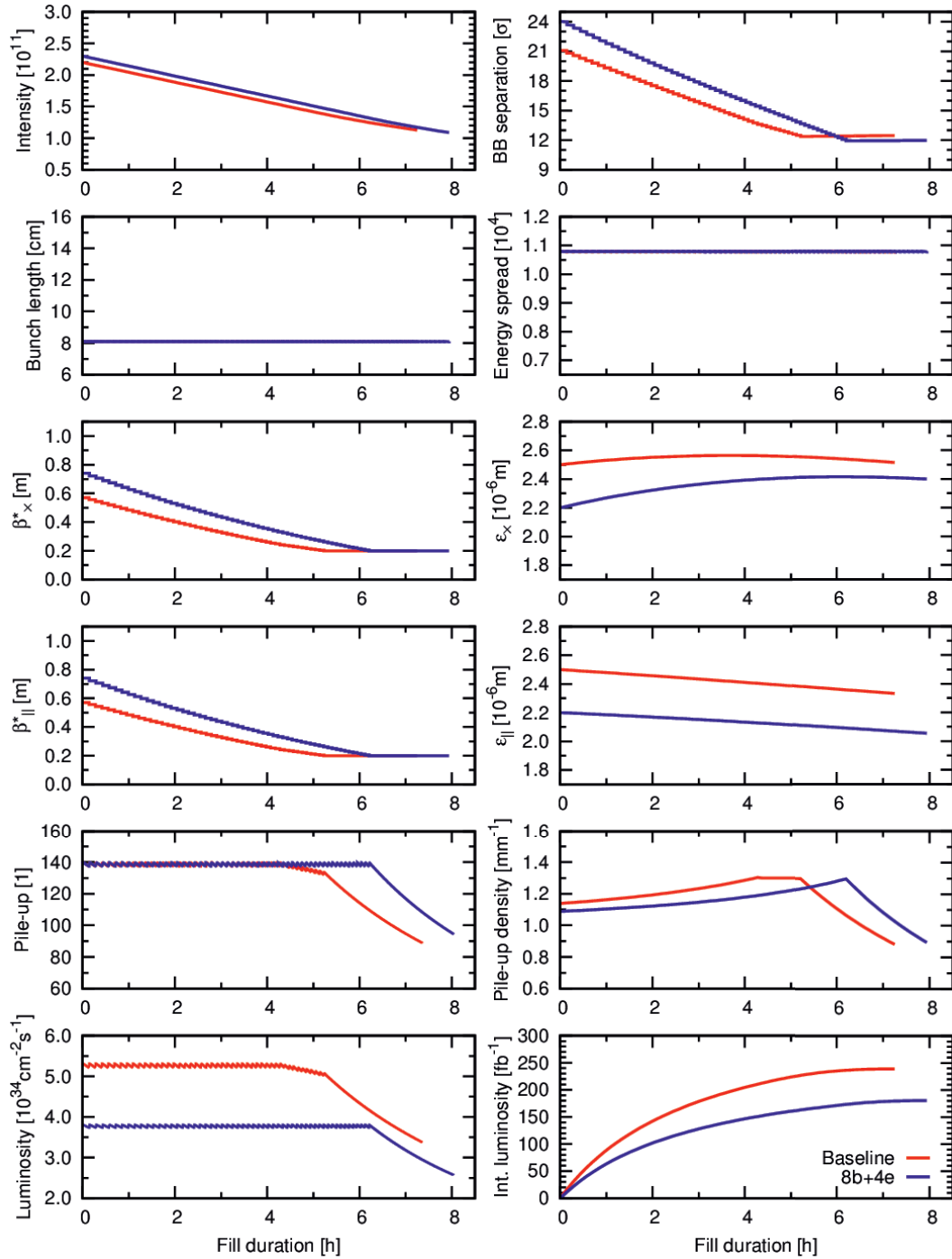


Figure 2-30: Performance comparison of the HL-LHC baseline (red) to the alternative 8b+4e filling scheme (blue). A reduction on the integrated luminosity of about 25% is observed in the 8b+4e scenario.

Table 2-17: Parameters of the HL-LHC baseline scenarios and main alternatives.

Parameter	Baseline		8b+4e	200MHz	No CC	
	Round	Flat			No wire	Wire
Beam energy in collision [TeV]	7	7	7	7	7	7
Particles per bunch, N [10^{11}]	2.2	2.2	2.3	2.2	2.2	2.2
Number of bunches per beam	2748	2748	1968	2748	2748	2748
Number of collisions in IP1 and IP5	2736	2736	1960	2736	2736	2736
N_{tot} [10^{14}]	6.0	6.0	4.5	6.0	6.0	6.0
Beam current [A]	1.10	1.10	0.82	1.10	1.10	1.10
Crossing angle in IP1 and IP5 [μrad]	510	344	480	510	344	281
Norm. long-range beam-beam sep. [σ]	12.5	11.9	12.5	12.5	11.9	9.7
Minimum β_x^* [cm]	20	40	20	20	40	40
Minimum β_y^* [cm]	20	15	20	20	15	15
ϵ_n [μm]	2.5	2.5	2.2	2.5	2.5	2.5
ϵ_L [eVs]	2.5	2.5	2.5	2.5	2.5	2.5
R.M.S. energy spread [0.0001]	1.08	1.08	1.08	1.00	1.08	1.08
R.M.S. bunch length [cm]	8.1	8.1	8.1	15.0	8.1	8.1
IBS horizontal [h]	18.8	17.3	13.6	33.4	17.3	17.3
IBS longitudinal [h]	20.6	21.1	16.9	31.7	21.1	21.1
Piwinski parameter	2.53	1.20	2.5	4.69	1.20	0.98
R_0 w/o crab cavities at min. β^*	0.369	0.623	0.369	0.210	0.623	0.692
R_1 with crab cavities at min. β^*	0.715	0.907	0.740	0.383	N/A	N/A
Beam-beam per IP [10^{-2}]	1.00	1.07	1.23	0.67	0.77	0.86
Peak luminosity w/o CC [$10^{34} \text{cm}^{-2}\text{s}^{-1}$]	6.52	9.00	5.8	3.71	9.00	9.99
Peak luminosity with CC [$10^{35} \text{cm}^{-2}\text{s}^{-1}$]	1.26	1.31	1.16	0.68	N/A	N/A
Pile-up without levelling and CC	172	237	213	98	237	263
Levelled luminosity [$10^{34} \text{cm}^{-2}\text{s}^{-1}$]	5.3	5.3	3.8	5.3	5.3	5.3
Events/xing μ (with levelling and CC)	140	140	140	140	140	140
Peak pile-up density [events/mm]	1.3	1.07	1.3	1.3	1.3	1.3
Levelling time [h]	5.14	5.03	6.2	2.36	4.47	4.22
Integrated luminosity [fb^{-1}]	239	241	181	206	214	225
Number of collisions IP2	2452	2452	1163	2452	2452	2452
Number of collisions IP8	2524	2524	1868	2524	2524	2524
N at injection [10^{11}]	2.3	2.3	2.4	2.3	2.3	2.3
Maximum n. of bunches per injection	288	288	224	288	288	288
N_{tot} per injection [10^{13}]	6.6	6.6	5.4	6.6	6.6	6.6
ϵ_n at SPS extraction [μm]	2	2	1.7	2	2	2

2.5.3 Sub-harmonic RF system 200 MHz

A 200 MHz RF system in the HL-LHC might allow to provide bunches as long as 20 cm. Simulations have shown that this bunch length highly suppresses electron cloud in the dipoles [223]. Figure 2-31 shows that a 15 cm bunch length mitigates the heat load for an SEY of 1.4. Electron cloud is most critical at injection for emittance dilution (due to the lower beam rigidity) and during the energy ramp for the total heat deposition in the beam screens (due to the reduction of the bunch length at the beginning of the ramp and to the increasing number of seed electrons generated by photoemission on the beam screen wall from synchrotron radiation). Once at flattop the bunch length could be optimized to find a balance between electron cloud effects and luminosity production, possibly allowing levelling luminosity with bunch length. 6 MV in the 200 MHz RF

system and 3 MV in the 400 MHz system are required to have 20 cm bunch length along the cycle. Shortening of the bunch length down to 8.1 cm would require a stronger 400 MHz system, closer to the current LHC configuration. It must be noted that operation with longer bunches will imply a different mode of operation of the triplet BPMs that will entail a reduction of their precision.

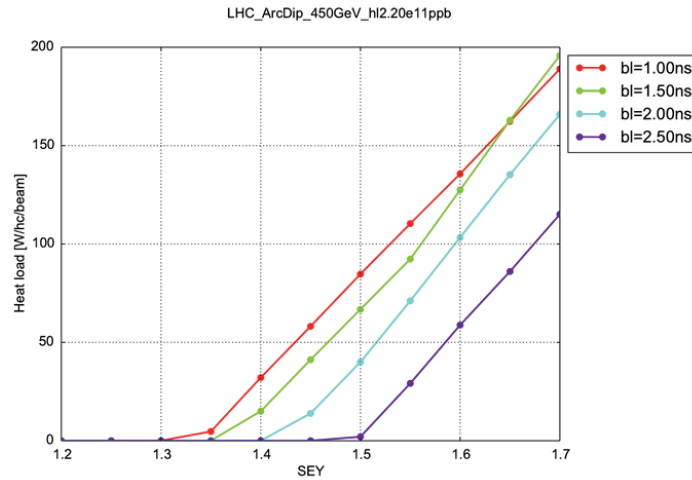


Figure 2-31: Heat load per half-cell and per aperture at injection induced by electron cloud in dipoles versus SEY for 4 different bunch lengths: 7.5, 11.2, 15 and 19 cm (corresponding to a 4σ bunch duration of 1, 1.5, 2 and 2.5 ns). A very low heat load is achieved already for an SEY of 1.4 and a bunch length 15 cm.

Figure 2-32 compares the HL-LHC baseline fill evolution to the 200 MHz alternative assuming 15 cm bunch length and the possibility of reducing the bunch length along the fill. The parameters for the considered scenario can be found in Table 2-17. If electron cloud would not allow for the reduction of bunch length below 15 cm the integrated luminosity would be about 14% lower.

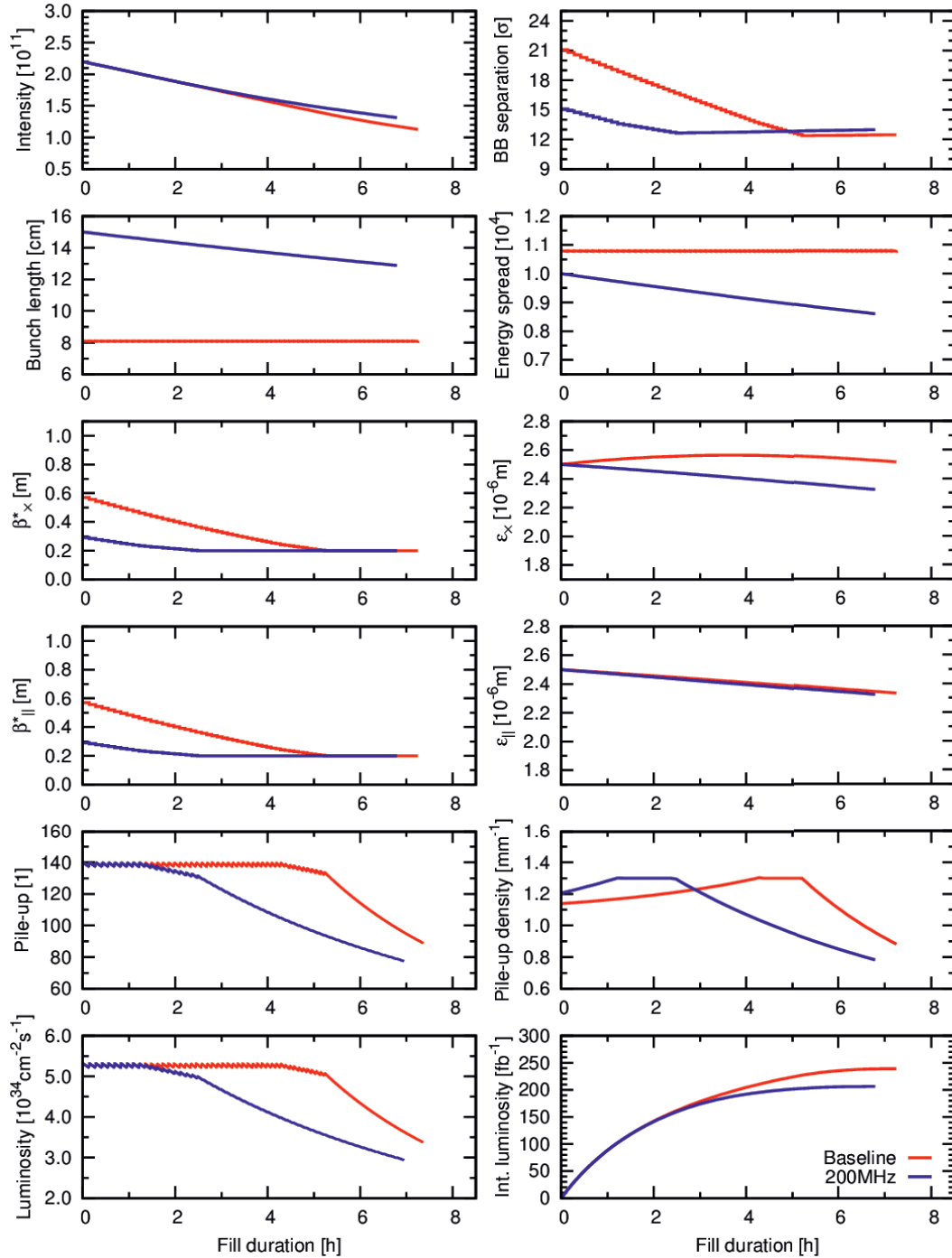


Figure 2-32: Performance comparison of the HL-LHC baseline (red) to the alternative of 200 MHz (blue) in order to suppress the electrons cloud effects. A bunch length of 15 cm is assumed at the start of the fill and then reduced to maximize luminosity.

2.5.4 Flat optics without crab cavities

SPS tests, machine protection issues, crab cavity impedance, or emittance growth due to RF phase noise might eventually suggest that crab cavities cannot be operated in the HL-LHC. In this scenario, it is possible to recover partially the performance loss by resorting to flat optics with larger beam size in the crossing plane at the IP. Current bearing wires or electron beams [224-226] might be installed in order to compensate for the long-range interactions allowing for a reduction of the crossing angle and therefore increasing the luminous

region. The configuration of the wires is still not finalized as these might require to be installed closer to the beam than the tertiary collimators. To make this possible an electron beam wire might be used or a compromise between wire position and settings of the nearby tertiary collimators could be found.

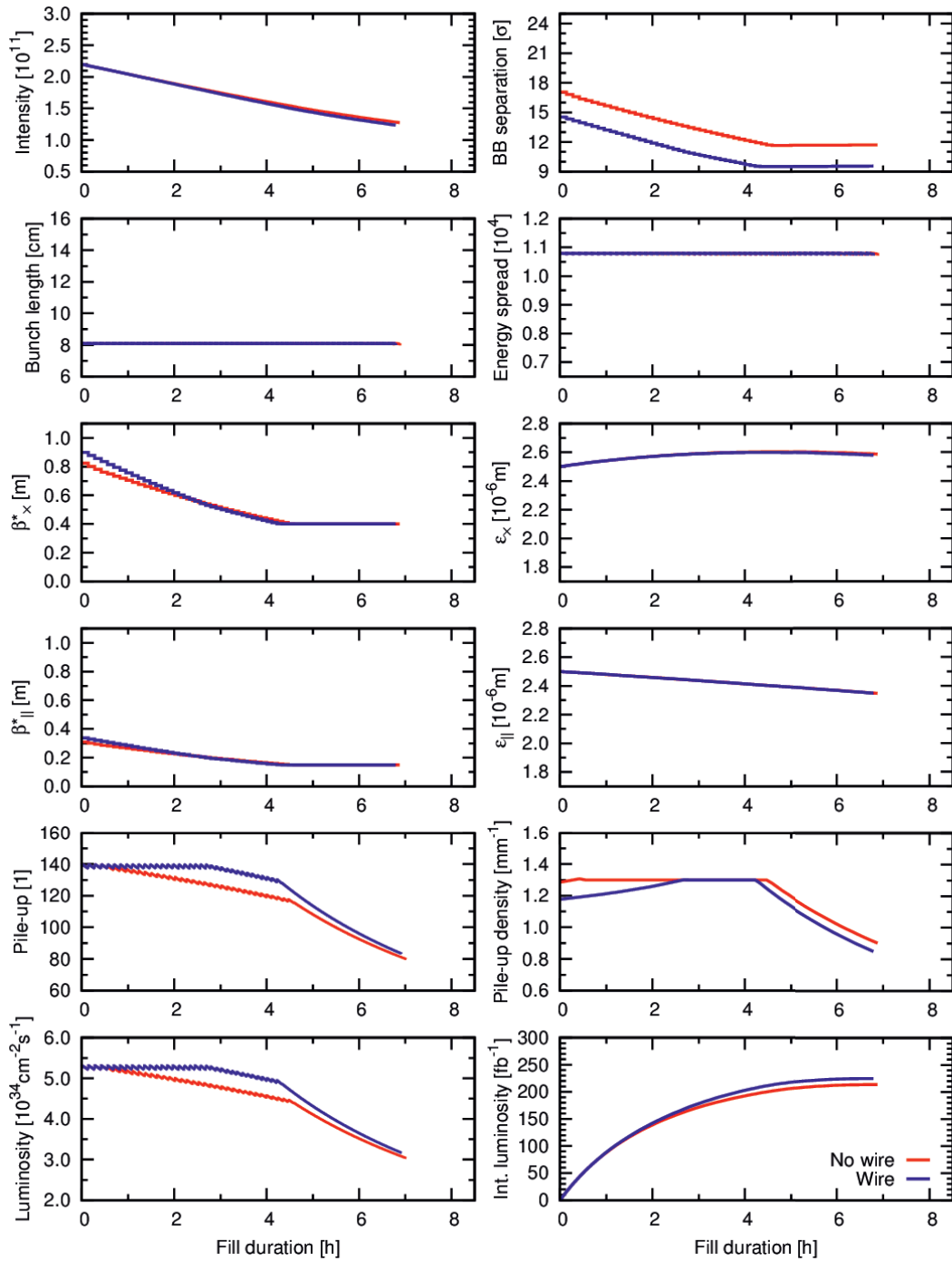


Figure 2-33: Performance comparison of two alternatives without crab cavities using flat optics with beam-beam long-range compensation (blue) and without (red).

Figure 2-33 compares the performance of the two scenarios considered above with and without long-range compensation. The peak pile-up density is limited to 1.3 events/mm. The configuration for the case without wire compensation has been derived from simulations in [220-222] for a crossing angle of 11.9 sigma and flat optics with $\beta^*=40/15$ cm as discussed in Section 2.5.1. For the case using wire compensators

simulations in [226] suggest that a 280 μrad crossing angle provides sufficient DA with $\beta^*=40/15$ cm in the presence of beam-beam effects although only IP1 and IP5 have been considered in the simulations and no magnetic field errors have been assumed.

The absence of crab cavities reduces the baseline performance by about 11%, while the beam-beam long-range compensation allows reducing the crossing angle and it improves the performance (luminosity loss only of 6%, instead of 11%) at constant peak pile-up density. The beam and machine parameters corresponding to these cases can be found in Table 2-17.

2.5.5 80 bunch filling scheme

The number of bunches in the PS trains could be increased from 72 to 80 in order to increase the integrated luminosity without affecting peak pile-up density [227]. In [228] various fillings schemes have been considered offering an increase in integrated luminosity of 2.3% in IP1 and IP5 and of 6.7% in IP8. Further optimizations in IP1 and IP5 result in a large penalty for IP8. The only drawback of the 80 bunch filling scheme is the slightly larger number of bunches at injection (from 288 to 320) to be considered for machine protection matters. Nevertheless, this represents only an 8% increase in transverse beam density.

2.5.6 Pile-up density control

Pile-up density control can be achieved without any extra hardware only slowing down the baseline β^* levelling to ensure a pile-up density below a pre-defined value. Since in the baseline the largest peak pile-up is reached for a short time at the end of the levelling process, it is possible to reduce this largest peak pile-up with little or negligible impact in the integrated luminosity [155][223].

Crab kissing [229] uses flat bunches in the longitudinal plane and additional crab cavities in the separation plane to maximize the luminous region. The flat bunches might be generated with a higher harmonic of the RF system or by introducing an RF phase modulation [230]. Crab kissing requires 4 crab cavities per IP side, per beam and acting in both of the transverse planes.

Control of the pile-up density becomes even more important for the operation at ultimate luminosity with a larger maximum average pile-up of up to 200 events per bunch crossing. The reduction of the pile-up density can be obtained by just slowing the reduction of β^* . In this configuration, an integrated luminosity of 271 fb^{-1} per year could be attained by levelling at a maximum pileup density of 1.74 events/mm. Figure 2-34 summarizes the performance for the scenarios discussed in this Section.

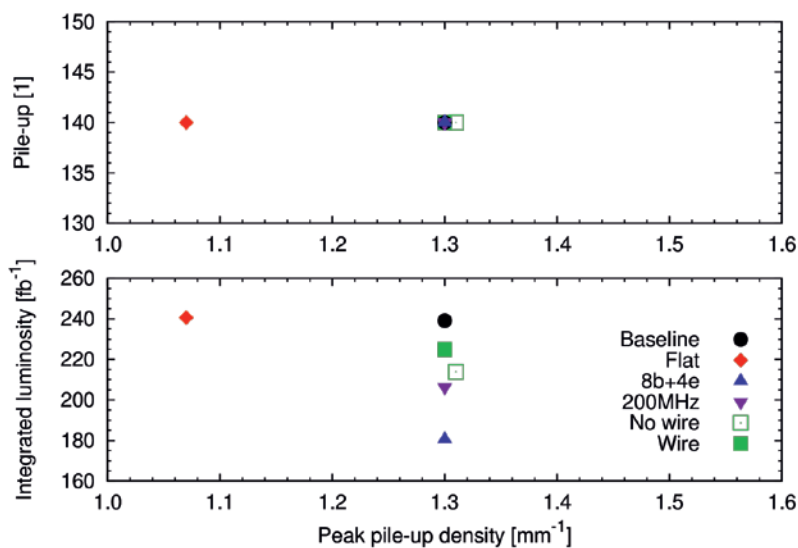


Figure 2-34: Summary chart showing pile-up (top) and integrated luminosity per year (bottom) versus peak pile-up density for the various scenarios considered Section.

2.6 The HL-LHC as a nucleus–nucleus collider

The LHC’s second major physics programme provides nucleus–nucleus (full stripped lead ions $^{208}\text{Pb}^{82+}$) and proton–nucleus collisions to ALICE, ATLAS and CMS. The principal overall goal of the programme is ultimately to accumulate 10 nb^{-1} of Pb–Pb luminosity in the ALICE experiment from LS2 to LS4 [156,231-233] with some heavy-ion runs devoted to p-Pb or reference p-p data taking. The requirements of the other experiments are assumed to be similar. The shorter p-Pb operational period is not considered here but the successful run in this mode in 2013 shows that the luminosity goals are within reach [156, 234-235]. The heavy-ion programme also requires p–p runs at specific energies to provide reference data (see Section 16.5.1) and further special Pb-Pb runs. Nuclei other than $^{208}\text{Pb}^{82+}$ have not been requested by the experiments but they remain as possible options with potential performance to be evaluated.

The heavy-ion luminosity upgrade aims at increasing integrated rather than peak luminosity and is therefore focused mainly on injecting the maximum beam current possible. With the expected upgrade to remove the event rate limit of the ALICE experiment [232], luminosity levelling will no longer be a necessity but may be employed to mitigate the rapid luminosity decay due to the large electromagnetic cross-sections [156][236]. Low values of β^* are required at three interaction points so the ATS optics will not be used. The main elements of the heavy-ion luminosity upgrade should be in place a few years before those of the proton–proton part of the project.

Upgrades to the heavy-ion injector chain [237][238] would normally aim to increase both the number of bunches and the intensity per bunch, but these two quantities are not independent. Injecting long trains from the SPS lengthens the injection plateau in the SPS, subjecting some bunches to higher losses from the effects of intra-beam scattering, space charge, and RF noise [156][239]. On the other hand, injecting a larger number of short trains from the SPS increases the average bunch intensity but leaves more gaps in the LHC bunch train and increases the LHC’s injection time, reducing overall efficiency and subjecting some bunches to more emittance growth at LHC injection. In all cases, there is a broad distribution of bunch parameters in collision in the LHC. Optimization of the injection and filling schemes has to take all these interdependencies into account [239] and will likely have to be done anew each year as a function of injector performance.

The previous performance estimates were based on an injection scheme that assumes that the maximum 12 PS batches of four bunches are assembled into a batch in the SPS, with a 50 ns bunch spacing achieved by slip-stacking. This is repeated 26 times to assemble a train of up to 1248 bunches in the LHC (practical filling scheme details will reduce this by some percent) and yielding a distribution of individual bunch-pair luminosities at the start of colliding beams as shown in Figure 2-35. Simulation of the evolution of these individual bunches, taking into account luminosity burn-off, IBS, and radiation damping [239] leads to the total luminosity shown in Figure 2-36. Depending on the turnaround time (between beam dump and the next declaration of stable beams for physics), the fill length can be optimized to give the ideal average daily luminosity shown.

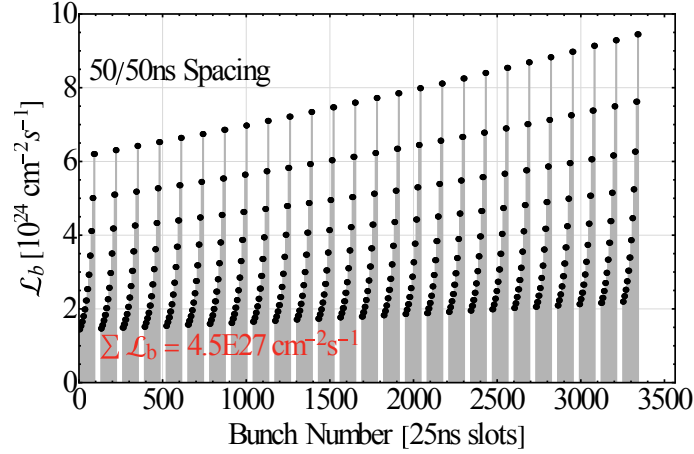


Figure 2-35: Initial luminosity for each colliding bunch pair along the full train in the LHC.

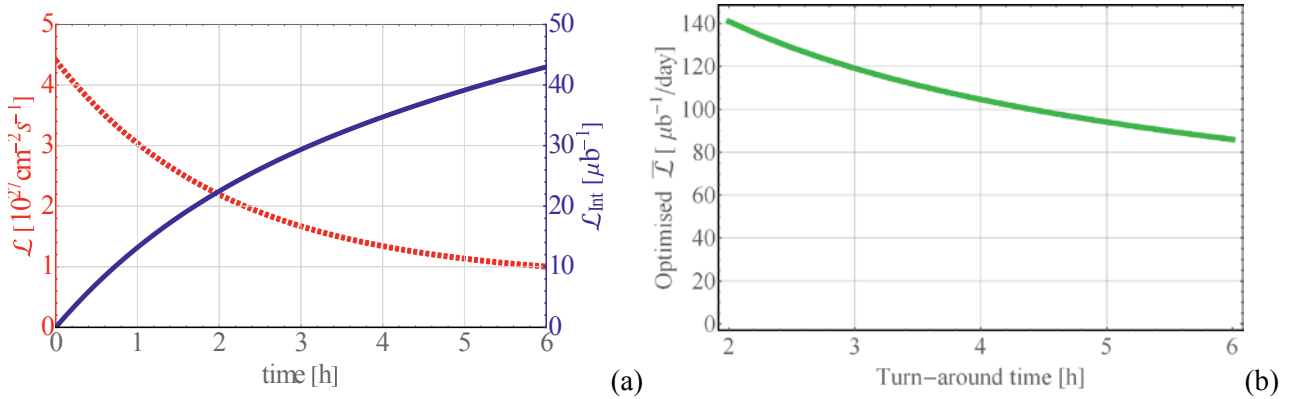


Figure 2-36: (a) Total luminosity (red) and integrated luminosity (blue) during a fill starting with the bunch-pair luminosities shown in Figure 2-35. (b) Average luminosity per day as a function of turnaround time (dump to next stable beams) when fill lengths are optimized, with lengths varying between 3 h and 6 h, with the luminosity dependence shown in the left plot.

The rapid luminosity decay is due to the large cross-sections of electromagnetic processes in the collisions [236][240]. The peak luminosity is expected to be substantially above the quench limit from losses due to the bound-free pair-production process and new collimators (TCLD) are required in the dispersion suppressors around IR2 (see Chapter 5, Section 5.2) in the connection cryostat zone. Intensity limitations may also arise from losses due to collimation inefficiency, which is higher for ion beams, because of the more complicated nuclear interactions with collimators [241][242][241-242]. These losses should be reduced by the installation of TCLD collimators in two 15 m long units (each consisting of two 11T dipoles and a TCLD collimator) replacing two main dipoles on the dispersion suppressors, one on each side of the IR7.

The 50 ns bunch spacing introduces close parasitic beam-beam encounters near to the ALICE experiment, which may require the half-crossing angle to be increased beyond the 60 μrad limit imposed up to Run 2 for optimum operation of the zero-degree calorimeters. Optimisation of the apertures of injection elements in IR2 should allow half-crossing angles up to 100 μrad . The minimum acceptable value at the low Pb bunch charge will be determined empirically [156] or, possibly, from future simulation studies. The crossing angles for ATLAS and CMS are unrestricted and can be taken over from proton operation.

The principal beam parameters determining the luminosity are summarized in Table 2-18. Other parameters will be similar to those given in Ref. [243].

Higher injected intensities would be required to reach the integrated annual luminosity target of 2.85 nb^{-1} requested by the ALICE experiment [232] in a typical one-month Pb-Pb run, assuming an LHC performance efficiency of 50%. The required values have been computed [233] with the simplifying assumption that all

bunches have the same intensity, i.e., the intensity decay along the SPS bunch trains shown in Figure 2-35 has been eliminated. Parameters for this configuration are given in the last column of Table 2-18 and can be regarded as specifying a goal for the injectors.

The estimated performance of the injectors after the baseline upgrade has been recently reviewed [238] and the expected beam parameters at the LHC in collision are listed in the third column of Table 2-18. In the same table the expected beam parameters for an option (not part of the LIU baseline) based on a 25 ns spacing beam are also presented (column 4). The feasibility of operating the LHC with 25 ns and a half crossing angle of 100 μrad must still be investigated.

Table 2-18: Average values of principal beam parameters at the start of physics [233][238].

Parameter	Nominal LHC (design report)	HL-LHC (projected)	HL-LHC (LIU baseline)	HL-LHC (25 ns option)	HL-LHC (required)
Beam energy in collision [TeV]	574	574	574	574	574
Beam energy per nucleon in collision [TeV]	2.76	2.76	2.76	2.76	2.76
Particles per bunch, N [10^7]	7	10.4	15	15	19
Number of bunches per beam	592	1248	1152	1680	1248
Colliding pairs at IP2	592	1100	1000	1500	1100
N_{tot} [10^9]	41.4	121.7	173	252	222.3
Beam current [mA]	6.12	18.0	25.6	37.2	32.8
Minimum β^* [m]	0.5	0.5	0.5	0.5	0.5
ϵ_n [μm]	1.5	1.6	1.6	1.6	1.5
ϵ_L [eVs/charge]	2.50	2.50	2.50	2.50	2.50
RMS energy spread [0.0001]	1.10	1.10	1.10	1.10	1.10
RMS bunch length [cm]	7.94	7.94	7.94	7.94	7.94
IBS horizontal [h]	7.7	4.5	2.8	2.8	2.2
IBS longitudinal [h]	13	7.5	4.7	4.7	3.7
Half-crossing angle at IP2 [μrad]	60	100	100	100	100
Peak luminosity [$10^{27} \text{ cm}^{-2} \text{ s}^{-1}$]	1.00	4.5	4.5	6.8	8
Levelled luminosity [$10^{27} \text{ cm}^{-2} \text{ s}^{-1}$]	-	-	6-7	6-7	6-7
Levelling time [h]	-	-	-	0.6	1
Maximum number of bunches per injection	54	48	48	56	48

The expected integrated luminosity per year estimated for the beam parameters expected after the LIU baseline upgrade for a performance efficiency of 50% is approximately 1.9 nb^{-1} . This could increase to 2.7 nb^{-1} for the 25 ns optional scenario, approaching the annual target of 2.85 nb^{-1} given by ALICE. The expected integrated luminosity depends on the expected performance efficiency: this was 43% for the 2011 Pb-Pb run and 62% for the 2015 Pb-Pb run.

2.7 Acknowledgements

The volunteers of the LHC@home project are warmly acknowledged for their generous contribution of CPU time for the numerical simulations of dynamic aperture.

2.8 References

- [1] R. Jacobsson, Future wishes and constraints from the experiments at the LHC for the proton–proton programme, ICFA Mini-Workshop on Beam-Beam Effects in Hadron Colliders (BB2013), CERN, Geneva, Switzerland, 18 - 22 Mar 2013, Eds. W. Herr and G. Papotti. [CERN-2014-004](#) (2014), pp. 167–176.
- [2] G. Apollinari, I. Bejar Alonso, O. Brüning, M. Lamont, L. Rossi, eds., High Luminosity Large Hadron Collider (HL-LHC): Preliminary Design Report. [CERN-2015-005](#).
- [3] G. Apollinari, I. Bejar Alonso, O. Brüning, M. Lamont, L. Rossi, eds., High Luminosity Large Hadron collider (HL-LHC) Technical Design Report V0, EU Deliverable D1-10, [EDMS 1558149](#).
- [4] O. Brüning, L. Rossi, eds., The High Luminosity Large Hadron Collider: the new machine for illuminating the mysteries of Universe, Advanced Series on Directions in High Energy Physics: [Volume 24](#) (2015), World Scientific.
- [5] The ATLAS and CMS Collaborations, Expected pile-up values at HL-LHC. [ATL-UPGRADE-PUB-2013-014](#), CERN (30 September 2013).
- [6] O.S. Brüning and F. Zimmermann, Parameter space for the LHC High Luminosity Upgrade, Proc. 3rd International Particle Accelerator Conf., New Orleans, 20–25 May 2012, Conf. Proc. C1205201 (2012) pp.[MOPPC005](#).
- [7] D. Contardo, private communication, 3 December 2014.
- [8] G. Arduini, O. Brüning, R. De Maria, R. Garoby, S. Gilardoni, B. Goddard, B. Gorini, M. Meddahi, G. Rumolo and R. Tomás, Beam parameters at LHC injection. [CERN-ACC-2014-0006](#) (2014).
- [9] A. Apollonio, LHC Machine availability, Experiment Data Quality Working Group Meeting held on 30th August 2016, [INDICO 542713](#)
- [10] L. Rossi, Short recap of recent changes to baseline, 16th HL-LHC Parameter and Layout Committee Meeting, 16th July 2015, [EDMS 1567268](#)
- [11] O. Brüning, HL-LHC parameter space and scenarios, Chamonix 2012 Workshop on LHC Performance, Chamonix, France, 6 - 10 Feb 2012, pp.315-324 ([CERN-2012-006](#)) DOI 10.5170/CERN-2012-006.315.
- [12] S. Fartoukh and F. Zimmermann, The HL-LHC accelerator physics challenges, [CERN-ACC-2014-0209](#) (2014) Advanced Series on Directions in High Energy Physics: Volume 24 (2015), World Scientific Chapter 4, pp. 45-96
- [13] V. Kain, C. Bracco, M. Fraser, Y. Kadi, A. Lechner, F. Maciariello, M. Maddahi, A. Mereghetti, G. Steele, F. Velotti Concerns with low emittance beams operation, Proc. Chamonix 2014 Workshop on LHC Performance, Chamonix, France, 22–25 September 2014, Ed. M. Draper, CERN–2015–002, pp. 176-179. DOI: [10.5170/CERN-2015-002.176](#)
- [14] V. Kain et al., Injection protection: are we taking it seriously, how can we make it safer?, Proc. 2nd Evian Workshop on LHC Beam Operation, Evian, France, 7–9 December 2010, Ed. B. Goddard, [CERN-ATS-2011-017](#), pp. [143–149](#).
- [15] E. Métral, Pushing the limits - beam, Proc. Chamonix 2011 Workshop on LHC Performance, Chamonix, France, 24–28 January 2011, Ed. C. Carli, CERN-ATS-2011-005, pp. [252–260](#).
- [16] R.W. Assmann, Implications of higher intensities in the LHC, Proc. Chamonix 2011 Workshop on LHC Performance, Chamonix, France, 25–29 January 2010, Ed. C. Carli, CERN-ATS-2010-026, pp. [328–333](#).
- [17] R. Calaga, R. Tomás and F. Zimmermann, LHC Crab-Cavity Aspects and Strategy, Proc. 1st International Particle Accelerator Conf., Kyoto, Japan, 23–28 May 2010, Eds. A. Noda, C. Petit-Jean-Genaz, V. Schaa, T. Shirai and A. Shirakawa, pp. [1240–1242](#).

- [18] J. Coupard, H. Damerou, A. Funken, R. Garoby, S. Gilardoni, B. Goddard, K. Hanke, A. Lombardi, D. Manglunki, M. Meddahi, B. Mikulec, G. Rumolo, E. Shaposhnikova, M. Vretenar, eds., LHC Injectors Upgrade, Technical Design Report – Volume I: Protons. CERN-ACC-2014-0337 – 15 December 2014.
- [19] M. Meddahi, G. Rumolo, Introductory remarks: LIU baseline and beam parameters through the chain, LHC Performance Workshop (Chamonix 2016), Chamonix, France, 25–28 January 2016, INDICO 448109
- [20] G. Rumolo et al., Session 6: LIU, Summary session of LHC Performance Workshop - Chamonix 2016, CERN, 3 March, 2016, INDICO 486336
- [21] H. Bartosik, T. Argyropoulos, B. Goddard, G. Iadarola, Y. Papaphilippou, G. Rumolo and E. Shaposhnikova, Can we ever reach the HL-LHC requirements with the injectors?, Proc. Review of LHC and Injector Upgrade Plans Workshop, Archamps, 29–31 October 2013, Eds. B. Goddard, F. Zimmermann, CERN-2014-006, pp. 95-104
- [22] HL-LHC Parameter and Layout Committee Parameter table v 6.10 (25/10/2016). https://espace.cern.ch/HiLumi/TCC/_layouts/15/WopiFrame.aspx?sourcedoc=/HiLumi/TCC/SiteAssets/HL_LHC_Parameter_Table.xlsx&action=default
- [23] G. Arduini, “New Performance Reach”, 9th HL-LHC Technical Coordination Committee, 23rd June 2016, INDICO 515632
- [24] HL-LHC/LARP International Review of the Inner Triples Quadrupoles (MQXF) Design, CERN, 10-12 December 2014, INDICO 355818
- [25] The HL-LHC and LIU Cost and Schedule Review, CERN, 9-11 March, 2015, <https://espace.cern.ch/project-HL-LHC-Technical-coordination/CandS/default.aspx>
- [26] Conceptual Design Review of the Magnet Circuits for the HL-LHC , CERN, 21-23 March 2016, INDICO 477759
- [27] L. Rossi, “Outcome of the HL-LHC budget review”, 9th HL-LHC Technical Coordination Committee, 23rd June 2016, INDICO 515632
- [28] C. Garion, “Update on the beam screen/cold bore tolerances and apertures in the triplet area”, 7th HL-LHC Technical Coordination Committee, 28th April 2016, INDICO 515629
- [29] R. Bruce, A. Marsili and S. Redaelli, Cleaning performance with 11 T dipoles and local dispersion suppressor collimation at the LHC, Proc. 5th International Particle Accelerator Conference, Dresden, Germany, 15 - 20 June 2014, Eds. C. Petit-Jean-Genaz, pp.MOPRO042.
- [30] K. Ohmi, Beam-beam effects under the influence of external noise, Proc. ICFA Mini-Workshop on Beam-Beam Effects in Hadron Colliders, CERN, Geneva, Switzerland, 18-22 March 2013, Eds. W. Herr and G. Papotti, CERN-2014-004, pp. 69–74.
- [31] J. Qiang, J. Barranco, T. Pieloni, K. Ohmi, Beam-beam simulation of crab cavity white noise for LHC upgrade, , Proc. 6th International Particle Accelerator Conf., Richmond, VA, USA, 3-8 May 2015, pp.TUPTY076.
- [32] S. Fartoukh, Pile-up density management at HL-LHC and the crab-kissing scheme, HL-LHC brainstorming coordination meeting, July 2013, INDICO 263083
- [33] S. Fartoukh, Optics challenges and solutions for the LHC insertion upgrade phase I, Workshop on LHC Performance, Chamonix, France, 25–29 January 2010, Ed. C. Carli, CERN-sLHC-PROJECT-Report-0038, pp. 262–290.
- [34] S. Fartoukh, Layout and optics solution for the LHC Insertion Upgrade Phase I, 1st International Particle Accelerator Conference, Kyoto, Japan, 23 - 28 May 2010, pp.THPE018 .
- [35] S. Fartoukh, R. Tomás and J. Miles, Specification of the closed orbit corrector magnets for the new LHC inner triplet. CERN-sLHC-PROJECT-Report-0030 (2009).

- [36] S. Fartoukh, Towards the LHC Upgrade using the LHC well-characterized technology. [CERN-sLHC-PROJECT-Report-0049](#) (2010).
- [37] S. Fartoukh, Breaching the phase I Optics Limitations for the HL-LHC. [CERN-sLHC-PROJECT-Report-0053](#) (2011).
- [38] S. Fartoukh, An achromatic telescopic squeezing (ATS) scheme for the LHC upgrade, Proc. [2nd International Particle Accelerator Conference](#), San Sebastian, Spain, 4 - 9 Sep 2011, pp.[WEPC037](#).
- [39] S. Fartoukh, B. Goddard, W. Höfle, M. Lamont, R. de Maria, R. Miyamoto, G. Müller, L. Ponce, S. Redaelli, R. Steinhausen, M. Strzelczyk, R. Tomás, G. Vanbavinckhove and J. Wenninger, The achromatic telescopic squeezing scheme: Basic principles and first demonstration at the LHC, Proc. [3rd International Particle Accelerator Conference 2012](#), New Orleans, LA, USA, 20 - 25 May 2012, pp.[TUPPR068](#).
- [40] S. Fartoukh, Achromatic telescopic squeezing scheme and application to the LHC and its luminosity upgrade, *Phys. Rev. Spec. Top. Accel. Beams* 16 (2013) 111002. [DOI: 10.1103/PhysRevSTAB.16.111002](#)
- [41] S. Fartoukh, G. Vanbavinckhove, M. C. Alabau Pons, R. Alemany Fernandez, R. Assmann, A. Butterworth, M. Giovannozzi, B. Goddard, P. Hagen, W. Höfle, D. Jacquet, R. de Maria, R. Miyamoto, G. Müller, S. Redaelli, R. Steinhausen, M. Strzelczyk, R. Suykerbuyk, E. Todesco, R. Tomás, W. Venturini, J. Wenninger and F. Zimmermann, The achromatic telescopic squeezing (ATS) MD part I, [CERN-ATS-Note-2011-033 MD](#) (2011) 17 p.
- [42] S. Fartoukh, M. Lamont, R. De Maria, R. Miyamoto, G. Müller, L. Ponce, S. Redaelli, M. Strzelczyk, R. Tomás, G. Vanbavinckhove, J. Wenninger, M. Albert, R. Giachino, M. Giovannozzi, B. Goddard, P. Hagen, W. Höfle, V. Kain, A. Macpherson, L. Normann, G. Papotti, R. Steinhausen, D. Valuch and D. Wollman, The achromatic telescopic squeezing (ATS) MD part II, [CERN-ATS-Note-2011-060 MD](#) (2011) 26p.
- [43] S. Fartoukh, R. Tomás, B. Goddard, W. Höfle, D. Jacquet, G. Kruk, M. Lamont, R. de Maria, R. Miyamoto, G. Müller, M. Pojer, L. Ponce, S. Redaelli, N. Ryckx, R. Steinhausen, M. Strzelczyk, G. Vanbavinckhove and J. Wenninger, The achromatic telescopic squeezing (ATS) MD part III, [CERN-ATS-Note-2011-132 MD](#) (2011) 8p.
- [44] S. Fartoukh, V. Kain, Y. Levinsen, E. Maclean, R. de Maria, T. Person, M. Pojer, L. Ponce, P. Skowronski, M. Solfaroli, R. Tomás and J. Wenninger, The 10 cm beta* ATS MD. [CERN-ATS-Note-2013-004 MD](#) (2013).
- [45] S. Fartoukh, First demonstration with beam of the Achromatic Telescopic Squeezing (ATS) scheme, Proc. [Chamonix 2012 Workshop on LHC Performance](#), Chamonix, France, 6 - 10 Feb 2012, pp.128-134 (CERN-2012-006) DOI: [10.5170/CERN-2012-006.128](#).
- [46] E. Todesco, H. Allain, G. Ambrosio, G. Arduini, F. Cerutti, R. De Maria, L. Esposito, S. Fartoukh, P. Ferracin and H. Felice et al., A first baseline for the magnets in the High Luminosity LHC insertion regions, [CERN-ACC-2014-0036](#) (2014) [23rd International Conference on Magnet Technology](#), Boston, MA, USA, 14 - 19 Jul 2013, pp.4003305.
- [47] S. Fartoukh and R. De Maria, Database of baseline scenarios and variants: Milestone: MS17. [CERN-ACC-2014-0069](#) (2014).
- [48] S. Fartoukh and R. De Maria, Optics and layout solutions for HL-LHC with large aperture Nb₃Sn and Nb-Ti inner triplets, Proc. 3rd International Particle Accelerator Conference 2012, New Orleans, LA, USA, 20 - 25 May 2012, , *Conf. Proc.* C1205201 (2012) pp.[MOPPC011](#)
- [49] R. De Maria, S. Fartoukh, A. Bogomyagkov and M. Korostelev, HLLHCV1.0: HL-LHC layout and optics models for 150 mm Nb₃Sn Triplets and local crab-cavities, Proc. 4th International Particle Accelerator Conference, Shanghai, China, 12 - 17 May 2013, pp.1358-1360. [CERN-ACC-2013-0129](#).

- [50] R. De Maria, S.D. Fartoukh, M. Fitterer, HLLHC V1.1 Optics Version for the HL-LHC Upgrade, Proc. 6th International Particle Accelerator Conference, Richmond, VA, USA, 3 - 8 May 2015, , pp. 2090-2092. [CERN-ACC-2015-0175](#)
- [51] R. De Maria, M. Fitterer, Optics and Layout V1.2, 53rd WP2 Task Leader meeting, 24 July 2015, [INDICO 394926](#)
- [52] B. Vazquez, I. Zurbano, P. Fessia, H. Prin, Drawing HL-LHC LONG STRAIGHT SECTIONS - RIGHT OF POINT 5, [EDMS 1395366](#)
- [53] R. De Maria, Layout and optics update, 76th HiLumi WP2 Task Leader Meeting, 2nd September 2016, [INDICO 556766](#)
- [54] R. Calaga, R. De Maria et al., 9th HL-LHC PLC meeting Crab cavity integration in the layout (longitudinal space requirements) with the new baseline of 4 cavities per beam and side of the IP (2014) [INDICO 315418](#)
- [55] M. Giovannozzi et al., Optics and layout update, 3rd Joint HiLumi LHC– 22nd LARP Collaboration Meeting, 7–8 May 2014, BNL, USA, <https://indico.bnl.gov/conferenceDisplay.py?confId=730>
- [56] M. Fitterer, S. Fartoukh, M. Giovannozzi and R. De Maria, Crossing scheme and orbit correction in IR1/5 for HL-LHC, [6th International Particle Accelerator Conference](#), Richmond, VA, USA, 3 - 8 May 2015, pp.TUPTY036. [CERN-ACC-2015-0014](#).
- [57] L. Esposito, F. Cerutti, Energy deposition for HL-LHC v1.1: TAN/D2/Q4, Joint HiLumi LHC-LARP Annual Meeting, Tsukuba, Japan, 17 – 21 November, 2014, [INDICO 326148](#)
- [58] P. Fessia, C. Garion. T. Lefevre, Interconnection length for triplet magnets, 13th HL-LHC Parameter and Layout Committee Meeting, 22 January 2015, [INDICO 364435](#)
- [59] I. Efthymiopoulos et al., WP8 bi-weekly meetings, 2015, [INDICO 5646](#) /
- [60] R. De Maria, T. Lefevre, Specification BPM blind area, 61st HiLumi WP2 Task Leader Meeting, 27th November 2015, [INDICO 402184](#)
- [61] B. Vazquez, D. Duarte, E. Todesco, H. Prin, P. Ferracin, Discussion about the possibility of moving the BPM in Q1-Q2A towards the IP, HL-LHC Integration Meeting, 24/6/2016, [INDICO 502018](#)
- [62] M. Giovannozzi, “Operating temperature for Q6 in IR1&IR5”, 4th HL-LHC Technical Coordination Committee, 10th March 2016, [INDICO 476960](#)
- [63] E. Todesco, “ECR: Magnet temperatures in matching section”, 7th HL-LHC Technical Coordination Committee, 28th April 2016, [INDICO 515629](#)
- [64] P. Fessia, "Comparison in terms of cost and planning between 1.9 K and 4.5 K options for Q5 in Pt6”, 2nd HL-LHC Technical Coordination Committee, 11th February 2016 [INDICO 476957](#) and [minutes of the meeting](#).
- [65] M. Giovannozzi, S. Fartoukh and R. De Maria, Specification of a system of correctors for the triplets and separation dipoles of the LHC upgrade, Proc. 4th International Particle Accelerator Conference, Shanghai, China, 12 - 17 May 2013, pp. 2612-2614. [CERN-ACC-2013-0168](#)
- [66] M. Giovannozzi, S. Fartoukh and R. De Maria, Initial models of correction systems. [CERN-ACC-2014-0010](#) (2014).
- [67] R. Bruce, R. De Maria, S. Fartoukh, M. Giovannozzi, S. Redaelli, R. Tomás, J. Wenninger, Parameters for HL-LHC aperture calculations and comparison with aperture measurements. [CERN-ACC-2014-0044](#).
- [68] M. Fitterer, Budget for HL-LHC Orbit Correctors, HSS meeting 14 April 2014. http://ab-dep-abp.web.cern.ch/ab-dep-abp/HSS/HSS_meetings/2014/20140414/HSSMeeting14042014.pdf
- [69] M. Fitterer and R. De Maria, IT BPM tolerances for HL-LHC orbit correction, HSS meeting 26 May 2014. http://ab-dep-abp.web.cern.ch/ab-dep-abp/HSS/HSS_meetings/2014/20140526/HSSMeeting26052014.pdf

- [70] R. Calaga, M. Fitterer, “Crab cavity beam base alignment needs”, 51st HiLumi WP2 Task Leader Meeting, 19th June 2015, [INDICO 394922](#)
- [71] P. Fessia, C. Magnier, R. De Maria, H. Prin, Additional Q5 in IR6 (status of cold-mass and integration study), 15th HL-LHC Parameter and Layout Committee Meeting, 4 June 2015, [INDICO 396467](#)
- [72] C. Garion, R. Kersevan, N. Kos, Preliminary Design of the HiLumi-LHC Triplet Area Beam Screen, [5th International Particle Accelerator Conference](#), Dresden, Germany, 15 - 20 Jun 2014, pp.2378. [CERN-ACC-2014-0268](#).
- [73] R. Bruce, Aperture in case of an asynchronous beam dump with ATS optics, 5th Joint HiLumi LHC-LARP Annual Meeting 2015, CERN, 26-30 October 2015, [INDICO 400665](#)
- [74] R. De Maria, “Review on aperture (N1 + mechanical) between D1 and Q6 in HLLHC IR1/5”, 67th ColUSM Meeting (5/02/2016), [INDICO 493012](#) .
- [75] R. Bruce, LHC machine configuration in the 2016 proton run, LHC Performance Workshop (Chamonix 2016), Chamonix, France, 25–28 January 2016, [INDICO 448109](#)
- [76] R. Bruce, R. De Maria, M. Giovannozzi, P. Hagen, S. Redaelli, M. Solfaroli Camillocci, E. Todesco, R. Tomas, J. Wenninger, Validation of new optics with favourable phase advance, 254th LHC Machine Committee Meeting, 16th March 2016, https://espace.cern.ch/lhc-machine-committee/_layouts/15/WopiFrame.aspx?sourcedoc=/lhc-machine-committee/Presentations/1/lmc_254/LMC_20160316_Optics_Validation_giovannozzi.pptx&action=default
- [77] S. Fartoukh, Asynchronous free ATS optics for LHC & HL-LHC, 61st HiLumi WP2 Task Leader Meeting, 27 November 2015, [INDICO 402184](#)
- [78] O. S. Brüning, P. Collier, P. Lebrun, S. Myers, R. Ostojic, J. Poole and P. Proudlock (Eds.), LHC Design Report, v.1: The LHC Main Ring. [CERN-2004-003-V-1](#) (2012).
- [79] V. Baglin, N. Kos, Beam screens for the LHC long straight section, LHC-VSS-ES-0002 Rev. 1.3, [EDMS 334961](#), CERN.
- [80] J.-B. Jeanneret, Geometrical tolerances for the qualification of LHC magnets, [LHC Project Report 1007](#) (2007).
- [81] R. De Maria, Parametric study of optics options for the HL-LHC project, Proc. 3rd International Particle Accelerator Conference 2012, New Orleans, LA, USA, 20 - 25 May 2012, pp.142-144. [CERN-ATS-2012-137](#)
- [82] B.J. Holzer, R. De Maria, S. Fartoukh, A. Chancé, B. Dalena, J. Payet, A. Bogomyagkov, R. B. Appleby, S. Kelly, M. B. Thomas, L. Thompson, M. Korostelev, K. M. Hock, A. Wolski, C. Milardi, A. Faus-Golfe and J. Resta Lopez, Optics design and lattice optimisation for the HL-LHC Proc. 4th International Particle Accelerator Conference, Shanghai, China, 12 - 17 May 2013, pp. 1385-1387. [CERN-ACC-2013-0134](#)
- [83] B. Dalena, J. Payet and A. Chancé, R. De Maria, S. Fartoukh, High Luminosity LHC matching section layout vs crab cavity voltage, Proc. 4th International Particle Accelerator Conference, Shanghai, China, 12 - 17 May 2013, pp. 1328-1330. [CERN-ACC-2013-0126](#)
- [84] M. Fitterer, R. Bruce, R. De Maria and S. Fartoukh, Optics Considerations for PIC and US1 scenarios for HL-LHC in the framework of the RLIUP review. [CERN-ACC-NOTE-2014-0031](#) (2014).
- [85] B. Dalena, J. Payet, A. Chancé and R. De Maria, Alternative high luminosity LHC matching section layout, Proc. 5th International Particle Accelerator Conference, Dresden, Germany, 15 - 20 June 2014, pp. 990-992. [CERN-ACC-2014-0174](#)

- [86] M. Korostelev, A. Wolski, R. De Maria and S. Fartoukh, Optics Transition between Injection and Collision Optics for the HL-LHC Upgrade Project, Proc. 4th International Particle Accelerator Conference, Shanghai, China, 12 - 17 May 2013, pp. 1460-1462. [CERN-ACC-2013-0127](#)
- [87] M. Korostelev, Transition between injection optics and collision optics (including ATS squeeze), 3rd Joint HiLumi LHC-LARP Annual Meeting, 11–15 November 2013, [INDICO 257368](#)
- [88] M. Fitterer, IR6 Squeeze update, 57th WP2 meeting, 9/10/2015, [INDICO 402177](#)
- [89] Q. King, M. Giovannozzi, Analysis of time required for pre-squeeze, squeeze, and ramp down, WP2 Task 2.2 meeting, 19 February 2015, [INDICO 369635](#)
- [90] G. Arduini, A. Ballarino, J-P. Burnet, R. De Maria, S. Fartoukh, M. Fitterer, M. Giovannozzi, E. Todesco, Powering aspects for discussion, WP2 Task 2.2 Meeting, 29 April 2015, [INDICO 342270](#)
- [91] J. P. Burnet, Power converters for HL-LHC insertion region magnets considerations for alternative powering schemes, 22nd HL-LHC Technical Committee, 30 April 2015, [INDICO 373541](#)
- [92] M. Fitterer, S. Fartoukh, M. Giovannozzi and R. De Maria, Beam Dynamics Requirements for the Powering Scheme of the HL-LHC Triplet, Proc. 6th International Particle Accelerator Conference, Richmond, USA, 3 - 8 May 2015, pp. 2082-2084. [CERN-ACC-2015-0174](#)
- [93] M. Fitterer, S. Fartoukh, M. Giovannozzi and R. De Maria, Powering Schemes for Triplet and Matching Sections, 4th Joint HiLumi LHC-LARP Annual Meeting, Tsukuba, Japan, 17 – 21 November 2014, [INDICO 326148](#)
- [94] M. Fitterer, S. Fartoukh, M. Giovannozzi and R. De Maria, Powering Schemes for Inner Triplet, Q4 and D1/D2, HL-LHC Technical Committee, 16 April 2015, [INDICO 373539](#)
- [95] M. Fitterer, M. Giovannozzi and R. De Maria, Follow up of powering schemes for IT, Q4 and D1/D2, HL-LHC Technical Committee, 30 April 2015, [INDICO 373541](#)
- [96] J.-P. Burnet, private communication (2015).
- [97] M. Cerqueira Bastos, private communication (2015).
- [98] M. Cerqueira, Power converter noise, 66th WP2 Meeting, 19/4/2016, [INDICO 463032](#)
- [99] R. Calaga, R. Miyamoto, R. Tomás and G. Vanbavinckhove, Beta* Measurement in the LHC Based on K-modulation. [CERN-ATS-2011-149](#).
- [100] J. Coello de Portugal, F. Carlier, A. Garcia-Tabares, A. Langner, E.H.Maclean, L. Malina, T. Persson, P. Skowronski, R. Tomás, Local Optics Corrections in the HL-LHC IR, Proc. 7th International Particle Accelerator Conference 2016, Busan, South Korea, 8-13 May 2016, , pp. 3480-3482 and references therein. [CERN-ACC-2016-176](#)
- [101] J. Coello de Portugal, Optics correction update, 73rd HiLumi WP2 Task Leader Meeting, 9th August 2016, [INDICO 544551](#)
- [102] R. De Maria, Update of the requirements on circuits parameters from beam physics (current, acceleration and ramp rates, ripple and stability), 26th LARP Hi-Lumi Collaboration Meeting, 18-21 May 2016, SLAC, USA, <https://indico.fnal.gov/getFile.py/access?contribId=55&sessionId=5&resId=0&materialId=slides&confId=11049>
- [103] C. Tambasco, Specification of separation collapsing speed, 67th HiLumi WP2 Task Leader Meeting, 26th April 2016, [INDICO 512381](#)
- [104] M. Giovannozzi et al., LHC@Home: A Volunteer computing system for Massive Numerical Simulations of Beam Dynamics and High Energy Physics Events, Proc. 3rd International Particle Accelerator Conference 2012, New Orleans, LA, USA, 20 - 25 May 2012, , pp. 505-507. [CERN-ATS-2012-159](#)

- [105] S. Fartoukh and M. Giovannozzi, Dynamic aperture computation for the as-built CERN Large Hadron Collider and impact of main dipoles sorting, Nucl. Instrum. Methods Phys. Res., A 671 (2012) 10–23. [CERN-ATS-2012-001](#)
- [106] F. Schmidt, SixTrack – Version 4.2.16 – Single particle tracking code treating transverse motion with synchrotron oscillations in a symplectic manner – Users’ reference manual. [CERN-SL-94-56](#) update (2012).
- [107] SixTrack web site <http://sixtrack-ng.web.cern.ch/sixtrack-ng/>
- [108] <https://espace.cern.ch/HiLumi/WP2/task4/SitePages/Home.aspx> and </afs/cern.ch/eng/lhc/optics/SLHCV3.1b/errors/>
- [109] <https://espace.cern.ch/HiLumi/WP2/task4/SitePages/Home.aspx> and </afs/cern.ch/eng/lhc/optics/HLLHCV1.0/errors/>
- [110] R. de Maria, S. Fartoukh, M. Giovannozzi, E. McIntosh, Y. Nosochkov, Y. Cai and M.-H. Wang, HiLumi LHC Deliverable Report D2.2: Magnet Field Quality Specifications, [CERN-ACC-2014-0295](#) (2014)
- [111] Y. Nosochkov, Y. Cai, M.-H. Wang, R. de Maria, S. Fartoukh, M. Giovannozzi and E. McIntosh, Optimization of Triplet Quadrupoles Field Quality for the LHC High Luminosity Lattice at Collision Energy, Proc. 4th International Particle Accelerator Conference, Shanghai, China, 12 - 17 May 2013, , pp. 1364-1366. [CERN-ACC-2013-0132](#)
- [112] <https://espace.cern.ch/HiLumi/WP3/SitePages/MBXF.aspx>
- [113] <https://espace.cern.ch/HiLumi/WP3/SitePages/D2.aspx>
- [114] E. Todesco, private communication (2014).
- [115] R. De Maria, M. Giovannozzi, E. McIntosh, Y. Cai, Y. Nosochkov, M.-H. Wang, Dynamic Aperture, Studies for the LHC High Luminosity Lattice, Proc. 6th International Particle Accelerator Conference, Richmond, USA, 3 - 8 May 2015, pp. 705-707. [CERN-ACC-2015-0177](#)
- [116] Y. Nosochkov, Y. Cai, M. Giovannozzi, R. De Maria, E. McIntosh, Field Quality and Dynamic Aperture Optimisation, 26th LARP Hi-Lumi Collaboration Meeting, 18-21 May 2016, SLAC, USA, <https://indico.fnal.gov/getFile.py/access?contribId=75&sessionId=5&resId=0&materialId=slides&confId=11049>.
- [117] S. Kelly, M.B. Thomas, R. Appleby, L. Thompson, B. Holzer, R. De Maria and S. Russenschuck, Study of the impact of fringe fields of the large aperture triplets on the linear optics of the HL-LHC, Proc. 4th International Particle Accelerator Conference, Shanghai, China, 12 - 17 May 2013, pp. 2642-2644. [CERN-ACC-2013-0174](#)
- [118] A. Bogomyagkov et al., Analysis of the non-linear fringe effects of large aperture triplets for the HL LHC project, Proc. 4th International Particle Accelerator Conference, Shanghai, China, 12 - 17 May 2013, pp.2615-2617. [CERN-ACC-2013-0169](#)
- [119] B. Dalena et al., Fringe fields modelling for the High Luminosity LHC large aperture quadrupoles, Proc. 5th International Particle Accelerator Conference, Dresden, Germany, 15 - 20 June 2014, pp.993-995. [CERN-ACC-2014-0175](#)
- [120] S. Jones, D. Newton and A. Wolski, Initial estimate of fringe field effects in HL-LHC using frequency map analysis, Proc. 5th International Particle Accelerator Conference, Dresden, Germany, 15 - 20 June 2014, pp.1067-1070.
- [121] https://lhc-div-mms.web.cern.ch/lhc-div-mms/tests/MAG/docum/hilumi/Magnets/field_quality.xlsx
- [122] M. Giovannozzi, Y. Cai, Y. Nosochkov, M.-H. Wang, R. de Maria, E. McIntosh, Field quality update and recent tracking results, Talk at the HiLumi annual meeting, November 2015, [INDICO 400665](#)
- [123] /afs/cern.ch/eng/lhc/optics/HLLHCV1.0/errors2/MCBXFAB_errortable_v1

- [124] Y P Sun, R. Assmann, J. Barranco, R. Tomás, T. Weiler, F. Zimmermann, R. Calaga and A. Morita, Beam dynamics aspects of crab cavities in the CERN Large Hadron Collider, Phys. Rev. ST Accel. Beams 12 (2009) 101002. [EuCARD-PUB-2009-031](#)
- [125] J. Barranco García et al., Study of multipolar RF kicks from the main deflecting mode in compact crab cavities for LHC, Proc. 3rd International Particle Accelerator Conference 2012, New Orleans, LA, USA, 20 - 25 May 2012, pp.1873-1875. [CERN-ATS-2012-120](#)
- [126] D. R. Brett et al., Comparison of Taylor maps with RF multipoles in a thin lens 6D tracking code, Proc. 4th International Particle Accelerator Conference, Shanghai, China, 12 - 17 May 2013, Eds. Z. Dai, C. Petit-Jean-Genaz, V. Schaa, C. Zhang, pp. 2687-2689.
- [127] R. Appleby et al., Modelling and long term dynamics of crab cavities in the LHC, Proc. 5th International Particle Accelerator Conference, Dresden, Germany, 15 - 20 June 2014, pp. 1578-1580. [CERN-ACC-2014-0173](#)
- [128] E. Métral et al., Summary of the 2-day internal review of LHC performance limitations (linked to transverse collective effects) during run I (CERN, 25-26/09/2013). [CERN-ACC-NOTE-2014-0006](#).
- [129] E. Métral, Initial estimates of intensity limitations Milestone: MS30. [CERN-ACC-2014-0074](#) (2014).
- [130] E. Métral, Update of the stability limits including the effect of electron cloud, implications for machine and HW parameters (e.g. ramp rates), 26th LARP Hi-Lumi Collaboration Meeting, 18-21 May 2016, SLAC, USA, <https://indico.fnal.gov/getFile.py/access?contribId=18&sessionId=1&resId=0&materialId=slides&confId=11049>
- [131] L. Carver et al., Current status of instability threshold measurements in the LHC at 6.5 TeV, Proc. 7th International Particle Accelerator Conference 2016, Busan, South Korea, 8-13 May 2016, pp. 1434-1437. [CERN-ACC-2016-234](#)
- [132] N. Mounet, DELPHI: an Analytic Vlasov Solver for Impedance-Driven Modes, CERN HSC meeting, 07/05/2014, <https://espace.cern.ch/be-dep/ABP/HSC/Meetings/DELPHIexpanded.pdf>
- [133] E. Métral, Initial estimate of machine impedance, [CERN-ACC-2014-0005](#) (2014).
- [134] N. Biancacci et al., HL-LHC impedance and beam stability, 5th Joint HiLumi LHC-LARP Annual Meeting, CERN, 28-10-2015, https://indico.cern.ch/event/400665/contributions/1843458/attachments/1177720/1703472/HLLHC_CERN_28102015_NB.pdf
- [135] E. Métral, Transverse resistive-wall impedance from Zotter 2015's theory, CERN-GSI bi-lateral working meeting on Collective Effects – Coordination of Theory and Experiments, GSI, Darmstadt, Germany, 30-31 March 2006, <http://care-hhh.web.cern.ch/care-hhh/Collective%20Effects-GSI-March-2006/default.html>
- [136] E. Métral et al., HL-LHC operational scenarios, (2015). [CERN-ACC-NOTE-2015-0009](#)
- [137] G. Iadarola, LHC Performance Workshop (Chamonix 2016), Electron Cloud Effects, Chamonix, France, 25–28 January 2016, [INDICO 448109](#)
- [138] HOM impedance with fabrication errors, [EDMS 1518298](#)
- [139] RFD-SPS-test-cavity-HOM-Qext-and-Impedance SLAC/ODU, [EDMS 1523249](#)
- [140] N. Biancacci et al., Impedance and beam stability, 30th HL-LHC Technical Committee Meeting, 5th November, 2015, [INDICO 450955](#)
- [141] N. Biancacci et al., The HL-LHC impedance model and aspects of beam stability, Proc. 7th International Particle Accelerator Conference 2016, Busan, South Korea, 8-13 May 2016, pp. 606-609. [CERN-ACC-2016-309](#)
- [142] E. Métral, Impedance update (other components than Crab Cavities), 26th LARP Hi-Lumi Collaboration Meeting, 18-21 May 2016, SLAC, USA,

<https://indico.fnal.gov/getFile.py/access?contribId=13&sessionId=1&resId=0&materialId=slides&confId=11049>

- [143] E. Métral, GH. Hoffstätter, F. Willeke; Destabilising effect of linear coupling in the HERA proton ring, Proc. of EPAC'2002, Paris, France, June 3-7, 2002. [CERN-PS-2002-021-AE](#)
- [144] O. Brüning et al., LHC luminosity and energy upgrade: A feasibility study (2002). [LHC Project Report 626](#)
- [145] F. Ruggiero and F. Zimmermann, Luminosity optimization near the beam-beam limit by increasing the bunch length or crossing angle (2002). [CERN-SL-2002-005-REV-AP](#)
- [146] F. Ruggiero and F. Zimmermann, Possible scenario for an LHC upgrade, Proc. HHH 2004 Workshop, Geneva, November 2004, CARE-Conf-05-002-HHH pp.1-13.
- [147] T. Linnecar and E. Shaposhnikova, An RF system for Landau damping in the LHC (2007). [LHC Project Note 394](#)
- [148] C. Bhat, Bunch shaping in the LHC: A quick look, CERN 97th LMC meeting, 22 June 2011, https://espace.cern.ch/lhc-machine-committee/Presentations/1/lmc_97/lmc_97d.pdf
- [149] T. Mertens et al., Emittance growth, debunching and integrated luminosity in the LHC with a higher harmonic RF system (2011). [CERN-AT-Note-2011-071 PERF](#)
- [150] D. Shatilov and M. Zobov, On the possibility of utilizing flat longitudinal beam profiles to increase the luminosity in collisions with large Piwinski angle, 14 April 2012, unpublished note. https://espace.cern.ch/HiLumi/WP2/task4/Shared%20Documents/flat_long_en.docx
- [151] E. Shaposhnikova, Harmonic System for the LHC, 4th Joint HiLumi LHC - LARP Annual Meeting, 17-21 November 2014, KEK, Japan, [INDICO 326148](#)
- [152] L. Ficcadenti et al., Summary of the 800 MHz RF design, CERN meeting on High Harmonic RF System Review, 27 May 2013. [INDICO 254151](#)
- [153] E. Métral et al., Beam intensity limitations, 4th Joint HiLumi LHC-LARP Annual Meeting, KEK, Japan, 17-21 November 2014, [INDICO 326748](#)
- [154] K. Li et al., HL-LHC transverse beam stability studies – some updates, 18th CERN HiLumi WP2 Task 2.4 meeting, 10th December 2014, [INDICO 354942](#)
- [155] R. Tomás et al., HL-LHC: Exploring alternative ideas, Proc. Review of LHC and Injector Upgrade Plans Workshop (RLIUP), Archamps, France, 29–31 October 2013, Eds. B. Goddard and F. Zimmermann, CERN–2014–006, pp. 119-126.
- [156] J.M. Jowett et al., Future heavy-ion performance of the LHC, Proc. Review of LHC and Injector Upgrade Plans Workshop (RLIUP), Archamps, France, 29–31 October 2013, Eds. B. Goddard and F. Zimmermann, CERN–2014–006, pp. 167-184.
- [157] K. Li, Pros and Cons of the 200 MHz system, 26th LARP Hi-Lumi Collaboration Meeting, 18-21 May 2016, SLAC, USA, INDICO: [11049](#)
- [158] S. Fartoukh, The sign of the LHC octupoles, 141st LMC meeting, CERN, 11 July 2012. https://espace.cern.ch/lhc-machine-committee/Presentations/1/lmc_141/lmc_141h.pdf
- [159] C. Tambasco et al., HL-LHC Stability diagrams during the squeeze and collapse, CERN 22nd HiLumi WP2 Task 2.4 (and 2.7) meeting, 29th April 2015, [INDICO 390084](#)
- [160] G. Iadarola et al., Beam induced heat load in the cold elements of the IRs, 4th Joint HiLumi LHC - LARP Annual Meeting, 17-21 November 2014, KEK, Japan, [INDICO 326148](#)
- [161] A. Romano et al., Effect of the LHC beam screen baffles on the electron cloud buildup, Proc. 7th International Particle Accelerator Conference 2016, Busan, South Korea, 8-13 May 2016, pp. 1454-1457. [CERN-ACC-2016-256](#)
- [162] G. Iadarola et al., Electron Cloud Effects: Heat Load and Stability Issues, Joint HiLumi-LARP meeting & 24th LARP Collaboration Meeting, 11-13 May 2015, Fermilab, Chicago, USA,

- <https://indico.fnal.gov/getFile.py/access?contribId=62&sessionId=4&resId=0&materialId=slides&confId=9342>
- [163] K. Li et al., Electron cloud observations during LHC operation with 25 ns beams, Proc. 7th International Particle Accelerator Conference 2016, Busan, South Korea, 8-13 May 2016, pp. 1458-1461. [CERN-ACC-2016-255](#)
- [164] G. Rumolo et al., Electron cloud in the CERN accelerator complex, Proceedings of the 57th ICFA Advanced Beam Dynamics Workshop on High-Intensity and High-Brightness Hadron Beams, Malmö, Sweden, 3-8 July 2016, Eds. D. Gous, M. Marx, R. Mueller (GSI, Germany), J. Olander, V.R.W. Schaa, G. Trahern, pp. 266-271. [CERN-ACC-2016-0099](#)
- [165] K. Li et al., Update on Landau octupoles settings at injection, 65th LHC Beam Operation Committee meeting, CERN, 23rd August 2016, [INDICO 564033](#)
- [166] E. Métral et al., Measurement and interpretation of transverse beam instabilities in the CERN Large Hadron Collider (LHC) and extrapolation to HL-LHC, Proceedings of the 57th ICFA Advanced Beam Dynamics Workshop on High-Intensity and High-Brightness Hadron Beams, Malmö, Sweden, 3-8 July 2016, Eds. D. Gous, M. Marx, R. Mueller (GSI, Germany), J. Olander, V.R.W. Schaa, G. Trahern, pp. 254-259. [CERN-ACC-2016-0098](#)
- [167] G. Iadarola, Electron cloud studies for CERN particle accelerators and simulation code development, [CERN-THESIS-2014-047](#)
- [168] K. Li et al., Mitigation of electron cloud instabilities in the LHC using sextupoles and octupoles, Proc. 3rd International Particle Accelerator Conference 2012, New Orleans, LA, USA, 20 - 25 May 2012, pp. 3084-3086. [CERN-ATS-2012-138](#)
- [169] E. Benedetto, Emittance growth induced by electron cloud in proton storage rings, Ph.D. dissertation, Politecnico di Torino, 2006, [CERN-THESIS-2008-096](#)
- [170] M. Schenk et al., Use of RF quadrupole structures to enhance stability in accelerator rings, Proceedings of the 57th ICFA Advanced Beam Dynamics Workshop on High-Intensity and High-Brightness Hadron Beams, Malmö, Sweden, 3-8 July 2016, Eds. D. Gous, M. Marx, R. Mueller (GSI, Germany), J. Olander, V.R.W. Schaa, G. Trahern, pp. 505-510. [CERN-ACC-2016-0096](#)
- [171] K. Li et al., Do we need a wide-band transverse feedback in the LHC / HL-LHC?, 75th WP2 Task Leader meeting, 23rd August 2016, [INDICO 544550](#)
- [172] W. Herr et al., Observations of beam-beam effects in the LHC in 2011, Proc. Chamonix 2012 Workshop on LHC Performance, Chamonix, France, 6–10 Feb 2012, Ed. C. Carli, CERN-2012-006 (2012), pp. 99-104. [CERN-ATS-2011-154](#)
- [173] Y. Luo and F. Schmidt, Dynamic aperture studies for LHC optics Version 6.2 at Collision. [LHC-PROJECT-NOTE-310](#)
- [174] A. Valishev et al., Simulation of beam-beam effects and Tevatron experience, JINST 7 (2012) [P12002](#).
- [175] J. Qiang et al., A parallel particle-in-cell model for beam–beam interaction in high energy ring colliders, J. Comp. Phys. 198 (2004) 278.
- [176] T. Pieloni, A study of beam-beam effects in hadron colliders with a large number of bunches, Ph.D. thesis, EPFL, 2008, CERN-THESIS-2010-056.
- [177] W. Herr, X. Buffat, R. Calaga, R. Giachino, G. Papotti, T. Pieloni and D. Kaltchev, Long range beam-beam effects in the LHC, Proc. ICFA Mini-Workshop on Beam-Beam Effects in Hadron Colliders, CERN, Geneva, Switzerland, 18-22 March 2013, Eds. W. Herr and G. Papotti, CERN-2014-004, pp. 87–92 (2014).
- [178] T. Pieloni, X. Buffat, D. Banfi, J. Barranco, G. Arduini, E. Mounet, N. Mounet, S.M. White and J. Qiang, Two beam effects, Proc. 5th Evian Workshop on LHC beam operation, Evian, France, 2–4 June 2014, Eds. B. Goddard, S. Dubourg, CERN-ACC-2014-0319 (2014), pp. 69-79.

- [179] T. Pieloni, Levelling Scenarios: present and future perspectives, LARP-HiLumi Meeting, INFN Frascati, Frascati, Italy, 14–16 November 2012, INDICO: 183635
- [180] X. Buffat, D. Banfi, G.R. Coombs, W. Herr and T. Pieloni, Beam-Beam Effects in Different Luminosity Levelling Scenarios for the LHC, Proc. 5th International Particle Accelerator Conference, Dresden, Germany, 15 - 20 June 2014, Eds. C. Petit-Jean-Genaz, G. Arduini, P. Michel and V.R.W. Schaa, pp. 1061-1063.
- [181] D. Banfi, J. Barranco, T. Pieloni and A. Valishev, Weak-Strong Beam-Beam Simulations for the HL-LHC, Proc. 5th International Particle Accelerator Conference, Dresden, Germany, 15 - 20 June 2014, Eds. C. Petit-Jean-Genaz, G. Arduini, P. Michel and V.R.W. Schaa, pp. 3079-3081.
- [182] M. Giovannozzi, Dynamic Aperture: Simulations vs. Experiments and first DA results in the LHC, 14th HiLumi WP2 Task Leader Meeting, 27th August 2013.INDICO: [267840](#)
- [183] T. Pieloni et al., Beam-beam effects and limitations in the HL-LHC, LARP-HiLUMI Collaboration Meeting, Brookhaven National Laboratory, Upton, NY, USA, 7–9 May 2014, INDICO: 730
- [184] M. Giovannozzi et al., Dynamic aperture performance for different collision optics scenarios for the LHC luminosity upgrade, Proc. 4th International Particle Accelerator Conference, Shanghai, China, 12 - 17 May 2013, Eds. Z. Dai, C. Petit-Jean-Genaz, V. Schaa, C. Zhang, pp. 2609-2611.
- [185] T. Pieloni et al., Preliminary studies of beam-beam long-range effects: Orbit, tune, chromaticity for HL-LHC, 35th HiLumi WP2 Task Leader Meeting, 10 October 2014, <https://indico.cern.ch/event/341000/>
- [186] A. Valishev et al., Preliminary estimates of beam-beam effects, HiLumi LHC Milestone Report, CERN-ACC-2014-0066 (2014).
- [187] J. Qiang et al., Strong-strong beam-beam simulation for LHC upgrade, Proc. 5th International Particle Accelerator Conference, Dresden, Germany, 15 - 20 June 2014, Eds. C. Petit-Jean-Genaz, G. Arduini, P. Michel and V.R.W. Schaa, pp. 1006-1009.
- [188] D. Pellegrini, Y. Papaphilippou, S. Fartoukh, F. Antoniou and G. Iadarola, BBLR studies and possible reduction of the crossing angle: simulations, LBOC Meeting No 64, 16 Aug 2016, INDICO: 561910
- [189] A. Valishev et al., 42nd HiLumi WP2 Task Leader Meeting, 6 March 2015, INDICO: 371768
- [190] D. Banfi, Beam-beam effects for round optics: DA simulations summary, 44th HiLumi WP2 Task Leader Meeting, CERN, 20 March 2015,INDICO: 376192
- [191] T. Pieloni, Field Quality Requirements Including Beam-Beam Effects, Joint HiLumi-LARP meeting & 24th LARP Collaboration Meeting, 11-13 May 2015, Fermilab, Chicago, USA, <https://indico.fnal.gov/getFile.py/access?contribId=27&sessionId=4&resId=0&materialId=slides&confId=9342>
- [192] S. Fartoukh, A. Valishev, Y. Papaphilippou, and D. Shatilov, Compensation of the long-range beam-beam interactions as a path towards new configurations for the high luminosity LHC, Phys. Rev. Accel. Beams 18, 121001, 1 December 2015
- [193] E. Métral et al., Lessons learnt and mitigation measures for the CERN LHC equipment with RF fingers, Proc. 4th International Particle Accelerator Conference, Shanghai, China, 12 - 17 May 2013, Eds. Z. Dai, C. Petit-Jean-Genaz, V. Schaa, C. Zhang, pp. 1802-1804.
- [194] R. Veness et al., Specification of new vacuum chambers for the LHC experimental interactions, Proc. 2nd International Particle Accelerator Conference, San Sebastian, Spain, 4 - 9 Sep 2011, Eds. C. Petit-Jean-Genaz, A. Blanco, I. Etxebarria, F. Perez, A. Wolski and V. Schaa, pp. 1584-1586.
- [195] B. Salvant et al., Attempt at impedance studies for the experimental beam pipes 10th LEB Technical Meeting, CERN, 15 June 2012, https://espace.cern.ch/LEBC/Shared%20Documents/Impedance_studies_for_the_experimental_beam_pipes2.pdf

- [196] R. Wanzenberg and O. Zagorodnova, Calculation of wakefields and higher order modes for the new design of the vacuum chamber of the CMS experiment for the HL-LHC, CERN-ATS-Note-2013-018 TECH (2013).
- [197] B. Salvant et al., Heat load from impedance on existing and new hardware in the LHC era, 3rd Joint HiLumi LHC-LARP Annual Meeting, Daresbury, UK, 11–15 November 2013, <https://indico.cern.ch/event/257368/session/2/contribution/12/attachments/452047/626807/Daresbury.pptx>
- [198] B. Salvant et al., Impedance of new ALICE beam pipe, 2nd LHC Tunnel Region Experiments Working Group (TREX) meeting, CERN, 31 July 2014, https://indico.cern.ch/event/333087/contribution/2/attachments/649619/893336/Impedance_for_new_ALICE_beam_pipe.pptx
- [199] B. Salvant, Heat load estimates for the experimental vacuum chambers and potential limitations, 74th HiLumi WP2 Task Leaders Meeting, CERN, 16 August 2016, https://indico.cern.ch/event/556760/contributions/2243233/attachments/1323597/1986054/Heat_load_estimates_for_the_experimental_vacuum_chambers_WP2_Aug16_v3.pptx
- [200] E. Métral and C. Zannini, Temperature effects on image current losses in the HL-LHC triplets – Part 2, 33rd HiLumi WP2 Task Leaders Meeting, CERN, 5 September 2014, INDICO: 323863
- [201] N. Mounet et al., Impedance considerations for the design of the triplet/D1 beam screen, Technical Meeting on Vacuum for HL-LHC, CERN, 5 March 2014, INDICO [304605](#)
- [202] E. Métral et al., Expected impedance and heat load of the present design of the HL- LHC BPMs, 28th HiLumi WP2 Task Leaders Meeting, CERN, 23 May 2014, INDICO: [315532](#)
- [203] H. Day et al., TCTP summary of power loss and heat load calculations (with attention paid to the heat load of the ferrite damping material), 149th LHC collimation working group meeting, CERN, 1 October 2012, https://indico.cern.ch/event/209417/contribution/0/attachments/324935/453137/hday_TCTP_heating_summary_CollWG_01-10-12.pdf
- [204] H. Day, Measurements and Simulations of Impedance Reduction Techniques in Particle Accelerators, Ph.D. thesis, Manchester University, CERN-THESIS-2013-083, 2013.
- [205] B. Salvant et al., Impedance aspects of crab cavities, HiLumi-LHC/LARP Crab Cavity System External Review, BNL, USA, 5–6 May 2014, <https://indico.bnl.gov/getFile.py/access?contribId=16&sessionId=5&resId=1&materialId=slides&confId=728>
- [206] M. Wendt, Wakefield analysis of the LHC BSRT mirror holder, Internal Impedance Meeting, CERN, 9 September 2013, https://impedance.web.cern.ch/impedance/documents/Imp_meetin_09-09-2013/MW.pdf
- [207] R. Cimino, I. R. Collins, M. A. Furman, M. Pivi, F. Ruggiero, G. Rumolo, and F. Zimmermann, Can Low-Energy Electrons Affect High-Energy Physics Accelerators?, Phys. Rev. Lett., vol. 93, p. 014801, Jun 2004.
- [208] H. Damerau et al., LIU: Exploring Alternative Ideas, Proc. Review of LHC and Injector Upgrade Plans Workshop (RLIUP), Archamps, France, 29–31 October 2013, Eds. B. Goddard and F. Zimmermann, CERN–2014–006, pp. 127-137.
- [209] G. Iadarola, H. Bartosik, K. Li, L. Mether, A. Romano, G. Rumolo, M. Schenk, Performance limitation from electron cloud in 2015, Proc. 6th Evian Workshop on LHC beam operation, Evian, France, 15-17 June 2016, Eds. B. Goddard, S. Dubourg, INDICO: [434129](#)
- [210] G. Iadarola and G. Rumolo, 200 MHz Scenario: e-cloud, 68th HiLumi WP2 Meeting, 3 May 2016, INDICO: [523881](#)

- [211] E. Metral, G. Iadarola, A. Rossi, Summary heat-loads for the different beams screens including image currents, electron cloud and synchrotron radiation, 63rd HiLumi WP2 Meeting, 15 Mar 2016, INDICO: [463028](#)
- [212] V. Baglin, G. Bregliozzi, R. Kersevan., Coupled Simulations of the Synchrotron Radiation and Induced Desorption Pressure Profiles for the HL-LHC Triplet area and Interaction Points, Proc. 5th International Particle Accelerator Conference, Dresden, Germany, 15 - 20 June 2014, Eds. C. Petit-Jean-Genaz, G. Arduini, P. Michel and V.R.W. Schaa, pp. 2381-2383.
- [213] V. Baglin, G. Bregliozzi, R. Kersevan, Synchrotron Radiation Distribution and Related Outgassing and Pressure Profiles in the HL-LHC Final Focus Magnets, Proc. 6th International Particle Accelerator Conference, Richmond, USA, 3 - 8 May 2015, Eds. S. Henderson, E. Ayers, T. Satogata, V.R.W. Schaa, pp. 3127-3130.
- [214] G. Iadarola, E. Metral, G. Rumolo, Expected heat load for the two bore magnets in the IRs of the HL-LHC, CERN-ACC-2016-0112.
- [215] G. Arduini, Performance Limitations in HL-LHC after LIU Upgrade, LHC Performance Workshop (Chamonix 2016), Chamonix, France, 25–28 January 2016, INDICO: [448109](#)
- [216] G. Antchev et al., Luminosity-independent measurements of total, elastic and inelastic cross sections at $\sqrt{s}=7$ TeV, CERN-PH-EP-2012-353 (2012).
- [217] G. Antchev et al., Luminosity-independent measurements of the proton–proton total cross section at $\sqrt{s}=8$ TeV, CERN-PH-EP-2012-354 (2012).
- [218] G. Arduini et al., PICS: What do we gain in beam performance, Proc. Review of LHC and Injector Upgrade Plans Workshop, Archamps, 29–31 October 2013, Eds. B. Goddard, F. Zimmermann, CERN-2014-006, pp. 49-56.
- [219] L. Medina, R. Tomas, Performance and Operational Aspects of HL-LHC Scenarios, Proc. 7th International Particle Accelerator Conference 2016, Busan, South Korea, 8-13 May 2016, Eds. C. Petit-Jean-Genaz, D. E. Kim, K. S. Kim, I. S. Ko, K. R. Kim, V.R.W. Schaa, pp. 1516-1518.
- [220] A. Valishev, S. Fartoukh and D. Shatilov, BBLR compensation for HL-LHC, 3rd Joint HiLumi LHC–22nd LARP Collaboration Meeting, 7–8 May 2014, BNL, USA, INDICO: 730
- [221] D. Banfi, J. Barranco, T. Pieloni, A. Valishev, “Task 2.5: Beam-beam studies”, 20th HiLumi WP2 Task Leader Meeting, 25 October 2013, CERN, INDICO: 278765
- [222] D. Banfi, J. Barranco, T. Pieloni, A. Valishev, Beam-beam effects for round and flat optics: DA simulations, 4th Joint HiLumi LHC - LARP Annual Meeting, 17-21 November 2014, KEK, Japan, INDICO: 326148
- [223] R. Tomás et al., HL-LHC Alternative Scenarios, Proc. Chamonix 2014 Workshop on LHC Performance, Chamonix, France, 22–25 September 2014, Ed. M. Draper, CERN–2015–002, pp.217-224.
- [224] J.P. Koutchouk, Principle of a Correction of the Long-Range Beam-Beam Effect in LHC using Electromagnetic Lenses, LHC-Project-Note 223, CERN, Geneva, Switzerland, 2000.
- [225] A. Valishev and G. Stancari, Electron Lens as Beam-Beam Wire Compensator in HL-LHC, FERMILAB-TM-2571-APC, arXiv:1312.1660
- [226] S. Fartoukh, A. Valishev, D. Shatilov, An alternative High Luminosity LHC with flat optics and long-range beam-beam compensation, Proc. 6th International Particle Accelerator Conference, Richmond, USA, 3 - 8 May 2015, Eds. S. Henderson, E. Ayers, T. Satogata, V.R.W. Schaa, pp. 2199-2202.
- [227] H. Bartosik et al., Other Means to increase the SPS 25 ns Performance - Transverse Plane, Proc. Chamonix 2014 Workshop on LHC Performance, Chamonix, France, 22–25 September 2014, Ed. M. Draper, CERN–2015–002, pp. 180-184.
- [228] R. Tomás et al., 80 bunch scheme option for HL-LHC - physics potential, 14th HL-LHC Parameter and Layout Committee Meeting, 12 March 2015, CERN, INDICO: 378400

- [229] S. Fartoukh, Pile up management at the High Luminosity LHC and introduction to the crab-kissing concept, *Phys. Rev. ST Accel. Beams*, 17, 111001 (2014).
- [230] E. Shaposhnikova et al., Flat bunches in the LHC, *Proc. 5th International Particle Accelerator Conference*, Dresden, Germany, 15 - 20 June 2014, Eds. C. Petit-Jean-Genaz, G. Arduini, P. Michel and V.R.W. Schaa, pp. 1413–1415.
- [231] J.M. Jowett, R. Alemany-Fernandez, R. Assmann, P. Baudrenghien, G. Bellodi, S. Hancock, M. Lamont, D. Manglunki, S. Redaelli, M. Sapinski, M. Schaumann, M. Solfaroli, R. Versteegen, J. Wenninger and D. Wollmann, Heavy ions in 2012 and the programme up to 2022, *Proc. Chamonix 2012 Workshop on LHC Performance*, Chamonix, France, 6–10 Feb 2012, Ed. C. Carli, CERN-2012-006 (2012), pp. 200–215.
- [232] ALICE upgrade Letter of Intent (<http://cds.cern.ch/record/1475243>) endorsed by the LHCC on 27 Sep 2012 and approved by the Research Board on 28 Nov 2012 (<http://cds.cern.ch/record/1499619/files/M-202.pdf>)
- [233] J. Jowett, Functional Specification HL-LHC Heavy-Ion Beam Parameters at LHC Injection, EDMS 1525065, <https://edms.cern.ch/file/1525065/0.2/HL-LHC-IONS-1525065-00-20.pdf>
- [234] C.A. Salgado, J. Alvarez-Muniz, F. Arleo, N. Armesto and M. Botje et al., Proton–nucleus collisions at the LHC: Scientific opportunities and requirements, *J. Phys. G39* (2012) 015010.
- [235] J.M. Jowett, R. Alemany-Fernandez, P. Baudrenghien, D. Jacquet, M. Lamont, D. Manglunki, S. Redaelli, M. Sapinski, M. Schaumann, M. Solfaroli, Camillocci, R. Tomás, J. Uythoven, D. Valuch, R. Versteegen and J. Wenninger, Proton nucleus collisions in the LHC, *Proc. 4th International Particle Accelerator Conference*, Shanghai, China, 12 - 17 May 2013, Eds. Z. Dai, C. Petit-Jean-Genaz, V. Schaa, C. Zhang, pp.49-51.
- [236] R. Bruce, D. Bocian, S. Gilardoni and J.M. Jowett, Beam losses from ultraperipheral nuclear collisions between 208Pb82+ ions in the large hadron collider and their alleviation, *Phys. Rev.ST Accel. Beams* 12 (2009) 071002.
- [237] M. Bodendorfer et al., Ions: Baseline, Studies Plan and Strategy for Pending Options, *Proc. Chamonix 2014 Workshop on LHC Performance*, Chamonix, France, 22–25 September 2014, Ed. M. Draper, CERN–2015–002, pp. 192-197.
- [238] J. Coupard, H. Damerau, A. Funken, R. Garoby, S. Gilardoni, B. Goddard, K. Hanke, D. Manglunki, M. Meddahi, R. Scrivens, G. Rumolo, E. Shaposhnikova, eds., *LHC Injectors Upgrade Technical Design Report – Volume II: Ions*, EDMS 1626950 (April 2016)
- [239] M. Schaumann, Semi-empirical model for optimising future heavy-ion luminosity of the LHC, *Proc. 5th International Particle Accelerator Conference*, Dresden, Germany, 15 - 20 June 2014, Eds. C. Petit-Jean-Genaz, G. Arduini, P. Michel and V.R.W. Schaa, pp. 1033–1035.
- [240] J.M. Jowett, H.-H. Braun, M.I. Gresham, E. Mahner and A.N. Nicholson, et al., Limits to the performance of the LHC with ion beams, *Proc. 9th European Particle Accelerator Conference*, Lucerne, Switzerland, 5 – 9 July 2004, Eds. J. Chrin, C. Petit-Jean-Genaz, J. Poole, C. Prior, H.-A. Synal, pp. 578–580.
- [241] H.-H. Braun, R.W. Assmann, A. Ferrari, J.-B. Jeanneret, J.M. Jowett and I.A. Pshenichnov, Collimation of heavy ion beams in LHC, *Proc. 9th European Particle Accelerator Conference*, Lucerne, Switzerland, 5 – 9 July 2004, Eds. J. Chrin, C. Petit-Jean-Genaz, J. Poole, C. Prior, H.-A. Synal, pp. 551–553.
- [242] H.-H. Braun, A. Fassò, A. Ferrari, J.M. Jowett, P.R. Sala and G.I. Smirnov, Hadronic and electromagnetic fragmentation of ultrarelativistic heavy ions at LHC, *Phys. Rev. ST Accel. Beams* 17 (2014) 021006.

- [243] O. S. Brüning, P. Collier, P. Lebrun, S. Myers, R. Ostojic, J. Poole and P. Proudlock (Eds.), LHC Design Report, v.1: The LHC Main Ring, CERN-2004-003-V-1 (2012) Chapter 21, The LHC as a Lead Ion Collider, Tables 21.1-21.3.

Chapter 3

Insertion Magnets

3 Insertion magnets

3.1 Overview

The layout of the HL-LHC insertion magnets is shown in Figure 3-1 and compared to those of the LHC in Figure 3-2. The main technical choices can be summarized as follows [1, 2]:

- Maintain the distance from the first magnet to the collision point at 23 m. This allows preserving the most critical boundaries with the detectors.
- Increase the quadrupole triplet coil aperture from 70 mm to 150 mm to allow a smaller β^* . Nb₃Sn technology has been selected for the quadrupoles [3], allowing an increase in the aperture while keeping the magnet length at acceptable values. The choice of a large coil width (about 36 mm, arranged in two layers of 18-mm-wide cable) aims at reaching maximum performance in terms of gradient [1, 4]. The operational current has been first set at ~80% of the load line critical current, which is a good compromise between risk and performance [5, 6]. During the design the margin gradually reduced, with operating current set at 81% to take into account the details of the heads and of the cross-section. Therefore, following the suggestion of the design review in December 2014, it has been decided to lower the operational current to 76% of load line critical current, considering the lack of experience with 7-m-long coils and the difficulties in reaching the specified critical current for the strand production. This reduction of gradient from 140 T/m to 132.6 T/m [7] is compensated by a longer coil (from 4.0 to 4.2 m in the Q1/Q3, and from 6.8 m to 7.15 m in Q2a and Q2b magnets), corresponding to a triplet length of ~31 m, compared to ~24 m in the LHC.
- Reduce the critical current specification from 1400 to 1280 A/mm² at 15 T and 4.2 K; this brings the operational gradient of 132.6 T/m at 78% of the load line critical current. This reduction has been done to avoid the rejection of non-negligible fractions of the conductor production, i.e. lowering the strand cost.
- To recover the 10 m of additional space allocated to the triplet and the correctors, and gain further space for inserting the crab cavities (see Chapters 2 and 4), three steps are taken.
 - o Increase the strength of the separation/recombination dipoles from 26 T·m to 35 T·m, thus reducing the distance between the D1 and D2 centres from 90 to 75 m and recovering ~15 m.
 - o Replacing the 20-m-long normal conducting magnet D1 operating at 1.28 T with a superconducting 6.27 m long magnet, operating at 5.6 T [8], thus recovering ~15 m.
 - o The busbars for the triplet and D1 are not connected through a feedbox placed between D1 and the triplet as in the LHC (indicated by DFB in Figure 3-2), but through a service module on the non-IP side of D1 (not shown in Figure 3-1). This allows a shifting of D1 towards the IP by a few metres, at the price of having the triplet and corrector busbars going through D1.

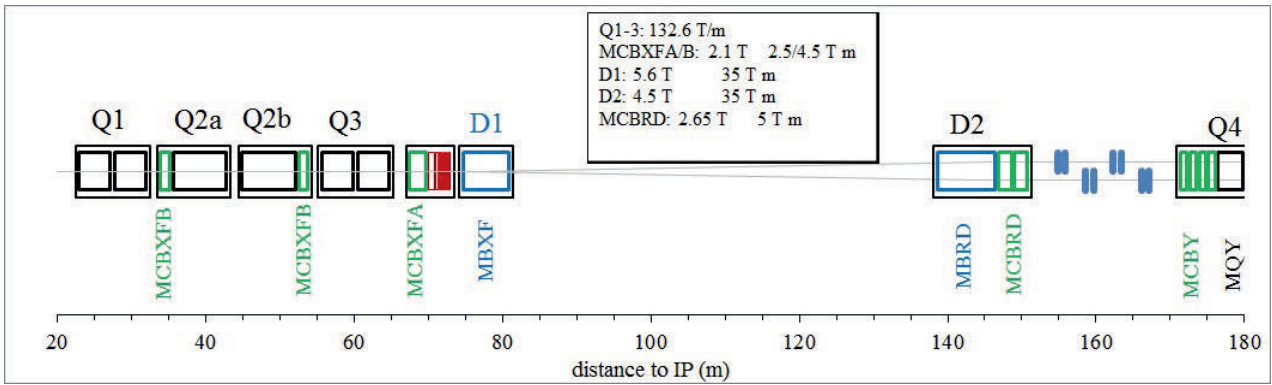


Figure 3-1: Schematic layout of the IR region of HL-LHC. Thick boxes are magnets, thin boxes are cryostats.

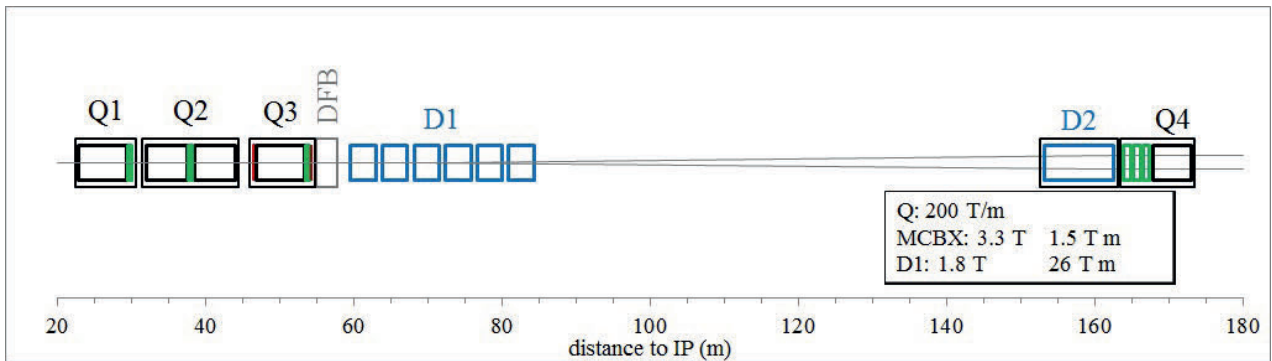


Figure 3-2: Schematic layout of the current IR region of the LHC. Thick boxes are magnets, thin boxes are cryostats.

- The apertures of the magnets between the triplet and the dispersion suppressor have to be increased: D1 from 60 mm to 150 mm, D2 from 80 mm to 105 mm, and Q5 from 56 mm to 70 mm. Q4 aperture is at 70 mm as it is in the LHC today, using MQY spares, and Q5 is replaced by the present Q4 in the LHC. For the new dipoles D1 and D2, Nb-Ti superconductor has been chosen [1, 2], since requirements are within reach of this technology, and the potential performance improvement given by Nb₃Sn is not sufficient to justify the additional cost and complexity. Since the size of the magnet is limited by the cryostat, and the aperture is enlarged, we selected a one layer coil reusing the LHC outer dipole cable (15 mm width) to have enough space for the iron yoke to magnetically separate the apertures and to reduce fringe fields in the tunnel. Using the LHC cable allows to reduce the risks (the cable properties are well known), to ease the schedule (lengths are already available) at the price of a larger operational current.
- All new magnets, plus Q4 and Q5, will operate at 1.9 K to have the maximum superconductor performance. This is an important change with respect to the LHC, where the D2, Q4, Q5, and Q6 operational temperature is 4.5 K. For Q6, there is no requirement of additional strength and therefore operational temperature is kept at 4.5 K to minimize the cost and the workload.
- Three horizontal/vertical orbit correctors are required in the triplet. The strength is increased from 1.5 T·m (LHC value) to 2.5 T·m for the correctors close to Q2a/b, and to 4.5 T·m for the corrector close to Q3. The position with respect to the quadrupole magnets is the same as in the LHC layout, with the exception of the corrector between Q2a and Q2b, which is moved to between Q2b and Q3. Correctors are nested (like in the present LHC), providing both horizontal and vertical field in the same longitudinal location, to keep a compact triplet layout.
- A skew quadrupole is used to correct the triplet tilt, as in the LHC. Non-linear correctors of the order 3, 4, 5, and 6 are required, both normal and skew. With respect to the LHC layout, normal and skew decapole correctors and a skew dodecapole corrector are added. Experience with LHC operation and

field quality of the triplet short models will confirm whether these correctors are needed. Anyway, the longitudinal space required for a single corrector is about 15 cm, and therefore it does not have a large impact on the layout.

- Horizontal and vertical orbit correctors are also required close to D2 and to Q4 (note that they were present only in Q4 in the LHC) with a nominal strength of 5 T·m. For D2, we will use a canted costheta design (CCT), whose field is limited to 2.65 T due to the magnetic cross-talk between the apertures, giving a 1.89 m magnetic length. Four MCBY units, each giving 2.7 T·m in each plane, will be assembled in the Q4 cold mass.
- With an ultimate luminosity 7.5 times larger than the nominal design goal of the LHC, a new absorber, using 8- and 16-mm-thick tungsten (W) shielding attached to the outer surface of the beam screen (Figure 3-3) is foreseen to reduce the effect of collision debris. For nominal integrated luminosity, the tungsten shielding will limit in the region Q1 to D1 the radiation dose to 20 MGy in most parts of the coils, with few locations reaching 40 MGy (see Chapter 10). A switch of the crossing angle plane between IP1 and IP5 allows to further reduce the dose by 30%. All magnets components are designed to withstand a radiation dose of 35 MGy. The peak energy deposition is 2 mW/cm³, i.e. about half of the nominal LHC [9]. These values are similar to the expected heat load and radiation doses for the nominal LHC [10]. The cryogenic system from the triplet to D1 has to absorb 1.3 kW steady-state at ultimate luminosity. Approximately half of this is intercepted by the cold mass at 1.9 K and half by the beam screen at 40–60 K. For the region D2 to Q6, the maximum dose is 20 MGy and the peak energy depositions are 2 mW/cm³.

The main parameters of the magnets are listed in Table 3-1.

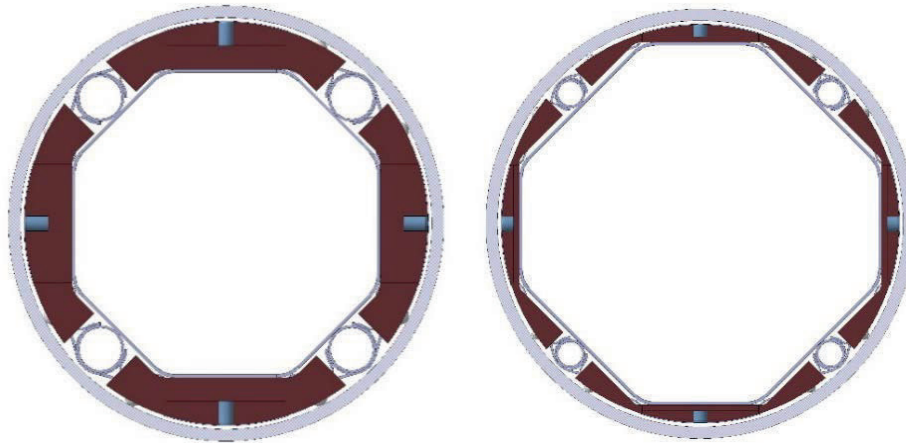


Figure 3-3: Beam screen (grey) with tungsten shielding (dark brown) and cooling tubes in Q1 (lefthand side) and in Q2-D1 (righthand side).

3.2 Low- β Quadrupoles

Function, operational modes, and powering: The triplet magnets, denoted by MQXF, ramp with the energy of the LHC, with a nominal gradient of 8.5 T/m at 450 GeV, and a maximal operational gradient of 132.6 T/m at 7 TeV. During squeeze, its gradient is constant or decreases by not more than 10%. The triplet quadrupoles are powered in series, with a 2 kA powering trim acting on Q1 and another one on Q3. A 120 A trim is acting on Q2b, to compensate for differences in the gradient between Q2a and Q2b of the order of 0.1% or less. The quadrupoles Q1 and Q3 are developed by US-LARP and Q2a and Q2b by CERN.

Table 3-1: Overview of the main parameters of the insertion magnets – see the text for definitions of footnotes.

		Triplet		Short orbit	Long orbit	Separation	Recomb.	Orbit	Large ap. Q	Orbit	Large ap. Q
		Q1/Q3	Q2a/b	corrector	corrector	dipole	dipole	corrector	2-in-1	correcto	2-in-1
		MQXFA	MQXFB	MCBXFB	MCBXFA	D1	D2	MCBRD	Q4	MCBY	Q5
						MBXF	MBRD	MCBRD	MQY	MCBY	MQY
Aperture ¹	(mm)	150	150	150	150	150	105	105	70	70	70
Field	(T)			2.10	2.10	5.58	4.50	2.80		3.00	
Gradient	(T/m)	132.6	132.6						200		200
Magnetic length ²	(m)	4.20	7.15	1.20	2.20	6.27	7.78	1.8	3.4	0.9	3.4
Int field	(T m)			2.5	4.5	35.0	35.0	5.0		2.7	
Int gradient	(T)	557	948						680		680
Number of apertures		1	1	1	1	1	2	2	2	2	2
Distance between apertures ¹	(mm)						188	188	194	194	194
Number of circuits		4	4	16	8	4	4	16	8	16	8
Units needed		16	8	8	4	4	4	8	4	16	4
Spares		4	2	2	2	2	2	4	-	-	-
Cable data											
Material		Nb ₃ Sn	Nb ₃ Sn	Nb-Ti	Nb-Ti	Nb-Ti	Nb-Ti	Nb-Ti	Nb-Ti	Nb-Ti	Nb-Ti
Cable thick. in. ³	(mm)	1.462	1.462	0.819	0.819	1.362	1.362	1.129	0.77	1.129	0.77
Cable thick. ou. ³	(mm)	1.588	1.588	0.871	0.871	1.598	1.598	1.441	0.92	1.441	0.92
Cable width ³	(mm)	18.15	18.15	4.37	4.37	15.10	15.10	8.30	8.30	8.30	8.30
Ins. thick radial ⁴	(mm)	0.145	0.145	0.105	0.105	0.155	0.150	0.08	0.08	0.08	0.08
Ins. thick azimuth. ⁴	(mm)	0.145	0.145	0.105	0.105	0.135	0.130	0.08	0.08	0.08	0.08
No. strands		40	40	18	18	36	36	22	34	22	34
Strand diameter ³	(mm)	0.850	0.850	0.480	0.480	0.825	0.825	0.735	0.48	0.735	0.48
Cu/NonCu		1.20	1.20	1.75	1.75	1.95	1.95	1.25	1.75	1.25	1.75
Filling factor ⁵		0.31	0.31	0.25	0.25	0.24	0.24	0.34	0.26	0.34	0.26
Coil design											
N. layers		2	2	2+2	2+2	1	1	2	3	2	3
N. turns/pole		50	50	139 / 187	139 / 187	44	31	22	52	22	52
Cable length/pole	(m)	470	750	420/560	700/920	600	500	200	404	200	404
Operational parameters											
Peak field ⁶	(T)	11.4	11.4	4.1	4.1	6.6	5.1	3.1	7.6	3.6	7.6
Temperature	(K)	1.9	1.9	1.9	1.9	1.9	1.9	1.9	1.9	1.9	1.9
Current	(kA)	16.47	16.47	1.60 / 1.47	1.60 / 1.47	12.00	12.05	0.43	4.51	0.088	4.51
j overall ⁷	(A/mm ²)	462	462	331 / 304	331 / 304	445	450	369	531	369	531
Loadline fraction ⁸	(adim)	0.78	0.78	0.50	0.50	0.76	0.65	0.82		0.82	
Temperature margin	(K)	5.0	5.0	4.1	4.1	2.5	3.0	1.6		1.6	
Stored energy/m	(MJ/m)	1.17	1.17	0.100	0.100	0.342	0.281	0.435		0.435	
Inductance/m	(mH/m)	8.21	8.21	15.2 / 24.2	15.2 / 24.2	4.01	3.51	21.7		21.7	
Stored energy ⁹	MJ	4.91	8.37	0.122	0.223	2.15	2.19	1.48		1.48	
Mechanical structure											
Forces x	(MN/m)	2.47	2.47	0.322	0.322	1.53	0.64				
Forces y	(MN/m)	-3.48	-3.48	0.402	0.402	-0.64	-0.40				
F _{mag} stress ¹⁰	(MPa)	114	114	135	135	100	50				
Protection											
Circuit inductance ¹¹	(mH)	138	117	18 / 29	32 / 51	27	25	73.8		73.8	
Coil energy density ¹²	(J/mm ³)	0.082	0.082	0.007	0.007	0.072	0.042	0.076		0.076	

¹Aperture is the coil inner diameter at room temperature, excluding ground insulation, cold bore, and beam screen; distance between apertures is given at 1.9 K.

²Magnetic length is given at 1.9 K.

³Strand/cable dimensions are given at room temperature, in the case of Nb₃Sn before reaction.

⁴Insulation dimensions are given at room temperature.

⁵Filling factor is defined as the fraction of superconductor in the insulated cable.

⁶Peak field in the coil is given including the contribution of the strand where the peak is located.

⁷Overall current density is the average over the whole cross-section of the insulated cable at 1.9 K (i.e. including voids or impregnation and insulation, but not copper wedges).

⁸Load line fraction is the ratio between the operational current and the critical current on the load line.

⁹Stored energy is given for the whole magnet: in the case of independently powered apertures or nested magnets, stored energy is given for both circuits powered with maximum nominal current.

¹⁰Stress is an estimate given by the accumulation of the azimuthal Lorentz forces at nominal current divided by the coil radial width – the impact of the structure, preload, and bending is not considered.

¹¹Circuit inductance is the differential inductance of the circuit at maximum nominal current.

¹²Energy density is given over the coil volume at 1.9 K, including insulation but not coil parts such as copper wedges and pole pieces.

Conductor: The Nb₃Sn cable has 40 strands, with 0.85 mm diameter [7]. The main specifications are:

- A minimum non-copper critical current density of 1280 A/mm² at 15 T and 4.2 K; this value has been lowered in 2015 with respect to the initial specification of 1400 A/mm² to avoid the rejection of a significant part of the production.
- The cable keystone angle has been lowered from 0.55° to 0.40° to reduce the critical current degradation below the 5% specified value. This entails a minor change in the cross-section, keeping the same 4 blocks with the same number of turns per block. The short model program will have ~10 coils with the first cross-section, and from 2015 the new cross-section will be produced.
- A strand RRR larger than 150, and a Cu/no Cu ratio of 1.2 (54.5% of copper in the strand). The cable has S2TM glass braided insulation, whose thickness is 145 μm at 5 MPa before reaction. The cable contains a 12-mm-wide, 25-μm-thick stainless steel core to control and reduce the dynamic effects.

Coil, current density, and margin: with two layers one can reach the operational gradient of 132.6 T/m at 78% of the short sample limit on the load line (i.e. 22% of load line margin). Each layer has a copper wedge to tune field quality.

Lengths and transverse size: the triplet is made of Q1 and Q3 magnets, each unit requiring a magnetic length of 8.4 m; plus Q2a and Q2b, each one with a 7.15-m-long magnetic length. The US-LARP collaboration, in charge of Q1 and Q3 development, has proposed splitting both Q1 and Q3 into two 4.2-m-long magnets assembled in the same cold mass. The Q1, Q2, and Q3 cross-sections are identical, and make use of the same design, technologies, and components. These lengths refer to the new operational gradient of 132.6 T/m, described in the previous section. The first long prototype of Q1/Q3 will have a length of 4.0 m (previous design), while the successive prototypes will all be 4.2 m long. The Q2a/b will have the length of 7.15 m already in the first prototype. The cold mass cross-section has a 630 mm diameter, i.e. 60 mm more than the LHC dipoles including the stainless steel vessel.

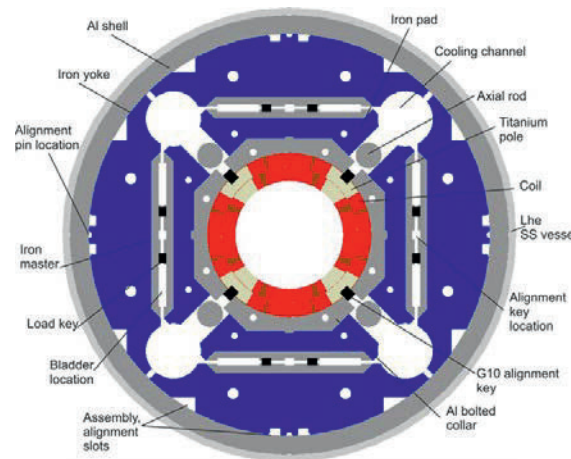


Figure 3-4: Sketch of triplet quadrupole magnet cross-section.

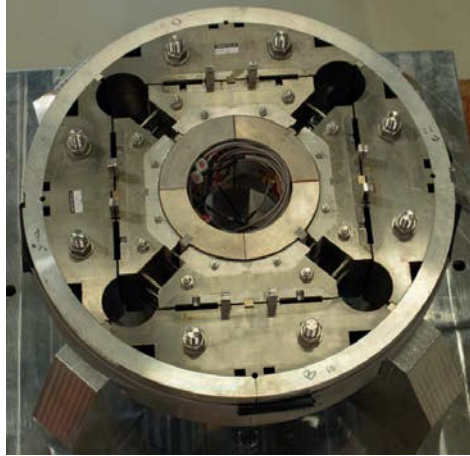


Figure 3-5: 200 mm slice of MQXF used to test assembly procedures and validate mechanical structure.

Mechanical structure: the quadrupole makes use of a shell-based structure developed at LBNL and within the LARP collaboration with a series of short models called TQS [11]. The structure scale-up to a length of 3.4 m, was demonstrated in the LARP LR and LQ quadrupole models [12], and features to assure alignment in operational conditions have been included in the 120 mm aperture HQ short model quadrupole [13]. The MQXF cross-section is a scaling up of the HQ design. Coils are mainly pre-stressed by the Al shell during cool-down, acting as the structure to contain the Lorentz forces during powering up. The level of stress is fine-tuned during the loading of the coil, which is done at room temperature using water-pressurized bladders and interference keys. Typically one has ~ 70 MPa of azimuthal coil compression at room temperature, which becomes ~ 150 MPa at 1.9 K thanks to the interplay of the thermal contractions of the different components. The structure keeps the coil under compression up to the ultimate current, corresponding to 143.2 T/m (8% above nominal).

Protection: the energy density in the coil is ~ 0.08 mJ/mm³ (including insulation, but excluding wedges), which is $\sim 50\%$ larger than the LHC main magnets [14]. This makes quench protection challenging. Since the circuit inductance is of the order of 100 mH, only a small fraction ($\sim 5\%$) of the energy can be extracted on a dump resistor. Therefore we have to rely on quench heaters on the outer layer of the coil, and no dump resistor is included in the circuit. Quench heaters are 25 μ m stainless steel strips with a 50 μ m polyimide layer to ensure proper insulation. The heaters will have heating stations of 40 mm length, separated by 120 mm sections with lower resistance due to a 10 μ m copper cladding (see Figure 3-6, left). The width of the heating stations is 20 mm, and a 7.15-m-long magnet will have ~ 40 heating stations. Two independently powered strips will cover the two blocks of the outer layer. The typical time needed to quench the coil at nominal current is of the order of 15–20 ms following heater firing [15]. Assuming 5 ms for detection time, a validation window of 10 ms and a few ms for switch opening, this brings the hotspot temperature to ~ 350 K [16]. To reduce this value and to ensure some redundancy, we are studying the options of heaters on the inner layer, and the CLIQ system [17], recently developed at CERN, based on coil heating induced by an induced oscillating current in the magnet. For the inner layer, heating stations are also needed, with a more complex geometry since $\sim 50\%$ of the surface must be left free for heat removal. A single strip slaloms between the two blocks, with 25 mm long heating stations and 40 mm long cladding (see Figure 3-6, right). The CLIQ system has the interesting feature of acting rapidly on the inner layer, and is therefore complementary to the outer layer quench heaters, with the price of additional leads and a more complicated circuit. The integration of several units in the triplet circuit is being studied at the moment of writing this report.

INSERTION MAGNETS

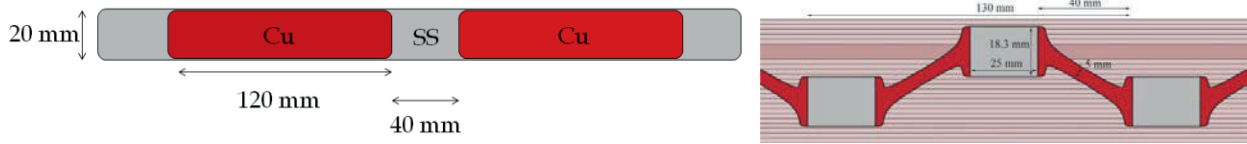


Figure 3-6: Quench heaters for the outer layer (left); a design for the inner layer (right). Stainless steel (SS) in grey and copper cladding in red. A ~300 mm long portion, out of the 4/7 m long strip, is shown.

Field quality: allowed field harmonics (b_6, b_{10}) are optimized for operation at high field, and are expected to be below one unit in absolute value. Contributions from the coil ends are also taken into account and compensated when possible through the straight part [18]. Fine-tuning of b_6 can be done in the short model phase through small changes to the coil cross-section. Random components are estimated for a 25 μm random error in the block positioning for non-allowed, and 100 μm for allowed (see Table 3-2); most critical components are low-order harmonics (b_3, a_3, b_4, a_4). To minimize these components we opted a strategy similar to that used in the RHIC magnets [19], with magnetic shims to be inserted in the bladder location [20]. This allows correcting (i) ± 5 units of b_3 ; (ii) ± 5 units of a_3 ; (iii) ± 3 units of b_4 ; (iv) ± 1 units of a_4 , for a maximum of two harmonics at the same time, through an asymmetric magnetic shimming.

Table 3-2: Expected field quality in the triplet, multipoles in units at 50 mm reference radius.

Normal	Straight part										Ends		Integral				
	Systematic					Uncertainty		Random			CS	NCS	Q1/Q3		Q2a/b		
	Geometric	Ass. & cool	Saturation	Persistent	Injection High Field	Injection High Field	Injection High Field	Injection High Field	Injection High Field	Injection High Field			Injection High Field	Injection High Field	Injection High Field		
2																	
3	0.000	0.000	0.000	0.000	0.000	0.000	0.820	0.820	0.820	0.820			0.000	0.000	0.000	0.000	
4	0.000	0.000	0.000	0.000	0.000	0.000	0.570	0.570	0.570	0.570			0.000	0.000	0.000	0.000	
5	0.000	0.000	0.000	0.000	0.000	0.000	0.420	0.420	0.420	0.420			0.000	0.000	0.000	0.000	
6	-2.200	0.900	0.660	-20.000	-21.300	-0.640	1.100	1.100	1.100	1.100	8.943	-0.025	-16.692	0.323	-18.593	-0.075	
7	0.000	0.000	0.000	0.000	0.000	0.000	0.190	0.190	0.190	0.190			0.000	0.000	0.000	0.000	
8	0.000	0.000	0.000	0.000	0.000	0.000	0.130	0.130	0.130	0.130			0.000	0.000	0.000	0.000	
9	0.000	0.000	0.000	0.000	0.000	0.000	0.070	0.070	0.070	0.070			0.000	0.000	0.000	0.000	
10	-0.110	0.000	0.000	4.000	3.890	-0.110	0.200	0.200	0.200	0.200	-0.189	-0.821	3.119	-0.175	3.437	-0.148	
11	0.000	0.000	0.000	0.000	0.000	0.000	0.026	0.026	0.026	0.026			0.000	0.000	0.000	0.000	
12	0.000	0.000	0.000	0.000	0.000	0.000	0.018	0.018	0.018	0.018			0.000	0.000	0.000	0.000	
13	0.000	0.000	0.000	0.000	0.000	0.000	0.009	0.009	0.009	0.009			0.000	0.000	0.000	0.000	
14	-0.790	0.000	-0.080	1.000	0.210	-0.870	0.023	0.023	0.023	0.023	-0.545	-1.083	0.033	-0.856	0.106	-0.862	
Skew																	
2									10.000	10.000	-31.342		-2.985	-2.985	-1.753	-1.753	
3	0.000	0.000	0.000	0.000	0.000	0.000	0.650	0.650	0.650	0.650			0.000	0.000	0.000	0.000	
4	0.000	0.000	0.000	0.000	0.000	0.000	0.650	0.650	0.650	0.650			0.000	0.000	0.000	0.000	
5	0.000	0.000	0.000	0.000	0.000	0.000	0.430	0.430	0.430	0.430			0.000	0.000	0.000	0.000	
6	0.000	0.000	0.000	0.000	0.000	0.000	0.310	0.310	0.310	0.310	2.209		0.210	0.210	0.124	0.124	
7	0.000	0.000	0.000	0.000	0.000	0.000	0.190	0.190	0.190	0.190			0.000	0.000	0.000	0.000	
8	0.000	0.000	0.000	0.000	0.000	0.000	0.110	0.110	0.110	0.110			0.000	0.000	0.000	0.000	
9	0.000	0.000	0.000	0.000	0.000	0.000	0.080	0.080	0.080	0.080			0.000	0.000	0.000	0.000	
10	0.000	0.000	0.000	0.000	0.000	0.000	0.040	0.040	0.040	0.040	0.065		0.006	0.006	0.004	0.004	
11	0.000	0.000	0.000	0.000	0.000	0.000	0.026	0.026	0.026	0.026			0.000	0.000	0.000	0.000	
12	0.000	0.000	0.000	0.000	0.000	0.000	0.014	0.014	0.014	0.014			0.000	0.000	0.000	0.000	
13	0.000	0.000	0.000	0.000	0.000	0.000	0.010	0.010	0.010	0.010			0.000	0.000	0.000	0.000	
14	0.000	0.000	0.000	0.000	0.000	0.000	0.005	0.005	0.005	0.005	-0.222		-0.021	-0.021	-0.012	-0.012	
	Magnetic length straight part				Q1/Q3	3.459	Q2a/b	6.409	Mag. Len. Ends	0.400	0.341						

Cooling: The magnet is in a static bath of pressurized HeII, with a welded stainless-steel shell placed outside the Al structure acting as a helium vessel. Cooling is ensured via two heat exchangers of 68 mm inner diameter, in which a saturated HeII bath is formed, housed in the 77 mm diameter holes of the iron located in the upper part, see Figure 3-4 [21]. The heat exchanger cools the triplet and the short orbit correctors MCBXFB, with the separation dipole and corrector package on a different circuit (see Section 3.1.1 for more details). With this design, one can comfortably remove ~800 W of heat load from the triplet, i.e. 675 W on the cold mass given by debris (see Table 3-1), plus a 125 W budget for other loads (among them the 25 W load of collision debris ending on interconnections), at the ultimate peak luminosity. For the Nb-Ti coils in the LHC, the peak heat deposition target was set at 4 mW/cm^3 ; this has a factor of 3 safety on 12 mW/cm^3 , which was considered to be the hard limit. Later experience showed that the hard limit is at least a factor of two larger. In the HL-LHC, thanks to the tungsten shielding, we are always below the 4 mW/cm^3 target, as shown in Table 3-1. The Nb_3Sn superconductor in the present MQXF design is expected to have a peak power limit of the order of 50 mW/cm^3 , i.e. one order of magnitude larger than the load in HL-LHC. The heat loads from the coils, from the

cold mass and from the beam-pipe area can only be evacuated to the two heat exchangers by means of pressurized HeII. To this aim the cold mass design incorporates the required helium passages: 1.5 mm annular spacing between cold bore and inner coil-block, and free passage through the coil pole and subsequent G10 alignment key. The free passage needed through the coil pole and G10 alignment key in the transverse direction is given by 8 mm diameter holes repeated every 50 mm.

Cryostat: independent cryostats are used for Q1, Q2a, Q2b, and Q3. The Q1 and Q3 cryostats contain two 4.2-m-long magnets. The Q2a and Q2b cryostats contain each one 7.15-m-long magnet plus the orbit correctors described below. The cryostat size should be able to accommodate the cold mass, the thermal shielding, and the cooling pipes. First estimates show that the LHC standard vacuum vessel size of 980 mm (including flanges) is a tight fit for all of these components. To solve this problem, we use asymmetric centering to make room for the piping in the upper part of the cryostat (see Figure 3-7).

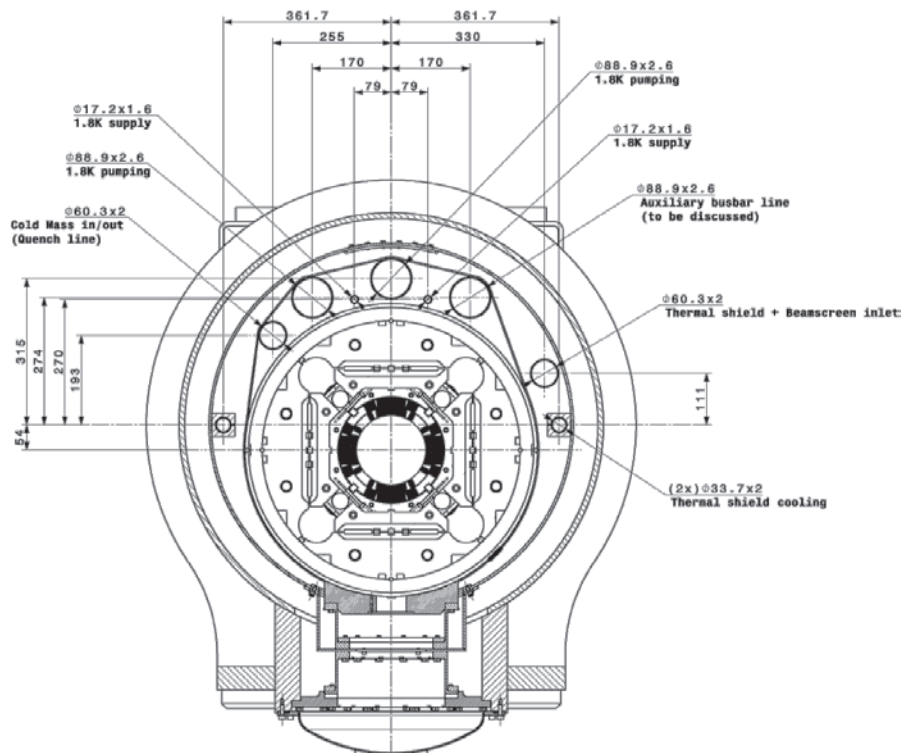


Figure 3-7: Cross-section of the cryostat.

3.3 Orbit correctors

Function and operational modes: the orbit correctors are single-aperture magnets. Two versions are required, providing 2.5 T·m and 4.5 T·m integrated fields. To have a more compact layout in this region where longitudinal space affects performance, a nested design has been adopted, with the horizontal and vertical dipole coil in the same cross-section (see Figure 3-8). The field in each plane has been limited to 2.1 T, giving a maximum combined field of 3 T. Powering will be allowed in a square in the horizontal/vertical plane, with both positive and negative currents. These magnets generate the crossing angle and correct the quadrupole misalignment. Orbit correctors are being developed by CIEMAT [23].

Cable: the 4.5-mm-wide Nb-Ti cable developed for the SLHC corrector [24] has been adopted. This is based on a 0.48 mm diameter strand, arranged in a Rutherford cable with 18 strands.

Coil, current density and margin: with two-layer coils per dipole direction, it can reach the operational field of 2.1 T simultaneously in both planes at less than 50% of the load line. The two layers allow to increase the margin and to lower the operational current.

Lengths and transverse size: the magnetic length is 1.2 m for the short version (MCBXFB) and 2.2 m for the long one (MCBXFA). The magnet cross-section has a 630 mm diameter, including the stainless steel helium vessel (not shown in Figure 3-8), i.e. as in the HL-LHC triplet.

Mechanical structure: the magnet makes use of self-supporting collars. Stainless steel collars are used for keeping the inner and outer coils in place. Their thickness is 25 mm. Due to the nested coil arrangement, a complex collaring based on two consecutive steps (first the inner, then the outer) is needed. The inner collars are closed with two round pins; the outer ones will be kept in place by four prismatic keys. A particular difficulty is that when both horizontal and vertical coils are powered, Lorentz forces push the inner coil towards the centre of the aperture: this could require a structure between the inner coil of the inner dipole and the cold bore to prevent movement. Since the size of this movement is at the limit of what is tolerable, a titanium tube could be inserted to prevent motion, given that its contraction coefficient is lower than those of the other materials. This feature will be tested on the first prototype.

Protection: The magnet can be protected via quench heaters or energy extraction. A cost and risk analysis is under way to select one of these two options.

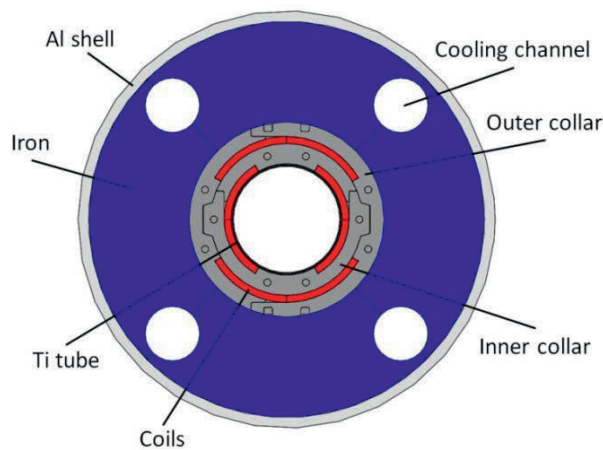


Figure 3-8: Sketch of orbit corrector cross-section (short version MCBXFB, in the cold mass of the triplet magnets Q2a and Q2b).

3.4 High-order correctors

Function, design and operational modes: The high-order correctors (skew quadrupole, normal and skew sextupole, octupole, decapole, and dodecapole) are specified on the expected field quality and alignment errors (see Chapter 2), with a safety factor of 2 for the quadrupole, sextupole, and octupole, and 1.5 for the decapole and dodecapole. The magnets will operate with nominal settings based on the measured field errors of the triplet and of the separation dipole. To ease operation, a non-nested layout (see Figure 3-9) has been adopted, using a superferric technology (see Figure 3-10 and Figure 3-11), already developed for the SLHC-PP [25]. Nb-Ti racetrack coils provide the ampere-turns, with iron giving the required field shape. The aperture is 150 mm, as for the triplet and D1. The high-order correctors are being developed by LASA laboratories of INFN-Milano.

Cable: the cable is a single Nb-Ti strand, of 0.7 mm diameter for the quadrupole and of 0.5 mm diameter for the higher order multipoles. Insulation is made with a 0.07 mm thick S2 glass. Ground insulation is added on the external side of the coil.

Coil, current density, and margin: we chose to operate at 40% on the load line. The optimized current density is of the order of 300 A/mm² [26], with peak fields on the coil in the range 2.0–2.3 T for the nonlinear correctors and 3.0 T for the skew quadrupole (see Table 3-3). Coils are dry-wound and then vacuum impregnated with CTD-101[®]. Currents are in the range of 120-180 A. An iteration of the design is ongoing to bring all these

currents below 105 A, thus allowing using 120 A power converters already developed for the LHC. This change can be done either using a larger coil or a wire with smaller diameter.

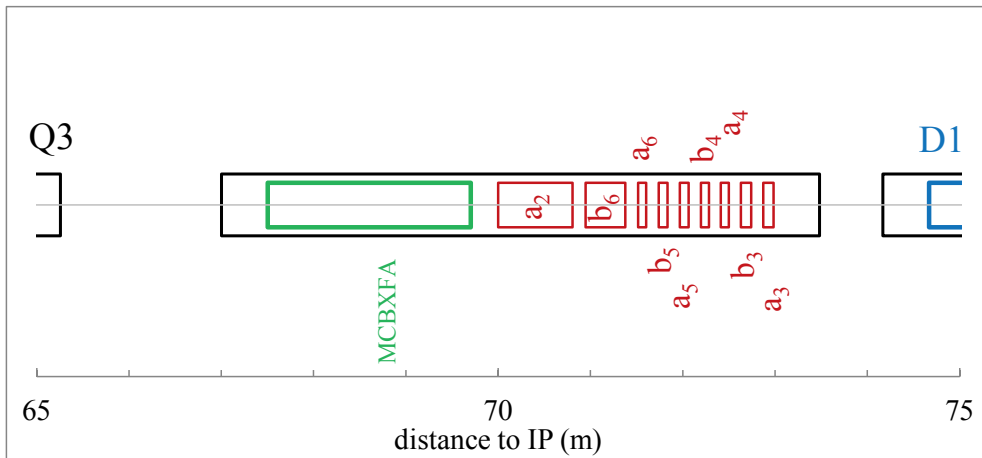


Figure 3-9: Layout of the corrector region.

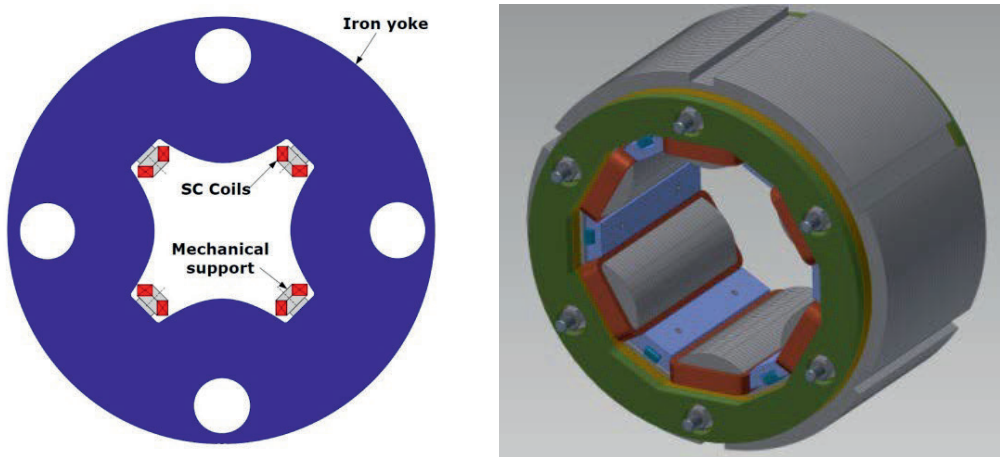


Figure 3-10: Cross-section of the skew quadrupole (left, with obsolete position of cooling holes at 90°) and 3D view of a sextupole (right).

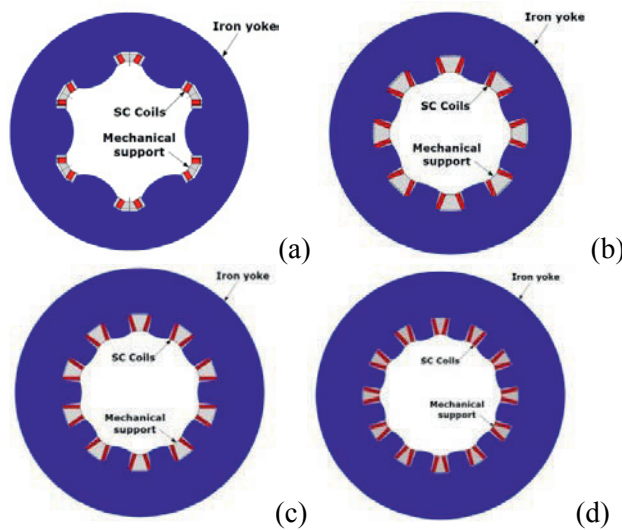


Figure 3-11: Sketch of nonlinear corrector cross-sections of (a) normal sextupole; (b) normal octupole; (c) normal decapole; (d) normal dodecapole correctors.

Lengths and transverse size: the magnet coil lengths are ~0.1 m for the sextupole, octupole, decapole, and skew dodecapole (see Table 3-3). The normal dodecapole and the skew sextupole require greater strengths, giving a coil length of ~0.45 m and ~0.84 m, respectively. The skew quadrupole needs a 460 mm diameter iron yoke that has to include the cooling holes for the D1 heat exchanger and orbit corrector. The nonlinear correctors can have an iron yoke diameter of 320 mm, which fits inside the cooling holes. Spacers are required to match the transverse size of the correctors to the same value of the MCBXFA orbit correctors, and to maintain alignment within the cold mass. Heat exchangers will go through these spacers to cool the whole cold mass.

Mechanical structure: the mechanical support for the correctors coils are under study. The forces are of the order of 60 kN/m for the quadrupole and 10–30 kN/m for the other magnets.

The main parameters of the correctors are given in Table 3-3.

Table 3-3: Overview of the main parameters of the triplet corrector magnets.

	Unit	MCQSX	MCSX/MCSSX	MCOX/MCOSX	MCDX/MCDSX	MCTX	MCTSX
Order		2	3	4	5	6	6
Aperture	[mm]	150	150	150	150	150	150
Integrated strength¹	[T m]	1.000	0.063	0.046	0.025	0.086	0.017
Coil length²	[mm]	841	123	99	107	449	102
Gradient	[T/m ⁿ⁻¹]	25	11	3690	50600	640000	613000
Number of apertures		1	1	1	1	1	1
Number of circuits		1	2	2	2	1	1
Units needed		4	8	8	8	4	4
Spares		2	4	4	4	2	2
Cable data							
Strand diameter	[mm]	0.700	0.500	0.500	0.500	0.500	0.500
Insulation thickness	[mm]	0.070	0.070	0.070	0.070	0.070	0.070
Cu/No_Cu		2.3	2.3	2.3	2.3	2.3	2.3
Coil design							
Material		Nb-Ti	Nb-Ti	Nb-Ti	Nb-Ti	Nb-Ti	Nb-Ti
N. turns/pole		320	214	344	256	154	172
Cable length/pole	[m]	604	79	88	67	144	42
Operational parameters							
Coil peak field	[T]	2.97	2.33	2.41	2.34	2.04	2.01
Temperature	[K]	1.9	1.9	1.9	1.9	1.9	1.9
Current	[A]	182	132	120	139	167	157
j overall³	[A/mm ²]	303	353	314	360	259	284
Loadline fraction		0.60	0.60	0.60	0.60	0.60	0.60
Differential inductance	[mH]	1247	118	152	107	229	52
Stored energy	[kJ]	24.6	1.24	1.41	1.39	4.35	0.92
Dose and heat load							
Heat load cold mass	[W]	70					
Heat load beam screen	[W]	45					
Peak dose	[MGy]	35					

¹Integrated strength is defined as the field at the 50 mm reference radius times the magnetic length.

²Coil length refers to the physical coil length, and not to magnetic length.

³The overall current density includes 0.07 mm thick strand insulation and the coil ground insulation.

3.5 Separation dipole D1

Function and operational modes: the separation dipole is ramped with the energy of the LHC, and is constant during squeeze. On each side of the IP, D1 is individually powered. The option of powering D1 in series with D2 is considered since, notwithstanding different operational fields, their nominal currents turn out to be the same within 1%. In this case, allowing to reduce both the number of power converters and the total current of the links, a fine tuning of D2 magnetic length will be done to have agreement of the D1 and D2 nominal currents within 0.01%. The separation dipole is being developed by KEK.

Cable: the 15-mm-width Nb-Ti cable used for the outer layer of the main LHC dipole is adopted. The required unit length is smaller than the main LHC dipole outer cable unit length (780 m).

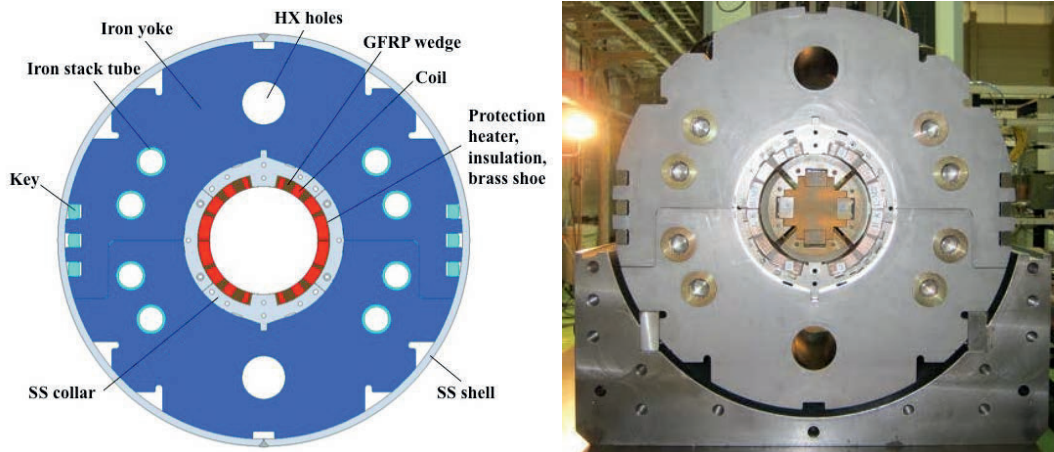


Figure 3-12: Sketch of separation dipole cross-section (left) and yoking test (right).

Coil, current density and margin: for the initial choice of 70% operational level, the magnet length was slightly longer than the KEK test station [8, 27]. We therefore fixed the operational current at 76% of the load line, with a bore field of 5.6 T. This allows fitting the vertical test station without significantly increasing the risk related to the lower margin.

Lengths and transverse size: Magnetic length is 6.27 m. The magnet cross-section has a 570 mm diameter, including the stainless steel vessel, i.e. the same as the LHC dipoles. A larger diameter has been excluded to be able to reuse the yoking tooling used for J-PARC at KEK.

Mechanical structure: Forces are contained by the iron yoke, with thin spacers between the iron and the coil, as the J-PARC [28], RHIC magnets [29], and LHC Q1/Q3 [30]. Here the pre-stress is given by the iron laminations, horizontally split, that are locked through keys (see Figure 3-12). A thin stainless-steel collar acts as a spacer between the coil and the iron yoke. An alignment notch at 90° and 270° has been added after a first collaring test. An average pre-stress of 90 MPa is given at room temperature during the so-called ‘yoking’. During cool-down the pre-stress lowers to 70 MPa, which is enough to counteract the Lorentz forces during powering.

Protection: the initial baseline of protection through a dump resistor has been changed to quench heaters due to the lower cost. Simulations show that with LHC dipole-like quench heaters the hotspot temperature in the adiabatic approximation is 220 K for the nominal current of 12 kA. CLIQ [17] is also considered as an alternative option.

Field quality: the main issue here is the saturation component [8], which is optimized via the iron shaping (see Table 3-4). Following the analysis given in Refs. [31, 32], the random components are estimated through random positioning of the coil block with different amplitudes for each family of harmonics, namely 40 μm for the allowed b_{2n+1} , 30 μm for the even skew a_{2n} , 15 μm for the odd skew a_{2n+1} , and 10 μm for the even normal multipoles b_{2n} .

Cooling: the magnet is in a static bath of pressurized HeII, with a stainless steel shell acting as a helium vessel. First baseline, showed in Figure 3-12, had cooling is ensured via two heat exchangers, of 49 mm inner diameter, housed in the 60 mm diameter holes through the iron. Later studies on interconnection proved that the heat exchanger position should be the same as in the triplet. An iteration on the yoke design is ongoing at the moment of writing.

Cryostat: the cryostat has the same geometry as the triplet cryostat (see Figure 3-7).

Table 3-4: Expected field quality of D1, multipoles given in units at 50 mm reference radius. Straight part.

Normal	Systematic					Uncertainty		Random	
	Geometric	Saturation	Persistent	Injection	High Field	Injection	High Field	Injection	High Field
2	0.000	0.000	0.000	0.000	0.000	0.200	0.200	0.200	0.200
3	-1.800	0.900	-14.200	-16.000	-0.900	0.727	0.727	0.727	0.727
4	0.000	0.000	0.000	0.000	0.000	0.126	0.126	0.126	0.126
5	0.500	-0.500	-1.000	-0.500	0.000	0.365	0.365	0.365	0.365
6	0.000	0.000	0.000	0.000	0.000	0.060	0.060	0.060	0.060
7	1.600	-1.200	-0.700	0.900	0.400	0.165	0.165	0.165	0.165
8	0.000	0.000	0.000	0.000	0.000	0.027	0.027	0.027	0.027
9	-0.680	0.090	0.020	-0.660	-0.590	0.065	0.065	0.065	0.065
10	0.000	0.000	0.000	0.000	0.000	0.008	0.008	0.008	0.008
11	0.440	0.030	0.000	0.440	0.470	0.019	0.019	0.019	0.019
12	0.000	0.000	0.000	0.000	0.000	0.003	0.003	0.003	0.003
13	0.000	0.000	0.000	0.000	0.000	0.006	0.006	0.006	0.006
14	0.000	0.000	0.000	0.000	0.000	0.001	0.001	0.001	0.001
15	-0.040	0.000	0.000	-0.040	-0.040	0.002	0.002	0.002	0.002
Skew									
2	0.000	0.000	0.000	0.000	0.000	0.679	0.679	0.679	0.679
3	0.000	0.000	0.000	0.000	0.000	0.282	0.282	0.282	0.282
4	0.000	0.000	0.000	0.000	0.000	0.444	0.444	0.444	0.444
5	0.000	0.000	0.000	0.000	0.000	0.152	0.152	0.152	0.152
6	0.000	0.000	0.000	0.000	0.000	0.176	0.176	0.176	0.176
7	0.000	0.000	0.000	0.000	0.000	0.057	0.057	0.057	0.057
8	0.000	0.000	0.000	0.000	0.000	0.061	0.061	0.061	0.061
9	0.000	0.000	0.000	0.000	0.000	0.020	0.020	0.020	0.020
10	0.000	0.000	0.000	0.000	0.000	0.025	0.025	0.025	0.025
11	0.000	0.000	0.000	0.000	0.000	0.007	0.007	0.007	0.007
12	0.000	0.000	0.000	0.000	0.000	0.008	0.008	0.008	0.008
13	0.000	0.000	0.000	0.000	0.000	0.002	0.002	0.002	0.002
14	0.000	0.000	0.000	0.000	0.000	0.003	0.003	0.003	0.003
15	0.000	0.000	0.000	0.000	0.000	0.001	0.001	0.001	0.001

3.6 Recombination dipole D2

Function and operational modes: the recombination dipole is ramped with the energy of the LHC, and is constant during squeeze. The two D2 apertures are in series. In D2, the fields point in the same direction in both apertures; this makes field quality control much more challenging than in the LHC dipoles, where the fields point in opposite directions. The design of the recombination dipole is being studied by INFN-Genova, that is also in charge of the model and prototype construction.

Cable: the 15-mm-wide Nb-Ti cable used for the outer layer of the main LHC dipole is adopted. The required unit length is not longer than that of the LHC main dipole’s outer layer unit length (780 m).

Coil, current density and margin: we selected a conservative margin, operating at 65% of the load line with a 15 mm width coil, and an operational field of 4.5 T. In these conditions, the approach used in the present D2 design, that is using iron to magnetically decouple the two apertures, leads to large saturation effects. An alternative approach using left–right asymmetric coils was therefore adopted [33] to compensate for the cross-

talk between the two apertures (see Figure 3-13). A very careful optimization is needed to find the best solution. After several iterations, a cross-section was found where the left–right asymmetry is only given by the angles of the blocks, but the number of cables per block is the same [34]. This allows for much simpler coil heads.

Lengths and transverse size: the magnetic length is 7.78 m. The magnet requires an adequate iron thickness to reduce the fringe field. An elliptical iron yoke is proposed, of 570 mm vertically and 630 mm horizontally.

Mechanical structure: The accumulation of Lorentz forces corresponds to a pressure in the midplane of about 40 MPa. A self-supporting stainless-steel collar, one per aperture, is considered. The two apertures are then inserted in a Al skin providing the relative alignment. The whole pack is inserted in the iron. Peak stress during collaring is of the order of 100 MPa [35].

Protection: protection will be based on quench heaters using the standard LHC dipole technology (used also in D1). Hotspot temperature is estimated to be below 250 K.

Field quality: this is the main issue for this magnet: the square design of the central aperture in the iron is imposed by field quality optimization, namely the reduction of the field harmonics due to saturation. Cross-talk is optimized via the asymmetric cross-section, and the saturation through an iron shaping. The field quality estimate is given in Table 3-5.

Table 3-5: Expected field quality of D2, multipoles given in units at 35 mm reference radius.

Normal	Straigh part									Ends		Integral	
	Systematic					Uncertainty		Random		CS	NCS	Injection	High Field
	Geometric	Saturation	Persistent	Injection	High Field	Injection	High Field	Injection	High Field				
2	-0.800	1.800	0.000	-0.800	1.000	0.200	0.100	0.200	0.100	94.000	-64.800	2.118	3.729
3	-2.400	3.000	-14.000	-16.400	0.600	0.727	0.300	0.727	0.300	2.500	0.200	-14.524	0.697
4	0.800	-0.400	0.000	0.800	0.400	0.126	0.040	0.126	0.040	-5.500	0.800	0.419	0.060
5	0.800	-0.400	-1.000	-0.200	0.400	0.365	-0.040	0.365	-0.040	-9.600	-6.700	-1.056	-0.518
6	0.000	0.000	0.000	0.000	0.000	0.060	0.060	0.060	0.060	-0.600	1.500	0.030	0.030
7	0.200	0.100	-0.700	-0.500	0.300	0.165	0.165	0.165	0.165	-4.000	-0.200	-0.699	0.018
8	0.000	0.000	0.000	0.000	0.000	0.027	0.027	0.027	0.027	-0.700	1.000	0.002	0.002
9	0.000	0.090	0.020	0.020	0.090	0.065	0.065	0.065	0.065	-2.700	-4.200	-0.331	-0.268
10	0.000	0.000	0.000	0.000	0.000	0.008	0.008	0.008	0.008	-0.040	0.500	0.020	0.020
11	0.000	0.030	0.000	0.000	0.030	0.019	0.019	0.019	0.019	-2.500	-3.100	-0.288	-0.261
12	0.000	0.000	0.000	0.000	0.000	0.003	0.003	0.003	0.003	-1.600	1.600	-0.026	-0.026
13	0.000	0.000	0.000	0.000	0.000	0.006	0.006	0.006	0.006	-1.900	-1.900	-0.199	-0.199
14	0.000	0.000	0.000	0.000	0.000	0.001	0.001	0.001	0.001	-0.090	0.800	0.030	0.030
15	0.000	0.000	0.000	0.000	0.000	0.002	0.002	0.002	0.002	-0.070	-0.700	-0.035	-0.035
Skew													
2	0.000	0.000	0.000	0.000	0.000	0.679	0.679	0.679	0.679	-14.500	0.000	-0.878	-0.878
3	0.000	0.000	0.000	0.000	0.000	0.282	0.282	0.282	0.282	0.500	0.000	0.030	0.030
4	0.000	0.000	0.000	0.000	0.000	0.444	0.444	0.444	0.444	5.500	0.000	0.333	0.333
5	0.000	0.000	0.000	0.000	0.000	0.152	0.152	0.152	0.152	-1.000	0.000	-0.061	-0.061
6	0.000	0.000	0.000	0.000	0.000	0.176	0.176	0.176	0.176	-1.400	0.000	-0.085	-0.085
7	0.000	0.000	0.000	0.000	0.000	0.057	0.057	0.057	0.057	0.000	0.000	0.000	0.000
8	0.000	0.000	0.000	0.000	0.000	0.061	0.061	0.061	0.061	0.200	0.000	0.012	0.012
9	0.000	0.000	0.000	0.000	0.000	0.020	0.020	0.020	0.020	0.200	0.000	0.012	0.012
10	0.000	0.000	0.000	0.000	0.000	0.025	0.025	0.025	0.025	-0.200	0.000	-0.012	-0.012
11	0.000	0.000	0.000	0.000	0.000	0.007	0.007	0.007	0.007	-0.100	0.000	-0.006	-0.006
12	0.000	0.000	0.000	0.000	0.000	0.008	0.008	0.008	0.008	0.000	0.000	0.000	0.000
13	0.000	0.000	0.000	0.000	0.000	0.002	0.002	0.002	0.002	0.000	0.000	0.000	0.000
14	0.000	0.000	0.000	0.000	0.000	0.003	0.003	0.003	0.003	0.000	0.000	0.000	0.000
15	0.000	0.000	0.000	0.000	0.000	0.001	0.001	0.001	0.001	0.000	0.000	0.000	0.000
Magnetic length straight part					6.966				Mag. Len. Ends	0.471	0.343	Total length	7.78

Cooling: the magnet is in a static bath of pressurized HeII. Cooling is ensured via two heat exchangers, of 51 mm diameter, housed in a 60 mm diameter hole in the iron, located in the upper part.

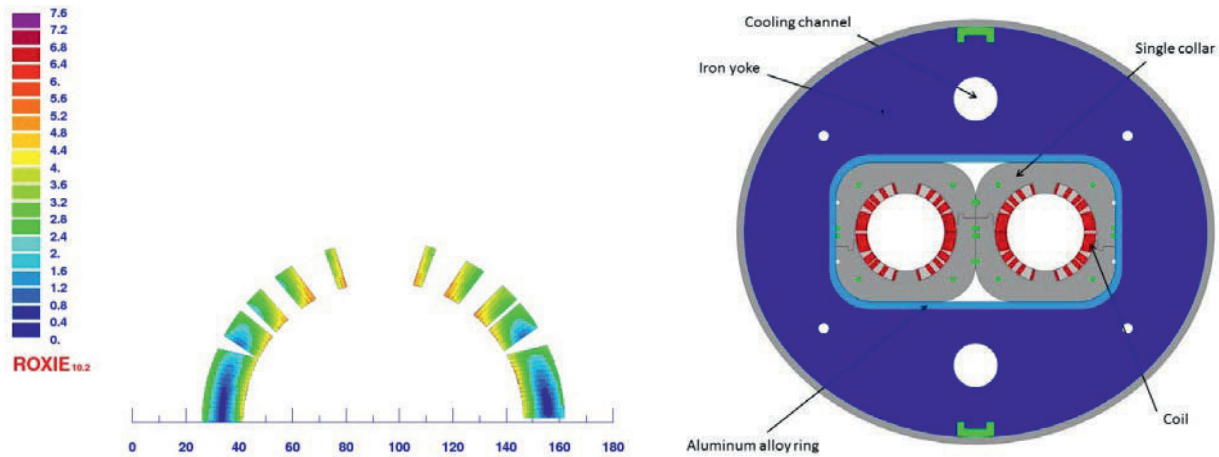


Figure 3-13: Sketch of recombination dipole cross-section. Asymmetric coil (left) and magnet cross-section (right). Note the elliptical shape of the yoke.

3.7 D2 correctors

Function and operational modes: D2 needs orbit correctors for each beam and each plane (horizontal and vertical), with an integrated strength of 5 T·m, and an aperture of 105 mm. These correctors are used to control the crossing angle and to correct the closed orbit, and therefore they should be powered in any configuration. The large electromagnetic coupling and the stringent field quality requirement (for all combinations of currents) limit the main field to 2.65 T; this gives a magnetic length is 1.89 m. Horizontal and vertical correctors share the same longitudinal position for beam 1 and 2 respectively, and are followed by a vertical (beam1) and horizontal (beam2) corrector. In this configuration the magnetic cross-talk is less severe than in a case with horizontal-horizontal (or vertical/vertical) correctors in both beams (see Figure 3-14). These requirements make the D2 corrector as the ideal test bed for the canted cos-theta design, which provides the advantage of low operational current, and simple components and assembly procedures [36]. It will be the first time that a magnet based on this design will be used in a high energy physics accelerator.

Cable, current density, and margin: First concepts consider with a single wire wound on 5 layers, with the 0.825 mm strand of the LHC outer layer cable. This gives an operational field of 2.6 T, peak field of 3.1 T, and an operational current below 500 A, and a loadline margin of 50%.

Field quality: the challenge in these magnets is the cross-talk between the apertures. Since for D2 the beam distance is 188 mm, and the aperture is 105 mm, little space is left for the iron to decouple the two apertures [37]. No optimization can be made through the coil cross-section as is the case in D2, since these magnets have to be powered with any combination of currents. The solution is to keep a thin coil, and to maximize the iron thickness. Requirements on field quality are stringent, especially on b_3 where the tolerance is of the order of 1.5 units.

Cooling: the magnets will share cooling with D2, so will have heat exchangers in the same position.

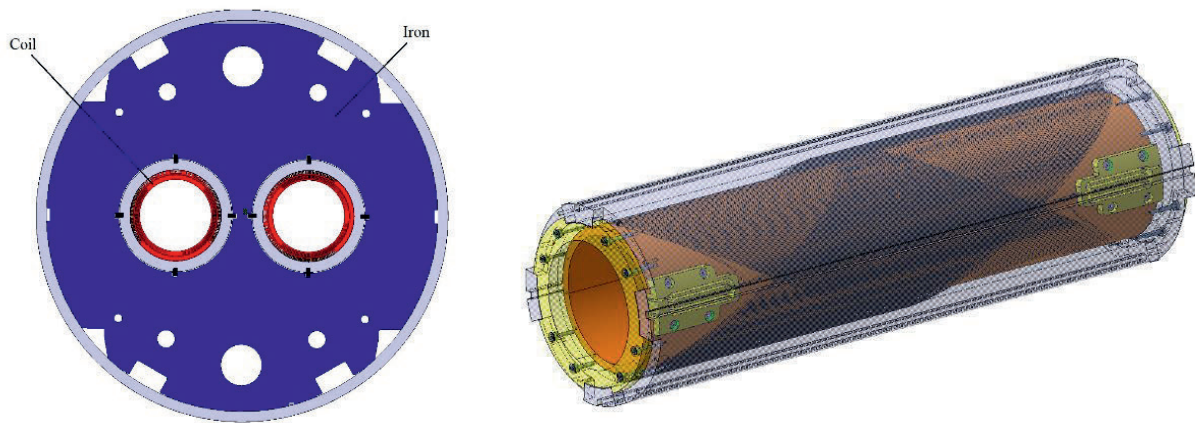


Figure 3-14: Cross-section of D2 orbit corrector (left) and 3D view of the short model coil (right).

3.8 Q4, Q5 and Q6

The Q4 magnet will be the LHC 70 mm aperture MQY [38]. As for D2, orbit correctors of 5 T·m integrated field in H and V respectively are needed: the MCBY correctors provide 2.7 T·m at 1.9 K, so two of them in each plane are needed. The magnet Q4 could work at 4.5 K, since the integrated gradient satisfies the 440 T requirement, but in this case we would need three MCBY per plane. For this reason the operational temperature is fixed at 1.9 K. Four new cold masses (two per IP side) will be built, each one containing one MQY and two MCBYH and two MCBYV (see Figure 3-1).

The present LHC Q4 cold mass will be reused as Q5, with a modification to make it able to operate at 1.9 K. This allows to satisfy the integrated gradient requirement of 680 T, with 200 T/m operational gradient, an operational current of 4510 A and 20% margin on the loadline. As for Q4, apertures of Q5 are independently powered. The four new Q5 cold masses also contain three MCBY correctors, see Figure 3-1. They will be recovered from IP1 and IP5 in the Q4 position during LS3, modified and installed in Q5 location.

The Q6 magnet will not be modified, and will be operated at 4.5 K as it is today in the LHC.

For Q4, a 90 mm aperture magnet is also under study; this magnet, called MQYY, is not in the baseline, but it is included in the R&D part of the project. This would give more aperture margin, required for the flat beams operational mode. A short model will be developed by CEA-Saclay [39], and two prototypes will be built by industry within the QUACO EU supported initiative based on the Pre-Commercial Procurement (PCP) scheme (Grant Agreement no. 689359). The magnet will be a scale up of the MQM LHC magnet, with two layers coil, separate mechanical structure based on collars, 4 kA operational current and 20% margin on the loadline. IT would provide 120 T/m over a magnetic length of 3.67 m to satisfy the beam dynamics requirement of 440 T integrated gradient. A cross-section is shown in Figure 3-15.

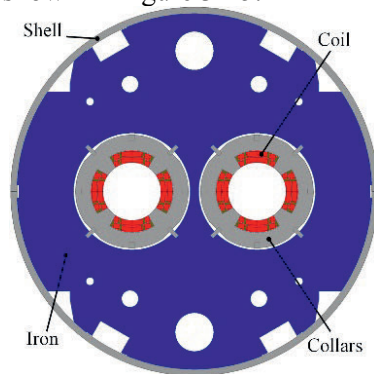


Figure 3-15: MQYY 90 mm aperture cross-section.

3.9 Other interventions: Sextupole (MS) in Q10 and Q5 in IR6

The four cold masses of Q10 around IP1 and IP5 require a modification to include a lattice sextupole (MS) corrector.

For Q5 in IR6, an increase in the strength is needed; in the LHC the cold mass includes a MQY units operating at 4.5 K, giving an integrated gradient of 544 T. First option considered the use of a new cold mass with two MQY, operating at 4.5 K, doubling the integrated gradient. Later on, the option of a simple increase of gradient from 544 to 680 T through lowering the operational temperature to 1.9 K has been retained. This has the advantage of not requiring two additional MQY, and reusing the present cold mass with a simple modification to make it able to operate at 1.9 K, as done for the Q5. Modifications of the QRL service modules will be necessary, too.

3.10 Resistive magnets

Few of the MBW and MQW in IR3 and IR7 will have in the HL LHC era a radiation dose above the safe limit [40]. Besides some consolidation actions taken to make these magnets able to survive the expected integrated luminosity of the LHC, four MQW (plus two spares) able to resist the radiation dose will be built and installed in LS3. For MBW, four magnets will be refurbished with new radiation resistant coils and installed in LS3. This action, increasing reliability, will also reduce the risk to expose workers to the high dose in this area in case of unforeseen maintenance.

3.11 Powering

The powering is from the non-IP side of D1, allowing a more compact layout with respect to the LHC, where this is done through a distribution feedbox taking a few metres between the triplet and D1. This choice improves performance at the price of having triplet and corrector cables going through (or along) the separation dipole. The second important choice is that magnets are fed by a superconducting link: therefore the transition from superconducting to resistive leads is displaced from the LHC tunnel to the new underground service gallery UR (Chapter 15). The baseline of the powering scheme of the triplet is shown in Figure 3-16, with Q1 Q2a, Q2b and Q3 in series on one 18 kA power converter, plus a 2 kA trims on Q1 and Q3 and 120 A trim on Q2a, and plus the CLIQ unit cables option. Diodes are required to reduce the voltage during quench within acceptable limits.

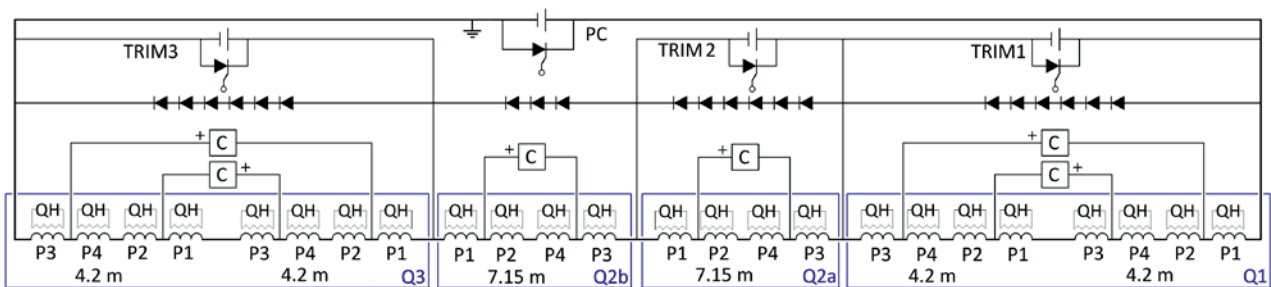


Figure 3-16: Baseline for triplet powering.

Besides the triplet, for each side of IP1 and IP5 one has two 13 kA circuit for D1 and D2, six 2 kA circuits for the orbit correctors, plus the nine correctors rated at 200 A (possibly lowered at 120 A). In the baseline case, one has a total of ~45 kA of current to bring in and out of the triplet–D1 area through the link (see Chapter 6B). The D2 is fed by a second superconducting link, bringing current to the D2, and the orbit correctors.

For the busbar the baseline is to place it inside the magnet (as in the LHC main cell), through the iron holes that are not used by the heat exchangers; two other options are also under study:

- busbar inside the cryostat, but outside the cold mass, in a separate line (as the M line in the LHC cell, carrying some correctors busbars);

- busbar outside the cryostat in a separate cryostat, in this case each magnet is fed by a bypass of the busbar cryostat.

3.12 Cooling

The whole string of magnets from Q1 to Q5 will be cooled at 1.9 K, while keeping only Q6 at 4.5 K. The static heat load on the cold mass is mainly due to collision debris: 430 W on the triplet, 75 W on the corrector package, and 135 W on the separation dipole. These numbers refer to the nominal luminosity of $5 \times 10^{34} \text{ cm}^{-2} \text{ s}^{-1}$; the system must be able to remove the heat load, without margin, at the ultimate luminosity of $7.5 \times 10^{34} \text{ cm}^{-2} \text{ s}^{-1}$. The heat load on the triplet is removed via two 68 mm inner diameter heat exchangers, ultimately providing the ability to remove up to 1000 W (see Figure 3-17). To cope with these high heat loads, an additional low pressure pumping is added between Q2a and Q2b to keep the two-phase vapour flow velocity below 7 m/s, above which the HXs would not function correctly. These heat exchangers also cool the 1.2 m long orbit corrector. Simulations show that a solution with one (or more) heat exchangers cooling the whole string triplet–D1 is not viable. Therefore, a second system of heat exchangers is used to cool the corrector package and D1. Here the baseline is to have two heat exchangers of 49 mm inner diameter, able to remove 250 W. One heat exchanger would provide only 125 W. Additional low pressure pumping is added between Q2a and Q2b.

The beam screen receives $\sim 500 \text{ W}$ in the triplet–correctors–D1 region (see Table 3-1, including 55 W from the interconnections). Given the 100 W budget for the residual effect of electron cloud, and the 50% margin for getting to ultimate luminosity, the system has to remove $\sim 1000 \text{ W}$ over 55 m, i.e. $\sim 17 \text{ W/m}$. Heat is removed at 40–60 K [41]. The cooling tubes inner diameter is $\sim 7 \text{ mm}$, due to an increase of the pressure of the helium to 18 bar. This choice is more challenging for the piping system but allows minimization of the space taken by the cooling pipes, which reduce the aperture available to the beam.

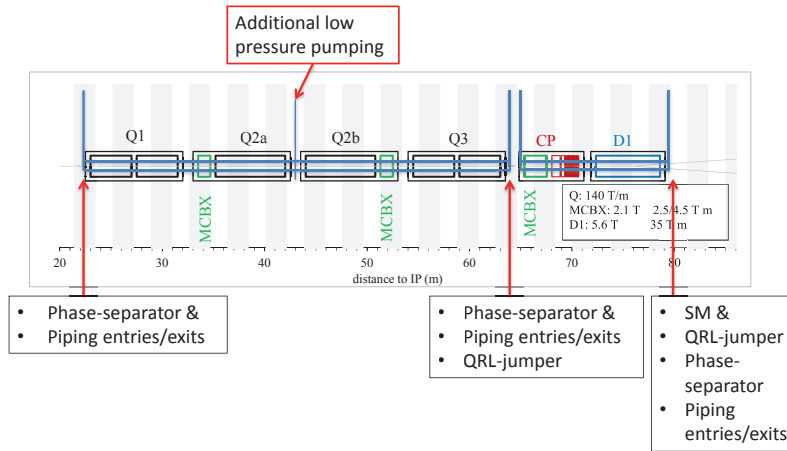


Figure 3-17: Sketch of the cooling system.

For the stand-alone magnets it has been decided to adopt a glove type of heat exchanger and not the previously adopted solution of bayonet heat exchanger. This provides more flexibility in the jumper positioning, making it independent from the slope. This choice cannot be taken for the triplet, because of the highest heat load to be evacuated. So the jumper is on the D1 side, requiring an additional return pipe.

3.13 Instrumentation

We give here a short summary of the instrumentation foreseen for the IR magnets.

- Quench protection requires voltage taps; for dipoles and quadrupoles we foresee the possibility of monitoring the voltage on each coil. Quench detection is therefore based on an analysis of the difference between signals of different coils, thus allowing cancelling of the inductive voltage.

INSERTION MAGNETS

- Beam loss monitors will be located inside the triplet cold mass to have the possibility of monitoring beam losses closer to the beam pipe and to the coil. Installation of special beam loss monitors in one of the iron holes not used by the heat exchangers or by the busbars is foreseen.
- Temperature sensors: one per cold mass, plus a spare, as in the LHC.
- Beam position monitors will be placed in the interconnections between Q1 and Q2a, Q2b and Q3, Q3 and the corrector package, and between the corrector package and D1. Moreover they will be present at positions close to D2, Q4 and Q5.

3.14 Test

In general, magnets will be tested individually in a vertical test station, and then horizontally in the final cold mass assembly within the final cryostat, with the exception of Q2 and D2 whose length does not allow vertical testing. In some cases the first test will be possible in laboratories collaborating with CERN (for instance BNL for vertical test of Q1/Q3, FNAL for horizontal test of Q1/Q3, KEK for vertical and horizontal test of D1, LASA for vertical test of correctors). The second test will be carried out at CERN. A string including the magnets from Q1 to D1 will be assembled in the CERN test facility (SM18) (See Chapter 16). Magnetic measurements at 1.9 K with the rotating coil technique will be carried out for all main magnets and for all the low-order (dipole and quadrupole) correctors.

3.15 Summary of baseline modifications with respect to the previous version of the Design Report

Major changes:

- For the Q4, one MQY magnet and four MCBY correctors will be reused from LHC to build four new cold masses, operating at 1.9 K. Therefore the aperture will be 70 mm, with respect to the 90 mm option considered in the initial phase of the project.
- The Q6 will be kept at 4.5 K operational temperature.
- The Q5 in IR6 will reuse the present cold mass, lowering operational temperature from 4.5 K to 1.9 K, providing a 680 T integrated gradient. Previous baseline was to building a new cold mass containing two MQY, with 4.5 K operational temperature and 1088 T integrated gradient.
- All dump resistors have been removed (Triplet, D1, D2), and protection relies on quench heaters. Dump resistor still considered as an option for MCBXFA and for the D2 correctors.
- The triplet will be on one 18 kA circuit with three trims, instead of on two 18 kA circuits.
- The design of D2 corrector magnet has been changed from a Rutherford cable to a canted cos theta concept, lowering the current from 3 kA to 500 A.

Fine tuning:

- The specification on the critical current of the Nb₃Sn strand has been lowered by 10% to avoid rejecting large quantities of strand. The reason is the reduction of cost (keeping the previous value would have significantly increased the strand cost).
- The operational current of the triplet has been lowered by 6.4%. The lower gradient is compensated by a 5% longer length of the magnet, with a loss of performance of the order of 1%. The reason is the reduction of risk associated to the performance of long Nb₃Sn coils. Taking into account of the gradient reduction and of the critical current reduction, the loadline margin is increased from 19% to 22%.
- The keystone angle of the cable has been reduced from 0.55° to 0.4° degrees. This gives minor changes in the angles of the four blocks making the magnet coil. Therefore we will have 10 short coils for models manufactured with a first generation cross-section using the 0.55° keystone angle cable, followed by the second generation. The reason is the reduction of critical current degradation due to cabling.

- The strength of the D2 and Q4 correctors has been increased from 4.5 to 5.0 T·m. This has been realized with a 0.30 m increase of the magnetic length, keeping the same operational field. The reason comes from the beam dynamics studies.
- The number of spares for the resistive magnets MQW have been reduce from 4 to 2, so 6 magnets plus one prototypes will be needed. We will not have new MBW magnets but new coils will be installed in the present available spares.
- The number of spares MCBXFB has been increased from 2 to 4; the number of spares sextupole, octupole and decapole correctors have been increased from 2 each to four each. In both cases the new baseline is to have enough two full IP sides as spares.
- The D2, Q4, Q5 heat exchanger design has been changed from bayonet type to glove type and the magnet will be therefore cooled by conduction.

3.16 References

- [1] O. Bruning, L. Rossi, Eds. “The High Luminosity Large Hadron Collider”, Advances Series on Directions in High Energy Physics **24**, (World Scientific, Singapore 2015). DOI: [10.1142/9581](https://doi.org/10.1142/9581)
- [2] E. Todesco *et al.*, A first baseline for the magnets in the high luminosity LHC insertion regions, *IEEE Trans. Appl. Supercond.* **24** (2014) 4003305. DOI: [10.1109/TASC.2013.2288603](https://doi.org/10.1109/TASC.2013.2288603)
- [3] G. Sabbi, Nb₃Sn IR Quadrupoles for the High Luminosity LHC, *IEEE Trans. Appl. Supercond.* **23** (2013) 4000707.
- [4] L. Rossi and E. Todesco, Electromagnetic design of superconducting quadrupoles, *Phys. Rev. Spec. Top. Accel. Beams* **9** (2006) 102401. [CERN-AT-2006-016-MCS](https://arxiv.org/abs/2006.016-MCS)
- [5] A. Tollestrup *et al.*, The development of superconducting magnets for use in particle accelerators: from Tevatron to the LHC, *Rev. Accel. Sci. Technol.* **1** (2008) 185-210. DOI: [10.1142/S1793626808000101](https://doi.org/10.1142/S1793626808000101)
- [6] P. Ferracin *et al.*, Limits to high field magnets for particle accelerators, *IEEE Trans. Appl. Supercond.* **22** (2012) 4003106. DOI: [10.1109/TASC.2011.2181143](https://doi.org/10.1109/TASC.2011.2181143)
- [7] P. Ferracin *et al.*, Magnet design of the 150 mm aperture low-beta quadrupoles for the high luminosity LHC, *IEEE Trans. Appl. Supercond.* **24** (2014) 4002306.
- [8] Q. Xu *et al.*, Design optimization of the new D1 dipole for HL-LHC upgrade, *IEEE Trans. Appl. Supercond.* **24** (2014) 4000104. DOI: [10.1109/TASC.2013.2280812](https://doi.org/10.1109/TASC.2013.2280812)
- [9] L. Esposito *et al.*, Fluka energy deposition studies for the HL-LHC, IPAC (2013) 1379–1381. Conf. Proc. C130512 (2013) pp.TUPFI021 [CERN-ACC-2013-0283](https://arxiv.org/abs/2013-0283)
- [10] N. Mokhov *et al.*, Protecting LHC IP1/IP5 component against radiation resulting from colliding beam interactions, [LHC-project-report-633](https://arxiv.org/abs/2003-633) (2003) p. 55.
- [11] S. Caspi *et al.*, Test results of LARP Nb₃Sn quadrupole magnets using a shell-based support structure (TQS), *IEEE Trans. Appl. Supercond.* **19** (2009) 1221–1225. DOI: [10.5170/CERN-2009-001.117](https://doi.org/10.5170/CERN-2009-001.117)
- [12] G. Ambrosio *et al.*, Test results of the First 3.7 m long Nb₃Sn quadrupole by LARP and future plans, *IEEE Appl. Supercond.* **21** (2011) 1858–1862.
- [13] H. Felice *et al.*, Design of HQ – A high field, large bore, *IEEE Trans. Appl. Supercond.* **19** (2009) 1235–1239.
- [14] E. Todesco, Quench limits in the next generation of magnets, CERN Yellow Report 2013-006 (2013) 10–16. DOI: [10.5170/CERN-2013-006.10](https://doi.org/10.5170/CERN-2013-006.10)
- [15] T. Salmi *et al.*, Modeling heat transfer from quench protection heaters to superconducting cables in Nb₃Sn magnets, *CERN Yellow Report* **2013-006** (2013) p. 30–37. DOI: [10.5170/CERN-2013-006.30](https://doi.org/10.5170/CERN-2013-006.30)
- [16] V. Marinozzi *et al.*, Study of quench protection for the low β quadrupole for the LHC luminosity upgrade. *IEEE Trans. Appl. Supercond.* **25** (2015) 4002905. DOI: [10.1109/TASC.2014.2383435](https://doi.org/10.1109/TASC.2014.2383435)
- [17] E. Ravaioli *et al.*, New coupling loss induced quench protection system for superconducting accelerator magnets, *IEEE Trans. Appl. Supercond.* **24** (2014) 0500905. DOI: [10.1109/TASC.2013.2281223](https://doi.org/10.1109/TASC.2013.2281223)

- [18] S. Izquierdo Bermudez *et al.*, Coil end optimization of the low β quadrupole for the high luminosity LHC, Applied Superconductivity Conference 2014, Charlotte, NC, USA, 10 - 15 Aug 2014
- [19] R. Gupta, Tuning shims for high field quality in superconducting magnets, *IEEE Trans. Magn.* **32** (1996) 2069–2073.
- [20] P. Hagen, Study of magnetic shimming in triplet magnets, Milestone Report 36 of HiLumi project. <http://www.cern.ch/hilumi/wp3>
- [21] R. Van Weelderden, Superfluid helium cooling, Milestone Report 42 of HiLumi project. <http://www.cern.ch/hilumi/wp3>
- [22] D. Duarte Ramos *et al.*, talk given at WP3 meeting on 28 January 2014. <https://espace.cern.ch/HiLumi/WP3/SitePages/Minutes%20and%20Presentations.aspx>
- [23] J. Garcia Matos *et al.*, talk given at WP3 meeting on 17 July 2014. <https://espace.cern.ch/HiLumi/WP3/SitePages/Minutes%20and%20Presentations.aspx>
- [24] M. Karppinen, Corrector magnets for the LHC upgrade phase-1, CERN EDMS [1039976](#), and R. Ostojic *et al.*, Conceptual design of the LHC interaction region upgrade: Phase I, [LHC Project Report 1163](#) (2008) p. 42.
- [25] F. Toral *et al.*, Development of radiation resistant superconducting corrector magnets for the LHC upgrade, *IEEE Trans. Appl. Supercond.* **23** (2013) 4101204.
- [26] G. Volpini *et al.*, Nb-Ti superferric corrector magnets for the LHC luminosity upgrade, submitted to *IEEE Trans. Appl. Supercond.* **25** (2015) 4002605.
- [27] T. Nakamoto *et al.*, Model magnet development of D1 beam separation dipole for the HL-LHC upgrade, *IEEE Trans. Appl. Supercond.* **25** (2015) 4000505. DOI: [10.1109/TASC.2014.2361404](#)
- [28] T. Nakamoto *et al.*, Construction of superconducting magnet system for the j-PARC neutrino beam line, *IEEE Trans. Appl. Supercond.* **20** (2010) 208–213.
- [29] M. Anerella *et al.*, The RHIC magnet system, *Nucl. Instrum. Meths. A* **499** (2003) 280–315.
- [30] Y. Ajima *et al.*, The MQXA quadrupoles for the LHC low-beta insertions, *Nucl. Instrum. Meths. A* **550** (2005) 499–513.
- [31] B. Bellesia, J. P. Koutchouk and E. Todesco, Field quality in low-beta superconducting quadrupoles and impact on the beam dynamics for the Large Hadron Collider, *Phys. Rev. STAB* **10** (2007) [062401](#).
- [32] B. Bellesia, C. Santoni and E. Todesco, Random errors in superconducting dipoles, 10th European Particle Accelerator Conf. (2006) 2601–2603. [CERN-AT-2006-010-MAS](#)
- [33] V. Kashikhin, *et al.*, Design study of 2-in-1 large aperture IR dipole (D2) for the LHC luminosity upgrade Particle Accelerator Conference (2007) 464-6, and G. Sabbi *et al.*, Conceptual Design Study of the High Luminosity LHC Recombination Dipole, 5th International Particle Accelerator Conf., (2014) 2712-4.
- [34] P. Fabbriatore *et al.*, talk given at WP3 meeting on 17 September 2014. <https://espace.cern.ch/HiLumi/WP3/SitePages/Minutes%20and%20Presentations.aspx>
- [35] S. Farinon *et al.*, talk given at WP3 meeting on 17 September 2014. <https://espace.cern.ch/HiLumi/WP3/SitePages/Minutes%20and%20Presentations.aspx>
- [36] G. Kirby, J. Rysti, *et al.*, HL LHC twin aperture orbit correctors, *IEEE Trans. Appl. Supercond.* **27** (2017), presented at ASC 2016.
- [37] J. Rysti *et al.*, talk given at WP3 meeting on 17 September 2014. <https://espace.cern.ch/HiLumi/WP3/SitePages/Minutes%20and%20Presentations.aspx>
- [38] G. Kirby *et al.*, Performance of the 1-m model of the 70 mm twin aperture superconducting quadrupole for the LHC insertions, *IEEE Trans. Appl. Supercond.* **11** (2001) 1641. P. P. Granieri *et al.*, Thermally enhanced cable insulation for the Nb-Ti high luminosity LHC inner triplet model, *IEEE Trans. Appl. Supercond.* **22** (2012) 7700404.
- [39] M. Segreti *et al.*, A Nb-Ti 90 mm double aperture quadrupole for the high luminosity LHC upgrade, *IEEE Trans. Appl. Supercond.* **25** (2015) 4001905. DOI: [10.1109/TASC.2014.2366517](#)

- [40] N. Mariani, P. Fessia, et al., talk given at WP3 meeting on 31 August 2015. <https://espace.cern.ch/HiLumi/WP3/SitePages/Minutes%20and%20Presentations.aspx>
- [41] V. Baglin *et al.*, Cryogenic beam screens for high energy particle accelerators, International Cryogenic Engineering Conf., [CERN ATS-2013-006](#) (2013).

Chapter 4

RF Systems

4 RF systems

4.1 Introduction

Deflecting (aka crab) RF systems are a part of the HL-LHC upgrade to potentially enhance the integrated luminosity performance by a factor of 5-6 per year. Crab cavities are used for compensation of the geometric crossing angle at the interaction point (IP) to recover the loss in luminosity.

Additional harmonic RF systems are under investigation for bunch manipulation and longitudinal beam stability which includes the option of a lower frequency towards an operation with longer bunches. An upgrade of the transverse damper for higher bandwidth, power and low noise is also studied. At present, only the crab cavities are considered baseline while the other two systems are studied as optional. The above RF systems are described with relevant technical details below. The beam and machine parameters from Appendix A are used to design the RF systems.

4.2 Crab cavities

The HL-LHC will use a 45 m common focusing channel plus 21 m common drift space and 6.7 m common dipole channel on each side of the interaction region (IR), where the two counter-rotating beams have to be separated transversely to avoid parasitic collisions. Separation is accomplished by introducing a crossing angle at the interaction point (IP), which needs to increase with the inverse of the transverse beam size at the collision point in order to maintain a constant normalized beam separation. The non-zero crossing angle implies an inefficient overlap of the colliding bunches. The luminosity reduction compared to that of a zero crossing angle, assuming a Gaussian distribution, can be conveniently expressed by a reduction factor,

$$R_{\Phi} = \frac{1}{\sqrt{1+\Phi^2}}, \quad (4-1)$$

where $\Phi = \sigma_z \varphi / \sigma_x$ is the aspect ratio of the longitudinal (σ_z) to the transverse (σ_x) beam sizes multiplied by the half crossing angle φ ; Φ is also known as the Piwinski angle [1]. Alternatively the reduction can be viewed as an increase in the transverse beam size at the collision point to effective beam size given by $\sigma_{\text{eff}} = \sqrt{\sigma_x^2 + \sigma_z^2 \varphi^2}$ and a reduction of the luminous region. For HL-LHC beam parameters, the reduction compared to the case of a head-on collision can be 70% or larger, depending on the final β^* value and the beam emittance. Therefore, the effective gain in luminosity by simply reducing the beam size at the collision point diminishes rapidly.

To recover the loss, it was first proposed and used [2, 3] RF deflectors (also known as crab cavities). The time-dependent transverse kick from an RF deflecting cavity is used to perform a bunch rotation, in the x - z plane or y - z plane depending on the crossing angle orientation, about the barycentre of the bunch (see Figure 4-1). The kick is transformed to a relative displacement of the head and the tail of the bunch at the IP to impose a head-on collision while maintaining the required beam separation to minimize parasitic collisions. The upstream RF deflector is used to reverse the kick to confine the bunch rotation to within the IR. The crab crossing scheme in a global compensation using only a single cavity per beam was successfully implemented at the e^+e^- collider at KEKB in Japan to achieve record luminosity performance [4].



Figure 4-1: Bunches colliding with a crossing angle without crab crossing (left); with the crab crossing (right).

Since the luminosity gain is substantial, the crab crossing scheme is adopted as a baseline for the HL-LHC upgrade. The time-dependent transverse kick can equally be used to regulate the crossing angle at the IP and therefore allows for a natural knob to control the total number of events per crossing (luminosity levelling), a feature highly desired by the experiments. Levelling by means of collision offsets is already used at LHCb and ALICE. More sophisticated means of levelling to control the density of the events along the luminous region by means of crab cavities are under investigation [5].

4.2.1 Beam and RF system parameters

The required HL-LHC crossing angle together with the beam optics requires crab cavities to provide a total voltage of 12–13 MV per beam per side of each collision point at a frequency of 400.79 MHz. Since the crossing plane in the two experiments is different, a local crab cavity system is a prerequisite. The nominal configuration will use a two-cavity cryomodule as the basic unit providing a deflecting voltage of 6.8 MV (3.4 MV each). A total CC voltage of ca. 11-12 MV is required per IP side per beam to perform the complete bunch rotation. Assuming a maximum voltage of 3.4 MV per, only a partial compensation w.r.t the initial plan of four cavities will be possible. However, only half the system, 16 cavities, are to be installed after the re-baselining in 2016. Space will be reserved to optionally install the second half at a later stage after LS3.

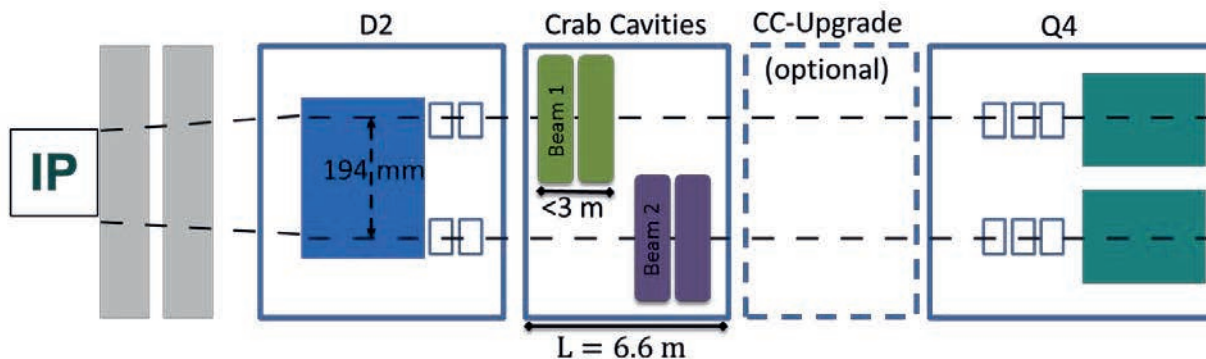


Figure 4-2: Schematic layout of the crab cavities in the LHC Point 1 and 5 w.r.t the interaction point.

Two spare cryomodules (four cavities) are required: One designed for horizontal crossing and the other for vertical crossing for P5 and P1, respectively. The low frequency of 400.79 MHz is required to minimize the RF curvature for the long LHC bunches (see Appendix A). The machine constraints near the interaction region require cavities with a transverse dimension compatible with the location of the adjacent beam pipe which is only 194 mm centre to centre. The RF and machine parameters directly relevant to the crab cavities are shown in Table 4-1. An operating temperature of 2 K is chosen as a baseline. A pressure stability on the cavity surface should be minimized to less than 1 mbar. The static and dynamic heat load is expected to be approximately 30 W to the 2 K bath for a two-cavity module. A cavity vacuum level to better than 10^{-10} mbar is required to assure stable performance.

The input RF power of 80 kW, provided by the Inductive Output Tubes (IOTs), is required to power each of the eight cavities to their nominal voltage with sufficient margin to cope with potential beam loading caused by beam offset. The low level RF (LLRF) will include a regulation loop around the IOT amplifier (to

reduce the RF amplitude and phase noise in a band extending to a few tens of kHz), plus an RF feedback to control the vector sum precisely on the two sides of the interaction region to cancel the crab kick elsewhere in the ring. Eight longitudinal pickups (PUs) located close to the crab cavities (one per IP per side and per beam) are used to regulate the slow drifts of the deflecting voltage with respect to the average bunch centre. To stay within the specified RF power limits the total orbit offset including mechanical tolerances must not exceed 1 mm with stable beams at flat-top. The cavity is kept on tune at all times. The resonant frequency should be precisely controlled by a tuning system to a level well below 80 Hz (approximately one tenth of the cavity bandwidth) to be compatible with the RF power limits.

Table 4-1: Relevant RF parameters for HL-LHC crab cavities.

Characteristics	Units	Value
Resonance frequency	[MHz]	400.79
Bunch length	[ns]	1.0 (4σ)
Maximum cavity radius	[mm]	≤ 145
Nominal kick voltage	[MV]	3.4
R/Q (assumed, linac convention)	[Ω]	400
Q_0		$\geq 1 \times 10^{10}$
Q_{ext} (fixed coupling)		5×10^5
RF power	[kW]	80
LLRF loop delay	[μ s]	≈ 1
Cavity detuning (if parked, optional)	[kHz]	≈ 1.0

4.2.2 RF cavity design

In order to sustain the surface fields at the required Continuous Wave (CW) kick voltage of 3.4 MV cavity for the LHC, crab crossing superconducting technology is essential; space restrictions, voltage requirements, and impedance considerations strongly rule out a normal conducting option. ‘Conventional’ superconducting elliptical cavities, which have already been used at KEK, have significant integration problems in the LHC at the operating frequency of 400 MHz due to their transverse size.

This led to the concept of ‘compact’ cavities. These cavities have unconventional geometries not widely used in superconducting technology. A few concepts with complex shapes exist primarily in the field of heavy ion acceleration. Such structures fit within the LHC space constraints in the existing tunnel and reveal significantly better surface field characteristics than the conventional cavities for beam deflection. As a result of an intense R&D programme within the EuCARD and LARP programmes and with other external collaborators during the past four years, three compact designs at 400 MHz have emerged as potential candidates. Their topologies are shown in Figure 4-3 The three proposed designs are at least four times smaller in the plane of crossing compared to an elliptical cavity with a ratio of the kick gradient to the peak surface fields lower by a factor of 2.

As a part of the R&D phase, it was decided to prototype full-scale cavities for all three designs for a field validation at the nominal kick voltage. Following the recommendation by the Crab Cavity Advisory Panel prototype cryomodules in a two-cavity configuration of the same type will be tested with beam in the SPS machine with LHC type beams [6]. These tests will help validate the cavity performance and operation with beam and understand the effects on protons as well as relevant machine protection aspects. The three prototype cavity types were fabricated in 2012–2013 and their performance validated at or beyond the nominal kick voltage [7–9]. The cavity designs including the fundamental power coupler and higher order mode couplers have evolved significantly from the prototype to meet the impedance requirements of the LHC. Following the recommendation of the May 2014 technical review [10], only two of the cavity designs have been considered for SPS testing, the Double Quarter Wave (DQW) and the RF Dipole (RFD).

The development of a two-cavity cryomodule for the SPS tests in 2018 is at an advanced stage. An overview of crab cavity planning spanning approximately ten years until full installation in the LHC is shown in Table 4-2. A more detailed plan for the SPS and the LHC, including the pre-series and series production, can be found in Ref. [11]. Since the 2015 LIU and HL-LHC Cost & Schedule review, a new baseline has been established with the installation of only 16 cavities in the long shutdown 3 (LS3).

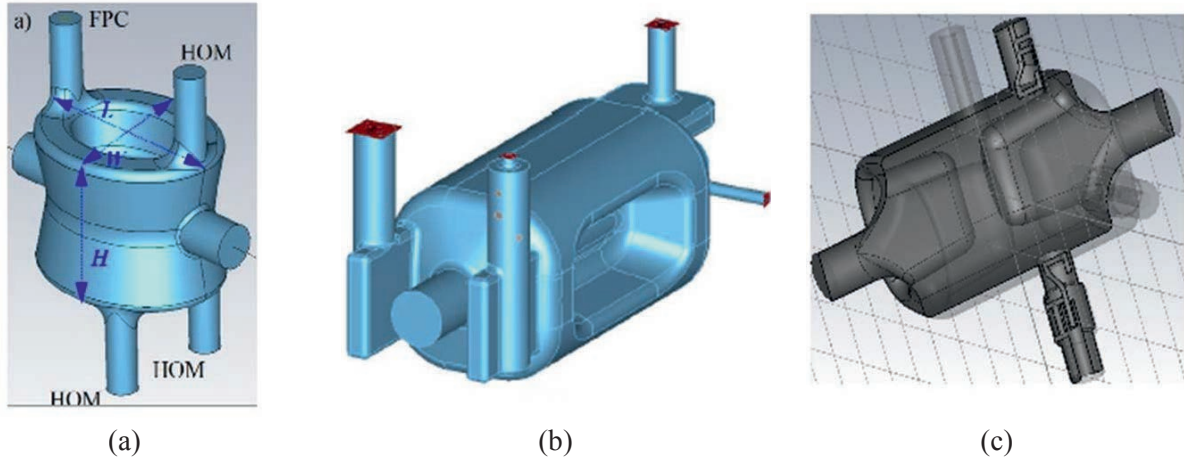


Figure 4-3: Compact cavities. (a): Double quarter wave cavity (DQW), Brookhaven National Lab. (b) RF dipole cavity (RFD), Old Dominion University. (c) Four-rod cavity, Lancaster University.

Table 4-2: Overview of crab cavity planning from R&D to installation in the LHC.

2013–2015	2015–2018	2017–2021	2020–2024	2024–2025
Cavity testing and prototype cryomodule	SPS cryomodule fabrication	SPS tests and LHC pre-series cavities	LHC cryomodule construction and SM18 testing	LHC installation

4.2.3 Beam loading and RF power

In deflecting cavities operated in the crabbing mode, the RF phase and the RF component of the beam current are in quadrature ($\phi_s = 0$, synchrotron convention). For a beam transversely centred, there is no beam loading: the RF generator does not pass power to the beam. With a superconducting cavity (negligible surface losses) the RF power required to maintain the cavity voltage decreases monotonically with Q_L . Therefore, with a perfectly centred beam, the choice of Q_L only requires sufficient bandwidth for unavoidable frequency transients due to external perturbations (see 4.2.10.4).

The situation is different for a beam circulating at an offset Δx . The beam-induced voltage due to an orbit offset is given by

$$\Delta V = I_b \cdot \frac{R_T}{Q_0} \cdot Q_L \cdot \Delta x, \quad (4-2)$$

where I_b is the average beam current, R_T is the transverse shunt impedance in Ω , and Δx is the offset. A sufficient bandwidth and the corresponding RF power are required to compensate for the unavoidable orbit offsets and frequency drifts. Figure 4-4 shows the required forward power as a function of the Q_L for a beam that is centred (red), off-centred by 1 mm (green) and 2 mm (blue). It is expected that the orbit will be kept within 0.5 mm at top energy of the LHC; another 0.5 mm should be added for mechanical tolerances. At injection and ramp, the operating voltage is kept to 10-15% of the nominal voltage. Therefore, the tolerance is relaxed to 3 mm with the available RF power.

The required RF power has a broad minimum (≤ 40 kW) from a Q_L of about $3.0 \cdot 10^5$ to $1.5 \cdot 10^6$ for an offset specification of ≤ 1 mm. Selection of an optimal Q_L value in the broad minimum is a compromise between the feasible tuning precision and the minimization of the field fluctuations from the amplifier

electronics. For larger bandwidth (leading to more stability), lower Q_L values are favoured – the cross-hatched area in Figure 4-4 was chosen as a compromise. A lower Q_L is also favourable for the tuning system as it relaxes the precision needed by a mechanical system and the power needed to compensate for fast frequency changes. The input RF power of 80 kW specified above will leave enough margin to cope with the specified offset and with short excursions even beyond this limit.

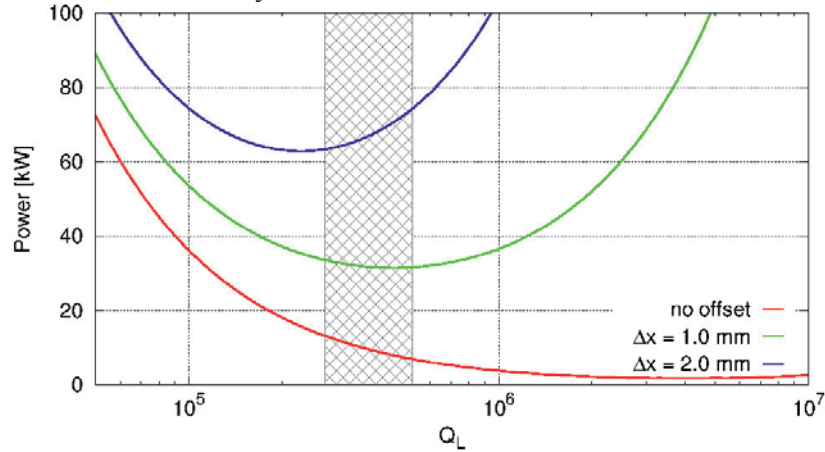


Figure 4-4: Forward power vs. cavity Q_L for centred (red), 1 mm offset (green), and 2 mm offset (blue) beams. Assumed $R_T/Q = 400 \Omega$, 3.4 MV RF, 1.1 A DC.

4.2.4 RF power coupler

The RF power coupler was designed in view of the HL-LHC requirements; additional constraints (common platform) were introduced to limit the variances between the alternative designs in view of the SPS tests.

The adopted crab cavity power coupler will use a single coaxial disk-type window to separate the cavity vacuum and the air side. The antenna shape is specific to each cavity type as the coupling mechanisms for the different cavities are not identical. However, a common platform starting from the cavity flange followed by the ceramic and double wall tube is imposed. To comply with the common platform, the inner antenna has a 27 mm diameter with an outer coaxial line of 62mm diameter for a maximum power capability of approximately 100kW. The double-wall tube is Stainless Steel 316LN with the inner surface coated with copper. The vacuum-to-air separation is achieved with a coaxial ceramic window (Al_2O_3) with an outer flange made of titanium. The rest of the items are built from massive Oxygen Free Electronic (OFE) 3D forged copper blocks. The coupler body is made of a conical with an increased diameter near the ceramic to limit arcing with the primary aim to maximize the air side diameter while keeping the 62 dimensions for the input antenna on the vacuum side. A coaxial-to-waveguide transition is implemented with a half-height WR2300 waveguide with proper impedance matching (see Figure 4-5).

The air side of the coupler will be air-cooled while the antenna itself will be water-cooled. The waveguide design includes the possibility of DC polarization in order to suppress multipacting.

Each coupler is equipped with one single port for a vacuum gauge. The vacuum gauge is mandatory to protect the window during conditioning as well as during operation. It will be oriented along the air line in order to minimize the cryomodule flange size.

Special quarter-wave test boxes to condition the couplers were designed (see Figure 4-5) and built. The coupler ports are designed to come out on the top of the cryomodule, perpendicular to the beam axis for ease of integration with the WR2300 waveguide transition. The cavity's helium vessel is designed to withstand the weight of the couplers and the waveguide (approximately 35 kg). The alternating crossing angle scheme will require that the orientation of a coupler assembly be robust for horizontal and vertical deflections.

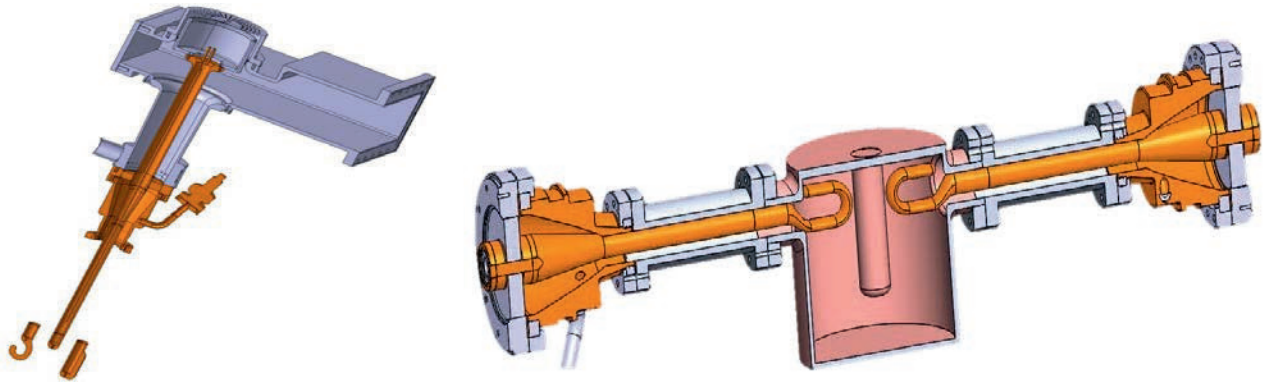


Figure 4-5: (left) Input coupler assembly; (right) test box for RF conditioning.

4.2.5 Coupled bunch instabilities, Fundamental Mode

The crab cavities must cope with the various modes of the collider cycle: filling, ramping, and physics. During filling of the nominally 2748 bunches into the LHC, energy ramping, or operation without crab cavities, the system will be inhibited by making the cavities transparent to the beam (crabbing off). Since more than one cavity is used, counter-phasing to make the effective kick voltage zero while always keeping accurate control of the cavity field is used as the baseline scenario. The counter-phasing ensures both zero effective voltage and beam stability on tune – in fact, it has been found that this is the preferred scenario [12]. Another possibility to operate with ‘crabbing off’ can be achieved by detuning the cavity; but a small field should be kept for the active tuning system. This is referred to as ‘parking’. Parking the cavity half the distance between two revolution frequency sidebands would be ideal for stability.

If detuning is used with a positive non-integer tune ($Q_h = 64.3$), the cavity should be tuned above the RF frequency to make the mode $l = -64$ stabilizing [12]. Although RF feedback is not mandatory for stability with a detuned cavity, it is preferred for accurate knowledge about, and control of, the cavity’s resonance frequency and field. Active feedback will also keep the beam-induced voltage zero if the beam is off-centred. The additional RF power is used as a measurement of beam loading to guide beam centring. The RF signal picked up through the HOM couplers might also be used.

On the flat-top detuning can be reduced (but keeping the total kick voltage initially at zero). The RF feedback keeps the cavity impedance small (beam stability) and compensates for beam loading as the cavity moves to resonance. Once the cavity detuning is reduced to zero, we drive counter-phasing to zero and use the functions to synchronously change the voltage in all crab cavities as desired (crabbing on). In a physics run, with crabbing on, the active RF feedback will continue to provide precise control of the cavity field. The RF feedback reduces the peak cavity impedance and transforms the high Q resonator to an effective impedance that covers several revolution frequency lines. The actual cavity tune then has no big importance for stability anymore. The growth rates and damping rates are much reduced, and we have no more dominant mode as shown in Figure 4-6.

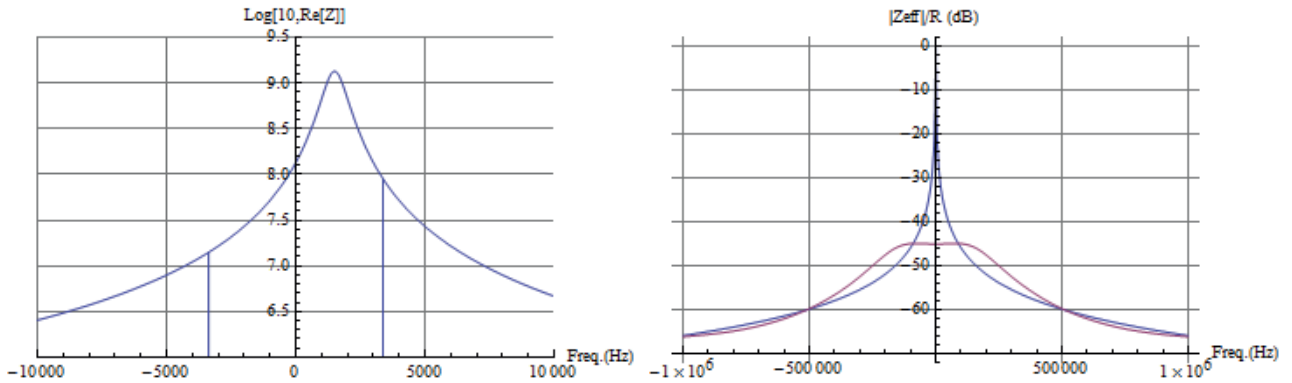


Figure 4-6: (left) Real part of the deflecting mode impedance with a detuning of 1.5 kHz from 400 MHz. The vertical lines represent the difference in $\Re\{Z\}$ evaluated at $\pm 0.3 f_{rev}$ for the computation of damping rate (mode $l = -64$). (right) Modulus of the cavity impedance seen by the beam with the RF feedback on (red) and off (blue) normalized to the cavity impedance at the fundamental mode.

4.2.6 Impedance budget, Higher Order Modes

On resonance, the large impedance of the fundamental deflecting (dipole) mode is cancelled between the positive and negative sideband frequencies, which are symmetric around ω_{RF} . The active feedback will reduce the growth rates by a large factor.

For higher order modes (HOMs), both narrowband and broadband impedance should be minimized during the entire machine cycle as the LHC will accelerate and store beams of currents exceeding 1.1 A (DC). Tolerances are set from impedance thresholds estimated from Ref. [13].

The longitudinal impedance has approximately a quadratic behaviour vs. f in the region of interest with the minimum threshold value at 300–600 MHz. The total maximum allowed impedance from each HOM, summing over all cavities in one beam, assuming that the HOM falls exactly on a beam harmonic, is set at $<200 \text{ k}\Omega$, so if all 8 cavities have identical HOM frequencies, the longitudinal impedance must not exceed $25 \text{ k}\Omega$ per cavity. For frequencies higher than 600 MHz, the threshold is higher ($\propto f^{5/3}$), but the same threshold was imposed. Modes with frequencies above 2 GHz are expected to be Landau-damped due to natural frequency spread and synchrotron oscillations.

In the transverse plane, the impedance threshold is set by the bunch-by-bunch feedback system with a damping time of $\tau_D = 5 \text{ ms}$ [13]. Eight effective cavities per beam per transverse plane (16 total per beam) are assumed due to the alternate crossing angles at the two experiments. The single bunch studies show that integrated R/Q over the frequency for all the HOMs per cavity should be suppressed to below $2 \text{ k}\Omega/\text{m}$ (without accounting for β -function) from stability considerations [15]. From multi-bunch considerations and assuming the pessimistic case that the HOM frequency coincides with the beam harmonic and identical HOM frequencies between the cavities, the maximum total impedance in each plane is set to be $160 \text{ k}\Omega/\text{m}$ [15]. Assuming well separated HOM spectrum and including beam size levelling at the IP, the allowed impedance per cavity can be relaxed to $0.5 \text{ M}\Omega/\text{m}$. Analogous to the longitudinal modes, frequencies above 2 GHz are expected to be Landau-damped due to natural frequency spread, chromaticity, and Landau octupoles.

Due to the very tight impedance thresholds, the distribution of HOM frequencies as mentioned above due to manufacturing errors can help relax the tolerances. The beam power deposited in the longitudinal HOMs can become significant when the frequencies coincide with bunch harmonics. The HOM couplers were dimensioned to accept a maximum of 1 kW to be able to cope with HL-LHC beams [14].

4.2.7 Higher order mode couplers

The first design goal of the HOM filter is to block the transmission of the main deflecting mode, while transmitting all remaining HOMs. Several HOM coupler designs were developed and optimized for different

cavity geometries. Two high-pass filter designs, incorporating a notch filter at the fundamental frequency, are shown in Figure 4-7 with both HOMs using hook-like antennae to couple to the HOMs.

Simulations show that the HOM coupler must have a superconductive surface due to the high fields of the fundamental mode. A second design constraint requires that HOM couplers be able to efficiently remove the power in the HOMs (up to 1 kW) and the heat dissipated by the fundamental mode in the inner part of the HOM coupler from the cavity. High purity bulk niobium with sufficient cooling can ensure this. The required cooling may be possible by conduction, but the possibility of actively cooling with superfluid liquid helium or immersion in a small He tank is also under study.

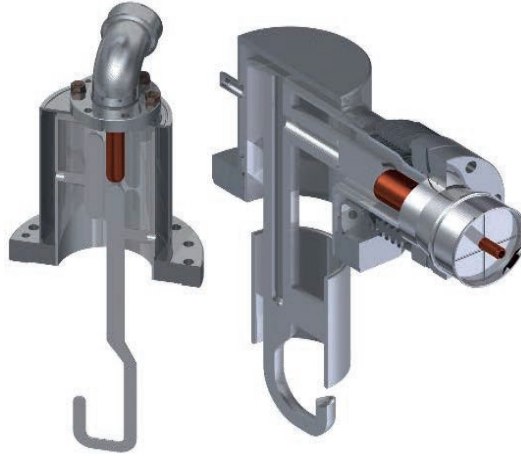


Figure 4-7: HOM filter for the RFD (left) and the DQW (right).

4.2.8 RF multipoles

The crab cavity designs presently considered are such that they lack axial symmetry. Therefore, they can potentially exhibit all higher order components of the main deflecting field. Due to the placement of the cavities at high beta-function locations, the higher order components of the main deflecting mode can affect long-term particle stability. RF multipole components b_n of the RF deflecting field can be approximated and hence expressed in a similar fashion to magnets [16]:

$$b_n = \int_0^L \frac{1}{qc} F_{\perp}^n dz \text{ [T m}^{2-n}\text{]}. \quad (4-3)$$

The quadrupolar component b_2 is zero in the case of perfect symmetry; due to fabrication errors and ancillary components it is non-zero – it must be smaller than 10 units leading to a tune shift in the order of $\Delta Q \approx 10^{-4}$. The first systematic multipole is the sextupolar component, b_3 . Long-term simulations with the optical functions of the HL-LHC indicate that the b_3 component should be limited to approximately $1000 \pm 10\%$ units, which results in an acceptable degradation of the dynamic aperture below 1σ for orbit offsets of 1.5 mm [13]. Both the DQW and the RFD conform are below the specified tolerance for b_3 . No specifications are yet provided for higher order terms, but it is expected that they can be controlled to smaller values than the neighbouring D2 dipole magnet.

For $n \geq 4$, assuming a very approximate scaling of the additional kick from an orbit offset via b_n , the b_n must be kept below $\propto O(10^n)$. Better estimates are pending; results from long-term tracking are needed to confirm the exact specifications.

4.2.9 Lorentz force detuning and multipacting

When the cavity contains RF fields there is a Lorentz force on the cavity surface resulting from the high radiation pressure on the cavity walls. This results in a detuning of the cavity frequency. The Lorentz force detuning is kept small (≤ 0.6 kHz) at the nominal field.

Another common problem in complex RF structures is multipacting. This is a resonant phenomenon where the electrons will absorb RF power, limiting the field to a finite level and depositing additional heat load in the walls. Multipacting was modelled in all cavities and couplers using two codes with different methodologies to identify multipacting. CST Particle Studio® uses particle tracking with accurate secondary emission models to simulate the growth in electrons with time, while Track3P tracks a single particle in the RF fields and looks for resonant trajectories.

In CST, three secondary electron yield (SEY) models were used to look at the effect of surface cleanliness. The models were for wet-treated, baked, and processed niobium surfaces. While multipacting in all cavities was found for the wet-treated and baked models, no multipacting trajectories were found for the processed surface, suggesting that any multipacting would be soft and easily processed. Similarly, Track3P found multipacting at low field. This is in good agreement with the results from the prototype tests, where multipacting was observed and could be processed away easily.

4.2.10 Cryomodule and integration

4.2.10.1 Temperature choice

The Bardeen-Cooper-Schrieffer (BCS) resistance of niobium at 4.5 K and 400 MHz is around 50 n Ω , which is more than 10 times larger than the value at 2 K. The complex shapes of the cavities may also be susceptible to microphonics caused by liquid He boil-off, hence operation below the lambda point of He is preferred. For these reasons operation at 2 K is baseline. This will require the provision of liquid He at 2 K to the crab cavity location in the LHC. The current heat load limits for the LHC are not currently known, but are likely to be around 3 W of dynamic load per cavity at 2 K.

4.2.10.2 Cavity interfaces and cold mass

Following the recommendation of the May 2014 technical review [10], only two cavity designs are considered for the engineering design towards the SPS tests and ultimately the LHC (DQW and RFD). The cavities were dimensioned to cope with several mechanical constraints: ensure elastic deformation during maximum pressure as well as during all transport and handling conditions; maximize tuning range; minimize sensitivity to pressure fluctuation; avoid buckling due to external pressure; and maximize the frequency of the first mechanical natural mode. The final mechanical design of the cavities including all external interfaces is shown in Figure 4-8.



Figure 4-8: Schematic view of the cavity with interfaces (left) DQW; (right) RFD.

The superconducting resonators are fabricated from bulk niobium sheets by electron-beam welding of deep-drawn parts. A final thickness of 4 mm was calculated to be acceptable in order to cope with all the

mechanical constraints as well as minimizing the cost of cavity production. The cavities are bath-cooled by saturated superfluid helium at 2 K. Each cavity (aka dressed cavity) is equipped with: a helium tank, internal magnetic shield, a tuning system, a fundamental RF power coupler, a field probe, and two or three HOM couplers. Functional specifications including all tolerances for the cavities with their interfaces to develop manufacturing drawings for the DQW and the RFD are shown in Figure 4-9 and Figure 4-10, respectively.

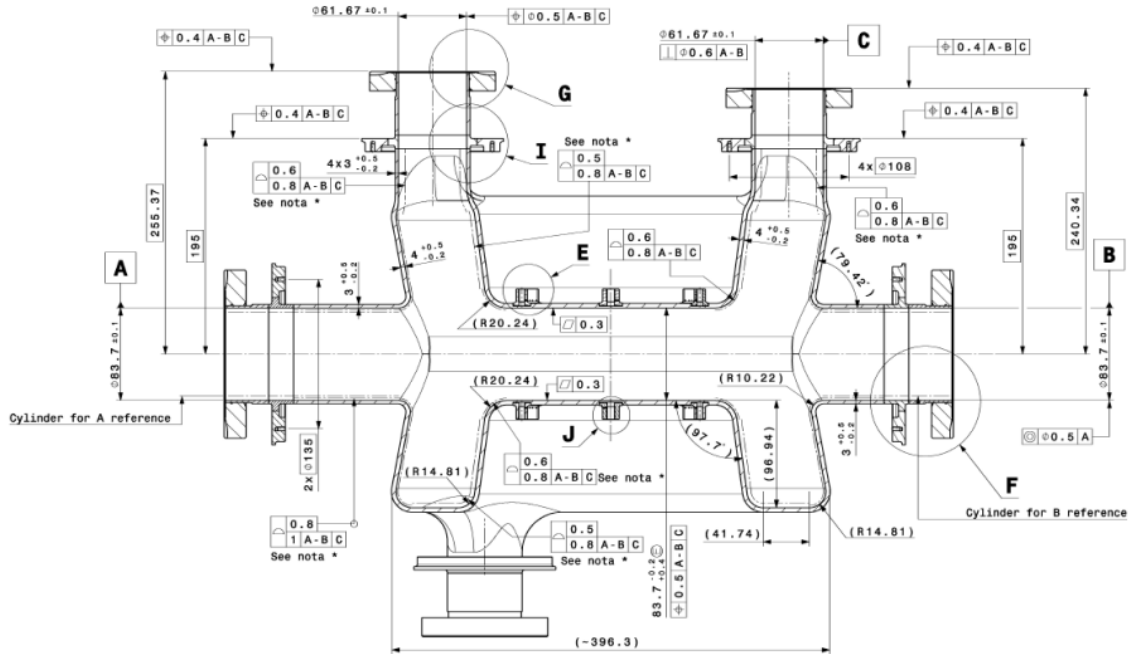


Figure 4-9: Dimensional plot with tolerances of the DQW cavity.

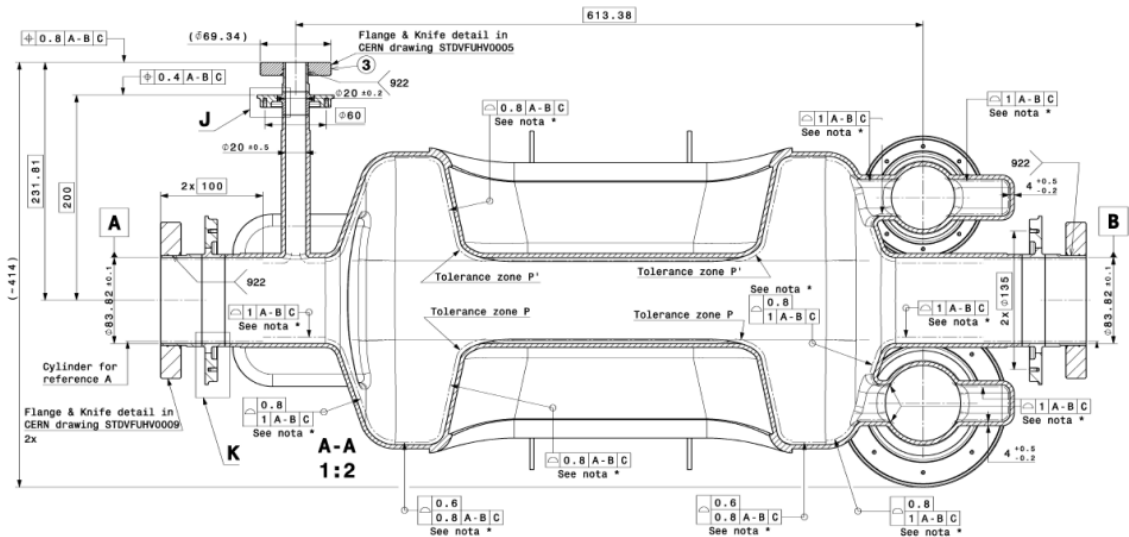


Figure 4-10: Dimensional plot with tolerances of the RFD cavity.

4.2.10.3 Helium vessel and dressed cavity unit

The helium tank will contain saturated superfluid helium at 2 K, cooling the cavity and allowing the extraction of the heat dissipated in the cavity and adjacent cold components. Superfluid helium is an excellent thermal conductor for small heat flux. Above a critical heat flux, the temperature increases drastically and eventually superfluidity is lost. The geometry of the helium tank has been determined to allow this maximum heat extraction while optimizing the quantity of the helium to be used.

Two choices of material have been studied for the helium tank: stainless steel and titanium. Titanium has the advantage of nearly the same thermal contraction as niobium (in the order of 1.5 mm/m from ambient temperature to 2 K), while the thermal contraction of stainless steel is twice as large, leading to larger thermal stresses. The advantage of stainless steel is the manufacturability and thus the cost. However, for the unconventional geometries of the crab cavities, titanium grade 2 was chosen as the optimum material for the helium tank, allowing for rigid connection of cavity ports to the helium vessel. An initial design based on fully welded joints is now replaced with a bolted design with additional leak proof welds to minimize the stress on the cavity during the assembly of the Helium vessel Figure 4-11. A dummy prototype for the DQW cavity is under fabrication to validate the principle and its functioning at nominal operating temperature with superfluid Helium.

The helium tank has a structural role, and its rigid connection to the cavity ports ensures optimum boundary conditions for the cavity during mechanical loading, in particular during maximum pressure loading and tuning. The helium tank geometry was chosen to limit the maximum stress on the cavity to tolerable values [13]. Figure 4-11 shows a qualitative stress distribution in the cavity wall during maximum pressure for the DQW cavity. The red colour indicates only small areas of high stress, which are tolerable. This distribution, as well as the maximum values, are directly influenced not only by the cavity geometry but also by the helium tank configuration. Similar calculations were carried out for the RFD cavity and validated.

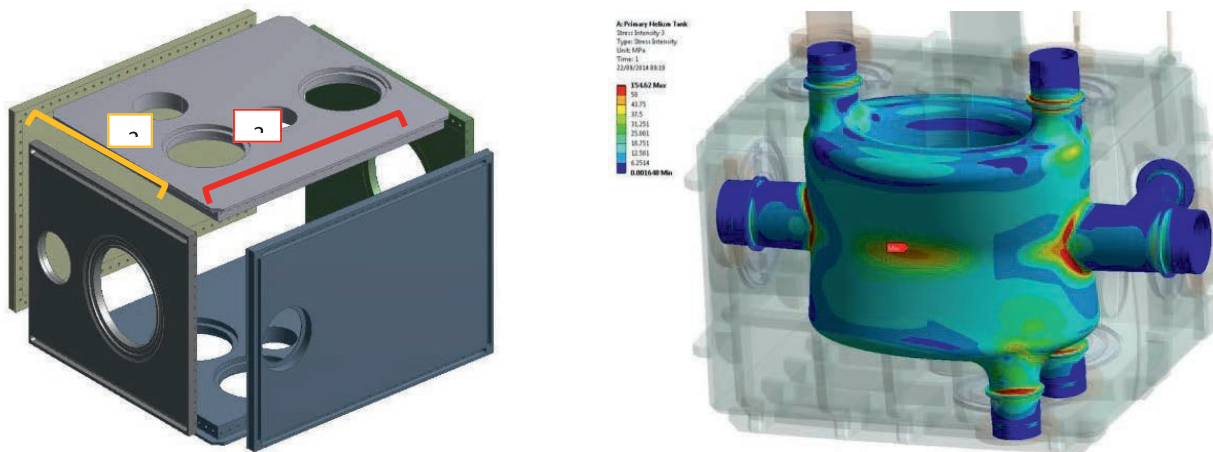


Figure 4-11: Schematic of the Helium vessel assembly of the bolted design (left). Mechanical stress induced by maximum pressure on the DQW cavity inside its helium tank (right). Red indicates regions with highest stress, which can be tolerated if confined to small areas.

A major concern for the mechanical design was the transitions from the helium tank to all of the adjacent components, in particular the main coupler, HOM couplers, and the flanges for connection to the beam pipes and helium pipes. All flange connections are stainless steel to stainless steel connections. Due to its proximity, the second beam pipe had to be integrated inside the helium vessel and consequently will be at 2 K; it is proposed to use a niobium beam pipe. A schematic view of the DQW and RFD cavities inside their helium tanks and equipped with the required ancillary equipment are shown in Figure 4-12 and Figure 4-13.

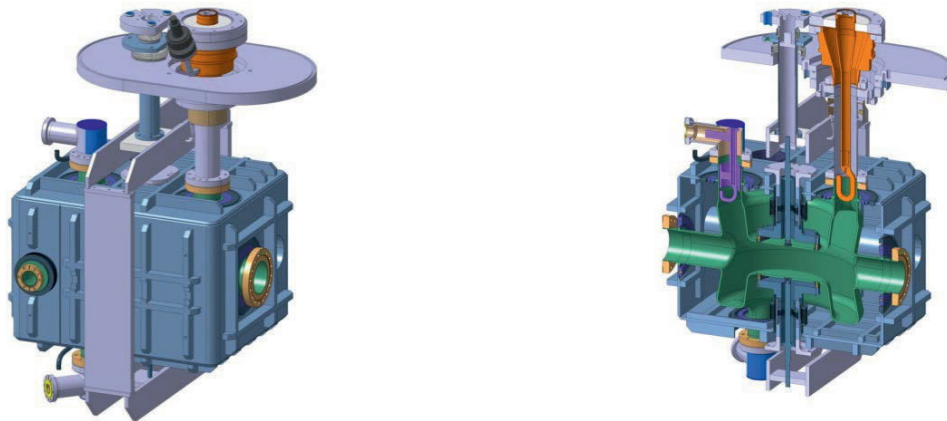


Figure 4-12: (left) The DQW cavity inside its helium tank with the field probe port (front), beam port (right) and tuner frame around. (right) Sectional view of the DQW cavity inside its helium tank with the power coupler (top right, orange), HOM coupler (left, top and bottom), and tuner (centre, top, and bottom).

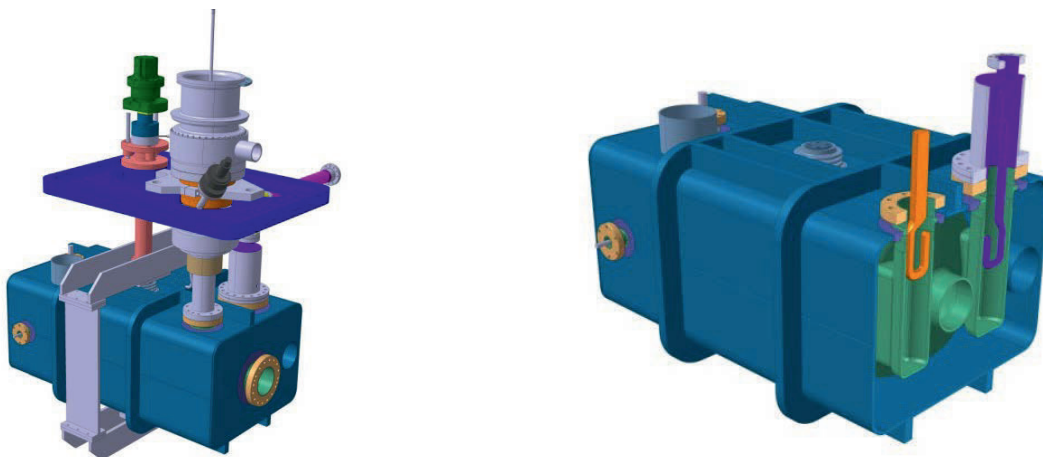


Figure 4-13: (left) The RFD cavity inside its helium tank with the field probe port (centre left), beam port (centre right), tuner frame around helium vessel and tuner actuation (top centre). (right) Schematic sectional view of the RFD cavity inside its helium tank with the power coupler (orange) and HOM coupler (violet).

4.2.10.4 Frequency tuning

The final resonance frequency of the cavity will depend on a number of fabrication and handling steps and cool-down (shifts by hundreds of kHz). A ‘slow’ mechanical tuning system is required to compensate for the uncertainties of the above steps by altering the cavity shape – this will dominate the tuner requirement. At 2K it must be possible to tune the cavity to $f_{\text{res}} = f_{\text{operation}} \pm \Delta f_{\text{LFD}}$, where Δf_{LFD} denotes Lorentz force detuning occurring during cavity filling. In the SPS, the operating frequency can vary by an additional 60 KHz (see 4.2.18.5). Despite the large resulting tuning range ($\approx \pm 200$ kHz) the resolution of the tuner should allow at least ten steps inside the cavity bandwidth (≈ 800 Hz); backlash and hysteresis must be small.

The tuning system, similar for both cavities (DQW and RFD), is shown in Figure 4-12 and Figure 4-13. It consists of an actuation system that is placed outside the cryomodule, and operated at room temperature and at atmospheric pressure, which makes it accessible and thus maintainable. The actuation system consists of a stepper motor, a harmonic gearbox, a roller screw, and linear guide bearings. The concept is based on a design developed and already in use at JLAB. The details of the prototype actuation system are shown in Figure 4-14.

Since the cavity will be operated in continuous wave mode and frequency variations are expected to be small, active tuning with piezoelectric actuators may not be needed in the final design. A piezo is, however, foreseen for the first cavity tests to validate this assumption.

Actuation induces a relative movement between two titanium cylinders. The inner cylinder is directly connected to the top of the cavity, the outer cylinder to the bottom via a titanium frame. A symmetric deformation is thus applied simultaneously to the top and bottom of the cavity.

A stepper motor drives with a high resolution (1.8 deg/step) a harmonic gearbox with a 100:1 ratio. A roller screw, allowing smaller pitch (1 mm) compared to a ball screw with less friction, transforms the rotation in a linear motion, guided by linear roller bearings on precision guides. The estimated mechanical resolution of the tuning system at the connection to the cavity is estimated to be in the order of 10nm or less, which is equivalent to a few tens of Hz for both cavities, allowing for at least 10 micro-steps inside the cavity RF frequency bandwidth. The cryostat vacuum exerts a non-negligible force on the tuner mechanism, as it remains floating with respect to the vacuum vessel. A pressure compensation feature is added to minimize this force. A study is also underway to orient the tuner mechanism in the horizontal direction using flexure guides to alleviate space constraints directly on top of the cavity.

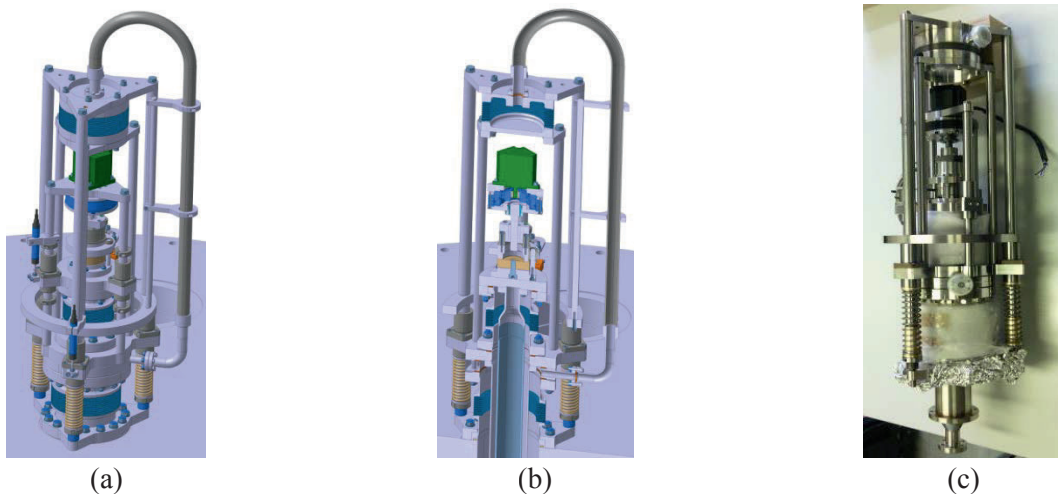


Figure 4-14: (a) Actuation system of the prototype tuning system for DQW and RFD cavities. (b) Cross-section. (c) The prototype tuning system manufactured for the test in SM18 vertical test.

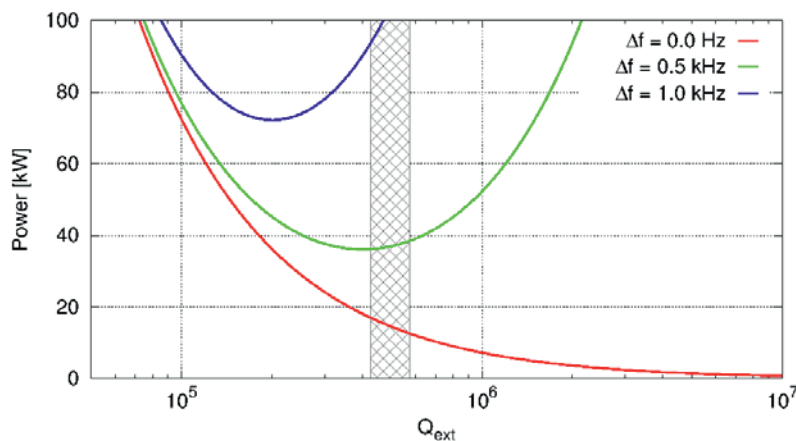


Figure 4-15: Forward power required as a function of Q_{ext} for different frequency detuning of the cavity from its nominal value. The cross-hatched area indicates the nominal range of Q_{ext} .

Low frequency mechanical resonances (below 150 Hz) should be avoided to minimize cavity perturbation due to both helium pressure fluctuations $\mathcal{O}(1 \text{ mbar})$ and external noise sources. Resonances above 150 Hz are considered to be benign. If fast-acting tuners (piezos) are deemed necessary, they should be able to compensate for deformations of $\leq 10\text{--}20 \text{ }\mu\text{m}$ to reduce the RF power overhead (see Figure 4-15).

4.2.10.5 Space, modularity, and the second vacuum chamber

Machine architecture and integration studies for the LHC led to the choice of housing two individual cavities in one stand-alone cryomodule, individually connected to a cryogenic distribution line cryostat running in parallel with the main line. The nominal configuration will use a two-cavity cryomodule as a basic unit. As a consequence, a total of eight cold-to-warm transitions for the beam tube and four connections to the cryogenic distribution line are required for one side of an LHC interaction region (Figure 4-16).

The length of the cryomodule depends on the cavity type and, for the longest cavity, results in a total of 6.7 m for four cavities (two cryomodules) per side of the LHC interaction region for both beams including gate valves from the interconnection plane, as shown in Figure 4-16. For each two-cavity module, two gate valves inside the cryomodule vacuum (see Figure 4-17) and two valves outside at ambient temperature are foreseen.

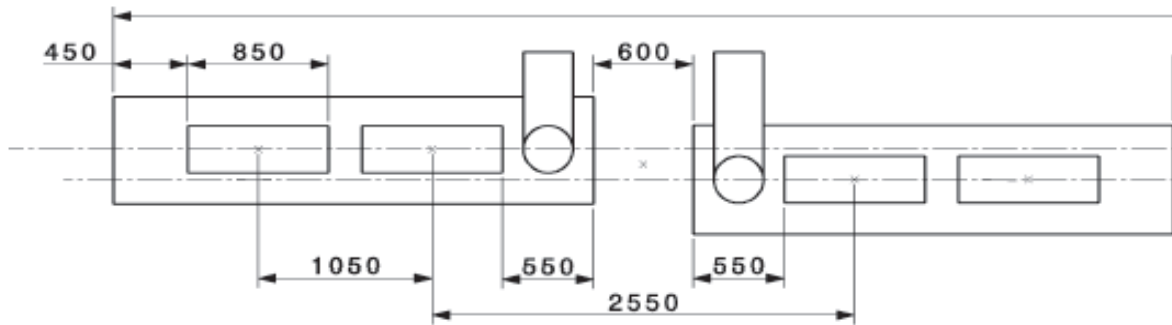


Figure 4-16: Cryomodule layout for one side of the interaction region in the LHC.

A detailed view of the cryomodule containing two DQW and RFD cavities is illustrated in Figure 4-17. The fixed RF coaxial coupler, with a single ceramic window, providing 80 kW average power, is mounted onto the cavity via a ConFlat[®] flange assembly equipped with a specific vacuum/RF seal designed at CERN and widely used elsewhere.

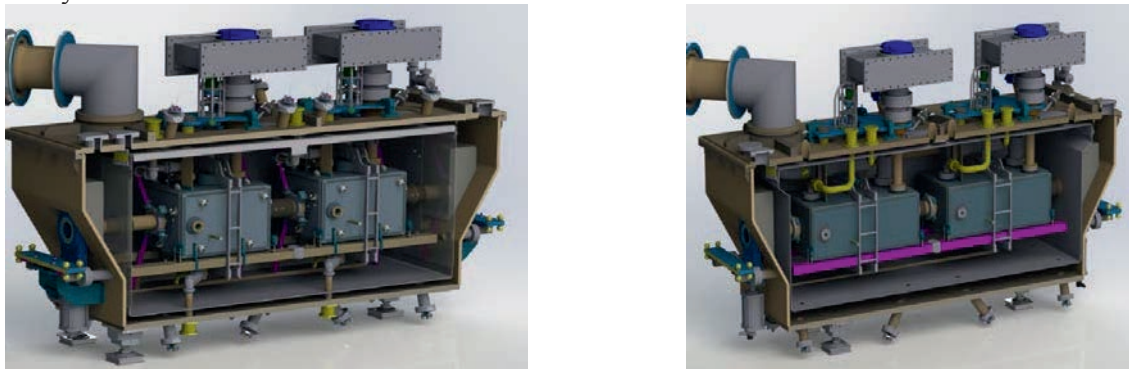


Figure 4-17: Cryomodules for (left) DQW cavity; (right) RFD cavity.

The RF coupler is mounted on the cavity in the clean-room, constraining the assembly of subsequent components of the cryomodule due to its size. The vacuum vessel is designed in two main parts – a lower vacuum tank and a top plate – with lateral windows for access to each cavity. It uses a top-down assembly procedure for the cavity string inside the vessel [18]. This allows the possibility of cavity alignment with optical

devices (laser trackers, for example) while making fine adjustments through the adjustable supports before closing the cryomodule lateral covers.

The cavity supporting concept uses the external conductor of the RF coupler as the main mechanical support of the dressed cavities. An additional supporting point to keep cavity alignment stability within requirements is obtained by the inter-cavity support. In the RFD cavity, the power coupler is transversely offset from the cavity axis, which requires additional vertical support, as shown in Figure 4-17.

For the LHC cryomodule, two options are considered. The baseline consists of two cryomodules per side per IP, each with two cavities similar to the SPS test prototype cryomodule. This would have the advantage of a topology similar to that having been tested in the SPS. The overall design would probably become simpler than for the SPS test prototype cryomodule. As a second option, a single four-cavity cryomodule could be considered, optimized for LHC operation requiring less access and minimizing cold-to-warm transitions.

Currently only the SPS test cryomodule exists with full technical specifications. The cryomodules are designed to have a rectangular outer vacuum vessel with removable side panels such that the dressed cavities remain accessible [18]. Loading of the complete cavity string into the vacuum vessel is from the top, with plug valves fitted with closing end-plates integrated in the cavity string. All external connections except the beam pipes are on the top of the cryomodule. The cavities are supported by the power couplers. This allows easy access to the cavities and ancillaries, as required for a prototype. The vacuum vessel is fitted with stiffening ribs to keep the stress within reasonable limits when placed under vacuum pressure and during cool-down. The designs for both cavity variants are kept as similar as possible. The second beam pipe for the counter-rotating beam is missing in the SPS DQW prototype.

4.2.10.6 Magnetic and thermal shielding

Assuming a cavity geometric factor of $\approx 100 \Omega$, the additional surface resistance due to trapped flux R_{mag} is required to be below 1–2 n Ω in order to stay in the shadow of the total surface resistance specification of 10n Ω . To achieve this, magnetic shielding in the cryostat should reduce the external magnetic field on the outer surface of the cavity by a factor of at least 100 (reducing the earth's magnetic field to $<1 \mu\text{T}$).

The external warm magnetic shield is made of 3 mm thick mu-metal and will be directly attached to the vacuum vessel. Due to the large apertures in the shielding for couplers and beam pipes, this layer on its own is not sufficient to completely shield the earth's magnetic field to the required level with sufficient safety margin. Figure 4-18 (right) shows the magnetic field amplitude inside a two-cavity cryomodule without an internal shield for an applied external shield of 60 μT in the longitudinal direction. To meet the magnetic field requirements a second shield is required close to the cavity. In order to reduce the size of the holes in the internal shield the cold magnetic shielding will be integrated inside the helium vessel, as presented in Figure 4-18. The internal shield is 1 mm thick and will be made from Cryoperm[®] or Aperam Cryophy[®]. Magnetization of both materials is adversely affected by stress. Hence, degradation of the shielding material during assembly and handling should be carefully studied and monitored. Effects of weight and thermal stresses were modelled in ANSYS. The simulations indicate that while the maximum stress is 439 MPa in the titanium supports, the stress on the shield is kept to less than 150 MPa. It is possible that this may affect the magnetization locally, but the effect is comparable to that of a small hole in the shield. Simulation results from OPERA, assuming the worst case field orientation, show that the use of the proposed two-layer shielding solution to achieve magnetic fields well below 1 μT is feasible, as shown in [19].

The thermal shield is made of rolled aluminium sheets. The shield is suspended from the vacuum vessel via flexible guides made from titanium alloy that also copes, through angular movements, with its thermal contractions. The absence of mechanical contact between the shield and the string of cavities eliminates the risk of interference with the alignment of the cavities induced by differential contractions and cooling transients. The cryomodule contains a single thermal shield, actively cooled in the LHC between 50 and 80 K by a cryogenic cooling line containing pressurized helium gas. For the SPS tests, similar solution using pressurized He will be applied and will replace initially foreseen N₂ circuit. A 30-layer prefabricated Multi-

Layer Insulation (MLI) blanket protects the thermal shield whereas a 10-layer blanket is mounted around each helium vessel.

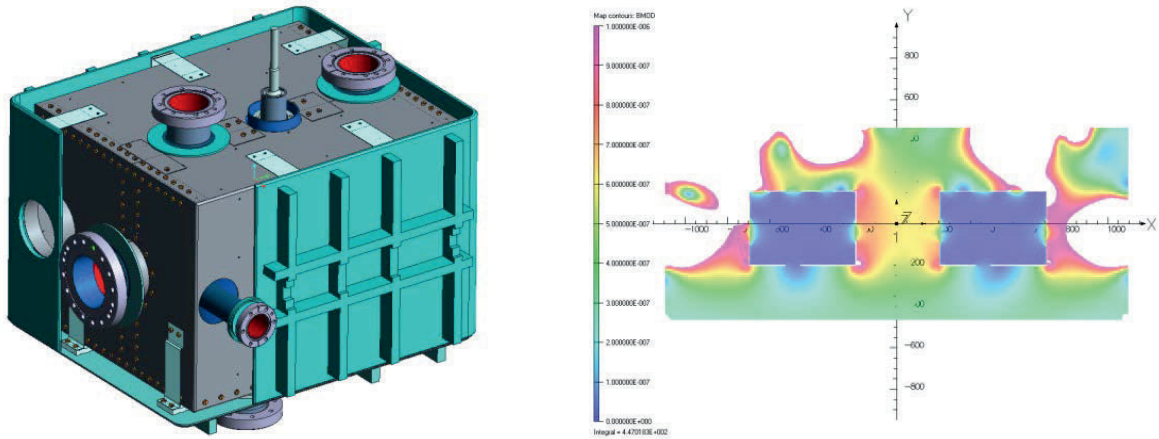


Figure 4-18: (left): Cold magnetic shielding inside the helium vessel; (right): magnetic field amplitude inside the two-cavity CM without the second internal cold magnetic shield, scale 0 to 1 μT . An external field of 60 μT in the direction parallel to X (longitudinal) is used.

4.2.10.7 Cavity Alignment and support

Successful operation of the RF cavities depends on their correct position. The transverse and longitudinal alignment tolerances described in the LHC performance requirements [13] define the configuration constraints:

- Cavity rotation in the X-Y plane (“roll”, R_z , Figure 4-19) – it is required that this rotation has to be $< 0.3^\circ = 5.2 \text{ mrad}$ (2σ) per cavity;
- Cavity “yaw” (R_y) and “pitch” (R_x) with respect to the cryostat axis should be less than $< 1 \text{ mrad} = 0.057^\circ$ (3σ), Figure 4-19. Similar tolerances are assumed for the alignment between cryostats.
- Transverse displacement of cavities w.r.t each other inside a cryostat: intra-cavity alignment in the transverse plane with respect to the cryostat axis should not exceed the 0.5 mm (3σ) tolerance set by the multipolar effects.

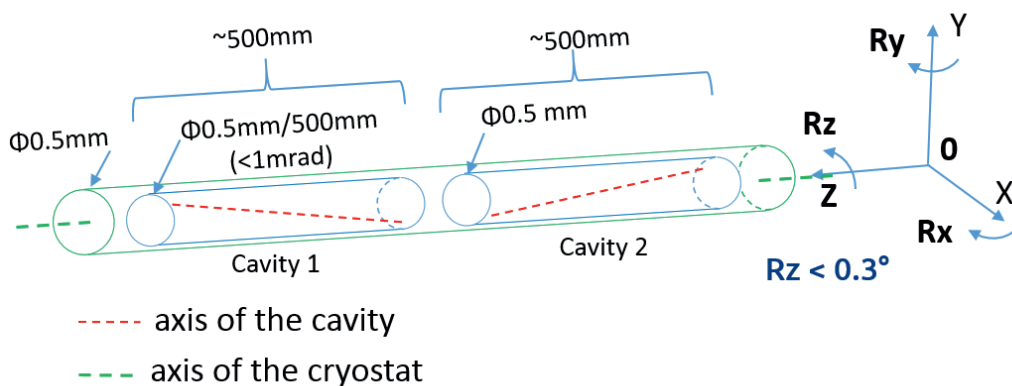


Figure 4-19: Crab-cavities alignment tolerances inside the cryostat.

The dressed cavity’s geometry can only be measured accurately by means of CMM (Coordinate Measurement Machines) at room temperature. After cool-down the CMM data is corrected through models using the materials contraction coefficients. This is not trivial considering the nonlinear behaviour of the materials’ contraction coefficients and the complex design of the cavities. However, the use of Titanium that

has a contraction coefficient similar to Niobium and the fact that the cavity is much less stiff than the tank should make the change in shape as linear as possible. The temperature gradient between the sensor head and the object may have impact on the result of the measured values. Therefore, non-contact methods are preferred. The components of the monitoring system will have to be radiation hard and keep stable properties over time. Before operation, the orientation and position of the cavity is adjusted by means of a plate rigidly connected to the dressed cavity. Such a plate is supported isostatically in 3 points (Figure 4-20). Its position and altitude can be modified by setting the position of these 3 support points. The rigid connection between the cavity and the alignment plate is obtained by means of the fundamental power coupler (FPC) and a set of additional supports as shown in Figure 4-20.

A ‘blade’ type flexure arrangement is used for the supporting system on the dressed cavities. This arrangement gives an increase in overall stiffness whilst still allowing for thermal contraction on cool-down to 2 K towards the fixed point, which is the input coupler. Further analyses with detailed models of each cavity type are foreseen following the complete integration of the vacuum vessel. This will assess the final deformation expected as well as tuning vibration modes to ensure excitation of the cavities is minimised.

The Frequency Scanning Interferometry (FSI, [21]) is chosen as a baseline solution crab cavity alignment system in the LHC. The FSI system offers absolute interferometric distance measurement capability at sub-micron level. Only passive components (mirror, collimator, fibres) are needed at the points of measurement, which makes the application suitable for a high radiation level of operation. FSI is a measurement technique that allows the determination of absolute distances (0.2-20 m) with high accuracy with a measurement uncertainty (95%) of $0.5 \mu\text{m/m}$. The FSI unit consists of a reference interferometer and a measurement interferometer that use tuneable lasers (from 1410 nm to 1510 nm). An additional second laser tuned in the direction opposite to the reference laser is required to remove the errors arising from drifts and account for internal frequency and phase changes from the laser itself. The gas cell ensures stability of the reference interferometer. Each cavity features several FSI heads (8 per cavity) and several lengths between the FSI system heads and the reflective targets are measured in order to determine the position of the dressed cavities (Figure 4-20).

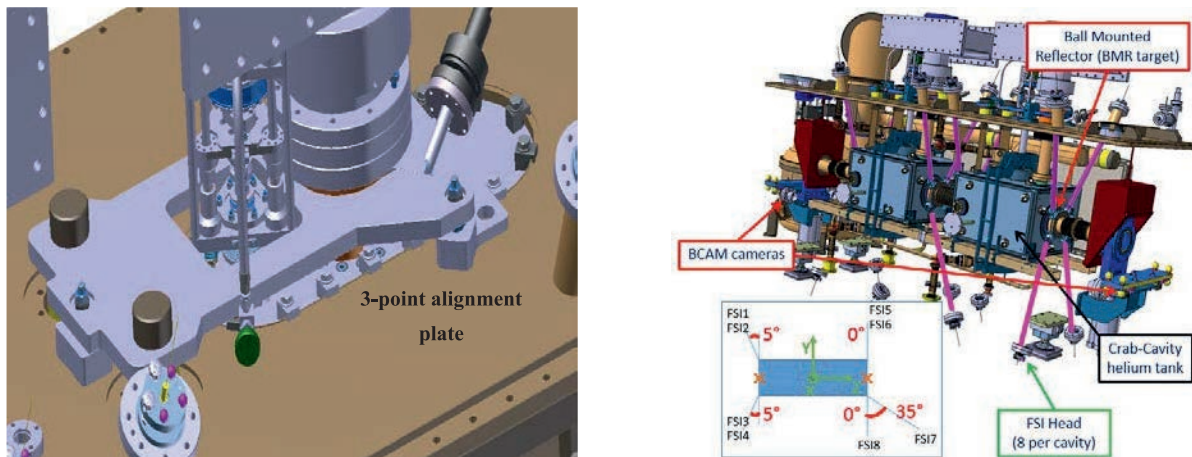


Figure 4-20: (left) Alignment plate in blue with the supports used for attitude and position actuation. (right) Frequency scanning interferometry (FSI) system for alignment monitoring.

In order to verify the performance of the FSI system during the preliminary prototype tests, a second solution based on the Brandeis CCD Angle Monitor (BCAM) is chosen [22]. The BCAM system is not radiation-hard and only allows to control the crab cavities position during the installation and preliminary tests. The basic concept is the creation of a closed geometrical network continuously monitored using a set of opto-electronic sensors linked to external references defined in the cryostat coordinate system. The positions of the cavities are measured in this geometrical frame. Double-sided BCAM cameras installed on precise metrological tables on the cryostat sides look at each other and at four target ‘‘fingers’’ attached to the cavities. Therefore, two external lines of sight are created, allowing the reconstruction of the position of the cavities.

4.2.10.8 Vacuum Vessel

The main constraints in the design of the vacuum vessel are the integration steps. The shape and the openings must allow the assembly and positioning of all the system in their right location. The dimensions of the vessel have to conform to the maximum available envelope in the LHC tunnel, including all systems external to the vacuum vessel, Figure 4-21:

- 2900 mm longitudinally for the RFD, 2750 mm for the DQW
- 1050 mm laterally (and proper position with respect to the beam for both axis)
- 2350 mm height (1400 mm above the beams, 950 mm below)

The detailed design also depends on the deformation induced by the difference of pressure between the outside (atmosphere) and the inside (vacuum); the design should limit the deformation to a minimum. Special care is required at each interface with the dressed cavity through the support and alignment. Figure 4-22 shows a trapezoidal concept adopted for the SPS tests with a top plate assembly of the dressed cavity string which is lowered into the vacuum vessel.

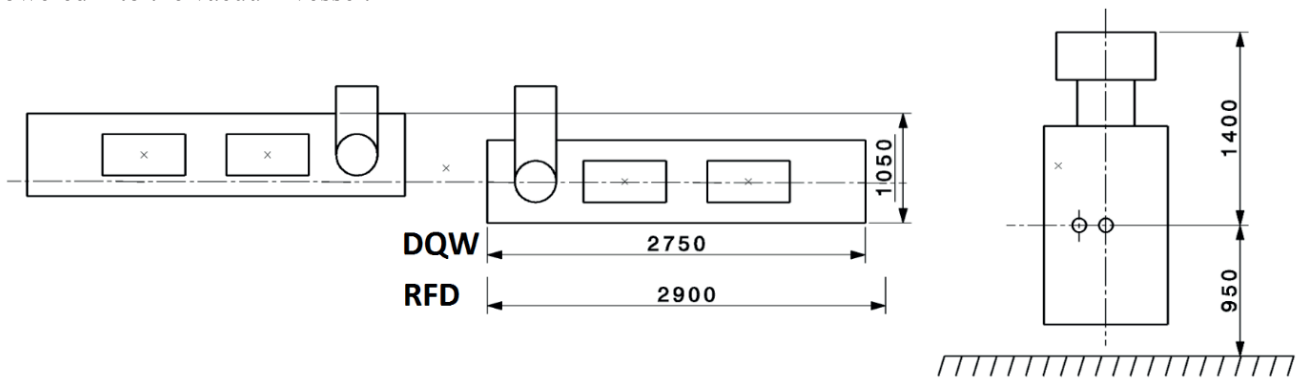


Figure 4-21: A section layout in the LHC for Beam 1 and Beam 2 with a two-cavity cryomodule (left). Maximum vertical envelope for the cryomodules including the RF and cryogenic services with interfaces on the top.

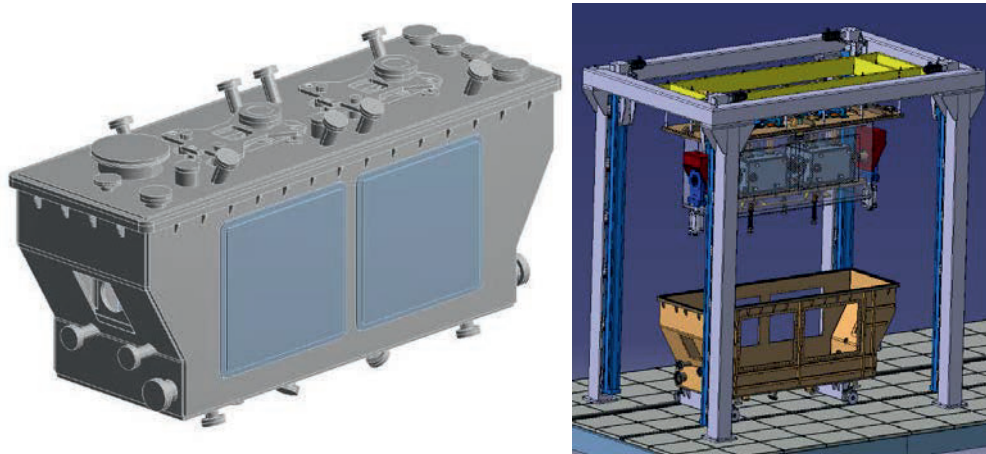


Figure 4-22: The design of the vacuum vessel for the SPS tests with lateral plates in Aluminium for maximum access to the cavity components during assembly and maintenance (left); Assembly concept of the dressed cavity string on the top plate of the vacuum vessel (right).

The use of ribs is foreseen in order to limit the deformation and control the total mass. Preliminary calculations, however, show that the deformation at the interface with the cavity support is about 100 μm . The thickness of the plates (in stainless steel) is 15 mm with the ribs thickness of 50 mm.

4.2.11 RF powering and control architecture

The overall architecture and approximate volume of the RF infrastructure is shown schematically in Figure 4-23. Near P1 and P5, the existing caverns closest to the cavity (RR caverns) are approximately 80 m away, while requiring a large space in the tunnel to pass the RF transmission lines along this distance. Radiation concerns rule out the installation of highly sensitive RF electronics in those caverns. A baseline surface option for the RF services is now replaced by a common underground service gallery (see chapter 15). In the present baseline, the circulators are placed in an RF gallery placed directly above the LHC tunnel with 1m diameter pits connecting the RF power lines. The circulator to cavity transmission lines will be waveguide WR2300 whilst amplifiers to circulators transmission lines will be coaxial lines. The RF gallery is then connected to the main service gallery via a perpendicular tunnel, which is used to host power amplifiers and LLRF and also used for passage (see Figure 4-24). The caverns shall be accessible at any time and adequate shielding is foreseen.

An independent powering system using SPS-type 400 MHz IOT, of 80 kW is assumed. In the SPS, the power requirement is approximately 40 kW for the maximum beam current foreseen for the beam tests. Recent advances in solid-state technology could eventually lead to power sources in the required power range and may provide a flexible platform.

The IOTs provide adequate power overhead in a compact footprint. This scheme would also allow for fast and independent control of the cavity set point voltage and phase to ensure accurate control of the closed orbit and the crossing angle in the multi-cavity scheme. Most importantly, fast control of the cavity fields will minimize the risk to the LHC during an abrupt failure of one of the cavities, ensuring machine protection before the beams can be safely extracted. For such fast and active feedback, a short overall loop delay between the RF system and the cavity is required [12].



Figure 4-23: Schematic of the RF system layout (four per IP side) in the underground cavern above the LHC tunnel lateral view (top); and top view (bottom); Note that these are only estimated values of space requirements.

To provide strong feedback, the low-level RF system requires the total loop delay to be approximately $< 2\mu\text{s}$, including the group delay from the driver, amplifier, circulator, and cable delays. Therefore, a distance of less than 100 m is desired for the separation between the amplifier, electronics, and the cavity in the tunnel. Such a short delay is already in place for the ACS main RF system in P4 (650 ns loop delay) with a service gallery running parallel to the tunnel.

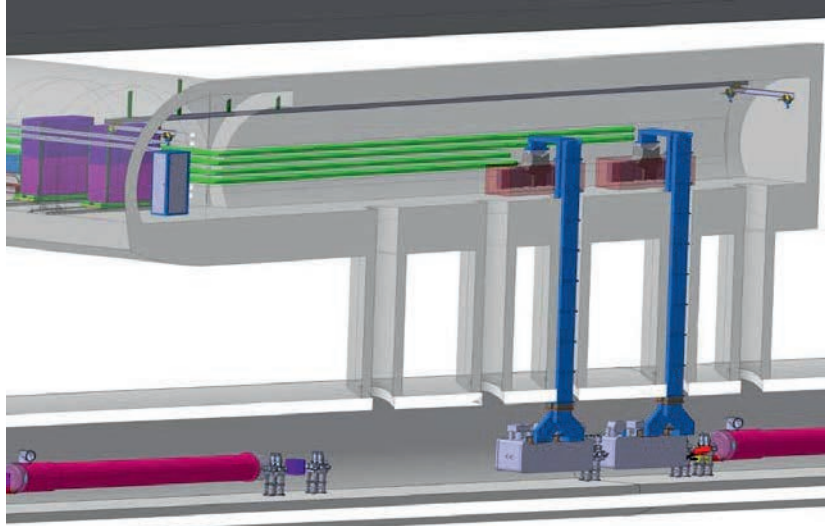


Figure 4-24: Preliminary sketch of a high-power RF, controls and LLRF layout in the underground RF cavern.

The controls and driver electronics are required to be located in a radiation-minimized zone. Assuming one IOT per cavity to provide 80 kW and electronics racks required for drivers, PLC, LLRF, and fast interlocks for eight cavities per IP side, an area of approximately 100 m² is needed near the cavities. The high-voltage power supplies and the power controls would need an additional 85 m². Both the high power and the low level control systems are placed in the nearby underground gallery (UA). The proximity of the circulator and RF loads in the present configuration allows for smaller RF transmission lines from the amplifier to the circulators. The required electrical interfaces are specified in Ref. [20]. Despite the reduction of cryomodules to be installed after the re-baselining in 2016 the space required for a full installation will be maintained.

4.2.12 Low level RF architecture and operational scenarios

The RF control system, also commonly referred as the low level RF system (LLRF), includes several functionalities. First, a tuning control is required to keep the cavity resonant frequency on-tune with the beam during the crabbing operation. If required, the LLRF also has to ensure that the cavity is safely parked at an optimal detuned position during filling, ramping, and collisions without crabbing. This system also synchronizes the phase of the RF kicks with the exact passage of the bunches for both beams. The LLRF includes a regulation loop around the amplifier (to reduce the RF amplitude noise and phase noise in a band extending to a few tens of kHz), plus an RF feedback to precisely control the cavity field. The feedback loop consists of both a local loop around the cavity-amplifier and a global loop regulating the vector sum of voltages on the two sides of the interactions' region. The global loop will reduce beam perturbation following a single cavity trip, by quickly reducing the field in the companion cavities to track the uncontrolled voltage in the faulty cavity. The beam dump system has a three-turn (270μs) response delay.

For each ring, the eight accelerating cavities (ACS) are driven from a single reference generated in a surface building above IP4. These two signals must be sent over phase-compensated links to IP1 (ATLAS) and IP5 (CMS). The up to eight crab cavities of a given ring at each IP are coupled with an 8-in, 8-out multi-cavity feedback (MFB). Figure 4-26 shows the proposed architecture. Operation with the initially installed four crab cavities for one IP and beam is equally possible.

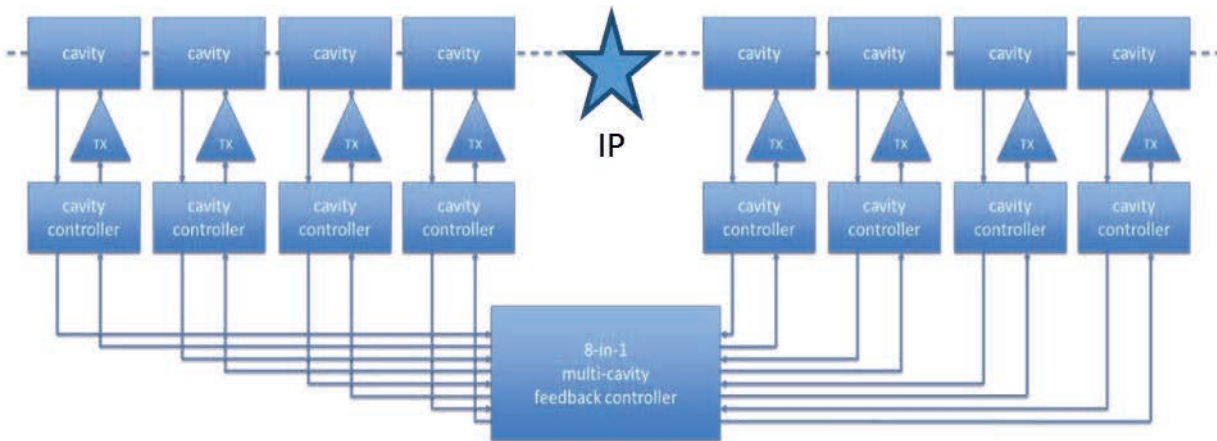


Figure 4-25: Proposed LLRF architecture for one ring at one IP for operation with a final installation of eight cavities. The same architecture is used for the initial stage of four cavities per IP.

A central controller receives measurements from all relevant cavities on each ring and IP, and makes corrections to the drive of each individual RF transmitter (TX). If the field starts changing in a cavity, the MFB will adjust the field in the other cavities on both sides of the IP, such that the orbit distortions remain local. As described in Section 4.2.5 on flat-top, counter-phasing is nulled while keeping the voltage set point small. The RF feedback keeps the cavity impedance small (beam stability) and compensates for beam loading as the cavity moves to resonance. The voltage set points are ramped to synchronously change the voltage in all crab cavities as desired. Any levelling scheme is possible. With a circulator between amplifier and cavity, the TX response is not affected by the cavity tune.

At present the spacing between LHC bunches within a batch is strictly constant along the ring. A large amount of RF power is used in the ACS system to fully compensate the transient beam loading caused by the $3\mu\text{s}$ long abort gap and the smaller gaps required for the injection kicker ('half detuning'). This scheme cannot be extended into the HL-LHC era as it would require excessive RF power. The power required is minimized by optimally detuning the cavity ('full detuning') and adapting the cavity set-point phases bunch by bunch. It results in bunch arrival time modulation of up to $\pm 42\text{ps}$ [25]. This may be acceptable given the 1 ns bunch length. There is no effect on the luminosity as the modulation is identical in both beams, only the vertex position is modulated around the nominal vertex by a maximum of $1\mu\text{m}$ over one turn. The bunch-to-bunch variation within a batch is at least an order of magnitude smaller. If not, the LLRF must synchronize the bunch-by-bunch crabbing field with the actual phase modulation.

The "slow" control is based on programmable logic controllers (PLC) similar to that of the ACS and LINAC4 cavities with the primary role to ensure safety and protection of the RF system. This includes the RF veto and vacuum signals, amplifier control, cavity tuning, high power interlocks, HOM interlocks, beam interlocks, cavity cryogenic interface and access in the RF zone. Each two-cavity cryomodule will be equipped with a single PLC controller with the hardware. The expected PLC cycle time is estimated to 2 ms and the fast interlock cycle time is $15\mu\text{s}$. Remote operation and monitoring will be provided using the standard CERN infrastructure.

4.2.13 Cavity failure scenarios

Crab cavity failures can lead to a fast voltage and/or phase change with a short time constant. This can lead to large, global head-tail oscillations, or coherent betatron oscillations with a change in transverse beam trajectories of 1.7σ for a single cavity failure; the effect is cumulative with the number of failing cavities. These failures can be broadly classified into two categories.

- Fast failures, single or few turns. For example, a sudden cavity quench or breakdown.

- Slow failures, several tens of turns or greater (caused by vacuum degradation, voltage and phase drifts, or similar).

Due to the relatively high quality factor in the superconducting cavity, the stored energy inside the cavity can typically only be extracted with a time constant determined by Q_L , which results from the strong coupling to the cavity via the power coupler. The stored energy will decay with a time constant $\tau = 2Q_L/\omega_0$. For $Q_L = 5 \times 10^5$, the time constant is approximately $400\mu\text{s}$. The three turn delay time ($267\mu\text{s}$) for a beam dump trigger is an important consideration during a RF source failure, where the cavity field decays to roughly half its value before the beam can be safely aborted. In the case of a quench, the time constant of field decay may be dominated by the quench dynamics rather than Q_L . The situation is similar to strong and sudden electron loading due to multipacting or other phenomena.

The cavity quench mechanism described above and the measurements from KEKB crab cavities [26] indicate that typically a quench is a slow thermal process (typically of the order of several milliseconds). Once the temperature of a sufficiently large area exceeds the critical temperature of niobium, the quench can propagate very quickly to completely quench the cavity or cause RF breakdown. However, any change in cavity quality factor well before reaching a critical temperature limit could be easily detected from the requested forward power (fast) or changes in the cavity temperature bath (slow). An interlock on the forward power, except due to induced orbit excursion, can cut the RF to slow down or stop quench propagation. A beam abort, if required, can be triggered simultaneously (a few μs) for machine protection.

4.2.14 Failure scenario mitigation

The choice of low operating temperature (2 K) and moderate surface field levels allow operation with ample margin over quench temperature and field limits. The significantly better thermal conductivity of superfluid helium should also improve the thermal performance and stability of the cavity. Additional measures in the cryomodule design are being considered to dimension the helium enclosures with sufficient margin for heat flux. The cavity thermal and RF stability will be thoroughly tested in the SM18 test facility and during the SPS beam tests.

To minimize the perturbation on the beam during a cavity failure, the MFB will adjust the field in the other cavities on both sides of the IP, such that the orbit distortion remains local. Figure 4-26 shows the cavity control of two cavities across the IP with one cavity failure and the RF controller to adjust the second cavity to follow. The rapid change in field will also result in a detuning of the cavity; however, the mechanical tuning system is unable to adjust the tune within $400\mu\text{s}$. Since a rapid breakdown of a failed cavity may become unpredictable, it is probably safest to ramp down the cavities synchronously. However, small and slow changes in one of the cavities can be adjusted for without aborting the beam.

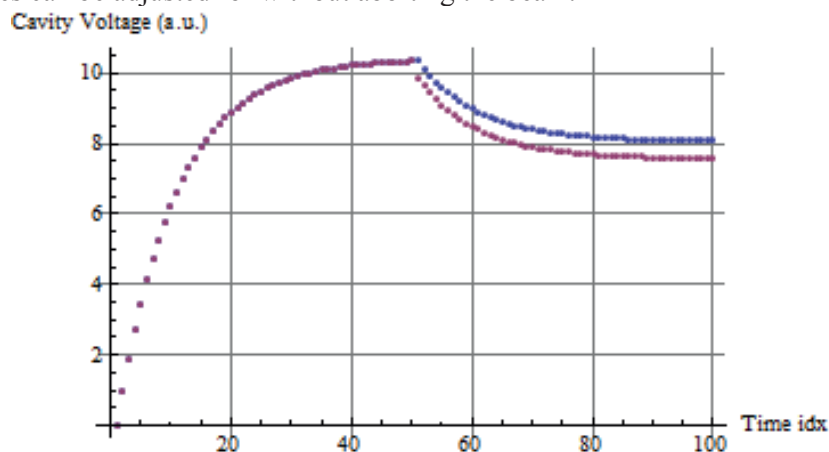


Figure 4-26: Voltage response with strongly coupled cavities across the IP as a function of time [μs]. At $50\mu\text{s}$, one cavity trips (red trace) and the other one is forced by the RF controller to follow (blue trace).

The cavities can be equipped with a fast tuning system such as a piezo mechanism. If the speed of such tuning devices is sufficient, it could compensate for Lorentz force detuning during transients and thus keep the tune within the bandwidth of the feedback system. If the SPS tests show fast tuning to compensate for cavity transients, piezo stacks can be added to the actuation within a limited range.

An additional mitigation to avoid large beam losses (and hence deposited energy) in the case of single or multiple cavity failures is a robust measurement and interlocking of the tail population and eventual head–tail oscillations. The addition of halo depletion methods (e.g. a hollow electron lens) for cleaning of the bunch tails to ensure a low particle density in the beam halo and interlocking with improved diagnostics like fast head–tail monitors and/or fast beam loss monitors (e.g. diamond monitors) are under investigation.

4.2.15 Heat loads and cryogenics

The cavities are housed in individual titanium helium tanks connected by a 100 mm diameter two-phase He pipe placed above the cavities along with a 20 mm diameter cool down bypass lines placed below the tanks. The two-phase pipe ensures that the liquid is fed to the cavities by gravity, and is also used as a pumping line for gaseous helium. A saturated helium bath maintains the cavities operating temperature at 2 K. Liquid helium is supplied to the two-phase pipe through a 10 mm supply line. It is proposed to fill the cryostat from one single point at the extremity opposite to the pumping outlet of the two-phase pipe, and to control the He level at about half of the two-phase pipe diameter.

The bottom bypass of 20 mm diameter will be used during cool down for parallel helium distribution to two helium tanks allowing for progressive cavity cool down from the bottom to the top. This bypass will have also the function to equilibrate the quantity of helium between two tanks in cases when the two-phase pipe will be out of this function (transients – e.g. filling, special tests). The static plus dynamic heat loads are expected to be approximately 30 W to the 2 K bath for a two-cavity module. The cryogenic limits in the LHC are not precisely known at this time. However, the 15 W per cavity heat load at 2 K is small compared to the LHC heat load capacity; the total heat load of the LHC crab cavity systems is estimated at 0.5 kW at 2 K.

4.2.16 Vacuum system

The crab cavity system has three independent types of vacuum systems: the cavity vacuum, the adjacent beam pipe, and the cryostat. The two-cavity common vacuum is pumped at room temperature with two ion pumps mounted at each end of the modules. However, at 2 K, the cryogenic pumping of the cavity walls is the dominating feature, with a pumping speed of 10 000 L/s. The background pressure without RF is expected to be much better than 10^{-10} mbar and likely limited by the measurement devices such as Penning gauges. Pressure signals provided for RF control are a hardware interlock from the ion pumps to cut the high voltage and readout from the Penning gauges, one per coupler, to limit the RF power. The cavity vacuum can be isolated by four all-metal valves at the ends of each module (two interior and two exterior to the cryomodule), to maintain vacuum during transport and installation.

The second beam pipe for the counter-rotating beam has to pass through the cavity helium vessel due to its proximity. It is planned that this will be made of niobium and will remain superconducting at close to 2 K to preserve the same surface conditions as in the cavity. The use of carbon coating in the warm regions near the crab cavities to reduce the pressure and to avoid electron cloud effects is currently not considered; this would risk contamination of the cavities.

The insulation vacuum is less demanding in terms of pressure, the modules being pumped to 10^{-5} mbar before being cooled down. When cold, the insulation vacuum also benefits from the cryogenic pumping of the cold surfaces and the operating pressure will decrease to 10^{-7} mbar. Turbo molecular pumps are used and pressures are measured using Penning gauges.

4.2.17 Interlocks for machine protection

Due to the immense stored energy of the beam (>700 MJ), the transient behaviour of the crab cavities is of concern. The crab cavity system will be equipped with several levels of interlocks both for machine protection and to protect the RF system itself. Slow and fast interlocks, including specific RF interlocks (reflected power, signal level, arc detection, etc.) will ensure safe operation under all conditions and cope with transients; the interlock system will be fully embedded in the overall machine interlock system. All RF systems, including amplifiers, circulators, and loads are designed to withstand full reflection in the case of a malfunction in the RF chain.

4.2.18 SM18 and SPS beam tests

The addition of crab cavities to the LHC should ensure robust functioning through the entire sequence of the LHC physics cycle. Since crab cavities of this type have yet to be realized and used with hadrons, beam tests with a prototype two-cavity cryomodule are a prerequisite to identifying potential risks from the technology to safe and reliable operation of the LHC. Therefore, an essential milestone for a crab cavity in the SPS is to demonstrate the operational reliability, ensure machine protection and cavity transparency. All RF manipulations and cavity-beam interactions will first be validated and commissioned in the SPS with the prototype module. The beam tests are planned as machine development studies during the run 2018–2019. Successful validation of the crab cavities in the SPS is a prerequisite for installation in the LHC.

4.2.18.1 Tests before installation

The two-cavity cryomodule will be assembled in SM18 with the cold masses (cavities, helium vessels, HOMs, and tuner) with contributions from the USLARP and UK collaborations. The cold masses are first tested and qualified to their final specification at the SM18 facility. The assembly of the power coupler is foreseen as a final assembly step prior to the string assembly of the two cold-masses in the SM18 clean room due to the risk associated with damage during transport.

The SPS cryomodule in its final assembly, along with all of the other major components, will be tested for vacuum integrity, RF performance, and operational reliability in the SM18 horizontal bunker to their nominal specifications prior to installation in the SPS. The RF control and interlock system will also be validated in SM18 as intense gamma radiation could be produced during cavity RF conditioning and operation of high fields.

4.2.18.2 SPS environment

The LSS6 region in the SPS ring will be equipped with a set of Y-chambers with mechanical bellows that allow for transverse displacement. This allows for a test module to be moved out of the beam line during regular operation of the SPS and only be moved into the beam line during the periods dedicated to machine development with crab cavities. This is essential both due to aperture limitations of the crab cavities and the risk associated with leaving the cavities in the beam line with different modes of operation in the SPS. The cryomodule is placed on a motorized transfer table that can move sideways by 510 mm (see Figure 4-27). The transfer table will also support the Y-chambers, the two RF circulators and loads and a cryogenic valve box. Due to limited space, hosting the RF and cryogenic refrigeration systems in the tunnel is not feasible. RF power amplifiers will be installed in the surface building BA6 and RF power routed via coaxial cables to the cryomodule. To limit heat losses and ease integration, the warm part of the cryogenic refrigeration system (compressor, oil removal system) is installed in BA6, while a cold-box is installed in an underground alcove to provide the required liquefaction capacity. Liquid helium will be routed to the cryomodule via a 110 m long cryogenic distribution line. A local dewar and two helium pumps for 2 K refrigeration complete the proximity cryogenics. Oxygen Deficiency Hazard detectors and acoustic alarms will cover the zone to protect personnel against cold helium release in the tunnel.

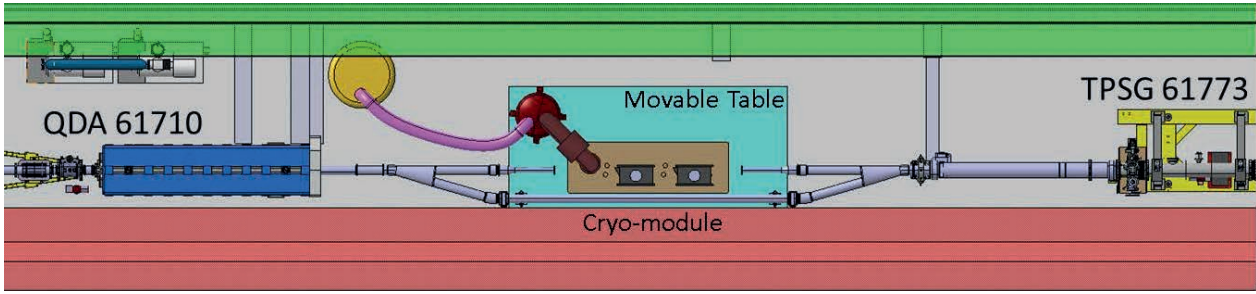


Figure 4-27: Top view of the integration of the cryomodule, RF assembly, and the cryogenics in the SPS-LSS6 region. The zone marked in red and green are stay clear zones for transport and cabling respectively.

Beam vacuum layout will be modified, creating a new vacuum sector for the cryomodule and beam bypass. To reduce Secondary Electron Yield for electron cloud mitigation, thus ensuring the low vacuum conditions required for crab-cavity operation, all vacuum chambers adjacent to the cryomodule will be carbon-coated. Suitable interlocks for circulating beam and beam extraction with respect to the transfer table position and status will ensure machine protection.

The relevant cryomodule envelope dimensions for the SPS tests is given in Table 4-3. In general, the SPS constraints are tighter than those of the LHC.

Table 4-3: Cryomodule envelope dimensions.

Description	Distance [mm]
Cryomodule length (plug gate valve to plug gate valve)	3000
Horizontal distance cavity axis to inner edge of cryomodule volume	420
Vertical distance, floor to cavity axis	1200
Maximum height above cavity axis	1200
Inner diameter of cavity beam pipe	84
Horizontal distance cavity axis to bypass beam pipe axis	510

4.2.18.3 SPS RF system and operation

Specially designed WR2300 waveguides will feed the RF power from the circulator to the respective cavity. An LHC-type circulator, although over-dimensioned, is preferred for reasons of maintenance and spares policy. Smaller coaxial lines will ensure the RF transmission from each amplifier to the respective circulator and load. A 3D integration of the cryomodule and the RF assembly is shown in Figure 4-28. To avoid stresses on the waveguides, the feeding coaxial cables are fixed on the transfer table.

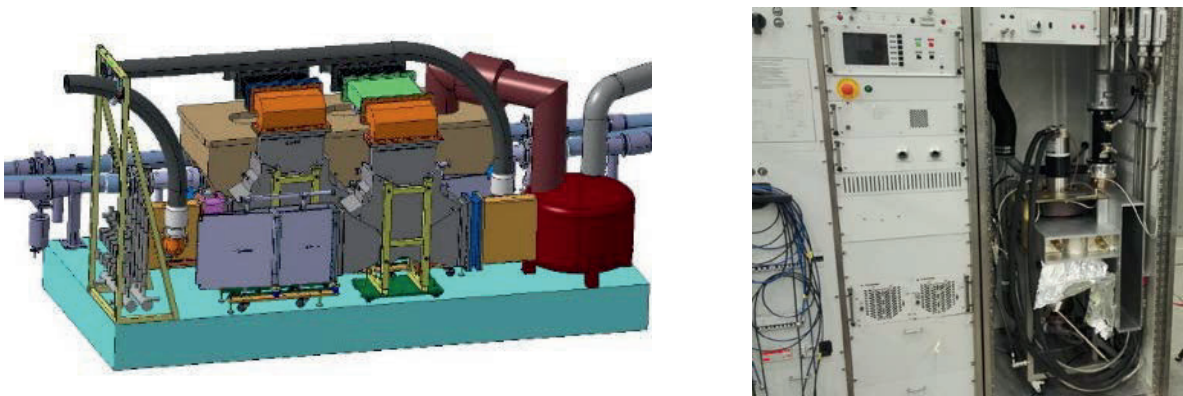


Figure 4-28: (left) Cryomodule and RF system layout; (right) a modified SPS-IOT at 400 MHz under test.

In the LHC, the two cavities per IP side and beam are always powered on tune, initially with a small voltage (10%–15% of the nominal) and counter-phased with active feedback to guarantee maximum beam stability during the entire cycle. Therefore, beam injection with counter-phased cavities with low voltage requires testing in the SPS. Other issues related to beam loading and transient effects with and without RF feedback and slow orbit control will be studied to evaluate the stability and tolerances required from the feedback systems. Induced RF trips and their effects on the beam will be studied in detail to guarantee machine protection and to devise appropriate interlocks. Long-term effects with crab cavities on coasting beams at various energies will also be tested.

4.2.18.4 SPS cryogenics requirements

With the aim of covering both the SPS crab-cavity testing program and to allow for cold operation of the LHC ACS in point 4 independently of the magnet cooling, a new mobile refrigerator is under procurement. The compressor, located at the surface in BA6, will be connected to the cold-box underground by two warm lines for high and low pressure gas. Integration is studied to allow for removal and relocation of both the warm equipment and the cold-box, with the remaining infrastructure remaining in place. The capacity of the new cold box was specified to cover crab cavity static and dynamic heat losses including a contingency factor of 1.5 (at least 48W at 2 K, equivalent to 2.06 g/s. Nitrogen precooling of the cold-box is under study. With this approach all operations at 4.5 K such as cool down and filling should be performed reliably. The first limitation from the new system is expected to be on low pressure helium pumping for normal operation at 2 K: careful design of all connections will help minimizing the global heat loss.

4.2.18.5 SPS tuning requirements

For beam tests in the SPS a slow mechanical tuner system is required to bring the cavity on resonance in the energy range of the SPS (0 – 60 kHz). In addition, the tuner must allow detuning of the cavity to its parking position, and it has to be precise enough to work together with the RF feedback. Table 4-4 summarizes the potential energies at which the SPS can be operated for crab cavity tests and their corresponding RF frequencies compared with that of LHC operation.

Table 4-4: Detuning ranges for the LHC and SPS.

Parameter	Unit	LHC	SPS		
Energy	GeV	450–7000	120	270	450
Frequency	MHz	400.79	400.73	400.78	400.79
$f - f_0$	kHz	0	-58.2	12.2	-2.4
Bandwidth	kHz	0.4–4	0.4–4	0.4–4	0.4–4
Max Detuning	Hz	± 5.5	± 21.7		

The detuning required to tune the cavity in its parking position (between betatron lines) is approximately ± 21.7 kHz in the SPS. The detuning requires a resolution of at least one-quarter of the final cavity bandwidth due to available power limits. Additional studies are required to determine the need for tuning system than that possible with the present mechanical tuner if limitations arise from feedback and/or orbit control.

4.2.18.6 SPS test objectives

A detailed report on the potential of the SPS test program with crab cavities can be found in Ref. [24]. The test programme objectives in the SPS are given below.

- Demonstrate cavity deflecting field with proton beam including injection, energy ramp, and coast at energies ranging from 26– 450 GeV.
- Verify and control the cavity field (amplitude and phase), frequency, tuning sensitivity, input coupling, power overhead, and HOM signals. Establish and test operational cycle with crab cavities.

- Demonstrate the possibility to operate without crab cavity action (make them invisible) by both counter-phasing the two cavities or by appropriate detuning (to parking position) at energies ranging from 26– 450 GeV. The precision phasing between the two cavities including the cable delays to represent the LHC scenario of cavities separated across the IP will be tested.
- Measure beam orbit centering, crab dispersive orbit, and bunch rotation with available instrumentation such as BPMs and head–tail monitors.
- Demonstrate MFB operation.
- Demonstrate non-correlated operation of two cavities in a common cryomodule – trigger quench in one cavity without inducing quench in the other.
- Define and implement interlock hierarchy. Verify machine protection aspects and functioning of slow and fast interlocks.
- Test HOM coupler operation with high beam currents, different filling schemes, and associated power levels. Measurement of impedance and instability thresholds for nominal mode and HOMs.
- Measure emittance growth induced by the crab cavities as far as possible.

4.2.18.7 Outline of an SPS test programme

- Initial RF commissioning with the cryomodule with high power RF in the out-of-beam position (no dedicated Machine Development (MD) required).
- RF commissioning with low-intensity beam, single bunch to a few bunches. Establish the proper RF parameters, including cavity tune, operating frequency, amplitude, and phase. Verify crab cavity active and invisible.
- High intensity single bunches to trains of bunches to investigate the effect of cavity performance, impedance, and machine protection; and characterize the transient behavior of the crab cavity system as a function of beam current. Verify cavity stability over many hours (as relevant for LHC physics fill).
- Long-term behavior of coasting beams in the SPS with relatively low intensity to study the effects of cavity drifts, emittance growth and possibly non-linear effects such as RF multipoles

4.3 Harmonic systems

A harmonic cavity is presently not part of the HL-LHC baseline. However, two types of harmonic systems are considered as options [25], [27].

- A higher harmonic (800 MHz) system can be used either for changing the bunch profile (in bunch lengthening mode (BL)) or for increasing the synchrotron frequency spread (in BL or bunch shortening mode (BS)). Depending on the mode of operation, this RF system can help to reduce the beam-induced heating, effect intra-beam scattering, improve longitudinal beam stability, and in some scenarios increase or level luminosity.
- A sub-harmonic (200 MHz) system could either completely replace the existing main RF system or work jointly with the 400 MHz RF system, which in this case will act as the second harmonic. The lower harmonic RF system will improve the capture efficiency for longer SPS bunches with very high intensity. The benefits of the combined 200 MHz and 400 MHz system are similar to the above double-harmonic system but with the primary aim of luminosity improvement.

For the higher harmonic system (800 MHz), a maximum of 8 MV longitudinal voltage can be provided from approximately four to ten cavities depending on the mode of operation [25]. The relevant RF parameters are listed in Table 4-5. A maximum of 300 kW input power assumed to be feasible [28]. The BS mode, with the full-detuning scheme in the fundamental 400 MHz cavities, requires significantly lower RF power. Therefore, a four-cavity system is more than adequate to provide the required 8 MV with a maximum power

of 300 kW per cavity. In the BL mode, the required RF power at 1 MV already exceeds 300 kW. Therefore, approximately 10 cavities are needed to provide for the 8 MV required to stay below the RF power limit.

Table 4-5: Relevant RF parameters for 800MHz RF cavities.

Characteristics	Units	Value
Resonance frequency	MHz	801.58
Total accelerating voltage	MV	8.0
Number of Cavities		4 (BS), ~ 10 (BL)
Residual resistance R_s	n Ω	~ 250
R/Q	Ω	~ 45
Q_0		$\geq 1 \times 10^9$
Q_{ext}	–	10^5 (BS), ~ 10^4 (BL)
RF power per cavity	kW	10^5 (BS), ~ 10^4 (BL)
Operating temperature	K	4.5

Replacing the existing acceleration system with a sub-harmonic system (200 MHz) will require a minimum of 3 MV of longitudinal voltage to capture, accelerate, and store the HL-LHC beams [29]. This can be provided from two to four compact quarter wave cavities, where the number of cavities also depends on power requirements and technology constraints [25]. Some relevant RF parameters for the 200 MHz cavities are listed in Table 4-6.

Table 4-6: Relevant RF parameters for 200 MHz RF cavities.

Characteristics	Units	Value
Resonance frequency	MHz	200.4
Total accelerating voltage	MV	3– 6
Residual resistance R_s	n Ω	≤ 10
R/Q	Ω	≈ 50
Q_0		$\geq 1 \times 10^{10}$
Q_{ext}		$\sim 2 \times 10^4$
RF power (assumed)	kW	500
Operating temperature	K	4.5

The total static and dynamic heat load for either system has to be evaluated in detail during the engineering phase of the cryomodule. A cryogenic sectorization of two cavities per cryomodule is assumed for modularity, maintenance, and reliability. For 200 MHz, a preliminary estimate of 120 W for a two-cavity module at 4.5 K can be assumed where each cavity operates at 3 MV. The cavity technology (bulk niobium or Nb-coated copper cavities) can play a role in the final quality factor of the cavity and hence the heat loads at the operating gradient.

For the 800 MHz system, the frequency dependence of the surface resistance gives 250 n Ω leading to approximately 50 W at 4.5 K due to dynamic RF losses. This is only 1 W at 2 K. A geometric factor of 230 Ω and a cavity voltage of 2 MV are assumed. Therefore, it is preferable to operate the 800 MHz system at 2 K to both take advantage of the lower surface resistance and superior properties of superfluid helium. Assuming a baseline of 4.5 K, approximately 200 W can be assumed as an upper limit for a two-cavity module.

4.4 Transverse damper (ADT) upgrade

The LHC requires a transverse feedback to damp injection oscillations and provide stability for impedance-driven transverse instabilities, thus guaranteeing preservation of beam intensity and emittance [25]. The existing coupled bunch feedback system ADT, installed in P4 of the LHC, was fully commissioned in 2010 [31]. It damps transverse instabilities within a bandwidth of 20 MHz, correcting the oscillations of the centre of gravity of the individual bunches about their orbit.

For the upgrade of the ADT system, three possible routes have been identified in the past [32]: increase of kick strength, reduction of noise, and increase of bandwidth. A space reservation of approximately 5 m on each side was made in the original design of the LHC to install more kickers adjacent to the existing ADTs in P4 [34].

Following the experience of the LHC Run 1, priority was given to an upgrade of the pick-up and signal processing systems aimed at reducing the noise floor, one of the options already foreseen in 2006. This includes new electronics and a doubling of the number of pick-ups, from two to four per beam and plane, with commissioning foreseen after LS1 [34]. The experience of Run 1 has also shown that an increase in kick strength may not be required, as injection errors are on average more than a factor of 4 smaller than originally assumed, and fast damping times of less than 20 turns for the injection errors can be achieved with the existing system. During Run 1, improvements in ADT signal processing were tested to address single bunch oscillations observed, which were different in nature from the coupled bunch oscillations typically driven by the resistive wall impedance, which falls off in frequency towards 20 MHz. The nature of some of these observed instabilities was not entirely unravelled during Run 1, and new diagnostics such as the multiband instability monitor (MIM) were added to the LHC to better characterize these instabilities [35]. Improvements in ADT signal processing tested during Run 1 permit running with a flat frequency response of up to approximately 20 MHz [36]. Beyond 20 MHz, the kicker and ADT power amplifier system cannot be used.

For the HL-LHC, a transverse kicker system with a larger bandwidth than 20 MHz would be an asset in view of the high bunch intensity.

In the SPS a development was started in 2008 within the USLARP program to design a high bandwidth transverse feedback system [37, 38] that aims at damping intra-bunch motion. The system consists of pick-ups, kickers, power amplifiers, and signal processing. Both slot-line and strip-line kickers are studied for this system; slot-line kickers could offer broadband response of up to 1.2 GHz [39]. The system can also be used to damp and attenuate intra-bunch motion caused by the electron cloud, impedance-driven instabilities, or other perturbations driven, for example, by beam–beam effects or crab cavities. With its generic approach the results of the SPS development are relevant to other accelerators, including the LHC and other large colliders.

At 1 GHz four slotlines, as developed for the SPS LIU project [39], with 2 kW amplifier power per coupling port can develop a transverse voltage of 37 kV. Consequently, the beam can be kicked by 82 nrad at 450 GeV and 5 nrad at 7 TeV. Assuming a reference beta function value of 180 m, at pick-up and kicker, the kick strength corresponds to removing 15 μm of oscillation at 450 GeV and 0.9 μm at 7 TeV, within a single turn. As a feedback system with a gain corresponding to 500 turns damping time, saturation would occur at 3.7 mm at 450 GeV and 225 μm at 7 TeV.

But the Wide Band Feedback system options are, at least for the moment, not part of the LIU and HL-LHC baseline upgrade ingredients and are only considered as an option for both upgrade projects [40].

4.5 References

- [1] A. Piwinski, Nucl. Instr. and Meth. 81, 199 (1970).
- [2] R. Palmer, Energy scaling, crab crossing and the pair problem, [SLAC-PUB-4707](#), 1988.
- [3] K. Oide, K. Yokoya, The crab crossing scheme for storage-ring colliders, [SLAC-PUB-4832](#) (1989).
- [4] Y. Funakoshi, Operational Experience with Crab Cavities at KEKB, ICFA Mini-Workshop on Beam-Beam Effects in Hadron Colliders, CERN, Geneva, Switzerland, 18 - 22 Mar 2013, pp.27-36 (CERN-2014-004) (2014). DOI: [10.5170/CERN-2014-004.27](https://doi.org/10.5170/CERN-2014-004.27)
- [5] S. Fartoukh, Pile up management at the High Luminosity LHC and introduction to the crab kissing concept, CERN-ACC-2014-0076 (2014). DOI: [10.1103/PhysRevSTAB.17.111001](https://doi.org/10.1103/PhysRevSTAB.17.111001)
- [6] G. Arduini et al., Summary of the LHC-CC11 Crab Cavity Workshop, [CERN-ATS-2012-055](#), 2012.

- [7] S. De Silva et al., Compact Superconducting RF-dipole Cavity Designs for Deflecting and Crabbing Applications, 4th International Particle Accelerator Conference, Shanghai, China, 12 - 17 May 2013, pp.[2483-2485](#) (2013).
- [8] B. Hall et al., Analysis of the Four Rod Crab Cavity for HL-LHC, in the proceedings of IPAC12, New Orleans, 2012; G. Burt et al., Manufacture of a Compact Prototype 4R Crab Cavity for HL-LHC, 4th International Particle Accelerator Conference, Shanghai, China, 12 - 17 May 2013, pp.[2420](#) (2013). [CERN-ACC-NOTE-2014-0076](#)
- [9] R. Calaga et al., A Double Quarter-Wave Deflecting Cavity for the LHC, 4th International Particle Accelerator Conference, Shanghai, China, 12 - 17 May 2013, pp.[2408](#) (2013); Q. Wu et al., Mechanical Study of 400 MHz Double Quarter Wave Crab Cavity for LHC Luminosity Upgrade, 4th International Particle Accelerator Conference, Shanghai, China, 12 - 17 May 2013, pp.[2417](#) (2013).
- [10] A. Yamamoto et al., Crab cavity system external review report, [CERN-ACC-2014-0093](#), 2014.
- [11] R. Calaga, A. Ratti, presented at the 4th HiLumi-LHC Meeting, KEK, 2014.
- [12] P. Baudrenghien, LLRF for Crab Cavities, presented at the 2nd HiLumi-LHC Meeting, Frascati, 2012.
- [13] P. Baudrenghien et al., Functional specification of the LHC prototype crab cavity system, [CERN-ACC-Note-2013-003](#), 2013.
- [14] R. Calaga, B. Salvant, Comments on crab cavity HOM power, [CERN-ACC-NOTE-2015-0024](#).
- [15] N. Biancacci et al., HL-LHC impedance and stability studies, presented at the 4th HiLumi-LHC workshop, KEK, 2014.
- [16] M. Navarro-Tapia, R. Calaga, A. Grudiev, RF multipoles from crab cavities, in the proceedings of IPAC13, Shanghai, 2013.
- [17] K. Brodzinski, S. Claudet, Private communication.
- [18] S. Pattalwar et al., Key Design features of the Crab-Cavity cryomodule for HiLumi-LHC, 5th International Particle Accelerator Conference, Dresden, Germany, 15 - 20 Jun 2014, pp.[WEPR1045](#).
- [19] T. Jones et al., presented at the Crab cavity manufacturing readiness meeting, INDICO: 334041, CERN, 2014.
- [20] L. Arnaudon et al., Conceptual specification of the crab cavity RF system, EDMS 1363181, 2014.
- [21] <http://www.npl.co.uk/science-technology/dimensional/frequency-scanning-interferometry-research>
- [22] BCAM “Brandeis CCD Angle Monitor”, <http://alignment.hep.brandeis.edu>
- [23] P. Fessia et al., Private communication.
- [24] G. Arduini, R. Calaga, A. Castilla, R. Jones, CERN-ATS-2016, 2016
- [25] R. Calaga, Chamonix 2014, in the proceedings of the LHC Performance Workshop, Chamonix 2014.
- [26] K. Nakanishi et al., Beam Behaviour due to Crab Cavities Break down, in the proceedings of IPAC10, Kyoto, 2010.
- [27] R. Calaga et al., Conceptual specification of the LHC RF harmonic system, EDMS [1363179](#), 2014.
- [28] E. Montesinos, Private communication.
- [29] E. Shaposhnikova, Harmonic system for the LHC, presented at the 4th HiLumi-LHC Meeting, KEK, 2014.
- [30] O. Brüning et al. (ed.), LHC Design Report, [CERN-2004-003](#), CERN, Geneva (2004), p. 140-142.
- [31] W. Hofle, D. Valuch, Transverse Feedback: high intensity operation, AGC, IGC, lessons for 2012, LHC Beam Operation Workshop, Evian, December 2011, [CERN-ATS-2012-083](#), CERN, Geneva (2012), p. 97-100.
- [32] W. Hofle, Transverse Feedback Systems in LHC and its Injectors: Projected Performance and Upgrade Paths, 3rd CARE-HHH-APD Workshop, LHC-Lumi-06, Valencia, 16-20 October 2006, CERN-2007-002, CERN Geneva (2007), p. 177-179. DOI: [10.5170/CERN-2007-002.177](#)
- [33] CERN CDD Drawing LHCLJ4GA0007 AH, EDMS [376008](#) March 2007

- [34] W. Hofle, G. Kotzian, T. Levens and D. Valuch, Transverse feedback, in the proceedings of the 5th Evian Workshop, [CERN-ACC-2014-0319](#) (2014).
- [35] R.J. Steinhagen, M.J. Boland and T.G. Lucas, A multiband-instability-monitor for high-frequency intra-bunch beam diagnostics, 2nd International Beam Instrumentation Conference, Oxford, UK, 16 - 19 Sep 2013, pp.[TUBL3](#).
- [36] W. Hofle, F. Dubouchet, G. Kotzian and D. Valuch, Performance of the LHC transverse damper with bunch trains, 4th International Particle Accelerator Conference, Shanghai, China, 12 - 17 May 2013, pp.[3022](#).
- [37] R. Thompson et al., Initial Simulation of Damping System for Electron Cloud Driven Instabilities in the CERN SPS, Particle Accelerator Conference 2009, Vancouver, Canada, 04 - 08 May 2009, pp.[FR5RFP076](#).
- [38] J.D. Fox et al., First Results and Analysis of the Performance of a 4 GS/s Intra-Bunch Vertical Feedback System at the SPS, 4th International Particle Accelerator Conference, Shanghai, China, 12 - 17 May 2013, pp.[3070](#).
- [39] J. M. Cesaratto et al., SPS Wideband Transverse Feedback Kicker: Design Report, [CERN-ACC-NOTE-2013-0047](#)
- [40] LIU-SPS Wideband Feedback Review, INDICO: [510321](#) CERN, 2016.

Chapter 5

Collimation System

5 Collimation system

5.1 LHC multi-stage collimation system

5.1.1 Motivation

A variety of processes can cause unavoidable beam losses during normal and abnormal operation. Because of the high stored energy above 700 MJ and the small transverse beam sizes, the HL-LHC beams are highly destructive. Even a local beam loss of a tiny fraction of the full beam in a superconducting magnet could cause a quench, and larger beam losses could cause damage to accelerator components. Therefore, all beam losses must be tightly controlled. For this purpose, a multistage collimation system has been installed [1–8] to safely dispose of beam losses. Unlike other high-energy colliders, where the main purpose of collimation is to reduce experimental background, the LHC and the HL-LHC require efficient beam collimation during all stages of operation from injection to top energy.

The HL-LHC poses increased challenges to the collimation system. Assuming that primary beam loss conditions were the same as in the LHC, the factor ~ 2 increase in total stored beam energy foreseen from the HL-LHC parameters will require a corresponding improvement of cleaning performance to achieve the same losses in cold magnets. Total losses might also exceed the robustness limit of collimators. The LHC system was designed to safely withstand beam lifetime drops down to 0.2 h during 10 s, corresponding to peak losses of up to 500 kW. As mentioned above, these loss levels scale with the total beam intensity so they will increase by about a factor of 2 for the HL-LHC parameter set. The collimation system must be upgraded to cope with these higher loss levels. It is clear that the lifetime control and optimization of beam halo losses will be crucial for the LHC upgrade. The larger stored energy, together with smaller beam sizes achieved through higher brightness beams, also imposes more severe challenges for collimator robustness against design loss scenarios for cleaning. In the case of single-turn beam failures, brighter beams significantly increase thermo-mechanical loads on collimator materials and components. The higher peak luminosity challenges entail the definition of new concepts for physics debris cleaning and an overall redesign of the IR collimation layouts. For example, in the present LHC layout, the inner triplet represents the IR aperture bottleneck and is protected by two dedicated tertiary collimators per plane per beam. Future optics scenarios might add critical aperture restrictions at magnets further away from the IP, requiring additional cleaning and protection.

Additional concerns for the HL-LHC collimation system are raised by possible beam instabilities triggered by the large electrical resistivity of the materials used for LHC primary and secondary collimators. As discussed in Chapter 2, given the higher bunch population and brightness of the beams required for HL-LHC and the fact that almost the maximum values in chromaticity and Landau octupoles current have been used since 2012, it is crucial for HL-LHC to minimize the transverse impedance to better conditions for beam stability. The identification of collimator materials greatly improving their electrical conductivity while maintaining the structural robustness of existing LHC collimators is therefore a crucial objective in the design of a new low-impedance collimation system. Note the HL-LHC also relies significantly on operational efficiency as it is based on a levelled luminosity. Improvements of the collimator setup time and of downtimes from collimator faults also call for an update of the present system.

To meet the new challenges, the HL-LHC collimation system therefore builds on the existing LHC collimation system, with the addition of several upgrades.

5.1.2 Collimation system inherited from the LHC

The backbone of the HL-LHC collimation system will remain, as for the current LHC, the betatron (IR7) and momentum (IR3) cleaning systems installed in two separated warm insertions [1]. A very efficient halo cleaning, as required to operate the LHC with unprecedented stored beam energies in a superconducting collider, is achieved by very precisely placing blocks of materials close to the circulating beams, while respecting a pre-defined collimator hierarchy that ensures optimum cleaning in a multi-stage collimation process. This is illustrated schematically in Figure 5-1. Most collimators consist of two movable blocks referred to as ‘jaws’, typically placed symmetrically around the circulating beams. The present system, deployed for LHC operation between 2010 and 2013, provided a cleaning efficiency of above 99.99% [2], i.e. it ensured that less than 10^{-4} of the beam losses are lost in superconducting magnets. Even if there are important upgrades foreseen for HL-LHC, addressing several potential limitations of the present system, about 30-40 % of the present system will have to remain operational throughout the HL-LHC era as part of the HL-LHC system. These collimators will need to be kept fully operational to ensure an efficient operation of HL-LHC.

The LHC collimators are built as high-precision devices. With beam sizes as small as $200\ \mu\text{m}$, outstanding mechanical precision is needed in order to ensure the correct hierarchy of devices along the 27 km ring. Details of the collimator design can be found in [9]. Key features of the design are (i) a jaw flatness of about $40\ \mu\text{m}$ along the 1 m long active jaw surface; (ii) a surface roughness below $2\ \mu\text{m}$; (iii) a $5\ \mu\text{m}$ positioning resolution (mechanical, controls); (iv) an overall setting reproducibility below $20\ \mu\text{m}$ [10]; (v) a minimal gap of $0.5\ \text{mm}$; (vi) capability of evacuating heat loads of up to 6 kW in a steady-state regime (1 h beam lifetime) and of up to 30 kW in transient conditions (0.2 h beam lifetime). Two photographs of the present LHC collimator are given in Figure 5-2 and Figure 5-3, where a horizontal collimator and a 45° tilted collimator are shown. An example of the tunnel installation layout for an IR7 collimator is given in Figure 5-4. The complete list of collimators, including injection protection collimators in the transfer lines and in the ring (TCDis, TCLIs, TCDD), is given in Table 5-1. For completeness, the injection protection TDI absorbers and the one-side beam dump collimator TCDQ (which are part of beam transfer system (see Chapter 14) rather than of the LHC collimation system, but designed with a similar concept) are also listed. The full system deployed for the LHC Run 2 in 2015 comprises 118 collimators, 108 of which are movable and 10 of which are fixed-aperture absorbers.

Since the collimator jaws are close to the beam (e.g. the minimum collimator gap during the 2012 run was $2.1\ \text{mm}$, i.e. jaws were $1.05\ \text{mm}$ from the central orbit of the circulating beam), the collimation system also has a critical role in the passive machine protection in case of beam failures that cannot be counteracted by active systems. Primary and secondary collimators in IR7 are the closest to the beam; their jaws are mainly made of robust carbon-fibre carbon composites (CFC), and are designed to withstand beam impacts without significant permanent damage from the worst failure cases such as impacts of a full injection batch of $288 \times 1.15 \times 10^{11}$ protons at 450 GeV and of up to $8 \times 1.15 \times 10^{11}$ protons at 7 TeV [11]. Given the low electrical conductivity of CFC and their vicinity to the beam, these collimators contribute significantly to the machine impedance, which is particularly critical at top energy. Impedance constraints determine the smallest gaps that can be used in IR3 and IR7 and hence may become an additional limiting factor for the minimum β^* in the experiment [3]. Other absorbers and tertiary collimators are positioned at larger gaps in units of the local beam size. They can be less robust, in term of resistance to beam impacts, compared to primary and secondary collimators because they are less exposed to beam losses. Thus, metal-based jaws that are more effective in absorbing particles can be used. For example, tertiary collimators, with jaws made of a heavy tungsten alloy (Inermet 180), protect efficiently the inner triplet magnets around the experiments.

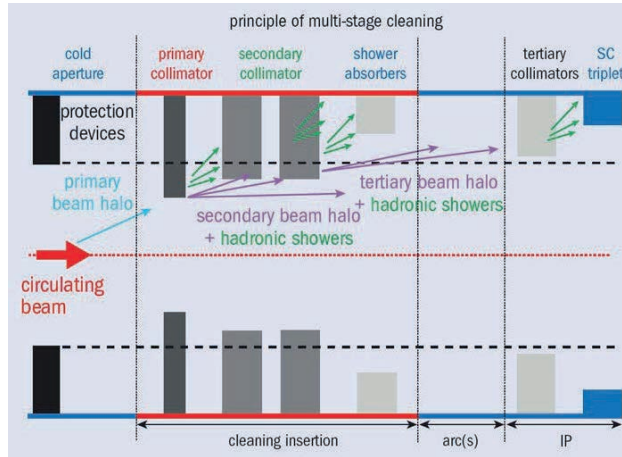


Figure 5-1: Schematic illustration of multi-stage collimation cleaning at the LHC. Primary and secondary collimators (darkest grey) are the devices closest to the circulating beam and are made of robust carbon-fibre composites. Shower absorbers and tertiary collimators (lighter grey) sit at larger apertures and are made of a tungsten alloy to improve absorption. Collimators of different families are ordered in a pre-defined collimation hierarchy that must be respected to ensure the required system functionalities. The collimator hierarchy is ensured by defining collimator settings in units of local beam size at the collimator location.

Table 5-1: Collimators for the LHC Run 2, starting in 2015. For each type, acronyms, rotation plane (horizontal, vertical or skew), material and number of devices, summed over the two beams, are given. For completeness, movable injection and dump protection devices are also listed. In addition, the collimation system comprises 10 fixed-aperture absorbers in IR3 and IR7 to reduce total doses to worm magnets of the cleaning insertions.

Functional type	Name	Plane	Number	Material
Primary IR3	TCP	H	2	CFC
Secondary IR3	TCSG	H	8	CFC
Absorber IR3	TCLA	H, V	8	Inermet 180
Primary IR7	TCP	H, V, S	6	CFC
Secondary IR7	TCSG	H, V, S	22	CFC
Absorber IR7	TCLA	H, V, S	10	Inermet 180
Tertiary IR1/IR2/IR5/IR8	TCTP	H, V	16	Inermet 180
Physics debris absorbers IR1/IR5	TCL	H	12	Cu, Inermet180
Dump protection IR6	TCDQ	H	2	CFC
	TCSP	H	2	CFC
Injection protection (transfer lines)	TCDI	H, V	13	Graphite
Injection protection IR2/IR8	TDI	V	2	hBN, Al, Cu/Be ¹
	TCLI	V	4	Graphite, CFC
	TCDD	V	1	Copper

¹ During the end-of-year technical stop 2015-16, the TDI collimator absorbing materials were changed to Gr, Al, CuCrZr.

The initial LHC collimator design has been improved by adding two beam position monitors (BPM pickups) on both extremities of each jaw [12]. Eighteen collimators (16 TCTP and 2 TCSP) were already upgraded with this new design during LS1. This concept allows for fast collimator alignment as well as a continuous monitoring of the beam orbit at the collimator, while the alternative BLM-based alignment can only be performed during dedicated low-intensity commissioning fills. The BPM pickups will improve significantly the collimation performance in terms of operational flexibility and β^* reach [3]. The BPM collimator design is the baseline for future collimation upgrades, and the BPM design is equally applicable to all collimators regardless of the jaw material. The concept has been tested extensively at the CERN SPS with a collimator prototype with BPMs [13–15]. An example of a CFC jaw prototype with in-jaw BPMs is shown in Figure 5-4.

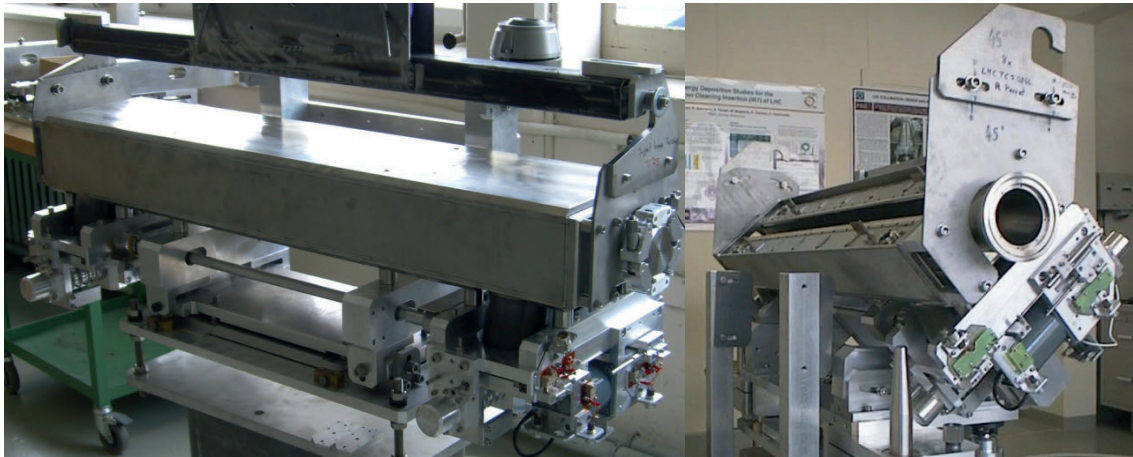


Figure 5-2: (a) horizontal LHC collimator; (b) skew LHC collimator. The latter has the vacuum tank open to show the two movable CFC jaws.



Figure 5-3: Photograph of the active absorber TCLA.B6R7.B1 as installed in the betatron cleaning insertion.

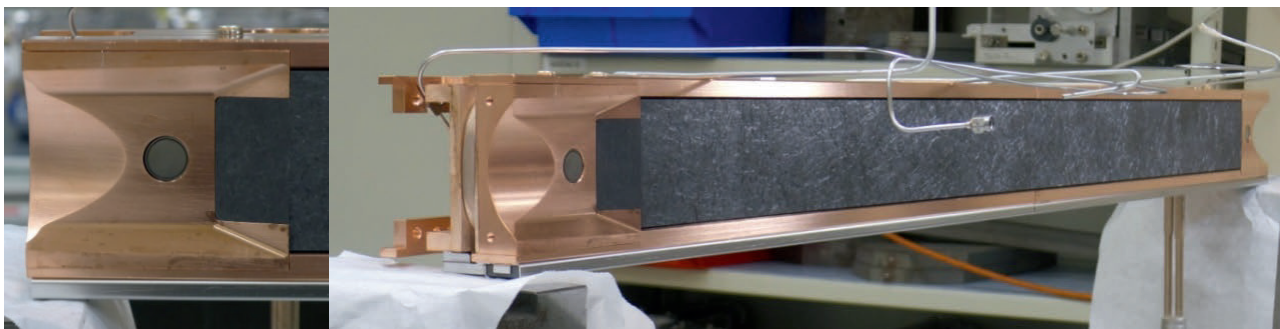


Figure 5-4: New CFC collimator jaw with integrated BPMs at each extremity ('buttons') to be installed as the secondary collimator in the dump insertion IR6. A detail of the BPM is given on the left-hand side. A variant of this design, made with a Glidcop support and tungsten inserts on the active jaw part, will be used for the tertiary collimators in all IRs.

In addition to beam halo cleaning, the collimation system fulfils other important roles.

- **Passive machine protection:** the collimators are the closest elements to the circulating beam and represent the first line of defense in case of various normal and abnormal loss cases. Due to the damage potential of the LHC beams, this functionality has become one of the most critical aspects for LHC operation and commissioning. In particular, it must be ensured that the triplet magnets around the experiments are protected during the betatron squeeze [3].
- **Active cleaning of collision debris products:** this is achieved with dedicated collimators (TCL) located on the outgoing beams of each high luminosity experiment, which catch the debris produced by the collisions. These collimators keep losses below the quench limit of the superconducting magnets in the matching sections and dispersion suppressors close to the interaction points.
- **Experiment background optimization**, i.e. reduction of perturbations from halo- and machine-induced signals in the detector measurements: this is one of the classical roles of collimation systems in previous colliders like the ISR, the SppS, and the Tevatron. For the LHC, the contribution to background from beam halo has always been expected to be small due to effective IR7 collimation cleaning that induces only limited losses close to the experiments. The initial run confirmed this expectation [4].
- **Concentration of radiation losses:** for high power machines, it is becoming increasingly important to be able to localize beam losses in confined and optimized 'hot' areas rather than having a distributed activation of equipment along the machine. This is an essential functionality to allow easy access for maintenance in the largest parts of the machine.
- **Local protection of equipment and improvement of its lifetime:** dedicated movable or fixed collimators are used to shield equipment. For example, eight passive absorbers are used in the collimation insertions in order to reduce the total dose to warm dipoles and quadrupoles that otherwise would have a short lifetime in the high-radiation environment foreseen during nominal LHC operation.
- **Beam halo scraping and halo diagnostics:** collimator scans in association with the very sensitive LHC beam loss monitoring system proved to be a powerful way to probe the population of beam tails [5, 6], which were otherwise too small compared to the beam core to be measured by conventional emittance measurements. Thanks to their robustness, the present primary collimators can also be efficiently used to scrape and shape the beams, as in Ref. [7].

In order to fulfil all these functionalities, the LHC collimation system features an unprecedented complexity compared to the previous state-of-the-art in particle accelerators. The Run 1 system required managing about 400 degrees of freedom for collimator movements [8]. As a comparison, the Tevatron collimation system had less than 30 degrees of freedom. For this reason, the possibility of reliably operating the collimation system has always been considered to be a major concern for LHC performance. Upgrade scenarios must address improved operational aspects, as the HL-LHC goal relies on machine availability.

5.2 Baseline and option upgrades to the LHC collimation system

To cope with the increased challenges in the HL-LHC, several of the functionalities of the LHC collimation system must be upgraded. In the following sections, we discuss technical solutions to improve the cleaning performance, the impedance, and the collimation in the experimental IRs. Here, for each upgrade topic, we present what is part of the ‘baseline’ and what is an ‘option’ upgrade. The latter are not part of the present project budget plan as at this stage we cannot yet determine, based on the LHC operation experience during Run 1, if and which ‘option’ items are needed for HL-LHC. A graphical view of the different items is given in Figure 5-5. This includes also the list of present LHC collimators that will be used for HL-LHC. In Figure 5-6, the same scheme of the project items is shown using the equipment code of each hardware type.

Technical solutions are under study both for baseline and options upgrade categories. It is planned to decide about baseline and option items during the LHC Run 2 at 6.5 TeV, after enough operational experience with high-intensity beams will be accumulated. In particular, it is important to address the analysis of beam losses, the experimental verification with beam of superconducting quench limits, the measurements of collimator impedance with beam and the analysis of beam losses with ion beam operation.

LHC operation in Run 2 started with rather relaxed collimator settings and β^* in 2015, and deployed tighter settings in 2016, which were closer to the HL-LHC baseline and hence more useful for studies of potential limitations. Note in particular that in 2016 the LHC has been limited in total intensity (maximum number of bunches is 2220 and maximum bunch population of about $1.1 \cdot 10^{11}$ protons). Some beam studies have already been performed at 6.5 TeV on these mentioned topics [70,72,73,74], however, firm conclusions cannot yet be drawn. The duration of this process will be determined by the progress of the LHC operation in Run 2.

5.2.1 Upgrades for cleaning improvement

5.2.1.1 Upgrades of the betatron and momentum cleaning systems

Protons and heavy ions interacting with the collimators in IR7 emerge from the IR with a modified magnetic rigidity. This represents a source of local heat deposition in the cold dispersion suppressor (DS) magnets downstream of IR7, where the dispersion starts to increase (see Ref. [16] and references therein): these losses are among the highest cold losses around the ring. They may pose a certain risk for inducing magnet quenches, in particular in view of the higher intensities expected for the HL-LHC. Although the intensities of heavy-ion beams are lower, they undergo numerous nuclear and electromagnetic interactions with the material of the primary collimators that can change their mass and charge. Collimation of heavy-ion beams is therefore much less efficient than that of proton beams.

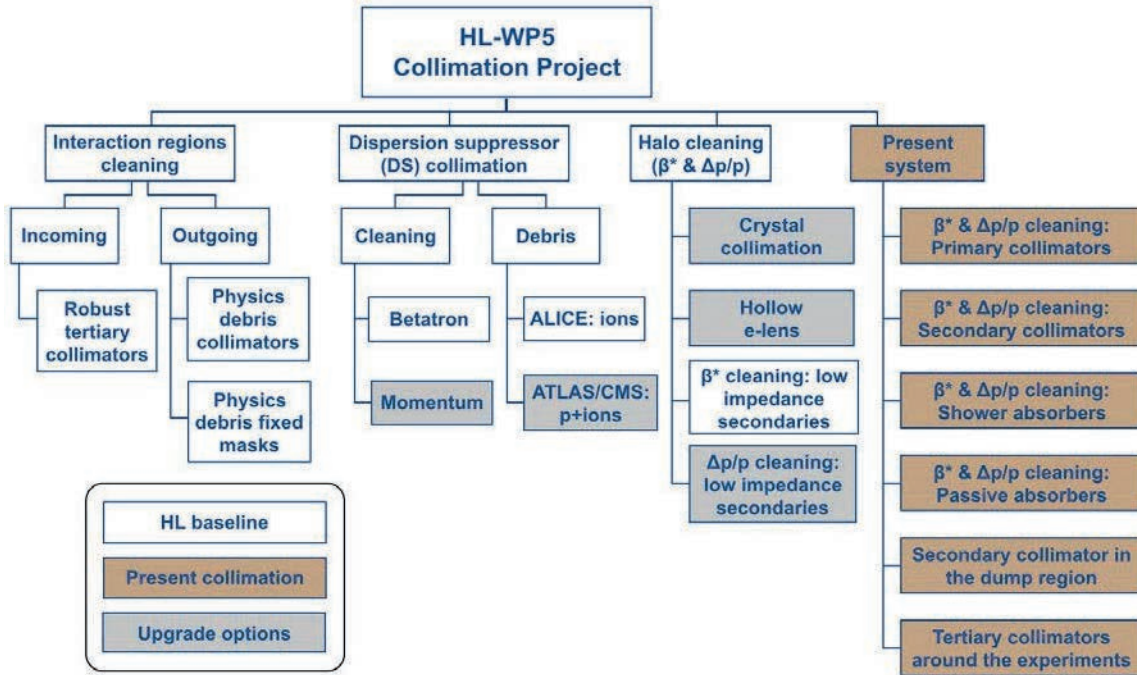


Figure 5-5: Block chart with baseline (white background boxes) and option (grey) collimation upgrade items. The LHC collimators that will continue to be part of the HL-LHC collimation system, which at this stage are considered to be adequate for the HL-LHC beam parameters, are also shown (brown).

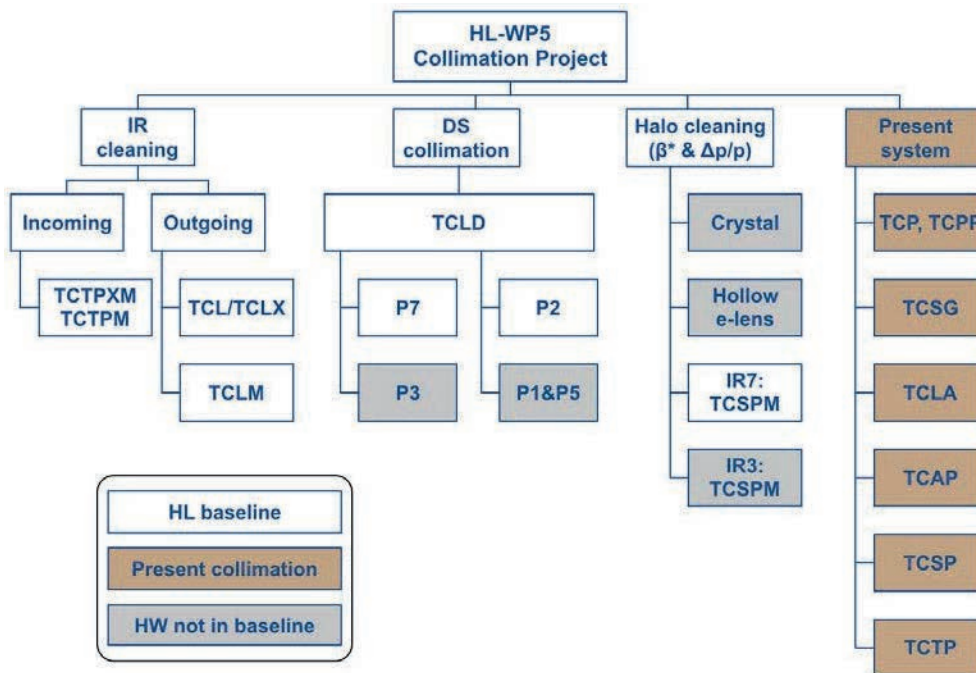


Figure 5-6: Diagram as that of Fig. 5.5 where equipment codes are used – when already available – as labels instead than the equipment functionality.

A possible solution to this problem is to add local collimators in the dispersion suppressors, which is only feasible with a major change of the cold layout at the locations where the dispersion starts rising. Indeed, the present system’s multi-stage cleaning is not efficient at catching these dispersive losses. Clearly, the need for local collimation depends on the absolute level of losses achieved in operation and the quench limit of

superconducting magnets. In this design phase, where the quench limits and the operational performance are not yet known accurately enough at beam energies close to 7 TeV, it is important to take appropriate margins to minimize the risk of being limited in the future (LHC operation at beam intensity above nominal design, and even more in the HL-LHC era).

A strategy to strongly reduce any risk of quench is the installation of DS collimators, referred to as TCLD collimators, where the dispersion has already started rising. In order to make space for the new collimators, it is envisaged to replace, for each TCLD, an existing main dipole with two shorter 11 T dipoles with the TCLD in between, as shown in Figure 5-7. This is a modular solution that can be applied to any dipole without additional changes to the adjacent superconducting magnets or other cold elements, should a space in the continuous cryostat be needed for any reason in the future [17].

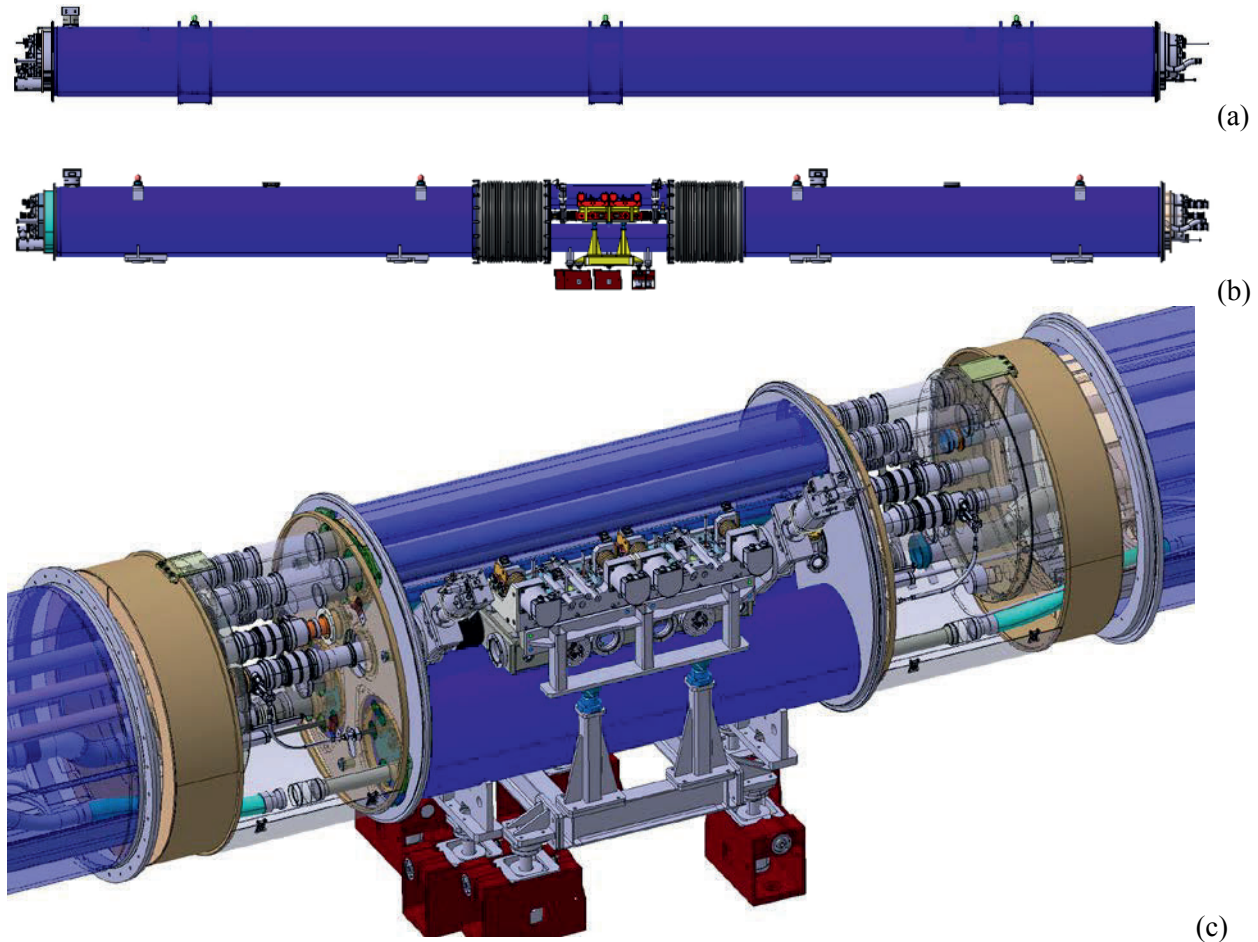


Figure 5-7: (a–b) Schematic view of the assembly of two shorter 11 T dipoles with a collimator in between, which can replace one standard main dipole. (c) 3D model of a TCLD assembly showing the collimator (in grey, at the centre), the two short dipole cryostats and the connection cryostat. Note the very tight space available for the collimator unit.

Extensive tracking and energy deposition simulations have been performed to assess the effect of the TCLDs [18–22]. The options of adding one or two TCLDs per side of P7 have been studied in detail, based on the assumption that the dipoles MB.B8R7 and optionally also MB.B10R7 are substituted for cleaning B1, and MB.B8L7 and optionally MB.B10L7 for cleaning B2. The different layout options are illustrated in Figure 5-8 and an example of the simulated power deposition in the DS magnets for the case of 0.2 h lifetime in the nominal LHC beam is illustrated in Figure 5-98 for the case of two TCLDs, compared to the case without.

More quantitatively, the proton energy deposition profile over the various DS elements, as simulated with FLUKA [69], is shown in Figure 5-10, assuming nominal LHC parameters at beam lifetime of 0.2 h (the

relative gain factors are expected to be similar for HL-LHC, while the absolute values of power deposition are expected to be about a factor 2 higher). The presence of one local DS collimators reduces the peak power deposition from 13.4 mW/cm^3 (found in cell 8) to 3 mW/cm^3 in (in cell 11). Effectively, this brings the power load in cells 8 and 11 down to about the same level, providing an overall gain factor of about 4.5.

With two TCLDs, the gain in local power deposition is minor compared to the case with one TCLD only, since the power leak in the 11T dipole in cell 10, caused by the shower from the TCLD, is not so much lower than the previous peak in a standard dipole. However, a relevant gain is still expected, since the quench limit of the 11T dipoles is expected to be higher than for the standard dipoles. Furthermore, TCLD collimators also make the cleaning performance more robust against various errors of the collimation system, of the optics, and of the orbit [22], as they remove the off-momentum particles at the first high-dispersion location downstream of IR7. This is of particular concern for the baseline HL-LHC optics solutions based on the Achromatic Telescopic Squeeze (ATS), which requires modified optics in the cold arcs. Indeed, for the HL baseline optics, the second TCLD almost eliminates additional losses predicted around the ring coming from the telescopic squeeze [51].

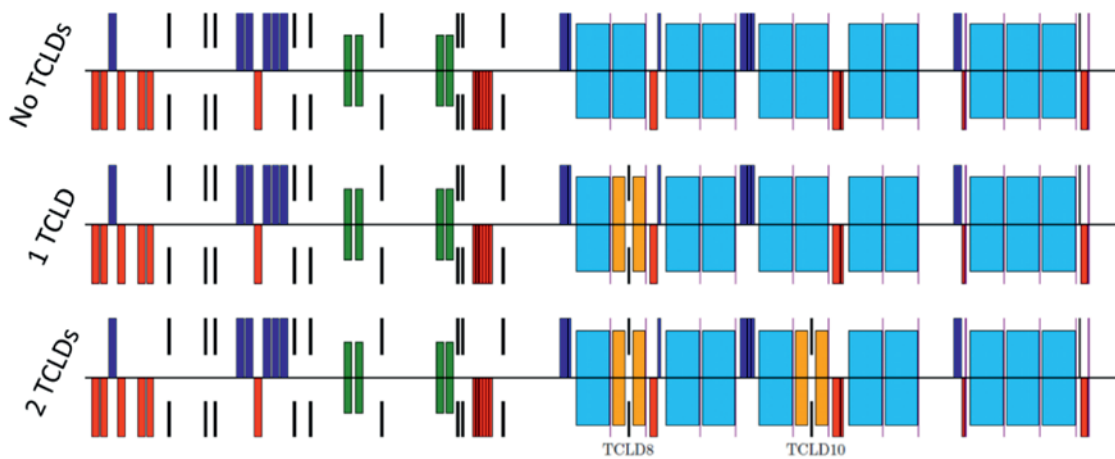


Figure 5-8: Schematic layout in the P7 DS without TCLDs (top), with 1 TCLD in cell 8 (middle) and with 2 TCLDs in cells 8 and 10 (bottom).

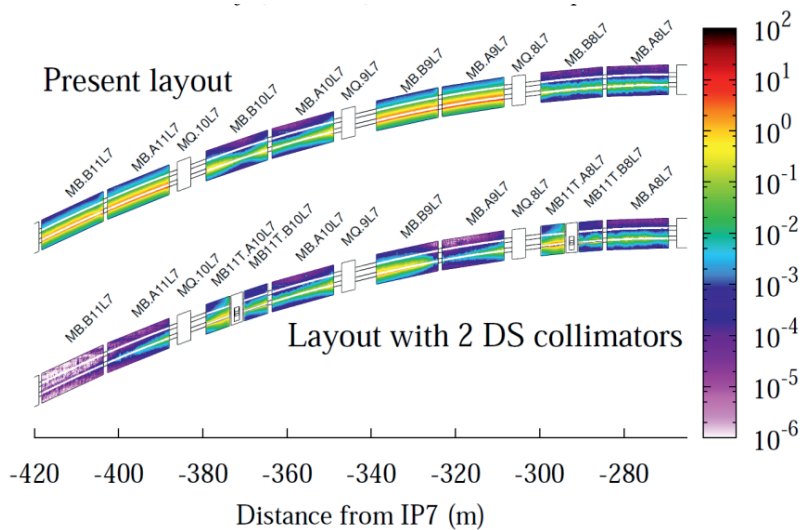


Figure 5-9: Illustrative scheme with power deposition profiles in the horizontal plane of the P7 dispersion suppressor (B1). The map makes a comparison between the present layout without TCLD collimators (top) and a layout with two TCLDs (bottom). Results correspond to relaxed collimator settings. Beam direction is from the right to the left. From Ref. [19].

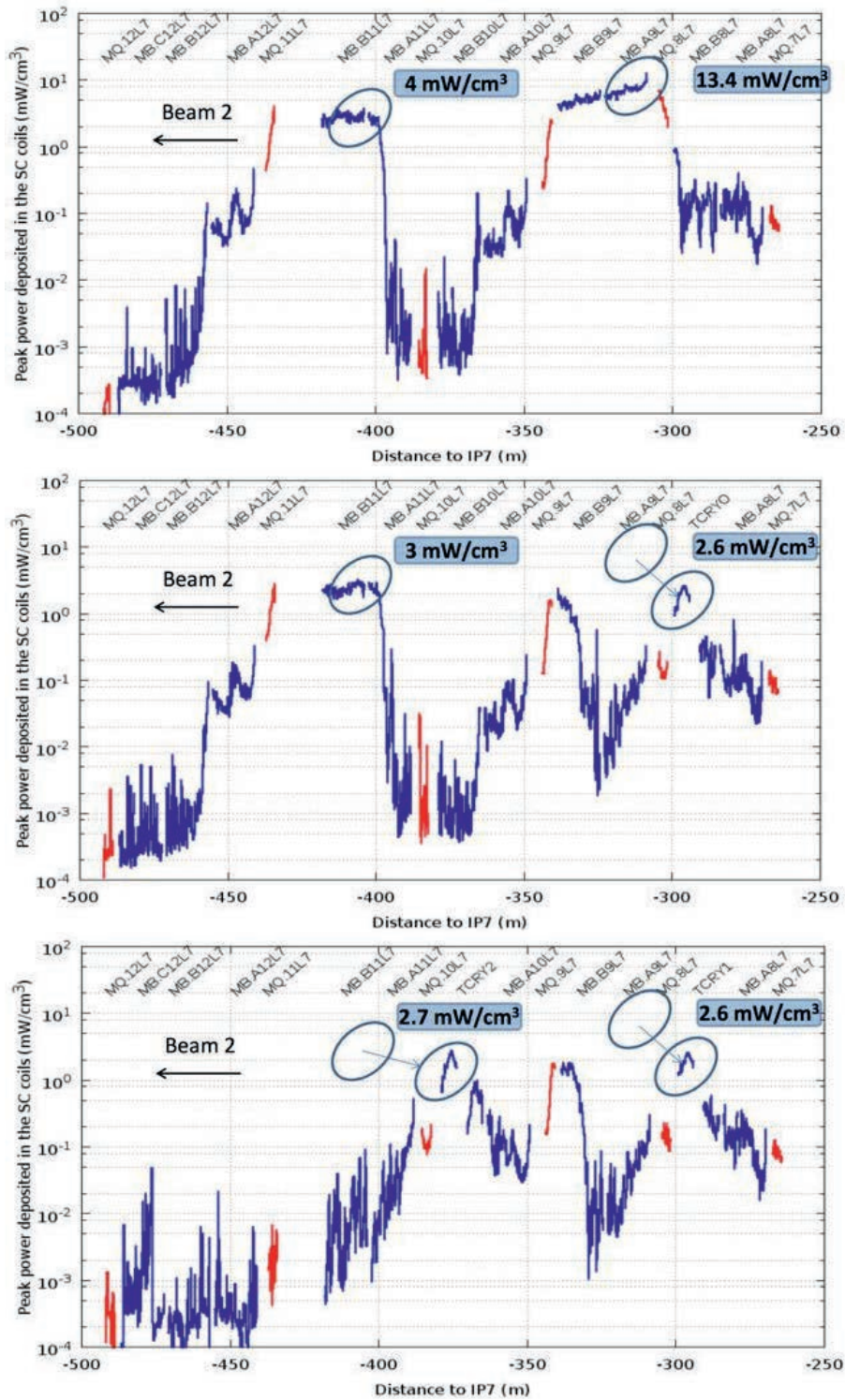


Figure 5-10: Proton energy deposition profiles in DS downstream of IR7 simulated with FLUKA, for the cases of no TCLDs (top), 1 TCLD (middle) and 2 TCLDs (bottom). Nominal LHC beam parameters are assumed and about a factor 2 higher numbers should be expected for HL-LHC. [69].

Furthermore, the improvement in cleaning could be very beneficial for LHC operation even if this is not limited by the collimation losses. For example, a better cleaning performance might allow relaxation of the opening of some secondary collimators with a subsequent reduction of machine impedance. It should also be noted that the DS collimation solution might also mitigate issues related to radiation damage to cold magnets protected by the TCLD collimators and the activation of near-by components.

The TCLDs could also be very beneficial for heavy-ion operation. Heavy ions hitting the primary collimator undergo fragmentation processes and a number of isotopes with different magnetic rigidities can scatter out of the collimator. Like single-diffracted protons, these isotopes could pass the secondary collimators and instead hit the aperture in the DS region where the dispersion increases. The heavy-ion collimation inefficiency in this region has been measured and simulated to be two orders of magnitudes worse than that of protons [52][53] because of the significant cross sections for nuclear fragmentation. This could become a limiting factor for the attainable luminosity, in spite of the much smaller heavy-ion beam intensities.

The quench limit of the DS magnets was probed using Pb beams in a dedicated test in 2015 at 6.37 Z TeV [70]. In this test, using the standard operational collimator settings in 2015, high losses were excited on the primary collimator and the debris leaking out of IR7 caused the dipole MBB.9L7.B2 to quench. The quench occurred at a beam power loss of around 15 kW on the primary collimator. A simple scaling of the experimental result gives at hand that, assuming a beam lifetime of 0.2 h, the maximum possible Pb ion intensity is less than 50% of the request for HL-LHC [70]. On top of this comes the scaling down of the quench limit from 6.37 TeV to 7 TeV, which makes the intensity limitation even lower.

It is therefore very important that solutions are found to improve the cleaning inefficiency for ions in the DS around IR7. Tracking simulations show that this could be achieved with the installation of TCLDs [52][71], where the solution with two TCLDs gives the best cleaning. However, final conclusion of the effectiveness of one or two TCLDs with ions have to be drawn based on energy deposition studies underway.

It is clear from the present state of the art of experimental and theoretical studies that the best solution for both protons and heavy ions is to install two TCLDs and the last collimation project review recommended that the preparation of DS collimation in IR7 be pursued with a high priority [23]. However, firm conclusions for the need of two units per beam cannot be drawn until more operational experience at 6.5 TeV, and if possible at 7 TeV, has been accumulated, including in particular further quench tests with beam for both particle types. Given this uncertainty, and the significant cost of producing more units of the 11T magnets, it is a reasonable compromise between cost and performance to include only one TCLD per beam in the HL-LHC baseline, scheduled for installation already in LS2.

In conclusion, it seems at this stage that one TCLD per beam can be acceptable for the performance; on the other hand this should be reviewed later in light of the Run 3 performance. The present baseline allows the technology for the 11 T dipoles to be developed and demonstrated in LS2, so that and if future studies show a strong need to install also the second TCLD in each beam, this could be done still be done in LS3 or even LS4.

The TCLD collimators design is derived from one of the standard LHC collimators [24]. In particular, it incorporates the latest design improvements, such as in-jaw BPMs; The absorbing elements of the two TCLD jaws are made of Inermet 180; each jaw is independently actuated by two motors, maintaining two degrees of freedom in the horizontal plane, as in standard collimators, while the suppression of the vertical adjustment permitted to reduce the jaw height to roughly a half of a standard collimator. In spite of less demanding thermo-mechanical requirements, partly because of lower losses compared to other collimators, the system design is made particularly complex by the very limited space allowances, imposed by the configuration of the surrounding cryogenic equipment. The key design parameters are listed in Table 5-2.

The new baseline that relies on shorter 11 T dipoles has been reviewed from the integration point of view [25]. Given the limited space budget, the length of all components and transitions must be carefully optimized. The present baseline is that the TCLD will have an active jaw length of 600 mm, which has proved to be sufficient to improve cleaning in all relevant cases. Tungsten heavy alloy is assumed for the material because the TCLD will rarely be exposed to a large beam load, so there is no need at this stage to consider

advanced materials. From the RF view point, a design with transverse RF contacts (as in the present system) has been favoured over ferrite tiles to absorb high-order modes (as in the collimators with BPMs). Present design is shown in Figure 5-11, where a detail of the collimator jaw extremity is given.

Table 5-2: Key parameters of TCLD collimators.

Characteristics	Units	Value
Jaw active length	[mm]	600
Jaw absorbing material	-	Inermet 180
Flange-to-flange distance	[mm]	1080
Number of jaws	-	Two
Orientation	-	Horizontal
Number of BPMs per jaw	-	Two
RF damping	-	RF fingers
Cooling of the jaw	-	Yes
Cooling of the vacuum tank	-	No
Minimum gap	[mm]	<2
Maximum gap	[mm]	50
Stroke across zero	[mm]	5
Number of motors per jaw	-	Two
Angular adjustment	-	Yes
Transverse jaw movement (fifth axis)	-	No

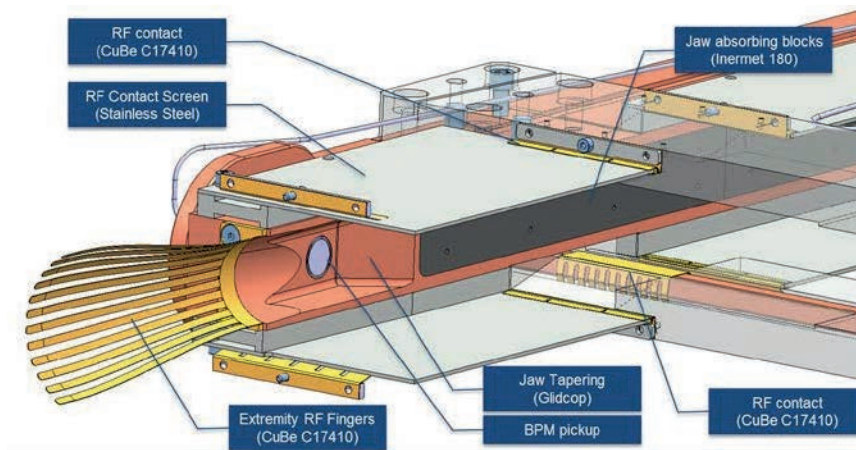


Figure 5-11: Detail of one extremity of the TCLD collimator to be installed in the DS between two new 11 T dipoles. The present design foresees a 60 cm-long jaw made of tungsten heavy alloy (the first of three 20 cm Inermet 180 blocks is shown) and will have two jaws. The longitudinal RF contacts, based on Copper-Beryllium contacts and fingers, are also shown.

5.2.1.2 Upgrades for improved cleaning of physics debris in the matching section

The collimators on the outgoing beams, downstream of the experiments, must intercept both scattered primary beam particles and secondary particles created by the collisions, in order to protect the magnets downstream. In Run 1, this was done by a single horizontal collimator in cell 5, called TCL5, in IR1 and IR5. No physics debris collimators were installed at the low-luminosity experiments in IR2 and IR8.

For Run 2, starting in 2015, the collimation system in IR1 and IR5 has been upgraded with additional TCLs in cells 4 and 6 (8 new collimators), in order to cope with the expected higher luminosities and requirements from forward-physics experiments. Energy deposition studies [25][55] have shown that the Run

COLLIMATION SYSTEM

2 layout with three TCLs should provide sufficient protection against luminosity debris also for proton operation in HL-LHC, provided the TCL4 is upgraded to have thicker jaws, with the active part made of Tungsten heavy alloy instead of copper [55-57]. This collimator is preliminarily called TCLX.

As a first design sketch of the TCLX, together with the present, thinner TCL, is shown in Figure 5-12. This illustrates the needed thickness of the jaw for sufficient protection, according to the FLUKA model of the TCLX. It should be noted that the jaw material is changed from copper to tungsten heavy alloy for better protection. The region between the D2 separation dipole and the TAXN, where the beams are recombined in a common vacuum chamber, is particularly critical from the integration point of view. Detailed studies [64] have shown that the TCLX with thicker jaws would not easily fit into this region because of transverse integration conflicts with the pipe of the other beam, which is larger at the HL-LHC than that of the LHC. A similar problem occurs for the horizontal tertiary collimator in this region, see below. In order to overcome this problem, a new two-in-one collimator design has been conceived. A preliminary drawing of this new design is shown in Figure 5-13. A single vacuum tanks houses at the same location the movable jaws acting on one beam and the vacuum chamber of the opposing – non collimated – beam. Details like the vacuum coupling of the two beams as well as the impedance budget of these design need to be studied in detail, but this proposed solution seems suitable for HL-LHC.

With the TCLX, no fixed masks are needed in front of D2 or Q4, allowing valuable gains in longitudinal space. Nevertheless, the longitudinal integration required the TAXN to be shortened somewhat compared to its previous design. Considering the total TAXN length of 3.33 m, this should not have any impact on the protection that the TAXN provides. Additional fixed masks are still needed on the IP side of Q4, Q5 and Q6.

The power deposition profile with this baseline layout, as simulated with FLUKA, is presented in detail in Chapter 10. The simulations show that the protection is adequate both for damage caused by long-term irradiation, as well as the instant heat load from physics debris that could bring the D2 close to the quench limit. It should be noted, however, that the transverse integration in this complex region is not yet fully finalized. Simulations will need to be repeated for the final layouts. While some changes might be revealed, we believe that the satisfactory performance of the proposed layout will be confirmed.

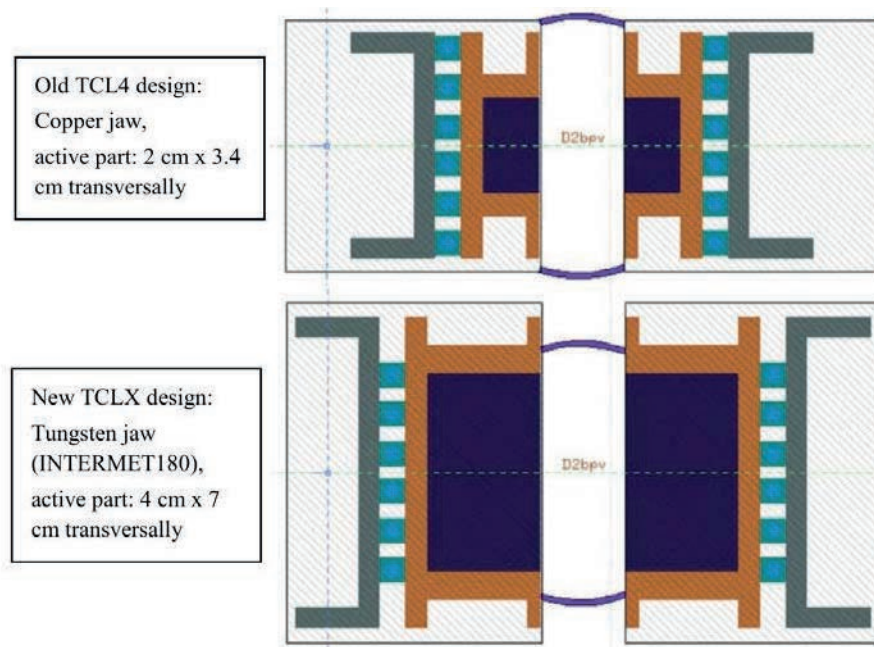


Figure 5-12: A schematic of the transverse cross section of the TCL design, as implemented in FLUKA (top), together with a first guess on the TCLX design (bottom), including thicker jaws, where the jaw material should be changed from copper to tungsten heavy alloy. Figure from Ref. [55].

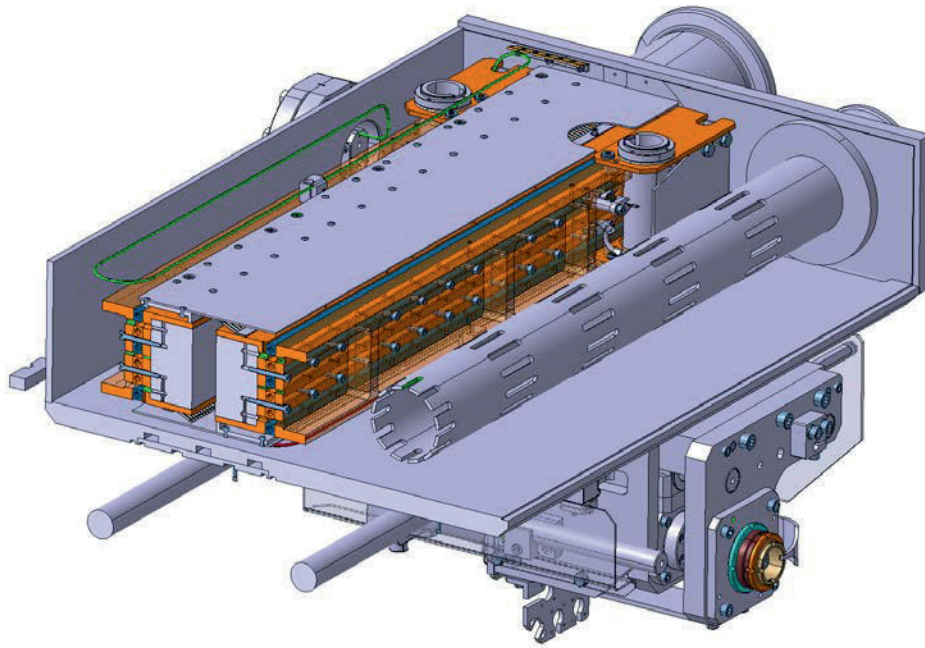


Figure 5-13: Design of new two-in-one collimator with a common vacuum tank housing both the movable jaws (left part) and the vacuum chamber of the opposing beam. This new design is required for the horizontal collimators to be installed in the regions of IR1/5 between D2 and TAXN, where transverse integration constraints prevent installing the standard single-beam collimators.

5.2.1.3 Upgrades for luminosity-generated losses in the dispersion suppressor

When heavy ions undergo ultra-peripheral interactions in the collision points of the experiments, secondary ion beams with a modified magnetic rigidity are generated [28][27]. These ions represent a source of local heat deposition in the adjacent dispersion suppressor regions where the dispersion function starts rising. The dominating processes are bound-free pair production (BFPP), where electron-positron pairs are created and one (BFPP1) or two (BFPP2) electrons are caught in a bound state of one of the colliding nuclei, thus changing its charge, and 1- or 2-neutron electromagnetic dissociation (EMD1 and EMD2) where one nucleus emits one or two neutrons, thus changing mass. Further photon-induced processes also take place, but the four mechanisms mentioned here have the higher cross-sections. An example of ion beams produced in collisions of $^{208}\text{Pb}^{82+}$ nuclei in IR2 is given in Figure 5-15

As can be seen, these secondary beams are lost very locally due to the big and sudden change of magnetic rigidity gained at the interaction with the opposite beam. After the LS2 ALICE upgrade, aiming at a peak luminosity of $6 \times 10^{27} \text{cm}^{-2} \text{s}^{-1}$ (about six times higher than the nominal one), the dominant BFPP1 beam can carry about 155 W, resulting in a power load in the coils of the MB.B10 dipole of about 44mW/cm^3 [29] on both sides of ALICE. Similar ion losses also occur in the DS regions around ATLAS and CMS, however at different locations than in IR2. A beam loss experiment carried out during the 2015 Pb-Pb run at 6.37 Z TeV [76] confirmed the long-standing presumption that BFPP1 ions risk to quench magnets [27][28]. The experiment was carried out around CMS because it was running at higher peak luminosity than ALICE. During standard operations, special bumps were deployed around ATLAS and CMS to steer the BFPP1 losses into the locations of the connection cryostat. In the quench experiment, BFPP1 losses were deliberately shifted inside a dipole using an orbit bump, and the heat deposition in the magnet was selectively increased in steps by reducing the beam separation [76]. The dipole eventually quenched at a luminosity of $2.3 \times 10^{27} \text{cm}^{-2} \text{s}^{-1}$. First results from particle shower simulations indicate that the peak power achieved during the test was around 15mW/cm^3 [76]. Studies continue to assess in more detail the loss conditions that led to the quench. Nevertheless, the test confirmed that BFPP1 ions would limit the luminosity below the HL-LHC target of $6 \times 10^{27} \text{cm}^{-2} \text{s}^{-1}$

and therefore the full exploitation of the ALICE detector upgrade. Note also that the beam energy was lower than nominal in this test.

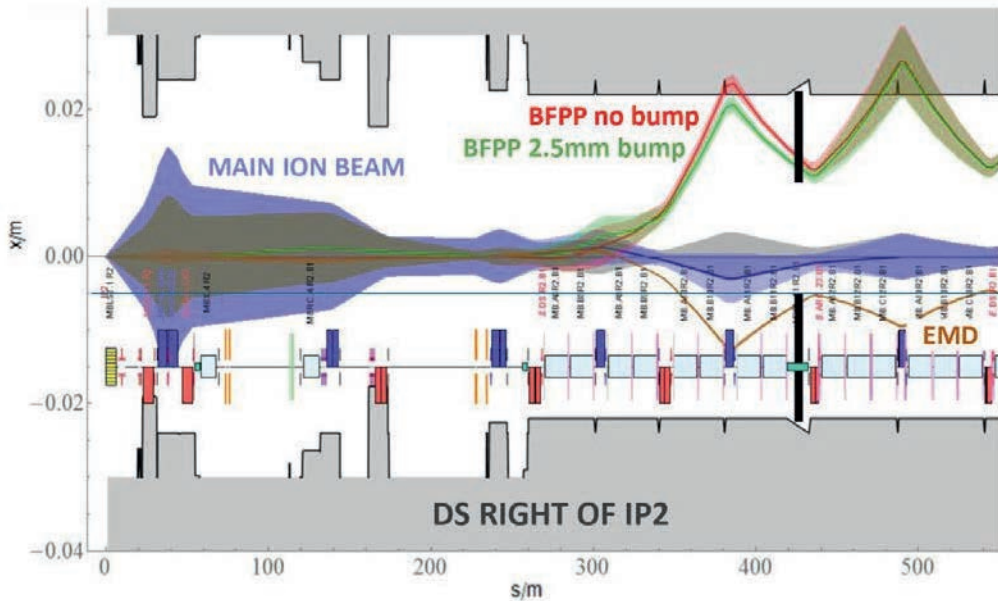


Figure 5-14: 1σ envelope of the main Pb^{82+} beam (violet) together with the dispersive trajectories of ions undergoing BFPP1 (red) and EMD1 (brown), coming out of the ALICE experiment (IP2). The DS collimator jaws appear as a black lines. The green line indicates the shifted BFPP1 orbit using a closed orbit bump, which is necessary to intercept the beam with the collimator. The EMD1 beam can be intercepted with the other jaw.

A strategy to eliminate any risk of ion-induced quenches in the DS next to IR2 is the installation of TCLD collimators, as shown schematically in Figure 5-15. One collimator per side of the ALICE experiment is sufficient to intercept the secondary beams from the most dominant processes (BFPP1 and EMD1) in a location where these ions are well separated from the main beam. Instead of substituting a dipole with a TCLD and a pair of 11T magnets like it is foreseen around P7, the baseline for IR2 is to install the collimators in the connection cryostat in cell 11. Since the BFPP ions would impact on the magnet aperture upstream of the connection cryostat, this solution requires the implementation of a closed orbit bump which makes the BFPP1 beam miss the first maximum of the locally generated dispersion since IP2 and redirects the beam onto the TCLD jaw. At the same time, the EMD1 beam, which carries ~ 56 W at a luminosity of $6 \times 10^{27} \text{cm}^{-2} \text{s}^{-1}$, could be intercepted with the other jaw. The feasibility of operating with closed orbit bumps of a few mm over more than 100 m has been successfully demonstrated in the 2015 Pb-Pb run [75].

In order to minimize design and production efforts, the same collimator length (60 cm) and material (heavy tungsten alloy Inermet 180) is chosen as for the TCLDs around IR7. Particle shower simulations suggest that with such jaws the power deposition in the coils of downstream magnets are expected to remain below 1mW/cm^3 and therefore safely below the quench level if the BFPP1 and EMD1 beams impact at least 2 mm from the collimator edges [77][78]. The simulations further show that showers from the collimator pose no risk of quenching the bus bars in the newly designed connection cryostat [78].

Because of a different optics than in IR2, an alternative solution without collimators is envisaged for the DSs next to IR1 and IR5. As the BFPP1 loss location is close to the connection cryostat in cell 11, bumps allow redirecting the losses directly onto the cryostat beam screen. Such bumps have been routinely used in the 2015 Pb-Pb run, where a peak luminosity of $3\text{-}3.5 \times 10^{27} \text{cm}^{-2} \text{s}^{-1}$ was reached in IP1 and IP5 [75]. Simulation studies as well as the operational experience in 2015 suggest that the power deposition in the coils of downstream magnets and in bus bars would still remain safely below the quench level at the HL target luminosity 179[79]. Losing the ions in the connection cryostat also reduces the total heat load to be evacuated by the cryogenic

system [79]. A significant fraction of the power is expected to be deposited in the Pb shielding of the connection cryostat, which is less critical than the power deposited in the cold mass of magnets as the Pb shielding is mainly thermalized to the thermal screen (~60-65K) [79].

Like for heavy ion operation, losses in the DS regions also occur during proton operation. Protons that changed their magnetic rigidity due to interactions with the other beam cannot be efficiently intercepted by the TCLs installed in the matching section, where the dispersion is still low. These losses may pose a certain risk for quenching magnets next to IR1 and IR5. As a possible solution the losses could be reduced with two TCLD collimators per IR side. The need for such an implementation depends on the dipole quench limits and on the effectiveness of the physics debris reduction with TCL collimators. Layouts based on TCL collimators only might be sufficient but this requires further studies with the latest HL-LHC layouts that will estimate the peak energy deposited in the DS magnets. If required, the TCLDs would then complement the present system with TCLs. For the moment, simulation results indicate that the TCLDs around IR1/5 are not necessary for operating HL-LHC reliably below quench limits. These collimators are therefore not in the baseline.

5.2.2 Upgrades for impedance improvement

The LHC impedance budget is largely dominated by the contribution of the LHC collimators. For this reason, the present collimation system has been conceived in a way that can be easily upgraded to reduce the impedance [30]. Every secondary collimator slot in IR3 and IR7 features a companion slot for the future installation of a low-impedance secondary collimator. A total of 22 slots (IR7) and 8 slots (IR3) are already cabled² for a quick installation of new collimators – referred to as TCSPM in the present database naming convention – that can either replace or supplement the present TCSG collimators. Partial preparation of these slots has been carried out in LS1.

The importance of minimizing the machine impedance for the HL-LHC has been emphasized in [31–33] and during a LHC collimation review [23]. It is also important to stress that each new TCS collimator will also add the BPM functionality for a faster setup, which will be important to maximum the time for physics at the HL-LHC. We therefore foresee that, by the time of the full HL-LHC implementation (LS3), some or all of the available TCSPM slots might be equipped with advanced collimators using new materials, and possibly coatings, to reduce the machine impedance. A staged installation using the various technical stops and shutdowns after LS1 should be possible according to actual needs. Simulations predict that beam stability can be re-established for all HL-LHC scenarios if the CFC of present secondary collimators is replaced, at least in the betatron cleaning insertion, with a jaw material having an electrical conductivity a factor of 50 to 100 higher than CFC [34], [35]; this improvement would be easily achieved if the jaw material were made of highly conductive metals such as copper or molybdenum.

However, secondary collimators in IR7 also play a crucial role in LHC machine protection and might be exposed to large beam losses. Therefore, collimator materials and designs must also be robust against beam failure (at the least those exposed to horizontal losses). The driving requirements for the development of new materials are thus: (i) low resistive-wall impedance to avoid beam instabilities; (ii) high cleaning efficiency; (iii) high geometrical stability to maintain the extreme precision of the collimator jaw during operation despite temperature changes; and (iv) high structural robustness in case of accidental events like single-turn losses.

The latter requirement rules out the possibility to employ high-Z metals because of their relatively low melting point and comparatively large thermal expansion that impairs their resistance to thermal shocks [36]. The present baseline for the upgraded secondary collimators relies thus on novel carbon-based materials such as molybdenum carbide-graphite (MoGr), a ceramic composite, jointly developed by CERN and Brevetti Bizz[®], in which the presence of carbides and carbon fibres strongly catalyses the graphitic ordering of carbon during high temperature processing, enhancing its thermal and electrical properties (see Figure 5-16) [37],

² Present installations include cabling for the collimator controls but not for the read-out of the in-jaw BPMs, which were not part of the collimator design when these slots for system upgrade were prepared. Also missing are the last meters of radiation-hard cabling from the tunnel cable trails to the collimators.

[38]. To further improve their surface electrical conductivity, these materials could possibly be coated with pure molybdenum or other lower Z refractory coatings. Replacing all present CFC secondary collimators in both IR7 and IR3 with bulk MoGr or MoGr coated with 5 μm -thick pure Mo would reduce the total LHC impedance by 40% and 60% respectively (Figure 5-17), allowing, particularly if coating is adopted, to recover beam stability in practically all operation modes.

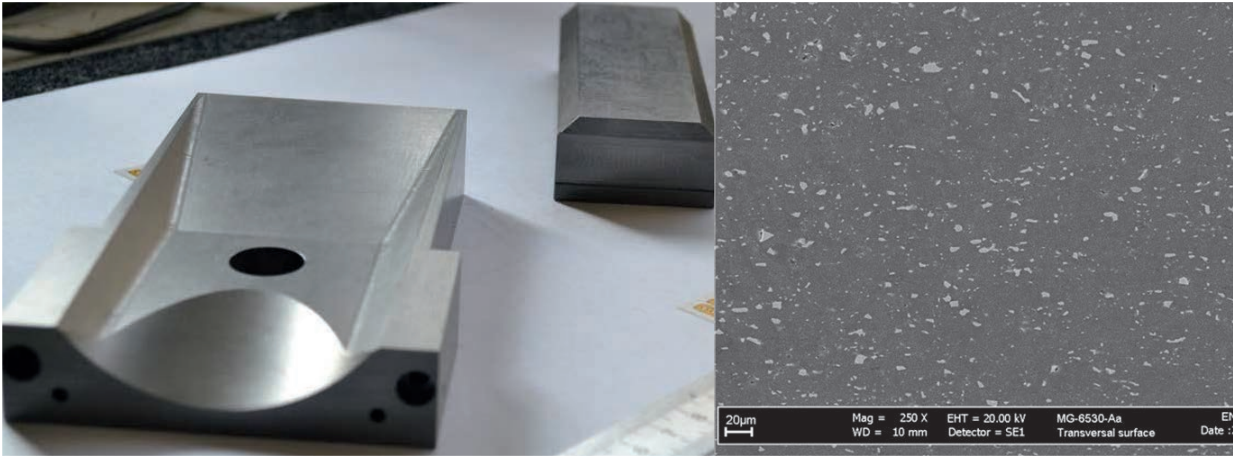


Figure 5-15: (a) MoGr components for a jaw prototype. Left: jaw extremity, dimensions: 147 x 88 x 25 mm³; right: jaw absorbing block, dimensions: 125 x 45 x 25 mm³. A jaw assembly includes 2 jaw extremities (taperings) and 8 blocks. (b) Detail of the microstructure, where the graphite matrix is visible together with molybdenum carbide grains of about 5 μm .

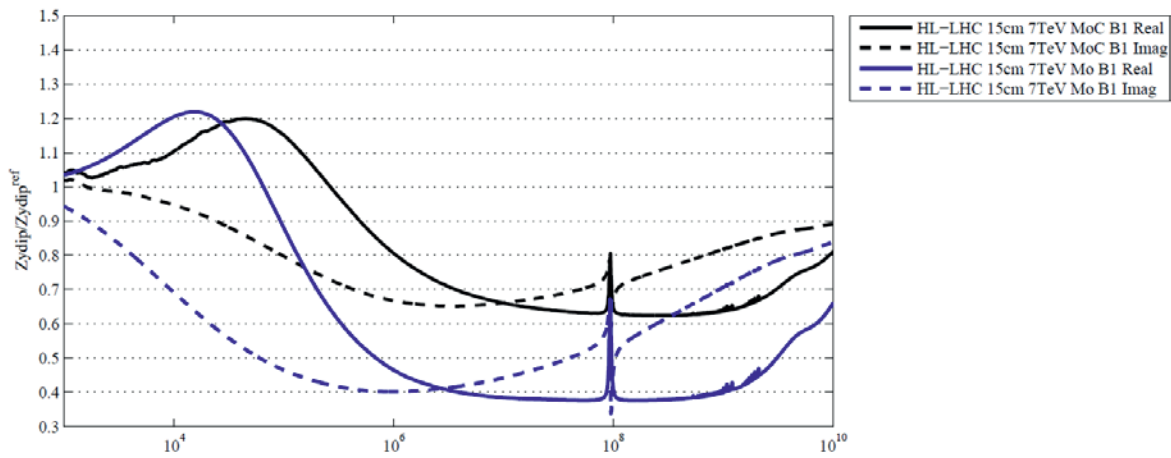


Figure 5-16: LHC machine impedance versus frequency: impedance ratio with respect to present CFC jaw of bulk MoGr (black) and 5 μm Mo-coated MoGr (blue) for the real (solid) and imaginary (dotted) parts [35]. The impedance is increased below ~ 1 MHz, but this not expected to be a problem because this frequency range is well within the transverse damper bandwidth of 20 MHz.

The new collimator design [39] along with novel materials and possible coatings alternatives must be validated for operation in the LHC. For these purposes, a rich programme of validation is in progress, involving:

- tests at HiRadMat, covering both material samples as well as full jaw validation;
- mechanical engineering prototyping;
- beam tests at the LHC, planned for 2017 (collimation installation in the 2016 year end technical stop);

- validation of new materials for operation with HUV and at high radiation doses.

HiRadMat tests were carried out very successfully in 2015 [65], demonstrating that a full-scale MoGr jaw could withstand without apparent damage the impact of a full injection train of brilliance beyond that of the LIU parameters (total intensity was still limited to about 60 % of the HL-LHC target, though). A CuCD jaw was also tested, showing that it is at least 15 times more robust than the Inernet jaw tested in HiRadMat in 2012. Irradiation tests of MoGr and other materials are also well advanced, thanks to ongoing collaborations with GSI and BNL [66]. Firm conclusions on the comparison between MoGr and CFC from the viewpoint of radiation resistance are expected by the beginning of 2017. It is also noted that the construction of a TCSPM collimator for beam tests in 2017 is well advanced.

In addition to the impedance improvements, the new TCSPM also feature a number of improvements in the mechanical design (Figure 5-18) [39]. They incorporate the BPM button design. The key hardware parameters are listed in Table 5-3.

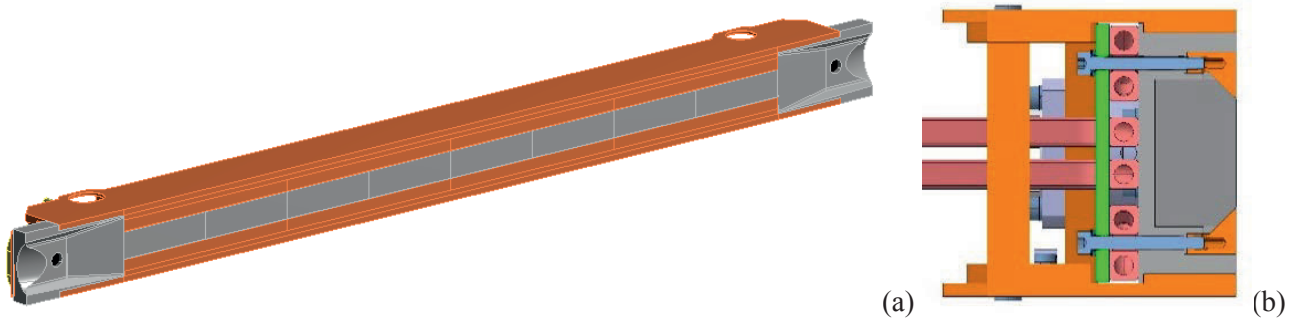


Figure 5-17: Design of the TCSPM jaw (a) and of its cross-section (b). The jaw assembly features 8 MoGr blocks. Also note that the jaw tapering is lengthened, further reducing its contribution to HOM RF instabilities in the geometrical transition zones.

Table 5-3: Parameters of TCSPM collimators.

Characteristics	Units	Value
Jaw active length	[mm]	1000
Jaw material	-	MoGr
Flange-to-flange distance	[mm]	1480
Number of jaws	-	2
Orientation	-	Horizontal, vertical, skew
Number of motors per jaw	-	Two
Number of BPMs per jaw	-	Two
RF damping	-	Fingers
Cooling of the jaw	-	Yes
Cooling of the vacuum tank	-	Yes
Minimum gap	[mm]	<1
Maximum gap	[mm]	60
Stroke across zero	[mm]	5
Angular adjustment	-	Yes
Jaw coating	-	To be decided
Transverse jaw movement (fifth axis)	[mm]	±10

5.2.3 Upgrades to the collimation of the incoming beam in the experimental IRs

The LHC Run 1 operation has shown that protection of the IR superconducting magnets and experiments is a key asset for machine performance: the available aperture, to be protected in all operational phases, determines

the collimation hierarchy. The present tertiary collimators (target collimator tertiary with pick-up (TCTP)) are located at positions that protect the triplet and are made of a heavy tungsten alloy (Inermet 180). They effectively protect the elements downstream but are not robust against high beam losses, in particular during very fast beam failures that might occur if the beam dumping system does not trigger synchronously with the abort gap (an asynchronous beam dump). Settings margins are added to the collimator hierarchy to minimize the risk of exposure of these collimators to beam losses in case of such failures [3]. A design with improved robustness would allow the reduction of these margins and, as a result, push further the β^* performance of the LHC, in particular for the HL optics baseline (ATS) that features an unfavourable phase between dump kickers and triplet magnets.

In addition to improvements from increased robustness, the HL-LHC layout has additional aperture constraints [2][3] because the aperture of the magnets up to Q5 is now smaller than in the present layout. Thus, up to four more tertiary collimators might be required in IR1/IR5 to protect the Q4 and Q5 quadrupole magnets, in addition to those installed to protect the triplet (two TCTP collimators – one horizontal and one vertical). The present baseline under study includes also a pair of new collimators in front of Q5. Ongoing studies are addressing: (i) the need for additional Q4 protection; and (ii) the need to keep tertiary collimators at the present locations in case additional tertiaries are added upstream.

A new design of tertiary collimators, referred to as target collimator tertiary with pick-up metallic (TCTPM), is under study to address the new challenges. This design will be based on novel materials to improve collimator robustness while ensuring adequate absorption, adequate cleaning, and protection of the elements downstream. The TCTPM design and material choice must also take impedance constraints under consideration to keep the collimator impedance under control.

Note that the present Inermet design is expected to undergo severe damage requiring a collimator replacement if hit by one single LHC nominal bunch of 10^{11} proton at 7 TeV. Other advanced materials are being studied as possible alternatives to further improve the robustness. The HL beam parameters with bigger charge and smaller emittance pose additional challenges in terms of beam damage potential.

Several alternative materials are currently considered for the new design; these include MoGr and Copper-Diamond (CuCD). The experimental experience of beam impacts on collimator material samples at HiRadMat [40] indicates that MoGr can improve the TCTP robustness by a factor of several hundreds. On the other hand, CuCD, compared to MoGr, features higher density (and hence better cleaning efficiency) and larger electrical conductivity. It may be considered particularly if the expected worst accident scenarios do not exceed an intensity equivalent to one full LHC bunch at 7 TeV.

A summary of the technical key parameters is given in Table 5-4.

For HL-LHC, with the larger β -functions in the high-luminosity insertions, the TCTs have to be opened to rather large gaps in mm to achieve the smaller normalized design openings in σ . To keep a maximum operational flexibility, it is desired to have the possibility of opening the TCTs to the same normalized aperture of the triplet, which could be as large as 14σ for the baseline optics with $\beta^*=15$ cm. In this case, a half gap of 33 mm, which goes up to 39 mm for flat optics [59]. These numbers account for the centre offset coming from the crossing and separation bumps, as well as an additional 3 mm tolerance for orbit variation. Even larger half gaps may be required if the optics is changed in order to have larger β -functions at the crab cavities, which would also result in larger β -functions at the TCTs. With the present TCT design, the half gap is limited to 30 mm, which means that the design has to be modified for HL-LHC. It may also lead to potential integration issues in the transverse plane, which is presently under study. Similar considerations apply also to the TCLs mentioned in Sec. 5.2.1.2. Indeed, it is also planned that the horizontal collimator in the D2/TAXN region uses the two-in-one design shown in Figure 5-13.

It is important to note that some collimators of type TCTP or TCL to be installed in cells 4, 5 and 6 might re-use the present TCTP collimators with BPM that are essentially of the same design. We believe that up to 8 collimators can be recuperated from the ones built for the present LHC (units installed in the machine or operational spares). For example, one could use the present Inermet TCTPs as vertical collimators – not

exposed to beam dump failures at top energy – or as single-beam horizontal TCLs that are at settings above 10σ – and built collimators based on advance materials for the horizontal TCTP slots. The other collimators for the IRs – TCLX, TCTPM, TCL collimator and masks, for a total of 20 movable collimators and 12 fixed masks – have to be built for HL-LHC. The decision to re-use existing collimator for HL-LHC was triggered by budget restrictions in June 2016. Clearly, evaluation of this proposed strategy must be made in due time, taking into account the extrapolation of radiation doses of collimators that will be operational until Run 3.

Despite being less critical because of the larger β^* values, upgraded TCTP's are under consideration also for IR2/8 because various luminosity scenarios in there IRs require the usage of tertiary collimators, although at relaxed settings compared to IR1 and IR5. For the time being, new collimators in IR2/8 are not considered part of the baseline because those IRs are not part of the high luminosity plan within HL. Clearly, the present collimators in these IRs must remain operational throughout the HL-LHC lifetime. Thus, adequate consolidation programs for these collimators must be ensured.

Table 5-4: Equipment parameters of the TCTPM.

Characteristics	Units	Value
Jaw active length	[mm]	1000
Jaw material	-	To be decided (CuCD, MoGr or other)
Flange-to-flange distance	[mm]	1480 (to be reviewed)
Number of jaws	-	Two
Orientation	-	Horizontal, vertical
Number of motors per jaw	-	Two
Number of BPMs per jaw	-	Two
RF damping	-	Fingers
Cooling of the jaw	-	Yes
Cooling of the vacuum tank	-	Yes
Minimum gap	[mm]	<1
Maximum gap	[mm]	>80
Stroke across zero	[mm]	>5
Angular adjustment	-	Yes
Jaw coating	-	No
Transverse jaw movement (fifth axis)	[mm]	± 10 mm (at least)

5.3 Advanced collimation concepts

In this section we discuss new, more advanced, collimation concepts and designs that still require R&D and are therefore not in the baseline. However, depending on the results of Run 2, some of these concepts may become an important asset for the LHC and the HL-LHC. In particular, in the present budget baseline a certain level of R&D on crystal collimation and hollow e-lenses is included, while the deployment of these solutions is part of the non-baseline options. These advanced solutions address in different ways the cleaning upgrade in IR7 and could therefore represent alternatives to the scheme based on 11 T dipoles and local DS collimation. The latter is considered as baseline at this stage because this technology is more mature, whereas more feasibility studies are deemed necessary before relying on crystals and hollow e-lenses as baseline.

5.3.1 Halo diffusion control techniques

The 2012 operational experience indicates that the LHC collimation would profit from halo control mechanisms. The operation at the beginning of Run 2 showed a less severe impact from halo losses however the scaling to HL-LHC beam parameters are sources of concerns. Halo control mechanisms were used in other machines like HERA and the Tevatron. The idea is that, by controlling the diffusion speed of halo particles, one can act on the time profile of the losses, for example by reducing rates of losses that would otherwise take

place in a short time, or simply by controlling the static population of halo particles in a certain aperture range. These aspects were recently discussed at a collimation review on the possible usage of the hollow e-lens collimation concept at the LHC [36], where it was concluded that hollow e-lenses could be used at the LHC for this purpose. In this case, a hollow electron beam runs parallel to the proton or ion beam that is on the axis of the cylindrical layer of electron. This hollow beam produces an electromagnetic field only affecting halo particles above given transverse amplitudes, changing their transverse speed. The conceptual working principle is illustrated in Figure 5-19(left). A solid experimental basis achieved at the Tevatron indicates this solution is promising for the LHC ([37] and reference therein).

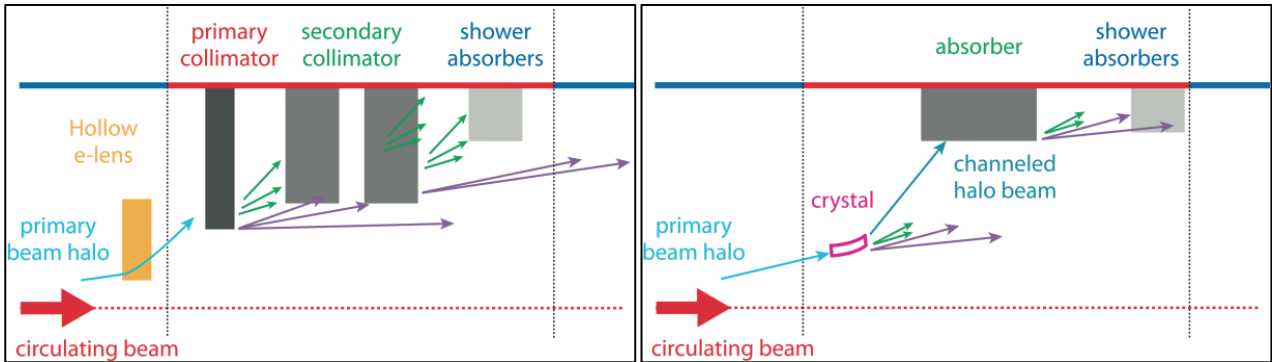


Figure 5-18: Illustrative view (left) of the collimation system with integrated hollow e-lens or equivalent halo diffusion mechanism; (right) an ideal crystal-based collimation. A simplified collimator layout to that in Figure 5-1 is adopted to show the betatron cleaning functionality only (one side only). Halo control techniques are used to globally change the diffusion speed of halo particles, and rely on the full collimation system remaining in place. Crystals entail a change of concept where the whole beam losses are concentrated, ideally, in one single beam absorber per plane.

The potential advantages of the electron lens collimation are several.

- Control of the primary loss rates, with potential mitigation of peak loss rates in the cold magnets, for a given collimation cleaning. Peak power losses on the collimators themselves can be optimized as well.
- Controlled depletion of beam tails, with beneficial effects in case of fast failures.
- Reduction of tail populations and therefore peak loss rates in the case of orbit drifts.
- Beam scraping at very low amplitudes ($>3\sigma$) without the risk of damage, as for bulk scrapers.
- Tuning of the impact parameters on the primary collimators with a possible improvement in cleaning efficiency.
- Controlled depletion of beam tails, opening the possibility to tighten primary collimator setting for a smaller β^* reach.

Since the main beam core is not affected, hollow electron beam (HEB) operation should in theory be transparent for the luminosity performance if this technique works as designed. This was demonstrated at the Tevatron for DC powering of the electron beams and is also expected at the HL-LHC for the proposed ‘S’ shape design that allows compensating edge effects at the entrance and exit of the e-beam.

The use of HEB requires the collimation system to be in place in order to dispose of the tail particles expelled in a controlled way. No losses occur at the HEB location and the tail control mechanism can be put in place in any ring location. Larger beam size locations are favourable as they entail reduced alignment accuracy for the hollow beam. IR4 is considered to be the best candidate for two HEB devices due to the larger than standard inter-beam distance (which eases integration of the device on the beam), cryogenics availability, low-radiation environment, and quasi-round beam.

While the functionality of HEB will provide clear benefits for LHC operation, the real need for such a scheme at the LHC and the HL-LHC has to be addressed after gaining sufficient operational experience at energies close to 7 TeV on quench limits, beam lifetime, and loss rates during the operational cycle and collimation cleaning. Fast failure scenarios for the crab cavities require a low tail population above about 4 beam σ : HEB is the only technique solidly validated experimentally in other machines that could in this case ensure safe operation [67].

The HEB is targeted at enabling active control of beam tails above 3 beam σ , with tail depletion efficiencies of the order of 90% over times of tens of seconds, in all phases of the operational cycle, specifically before and after beams are put into collision.

The HEB implementation should ensure:

- the possibility of pulsing the current turn-by-turn (as required to drive resonances in the linear machine before beams are in collision);
- a train-by-train selective excitation (leaving ‘witness’ trains with populated halos for diagnostics and machine protection purposes).

The main systems/components of a HEB can be summarized as:

- electron beam generation and disposal: electron gun and collector, with the required powering;
- several superconducting and resistive magnets: solenoids, dipoles, and correctors to stabilize and steer the electron beam;
- beam instrumentation for the optimization of the electron beam.

The parameters listed here are extracted from the conceptual design document [38] compiled by colleagues from FNAL who worked on this topic within the LARP collaboration. A detail engineering design is now on-going at CERN. The first goal will be to define the volumes for a full integration into the LHC. The present status of the 3D design of the LHC hollow e-lens is shown in Figure 5-20.

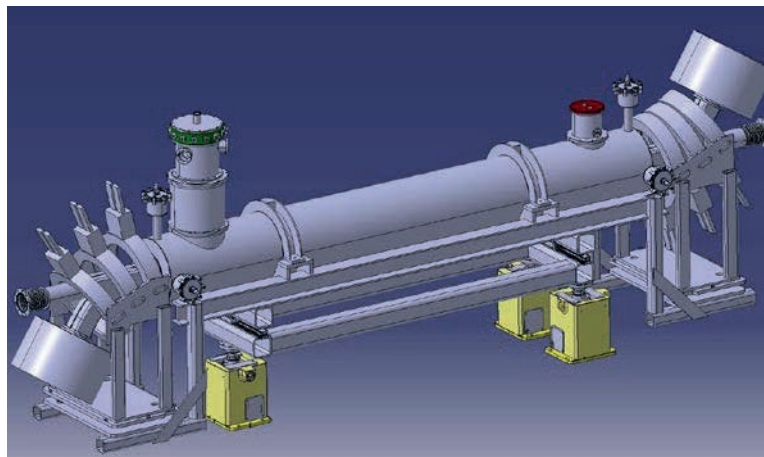


Figure 5-19: 3D design of the LHC hollow e-lens. An ‘S’ shape is proposed instead than the more conventional ‘U’ shape used at the Tevatron in order to compensate the contribution to the emittance growth from the asymmetry of the electron beams at entry and exit of the proton beam. Courtesy of D. Perini.

Table 5-5: Hollow electron beam equipment parameters.

Parameter	Value or range
<i>Geometry</i>	
Length of the interaction region, L [m]	3
Desired range of scraping positions	4–8
Inner/Outer cryostat diameter, [mm]	132 / \approx 500
Inner vacuum chamber diameter, [mm]	100 (80)
<i>Magnetic fields and magnet parameters</i>	
Gun and collector solenoid (resistive), B_g [T]	0.2–0.4
Main solenoid (superconducting), B_m [T]	2–6
Compression factor, B_m / B_g	2.2–5.5
Main solenoid current [A]	200–250
<i>Electron gun</i>	
Inner/outer cathode radius [mm]	6.75/12.7
Peak yield at 10 kV, I [A]	5
<i>Cryogenic requirements</i>	
Static heat load [W]	\leq 5
Dynamic heat load from electric powering [W]	\leq 0.5
Dynamic heat load from beam effects	negligible
<i>High-voltage modulator</i>	
Cathode-anode voltage [kV]	10
Rise time (10%–90%) [ns]	200
Repetition rate [kHz]	35

Source: Ref. [38]

At the collimation review [36], it became clear that, if loss spikes were limiting LHC performance after LS1, the hollow e-lens solution would not be viable because it could only be implemented in the next long shutdown at the earliest (driven by the time for integration into the cryogenics system). It is therefore crucial to work on viable alternatives that, if needed, might be implemented in an appropriate time scale. Two alternatives are presently being considered:

- tune modulation through a ripple in the current of lattice quadrupoles;
- narrow-band excitation of halo particles with the transverse damper system.

Though very different from the hardware point of view, both these techniques rely on exciting tail particles through resonances induced in the tune space by appropriate excitations. This works on the assumption of the presence of a well-known and stable correlation between halo particles with large amplitudes and corresponding tune shift in tune space (de-tuning with amplitude). Clearly, both methods require a solid experimental verification in a very low noise machine like the LHC, in particular to demonstrate that this type of excitation does not perturb the beam core emittance. Unlike hollow e-lenses, which act directly in the transverse plane by affecting particles at amplitudes above the inner radius of the hollow beam, resonance excitation methods require a good knowledge of the beam core tune even in dynamic phases of the operational cycle, so the possibility of using these techniques at the LHC remains to be demonstrated. For this purpose, beam tests at the LHC were performed to address the feasibility of alternative halo control method. While preliminary results are promising [68], it is clear at this stage that a viable alternative solution that fulfils all the functionality of hollow e-lenses has not been satisfactorily demonstrated yet. Ideally, these measurements would profit from appropriate halo diagnostic tools. We are, however, confident that conclusive measurements could be achieved in Run 2 with the techniques described, for example in Ref. [5].

5.3.2 Crystal collimation

Highly pure bent crystal can be used to steer high-energy particles that get trapped by the potential of parallel lattice planes. Equivalent bending fields of up to hundreds of tesla can be achieved in crystals with a length of only 3–4 mm, which allows in principle steering of halo particles to a well-defined point. As opposed to a standard collimation system based on amorphous materials, requiring several secondary collimators and absorbers to catch the products developed through the interaction with matter (Figure 5-1), one single absorber per collimation plane is in theory sufficient in a crystal-based collimation system [39]. This is shown in the scheme in Figure 5-19 (right). Indeed, nuclear interactions with well-aligned crystals are much reduced compared to a primary collimator, provided that high channelling efficiencies for halo particles can be achieved (particles impinging on the crystal to be channelled within a few turns). This is expected to significantly reduce the dispersive beam losses in the DS around the betatron cleaning insertion compared to the present system, which is limited by the leakage of particles from the primary collimators. Simulations indicate a possible gain of between 5 and 10 [40], even for a layout without an optimized absorber design. The crystal collimation option is particularly interesting for collimating heavy-ion beams thanks to the reduced probability of ion dissociation and fragmentation compared to the present primary collimators. SPS test results are promising [41].

Another potential advantage of crystal collimation is a strong reduction of machine impedance due to the facts that: (i) only a small number of collimator absorbers are required; and that (ii) the absorbers can be set at much larger gaps thanks to the large bending angle from the crystal (40–50 μrad instead of a few μrad from the multiple-Coulomb scattering in the primary collimator). On the other hand, an appropriate absorber design must be conceived in order to handle the peak loss rates in case of beam instabilities: the absorber must withstand continuous losses of up to 1 MW during 10 s while ensuring the correct collimation functionality. This is a change of paradigm compared to the present system, where such losses are distributed among several collimators. Other potential issues concern the machine protection aspects of this system (such as the implications of a crystal not being properly aligned and therefore channelling a large fraction of the total stored energy to the wrong place) and the operability of a system that requires mechanical angular stability in the sub- μrad range to be ensured through the operational cycle of the LHC (injection, ramp, squeeze, and collision).

Promising results were achieved in dedicated crystal collimation tests at the SPS performed from 2009 within the UA9 experiment [41–43]. On the other hand, some outstanding issues about the feasibility of the crystal collimation concept for the LHC can only be addressed by dedicated beam tests at high energy in the LHC. For this purpose, a study at the LHC has been proposed [44]: two goniometers housing crystals have been installed in IR7 during LS1 for horizontal and vertical crystal collimation tests. The main purpose of beam tests at the LHC is to demonstrate the feasibility of the crystal-collimation concept in the LHC environment, in particular to demonstrate that such a system can provide a better cleaning of the present high-performance system throughout the operational cycle. Until a solid demonstration is achieved, crystal collimation schemes cannot be considered for future HL-LHC baseline scenarios.

First beam tests at the LHC were very successfully carried out in 2015 and 2016. For the first time, channelling of 6.5 TeV proton beams was observed [80]. Channelling of ion beams was also seen at the record energy of 450 Z TeV (PB ion beam). These promising results also validated critical hardware component like the high-precision goniometer that allows controlling the crystal orientation with sub- μrad resolution. Tests will continue in 2016 to assess the cleaning performance of a crystal-based system.

5.3.3 Improved optics scenarios for collimation insertions

Alternative optics concepts in IR7 can be conceived in order to improve some present collimation limitations without major hardware changes. For example, non-linear optics schemes derived from the linear collider experience [45] were considered for IR7. The idea is that one can create a ‘non-linear bump’ that deforms the trajectories of halo particles and effectively increases their transverse amplitudes in a way that allows opening the gaps of primary and secondary collimators. These studies are well advanced from the optics point of view but at the present time it is not possible to easily find a layout solution providing the same cleaning as the

present system [46]. These studies, and others aimed at increasing the beta functions at the collimators, are ongoing.

5.3.4 Rotatory collimator design

The rotatory collimator design developed at SLAC under the LARP effort proposes a ‘consumable collimator’ concept based on two round jaws with 20 flat facets that can be rotated to offer to the beam a fresh collimator material in case a facet is damaged [47]. This design features a low impedance and is based on standard non-exotic materials. It was conceived for high-power operation, with a 12 kW active cooling system to withstand the extreme power loads experienced by the secondary collimators in IR7. A photograph of this device before closing the vacuum tank is given in Figure 5-21, where the rotatory glidcop (a copper alloy) jaws are visible. The first full-scale prototype of this advanced collimator concept has been delivered to CERN [48] and is being tested in preparation for beam tests. The ultimate goal is to validate the rotation mechanism after high intensity shock impacts at the HiRadMat facility, aimed at demonstrating that the concept of consumable collimator surfaces can indeed work for the LHC beam load scenarios. The precision accuracy of this prototype and the impedance are also being tested together with its vacuum performance. The vacuum measurements indicated that the SLAC prototype is suitable for installation in the SPS or even the LHC. An optimum strategy for beam tests is being established based on these new results.

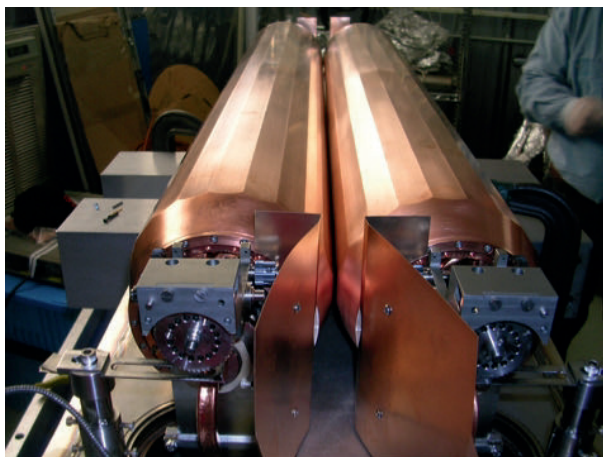


Figure 5-20: Photograph of the SLAC rotatory collimator prototype jaws before assembly in the vacuum tank.

5.4 Other collimators from the present system required in the HL-LHC

It is important to realize that 30-40 % of the present LHC collimators, which are not to be modified or replaced in the HL collimation upgrade baseline described above, must remain reliably operational for the HL-LHC era. Even devices whose design is deemed adequate for the HL-LHC parameters can hardly survive for the lifetime of the LHC machine without appropriate maintenance, substitution, or revamping. A long-term strategy must be put in place in order to ensure that the LHC collimation system can meet the performance and availability challenges of the HL-LHC project. In this section, the present LHC collimators that will also be needed for the HL-LHC, possibly with improved design and features, are described.

5.4.1 IR3 and IR7 primary collimators (target collimator primary and TCP with pick-up)

Carbon-based primary collimators, the target collimator primary (TCP), are used in the LHC to define the primary beam halo cut in the momentum and betatron cleaning insertion. One TCP collimator per beam is used in IR3 (horizontal orientation) whereas three collimators per beam are used in IR7 (horizontal, vertical, and skew orientations) for a total of eight primary collimators in the LHC. Since these collimators are closest to the circulating beams, their jaws are built with a robust carbon-fibre composite (CFC) that is designed to

withstand the design LHC failure scenarios at injection (full injection train of 288 bunches impacting on one jaw) and at 7 TeV (up to eight bunches impacting on one jaw in the case of an asynchronous dump) [1]. The need to improve the TCP collimator design in view of the updated beam parameters for the HL-LHC design is being assessed.

The LHC primary collimator might need to be upgraded for the HL-LHC if the present design:

- proves not to be adequate to cope with the design LHC failure scenarios updated for the upgraded HL-LHC beam parameters (larger bunch intensity and smaller emittances);
- proves not to be adequate for standard operational losses with a larger stored beam energy in the HL-LHC: for the same assumed minimum beam lifetime in operation, the total loss rates expected on the collimators might be up to a factor of 2 larger for the HL-LHC than for the LHC;
- can be improved in a way that the HL-LHC could profit from, e.g. improved materials or alignment features (integrated BPMs) for a more efficient operation.

The primary collimators are a fundamental element of the LHC multi-stage collimation hierarchy and are required in all operational conditions with beam in the machine. These are therefore high-reliability devices that must be compatible with operation in very high radiation environments and withstand standard operational losses and relevant failure cases without permanent damage that could jeopardize their functionality.

Note that a design with BPM-integrated jaw for primary collimators is currently being built for future consolidation of the TCPs. This design, referred to as TCP with pick-up (TCPP) currently uses the same CFC materials for the jaw but provides greatly improved operational features in terms of alignment speed and beam position monitoring. A new design that uses MoGr, as for the new secondary collimators, is also being produced. This design is also being considered for HL upgrades.

5.4.2 IR3 and IR7 secondary collimators (target collimator secondary graphite)

Carbon-based secondary collimators (target collimator secondary graphite (TCSG)) are used in the LHC for the secondary stage of the beam halo cut in the momentum and betatron cleaning insertion. Four secondary collimators per beam are used in IR3 whereas 11 collimators are used in IR7 for a total of 30 TCSG collimators in the LHC. Horizontal, vertical, and skew orientations are used in different locations. Since these collimators are among the closest to the circulating beams, their jaws are built with a robust CFC that is designed to withstand the same design LHC failure scenarios at injection and at 7 TeV as the primary collimators.

The present baseline for the HL-LHC is that new secondary collimators, TCSPM, based on advanced robust and low-impedance materials will be added in IR7, using existing TCSM slots [2]. In this scenario, the need to maintain the operability of the present CFC secondary collimators remains to be assessed. This depends, for example, on whether the new TCSPM collimators will be able to withstand the injection failure scenario. These aspects are presently under study. For IR3, the present TCSG collimators will not be replaced by a low-impedance design so adequate consolidation and spare policy must be established for these devices to ensure an efficient operation throughout the HL-LHC era.

5.4.3 IR3 and IR7 active shower absorbers collimators (target collimator long absorber)

Tungsten-based shower absorbers collimators (target collimator long absorber (TCLA)) are used in the LHC for the third or fourth stage of cleaning of beam halos in the momentum and betatron cleaning insertion. Four TCLA collimators per beam are used in IR3 whereas five collimators are used in IR7, with a total of 18 TCLA collimators in the LHC. Horizontal and vertical orientations are used depending on the location. Operationally, these collimators are not supposed to intercept primary or secondary beam losses. They are therefore built using a heavy tungsten alloy that maximizes efficiency in cleaning but which is not robust with respect to a beam impact of considerable power. The need to improve the TCLA collimator design in view of the updated beam parameters for the HL-LHC design is being assessed.

As for the previous case, the upgrade of the LHC shower absorber collimators might be needed for the HL-LHC if the present design proves not to be adequate for the standard operational losses with a larger stored beam energy in the HL-LHC and/or if it can be improved in a way from which the HL-LHC could profit (improved materials, BPM features).

The TCLA collimators are an important element of the LHC multi-stage collimation hierarchy and are required in all operational conditions with beam in the machine. Operation might continue temporarily in the case of isolated TCLA failures, but we assume here that HL operation for physics without TCLA collimators will not be possible. These are therefore high-reliability devices that must be compatible with operation in very high radiation environments and withstand standard operational losses and relevant failure cases without permanent damage that could jeopardize their functionality.

A joint study by the collimation team and the beam dump team has indicated the addition of two TCLA collimators per beam in IR6 in order to improve the protection of the Q4 and Q5 magnets immediately downstream of the dump protection devices [49]. The results indicate that this improvement was not necessary for post-LS1 operation.

5.4.4 IR6 secondary collimators with pick-up (target collimator secondary with pick-up)

Carbon-based secondary collimators with pick-up buttons (target collimator secondary with pick-up (TCSP)) are used in the LHC IR6 insertion as a part of the LHC protection system. Two collimators are used in the LHC, one per beam, as auxiliary dump protection devices in the horizontal plane. In LS1, the TCSG design without integrated beam position monitors (BPMs) was replaced with the new one with BPMs for improved alignment and local orbit monitoring. Since these collimators are among the closest to the circulating beams, and are expected to be heavily exposed to beam losses in case of asynchronous dumps, their jaws are built with a robust CFC that is designed to withstand the design LHC failure scenarios at injection (full injection train of 288 bunches impacting on one jaw) and at 7 TeV (up to eight bunches impacting on one jaw in case of an asynchronous dump). The need to improve the IR6 TCSP collimator design in view of the updated beam parameters for the HL-LHC design is being assessed.

5.4.5 Passive absorbers in IR3 and IR7 (TCAPA, TCAPB, TCAPC, TCAPD)

Tungsten-based passive shower absorbers collimators (target collimator absorber passive (TCAP)) are used in the LHC as fixed-aperture collimators in the momentum and betatron cleaning insertion to reduce radiation doses to the warm quadrupole and dipoles in these insertions. Two TCAP collimators per beam are used in IR3 whereas three collimators are used in IR7 for a total of 10 TCAP collimators in the LHC. Four variants of these collimators exist to match the dimensions and orientations of the aperture of the adjacent warm magnets: TCAPA, TCAPB, TCAPC, TCAPD. Operationally, these collimators are not supposed to intercept primary or secondary beam losses but rather to absorb shower products generated by halo particles impinging on primary and secondary collimators. They are built using a heavy tungsten alloy that maximizes shower absorption, surrounded by copper. The need to improve the TCAP collimator design in view of the updated beam parameters for the HL-LHC design is being assessed.

The TCAP collimators ensure that doses on warm magnets in the cleaning insertions are minimized. Doses are determined by the integrated luminosity and therefore the possibility to improve the warm magnet protection must be envisaged for the HL-LHC luminosity goal. The upgrade of the passive absorber collimators might be needed for the HL-LHC if the present design proves not to be adequate for HL-LHC operational loss cases and/or if it can be improved by increasing the lifetime of warm magnets due to radiation wear (e.g. new materials or improved layouts/designs).

As a part of the consolidation program of the warm magnets of type MQW and MBW in IR3 and IR7, it is planned to improve the passive cleaning of these magnets against large radiation doses. This work will require the preparation of new fixed-aperture absorbers to be installed next to the magnets. This activity already started in LS1 when 2 TCAP were added in IR3 to improve the passive protection of the Q5.

5.4.6 Tertiary collimators with pick-up in the experimental regions (target collimator tertiary with pick-up)

As discussed above, tungsten-based tertiary collimators with pick-up buttons (target collimator tertiary with pick-up (TCTP)) are used in the LHC to protect the superconducting triplets and the experiments in each experimental insertion against horizontal (TCTPH) and vertical (TCTPV) beam losses. A complete re-design of IR1 and IR5 collimation is imposed by the layout changes foreseen in the HL-LHC for LS3. The need to improve the present TCTP collimators in IR1/IR5 in view of the updated beam parameters for the HL-LHC design is also being assessed. In particular, consideration is being given to the possibility of replacing the TCTPs with more robust ones based on novel materials, at least in the horizontal plane, which is affected by beam dump failures.

5.4.7 Physics debris collimators in the experimental regions (Target Collimators Long (TCL))

Physics debris absorbers are used already in the present LHC to protect the matching sections and the dispersion suppressor of IR1 and IR5 from beam losses caused by collision products. The LHC IR layouts as of 2015 feature three horizontal (TCL) collimators per beam and per IR, for a total of 12 TCL collimators, installed in cells 4, 5, and 6. Their jaws are made of copper (TCLs in cells 4 and 5) and Inermet 180 (cell 6), as the latter were installed by recuperating tertiary collimators replaced in LS1 with the new TCTPs. Indeed, the tungsten based TCT can serve as TCL without design changes. The present baseline foresees changing all TCLs for HL by adding the BPM feature. The HL-LHC layouts require new TCLX design in the region between TAXN and D2. The present TCL collimators might be re-used for the HL-LHC by being moved to new layout positions, however the preferred solution (presently in the baseline) is to build new ones that feature the BPM design. Mechanical and radiation hardware should be studied for this scenario.

5.5 References

- [1] O. Brüning (Ed.) *et al.*, LHC Design Report Vol. 1, [CERN-2004-003-V-1](#) (2004).
- [2] R. Assman *et al.*, The final collimation system for the LHC, Proc. EPAC2006, Edinburgh, 2006. Conf. Proc. C060626 (2006) 986-988. Also as [CERN-LHC-PROJECT-REPORT-919](#) (2006).
- [3] R. Bruce *et al.*, LHC beta* reach in 2012, 3rd Evian Workshop on LHC beam operation, Evian-les-bains, France, 12 - 14 Dec 2011, pp.[117-124](#).
- [4] R. Bruce *et al.*, Sources of machine-induced background in the ATLAS and CMS detectors at the CERN Large Hadron Collider, *Nucl. Instrum. Methods Phys. Res. A* **729** (2013) 825–840. DOI: [10.1016/j.nima.2013.08.058](#)
- [5] G. Valentino *et al.*, Beam diffusion measurements using collimator scans at the LHC, *Phys. Rev. Spec. Top. Accel. Beams* **16** (2013) 021003. DOI: [10.1103/PhysRevSTAB.16.021003](#)
- [6] K.H. Mess and M. Seidel, Collimators as diagnostic tools in the proton machine of HERA, *Nucl. Instrum. Meth.* A351 (1994) 279–285.
- [7] H. Burkhardt, S. Redaelli, B. Salvachua and G. Valentino, Collimation down to 2 sigmas in special physics runs in the LHC, 4th International Particle Accelerator Conference, Shanghai, China, 12 - 17 May 2013, pp.1427. Also as [CERN-ACC-2013-0144](#) (2013).
- [8] S. Redaelli *et al.*, LHC collimator controls for a safe LHC operation, 13th International Conference on Accelerator and Large Experimental Physics Control Systems, Grenoble, France, 10 - 14 Oct 2011, pp.[1104-1107](#)
- [9] A. Bertarelli *et al.*, The mechanical design for the LHC collimators, 9th European Particle Accelerator Conference, Lucerne, Switzerland, 5 - 9 Jul 2004, pp.[545](#)
- [10] S. Redaelli *et al.*, Final implementation and performance of the LHC collimator control system, Particle Accelerator Conference 2009, Vancouver, Canada, 04 - 08 May 2009, pp.[FR5REP007](#).
- [11] A. Bertarelli *et al.*, Mechanical design for robustness of the LHC collimators, 21st IEEE Particle Accelerator Conference, Knoxville, TN, USA, 16 - 20 May 2005, pp.[913](#)

- [12] F. Carra *et al.*, LHC collimators with embedded beam position monitors: A new advanced mechanical design, 2nd International Particle Accelerator Conference, San Sebastian, Spain, 4 - 9 Sep 2011, pp.[TUPS035](#).
- [13] D. Wollmann *et al.*, First beam results for a collimator with in-jaw beam position monitors, 2nd International Particle Accelerator Conference, San Sebastian, Spain, 4 - 9 Sep 2011, pp.[THPZ027](#)
- [14] D. Wollmann *et al.*, Experimental verification for a collimator with in-jaw beam position monitors, Proc. HB2012. <http://accelconf.web.cern.ch/AccelConf/HB2012/papers/mop242.pdf>
- [15] G. Valentino *et al.*, Successive approximation algorithm for BPM-based LHC collimator alignment, Phys. Rev. ST Accel. Beams 17, 021005. DOI: [10.1103/PhysRevSTAB.17.021005](https://doi.org/10.1103/PhysRevSTAB.17.021005)
- [16] R. Bruce *et al.*, Energy deposition simulations for upgraded collimation layouts, [CERN-ACC-2014-0009](#)
- [17] Web site: Review of 11 T dipoles and cold collimation. INDICO: [155408](#)
- [18] A. Marsili, R. Bruce, L. Lari, S. Redaelli, Simulated cleaning for HL-LHC layouts with errors, INDICO: [257368](#). Presentation at the 3rd Joint HiLumi LHC-LARP Annual Meeting, Daresbury (UK), 2013.
- [19] A. Lechner *et al.*, Energy deposition with cryo-collimators in IR2 (ions) and IR7, INDICO: [257368](#). Presentation at the 3rd Joint HiLumi LHC-LARP Annual Meeting, Daresbury (UK), 2013.
- [20] R. Bruce, A. Marsili, S. Redaelli, Cleaning performance with 11 T dipoles and local dispersion suppressor collimation at the LHC, 7th International Particle Accelerator Conference, Busan, Korea, 8 - 13 May 2016, pp.WEPMW030. DOI: [10.18429/JACoW-IPAC2016-WEPMW030](https://doi.org/10.18429/JACoW-IPAC2016-WEPMW030)
- [21] A. Lechner *et al.*, Power deposition in LHC magnets with and without dispersion suppressor collimators downstream of the betatron cleaning insertion, 5th International Particle Accelerator Conference, Dresden, Germany, 15 - 20 Jun 2014, pp.[MOPRO021](#)
- [22] A. Marsili, R. Bruce, S. Redaelli, Collimation cleaning for HL-LHC optics with error models, 5th International Particle Accelerator Conference, Dresden, Germany, 15 - 20 Jun 2014, pp.163 [CERN-ACC-2014-0139](#)
- [23] Recommendation of 2013 Collimation Project review panel. INDICO: [251588](#)
- [24] L. Gentini, presentation at the 51st meeting of the Collimation Upgrade Specification working group.INDICO:[366694](#)
- [25] 2013 Collimation Project Review. INDICO: [251588](#)
- [26] LHC Collimation Review 2009. INDICO: [55195](#)
- [27] J.M. Jowett *et al.*, Heavy ion beams in the LHC, 20th IEEE Particle Accelerator Conference, Portland, OR, USA, 12 - 16 May 2003, pp.1682 [LHC-Project-Report-642](#)
- [28] R. Bruce *et al.*, Beam losses from ultraperipheral nuclear collisions between $^{208}\text{Pb}^{82+}$ ions in the Large Hadron Collider and their alleviation, *Phys. Rev. ST Accel. Beams* **12** (2009) 071002.
- [29] G. Steele *et al.*, Heat load scenarios and protection levels for ions, presentation at the 2013 LHC Collimation Project review. INDICO: [251588](#)
- [30] R. Assmann *et al.*, Collimation chapter of the LHC Design Report, Eds. O. Brüning *et al.* [CERN-2004-003-V-1](#) (2004)
- [31] HiLumi WP2 deliverable document D2.1. Optics and lattice files [CERN-ACC-2013-009](#)
- [32] HiLumi WP2 milestone document M29, Initial estimate of machine impedance. [CERN-ACC-2014-0005](#)
- [33] HiLumi WP2 milestone document M31, Preliminary estimates of beam-beam effect. [CERN-ACC-2014-0066](#)
- [34] N. Mounet, Transverse impedance in the HL-LHC era, presentation at the 3rd HiLumi Annual meeting, Daresbury, (2013).INDICO: [257368](#)
- [35] N. Biancacci, presentation at the 55th meeting of the Collimation Upgrade Specification working group INDICO: [390114](#)

- [36] A. Bertarelli, Beam Induced Damage Mechanisms and Their Calculation, 2014 Joint International Accelerator School: Beam Loss and Accelerator Protection, Newport Beach, CA, USA, 5 - 14 Nov 2014, pp.159-227 (CERN-2016-002) DOI: [10.5170/CERN-2016-002.159](https://doi.org/10.5170/CERN-2016-002.159)
- [37] A. Bertarelli *et al.*, Novel Materials for Collimators at LHC and its Upgrades, 54th ICFA Advanced Beam Dynamics Workshop on High-Intensity, High Brightness and High Power Hadron Beams, East-Lansing, USA, 10 - 14 Nov 2014, pp.438-442 [CERN-ACC-2015-0173](https://arxiv.org/abs/1501.0173)
- [38] A. Bertarelli *et al.*, Development and testing of novel advanced materials with very high thermal shock resistance, Tungsten, Refractory and Hardmetals Conference, Orlando, 2014 [CERN-ACC-2014-0306](https://arxiv.org/abs/1406.0306)
- [39] F. Carra *et al.*, Mechanical engineering and design of novel collimators for HL-LHC, 5th International Particle Accelerator Conference, Dresden, Germany, 15 - 20 Jun 2014, pp.369 [CERN-ACC-2014-0184](https://arxiv.org/abs/1406.0184)
- [40] A. Bertarelli *et al.*, An experiment to test advanced materials impacted by intense proton pulses at CERN HiRadMat facility, Nucl. Instr. Meth. B **308** (2013) 88 DOI: [10.1016/j.nimb.2013.05.007](https://doi.org/10.1016/j.nimb.2013.05.007)
- [41] Review of hollow e-lens for the LHC collimation. INDICO: [213752](https://indico.cern.ch/event/213752)
- [42] G. Stancari *et al.*, Conceptual design of hollow electron lenses for beam halo control in the Large Hadron Collider, FNAL note FERMILAB-TM-2572-APC (2014) and CERN [ATS Report CERN-ACC-2014-0248](https://arxiv.org/abs/1406.0248) (2014).
- [43] W. Scandale, Crystal-based collimation in modern hadron colliders, *Int. J. Mod. Phys. A* **25S1** (2010) 70–85 DOI: [10.1142/S0217751X1004992X](https://doi.org/10.1142/S0217751X1004992X)
- [44] D. Mirarchi *et al.*, Layouts for crystal collimation tests at the LHC, 4th International Particle Accelerator Conference, Shanghai, China, 12 - 17 May 2013, pp.966
- [45] W. Scandale *et al.*, Comparative results on collimation of the SPS beam of protons and Pb ions with bent crystals, *Phys. Lett. B* **703** (2011) 547–551 DOI: [10.1016/j.physletb.2011.08.023](https://doi.org/10.1016/j.physletb.2011.08.023)
- [46] W. Scandale *et al.*, Optimization of the crystal-assisted collimation of the SPS beam, *Phys. Lett. B* **726** (2013) 182–186
- [47] W. Scandale *et al.*, Strong reduction of the off-momentum halo in crystal assisted collimation of the SPS beam, *Phys. Lett. B* **714** (2012) 231–236 DOI: [10.1016/j.physletb.2012.07.006](https://doi.org/10.1016/j.physletb.2012.07.006)
- [48] Installation of the LUA9 Equipment in IR7 of the LHC EDMS: [1329235](https://arxiv.org/abs/1329235), LHC-TEC-EC-0001 (2013).
- [49] A. Faus-Golfe *et al.*, Non-linear collimation in linear and circular colliders, 10th European Particle Accelerator Conference, Edinburgh, UK, 26 - 30 Jun 2006, pp.1892
- [50] L. Lari *et al.*, Studies for an alternative LHC non-linear collimation system, 3rd International Particle Accelerator Conference, New Orleans, LA, USA, 20 - 25 May 2012, pp.544
- [51] J. Smith *et al.*, Design of a rotatable copper collimator for the LHC phase II collimation upgrade. 11th European Particle Accelerator Conference, Genoa, Italy, 23 - 27 Jun 2008, pp.[MOPC096](https://arxiv.org/abs/0806.096)
- [52] T. Markiewicz, Status of SLAC RC, presentation at the 3rd HiLumi annual meeting, Daresbury, 2013. INDICO: [257368](https://indico.cern.ch/event/257368)
- [53] Collimation Working group meeting. INDICO:[244412](https://indico.cern.ch/event/244412)
- [54] E. Skordis, presentation at the 51st Collimation Upgrade Specification Meeting. INDICO: [366694](https://indico.cern.ch/event/366694)
- [55] A. Marsili *et al.*, Simulations of Collimation Cleaning Performance with HL-LHC Optics, 4th International Particle Accelerator Conference, Shanghai, China, 12 - 17 May 2013, pp.987
- [56] G. Bellodi *et al.*, First Ion Collimation Commissioning Results at the LHC, 2nd International Particle Accelerator Conference, San Sebastian, Spain, 4 - 9 Sep 2011, pp.[TUPZ007](https://arxiv.org/abs/1109.007)
- [57] P.D. Hermes *et al.*, Studies on Heavy Ion Losses from Collimation Cleaning at the LHC, 54th ICFA Advanced Beam Dynamics Workshop on High-Intensity, High Brightness and High Power Hadron Beams, East-Lansing, USA, 10 - 14 Nov 2014, pp.[MOPAB43](https://arxiv.org/abs/1406.043)

- [58] P.D. Hermes et al., Betatron cleaning for heavy-ion beams with IR7 dispersion suppressor collimators, 6th International Particle Accelerator Conference, Richmond, VA, USA, 3 - 8 May 2015, pp.[TUPTY025](#).
- [59] L.S. Esposito and F. Cerutti, "Energy deposition for HL-LHC v1.1: TAN/D2/Q4", Presentation at the 4th Joint HiLumi LHC-LARP Annual Meeting, Tsukuba Japan, 2014.
- [60] R. Bruce et al., Technical Design IR Collimation : Deliverable: D5.6 [CERN-ACC-2015-0042](#)
- [61] R. Bruce et al., Verification of new IR Collimation Solution in Simulations. Possible Iteration in Design: Milestone: MS52. [CERN-ACC-2015-0041](#)
- [62] J.M. Jowett, presentation at the 54th Collimation Upgrade Specification Meeting. NDICO: [381344](#)
- [63] R. Bruce, presentation at the 58th Collimation Upgrade Specification Meeting. INDICO: [395463](#)
- [64] 67th Collimation Upgrade Specification Meeting (ColUSM), Feb. 6th, 2016. INDICO: [493012](#)
- [65] E. Quaranta *et al.*, "Towards optimum material choices for HL-LHC collimation upgrade", 7th International Particle Accelerator Conference, Busan, Korea, 8 - 13 May 2016, pp.WEPMW031. DOI: [10.18429/JACoW-IPAC2016-WEPMW031](#)
- [66] E. Quaranta *et al.*, "Radiation-induced effects on LHC collimator materials under extreme beam conditions", 7th International Particle Accelerator Conference, Busan, Korea, 8 - 13 May 2016, pp.WEPMW032. DOI: [10.18429/JACoW-IPAC2016-WEPMW032](#)
- [67] HL-LHC project review on "Needs for a hollow e-lens at the HL-LHC",INDICO: [567814](#)
- [68] J. F. Wagner *et al.*, "First attempts at using active halo control at the LHC", 7th International Particle Accelerator Conference, Busan, Korea, 8 - 13 May 2016, pp.WEPMW028. DOI: [10.18429/JACoW-IPAC2016-WEPMW028](#)
- [69] E. Skordis et al. "Updated power deposition simulations for DS collimators in IR7 (proton operation)", presentation in the Collimation Upgrade Specification Meeting (2015) INDICO: [366694](#)
- [70] P. D. Hermes, et al, "LHC Heavy-Ion Collimation Quench Test at 6.37Z TeV", [CERN-ACC-Note-2016-0031](#) (2016)
- [71] P. Hermes, Heavy-Ion Collimation at the Large Hadron Collider : Simulations and Measurements, PhD thesis, University of Munster (2016). [CERN-THESIS-2016-230](#)
- [72] B. Salvachua, et al, "Collimation quench test with 6.5 TeV proton beams", [CERN-ACC-NOTE-2016-0015](#) (2016)
- [73] J.F. Wagner, et al. "First Attempts at using Active Halo Control at the LHC", 7th International Particle Accelerator Conference, Busan, Korea, 8 - 13 May 2016, pp.WEPMW028 DOI: [10.18429/JACoW-IPAC2016-WEPMW028](#)
- [74] A. Mereghetti, et al., "Beta*-reach – IR7 Collimation Hierarchy Limit and Impedance", [CERN-ACC-NOTE-2016-0007](#) (2016)
- [75] J.M. Jowett, et al."The 2015 heavy-ion run of the LHC", Proceedings of IPAC16, Busan, Korea, TUPMW027, pp. 1493-1496. DOI: [10.18429/JACoW-IPAC2016-TUPMW027](#)
- [76] J.M. Jowett, et al. "Bound-free pair production in LHC Pb-Pb operation at 6.37 Z TeV per beam", Proceedings of IPAC2016, Busan, Korea, TUPMW028, pp. 1497-1500. DOI: [10.18429/JACoW-IPAC2016-TUPMW028](#)
- [77] C. Bahamonde Castro, et al. "Power deposition in LHC magnets due to bound-free pair production in the experimental insertions", Proceedings of IPAC2016, Busan, Korea, TUPMW006, pp. 1418-1421. DOI: [10.18429/JACoW-IPAC2016-TUPMW006](#)
- [78] C. Bahamonde Castro et al., "Needs for shielding in the connection cryostats in IR2 DS", Presentation at the 14th Meeting of the HL-TCC, Sept 2016, INDICO: [559125](#).
- [79] A. Lechner et al., "BFPP losses in the connection cryostat: power deposition and dose estimates for Run 2 (and some outlook to HL-LHC)", Presentation at the LMC Meeting, Sept 2015, INDICO:[442208](#).
- [80] W. Scandale et al. Observation of channeling for 6500 GeV/ c protons in the crystal assisted collimation setup for LHC. Phys.Lett. B758 (2016) 129-133. DOI: [10.1016/j.physletb.2016.05.004](#)

Chapter 6A

Cold Powering of the superconducting circuits

6A. Cold Powering of the superconducting circuits

6A.1 Overview

The electrical feed of the approximately 1700 Large Hadron Collider (LHC) superconducting (SC) circuits requires the transmission of more than ± 1.5 MA of current from the power converters to the magnets. This is done via conventional copper cables, for the room temperature path between power converters and current leads, and via High Temperature Superconducting (HTS) or resistive currents leads for the transfer to the 4.5 K liquid helium bath. Nb-Ti bus-bars operated in liquid helium at 4.5 K or in superfluid helium at 1.9 K provide the connection to the SC magnets. In the present LHC configuration, the power converters and the current leads are both located in underground areas: the former mainly in tunnel enlargements or alcoves situated adjacent to the machine tunnel, and the latter in cryostats that are near the LHC interaction points and in most cases in line with the SC magnets – only the leads housed in the five DFBL distribution feedboxes are in tunnel alcoves. The 60 A power converters for the dipole orbit correctors are located in the tunnel, underneath the main dipole magnets. Power converters and current leads at each of the eight interaction points feed the magnets occupying half of the two adjacent machine sectors. Some equipment in the tunnel is exposed to significant levels of radiation.

For the HL-LHC upgrade, novel superconducting lines (hereafter called “links”) are being developed to supply current to the magnets from remote distances [1]. The electrical layout originally envisaged the location of the power converters and current leads in surface buildings some hundred meters away from the tunnel. More recently power converters and leads have been located in underground areas (the so-called double decker solution (DD)) [2]. However, also in the chosen solution of locating the power converters in a technical gallery running aside the LHC tunnel, the current transport to the magnets is performed via SC links containing tens of cables feeding different circuits. A link will carry all together up to about $|150|$ kA. The benefits of this remote powering via SC links are several and can be summarized as follows:

- Access of personnel for maintenance, tests and interventions on power converters, current leads and associated equipment is in radiation free areas, in accordance with the principle of radiation protection that optimizes doses to personnel exposed to radiation by keeping them As Low As Reasonably Achievable (ALARA);
- Removal of the current leads and associated cryostats from the accelerator ring, thus making space available for other accelerator components. In the baseline hardware layout of the HL-LHC Interaction Regions (IR) around P1 and P5, no space is used for current leads and very limited one is taken by the cryostats in line with the magnets. Also, there is no space in the existing underground alcoves for locating the power converters feeding the HL-LHC circuits;
- Location of the power converters in radiation free, easy access areas. Access to this area may even be granted, under certain conditions, also during the HL-LHC run.

The Cold Powering work-package (WP6A) is presently focused on the development of SC links for potential integration at the LHC interaction Point 1 (P1), Point 5 (P5). A study was initially performed also for point 7 (P7).

Development of radiation hard power converters is carried out by the Power converters for superconducting magnets work-package (WP6B). In certain case, like P7, they can be effective solutions, however in other cases like for P1 and P5, the SC links offer a more complete approach for increased availability and reduced radiation dose to personnel.

6A.1.1 Cold Powering Systems

A Cold Powering System consists of:

- Current leads, located as near as possible to the power converters in a radiation free zone at about a hundred meters distance from the LHC tunnel. The leads are connected to the power converters via room temperature conventional cables;
- A dedicated cryostat (DFH), where the cold terminations of the leads are electrically connected to the cables in the link;
- A link, made of novel type of superconductor, MgB_2 , in form of round wire arranged in multi-stage cables, housed in a semi-flexible cryostat (DSH). The link is electrically connected to the leads to the magnet bus-bar inside a specific cryostat (DF);
- A cryostat (DF) in line with the magnets at the location where the link terminates in the LHC tunnel. In the DF cryostat, each cable of the link is connected to the Nb-Ti bus-bar feeding a magnet circuit. The helium cryogen required for the cooling of the Cold Powering System is supplied from this cryostat;
- Cryogenic instrumentation required for control, monitoring and interlock functions as well as electrical instrumentation needed for protection of superconducting components and current leads.

The Cold Powering System relies on cooling with helium gas. The superconducting part of the system spans the temperature range from 4.2 K up to 35 K - 50 K. The use of MgB_2 and HTS materials enables safe operation of the superconducting components, for which a temperature margin of at least 10 K is guaranteed.

In the tunnel, vapour generated in the DF cryostat from a two-phase helium bath is conveyed inside the superconducting link cold mass [3]. The gas cools the SC cables in the link and warms up to about 17 K while absorbing the static heat load of the cryostat. In the present HL-LHC baseline, the DSH cryostat includes a thermal shield actively cooled by forced flow of He gas at about 20 K. For the Cold Powering Systems at P1 and P5, the helium flow of the shield and of the cold mass are mixed at the level of the DFH to produce the flow of He gas, at about 30 K, required for the cooling of the current leads. The system that was studied for P7 did not need mixing - the helium flow in the superconducting link cold mass was sufficient for the cooling of the leads. The design of the current leads is such that the gas is recovered at room temperature at their warm end. Studies are under way to see if this last, simpler solution can be adapted also to P1 and P5 links, thus simplifying the baseline solution.

Until December 2014, activity was focused on the development of the Cold Powering Systems for LHC P7. Indeed for these systems, integration of the SC links in the tunnel in 2018 was an option. By end 2014, the following milestones were achieved:

- Concepts [4] and prototype [5] MgB_2 cables were developed and tested;
- Dedicated cabling machines conceived for production of long unit lengths of novel HTS or MgB_2 cables were designed, assembled and operated [6];
- A prototype Cold Powering System was developed and tested [7];
- Integration studies in the LHC were performed [8];
- New concepts of current leads and DFH cryostats optimized for easy transport and integration in the LHC underground areas at P7.

In December 2014, was decided not to integrate the SC links at P7 and to proceed with the consolidation of the power converters. It was nevertheless decided to complete the design study of the Cold Powering System for LHC P7 and to proceed with the construction and test of a prototype system aiming at validating the design concept.

The design of the Cold Powering Systems is such as to minimize the work done in the tunnel in terms of assembly of components. Ongoing design takes into account boundary conditions imposed by transport in the LHC underground areas. In particular, volumes of individual components have been minimized according to transport constraints and the main components (SC link, i.e. DSH cryostat with the SC cables inside, current leads, DFH and DF cryostats) are integrated as complete and pre-tested assemblies. Installation will account possible necessary tooling for the fixation of the link on the walls and the incorporation of means for length compensation plus the constraints impose by bends and maximum limited bending radius of the SC link itself. Activities after installation are limited to splicing between current leads and link and closure of the DFH cryostat, splicing between SC link and Nb-Ti bus-bar and closure of the DF cryostat, and connection of the conventional room temperature cables to current leads and power converters.

6A.1.2 Superconducting Link basic design and R&D

The superconducting link is a semi-flexible transfer line, which houses the MgB₂ cables connecting the cold end of the current leads to the Nb-Ti bus-bar of the magnet [1]. The transfer line consists of four corrugated concentric pipes that define the SC link cold mass, the actively cooled thermal shield and the external vacuum insulation wall.

The number of SC cables contained inside the link and their operating current vary for the different Cold Powering Systems that are to date under study. Inside the cold mass of each link there are tens of cables rated at different DC currents ranging from a minimum of 120 A up to a maximum of 18 kA. The cables are grouped in the form of compact cable assemblies with a total current capability of up to about |150| kA.

At LHC P1 and P5, four superconducting links, two right and two left of each interaction point, are being considered for integration in the LHC machine (Figure 6-1):

- Two SC links for the powering of the HL-LHC Insertions (low- β quadrupoles, D1 and corrector magnets);
- Two SC links for the powering of the HL-LHC Matching Sections.

The associated Cold Powering Systems replace or modify the LHC cryogenic feedboxes (DFBX, DFBL). New current leads and cryostats (DFHX and DFHM) connected to the link in a radiation free area away from the tunnel, are being developed.

Until the beginning of 2015, the baseline electrical layout envisaged the installation of the power converters and current leads in surface buildings. This called for development of superconducting links, about 300 m long, including a vertical section of about 80 m. By mid-2015, a global integration study (cryo-refrigerators, crab cavities, power converters, distribution feedboxes and associated equipment) opted for an underground installation (DD). Since then, the baseline electrical layout for LHC P1 and P5 foresees installation of power converters and current leads in the DD, parallel to the main ring. In this configuration, the links have a total length of about 100 m.

The baseline proposal envisages using MgB₂ conductor in the longest part of the SC links (from 4.2 K to 20 K), and HTS material (YBCO or Bi-2223) in the temperature range from 20 K up to 35 K – 50 K. The potential low cost of MgB₂ conductor and the possibility of cooling the superconducting link cold mass with He gas enabled the development of Cold Powering Systems with improved performance. There is a high temperature margin, at the benefit of a safer operation, and the total exergetic cost of the refrigeration is lower with respect to the conventional Nb-Ti solution. Figure 6-2 shows the cross section of the superconducting cable assembly proposed for the SC links powering the HL-LHC Insertion magnets at LHC P1 and P5. The total current transferred by these forty-four cables is about |150| kA. There are four 18 kA cables that are used

for powering the low- β insertion Nb₃Sn quadrupole magnets and the Nb-Ti separation dipole (D1), and two additional 18 kA cables that are integrated as spare units. The inclusion of the 18 kA spare units, made possible by the new powering lay-out with one main circuit for the low- β quadrupole instead of two, has been decided to mitigate any possible malfunctioning. The other cables feed corrector and trim circuits. Details of the cable assemblies developed for other Cold Powering Systems are presented elsewhere [1].

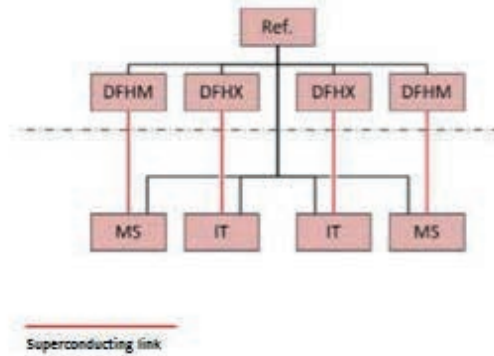


Figure 6-1: Superconducting links at LHC P1 and P5.

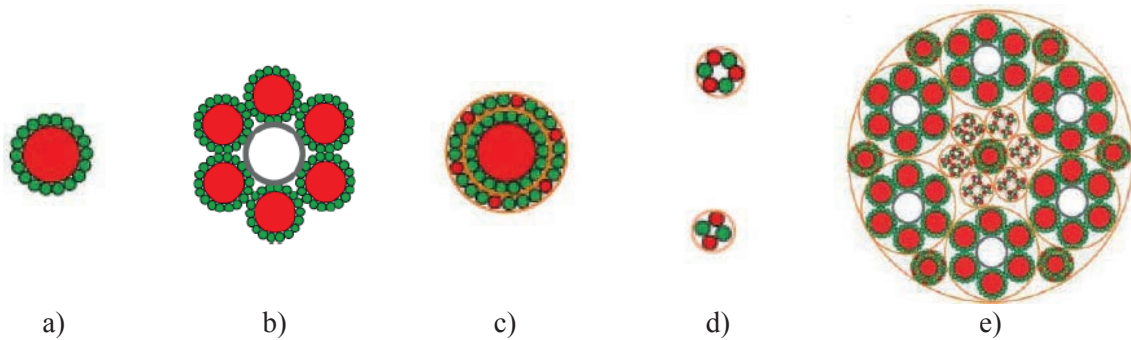


Figure 6-2: Cable assemblies for superconducting links at LHC P1 and P5. From left: a) Sub-unit of the 18 kA cable, $\Phi \sim 6.5$ mm, rated for 6 (??) kA; b) Complete 18 kA cable, $\Phi \sim 19.5$ mm; c) concentric 2 \times 3 kA cable, $\Phi \sim 8.5$ mm; d) 0.4 kA cable (top) and 0.12 kA cable (bottom), $\Phi < 3$ mm; e) 165 kA cable assembly for LHC P1 and P5 (6 \times 20 kA, 7 \times 2 \times 3 kA, 4 \times 0.4 kA, 18 \times 0.12 kA), $\Phi \sim 65$ mm. The cables are made of copper stabilizer (red) and MgB₂ wire (green).

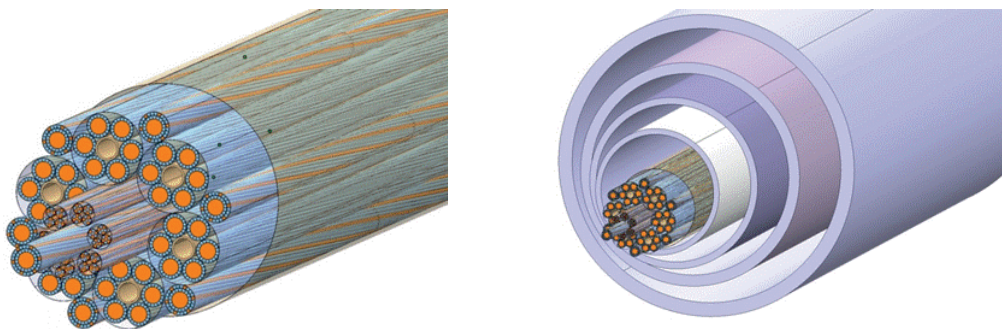


Figure 6-3: Cable assembly for superconducting links at LHC P1 and P5 (system powering the HL-LHC Insertions). From left: cable assembly; cable assembly inside the semi-flexible cryostat. The external diameter of the cryostat (vacuum wall), which includes an active thermal shield, is ~ 220 mm. The weight of the cryostat with the [150] kA cable assembly inside is ~ 20 kg/m.

The cable (Twisted-Pair of superconducting tapes or wires) and cable assemblies developed for LHC P7 were optimized for transport of 1 kA range current. Details of the cable concepts and results from tests performed in nominal operating conditions are presented elsewhere [5]. The cable assemblies are incorporated

in a semi-flexible cryostat of the CRYOFLEX® type. The proposal was to integrate in the LHC tunnel the cryostat with the cable assemblies already pulled in at the surface. To limit the risks associated with high-current resistive joints operated in helium gas environment, the cables were planned to be assembled in one single unit length with no splices between cables inside the link.

The main achievements to date are:

- The development of a the first MgB₂ Powder In Tube (PIT) round wire with electrical and mechanical performance that permit its use in high-current cables - work done in collaboration between CERN and Columbus Superconductors, Genova;
- The test of a 3 m long superconducting link of the type needed at LHC P7 [7];
- The design of a Cold Powering System optimized for integration at LHC P7 [6];
- The successful development and test of the first 2×20 m long cable made from MgB₂ round wire operated successfully up to 20 kA at 24 K [9].
- The conceptual design of Cold Powering Systems optimized for use of MgB₂ links.

Figure 6-4 shows the test station designed and successfully operated at CERN for the test of up to 20 m long superconducting links. As in the final configuration, the cables are cooled by forced flow of helium gas operating at any temperature from about 5 K to 35 K. Temperatures of up to 70 K can be achieved, enabling appraisal of cables made from different types of conductor.

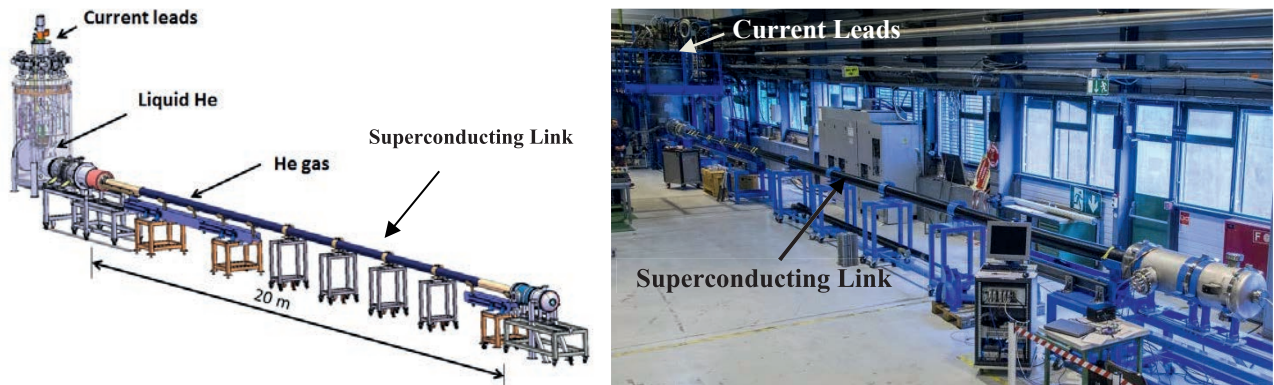


Figure 6-4: Test station designed and operated at CERN for the test of 20 m long superconducting links. The cables are cooled by forced flow of helium gas operating at any temperature from about 5 K to 35 K. Temperatures of up to 70 K can be achieved, enabling appraisal of cables made from different types of conductor.

6A.2 Cold Powering System design

In essence the Cold Powering System for the powering of the LHC magnets by superconducting links is a semi-flexible cryostat extended over a hundred metres. The novel design has to face several challenges never encountered previously.

6A.2.1 Cryostat for the superconducting link

The superconducting link cryostat (DSH) must maintain a stable and well defined cryogenic environment within which the superconducting cables are cooled by forced flow of helium gas. Unlike the liquid helium cooled superconducting bus-bars in the LHC machine, the cryogenic stability of the superconducting cables depends more critically on the cooling efficiency in helium gas environment within the superconducting link cold mass. The basic cryostat structure consists of an inner vessel surrounded by an actively cooled thermal shield and enclosed by an outer vessel as room temperature vacuum envelope. At present the reference design of the cryostat is analogous to the Nexan's 4-Tube Coaxial CRYOFLEX® transfer line, which can be

manufactured and delivered in one continuous length compatible to the cold powering requirements. It is essential to minimise the number of splices between cables inside the SC link cold mass due to their multiple circuit complexity and cooling challenges for high current resistive joints cooled by gaseous helium. As part of the HL-LHC design studies, pre-prototype cryostats in 5 m and 20 m lengths have been procured from Nexans and tested at CERN [9] and at the University of Southampton [7]. The working experiences have been positive so far and a 60 m long cryostat are being procured for integration tests in configurations similar to those in the LHC underground areas. However, in the frame of the R&D for SC links also other different and more simple cryostat configurations are under test. It is worth underling that SC links in the underground areas will be mostly horizontal – a vertical path of less than 10 m will be required, differently from the original baseline described in the HL-LHC Preliminary Design Report [10].

The gaseous helium in the cold mass of the SC link provides cooling for (a) steady-state heat load of the radial heat in-leak (conduction and radiation) from the surrounding thermal shield and heat conduction along the link and the inner vessel wall from the warmer end at 20 K and (b) transient heat load due to local disturbances in the link and/or thermal/vacuum instability in the cryostat. Under nominal operating conditions, the radial heat in-leak is dominant, estimated conservatively at below 0.2 W/m for a thermal shield temperature of ~ 60 K without multilayer insulation. The thermal shield will be actively cooled by flowing helium gas with an inlet temperature at 20 K. Further discussions on the cooling requirement can be found in [3].

6A.3 Interfaces to the superconducting link

The SC link has a colder (4.2 K) interface to the LHC machine at one end and a warmer (20 K) interface to the current leads at the level of the DFH cryostat. The two interfaces are an integral part of the Cold Powering System due to electrical continuity and synergy in the cooling arrangements.

The present LHC current leads consist of a self-cooled HTS section and a 20 K helium gas cooled resistive copper section [11]. The former is connected to the Nb-Ti bus-bar in helium and the latter extends from the warm end of the HTS at 50 K to room temperature. The Cold Powering System design seeks the integration of the different helium gas flows at the interface between the superconducting links and current leads.

6A.3.1 Electrical interface between the superconducting link and the current leads

Each of the multiple cables inside the superconducting link is spliced and connected to its corresponding current lead inside the DFH interconnection cryostat. The cryostat must allow easy access for making the electrical connections after the deployment of the superconducting link cable assembly in the semi-flexible DSH cryostat. The primary design focus is the reliable and secure handling of the SC cables via robust tooling and procedures. In addition, the design ensures in-situ completion of low resistance joints between the SC cables in the link and the current leads. Effective cooling of the resistive joints via the helium gas inside the link also requires integrated heat transfer features.

6A.3.2 Cryogenic interface between the superconducting link and the current leads

The interface between the superconducting link and the current leads involves several cryogenic aspects. First of all, the continuation of the helium gas from the superconducting link into the current leads and its mixing with additional cooling gas shall be assured. The present cooling proposal for the systems at P1 and P5 [3] uses the warm exit of the helium gas cooling the SC link thermal shield as the supplementary coolant for the current leads. Since the exit temperature of the shield cooling gas always exceeds the warm boundary condition of 20 K for the SC cable in the link, this option implicitly imposes the hydraulic separation of the helium spaces of the link and the leads. This is likely to be the scenario for P1 and P5, where the superconducting link cold mass requires ~ 1 g/s while the current leads require ~ 10 g/s for a total transfer of about | 150 | kA.

It is envisaged that the superconducting link cryostat (DSH) and current leads share a common vacuum space. A Paschen scenario will be avoided by ensuring that all the high tension side is surrounded by helium cooling gas at about 1 bar.

6A.3.3 Control

The stable operation of the Cold Powering System relies on maintaining two temperature boundary conditions, i.e. 20 K at the splice terminations between the superconducting link and the current leads and about 35 K to 50 K at the cold end of the resistive section of the current leads. The former is controlled by a heater to generate the required helium boil-off from the DF cryostat in the LHC tunnel while the latter is controlled by a valve at the helium warm exit of each current lead. If a single helium flow is adopted, like it was studied for P7, then appropriate override should be devised for the two controllers to work correctly in tandem. Specifically, in case more flow is required by the current leads, the boil-off heater must allow the temperature in the DF to drift below the set value of 20 K. Conversely, in case higher boil-off is necessary for the cooling of the interconnections, a pressure controlled cold bleed will be used to discharge the excess in order to avoid over-cooling of the current leads.

6A.4 Interface to the LHC machine

6A.4.1 General

The DF cryostat interfacing the superconducting link to the magnets cold mass performs the role of electrical, cryogenic and mechanical interface. It includes:

- The required connections to the HL-LHC cryogenic distribution line (QXL);
- A saturated liquid helium bath for the electrical splices between the cables in the link and the Nb-Ti cables;
- A hydraulic separation with respect to the superfluid helium bath cooling the magnets;
- The instrumentation required for cryogenic process control.

Two different variants of DF cryostats (DFX and DFM) are necessary for the Cold Powering Systems under study. The DF cryostats are vacuum insulated and equipped with an actively cooled thermal shield wrapped in multilayer insulation. Vacuum barriers are foreseen to separate the insulation vacuum of the DF cryostat from that of the link, in order to allow interventions on either equipment without the need for vacuum conditioning of the full system.

6A.4.2 Interface cryostat for the HL-LHC Insertions

A continuous cryostat of approximately 60 m in length is foreseen to house the magnets from Q1 to D1 in a common insulation vacuum, with the interface cryostat to the link (DFX) located at its non-IP extremity, after D1. This being the most suitable location from the machine optics point of view, it implies on the other hand that the DFX vacuum vessel and respective supports must be designed to withstand an axial force, of up to 10 tonnes, induced by the unbalanced atmospheric pressure. The DFX will include a jumper to the QXL with helium piping for the supply of both the superconducting link and part of the continuous cryostat.

The DFX may either be designed as an independent cryostat or as service module integrated in the D1 cryostat. The choice between these two configurations will be made not only on the basis of integration and engineering considerations, but most importantly taking into account the need for minimizing the residual radiation doses to personnel during specific interventions such as exchange of a magnet that may occur in the lifetime of the HL-LHC machine.

6A.4.3 Interface cryostat for the Matching Sections

The most compact solution for the Cold powering System of the Matching Sections is to include the connection to the link in the service module of the magnet cryostat (QCS). From there, a first link cooled by supercritical helium is routed up to the DFM cryostat that replaces the present LHC DFL feedbox. All cables are then gathered inside the DFM into a main link, this one connecting the DFM to the DFH in the technical gallery (UR). The supercritical helium arriving from the link in the tunnel is expanded inside the DFM in order to generate liquid for the splices and gas for the cooling of the SC link joining the UR. As such, this concept does not require a connection to the QXL at the level of the DFM.

It should be noticed that in summer 2016 a change to the powering of the MS has been carried, a solution where part of the exiting powering is kept unchanged. However, given the lack of time to present a complete and coherent plan for the new MS powering layout, it has been agreed that we keep in this TDR version the description of the old lay-out. An update description will follow soon.

6A.5 Integration of the Cold Powering Systems at LHC P1 and P5

Point 1 houses high luminosity insertions that have been totally redesigned to meet the HL-LHC performance requirements. The Inner Triplet quadrupoles, the D1-D2 separation dipoles and the Matching Sections will be replaced. Much higher current will be required to power the new magnets. Following the decision taken in 2015 to excavate a new underground gallery for housing the hardware of the high luminosity upgrade (cryo-refrigerators, crab cavities, power converters and distribution feedboxes), the present baseline configuration foresees power converters, current leads, distribution feedboxes and associated equipment to be located in this area. Integration studies, not yet finalized, are being made in the new configuration. The superconducting links will have a total length of up to about 100 m, with a vertical path of about 8 m.

It should be repeated that the new updated integration of the MS powering for P1 will be available soon.

Figure 6-5, Figure 6-6 and Figure 6-7 show the integration of the power converters and the superconducting links in P1.

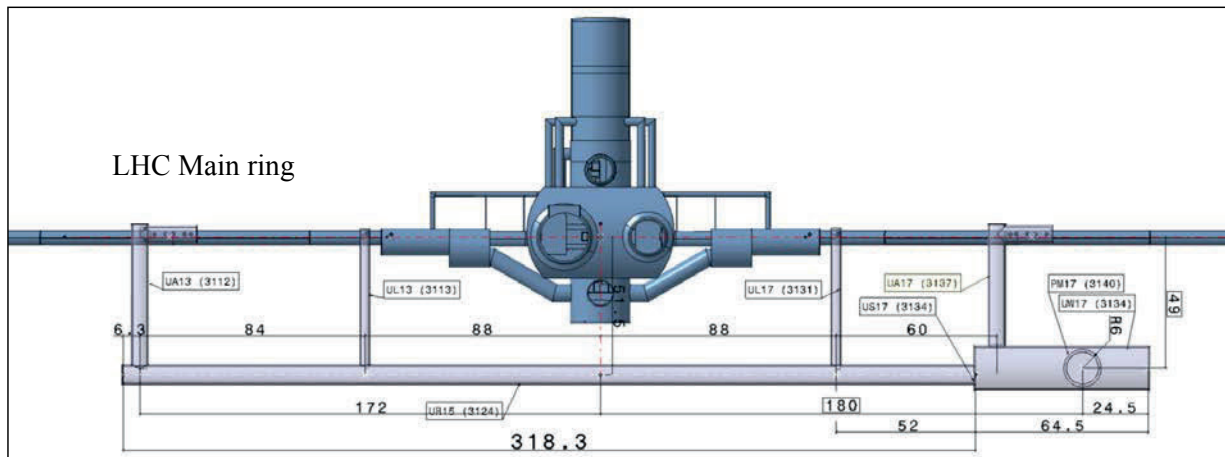


Figure 6-5: View of the LHC underground area at P1: service tunnel, parallel to the LHC main ring, where power converters and current leads will be located (HL-LHC baseline).

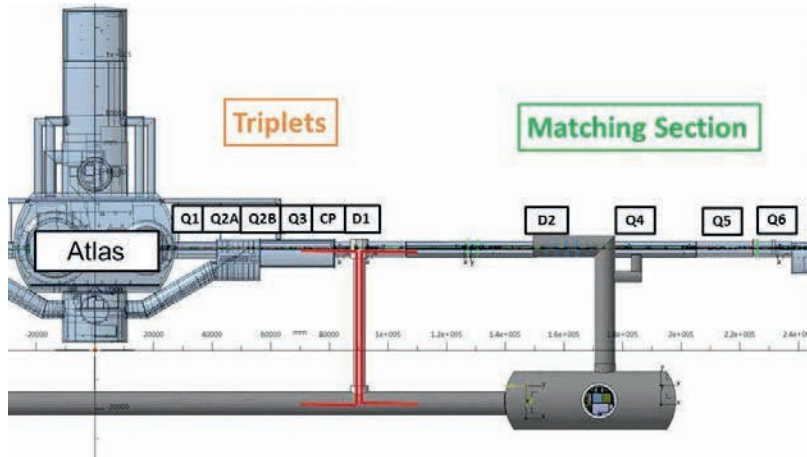


Figure 6-6: Schematic view of the LHC underground at P1 with the two superconducting links (red lines) routed from to the LHC main tunnel to new LHC service tunnel (HL-LHC baseline), where the power converters and the current leads will be located.

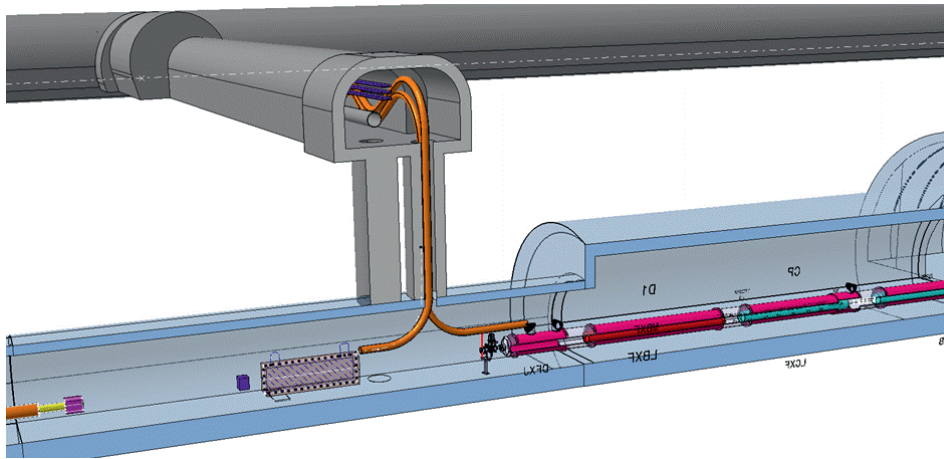


Figure 6-7: Schematic view of the LHC underground with the two superconducting links routed from to the LHC main tunnel to new LHC service tunnel (HL-LHC baseline). The vertical path of the links covers a difference in height of about 8 m.

6A.6 Reference

- [1] A. Ballarino, Development of Superconducting Links for the LHC Machine, Superconductor Science and Technology, vol. 27, 044024 (2014). DOI: [10.1088/0953-2048/27/4/044024](https://doi.org/10.1088/0953-2048/27/4/044024)
- [2] I. Bejar Alonso, HL-LHC: Decision Management - CE works P1 and P5 underground EDMS [1515107](#)
- [3] U. Wagner, A. Ballarino, Y. Yang, Cryogenic Scenarios for the Cold Powering System, HiLumi LHC Milestone Report MS57, FP7 High Luminosity Large Hadron Collider Design Study, [CERN-ACC-2014-0065](#) (2014)
- [4] A. Ballarino, Alternative Design Concepts for Multi-Circuit HTS Link Systems, Applied Superconductivity Conference 2010, Washington, DC, USA, 1 - 6 Aug 2010, pp.980-983 (2011). DOI: [10.1109/TASC.2010.2096378](https://doi.org/10.1109/TASC.2010.2096378)
- [5] A. Ballarino, J. Fleiter, J. Hurte, M. Sitko, G. Willering, First tests of twisted-pair HTS 1 kA range cables for use in superconducting links, Physics Procedia, vol. 36 (2012) [EuCARD-CON-2011-062](#).
- [6] A. Ballarino, M7.5.1: Final design report HTS link, [EuCARD-REP-2012-017](#) (2012)

- [7] Y. Yang, E. A. Young, W. O. S. Bailey, C. Beduz, A. Ballarino, Development of superconducting links for the Large Hadron Collider machine, Supercond. Sci. Technol. 27 (2014) 044024. DOI: [10.1088/0953-2048/27/4/044024](https://doi.org/10.1088/0953-2048/27/4/044024)
- [8] J. P. Corso, HL-LHC Integration SC links Point 7, CERN Engineering and Equipment Data Management Service, EDMS N. [1419773](#) (2014)
- [9] <http://phys.org/news/2014-04-cern-world-record-current-superconductor.html>
- [10] I. Bejar Alonso (ed), et al. High-Luminosity Large Hadron Collider (HL-LHC) : Preliminary Design Report HL-LHC Preliminary Design Report [CERN-2015-005](#). DOI: [10.5170/CERN-2015-005](https://doi.org/10.5170/CERN-2015-005)
- [11] A. Ballarino, Large capacity current leads, Physica C 468 , 15-20 (2008) 2143-2148. [CERN-AT-2008-001](#)

Chapter 6B

Power converters for superconducting magnets

6B Power converters for the new superconducting magnets

6B.1 Overview

The HL-LHC project has for main objective to increase the luminosity of experiments in Point 1 and Point 5. This requires new superconducting magnets in the insertion region with stronger magnetic field and larger aperture to reduce the β^* at the colliding point. These new magnets require higher currents to reach 11-12 T and a series of power converters needs to be replaced to deliver more current. A new underground infrastructure will be built to host various service as the cryogenic distribution. This new underground galleries UR (see Figure 6B-1 and chapter 15) has also been designed to install all the new power converters inside. In an early stage of the project, all the magnets from the Q1 to Q6 were replaced by new magnets which required 43 new power converters per interaction point (IP) side. In the last layout, this upgrade was reduced up to D2, leading to only 25 new power converters per IP side. The individual quadrupoles Q4, Q5, Q6 will re-use existing magnets and in the frame of the new project strategy they will be powered by the present hardware located in RR galleries.

6B.2 Superconducting magnets

6B.2.1 Insertion region layout

The new layout of the interaction region comprises the new Inner Triplet magnets (Q1-Q2a-Q2b-Q3) and associated correctors, the new separation/recombination dipole magnets (D1, D2) and associated correctors. The matching section (from Q4 to Q6) previously featured the use of new magnets for the Q4 plus the redeployment of LHC cold masses for Q5 and Q6. The latest layout version make use of LHC superconducting magnets for all these units. This leads to important saving by removing cost of new magnets, power converters and reducing the size of the UR galleries by keeping the powering of these magnets from the present RR galleries. The list of re-used superconducting magnets to be powered from the actual RR galleries is presented in Table 6B-1.

The list of new superconducting magnets to be powered from the new UR galleries is presented in Table 6B-2.

Table 6B-1: Superconducting magnets powered from the RR galleries.

Optic	DFH	Circuit	Magnet	Number of circuits/ IP side	Operating current 7 TeV [kA]
Q4	DFBL	Large aperture 2-in1 Quadrupole Q4	MQY	2	4.50
Q4	DFBL	Orbit correctors Q4	MCBY	8	0.072
Q5	DFBL	Present LHC Q4 magnet	MQY	2	4.51
Q5	DFBL	Orbit correctors present Q4	MCBY	6	0.072
Q6	DFBL	Insertion Quadrupole, 2-in1 aperture; Q6	MQML	2	4.31
Q6	DFBL	Orbit correctors Q6	MCBC	2	0.08

Table 6B-2: Superconducting magnets powered from the UR galleries.

Optic	DFHX	Circuit	Magnet	N.of circuits/ IP side	Operating current 7 TeV [kA]
IT	DFHX	Triplet Q1, Q2a, Q2b, Q3	MQXFA / B	1	16.5
IT	DFHX	Trim Q1			±2
IT	DFHX	Trim Q3			±2
IT	DFHX	Trim Q2a			±0.12
IT	DFHX	Orbit correctors Q2a/b - vertical	MCBXFVB	2	1.6
IT	DFHX	Orbit correctors Q2a/b - horizontal	MCBXFVBH	2	1.47
IT	DFHX	Orbit correctors CP - vertical	MCBXFVA	1	1.6
IT	DFHX	Orbit correctors CP - horizontal	MCBXFVAH	1	1.47
IT	DFHX	Superferric, order 2	MQSXF	1	0.182
IT	DFHX	Superferric, order 3, normal and skew	MCSXF / MCSSXF	2	0.105
IT	DFHX	Superferric, order 4, normal and skew	MCOXF / MCOSXF	2	0.105
IT	DFHX	Superferric, order 5, normal and skew	MCDXF / MCDSXF	2	0.105
IT	DFHX	Superferric, order 6	MCTXF	1	0.105
IT	DFHX	Superferric, order 6, skew	MCTSXF	1	0.105
D1	DFHX	Separation dipole D1	MBXF	1	12
D2	DFHM	Separation dipole D2	MBRD	1	12
D2	DFHM	Orbit correctors D2	MCBRD	4	0.5

6B.2.2 Integration and new civil engineering infrastructure

A new underground infrastructure is needed to distribute the cryogenic at both side of the interaction point for the superconducting magnets and crab cavities (CC) and to host the RF powering and controls of the latest. A long gallery called UR will be built in parallel of the LHC machine from the left-side CC to the right-side CC of the experiment (See Chapter 15). The UR gallery has been designed large enough to allow the installation of all equipment needed for this upgrade and especially all the new power converters as seen in Figure 6B-1. The layout of the underground galleries is identical for Point 1 and Point 5.

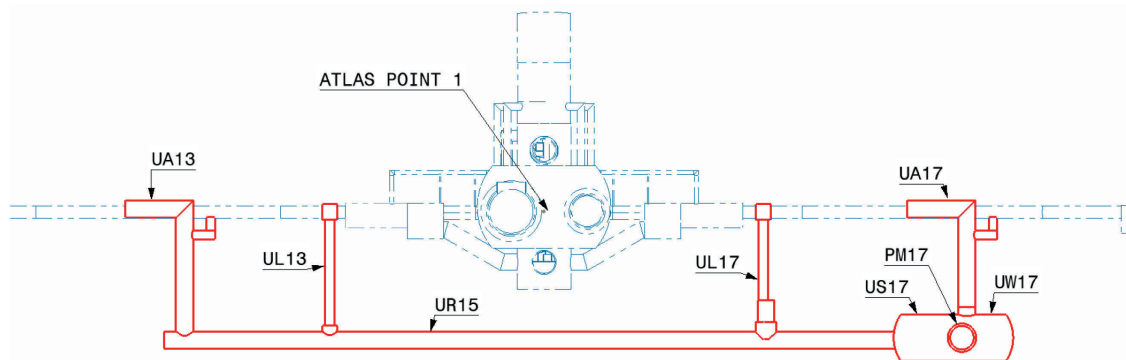


Figure 6B-1: New HL-LHC underground infrastructure at Point 1, top view.

The power converters and the DFHX and DFHM (electrical feed-boxes) will be placed in the UR gallery to reduce the length of water-cooled DC cables, see Figure 6B-2. The superconducting (SC) link will bring the DC current from the UR, through the UL, to the superconducting magnets in the LHC machine. The power converters will be water-cooled to ease the heat extraction and reduce the air-conditioning requirements. Two 18 kV line will bring electricity in the UR. Two dedicated 18 kV/400 V transformers will supply all the new power converters separating the feeding of the left and right part of the IP.

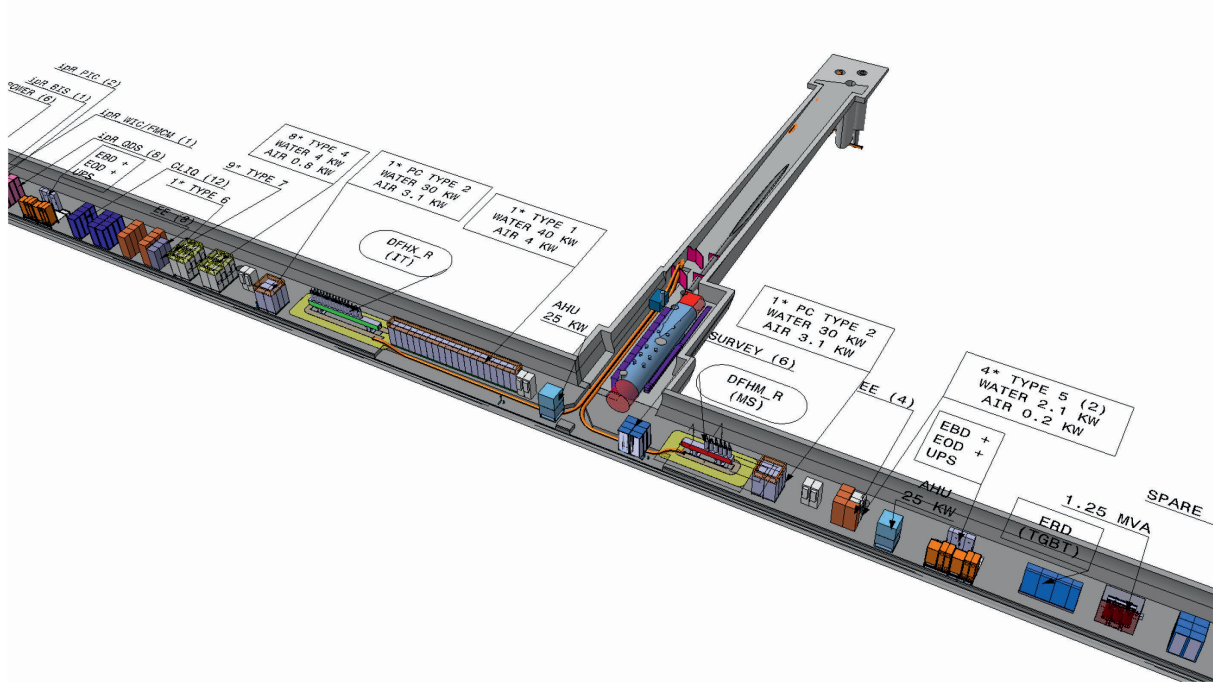


Figure 6B-2: Power converters installed in UR gallery.

6B.3 Circuit layout

The interaction region at Points 1 and 5 will be upgraded with new superconducting magnets. Figure 6B-3 and Figure 6B-4 show the present right-side magnet layout of the experiment and the new one with HL-LHC. The main parameters of the new circuits are shown in Table 6B-1. The next paragraphs will detail each circuit.

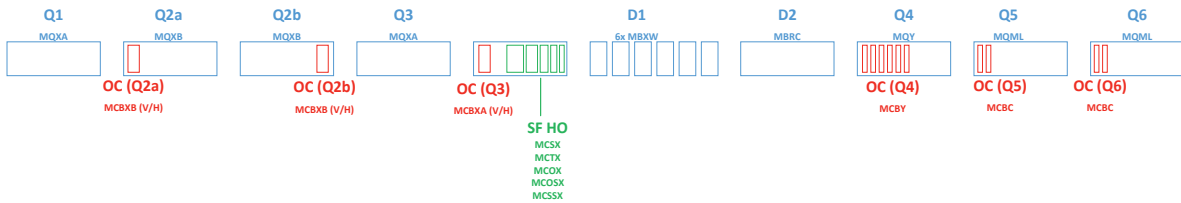


Figure 6B-3: Present LHC magnet layout

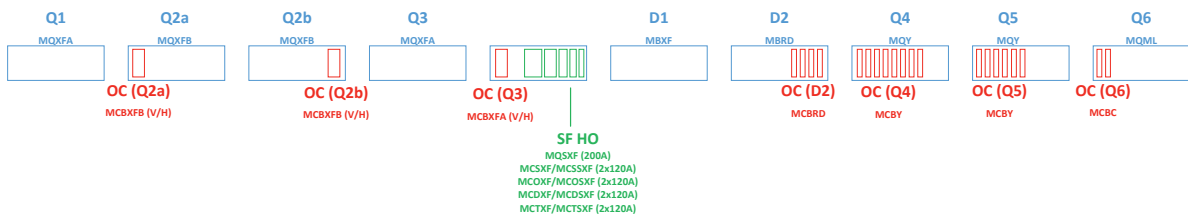


Figure 6B-4: New HL-LHC magnet layout (crab cavities not shown).

6B.3.1 Inner Triplet circuit

6B.3.1.1 Present Inner Triplet circuit layout

The baseline powering layout of the LHC Inner Triplets is shown in Figure 6B-5. This powering scheme consists of a nested circuit with three power converters and free-wheeling protection circuits. At the beginning of the LHC operation, this specificity generated somewhat longer down-times with respect to the other

electrical circuits. Thanks to the experience gained and to the development of diagnostic tools, the system has currently reached a good level of reliability. It should be noted that the ramp-down time of these circuits, which defines the minimum time before a beam injection, had to be slowed down with respect to that obtained with the free-wheeling process. This was done in order to avoid trips of the power converters generated by the nested configuration.

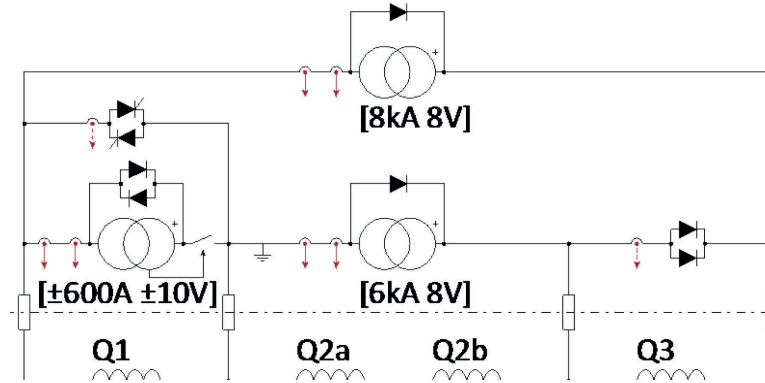


Figure 6B-5: Powering layout of the present LHC Inner Triplets.

6B.3.1.2 New Inner Triplet circuit layout

The new Inner Triplet circuit layout included the four cryo-magnet assemblies Q1-Q2a-Q2b-Q3. All these magnets will be powered in series to reduce the hardware cost, to ease the superconducting bus-bar layout inside the cryostat and to reduce the tune-shift due to current ripple discrepancy between magnets. The magnetic field needs to be adjusted in each magnet to play different beam optics. Q1, Q2a and Q3 magnets will have a dedicated trim power converter to adjust independently their current. The circuit layout is presented in Figure 6B-6.

- **Power converters:** The main power converter of the Inner Triplet circuit will have a rating of 18 kA. R&D work is being done to develop a new type of 2-quadrant power converter in order to apply positive and negative voltage to the magnets which is mandatory to ramp-down the current in the shadow of the main LHC dipole magnets. Two trim power converters will have a rating of ± 2 kA and the third one will be rated ± 120 A.
- **DC cabling:** Water-cooled cables will be placed between the power converters and the current leads of the DFHX, all placed inside the UR galleries, see Figure 6B-7. The SC Link dedicated for the Inner Triplet will bring the current to the superconducting magnets through the UL galleries.

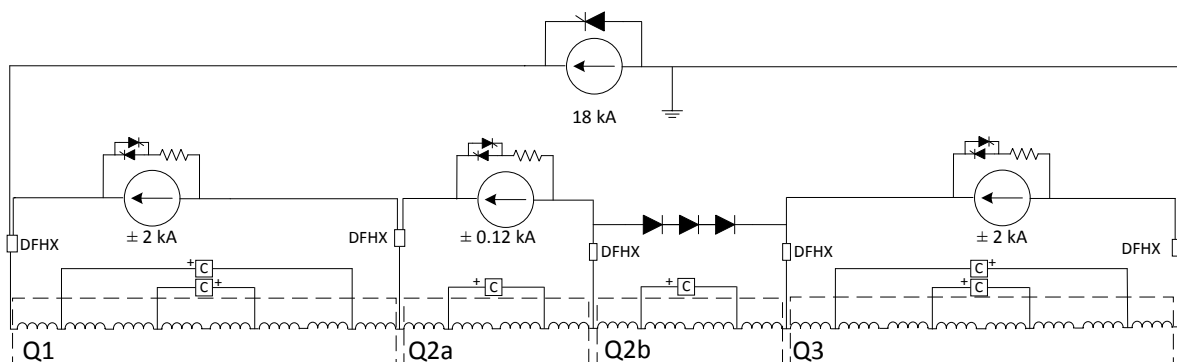


Figure 6B-6: Circuit layout of the HL-LHC Inner Triplet (MQXFA, MQXFB).

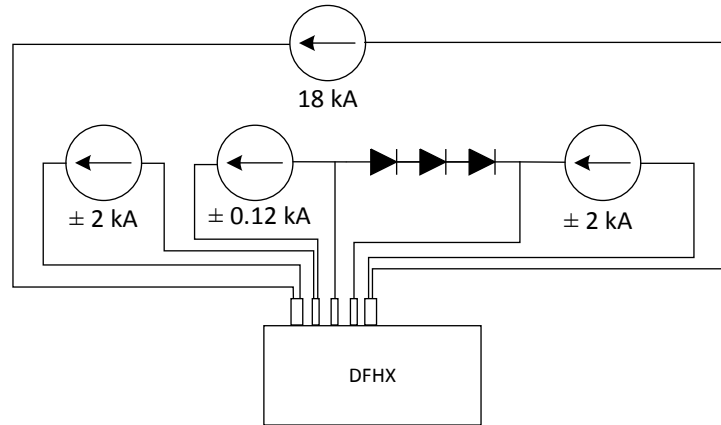


Figure 6B-7: Connections between the Inner Triplet power converters and the electrical feed-boxes.

6B.3.2 Inner Triplet orbit correctors

Six orbit correctors are needed (three nested magnet assemblies) for the Inner Triplet magnets (one vertical and one horizontal for Q2a, Q2b and CP). These corrector magnets will have a rating of ± 1.6 kA. The circuit layout is shown in Figure 6B-8.

- **Power converters:** One 4-quadrant power converter per circuit rated at ± 2 kA.
- **DC cabling:** Water-cooled cables will be placed between the power converters and the current leads of the DFHX, all placed inside the UR galleries. The Inner Triplet orbit corrector cables will be placed inside the same SC link feeding the main Inner Triplet circuit.

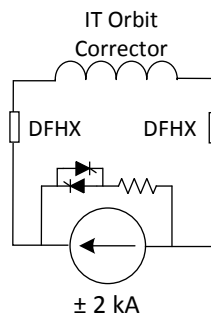


Figure 6B-8: Circuit layout of each Inner Triplet corrector circuit (MCBXF).

6B.3.3 Inner Triplet high order correctors

Nine high-order correctors (skew quadrupole, normal and skew sextupole, octupole, decapole and dodecapole) are needed for the Inner Triplet magnets. The second order corrector has a rating of ± 200 A whereas all the eight others correctors have a rating of ± 120 A. The circuit layout of these correctors is shown in Figure 6B-9.

- **Power converters:** One power converter per circuit rated ± 200 A or ± 120 A.
- **DC cabling:** Copper cables will be placed between the power converters and the current leads of the DFHX, all placed inside the UR galleries. The Triplet high-order corrector conductors will be placed inside the same SC link housing the main Inner Triplet circuit.

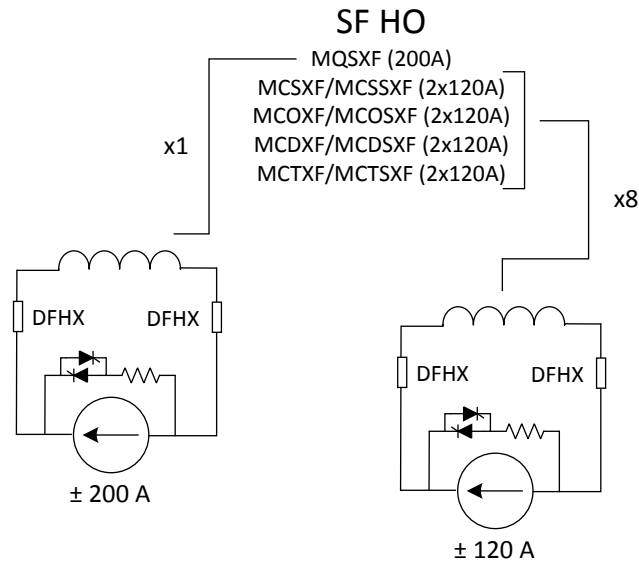


Figure 6B-9: High order correctors circuit layout (MCS, MCO, MCD, MCT, and MQSXF).

6B.3.4 Separation dipole D1

The new separation dipole D1 will be a superconducting cryo-magnet assembly substituting the present LHC six warm magnets. It has a single aperture and each magnet is independently powered. The circuit layout of these correctors is shown in Figure 6B-10.

- **Power converter:** One power converter per circuit rated at 13kA. This converter will be 1-quadrant type since no ramp-down issues are foreseen for this circuit. The time constant of the circuit is relatively low, estimated at 93 s.
- **DC cabling:** Water-cooled cables will be placed between the power converters and the current leads of the DFHX, all placed inside the UR galleries. The D1 circuit cables will be placed inside the same SC link housing Inner Triplet circuit.

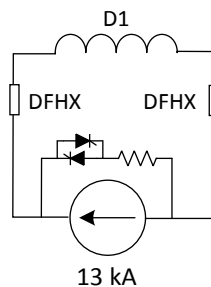


Figure 6B-10: D1 magnet circuit layout (MBXF).

6B.3.5 Recombination dipole D2

The new recombination dipole D2 will be a superconducting cryo-magnet assembly with two beam apertures. Each magnet is independently powered, and the two apertures are in series. The circuit layout is shown in Figure 6B-11.

- **Power converter:** One power converter per circuit rated at 13 kA. This converter will be 1-quadrant type since no ramp-down issues are foreseen for this circuit. The time constant of the circuit is relatively low, estimated at 100 s.

- **DC cabling:** Water-cooled cables will be placed between the power converters and the current leads of the DFHM (second electrical feed-box), all placed inside the UR galleries. The D2 circuit will have a dedicated SC Link.

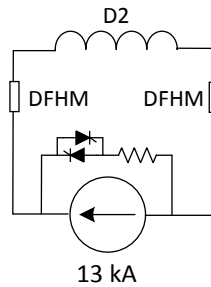


Figure 6B-11: D2 magnet circuit layout (MBRD).

6B.3.6 D2 orbit correctors

Four orbit correctors are needed for the D2 recombination cryo-magnet assembly (one vertical and one horizontal for each aperture). These corrector magnets will have a rating of ± 600 A. The circuit layout of these correctors is shown in Figure 6B-12.

- **Power converter:** One power converter per circuit rated ± 600 A.
- **DC cabling:** Copper cables will be placed between the power converters and the current leads of the DFHM, all placed inside the UR galleries. The D2 orbit corrector circuits will be included in the D2 dedicated SC Link.

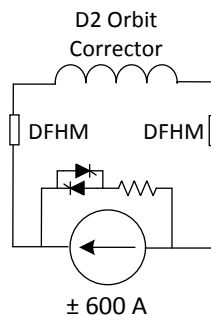


Figure 6B-12: D2 orbit correctors circuit layout (MCBRD).

6B.3.7 Individual powered quadrupole Q4, Q5 and Q6

The rearrangement of the layout of Q4, Q5 and Q6 is part of the latest HL-LHC re-baseline. The scope was reviewed and for LS3 installation no new superconducting magnets will be developed and the required cold mass will make use of existing LHC magnets (or LHC magnet design requiring the procurement of few new units). The powering scheme will remain the existing one through the DFBL and the power converters placed inside the RR galleries.

- **Power converter:** One power converter per beam aperture with a common return cable, see Figure 6B-13. The rating of the converters is 6 kA, 1-quadrant operation. For Q4, four warm cables are used instead of three to increase the operation margin [1].
- **DC cabling:** Water-cooled cables are placed between the power converters and the current leads of the DFBL (electrical feed-box inside RR galleries).

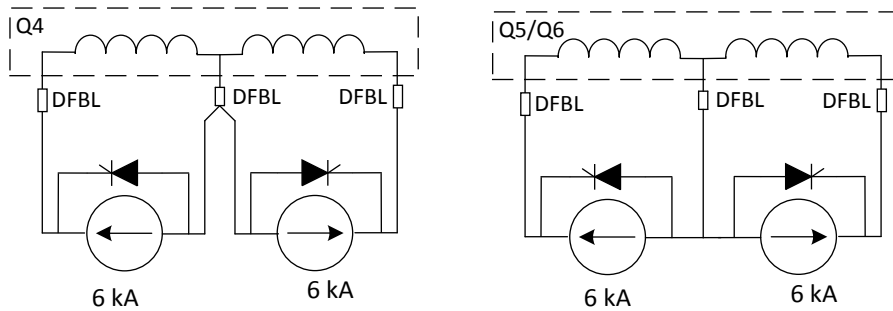


Figure 6B-13: Q4, Q5 and Q6 circuit layout (no change with respect to the present LHC layout).

6B.3.8 Q4, Q5 and Q6 orbit correctors

Sixteen orbit correctors are needed for Q4, Q5 and Q6 magnets (six more than the present scheme). Q4 will have eight corrector circuits, Q5 will have six corrector circuits and Q6 will have two corrector circuits.

- **Power converters:** One power converter per circuit rated at ± 120 A, see Figure 6B-14.
- **DC cabling and cold powering:** Several solutions are being studied in order to provide cold powering connections for the increased number of correctors. The solutions proposed are either to modify the DFBL and the DSL, or to provide local powering to the correctors magnets.

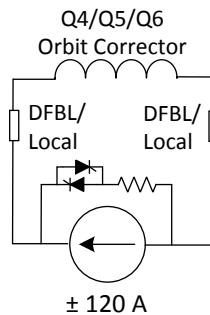


Figure 6B-14: Q4, Q5 and Q6 orbit corrector circuit layout.

6B.4 Power converters

The LHC was built with modular power converters to facilitate maintenance and integrate the redundancy principle [2][3]. Redundancy was included in power converters rated above 600 A. This has proven to be a real asset during operation. The $n+1$ redundancy allows the converter to be operated even with one module in fault. The advantages are the following:

- in case of fault, only one sub-converter is not operational and usually the fault does not generate a beam dump;
- the LHC can run with some faulty sub-converters and all interventions for repairing can be performed during a technical stop of the machine.

With the exception of dipoles, switch-mode technology was chosen for the LHC power converters in order to minimize their size and assure low output voltage ripple. All LHC power converters rated at currents above 120 A are water-cooled, inducing a size reduction of the hardware. All these design principles will be maintained for the new HL-LHC power converters.

6B.4.1 Power converter lists

The list of magnets and corresponding power converters needed for HL-LHC is reported in Table 6B-3. The list of new power converters to be built for HL-LHC is reported in Table 6B-4.

Table 6B-3: Magnets at each side of LHC P1 and P5.

Optic	Circuit	Magnet	L circuit [mH]	R circuit [mΩ]	Operating current 7 TeV [kA]	Converted rated current [kA]	Converted rated Voltage [V]
IT	Triplet Q1, Q2a, Q2b, Q3	MQXFA / MQFXB	255.0	0.21	16.5	18.00	±8
IT	Trim Q1		69.0	1.76	±2	2.00	±10
IT	Trim Q3		69.0	1.76	±2	2.00	±10
IT	Trim Q2a		69.0	7.97	±0.12	0.12	±10
IT	Orbit correctors Q2a/b - vertical	MCBXFBV	59.2	2.16	1.6	2.00	±10
IT	Orbit correctors Q2a/b - horizontal	MCBXFBH	134.8	2.16	1.47	2.00	±10
IT	Orbit correctors CP - vertical	MCBXFAV	108.5	1.91	1.6	1.60	±10
IT	Orbit correctors CP - horizontal	MCBXFAH	247.0	1.91	1.47	2.00	±10
IT	Superferric, order 2	MQSXF	1247.0	8.53	0.182	0.20	±10
IT	Superferric, order 3, normal and skew	MCSXF / MCSSXF	185.0	8.53	0.105	0.12	±10
IT	Superferric, order 4, normal and skew	MCOXF / MCOSXF	200.0	5.87	0.105	0.12	±10
IT	Superferric, order 5, normal and skew	MCDXF / MCDSXF	187.0	8.53	0.105	0.12	±10
IT	Superferric, order 6	MCTXF	576.0	8.53	0.105	0.12	±10
IT	Superferric, order 6, skew	MCTSXF	126.0	8.53	0.105	0.12	±10
D1	Separation dipole D1; MBXF	MBXF	25.0	0.27	12	13.00	8
D2	Separation dipole D2; MBRD	MBRD	27.0	0.27	12	13.00	8
D2	Orbit correctors D2	MCBRD	600	2.03	0.5	0.6	±10

Table 6B-4: List of new power converters for Inner Triplet and matching section magnets.

Equipment code	Power converter	Current	Voltage	Quantity per IP side	Quantity per UR
HCRPAFE	Type 1	18k A	±8 V	1	2
HCRPAFF	Type 2	13k A	8 V	2	4
HCRPBAA	Type 4	±2k A	±10 V	8	16
HCRPMBA	Type 5	±600 A	±10 V	5	10
HCRPLB	Type 6	±120 A	±10 V	9	18
Total				25	50

6B.4.2 Present LHC power converters

In the present LHC machine, 13 kA, 8 kA, 6 kA, 4 kA, ±600 A, ±120 A and ±60 A power converter types are already in operation [4].

The HL-LHC project will require the development of two new types of power converters:

- The 2-quadrant converter 18 kA/±8 V, which requires research of new power converter topologies. This development is mandatory for a ramp-down of the Inner Triplet magnets in less than 30 minutes.
- The 4-quadrant converter ±2 kA/±10 V, which will be based on a new topology developed for R2E 600 A power converters.

6B.4.3 R&D program

Based on the new integration layout, the length of the warm DC cables, between the power converters and the electrical feed-boxes is drastically reduced. Present DF BX are placed in the LHC machine close to the superconducting magnets while the new DFHX will be placed in the UR galleries very close to the power converters.

As the resistance of the DC cables becomes very low (less than 1 mΩ), the time constant of the circuit τ becomes very high (up to thousands of seconds). With classical 1-quadrant converter, the current ramp-down is done in free-wheeling process and the magnet energy is dissipated in the resistive part of the circuit: the cables. It takes around 5τ for the free-wheeling process to return to the injection current. In order to improve the ramp-down time, the power converter needs to be able to recover the magnet energy. A way to do so is by applying negative DC voltage on the magnets. The main power converter of the Inner Triplet circuit should then be 2-quadrant, the output current is always positive, the output voltage can be either positive or negative. The different modes of operation for power converters is depicted in Figure 6B-15.

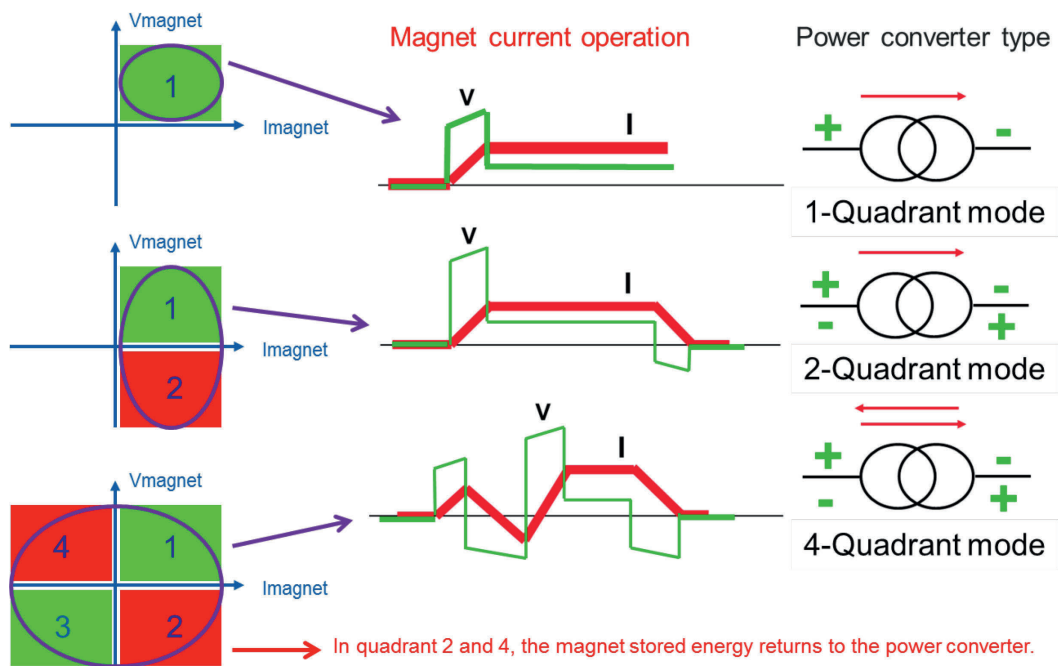


Figure 6B-15: The power converter type depends upon the operating cycle.

Today at CERN, only thyristor rectifiers can operate in 2-quadrant mode but with the drawback of low-order harmonics present in the spectrum of the DC voltage. These harmonics generate blow-up of the beam and shall be avoided to reach the high luminosity performance of HL-LHC.

The 2-quadrant R&D program is targeting power converter topologies able to operate in 2-quadrant which includes the management of the energy given back from the superconducting magnets to the converter during the ramp-down.

6B.4.3.1 High current 2-quadrant power converters

A new family 2-quadrant power converters should be developed using switch-mode technology in order to keep the same good principles of the present LHC power converters. Energy management will be studied to find the best way to control the recovered magnet energy. The most classical solution is to dissipate in the resistive part of the circuit but thanks to improvements of electrical storage like the last generation of batteries (driven by the development of electric vehicles), this energy could be stored and re-used during the next cycle. The proposed topology is shown in Figure 6B-16.

The introduction of energy storage brings another advantage by reducing the power taken from the grid. The sizing could be done as follow: only the losses of the transmission chain (losses in the converter, heat in the warm DC cables) will be taken from the grid while the magnet energy is provided and recovered by the electrical storage element. The energy flow between grid, storage and magnet should be optimized in order to maximize efficiency and lifetime of the storage element.

Researches will be focused on power converter topologies, energy management and energy storage system. The goal will be to keep reliability as high as possible, while improving size, power quality (harmonics on the grid as well as current ripple on the magnet) and efficiency. A first demonstration with prototypes is expected to be built by 2019.

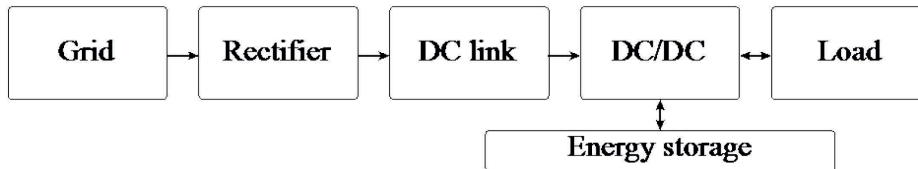


Figure 6B-16: Proposed layout of the new power converter topology.

6B.4.3.2 2kA 4-quadrant power converters

The powering of the corrector magnets usually requires operation in positive and negative current. Three families of 4-quadrant power converters were developed for the LHC machine to cover all corrector magnet families, ranked 60 A, 120 A and 600 A. With HL-LHC project, a new family of 4-quadrant power converter is required as the correction magnets are rated up to 1.6 kA. The present families are made with a unique power module rated at the maximum current, meaning without modularity nor redundancy. In the high current family, the redundancy principle has demonstrated all its interest for the maintenance and for the availability of the machine. In the framework of R2E, the 600 A converter was redesigned with introduction of redundancy. The power module is rated 300 A and two modules are placed in parallel to reach 600 A, see Figure 6B-17. In case of fault, and with a magnet current below 300 A, a power module failure will not stop the operation of the machine, as the second one will keep the magnet current constant. The redundancy is limited to 50% of the maximum current but most of the correctors operate far below their maximum current. This improvement shall reduce by 80% the beam dump due to 600 A failure.

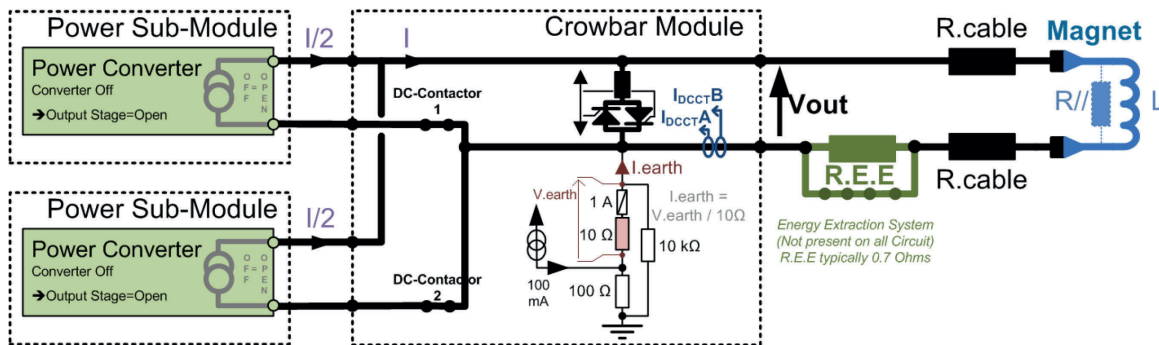


Figure 6B-17: Topology of new 600 A R2E power converter.

For the new 2 kA family, the same redundancy principle will be used. The power converter will be done with five power modules rated 400 A in parallel. They shall be identical or based on the recently developed 600 A power module.

6B.5 Power converter control and performances

Two main sets of terms and definitions will be introduced here to help readability and common understanding of fundamental parameters for the specification of power converter performances. The first set refers to metrology theory and the second to control theory.

Some useful metrology terms and definition taken from [5]:

- **Accuracy:** Closeness of agreement between a measurement and:
 - i) the true value of the measurand (absolute accuracy);
 - ii) an accepted reference value (relative accuracy).

Accuracy is a qualitative concept; it cannot be quantified.

- **Uncertainty:** Non-negative parameter characterizing the quantity values attributed to a measurand. This parameter can be a standard deviation (or a multiple of it).
- **Error of measurement:** Result of a measurement minus the true value of the measurand.
- **Precision:** Closeness of agreement between measured quantity values obtained by replicate measurements under specified conditions.
- **Repeatability and Reproducibility** are associated to the concept of precision and can be defined as the closeness of agreement between the results of successive measurements of the same measure and carried out under the same conditions (Repeatability) or carried out under changed conditions (Reproducibility).

In addition to the above stated terms, the following is also often used:

- **Stability:** It can be defined as an expression of the change in the measurement errors with time. One can more specifically refer to **Gain Stability** and **Offset Stability**. As stability depends on time, when expressing it, is necessary to state the time span/range of frequencies for which the parameter refers to.

In this chapter relative figures are always expressed in ppm (parts-per-million) of a given reference value; for circuits currents the reference value is the nominal value of the power converter current (which usually coincides with the maximum value of current that can be generated by the power converter and, at the same time, the nominal value of the current that can be measured by the DCCT). As an example the main power converter of the Triplet Q1-Q2a-Q2b-Q3, the HCRPAFE, is rated 18 kA whereas the operating current at 7 TeV is 16.5 kA; according to this convention one ppm amounts to 18 mA.

The term **Control** is hereby used to include two fundamental required functions (referred to a generic output quantity) [6]:

- **Regulation:** Ensuring that the effect of (non-decreasing) disturbances on the (plant) output are, in some sense minimized or eliminated.
- **Tracking:** Ensuring that the (plant) output tracks a (non-diminishing) reference signal with minimal or, ideally, zero steady-state error.

The term control therefore is not hereby used as synonym for monitoring or (online) diagnostics.

6B.5.1 Impact on the beam quality – Requirements from beam physics

Current understanding of requirements from beam physics is still not complete. A thorough review of the precision and accuracy requirements for all circuit types will be carried out in the coming months. The review process will aim at fully defining power converter performance requirements in terms of both regulation, or DC performance, and tracking.

6B.5.1.1 DC performance

Requirements dictated by beam quality performance are currently based on a rather simplified model of the full transfer function from power converter output (current or voltage delivered to the load) to the magnetic field experienced by the beam. The full transfer function is modelled as in the following equation:

$$B(f) = \begin{cases} T_{vacuum}(f) \times T_{ItoB}(f) \times I(f) & f < f_0 \\ T_{vacuum}(f) \times T_{ItoB}(f) \times T_{VtoI,load}(f) \times V(f) & f > f_0 \end{cases} \quad (6-1)$$

where f_0 is a parameter set by the (digital) current regulation of the power converter; for frequencies below f_0 the current regulation is fully active and the power converter is operating in “current control” mode, whereas for frequency above f_0 the electrical characteristics of the circuit dominate over the current regulation loop and the converter is considered to be operating in “voltage control” mode.

$T_{vacuum}(f)$ represents the transfer function between the B-field experienced by the beam and B-field produced by the magnet; this transfer function is associated with cold bores, absorbers, beam screens etc.

$T_{ItoB}(f)$ represents the transfer function between the B-field produced by the magnet and the current generated by the power converter and it depends on the magnet characteristics.

Both $T_{vacuum}(f)$ and $T_{ItoB}(f)$ are currently modelled as constant (as for LHC design). This approximation is rather accurate in the range of frequency where the power converter operates in “current control” and f_0 is in the range of few tenths of Hz to few Hz as for LHC and HL-LHC. However this approximation might be overly pessimistic for higher frequencies where both $T_{vacuum}(f)$ and $T_{ItoB}(f)$ can indeed introduce important attenuations due to different loss phenomena.

From the point of view of the magnetic flux Φ linked to the circuit the following equation is deemed more pertinent:

$$\frac{\Delta\Phi}{\Phi} = \frac{\Delta\Phi}{\Phi_{nom}} \approx \begin{cases} \frac{I(f)}{I_{nom}} & f < f_0 \\ \frac{V(f)}{2\pi f L_{dc} I_{nom}} & f > f_0 \end{cases} \quad (6-2)$$

Where $L_{dc} = \Phi_{nom}/I_{nom}$ is the constant “design” inductance of the magnet. This inductance is usually larger than the “apparent” or “differential” inductance which sets the time constant of the circuit together with the circuit resistance.

Requirements from beam physics however are usually formulated in terms of $\frac{\Delta B}{B}$ which could then be translated into:

$$\frac{\Delta B}{B} = \frac{\Delta B}{B_{nom}} \approx \begin{cases} \frac{I(f)}{I_{nom}} & f < f_0 \\ T_{vacuum}(f) \times T_{VtoB}(f) \times \frac{V(f)}{2\pi f L_{dc} I_{nom}} & f > f_0 \end{cases} \quad (6-3)$$

A dedicated task will be devoted to the modelling and experimental characterization of the currently neglected contributions of $T_{vacuum}(f)$ and either $T_{ItoB}(f)$ or $T_{VtoB}(f)$ in collaboration with the relevant other WPs. The main goal of the task will be avoiding over-specification of power converters ripple which can turn out in, probably large, over cost for the project.

Precision requirements are summarized in Table 6B-5; latest updates are derived from [7].

Table 6B-5: Summary of precision requirements per magnet.

Optics	Magnet	24h Uncertainty	½ hour Uncertainty
MQXF ¹ Q1-Q2-Q3	MQXFA	±1ppm	(noise better than) ±1ppm
CP	MCBXFA	±10ppm	±5ppm
	MCBXFB	±10ppm	±5ppm
	MCQSX	±100ppm	±10ppm
	MCTX	±100ppm	±10ppm
	MCTSX	±100ppm	±10ppm
	MCDX	±100ppm	±10ppm
	MCDSX	±100ppm	±10ppm
	MCSX	±100ppm	±10ppm
	MCSSX	±100ppm	±10ppm
	MCOX	±100ppm	±10ppm
	MCOSX	±100ppm	±10ppm
D1 (*)	MBXF	±1ppm	(noise better than) ±1ppm
D2 (*)	MBRD	±1ppm	(noise better than) ±1ppm
	MCBRD	±10ppm	±5ppm
Q4 (*)	MQYY	±1ppm	(noise better than) ±1ppm
	MCBYY	±10ppm	±5ppm
Q5	MQY	±10ppm	±5ppm
	MCBY	±100ppm	±10ppm
Q6	MQML	±10ppm	±5ppm
	MCBC	±100ppm	±10ppm

6B.5.1.2 Tracking

Requirements for maximum allowable error between reference current and actual circuit current during ramp-up and ramp-down phases will need to be specified in more details in the coming months based on the outcomes of WP2 optics studies. These requirements will impact mostly on power converter control technology for which EPC however has already a solution perfectly capable of handling this kind of performance. This system is based on a 2-degree-of-freedom RST digital control algorithm that has been successfully validated in LHC [3] and many other accelerators at CERN.

6B.5.2 Control electronics: FGC4

6B.5.2.1 Principles and current status

LHC power converter control is based on an “all-digital approach” [8][9][10]. The hardware that implements this “all-digital” control is called FGC (Function Generator/Controller); in particular, for LHC more than 1700 FGC2 (see Figure 6B-18 left) units are deployed with two main tasks:

- management of the voltage source state;
- regulation of the circuit current (by means of RST control algorithm).

The network interface of FGC2 is based on WordFIP 2.5 MHz fieldbus (see Figure 6B-19 left). Major effort was also devoted to make the controller radiation tolerant and capable of guaranteeing very high reliability.

¹[7] most recent figures - uniform distribution is assumed for noise

More recently it has been developed a new version of FGC [11]: FGC3 (see Figure 6B-18 right) which works with the same principles but is produced with up-to-date analogue and digital components. Its network interface is based on a dedicated implementation of 100 Mbps Ethernet (see Figure 6B-19 right) called FGC-Ether which is also used for very low jitter synchronization [12]. In addition to the FGC3 control unit itself a broad set of dedicated mixed analogue and digital boards have been developed by EPC under the name of RegFGC3; with this additional dedicated electronics the “all-digital” approach has been extended to the full control of the power converter (not limited anymore simply to current control).

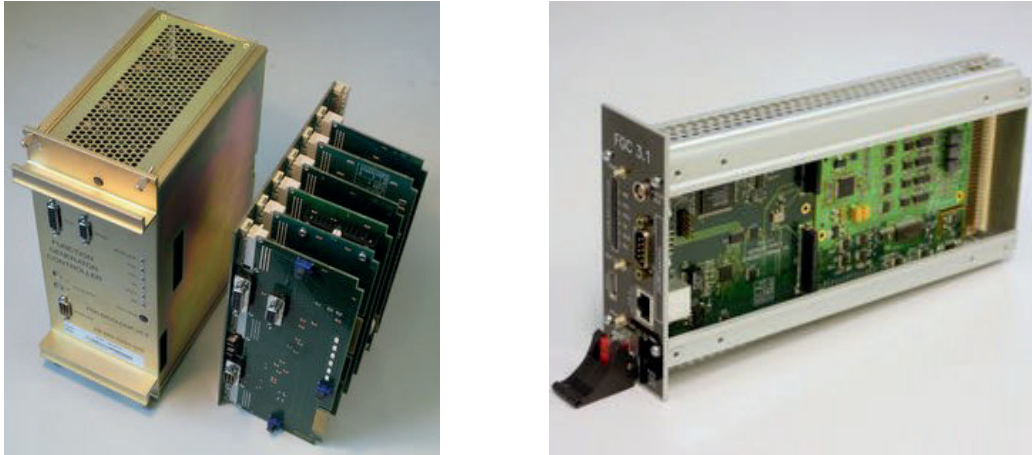


Figure 6B-18: FGC2 (left) and FGC3 (right) control units.

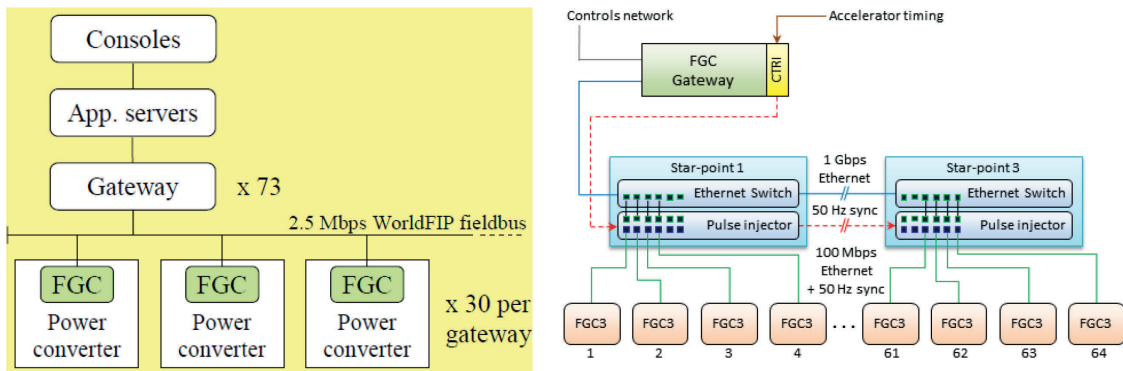


Figure 6B-19: LHC FGC2 network infrastructure (left), FGC3 network infrastructure (right).

6B.5.2.2 Upgrade of the control unit - Availability maximization

FGC3 is the outcome of a development phase that spanned from 2006 to 2011 and whose production started in 2012. It represents the standard for power converter control for current and upcoming accelerators. However, for HL-LHC, whose installation is foreseen in LS3 (effectively starting in 2024), FGC3 will likely suffer obsolescence. The development of its successor FGC4 is therefore needed. FGC4 will be based on the same principles that have been proven effective in LHC such as direct implementation of current regulation and management/monitoring of the voltage source, but will also allow the full control of the power converter (both current and voltage sources). This approach will allow complete freedom in the commercial strategies: procurement of fully functional voltage sources (as per LHC) or procurement “build-to-print” of power converters fully designed by CERN. In addition to a high reliability design of the control unit itself one of the main features of FGC4 will be the hardware support for the maximization of the availability of power converters strategies currently under development.

6B.5.2.3 Upgraded Monitoring Capabilities

The larger bandwidth offered by the 100 Mbps Ethernet will allow much better monitoring compared to the WordFIP network fieldbus currently adopted for LHC. New capabilities will be implemented both in hardware and in software (development of new libraries). These additional features will improve online diagnostics both for the LHC operators and beam physicists to perform their analysis and for the power converter experts to potentially speed up commissioning and troubleshooting.

6B.5.3 High precision measurement and regulation

6B.5.3.1 Principles

For operational purposes all LHC converters have been assigned to an “Accuracy Class” which summarizes its main precision performances. LHC accuracy classes are summarized in Table 6B-6.

The main principles of high precision measurement are depicted in Figure 6B-20 (with special reference to LHC Class 1) [13]:

- **DCCT:** DC Current Transformer is the transducer at the heart of the high precision measurement chain of the circuit current.
- **ADC:** For Class 1 power converters a special Delta-Sigma ADC is used [13]; the CERN designed DS22 was characterized by unprecedented precision when LHC was built. The final precision is also determined by the subsequent digital filter implemented in the FGC2 as the output of the DS22 is a 1-bit bitstream sent to FGC2 via optic fibre.
- **Redundancy:** Each power converter is equipped with two complete measurement “chains” comprising DCCTs and ADCs (CERN DS22 for Class 1); in normal operation the average of the two measured values of the circuit current is used for regulation whereas in case of a faulty component in one of the measurement chain the regulation can work with the single measurement supplied by the normal operating chain.
- **Remote Calibration:** The system is equipped with remote calibration capabilities (based on the CDC – CERN DCCT Calibrator [13]) in order to perform periodic calibration and keep the overall uncertainty within the tight limits imposed by Class 1.

Table 6B-6: LHC accuracy classes definition.

Accuracy Class	½ h stability [ppm]	24h reproducibility [ppm]	1 year accuracy [ppm]
1	3	5	50
2	5	10	70
3	10	50	200
4	50	100	1000
BT1	20	50	200
BT2	100	200	1000

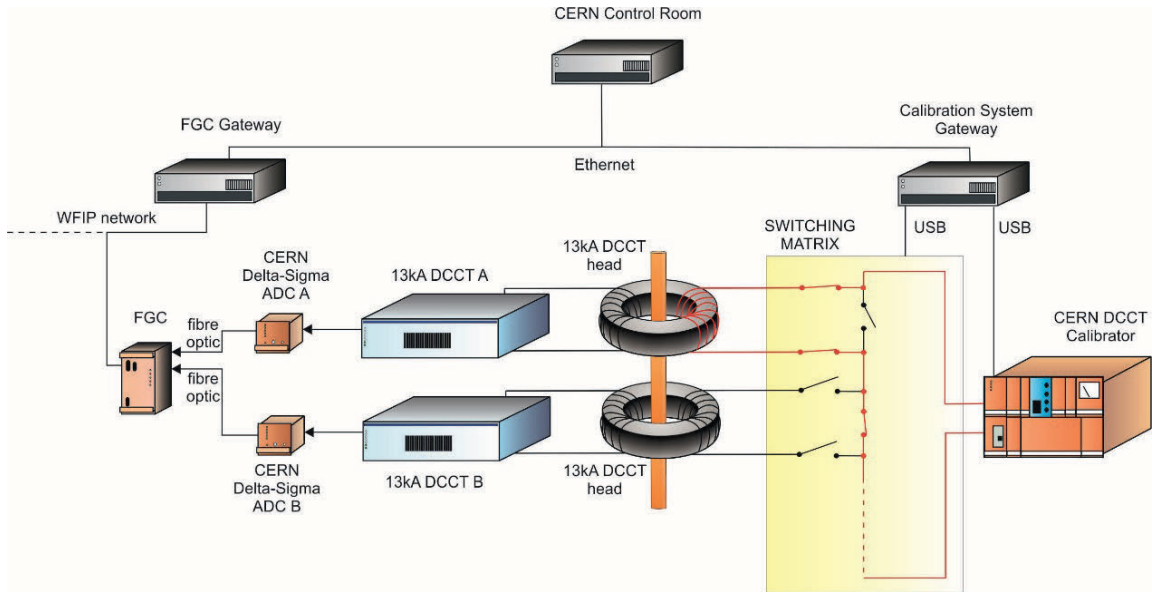


Figure 6B-20: Schematic representation of the full current measurement for the power converters equipping the main circuits of LHC (accuracy Class 1) including the remote calibration system.

For HL-LHC the same proven principles will be adopted, important R&D activities will be devoted to the update and potential performance improvement of existing LHC equipment.

6B.5.3.2 R&D DCCT

The DCCT is a mature and highly reliable technology, however some improvement might be achieved especially in the “current to voltage” conversion where the DCCT current (which can be assumed to be a known, small, fraction of the measurand current) is converted in voltage readily available for digitization [13]. The R&D activities will mostly focus on the high-precision current sensing resistors (a.k.a. the burden resistors) which represent a strategic know-how that CERN should keep in house as much as possible. Other aspects such as noise reduction by bandwidth optimization, minimization of modulation induced perturbations and optimization of the interface (to maximize common mode immunity) will also be considered.

6B.5.3.3 R&D ADC

The CERN DS22 is a 22-bit resolution Delta-Sigma ADC that currently equip Class1 LHC power converters. Its working principle, largely discussed in literature, is depicted in

Figure 6B-21. It was designed at the end of the 90’s expressly for LHC; as such it is now close to obsolescence and an R&D project was already launched with the main objective of its redesign with components that will need to be still available during HL-LHC operation. Another direction of R&D is a completely new design with comparable or improved performance; this will include market surveys for commercial ADCs that might have now filled the performance gap with respect to the CERN DS22.

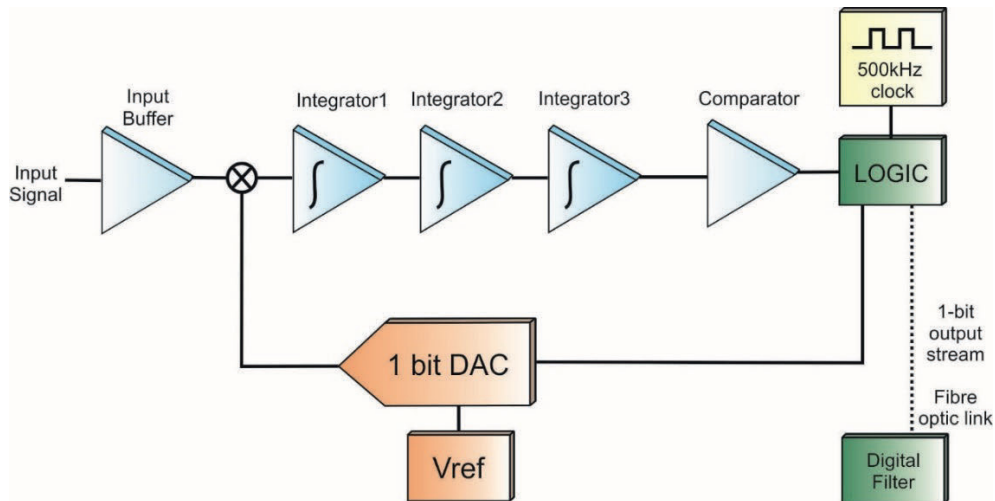


Figure 6B-21: Working principle of the CERN DS22 Delta-Sigma ADC.

6B.5.3.4 R&D calibration and test infrastructure

LHC calibration and test infrastructure up to 20 kA is depicted in Figure 6B-22 [14]. Such an infrastructure was crucial for the performance verification of the high precision DCCTs that equip LHC power converters. Such an infrastructure is going to be strategic for HL-LHC as well. This test setup is now close to obsolescence and it will require consolidation in coming years. A new (or refurbished) 20 kA power converter will also be needed together with new equipment of the reference cell.

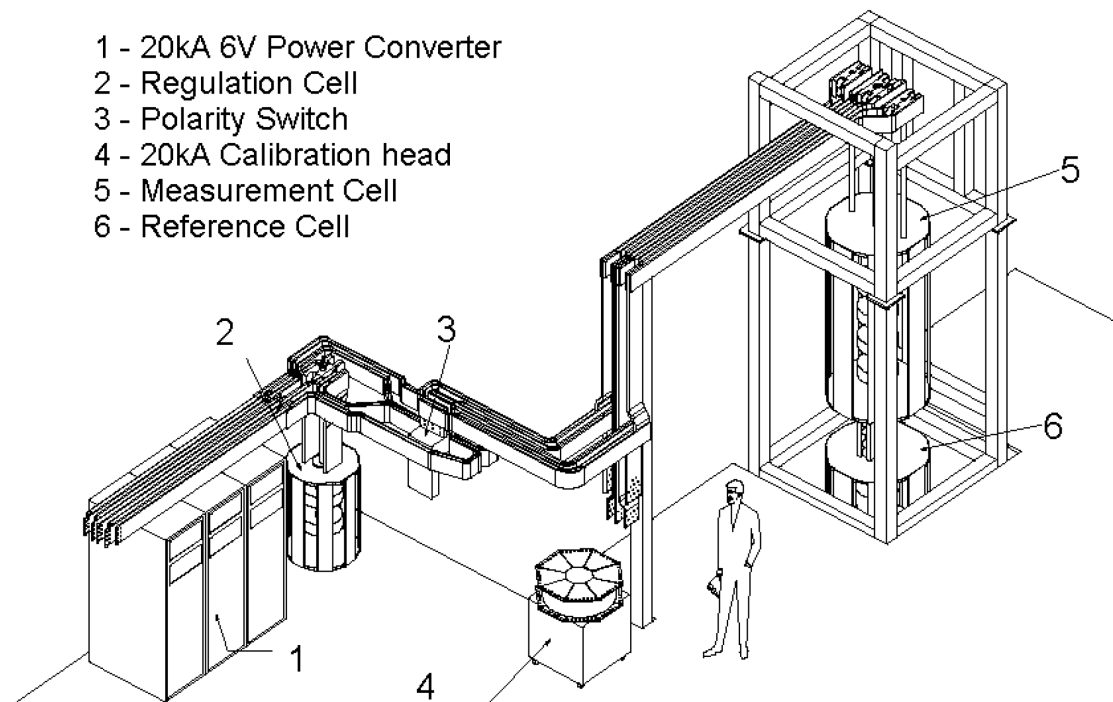


Figure 6B-22: LHC 20kA DCCT calibration test station.

6B.5.3.5 R&D control strategies

The main quadrupole circuits for the ITs of LHC comprise three nested circuits [3] (see Figure 6B-5). From the control point of view, this represents a MIMO (Multiple Input Multiple Output) system. The strategy

adopted for its control is based on the “decoupling” principle and it is realized by means of a dedicated hardware board (see Figure 6B-23). For HL-LHC ITs four nested circuits are foreseen in the baseline (see Figure 6B-6) so a new strategy is to be found. Given the upgraded monitoring and control capabilities of the control infrastructure based on Ethernet (which is going to drastically reduce “delays”) a fully software solution is to be developed. This will require the development of new libraries which will extend FGC control capabilities [15] beyond the current SISO (Single Input Single Output) paradigm.

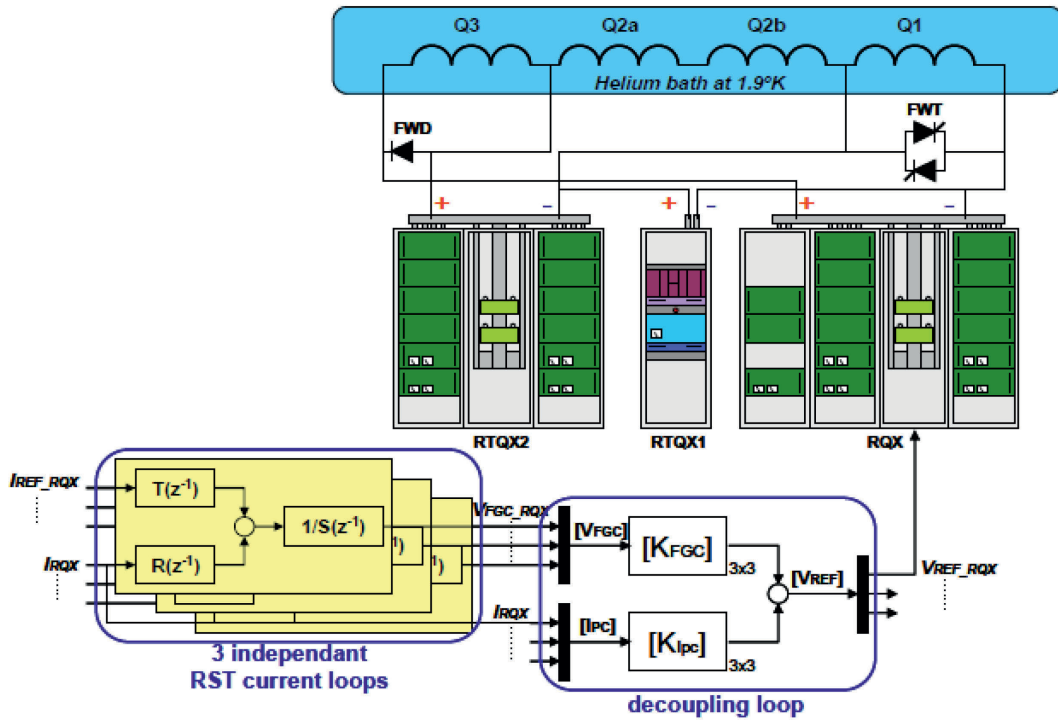


Figure 6B-23: Decoupling loop for the LHC Inner Triplets current control.

6B.6 Others performance improvements

The present LHC power converters are installed in underground areas. Of the 1710 total units, 1065 are exposed to radiation. During machine operation up to 2013, the power converters generated a number of beam-dumps due to single event effect (SEE). The faults due to SEE represented about 20% of the total power converter failures. A R2E programme was launched in 2010 to mitigate radiation issues for the whole LHC machine. In this framework, all power converters connected to the present DFBX (Inner Triplet magnets) were relocated to reduce their exposure to radiations. More shielding was added inside the RR alcoves to reduce particles fluences. A new radiation-tolerant version of the FGC system, called FGClite, was developed for integration in the machine in 2017.

6B.6.1 Radiation-tolerant power converters

The power converters currently in the RR alcoves will be replaced with radiation-tolerant converters. This development concerns the 600 A and the 4 kA, 6 kA, and 8 kA families. The replacement is planned to take place during Long Shutdown 2 (LS2). The new power converters will be able to withstand the doses and the fluences expected during the HL-LHC operation. These radiation-tolerant converters will be used to power the Q4-Q5-Q6 of the new HL-LHC configuration. No costs are foreseen for this part of the machine.

The present 60 A converters will not withstand the doses estimated during HL-LHC operation. They were designed for tolerating a maximum total dose of about 50 Gy, and the power converters placed in or close to the matching sections will receive a dose of up to 32 Gy/year. These converters will be replaced with new ones designed for withstanding a total dose of 200 Gy. This target corresponds to the maximum dose that can

be tolerated by a design based on commercial off-the-shelf (COTS) components. A rotation between highly exposed and less exposed power converters is also foreseen.

The 120 A power converters were not included in the present R2E project but as they are present in the RR galleries, a new radiation-tolerant version will be needed to guarantee a good availability of the LHC machine after LS3.

6B.6.2 Power converters and LHC machine availability

Global machine availability is affected by the pre-cycle needed to degauss the magnets and by the magnets ramp-down time. In the present LHC, the most limiting circuits are those of the Inner Triplet quadrupoles and of the main quadrupoles. All of these circuits are powered via 1-quadrant converters, which are the cause for the long ramp-down time. Two upgrades can be envisaged if machine availability needs to be improved:

- replacement of these power converters with 2-quadrant converter types;
- use of external dump resistors to accelerate the discharge.

As an illustration, by replacing the present 13 kA/18 V power converters of the main quadrupole circuits with two-quadrant 13 kA/±18 V power converters, the ramp-down of the machine can be reduced by 30 minutes. 2-quadrant power converter rated 6 kA/±10 V could be an option to reduce the squeeze time process. It is estimated that the replacement of both power converters powering the Inner Triplet quadrupole and main quadrupole circuits will increase the global availability of the machine by about 4%. More work is necessary to assess the best solution, also in conjunction with the LHC Consolidation project.

6B.7 References

- [1] V. Montabonnet, Y. Thurel, IPQ Circuit Powering Using 3 or 4 Cables, EDMS [1231467](#)
- [2] F. Bordry, H. Thiesen, LHC Inner Triplet Powering Strategy, 19th IEEE Particle Accelerator Conference, Chicago, IL, USA, 18 - 22 Jun 2001, pp.e-proc. 633 (2001). [LHC-Project-Report-476](#)
- [3] F. Bordry, D. Nisbet, H. Thiesen, J. Thomsen, Powering and Control Strategy for the Main Quadrupole Magnets of the LHC Inner Triplet System, 13th European Conference on Power Electronics and Applications, Barcelona, Spain, 8 - 10 Sep 2009, [CERN/ATS 2010-022](#) (2009)
- [4] F. Bordry, V. Montabonnet, H. Thiesen, Soft switching (ZVZCS) high current, low voltage modular Power converter (13 kA, 16 V), 9th European Conference on Power Electronics and Applications, Graz, Austria, 27 - 29 Aug 2001, pp.9 (2001)
- [5] Working Group 1 of the Joint Committee for Guides in Metrology (JCGM/WG 1); Evaluation of measurement data — Guide to the expression of uncertainty in measurement; [JCGM 100:2008](#)
- [6] W.A. Wolovich, P. Ferreira, Output Regulation and Tracking in Linear Multivariable Systems, IEEE Transactions on Automatic Control, 1979
- [7] G. Arduini, J. M. Coello de Portugal, R. De Maria, S. Fartoukh, M. Fitterer, M. Giovannozzi, R. Tomás, Operation and beam dynamics requirements, Conceptual Design Review of the Magnet Circuits for the HL-LHC, CERN, Geneva (2016)
- [8] J.C.L. Brazier, A. Dinius, Q. King, J.G. Pett, The all-digital approach to LHC Power converter Current Control, 8th International Conference on Accelerator and Large Experimental Physics Control Systems, San José, CA, USA, 27 - 30 Nov 2001, pp.e-proc. [THBT004](#) (2001)
- [9] H. Thiesen, M. Cerqueira-Bastos, G. Hudson, Q. King, V. Montabonnet, D. Nisbet, S. Page, High precision current control for the LHC main Power converters, 1st International Particle Accelerator Conference, Kyoto, Japan, 23 - 28 May 2010, pp.[WEPD070](#) (2010)
- [10] I. Barnett, D. Hundzinger, Q. King, J.G.Pett, Developments in the high precision control of magnet currents for LHC, 18th Biennial Particle Accelerator Conference, New York, NY, USA, 29 Mar - 2 Apr 1999, pp.e-proc. [3743](#) (1999)

- [11] D. Calcoen, Q. King, P.F. Semanaz, Evolution of the CERN Power converter Function Generator/Controller for Operation in Fast Cycling Accelerators, 13th International Conference on Accelerator and Large Experimental Physics Control Systems, Grenoble, France, 10 - 14 Oct 2011, pp.[939-942](#) (2013)
- [12] S.T. Page, Q. King, H. Lebreton, P.F. Semanaz, Migration from WorldFIP to a Low-Cost Ethernet Fieldbus for Power converter Control, 14th International Conference on Accelerator & Large Experimental Physics Control Systems, San Francisco, CA, USA, 6 - 11 Oct 2013, pp.[tuppc096](#) (2013)
- [13] M. Cerqueira Bastos, G. Fernquist, G. Hudson, J. Pett, A. Cantone, F. Power, A. Saab, B. Halvarsson, J. Pickering, High Accuracy Current Measurement in the Main Power Converters of the Large Hadron Collider: Tutorial 53, IEEE Instrumentation & Measurement Magazine, 2014
- [14] F. Bordry, G. Fernquist, B. Halvarsson, J-C. Perreard, J.G. Pett, High-Current Performance Evaluation of DCCT's, Electrical Power Technology in European Physics Research : EP2 Forum '98, Grenoble, France, 21 - 22 Oct 1998, [CERN-SL-98-069-PO](#)
- [15] Q. King, K. Lebioda, M. Margrans de Abril, M.Martino, R. Murillo, A. Nicoletti, CCLIBS: The CERN Power converter Control Libraries, 15th International Conference on Accelerator and Large Experimental Physics Control Systems, Melbourne, Australia, 17 - 23 Oct 2015, pp.WEPGF106 (2015),. DOI: [10.18429/JACoW-ICALEPCS2015-WEPGF106](#)
- [16] H. Thiesen, M. Cerqueira Bastos, G. Hudson, Q. King, V. Montabonnet, D. Nisbet, S. Page, High Precision Current Control for the LHC Main Power converters, 1st International Particle Accelerator Conference, Kyoto, Japan, 23 - 28 May 2010, pp.[WEPD070](#) (2010)

Chapter 7

Machine Protection, Interlocks and Availability

7 Machine protection, interlocks and availability

7.1 Machine protection with a 700 MJ beam

The combination of high intensity and high energy that characterizes the nominal beam in the LHC leads to a stored energy of 362 MJ in each of the two beams. This energy is more than two orders of magnitude higher than in any previous accelerator. For HL-LHC operation, it will increase by another factor of two as shown in Figure 7-1. With intensities expected to increase up to 2.3×10^{11} p/bunch with 25 ns bunch spacing and 3.7×10^{11} p/bunch with 50 ns bunch spacing [1], the damage potential of the HL-LHC beams is significantly larger than that of today's nominal beam parameters. Recent calculations that couple energy deposition and hydrodynamic simulation codes show that the nominal LHC beam can already penetrate fully through a 35 m long block of copper if the entire beam is accidentally deflected. Such an accident could for example happen if the beam extraction kickers deflect the beam at an incorrect angle. Hence, it becomes necessary to revisit most of the damage studies in light of the new beam parameters [2].

The damage limits of superconducting magnets due to instantaneous beam losses need to be determined, as they represent an important input for the choice of collimator materials and the design of protection absorbers. In addition, new failure scenarios will have to be considered following the proposed optics changes and the installation of new accelerator components such as crab cavities, hollow electron beam lenses and long range beam-beam compensators. Special care is required to find a trade-off between equipment protection and machine availability in view of the reduced operational margins (e.g. decreasing quench limits and beam loss thresholds versus increased beam intensity and tighter collimator settings, UFOs, etc.).

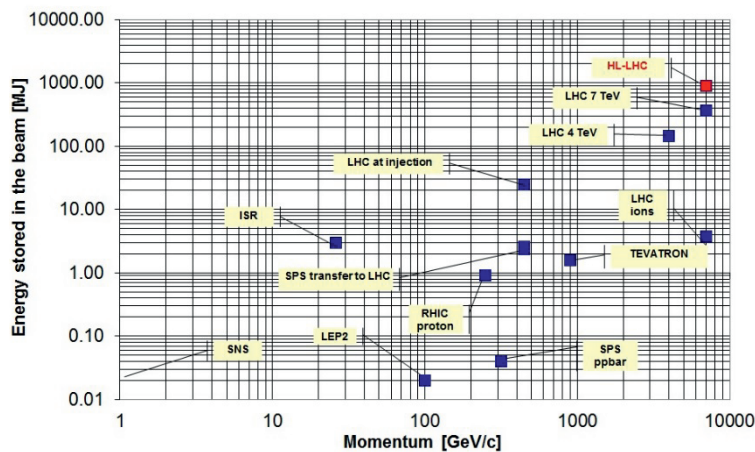


Figure 7-1: Stored beam energy as a function of beam momentum for various particle accelerators. The beam energy of about 700 MJ of each of the HL-LHC beams is shown in red.

Safe operation of the LHC currently relies on a complex system of equipment protection. The machine protection system (MPS) is designed to prevent the uncontrolled release of energy stored in the magnet system and damage due to beam losses, with very high reliability. An essential element of the active MPS system is the early detection of failures within the equipment. In addition, the beam parameters are monitored with fast and reliable beam instrumentation. This is required throughout the entire cycle, from injection to collisions.

Once a failure is detected by any of the protection systems, the information is transmitted to the beam interlock system (BIS), which triggers the extraction of the particle beams via the LHC beam dumping system (LBDS). It is essential that the beams are always properly extracted from the accelerator via the 700 m long transfer lines into the large graphite dump blocks. These are the only elements of the LHC that can withstand the impact of the full beams.

The current machine protection architecture is based on the assumption of three types of failure scenarios [3].

- **Ultra-fast failures:** failures within less than three turns, e.g. during beam transfer from the SPS to the LHC, during beam extraction into the LHC beam dump channel, or during beam extraction as a result of missing beam–beam deflection (1 LHC turn = 88.9 μ s). In the case of failures of this type, passive protection elements are required to intercept the beams and protect the accelerator equipment from damage, as no active protection is fast enough.
- **Fast failures:** failures on a timescale of several LHC turns (longer than 260 μ s and less than a few milliseconds) as a result of equipment failures with a fast effect on particle trajectories. The active extraction of the beams is completed within up to three turns after the detection of the failure and hence provides protection against such failures.
- **Slow failures:** multi-turn failures on timescales equal to or more than a few milliseconds, e.g. magnet powering failures, magnet quenches, RF failures, etc.

7.2 Protection against uncontrolled beam losses

Equipment failures or beam instabilities appearing on the timescale of multiple turns allow for dedicated protection systems to mitigate their effects on the circulating beams. Figure 7-2 shows a comparison of the failure detection times of different protection systems. As shown in the figure, the LHC beam loss monitoring system (BLM) has the fastest detection time down to 40 μ s. The BLM system is complemented with fast interlocks on the beam position in IR6, fast magnet current change monitors (FMCM) beam current change monitor (currently under development by the beam instrumentation group at CERN). All of these systems feature similar failure detection times in the 100 μ s to 1 ms range, providing diverse redundancy to the BLM system.

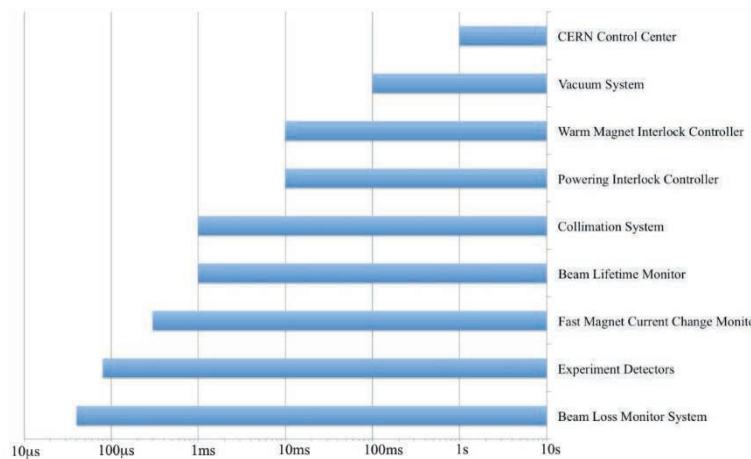


Figure 7-2: Some failure detection times at the LHC. The shortest failure detection time is currently assured by the BLM system, with the fastest integration time of 40 μ s, which is equivalent to half an LHC turn. Very fast beam loss detectors based on diamond detectors can achieve ns rise times. For the moment these detectors are only used for diagnostic purposes and not interlocked. This may change in the HL-LHC era.

Adding the additional time required to process the signal in the detection system and to transmit the detected failure through the LHC beam interlock system, the time required to synchronize the firing of the beam dump kickers with the abort gap as well as the time needed to completely extract the beam from the LHC

leads to an equivalent worst case MPS response time of four LHC turns after the appearance of the failure as depicted in Figure 7-3.

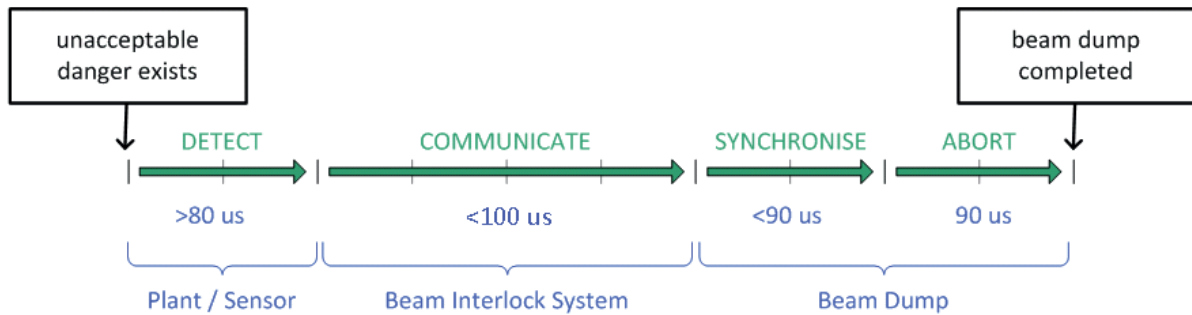


Figure 7-3: Current MPS response time from failure detection to completion of beam dump.

This reaction time is sufficient in the absence of failures occurring on timescales below 10 LHC turns. A failure of the normal conducting separation dipole D1 in IP1 and IP5 is currently considered the fastest possible failure with circulating beam. Therefore, this was the basis for the design of major parts of the current MPS system. Due to their location in areas with high beta functions and the fast decay of magnet current in the case of a magnet powering failure, these normal conducting magnets can induce fast changes of the particle trajectory. These changes lead to rapidly increasing beam losses in the LHC betatron cleaning insertion (IR7), which define the smallest aperture in the LHC. At nominal energy and intensity, the losses after this specific failure can reach collimator damage levels within just ten turns. Therefore, a dedicated protection system – the so-called fast magnet current change monitors (FMCM) – has been very successfully deployed on critical magnets in the LHC and its transfer lines in 2006 [4].

With the HL-LHC upgrade, the optics in the insertion regions will significantly change. For certain types of the so-called Achromatic Telescopic Squeezing (ATS) optics the β -function at the D1 separation dipole magnets in IR1 and IR5 will increase up to $\sim 17\,000$ m, which will enhance the effect of the dipole on the beam trajectory. However, the replacement of the D1 separation dipole magnets by a superconducting magnet will significantly increase the time constants of these circuits, hence eliminating the potential of fast failures originating from these magnets.

For HL-LHC operation, the use of crab cavities will introduce however new failure scenarios that can affect the particle beams on timescales well below the D1 failure mentioned above [5]. Studies of different failure scenarios are still ongoing. These studies require considerations of design details that might eventually be adopted for the crab cavity and the corresponding low-level RF systems. Both components, crab cavities and their low-level RF systems, have a significant impact on the circulating beams following a system failure, e.g. cavity quenches, trips of the RF power generator, or instabilities in the low-level RF loops. In addition, detailed measurements of the quench and failure behaviour of the chosen cavity designs have yet to be conducted. First experience with similar devices at KEK, however, shows that certain failures can happen within just a few turns, as depicted in Figure 7-4.

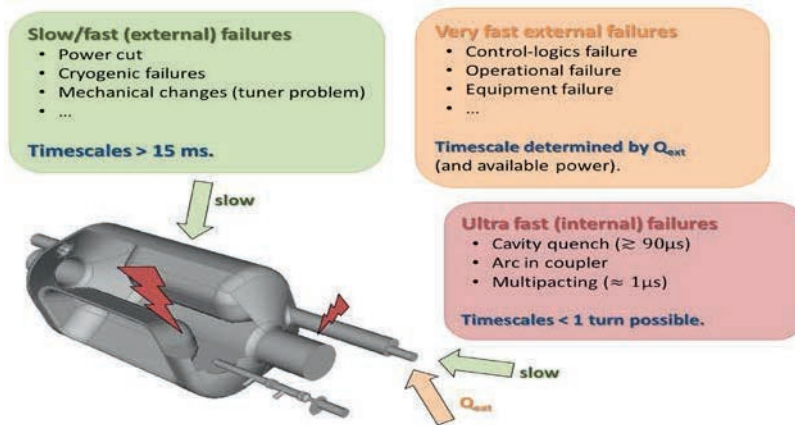


Figure 7-4: Schematic overview of crab cavity failure categories [5].

While protection against failures with time constants >15 ms is not expected to be of any concern, voltage and/or phase changes of the crab cavities will happen with a time constant τ , which is proportional to Q_{ext} . For a 400 MHz cavity with a $Q_{ext} = 1 \times 10^6$ this will result in a time constant as low as 800 μs . The situation becomes even more critical for cavity quenches, where the energy stored in the cavity can be dissipated in the cavity walls on ultra-fast timescales. Failures, believed to be caused by quenches, observed in cavities at KEKB show a complete decay of the cavity voltage within 100 μs , accompanied by an oscillation of the phase by 50° in only 50 μs . Such crab cavity failures can imply large global betatron oscillations, which could lead to critical beam losses for oscillation amplitudes above $1 \sigma_{nom}$. The appearance of multipacting in crab cavities, its timescale and consequences on the cavity voltage and phase has to be studied.

Highly overpopulated transverse tails compared with Gaussian beams were measured in the LHC (beam scrapings with collimators, van-der-Meer scans in the LHC experiments). Based on these observations the energy stored in the tails beyond 4σ are extrapolated to correspond to ~ 30 MJ for HL-LHC parameters. These levels are significantly beyond the specification of the collimation system, capable of absorbing up to 1 MJ for very fast accidental beam losses.

Mitigation techniques have to include a fast, dependable, and redundant detection and interlocking of a crab cavity failure on the mentioned timescales. Appropriate measures must be taken when designing the cavity and associated RF control to increase as much as possible the failure time constants:

- Avoid correlated failures of multiple cavities (on one side of an IP) through mechanical and cryogenic separation of the individual modules and appropriate design of the low-level RF [6].
- Investigate the use of fast failure detection mechanisms such as RF field monitor probes, diamond beam loss detectors, power transmission through input couplers, and head-tail monitors.
- Ensure the partial depletion of the transverse beam tails to reduce the energy stored in the beam halo, which would potentially be deflected onto the collimation system, below the design value of 1 MJ. For the current baseline this would require to deplete the halo for $1.7 \sigma_{nom}$ inside the primary collimators (i.e. from about $4 \sigma_{nom}$ to $5.7 \sigma_{nom}$), as this would be the possible transverse beam trajectory perturbation following an ultra-fast failure of a single crab cavity. An increase of the single cavity voltage will naturally lead to an increase of the trajectory perturbation, and therefore, has to be studied carefully. It is important to note that the partial depletion of the beam halo may have a negative effect on the available time to detect a failure with other machine protection systems like BLMs. All consequences of operation with a depleted beam halo need to be studied carefully.
- Decrease the reaction time of the MP system for such ultra-fast failures by, e.g. increasing the number of abort gaps, accepting the triggering of asynchronous beam dumps with potential local damage, adding direct links to the beam dumping system in IR6, and considering the installation of disposable absorbers.

7.2.1 Beam interlock system

The beam interlock system (BIS) is a highly dependable fast interlock system and a key element of CERN's accelerator machine protection systems. It is currently used in the LHC, SPS, and other parts of the injector chain at CERN. Its primary objective is to provide a fast and highly reliable link between users requesting a beam abort and the beam dumping system. The hardware implementation of the system is based on custom-made electronics, as industrial solutions have not been found to be adequate for the specific requirements of the system, especially regarding the reaction time combined with the geographical distribution of the system. Due to the obsolescence of electronics components and potential problems with the optical links the present system will need to be upgraded. To fulfil the requirements of the HL-LHC, the system will be equipped with additional input channels to connect additional user interfaces and to provide more flexibility in the configuration of the various user inputs. The number of required channels is subject to a future functional specification to be provided by the SPS and LHC machine protection panel (MPP). The possibility of implementing very fast interlock channels and direct links between the crab cavities and the LHC beam dumping system will be studied, but the feasibility and necessity cannot yet be confirmed. The new system will be equipped with advanced diagnostic features for all optical links allowing pre-emptive maintenance, e.g. in the case of degraded performance due to the enhanced radiation load on the optical fibres in the underground areas.

7.2.1.1 Equipment performance objective (BIS)

The upgraded Machine Protection System is supposed to reach the same performance level in terms of reliability as the present system, which qualitatively corresponds to a safety integrity level 3 (SIL3). The safety critical part of the BIS hardware architecture will be based on well-proven principles and solutions but adapted to state-of-the-art electronics components and assemblies. It is therefore probably possible to reuse a major part of the safety critical code, which is very well tested and fully validated. The design goal of the new BIS hardware is not to cause more than one spurious beam abort per year, in line with the present operational system.

The new BIS could be equipped with a new hardware controls interface, replacing obsolete architectures for communication buses and simplifying maintenance and potential upgrades. The BIS hardware will also feature advanced diagnostic tools for the system hardware and the optical links.

All of the proposed changes will require a major revision of the high-level supervision and controls software and afterwards the adaptation to the accelerator controls environment as at present.

7.2.2 Fast magnet current change monitor

The main function of the fast magnet current change monitors (FMCM) is to monitor fast current changes in electrical circuits with normal conducting magnets. A fast current change can be caused by sudden powering failures or perturbations on the supply network, which change the particle trajectories leading to fast beam losses. These monitors are required for electrical circuits with a short decay time constant and magnets installed in regions with high beta functions. Each monitor delivers a permit signal to the beam interlock system to request the extraction of particle beams before losses occur. Therefore, the FMCM provides a redundant protection to the beam loss monitors (BLM). A total of 26 monitors are presently installed to protect delicate parts of the LHC and SPS-LHC transfer lines.

7.2.2.1 Objectives for HL-LHC machine performance

The installation of FMCMs is required to ensure machine protection against powering failures in critical magnetic elements during all operational phases. Twelve monitors are currently installed in the LHC, namely for dump septa magnets in IR6, collimation insertion regions in IR3/IR7, Alice compensator circuits in IR2, and main separation dipoles D1 in IR1 and IR5 [6]. The latter will be replaced by superconducting magnets and most probably not require FMCMs anymore in the HL-LHC era. Additional input from WP3 (magnets)

and WP2 (accelerator physics) is required to clarify the necessity of additional FMCM units for the protection of the new magnet powering in the high luminosity insertion regions IR1 and IR5. In addition, new failure modes derived from the introduction of new elements (such as crab cavities) and combined failures need to be studied to understand the machine protection requirements and to estimate the number of monitors required to protect the accelerator equipment in the HL-LHC. These information are required by the latest by mid of LHC Run 3 (~end 2022) to allow sufficient time for design updates and production.

7.2.2.2 Equipment performance objective

FMCMs have successfully operated in the LHC and the SPS-LHC transfer lines for many years, and no missed dump has been identified since the start of operation. For the protection of the electrical circuits in the HL-LHC the use of the similar design is recommended. However, a review of the system needs, in view of the HL-LHC requirements, will be required. The review and potential redesign of the hardware is a mandatory step due to the aging and obsolescence of the electronics parts used in the current system and needs to be performed latest by the mid of LHC Run 3 (~ end 2022).

The aim of the upgrade of the FMCM will be to improve the maintainability of the system and to comply with the requirements of the HL-LHC.

7.3 Magnet powering protection

The quench protection systems in the LHC (including cold by-pass diodes and resistors) protect superconducting magnets, busbars, and current leads. The goal is to minimize peak temperatures and voltages in magnets and busbars due to a quench and to prevent quenches in the High Temperature Superconductor (HTS) leads. For HL-LHC this will also include the MgB₂ superconducting links powering the triplet and auxiliary circuits of IP1 and IP5. Magnet quenches can occur due to conductor movement, beam losses, heat propagation in the cryogenic system, and due to internal shorts. The main sources for busbar quenches are heat propagation in the cryogenic system due to magnet quenches, thermal coupling, bad splices, wrong helium levels in busbar lines and DFBs, and helium bubbles in superconducting links. Quenches in the HTS leads in current sharing regime can occur due to defective temperature sensors and regulation problems in the cryogenic system.

At present the magnet powering protection systems are protecting:

- 8 main dipole circuits (RB, $I_{nom}=11.85$ kA, 154 2-in-1 dipole magnets with both apertures powered in series per circuit);
- 8 main focusing quadrupole circuits (RQF) and 8 main defocusing quadrupole circuits (RQD) (RQ, $I_{nom}=11.87$ kA, one in each sector containing 47 or 51 magnets);
- 8 inner triplet circuits (ITs, IP1, IP2, IP5 and IP8 one per IP side, containing 4 magnets each, I_{nom} between 4.6 and 11.4 kA);
- 78 individually powered quadrupole circuits (IPQs, I_{nom} between 3.6 kA and 5.4 kA, operated at 1.9 or 4.5 K and K);
- 16 individually powered dipole circuits (IPDs, I_{nom} between 4.4 kA and 6.2 kA); 434 600 A circuits and
- 1052 60-120 A circuits.

Different protection strategies have been implemented for the circuits mentioned above. In the RB and RQ circuits, quench heaters and by-pass diodes guarantee the magnet protection, whereas energy extraction systems protect the bus-bars and the by-pass diodes. In the IPQ, IPD and triplet quadrupole circuits, quench heaters are simultaneously fired in all magnets of the circuit, which guarantees proper protection of the magnets and busbars. Protection of the magnets and busbars in the 600 A circuits varies depending on the type and number of magnets in the circuit. Protection is ensured by energy extraction systems, parallel resistors, or by the crow-bar of the power converter, or by any combination of these three methods. The 60-120 A circuits

contain self-protecting magnets and therefore have neither energy extraction systems nor parallel resistors. In this case the bus-bar protection is ensured by the crow-bar of the power converter, after switching it off.

Table 7-1 shows a list with the new circuits for HL-LHC including their current baseline key parameters and the proposed protection method.

Table 7-1: Circuits parameters.

	Circuits for HiLumi	Magnet Type	Number of circuits per IP side	Number of circuits	$I_{nominal}$ [kA]	$I_{ultimate}$ [kA]	I_{rated} [kA]	Quench Heaters	CLIQ	EE
Inner Triplet	Triplet Q1, Q2a, Q2b, Q3	MQXFA / MQFXB	1	4 (IR1/5)	16.5	17.8	18.0	Baseline (inner/outer layer)	Baseline	no
	Trim Q1		1	4 (IR1/5)	2		2.0			
	Trim Q3		1	4 (IR1/5)	2		2.0			
	Trim Q2a		1	4 (IR1/5)	0.12		2.0			
	Orbit correctors Q2a/b - vertical	MCBXFB	2	8 (IR1/5)	1.6	1.73	2.00	Baseline	no	Option
	Orbit correctors Q2a/b - horizontal	MCBXFB	2	8 (IR1/5)	1.47	1.59	2.00	Baseline	no	Option
	Orbit correctors CP - vertical	MCBXFA	1	4 (IR1/5)	1.6	1.73	2.00	Baseline	no	Option
	Orbit correctors CP - horizontal	MCBXFA	1	4 (IR1/5)	1.47	1.59	2.00	Baseline	no	Option
	Superferric, order 2	MCSXF	1	4 (IR1/5)	0.182	0.20	0.20	no	no	Option
	Superferric, order 3, normal and skew	MCSXF / MCSSXF	2	8 (IR1/5)	0.105	0.11	0.12	no	no	PC crowbar
	Superferric, order 4, normal and skew	MCOXF / MCOSXF	2	8 (IR1/5)	0.105	0.11	0.12	no	no	PC crowbar
	Superferric, order 5, normal and skew	MCDXF / MCDSXF	2	8 (IR1/5)	0.105	0.11	0.12	no	no	PC crowbar
	Superferric, order 6	MCTXF	1	4 (IR1/5)	0.105	0.11	0.12	no	no	PC crowbar
	Superferric, order 6, skew	MCTSXF	1	4 (IR1/5)	0.105	0.11	0.12	no	no	PC crowbar
D1	Separation dipole D1; MBXF	MBXF	1	4 (IR1/5)	12	13.0	13.0	Baseline	Option	no
D2	Separation dipole D2; MBRD	MBRD	1	4 (IR1/5)	12	13.0	13.0	Baseline	Option	no
	Orbit correctors D2	MCBRD	4	16 (IR1/5)	0.5	0.54	0.6	no	no	Option
Q4	Large aperture 2-in1 Quad; Q4	MQY	2	8 (IR1/5)	4.50	4.9	6.0	Baseline	no	no
	Orbit correctors Q4	MCBY	8	32 (IR1/5)	0.072	0.08	0.12	no	no	no
Q5	Present LHC Q4 magnet	MQY	2	8 (IR1/5)	4.51	4.9	6.0	Baseline	no	no
	Orbit correctors present Q4	MCBY	6	24 (IR1/5)	0.072	0.08	0.12	no	no	no
Q6	Insertion Quad, 2-in1 aperture; Q6	MQML	2	8 (IR1/5)	4.31	4.7	6.0	Baseline	no	no
	Orbit correctors Q6	MCBC	2	8 (IR1/5)	0.08	0.09	0.12	no	no	no
11T	11T dipole, MBH	11T dipole, MBH		2 (IR7)	11.85	12.798	13	Baseline	Option	existing RB EE
	Trim circuit			2 (IR7)	0.25	0.034	-0.3 / 0.1			

The circuits, busbars, and superconducting links will be equipped with quench detection systems (QDS) that detect changes in the superconducting state and activate, depending on the circuit, quench heaters, coupling loss induced quench systems (CLIQ), or energy extraction (EE) systems to safely extract the magnetic energy stored in the circuit.

Furthermore, the correct powering conditions have to be ensured for each circuit by a powering interlock system (PIC), which will interlock the powering of the circuit via the power converter and request a beam dump in the case of any failure in the powering systems. Therefore, the PIC is interfacing the quench detection and protection systems, the beam interlock system, the power converters, the cryogenic systems, and technical services such as uninterruptable power supplies (UPS), emergency stop buttons (AUG), and controls. In case of a quench in the new high-current circuits the beams should be dumped before circuit/magnet protection systems (quench heaters, CLIQ) are triggered. The effect of self-triggered quench heaters or CLIQ units on the circulating beam is currently under study.

The protection of the normal conducting magnets in the LHC and its injector complex is ensured by the warm magnet interlock system (WIC), which collects signals from thermo-switches installed on the magnets and status signals from the associated power converters.

As a failure in the magnet system will also impact the stored particle beams, these systems have to interface the magnet powering systems with the BIS and initiate a beam dump in case of a failure.

7.3.1 Circuit layout and protection concept of the new HL-LHC triplet circuits in IP1 and IP5

Following the recommendations of the *Conceptual Design Review of the Magnet Circuits for HL-LHC* [15], it was decided to power the new triplet magnets (Q1, Q2a, Q2b, Q3) on each side of the IR in series, both for IP1 and IP5, adding trim circuits for Q1, Q2a and Q3 to allow for the required flexibility of beam optics.

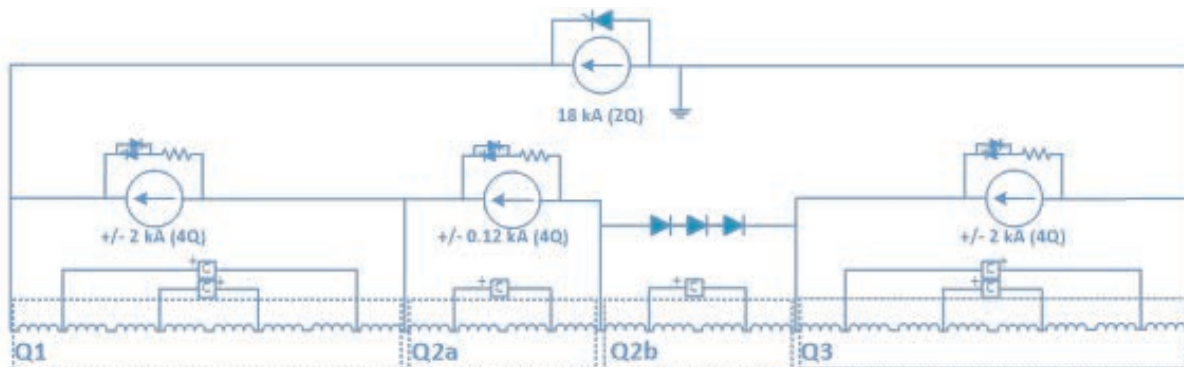


Figure 7-5: Schematic of the inner triplet (IP1/5) powering and protection layout.

A maximum allowable hotspot temperature of 350 K was defined for these high-field Nb₃Sn magnets. In addition, thermal gradients should be kept as small as possible, to minimize the risk of degradation of magnet performance due to thermal stresses. Due to the lack of experimental experience with full-size Nb₃Sn triplet quadrupoles, the quench protection scheme of this circuit is aiming for the lowest possible hot-spot temperatures and thermal gradients, sufficiently low inter-turn and inter-layer voltages, as well as low voltages to ground. To achieve this goal, each magnet will be equipped with 16 outer-layer heater strips (8 low-field and 8 high-field regions), which will be powered in 8 circuits, and 8 inner-layer heater strips, which will be powered in 4 circuits. In addition, Q1 and Q3 will each be equipped with two CLIQ units, whereas Q2a and Q2b each with one CLIQ unit (see 7.3.3), adding divers redundancy to the quench heaters. In total this corresponds to 48 outer-layer and 24 inner-layer quench heater circuits and 6 CLIQ units per triplet. Note that this describes the baseline until the performance of all protection systems has been fully validated in short model coils and long prototypes. Finally only one of the two systems - inner layer quench heaters or CLIQ - will be used in combination with the outer layer quench heaters. Warm parallel diodes and crowbars (with back-to-back thyristors) separate the protection of each quadrupole in the circuit and minimize the voltages in the circuit during a quench in case of non-zero currents in the trim circuits and differing discharge rates in the triplet quadrupoles due to tolerances and possible failures. Figure 7-5 illustrates the powering and protection layout of the new HL-LHC triplet circuits for IP1 and IP5.

Table 7-2 and Table 7-3 summarize the simulated hot spot temperatures and peak voltages to ground during a quench in case of the use of different combinations of the three protection systems. The given range indicates the spread of the simulation results depending on the quench location and the variation of cable parameters within their specifications. It can clearly be seen that a protection scheme only based on outer-layer quench heaters does not fulfil the requirements of a hot spot temperature below 350 K for the allowed/specified variation of cable parameters. Furthermore a combination of outer-layer quench heaters with either inner-layer quench heaters or CLIQ would provide a solid margin concerning the hot spot temperature even in case of ultimate circuit current. The worst-case peak voltages to ground during a quench are 39 V higher using a CLIQ system then with quench heaters only, due to the discharge of the CLIQ capacitors directly into the coil. It needs to be mentioned that in the case of quench heaters, the voltage between quench heater and coil is reaching a maximum in the order of 500 V.

Figure 7-6 shows the typical currents in the magnets and the parallel elements of the triplet circuit in case of a quench at nominal current (16.5 kA) and zero amperes in the trim circuits using outer-layer heaters and CLIQ. The oscillations introduced by the discharge of the six CLIQ units are clearly visible. The maximum dI/dt in the triplet circuit reaches 226 kA/s. All circuit elements (busbars, superconducting link, etc.) need to be designed to withstand this dI/dt and should avoid tripping neighbouring high current and corrector circuits through electromagnetic coupling.

Table 7-2: Hot spot temperature in the triplet magnets in case of a quench using outer-layer quench heaters (O-QH), outer- and inner-layer quench heaters (O-QH+I-QH) and outer-layer quench heaters and CLIQ (O-QH+CLIQ). The range indicates the spread of the simulation results depending on the quench location and the variation of cable parameters within their specification.

Hot spot	Cu/nCu, RRR, d	O-QH	O-QH+I-QH	O-QH+CLIQ
I_nominal	At min/max of spec	293-364 K	230-263 K	215-248 K
I_ultimate	At min/max of spec	312-389 K	253-290 K	237-273 K

Table 7-3: Peak voltage to ground in the triplet magnets in case of a quench using outer layer quench heaters (O-QH), outer and inner layer quench heaters (O-QH+I-QH), outer layer quench heaters and CLIQ (O-QH + CLIQ). The range indicates the spread of the simulation results depending on the variation of cable parameters within their specification.

Peak voltage to ground	Cu/nCu, RRR, d	O-QH	O-QH+I-QH	O-QH+CLIQ
I_nominal	At min/max of spec	304-619 V	438-592 V	521-658 V
I_ultimate	At min/max of spec	362-860 V	552-766 V	664-924 V

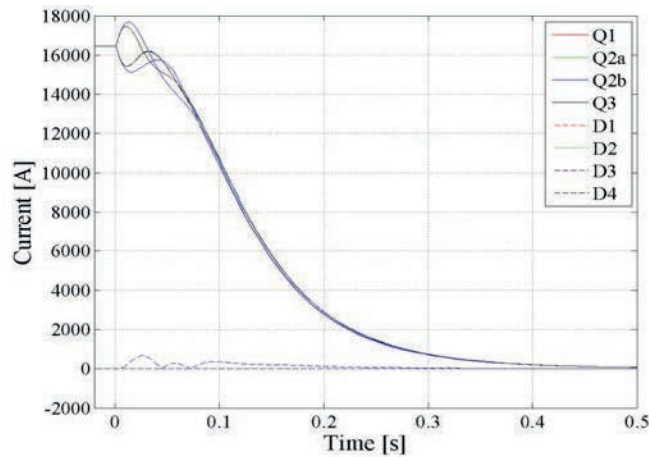


Figure 7-6: Simulated typical currents during a quench, when triggering outer-layer quench heaters and CLIQ. The current in the circuit before the quench is 16.5 kA. The currents in the trim circuits are all zero. D1, D2 and D4 are the currents through the crow-bar of the trim circuits for Q1, Q2a and Q3. D3 is the current through the parallel diodes of Q2b. Note: Q1=Q3, Q2a=Q2b and $I_{D1}=I_{D4}$, and $I_{D2}=I_{D3}$.

Table 7-4 shows the hot spot temperatures for the above mentioned combinations of protection systems in case of one (F1) or two (F2) quench heater circuits not functioning, for nominal circuit current and cable parameters. The temperature range indicates the spread of the simulation results due to the initial location of the quench. The results show clearly that the combination of two protection systems provides sufficient margin in case of such realistic failure scenarios. At ultimate circuit current the hot spot temperatures increase by about 20 K. In case of a non-functioning CLIQ system (O-QH+CLIQ) the hot spot temperatures would compare to the case of outer-layer heaters alone without failure. The currents in the parallel elements of the circuit would reach up to 2.5 kA for about 200 ms.

Table 7-4: Hot spot temperature in the triplet magnets in case of a quench, when one (F1) or two (F2) quench heater circuits do not function, using outer-layer quench heaters (O-QH), outer- and inner-layer quench heaters (O-QH+I-QH) and outer-layer quench heaters and CLIQ (O-QH + CLIQ). The range indicates the spread of the simulation results due to the initial location of the quench.

Hot spot	Cu/nCu, RRR,	Failure	O-QH	O-QH+I-QH	O-QH+CLIQ
I_nominal	nominal	-	330-345 K	251-253 K	236-238 K
I_nominal	nominal	F1	345-362 K	255-266 K	238-240 K
I_nominal	nominal	F2	363-384 K	277-283 K	239-242 K

7.3.2 Quench detection system (QDS)

The HL-LHC will incorporate new superconducting elements requiring dedicated protection systems. The upgrade of the quench detection system (QDS) will provide this functionality, including the related data acquisition systems, and the monitoring of the state of the protection systems and the protected elements. Special focus will be put on the quench detection systems for the Nb₃Sn magnets MQXA/B and the 11-T dipoles, due to the required faster reaction times and the effect of flux-jumps on the detection electronics.

The enhanced luminosity of the HL-LHC will increase the radiation levels in the dispersion suppressors to levels no longer compatible with the operation of radiation-tolerant electronics currently installed in those areas. The major part of the protection electronics will therefore be re-located to the new (radiation-free) underground galleries around IP1 and IP5 using long instrumentation cables or optical fibres to link to the protected elements. This facilitates the design of the quench detectors as well as the new communication links for supervision and data acquisition (DAQ), which can be entirely based on COTS components. Finally, advanced tools for remote diagnostics and maintenance will be provided.

7.3.2.1 Equipment performance objective

As requested by the magnet designers (see chapter 3) the reaction time of the QDS and magnet protection units has to be ~10x faster for Nb₃Sn magnets than for NbTi magnets. Simple and robust detection schemes have to be selected to achieve the required reliability and availability of the system. Instrumentation has a big impact on signal quality hence a sufficient amount of voltage taps and a clean signal-cable layout is crucial. Unlike for LHC's individually powered quadrupoles, superconducting bus-bar and magnet protection should be separated to avoid noise pick-up by the signal cabling.

Figure 7-7 shows an instrumentation scheme to protect a magnet assembly consisting of eight superconducting coils against single- and multiple coil quenches.

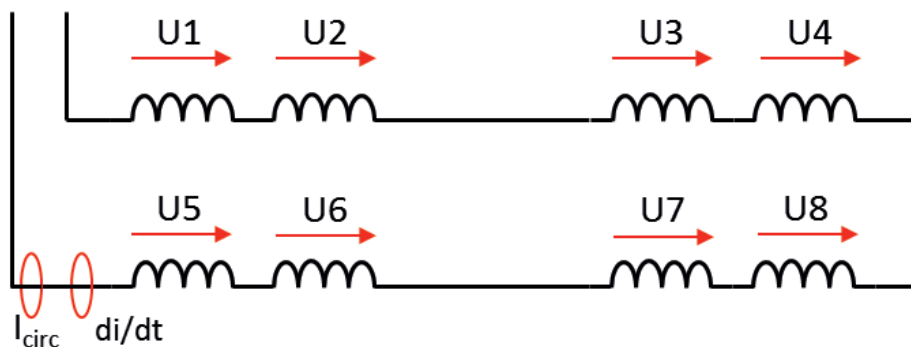


Figure 7-7: Instrumentation scheme to protect a magnet assembly consisting of eight superconducting coils against single- and multiple coil quenches. U1 – U8 are the voltages measured over the different 8 superconducting coils. I_{circ} is the circuit current and di/dt the first time derivative of the circuit current.

Comparing the coil voltages, the inductive part of the measured signal can be compensated. Quenches in single- or multiple coils can be detected depending on the comparison algorithm. The measurement of the circuit current as well as its derivative helps to protect the magnet against fully symmetric quenches. The voltages required for quench detection need to be provided by fully redundant voltage taps.

Nb₃Sn based magnets suffer from so-called flux jumps, which result in voltage spikes detected by the electronics. The QDS algorithm will therefore, be adapted in order to reduce its sensitivity to these signals. One possible implementation would be the use of operational state dependent parameters such as current dependent thresholds and evaluation times. This would require separate, galvanically isolated auxiliary input channels to measure the current in the circuit.

Due to the particularities of the protection scheme and isolation requirements, the quench detection algorithms will be implemented fully in the digital domain. This implies high-speed high-resolution sampling of the magnet signal to be able to detect quenches within the allowable time budget. Once a quench is detected, actions have to be taken by the detection electronics. Traditionally this is implemented with current loops opened and closed by electromechanical relays. Due to the small time budget, this technology has to be replaced by solid-state devices with switching times well below 1 ms.

The hardware capabilities of the data acquisition system (DAQ), the related communication links and the control system will be enhanced to allow for the required higher data transmission rates and advanced maintenance. Since the new galleries in P1 and P5 are free from ionizing radiation, an Ethernet based controls and DAQ system can be considered. The enhanced control system needs to be adapted to the foreseen accelerator controls environment.

7.3.2.2 Implementation

A unified approach is proposed for the HL-LHC quench detection system. All detection tasks are implemented using a universal quench detection system (uQDS) unit. This unit is equipped with 10 isolated polyvalent input channels. These channels amplify and digitize the signals and provide galvanic isolation. All signals are transmitted to an Field Programmable Gate Array (FPGA), which implements the quench detection algorithms. Each box is connected to the controls system via a dedicated communications interface. Figure 7-8 shows the system block diagram.

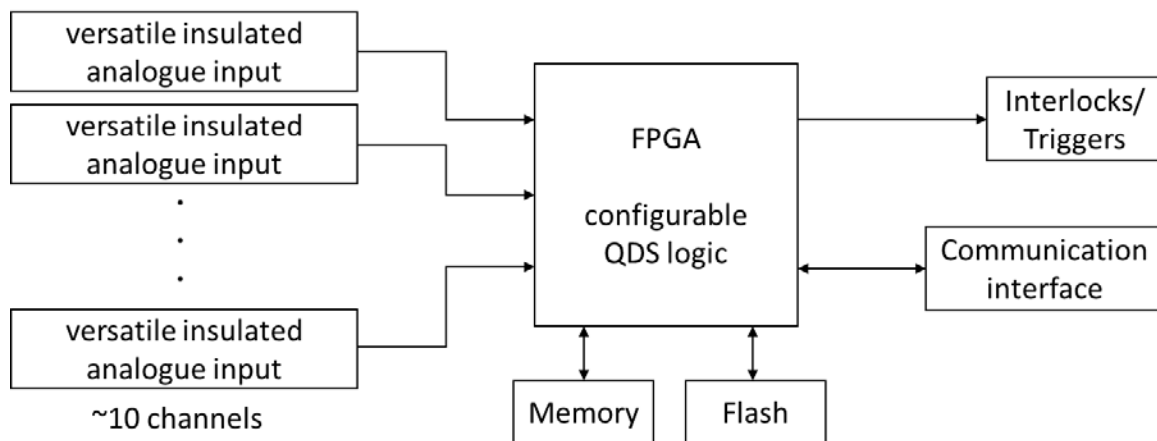


Figure 7-8: Block diagram of the universal quench detection system (uQDS) unit.

To ensure redundancy, two uQDS units are used in parallel. Multiple units can be connected in series to generate a common trigger for magnet assemblies requiring more than 10 channels for quench detection.

The polyvalent analogue input channel has a maximum input range of ±20 V. Equipped with pull-up resistors and without input voltage divider a safe detection of disconnected voltage taps is ensured. The programmable gain amplifier allows configuring each channel for various tasks like quench detection, current

lead protection, and splice supervision. Figure 7-9 shows a block diagram of one of the input channel designs under evaluation.

A dedicated high-density measurement unit with ~16 channels has to be designed for auxiliary tasks like quench heater supervision. Due to the large number of quench heater power supplies, a dedicated trigger distribution unit has to be implemented.

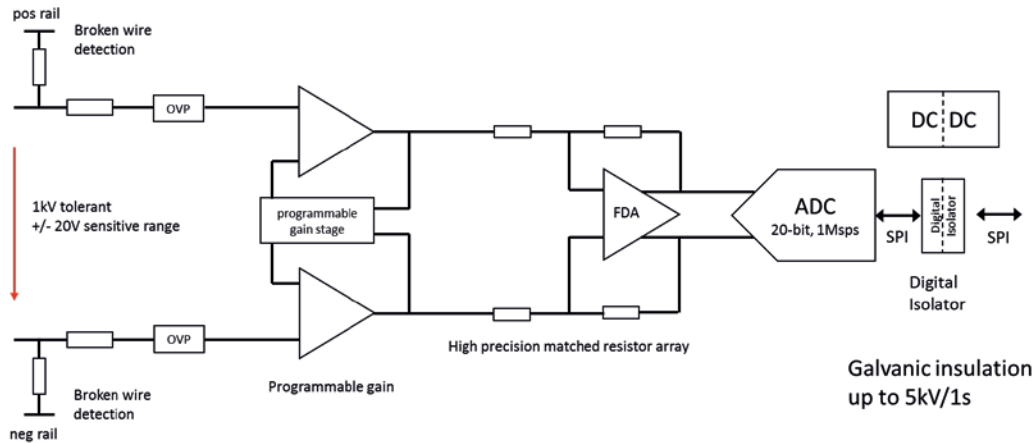


Figure 7-9: Block diagram of a polyvalent analogue input channel design under evaluation.

7.3.3 CLIQ

Coupling-Loss Induced Quench (CLIQ) is an innovative method for the protection of superconducting magnets after a quench [12-14]. Its fast and effective heating mechanism, utilizing coupling loss, and its robust electrical design make it a very attractive solution for high-magnetic-field coils. CLIQ technology has been successfully applied to magnets of different size, coil geometry, and type of superconductor.

The CLIQ system is schematized in Figure 7-10. It is composed of a capacitor bank C , a floating voltage supply S , two additional resistive current leads $CL1$ and $CL2$ connecting the system to the magnet, and a Bidirectional Controlled Thyristor (BCT) package. The positioning of connection of the current leads strongly affects the efficiency of the CLIQ system. These leads carry typically 10% of the nominal magnet current for about 100-200 ms, and can therefore be small. The capacitor bank is charged by S with a voltage U_C . Upon quench detection, the thyristors are activated resulting in a current I_C to be discharged through $CL2$. Part of this current flows through L_{2U} , whereas the remainder flows through L_{2L} . The BCT package allows continuous oscillations of I_C .

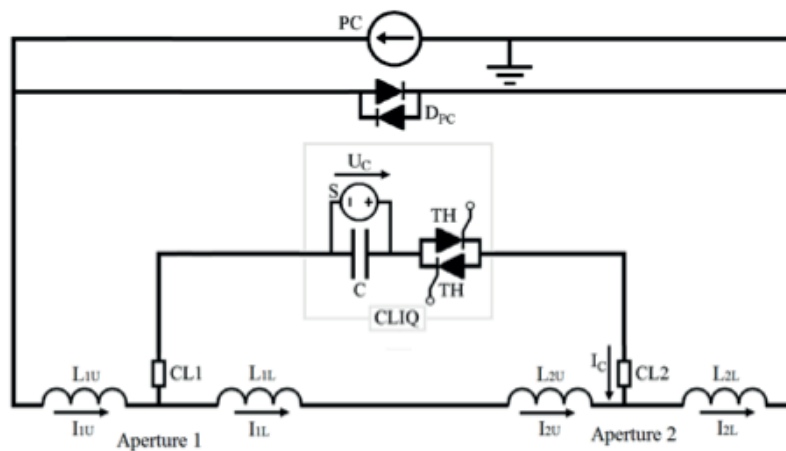


Figure 7-10: Schematic of a CLIQ unit connected to a magnet for its protection [12].

7.3.3.1 Equipment performance objectives

CLIQ in combination with the quench detection system assures that the peak temperatures and voltages to ground in the MQXF coils are maintained within safe limits. A detailed analysis of the magnet quench protection of the inner triplet circuits can be found in [14]. The CLIQ units connected to the magnets must comply with the same standards as quench heaters. As the units are directly connected to the magnets, every effort must be made for reducing the probabilities of a short circuit across a unit, or internal to a unit. A validation programme using prototype CLIQ units (developed and made at CERN), on HL-LHC model and prototype magnets, is on going within the different (present and future) magnet test programmes

7.3.4 Energy extraction system

Energy extraction systems (EE) are an integral part of the safety-critical quench protection systems, which are widely used in the existing LHC machine with a total of 234 installed facilities (202 for the 600 A corrector circuits and 32 for the main 13 kA dipole and quadrupole circuits). The systems are strongly circuit-specific, tailor-made for a particular set of requirements, and adapted to the local infrastructure.

The present 600 A electro-mechanical energy extraction switches will have to be replaced for the HL-LHC era. To allow for faster reaction times, which may be required for future superconducting magnets, the development of fast switches based both on semiconductors (IGBTs) and novel electro-mechanical vacuum switches is currently on-going. Alternatively, for slow switching times, classical electro-mechanical switches in combination with snubber capacitor banks, suppressing sparks, could be used.

Energy extraction systems for the high current circuits in HL-LHC (Triplet Q1-Q2a-Q2b-Q3, D1-D2 and Q4) have been removed from the protection schemes, as the amount of energy they are able to extract from the corresponding magnets is relatively small (in the 10% level). Their complexity, continuous power dissipation impacting operational costs, space required, and maintenance justify the study of alternative options. CLIQ systems constitute a solid protection method that together with quench heaters can provide sufficient protection for the circuits in the triplets.

The IGBT development programme for high current circuits is continuing as these IGBT switches will be required for the magnet and circuit tests at the superconducting magnet test facility (SM18) essential for the HL-LHC development programme. Recent results on the first IGBT prototype show very encouraging results.

The necessity of energy extraction systems for intermediate current levels (in the 1.5 to 2 kA range) is also under thorough analysis at the moment as most of the circuits in that range could also be protected by quench heaters. The pros and cons of these two options are being analysed. The complexity of integrating quench heaters in the coils has to be balanced versus the cost of developing new energy extraction systems based on mechanical switches. However, such development would anyhow be needed since new 600 A systems will be required for the LHC in the future due to a limited lifetime of the actual switches.

Finally, energy extraction for low-current (120-180 A), multi-pole correctors should be avoided by either designing self-protecting magnets or by including energy extraction resistors within the crow-bar of the converters. In the latter case, the maximum voltage across those resistors should be rated at 30-50 V as required by power converters.

If required, the new design of the extraction resistors (DQR) will be significantly different from those present in the LHC main circuits. The pursued characteristics and properties of these new energy absorbers are very fast recovery (cooling) times, compact design (minimized volume), and easily changeable resistance values.

7.3.4.1 Equipment performance objectives

The new energy extraction equipment for the HL-LHC will use a new generation of switches, incorporate the latest technology for high-current transmission, benefit from built-in features for facilitating diagnostics and

maintenance, offer systems that will minimize intervention time for accessing all parts of the facilities, and profit from the experience gained with the operation of the existing LHC energy extraction facilities.

7.3.5 Powering interlock system

The powering interlock system (PIC) ensures the presence of the correct powering conditions for the different electrical circuits with superconducting magnets in the LHC. At the same time, it guarantees the protection of the magnet equipment by interfacing the quench protection systems, the beam interlock system, the power converters, the cryogenic system, and technical services such as uninterruptable power supplies (UPS), emergency stop buttons (AUG), and controls. The PIC is a distributed system currently consisting of 36 individual powering interlock controllers, which manage the powering of each of the 28 powering subsectors [7].

7.3.5.1 Objective for HL-LHC machine performance

Magnet interlocks are required to guarantee safe magnet powering during all phases of operation from injection to collisions. In order to achieve this protection while maintaining the time constraints required for equipment protection, interlock electronics are usually installed close to the main clients (QPS and power converters) such as the UA, UJ, RR alcoves, UL or UR (see chapter 15). At the design luminosity for HL-LHC ($5 \times 10^{34} \text{ cm}^{-2} \text{ s}^{-1}$) the thermal neutron and high-energy hadron fluencies in the areas close to the tunnel will increase considerably with respect to the values for which the existing PIC has been designed. Additional changes and requirements from the new quench protection system will have to be reflected in the upgraded interlock system to assure the current dependability of the system during the HL-LHC era. For these reasons, a new design for the distributed I/O modules is required to cope with the increment of particle flux in the most sensitive areas. In addition, an upgrade of the industrial components used will very likely become necessary due to the obsolescence of the current PLC series and associated I/O modules being used.

7.3.5.2 Equipment performance objectives

The PIC was installed during 2006 and has been operating since the start of LHC operation in 2008. By the time the HL-LHC starts operation, the system will have been running for more than 15 years. Therefore, some of the electronics components will reach the end of their life expectancy, which can have an impact on the availability of the system. In addition, obsolescence of electronics parts needs to be addressed since some of the critical components of the system can no longer be purchased, affecting its maintainability. Furthermore, the increased radiation dose in certain areas will affect the most sensitive components of the PIC.

The upgrade of the PIC will address the issues mentioned above to adapt to HL-LHC requirements. In addition, the system will be reviewed to provide enhanced diagnostics of the safety-critical hardwired loops in line with the upgrades foreseen for the quench protection system. The implementation of triple redundancy in combination with two-out-of-three voting is being considered for the quench loop of main circuits, however detailed dependability studies have to confirm the expected benefits of such architectures.

7.4 Availability requirements to achieve HL-LHC goals for integrated luminosity

The challenging goals of total integrated luminosity of the HL-LHC project require a high level of accelerator availability and operational efficiency. The expected integrated luminosity production as a function of machine availability is discussed below. The following figures are to be considered when evaluating LHC availability:

- **The time with colliding beams (stable beams):** this quantity must be optimized by operators depending on the observed distributions of turnaround time, downtime and luminosity lifetime. Stable beam optimization will be particularly relevant for operation with leveled luminosity.
- **The turnaround time:** the time to go from the beam dump of a given fill during stable beams to the beginning of stable beams of the next fill, when no faults occur. This quantity has a minimum value determined by the durations of the LHC cycle phases. Efforts must be devoted to reaching this minimum

value. Parallelizing/combining machine modes (e.g. collide and squeeze) is one possibility to optimize the turnaround time.

- **The machine downtime:** the time to clear machine faults and recover operating conditions for beam injection. It includes the time for expert diagnostics and intervention, possibly requiring access to the LHC tunnel. Downtime of LHC injectors is considered also as downtime for the LHC, provided that the LHC is requiring beam. In the following, a distinction is made between the downtime following protection dumps (longer, as it includes beam-induced quenches, training quenches, loss of cryogenic conditions due to equipment failures, etc.) and the downtime following operator dumps (shorter, typically including time for beam setting-up in the injectors and minor equipment failures). While the last is not expected to change significantly for HL-LHC, the downtime following protection dumps is considered more susceptible to changes: it could increase due to the effects of increased energy and intensity or be reduced due to the improved operational experience (e.g. management of BLM thresholds).
- **The fraction of premature dumps:** the percentage of fills dumped by the protection systems due to failures.

For the following extrapolations of the expected total integrated luminosity per year during HL-LHC operation, a fraction of the 2016 LHC run (from 11th June to 25th July) is taken as a reference for the statistics. This represents a stable period of luminosity production (same number of injected bunches, filling scheme and optimal fill length), when the average turnaround time was about 4.5 h, after subtracting the faults occurred. A detailed analysis of the turnaround revealed that its duration is in first approximation independent from the reason of the dump of the previous fill (due to a failure or by an operator). The theoretical minimum turnaround time for the adopted filling scheme is 2.52 h, revealing margins for improvement. The main driver for the longer turnaround time is the injection process, which lasts on average about double the theoretical minimum. For HL-LHC operation, considering slightly longer current ramps due to the increased energy to 7 TeV, an optimized filling scheme with 288 bunches per injection (in the reference period the maximum number of injected bunches was limited by the degraded conditions of the SPS dump), and considering the additional complexity of running with higher brightness beams, 4.5 h is assumed as a realistic turnaround. The shorter luminosity levelling time of the new HL-LHC baseline leads to a reduction of the optimal stable beams duration. This makes the turnaround a sensitive parameter for the overall optimization of HL-LHC performance.

Making predictions for the downtime distribution for HL-LHC operation is not trivial, as many factors will play an important role. The increased energies and intensities will result in higher radiation levels, which could have a direct impact on the observed number of single event effects (SEE) per year and on long-term effects on components due to the total integrated dose (TID). Mitigations for these effects have been deployed during LS1, with a major relocation of sensitive equipment in protected areas of the LHC tunnel. These measures have proven to be effective in operation in 2015 and 2016. Furthermore, it is foreseen that a new generation of electronics systems will be designed before the HL-LHC era. New designs should cope with such radiation levels.

The increased beam energy and intensities may have an impact on the rate of Unidentified Falling Objects (UFO)-induced beam dumps due to localized losses. Experience shows that optimization of BLM thresholds, supported by an improved understanding of quench levels, helps in reducing the number of UFO dumps, while minimizing the number of quenches. Given the sensitivity of HL-LHC luminosity production on the turnaround time, machine availability should be preserved by reducing the number of unnecessary UFO-dumps and tolerating a limited number of quenches.

For what concerns equipment availability in the HL-LHC era, components will operate closer to design limits and partially reach their end-of-life. No significant increase of equipment failure rates (e.g. for magnet power converters) has been observed while increasing the energy from 4 TeV to 6.5 TeV. This gives confidence that the achieved equipment reliability could be maintained, provided that ageing effects will be mitigated. In

2016 equipment unavailability has been mainly dominated by long stops due to external events (e.g. perturbations of the cryogenics system and the electrical network, floods in the underground areas requiring the exchange of some cables of vital systems or the damage of electric network transformers).

The introduction of crab cavities will possibly give a notable gain of machine performance, but will also bring additional complexity and introduce new, very fast failure modes. The reliability of crab cavities in operation should be such that the resulting gain in integrated luminosity will be significant despite the occurrence of new failure modes. The SPS crab cavity test could give the first hints for an estimate of their reliability.

A Monte Carlo model [10], [11] of LHC availability was used to qualitatively assess the combined impact of all these factors on integrated luminosity production for HL-LHC. A sensitivity analysis has been carried out with respect to the average downtime following protection dumps and the fraction of premature dumps. The results for 160 days of HL-LHC operation are presented in Figure 7-11. Updated HL-LHC parameters were considered: 7 TeV, $5 \times 10^{34} \text{ s}^{-1} \text{ cm}^{-2}$ levelled luminosity, 5 h levelling time, 5 h luminosity lifetime (assuming an exponential decay) and 9.2 h optimal stable beams duration were assumed.

The results show that, considering availability figures from the reference period of 2016 (5.6 h average downtime and 50% premature dumps), about 270 fb^{-1} could be produced in 160 days of HL-LHC operation. This is equivalent to a stable beams efficiency of 45%, i.e. the percentage of time allocated for physics production, which is spent in stable beams. This needs to be compared to the goal of 250 fb^{-1} per year for the nominal HL-LHC and 320 fb^{-1} in case of ultimate performance.

It was estimated that for the same availability figures, the previous HL-LHC baseline described in the TDR.V0 would have achieved about 300 fb^{-1} , yielding 10% better performance with respect to the new baseline. The results of the sensitivity analysis can be used to provide guidelines for future system designs, indicating the reliability (i.e. number of provoked dumps for a given system) and maintainability (i.e. the resulting average downtime) targets to be achieved.

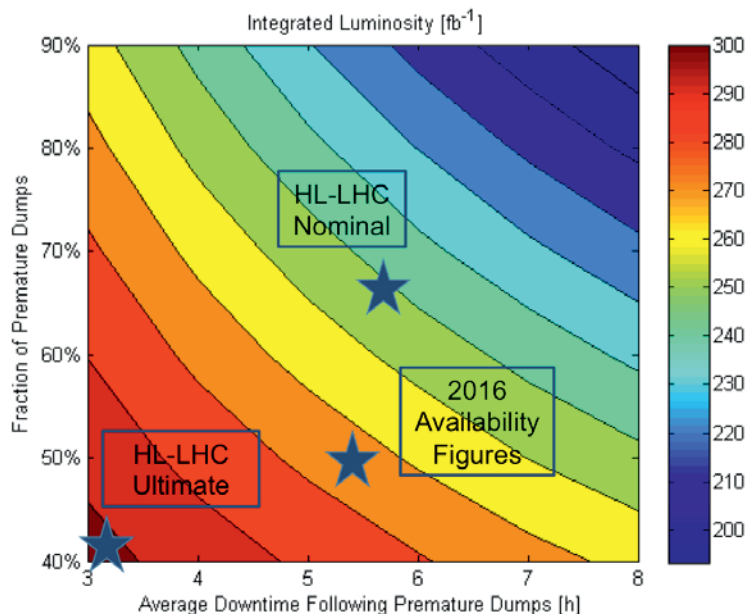


Figure 7-11: Sensitivity analysis of integrated luminosity over 160 days of operation to the machine failure rate and average fault time. The stars indicate the achievable yearly integrated luminosity based on the availability figures of the 2016 reference period and the goals for nominal (250 fb^{-1}) and ultimate (320 fb^{-1}) HL-LHC performance.

7.5 References

- [1] O. Bruning, HL-LHC Parameter space and scenarios, Proc. Chamonix 2012 workshop on LHC Performance, CERN-2012-006 (2012) p. 315. DOI: [10.5170/CERN-2012-006.315](https://doi.org/10.5170/CERN-2012-006.315)
- [2] N.A. Tahir, J.B. Sancho, A. Shutov, R. Schmidt and A.R. Piriz, Impact of high energy high intensity proton beams on targets: Case studies for Super Proton Synchrotron and Large Hadron Collider, *Phys. Rev. ST accel. Beams* **15** (2012) 051003. DOI: [10.1103/PhysRevSTAB.15.051003](https://doi.org/10.1103/PhysRevSTAB.15.051003)
- [3] R. Filippini, B. Goddard, M. Gyr, V. Kain, R. Schmidt, J. Uythoven and J. Wenninger, Possible causes and consequences of serious failures of the LHC machine protection systems, 9th European Particle Accelerator Conf., Lucerne, Switzerland, 5–9 July 2004, p. 620. [LHC-Project-Report-755](https://arxiv.org/abs/hep-ex/0407011)
- [4] M. Werner, Einrichtung zur Bestimmung der Stärke des Magnetfeldes eines Elektromagneten, Patent DE102005045537B3 28.12.2006, September 2005.
- [5] T. Baer et al., Very fast crab cavity failures and their mitigation, Proc. IPAC'12, May 2012, pp. 121–123, MOPPC003. [CERN-ATS-2012-106](https://arxiv.org/abs/1205.1066)
- [6] M. Werner, M. Zerlauth, A. Dinius and B. Puccio: Requirements for the fast magnet current change monitors (FMCM) in the LHC and SPS-LHC transfer lines, LHC-CIW-ES-0002, EDMS [678140](https://cds.cern.ch/record/678140).
- [7] R. Schmidt, B. Puccio, M. Zerlauth: The hardware interfaces between the powering interlock system, power converters and quench protection system', LHC-D-ES-0003, EDMS [368927](https://cds.cern.ch/record/368927).
- [8] P. Dahlen, R. Harrison, R. Schmidt and M. Zerlauth, The warm magnet interlock system for the LHC ring, LHC-CIW-ES-0003, EDMS [653548](https://cds.cern.ch/record/653548).
- [9] B. Todd *et al.*, Workshop on Machine Availability and Dependability for Post-LS1 LHC, Proc. Workshop, CERN (2013).
- [10] A. Apollonio *et al.*, HL-LHC: Integrated luminosity and availability, 4th International Particle Accelerator Conference, Shanghai, China, 12 - 17 May 2013, pp.1352. [CERN-ACC-2013-0066](https://arxiv.org/abs/1305.1066)
- [11] A. Apollonio *et al.*, Update on predictions for yearly integrated luminosity for HL-LHC based on expected machine availability, 5th International Particle Accelerator Conference, Dresden, Germany, 15 - 20 Jun 2014, pp. [TUPRO015](https://arxiv.org/abs/1406.1015).
- [12] E. Ravaioli, CLIQ. A new quench protection technology for superconducting magnets, PhD thesis University of Twente, 2015. [CERN-THESIS-2015-091](https://arxiv.org/abs/1509.09101)
- [13] V.I. Datskov, G. Kirby, and E. Ravaioli, "AC-Current Induced Quench Protection System", EP13174323.9, priority date: 28 June 2013.
- [14] E. Ravaioli *et al.*, Advanced Quench Protection for the Nb₃Sn Quadrupoles for the High Luminosity LHC, IEEE Trans. Appl. Supercond. 26 (2016) 4002006. DOI: [10.1109/TASC.2016.2524464](https://doi.org/10.1109/TASC.2016.2524464)
- [15] Conceptual Design Review of the Magnet Circuits for HL-LHC, 21.-23.03.2016, CERN, Switzerland. INDICO: [477759](https://indico.cern.ch/event/477759)

Chapter 8

Interface with experiments

8 Interface with experiments

8.1 Introduction

The High Luminosity LHC (HL- LHC) project aims to increase the integrated luminosity of LHC by a factor 10 beyond its design value for the two interaction regions in the ATLAS and CMS experiments, whilst maintaining beam collisions in all four experiments. In particular, the upgrade efforts, which are shared between the machine and the experiments, aim at operating the LHC accelerator with a peak luminosity of $5 \times 10^{34} \text{ cm}^{-2} \text{ s}^{-1}$ with levelling (140 PU), and deliver 250 fb^{-1} per year to achieve 3000 fb^{-1} in twelve years of operation. Key ingredients for the luminosity increase are larger apertures in the focusing sections around the experiments, higher beam intensities and optimised collision and luminosity levelling schemes, described in detail in Chapter 2. In Table 8-1 the targeted luminosities for HL-LHC proton operation are listed for the four experiments.

The HL-LHC will be more oriented towards high-luminosity/low β^* operation than the present LHC. Very high β^* running will have to end with LS3. The upper limit for β^* for physics at top energy is expected to get reduced to about 30 m.

Table 8-1: Nominal design luminosities for p-p operation for the HL-LHC. In parenthesis the value envisaged as “ultimate”. The luminosities for the LHC Run-2 are also included for comparison. Total targeted integrated luminosity in CMS and ATLAS is 3000 fb^{-1} about 12 years after upgrade.

Experiment	Peak Luminosity [$\text{cm}^{-2} \text{ s}^{-1}$]		IP
	HL-LHC	LHC	
ATLAS	$5(7.5) \times 10^{34}$	$1(2) \times 10^{34}$	1
CMS	$5(7.5) \times 10^{34}$	$1(2) \times 10^{34}$	5
ALICE	1×10^{31}	1×10^{31}	2
LHCb	2×10^{33}	2×10^{33}	8

The ATLAS and CMS experiments will be upgraded progressively during the planned LS2 and LS3 long-shutdowns of the accelerator, LS3 upgrade being the one addressing the challenges of the high luminosity regime. The experimental upgrade program focuses on the inner tracker, trigger system, calorimeter and muon detection systems, by replacing existing components with new ones capable of operating at the foreseen pile-up density, increased radiation environment and minimisation of activation, described in detail in several TDR documents submitted to LHCC [1][2][3][4].

Besides the high-luminosity experiments, the ALICE and LHCb experiments will be upgraded and continue operations during HL-LHC. The ALICE experiment, for which a detector upgrade is planned during LS2, will continue on the Pb-Pb ion and proton-Pb ion collision program aiming to collect in total 10 nb^{-1} Pb-Pb collision data up to LS4. As ion beams will be available during HL-LHC, i.e. after LS3, the ATLAS and CMS experiments will also participate in the Pb-Pb and p-Pb collision program within the capabilities and constraints from the upgraded inner triplet magnets and available apertures. The LHCb experiment plans for a major upgrade during LS2 to allow operating at instantaneous luminosities of $2 \times 10^{33} \text{ cm}^{-2} \text{ s}^{-1}$, that remains compatible with the present magnet layout of the machine in LSS8. The introduction of a TAN is planned to

protect the D2 dipole and the downstream cryogenic magnets from the collision debris. Operating in these conditions, LHCb expects to collect 50 fb⁻¹ of data until LS4, when a second major upgrade of the detector might be envisaged that would open the possibility of operating at around the LHC nominal luminosity of 2×10³⁴ cm⁻² s⁻¹, for collecting 300-500 fb⁻¹ of data to fully exploit the flavour physics potential of LHC. This later major upgrade is presently under study within the HL-LHC project, in particular to understand the implications on the beam operation and impact to the ATLAS and CMS experiments, and to anticipate modifications to the installed hardware in LSS8 in view of optimizing interventions before the increased activation levels. In Figure 8-1 shows a graphical representation of the planned LHC operation and key upgrade efforts for the four experiments. In the present considerations for the HL-LHC project, no forward physics experiments will be operated in the LHC tunnel after LS3 in LSS1 and LSS5, apart from the detectors required for the ion operation. The presently installed elastic scattering and diffractive physics experiments TOTEM and ATLAS/ALFA, AFP are assumed to be dismantled during LS3.

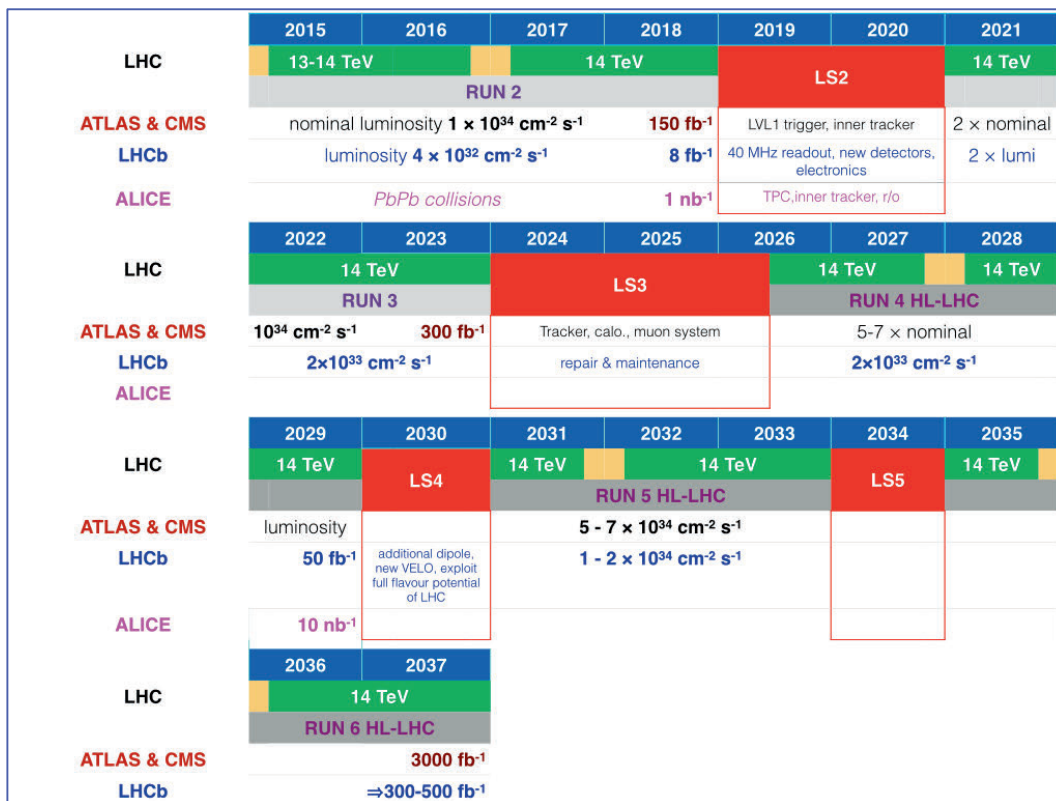


Figure 8-1: Graph showing the foreseen LHC and HL-LHC operation plans for the four experiments. The key activities per experiment are indicated, as well as the expected integrated luminosities. The periods in red indicate the long-shutdowns of the LHC accelerator, with the ones following LS3 considered as tentative only. The HL-LHC program starts after LS3 in 2026.

The definition of the Machine-Experiment Interface framework is described in [5] and done together with WP 2. The interface activities can be classified in three areas with obvious links between them:

- **Beam design:** definition of beam optics, layout and parameters, apertures, pile-up and impact to experiments, overall performance that lead to the set goal of the integrated luminosity as described above;
- **Beam operations:** signal exchange, machine and experiment protection, background conditions to assure the safe, high-efficiency operation of the machine and the experiments;

- **Equipment:** experimental beam pipe, shielding layout, passive forward absorbers for charged and neutral particles to protect machine equipment exposed in the high-flux of debris from the interaction point and also from secondary's produced at the beam impact on collimators.

8.2 Beam design

The key features of the beam design to match the requirements on the luminosity conditions for the ATLAS and CMS experiments are described in detail in Chapter 2. What remains a challenging task for the experiments is the handling of the expected pile-up density and the resulting requirements from the experiments. The main ideas to control pile-up and pile-up densities are exposed in the Chapter 2 of this report and many of them, especially for pile-up density control, are still at the level of options under study.

8.3 Beam operations

Extensive experience is gained so far with the operation of the LHC and the experiments during Run 1 and the present Run 2. The major operational issues on the machine-experiment interface are addressed, and viable solutions are found on issues like:

- signal exchange, for experiment and machine status and information;
- beam tuning for luminosity optimization during operations;
- safety interlock signals to protect sensitive experimental equipment from failure cases;
- beam induced background to the experiments.

The active beam monitoring system using the BLMs and potential fast 3-turns beam dump will be maintained for the Machine Protection system (see chapter 7) and further improved for HL-LHC possibly including signals from the inner or near-beam detectors from the experiments.

With the upgraded layout of the machine in the high-luminosity regions around IP1 and IP5 substantial effort must be invested to estimate the expected background to the experiments and possibly reduce their impact to the physics performance of the detectors. The LHC background working group brings together experts from the four LHC experiments (ATLAS, CMS, LHCb, ALICE) and coordinates the studies. Particular effort is made to develop common tools and share the knowledge and experience from the present LHC operation. The impact of the expected aperture model for background to the experiments is evaluated and feedback is given to the beam design teams. Beam induced backgrounds increased in Run 2 compared to Run 1. This was generally expected and can be attributed to:

- increased beam energy resulting in more synchrotron radiation and dynamic pressure rise;
- doubling the number of bunches, reducing the bunch spacing from 50 ns to 25 ns increasing electron cloud effects;
- reduced β^* and tighter collimator margins.

Details are presently under study. An early conclusion to be confirmed by further studies is, that backgrounds in fact significantly increased from Run 1 to Run 2, and that a further increase is expected for the HL-LHC, but that it is very likely that the signal to background ratios will remain well acceptable for the high luminosity experiments.

Studies involving experts from the machine and the experiments are ongoing on the possible operation scenarios including crabbing schemes, luminosity levelling, collision crossing angles, etc. The goal is to evaluate the limits from the detectors like the pile-up density that can be afforded whilst maintaining the high-efficiency for the physics signals. Furthermore, studies on possible accident scenarios and associated risks for the machine and experiments are initiated. The studies address failure scenarios of machine components during operation using particle tracking codes through the LSS magnetic elements like: crab cavity failures [6][7],

asynchronous beam dumps, or rarer events like mechanical failures with obstacles in the beam, to name the major ones.

The induced background and radiation to the experiment in the case of these events will be evaluated and protection measures will be suggested and studied to mitigate the risks. The radiological impact in these scenarios will be evaluated in the collaboration with WP10, Radio Protection experts and experts from the experiments and, when required, mitigation solutions will be developed like the correct choice of materials, special tooling and optimized procedures for maintenance and repair actions. This work will be part of the subject of the Working Group “Interventions in Radioactive Areas of HL-LHC” setup to provide the forum for exchange of information and expertise towards developing common optimized approaches within the project.

8.4 Equipment

The hardware and equipment involved in the machine-experiment interface for HL-LHC operation include:

- The experimental beam pipes, covering in particular the part around the interaction region but more widely the design, handling and operation procedures for the vacuum sector from Q1-left-to-Q1-right.
- The passive absorbers for charged (TAXS) and neutral (TAXN) particles designed to primarily protect the nearby superconducting magnets from the radiation coming out from the interaction region, and simultaneously provide a background reduction to the experiments for beam interactions in the collimators and beam gas,
- The forward shielding in the experimental caverns, in particular the part that is close to the LHC machine tunnels, is designed to minimize the background radiation in the detectors and to protect personnel from the highly activated elements during access and maintenance activities.

The design considerations and required upgrades and modifications for the HL-LHC operation are described in the next sections.

8.4.1 The experimental beam pipes

An upgrade program for the vacuum pipe in all four experiments is planned and for some realized already in LS1. In general, for all experiments the inner pipe diameter around the IP has been (or will be) reduced with respect to the initial one, to allow new or additional detectors to be placed closer to the interaction point. The new inner pipe diameters are shown in Table 8-2. The new apertures are compatible with the HL-LHC parameters and no operation with high- β values are foreseen. No further modification of that part would be required.

Table 8-2: Original and reduced inner beam pipe radii located at the IPs vicinity.

IP	Original r_{\min} [mm]	Reduced r_{\min} [mm]	Experiment	When
1	29	23.5	ATLAS	LS1
2	29	18.2	ALICE	LS2
5	29	21.7	CMS	LS1
8	5	3.5	LHCb, VELO	LS2

The activation levels in the experimental beam pipes, in particular for the high-luminosity experiments ATLAS and CMS, and the activation levels in vacuum chambers and the central tracking detectors need to be considered already during Run 2 but in particular after few years of operation in Run 3 at high-luminosity. The development of special handling tools and careful planning during maintenance activities and final dismantling would be needed to minimize the dose during interventions.

8.4.1.1 Beam pipe for ATLAS

For ATLAS the central beryllium beam vacuum chamber of 7.382 m length and placed around the interaction point was exchanged to a new one with reduced aperture of 47 mm to accommodate the new inner pixel detector layer (IBL) as shown in Figure 8-2.[8]

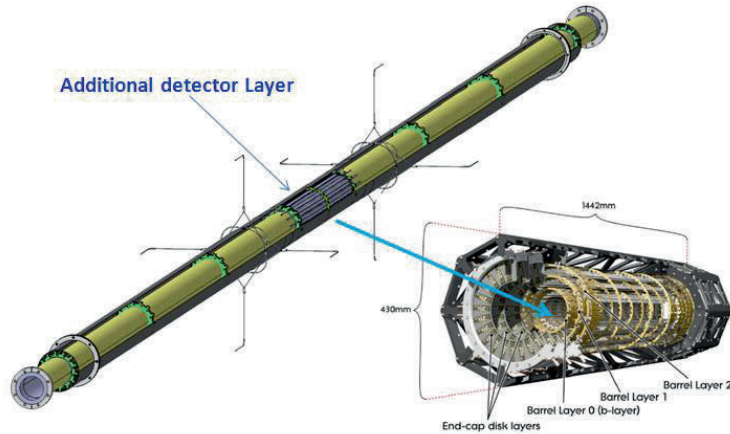


Figure 8-2: The updated ATLAS central vacuum chamber and the new inner detector.

The conical vacuum chambers up to the forward TAS absorber were also exchanged to new aluminium ones in order to minimize the material activation and dose during interventions. The already installed permanent bake-out system is maintained. The last part of the conical chambers upstream of the TAS and the chamber support system would have to be exchanged during LS3 to adapt to the new apertures and layout as explained in the following sections.

8.4.1.2 Beam pipe for CMS

A new 6.24 m long central beryllium vacuum chamber was installed in CMS during LS1. with a reduced aperture. The new chamber has an aperture of 58 mm which reduces down to 43.5 mm over the central length of 2.915 m, [9] The new reduced aperture central beryllium chamber allows space to accommodate an additional pixel detector layer as shown in Figure 8-3.

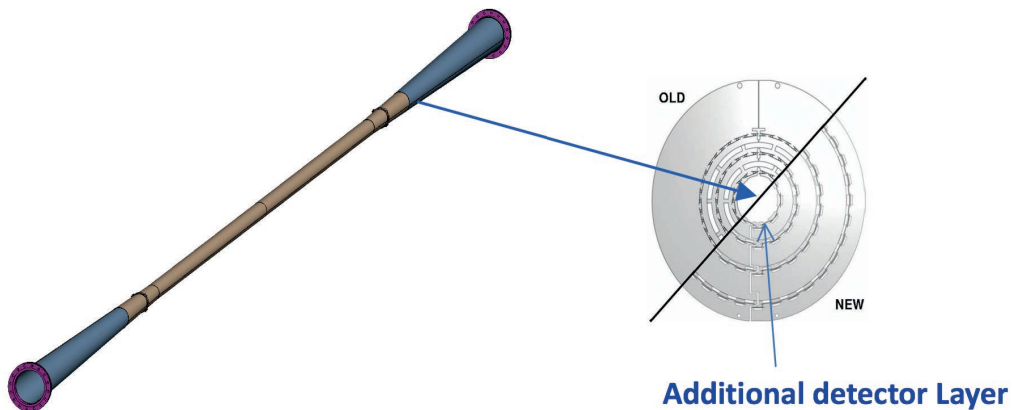


Figure 8-3: The updated CMS central vacuum chamber and the new configuration of the inner detector pixel layers.

The conical vacuum chambers up to the forward TAS absorber will be exchanged to aluminum ones during LS2 to minimize activation and dose during interventions. As for ATLAS, the last section will be further modified during LS3 to adopt to the new layout and apertures for HL-LHC operation. No permanent bake-out

system is installed. The pumping station presently installed at the end of the experiment will be moved forward towards the TAS region as indicated in Figure 8-4.

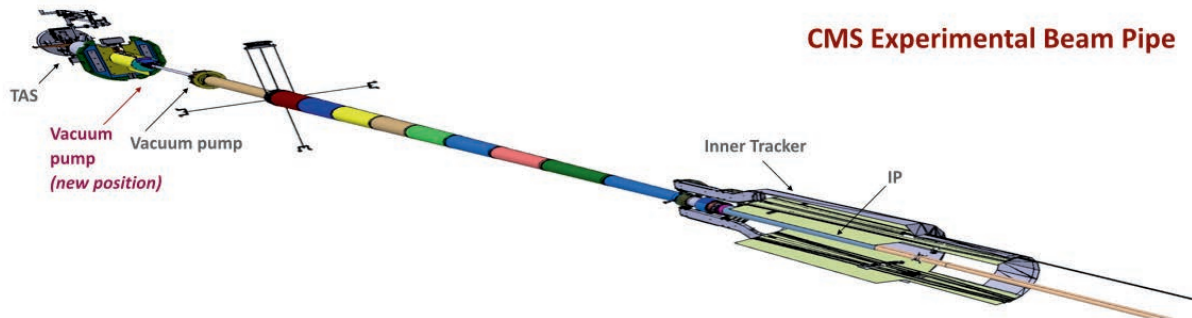


Figure 8-4: The full CMS vacuum chamber layout (single side) from the IP to the TAS. The present and future position of the proximity pumping station is indicated.

8.4.1.3 Beam pipes for ALICE and LHCb

New reduced-aperture central vacuum chambers will be installed during LS2 for ALICE and LHCb. No further changes to the vacuum chamber geometry and layout is needed for HL-LHC operation.

The LHCb updated VELO detector will operate in the same mode as presently: open to 30mm aperture during injection, ramp, squeeze and adjust and only moved to the 7 mm aperture once stable physics mode is established in the machine

8.5 The passive forward absorbers

The high-luminosity regions of LHC at P1/ATLAS and P5/CMS are equipped with passive absorbers for charged (TAS) [4] and neutral (TAN) [5] particles. They are installed on both sides of the interaction region at the transition of the experimental caverns to the LHC tunnel (TAS), and the transition to the separate beam pipes for the two beams (TAN). Their main function is to reduce the heat load and radiation for superconducting quadrupoles in the straight section, primarily the inner triplet quadrupoles Q1-Q3 for the TAS, but also D2 and Q4, from the collision debris out of the interaction region. In parallel the TAS completes the forward shielding of the experiments and both the TAS and TAN participate in the background reduction to the experiments.

For the HL-LHC operation, the following modifications are foreseen:

- New TAS and TAN absorbers on either side of **IP1** and **IP5**, called **TAXS** and **TAXN** respectively replacing the existing ones. The protection must be extended to D1 magnets that in HL-LHC will be superconducting (while it is normal conducting in the present LHC). The new absorbers must have an aperture adapted to the HL-LHC beam optics and operation and should be designed to cope with the increased energy deposition.
- A new **TAXN** absorber is planned for **IP8** designed to operate at the foreseen $\times 5$ higher luminosity ($2 \times 10^{33} \text{ cm}^{-2} \text{ s}^{-1}$), already after LS2. The TAXN absorber is a reduced version of the ones foreseen at IP1 and IP5 due to the reduced luminosity. The installation of a TAXS absorber around IP8 is not required for this luminosity. If in the future the operation of LHCb/IP8 foresees a higher luminosity, reaching the LHC nominal luminosity of $1-2 \cdot 10^{34} \text{ cm}^{-2} \text{ s}^{-1}$, a TAXS absorber would need to be installed in IR8, together with a full TAXN absorber as presently installed in IP1 and IP5. Preliminary studies showed that it would be possible to accommodate a TAXS installation around the LHCb experiment, however as this upgrade is not presently included in the HL-LHC project baseline, it is not further discussed in this document.

All new absorbers for P1 and P5 will be designed to operate at $5 \times 10^{34} \text{ cm}^{-2} \text{ s}^{-1}$ luminosity conditions during HL-LHC as defined above. As any other HL-LHC equipment, the engineering used to guarantee the nominal design operation may allow to enhance operation up to $L_{\text{levelling}}$ of $7-7.5 \times 10^{34}$.

8.5.1 The charged particle passive absorber - TAXS

The TAXS absorber is located at approx. 19 m from the interaction point on either side of IP1 or IP5. Its core is a 0.5 m diameter and 1.8 m long copper cylinder traversed on its axis by a constant aperture beam pipe. The design of the new TAXS absorbers for HL-LHC for IP1 and IP5 is based on the existing ones, thus maintaining the same shielding configuration, with the following modifications and improvements:

- The beam pipe aperture increases to at least 57 mm in diameter from the present 34 mm. Studies are ongoing to validate this aperture with all possible beam optics foreseen for HL-LHC operation and impact to the background conditions for the experiments. It may increase, however its internal diameter is limited to a maximum of 60 mm.
- The cooling power increases to dissipate the approx. 780 W deposited in the TAXS during beam operation conditions of HL-LHC including a safety margin (see [14]).
- The overall design of the TAXS remains compatible with the mechanical and envelope constraints from the surrounding shielding of the experiments.

The TAXS design is described in detail in the Technical Specifications Documents for IP1 [14] and IP5 [15] respectively. The key design and operation parameters are shown in Table 8-3 and Table 8-4 below.

Table 8-3: TAXS design parameters from ref. [14].

Characteristics	Units	Value
Distance from IP1 to front flange	[mm]	19050
TAXS absorber length	[mm]	1800
TAXS absorber diameter	[mm]	500
Nominal beam height from floor	[mm]	1100 at IP1 and 950 at IP5
Nominal longitudinal tunnel slope		+1.236 % at IP1 and -1.236 % at IP5
Nominal transverse tunnel slope		0.0 %
Maximum floor loading	[MPa]	<0.5
Flange types: rear front		CERN ConFlat, 316LN ss Helicoflex Quick Disconnect System Class 300
Beam tube straight absorber section (two beams in one tube) Inner radius	[mm]	29.8 IR
Mechanical tolerance (radius)	[mm]	± 0.2
Beam tube tapered section away from absorber section (two beams in one tube) IP side	[mm]	29.8 to 31.5 mm IR,
Q1 side	[mm]	29.8 to 50 mm IR,
Mechanical tolerance (radius)		± 0.2
Vacuum chamber to alignment fiducial tolerance	[mm]	± 0.6
Supports range of motion		± 30 mm at installation, 5.0 mm horiz. and vert. Stops in z (beam axis) at operation.
Absorber cooling		Water and ambient air

Table 8-4: TAXS operation parameters from ref. [15].

Characteristics	Units	Value
Aperture diameter	[mm]	60
Absorbed collision power at $5 \times 10^{34} \text{ cm}^{-2} \text{ s}^{-1}$	[kW]	0.5
24 hr average absorbed collision power (80%)	[kW]	0.4
Maximum internal beam tube temperature at $5 \times 10^{34} \text{ cm}^{-2} \text{ s}^{-1}$	[C]	<85
Peak power density	[mW/cm ³]	290
Peak dose	[GGy]	2
Baking temperature	[C]	200
Lifetime alignment operations [1 per opening]		20

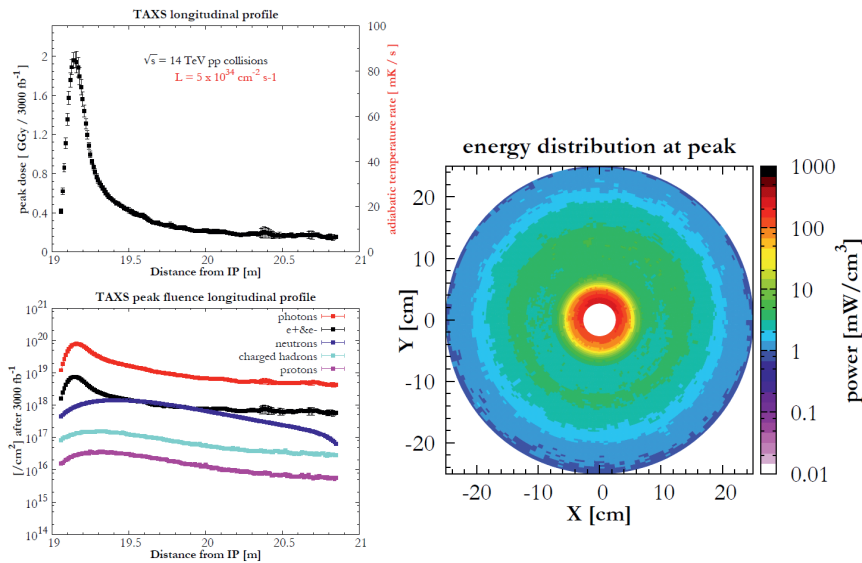


Figure 8-5: Energy deposition in the TAXS from FLUKA simulations. An aperture of 54mm is considered in these simulations.

Besides the TAXS upgrades, the equipment layout in the TAXS-Q1 region is modified with the following guidelines:

- Improve the precision on the beam position, important for the optimised beam levelling during HL-LHC operation.
- Eliminate the need of interventions in the TAS-Q1 region that are very difficult due to the constrained space and expected radiation levels.
- Provide a He insulation between the tunnel and the experimental side in order to allow safe work at the cavern.

In particular, the following modifications are foreseen:

- The warm BPM installed in the TAS-Q1 section is now embedded in the Q1 cryostat. This allows a better (direct) alignment of the BPM to the Q1 bore, for increased beam positioning precision and eliminates alignment and maintenance operations.
- All vacuum equipment (valves, pumping stations, gas injection lines) are moved to the upstream side of the TAXS towards the experiment. The installation on the experimental side requires some minor modifications to the installed forward shielding of the experiments. At the same time, it allows the optimization of the interventions, as much simpler space constraints exist any longer, adopting remote handling methods in compliance with the ALARA principle and minimizing the down-time for the

accelerator in case of problems. The impact on the required shielding modifications to the experiments is minimal.

- Q1 will be extended to include the BPM in the secondary vacuum, improving its alignment and reducing the need of interventions.

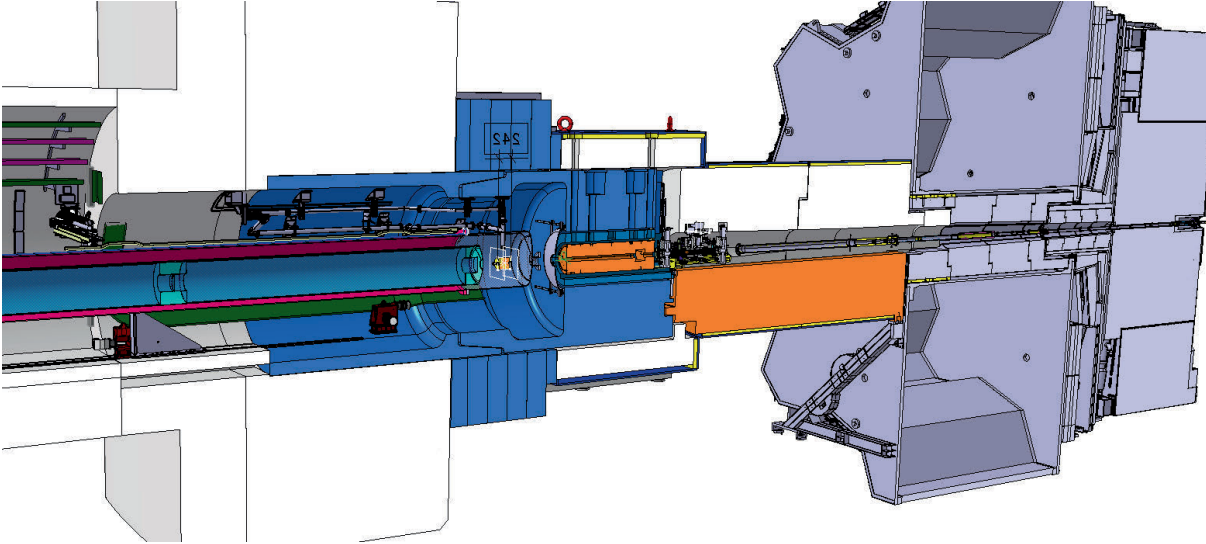


Figure 8-6: 3-D view of the TAXS region from Q1 (machine side, on the right) to ATLAS toroid (in grey). The layout corresponds to the run configuration. Q1 is shown on the left (in blue/red), followed by the TAXS absorber (in orange), and the vacuum assembly module. The foreseen modifications required to host it in the experimental area concern the JFC (upper shown in white, lower bridge shown in orange) and JTT (in grey), as described in the text. On the right of the TAXS, the Forward shielding elements surround the VAX and the beam pipe before the toroid. Inside the toroid, (in grey) the JTT shielding rings. In the figure, VAX is relocated as foreseen for HL-LHC. Note that Q1-TAXS region, inside the TX1S (blue area), is the area with the most difficult access of the whole machine. The gate valves and current VAX module will be moved to the experimental caverns.

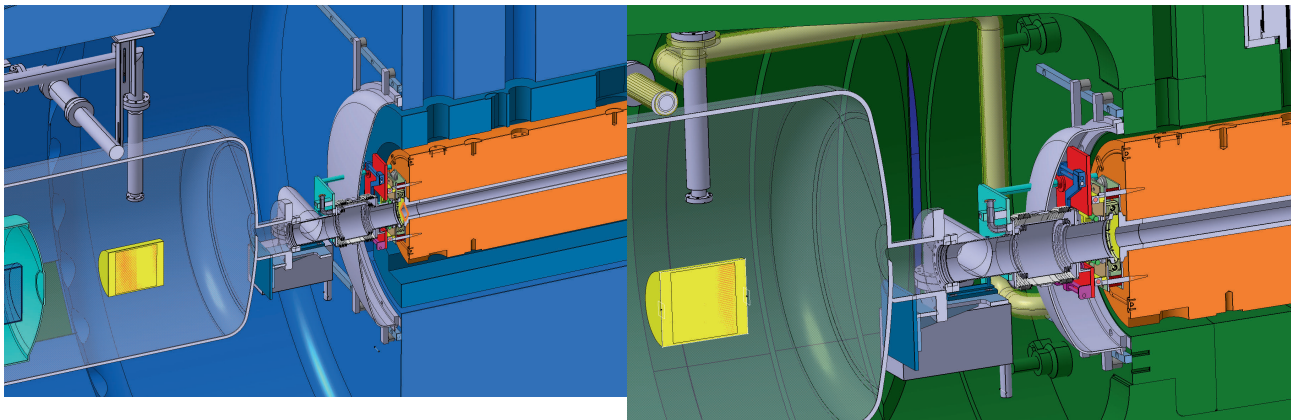


Figure 8-7: Right- Zoom into the IP1 Q1-TAXS region as foreseen for HL-LHC. TAXS (orange) is shown inside its cradle shielding (dark blue). BPM (yellow) will be placed inside Q1 secondary vacuum and quick connector, double pump which requires no access and the He tightness dome will remain in the very limited region (grey elements). The gate valves and current VAX module will be moved to the experimental caverns. Left Zoom on IP5 Q1-TAXS region as foreseen for HL-LHC.

The exchange from the TAS to TAXS could happen both at the beginning or after a few months of cool-down period during LS3. Studies have been performed and show that the effect of leaving the TAS in the

current location does not affect to the dose received for the operations performed in the experimental caverns [20]. The overall procedure is being optimized such as to minimize the exposure of personnel to radiation in compliance with the ALARA principle and the overall planning of the activities in the LHC tunnel and experimental caverns.

Details of the planned integration of the TAXS and adjacent vacuum equipment for ATLAS/IP1 and CMS/IP5 are presented in the following sections.

8.5.1.1 The TAXS absorber in ATLAS/IP1

The updated layout of the TAXS installation in ATLAS is shown in Figure 8-2. It is assumed that the present forward luminosity detector (LUCID), will be removed for HL-LHC. In its place on the IP side of the TAXS an assembly module of vacuum equipment will be installed. The module consists of two all-metal gate valves (DN63), the VAX module with ports for the ionic pump, the gas (Ne) injection/extraction line, the quick flanges and intermediate bellows as shown in Figure 8-9. The removal of the different modules and its ancillary services will be fully removed.

All elements will be positioned with respect to a baseplate that is attached on the JN monobloc (blue structure surrounding the TAXS, see Figure 8-6). The baseplate has an embedded alignment mechanism that can be manipulated from a distance. The baseplate also supports the last part of the experimental beam pipe, and eventually a new LUCID detector upgraded to operate at the HL-LHC environment if proposed by the experiment.

Bellows and quick disconnects installed on either side of the equipment allow for fast exchange with remote tools in case of problems. The installation of two flanges, one on the experiment side and one towards the machine, allows for redundancy and easy decoupling of vacuum sections in case of failures. A permanent bake-out system will be installed.

Minor modifications of ATLAS forward shielding elements will be required to integrate the relocated vacuum elements (VAX, all-metal gate-valves). Studies performed by ATLAS have shown that the overall shielding performance is not affected.

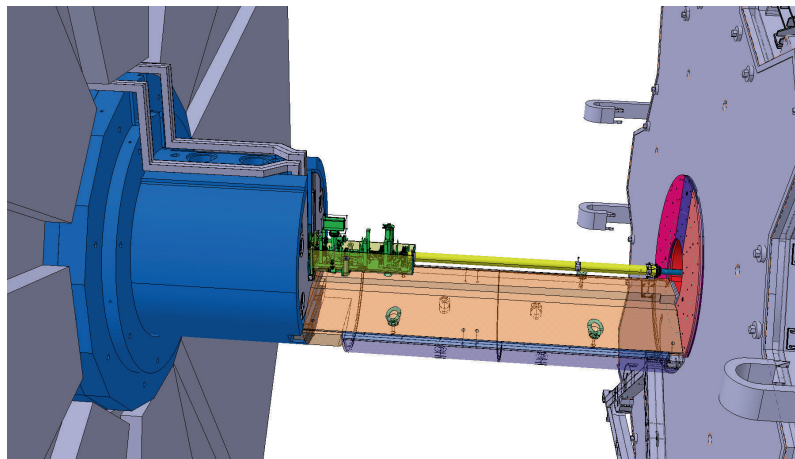


Figure 8-8: 3D view of the forward shielding region with the relocated VAXS and services. The layout corresponds to a phase in the detector access procedure where the octagonal and part of the JFC shieldings are removed. The passage of the services for the vacuum equipment module (cabling and gas injection/extraction pipes) is shown in grey.

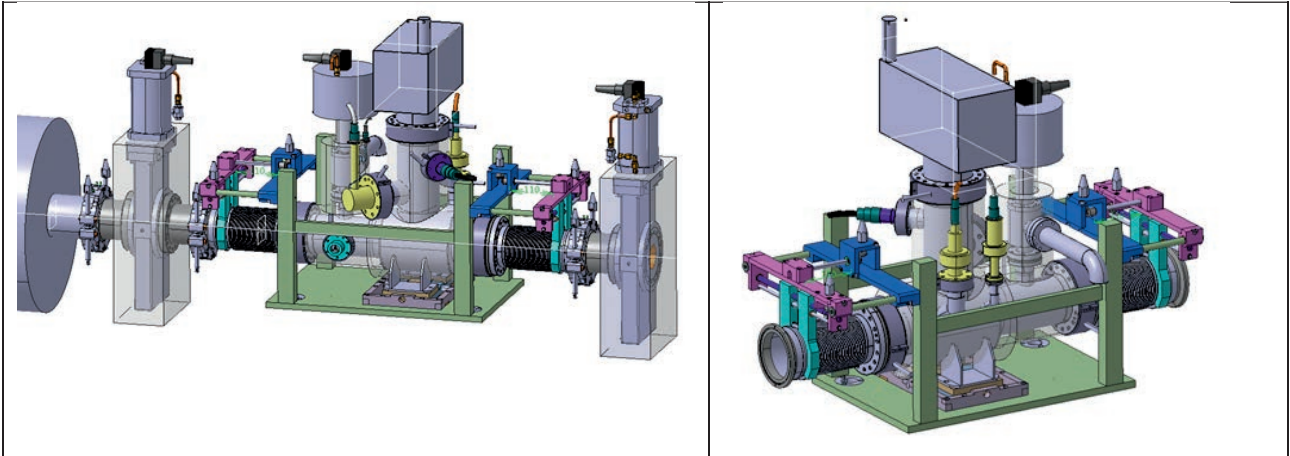


Figure 8-9: Right- Vacuum module assembly installed on the IP side of the TAXS with all-metal gate valves. The valves are closed in case of remote exchange of the vacuum pump module (left). Note that the cantilever support structure is not shown in the picture.

To allow the full opening of the ATLAS endcap without dismantling any vacuum component, the first disk of the plug shielding placed inside the toroid inner bore tube (JTT shielding [10]) needs to be modified. The present single block cylinder, will be replaced by a new one composed of an outer cylinder with a tailored shaped internal bore.

The internal bore will be fully compatible with the new vacuum equipment and will provide a safe clearance in case of the detector opening. Shielding performance will be kept by adding extra-material (nose-shape) onto the JFC2. Usual opening routine will not be affected.

As the proposed JTT modification preserves the shielding volume, should be transparent to the operation of the detector. It affects however the support of the experimental vacuum chamber, where a solution is being developed.

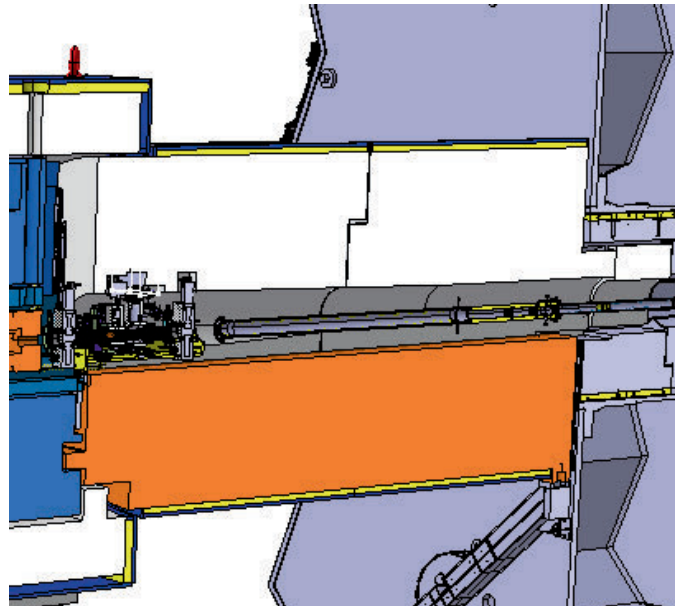


Figure 8-10: Detail cut view of ATLAS forward shielding structures that need to be modified. The shielding consists of two parts: The cylindrical core and the octagonal back. Three pieces called JFC1 ("the bridge, in orange"), JFC2 (white) and JFC3 (white) are used for the core and two pieces called "JFS3 upper" and "JFS3 lower" (on the left, surrounding the blue nose monobloc) are used for the octagonal back.

As the equipment installed on the IP side will be exposed to higher particle fluxes, resulting in higher ($\times 3$) residual doses, the use of optimised material such as Aluminium or low-carbon stainless steel will be promoted. Studies on the activation levels and impact to detector background are ongoing, to fully validate this baseline layout. [11]

Other minor shielding modifications (machining) are needed to accommodate the passage of services to the relocated VAX:

- TX1S (slots for cabling passage);
- JFC1 (machining below VAX support frame);
- JFC2 (machining slots for all-metal gate valve heads and VAX);
- JFC3 (include nose for shielding JTT);
- JTT1 (increase bore diameter to host VAX and all-metal gate valve heads).

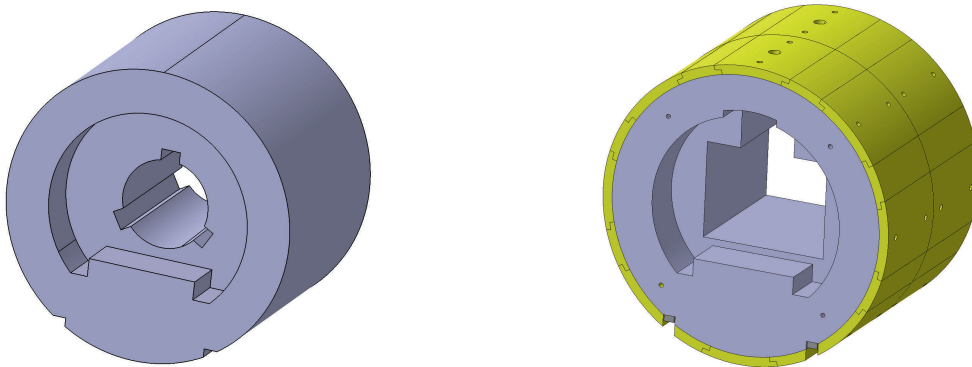


Figure 8-11: 3D view of the ATLAS Toroid shielding plug (JTT, in grey). Only the first of the four disks is shown. For present LHC configuration (left) the disk is a single block, while for HL-LHC (right) will be modified and shielding will be done two parts: an outer cylinder with a tailored bore, and an internal block attached to the JFC2 module (Figure 8-12). Polyethylene layer (yellow) is shown around the HL-LHC JTT.

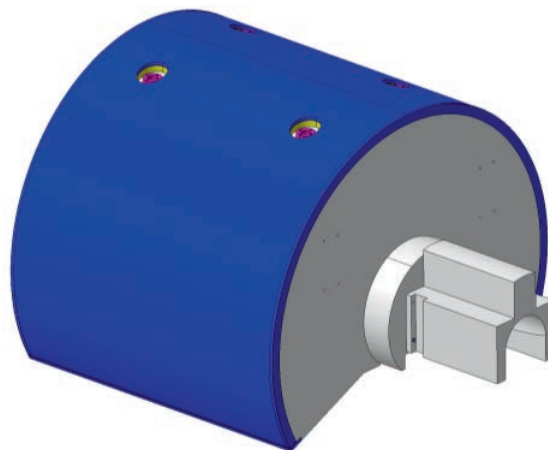


Figure 8-12: 3D view of the ATLAS JFC2 module. Presently the module is a cylindrical shaped block, while for HL-LHC an “extra nose” shielding will be added to fill the gap required in JTT for the detector opening without removing VAX.

FLUKA studies [11][21] have been performed to analyse the impact of the new equipment (support and vacuum modules), and the results show that the impact to the surroundings is minimal and no further protection for workers will be needed with respect to the LHC configuration.

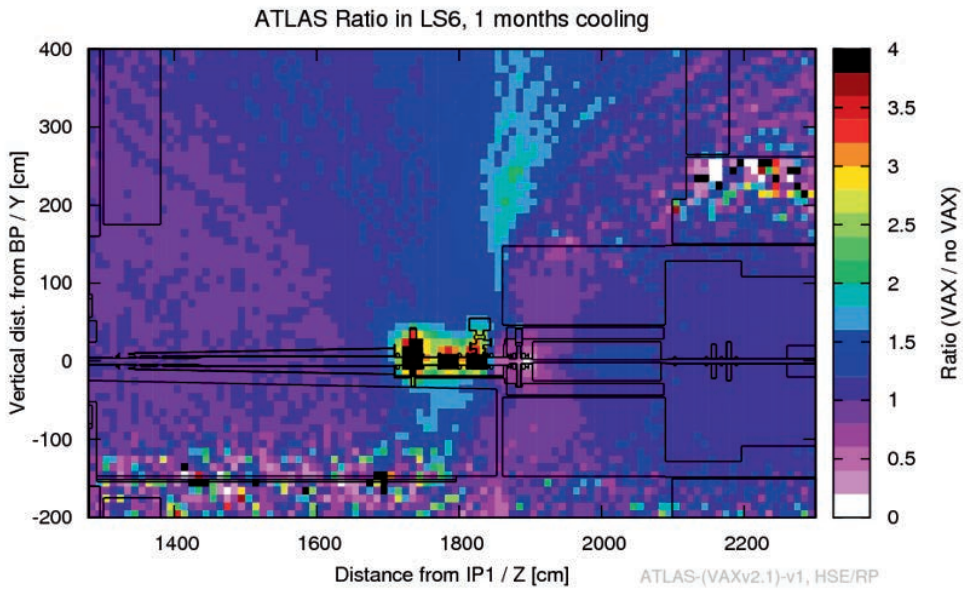


Figure 8-13: Ratio of $H^*(10)$ (ambient dose) in LS6 (ATLAS) showing the increase in dose rate with VAX after 1 month cooling. The calculation is conservative, as it assumes peak luminosity of $7.5 \times 10^{34} \text{ cm}^{-2}\text{s}^{-1}$ (levelling), integrated lumi of 300/fb per year in HL-LHC, 7+7 TeV pp-collisions, 80 mb inelastic cross section and 3 years operation-1 year shutdown x 3 periods until LS6. Results for LS4 and LS5 are similar [11]. The ATLAS forward shielding remains open during access and the routine operations at the detector are not affected. Right picture zooms in the ratio around the VAX region.

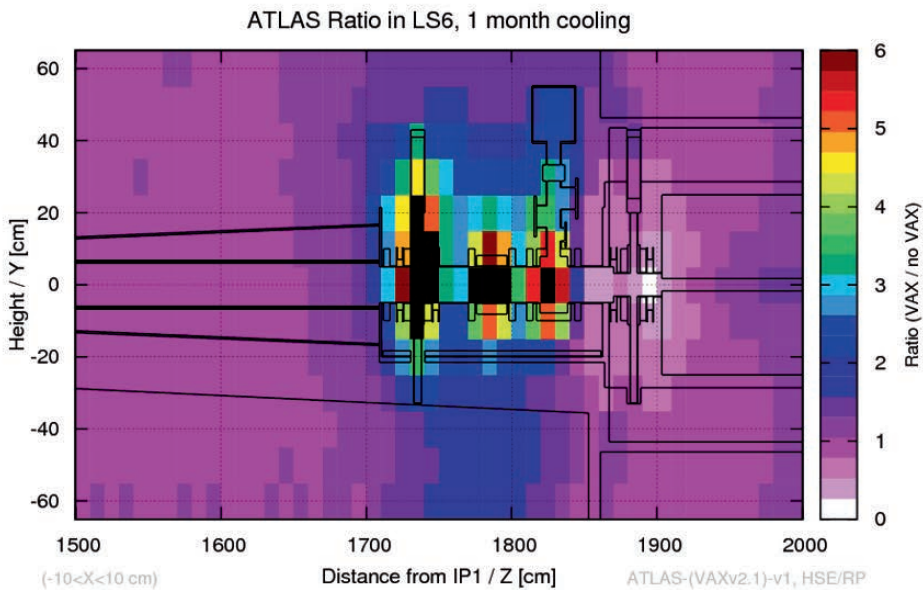


Figure 8-14: Ratio of $H^*(10)$ in LS6 (ambient dose in ATLAS) zooming around the VAX region. . The calculation is conservative, assuming peak luminosity of $7.5 \times 10^{34} \text{ cm}^{-2}\text{s}^{-1}$ (levelling), integrated luminosity of 300/fb per year in HL-LHC, 7+7 TeV pp-collisions, 80 mb inelastic cross section and 3 years operation-1 year shutdown x 3 periods until LS6. Results for LS4 and LS5 are similar [11]. The increase in dose rate with VAX after 1-month cooling is shown. The ATLAS forward shielding remains open during access and the routine operations at the detector are not affected.

8.5.1.2 The TAXS absorber in CMS/P5

The updated layout for the CMS experiment is shown in Figure 8-15. As for ATLAS, there are some conflicts with the presently installed shielding that can be easily resolved with minor modifications.

The assembly module for the vacuum equipment is similar to that for ATLAS, with minor modifications to adopt it to the shielding layout. A new plug for the fix iron nose will be built, and shielding “chicane” elements of the rotating shielding will be either removed or modified to allow the integration of the displaced VAX equipment, but there is no further conflict with the detector opening as basically the module will occupy the volume of the presently installed support module, shown in yellow in Figure 8-16 and Figure 8-18. The installation of the vacuum equipment (all metal gate valves-quick connectors), bellows and VAX module on the new beam pipe support will require the relocation of the services (Grey beam over the support at Figure 8-18 left). The passage of the services is challenging but also possible using the channels on the fixed iron nose left open when the rotating shielding closes.

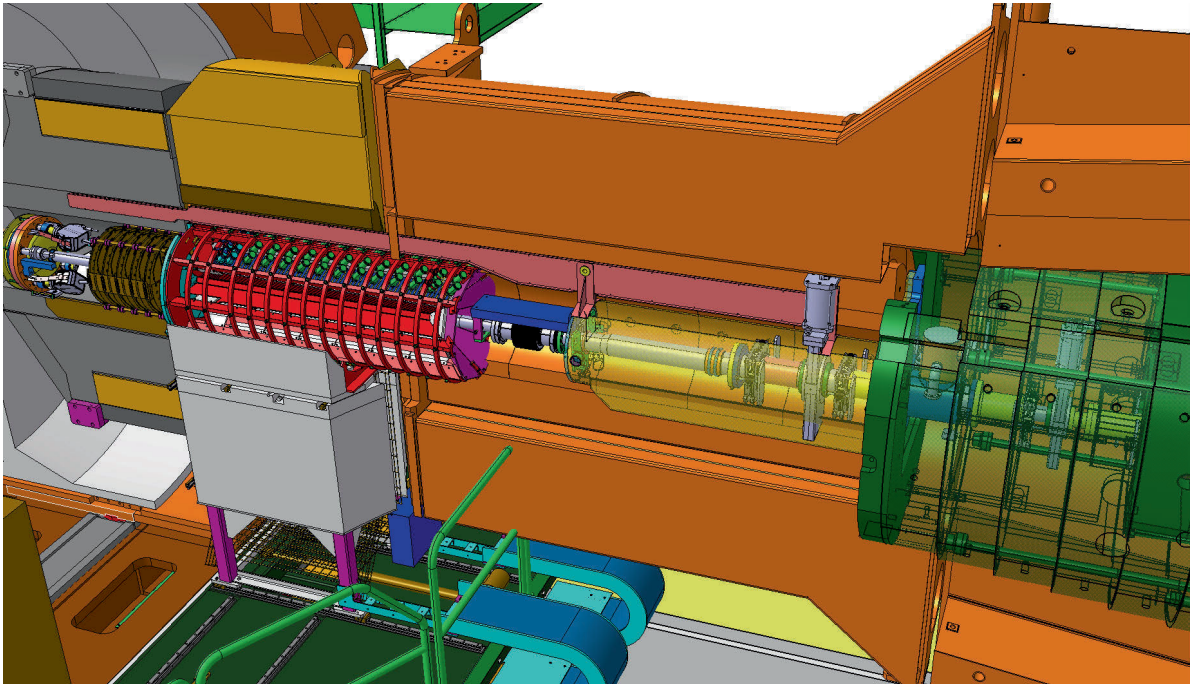


Figure 8-15: 3D view of the CMS forward shielding region with the TAXS and vacuum module. The layout corresponds to the run configuration. The TAXS absorber is on the left inside the FIN (green) and the surrounding rotating shielding (orange). The vacuum assembly module on the IP side is shown inside the baseplate support (transparent yellow).

INTERFACE WITH EXPERIMENTS

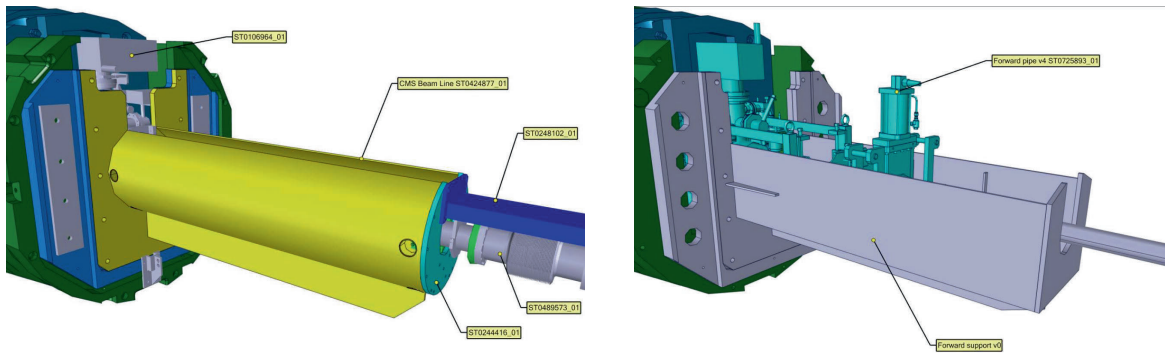


Figure 8-16: Right-3D view of the current CMS beam pipe support (yellow) in front of TAS. The layout corresponds to the open detector configuration. Left- The new support structure (grey) which supports the relocated VAX equipment (blue).

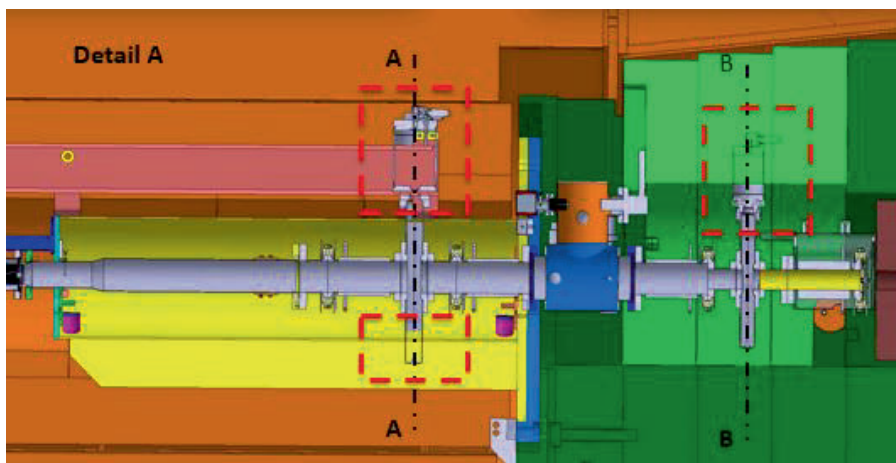


Figure 8-17: Cut of the CMS forward shielding showing the relocated VAX inside the yellow beam pipe support module. End of TAXS is shown at the right end. The required modifications in the Forward shielding (orange) and Fixed Iron nose (green) are inside the red boxes. the yellow beam pipe support module. Details of the beam pipe support and the cable tray to be modified are shown on the left.



Figure 8-18: Photos showing the CMS forward shielding during access. The small rotating shielding is open showing the yellow beam pipe support module. Details of the beam pipe support and the cable tray to be modified are shown on the left.

FLUKA studies **Error! Reference source not found.** have been performed to analyse the impact of the new equipment (support and vacuum modules), results had shown that the impact to the surroundings is minimal and no further protection for workers will be needed with respect to the LHC configuration.

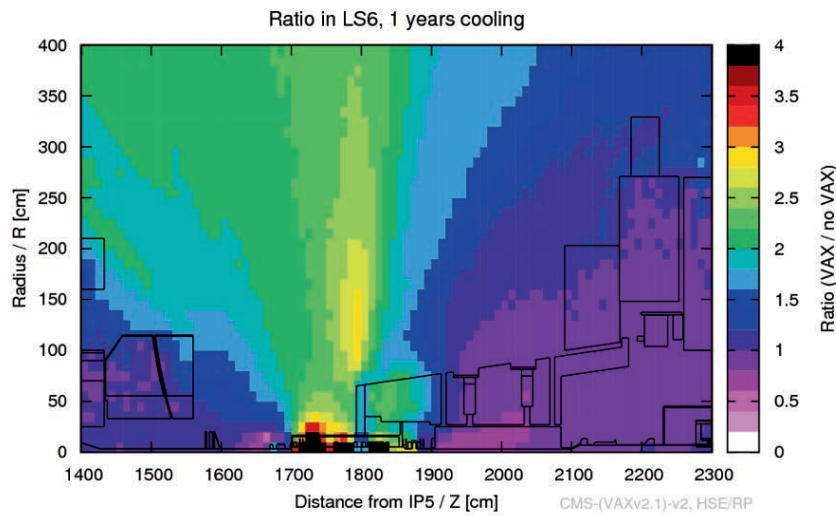


Figure 8-19: Ratio of $H^*(10)$ in LS6 (ambient dose in CMS) showing the increase in dose rate with VAX after 1 month cooling. The calculation is conservative, assuming peak luminosity of $7.5 \times 10^{34} \text{ cm}^{-2}\text{s}^{-1}$ (levelling), integrated lumi of 300/fb per year in HL-LHC, 7+7 TeV pp-collisions, 80 mb inelastic cross section and 3 years operation-1 year shutdown x 3 periods until LS6. Results for LS4 and LS5 are similar [11]. The CMS forward shielding remains open during access, and the routine operations at the detector are not affected.

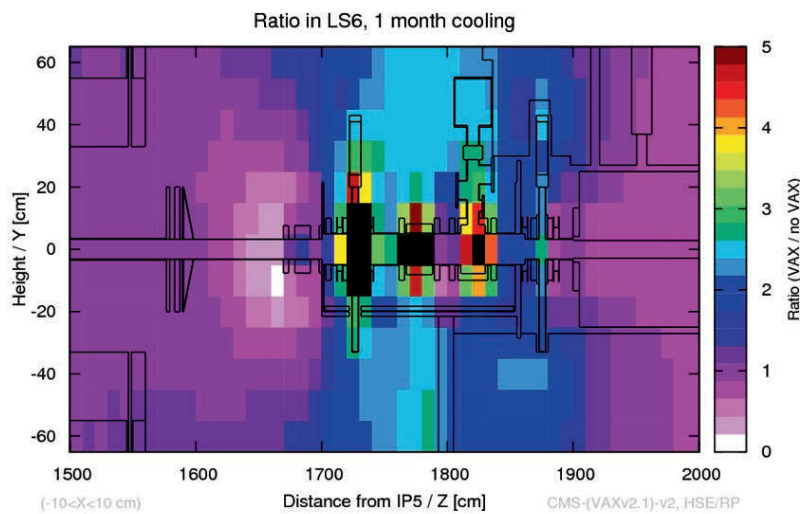


Figure 8-20: Ratio of $H^*(10)$ in LS6 (ambient dose in CMS) zooming around the VAX region. The increase in dose rate with VAX after 1-month cooling is shown. The calculation is conservative, assuming peak luminosity of $7.5 \times 10^{34} \text{ cm}^{-2}\text{s}^{-1}$ (levelling), integrated luminosity of 300/fb per year in HL-LHC, 7+7 TeV pp-collisions, 80 mb inelastic cross section and 3 years operation-1 year shutdown x 3 periods until LS6. Results for LS4 and LS5 are similar [11]. The CMS forward shielding remains open during access, and the routine operations at the detector are not affected.

8.5.2 The neutral particle passive absorber – TAXN

The TAXN absorber is designed to absorb the flux of forward high-energy neutral particles produced at the interaction region of P1 and P5. A TAXN absorber is installed in either side of IP1 and IP5 located between the separation/recombination dipole pair D1 and D2 and containing the transition from the single common beam pipe to the two separate pipes for the incoming/outgoing beams.

8.5.2.1 The TAXN for IP1 & IP5

The design of the new TAXN absorbers for P1 and P5 is based on that of the presently installed TAN, with the following modifications and improvements:

- In the HL-LHC layout, the position of the TAXN is displaced by approximately 14 m towards the IP compared to the present situation, and the available space is reduced by approx. 160 mm.
- The vacuum chamber has a fixed aperture, that combined with a specially designed TCLX collimator with movable jaws just downstream towards D2, provides the maximum protection efficiency at all beam optics scenarios for HL-LHC.
- Active water cooling will be required to dissipate the expected approx. 1.8 kW of power from the beam, expected during the operation during HL-LHC including safety margins. The expected peak dose is 4.5 GGy for 3000 fb⁻¹ (see [16]).
- Improvements in the mechanical design of the absorber will be incorporated to the design in order to allow optimized installation and maintenance activities. The bake-out needs for the absorber core in terms of thermal isolation jackets and optimised duration of the process will be included in the design.
- The slots for beam instrumentation for luminosity monitoring and, as at the beginning of Run 4 operation with ion beams is foreseen, experimental detectors will be maintained unless they impose important constraints to the TAXN design and maintenance.

The TAXN design is described in detail in the Technical Specifications Documents for P1 and P5 [17] respectively. The key design and operation parameters are shown in Table 8-5 and Table 8-6

Table 8-5: Key design parameters for the TAXN of P1 and P5.

Parameter	Unit	Value
Aperture separation (from the transition point)		
entrance	[mm]	148
end	[mm]	158.6
Distance from IP to front flange	[m]	130
TAXN length from flange to flange	[mm]	4900
Inner absorber length	[mm]	3900
Length of separated pipes	[mm]	3700
Maximum TAXN width	[mm]	1150
Absorber width	[mm]	1100
Maximum TAXN height (from two beam centreline)	[mm]	550
Shielding radius (from two beam centreline)	[mm]	530
Nominal beam height from floor	[mm]	1100
Maximum floor loading	[MPa]	<0.5
Beam tube facing IP (two beams in one tube)		
Inner radius	[mm]	106.0
Mechanical tolerance (radius)	[mm]	± 2.1
Transition section		
Inner radii	[mm]	106.0 to [41.0(h)-37.0(w)]
Mechanical tolerance (radius) [e/m/e]	[mm]	± 1.9 / ± 4.9 / ± 1.4

Beam tube away from IP5 (two beams in two tubes)	Inner radius	[mm]	38.0
	Mechanical tolerance (radius)	[mm]	± 1.0
Vacuum chamber to alignment fiducial tolerance		[mm]	± 0.6
Supports range of motion		[mm]	± 10.0 [h & v]
Absorber cooling			Demin. Water

Table 8-6: TAXN operational parameters.

Characteristics	Units	Value
Absorbed collision power at		
$5 \times 10^{34} \text{ cm}^{-2} \text{ s}^{-1}$	[kW]	1.0
$7.5 \times 10^{34} \text{ cm}^{-2} \text{ s}^{-1}$		1.5
24 hr average absorbed collision power at		
$5 \times 10^{34} \text{ cm}^{-2} \text{ s}^{-1}$	[KW]	0.91
$7.5 \times 10^{34} \text{ cm}^{-2} \text{ s}^{-1}$		1.37
Maximum internal beam tube temperature	[C]	85

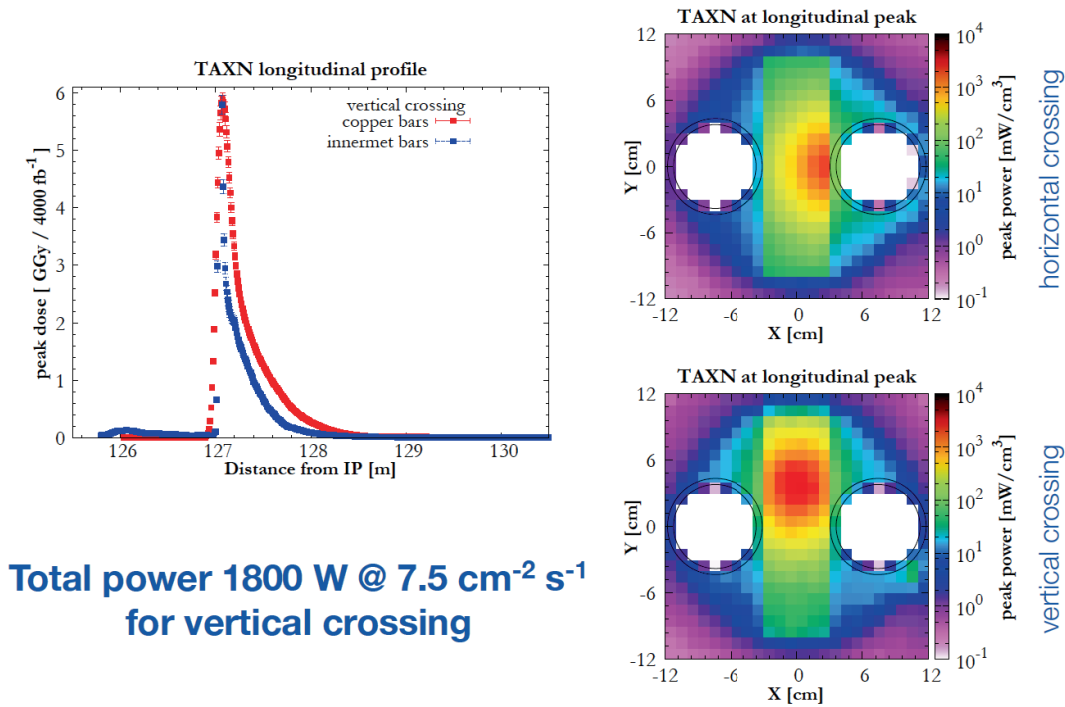


Figure 8-21: Results from FLUKA energy deposition studies for the TAXN at P1,P5. Left: the energy deposition longitudinal profile, Right: the transverse energy distribution at the peak location.

Optimisation studies on the TAXN absorber length were performed, showing that a shorter absorber with a denser material, Inermet180 instead of Cu, can be equally efficient, gaining about 1m in longitudinal length (see Figure 8-22). However, using tungsten as the core absorber material may lead to technical difficulties compared to copper, so this possibility is kept as option for the final technical design of the absorber.

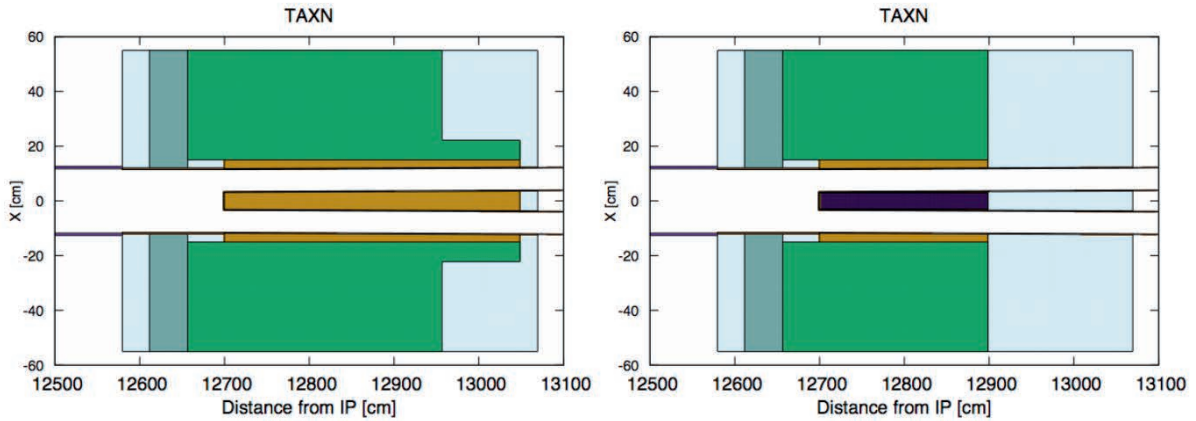


Figure 8-22: TAXN geometry using different material for the core absorber: Cu (left), Inermet180 (right). Maintaining the same efficiency (approx. 22-25 λ_{int}) a gain in length of 1.5m can be obtained.

8.5.2.2 The TAXN for IP8

During the LHC design stage, it was estimated that absorbers would become only necessary for luminosities above $L = 10^{33} \text{ cm}^{-2}\text{s}^{-1}$. The original request by LHCb has been for luminosities of up to $L = 4 \times 10^{32} \text{ cm}^{-2}\text{s}^{-1}$, such that IR8, where the LHCb experiment is located, could be designed without absorbers. More detailed studies on energy deposition in IR8 [22] have been made recently, to see to which extent absorbers are required for the luminosity upgrade of IR8 up to $L_{HL} = 2 \times 10^{33} \text{ cm}^{-2}\text{s}^{-1}$.

With $L_{HL} = 2 \times 10^{33} \text{ cm}^{-2}\text{s}^{-1}$ and the inelastic cross section $\sigma_{pp} = 85\text{mb}$, there will be 1.7×10^8 inelastic collisions per second at the LHCb. The inelastic collision power is carried off by neutrals (mostly neutrons and photons) and charged particles (mostly pions and protons), that leave in both directions from the Interaction Point (IP). Detailed Fluka simulations have estimated the energy deposition around IP8 at $2 \times 10^{33} \text{ cm}^{-2}\text{s}^{-1}$ luminosity without TAS and compared it with IP1 and IP5 at $1 \times 10^{34} \text{ cm}^{-2}\text{s}^{-1}$ luminosity with TAS. The studies have shown that the TAS is only really effective as protection for Q1. Nevertheless, the energy deposition in the triplet depends on the crossing angle in IP8. Changing the beam screen orientation has little effect on the energy deposition. As conclusion, the LHCb luminosity upgrade with $2 \times 10^{33} \text{ cm}^{-2}\text{s}^{-1}$ luminosity is compatible without TAS installation, and a protection (kind of minimal TAN) is recommended to reduce the heat load on the D2 magnets well below the quench level.

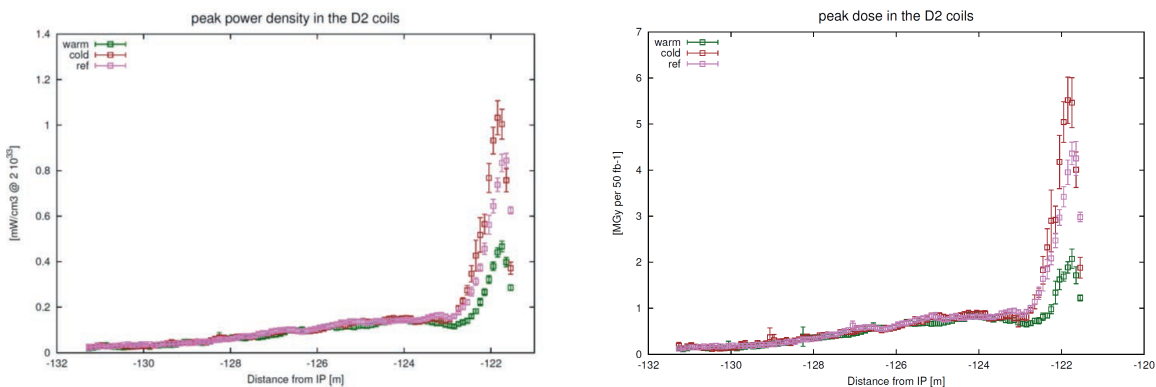


Figure 8-23. Peak power density (left picture) and peak dose (right picture) in the IP8 D2 coils.

New TAXN absorbers should be installed in P8 on either side of the interaction region in available slots upstream of D2, as shown in Figure 8-24. Several energy deposition studies with different configurations of absorbers and masks were performed. Conclusion is that a 340x200 mm mini-TAXN with a 500mm long Inermet180 absorber situated at ~ 1.9 m from the D2-IP face, would efficiently protect the D2 from the

interaction debris at the foreseen luminosity of $2 \times 10^{33} \text{ cm}^{-2} \text{ s}^{-1}$ for LHCb (See Figure 8-26). Three different options have been considered: a classical TAN located at the Y chamber (rose), a cold mask placed inside the D2 (red) and a mini-TAN situated at $\sim 1.9 \text{ m}$ from the D2-IP face (green). Protection levels of the latest are the highest.

In conclusion, there will be one mini-TAXN on either side of the interaction point. The integration of the mini-TAXN in the current LHC lay-out will require a relocation of the BPM's situated between D2 and TCTPH and the change of some vacuum elements (bellows & beam pipe) and will be installed during LS2.

The total weight of the new equipment is around 800 kg and will be transported as a single piece.

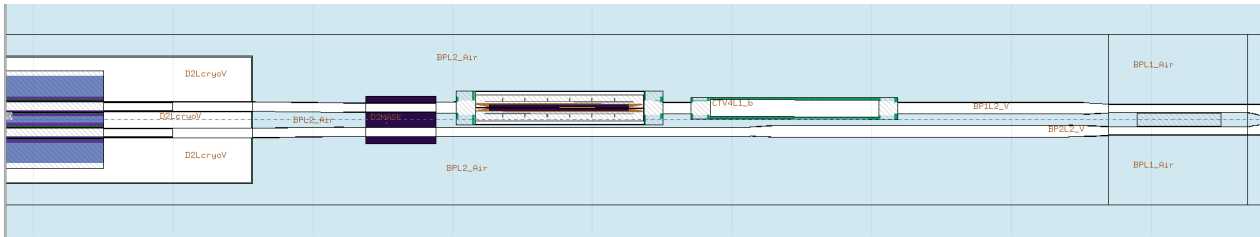


Figure 8-24: 2D layout (top view) of the D2 region as considered for the FLUKA analysis. The new TAXN (dark blue) is situated between D2 (white) and the TCTPH collimator Y-chamber is shown on the left of the picture.

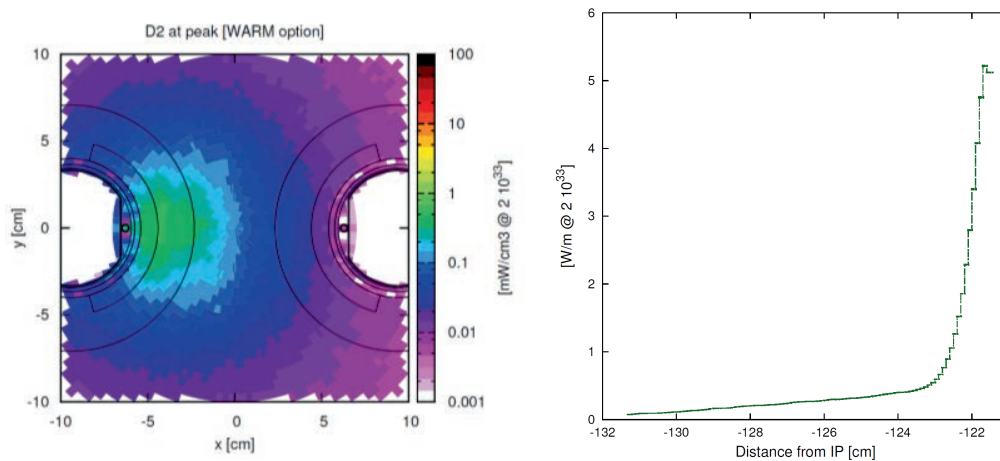


Figure 8-25: energy deposition in the D2 front face, in the layout including the 500 mm Inermet180 TAXN. A load increase of 6 W in D2 respect to LHC, 60% of which are absorbed in the first meter.

Quick connectors will be included allowing a fast exchange in case of need. A preliminary thermal analysis has been performed showing that the mini-TAXN will not need to be water cooled (estimated heat deposition is below 20W).

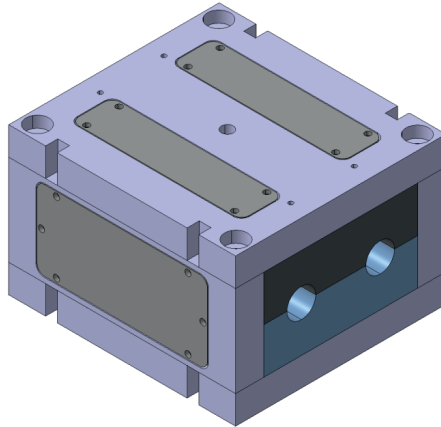


Figure 8-26: 3D conceptual drawing of a mini-TAXN to be installed in LSS8 currently under consideration. Inner part is made of INERMET 180, while the surrounding box provides baking capabilities. Support, survey & alignment structures not shown.

8.6 References

- [1] Letter of Intent for the Phase-II Upgrade of the ATLAS Experiment, ATLAS Collaboration [CERN-LHCC-2012-022](#). LHCC-1-023.
- [2] Technical proposal for the upgrade of the CMS detector through 2020, CMS Collaboration, [CERN-LHCC-2011-006](#). LHCC-P-004.
- [3] Technical Proposal for the Phase-II Upgrade of the CMS Detector, J. Butler et. al, [CERN-LHCC-2015-010](#). LHCC-P-008.
- [4] RD Collaboration Proposal: Development of pixel readout integrated circuits for extreme rate and radiation, J. Chistiansen, M. Garcia-Sciveres. [CERN-LHCC-2013-008](#)
- [5] Interface Machine-Experiments: Definition and Time Plan, Milestone 18. [CERN-ACC-2014-0304](#)
- [6] A. Santamaria et al., Machine Protection from Fast Crab Cavity Failures in the High Luminosity LHC, Proc. IPAC 2016
- [7] K. Sjobak et al., Time Scale of Crab Cavity Failures Relevant for High Luminosity LHC, 7th International Particle Accelerator Conference, Busan, Korea, 8 - 13 May 2016, pp.TUPMW025. DOI: [10.18429/JACoW-IPAC2016-TUPMW025](#)
- [8] M. Galilee, Reduction of ATLAS VI Diameter, LHC-VC11-EC-0001. EDMS [1230222](#).
- [9] M. Galilee, CMS Central chamber diameter reduction, LHC-VC5-EC-0001. EDMS [1230176](#).
- [10] Atlas shielding project <http://atlas.web.cern.ch/Atlas/GROUPS/Shielding/shielding.htm>
- [11] I. Bergstrom, H. Vincke, 39 th HL-LHC WP8 meeting. INDICO: [539877](#)
- [12] E. Hoyer et al., Interface Specification LHC IP1/IP5, Front Quadrupole Absorbers (TAS), LHC-TAS-ES-0003. EDMS: [111998](#).
- [13] E. Hoyer et al., LHC IP1/IP5 Neutral Beam Absorbers (TAN), LHC-TAN-ES-0100. EDMS: [108093](#).
- [14] Target Absorber for IP1 Insertion Region Secondary - Conceptual Specifications. EDMS: [1361111](#)
- [15] Target Absorber for IP5 Insertion Region Secondary - Conceptual Specifications. EDMS: [1361109](#)
- [16] IP1 Neutral Beam Absorber - Conceptual Specifications. EDMS: [1361107](#)
- [17] IP5 Neutral Beam Absorber - Conceptual Specifications. EDMS: [1361109](#)
- [18] IP8 Neutral Beam Absorber - Conceptual Specifications. EDMS: [1361110](#)
- [19] I. Bergstrom, H. Vincke. – 37th HL-LHC WP8 meeting (2016-08). INDICO: [526092](#)
- [20] C. Adorasio. - Overview of activation of LHC elements to be disassembled 48th HL-LHC Integration Meeting. INDICO: [502039](#)

- [21] C. Adorisio, 35th HL-LHC WP8 meeting, INDICO:[448624](#)
- [22] F. Cerutti, 45th HL-LHC WP15 Integration meeting & 40th HL-LHC WP8 Meeting. INDICO: [545143](#)

Chapter 9

Cryogenics for the HL-LHC

9 Cryogenics for the HL-LHC

9.1 Introduction

The upgrade of the cryogenics for the HL-LHC will consist of the following.

- The design and installation of two new 1.9 K cryogenic plants at P1 and P5 for high luminosity insertions. This upgrade will be based on a new sectorization scheme aimed at separating the cooling of the magnets in these insertion regions from the arc magnets, and on a new cryogenic architecture based on electrical feedboxes located at ground level and vertical superconducting links.
- The design and installation of a new 4.2 K cryogenic plant at P4 for the Superconducting Radio Frequency (SRF) cryo-modules and other future possible cryogenic equipment (e-lens, RF harmonic system).
- No new cryogenic circuits at P7 for the HTS links and displaced current feedboxes (baseline change).
- Cryogenic design support for cryo-collimators and 11 T dipoles.

Figure 9-1 shows the overall LHC cryogenic layout, including the upgraded infrastructure.

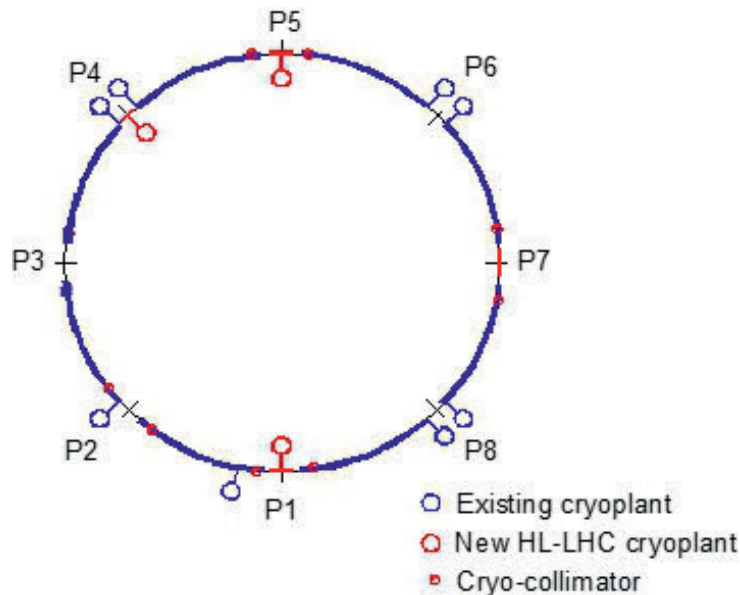


Figure 9-1: Overall LHC cryogenic layout, including the upgraded infrastructure.

9.2 LHC machine upgrades

9.2.1 Upgraded beam parameters and constraints

The main parameters impacting on the cryogenic system are given in Table 9-1. With respect to the nominal beam parameters, the beam bunch population will double and the luminosity in the detectors of the high luminosity insertions at P1 and P5 will be multiplied by a factor 5.

Table 9-1: LHC upgraded beam parameters for 25ns bunch spacing.

Parameter	Units	Nominal	Upgrade
Beam energy, E	[TeV]	7	7
Bunch population, N_b	[protons/bunch]	1.15×10^{11}	2.2×10^{11}
Number of bunches per beam, n_b	-	2808	2748
Luminosity, L	[$\text{cm}^{-2} \text{s}^{-1}$]	1×10^{34}	5×10^{34}
Bunch length	[ns]	1.04	1.04

These upgraded beam parameters will introduce new constraints to the cryogenic system.

- The collimation scheme must be upgraded by adding collimators to the continuous cryostat close to P2 and P7. The corresponding integration space must be created by developing shorter but stronger 11 T superconducting dipoles. As the new collimators will work at room temperature, cryogenic bypasses are required to guarantee the continuity of the cryogenic and electrical distribution. Figure 9-2 shows the nominal and upgraded layouts of the continuous cryostat. Halo control for the HL-LHC may require the installation of hollow electron lenses at P4, making use of a superconducting solenoid. While not yet in the HL-LHC baseline, this device may be the best option for controlling particle diffusion by depopulating the halo of the high-power hadron beams, thereby avoiding uncontrolled losses during critical operations such as the squeeze. Figure 9-3 shows the nominal and upgraded layouts of the P4 insertion region, anticipating the installation of an e-lens and a new SRF system.
- The increase of the level of radiation to the electronics could possibly require relocating power converters and related current feedboxes at ground level at P1 and P5. New superconducting links will be required to connect the displaced current feedboxes to the magnets. Figure 9-5 show the nominal and upgraded layouts of the insertion regions at P1 and P5.
- To better control the bunch longitudinal profile, reduce heating and improve the pile-up density, new cryo-modules of 800 MHz RF cavities could be added to the existing 400 MHz cryo-modules at P4 creating a high-harmonic RF system (see Figure 9-3). Alternatively, discussions are underway to see if a better scheme would be the installation of a new 200 MHz SRF system, rather than the 800 MHz. From the cryogenic point of view the requests are similar, so we will consider below the 800 MHz system that is in an advanced phase of study.
- To improve the luminosity performance by addressing the geometric luminosity reduction factor and possibly allowing the levelling of the luminosity, cryo-modules of crab-cavities (CC) will be added at P1 and P5 (see Figure 9-4).
- Finally, the matching and final focusing of the beams will require completely new insertion cryo-magnet assemblies at P1 and P5 (see Figure 9-4).

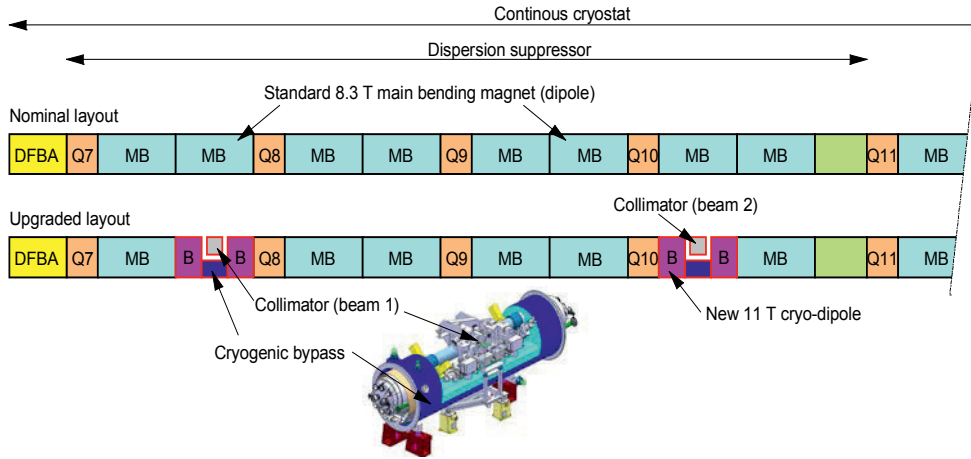


Figure 9-2: Upgraded layout of the continuous cryostat at P2 (as well at P1, P5, and P7).

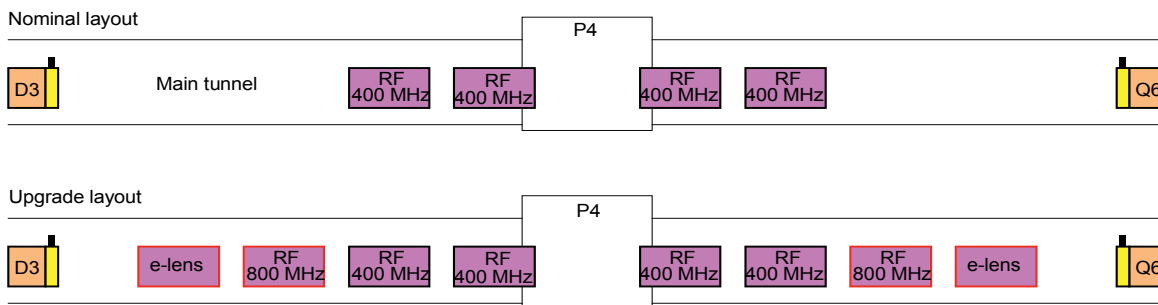


Figure 9-3: Possible upgraded layout of the P4 insertion region.

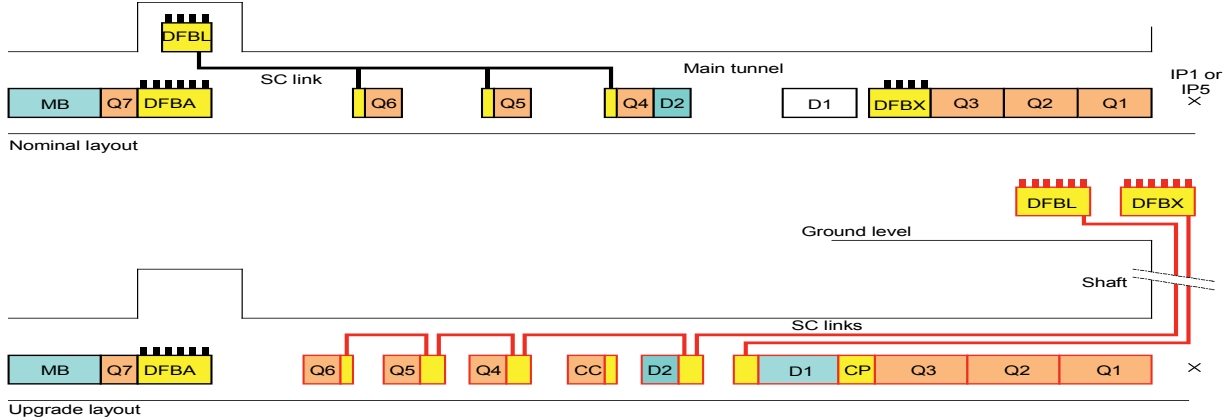


Figure 9-4: Upgraded layout of the P1/P5 insertion region (half insertion).

9.3 Temperature level and heat loads

Heat loads to the cryogenic system have various origins and uncertainties. As done for the LHC [1], two categories of heat loads are considered: static heat loads (Q_{static}) to be compensated just to reach the desired temperature level, and dynamic heat loads ($Q_{dynamic}$) due to energising or circulating beams. These heat loads are primarily considered without contingency to avoid piling-up margins. However, the cooling capacity to be installed has to include margins that vary for the static and dynamic heat loads to properly allow the nominal beam scenario. This margin vanishes for the ultimate beam scenario.

In Table 9-2 the static heat in-leaks are reported, for different temperature levels. For new equipment, the thermal performance of supporting systems, radiative insulation and thermal shields is considered identical to that of existing LHC equipment.

Table 9-2: Static heat in-leaks of HL-LHC machine (without contingency).

Temperature [k]	Equipment	Unit	Nominal	Upgrade
4.6–20	Beam screen circuit (arc + DS)	[mW/m]	140	140
	Beam screen circuit (IT)	[mW/m]	125	125
	Beam screen circuit (MS)	[mW/m]	578	578
1.9	Cold mass (arc + DS)	[mW/m]	170	170
	Cold mass (IT)	[mW/m]	1250	1250
	Crab cavities	[W per module]	0	25
4.5	Cold mass (MS)	[mW/m]	3556	3556
	400 MHz RF module	[W per module]	200	200
	800 MHz RF module	[W per module]	0	120
	Electron-lens	[W per module]	0	12
20–300	Current lead	[g/s per kA]	0.035	0.035

Table 9-3 gives the dynamic heat loads expected for the HL-LHC. The main concern is electron-cloud impingement on the beam screens, which can only be reduced by efficient beam scrubbing (dipole off) of the beam screens. This remains to be demonstrated. Without efficient beam scrubbing (dipole on), the e-cloud activity will remain high (more than 4 W/m and per beam) in the arcs and dispersion suppressors (DS). This heat deposition corresponds to about twice the local cooling limitation given by the hydraulic impedance of the beam screen cooling circuits. In addition, the corresponding integrated power over a sector (more than 25 kW) is not compatible with the installed capacity of the sector cryogenic plants. For e-cloud deposition in the arcs and dispersion suppressors, efficient (dipole off) or inefficient (dipole on) beam scrubbing is considered.

Table 9-3: Dynamic heat loads on HL-LHC machine (without contingency).

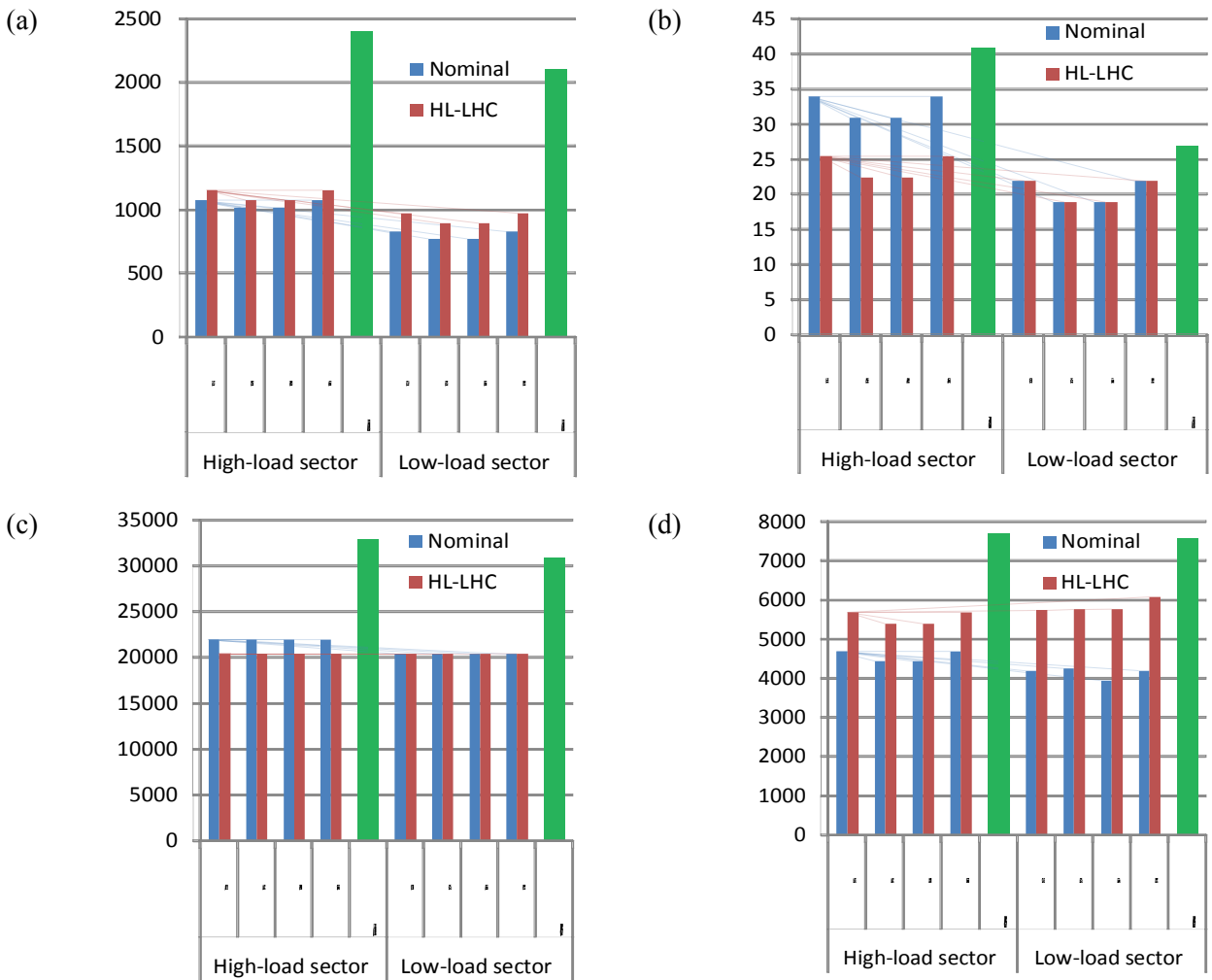
Temperature [k]	Equipment	Unit	Nominal	Upgrade
4.6–20	Synchrotron radiation (arc + DS)	[mW/m per beam]	165	310
	Image current (arc + DS + MS)	[mW/m per beam]	145	522
	Image current (IT low-luminosity)	[mW/m]	475	1698
	Image current (IT high luminosity)	[mW/m]	166	596
	E-clouds (arc + DS) (dipole off)	[mW/m per beam]	271	41
	E-clouds (arc + DS) (dipole on)	[mW/m per beam]	4264	4097
	E-clouds (IT high luminosity)	[mW/m]	5500	9455
	E-clouds (IT low-luminosity)	[mW/m]	5500	5500
	E-clouds (MS)	[mW/m per beam]	2550	383
	Secondaries (IT beam screen P1 and P5)	[W per IT]	0	650
1.9	Beam gas scattering	[mW/m per beam]	24	45
	Resistive heating in splices	[mW/m]	56	56
	Secondaries (IT cold mass P1 and P5)	[W per IT]	155	630
	Secondaries (DS cold mass P1 and P5)	[W per DS]	37	185
	SRF crab cavities	[W per module]	0	24
4.5	SRF 400 MHz	[W per module]	101	366
	SRF 800 MHz	[W per module]	0	183
	E-lens	[W per module]	0	2
20–300	Current lead	[g/s per kA]	0.035	0.035

The beam screens of the new inner triplets at P1 and P5 will be protected by tungsten shielding that will be able to absorb about half of the energy deposited by collision debris escaping the high luminosity detectors.

For simplicity at this stage, beam screen loads were considered to be between 4.6 K and 20 K as for the current LHC. However, the large dynamic power to be extracted could force consideration of the next possible temperature range compatible with beam vacuum requirements, i.e. the range 40 K to 60 K. Despite this thick W-shielding, the 1.9 K load, i.e. the energy that collision debris deposited onto the magnet coil and cold mass, increases by four times with respect to the nominal LHC case. The W-shielding, in any case, reduces the overall refrigeration cost and increases the lifetime of the inner-triplet coils.

9.4 Impact on existing sector cryogenic plants

With new cryogenic plants dedicated to the cooling of cryogenic equipment in P1, P4, and P5, the cooling duty of the existing sector cryogenic plants will be reduced and more equally distributed. Figure 9-6 shows the required cooling capacities for the different temperature levels and compares them to the nominal cooling requirements and to the installed capacities. The low-load sectors equipped with upgraded ex-LEP cryogenic plants have lower installed capacity than the four cryogenic plants specially ordered for the LHC’s high-load sectors. For the HL-LHC, sufficient capacity margin still exists providing that the beam scrubbing of dipole beam-screens is efficient (dipole off).



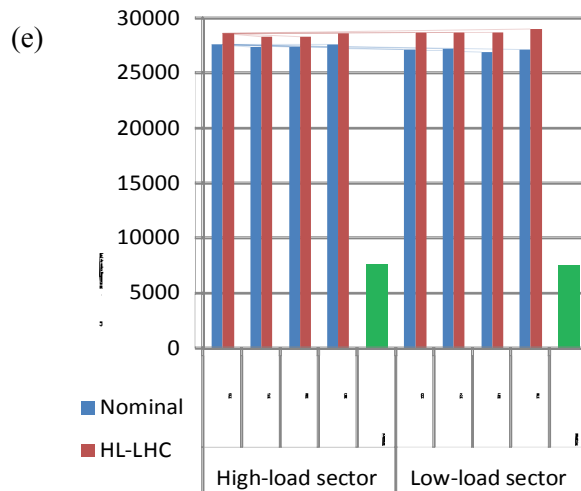


Figure 9-5: Cooling capacity requirement of sector cryogenic plants. (a) Cold mass; (b) current leads; (c) thermal shields; (d) beam screen (dipole off); (e) beam screen (dipole on).

9.5 New cryogenics for Point 4 insertion

Figure 9-6 shows the cryogenic architecture of the upgraded P4 insertion consisting of:

- a warm compressor station (WCS) located in a noise-insulated surface building and connected to a helium buffer storage;
- a lower cold box (LCB) located in the UX45 cavern and connected to a cryogenic distribution valve box (DVB), also located in the UX45 cavern;
- main cryogenic distribution lines connecting the cryo-modules to the distribution valve box;
- auxiliary cryogenic distribution lines interconnecting the new infrastructure with the existing QRL service modules (SM) and allowing redundancy cooling with adjacent-sector cryogenic plants;
- a warm-helium recovery line network.

Concerning the planned installed capacity ($Q_{\text{installed}}$) of the new cryogenic plant, some uncertainty (f_u) and overcapacity (f_o) margins have to be introduced as shown in Eq. 9.1:

$$Q_{\text{installed}} = f_o \times (Q_{\text{static}} \times f_u + Q_{\text{dynamic}}), \quad (9-1)$$

where $f_o = 1.5$ and $f_u = 1.5$.

Table 9-4 gives the installed capacity of the P4 cryogenic plant required at different temperature levels. The P4 cryogenic plant will require an equivalent capacity of about 6 kW at 4.5 K.

This is considered as the present baseline, with the evaluation of an alternative scenario for the refrigeration part. The alternative scenario would consist of an upgrade of one of the existing refrigerator of P4 (+2.5kW@4.5K equivalent to +14%) to fulfil the required cooling capacity of existing SRF modules with sufficient margin, while keeping the baseline new distribution scenario. As a complement, a new mobile refrigerator with a cooling capacity allowing RF tests of a single cryo-module during long shut-downs is under investigation, as all other cryogenic sub-systems would be stopped for maintenance and major overhauling.

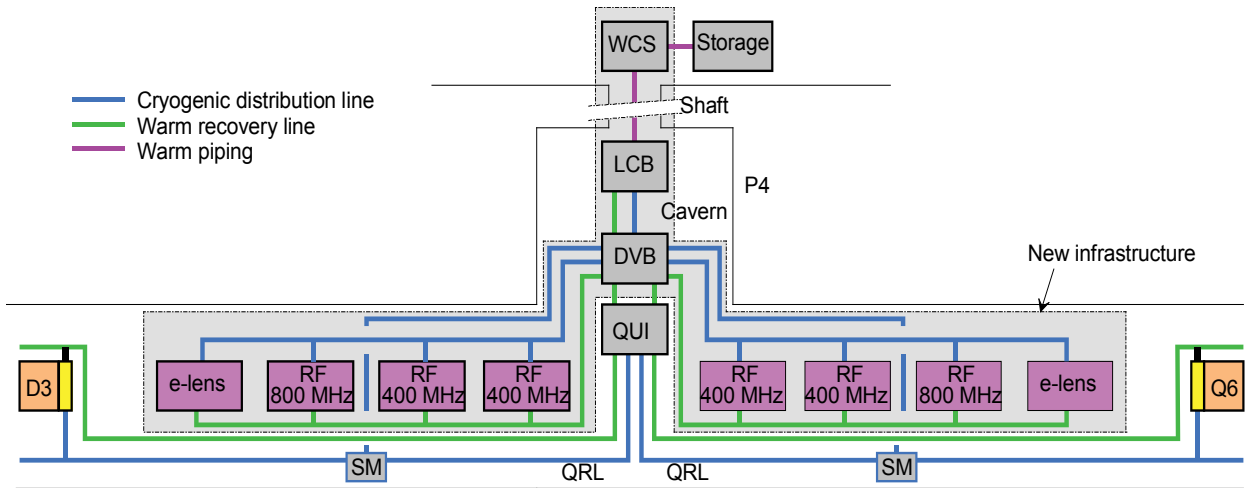


Figure 9-6: Upgraded cryogenic architecture at P4.

Table 9-4: Installed capacity requirements of the new cryogenic plant at P4.

Temperature level [K]	Static [W]	Dynamic [W]	Installed [W]	Equivalent installed capacity at 4.5 K [kW]	
4.5	1144	1736	5223	5.6	5.8
50–75	1000	0	2250	0.2	5.8

9.6 New cryogenics for high luminosity insertions at Point 1 and Point 5

Figure 9-7 shows the proposed cryogenic architecture of the P1 and P5 high luminosity insertions consisting of:

- a warm compressor station (WCS) located in a noise-insulated surface building and connected to a helium buffer storage;
- an upper cold box (UCB) located in a ground-level building;
- a quench buffer (QV) located at ground level;
- one or two cold compressor boxes (CCB) in an underground cavern;
- two main cryogenic distribution lines (one per half-insertion);
- two interconnection valve boxes with existing QRL cryogenic line allowing redundancy with the cryogenic plants of adjacent sectors.

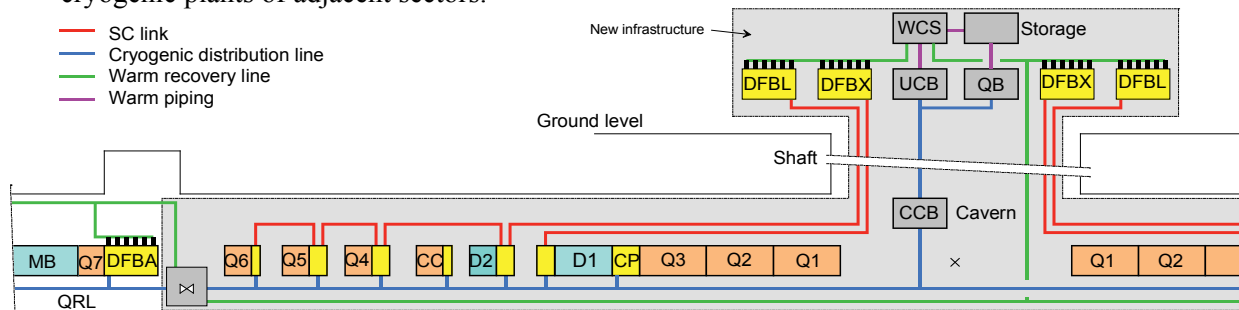


Figure 9-7: Upgraded cryogenic architecture at P1 and P5.

Table 9-5 gives the installed capacity of the proposed P1 and P5 cryogenic plants required at the different temperature levels and using the same uncertainty and overcapacity margins as those used for P4. The cryogenic plants will require an equivalent capacity of about 18 kW at 4.5 K, including 3 kW at 1.8 K.

Table 9-5: Installed capacity requirements of the new cryogenic plants at P1 and P5.

Temperature level [K]		Static	Dynamic	Installed	Equivalent installed capacity at 4.5 K [kW]	
1.9	[W]	433	1380	3045	12	18
4.5	[W]	196	8	452	0.5	18
4.6–20	[W]	154	2668	4348	2.4	18
50–75	[W]	4900	0	7350	0.5	18
20–300	[g/s]	16	16	59	2.6	18

At P1 and P5 the superconducting magnets of the ATLAS and CMS detectors are cooled by dedicated cryogenic plants. A possible redundancy with detector cryogenic plants could be interesting in the event of a major breakdown of the detector cryogenic plants. The corresponding power requirements are about 1.5 kW at 4.5 K for CMS and 3 kW at 4.5 K for ATLAS.

The cooling capacity of 3 kW at 1.8 K is higher than the 2.4 kW installed capacity of an LHC sector, which corresponds to the present state-of-the-art for the cold compressor size. Consequently:

- larger cold compressors have to be studied and developed;
- or parallel cold compressor trains have to be implemented (one 1.5 kW train per half insertion);
- or duplication of the first stage of cold compression to keep the machine within the available size.

9.7 Building and general service requirement

Table 9-6 gives the buildings and general services at P1, P4, and P5 required by the cryogenic infrastructure. At P4, the required surface and volume for the warm compression station and for the cold box are respectively available in the existing SUH4 building and in the UX45 cavern.

Table 9-6: Building and general service requirement.

Cryogenic system			P1 and P5	P4
Warm compressor building	Surface	[m ²]	700	400
	Crane	[t]	20	20
	Electrical power	[MW]	4.6	2.0
	Cooling water	[m ³ /h]	540	227
	Compressed air	[Nm ³ /h]	30	20
	Ventilation	[kW]	250	100
	Type	-	Noise-insulated (~108 dB_A)	
Surface SD building	Surface	[m ²]	30 × 10	N/A
	Height	[m]	12	N/A
	Crane	[t]	5	N/A
	Electrical power	[kW]	50	N/A
	Cooling water	[m ³ /h]	15	N/A
	Compressed air	[Nm ³ /h]	90	N/A
Cavern	Volume	[m ³]	200	300
	Local handling	[t]	2	2

	Electrical power	[kW]	100	20
	Cooling water	[m ³ /h]	20	20
	Compressed air	[Nm ³ /h]	40	30

9.8 Conclusions

The HL-LHC project will require a major cryogenic upgrade. The main challenges are given below.

- Cooling circuits for large heat deposition.
 - o Up to 13 W/m on 1.9 K cold masses for heat extraction from SC cables and sufficient quench energy margin. Accurate heat flow calculation in coil and yoke cross-section must be developed.
 - o Up to 23 W/m on inner-triplet beam screens possibly with a different operating range (40–60 K) and with a large dynamic range that will require specific cryogenic plant adaptation studies.
- Cooling of HTS SC links and current feedboxes.
- Cooling and pressure relief of crab cavities.
- Validation tests on SC link, crab cavities, magnets, beam screens, etc.
- Quench containment and recovery.
- Larger 1.8 K refrigeration capacities beyond the present state-of-the-art.
- Large capacity (1500 W/3000 W) sub-cooling heat exchangers.
- Larger turndown capacity factor (up to 10) on the 1.8 K refrigeration cycle.

9.9 References

[1] LHC Design Report Geneva : CERN, 2004. - 548 p. DOI: [10.5170/CERN-2004-003-V-1](https://doi.org/10.5170/CERN-2004-003-V-1)

Chapter 10

Energy Deposition and Radiation to Electronics

10 Energy deposition and radiation to electronics

10.1 Characterization of the radiation source

Proton–proton inelastic collisions taking place in the LHC inside its four detectors generate a large number of secondary particles with an average multiplicity of approximately 120 per single proton–proton interaction with 7 TeV beams, but with very substantial fluctuations over different events. Moving away from the interaction point (IP), this multiform population evolves, even before touching the surrounding material, because of the decay of unstable particles (in particular neutral pions decaying into photon pairs). Figure 10-1 illustrates the composition of the debris at 5 mm from the point of a 14 TeV centre of mass collision, featuring a ~30% increase in the number of particles, due to the aforementioned decays, and a clear prevalence of photons (almost 50%) and charged pions (~35%).

Most of these particles are intercepted by the detector and its forward region shielding, releasing their energy within the experimental cavern. However, the most energetic particles, emitted at small angles with respect to the beam direction, travel farther inside the vacuum chamber and reach the accelerator elements, causing a significant impact on the magnets along the insertion regions (IRs), in particular the final focusing quadrupoles and the separation dipoles. Figure 10-1 also shows the breakdown of the debris components going through the aperture of the Target Absorber Secondaries (TAS), a protection element consisting of a 1.8 m long copper core located 20 m from the IP and representing the interface between the detector and the accelerator. The TAS absorbers are only installed on each side of the high luminosity detectors, ATLAS in P1, and CMS in P5, since their protection role, which is in fact limited to the first focusing quadrupole, is not needed for luminosities up to $0.2 \times 10^{34} \text{ cm}^{-2} \text{ s}^{-1}$ [1].

Despite the fact that the number of particles per collision leaving the TAS aperture is more than one order of magnitude lower than the total number of debris particles, they carry about 80% of the total energy, implying that 40% of the released energy at the IP exits on each side of the experiments. At the nominal HL-LHC luminosity ($5 \times 10^{34} \text{ cm}^{-2} \text{ s}^{-1}$), this represents about 3800 W per side that is inevitably impacting upon the LHC elements and consequently dissipated in the machine and in the nearby equipment (e.g. electronics, racks, etc.) and in the tunnels walls.

It is fundamental to study how these particles are lost in order to implement the necessary protections for shielding sensitive parts of the LHC magnets and the machine. For these purposes, Monte Carlo simulations of particle interactions with matter play an essential role, relying on a detailed implementation of physics models and an accurate 3D description of the region of interest.

In addition to the luminosity debris, which dominates energy deposition in the vicinity of the collision points, regular and accidental beam losses represent other relevant sources of radiation. In particular, beam halo particles caught in the collimators (see Chapter 5) initiate hadronic and electromagnetic showers, mainly in the betatron and momentum cleaning IRs, but also from the tertiary collimators around the experiments. The same happens with injection and dumping protection devices (see Chapter 14). Moreover, secondary particle showers are also originated by beam interactions with the residual gas inside the vacuum chamber the length of the accelerator, as well as with dust fragments falling into the beam path.

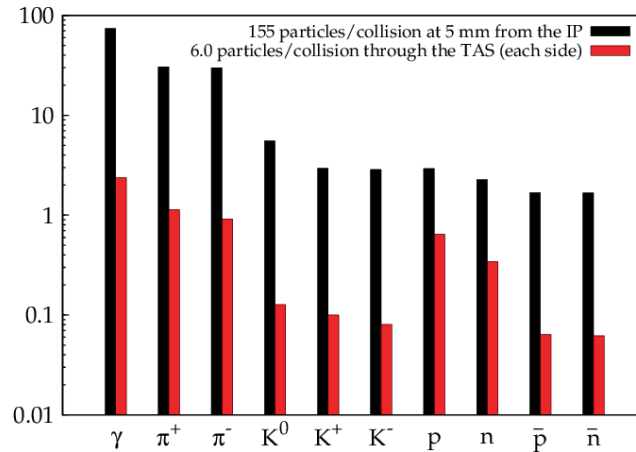


Figure 10-1: Breakdown of the debris particles per single proton–proton inelastic interaction at 5 mm from the interaction point (black) and at the exit of each 60 mm TAS aperture (red).

10.2 Power and dose evaluations concerning the triplet-D1 region

The LHC upgrade includes replacement of the triplet 70 mm Nb-Ti quadrupoles in P1 and P5 with the 150 mm coil aperture Nb₃Sn quadrupoles, along with the new 150 mm coil aperture Nb-Ti separation dipole (D1) and orbit correctors. Moreover, a corrector package (CP) that includes a skew quadrupole and eight high-order magnets (from sextupole to dodecapole, normal and skew, based on Nb-Ti technology) will be located between the triplet and D1.

As the first studies of radiation loads in the HL-LHC have shown [2, 3], one could provide the operational stability and adequate lifetime of the IR superconducting magnets by using tungsten-based inner absorbers in the magnets. The goals of the absorbers are:

- to reduce the peak power density in the inner Nb₃Sn cable to below the quench limit with a safety margin;
- to keep the peak dose in the innermost layers of insulation and radiation loads on inorganic materials in the hottest spots of the coils below the known radiation damage limits all over the HL-LHC lifetime;
- to keep the dynamic heat load to the cold mass at a manageable level.

10.2.1 FLUKA–MARS modeling

To design such a shielding system in a consistent and confident way, coherent investigations have been undertaken with two independent Monte Carlo codes benchmarked up to the TeV energy region and regularly used in such applications: FLUKA at CERN [4–7] and MARS15 (2014) at Fermilab [8–10]. The studies were done for 7 + 7 TeV p–p-collisions with a 295 μ rad half-angle vertical crossing in IP1 (which had previously been found to be the worst case) using DPMJET-III as the event generator [11].

An identical, very detailed geometry model was created and used in both codes with the same materials and magnetic field distributions in each of the components contained within the 80 m region from the IP through to the D1 dipole. An octagonal stainless steel beam screen, equipped with 6 mm tungsten absorbers on the mid-planes, is placed inside the cold bore along the triplet, the CP, and the D1, except in Q1, where the tungsten thickness is increased to 16 mm, compatible with the relaxed aperture requirements. The absorbers are between the beam screen and the 1.9 K beam pipe: they are supported by the beam screen, and thermally connected to it, whereas they have negligible contact with the cold mass. Therefore, from the point of view of energy deposition, the function of the absorber-equipped beam screen is two-fold:

- it shields the coils from the debris;

- it removes a sizable part of the heat load from the 1.9 K cooling system, intercepting it at a higher temperature.

The HL-LHC layout foresees six cryostats on each side of the IP: four for the triplet quadrupoles (Q1, Q2A, Q2B, and Q3), one for the CP and one for D1. The distance between the magnets in the interconnections is 1.5–1.7 m, and an interruption of the beam screen is necessary therein. In the preliminary calculations performed with the specific aim of comparing independent evaluations and reported in this section, we assumed a 500 mm interruption of the tungsten absorbers in the middle of the interconnects as a tentative baseline. Figure 10-2 and Figure 10-3 show a 3D view of the model and details in the inner parts of the quadrupoles and orbit correctors.

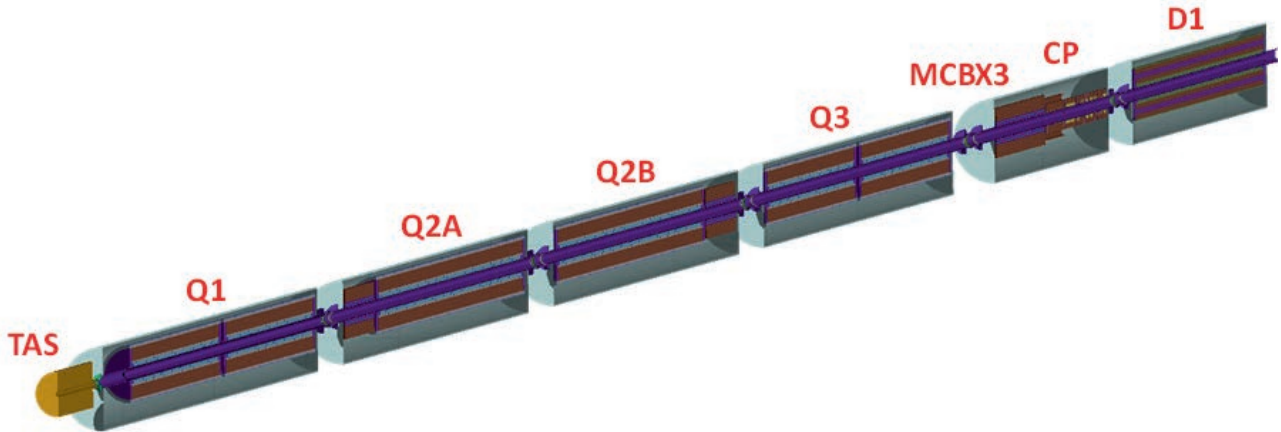


Figure 10-2: HL-LHC inner triplet with MCBX/CP correctors and D1 dipole.

Fine-mesh distributions of power density as well as absorbed dose, neutron fluence, and displacements-per-atom (DPA), along with dynamic heat load in every triplet component were calculated with FLUKA and MARS. The power density and dynamic heat load results are normalized to a luminosity of $5 \times 10^{34} \text{ cm}^{-2} \text{ s}^{-1}$, while all others are normalized to 3000 fb^{-1} integrated luminosity, corresponding to $\sim 10\text{--}12$ years of HL-LHC operation. The longitudinal resolution in the assessment of the quantity of interest is 10 cm, and the azimuthal one is 2° . Radially, power density is averaged over the superconducting cable width, while dose, fluence, and DPA are scored within the innermost layer equal to 3 mm or its thickness, whichever is thinner.

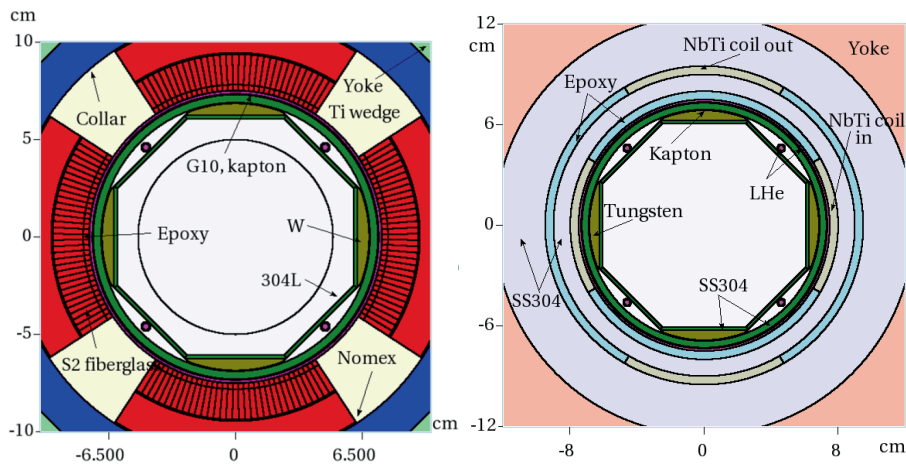


Figure 10-3: Details of the FLUKA-MARS model in the innermost regions of (left) the Q2–Q3 quadrupoles; (right) MCBX orbit correctors. A more advanced implementation is documented in section 10.3.

10.2.2 Operational radiation loads

Power density isocontours at the IP end of the cold mass of the Q2A quadrupole, as calculated by MARS, are shown in Figure 10-4(left). The longitudinal peak power density profile on the inner coils of the IT magnets at the azimuthal maxima is presented in Figure 10-4(right). Results from FLUKA and MARS are in excellent agreement. The observable discrepancies, which are naturally related to the use of fully independent tracking and scoring algorithms and physics models, are largely within the safety margin recommendable at the design stage. The peak value of 2 mW/cm^3 in the quadrupoles is 20 times less than the assumed quench limit of 40 mW/cm^3 in Nb_3Sn coils [2]. The peak value of $\sim 1.5 \text{ mW/cm}^3$ in the Nb-Ti based coils of the correctors and D1 dipole is almost ten times less than the known quench limit of 13 mW/cm^3 in such coils [12].

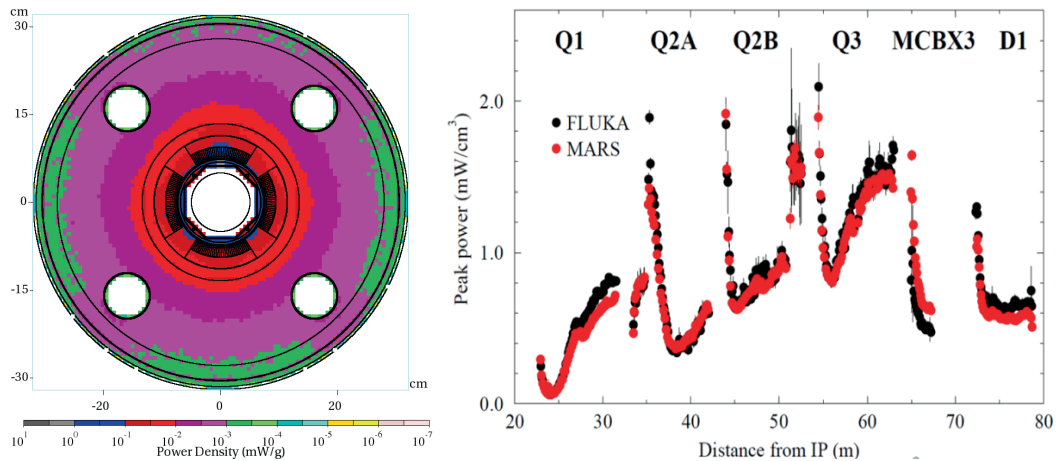


Figure 10-4: (left) Power density isocontours at the IP end of Q2A calculated by MARS; (right) comparison of the longitudinal peak power density profile on the inner coils of the triplet magnets for the MARS and FLUKA codes.

The total power dissipation in the triplet region from the IP1 collision debris splits roughly 50–50 between the cold mass and the beam screen with tungsten absorber, 630 W and 615 W, respectively, from the FLUKA calculations. MARS predicts values about 2% lower. For the 45 m effective length of the cold mass, the average dynamic heat load is $\sim 14 \text{ W/m}$.

More updated values, reflecting the evolution of the optics and layout baseline and the maturation of the various component design, are given in section 10.3 and should be taken as the most reliable reference.

10.2.3 Lifetime radiation loads

The peak dose and DPA – the quantities that define radiation damage and the lifetime of the insulators and non-organic materials of the triplet magnets, respectively – are calculated at the azimuthal maxima in the innermost layers of each triplet component shown in Figure 10-2.

The longitudinal peak dose profiles on the inner coils and insulating materials are presented in Figure 10-5(left). The values in the MCBX orbit correctors (located in the Q1–Q2A, Q2B–Q3, and Q3–D1 regions) are given for the epoxy layer (FLUKA) and kapton layer (MARS); see Figure 10-3 for details. Results from FLUKA and MARS are again in good agreement. The larger aperture triplet magnets and the simulated implementation of tungsten absorbers perform very well, reducing the peak values of both power density and absorbed dose in the HL-LHC IR to the levels that correspond to LHC nominal luminosity.

The maximum peak dose in the coils is about 25 MGy for quadrupoles and $\sim 15 \text{ MGy}$ for the D1 dipole. The integrated peak dose in the triplet magnet insulation reaches 30–36 MGy in the MCBX3 corrector, 28–30 MGy in the quadrupoles, and $\sim 22 \text{ MGy}$ in the D1 dipole. This is at or slightly above the common limits for kapton (25–35 MGy) and CTD-101K epoxy (25 MGy). Also in this case, a re-evaluation based on the latest project baseline can be found in section 10.3.

Degradation of the critical properties of inorganic materials in the magnets – Nb₃Sn and Nb-Ti superconductors, copper stabilizer, and mechanical structures – is usually characterized not by absorbed dose but by integrated neutron fluence and by DPA accumulated in the hottest spots over the magnet's expected lifetime. DPA is the most universal way to characterize the impact of irradiation on inorganic materials. In both FLUKA and MARS, all products of elastic and inelastic nuclear interactions as well as Coulomb elastic scattering (NIEL) of transported charged particles (hadrons, electrons, muons, and heavy ions) from ~1 keV to TeV energies contribute to DPA using energy-dependent displacement efficiency. For neutrons at <20 MeV (FLUKA) and <150 MeV (MARS), the ENDF-VII database with NJOY99 processing is used in both the codes.

The longitudinal peak DPA profiles on the triplet magnet coils are presented in Figure 10-5(right). The peaks are generally observed at the inner coils; therefore, the data is given for these areas. With the vertical crossing in IP1, the MCBX3 orbit corrector is the exception with the peak in the outer coil in the vertical plane (see Figure 10-3(right)). To see this effect, the MARS data in Figure 10-5(right) for MCBX3 is given for the outer coil, while FLUKA shows results for the inner coil as in all other magnets. Contrary to the power density and dose distributions driven by electromagnetic showers initiated by photons from π^0 decays, DPA peaks at the non-IP end of the Q1B quadrupole. At that location, about 70% of DPA is from neutrons with $E < 20$ MeV, ~25% from transported nuclear recoils above 0.25 keV/A, and the rest is due to other transported particles and non-transported recoils. The thicker Q1 shielding, while assuring a very effective dose reduction, plays a clear role in enhancing neutron production.

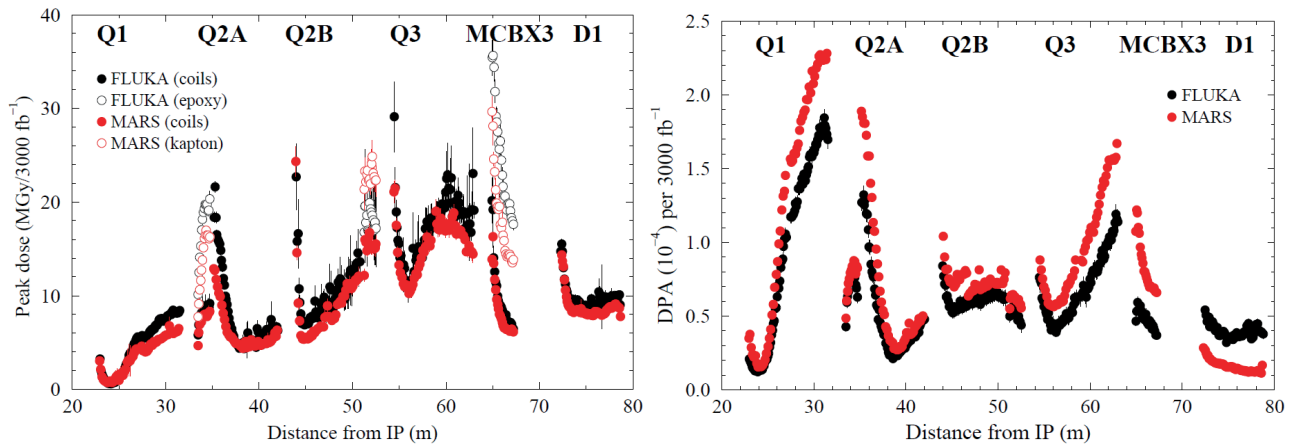


Figure 10-5: Longitudinal distributions of (left) peak dose on inner coils and nearby insulators; (right) peak DPA on inner coils.

The peak in the Q1B inner coil is about 2×10^{-4} DPA per 3000 fb^{-1} integrated luminosity. In other triplet components it is about $(1 \pm 0.5) \times 10^{-4}$. These numbers should be acceptable for the superconductors and copper stabilizer provided that there is periodic annealing during the collider shutdowns. Taking into account a good correlation of DPA with neutron fluence in the coils, one can also compare the latter with known limits. In the quadrupole coils, the peak fluence is $\sim 2 \times 10^{17} \text{ cm}^{-2}$ that is substantially lower than the $3 \times 10^{18} \text{ cm}^{-2}$ limit used for the Nb₃Sn superconductor. In the orbit corrector and D1 dipole coils, the peak fluence is $\sim 5 \times 10^{16} \text{ cm}^{-2}$ that is again lower than the 10^{18} cm^{-2} limit used for the Nb-Ti superconductor. The integrated DPA in the magnet mechanical structures are several orders of magnitude lower than the ~ 10 DPA limit for these materials. Corresponding neutron fluences range from $3 \times 10^{16} \text{ cm}^{-2}$ to $3 \times 10^{17} \text{ cm}^{-2}$, compared to the 10^{21} cm^{-2} to $7 \times 10^{22} \text{ cm}^{-2}$ limits.

Peak dose on the beam screen was found to be of the order of several hundred MGy after 3000 fb^{-1} integrated luminosity (up to 700 MGy in D1), mostly carried by electromagnetic particles. If the use of carbon coating is considered, its resistance to such a dose has to be assessed.

10.3 Update to HL-LHCv1.2

Since the completion of the original FLUKA–MARS intercomparison, as reported in the previous section, many relevant ingredients have evolved and their progressive implementation in the FLUKA model has led to more accurate results, accounted for in the following. In particular, since the beam screen equipped with tungsten absorbers represents the backbone element for the protection of the IR magnets, the details of its design play a crucial role in determining its actual effectiveness.

In this respect, the real absorber material, Inermet 180, which has a density of 18 g cm^{-3} , about 8% less than the one of pure tungsten initially assumed, was considered, implying a reduced shielding performance. Moreover, the reduction of the beam screen thickness (from 2 mm to 1 mm) was necessary to let the structure respond elastically to possible deformations occurring during a quench. In addition, the first prototype proposal embedding those modifications and applying to all magnets but Q1 (due to the thicker shielding included in the latter) was later reworked to extend the Inermet absorbers towards the quadrupole poles, in order to better cover the coils (see Figure 10-6(b) and (c)). This is needed because, starting from Q2, most of the charged debris is pushed by the magnetic field from the crossing angle side to the opposite side and the energy deposition peak moves through different azimuthal regions, which have to be properly shielded. However, the mentioned extension between the mid planes cannot be fulfilled along the whole magnet length, since the pumping slots entail longitudinal gaps limiting it to an effective filling factor, initially guessed at 0.5 and eventually reduced to 0.2 (meaning the alternation of 2 cm long Inermet pieces with 8 cm gaps at 45°).

Figure 10-6 shows the revised magnet models, where a more accurate coil design is implemented – especially different from the initial one in Figure 10-3 for the MCBX orbit correctors – and the aperture dimensions comply with a cold coil inner radius of 74.35 mm. The latter has to accommodate 0.25 mm coil insulation, a 1.5 mm superfluid Helium layer and a 4 mm thick cold bore wall as well as its 0.2 mm insulation, yielding an outer radial limit of 68.4 mm for the beam screen with the Inermet absorbers.

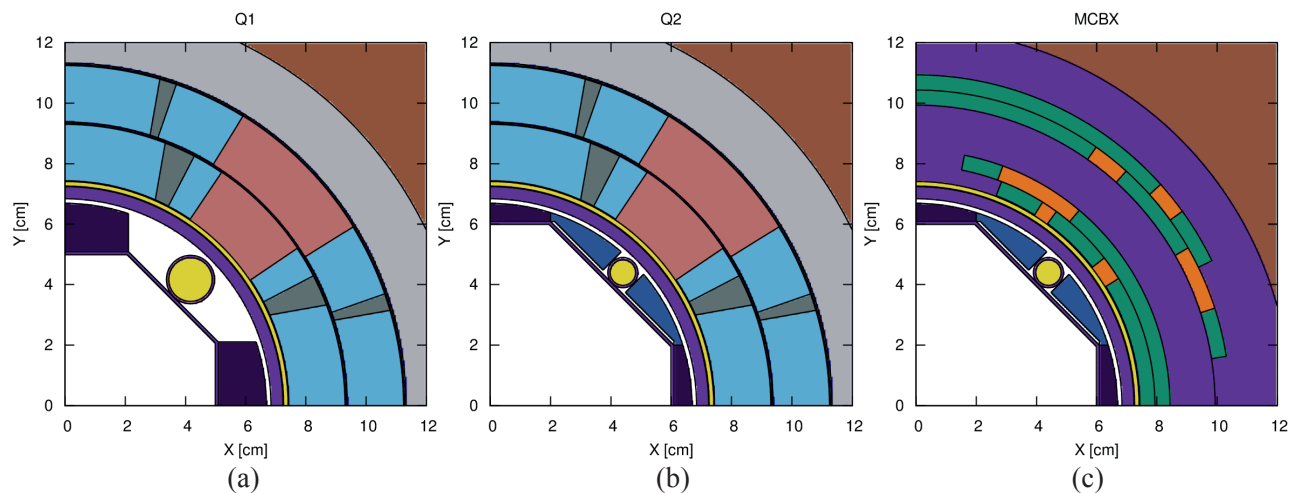


Figure 10-6: Cross-sections of triplet quadrupoles and orbit correctors: (a) Q1; (b) Q2; (c) MCBX. The extension of the Inermet absorbers around the Helium channel at 45° , implemented from Q2 onwards in alternation with pumping slot gaps, can be noted.

Another crucial aspect is the longitudinal interruption of the beam screen and its absorbers between two consecutive cryostats. As mentioned in the previous section, we initially assumed a 500 mm gap. With the elaboration of a realistic interconnect design, hosting a BPM as reproduced in the FLUKA model shown in Figure 10-7, the gap exceeds 700 mm, leaving the IP end of the following magnet less protected.

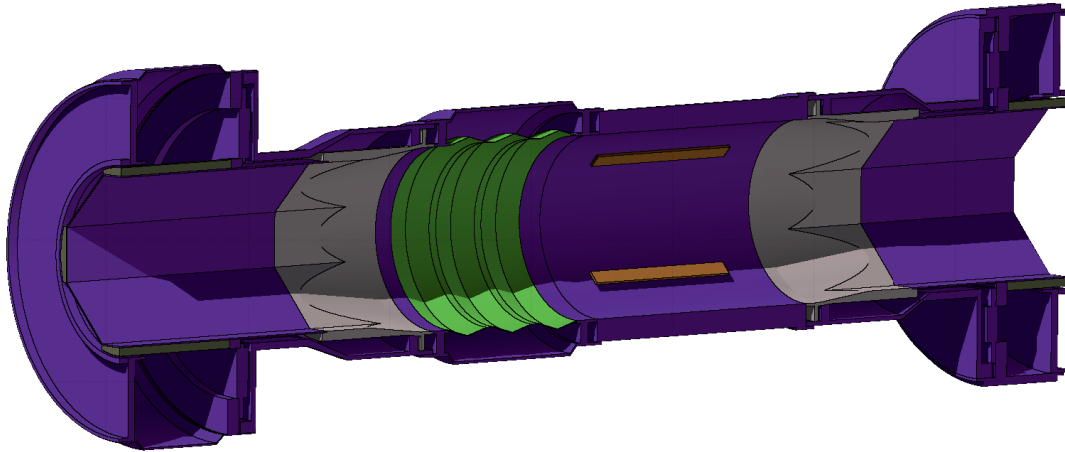


Figure 10-7: FLUKA model of triplet interconnects, including a circular BPM with its electrode strips (in brown).

The results reported in this section refer to the HL-LHCv1.2 optics and explore both crossing schemes, vertical in IP1 and horizontal in IP5, with a 295 μrad half-angle and round beams at the IP as already assumed initially. Table 10-1 lists the power absorbed by the triplet–D1 string elements, distinguishing what is taken by the absorber equipped beam screen from the amount collected in the 1.9 K cold mass. The fairly equilibrated sharing between the two cooling systems as well as the original estimate of about 600 W for each of them are substantially confirmed, with a natural increase on the cold mass as the presence of the absorbers out of the mid planes is (more realistically) reduced. For horizontal crossing, the total load is roughly 10% lower.

Table 10-1: Heat loads at $5 \times 10^{34} \text{ cm}^{-2} \text{ s}^{-1}$ for different crossing schemes and absorber implementations.

Cooling system	Round vertical 0.5 filling factor at 45°		Round horizontal 0.5 filling factor at 45°		Round vertical 0.2 filling factor at 45°	
	Magnet cold mass	Beam screen	Magnet cold mass	Beam screen	Magnet cold mass	Beam screen
	Absorbed power [W]					
Q1A + Q1B	111	167	117	171	113	170
Q2A + MCBX1	93	77	85	67	103	70
Q2B + MCBX2	113	98	119	102	121	85
Q3A + Q3B	124	102	107	83	141	86
MCBX3 + CP	57	71	39	49	56	69
D1	75	71	61	56	74	71
Beam tube prolongations	11	78	9	65	12	77
TOTAL	584	664	537	593	621	628

Figure 10-8 gives a re-evaluation of Figure 10-4(left), as far as vertical crossing is concerned, and adds the information for horizontal crossing. The two curves reflect the different coupling between the same magnetic configuration of the triplet (Focusing-Defocusing-Focusing in the horizontal plane for the outgoing beam) and the different crossing planes, where the debris is oriented by the transverse component of the colliding beam momentum. Peak power density remains well below design values overall. The effect of the interconnects, where the absorbers are interrupted, is clearly visible on the IP ends and becomes especially pronounced on Q2B for horizontal crossing.

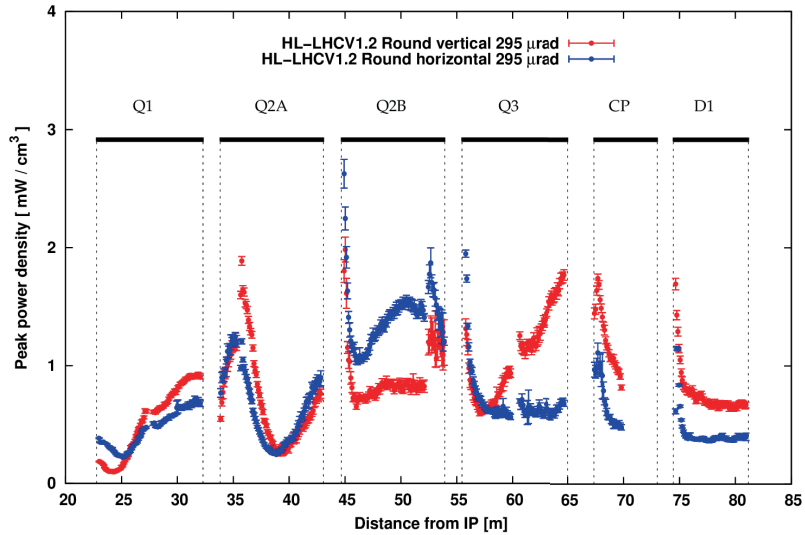


Figure 10-8: Peak power density profile in the magnet inner coils (radially averaged over the cable width), for vertical (red) and horizontal (blue) beam crossing. Error bars indicate statistical uncertainties. $L = 5 \times 10^{34} \text{ cm}^{-2} \text{ s}^{-1}$.

Similar features are displayed by the peak dose profile in Figure 10-9, not far from 40 MGy, after 3000 fb^{-1} in 295 μrad half-angle horizontal crossing, at the localized maximum on the Q2B IP end. There, a good 15% reduction can be achieved by a 7 cm prolongation of the beam screen absorbers inside the non-IP hand of the interconnect, deemed to be possible. Such a reduction would be doubled, dropping to a 25 MGy maximum, if the option of an octagonal BPM embedding the same absorbers is retained. It has to be noted that the highest values previously expected in the MCBX3 insulator, according to Figure 10-5 (left) and Figure 10-3(right), are actually falling in the collar region, after considering the revised orbit corrector design as in Figure 10-6(c).

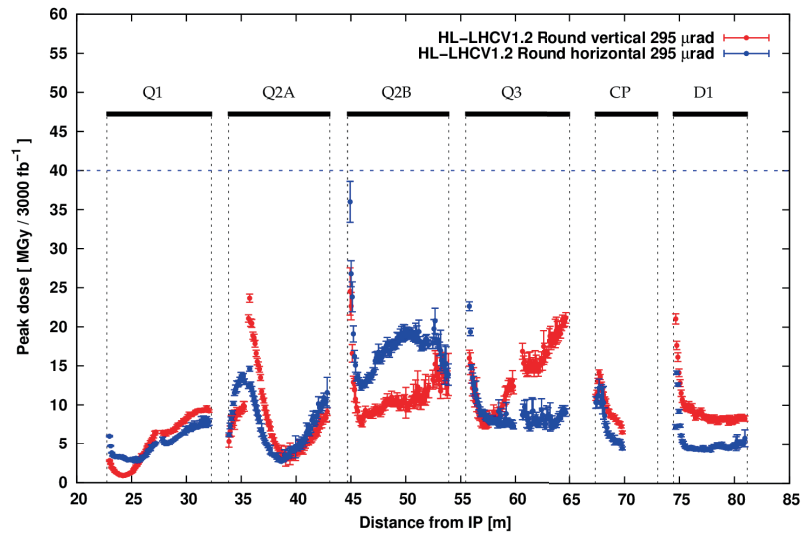


Figure 10-9: Peak dose profile in the magnet inner coils (radially averaged over the innermost layer, $\leq 3\text{mm}$), for vertical (red) and horizontal (blue) beam crossing. Error bars indicate statistical uncertainties. $L_{\text{int}} = 3000 \text{ fb}^{-1}$.

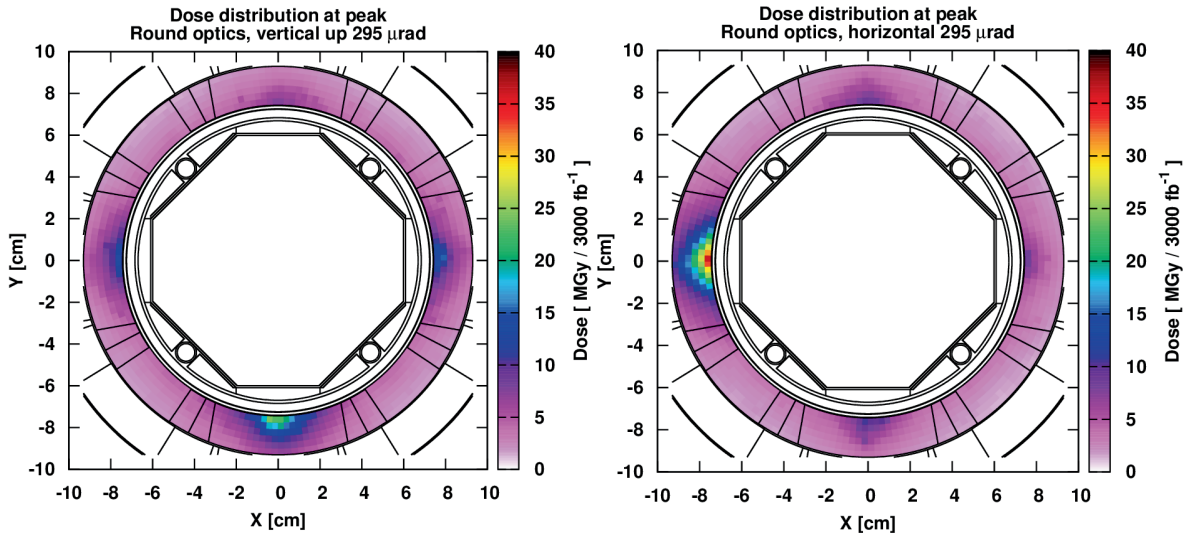


Figure 10-10: Dose two-dimensional distribution over the coil radial range, corresponding to the Q2B maximum as in Figure 10-9, for vertical (left) and horizontal (right) beam crossing.

Looking at the azimuthal dose distribution, shown in Figure 10-10 at the Q2B maximum, one can realize that the hot spot is well defined and lies opposite to the crossing angle side, where instead it is found inside Q1 and on the IP hand of Q2A. This feature could be exploited by changing the crossing plane and the vertical angle polarity during the run (the polarity of the horizontal angle has no degree of freedom, to avoid undesired bunch collisions in the machine near the D1 separation dipole). As originally proposed for the current LHC operation (concerning only the vertical crossing polarity in ATLAS, due to physical aperture limitations preventing the crossing plane swap), a mitigation technique of this kind divides the maximum dose among different mid plane positions and allows for a significant reduction of its value, yielding a valuable lifetime increase with respect to the worst fixed angle case [13]. This technique requires either rotation of the installed crab cavities or a swap of the IR1 and IR5 crab cavities during an extended technical stop. The operational implications of this procedure are still under study. Additionally, the possible adoption of a smaller crossing angle, as for instance envisaged for flat optics, provides a clear benefit, systematically lowering the peak energy deposition profile along the whole string.

10.4 Impact on the matching section and protection strategy

The HL-LHC upgrade foresees changes in the IR1 and IR5 matching section, implying a new Target Absorber Neutral (TAXN) absorber and a new recombination dipole D2 with its two new correctors. All new elements feature larger twin apertures, of 85 mm inner diameter for TAXN and 105 mm coil inner diameter for the magnets in the D2 cryostat. The option of a new 90 mm aperture Q4, accompanied by two new correctors, is now postponed, but was assumed in the study reported in this section, which refers again to the HL-LHCv1.2 round optics for both crossing schemes. The current baseline also foresees the Q5 replacement with the present Q4, providing an aperture increase from 56 mm to 70 mm, and the installation of crab cavities (two per side per beam, while the HL-LHCv1.2 study assumed twice as much). From Q6 onwards, no hardware modifications are expected inside the IRs.

With respect to the present LHC, the energy deposition in the matching section elements is mainly impacted by the variation of three ingredients. They are:

- the distance between the separation/recombination dipoles (reduced from 86 m to 65 m);
- the aperture of the upstream magnets (triplet quadrupoles, CP correctors and D1);
- the TAXN design, which has to comply with larger beam sizes.

As a consequence, the number of debris particles entering the matching section per primary collision is much larger than in the case of the current machine. This is illustrated in Figure 10-11, where the debris particle distribution at the exit of the TA(X)N outgoing beam pipe is shown for the LHC (Figure 10-11(left)) and the HL-LHC (Figure 10-11(right)). The number of protons is increased by about 30% (from 0.12 to 0.16 protons/collision), while the number of photons and neutrons is about seven times higher (from 0.06 to 0.41 particles/collision). Note that in the case of the HL-LHC optics the beam size at this location is about twice as large as that of the LHC optics. Therefore, a collimator set at the same aperture in beam σ turns out to be less effective in intercepting debris particles, as clearly revealed in the figure by the number of particles left inside the beam envelope.

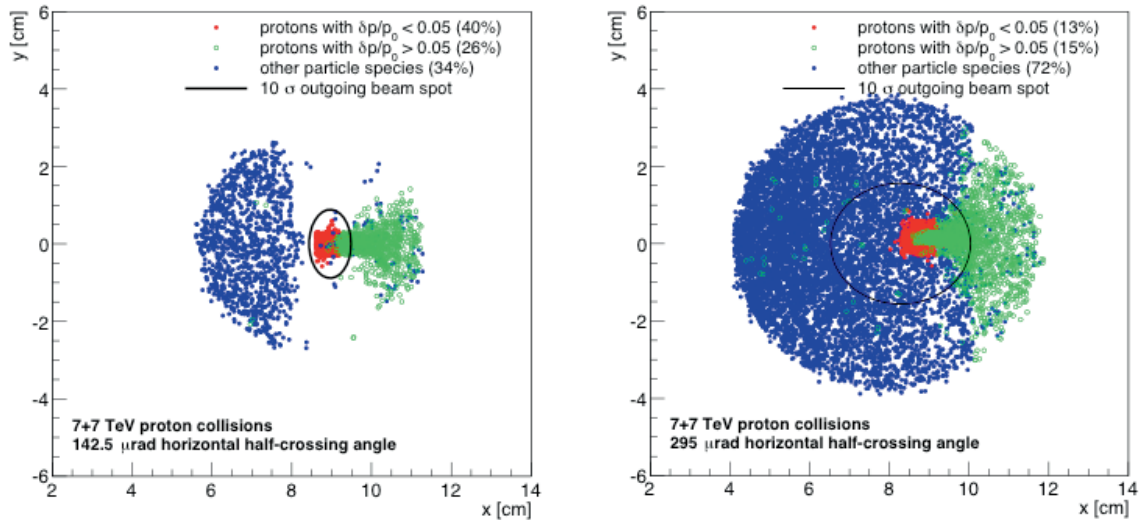


Figure 10-11: Debris particle distribution at the exit of the outgoing beam pipe of the TA(X)N, (left) for the LHC; (right) for the HL-LHC. Red points indicate protons with magnetic rigidity within 5% with respect to beam protons and green points indicate protons with lower magnetic rigidity. Blue points indicate neutral particles (photons and neutrons). The same number of collision is simulated in both cases. The black ellipse shows the 10σ outgoing beam envelope for round beam optics.

In the present LHC, a network of target long physics debris collimators (TCL) secures the protection of the cold magnets in the matching section. There is one copper TCL in front of D2 (TCL4, installed during LS1), one copper TCL in front of Q5 (TCL5, the only one already present and operating during Run 1), and one tungsten TCL in front of Q6 (TCL6, whose installation during LS1 was triggered by specific Roman pot operation scenarios). However, at nominal luminosity not all TCLs are necessary to keep the heat load below the quench level. It was shown that the single TCL4 set at 15σ is sufficient to maintain the peak power density below 0.3 mW/cm^3 in all matching section magnets [14].

Conversely, in the case of the HL-LHC, all of the TCLs are indispensable for magnet protection. For the purposes of the estimates presented here, the jaws of all the collimators are assumed to be made of tungsten (Inermet 180) because of its greater absorption efficiency (higher density and atomic number than copper). The first collimator, located between TAXN and D2, requires a special design with thicker jaws (TCLX4), in order to assure an adequate transverse coverage. Moreover, additional fixed target collimator long masks (TCLM) are needed downstream of the other two TCL collimators in order to further shield the aperture of the magnets in the Q5 and Q6 cryostats. Since the hottest spot is typically located on the IP side of each magnet, a shielding strategy based on a beam screen equipped with thick absorbers, as in the IT region, does not pay here. On the other hand, the Inermet masks, which are 1 m long and have the same aperture as the beam screen of the protected magnets and a radial thickness sufficient to shadow the coils, can ensure an effective interception of the shower coming from the upstream elements.

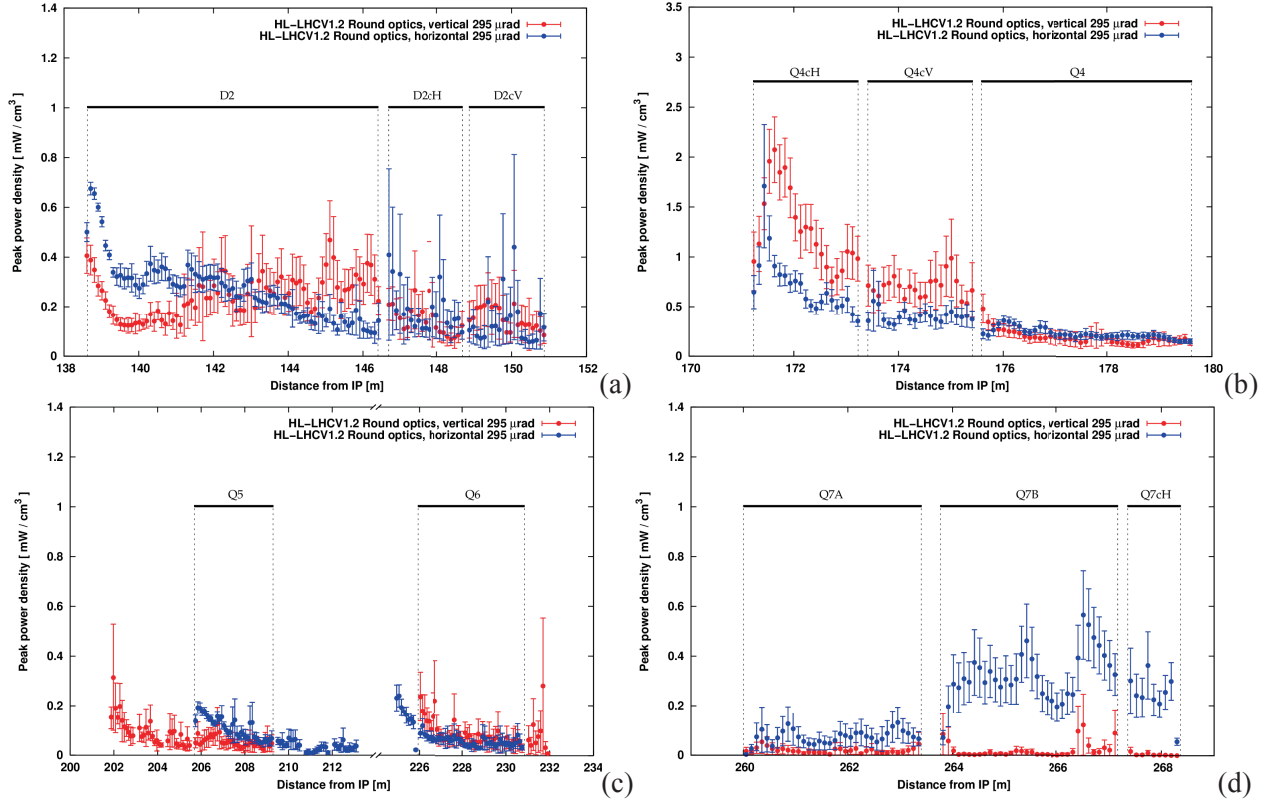


Figure 10-12: Peak power density profile in the magnet coils around the outgoing beam bore (radially averaged over the cable width), for vertical (red) and horizontal (blue) beam crossing, along the matching section cryostats: (a) D2; (b) Q4 (note the different vertical scale); (c) Q5 and Q6; (d) Q7. The position of the Q5 and Q6 correctors (three and one, respectively) varies between P1 (red, vertical crossing) and P5 (blue, horizontal crossing). The three TCL(X) opening is assumed to be 12σ (half gap). Error bars indicate statistical uncertainties. $L = 5 \times 10^{34} \text{ cm}^{-2} \text{ s}^{-1}$.

With this protection scheme in place, the power density in the quadrupole and corrector coils is kept at fully acceptable levels, as shown in Figure 10-12 for the outgoing beam bore. However, with the aperture of the Q4 cryostat magnets now maintained at 70 mm (coil inner diameter), differently from the 90 mm model assumed in Figure 10-12 (b), the hot spot on the IP end of the first Q4 corrector is expected to significantly worsen and calls for another TCLM in front (in the studied layout no protection element was deemed to be necessary for Q4 – as for Q7 –, also considering the integration challenges of the TAXN–Q4 region). Concerning lifetime goals, this additional Q4 mask will have to prove to suitably cure the corresponding increase in the maximum dose, which already reaches 25 MGy after 3000 fb^{-1} with the more favourable 90 mm aperture and no shielding. The situation on the incoming beam bore is more relaxed, provided that the tertiary collimators (TCTs) are not removed or fully opened, in particular the pair between TAXN and D2. In fact, they are meant to protect the triplet and the detector from incoming beam losses, but they turn out to play a critical role also for the D2 and Q4 protection from the collision debris, especially in case of vertical crossing.

In terms of total power loads, the leakage through the TAXN to the matching section is logically more severe for horizontal crossing and mainly impacts D2, which at $5 \times 10^{34} \text{ cm}^{-2} \text{ s}^{-1}$ absorbs 35 W (compared with almost 20 W for vertical crossing). For the crab cavities, a quite significant dependence on the upstream vacuum chamber profile, whose details are not yet defined, was found. The most exposed one (on the outgoing beam) can collect from few hundred mW up to 1 W. The maximum power density is located on the cavity internal plate and is in the range between 0.1 and 1 mW/cm^2 . It corresponds to 1 to several MGy after the target HL-LHC integrated luminosity.

10.5 Exposure of the superconducting links

Cold powering of the HL-LHC magnets foresees connecting lines made of MgB_2 [15]. The link cold mass contains SC cables that are connected at one end, in the tunnel, to the Nb-Ti magnet busbar operating in liquid helium; the other end is connected to the current leads maintained at a maximum temperature (T_{CL}) of about 20 K in a helium gas environment, see Figure 10-13 [16].

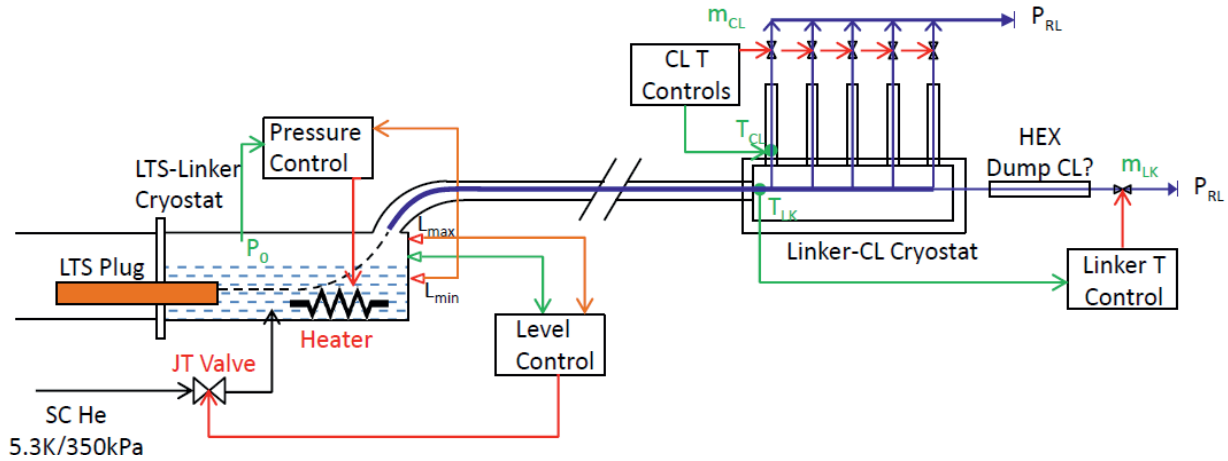


Figure 10-13: Cooling scheme of the cold powering system. Left-hand side: low temperature (LT) side, where there are the connections with the SC magnet cable. Right-hand side: connection with the current leads (CL).

The radiation impact on the MgB_2 SC links is evaluated from different points of view. Boron consumption by thermal neutrons is not a concern. The total number of neutrons escaping from the first quadrupole of the new triplet is of the order of 10^{21} , over an integrated luminosity of 3000 fb^{-1} . Considering the amount of ^{10}B in the links, consumption can be estimated to be much less than 0.01%.

The links in P1 and P5 consist of a multi-cable assembly as shown in Figure 10-14.

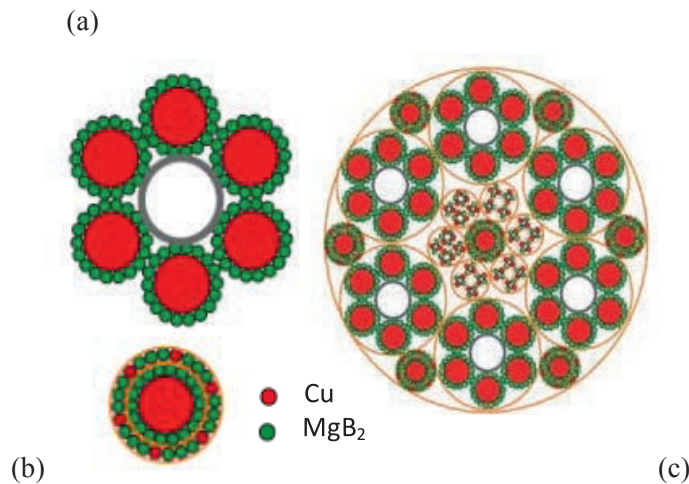


Figure 10-14: (a) 18 kA MgB_2 cable, $\varnothing = 19.5 \text{ mm}$; (b) two MgB_2 concentric cables for 3 kA total current, $\varnothing = 8.5 \text{ mm}$; (c) 165 kA cable assembly for LHC P1 and P5 ($6 \times 20 \text{ kA}$, $7 \times 2 \times 3 \text{ kA}$, $4 \times 0.4 \text{ kA}$, $18 \times 0.12 \text{ kA}$), $\varnothing = 65 \text{ mm}$. The cables are made of copper stabilizer (red) and MgB_2 wire (green).

The calculated dose maps for the horizontal and vertical routing of the SC link inside the shuffling module (i.e. the interface with the magnet cryostat) are shown in Figure 10-15 for P1. The obtained values (up to about 1 MGy) are not expected to affect the link operation (provided that the chosen insulator is radiation

resistant). The maximum DPA induced in the links is of the order of 10^{-6} . Preliminary simulations for P5 indicate the same outcome as for P1.

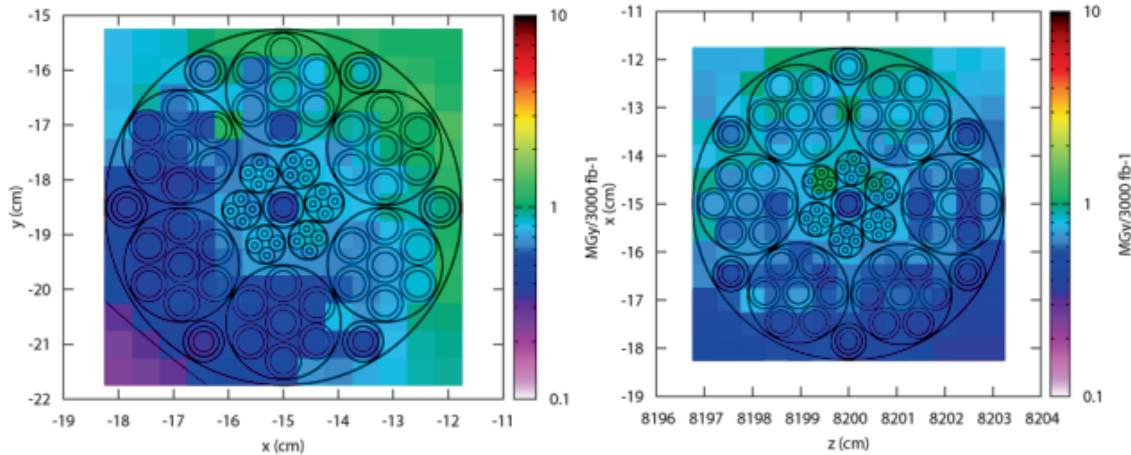


Figure 10-15: Maps of dose released in the SC Link in the P1 shuffling module. (left) Superconducting horizontal cable shuffle module dose; (right) Superconducting vertical cable shuffle module dose. Values (in MGy) are normalized to 3000 fb^{-1} .

10.6 Radiation To Electronics

A specific problem is represented by the sensitivity of electronics to radiation. The above described particle debris emerging from the IP (together with the additional loss contribution from beam-gas interactions, which however is not expected to bring a significant increase) will impact equipment present in the areas adjacent to the LHC tunnel (UJs, RRs). Installed (present or future) control systems are either fully commercial or based on commercial-off-the-shelf (COTS) components, both possibly affected by radiation. This includes the immediate risk of single event effects (SEE) and a possible direct impact on beam operation, as well as in the long-term cumulative dose effects (impacting the component/system lifetime) that additionally have to be considered.

For the tunnel equipment in the existing LHC, radiation was only partially taken into account as a design criterion prior to construction, and most of the equipment placed in adjacent and partly shielded areas was not conceived nor tested for their actual radiation environment. Therefore, given the large amount of electronics being installed in these areas, during the past years a CERN-wide project called Radiation To Electronics (R2E) [17] has been initiated to quantify the danger of radiation-induced failures and to mitigate the risk for nominal beams and beyond to below one failure per week. The respective mitigation process included a detailed analysis of the radiation fields involved, intensities and related Monte Carlo calculations; radiation monitoring and benchmarking; the behaviour of commercial equipment/systems and their use in the LHC radiation fields; as well as radiation tests with dedicated test areas and facilities [17, 18].

In parallel, radiation-induced failures were analysed in detail in order to confirm early predictions of failure rates, as well as to study the effectiveness of implemented mitigation measures. Figure 10-16 shows the actual number of SEE failures measured during 2011 and 2012 operations, the achieved improvement (note that the failure rate measured during 2011 already benefitted from mitigation measures implemented during 2009 and 2010), as well as the goal for operation after LS1 and during the HL-LHC era.

Aiming for annual luminosities of 250 fb^{-1} , it is clear that machine availability has to be maximized during the HL-LHC period in order to successfully achieve the physics goal. This implies that existing electronics control systems are either installed in fully safe areas, sufficiently protected by shielding, or are made adequately radiation tolerant.

The last statement implies that existing equipment, as well as any future equipment that may be installed in R2E critical areas, must be conceived in a specific way.

Radiation damage to electronics is often considered in space applications. However, it is important to note that the radiation environment encountered at the LHC, the high number of electronics systems and components partly exposed to radiation, as well as the actual impact of radiation-induced failures, differ strongly from the context of space applications. While design, test, and monitoring standards are already well defined for the latter, additional constraints, but in some cases also simplifications, have to be considered for the accelerator environment.

The mixed particle type and energy field encountered in the relevant LHC areas is composed of charged and neutral hadrons (protons, pions, kaons, and neutrons), photons, electrons, and muons ranging from thermal energies up to the GeV range. This complex field has been extensively simulated by the FLUKA Monte Carlo code and benchmarked in detail for radiation damage issues at the LHC [19, 20]. As discussed above, the observed radiation is due to particles generated by proton–proton (or ion–ion) collisions in the LHC experimental areas, distributed beam losses (protons, ions) around the machine, and to beam interaction with the residual gas inside the beam pipe. The proportion of the different particle species in the field depends on the distance and on the angle with respect to the original loss point, as well as on the amount (if any) of installed shielding material. In this environment, electronics components and systems exposed to a mixed radiation field will experience three different types of radiation damage: displacement damage, damage from the total ionizing dose (TID), and SEEs. The latter range from single event or multiple bit upsets (SEUs or MBUs), transients (SETs) up to possible destructive latch-ups (SELs), destructive gate ruptures, or burn-outs (SEGRs and SEBs).

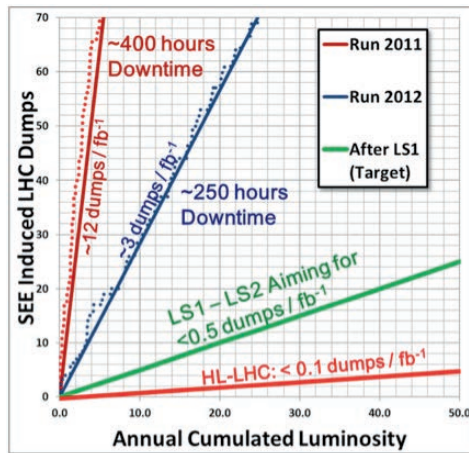


Figure 10-16: LHC beam dumps due to single event effects against beam luminosity. Dots (2011 and 2012) refer to measurements, whereas lines show annual averages for both past and future operations.

The first two groups are of cumulative nature and are measured through TID and non-ionizing energy deposition (non-ionizing energy losses (NIEL), generally quantified through accumulated 1 MeV neutron equivalent fluence), where the steady accumulation of defects causes measurable effects that can ultimately lead to device failure. As for stochastic SEE failures, they form an entirely different group, since they are due to ionization by a single particle, and are able to deposit sufficient energy to perturb the operation of the device. They can only be characterized in terms of their probability of occurring as a function of accumulated high energy (>20 MeV) hadron (HEH) fluence, incorporating also the weighted contribution of lower energy neutrons [21]. The probability of failure will strongly depend on the device as well as on the flux and nature of the particles. In the context of the HL-LHC, several tunnel areas close to the LHC tunnel, and partly not sufficiently shielded, are or are supposed to be equipped with commercial or not specifically designed electronics that are mostly affected by the risk of SEEs, whereas electronics installed in the LHC tunnel will also suffer from accumulated damage in the long term [22].

Three distinct areas are to be distinguished.

- The accelerator between the Triplet and Q6: in this area no active electronics is installed and any future installation should certainly be avoided as radiation levels clearly exceed the usability domain of

commercial components and also pose significant constraints to custom designs, including application specific integrated circuits (ASICs).

- The adjacent (shielded) areas: where the shielding has been maximized before and during LS1 and where radiation levels become acceptable for characterized and qualified custom electronics. The equipment and selected electronics components have to be qualified for both SEEs and TID. For the first, it is important that radiation tests are carried out in a representative radiation environment, or adequate safety margins have to be added [23]. Fully commercial systems (COTS based) are still to be avoided in these areas. In case they are required, their failure impact and respective mitigation has to be studied in the context of accelerator operation.
- The dispersion suppressor area: given the fact that the magnets have to be protected against quenches, it is likely that the leakage into this area must not increase significantly with respect to nominal LHC operation. A detailed quantification is, however, needed to coherently design the required control electronics, again both for SEE effects as well as for their lifetime (TID) to comply with the stringent availability requirement, as shown in Figure 10-16.

During the first years of LHC operation, the radiation levels in the LHC tunnel and in the (partly) shielded areas have been measured using the CERN RadMon system [24], which is dedicated to the analysis of radiation levels possibly impacting installed electronics equipment.

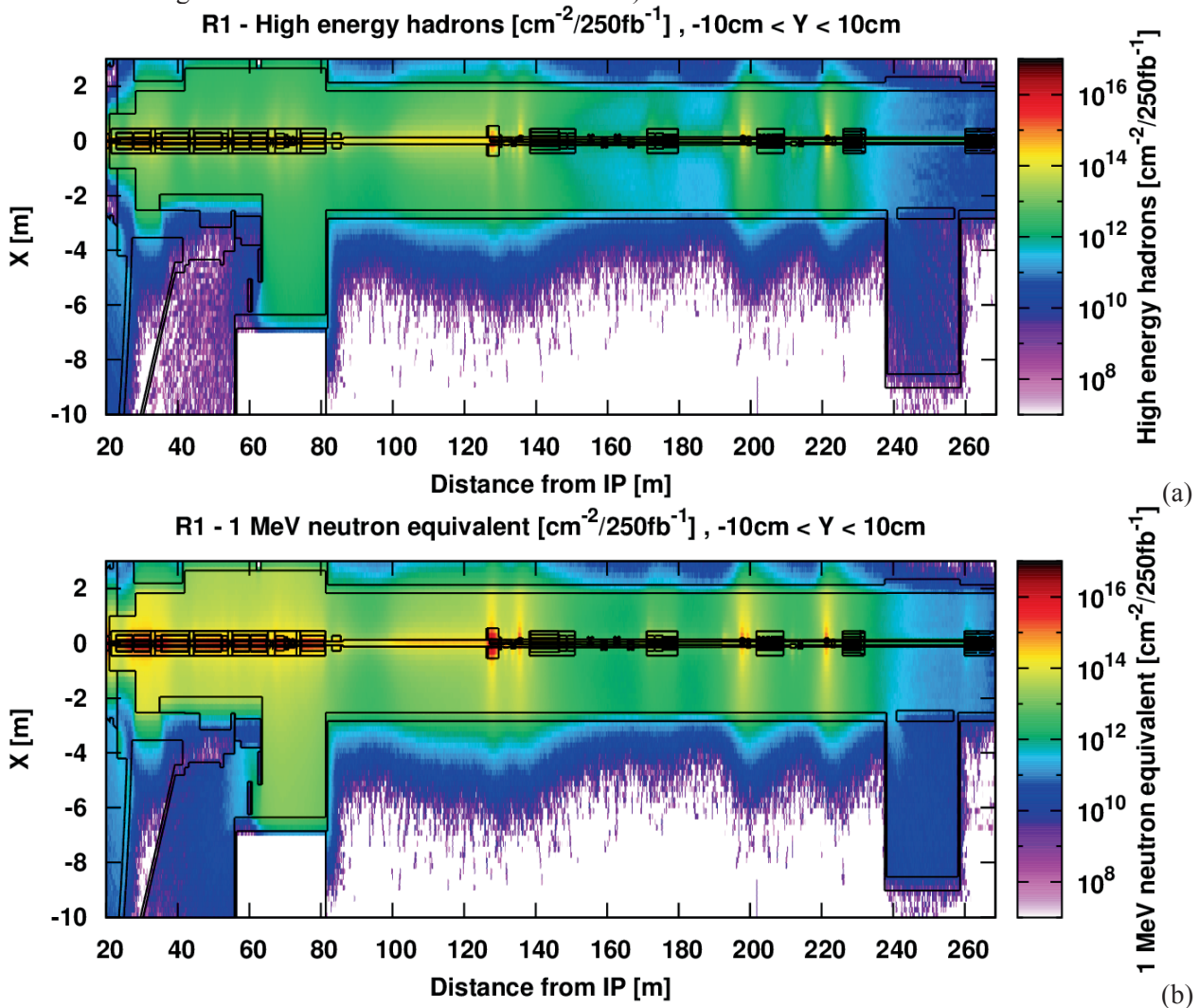
Table 10-2 summarizes the level of accumulated HEH fluence measured during 2012 for the most critical LHC areas where electronics equipment is installed and that are relevant for the HL-LHC project, together with the expected annual radiation levels for nominal LHC performance ($50 \text{ fb}^{-1}/\text{y}$). The HEH fluence measurements are based on the RadMon reading of the SEUs of SRAM memories whose sensitivity has been extensively calibrated in various facilities [25, 26]. The results obtained during the 2012 LHC proton operation show that the measurements compare very well with previously performed FLUKA calculations, and that observed differences can actually be attributed to changes of operational parameters not considered in the calculations [27]. In a first approximation, the measured radiation levels can also be used to extrapolate towards the HL-LHC by purely scaling with annual luminosity (see the last two columns of Table 10-2); keeping in mind, however, that operational and layout parameters (beam energy, crossing angle, TAXN design, absorbers and masks, collimator settings, etc.) can have a non-negligible impact on the final values, especially for the RRs close to the matching section. The resulting values clearly indicate that any equipment installed in the LHC tunnel will not only suffer SEE failures, but will also be heavily impacted by TID effects, thus limiting the its lifetime.

Table 10-2: Predicted and measured annual HEH fluence in critical shielded areas for a cumulated ATLAS/CMS luminosity of 15 fb^{-1} during 2012 operation, then extrapolated based on the measurement to the expected nominal and HL-LHC performance ($50 \text{ fb}^{-1}/\text{y}$ for nominal and $250 \text{ fb}^{-1}/\text{y}$ for HL-LHC performance, except for P8 where 2012 can already be considered as almost nominal and HL-LHC refers to a five-fold increase). For the HL-LHC an estimate for corresponding annual TID levels is also given.

LHC	Prediction	Measured	Nominal	HL-LHC	HL-LHC
UJ14/16	1.4×10^8	1.6×10^8	5×10^8	3×10^9	6
RR13/17	4.0×10^7	2.5×10^7	8×10^7	5×10^8	1
UJ56	1.6×10^8	1.5×10^8	5×10^8	3×10^9	6
RR53/57	4.0×10^7	2.5×10^7	8×10^7	5×10^8	1
UJ76	2.1×10^7	6.0×10^7	2×10^8	1×10^9	2
RR73/77	2.9×10^7	5.0×10^7	2×10^8	1×10^9	2
UX85B	4.3×10^8	3.5×10^8	4×10^8	2×10^9	4
US85	1.3×10^8	8.8×10^7	9×10^7	4×10^8	1

Dedicated maps of R2E relevant quantities in the tunnel and adjacent areas of the high luminosity experimental insertions (P1 and P5), in their HL-LHC configuration, are available by FLUKA simulations, as shown in Figure 10-17. In the UJ area, on the side of the inner triplet, the expected annual value of HEH fluence behind the shielding confirms the respective extrapolation reported in the first row of Table 10-2. On the other hand, inside the RR area at the far end of the matching section, the calculated level exceeds by more than one order of magnitude the $5 \times 10^8 \text{ cm}^{-2}/\text{y}$ value scaled up from past measurements. The reason for this substantial increase is the use of the TCL6 collimator, which becomes the dominant source of radiation due to its position, as clearly visible in the figure.

Any control equipment (commercial or based on commercial components) to be installed in these areas clearly has to be proven to be sufficiently radiation tolerant. For comparison, as mentioned earlier, during the last years of operation we have already observed a number of radiation-induced failures of commercial equipment at radiation levels corresponding to $10^8\text{--}10^9 \text{ cm}^{-2}/\text{y}$ (which is about 1 000–10 000 times more than what one would get at the surface due to cosmic radiation).



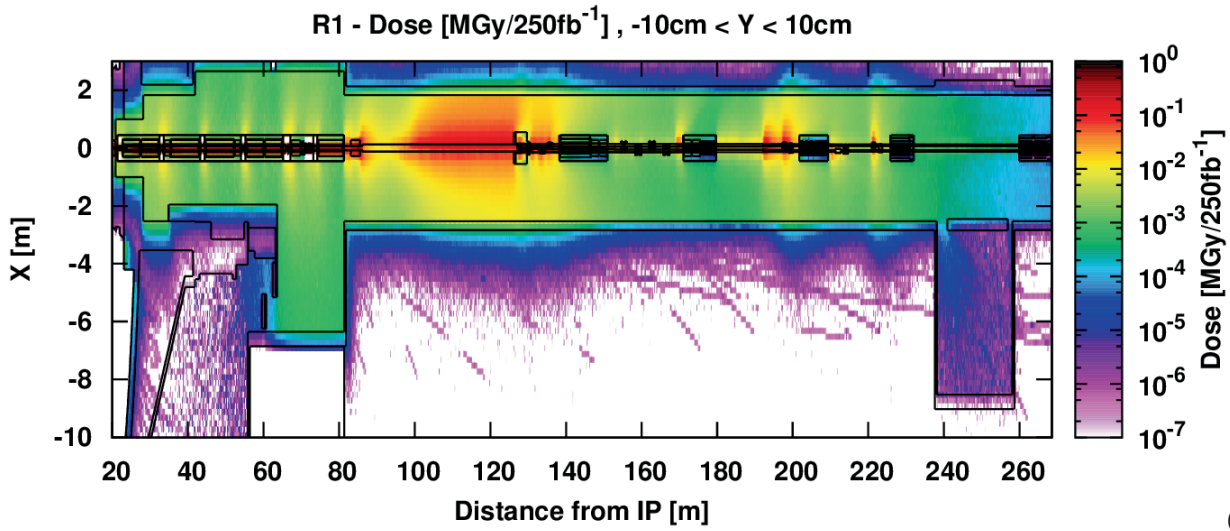


Figure 10-17: Annual radiation levels in the LSS and in the adjacent UJ, UL and RR areas at P1 during the HL-LHC era (per 250 fb⁻¹), calculated with the HL-LHCv1.2 round optics: (a) HEH fluence; (b) 1 MeV neutron equivalent fluence; (c) absorbed dose. The three TCL(X) collimators are set at 12 σ half gap.

The analysis of the performed radiation tests, as well as the experience acquired during LHC Run 1 operation allowed the deduction of an acceptable limit of $10^7 \text{ cm}^{-2} \text{ y}^{-1}$ annual radiation level, leading to the definition of so-called protected areas (in terms of overall risk of radiation-induced failures). Therefore, for the HL-LHC any installation of non-tested (and not specifically designed) electronics equipment in the UJs, part of the ULs, and RRs is clearly to be avoided or subjected to a detailed analysis process before an exceptional installation can be granted under the following conditions:

- the equipment is not linked to any safety system;
- the failure of the equipment will not lead to a beam dump;
- the failure of the equipment does not require quick access (thus lead to downtime);
- there is no other operational impact (loss of important data, etc.).

In all other cases requiring installation in critical areas, a respective radiation-tolerant electronics development must be considered from a very early stage onward. Related expertise exists at CERN within the equipment groups, the R2E project, and a dedicated working group [28].

In a first approximation and limiting the total number of exposed systems, the above-mentioned annual radiation design level of $10^7 \text{ cm}^{-2} \text{ y}^{-1}$ can also be chosen as acceptable, aiming to achieve an overall performance of less than one radiation-induced failure per one or two weeks of HL-LHC operation.

For operation-critical equipment, the HL-LHC project already foresees radiation-tolerant developments at an early stage of the design phase, taking into account that:

- for the LHC-tunnel: in addition to SEEs, cumulative damage also has to be considered for both existing and future equipment;
- for partly shielded areas (UJs, RRs, ULs): cumulative damage should be carefully analyzed but can most likely be mitigated by preventive maintenance (detailed monitoring is mandatory); however, radiation-tolerant design is mandatory in order to limit SEE-induced failures;
- the knowledge of radiation-induced failures and radiation-tolerant development within the equipment groups and in the overall accelerator and technology sector has to be maintained and further strengthened;

- the access and availability of radiation test facilities (both inside CERN and outside) has to be ensured, providing efficient support to equipment groups;
- building on the experience obtained during the LHC R2E project and in view of the HL-LHC time-scale, it is important that the expertise of and support to radiation-tolerant developments (currently available through the Radiation Working Group [28]) are maintained and ensured from the early project stages onwards.

10.7 References

- [1] L.S. Esposito *et al.*, Power load from collision debris on the LHC Point 8 insertion magnets implied by the LHCb luminosity increase, Conf. Proc. C130512 (2013) pp.TUPFI022. [CERN-ACC-2013-0285](#)
- [2] N.V. Mokhov and I.L. Rakhno, Mitigating radiation loads in Nb₃Sn quadrupoles for the CERN Large Hadron Collider upgrades, *Phys. Rev. ST Accel. Beams* **9** (2006) 101001.
- [3] L.S. Esposito, F. Cerutti and E. Todesco, Fluka Energy Deposition Studies for the HL LHC, Conf. Proc. C130512 (2013) pp.TUPFI021. [CERN-ACC-2013-0283](#)
- [4] G. Battistoni *et al.*, Overview of the FLUKA code, *Annals of Nuclear Energy* **82** (2015) 10-18. DOI: [10.1016/j.anucene.2014.11.007](#)
- [5] A. Ferrari *et al.*, FLUKA: A multi-particle transport code (Program version 2005), CERN-2005-010. <http://www.fluka.org> DOI: [10.5170/CERN-2005-010](#)
- [6] V. Vlachoudis, FLAIR: A powerful but user friendly graphical interface for FLUKA, Proc. Int. Conf. Mathematics, Computational Methods & Reactor Physics, Saratoga Springs, New York, 2009, on CD-ROM, American Nuclear Society, LaGrange Park, IL (2009) 1-11.
- [7] A. Mereghetti *et al.*, The FLUKA LineBuilder and Element DataBase: Tools for Building Complex Models of Accelerator Beam Lines, IPAC2012, Conf. Proc. C1205201 (2012) pp.WEPPD071 [CERN-ATS-2012-266](#)
- [8] N.V. Mokhov and C. James, The MARS Code System User's Guide. <http://www-ap.fnal.gov/MARS>
- [9] N.V. Mokhov and S.I. Striganov, MARS15 Overview, Proc. of Hadronic Shower Simulation Workshop, Fermilab, AIP Conf. Proc. **896** (2007) pp. 50–60.
- [10] N.V. Mokhov *et al.*, MARS15 code developments driven by the intensity frontier needs, *Prog. Nucl. Sci. Tech.* **4** (2014) 496–501. [FERMILAB-CONF-12-635-APC](#)
- [11] S. Roesler, R. Engel and J. Ranft, The Monte Carlo event generator DPMJET-III, Proc. Monte Carlo 2000 Conference, Lisbon, October 23-26 2000, A. Kling, F. Barao, M. Nakagawa, L. Tavora, P. Vaz eds., Springer-Verlag Berlin, (2001) pp. 1033-1038. DOI: [10.1007/978-3-642-18211-2_166](#)
- [12] N.V. Mokhov *et al.*, Protecting LHC IP1/IP5 components against radiation resulting from colliding beam interactions, [CERN-LHC-Project-Report-633](#). 17 Apr 2003. - 56 p.
- [13] M.I. Besana *et al.*, Assessment and mitigation of the proton–proton collision debris impact on the FCC triplet, IPAC2016, Conf. Proc. (2016) pp. TUPMW004
- [14] L.S. Esposito and F. Cerutti, FLUKA simulations of collision debris with TCL6, presentation at LHC Collimation Working Group #163.INDICO [267815](#)
- [15] A. Ballarino, Development of superconducting links for the LHC machine, EEE/CSC & ESAS Superconductivity News Forum (global edition), October 2013. DOI: [10.1088/0953-2048/27/4/044024](#)
- [16] A. Ballarino, Preliminary report on cooling options for the cold powering system, June 2013. <http://cds.cern.ch/record/1557215/files/CERN-ACC-2013-010.pdf>
- [17] R2E website. www.cern.ch/r2e
- [18] M. Brugger *et al.*, R2E Experience and outlook for 2012, Proc. LHC Performance workshop, Chamonix 2012. DOI: [10.5170/CERN-2012-006.163](#)

- [19] K. Roed *et al.*, FLUKA simulations for SEE studies of critical LHC underground areas, *IEEE Trans. Nucl. Sci.* **58**, (2011) 932. DOI: [10.1109/TNS.2010.2097605](https://doi.org/10.1109/TNS.2010.2097605)
- [20] M. Brugger *et al.*, FLUKA capabilities and CERN applications for the study of radiation damage to electronics at high-energy hadron accelerators, *Prog. Nucl. Sci. Tech.* (2010) PNST10184-R1.
- [21] K. Roed *et al.*, Method for Measuring Mixed Field Radiation Levels Relevant for SEEs at the LHC, *IEEE Trans. Nucl. Sci.* **59**, (2012) 1040.
- [22] K. Roed, M. Brugger and G. Spiezia, An overview of the radiation environment at the LHC in light of R2E irradiation test activities, CERN publication, [CERN-ATS-Note-2011-077 TECH](https://cds.cern.ch/record/1311111/files/CERN-ATS-Note-2011-077_Tech.pdf) (2011).
- [23] R. García Alía *et al.*, SEL Hardness Assurance in a Mixed Radiation Field, *IEEE Trans. Nucl. Sci.* **62**, (2015) 2555. [CERN-ACC-NOTE-2016-0048](https://cds.cern.ch/record/1311111/files/CERN-ACC-NOTE-2016-0048.pdf)
- [24] G. Spiezia *et al.*, A New RadMon Version for the LHC and its Injection Lines, *IEEE Trans. Nucl. Sci.* **61**, (2014) 3424. DOI: [10.1109/TNS.2014.2365046](https://doi.org/10.1109/TNS.2014.2365046)
- [25] D. Kramer *et al.*, LHC RadMon SRAM detectors used at different voltages to determine the thermal neutron to high energy hadron fluence ratio, *IEEE Trans. Nucl. Sci.* **58**, (2011) 1117. DOI: [10.1109/TNS.2011.2105891](https://doi.org/10.1109/TNS.2011.2105891)
- [26] S. Danzeca *et al.*, Qualification and Characterization of SRAM Memories Used as Radiation Sensors in the LHC, *IEEE Trans. Nucl. Sci.* **61**, (2014) 3458. DOI: [10.1109/TNS.2014.2365042](https://doi.org/10.1109/TNS.2014.2365042)
- [27] G. Spiezia *et al.*, R2E Experience and Outlook, LHC Beam Operation Workshop, Chamonix, France, 6 - 10 Feb 2012, pp.163-169 (CERN-2012-006) DOI: [10.5170/CERN-2012-006.163](https://doi.org/10.5170/CERN-2012-006.163).
- [28] CERN Radiation Working Group (RadWG). www.cern.ch/radwg

Chapter 11

11 T Dipole and New Connection Cryostat for the Dispersion Suppressor Collimators

11 11 T dipole and new connection cryostat for the dispersion suppressor collimators

11.1 Introduction

A few pairs of 11 T dipoles will replace some of the main dipoles (MB) in the dispersion suppressor (DS) regions of the LHC to create space for additional collimators. The upgrade of the collimation system is necessary to cope with beam intensities that are larger than nominal, such as in the baseline of the High Luminosity LHC (HL-LHC) project [1]. This solution will be used around IP7 where one collimator per beam is needed for both proton and heavy-ion collimation losses [2]. The installation of collimators for heavy-ion secondary beams around IP2, which was originally foreseen at the location of the MBs in A10L2 and A10R2, is now requested at the location of the connection cryostats in between the first MB and the first quadrupole, Q11, of the DS region next to the arc [3], [4]. Therefore, 11 T dipole magnets are no longer needed for IP2. Instead, new connection cryostats are needed to create the room temperature longitudinal space required for the collimators and to ensure continuity of the continuous cryostats and sub-systems such as the beam pipes, the bus bars, and the helium heat exchanger tube.

A joint research and development (R&D) programme was initiated in October 2010 at the Fermi National Laboratory (FNAL) in the US, and in the middle of 2011 at CERN, with the goal of developing the necessary technology for the fabrication of a full-length two-in-one aperture accelerator quality Nb₃Sn dipole prototype, exploiting the synergy between the goals of the High Field Magnet development program in the US and the need for magnets suitable for installation in the LHC [5], [6]. After the successful design, fabrication, and test of a number of short models with a length of 1 m and 2 m, FNAL slowed down the research effort, while CERN gradually ramped up with the fabrication of 2 m long models and the preparation of the tooling for full-length prototypes to be installed in LHC. The design of the 11 T dipole described in this chapter features the solutions developed in the framework of the CERN programme. The CERN design comprises some innovations, like the pole loading concept, the cable insulation scheme, and a different geometry for the components of the magnetic yoke and of the structure. Other features are specific to full-length magnets. However, many solutions used at CERN are largely based on the results of the R&D programme conducted at FNAL.

11.2 The 11 T dipole full assembly

11.2.1 Description

An main dipole cryo-magnet assembly (MB) will be replaced with a string of three independently installed and aligned cryo-magnet assemblies: two of these will each house an 11 T dipole, referred to below as the MBH, with a bypass cryostat installed between them. This new assembly will be called 11 T dipole full assembly. The bypass cryostat ensures the continuity of the cryogenic and electrical circuits and comprises cold to warm transitions on the beam lines in order to create a room temperature vacuum sector sufficiently long to install the collimator.

Figure 11-1 shows a schematic layout of the string of cryo-assemblies composing the 11 T dipole full assembly, which will replace an main dipole cryo-magnet assembly.

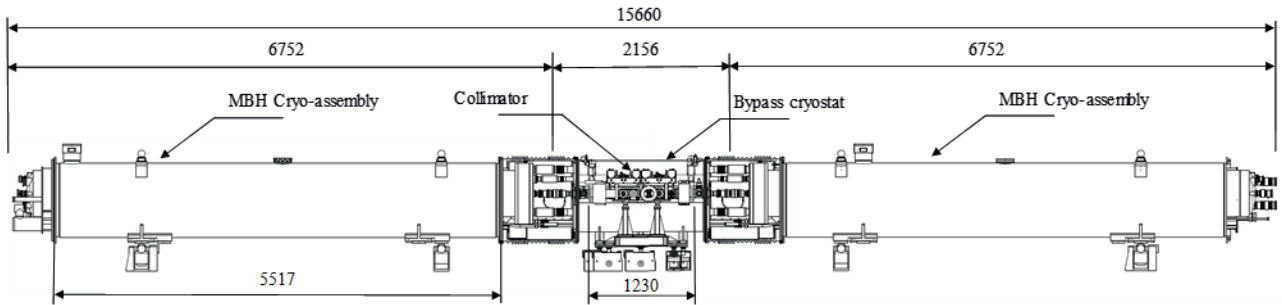


Figure 11-1: Side view of the 11 T dipole full assembly showing the collimator installed between cold-to-warm transitions.

The cryostat for the MBH follows the same design and fabrication principles as the other arc cryostats; it complies with the static heat loads specified by the Heat Load Working Group [7]. Standard LHC cryostat performance in terms of alignment tolerances and geometrical stability are ensured.

The design of the bypass cryostat is compatible with the integration of the collimator and of the RF-shielded gate valves at the extremity of the cold-to-warm transitions shown in Figure 11-2. All cryogenic lines and powering busbars have their continuity ensured across the bypass cryostat. Enlarged end covers at the extremity of the MBH cold mass interfacing with the collimator allows for all lines to run straight across the bypass cryostat as illustrated in Figure 11-3.

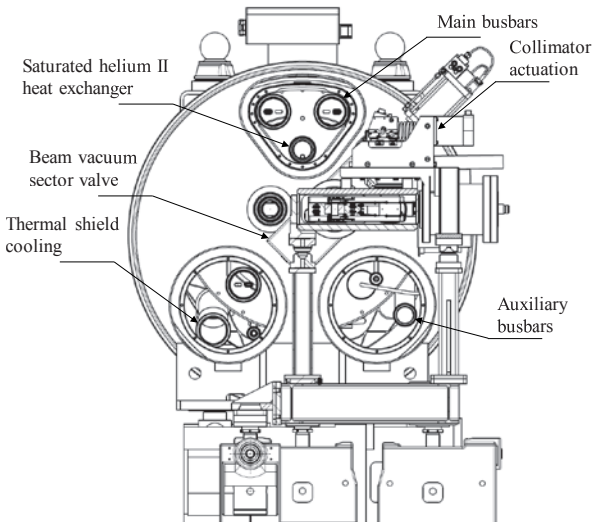


Figure 11-2: Cross-section of the bypass cryostat and collimator. The three main busbar lines have been moved away from the beam lines radially in order to create space for the collimator and the beam vacuum sector valves.

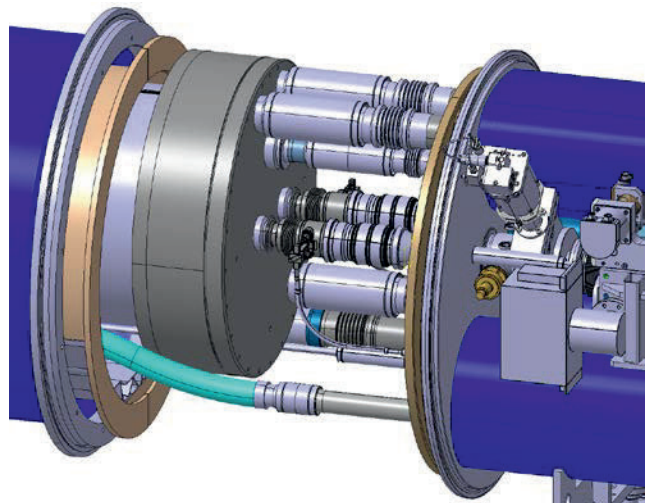


Figure 11-3: View of the enlarged cold mass end cover and interconnect to the bypass cryostat .

Independent installation and alignment of the three cryostats is foreseen. In addition, the TCLD collimator is supported directly onto the tunnel floor so as not to be affected by deformations of the cryostat vacuum vessels due to alignment or pressure-induced forces.

A solution with a cold vacuum chamber for the beam line without collimator and equipped with a beam screen was preferred to a warm chamber because this reduces the total number of sector valves that are needed. This makes the overall integration simpler, and more reliable thanks to fewer number of sector valves.

11.2.2 Equipment parameters

The main parameters of the 11 T dipole full assembly are given in Table 11-1. The dimensions of the cryogenic pipes are equivalent to those of a standard LHC arc continuous cryostat.

Table 11-1: Main parameters of the 11 T dipole full assembly.

Characteristics	Unit	Value
Total length including interconnects	[mm]	15660
Upstream cryostat length between interconnect planes	[mm]	6752
Downstream cryostat length between interconnect planes	[mm]	6752
Bypass cryostat length between interconnect planes	[mm]	2156
Beam line cold bore diameter (inner)	[mm]	50
Length of room temperature beam vacuum sector measured between cold-to-warm transition flanges	[mm]	1230
Compatible active length of the collimator jaws	[mm]	600

The design of the 11 T dipole full assembly is based on the following baseline.

- The length of the jaws of the collimator is 600 mm and this is valid for all the locations envisaged for installation, in particular for proton and ion cleaning (See Chapter 5).
- The interface between the cold beam lines of the MBH cryostats and the beam vacuum sector of the collimator requires sectorization by RF-shielded gate valves.
- As opposed to other collimators in the machine, residual radiation to personnel is assumed to be compatible with the removal and installation of the TCLD collimator without remote handling equipment. Given the integration constraints in the LHC dispersion suppressors, the design of a collimator compatible with remote handling is most likely not achievable.
- Radiation doses on the cryostat throughout the HL-LHC lifetime are compatible with the usage of LHC standard cryostat materials.
- Magnetic shielding is not required on the bypass cryostat. It is assumed that the magnetic field created by the busbar currents will not be detrimental to the accuracy of the TCLD instrumentation and controls.

11.3 The 11 T dipole

The design of the MBH is based on the two-in-one concept, i.e. the cold mass comprises two apertures in a common yoke and shell assembly. There are two types of cold mass per 11 T dipole full assembly, the cold mass LMBHA that will be installed on the left-hand side of the collimator (for an observer looking from the centre of the accelerator), and the cold mass LMBHB that will be installed on the right-hand side of the collimator. These cold masses will have all the features to make them compatible to any of the installation locations of the collimators on either side of IP7.

The LMBH cold masses have a length of 6.252 m between the datum planes C and L that are shown on the end covers, see Figure 11-4-a and b. The coils have a length of 5.417 m without the outermost end spacers (called saddles), and 5.559 m with the saddles, see Figure 11-5. A pair of MBHs is needed to produce an integrated field of 119 T·m at 11.85 kA, which corresponds to the bending strength of the MB. The MBHs need to be compatible with the LHC lattice and its main systems. They will be connected in series with the MBs.

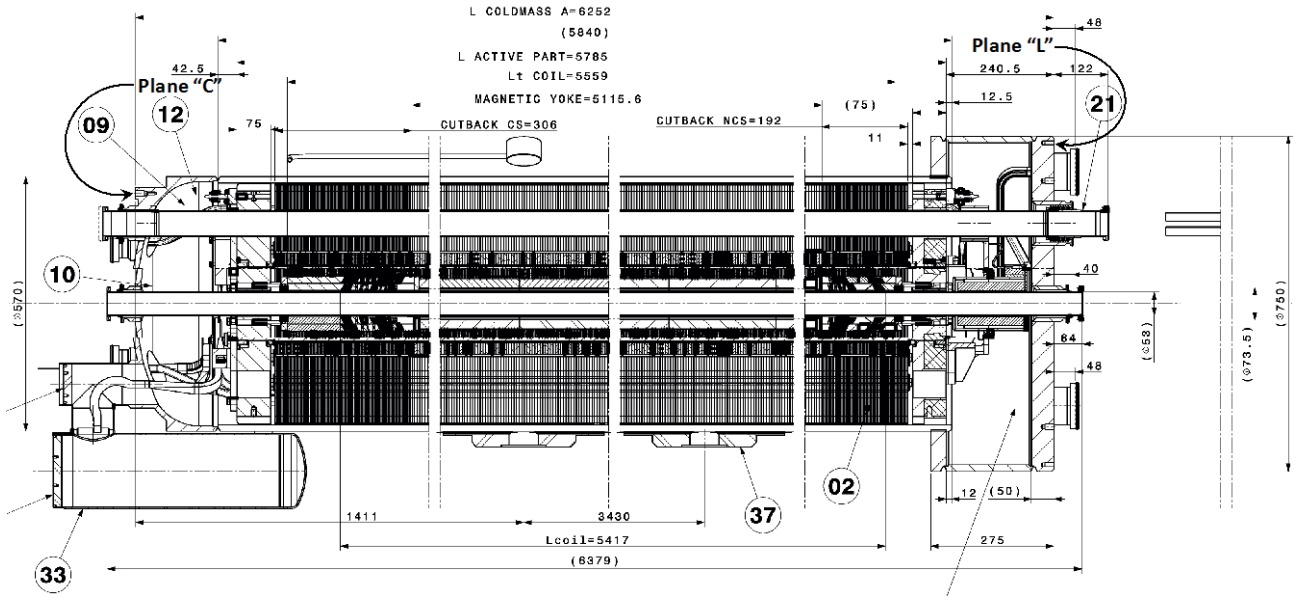


Figure 11-4-a: Longitudinal section of the cold mass assembly LMBHA, retrieved from drawing LHCLMBH_0001.

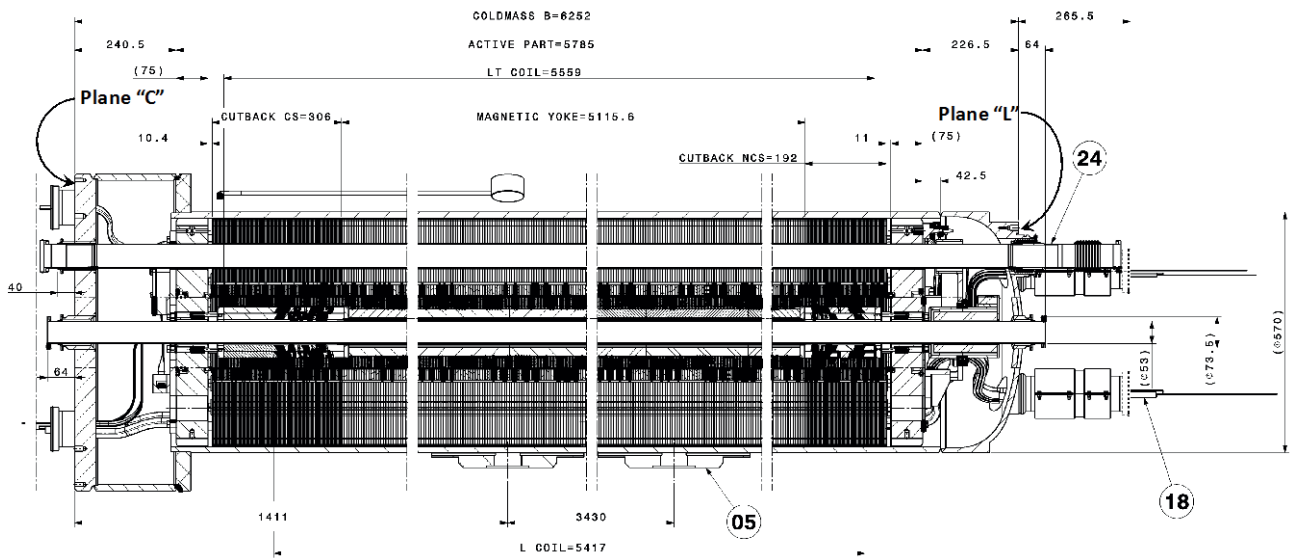


Figure 11-4-b: Longitudinal section of the cold mass assembly LMBHB, retrieved from drawing Nb. LHCLMBH_0005.

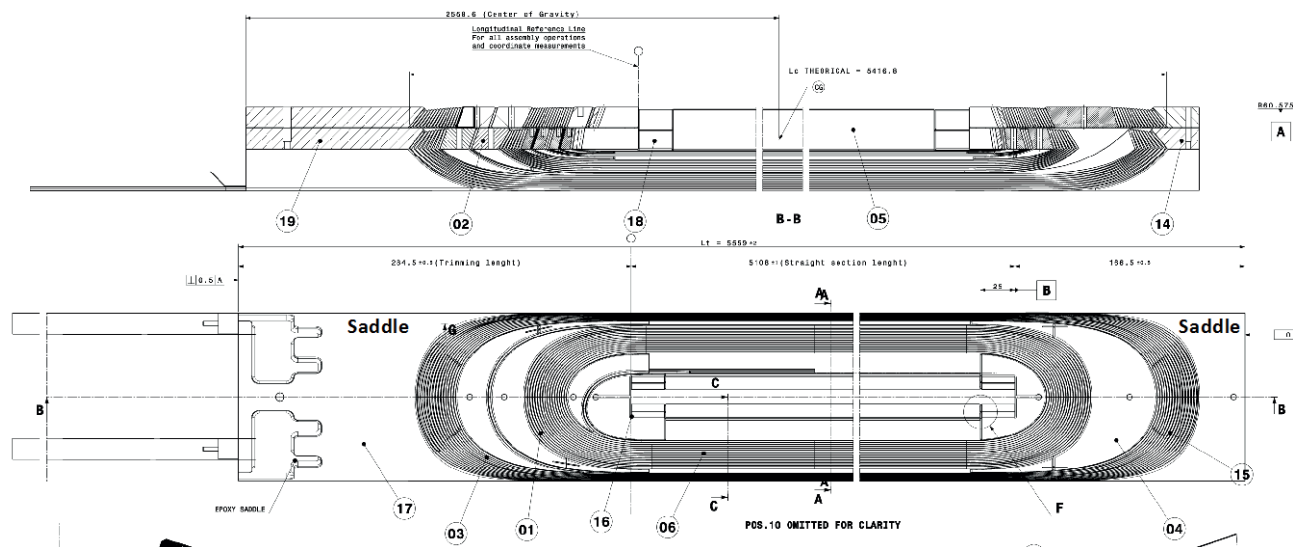


Figure 11-5: Top and side views of the coil, retrieved from drawing Nb. LHCMBH_C0005.

11.3.1 Description

The coils of the MBH are made of two layers and six blocks with Nb₃Sn keystoneed Rutherford-type cable as shown in Figure 11-6. Each coil comprises 56 turns, with 22 in the inner layer and 34 in the outer layer. There is no splice at the layer jump, i.e. the two layers are wound from the same cable unit length. The cable is made by 40 strands of 0.7 mm diameter wire. Two manufacturing routes are considered for the strand: the restacked rod process (RRP) and the powder-in-tube (PIT) process. The first four MBHs will be made with RRP conductor, and a cable keystone angle of 0.79°, whereas the two additional MBHs needed as spare units will be made with PIT conductor, and a cable keystone angle of 0.50°. The reduction of keystone angle for the PIT route was necessary to avoid excessive degradation of the critical current after cabling, and keep it below the allowable limit of 5 % [8][9]. The cable mid-thickness will be the same, 1.25 mm, for the two types of conductor.

The cable insulation is composed of:

- A Mica tape type COGEBI FIROX® of 80 µm thickness shaped in the form of a “C” around the cable. This tape is made of phlogopite mica assembled on an E-glass backing strip providing a dielectric strength of 800 V;
- An S2-Glass layer covering the Mica tape. This S2-Glass layer is made of 32 threads over-braided bundles of 9 yarns for each thread. The Yarn is AGY S-2® 11TEX 636, and there are 12 threads every 20 mm.

To complete the electrical insulation, the coils are impregnated under vacuum with an Epoxy resin system CTD-101K® from the company Composite Technology Development, Inc.

The mechanical structure comprises separate austenitic steel collars for each aperture to balance the electromagnetic forces, and a vertically split iron yoke surrounded by a welded stainless steel shrinking cylinder, which contributes to the overall rigidity of the assembly. The axial component of the electromagnetic forces is also transferred to the shrinking cylinder via thick end plates, which are welded to it, and bolts in contact with the saddles. The bolts are screwed into the end plates. The cold mass envelope is closed at the ends by a dished cover on the side of the assembly facing the existing MBs and by a flat cover of a larger diameter on the side of the assembly facing the collimator, see Figure 11-1. A larger diameter is needed on that side to allow the routing of the busbars across the bypass cryostat within the limits of the radial and longitudinal space available.

A cross-section through the MBH is shown in Figure 11-6, where the key parts of the collared coils are also identified.

In order to suppress the peak field at the transition region between the straight part and the ends of the coils, which is critical in terms of mechanical structure singularities, a cutback at the yoke extremities has been introduced. The yoke cutback consists in replacing a number of low-carbon steel laminations by laminations made of non-magnetic steel. This will reduce the amplitude of the field in these regions, and move the peak field in the straight part, which is mechanically more robust. The length of the yoke cutback is 192 mm on the non-connection side and 306 mm on the connection side.

For powering, the two MBH's will be connected in series as shown in Figure 11-7. There will be two powering directions depending on the direction of circulation of the beam. In one case, current coming from the RB circuit in the M3 line will enter in Aperture 1 of LMBHA (or Aperture 2), then will go in Aperture 1 of LMBHB via the by-pass cryostat, then will go in Aperture 2 of LMBHB, and finally will go in Aperture 2 of LMBHA via the by-pass cryostat before continuing in the RB circuit towards the next MB. In the other case, current will be circulating in the opposite directions.

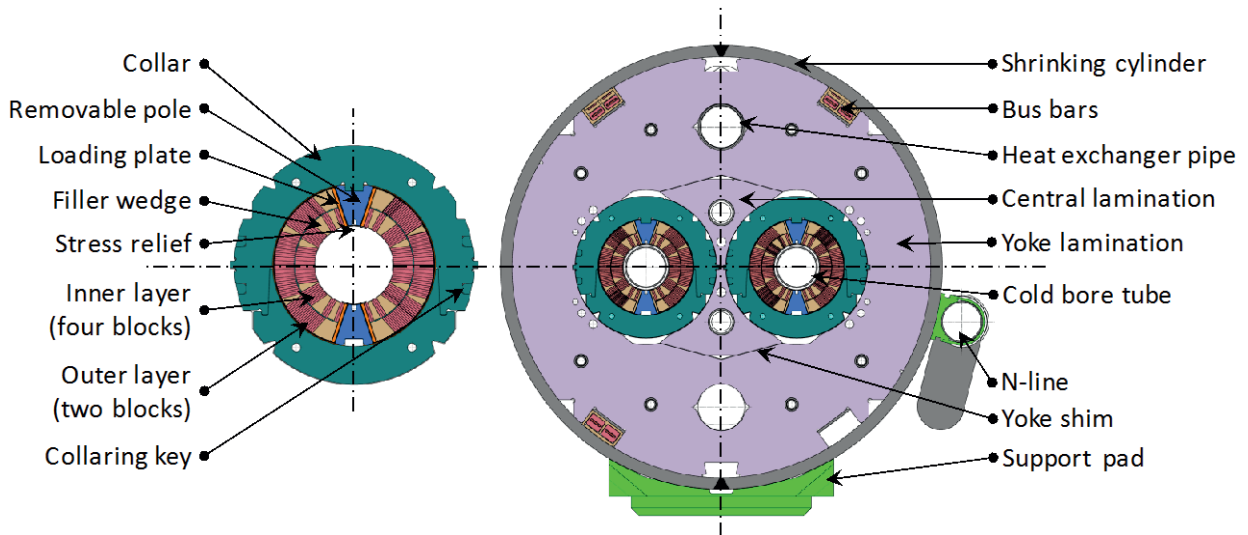


Figure 11-6: Cross-section through (left) the 11 T dipole collared coil; (right) the cold mass assembly.

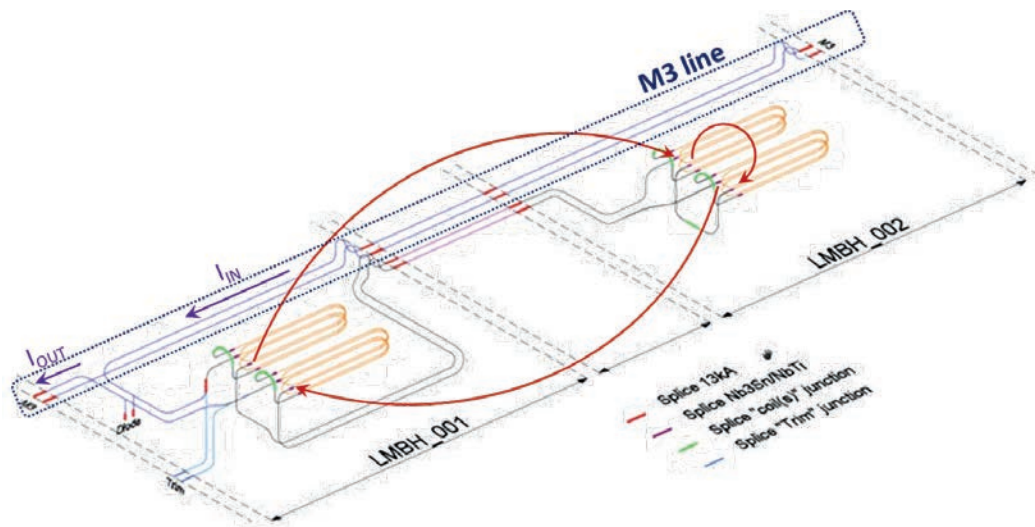


Figure 11-7: Powering scheme of a pair of MBH inside the cold mass assembly.

To avoid deformation of the beam closed orbit, the integrated transfer function of a pair of MBHs shall be identical to that of the MB. However, this is not possible across the entire range of current during ramping up to nominal, as shown in Figure 11-8. The design is such that a pair of MBHs provides the same integrated field of 119 T·m as a standard MB at the nominal current of 11.85 kA.

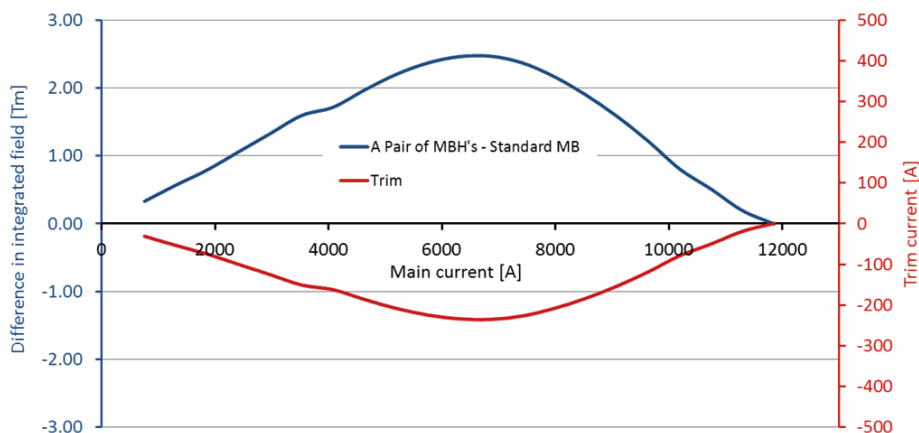


Figure 11-8: The blue line shows the difference in integrated field between a pair of MBHs and an MB, both delivering 119 T·m at 11.85 kA. The red line shows the trim current needed to correct the difference at currents below 11.85 kA.

The MBH is stronger at lower currents (it has more turns) with a peak difference in integrated field around 6.5 kA. This can be mitigated by adding a dedicated trim power converter for ± 250 A / ± 10 V. In the absence of trim current, the resulting orbit distortion could be mitigated by means of the standard orbit correctors in the LHC lattice. However, a fully validated solution including machine protection, reliability, and availability is not currently available (for example, the operation of LHC would be compromised in the case of failure of an orbit corrector). The correction of the transfer function with a trim current is the baseline. It will allow simpler and more transparent operation. More details on the powering requirements are given in section 11.3.6.

Unlike the MB, which is curved in the horizontal plane, the MBH will be straight because of the brittleness of Nb₃Sn after reaction. Even though the MBH has an aperture of 60 mm against 56 mm for the MB, it will be equipped with the same cold bore tube and beam screen as the present curved MB, in order to facilitate integration. To mitigate for the corresponding reduction of mechanical aperture, the two MBHs of an 11 T dipole full assembly will be assembled with an angle of 2.55 mrad relative to each other, and shifted by 0.8 mm towards the centre of the machine.

Depending on the location, the MB to be replaced may be of type A or type B, i.e. it will have both a magnet corrector sextupole (MCS) on the lyre side (i.e. downstream), and a nested magnet corrector decapole/octupole (MCDO) on the connection side (i.e. upstream), respectively, or only an MCS on the lyre side. The LMBHB, which is on the right-hand side of the collimator for an observer looking at the machine from its centre, will have only an MCS on the lyre side. It is also planned to install an MCDO on the connection side of the LMBHA that is installed on the left-hand side of the collimator. The MCDO may be connected during installation, or not, depending on the installation location of the 11 T dipole full assembly.

11.3.2 Instrumentation

The instrumentation foreseen in the 11 T dipole full assembly is much reduced when compared to that installed in the MBH models (1 to 2 m in length) and prototypes (full length). However, it is significantly increased when compared to the instrumentation of the MBs that will be replaced.

11.3.2.1 Voltage Taps

The voltage taps installed along the electrical circuit are used to detect quenches in the coils and to monitor the electrical resistance of the splices between the different coils and bus bars, and the electrical resistance of the joints which are part of the diode leads. The present scheme uses one V-Tap on each side of each splice in the cold mass assembly. The 14 V-Taps distributed along the dipole and spool pieces circuits inside an MBA (respectively 10 for an MBB) amount to 30 in the LMBHA, and 18 in the LMBHB. They are shown in Figure 11-9 with "EExxx" labels. This figure illustrates the 13 kA circuits, the integration of the trim circuit, and the associated Taps. Eighteen V-Taps are used to monitor the Nb-Ti to Nb-Ti and Nb-Ti to Nb₃Sn splices between the poles and apertures. The LMBHA cold mass is equipped with 6 additional V-Taps to monitor the joints along the diode and trim circuits, and 2 I-Taps, which can be used for specific quality control tests. Four additional wires for the MCDO and 2 for the MCS spool pieces circuits are installed respectively in LMBHA and LMBHB, as shown in Figure 11-10.

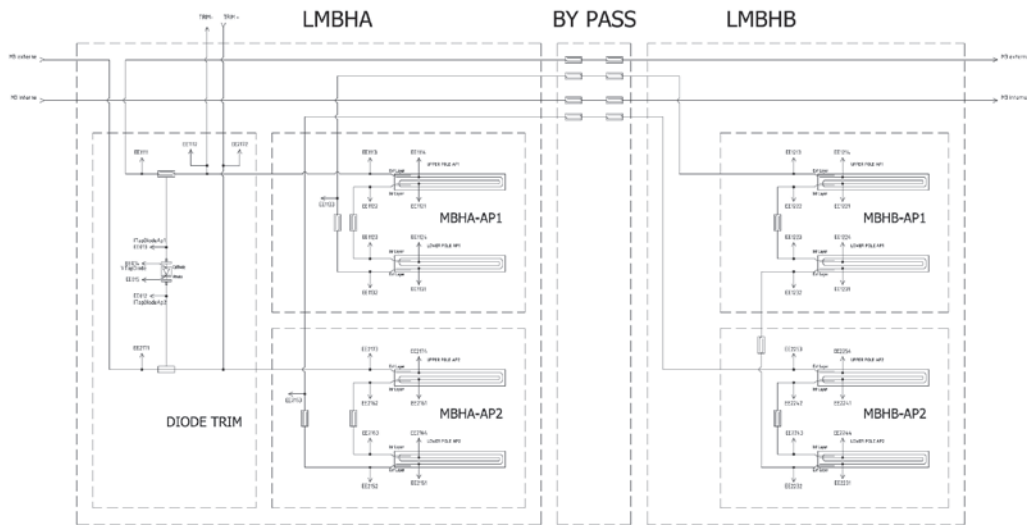


Figure 11-9: Instrumentation scheme in the main/trim circuits of the 11 T dipole full assembly substituting a standard MB_L.

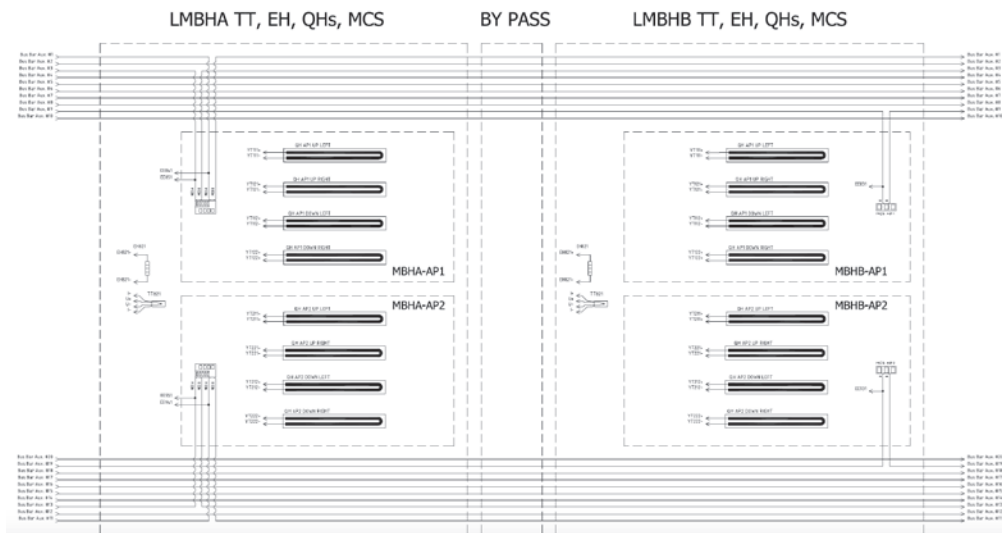


Figure 11-10: Instrumentation scheme for the temperature sensor, cryo-heater, spool pieces, and quench heaters in the 11 T dipole full assembly substituting a standard MBA.

11.3.2.2 Cryo-heater

A cryo-heater is installed at the bottom of each LMBHA and LMBHB cold mass on the magnet end plate at the connection side. It can be used during warm-up phases to vaporise the helium possibly remaining in the cold mass. The powering circuit of the cryo-heater comprises 2 wires.

11.3.2.3 Temperature sensor

In each LMBHA and LMBHB cold mass, a temperature sensor is attached to the lower part the yoke, inside the magnet 2 m away from the end plate, on the connection side. It is the same as those used in the MBs (type CERNOX™). Each temperature sensor is equipped with 4 wires arranged in a cable.

11.3.2.4 Instrumentation and feed-through system

The instrumentation feed-through system (IFS) provides path for the cabling of the electrical instrumentation and quench heaters via a capillary tube running from the cold mass envelope to the envelope of the cryostat.

For the sake of standardization, the design of the cover flange will be the same as that used in the MBs. It is equipped with 40 feedthru pins, and the capillary tube can route a maximum of 40 wires. Because the section of the 16 quench heater wires has been increased, and it was decided to keep the same diameter for the capillary tube as in the MBs, two IFS systems per MBH are needed.

11.3.3 Equipment parameters

A pair of MBHs will provide an integrated field of 119 T·m at the nominal operation current of the MBs, 11.85 kA. This corresponds to a nominal magnetic flux density of 11.23 T at the centre of the bore. This goal shall be obtained with a margin of ~20% on the magnet load line.

The geometric field quality will be optimized to keep the low-order field errors below 1 unit. The different contributions to the field errors are given in Table 11-2. These include the contributions of the coil ends, cryostat, and the effects of the persistent currents. The geometric multipoles measured on the model MBHDP101 are given in Table 11-3. These geometric multipoles are defined as the average of the measured values, at a constant current of 5 kA, on both up- and down-ramp branches of the stair-step cycle at 1.9 K. Table 11-3 shows the measured multipoles in the central section of the models compared with the values determined by modelling the nominal coil dimensions in 2D.

Table 11-2: Field errors – $R_{ref} = 17$ mm.

Normal	Systematic					Uncertainty		Random	
	Geometric	Saturation	Persistent	Injection	High field	Injection	High field	Injection	High field
2	0.000	-12.200	1.010	1.010	-12.200	1.930	1.930	1.9300	1.930
3	7.459	-0.279	-1.299	6.160	7.180	1.240	1.240	1.2400	1.240
4	0.000	-0.400	0.070	0.070	-0.400	0.600	0.600	0.6000	0.600
5	-0.014	0.514	6.594	6.580	0.500	0.310	0.310	0.3100	0.310
6	0.000	-0.020	0.000	0.000	-0.020	0.180	0.180	0.1800	0.180
7	-0.093	0.062	-0.688	-0.780	-0.030	0.110	0.110	0.1100	0.110
8	0.000	0.000	0.000	0.000	0.000	0.060	0.060	0.0600	0.060
9	0.912	0.028	1.024	1.936	0.940	0.030	0.030	0.0300	0.030
10	0.000	0.000	0.000	0.000	0.000	0.010	0.010	0.0100	0.010
11	0.450	0.000	-0.090	0.360	0.450	0.010	0.010	0.0100	0.010
12	0.000	0.000	0.000	0.000	0.000	0.000	0.000	0.000	0.000
13	-0.115	-0.006	-0.028	-0.143	-0.121	0.000	0.000	0.000	0.000
14	0.000	0.000	0.000	0.000	0.000	0.000	0.000	0.000	0.000
15	-0.032	-0.002	-0.008	-0.040	-0.034	0.000	0.000	0.000	0.000

Skew	Systematic					Uncertainty		Random	
	Geometric	Saturation	Persistent	Injection	High field	Injection	High field	Injection	High field
2	0.000	-0.261	0.000	0.000	-0.261	1.660	1.660	1.660	1.660
3	-0.130	0.050	0.000	-0.130	-0.080	1.000	1.000	1.000	1.000
4	0.000	-0.010	0.000	0.000	-0.010	0.640	0.640	0.640	0.640
5	0.080	0.000	0.000	0.080	0.080	0.380	0.380	0.380	0.380
6	0.000	0.000	0.000	0.000	0.000	0.200	0.200	0.200	0.200
7	0.030	0.000	0.000	0.030	0.030	0.090	0.090	0.090	0.090
8	0.000	0.000	0.000	0.000	0.000	0.050	0.050	0.050	0.050
9	0.000	0.000	0.000	0.000	0.000	0.030	0.030	0.030	0.030
10	0.000	0.000	0.000	0.000	0.000	0.020	0.020	0.020	0.020
11	0.000	0.000	0.000	0.000	0.000	0.010	0.010	0.010	0.010
12	0.000	0.000	0.000	0.000	0.000	0.000	0.000	0.000	0.000
13	0.000	0.000	0.000	0.000	0.000	0.000	0.000	0.000	0.000
14	0.000	0.000	0.000	0.000	0.000	0.000	0.000	0.000	0.000
15	0.000	0.000	0.000	0.000	0.000	0.000	0.000	0.000	0.000

Table 11-3: Modelled and measured geometric multipoles. The reference radius is 17 mm.

n	2D model		MBHDP101 106-108		MBHDP101 109-111	
	bn	an	bn	an	bn	an
2	-0.07	0.00	-1.80	4.17	-0.09	6.30
3	7.46	0.00	11.85	-1.12	11.54	0.13
4	0.00	0.00	-0.31	0.15	-0.65	0.99
5	-0.01	0.00	1.25	-0.01	1.58	-0.65
6	0.00	0.00	-0.13	-0.11	-0.17	0.31
7	-0.09	0.00	0.15	-0.11	0.21	-0.18
8	0.00	0.00	-0.04	0.04	-0.05	0.02
9	0.91	0.00	0.65	0.06	0.70	-0.31

The effect of the persistent currents is generally larger than expected below 2 kA. Figure 11-11 shows the measured b_3 , as function of the excitation current for the magnet model MBHDP101, and the values determined by modelling of the specific superconducting cable used in this model.

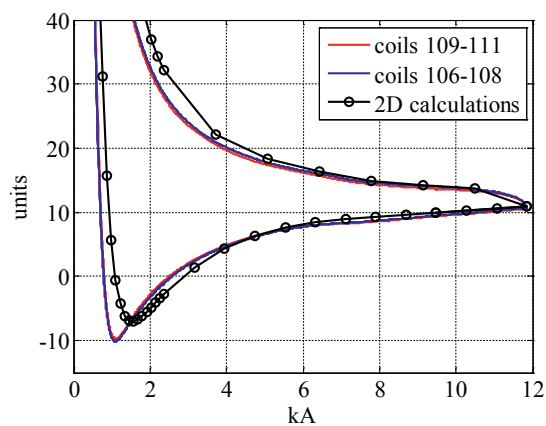


Figure 11-11: Persistent current effect on b_3 , in DC conditions as function of the excitation current, for the two apertures of MBHDP101, compared to calculations. An artificial offset is added on purpose to the curve for the 2D calculations to facilitate the comparison. The reference radius is 17 mm.

For the transfer function, Figure 11-12 shows the results of the measurements for the average of up- and down ramp branch of a measurements cycle for the magnet model MBHDP101, and the expected curve computed with the 2D model.

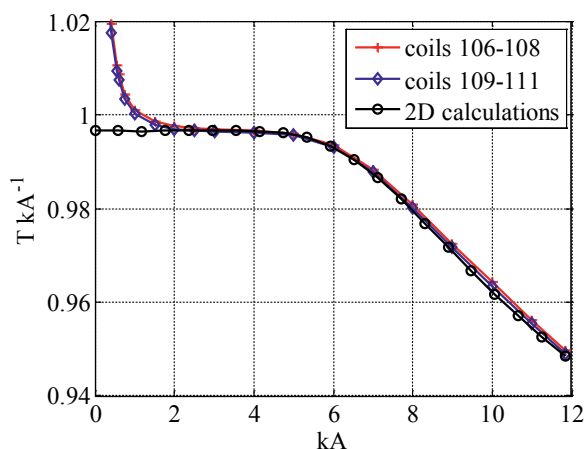


Figure 11-12: Measured and modelled transfer function as a function of the excitation current in DC conditions.

The main parameters of the MBH are listed in Table 11-4.

Table 11-4: Main parameters of the MBH.

Characteristics	Unit	Value
Aperture	[mm]	60
Number of apertures	-	2
Distance between apertures at room temperature/1.9 K	[mm]	194.52/194.00
Cold mass outer diameter	[mm]	570
Magnetic length	[m]	5.307
Coil physical length, as per magnetic design	[m]	5.417
Magnet physical length: active part (between the end plates)	[m]	5.785
Magnet physical length: cold mass (between datum planes C and L)	[m]	6.252
Cold mass weight	[tonne]	~8
Nominal operation current	[kA]	11.85
Bore field at nominal current	[T]	11.23
Peak field at nominal current (without strand self-field correction)	[T]	11.59
Operating temperature	[K]	1.9
Load line margin	(%)	20
Stored energy/m at I_{nom}	[MJ/m]	0.896
Differential inductance/m at I_{nom}	[mH/m]	11.97
Number of layers	-	2
Number of turns (inner/outer layer)	-	56 (22/34)
Superconductor	-	Nb ₃ Sn
Cable bare width before reaction	[mm]	14.7
Cable bare mid-thickness before reaction	[mm]	1.25
Keystone angle RRP / PIT	[degree]	0.79 / 0.50
Cable unit length for the two layers (no layer jump splice)	[m]	~600
Strand diameter	[mm]	0.700 ± 0.003
Number of strands per cable	-	40
Cu to non-Cu ratio	-	1.15 ± 0.10

RRR, after reaction	-	>150
Minimum strand critical current, I_c , without self-field correction (12 T, 4.222 K)	[A]	438
Minimum strand current density, J_c , at 12 T, 4.222 K	[A/mm ²]	2560
Cable insulation thickness per side azimuthal, before/after reaction	[mm]	0.155/0.100
Heat exchanger hole diameter	[mm]	60
Heat exchanger distance from centre (same position as in the MB)	[mm]	180
Cold bore tube inner diameter/thickness (same as in the MB)	[mm]	50/1.5
Gap CBT to coil	[mm]	2.7

11.3.4 Quench performance

The quench performance of the 11 T dipole was verified on a number of magnet models, first at FNAL, and later at CERN. We are reporting here on the results of the single aperture models made in the two laboratories.

At FNAL, three single aperture models and a two-in-one model were built. These were tested between June 2012 and March 2015. A mirror assembly was also made, MBHSM01, and tested in December 2013 – January 2014. The first model, referred to as MBHSP01, was a demonstrator made of 2-m long coils aiming at showing feasibility in a reasonably short time. The quench performance of this model is shown in Figure 11-13 [10]. The degradation of performance observed can be possibly attributed to conductor damage at the mid-plane during the coil fabrication, or during the magnet assembly. Because of the conductor damage, quenches were observed during a current plateau at 9 kA and above, sign of a time-dependent behaviour. The next 2 models, referred to as MBHSP02 and MBHSP03, were made of 1 m long coils with, for the first time, a stainless steel core in the cable to reduce the effect of persistent currents and ramp-rate dependence. The quench performance of these models is shown respectively in Figure 11-14 [11] and in Figure 11-15 [12]. A bore field of 11.7 T was reached in MBHSP02. In MBHSP02, quenches were also observed during current plateaus, at higher current levels above 11 kA. This time-dependent behaviour was not observed in MBHSP03. The two-in-one model, MBHDP01, was made from the collared coils of the single aperture models MBHSP02 and MBHSP03. The collared coils of MBHSP03 were de-collared in order to add 75- μ m thick shims before integration in the two-in-one structure. The goal was to increase the pre-stress in order to, hopefully, suppress the instability observed in the last part of the training curve, attributed to insufficient pre-stress. This two-in-one model reached a bore field of 11.5 T at 12.1 kA, with a quench behaviour similar to that of the single aperture models, and a limitation attributed to conductor degradation in the coils of MBHSP02. The quench performance of this model is shown in Figure 11-16 with the training curves of the models MBHSP02 and MBHSP03 for comparison. This model MBHDP01 was retesed in June-July 2016 in order to verify how it behaves in terms of training memory and to carry out field quality measurements. The quench performance results are shown in Figure 11-17.

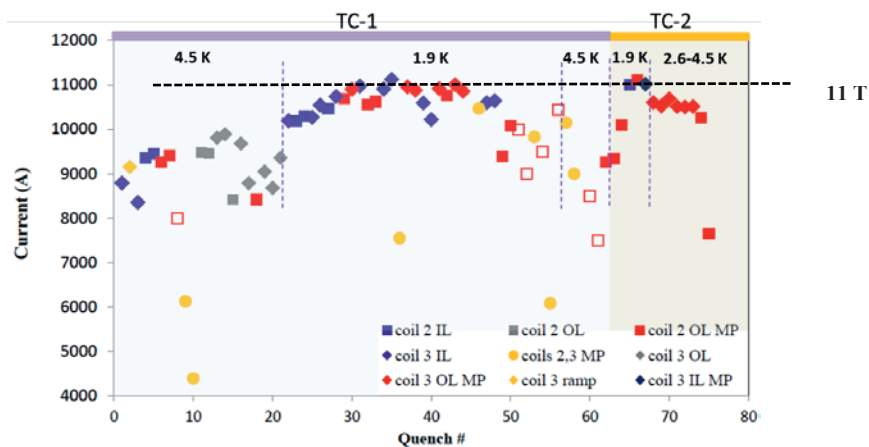


Figure 11-13: Quench performance of single aperture model MBHSP01.

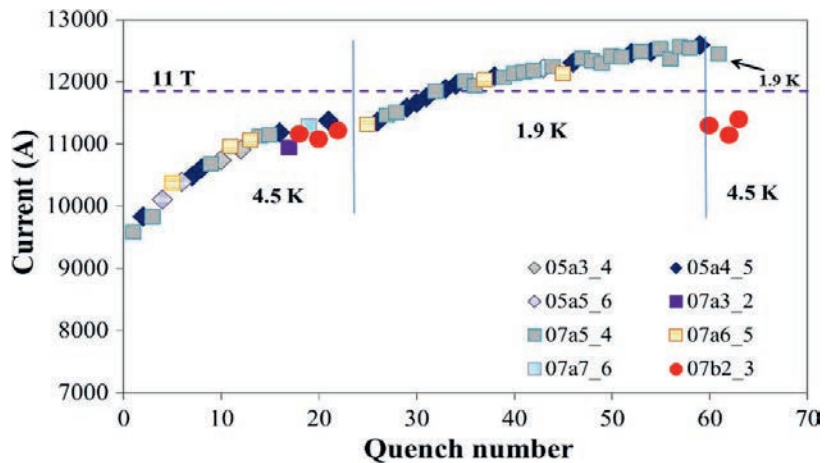


Figure 11-14: Quench performance of single aperture model MBHSP02.

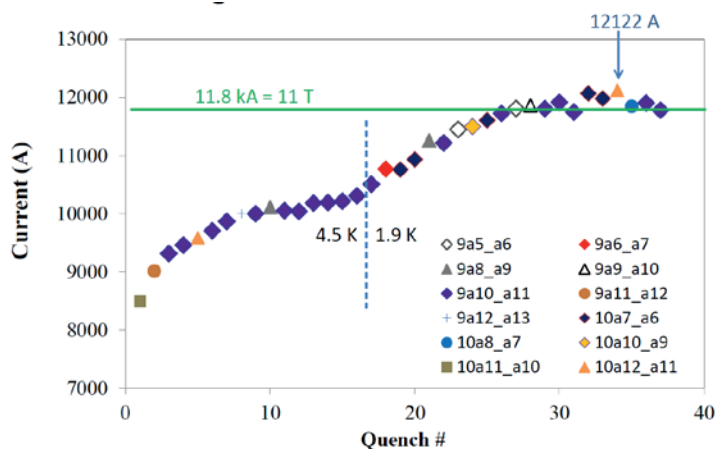


Figure 11-15: Quench performance of single aperture model MBHSP03.

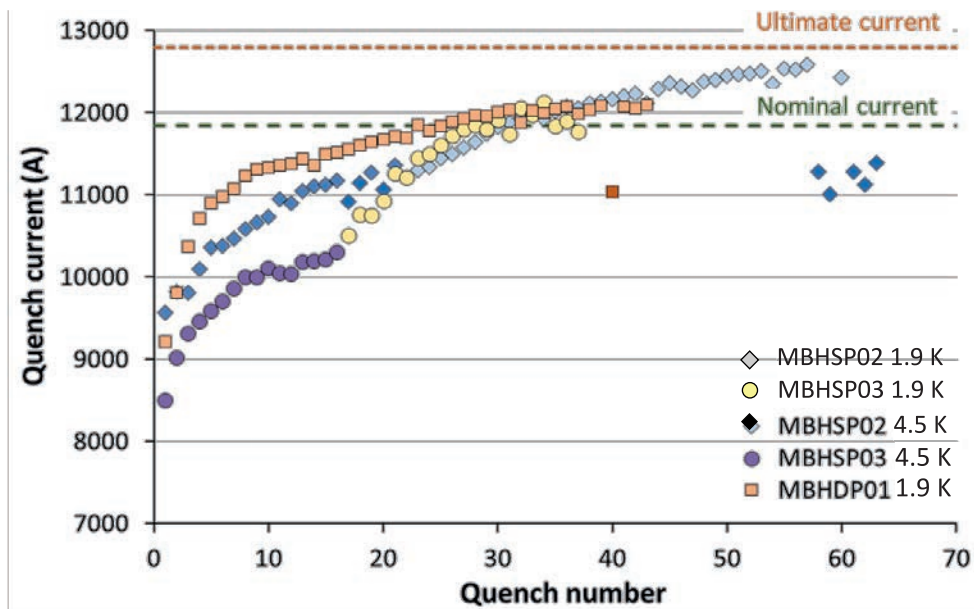


Figure 11-16: Quench performance of the two-in-one model MBHDP01 during the original training carried out in the beginning of 2015.

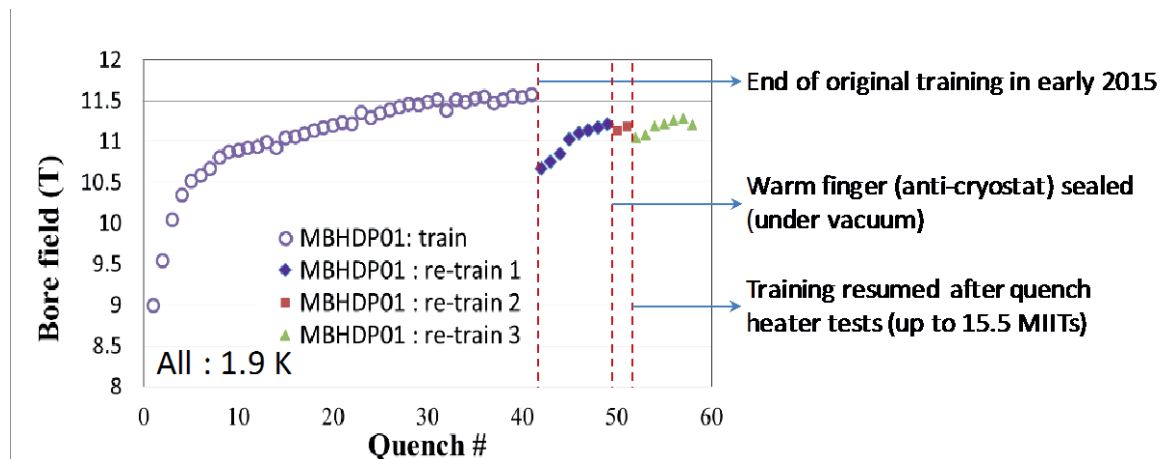


Figure 11-17: Quench performance of the two-in-one model MBHDP01 during the second test campaign carried out in June-July 2016.

At CERN, four single aperture models were made, and tested between October 2013 and July 2016. The quench performance of these four models is shown in Figure 11-18, to Figure 11-21 [13].

Although the first model, MBHSP101, reached nominal current, significant degradation was observed during the first run at 1.9 K and the model did not recover after thermal cycle. Most of the quenches occurred in coil #107. After disassembly, a shim of 250 μm was found in the mid-plane, i.e. in between the two coils, on the entire length of the straight part. Hence, the heads were unloaded with a sharp transition between them and the straight part, provoking likely excessive shear. The good coil, coil #106, was reused and assembled with a virgin coil, coil #108, in MBHSP102. This second model performed well, passing nominal current after 5 quenches, and reaching nearly ultimate field after a thermal cycle. It also showed stable current conditions during a 2.5 hour test at 12.5 kA and a 10 hour test at nominal current. The third model MBHSP103 performed also very well, passing over nominal current after 13 quenches. It reached the test target after 3 more quenches, where it remained stable during the 1 hour plateau. During about 20 following cycles to nominal current with ramp rates up to 300 A/s and quench heater tests, the magnet did not quench and reached again without retraining its target of 12.8 kA, stable for 1 hour.

The quench performance of the model MBHSP104 did not meet expectations. Coil #113 was clearly limiting the performance of this model with one weak spot in the layer jump showing repetitive quenching and strong ramp rate and current cycle dependencies, and another weak spot in the mid-plane. Coil # 113 had 17 training quenches, and coil #112 had only 3 training quenches. This model reached a maximum current of 12.24 kA at 1.9 K, corresponding to 88 % of the short sample limit. The limitation at the layer jump is ramp-rate dependent. It is associated to unusual quench propagation velocity beyond 150 m/s. Current redistribution due to a local defect may be the cause of the layer jump limitation. In the mid-plane, a local degradation, e.g. damage of the wire, or conductor limitation due to higher strain concomitant with the high field region, may be the cause of the limitation. The model will be dismantled in order to allow a thorough examination of the coil #113.

A first two-in-one model was made with the collared coils of the models MBHSP102 and MBHSP103. The training of this two-in-one model, MBHDP101, turned out to be very fast, as no quench occurred at the first ramp up to 11.87 kA. Then, the test had to be interrupted due to a joint quenching in the test station. When the cold tests were resumed, only two quenches were needed to exceed the ultimate field of 12 T. Thereafter, a number of quenches were made to understand the magnet behaviour under high MIITs, as part of magnet protection studies. During these tests, 94 % of the short sample limit was reached, concurring with the mechanical limit of the MBH structure. The quench performance of MBHDP101 is illustrated in Figure 11-22 with the results of the single aperture models MBHSP102 and 103 for comparison[14]. The better performance of the MBHDP101 is attributed to the fact that (1) the coils were trained when tested in the single aperture

structure, and (2) the collaring parameters, in particular the thickness of the collaring shims allowing to tune the level of prestress in the coils, were optimized for the two-in-one structure. The collared coils were not dismantled, meaning that the collaring shims were not changed, when the collared coils were transferred in the two-in-one structure. However, the thickness of the shims installed between the collars and the yoke were increased by 50 μm for the collared coils originally assembled in MBHSP102.

The following conclusions can be drawn out from the cold performance tests of the models made at CERN:

- The training memory of the single aperture models MBHSP102 and 103 was excellent up to ultimate field after their collared coils were placed in the two-in-one model MBHDP101;
- In the two-in-one structure, the erratic quenches, which were observed in the pole turns mainly in MBHSP102 between 11.8 and 12.8 kA, disappeared. This is attributed to a slightly higher pre-stress at the location of the pole in the two-in-one structure, which provides better stability. This is supported by the results of the strain gauge measurements and the structural analysis;
- The single aperture model MBHSP104 did not show any erratic or detrainning quenches up to 12.2 kA;
- The models MBHDP101 and MBHSP104 were both limited, when pushing current to the highest possible levels, in the inner layer mid-plane of the magnet.

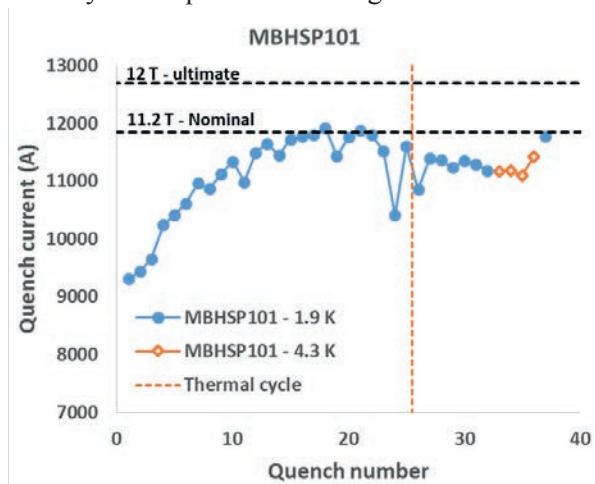


Figure 11-18: Quench performance of the single aperture model MBHSP101.

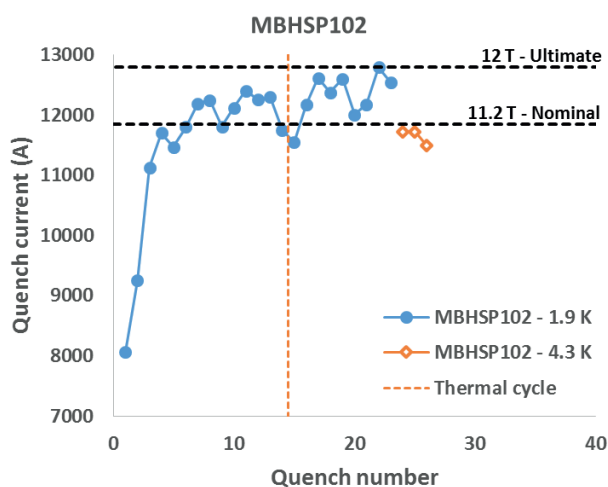


Figure 11-19: Quench performance of the single aperture model MBHSP102.

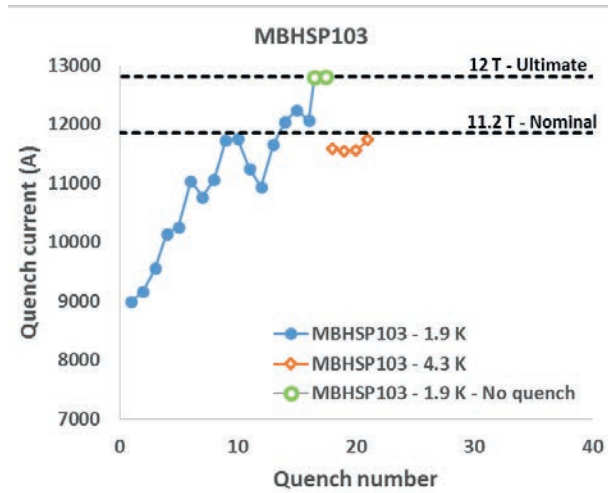


Figure 11-20: Quench performance of the single aperture model MBHSP103.

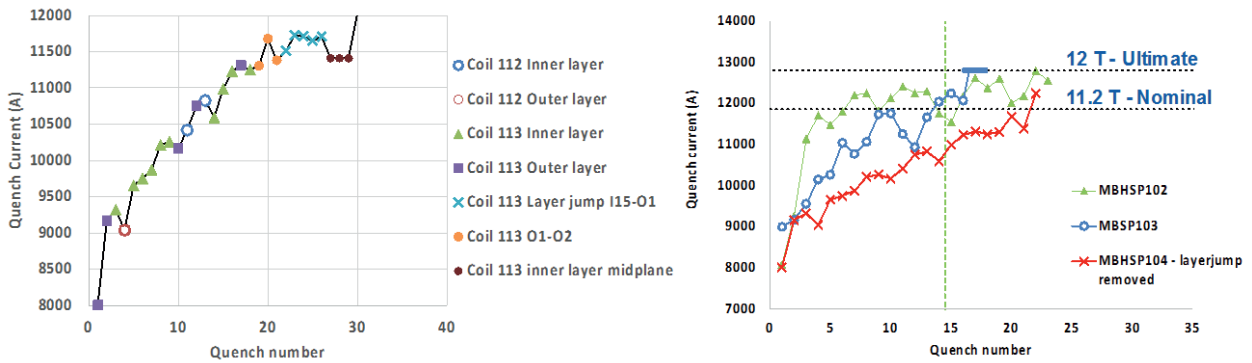


Figure 11-21: Quench performance of the single aperture model MBHSP104, compared to the models MBHSP102 and MBHSP103 on the right.

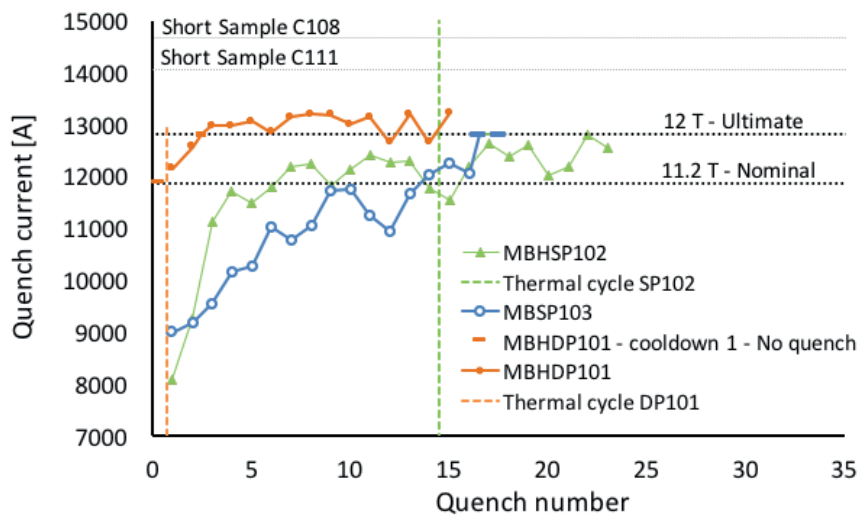


Figure 11-22: Quench performance of the two-in-one model MBHDP101.

11.3.5 Protection

The MBH will be protected with quench heaters and a bypass diode operating at cold, integrated with the cold mass assembly. At the current stage of development, it is foreseen to use one bypass diode for the two MBHs of an 11 T dipole full assembly. However, this needs to be validated. It would be located in LMBHA at the same location as in the MB's so that it can be accessed and repaired, or replaced, as needed.

The energy density in the conductor is 0.130 MJ/m^3 , which is about a factor two larger than in the MBs of LHC, making quench protection particularly challenging. Magnet protection relies on outer layer quench heaters. The quench heaters are designed to quench the coils as uniformly as possible, and to avoid a hot spot temperature in the coil in excess of 350 K, in all conditions. The stainless steel strips are copper plated in order to reduce the resistance of the heaters and thus, limit the voltage across them to $\pm 450 \text{ V}$ (using only stainless steel strips would imply excessive voltage for 5.5 m long heaters). The quench heaters are made of a polyimide-stainless steel laminate, which is copper-plated on the steel side. The $25 \mu\text{m}$ thick stainless steel strip is glued on a $50 \mu\text{m}$ thick foil made of polyimide to form the laminate, which can be purchased as standard product. The glue between the two layers has a thickness of $25 \mu\text{m}$. the copper-plating has a thickness of $5 \mu\text{m}$. There will be 2 quench heater circuits per coil (i.e. per pole) meaning a total of 8 quench heater circuits per MBH, and 16 quench heater circuits per 11 T dipole full assembly. Figure 11-23 illustrates the installation layout of the quench heaters for one aperture of an MBH, and the geometry of the quench heater strips. Figure 11-10 illustrates the wiring scheme of the quench heaters. Although the quench heaters used to be glued on the outside surface of the coil after impregnation, it is foreseen to have them embedded, i.e. impregnated with the coil, in order to reduce their time delay, i.e. their overall efficiency. Measurements on short coils have shown that minimizing the thermal insulation between the heater and the coil allows reducing the quench heater delay from 20 ms to 10 ms at nominal current, and decreasing the hot spot temperature by about 45 K [15]. With a validation time of 10 ms and 5 ms for the switch opening, the thermal analysis gives a hot spot temperature of 325 K. In case of failure of two quench heater circuits, the hot spot temperature would rise up to 345 K.

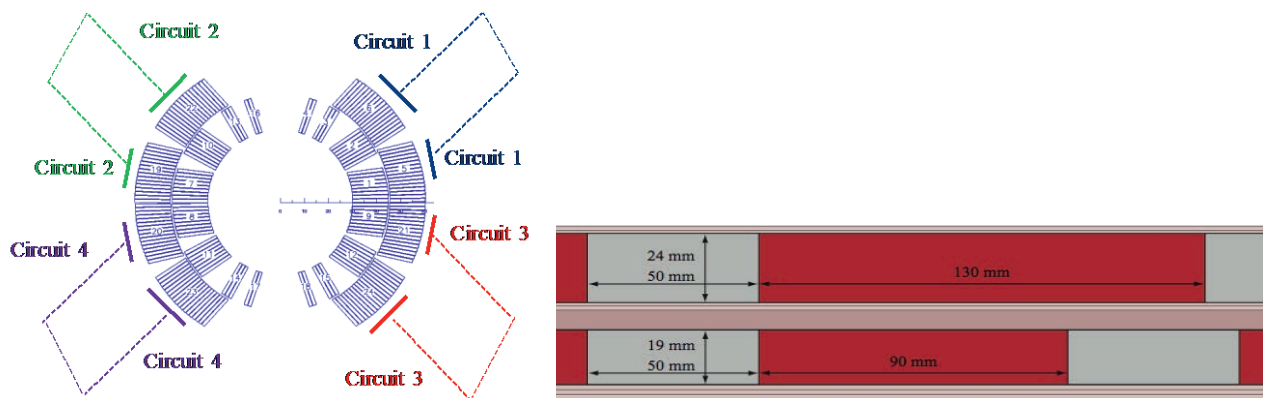


Figure 11-23: Schematic of the quench heater circuits for one aperture of an MBH (left), and quench heater geometry (right).

11.3.6 Powering

The MBHs will be integrated in the circuits RB.A67 and RB.A78. As quoted above, the 11 T dipole full assembly will be connected in series with the chain of MBs. Each chain of MBs is powered by a converter rating $\pm 190 \text{ V}$ and 13 kA [16]. As the 11 T dipole full assembly does not have the same transfer function as the MB, a trim circuit comprising a specific power converter, which can extract or inject current, is introduced. The difference between the transfer functions and the required trim current to compensate for this are shown in Figure 11-24, Figure 11-25 and Figure 11-26 show the new layout for the RB circuits RB.A67 and RB.A78 with the main power converter and the trim circuit. For the circuit RB.A78 the 11 T dipole full assembly will

be placed after the second energy extraction system (Figure 11-26), creating a little dissymmetry in the RB circuit.

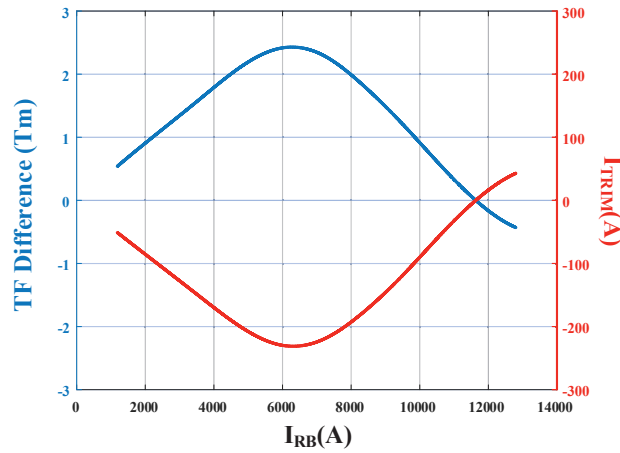


Figure 11-24: Transfer function difference between the 11 T dipole full assembly and the MB, and required trim current (in red) to compensate for the difference.

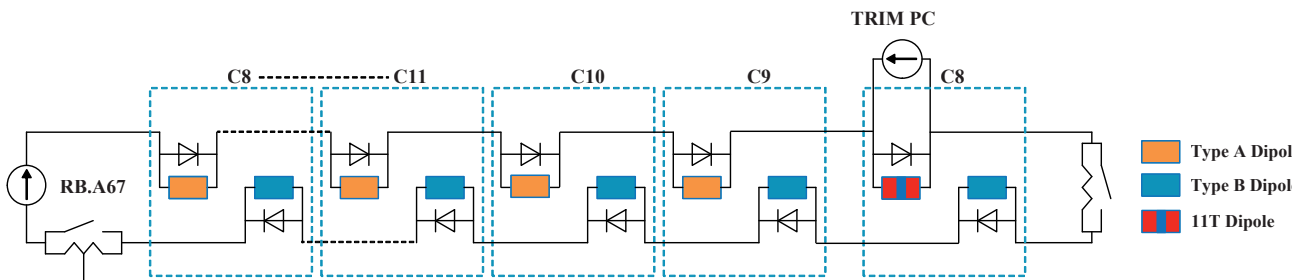


Figure 11-25: Main dipole circuit (RB.A67) configuration for the HL-LHC with the 11T trim power converter.

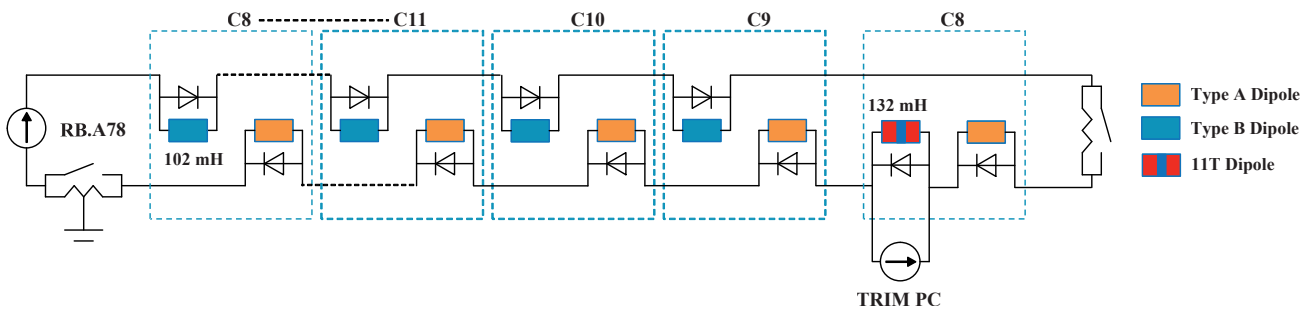


Figure 11-26: Main dipole circuit (RB.A78) configuration for the HL-LHC with the 11 T trim power converter.

11.3.6.1 RB circuit characteristics modification

The difference in inductance between the MB (0.102 H) and the 11 T dipole full assembly (0.132 H) will alter the circuit characteristics. However, this change will have low impact since only one MB out of 154 is replaced. Table 11-5 shows the new characteristics of the RB circuit after the introduction of the 11 T dipole full assembly.

Table 11-5: RB circuit characteristics in the current LHC configuration and after the introduction of 11 T dipole full assembly for circuits RB.A67 and RB.A78.

	Circuit	LHC Configuration	HL-LHC Configuration
Maximal Required PC Voltage	RB.A67 - RB.A78	171 V	171.6 V
Total Circuit Inductance (L_{TOT})	RB.A67 - RB.A78	15.708 H	15.738 H
Circuit Time Constant (τ)	RB.A67 - RB.A78	15700s	15740s
Energy Extraction Time Constant	RB.A67 - RB.A78	112s	113s
Maximum Common Voltage of the Trim Circuit in Case of Energy Extraction	RB.A67	420 V	433 V
	RB.A78	420 V	425 V
Maximum Common Voltage of the Trim Circuit in Case of Energy Extraction + Earth Fault	RB.A67 - RB.A78	910 V	910 V

11.3.6.2 Operation of the trim circuit

The operating current of the trim circuit depends on the energy level of the RB circuit operation. Figure 11-27 shows the RB current and the trim current for 3 energy levels of HL-LHC: 6.5 TeV (run 2 energy), 7 TeV (nominal energy), and 7.5 TeV (ultimate energy). The minimum current of the trim circuit is -250 A when the RB circuit current is around 6500 A. In this case, the corresponding energy of LHC (or HL-LHC) is around 3.5 TeV. It should be noted that some continuous runs at around 3.5 TeV are envisaged. Therefore, the trim circuit should be designed in order to deliver -250 A in a continuous operation.

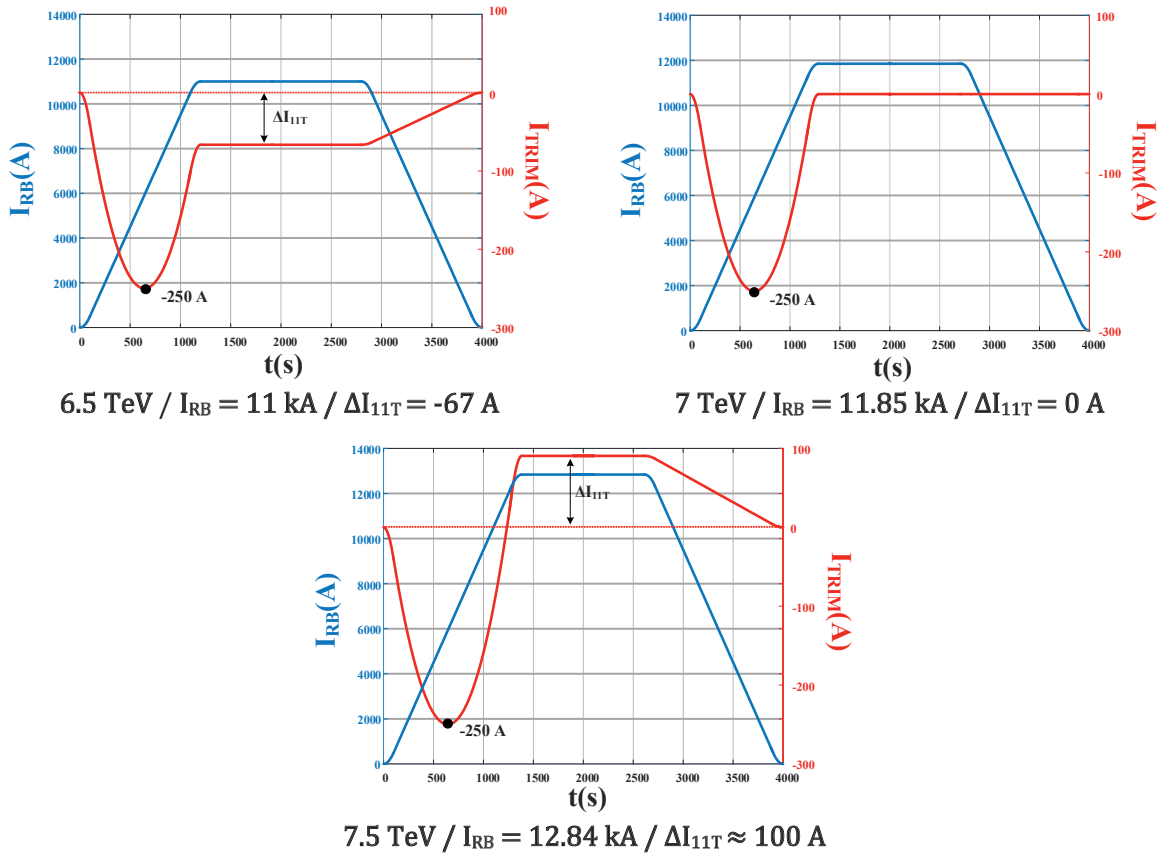


Figure 11-27: 11T trim currents for three LHC energy levels (run2, nominal and ultimate).

11.3.6.3 Design considerations for the trim circuit

Several design considerations for the trim circuit are taken into account:

- When the energy extraction systems in either the RB.A67 or the RB.A78 circuit are fired, a total voltage of around 15 V is seen across the 11 T dipole full assembly. The crowbar resistance value (refer to Figure 11-28) is chosen in order to limit the currents in the trim circuit to 250 A, respecting the cold powering constraints. However, PC failures with trim currents more than 50 A will lead to the conduction of the bypass diode for several seconds. The impact of this scenario will be tested in SM18 in the last quarter of 2016.
- The trim power converter is designed to operate in 4 quadrants (positive and negative currents and voltages) and to attain all the operation points represented in the loci represented on Figure 11-29.
- The trim circuit should withstand a common voltage of 1500 V during tests (corresponding to 910 V maximum operation voltage + margin).

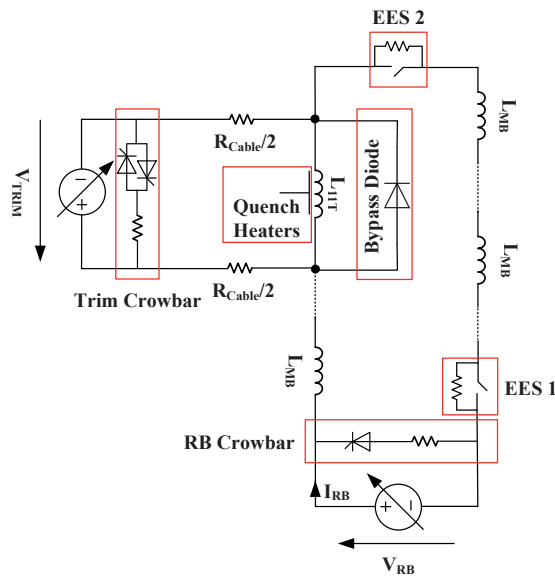


Figure 11-28: Circuit representation of the RB circuit with the 11T magnets and the power converter (crowbar included).

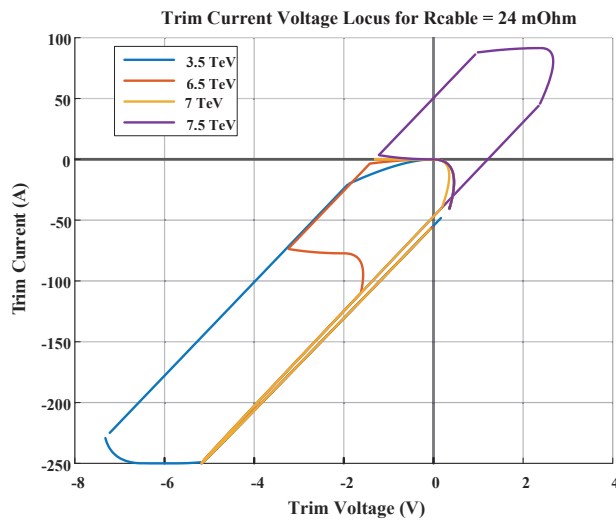


Figure 11-29: Trim PC current-voltage locus for nominal operation and operation extremums.

11.3.6.4 Trim power converter

Three trim power converters will be installed during LS2. There are two possible power converter designs for the trim power converter:

- COMET ($\pm 250\text{A}/\pm 120\text{V}$)
- R2E-LHC600A-10V ($\pm 600\text{A}/\pm 10\text{V}$)

The designs will be adapted to respect the design considerations of the trim circuit. Table 11-6, Table 11-7, Table 11-8, Table 11-9 and Table 11-10 summarize the different aspects of the trim power converter.

Table 11-6: Power converter main performance requirements.

Parameter	Data – Comments
Output Current Range	$\pm 250\text{ A}$
Output Voltage Range	$\pm 10\text{ V}$
Operating Power Range	$[-0.016; 2.5]\text{ kW}$ for 20 mins (2.5 kW continuous for 3.5 TeV Operation).
Maximum current variation in the output current range [9].	26 mA _{pk-pk} (+/- 13 mA _{pk-pk}) 1 ppm of 13 kA (RB current) = 13mA; the system accuracy over 1 year. Additionally, voltage Ripple @ 50 Hz < 40 mV _{rms} will induce I _{noise,max} @ 50 Hz expected $\approx 2\text{ mA}_{\text{rms}}$ based on: L _{magnet,300 Hz} = 0.095 H (Extrapolation from the experimental values of the 2m model).
Operation mode	Regulated DC-mode
Bandwidth I V	I _{FGC} : 3 Hz V _{PWR SOURCE} : 1 kHz (The bandwidth is defined not to excite resonating frequencies in the RB circuit – to be verified with simulations from MPE).
Voltage output noise	40 mV _{rms max} for each freq. in @ [50Hz; 20MHz]
Current output noise	In this case, the total output current noise in [50 Hz; 20 MHz] is less than 2 mA _{rms} .
Topology Efficiency	4 Quadrant, > 6 kHz switching mode efficiency > 50 % on power range.

Table 11-7: Interlock systems.

Item	Required	Comments
PIC (Powering Interlock Controller)	Yes	The schematic of the PIC is to be determined: Failure scenarios analysis, criticalness of failures and action to be taken.
BIS (Beam Interlock System)	No	
SIS (Software Interlock System)	No	
EIS (Equipement Important for Safety)	No	

Table 11-8: Power converter electrical protection.

Functionality	Description
Earth leakage current detection	The converter is floating. Therefore, no earth leakage current detection. This functionality is guaranteed by the RB main converter.
Discharge crowbar	The crowbar has a value between 50 - 100 mΩ. No values less are allowed since it is necessary for the limitation of overcurrent in the trim current leads in case of failure. The crowbar dissipates a maximum energy of 4 kJ @ 2kW maximum.

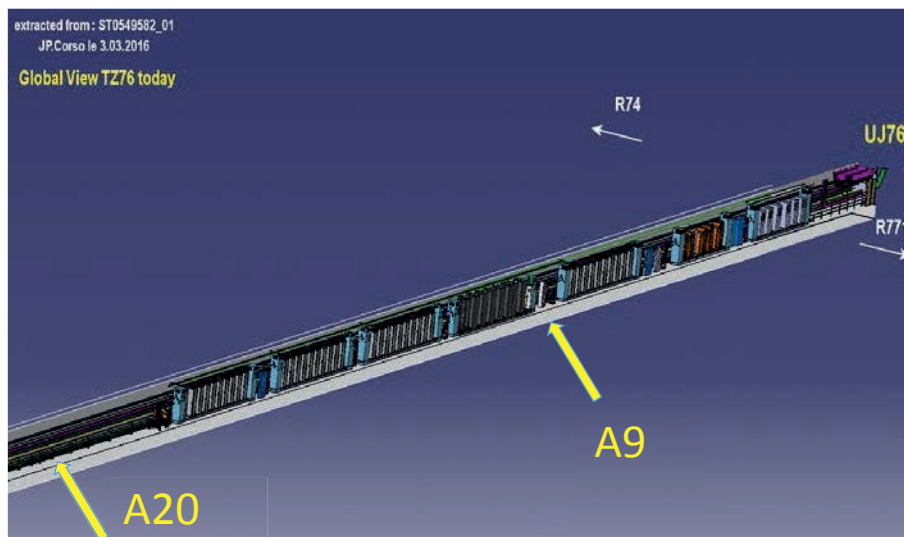
Table 11-9: Power converter interfaces.

Interfaces	From / To	Data - Value - Comments
AC connexion	AC distribution	Rack Bottom for both PCs COMET: 3x400V/50Hz - 63Arms /rack (c.f. table 11-6 for total number of racks). R2E-LHC600A-10V : (3+N)x230V/50Hz - 16Arms /rack
DC connexion		COMET : Rack Bottom R2E-LHC600A-10V : Rack Top DC cable cross-section: up to 3x 400 mm ² per polarity.
Water Cooling	Services or infrastructure: Water cooling System	COMET : Air Forced Cooling R2E-LHC600A-10V : 6l/min @ 3 bars of differential pressure drop
Air Cooling	Services or infrastructure: Air cooling System	Total losses (Incl. DCTT + FGC)/rack: COMET : 3000 W R2E-LHC600A-10V : 700 W (to be confirmed)
PIC	Services or infrastructure: Interlock system	Compatible PIC for both PCs. (Fast-Abort, Ppermit & Powering Failure signals). 12-pin female chassis burndy connector.

Table 11-10: Power converter rack space requirements.

Converter Base	Data - Value - Comments
COMET	1 converter/rack => 3 racks of (lxwd) 230 cm x 80 cm x 90 cm (2 Converters + 1 Spare). Space is required to have an access from front and back of the racks in the case of the COMET. One additional rack is required for the gateway and converter start points that should be installed in the tunnel (Ethernet Technology). Therefore, a space of around 9m is required.
R2E-LHC600A-10V	2 converters/rack => 2 racks of 230 cm (5U) x 60 cm (19") x 90 cm (lxwd). No Space is required between racks. Therefore, a space of around 2m is required (to be confirmed).

The power converters will be placed in the TZ76 tunnel. Position A9 can be considered if the technology based on R2E-LHC600A-10V is chosen. If the COMET technology is chosen, A 20 will be considered.



11.3.7 Radiation

The MBH will, inevitably, see a shower of particles from the DS collimator. The dose estimates at the foreseen locations of the 11 T dipole full assemblies around IP7, including at the level of the cold diode, have been

recently computed [17]. The peak dose in the coils remains below 2 MGy, and will be limited to few kGy at the level of the cold diode. These levels of radiation are acceptable for the magnet components.

11.3.8 Installation and dismantling

The cold mass of the MBH will be equipped with standard features in the ends facing the existing MBs in the tunnel to facilitate the installation and connection, e.g. M-flanges and bellows, preparation of the busbar extremities with regard to splicing, end flanges on the X/V lines, etc. The ends facing the collimator need to be specific; however, standard elements will be used as much as possible.

11.3.9 Cryogenics

11.3.9.1 Cooling

Although the cooling layout is similar to that of an MB, the heat extraction capacity in the MBH is reduced by approximately an order of magnitude in the MBH due to construction specificities of the Nb₃Sn coils, in particular the fact that they are impregnated. In both cases, the cold source is formed by a bayonet heat exchanger protruding the upper yoke-hole. Whereas the MB has radial connections open to helium from the annular space in between the coil-inner layer and beam-pipe to this cold source, the coils of the BMH do not. Adding such radial connections in sufficient amount for a measurable improvement in effective cooling, specifically through the titanium pole of the coils, is for the moment considered not feasible. Therefore instead of radially, the heat extraction will be via conduction over the magnet length through the helium contained in the annular space between beam-pipe and inner-coil layer towards the magnet ends. Given a cold bore of 54.5 mm diameter (53 mm + Kapton® insulation), an inner coil diameter of 59.8 mm and a magnet length of 5.5 m, the maximum heat extraction capacity at 2.1 K is evaluated to 1.7 W/m (9.3 W total). This is approximately a factor 3 above the requirement. Therefore, radial cooling channels through the coil will not be required as long as the annular space around the beam pipe towards the magnets-ends remains unobstructed and thus free for the helium.

11.3.9.2 Quench-induced pressure

In the absence of radial escape channels for the helium from the annular space around the beam-pipe an assessment of possible pressure build-up in this area has to be made. This with reference to experience with the MBs where, in case this radial escape path was blocked, dangerously high pressures develop [18][19]. At first sight, we do not expect this to be an issue due to the fact that:

- The Nb₃Sn coil is fully impregnated, thus eliminating the effects due to helium in close contact with the cable;
- The helium escape path along the annular space around the beam-pipe is much wider than in the MB;
- The escape path is much shorter as the magnet is only ~5.5 m long.

For completeness, a numerical assessment is being prepared and annular space quench pressure measurements for upcoming model-magnet tests are envisaged.

11.4 Connection cryostats for integration of dispersion suppressor collimators in IR2

In IR2, orbit bumps can be applied to steer the primary bound-free pair production (BFPP) losses in collimators located in the connection cryostat. Therefore, 11 T dipole magnets are not needed in IR2. Instead, special connection cryostats will be used to create the room temperature longitudinal space required for the collimators and to ensure continuity of the continuous cryostat and sub-systems such as the beam pipes, the bus bars and the helium heat exchanger.

On both sides of IR2, the existing connection cryostat cryo-assembly will be replaced with a string of three independently installed and aligned cryo-assemblies: two of these will be new connection cryostats

(CCC), with a bypass cryostat (QEN) installed between them. This new assembly will be called connection cryostat full assembly.

There are two types of cold mass per cryo-assembly: the cold mass CCC_001 that will be installed on the left hand side of the collimator (for an observer looking from the center of the accelerator), and the cold mass CCC_002 that will be installed on the right hand side of the collimator. These cold masses will have all the features to make their installation compatible with the location of the collimators on either side of the IR2.

The CCC cold mass assembly has a length of 5309 mm between the datum plane C and L at the end covers. The CCCs need to be compatible with the LHC lattice and its main systems. They will be connected in series with the MBs and MQs.

11.4.1 Description

The cold mass of the CCC is made of a mechanical structure holding several pipes ensuring continuity of the cryogenic circuits. Specific busbars are installed inside the cold mass for continuity of the main and auxiliary powering circuits.

The mechanical structure is based on three 25 mm thick stainless steel plates assembled with screws to form a H type beam. This beam is reinforced by intermediate plates to insure mechanical stability of the assembly when loaded.

A cross-section through the CCC is shown in Figure 11-30.

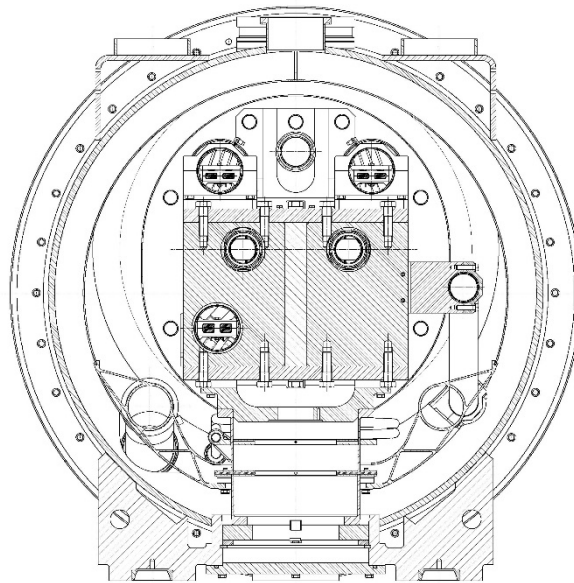


Figure 11-30: Cross-section of the CCC.

The cold mass is finished by a flat plate on the side of the assembly facing the existing MBs or MQs (see Figure 11-31) and by a dished end of a larger diameter on the side of the assembly facing the collimator (see Figure 11-32).

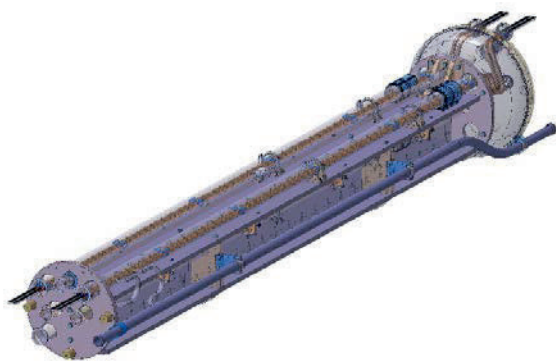


Figure 11-31: CCC Cold Mass (MBs side)

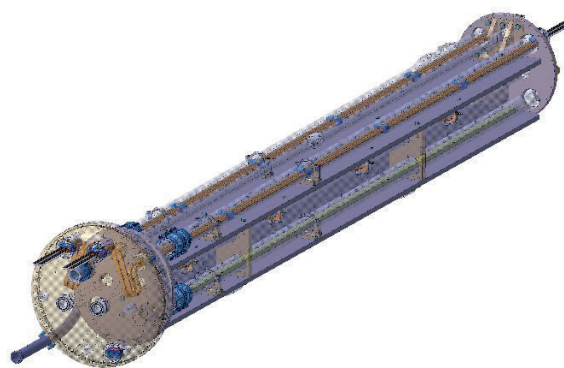


Figure 11-32: CCC Cold Mass (QEN side)

The cryogenic circuit is composed of three pipes housing the main busbars and a heat exchanger pipe connected to a “shuffling module” composed of two dished ends. On the MBs or MQs side, the pipes housing the busbars are placed in the same position as in a standard interconnection. On the collimator side, the busbar are placed further away from the beam lines to allow the routing of the busbars accros the bypass cryostat. The shuffling module is made large enough to hold the lyras of the busbars, and is used also to make the transtision between the position of the busbar in a standard interconnection and their position in the bypass cryostat.

The CCC will be equipped with the same cold bore tube and beam screen as the present connection cryostats to facilitate integration. The cold bore is installed inside a larger pipe hydraulically connected to the main cryogenic circuit of the CCC to insure low temperature cryo-pumping on the the beam vacuum surface. This configuration guarantees the temperature of the cold bore walls to be at 1.9 K in operation.

11.4.2 Equipment parameters

The main parameters of the CCC are listed in Table 11-11.

Table 11-11: Main parameters of the CCC.

Characteristics	Unit	Value
Cold bore tube inner diameter/thickness	[mm]	50/1.5
Number of apertures	-	2
Distance between apertures at room temperature/1.9 K	[mm]	194.52/194.00
Cold mass physical length (between datum planes C and L)	[m]	6.252
Cold mass weight	[tonne]	~2
Nominal operation current	[kA]	11.85
Operating temperature	[K]	1.9
Heat exchanger hole inner diameter	[mm]	60
Heat exchanger distance from centre (same position as in the MB)	[mm]	180

11.4.3 Installation and dismantling

The cold mass of the CCC will be equipped with standard features in the ends facing the existing MBs and MQs in the tunnel in order to standardize the installation and connection procedures such as M-flanges and bellows, preparation of the busbar extremities with regard to splicing, end flanges on the X/V lines, etc. The ends facing the collimator need to be specific; however, standard elements will be used as much as possible.

11.5 Inventory of units to be installed and spare policy

Two full-length MBH prototypes will be fabricated to validate the design, the overall performance in nominal operation conditions (to be checked on horizontal test benches in building SM18 at CERN), and the different interfaces with the neighbour systems. One prototype will be made with RRP conductor and the other one with PIT conductor after validation with short models.

For LS2, around IP7, two 11 T dipole full assemblies shall be fabricated in order to replace the MBs MBA-B8L7 and MBB-B8R7, i.e. 4 MBHs and two bypass cryostats are required for installation. It is planned to fabricate one spare 11 T dipole full assembly. It shall be ready by end 2021.

For LS2 around IP2, two connection cryostat full assemblies in order to replace the existing connection cryostats located in between the first MB and the first quadrupole, Q11, of the DS region next to the arc. It is planned to fabricate one spare connection cryostat full assembly.

11.6 Quality Assurance

The fabrication of the parts of the 11 T dipole full assembly and of the connection cryostat full assembly comply with the HL-LHC Quality Assurance Plan, whose implementation started at the beginning of the prototyping phase. A dedicated Quality Assurance team ensures systematic update of the relevant documentation: drawings, test reports, technical specifications, work instructions, and Manufacturing and Inspection Plans (MIP). The documentation is classified in the CERN reference databases, EDMS and CDD, where it can be easily retrieved.

Each production step is checked and documented following the MIP in order to provide adequate traceability level for each performed operation.

11.7 References

- [1] L. Rossi, LHC Upgrade Plans: Options and Strategy, 2nd International Particle Accelerator Conference, San Sebastian, Spain, 4-9 Sep 2011, pp.TUYA02. [CERN-ATS-2011-257](#)
- [2] P. D. Hermes et al., LHC Heavy-Ion Collimation Quench Test at 6.37 Z TeV, [CERN-ACC-Note-2016-0031](#), (2016).
- [3] J. Jowett et al., Bound-Free Pair Production in LHC Pb-Pb Operation at 6.37 Z TeV Per Beam, Proceedings of IPAC2016, Busan, Korea 2016, DOI: [10.18429/JACoW-IPAC2016-TUPMW028](#).
- [4] C. Bahamonde Castro et al., Power Deposition in LHC Magnets due to Bound-Free Pair Production in the Experimental Insertions, Proceedings of IPAC2016, Busan, Korea 2016, DOI: [10.18429/JACoW-IPAC2016-TUPMW006](#).
- [5] M. Karppinen *et al.*, Design of 11 T twin-aperture Nb₃Sn dipole demonstrator magnet for LHC upgrades, CERN-ATS-2013-025 (2013). DOI: [10.1109/TASC.2011.2177625](#)
- [6] F. Savary et al., Status of the 11 T Nb₃Sn dipole project for the LHC, Applied Superconductivity Conference, USA, 10 – 15 Aug. 2014, DOI: [10.1109/TASC.2014.2375914](#).
- [7] Heat Load Working Group, <http://lhc-mgt-hlwg.web.cern.ch/lhc-mgt-hlwg/default.htm>
- [8] S. Izquierdo Bermudez et al., “Design Optimization of the Nb₃Sn 11 T Dipole for the High Luminosity LHC”, submitted for publication at ASC 2016 Denver.
- [9] J. Fleiter et al., “Optimization of Nb₃Sn Rutherford cables geometry for the High Luminosity LHC”, IEEE Trans. Appl. Supercond. **27** (2017) 4004305 DOI: [10.1109/TASC.2017.2672903](#)
- [10] A. V. Zlobin et al., “Development of Nb₃Sn 11 T single aperture demonstrator dipole for LHC upgrades,” in Particle Accelerator Conference, New York City, NY, USA, 28 Mar - 1 Apr 2011, pp.WEOCS2, p. [1460](#).
- [11] A. Zlobin et al., “Quench Performance of a 1 m Long Single-Aperture 11 T Nb₃Sn Dipole Model for LHC Upgrades”, IEEE Trans. Appl. Supercond. **24** (2014) 4000305, DOI [10.1109/TASC.2013.2281782](#).

- [12] A. Zlobin et al., "Status of 11 T 2-in-1 Nb₃Sn Dipole Development for LHC", Proceedings of IPAC 2014, [WEPRI097](#).
- [13] G. Willering et al., "Cold powering tests of 11-T Nb₃Sn Dipole models for LHC upgrades at CERN", IEEE Trans. Appl. Supercond., vol. **26**, no. 4, Jun. 2016. DOI: [10.1109/TASC.2016.2540604](#)
- [14] G. Willering et al., "Cold powering performance of the first 2 meter Nb₃Sn DS11T twin aperture model magnet at CERN", submitted for publication at ASC 2016 Denver.
- [15] S. Izquierdo Bermudez et al., Quench Protection Studies of the 11-T Nb₃Sn Dipole for the LHC Upgrade, IEEE Trans. Appl. Supercond. **26** (2016) 4701605, DOI: [10.1109/TASC.2016.2536653](#).
- [16] LHC Design Report Geneva : CERN, 2004. - 548 p. DOI: [10.5170/CERN-2004-003-V-1](#)
- [17] A. Lechner et al., "Update of dose estimates at the level of the cold diode for the 11 T magnets", 10th meeting of the HL-LHC Technical Coordination Committee, 30 June 2016. INDICO [515633](#)
- [18] Lebrun, P. ; Wahlström, T. ; Van Weelderen, R. ; Williams, L., "Investigation of quench pressure transients in the LHC superconducting magnets", [CERN-AT-94-16-CR-MA](#), 27 Jun 1994. - 5 p, 15th International Cryogenic Engineering Conference, Genoa, Italy, 7 - 10 Jun 1994, pp.705-708.
- [19] Wahlström, T., "Investigation of quench pressure transients in the LHC superconducting magnets", 20 Dec 1994. - 55 p. [CERN-AT-94-46](#)

Chapter 12

Vacuum System

12 Vacuum system

12.1 Overview

The luminosity upgrade programme (HL-LHC) requires modifications of the present LHC's vacuum system, in particular in the triplets, crab cavities, matching section and experimental areas. Such modifications must follow guidelines similar to those followed for the present machine. The increased stored current implies a higher thermal power in the beam screen from the image current moving along with the stored particles and stronger synchrotron radiation (SR) and electron cloud (EC) effects, which in turn translate into higher degassing rates.

One of the main tasks of the vacuum HL-LHC work package is to define the geometry of the vacuum equipment in the new superconducting (SC) focusing triplet (FT) and D1 magnets. It is also necessary to define a strategy for assembling and inserting high-density shielding material into the SC Insertion Region (IR) magnets. This is mandatory for protecting the magnets from collision debris coming from the experiments' interaction points (IPs). A balance between cold bore size and vacuum pumping system will be defined based on experience gained with the present machine and recent advances with new materials. A number of new ideas have emerged recently – for example, amorphous carbon (a-C) coating for which validation is ongoing and laser structure surface currently under study.

The change of the aperture of the triplets at IR1 and IR5 implies that the experimental vacuum chambers of CMS and ATLAS will require a review of aperture, impedance, and vacuum (dynamic and static). From preliminary analyses, the forward regions of CMS and ATLAS will need to be adapted to cope with the new beam geometry in IR1 and IR5. New materials will likely be needed to mitigate the additional activation from the increased luminosity. New access procedures will be needed to allow the minimization of the integrated dose to personnel. With the HL-LHC, less flexibility will be available for the optics of LHCb and ALICE; therefore, the vacuum chambers at IR2 and IR8 must be validated for operating conditions to ensure that these chambers do not impose a limitation. *In-situ* a-C coating of the beam screens focussing triplet magnet, located in LSS2 and 8, is under validation to reduce the electron cloud heat load onto the cryogenic system. Positions of mechanical supports, pumps, and gauges must be analyzed to ensure that layouts are optimized for the new machine configuration. Bake-out equipment will be redefined depending on activation and specific needs. All experimental chambers must be treated with Non-Evaporative Getter (NEG) or equivalent to minimize secondary electron yield (SEY), thus reducing electron cloud effects.

12.2 Beam vacuum requirements

The HL-LHC beam vacuum system must be designed to ensure the required performance when beams with HL-LHC nominal parameters circulate. The system must be designed for HL-LHC ultimate performance, without a margin.

The vacuum system must be designed to avoid pressure runaway induced by ion-stimulated desorption. It must also be designed to take into account the effects of synchrotron radiation, electron cloud, and ion-stimulated desorption from the walls. Heat load onto the beam vacuum chamber walls or flanges and beam impedance effects must also be taken into account [1].

The system must be compatible with the global LHC impedance budget and the designated machine aperture.

The average gas density along the IRs must satisfy the level defined by the 100 h vacuum lifetime due to nuclear scattering, i.e. less than 1.2×10^{15} H₂ molecules m⁻³ equivalent in the LHC [2]. This gas density limit decreases proportionally to the inverse of the beam current. Table 12-1 gives the molecular gas densities yielding a 100 h vacuum lifetime in the LHC and the HL-LHC assuming the presence of a single gas in the vacuum system. The average gas density along IR1, IR2, IR5, and IR8 must also ensure that the background to the LHC experiments remains at acceptable levels [3, 4]. In the absence of specified values from the LHC experiments themselves, the LHC design value will be scaled to HL-LHC parameters.

Table 12-1: Single gas species molecular gas density (m⁻³) to satisfy 100 h vacuum lifetime in the LHC and the HL-LHC assuming a single circulating beam [2].

Machine	I [A]	H ₂ [m ⁻³]	CH ₄ [m ⁻³]	H ₂ O [m ⁻³]	CO [m ⁻³]	CO ₂ [m ⁻³]
LHC	0.58	1.2×10^{15}	1.8×10^{14}	1.8×10^{14}	1.2×10^{14}	7.9×10^{13}
HL-LHC	1.09	6.4×10^{14}	9.6×10^{13}	9.6×10^{13}	6.4×10^{13}	4.2×10^{13}

12.3 Vacuum layout requirements

The vacuum layout must ensure the vacuum requirements for circulating beams with HL-LHC nominal parameters. The system must be designed for the HL-LHC ultimate luminosity (i.e. 7.5×10^{34} cm⁻² s⁻¹), without margin.

- All beam vacuum elements must be leak tight (leak rate less than 10^{-11} mbar⁻¹/s He equivalent), clean according to CERN vacuum standards, and free of contamination *e.g.* grease, oil, fingerprints.
- According to the LHC baseline [2], the vacuum system in the Long Straight Sections (LSS) must be sectorized with gated valves. The vacuum sectorization is delimited by cold-to-warm transitions, length of vacuum sectors, or specificity of components (fragility, maintenance, etc.) [5].
- Vacuum sector valves must be installed at each cold-to-warm transition in order to decouple the room temperature and cryogenic temperature vacuum systems during bake-out, cool-down, installation and commissioning phases.
- The distance between the vacuum sector valve and the cold-to-warm transition must be minimized in order to reduce the length of the beamline that is not baked-out in situ.
- Dedicated vacuum instrumentation must be provided close to and on either side of each sector valve and along each vacuum sector.
- Sector valves must be remotely controlled and interlocked in order to dump the circulating beam in the case of malfunctioning. The LHC and HL-LHC vacuum sectorizations delimit two types of vacuum system:
 - o room temperature vacuum system;
 - o cryogenic temperature vacuum system.
- The vacuum system shall be integrated in the tunnel and cavern volumes with the permanent/mobile bake-out system, bake-out racks, quick flanges collars, mobile pumping systems, and diagnostics systems. The corresponding space must be reserved into the tunnel integration to allow a proper access and operation of the vacuum system.
- Integration studies must also be performed for installation and un-installation phases of equipment to identify potential conflicts.

VACUUM SYSTEM

- Integration and installation drawings must be circulated and validated before installation in the tunnel and caverns.
- The vacuum chamber aperture is defined by the beam optics system, the beam impedance, by machine protection, and background considerations of the experiments. The aperture of the vacuum chamber must not be the limiting aperture.
- All components to be installed into the vacuum systems must be approved and their vacuum performance validated before installation.
- A maximum number of LHC beam vacuum components will be reused for the HL-LHC upgrade.
- High radiation areas along the LSS must be clearly identified at an early stage of the design, in particular to highlight positions where remote handling/tooling might be preferred and positions where instrumentation must be radiation resistant.
- When needed, irradiation tests of specific components (instruments, bake-out jackets, cables, electronics, O-rings, etc.) must be conducted to meet the radiation dose specifications.
- The spares policy will follow the general A&T sector policy. A spares policy must be defined and made available from early on during procurement to benefit from large quantity orders, in particular for highly specialized equipment such as beam screens, modules, etc.
- Cryogenic elements must be installed first; then room temperature vacuum sector valves, followed by completion of the room temperature vacuum sectors.
- Time, resources, and space to allow the temporary storage of LHC vacuum components, which need to be dismantled to allow HL-LHC infrastructure modifications and equipment installation, will be evaluated in the next phase of the project.

12.3.1 Room temperature vacuum system requirements

Standard vacuum chambers and vacuum modules will connect the machine components.

In order to accommodate thermal expansion during bake-out and sustain ‘vacuum forces’ due to the differential pressure, each component containing a beam pipe must have a single fixed point. Other supporting points, if any, must be sliding.

All machine components operating at room temperature must be bakeable. The required bake-out temperature is $230^{\circ}\text{C} \pm 20^{\circ}\text{C}$ for NEG coated vacuum chambers and $300^{\circ}\text{C} \pm 20^{\circ}\text{C}$ for uncoated stainless steel beam pipes. To optimize the bake-out duration while minimizing the mechanical strength and radiation to personnel, the applied heating rate during bake-out is 50°C/h .

The vacuum system layout must be designed to fulfil the stated requirements throughout a full run. In particular, the impact of the outgassing rate of specific components, e.g. collimators, must be taken into account during the layout definition phase. No NEG coating re-activation can be foreseen during short stops to recover loss of pumping performance.

A vacuum module equipped with a bellow must be inserted between each machine component and vacuum chamber, and between the vacuum chambers themselves. These vacuum modules must be screened by an RF bridge for impedance reasons.

For the sake of cost, reliability, spares policy, and standardization, the maximum number of vacuum module variants must be reduced with respect to the LHC baseline.

The warm vacuum chambers must be circular and bakeable. The current LHC variants are 80 mm, 100 mm, 130 mm, and 212 mm ID: any further variants needed for the HL-LHC will be kept to the minimum necessary.

Special chambers may be designed if needed but the quantity must be kept to a minimum. A typical case is that of the recombination chambers installed into the TAN absorber, which by definition is not circular.

Vacuum chamber transitions (VCT), which give offsets and adaptations between pipe apertures, must be integrated at the early design stage into the concerned equipment by the equipment owners themselves, e.g. beam monitors, superconducting cavities, quadrupole masks, etc. in agreement with the vacuum, surface and coating group of the CERN Technology department.

The vacuum chambers are aligned within ± 3 mm accuracy. Better tolerance will require the installation of survey targets on the vacuum chamber and their alignment by the survey group. Alignment of other equipment is the responsibility of the survey group.

The choice of the vacuum chamber material between Cu-alloy and stainless steel (either Cu coated or bare) is dictated by beam impedance constraints. Al- alloys are preferred in high-radiation areas.

Connections between equipment must be made by ConFlat® bolt technology unless radiation issues and/or remote handling require the use of quick-release flanges with, for example, chain clamps.

12.3.2 Cryogenic temperature beam vacuum system requirements

The cryogenic beam vacuum system must be tightly decoupled by sector valves from the room temperature vacuum system. Dedicated instruments must be provided close to the sector valves to allow atmospheric evacuation roughing, monitoring, and safety against overpressure of the beam vacuum vessel.

A cold-to-warm transition must be integrated into the cryogenic beam vacuum sector at each extremity of the cryogenic system.

A continuous cold bore, i.e. without penetrating welds between the beam vacuum and helium enclosure, ensures leak-tightness between the superfluid helium and beam vacuum along the cryogenic beam vacuum sector. The LHC nominal cold bore temperature is 1.9 K in the arcs.

A beam screen must be inserted into the cold bore to extract the beam-induced heat load at a temperature higher than 1.9 K. The beam screen must be perforated with slots (4% transparency) to allow pumping into the cold bore space [2]. The LHC beam screen operates from 5 K to 20 K. The HL-LHC beam screens of the FT + D1 will run at a higher temperature (between 40 K and 60 K) due to a much higher heat load. In situ heating of the beam screen up to 90 K, with cold bore < 3 K, is required to flush the condensed gas present on the beam screen inner surfaces towards the cold bore. This heating cycle may be required after a long technical stop or even between physics fills. For the new beam screens built for the HL-LHC project, the beam screen perforation percentage will be scaled to HL-LHC parameters and therefore increased as compared to the LHC.

When a cold bore operates at 4.5 K, cryo-absorbers are installed outside the beam screen in order to provide hydrogen pumping speed and capacity.

In the LHC, the maximum length without beam screen is less than 1 m (with the exception of superconducting cavities). This LHC design value will be scaled to HL-LHC parameters and therefore reduced.

For the HL-LHC, the beam screen aperture will be derived from beam optics and magnet aperture inputs.

12.4 Insulation vacuum requirements

The insulation vacuum system ensures the required performance of the cryogenic system by eliminating the heat losses due to gas convection. The insulation vacuum systems under the responsibility of TE-VSC include the cryogenic distribution line (QRL) and cryogenic machine components, but exclude transfer lines outside the LHC tunnel and those of the experimental cavern.

The requirements of the insulation vacuum system for the HL-LHC can be summarized as follows:

- the pressure must be below 10^{-5} mbar;

VACUUM SYSTEM

- the helium leak rate, at the component level, must be below 10^{-10} mbar L/s;
- it must be compatible with the LHC insulation vacuum system [2];
- it must be built with the same standards used for the LHC insulation vacuum system.

The QRL and the magnet cryostats are mechanically connected via specific bellows and pipes assemblies called jumpers. However, the insulation vacuum of the QRL and continuous cryostat is sectorized through vacuum barriers. There is no sectorization of the QRL in the LSS of the LHC. Sectorization of the HL-LHC cryostats shall ensure that longitudinal leak location techniques can be employed. Connection to cryo-plant or transfer lines outside the LHC tunnel shall be delimited by vacuum barriers.

The insulation vacuum relies on cryopumping in normal operation. Fixed turbomolecular pumping groups are used for pumping before cool-down. This system also mitigates the impact of helium leaks during operation. Such pumps are also used for the detection of helium or air leaks. Dedicated pumping ports are used for rough pumping groups, pressure gauges, pressure relief valves, longitudinal leak localization techniques, and additional pump placement in case of operational leaks. A bypass equipped with isolation valves is installed between subsectors. The standard for pumping ports is the ISO-K DN 100 flange. Each insulation vacuum volume has to be equipped with pressure relief valves. Elastomer seals (Viton, NBR) are used where system demountability is necessary (interconnections, instrumentations, etc.).

For the HL-LHC project, in the areas of expected high irradiation, specific seals (metals or hard-rad polymers) have to be installed on new equipment and be used to replace standard seals on any retained equipment.

Regular preventive maintenance will be carried out on turbomolecular pumping groups during technical stops.

12.5 Experimental vacuum system requirements

The experimental vacuum system is located between Q1L and Q1R of each interaction point. Similarly to the LSS, the vacuum layout of each experimental vacuum system must ensure the vacuum requirements when beams with HL-LHC nominal parameters circulate. The system shall be designed for HL-LHC ultimate parameters, without margin. Therefore, all constraints and requirements defined in Section 12.3 apply in this section.

During long beam stops (>10 days), neon venting is needed to protect the fragile experimental vacuum chambers from deformations caused by mechanical shocks. The baseline is that there will be no work in the vicinity of the vacuum chambers while they are under vacuum.

The vacuum chamber supporting system must be compatible with standard activities performed in the experimental cavern during short stops (e.g. winter technical stops). In particular, no personnel are allowed in the vicinity of the beam pipe (<2 m radius) during these phases.

The decoupling between the two complex and delicate inner triplet and experimental vacuum sectors is done by two vacuum sector valves sitting almost side by side. The vacuum sector defined by these two sector valves is named hereafter 'buffer'. This buffer ensures a full decoupling of the room temperature experimental vacuum system and the cryogenic temperature vacuum system during bake-out and cryogenic temperature transients. It brings also redundancy for the sectorization of these important vacuum sectors.

A first vacuum sector valve is located at each TAXS extremity inside the cavern of ATLAS and CMS and installed at the Q1 extremity inside the tunnel for the other experiments. These sector valves are interlocked to the circulating beam.

A second vacuum sector valve is installed inside the cavern between TAXS and the interaction point on the left-hand and right-hand sides of the ATLAS and CMS experiments. On the left-hand and right-hand sides of the ALICE and LHCb experiments, the second sector valve is installed inside the tunnel between Q1 and the cavern shielding. These valves are blocked open during operation, i.e. they are out of the interlock chain.

A rupture disk is installed in the buffer zones in order to protect the experimental vacuum chambers in case of liquid helium inrush.

As for the present LSS vacuum system, all machine components operating at room temperature must be bakeable and NEG coated.

Accidental or scheduled air venting for repair or maintenance of any of the vacuum sectors of the experimental vacuum system implies a complete NEG recommissioning of the beam pipes, i.e. two bake-out cycles, the first for the bake-out of the metallic part, the second for NEG activation.

An ultra-pure neon venting system is installed in the buffer zone (for ATLAS, CMS, and ALICE) or in the detector itself (i.e. in the LHCb vertex locator, VELO) to allow remote venting of the experimental vacuum system during long stops (>10 days).

12.5.1 High luminosity experiments: ATLAS and CMS

ATLAS and CMS LHC vacuum layout drawings are described in [6] and [7].

On both sides of ATLAS and CMS, a pumping system, shown in Figure 12-1, is installed in the buffer zone to allow pump-down and vacuum commissioning during NEG activation of the ATLAS and CMS experiment.

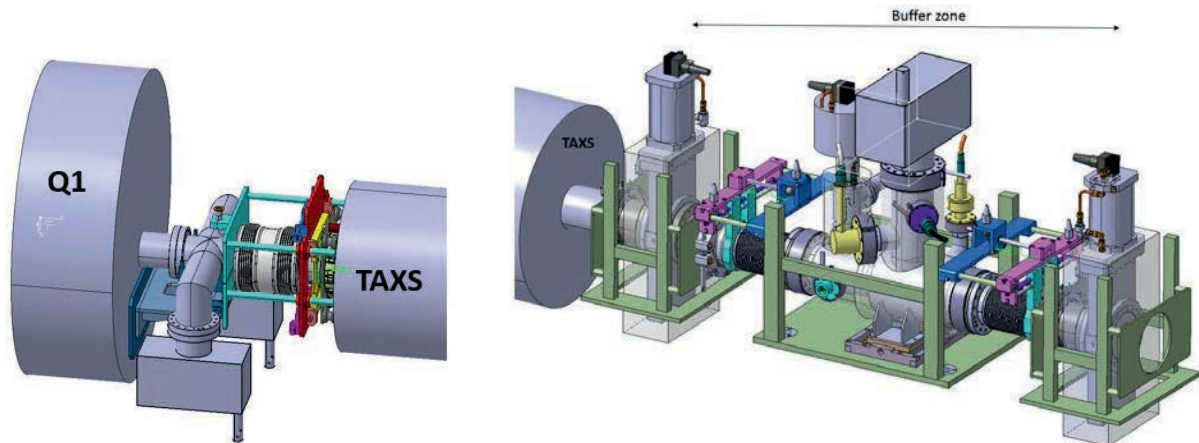


Figure 12-1: Schematic of HL-LHC high luminosity experiments instrumentation areas. Left, connection between Q1 and TAXS. Right, buffer zone between sector valves.

In the Q1–TAXS areas instrumentation must be minimized. The present baseline foresees a simple connecting bellow and two ion pumps between Q1 and TAXS chambers. The connecting bellow is surrounded by an insulating vacuum to minimise the impact of potential leaks into the beam vacuum system.

The following are required to avoid personnel intervention in a high radiation area.

- A pumping and neon systems must be installed in the buffer zone on the right-hand side of ATLAS to complement the left-hand side.
- Remote tooling and handling must be foreseen to avoid personnel intervention. Quick type flanges are mandatory. Welds are preferred to flanges.
- Installed components must be robust: in particular, sliding fingers in RF bridges are forbidden.
- The bake-out system must be permanent and fully integrated with the other systems from the design phase.
- Detector modifications shall be designed taking into account movement and intervention of personnel. They shall also take into account the beam pipe system and flanges for detector movements. It must be ensured that standard interventions during technical stops and chamber replacements are thoroughly

studied during the design phase with the aim of minimizing the radiation dose to personnel during the detector and chamber lifecycle.

ATLAS is equipped with a permanent bake-out system while CMS is not. However, the HL-LHC might require the use of permanent bake-out systems for both detectors due to radiation issues. In CMS, a specific design of the jackets, thermocouple, and cable layouts must also comply with radiation requirements.

The vacuum modules are not screened by sliding RF finger because of access and space constraints, radiation protection reasons, and potential risk of aperture loss.

The alignment of the vacuum chambers shall be performed remotely with appropriate hardware.

The choice of the vacuum chamber material between Cu-alloy and stainless steel (either Cu coated or bare) is dictated by beam impedance requirements. Al-alloys are preferred in high-radiation areas.

The connection between equipment shall be done by Conflat bolted technology unless there are radiation issues and/or remote handling that requires the use of quick-release flanges.

It is assumed that the ATLAS central beam pipe inner diameter, as installed during LS1, remains the same until at least LS3 [8].

According to Ref. [9], the following are assumed.

- The CMS central beam pipe inner diameter, as installed during LS1 remains the same until at least LS3.
- End cap, HF, CT2, and forward pipes of the CMS vacuum system must be upgraded to Al bulk material during LS2. No mechanical intervention between TAS L and TAS R is therefore expected during LS3.

Any new chamber to be installed in the future must be compatible with remote tooling, e.g. equipped with a 'quick flange' type system.

Since the TAS needs to be replaced during LS3, the vacuum system located inside the experimental cavern needs to be recommissioned, i.e. NEG activation even if no changes to the vacuum system inside the cavern is foreseen.

12.5.2 ALICE and LHCb experiments

On the right-hand side of ALICE, a pumping system is installed in the buffer zone to allow pump-down and commissioning during NEG activation of the beam pipes.

In the ALICE cavern, a manual valve, located on the left-hand side of the beryllium central beam pipe, allows the isolation of the detector vacuum sector from the vacuum sector located in RB24 cavern. Consequently, the vacuum chambers in the RB24 area can be dismantled during long shutdowns if needed.

The ALICE vacuum layout drawing is described in [10].

The ALICE central beryllium beam pipe is not equipped with a permanent bake-out system. The beam pipes located in the RB26 area of the ALICE cavern (i.e. the right-hand side of the IP) are equipped with a permanent bake-out system. From the left of the central beam pipe to the end of RB26, the vacuum modules are not screened by sliding RF fingers because of access and space constraints, radiation issues, and the potential risk of aperture loss.

In LHCb, the vertex locator (VELO) detectors are installed into a secondary vacuum system which is isolated from the beam vacuum system by a thin RF shield. The RF shield mechanical integrity is protected during pumping and venting phase by an automatic gas balance system to maintain the pressure difference within a mechanically stable range.

At the VELO, an automatic pumping system is installed to allow pump-down and commissioning during NEG activation while protecting the VELO RF shield.

At the VELO, an ultra-pure neon venting system is installed to allow remote venting of the LHCb with an automatic gas balance system while protecting the VELO RF shield during long stops (>10 days).

The LHCb beam pipes are not equipped with a permanent bake-out system. However, it is foreseen that part of the vacuum chamber named UX85/3 and located in the region of the calorimeter will be equipped with permanent bake-out for LS2 [11, 12].

The VELO beam pipe must be baked for 48 h at a minimum of 180°C to suppress electron cloud.

From the right-hand side of the VELO beam pipe to the end of UX85 cavern, the vacuum modules are not screened by sliding RF fingers because of access and space constraints, radiation issues, and the potential risk of aperture loss.

Wake-field suppressors are installed at the VELO beam pipe extremities for impedance reasons.

The LHCb vacuum layout drawing is described in Ref. [12].

According to Ref. [13], it is assumed that the ALICE central beam pipe inner diameter will be changed during LS2 and remains unchanged afterward.

According to Ref. [11], the following are assumed.

- The LHCb VELO beam pipe will be changed during LS2 and remains in the ring afterward.
- The 2 m long Cu-alloy vacuum chamber, VCDBV, located on the right-hand side of the VELO will be replaced by an Al-alloy beam pipe. This change will take place during LS2. No modification is expected afterward.
- Part of the UX85/3 vacuum chamber in the calorimeter region will be equipped with permanent bake-out jackets during LS2. It is also assumed that there will be no more installation of permanent bake-out jackets after LS2.

12.6 Beam screen requirements

Beam screens are inserted into cryogenic cold bores in order to guarantee vacuum performance. They are part of the LHC vacuum system baseline [1]. The requirements of the HL-LHC beam screen can be summarized as follows.

- The system lifetime must be longer than the HL-LHC lifetime, i.e. 40 years of operation and 50 quenches.
- The system must fulfil the required vacuum performance in terms of vacuum stability, vacuum lifetime, and background to the experiments.
- The shielded beam screen must be perforated (or be shadowing) in order to fulfil the vacuum performance in a way to allow the pumping of molecules onto the cold bore.
- The cold bore temperature must be held below 3 K to allow cryo-absorption of all molecules with the exception of helium.
- The shielded beam screen must be heatable to allow a transfer of the gas onto the shielded beam screen towards the cold bore during machine stops.
- The shielded beam screen must withstand the Lorentz forces induced by eddy currents during a quench.
- The temperature of the shielded beam screen must be actively controlled in a given temperature range.
- To minimize the heat load on the shielded beam screen due to the electron cloud, a coating, e.g. amorphous carbon or a clearing electrode system, must be studied, validated, and implemented. The e-cloud mitigation measures must be applied not only to the new high-luminosity insertion regions, IP1 and IP5, that will be renovated. They will be applied also to the interaction regions of IP2 and IP8. These

VACUUM SYSTEM

are indeed low-luminosity insertions, however the beam pattern will be the same as in the high-luminosity insertions. This point is quite recent and mitigation measures are currently under investigation.

- The system must be compatible with the impedance budget.
- The system must be compatible with the machine aperture.
- The surface of the beam screen must withstand a dose of several hundred MGy during its lifetime.

In order to operate properly, the beam vacuum system must be evacuated for five consecutive weeks, at least, prior to cool-down to allow the outgassing rate of adsorbed water to be reduced to acceptable levels.

During cool-down of a cryogenic system, the cold bore must be cooled first in order to minimize gas condensation onto the beam screen.

In the case where gas condenses onto the beam screen during operation, e.g. after a magnet quench, a transfer of this gas towards the cold bore via beam screen heating is needed. This procedure should be carried out in a couple of days.

The HL-LHC beam screen must be inserted during the cryostating phase prior to tunnel installation. The surface of the beam screens must be kept clean during assembly. This implies that the beam screen is installed at the last stage of cryostating. Without specific tooling and procedures, no probe or device can be inserted into the vacuum system once the beam screens are installed.

The cooling tubes must be dimensioned to allow a proper cooling of the system during operation within the limits defined above.

According to vacuum standards, full penetrating welds are forbidden in the vessel wall separating the beam vacuum and helium enclosures. However, given the limited number and length of new vacuum elements to be installed, this general rule might be revised in the case of compelling reasons, if compensated for by adequate measures of risk mitigation.

Depending on the location, two types of beam screens may exist: shielded and non-shielded beam screens. The shielded beam screens intercept part of the debris produced at the high luminosity IPs, thereby protecting the cold masses from radiation-induced damaged.

Amorphous carbon (a-C) coating is at present the baseline for the inner surface of the HL-LHC shielded and non-shielded beam screens. Due to a-C's properties, strong electron cloud suppression in these HL-LHC components is expected. Amorphous carbon coating will be applied to HL-LHC beam screens if needed for the reduction of heat load to cryogenic systems, reduction of background to experiment, and/or beam physics requirements.

A demonstration of the electron cloud suppression must be performed with a dedicated set up such as COLDEX in SPS LSS4 [14]. Studies will be held during SPS scrubbing runs and dedicated machine development. Experimental results must be supported by theoretical expectations derived from simulations codes such as Ecloud or PyCloud.

Amorphous carbon coating should be the last step of beam vacuum preparation before lowering the magnet into the tunnel, avoiding any subsequent insertion of tooling or other devices into the beam vacuum line.

For IP2 and IP8, in situ coating of the present beam screen (or alternatively the placement of a clearing electrode) must be studied and conducted during the long shutdown (LS2 or LS3). If in situ coating is not possible, removal of the magnet cryostat will be considered to allow beam screen exchange.

If needed, a sawtooth structure can be produced on the beam screen walls (dipoles and quadrupoles). The sawtooth must be designed to intercept the synchrotron radiation at perpendicular incidence and to reduce the forward scattering of light.

12.6.1 Shielded beam screen

HL-LHC shielded beam screens are to be inserted into HL-LHC D1 and FT of LSS1 and LSS5. These beam screens ensure the vacuum requirements, the shielding of the cold mass from physics debris, and the screening of the 1.9 K cold bore cryogenic system from beam-induced heating.

As a baseline, the shielded beam screen is assumed to fulfil the vacuum requirements with a-C coating operating at 40–60 K [15].

The shielded beam screen is estimated to operate in the 40–60 K \pm 10 K temperature range. The operating temperature range will be defined by the available cooling power, the expected beam-induced heat load, and compatibility with the vacuum requirements.

The selected shielding material is Inermet, a tungsten alloy. Inermet is a sintered tungsten-based composite material with around 3.5 wt% of nickel and 1.5 wt% of copper. The electrical, thermal, magnetic and mechanical properties of the Inermet 180 have been measured at room and cryogenic temperatures [16].

Depending on the purity, the electrical resistivity of tungsten varies a few orders of magnitude at cryogenic temperature. The electrical resistivity of the Inermet 180 has been measured between 4.2 and 300 K. Different batches have been tested to assess possible variations during the manufacturing. The samples have been machined from sintered blocks. Two different geometries have been considered to evaluate the impact of the machining and the local surface modifications. The measurements are given in Figure 12-2. Neither significant influence of the batch nor of the sample geometry has been observed at cryogenic temperatures.

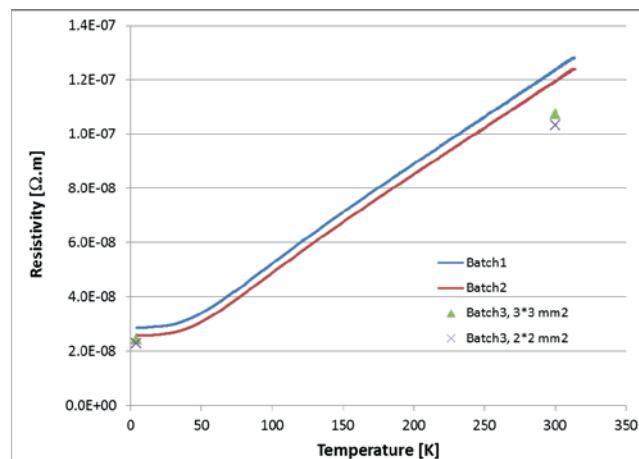


Figure 12-2: Measured electrical resistivity of Inermet 180 as a function of temperature. Batch 1 corresponds to reference number 8017006 and Batch 2 to reference 802482. The sample dimensions of Batch 1 and 2 have been 2 mm x 2 mm x 73 mm.

The magnetic permeability has been measured using a vibrating sample magnetometer. Three different samples, 8 x 4 x 2 mm³ each, have been extracted by electro discharge machining at different position from a machined tungsten piece and have been tested. The measurements have been carried out between 4 K and 300 K with a magnetic field, H, up to 90 kOe (7162 kA/m). The magnetic permeability curves are given as a function of the temperature and the magnetic field in Figure 12-3. The Inermet 180 magnetic permeability is less than 1.0003 at all measured fields and temperatures. No significant deviation has been observed between these three specimens. The magnetic susceptibility is in the order of 10⁻⁴ in the temperature range of 40-60 K. This is more than one order of magnitude lower than the magnetic susceptibility of the specific high-Mn austenitic stainless steel used for the beam screen wall.

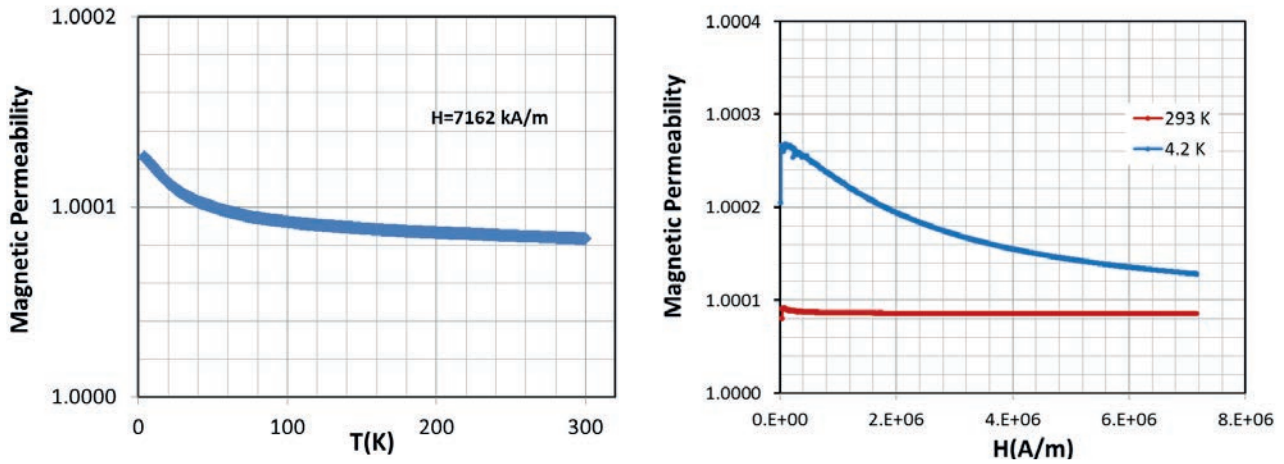


Figure 12-3: (left) Typical Inermet 180 magnetic permeability as a function of temperature. Values obtained from measurement at H=7162 kA/m.(right) Typical Inermet 180 magnetic permeability as a function of magnetic field. Values at room temperature and 4.2K.

The absolute measurement method was used to determine thermal conductivity as $\lambda = \dot{Q} \cdot L / (A \cdot \Delta T)$ and has been carried out between 3.8 K and 280 K on two 8 mm x 8 mm x 50 mm samples. Samples identical to those used for the thermal contraction measurement have been used to determine the thermal conductivity. An active length of 30 mm has been chosen for the measurement of the temperature difference. Figure 12-4 shows the measured thermal conductivity as a function of temperature for both specimens. No significant deviation has been observed between the two samples. The relative measurement error, equation (12-1), was estimated to be the maximum error taking into account errors in the measurement of the applied heat load Q, the sample length L, the sample cross section A, and the recorded temperature difference, ΔT, along the sample length.

$$\Delta\lambda / \lambda = \left| \frac{\partial\lambda}{\partial\dot{Q}} \Delta\dot{Q} \right| + \left| \frac{\partial\lambda}{\partial L} \Delta L \right| + \left| \frac{\partial\lambda}{\partial A} \Delta A \right| + \left| \frac{\partial\lambda}{\partial T} \Delta T \right| \tag{12-1}$$

The calculated relative measurement error varies from about 2.5 % to 6.5 % depending on the temperature range of measurements. The respective error bars for the thermal conductivity values are shown in Figure 12-4. The error for the absolute temperature is related to the uncertainty of the used calibrated temperature sensor of ±8 mK at 4.2 K and ±120 mK at room temperature.

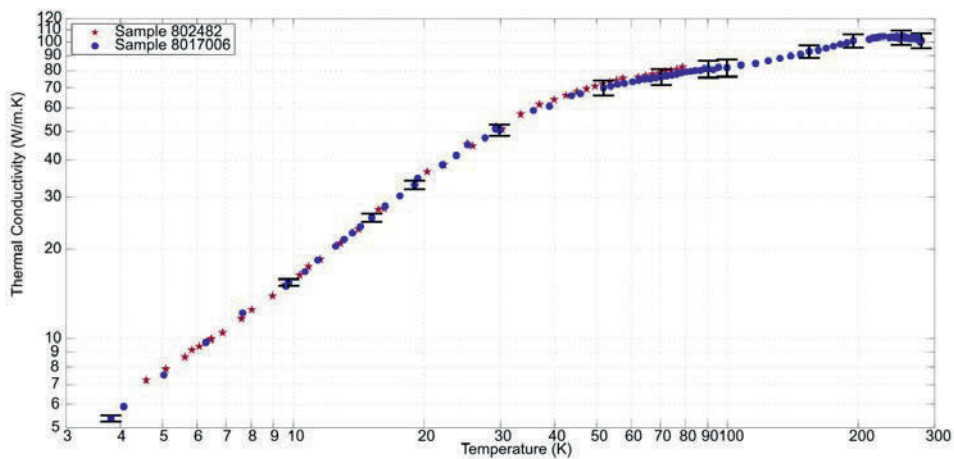


Figure 12-4: Graph of the Inermet 180 thermal conductivity as a function of temperature. The thermal conductivity of one sample (802482) has been measured up to 70 K, while for the other (8017006) the temperature range has been extended up to room temperature.

The shielding is made of 40 cm long Inermet 180 blocks, which must be accommodated on the beam screen structure [17]. Figure 12-5 shows a concept based on a mechanical assembly of the tungsten absorbers [18]. As for the standard LHC beam screen, the shell is perforated with oblong holes to provide sufficient pumping speed of the desorbed gas. The cooling is provided by four tubes, whose diameter depends on the type of magnet (external diameter of 16 mm and 10 mm for the Q1 and Q2-D1, respectively). The tungsten blocks are positioned on the beam screen by pins, welded onto the shell. Dedicated slots are used on one side of the block to allow differential thermal contraction; an overlap is used to reduce the number of pins. Copper strips are installed between the absorbers and the cooling tubes to assure a good heat transfer.

The fast decay of the magnetic field leads to the development of Foucault currents that induce Lorentz forces, especially in high electrical conductivity material such as copper. The behaviour of the assembly is driven by the 80 μm thick copper layer and the tungsten alloy absorbers; their electrical resistivities have been assumed to be $1.9 \cdot 10^{-10} \Omega \cdot \text{m}$ and $3 \cdot 10^{-8} \Omega \cdot \text{m}$, respectively. The specific resultants of the Lorentz forces, per quadrant, are around 230 N/mm and 310 N/mm for the copper layer and tungsten absorbers, respectively. The beam screen assembly has been designed to be rather elastic and therefore, during a magnet quench, the tungsten absorbers go in contact with the 4 mm thick cold bore, which can withstand the high magnetic forces (Figure 12-6). The contact force between the tungsten and the cold bore is around 370 N/mm. The maximum Von Mises stress in the cold bore is around 650 MPa (Figure 12-7) which is below the yield strength (860 MPa). The maximum stress in the beam screen wall is around 840 MPa, whereas the yield stress is around 1150 MPa. This value is driven by the initial gap between the tungsten and the cold bore.

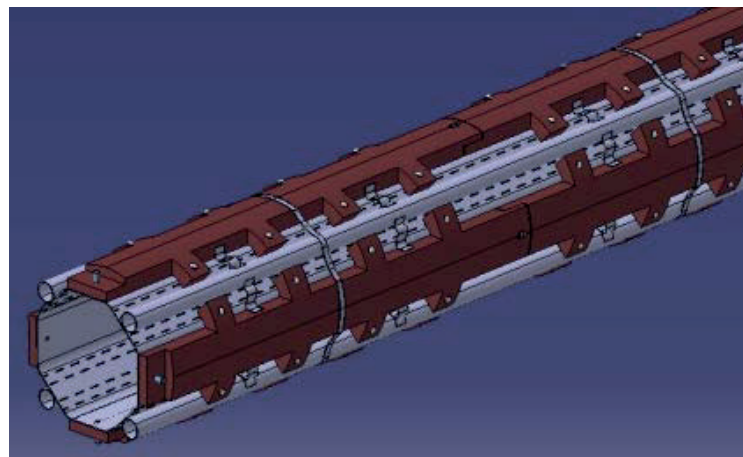


Figure 12-5: Mechanical design of the beam screen with shielding.

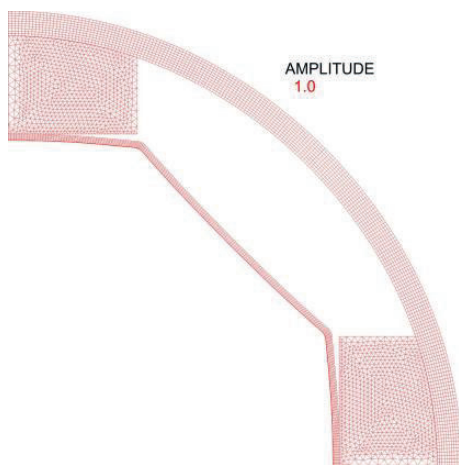


Figure 12-6: Deformation of the beam screen during a magnet quench.

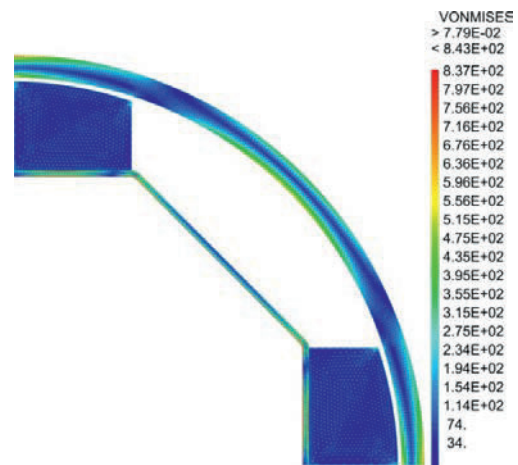


Figure 12-7: Von Mises stress field in the beam screen and cold bore during a magnet quench.

The heat deposited on the tungsten absorbers is transferred by thermal links to the cooling tubes, in which a helium flow is imposed. The specific thermal load for the whole beam screen is 20 W.m^{-1} . A thermal analysis has been carried out based on the model presented Figure 12-8.

The thermal conductivities for the copper, stainless steel and the tungsten alloy have been considered temperature dependent. It is assumed that the copper thermal link is perfectly bounded to the tungsten absorbed and to the stainless steel strip used as the interface with the cooling tube. This interface is welded to the cooling tube on three edges. The nominal cross section area of each thermal link is assumed to be 10 mm^2 . The heat transfer by convection, between the helium and the cooling tube, has been estimated by several empirical formulae. A conservative value of $150 \text{ W.K}^{-1}.\text{m}^{-2}$ has been assumed. A helium flow rate of 1 g/s per cooling tube is considered. The inlet helium temperature is 40 K .

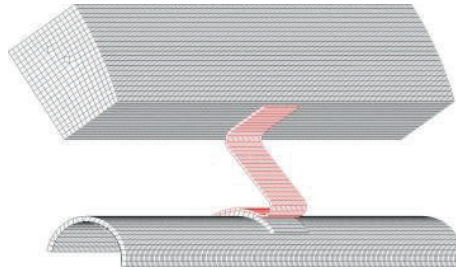


Figure 12-8: Model of the thermal link between the tungsten absorber and the cooling tube.

The typical temperature profile is shown in Figure 12-9. The temperature difference between the cooling gas and the tungsten blocs is around 13 K . The helium temperature gradient, along the cooling tube, is 0.5 K.m^{-1} . The number of thermal links or their cross section can be increased to improve the thermal performance (Figure 12-10).

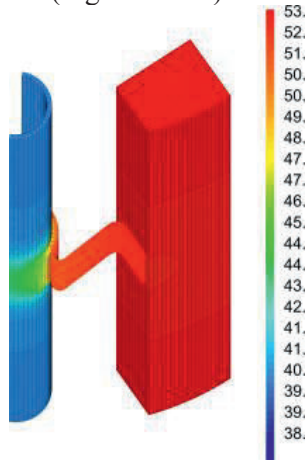


Figure 12-9: Temperature profile of the heat transfer from the tungsten absorber to the cooling tubes.

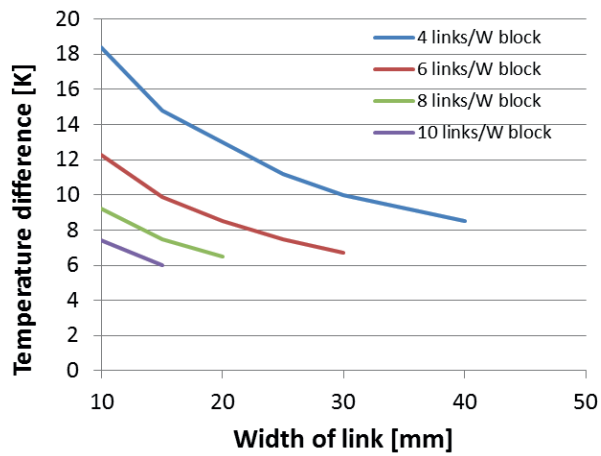


Figure 12-10: Influence of the number and width of the thermal links (0.5 mm thick) on the temperature difference between the cooling He gas and the W absorbers.

12.6.2 Non-shielded beam screen

HL-LHC non-shielded beam screens are to be inserted into HL-LHC D2, Q4, Q5, and Q6 of LSS1 and LSS5 and, if needed, in D1, DFBX, and IT of LSS2 and LSS8. Such beam screens ensure the vacuum requirements together with screening of the 1.9 K cold bore from beam-induced heating.

As a baseline, the a-C beam screen is assumed to fulfil its vacuum requirements with a-C coating operating at $5\text{--}20 \text{ K}$ [15].

In LSS1 and LSS5, the a-C beam screen is part of the new D2 and Q4 system for the HL-LHC, which will replace the present ones. The beam screens of Q5 and Q6 are recovered from the LHC matching section system.

In LSS2 and LSS8, the a-C coated beam screens will replace part of the present beam screens. The dismantling of the D1, DFBX, and IT of LSS2 and LSS8 is needed unless the cryogenic system can be upgraded.

The a-C coated beam screen is estimated to operate in the 5–20 K \pm 3 K temperature range. The operating temperature range will be defined by the available cooling power, the expected beam-induced heat load and compatibility with the vacuum requirements.

The selected a-C coated beam screen material is P506 non-magnetic stainless steel. It is similar to that used for the present beam screens. Copper will be co-laminated for impedance reasons. The proposed thickness of the Cu layer is 60 μ m.

12.6.3 Vacuum beam line interconnection

HL-LHC shielded beam screens are to be inserted into HL-LHC D1 and IT of LSS1 and LSS5. Beam vacuum interconnections ensure the continuity of the beam vacuum envelope, a smooth transition between adjacent beam screens, and the electrical continuity of the image current. The beam screens are fixed on one side to the cold mass; on the other side, a compensation bellows between the beam screen extremity and the cold mass has to be integrated to cope with the differential thermal displacements between the beam screens and the cold mass.

The HL-LHC beam screens rely on cooling tubes larger than those currently used. The routing of these cooling tubes, in and out of the cold bore, requires exit pieces with significant longitudinal space. Through-wall welds on the helium circuit are forbidden in the beam vacuum. Automatic welds have to be used in the insulation vacuum.

Bellows between two adjacent beam screens has to be integrated to allow thermal contraction as well as to compensate for the mechanical and alignment tolerances. In the transitions, collisions debris shielding with a circular aperture and non-sliding RF fingers are foreseen and are being studied.

The vacuum beamline interconnections in the triplets integrate BPM as well. They define the interconnection length. Therefore, iteration and optimization of the different elements are required to complete machine integration.

12.7 References

- [1] O. Gröbner, Overview of the LHC vacuum system. *Vacuum* **60** (2001) [25–34](#).
- [2] LHC Design Report, [CERN-2004-003](#) (2004).
- [3] A. Rossi, Residual Gas Density Estimations in the LHC Insertion Regions IR1 and IR5 and the Experimental Regions of ATLAS and CMS for Different Beam Operations. CERN [LHC Project Report 783](#) (2004).
- [4] A. Rossi, Residual gas density estimations of the LHC experimental interaction regions. CERN LHC Project Report 674 (2003). EDMS [410413](#), 2003-11-19.
- [5] Model of LSS layout LHCLJV_L0011. EDMS [356208](#)
- [6] ATLAS vacuum layout Q1/Q1. LHCVC1__0007. EDMS [1317281](#)
- [7] CMS vacuum layout Q1/Q1. LHCVC5__0006. EDMS [903240](#)
- [8] M. Gallilee, TE-VSC & ATLAS work packages consolidation and upgrade of the beam vacuum systems. EDMS [1065775](#) (2013).
- [9] M. Gallilee, TE-VSC & CMS work packages consolidation and upgrade of the beam vacuum systems. EDMS [1065775](#) (2013).

- [10] ALICE vacuum layout Q1/Q1. LHCVC2__0001. EDMS [946914](#)
- [11] M. Gallilee, TE-VSC & LHCb work packages consolidation and upgrade of the beam vacuum systems. EDMS [1065775](#) (2013).
- [12] LHCb vacuum layout Q1/Q1. LHCVC8B_0151. EDMS [932121](#)
- [13] M. Gallilee, TE-VSC & ALICE work packages consolidation and upgrade of the beam vacuum systems. EDMS [1065775](#) (2013).
- [14] V. Baglin *et al.*, Performance of a cryogenic vacuum system (COLDEX) with a LHC type beam. *Vacuum* **73** (2004) [201–206](#)
- [15] HL-LHC Decision Management: Temperature beam screens Q1 to Q6. EDMS [1601082](#), (2016).
- [16] C. Garion *et al.*, Material characterisation and preliminary mechanical design for the HL-LHC shielded beam screens operating at cryogenic temperatures, Advances in Cryogenic Engineering - Materials: International Cryogenic Materials Conference, Tucson, AZ, USA, 28 Jun - 2 Jul 2015. DOI: [10.1088/1757-899X/102/1/012013](#)
- [17] C. Garion *et al.*, Preliminary design of the high-luminosity LHC beam screen with shielding, 6th International Particle Accelerator Conference, Richmond, VA, USA, 3 - 8 May 2015, pp.[MOBD1](#).
- [18] R. Kersevan *et al.*, Preliminary design of the HiLumi-LHC triplet area beam screen. 5th International Particle Accelerator Conference, Dresden, Germany, 15 - 20 Jun 2014, pp.[2378](#)

Chapter 13

Beam Instrumentation and Long-Range Beam–Beam Compensation

13 Beam instrumentation and long-range beam–beam compensation

13.1 Introduction

The extensive array of beam instrumentation with which the LHC is equipped has played a major role in its commissioning, rapid intensity ramp-up, and safe and reliable operation. In addition to all of these existing diagnostics, the HL-LHC brings a number of new challenges in terms of instrumentation that are currently being addressed.

The beam loss monitor system, designed to protect the LHC from losses that could cause damage or quench a superconducting magnet, will need a significant upgrade in order to be able to cope with the new demands of the HL-LHC. In particular, cryogenic beam loss monitors are under investigation for deployment in the new inner triplet magnets to distinguish between collision debris and primary beam losses. Radiation-tolerant integrated circuits are also under development to allow the front-end electronics to sit much closer to the detector, so minimizing the cable length required and reducing the influence of noise.

The use of crab cavities and possible use of long-range beam-beam compensators and hollow-electron lenses also implies new instrumentation in order to allow for optimization of their performance. Several additional diagnostic systems will therefore be considered. Very high bandwidth pick-ups and a streak camera installation to perform intra-bunch transverse position measurements are being investigated, along with new techniques for transverse beam size measurements such as a beam gas vertex detector.

An upgrade to several existing systems is also envisaged, including the beam position measurement system in the interaction regions and the addition of a halo measurement capability to synchrotron light diagnostics.

13.2 Beam loss measurement

Monitoring of beam losses is essential for the safe and reliable operation of the LHC. The beam loss monitoring (BLM) system provides knowledge of the location and intensity of such losses, allowing an estimation to be made of the energy dissipated in the equipment along the accelerator. The information is used for machine protection, to qualify the collimation hierarchy, to optimize beam conditions, and to track the radiation dose to which equipment has been exposed. This is currently done using nearly 4000 ionization monitors distributed around the machine positioned at all probable loss locations, with the majority mounted on the outside of the quadrupole magnets, including those in the inner triplet regions. Approximately one-third of the arc monitors have recently been relocated in order to optimize the system for protection against fast beam losses believed to be caused by dust particles falling across the aperture of the vacuum pipe. While the existing system is believed to meet the needs of the HL-LHC for the arcs, this will no longer be the case for the high luminosity interaction points.

In the HL-LHC high luminosity insertions the magnets will be subjected to a greatly enhanced continuous radiation level due to the increase in collision debris resulting from the higher luminosity. With the presently installed configuration of ionization chambers in this region the additional signal from any dangerous

accidental losses would be completely masked by that coming from collision debris. This is a critical issue for LHC machine protection and therefore R&D has started to investigate possible options for placing radiation detectors inside the cryostat of the triplet magnets as close as possible to the superconducting coils. The dose measured by such detectors would then correspond much more precisely to the dose deposited in the coils, allowing the system to be used once again to prevent a quench or damage.

The quench level signals estimated for 7 TeV operations are, for some detectors, very close to the noise level of the acquisition system. This is mainly determined by the length of cable required to bring the signal from the radiation hard detector to the more radiation-sensitive front-end electronics. Although qualified for use in the low radiation environments of the LHC arcs, the current electronics cannot be located close to the detectors in the higher radiation insertion regions. Development to implement this electronics in a radiation-hard application-specific integrated circuit (ASIC) has therefore been started.

13.2.1 Beam loss monitors for the HL-LHC triplet magnets

Three detectors are currently under investigation as candidates for operation at cryogenic temperatures inside the cryostat of the triplet magnets [1]:

- single crystal chemical vapour deposition (CVD) diamond with a thickness of 500 μm , an active area of 22 mm^2 , and gold as the electrode material;
- $\text{p}^+\text{-n-n}^+$ silicon wafers with a thickness of 280 μm , an active area of 23 mm^2 and aluminum as the electrode material;
- liquid helium ionization chambers.

Experiments have already been performed to observe the behaviour of such detectors in a cryogenic environment and on the radiation effects at such temperatures upon silicon and single crystal diamond. Irradiation at up to 2 MGy (0.8×10^{16} protons/ cm^2) showed degradation in the charge collection efficiency for CVD diamond by a factor of 15 and for Si by a factor of 25 (see Figure 13-1). The major downside of silicon compared to diamond, its much higher leakage current when irradiated, has been observed to disappear at liquid helium temperatures, with the leakage current remaining below 100 pA at 400 V, even under forward bias for an irradiated diode. Further experiments combining irradiation with cryogenic temperatures will be necessary to optimize the final detector design. These experiments will be accompanied by tests of detectors mounted inside the cryostats of existing LHC magnets with the aim of gaining experience with the long-term performance of such detectors under operational conditions. The technology chosen will need to be able to withstand irradiation up to 20 MGy at 4.5K.

Up to six detectors will be installed inside the cold mass of each main triplet quadrupole magnet, which leads to a baseline procurement of 100 detectors (96 installed and four spares). If the option of equipping the 11 T dipole and all the spare triplet magnet assemblies is also taken into account, then a total procurement of 150 detectors would be required. They are foreseen to be housed in existing holes in the iron yoke within the cold mass of the magnet. Each detector will be equipped with a single semi-rigid coaxial cable that will provide the necessary high voltage (up to 1000 V) and extract the loss signal from each detector. Feedthroughs allowing a total of six coaxial cable connections will have to be integrated into each of the main triplet quadrupole cryostats with the location of the feedthrough chosen so as to minimize the cable length required.

As part of the machine protection system these components need to be highly reliable and maintenance-free. In the event that some of these monitors stop functioning the existing external BLM system should still provide adequate protection against damage due to excessive beam loss, but will probably not be able to distinguish quench provoking losses from the experimental background.

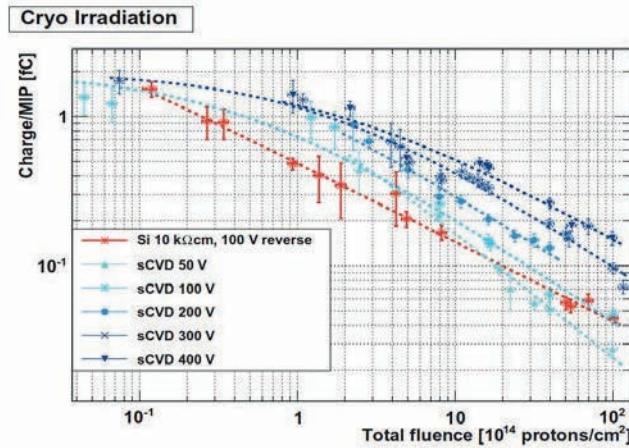


Figure 13-1: Charge collection efficiency for silicon and diamond detectors with increasing radiation fluence in a cryogenic environment.

13.2.2 A radiation-tolerant application-specific integrated circuit for the HL-LHC beam loss monitoring system

The current front-end electronics for the LHC BLM system, while providing a 40 μs integration time, is limited in the dynamic range it can handle and is only radiation tolerant up to ~500 Gy. The latter implies the use of long cables in the higher radiation LSS regions, which further limits the dynamic range and in some cases brings the noise floor close to the quench level signal at 7 TeV. Instead of the discrete component currently used, an optimized ASIC is therefore under development. This is still based on the current-to-frequency conversion used in the existing system, but is packaged in a compact, radiation-tolerant form with an increased dynamic range. The technique employed allows the digitization of bipolar charge over a 120 dB dynamic range (corresponding to an electric charge range of 40 fC–42 nC) with a 40 μs integration time and a conversion reference provided by an adjustable, temperature-compensated current reference [2].

Figure 13-2 shows the block diagram of the integrated circuit. It is composed of a bipolar, fully-differential integrator that converts the charge received from the detector into a voltage input for a synchronous comparator system. A three-level digital-to-analog converter (DAC) drives the discharge current for the integrator and is connected in a feedback loop to the comparator output. The first logic block is used to select the gain in the integrator, the current step in the DAC, and the threshold in the comparators, while a second logic block encodes the output signal from the comparators. The results of both of these are used by a third block to assemble the final, correctly weighted, output word.

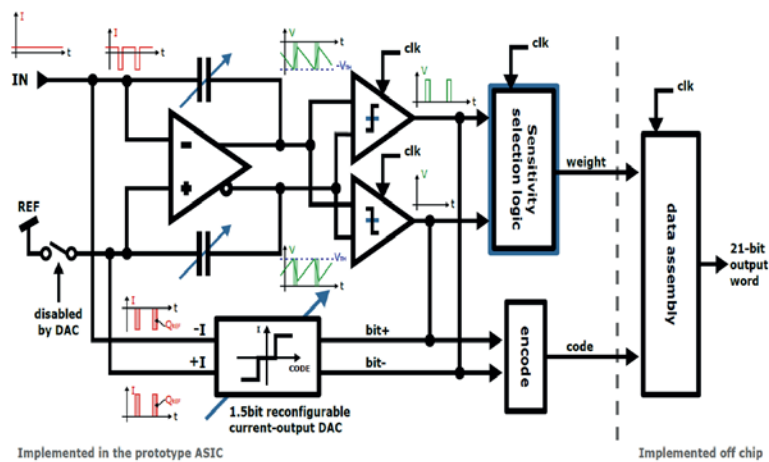


Figure 13-2: Schematic representation of the ASIC implementation currently under development.

The prototype ASIC is designed with commercial CMOS technology and has two analog-to-digital (A/D) channels and a sensitivity selection logic that can be disabled to implement the circuitry externally. This strategy has been useful for testing the device and improving the algorithm. Its measured characteristics are listed in Table 13-1.

Table 13-1: Characteristics of the prototype HL-LHC BLM system ASIC.

ASIC	Parameter	Value
A/D converter		
	Integration time	40 μ s
	Input current range	-1.05-1.05 mA
	Input charge range	-42-42 nC
	Offset	<40 aC at 40 μ s integration, <1 pA
	Default least significant bit step	50 fC \pm 20%, adjustable
	Dynamic range	120 dB
	Linearity error	< \pm 5%
	Peak signal/noise ratio	53 dB
	SFDR at 999 Hz, 1 mA	50 dB
	Total ionizing dose	10 Mrad (Si)
	Supply voltage	2.5 V
	Clock	12.8 MHz
	Power	40 mW
Reference charge		
	Drift with TID	3% at 10 Mrad (Si)
	Drift with temperature	<600 \times 10 ⁶ / $^{\circ}$ C

The measured linearity is limited by transistor matching imperfections in the DAC, introducing an error at the transition between the sensitivities. However, overall the error is less than 5% and well inside specification (<10%).

Total ionizing dose (TID) effects on the ASIC have been investigated using an X-ray beam with 20 keV peak energy. The characteristics of the device were measured up to 100 kGy (Si), followed by a one-week annealing cycle at 100 $^{\circ}$ C. From the beginning to the end of the irradiation cycles, the functionality was always preserved, with the conversion offset remaining below 1 least significant bit (LSB) and the value of the full-scale charge drifting by less than 3%. Development will now continue to address the issues found using the prototype and to implement more advanced logic blocks within the ASIC.

It is foreseen that a total of some 300 detectors, mainly located in the LSS regions, will be equipped with such a front-end ASIC.

13.3 Beam position monitoring

With its 1070 monitors, the LHC beam position monitor (BPM) system is the largest BPM system in the world [3]. Based on the wide band time normalizer (WBTN) principle, it provides bunch-by-bunch beam position over a wide dynamic range (~50 dB). Despite its size and complexity (3820 electronics cards in the accelerator tunnel and 1070 digital post-processing cards in surface buildings) the performance of the system to date has been excellent, with greater than 97% overall availability.

13.3.1 Current performance and limitations

The position resolution of the LHC arc BPMs has been measured to be better than 150 μ m when measuring a single bunch on a single turn and better than 10 μ m for the average position of all bunches. The main limitation on the accuracy and reproducibility of the BPM system is linked to temperature-dependent effects in the

acquisition electronics, which can generate offsets of up to a millimetre over a timescale of hours. On-line compensation was initially introduced to limit this effect during operation in LHC Run 1, and temperature-controlled racks were installed in LS1, eliminating this limitation for Run 2.

The non-linearity of the BPMs located near the interaction points has proven to be problematic, in particular for accurate measurements during the beta squeeze and during machine development periods. A new correction algorithm has therefore been developed, based on exhaustive electromagnetic simulations, with the aim of bringing down the residual error to below 20 μm over most of the useable BPM area [4]. Developed to be able to distinguish between the positions of the two counter-rotating beams in the same beam pipe, these BPMs also suffer from non-optimal decoupling between the beams, which is something that will need to be addressed for the HL-LHC.

13.3.2 A high resolution orbit measurement system for the HL-LHC

Originally developed to process signals from BPM buttons embedded in LHC collimator jaws, orbit measurement using a compensated diode detector scheme [5] was demonstrated to be simple and robust, and to provide a position resolution down to the nanometre level. A comparison of the orbit measured on a single BPM during a Van der Meer scan by the current orbit system and the new diode orbit system is presented in Figure 13-3, where the resolution of the new system can be seen to be over 50 times better. All new LHC collimators will have BPMs using this acquisition system installed with them, with plans to also equip the BPMs in all four LHC interaction regions. It is important to note, however, that the new system does not provide the bunch-by-bunch measurement capability of the existing system.

At the start of the HL-LHC era the existing BPM system will have been operational for over 15 years, using components that are over 20 years old. It is therefore likely that a completely new system will need to be installed for HL-LHC operation. One candidate would be to extend the new diode orbit system to the whole machine for accurate global orbit measurements, and complement this with a system capable of providing the high-resolution bunch-by-bunch, turn-by-turn measurements required, in particular, for optics studies and the many other accelerator physics experiments that will be needed to understand and optimize HL-LHC performance.

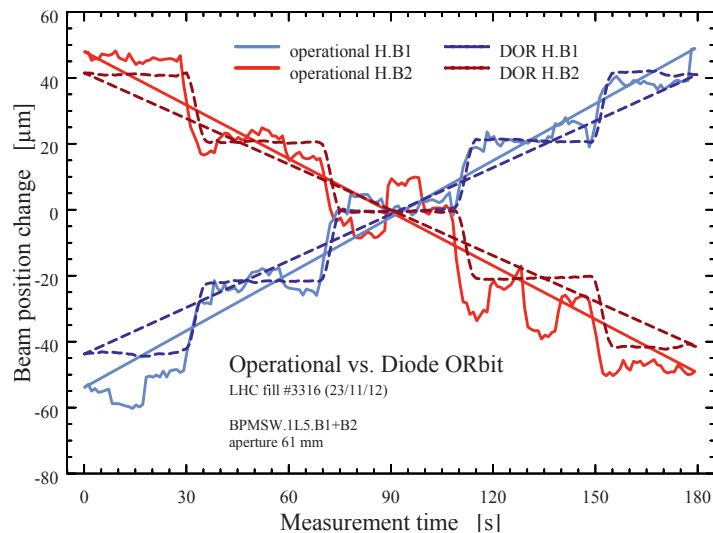


Figure 13-3: Comparison of the new LHC orbit system electronics with the existing system during a Van der Meer scan.

With the higher bunch intensities foreseen, the dynamic range of the BPM system for the HL-LHC will need to be increased accordingly. The present system implements two sensitivity ranges, optimized for pilot and nominal bunch intensities. Issues have been observed in the first three years of operation with BPMs giving large errors when reaching the limit of their dynamic range. For the interlock BPMs located in P6, this can

trigger false beam dumps, which clearly have an impact on machine availability. Although improvements have already been made to this interlock system for Run 2, a full consolidation of this system is currently underway, involving the development of dedicated electronics optimized for both high reliability and availability.

13.3.3 High directivity strip-line pick-ups for the HL-LHC insertion regions

In the BPMs close to the interaction regions, the two beams circulate in the same vacuum chamber. Directional strip-line pick-ups are therefore used to distinguish between the positions of both beams. When the two beams pass through the BPM at nearly the same time, the two signals interfere due to the limited directivity of the strip-line that, in the present design, only gives a factor of 10 isolation between the wanted signal and the signal coming from the other beam. This effect can be minimized by installing the BPMs at a location where the two beams do not overlap temporally. This is a constraint included in both the present and future layout, but which cannot be satisfied for all BPM locations. The ideal longitudinal location corresponds to $(1.87 + N \times 3.743)$ m from the IP where N is an integer. Any deviation from this will diminish the ability of the system in distinguishing one beam from the other. A total of 7 directional strip-line BPMs are foreseen for the HL-LHC upgrade at the following locations: in front of Q1, in front of Q2A, between Q2A and Q2B, in front of Q3, between Q3 and the corrector package, in front of, and behind, D1.

For the HL-LHC BPM between the Q2A and Q2B magnets and possibly also those in front of Q2A and Q3, there is the additional constraint that tungsten shielding is required in the cold bore to minimize the integrated radiation dose deposited in these magnets. A mechanical re-design of the existing LHC monitors coupled with extensive electromagnetic simulations is therefore necessary to optimize the directivity under these constraints.

As part of the critical beam position system required to maintain optimised collisions in HL-LHC these components need to be highly reliable and maintenance-free. The system should be able to measure the beam position for each beam with a resolution of 1 μm and a medium term (fill to fill) reproducibility of 10 μm .

In the current HL-LHC layout for the HL-LHC high luminosity insertion regions, two types of cold strip-line BPMs, measuring simultaneously the position of both beams in both planes, are foreseen. The BPMs located in the interconnect between Q2A and Q2B as well as, possibly, in front of Q2A and Q3 magnets will be cold strip-line BPMs, rotated by 45° to allow the insertion of tungsten shielding in the median planes of both horizontal and vertical axes. All the other common beampipe insertion region BPMs will be cold strip-line BPMs with orthogonally positioned electrodes without the tungsten shielding.

The signal from all of these BPMs will be extracted using eight semi-rigid, radiation-resistant coaxial cables per BPM. Two feedthroughs with four coaxial cable connections will be integrated into the Q1, Q2A, Q2B, and Q3 cryostats and into the cryostat of the triplet corrector magnet package, with four such feedthroughs integrated into the D1 cryostat. The outputs of these feedthroughs will be connected to standard 1/2" coaxial cables taking the signal to the electronics in the UA/UJ.

A total of 28 new strip-line BPMs will be installed in the common beam-pipe sections of the high luminosity regions.

13.3.4 Button Electrode Beam Position Monitors for the HL-LHC insertion regions

New button electrode beam position monitors are foreseen for the modified regions where the beams travel in separate vacuum chambers, specifically 2 warm BPMs (one per beam) in front of D2, new cold BPMs in Q4 and Q5, as well as one trigger BPM for the experiments between Q4 and Q5 on the incoming beam each side of the interaction point. These will be based on original LHC designs. A total of 28 new button BPMs will therefore need to be produced for HL-LHC.

13.3.5 Collimator beam position monitors

All next-generation collimators in the LHC will have button electrodes embedded in their jaws for on-line measurement of the jaw-to-beam position [4]. This is expected to provide a fast and direct way of positioning the collimator jaws and subsequently allow constant verification of the beam position at the collimator location, improving the reliability of the collimation system as a whole. The design of such a BPM was intensively simulated using both electromagnetic (EM) and thermo-mechanical simulation codes. In order to provide the best accuracy, the BPM readings must be corrected for the nonlinearity coming from the varying geometry of the collimator jaws as they are closed and opened, for which a 2D polynomial correction has been obtained from EM simulations and qualified with beam tests using a prototype system installed in the CERN SPS. This system has subsequently been deployed for operation with excellent results on all TCT collimators in the LHC.

The collimator BPM hardware, i.e. the button electrode located in the jaw, the cable connecting the electrode to the electrical feedthrough mounted on the vacuum enclosure, and the feedthrough itself have been chosen to withstand the radiation dose of 20 MGy expected during the lifetime of the collimator.

13.4 Beam profile measurements

The LHC is currently fitted with a host of beam size measurement systems used to determine beam emittance. These different monitors are required in order to overcome the specific limitation of each individual system. Wire scanners are used as the absolute calibration reference, but can only be operated with a low number of bunches in the machine due to intensity limitations linked to wire breakage. A cross-calibrated synchrotron light monitor is therefore used to provide beam size measurements, both average and bunch-by-bunch, during nominal operation. However, the small beam sizes achieved at 7 TeV, the multiple sources of synchrotron radiation (undulator, D3 edge radiation, and central D3 radiation), and the long optical path required to extract the light imply that the correction needed to extract an absolute value is of the same order of magnitude as the value itself. This requires an excellent knowledge of the error sources to obtain meaningful results. The third system installed is an ionization profile monitor, which is foreseen to provide beam size information for lead ions at injection, when there is insufficient synchrotron light. The monitor has also been used for protons, but suffers from significant space charge effects at energies above 2 TeV.

Whilst efforts are ongoing to improve the performance of all the above systems, alternative techniques to measure the transverse beam size and profile are also under study for the HL-LHC, as these are crucial measurements for machine optimization and to understand any bunch by bunch luminosity variations.

13.4.1 A beam gas vertex profile monitor (BGV)

The VELO detector of the LHCb experiment has shown how beam-gas interactions can be used to reconstruct the transverse beam profile of the circulating beams in the LHC [6]. The new concept under study is to see whether a simplified version of such a particle physics tracking detector can be used to monitor the beams throughout the LHC acceleration cycle. This concept has, until now, never been applied to the field of beam instrumentation, mainly because of the high level of data treatment required. However, the advantages compared to the standard beam profile measurement methods listed above are impressive: high resolution profile reconstruction; single bunch measurements in three dimensions; quasi non-destructive; no detector equipment required in the beam vacuum; and high radiation tolerance of the particle detectors and accompanying acquisition electronics.

Such a beam shape measurement technique is based on the reconstruction of beam-gas interaction vertices, where the charged particles produced in inelastic beam-gas interactions are detected with high-precision tracking detectors. Using the tracks left in the detectors, the vertex of the particle-gas interaction can be reconstructed so, with enough statistics, building up a complete 2D transverse beam profile (Figure 13-4). The longitudinal profile could also be reconstructed in this way if relative arrival time information is additionally acquired by the system, which is not currently planned.

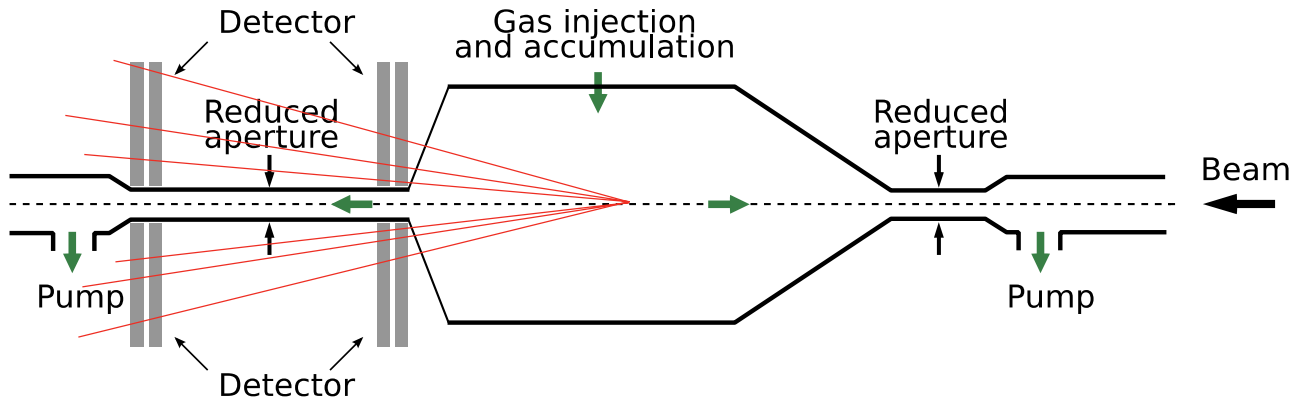


Figure 13-4: A sketch demonstrating the beam gas vertex measurement concept.

Unlike LHCb, where the detector is placed very close to the beam and can therefore only be used during stable beams, the aim with the beam gas vertex profile monitor (BGV) detector is to design a robust instrument that can be used for beam size measurements throughout the LHC cycle. Its final specifications are to provide:

- transverse bunch size measurements with a 5% resolution within 1 minute;
- average transverse beam size measurements with an absolute accuracy of 2% within 1 minute.

The main subsystems are: a neon gas target at a pressure of 6×10^{-8} mbar; a thin aluminium exit window; tracking detector based on scintillating fibre modules read out by silicon photomultipliers; hardware and software triggers; and a readout and data acquisition system based on that used for LHCb. As the tracking detector is external to the vacuum chamber, no movable parts are needed. The final design of the prototype is shown in Figure 13-5.

A proof-of-principle demonstrator has been installed on the left-hand side of LHC IP4 on Beam 2 during LS1, with a second system for Beam 1 foreseen for installation on the right-hand side of IP4 in LS2. A full upgrade of these systems, to include a third detector layer and upgraded electronics, may be required in LS3 to reach the full design goals outlined above. This upgrade is currently not part of the HL-LHC baseline.

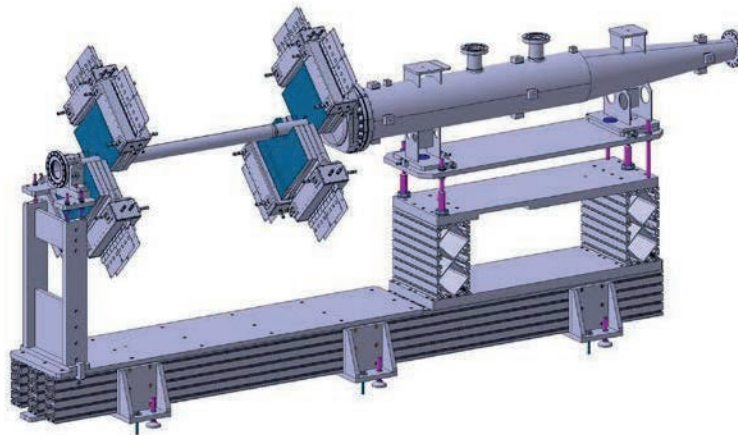


Figure 13-5: The demonstrator beam gas vertex detector installed in the LHC during LS1.

13.4.2 Gas Jet Monitoring

Another candidate for non-destructive monitoring is a gas monitor where the particle beam interacts with either residual gas particles or a dedicated supersonic gas jet target shaped into a pencil or curtain, causing either ionization or fluorescence. The electrons or ions resulting from ionization can be collected by means of an electric field and imaged onto a position-sensitive detector to provide information on the beam profile. Alternatively, the light emitted by the gas particles can be detected with photon detectors providing a full 2D

beam image. If a suitable design is chosen the number of particles from the primary beam interacting with the gas can be negligible compared to the number of particles in the beam and the monitor can be considered as non-invasive.

Gas jet monitors have been shown to operate in an ultra-high vacuum environment in the order of 10^{-11} mbar and to probe high energy proton beams [14],[15]. These designs typically rely on a neutral gas jet, shaped into a thin sheet. The gas jet travels perpendicularly to the particle beam's propagation axis, crossing the particle beam with its plane tilted at 45° . At the point of interaction, ionization occurs and the ions or electrons produced are accelerated by an external electric field toward a microchannel plate detector (MCP). Every ion or electron incident on the MCP produces a cascade of electrons which are incident on a phosphor screen. The light emitted by the phosphor screen is then detected by a CCD camera. After interaction with the beam, the jet enters a dumping chamber, where a turbo molecular pump evacuates the non-ionized gas. This monitor allows for 2-dimensional transverse beam profile imaging due to the 45° of inclination of the gas jet plane, which acts as a mirror reflecting the beam's transverse profile onto the MCP.

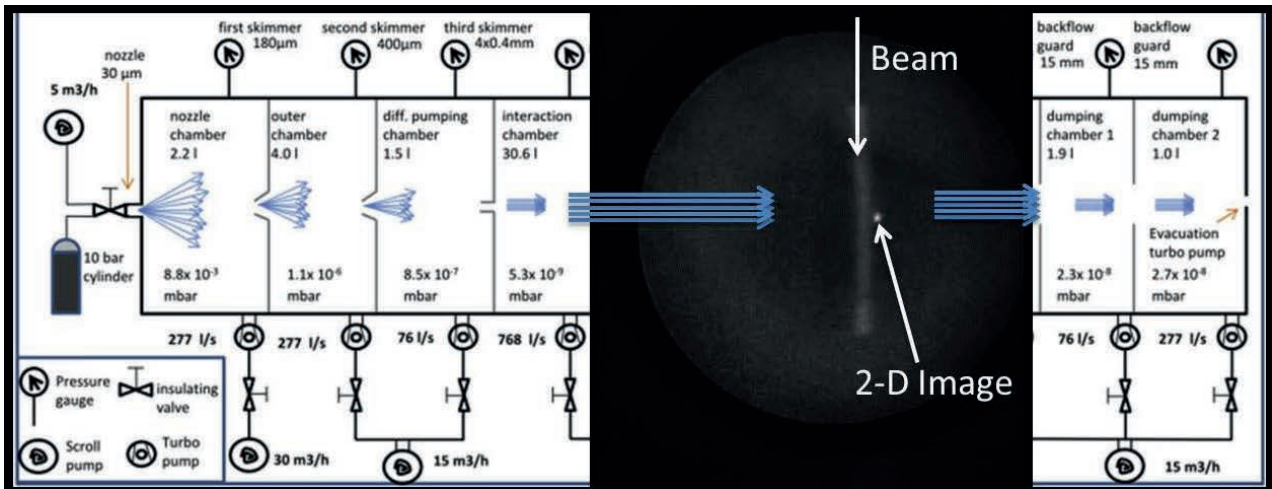


Figure 13-6: Gas jet profile monitoring set-up.

It is foreseen to develop this technique further for application to HL-LHC, combining the neutral gas jet with electron/ion, luminescence or fluorescence detection. This will include optimisation of the optical and mechanical design, as well as studies related to issues with potential gas condensation and to ascertain the overall monitor resolution. The main applicability of the technique is currently geared towards the measurement of a dense electron beam in the presence of a high energy proton beam, foreseen as diagnostics for the eventual use of a hollow-electron lens for collimation or electron-beam based long-range beam-beam compensation.

13.5 Diagnostics for crab cavities

The crab cavities for the HL-LHC are proposed to counter the geometric reduction factor and so to enhance luminosity. These cavities will be installed around the high luminosity interaction points (IP1 and IP5) and used to create a transverse bunch rotation at the IP. The head and tail of each bunch is kicked in opposite directions by the crab cavities such that the incoming bunches will cross parallel to each other at the interaction point. These intra-bunch bumps are closed by crab cavities acting in the other direction on the outgoing side of the interaction region. If the bumps are not perfectly closed the head and tail of the bunch will follow different orbits along the ring. Monitors capable of measuring the closure of the head-tail bump and any head-tail rotation/oscillation outside of the interaction regions are therefore required.

13.5.1 Bunch shape monitoring using electromagnetic pick-ups

Electromagnetic monitors for intra-bunch diagnostics are already installed in the LHC. These so-called ‘head–tail’ monitors mainly provide information on instabilities and have a bandwidth of approximately 2 GHz. To go to a higher resolution within the bunch a bandwidth of 10 GHz or more is desirable. This will be important to better understand instabilities in the HL-LHC and to help with the tuning of the crab cavities, with several of these systems foreseen for installation around the interaction points. In addition to studies aimed at improving the existing electromagnetic pick-ups, which include optimization of the pick-up design and the testing of faster acquisition systems, pick-ups based on electro-optical crystals in combination with laser pulses are also being considered [7]. Such pick-ups have already demonstrated fast time responses in the picosecond range [8]. Developed mainly for linear accelerators, this technology is now also being considered for circular machines, with a design for a prototype to be tested on the CERN SPS recently initiated.

13.5.2 Bunch shape monitoring using streak cameras

The use of synchrotron light combined with a streak camera may be an easier alternative to electromagnetic or electro-optical pick-ups for high resolution temporal imaging. Using an optical system to re-image the synchrotron light at the entrance of a streak camera allows the transverse profile of the beam to be captured in one direction (X or Y) with a very fast time resolution (below the picosecond level). Only one transverse axis can be acquired with a given setup, while the other is used for the streaking. Using a sophisticated optical setup it is, however, possible to monitor both axes at the same time, as was performed in LEP [9].

Streak cameras can be used to observe a number of parameters simultaneously: bunch length, transverse profiles along the bunch, longitudinal coherent motion, head–tail motion, etc. The main limitation of the streak camera is the repetition rate of the acquisition, typically <50 Hz, and the limited length of the recorded sample, given by the CCD size. Double scan streak cameras exist that allow an increase in the record length. By using a CCD with 1000×1000 pixels working at 50 Hz and adjusting the optical magnification and scan speed such that the image of each bunch covers an area of about 100×100 pixels, it is possible to record a maximum of 100 bunch images per 20 ms, i.e. 5000 bunches/s. This is clearly just an optimistic upper limit with other factors likely to reduce this value.

The longitudinal resolution of around 50 ps required for the HL-LHC is rather easy to achieve using streak cameras, where measurements down to the sub-picosecond range are now possible. In terms of transverse resolution two distinctions have to be made.

- Measurement of the beam width is affected by diffraction due to the large relativistic gamma of the beam, with the diffraction disk of the same order as the beam size. This will significantly reduce the resolution of such measurements.
- The centroid motion (i.e. the centre of gravity) is not directly affected by diffraction, which produces a symmetrical blur, and therefore the resolution for this type of measurement will be much better.

For determining crab cavity non-closure only the average position along the bunch is of importance, and not changes to the beam size. The streak camera should therefore be able to achieve a resolution of a few percent of the beam sigma for this measurement.

Streak cameras are expensive and delicate devices not designed for the harsh environment inside an accelerator. Radiation dose studies are therefore required in order to verify if a streak camera can be installed directly in the tunnel or if, which seems more likely, it has to be housed in a dedicated, shielded, hutch. The latter would imply an optical line to transport the synchrotron light from the machine to the camera, something for which an integration study will be initiated.

Another point to consider is the synchrotron light source. Currently, two synchrotron light telescopes are installed in the LHC, one per beam. These telescopes already share their light amongst three different instruments, the synchrotron light monitor, the abort gap monitor, and the longitudinal density monitor, and in the future will also have to accommodate halo diagnostics. It will therefore be difficult to integrate yet another

optical beam line for the streak camera. The installation of additional light extraction mirrors will therefore be necessary to provide the light for the streak cameras. Since the crab cavities are only needed at high energy, dipole magnets can be used as the source of the visible synchrotron radiation for the streak cameras, with no need for the installation of additional undulators that are only required at injection energy, where the dipole radiation is in the infra-red. The best location and corresponding light extraction system for such an additional synchrotron radiation source is currently under study.

13.6 Halo diagnostics

Population of the beam ‘halo’, i.e. particles in between the beam core and the limits set by the primary collimators, can lead to important loss spikes through orbit jitter at the collimator locations. Measurement of the beam halo distribution is therefore important for understanding and controlling this mechanism. Such measurements are also important to determine the effectiveness of equipment that influences the beam halo, such as hollow electron lenses or long-range beam-beam compensators. Moreover, in the HL-LHC, any failure of a crab cavity module could result in the loss of the halo in a single turn. If the halo population is too high this could cause serious damage to the collimation system or to other components of the machine. In order to fulfil all of these diagnostic requirements for halo observation in the HL-LHC, the final system should be capable of measuring halo populations at the level of 10^{-5} relative to that of the core.

Three techniques are currently being considered for halo monitoring in the HL-LHC:

- the use of high dynamic range cameras combined with apodization;
- core masking followed by acquisition using standard cameras;
- use of the beam gas vertex detector.

The first two techniques make use of synchrotron light and, as for the streak cameras, may require an additional light source for the final HL-LHC configuration.

Although commercial high dynamic range (HDR) cameras suitable for detecting the halo exist (with dynamic ranges exceeding 7 orders of magnitude), an HDR halo monitor based on synchrotron radiation has to cope with the additional difficulties of diffused and scattered light, and diffraction.

Light diffusion and scattering can be minimized by blackening all the surfaces around the monitor (including the vacuum chambers), adding baffles to stop any light rays arriving from outside the required aperture, using only high grade optical components and avoiding dust in the system. The implementation of all of these are complicated by the harsh environmental and space constraints of HL-LHC.

The effect of diffraction can be mitigated by the use of apodization or of a coronagraph. Both of these techniques are under investigation as part of the halo monitoring system for HL-LHC.

Apodization consists in shaping the light distribution at the entrance of the optical system using special masks, such that the interference pattern on the image plane reduces the effects of diffraction at the expense of resolution [16]. A system based on an HDR camera with apodizing optics would allow the capture of the full beam image with the core and the halo visible at the same time.

The core masking technique is based on the Lyot coronagraph, which was invented in order to allow the observation of the sun’s corona without the need for a total solar eclipse. The optics contains several stages of re-imaging and masks (stops) such that at the final image plane the bright core is masked and the diffraction rings shifted outside of the image, leaving enough room for observation of the corona. Similar setups have already been used for the observation of beam halo in particle accelerators [17]. For HL-LHC a coronagraph similar to the one reported in [17] is under study. In this case there is no need for an HDR camera as the core of the beam is masked. This does, however, imply that it is not possible to observe the core and the halo at the same time. Nevertheless it would still be possible to take consecutive images with and without the mask (adjusting the attenuation filters accordingly), to compose a synthetic image that includes both the core and the halo.

13.7 Luminosity measurement

The measurement of the collision rate at the luminous interaction points is very important for the optimization of the machine. The LHC experiments can certainly provide accurate information about the instantaneous luminosity, but this information is often not available until stable collisions have been established, and is often missing altogether during machine development periods. For this reason simple and reliable collision rate monitors, similar to those now used in the LHC, are also needed for the HL-LHC. This measurement is currently obtained by measuring the flux of forward neutral particles generated in the collisions using fast ionization chambers installed at the point where the two beams are separated into individual vacuum chambers. The detectors (BRAN) are installed inside the neutral shower absorber (TAN) whose role is to prevent neutral collision debris, and the secondary showers that this induces, from reaching downstream machine components. The luminosity monitors therefore already operate in a very high radiation area, which for the HL-LHC is anticipated to be a further ten times the nominal LHC value. For this reason the technology chosen for the HL-LHC is likely to be based on the radiation-hard LHC design [10], with the geometry adapted to the new TAXN design. In order to further increase the radiation resistance some current features, such as their bunch-to-bunch capability, may need to be sacrificed and redundancy added.

13.8 Long-range beam–beam compensation

The simulated strong effect of the LHC long-range interactions inspired a proposed long-range beam–beam compensation for the LHC based on current-carrying wires [11]. In order to correct all non-linear effects the correction must be made individually in each high luminosity interaction point, with the wire generating the same integrated transverse force as the opposing beam at the parasitic long-range encounters.

The ideal location for compensation of the long-range beam–beam tune-spread is found where the beta functions are equal; there is little phase advance difference with respect to that between the long-range encounters and the IP, and where the beams are sufficiently well separated. Hence for the HL-LHC the proposed layout features compensators placed after the D1 separation dipole in IP1 and IP5 (Figure 13-7). In order to get the compensation correct for all multipoles the transverse location of a wire compensator must be on the inside of the compensated beam, i.e. between the two circulating beams, at a distance equivalent to the average long-range beam–beam separation. This poses significant technical constraints since, at the ideal longitudinal position, the transverse separation of the beams is only a few centimetres in a region with a high flux of secondary neutrons, and the transverse wire position is only a few mm from the beam. Placing and aligning a ‘wire’ at these locations, in particular between the two counter-rotating proton beams, will be very difficult. An alternative is to replace the ‘wire’ with an electron beam produced in a manner similar to that of well-established electron coolers (Figure 13-8).

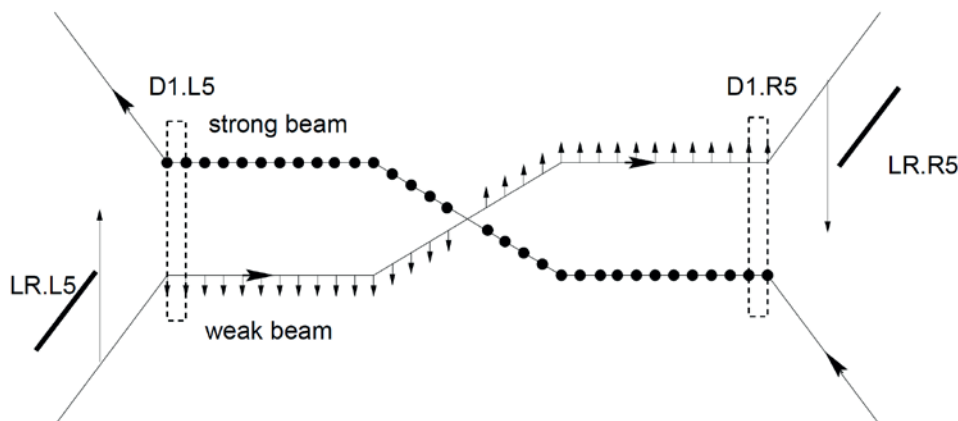


Figure 13-7: Illustration of the compensation principle [12]. Here LR.L5 and LR.R5 indicate schematically the potential position of compensating wires.

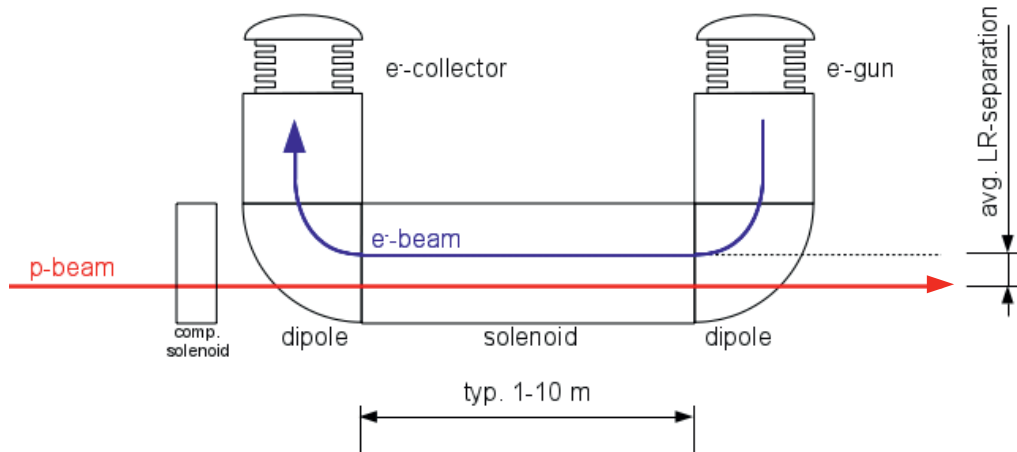


Figure 13-8: Sketch of an electron cooler type layout for long-range beam-beam compensation.

Although such systems have been used for head-on beam-beam compensation at both the Tevatron (FNAL) [12] and RHIC (BNL) [13], the implementation required for the HL-LHC is beyond what has been achieved so far. Assuming an effective length of 6 m on both sides of the IP, an electron beam current of about 15–20 A would be needed, significantly higher than for previous implementations. Compensation with one system per beam in both IR1 and IR5 is also possible, and would reduce the necessary infrastructure by a factor of two, but implies electron currents of up to 40 A, almost an order of magnitude larger than what has been achieved so far.

Preliminary simulations and integration studies started to look into the feasibility of such an implementation in the LHC. However, it is clear that such infrastructure could only be installed at the same time as the upgrade of the interaction regions for the HL-LHC, ruling out the possibility of testing such a long-range beam-beam compensator beforehand. Since long-range beam-beam compensation has, so far, never been demonstrated at a long-range beam-beam limited machine, it was deemed essential to install a prototype in the LHC as soon as possible. With a test of the electron beam solution ruled out in the short term, a fall-back solution relying on wires will be pursued, with a view to installing a demonstrator in the 2016/2017 end-of-year technical stop.

13.8.1 Long-range beam-beam demonstrator

One of the few solid objects that can approach the beam accurately to within 10σ or less are the LHC collimators. By embedding a wire in such a collimator it would be possible to use the collimator as a host for a demonstrator version of a long-range beam-beam compensator. The best compensation effect in this scenario is obtained by a wire in the tertiary collimators (TCT) located just in front of the D2 magnet. A 1 m long wire at this location would require a DC current of some 180 A at a distance of 9.5σ to the beam or over 200 A at a distance of 11σ . These values correspond to a symmetric layout with one compensator left of the IP and another on the right-hand side, a set-up which will probably be necessary since the ratio of the horizontal and vertical beta functions are not equal at the TCT locations.

Integration of DC-powered wires into collimator jaws seems the only possibility to make realistic beam tests before embarking on a final implementation of the wires for LHC high luminosity operation. This integration itself requires the solution of many important technical issues:

- no interference of the wires with the nominal operation of the collimators;
- transfer of 1 kW resistive heat loss in the wire by heat conduction to the water-cooled collimator jaw;
- shielding of the wire from the beam with a thin metallic layer for impedance reasons.

The design of such a wire-in-jaw tertiary collimator is well advanced (Figure 13-9) and the production of four such collimators started in early 2016. The necessary DC cables and power converted infrastructure were already installed during LHC LS1.

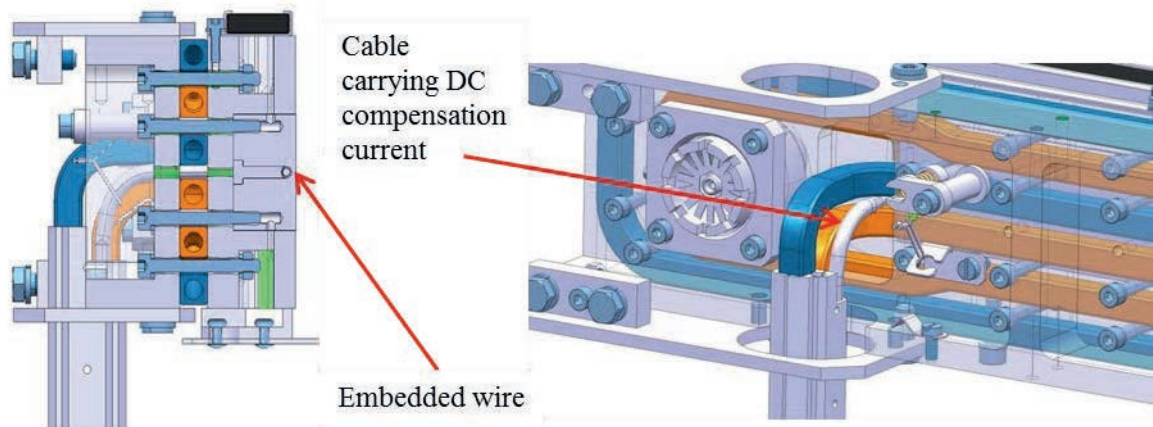


Figure 13-9: Technical drawing of the wire-in-jaw collimator design.

The earliest date at which such collimators equipped with a long-range beam–beam compensation wire can be installed in the LHC is the end of year technical stop 2016/2017. Machine experiments are then planned to validate predictions by simulation, which would then allow a decision to be taken on whether such technology should be pursued for full implementation in the HL-LHC era.

13.9 References

- [1] C. Kurfuerst *et al.*, Radiation tolerance of cryogenic beam loss monitor detectors, 4th International Particle Accelerator Conference, Shanghai, China, 12 - 17 May 2013, pp.3240. J.M. Raby, Biophysical aspects of radiation quality, IAEA, Technical Reports Series No. 58 (1966). [CERN-ACC-2013-0188](#)
- [2] G. Venturini, F. Anghinolfi, B. Dehning and M. Kayal, Characterization of a wide dynamic-range, radiation-tolerant charge-digitizer ASIC for monitoring of beam losses, Proc. IBIC12, Tsukuba, Japan, 2012. [CERN-ATS-2012-281](#)
- [3] E. Calvo *et al.*, The LHC orbit and trajectory system, Proc. DIPAC03, Mainz, Germany, 2003, p. 187. [CERN-AB-2003-057-BDI](#)
- [4] A. Nosych *et al.*, Electromagnetic simulations of an embedded BPM in collimator jaws, Proc. DIPAC11, Hamburg, Germany, 2011, p. 71. [CERN-BE-2011-022](#)
- [5] M. Gasior, J. Olexa and R.J. Steinhagen, BPM electronics based on compensated diode detectors – results from development systems, Proc. BIW12, Newport News, Virginia, 2012. [CERN-ATS-2012-247](#).
- [6] LHCb Collaboration, Absolute luminosity measurements with the LHCb detector at the LHC, *J. Instrum.* 7 (2012) P01010, IOP and SISSA. DOI [10.1088/1748-0221/7/01/P01010](#)
- [7] M.A. Brubaker *et al.*, Electro-optic beam position and pulsed power monitors for the second axis of DARHT, 19th IEEE Particle Accelerator Conference, Chicago, IL, USA, 18 - 22 Jun 2001, pp.e-proc. [534](#).
- [8] Y. Okayasu *et al.*, The first electron bunch measurement by means of organic EO crystals, Proc. IBIC12, Tsukuba, Japan, 2012. MOCC03 pp 29-33
- [9] E. Rossa, Real time single shot three-dimensional measurement of picosecond photon bunches, 6th Beam Instrumentation Workshop, 6th Workshop on Beam Instrumentation, Vancouver, Canada, 3 - 6 Oct 1994, pp.148-159. [CERN-SL-94-79-BI](#)
- [10] J.F. Beche, A. Ratti, *et al.*, Rad hard luminosity monitoring for the LHC, 10th European Particle Accelerator Conference, Edinburgh, UK, 26 - 30 Jun 2006, pp.[580](#).

- [11] J.-P. Koutchouk, Principle of a correction of the long-range beam-beam effect in LHC using electromagnetic lenses, [LHC Project Note 223](#) (2000).
- [12] F. Zimmermann, P. Lebrun, T. Sen, V. Shiltsev and X.L. Zhang, Using the Tevatron electron lens as a wire and other TEL studies at FNAL, [CERN AB-Note-2004-041](#) (2004).
- [13] W. Fischer, R. Calaga, U. Dorda, J.-P. Koutchouk, F. Zimmermann, V. Ranjbar, T. Sen, J. Shi, J. Qiang and A. Kabel, Observation of long-range beam-beam effect in RHIC and plans for compensation, 10th European Particle Accelerator Conference, Edinburgh, UK, 26 - 30 Jun 2006, pp.[2158](#)
- [14] V. Tzoganis, C. P. Welsch, A non-invasive beam profile monitor for charged particle beams', Applied Physics Letters 104, [204104](#) (2014).
- [15] Y. Hashimoto *et al.*, Development of a beam profile monitor using a nitrogen-molecular jet for the J-PARC MR, Proc. IBIC13, Oxford, UK, 2013.
- [16] M.A. Cagigas *et al.*, Super-Gaussian apodization in ground based telescopes for high contrast coronagraph imaging, Optics Express, vol. 21 (2013), issue 10, p. 12744.
- [17] T. Mitsuhashi, Beam Halo Observation by Coronagraph, Proc. DIPAC 2005, Lyon, France, 2005, pp.[7](#).

Chapter 14

Injection and Dumping Systems

14 Injection and dumping systems

14.1 Injection and dumping systems overview

The beam transfer into the LHC is achieved by the two long transfer lines TI2 and TI8, together with the septum and injection kickers, plus associated systems to ensure the protection of the LHC elements in case of a mis-steered beam. In the nominal scheme the LHC is filled with approximately 10 injections per beam. The MKI injection kicker magnet pulse length consists of a flat-top of up to $8 \mu\text{s}$, with a rise time of $0.9 \mu\text{s}$ and a fall time of $3 \mu\text{s}$. Filling each ring takes at least 8 minutes (when injecting trains of 288 bunches at the time) with the SPS supplying interleaved beams to other facilities. The foreseen increase in injected intensity and brightness for the HL-LHC means that the protection functionality of the beam-intercepting devices needs upgrading [1]. In addition, the higher beam current significantly increases the beam-induced power deposited in many elements, including the injection kicker magnets in the LHC ring.

The beam dumping system is also based on DC septa and fast kickers, with various beam intercepting protection devices including the beam dump block. Again, the significant change in the beam parameters for the HL-LHC implies redesign of several of the dump system devices, both because of the increased energy deposition in the case of direct impact and because of increased radiation background that could affect the reliability of this key machine protection system [1].

In the following sections the changes planned in light of the HL-LHC for the different LHC beam transfer systems are described.

14.2 Injection systems

The high injected beam intensity and energy mean that precautions must be taken against damage and quenches, by means of collimators placed close to the beam in the injection regions [2], [3]. The layout of the injection region and associated protection devices is shown schematically in Figure 14-1. The beam to be injected passes through five horizontally deflecting steel septum magnets (MSI) with a total deflection of 12 mrad, and four vertically deflecting MKI kickers with a nominal total kick strength of 0.85 mrad. Uncontrolled beam loss resulting from errors (missing, erratic, partial, badly synchronized, or wrong kick strength) in the MKI could result in serious damage to the downstream equipment in the LHC injection regions, in particular the superconducting separation dipole D1, the triplet quadrupole magnets near the ALICE or LHCb experiments, or in the arcs of the LHC machine itself. Damaging detector components, in particular those close to the beam pipe, with excessive showers generated by lost protons, is also possible.

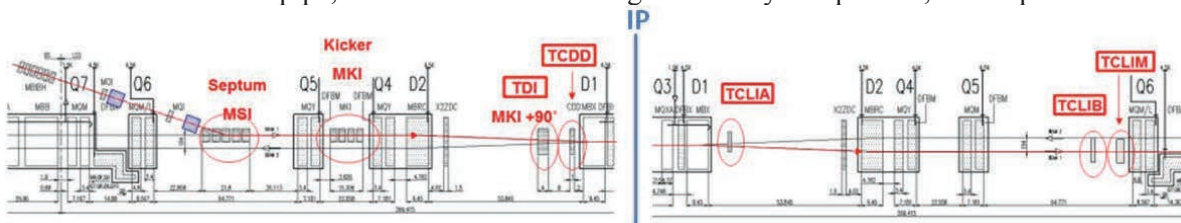


Figure 14-1: Overview of the present injection system into the LHC and the associated protection devices (Beam 1, IR2). The beam is injected from the left hand side.

14.2.1 Upgrade of the primary injection absorbers (TDIS)

The presently installed TDI is a movable two-sided vertical absorber. Its purpose is to protect machine elements in case of MKI malfunctions and to intercept low-intensity bunches during set-up or commissioning of the injection system. Protection must be provided both in case of mis-deflections of the injected beam due to MKI faults as well as in case of accidental kicks of the stored beam due to MKI erratics or timing errors. In the first case, too little or zero kick strength causes the incoming beam to impact the upper TDI jaw. In the second case, the miskicked stored beam impacts on the lower TDI jaw. The protection objectives should be met for any impact condition, including cases where beams are swept over the aperture (beam affected by MKI rise or fall time) or where a full batch is grazing the TDI jaw due to a non-nominal MKI kick strength. The maximum possible impact parameter (vertical distance between jaw edge and impact position) on the absorber front face is estimated to be 36 mm. The largest energy deposition in downstream magnets and the highest stresses in the absorber blocks themselves are expected for small impact parameters (around $1-2\sigma$, which is about 0.5-1 mm from the absorber edge), which could occur in the case of a high voltage breakdown in one magnet during injection.

The jaws of the TDIs at present installed in the LHC [4] are 4.185 m long and accommodate blocks of graphite (6×47.1 cm), aluminium (1×60 cm) and CuCr1Zr (1×70 cm). The two latter blocks are retracted by 2 mm with respect to the graphite to avoid direct beam impact on these materials, which could lead to an excessive heating and stresses of these blocks. During the first years of LHC operation, mechanical problems with the present design have become apparent due to the very long length of the jaws. Instead of having one long jaw as in the present TDI, the new TDI (called TDIS, where the S stands for Segmented) will comprise three shorter absorbers most likely accommodated in separate tanks (see Figure 14-2).

The jaws of the three TDIS modules will all be identical except for the active absorber material. For robustness reasons, the two upstream modules will accommodate low-Z absorber blocks. The baseline is to use the same grade of Graphite as in the present TDI and transfer line collimators (SIGRAFINE[®] R4550, 1.83 g/cm^3), the final decision of the material is pending further material tests. The third module is foreseen to host higher-Z absorber materials to partially absorb and efficiently attenuate the particle showers from the low density absorber blocks upstream. The final choice of materials for this module is subject to further studies. The active absorber length of each jaw will be approximately 1.5 m. The new TDISs will be at the same position as the present TDIs, as they need to be at 90° betatron phase advance relative to the MKIs. The total length including vacuum transition chambers will be the same as the present TDI, i.e. not requiring any modification of nearby vacuum equipment.

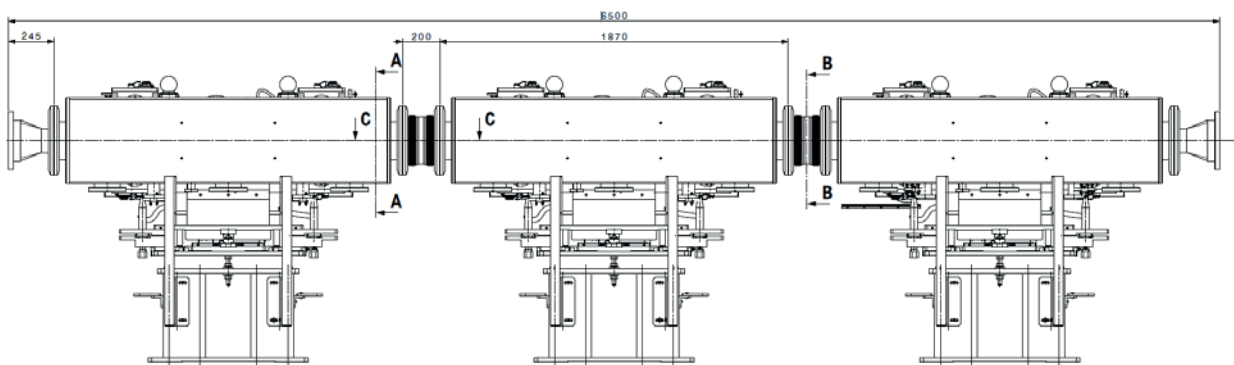


Figure 14-2: Preliminary design of the three TDIS tanks, supports and vacuum transition chambers.

The correct vertical positioning of the TDIS jaws around the beam is a vital element of the machine protection system during injection. A beam energy tracking system (BETS) is foreseen to guarantee the correct position at injection energy. For a multi-module TDIS system the correct alignment with beam between the different modules will be very important, as is illustrated in Figure 14-3. The jaws of the third module need to be slightly retracted compared to the upstream jaws to avoid direct beam impact on the higher-Z absorber blocks.

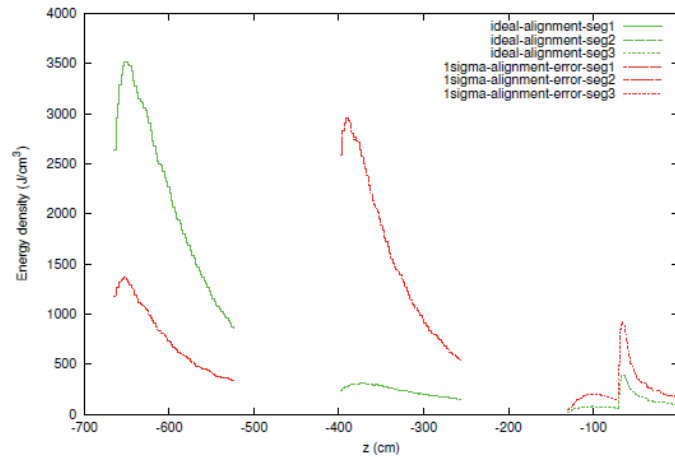


Figure 14-3: Energy deposition in a TDIS consisting of three modules (graphite, graphite and aluminium - copper) for grazing beam impact and showing the effect of a 1σ alignment difference between the first and second module.

14.2.1 Supplementary shielding of D1 coils

The superconducting D1 separation dipole is located just downstream of the TDIS. The largest energy deposition in the D1 coils can be expected if bunches impact close to the edge of the leading TDIS absorber block or if they graze along the jaws since secondary particle showers can escape through the TDIS gap. During the design of the present TDI, it was found necessary to add a complementary mask in order to prevent damage to the D1 coils for such accident scenarios, see Figure 14-1. The masks, called TCDD in IR2 and TCDDM in IR8, are 1 m long Cu blocks, which are movable in IR2 to provide enough aperture for the ALICE ZDC detector during data taking. The TCDDs have a rectangular opening ($70 \times 42 \text{ mm}^2$), which is smaller than the inner diameter of the D1 coils (80 cm). The drift space between the TCDD/TCDDM and the D1 front face amounts to almost 3 m and is presently occupied with room temperature vacuum equipment, a beam position monitor, as well as a 50 cm long cold-to-warm transition inside the magnet cryostat. The masks provide an asymmetric protection of the D1 coils since they are centred around the machine axis while particle showers from the TDI/TDIS give rise to an asymmetric load on the D1 front face since the beam trajectories are not parallel to the magnet axis due to the TDI being located between the separation dipoles.

Detailed particle shower simulations were carried out to determine if the efficacy of the protection system needs to be improved for HL-LHC beam parameters. Considering the present understanding of the damage limit of superconducting coils and accounting for a suitable safety margin (factor 3) due to inevitable approximations in the simulation model, it cannot be excluded that the D1 damage limit is exceeded for some failure cases if the shielding of particle showers from the TDIS is not improved. Increasing the length of the TDIS would only result in a limited additional gain in protecting the D1 and therefore the active absorber length is left almost unchanged compared to the present TDI as already described in the previous section.

Two alternative concepts have been studied to enhance the shielding of showers from the TDIS, one based on the redesign of the TCDD and TCDDM masks while the other one relies on a complementary shielding inside the D1 cryostat. The effectiveness of the TCDD and TCDDM in intercepting shower particles can only be sufficiently improved if both their opening is reduced and they are moved closer to the D1. Owing to the stringent aperture requirements for the circulating beams, the mask dimensions can only be modified by a few millimetres. The minimum acceptable dimensions differ between IR2 and IR8 due to different crossing and separation schemes. The maximum distance the TCDD/TCDDM can be moved towards the D1 is about 50 cm and would require the displacement of a beam position monitor. Although some reduction of the energy density in the D1 coils can be achieved with these measures, it is more efficient to complement the present TCDD/TCDDM with another mask-like protection element inside the insulation vacuum of the D1 cryostat (TCDDXM). This solution offers the advantage of intercepting shower particles closer to the magnet and would

not affect the present machine aperture. Made of a heavy material to optimize its protection efficiency (e.g. tungsten alloy or steel), such a mask could be placed upstream of the cold mass endcap, tightly enclosing the cold bore which protrudes from the D1 cold mass assembly (see Figure 14-4). A radial thickness of 1 cm would be sufficient to effectively shield the coil cross section. The length of the mask could be between 14 cm and 17.5 cm depending on the detailed integration.

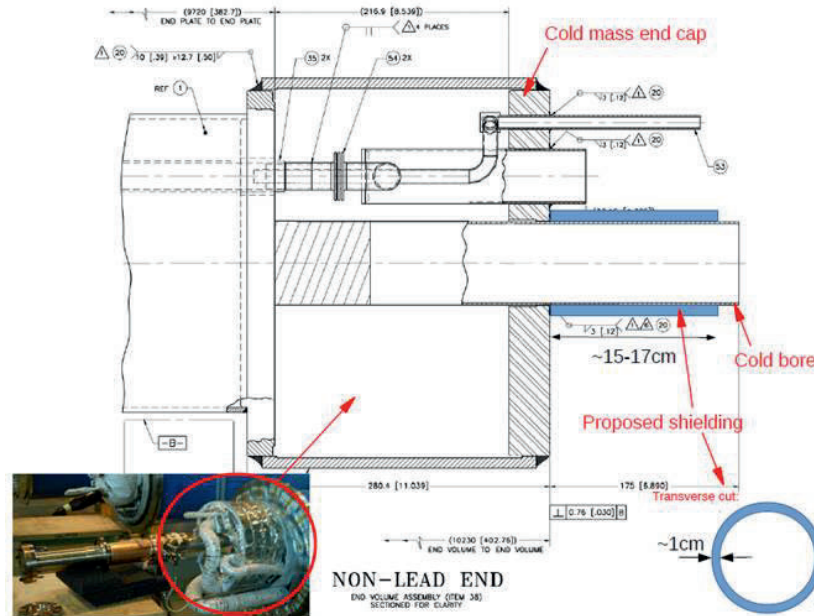


Figure 14-4: Possible shielding inside the D1 cryostat.

14.2.2 Injection protection devices retained from the LHC

Besides the TCDD and TCDDM masks described in the previous section, detailed studies have shown that several other protection elements can be retained from the LHC without any modification. This includes two auxiliary collimators, TCLIA and TCLIB, as well as a fixed mask (TCLIM) downstream of the TCLIB. The position of these devices is shown in Figure 14-1. The TCLIA is located between the separation dipoles D1 and D2, while the TCLIB and TCLIM are installed upstream of the matching section quadrupole Q6. Owing to its position close to the D1, the TCLIA also hosts the other circulating beam. By design, the collimators are at phase advances of $\pm 20^\circ$ (modulo 180°) relative to the TDIS in order to provide additional protection in case of phase errors. Both devices have two opposite jaws with an active length of 1 m. The TCLIA accommodates absorber blocks made of Graphite (SIGRAFINE[®] R4550, $\sim 1.83 \text{ g/cm}^3$), while the TCLIB is identical to secondary collimators presently installed in the LHC, which use CfC as absorber material (AC150K by Tatsuno/Across Corporation, $\sim 1.67 \text{ g/cm}^3$). Owing to the proximity of the TCLIB to the Q6, the collimator is complemented by a 1 m long TCLIM mask, which intercepts secondary showers from the TCLIB. No mask is installed downstream of the TCLIA as it is placed more than 40 meters upstream of the D2.

Depending on the injection kicker strength, badly injected beam will be intercepted by TDIS, TCLIA, or TCLIB. It is shown in Figure 14-5 that the TCLIB intercepts up to 28% of the particles contained in the 5σ area of a single particle emittance for injection kicker failures of $\pm 10\%$ nominal kick strength. This corresponds to a grazing impact of the beam on the TDIS. These studies accounted for different sources of machine imperfections such as quadrupole misalignments, field errors, and jaws misalignment. Tracking simulations indicate that, in the worst case, about 11% of the bunch train intensity can impact on the TCLIB, and less than 5% on the TCLIA. In such cases, the energy deposition in superconducting coils of the neighbouring magnets is estimated to not exceed a few J/cm^3 for HL-LHC beams. The risk of damaging magnets is therefore considered not significant. The same conclusion applies to the TCLIA and TCLIB themselves, as well as the downstream mask. Hence no modification of these protection devices is foreseen, except for a small increase

of the TCLIA jaw stroke in order to improve the angular acceptance of the ALICE ZDC. Besides this minor modification, the TCLIA is foreseen to be moved by about 1.8 m towards the IP to further increase the ZDC acceptance.

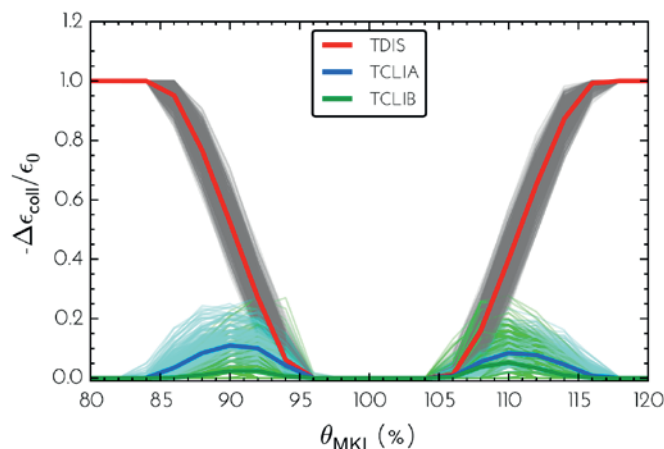


Figure 14-5: Fraction of 5σ single particle emittance absorbed by the different injection protection absorbers TDIS, TCLIA, or TCLIB for different injection kicker amplitudes.

14.2.3 Injection kicker magnet (MKI)

The injection kicker magnets MKI installed in IR2 and IR8, see Figure 14-1, deflect the injected beam vertically onto the LHC closed orbits. During Run 1 a number of issues have been encountered with the MKI magnets installed prior to LS1. These include beam-induced heating of the ferrite yoke, inefficient cooling of the ferrite yoke, electrical flashovers, beam losses due to macro particles falling into the beam, and electron cloud related vacuum pressure rise [5], [6] and [7].

If the ferrites of the injection kicker magnets reach a temperature above the Curie temperature their magnetic properties are temporarily compromised and the beam cannot be injected. Reducing beam-induced heating, additional cooling, and/or ferrites with a higher Curie temperature would avoid waiting periods before the beam can be injected into the LHC. A reduced magnetic field from the injection kickers is also a machine protection risk, possibly leading to quenches of the downstream magnets. The beam impedance of the MKI magnets has been reduced in LS1 by increasing the number of beam screen conductors from 15 to 24, see Figure 14-6. The increased number of conductors is expected to limit the ferrite yoke temperature to a maximum of 80°C for 2808 bunches of 25 ns beam with 1.15×10^{11} ppb and an average bunch length of 1.0 ns. Run 2 data to date confirms the reduction of the ferrite temperature with the additional screen conductors and is consistent with predictions obtained from beam impedance and thermal models. However, it cannot be guaranteed that this will sufficiently reduce beam-induced heating for HL-LHC operation. The heating depends critically on the bunch length and further studies and experimental data with high intensity LHC beam are required to predict the ferrite temperatures for ultimate LHC beams.

Operational experience during Run 1 showed that a beam power deposition of about 160 W/m occasionally limited the ability to inject beam. The present power deposition estimate with HL-LHC beams, for the MKIs with the upgraded beam screen, is approximately 200 W/m. Furthermore, operational experience from Run 2, together with improved modelling, shows that the beam induced power is not distributed equally throughout the ferrite yoke, but is mainly concentrated towards the capacitively coupled end. A prototype MKI magnet with reduced power deposition at the capacitively coupled end of the ferrite yoke and additional cooling will be developed for HL-LHC. In addition different ferrite types are being considered: a ferrite such as CMD10, which has a higher Curie temperature than the present MKI ferrite, would permit high intensity beam operation with better availability. However, a concern of operating at higher yoke temperatures is the higher pressure in the vacuum tank, which may result in an increased electrical breakdown and surface flashover rate. Further optimization of the capacitively coupled end of the beam screen is therefore being carried out to further

decrease beam coupling impedance and reduce the electric field strength in this area. Run 2 experience in this respect is relatively good: during 2015 there was a total of $\sim 6.2 \times 10^5$ pulses, for the 8 MKI kicker magnets and 5 flashovers, corresponding to a breakdown rate of $\sim 8 \times 10^{-6}$ per pulse [8].

Electron cloud in the ceramic tube results in a pressure increase, which may result in an increased electrical breakdown and surface flashover rate. This has been an issue when MKI magnets have been replaced - conditioning with beam is slow, requiring above 300 hours. In 2016 the resulting pressure rise (which for reasons which are not understood is worse in the Q5-MKID interconnect) has been the main limitation to date for the total injected beam intensity, despite operation with only 2020 bunches. A low SEY coating, such as Cr_2O_3 , or Laser Engineered Surface Structure (LESS) could eliminate multipactoring, and thus the related pressure rise, permitting more reliable operation of the injection kickers. Research and development of special coatings and LESS for the inner surface of the ceramic tube is being carried out, and it is planned to modify the inner surface of the ceramic tube of the prototype MKI. SEY measurements on alumina samples magnetron sputtered with Cr_2O_3 are showing great promise. The installation of a short (~ 0.5 m) coated liner in the SPS is being considered, possibly during the 2016-2017 EYETS, to qualify the Cr_2O_3 coating in an accelerator environment, before coating a 3 m long ceramic chamber for the prototype MKI.

After a comprehensive study programme in 2011, the macro particles causing ‘UFO’ beam losses around the MKIs were identified as fragments originating from the ceramic tube inside the MKI magnets [7]. The ceramic tube of MKI8D installed during a Technical Stop 3 (TS3) of 2012, towards the end of LHC Run 1, was subjected to improved cleaning, which included iterations of flushing of the inside of the tube with N_2 at 10 bar and dust sampling, until no significant further reduction of macro particles was noted. Before TS3, MKI8D exhibited the highest rate of beam-dust particle interactions of all MKIs in P8. The replacement MKI8D, in operation after TS3, exhibited the lowest rate. Extensive additional cleaning was carried out on the ceramic tubes of all eight MKI magnets installed during LS1: in 2015 the MKIs have vanished completely from the UFO statistics at 6.5 TeV compared to 2012 [9], which validates the new preparation procedures for the MKI beam screen.

Despite the continued issues and limitation a full scale modification of the series of the MKI magnets is not yet part of the HL-LHC baseline. The necessity of the described changes for the series of magnets depends on the Run 2 performance of the magnets installed in LS1 and the final beam parameters to be used for the HL-LHC beams (especially the bunch length). The installation of a prototype magnet to test the developed technologies is foreseen during the YETS in 2017-2018.

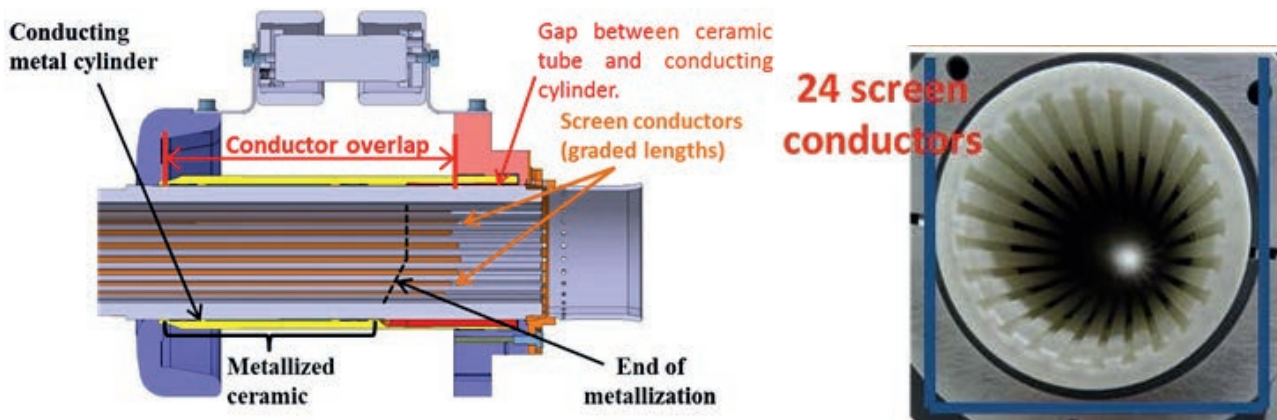


Figure 14-6: View of the capacitively coupled extremity of the MKI beam screen supporting the 24 screen conductors and the conductor overlap.

14.3 Beam dumping system

The beam in the LHC is aborted or dumped by a dedicated system based on pulsed extraction kickers MKD and DC septum magnets MSD located in the dedicated insertion in LHC point 6, followed by a dilution kicker system MKB, a long drift chamber, and a graphite beam dump absorber block (TDE) kept under N_2 gas at higher than atmospheric pressure. The $3 \mu s$ rise time of the extraction kicker field is synchronized by a highly reliable timing and synchronisation system TSU to a beam-free abort gap in the circulating bunch pattern. The horizontal and vertical dilution kickers are powered with anti-phase sinusoidal currents in order to paint the bunches onto the TDE with an elliptical shape, see Figure 14-7. The present system comprises 6 vertical and 4 horizontal kickers.

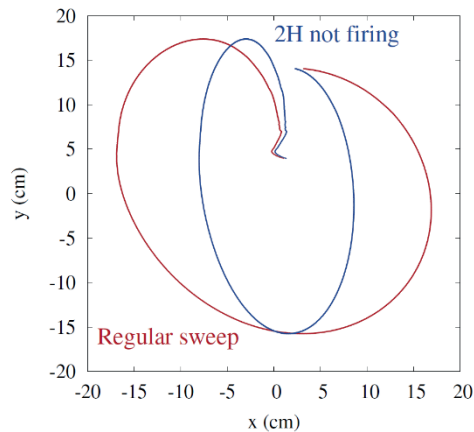


Figure 14-7: Sweep path of 25 ns spacing LHC beam on TDE dump block in case of a regular dump and in case 2 horizontal dilution kickers would not be firing.

14.3.1 Beam dump (TDE)

The LHC beam dump TDE and its entrance and exit windows [10], [11] will need to withstand the repeated dumping of high intensity HL-LHC beams. The TDE has a length of 8.4 m and accommodates different high- and low-density Graphite segments inside a 12 mm thick stainless steel jacket. The high-density segments are made of polycrystalline Graphite, whereas the 3.5 m long low-density part consists of a stack of 2 mm thick flexible Graphite sheets. Simulation studies show that, in case of a regular dump of HL-LHC beams, the maximum energy density in the TDE core exceeds 3.5 kJ/g (see Figure 14-8), generating a peak temperature of more than 2000°C. In case two horizontal dilution kickers would not fire, the peak energy density is estimated to reach more than 6 kJ/g (see Figure 14-8), which is expected to cause local damage to the dump core. The likelihood of different dilution failures and the consequences for the dump are under study. Thermo-mechanical simulations are being carried out to assess the stresses induced in the dump core, both for regular dumps and in case of a sweep failure. Similar studies have to be performed for the entrance and exit windows of the TDE. In case the load on the TDE is found not to be acceptable, the installation of additional dilution kicker magnets on the beam dump lines TD62 and TD68 could be required, with an increase of the sweep frequency to increase the path length and reduce the peak energy deposition. The installation of additional kickers or a modification of the TDE are not part of the baseline.

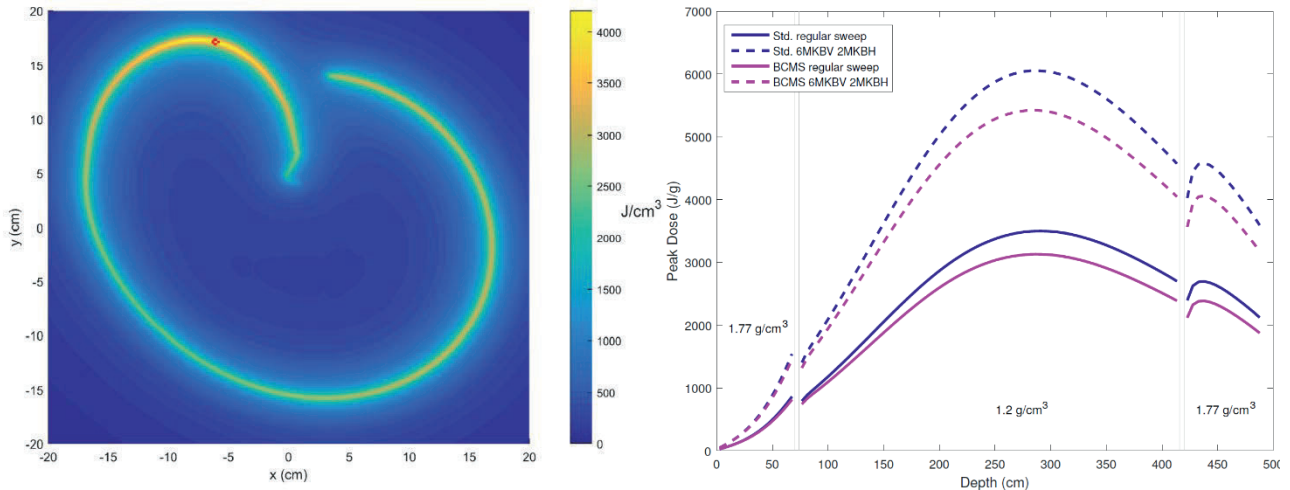


Figure 14-8: Transverse energy density distribution in the TDE core for a regular dump of HL-LHC beams, and longitudinal energy density distribution along the core for a regular dump and for a case where 2 horizontal dilution kickers are not firing. The figure on the right shows results both for standard HL-LHC beams with 2.3×10^{11} protons per bunch and an emittance of $2.1 \mu\text{m rad}$, and for BCMS beams with 2.0×10^{11} protons per bunch and an emittance of $1.37 \mu\text{m rad}$.

14.3.2 Beam dumping system absorbers (TCDQ and TCDS)

Several failure modes exist in the synchronization system and in the kicker switches that could lead to an asynchronous dump, in which part of the beam would be swept across the LHC aperture by the rising kicker field. Without dedicated protection devices this would lead to a massive damage of the LHC magnets in IR6 and the downstream arcs 5–6 and 6–7 and, depending on the operational configuration, a number of collimators and possibly experimental triplet magnets. The protection devices against asynchronous beam dumps are shown in Figure 14-9: the TCDS is a fixed absorber that directly protects the downstream extraction septum MSD, while the TCDQ is a movable absorber that, together with the secondary collimator TCSP, protects the superconducting quadrupole Q4 and further downstream elements, including the arc and the tertiary collimators (TCTs) around the experiments. A fixed mask (TCDQM) is installed right upstream of Q4 to intercept secondary particle showers produced at the TCDQ/TCSP and thus reduce the energy deposition in the superconducting coils.

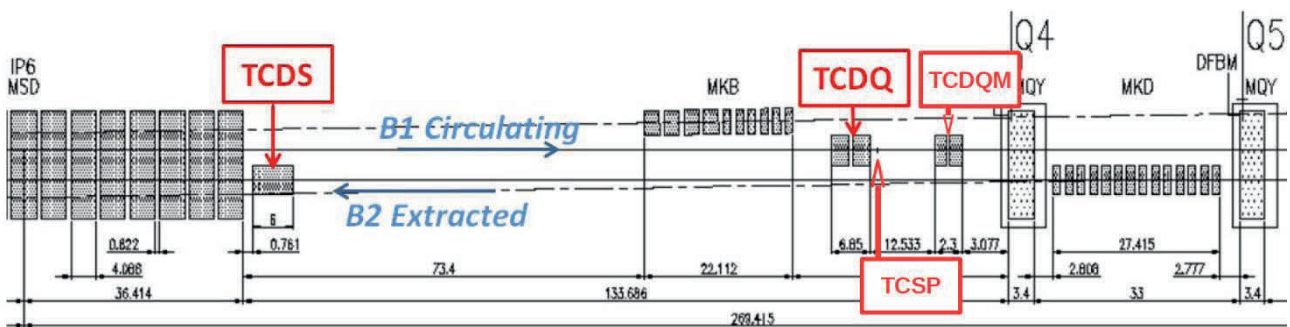


Figure 14-9: Schematic layout of the beam dump area right of P6 as used during LHC Run 1, showing the extraction absorber element TCDS on Beam 2 and the TCDQ on Beam 1.

The TCDQ was upgraded in LS1. The new design, which is described in detail in [12], includes an extension of the absorber length from 6 m to 9 m, and the replacement of the higher density graphite absorber material with different grades (1.4 g/cm^3 and 1.8 g/cm^3) of carbon fibre composites (CfC). During the reliability runs performed in 2015 a new type of MKD erratic (Type 2), with a different rise time than the standard one (Type 1), was identified. This case is more critical since a higher number of bunches can impact the TCDQ

with a large density close to the jaw surface (see Figure 14-10). New studies are being carried out to verify the robustness of the TCDQ and the provided protection to the downstream elements also for this new failure scenario. A further TCDQ upgrade is not part of the HL-LHC baseline.

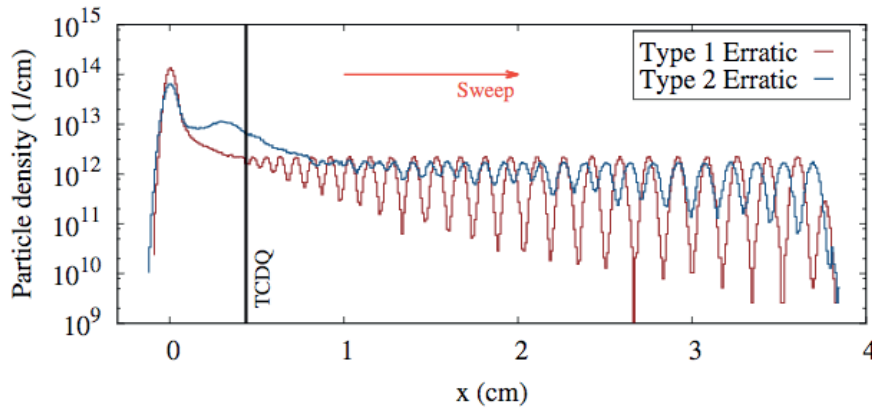


Figure 14-10: Particle density at the TCDQ in case of Type 1 and Typ2 MKD erratics.

FLUKA simulations were performed for standard LHC, HL-LHC and BCMS beams (the beam parameters are shown in the legend of Fig. 14-11) in case of a Type 2 MKD erratic. The energy density along the TCDQ jaw is strongly dependent on the bunch intensity while it is only marginally affected by the beam emittance (Figure 14-11). A maximum peak of $\sim 3\text{-}3.5 \text{ kJ/cm}^3$ is found, for the HL-LHC beam, in the low- and high-density blocks of the upstream module, corresponding to an absolute temperature $\geq 1300 \text{ }^\circ\text{C}$. In this condition, the mechanical stresses could be close to the damage limits and thermo-mechanical calculations have to be performed to evaluate the possible effects on the jaw. It is important to notice that the present transverse position of the TCDQ ($\sim 4 \text{ mm}$ at 7 TeV) depends on the optics and in particular on the β function at the TCDQ location. Any change inducing a reduction in the TCDQ gap (smaller β , larger local orbit excursion, etc.) would translate in an even higher energy density and thus in an increased risk of damage. Possible mitigations (i.e. Type 2 erratic prevention, improved monitoring of the local orbit, suitable optics conditions, etc.) are being evaluated and, together with the outcome of the ANSYSTM calculations, will allow to assess if the upstream part of the TCDQ jaw has to be upgraded with more robust materials (e.g. 3D C-C).

The TCSP collimators were upgraded in LS1 with integrated button BPMs in the jaws, which allows for faster and more accurate setup. No TCSP robustness related issue is expected for the HL-LHC era.

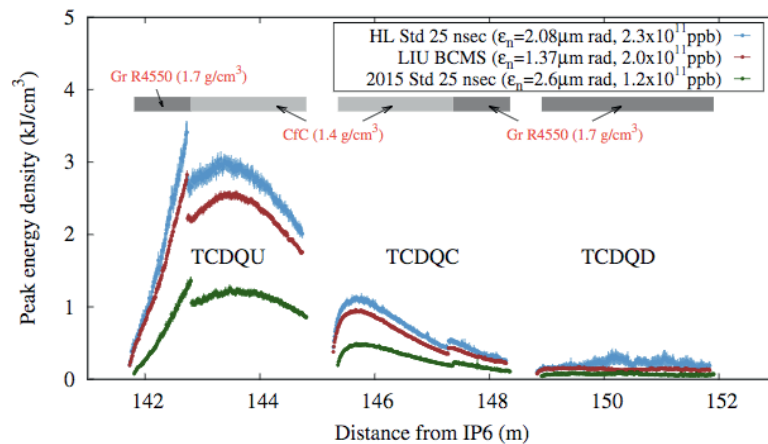


Figure 14-11: Energy density distribution along the present TCDQ absorber in case of a Type 2 MKD erratic for standard HL-LHC, BCMS and LHC beams.

In case of a Type 2 erratic, the simulations indicate a peak energy density of 17 and 30-40 J/cm³ in the coils the downstream Q4 and Q5 quadrupoles, respectively. The damage limit for the Nb-Ti coils for ultra-fast losses is not exactly known; nevertheless a damage limit of 87 J/cm³ was assumed during the design of the LHC protection devices. Ideally, a factor of three has to be accounted as a safety margin between the calculated energy density and the damage limit. HiRadMat tests are foreseen to improve the knowledge of the damage limit and, depending on the outcome, an improved protection might be considered for the Q5s in IR6, equivalent to the TCDQM. This will be difficult to integrate due to the location of the MKD kickers on the other beam, and is presently not in the HL-LHC baseline.

The robustness of the present TCDS and the protection of the MSD magnets, in case of an asynchronous beam dump with full intensity HL-LHC beams, is also being verified (Type 2 erratic, LHC, HL-LHC and BCMS beams see Figure 14-12). A maximum energy density of 2.5 kJ/cm³ (~1150 °C) was calculated in the low-density blocks (graphite and CfC) and of >1 kJ/cm³ in the Ti block. Thermo-mechanical studies are needed for the final assessment but there are clear indications that the Ti block has to be replaced either with a more robust high Z material or with a low Z material provided that a third module is added. Any additional length will slightly reduce the aperture for the circulating or extracted beams by a small fraction of a sigma, which should be acceptable. The TCDS upgrade is included in the HL-LHC baseline.

The calculated energy deposition at the first downstream MSD septum corresponds to a temperature increase of less than 100 K (~130 °C absolute temperature). This temperature is not critical concerning possible changes in the magnetic properties of the steel (up to 150 °C is considered acceptable). Moreover the peak temperature is reached in a peripheral part of the yoke so that no issue is expected for the insulation of the coils. Further studies are needed to evaluate if a temperature increase of up to 100 K could induce a deformation of the vacuum chamber of the circulating beam. Moreover FLUKA and ANSYSTM calculations have to be performed to quantify the temperature increase of the water in the MSD cooling pipes and thus evaluate the pressure rise and the consequent risk of shockwaves.

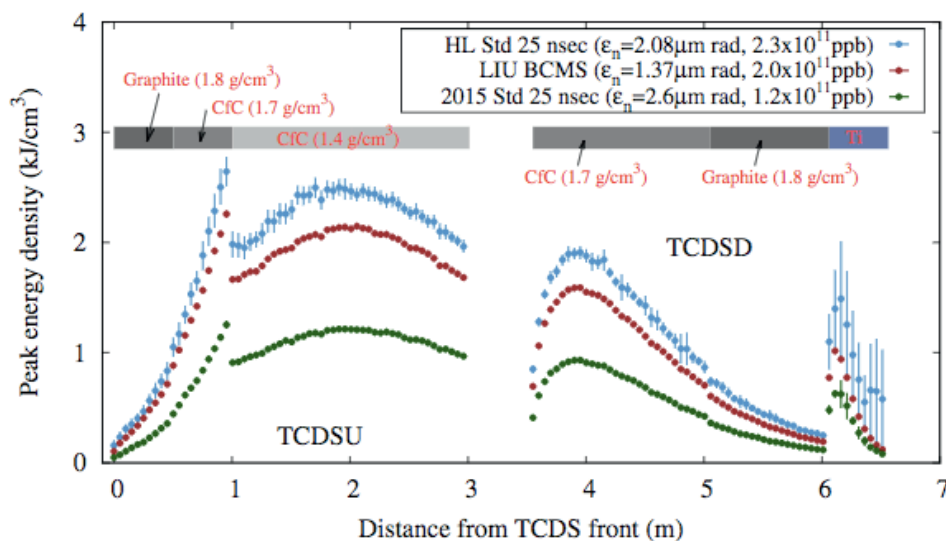


Figure 14-12: Energy density distribution along the present TCDS absorber in case of a Type 2 MKD erratic for standard HL-LHC, BCMS and LHC beams.

14.3.3 Extraction kicker generator and control system

During the several months of reliability running at the end of LS1, the generators of the beam dumping system extraction kickers (MKD) initially showed a large number of erratic triggers due to electric breakdowns. This was explained by the higher operational voltages required by the higher beam energy of Run 2. The breakdowns were located at regions with large electrical fields of around 3 MV/m at the edges of insulators in the generators. Replacing the critical insulators and cleaning of the critical areas in the generator allowed for a

reliable operation of the MKD system during the 2015 run at 6.5 TeV. However, operational margins are considered too small for long-term reliable operation at 7.0 TeV for HL-LHC. For this reason a redesign of the switch stacks of the MKD generators is ongoing with the aim of keeping the electrical field below 1.5 MV/m in all areas [13]. Replacement of the generator switch stacks is foreseen for LS2.

Simultaneously with the upgrade of the MKD switch stacks the power triggering and retriggering system of the MKD switches will be upgraded. The power triggers are presently rated at a current of 500 A and a di/dt of 400 A/ μ s for a voltage of 3.5 kV. The upgraded system will double the current and almost double the di/dt for a reduced voltage of 3.0 kV. The new parameters are better in line with the specifications of the manufacturer and will increase the lifetime of the GTO switches, result in a shorter rise time and will make the power trigger less sensitive to radiation. The retrigger system triggers all the extraction and dilution kickers as quickly as possible in case of an erratic closing of an extraction kicker switch. The present retrigger delay is about 900 ns and the aim is to reduce this to 700 ns, which will reduce the load on the ring elements, in particular the tertiary collimators, in case of an asynchronous dump. At the same time the electronics of the retriggering system, which is becoming obsolete, will be replaced.

14.4 References

- [1] J. Uythoven *et al.*, Upgrades to the injection and beam dumping systems for the HL-LHC project, Proc. 5th International Particle Accelerator Conference, Dresden, Germany, 15 - 20 Jun 2014, pp. [MOPRO032](#)
- [2] J. Uythoven *et al.*, Injection protection upgrade for the HL-LHC, Proceedings of the 6th International Particle Accelerator Conference 3 – 8 May 2015, Richmond, USA. [CERN-ACC-2015-359](#)
- [3] A. Lechner *et al.*, Protection of superconducting magnets in case of accidental beam losses during HL-LHC injection, Proceedings of the 6th International Particle Accelerator Conference 3 – 8 May 2015, Richmond, USA. [TUPTY049](#)
- [4] B. Goddard, V. Kain and M. Lamont, Function and operating conditions of the TDI beam absorber, functional specification, EDMS [508735](#) (2004).
- [5] M.J. Barnes *et al.*, Upgrade of the LHC injection kicker magnets, 4th International Particle Accelerator Conference, Shanghai, China, 12 - 17 May 2013, pp. 729 [CERN-ACC-2013-0077](#)
- [6] T. Baer *et al.*, UFOs: Observations, statistics and extrapolations, Proc. LHC Beam Operation workshop, Evian, 17–20 December 2012.
- [7] B. Goddard *et al.*, Transient beam losses in the LHC injection kickers from micron scale dust particles, IPAC'12, 2012, [TUPPR092](#).
- [8] M.J. Barnes *et al.*, Operational experience of the upgraded LHC injection kicker magnets, 7th International Particle Accelerator Conference, Busan, Korea, May 2016. DOI: [10.18429/JACoW-IPAC2016-THPMW033](#)
- [9] G. Papotti, M. Albert, B. Auchmann and A. Lechner, “Busting UFOs –part 1”, LMC 22/07/2015, INDICO: [434116](#).
- [10] J. Zazula and S. Peraire, LHC beam dump design study: 1, simulation of energy deposition by particle cascades; implications for the dump core and beam sweeping system, [CERN-LHC-Project_Report-80](#) (1996).
- [11] B. Goddard *et al.*, A large diameter entrance window for the LHC beam dump line, [LHC Project Report 823](#) (2005).
- [12] R. Versaci, B. Goddard and V. Vlachoudis, LHC asynchronous beam dump: Study of new TCDQ model and effects on downstream magnets, [CERN-ATS-Note-2012-084-MD](#) (2012).
- [13] B. Goddard *et al.*, “Proposed MKD generators consolidation”, LMC 29/07/2015, INDICO: [435579](#).

Chapter 15

Integration, (de-)installation and alignment

15 Integration, (de-)installation and alignment

15.1 Geographical distribution of HL-LHC upgrade interventions

The HL-LHC will require modifying the machine and infrastructure installations of the LHC in several points along the ring, in particular: P1, P2, P4, P5, P6 and P7.

Modifications and improvement in P4, P6 and part of P7 shall be completed during LS2 and be operational for LHC Run 3, while the equipment in P1, P2, P5, and rest of P7 are meant to be installed during Long Shutdown 3 (LS3). The activities required point by point will be therefore listed and analysed here below according to the above mentioned sequence that follows the present the HL-LHC schedule.

In P2, P4, P8 various machine equipment will be installed between LS2 and LS3, but at the present design stage, they do not look to present relevant challenges for the integration activities and therefore they are not described here.

15.2 Point 4

15.2.1 Cryogenic system upgrade

P4 will receive an upgrade of the cryogenic system to address the additional cryogenic load from the new installations.

Two options have been analysed for the cryogenic upgrade. The first foresees the installation of a new dedicated fixed plant and the second an installation with a mobile cold box and the upgrade of the existing cryogenic infrastructure. In both cases the cryogenic distribution will be sectorized to allow independent operation. The second option has a lower cost and its installation will be simpler, but requires a very careful analysis of the HL-LHC cryogenic needs through the different phases (installation, commissioning, RF conditioning, operation ...). As the first option has the largest impact and is more challenging from an integration point of view, the following paragraph will provide the selected installation solutions to fit it in the present LHC civil engineering infrastructures.

The installation will require:

- surface: installation of the warm compressor systems in SU4;
- junction surface to the underground cavern via PX46;
- underground: installation of the cold box in TX46 (see Figure 15-1);
- connection between the cold box and QRL via UX45;
- QRL modification between -25 m and $+25$ m around IP4. This will require modification of the LHC tunnel inside the UX45 with the increase of the tunnel height via the modification of the prefabricated structure supporting the closing slabs, and the relocation of the cooling ventilation services. All modifications shall ensure maintainability of the LHC RF systems including RF cryo-modules changes.

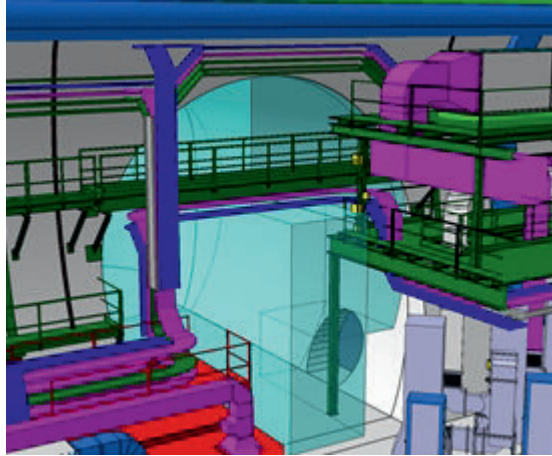


Figure 15-1: Volume reserved for the installation of the new cold box unit dedicated to RF system cooling (light blue).

The solutions presently adopted make the maximum use of existing volumes, requiring very limited civil engineering work, mainly devoted to the routing of the piping from SU4 to SX4 and to the vertical wall of PX46. The whole system installation shall be completed for the end of LS2. Figure 15-2 provides a schematic of the P4 buildings.

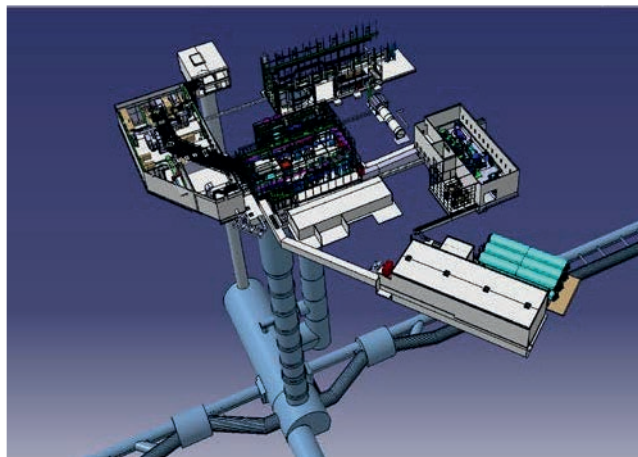


Figure 15-2: View of the LHC civil works at P4.

15.2.2 New beam line elements

The following elements are foreseen to be installed in the long straight section at Point 4 for HL-LHC. Their installation will take place between LS2 and LS3:

- **Synchrotron light diagnostics:** New synchrotron light diagnostics, looking at photon emission from the D4 bending magnet, on the beams heading to IP4 including an extraction mirror located ~20 meters from D4 toward D3 and an optical path to bring the synchrotron light to a light detector located in a hutch in the UA gallery, through a duct to be drilled in the shielding wall. This installation is foreseen on both beams, one on each sides of IP4.
- **Synchrotron light monitors:** The present synchrotron light monitors, looking at photon emission from the undulator magnet, on the beams heading away from IP4, will be upgraded and also installed in optical hutches in the UA's galleries. This will require to install an optical path and the drilling of the corresponding ducts in the RA-UA shielding walls.

- **Fast wire-scanners:** New fast wire-scanners will complement the existing beam profile monitors. Two wire-scanners for each plane are foreseen, located in the D3-D4 drift space, on beam 1 right of IP4 and a similar setting will be installed on beam 2 left of IP4.
- **Transverse feedback system:** A transverse feedback system (ADT) upgrade with higher bandwidth will be installed in to cure single and multi-bunch instabilities outside the 20 MHz covered by the existing system.

Not part of the present baseline but under study:

- **RF Cryo-cavities:** Additional RF cryo-cavities could be installed to provide a harmonic system with the present ACS cavities. A higher harmonic (800 MHz) could improve beam stability in bunch-lengthening or shortening mode.
- **Hollow-electron lens:** They could complete the collimation system by providing an active control of the beam halo population and of the beam loss rate.

The ADT, 800 MHz cryo-cavities and hollow e-lens could require transverse space that is only available in the central region of the long straight section at IP4, between D3 Left and D3 Right, where the beam separation is 420 millimetres. Longitudinal space to accommodate these new elements is limited and the integration optimisation is still in progress.

15.3 Point 6

In P6 the two Q5 quadrupole magnets will be modified in order to fulfil the needs of the new HL-LHC ATS optics. The previous HL-LHC baseline foresaw the replacement of the present Q5 with a new longer element featuring two MQY quadrupoles in series, and one MCBY corrector.

Design and cost optimisation has led to the decision to keep the present cryo-assembly magnets but to lower their operational temperature from 4.5 K down to 1.9 K. This will require the modification of the cold mass cooling and therefore the cryostat piping. The new temperature will provide enough margin to operate at the required higher gradient. In order to provide the required cryogenic supply the QRL shall be modified accordingly with the substitution of the present service modules with new ones featuring the required 1.9K supply in the jumpers.

This intervention will be performed in LS3.

15.4 Point 7

In order to protect the superconducting magnets (excess heat deposition) from off-momentum proton leakage from the main collimator system itself, some special collimators must be installed in the dispersion suppression region, i.e. in the continuous cryostat. The installation will take place during LS2.

In order to cope with the proton losses in the dispersion suppressor area it has been decided to install two collimators on each side of the IP. In order to do so it will be necessary to:

- remove MB.B8L7 and the symmetric MB.B8R7;
- substitute each removed dipole with a unit composed of two 11 T dipoles (Chapter 11) separated by a cryogenic bypass;
- install the collimator on the top of the cryogenic bypass (Chapter 5).

The magnet installation will probably also require a new dedicated quench protection system and a trim circuit with its own power converter. The location and the installation approach for this equipment are still under evaluation, but very probably it will be located in the nearby RR, while the trim power supply will be installed in the TTZ tunnel.

15.5 Point 2

In order to limit the heat deposition from secondary beams in the superconducting magnets during the ion run, collimators in the dispersion suppressor will also be installed in P2 (Chapter 5). In this case the installation will take place only in one slot on each side of the IP. The previously proposed strategy relying on the installation of two 11 T units with the related by-pass and collimators has been changed in replacing the interconnection cryostat with a modified version of the by-pass cryostat development for the 11 T collimator installation. This approach is much more cost effective and it has been made possible thanks to the study and tests performed during Run 2 that have put in evidence the possibility to steer the ion secondary beam in these locations.

15.6 Point 1 and Point 5

The largest part of the new equipment required to meet the HL-LHC performance objectives will be installed in P1 and P5. The items to be installed and actions to be carried out are listed below, and are applicable to both points, if not otherwise specified. The list is organized by geographical areas.

15.6.1 LHC machine tunnel

De-installation:

- All the machine equipment from the interface with the experimental cavern (TAS included) until the DFBA (excluded) requires removal.
- The present QRL will be removed from the same area. A new return module will be installed near the DFBA in order to allow separation of the coolant flows coming from the LHC QRL and one of the new HL-LHC QXLs that will feed the part of the machine from Q1 to Q6. This return module should also provide the possibility, if required, to connect the LHC QRL with the HL-LHC QXL, ensuring an increased level of redundancy in the system.
- Services linked to the above de-installed equipment.

Preparation for re-installation:

- Minor works could be necessary in order to prepare the tunnel floor and wall to receive the installation of the new equipment (for larger and dedicated civil engineering see the next paragraphs).

Installation. Installation of the new equipment, probably in the following sequence:

- TAXS;
- services;
- QXL with related valve and service modules;
- horizontal superconducting links from the DFM to the magnets to be fed;
- magnets and crab cavity support system;
- magnets and crab cavity;
- distribution feedboxes (DFX) for the Q1 to D1 magnet system and distribution feedboxes (DFM) for the D2 to Q6 magnet system.

The sequence of installation of the vertical superconducting links to be connected to the DFX and DFM still need to be assessed according to the options retained for their routing.

In addition to the interventions described above, it may be necessary to strengthen the collimation system with new collimators in the dispersion suppressor as described for P2 in 15.5.

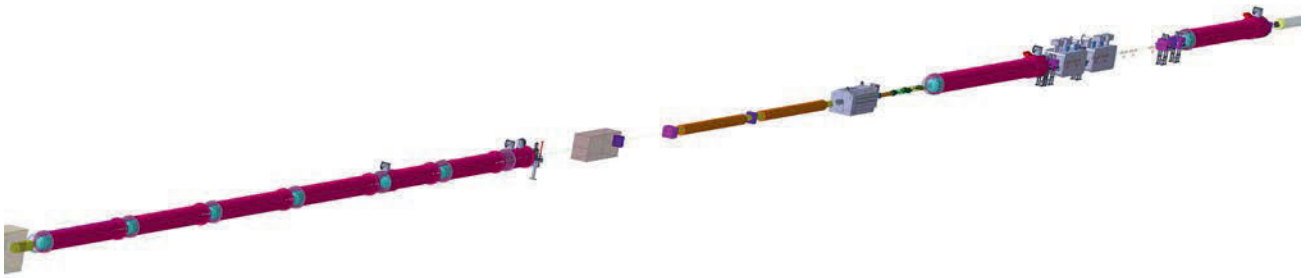


Figure 15-3: Integration 3D model of the HL-LHC machine. From left to right: Q1, Q2,Q3, D1, Corrector Package, DFX, DFM, LBBR compensators, TAXN, D2, 4 Crab Cavities cryo modules, Q4.

15.6.2 Existing LHC tunnel service areas

The RRs on both sides of P1 and P5 will need to be re-organized, and in particular the following actions will be necessary.

- De-install the power converter and other related systems (e.g. the quench detection system) linked to the powering of the removed LHC matching section.
- Re-organize the remaining equipment in order to have the most efficient space occupation, increase if necessary the radiation shielding, and place the most radiation-sensitive equipment in the most protected areas. Possible equipment replacement with new radiation-hard elements can be envisaged.

At present no civil work interventions are foreseen in the RRs areas

15.6.3 New HL-LHC tunnel service areas

15.6.3.1 General concepts

The installation of the new cryogenic plant in P1 and P5 will have two objectives:

- provide independent and redundant cooling capacity to feed the final focus and matching sections left and right of each of the two high luminosity insertions for the LHC;
- provide redundancy to the cryogenic plant installed to cool the detector magnets.

The cold boxes shall be installed in underground areas. At present the required volume does not exist. The maximum difference in level between the cold box outlet and the QXL distribution line shall be less than 20 m. Items that need to be taken into account include:

- the above mentioned allowed height difference;
- the need to build tunnels to distribute the cryogenic fluids from the cold box to the left and right of the IP;
- the advantage for the crab cavities to have the RF equipment installed in the proximity, providing easier exploitation and simplifying the equipment installation;
- the possible synergy with the magnet power converter system installation;
- the lack of space to integrate the RF waveguides or coaxial lines in the LHC tunnel.

The HL-LHC project has identified as baseline the construction of an underground cavern plus gallery system to host:

- the cold box and the connection to the QXL;

- the RF ancillaries (powering and control, space will be reserved for possibly doubling of the HL-LHC baseline crab cavity system);
- the magnet power converters;
- the related technical services (cooling and ventilation, electrical supply, access control systems,...);
- the necessary safety related equipment (smoke extraction, fire suppression, safety room,...);

The installation approach shall guarantee the access to the power converters and to relevant part of the RF ancillaries also during beam-on periods therefore insuring no or very limited radiation coming from the LHC tunnel and no risk of oxygen deficiency in case of He release from the cryogenic system installed in the LHC machine.

The proposed solution has been identified with the nick name of double decker (DD) and it makes use of the allowed height difference between the cold box and the QXL in order to fulfil the technical, operational and safety requirements (Figure 15-4 and Figure 15-5). The floor of the new structure will be placed at a higher level respect to the LHC tunnel floor, in such a way that the vertical distance between the cold box outlet and the QXL is less than the required 20 m. The transverse connection (UA, UR) tunnels where the cryogenic link, the superconducting links and the RF ancillaries will be installed will extend from the UR tunnel (parallel to the LHC machine tunnel at a distance of about 40 m) to the top of the LHC machine in the vertical point as near as possible of the equipment that need to be fed. In this point the rock layer between the LHC tunnel vault and the UL galleries will be about 4.5 m. Vertical cores will provide the path through which the cryogenic lines, the SC links and the RF powering will dive into the LHC tunnel. To guarantee the escape to safe area in all the envisaged incident scenarios it has been decided to build two escape ways joining the UA extremities to the LHC tunnel.

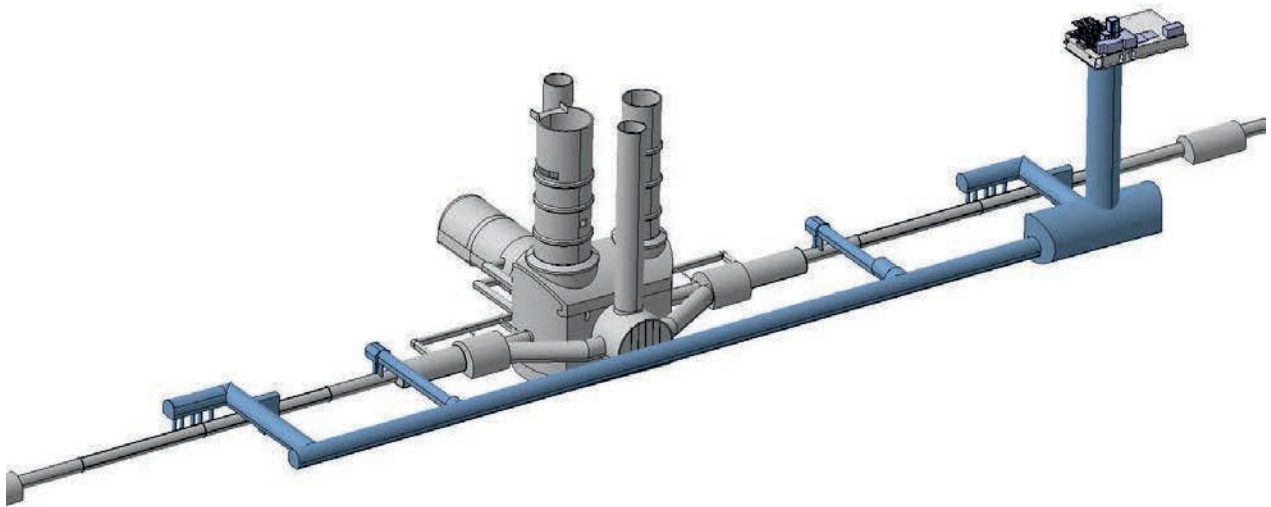


Figure 15-4: Assonometric view of the HL-LHC underground civil engineering infrastructures as it would appear in IP1.

The main elements of the new underground structures and their code names are:

- PM: shaft joining the surface to the underground structure.
- US: cavern for the installation of the cryogenic cold box.
- UR: gallery parallel to the LHC tunnel, about 40 meter away, and extending from the location of the crab cavity system on the right of the IP to the point where the crab cavity are installed on the left of the IP. Approximately 300 m long.
- UA: two galleries per LHC point, distributed symmetrically respect to the IP and joining the URs to the top of the LHC over the crab cavities.

- UL: two galleries per LHC point, distributed symmetrically respect to the IP and joining the URs to the top of the LHC over the DFX near the D1 magnet.

In the following paragraph the installation approach for the many equipment shall be discussed.

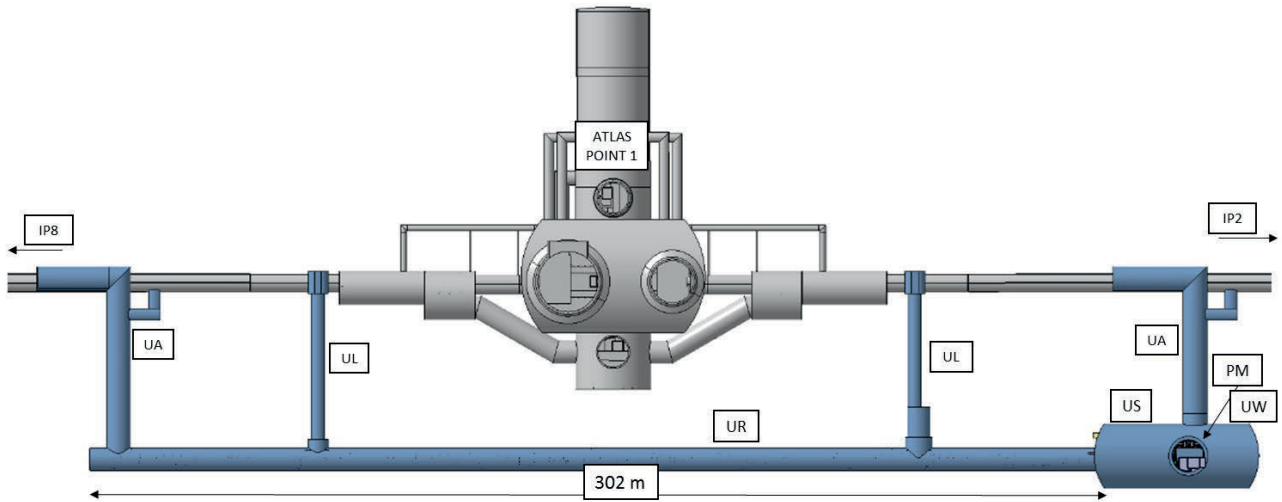


Figure 15-5: Top view of the HL-LHC underground civil engineering infrastructures as it would appear in IP1.

15.6.3.1 The cryogenic installation

The HL-LHC cold box will be installed in the US (Figure 15-6), from here one line will join the distribution box in the alcove of the nearest UL. From this valve box two lines will exit feeding the QXLs left and right of the IP. The first one would run along the UL and connect into the LHC tunnel via a vertical core. The second will run through the UR length and then (as for the first one) will join the other UL and will dive down through the core to be connect to the LHC QXL.

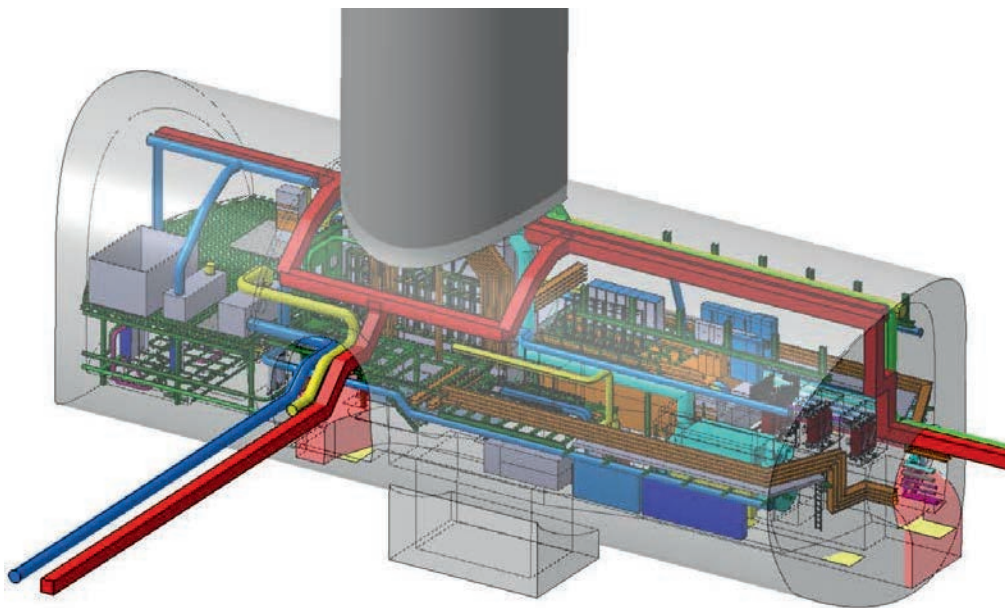


Figure 15-6: The cavern (US) hosting the cold box with other technical services.

15.6.3.2 The Superconducting links

The superconducting links will be four per IP, two per side. One will connect the DFXH to the DFX in order to feed the superconducting magnets installed from Q1 to D1, the second will connect the DFXM to the DFM to feed the D2 magnet. The design optimisation of this second link is still undergoing.

The DFXH and DFMH will be installed in the URs near the power converters that will feed them and as close as possible to the ULs (Figure 15-7). The SC links through the UL will reach, together with the cryogenic lines, the vertical crossing of the LHC and they will dive down through cores to be connected to the DFX and DFM that will be installed in the LHC tunnel parallel and near the beam lines (Figure 15-8).

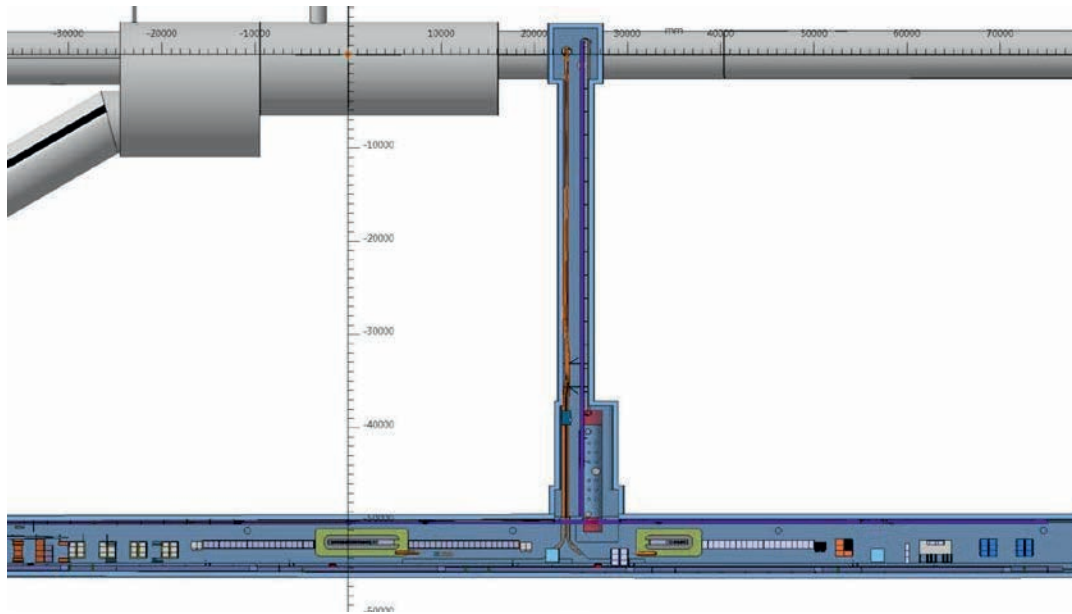


Figure 15-7: Installation of the DFX in the UR and routing of the SC link to the top of the LHC machine tunnel via the UL gallery. Top view.

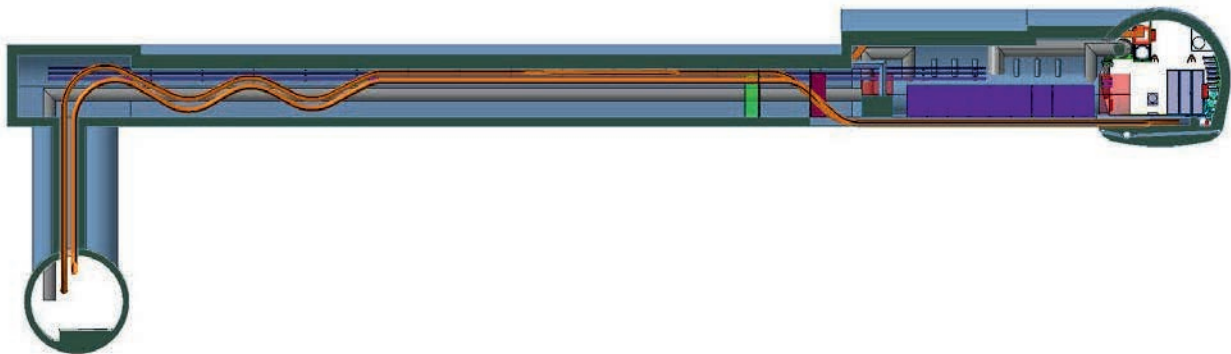


Figure 15-8: The UL gallery with the cryogenic and superconducting link routing and their vertical connection to the LHC machine tunnel.

15.6.3.3 The Power converters

The power converters feeding the DFXH and DFMH will be installed in the URs (8) around these units; optimising current distribution via the warm cables. The power converters are the main source of space and of cooling power requirement in the URs, therefore any possible optimisation on the electrical scheme (reduction of the number of circuit or of the circuit current) will also have relevant impact on the underground space requirement and on the cooling capacity to be installed.

15.6.3.4 The RF ancillaries

The waveguides joining the RF superconducting cavities (crab cavities) to the circulator will require eight large cores per IP side (Figure 15-9). These cores and safety escape ways to the LHC tunnel will represent the two paths through which radiation could propagate from the LHC machine into the UA and therefore to the UR. The foreseen arrangement is as follows:

- On the vertical of the crab cavity installation in the LHC tunnel, five large cores will be drilled: two for immediate use for the crab installation (each one housing two waveguides), one for the instrumentation and control cables, two for possible future doubling of the crab installation.
- The waveguides will exit inside a tunnel running parallel to the LHC tunnel on its top and separated from it by a rock frame.
- The waveguides will be then connected to the loads and circulators. These elements are not radiation sensitive and therefore they could be installed just at the exit of the cores or farther in the UAs. The first option would allow reducing the waveguide length making easier the installation of the maze required for radiation attenuation.

A maze will be installed at the junction of the gallery and the UAs in order to reduce the radiation to a level allowing access in beam also in case of incidental scenario (full beam loss on a massive block placed under to the cores entrance along the LHC beam orbit). Tetrodes and RF power supplies will be installed in the UAs, between the maze and the junction between the UAs and the URs they will be connected to the circulator by coaxial cables. The RF control racks will be placed in a shielded faraday cage. The safety escape ways has been designed in order to fulfil the same radiological requirements

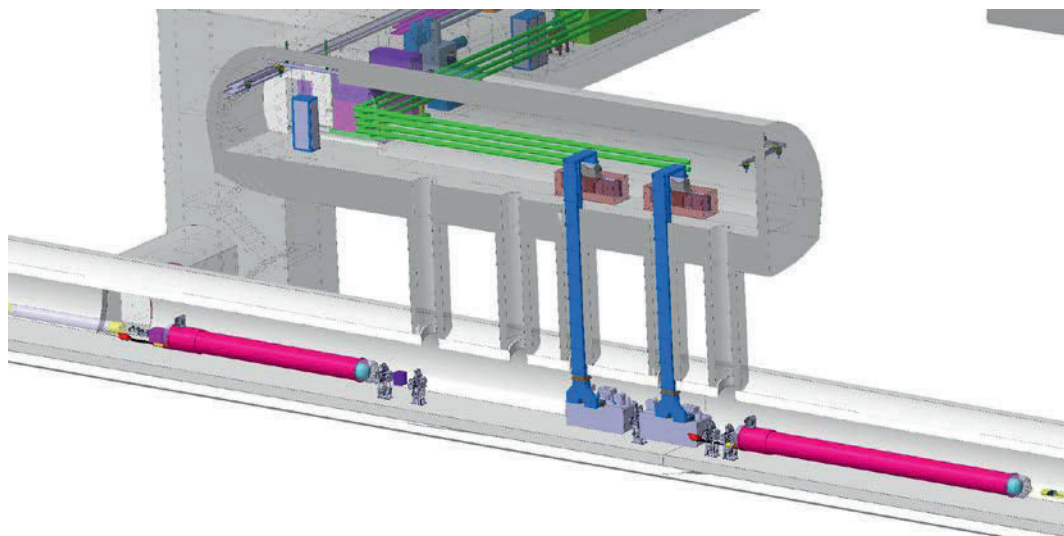


Figure 15-9: The axonometric view the UA with the waveguide providing RF powering to the crab cavity installed in the LHC and the tetrodes installed along the UA.

15.6.4 New surface installation

With the adoption of the double decker solution all the system directly linked with the HL-LHC machine equipment will be installed underground with the exception of warm compressor of the cryogenic system. On the surface it will be necessary to build, both at Point 1 and Point 5, new buildings to host the general services. Detailed description of these buildings and of the equipment to be installed there are not the object of this chapter, and therefore here the description will be limited to the list of the required building and their main function

- SD: access to the PM shaft connecting the surface to the new underground UR complex;

- SU: ventilation service building;
- SDH: helium unloading service building;
- SE: electrical service building;
- SHM: compressor building;
- SF: cooling towers;
- SR: RF power converters if the powering of the crab cavities will make use of IOT option;

In addition various technical galleries and concrete platform for equipment to be installed open air will be required.

The present provisional lay-out for the Point 1 and Point 5 are in Figure 15-10 and Figure 15-11.



Figure 15-10: The LHC Point 5 with the new HL-LHC surface building.



Figure 15-11: The LHC Point 1 with the new HL-LHC surface building.

15.6.5 Activity sequence considerations

Concerning the execution of the underground works, vibration propagation studies and LHC optics studies have put in evidence the high risk to perturb the LHC operation if the activities of excavation are performed during beam time. Consequently the project has decided to anticipate the excavation during the LS2 in order to avoid risk for LHC operations. In order to avoid disruption in the LS2 into the LHC machine, the connections between the new underground infrastructures and the LHC tunnel will be dig during LS3.

For what it concerns the installation, while the sequence of intervention on the underground LHC installed equipment (machine and RR) is quite clear and linked to the end of the LHC Run 3, the sequence for the other installation and surface civil work activities is still under evaluation.

15.7 Alignment and internal metrology

15.7.1 General objectives, requirements and constraints

The HL-LHC performance heavily relies on precise alignment of the magnets, RF systems or beam diagnostics components. The alignment and internal metrology of these components can be divided into 3 steps: the fiducialisation, the absolute alignment of the components w.r.t underground geodetic network (“standard alignment”) and the relative alignment (smoothing) of the components using sensors and actuators to determine their position and readjust them remotely. The fiducialisation (or internal metrology) will determine the position of the magnetic axis at cold and at warm w.r.t. the external alignment targets used to align the cryostats in the tunnel. The absolute alignment of the HL-LHC components in the tunnel will imply first a redetermination of the underground geodetic network, using the good geometry of the LHC components, before their dismantling. Then, the heads of jacks will be aligned w.r.t this network, as well as the new components once installed. Such “standard” alignment will allow the implementation of the alignment systems (sensors and actuators) that will perform the smoothing and continuous determination of the position of the components from Q1 to Q5, according to 6 degrees of freedom. The cold mass monitoring systems will determine continuously the position of the cold mass inside its cryostat according to 5 degrees of freedom, from their fiducialisation to their installation in the tunnel, with the follow-up of the impact of vacuum and cold on the position of the cold mass in the coordinate system of the cryostat.

The general schedule of LS3 will integrate the re-determination of the underground geodetic network, based on the LHC components, prior to their dismantling, to preserve the good LHC beam geometry. This step is needed to install all the components in the measurement range of the alignment systems and in the adjustment range of the actuators.

From the integration point of view of the new HL alignment systems, several constraints shall be satisfied:

- Sensors will be located at the vertical of the jacks to avoid level arm effects
- A straight line of sight along the components to be monitored is booked from Q1 to Q5, on the transport side, for the stretched wire
- Horizontal levels along the components with a difference of height from 0.5 to 1 m between the levels must be preserved in the tunnel for the hydraulic networks from Q1 to Q5.

From the global schedule point of view, the following major steps can be identified:

- The absolute alignment step will take place once the cryostats are installed on their jacks, before the interconnection and cool-down operations.
- The alignment systems (sensors part) will have to be in operation before the pumping of the insulation vacuum and cool-down start up in order to monitor possible position changes during these steps.
- The final smoothing of all the components of LSS will take place once the magnets are connected, under vacuum and cooled-down

As-built measurements using laser scanner will be carried out in all the newly equipped area, once all components, the technical systems and cables are in place.

The installation of such continuous and remote alignment systems, allowing to determine the position of the components of the LSS and readjust the components remotely (between Q1 and Q5), will allow to considerably reduce the doses taken by the surveyors in these area and limit their exposition to risks of a cryogenic accident. The access in these area will only be needed for corrective maintenance of the alignment systems.

In order to perform measurements in high radioactive areas, the alignment systems will consist of capacitive WPS and HLS sensors. These sensors are made of passive materials: their electronics is not integrated inside the sensor. Nevertheless, the maximum distance between the sensor and its remote electronics should be inferior to 30 m to keep noise on the signal at an acceptable value. The remote electronics must be located in low radiation area as it can only stand up to 500 Gy as a cumulative dose without failure [1]. The acquisition units of the alignment sensors and the control/command units of the actuators to adjust remotely the components will have to be located in an area with no level of radiations.

Preliminary estimation of total ionising doses during HL-LHC operation received by the WPS and HLS sensors installed on the cryostats at a maximum level of 1 MGy.

The monitoring of cold masses inside each cryostat of inner triplet, combined with the continuous determination of the position of each cryostat, will considerably improve the alignment of the inner triplet compared to the LHC era. The new instrumentation will take into account the misalignment occurring after cooling, due to mechanical stress.

The continuous determination of the cryostats position, carried out from Q1 to Q5 will offer a remote fine tuning of the alignment of the inner triplet w.r.t the other components of the LSS after the cool-down.

Such systems will allow to fulfil the assumptions considered in the report [2] to reduce the strength of orbit correctors, considering ± 0.5 mm transverse error for the inner triplet (± 0.27 mm at 1σ).

15.7.2 Internal metrology

The determination of the coordinates of the fiducials, located on the cryo-assembly magnets, with respect to the as-built mechanic and magnetic axis of the quadrupoles and dipoles, is the basic information necessary for all further alignment actions and is the object of the fiducialisation process [3].

Each cryostat will be equipped with 4 fiducials [4]. Some 1.5'' fiducials supports will be added on the cryostat to provide redundancy for laser tracker measurements if needed.

On the present triplets of the LHC, the fiducials measurements were carried out in warm and cold conditions at Fermi National Accelerator Laboratory (FNAL), initially with a simple control at CERN. As the results showed changes of the fiducialisation during ocean-going transport, the metrology of the quadrupoles was redone at warm using the tools and techniques used for all other LHC cryo-assembly magnets. For the HL-LHC triplets, all warm and cold measurements (both magnetic and geometric) will be performed at CERN using the existing LHC test benches, measurements tools and procedures that are well understood. The following improvements of the magnet metrology should be further implemented:

- The straightness of the cold mass and the position of the vacuum pipe should be controlled during the manufacturing phase of the cold mass.
- The position of the cold mass inside the cryostat should be controlled after the manufacturing phase within an uncertainty of measurement of ± 0.1 mm
- In order to determine if there is a displacement of the cold mass inside the cryostat during transport, a dedicated internal monitoring system will be installed in the low beta triplet cryostats.
- Additional reference points on the cold mass extremities will increase redundancy and allow to re-fiducialise the magnets in-situ if needed and to perform additional geometrical controls of the interconnections areas. The points should be referenced to the beam tubes during final magnet assembly.
- The positions of the fiducial targets on the cryostats and of the interface points with the jacks will be measured and re-adjusted if needed after magnet assembly to allow full range of the alignment system.

The same procedure than in the LHC will be carried out to determine the mechanical position of the BPM, the beam screens and the cartography at the ends of each cryo-assembly [5].

15.7.3 *Monitoring of cold mass and crab cavities*

15.7.3.1 Monitoring of the cold mass

As described in [2], the position of the magnetic axis and mechanical axis of each magnet w.r.t the alignment targets installed on top of the cryostat (materializing the referential frame of the cryostat) will have to be known within ± 0.1 mm (1σ). Such budget error includes the error of fiducialisation and the error of the cold mass monitoring.

To answer such requirements, a measurement system with an accuracy of 10 μm is needed, able to work at cold temperature, perform measurements along an important gradient of temperature (from the cryostat at room temperature to the crab cavities at 3 K) and in a high radiation environment. Non-contact measurements in that case are preferred, and the Frequency Scanning Interferometry (FSI) system answering all the requirements, has been chosen as the baseline, even if it is still under qualification.

FSI is a measurement technique allowing the determination of absolute distances with an interferometric accuracy: measurement uncertainty (95%) of 0.5 $\mu\text{m}/\text{m}$ between 0.2 and 20 m. Each distance measurement is performed between a collimator and an alignment target.

The configuration proposed for the cold mass monitoring consists of 8 distance measurements and an additional one for the longitudinal position of the cold mass. Each survey collimator will be located directly on the cryostat via a feedthrough that will allow its adjustment w.r.t. its corresponding alignment target located

on the cold mass interface. The feedthroughs will be equipped with alignment targets to determine their position in the referential frame of the cryostat and then in the referential frame of the tunnel.

15.7.3.2 Monitoring of crab cavities

As described in [13], the alignment requirements concerning the HL-LHC crab cavities are the following:

- The transverse rotation (roll R_z) of the individual cavities inside the cryostat should be inferior to 0.3° (3σ)
- The cavity roll w.r.t longitudinal cryostat axis should be less than 1 mrad
- The transverse displacement of cavities w.r.t each other inside their cryostat should not exceed 0.7 mm (3σ).

To answer such requirements, a solution based on FSI is proposed. The configuration of FSI consists of 16 distance measurements: 8 per crab cavities, as shown on Figure 15-12.

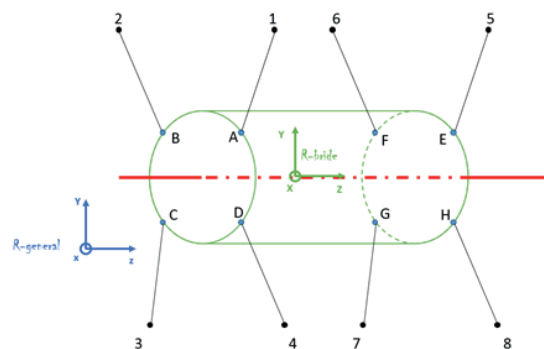


Figure 15-12: configuration of FSI channels per crab cavity.

Each FSI head interference point will be located on the top and bottom sides of the cryostat, while the reflector will be located on the flange of each crab cavity tank, see Figure 15-13 [6].

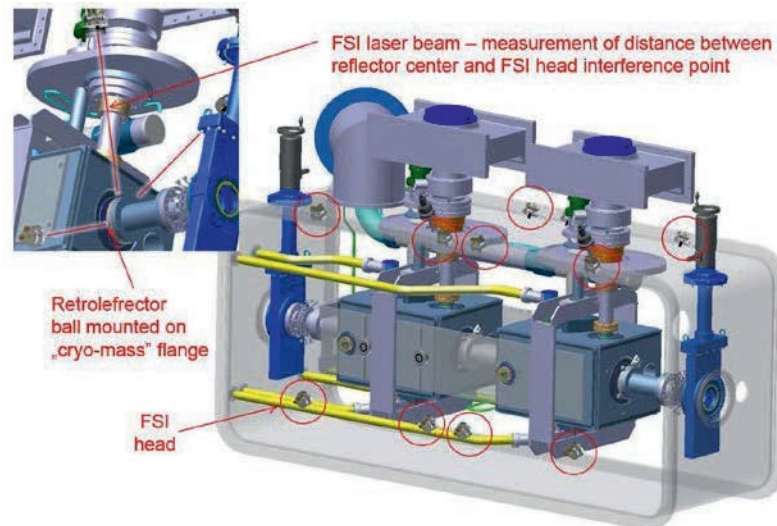


Figure 15-13: FSI system configuration to monitor the crab cavities.

15.7.4 Standard alignment

As mentioned before, in order to preserve the good beam geometry from Run 3, the underground network will be re-determined in the area where new components will be installed, from the old components, prior to their dismantling.

Then, using this re-determined underground network, preparatory works will be carried out once the old components are removed from the tunnel. First, the marking on the floor of the position of the new elements will take place, following the strategy used in the LHC [7]. Then, the heads of the jacks will be positioned within ± 2 mm before the installation of the cryo-magnets, with the adjustment screws in their middle range. Once the jacks are at their nominal position, they will be sealed on the floor [8].

Traditionally, in accelerators, the alignment of the cryo-assembly magnets is carried out into two steps: the initial alignment and the smoothing (relative alignment of cryo-assembly magnets with respect to each other, not using the underground geodetic network any more as a reference). In the case of HL-LHC and components from Q1 to Q5, only the first step will be carried out using standard alignment measurements. The second step will be carried out using the sensors and actuators [9].

The initial alignment takes place once the magnets are installed on their jacks, before the interconnection and cool-down operations are completed. Each cryostat is aligned independently with respect to the underground geodetic network using its external fiducials within ± 0.25 mm (1σ). Once the initial alignment has been carried out, the interconnection phase can start.

15.7.5 Alignment sensors and actuators

The requirements concerning the alignment of the components from Q1 to Q5, are the following [10]:

- The mechanical axes of the magnets included in a cylinder with a radius of 0.1 mm (Figure 15-14 left).
- The mean axis of the right side included in a cylinder with a radius of 0.15 mm around the mean axis of the left side (Figure 15-14 right).

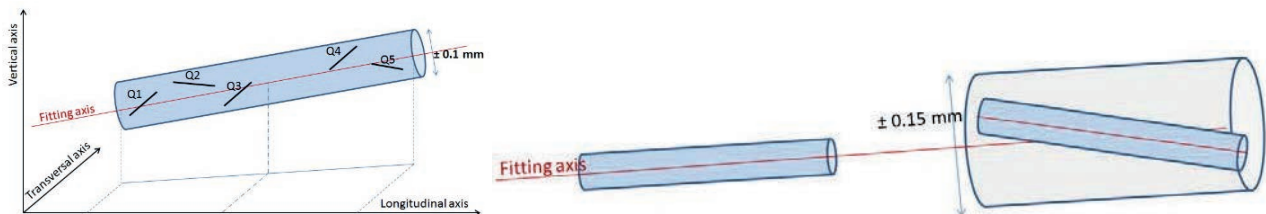


Figure 15-14: requirements concerning the mechanical axes of the magnets.

The same alignment solution than for the LHC low beta triplets is proposed [10], extended from Q3 to Q5.

Each cryostat from Q1 to Q5 will be equipped with 2 capacitive Wire Positioning Sensors (cWPS) and 3 Hydrostatic Levelling Sensors (HLS). The cWPS provide 4 DOF (pitch & yaw rotations, vertical and radial translations), and Hydrostatic Levelling Sensors (HLS) the roll plus redundancy in the determination of vertical translation and pitch rotation. The HLS sensors will also determine continuously the catenary shape of the stretched wire. In case of longer cryostats supported by an additional central jack to support the sag of the cryostat, a fourth HLS sensor will be installed on the cryostat on top of the 4th central jack. Figure 15-15 illustrates the configuration of sensors on the inner triplet.

The determination of the longitudinal position of each cryostat w.r.t to the tunnel floor will be achieved by installing a capacitive sensor on a special support on the tunnel floor. The capacitive sensor will measure the distance to a target rigidly linked to the cryostat.

Diagnostic devices associated with each alignment system will carry out the remote validation of the sensors. Prototypes are already in place in the LHC.

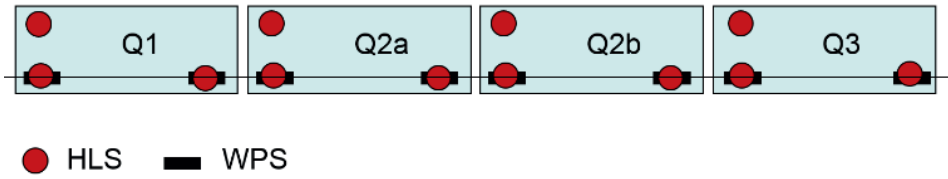


Figure 15-15: configuration of sensors on the inner triplet.

Several improvements are proposed for HL-LHC to limit the measurements interventions in the LSS areas around Point 1 and Point 5:

- A mechanical system will be designed to monitor continuously the difference of height between the 4 deep references used as vertical absolute reference in the tunnel (in RB14, RB16, RB54 and RB56) to the closest HLS sensor.
- A HLS located after Q5 will provide a LSS vertical reference for the levelling of the arcs.

To link the left and right sides of tunnels on each side of ATLAS and CMS caverns, the same solution presently used for the LHC is proposed, as it fulfils the requirements:

- A 120 m wire stretched in the dedicated UPS galleries and along the IP1 and IP5 cavern (same location than for the LHC) will be combined with cWPS, mechanical systems and capacitive sensors to determine at a micrometric accuracy the distances between tunnel and UPS wires, at 6 locations.
- Left and right sides of tunnel will be linked vertically by HLS system

Figure 15-16 and Figure 15-17 show a top view of the general configuration of sensors around the two sides of an experimental cavern respectively for the radial and vertical determination.

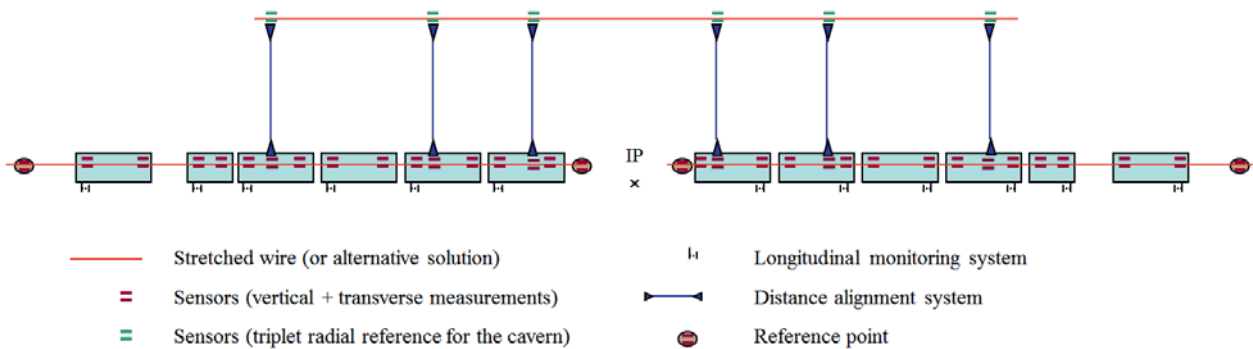


Figure 15-16: radial configuration of sensors around IP.

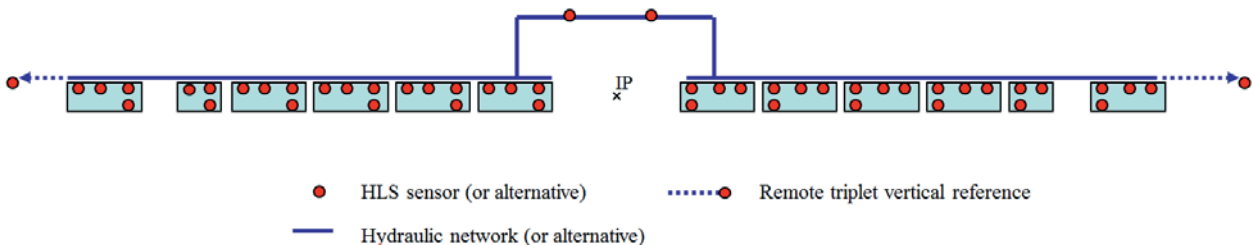


Figure 15-17: vertical configuration of sensors around IP.

The cWPS installed in the UPS galleries and the HLS sensors installed in the caverns will provide machine references in the experimental areas [11].

Once the position of the cryostats is determined by the sensors and if the misalignments become too important, the remote adjustment of each cryostat will be carried out. The jacks supporting the cryostat will be motorized according to 5 degrees of freedom (the longitudinal axis will be anchored on the ground for some of the components). The motorisation solution shall fulfil the following requirements: a resolution of displacement below 10 μm , over a stroke of ± 4 mm. The remote adjustment system shall provide a high stiffness to the cryostat support, with the first Eigen frequencies as high as possible.

The HL-LHC collimators located in the Q1-Q5 area, or just after, will be equipped with the same alignment systems than the other components to allow the remote determination of their position. This should be combined with a remote adjustment system. Dedicated solutions of remote determination and adjustment for the other collimators to be installed are under study [12].

15.8 References

- [1] Marin, A. et al., Radiation tolerance of positioning sensors and their conditioners used for LHC low beta magnets, 8th IWAA, CERN, 2004
- [2] Fitterer, M et al., Crossing scheme and orbit correction in IR1/5 for HL-LHC, 6th International Particle Accelerator Conference, Richmond, VA, USA, 3 - 8 May 2015, pp.TUPTY036. [CERN-ACC-2015-0014](#)
- [3] Missiaen D., Quesnel J.-P., Fiducialisation of the LHC Cryo-Dipole Magnets, EDMS: [110632](#), June 2000.
- [4] Quesnel J.-P., Alignment Targets, EDMS: [90314](#), March 1999.
- [5] High-Luminosity Large Hadron Collider (HL-LHC) : Preliminary Design Report DOI: [10.5170/CERN-2015-005](#)
- [6] Artoos, K. et al., Compact crab cavity cryomodule. [CERN-ACC-2015-0130](#)
- [7] Quesnel J.-P., Schmitt J., "Marking on the Floor in the LHC and Transfer Tunnels (TI2 & TI8)" – Interface specification, EDMS: [311753](#), November 2001.
- [8] Quesnel J.P, Positioning of the jacks of the cryomagnets, EDMS: [311752](#), March 2002.
- [9] Quesnel J.-P., The First Positioning of the LHC Cryomagnets (Arcs and DS), EDMS [311755](#), November 2001.
- [10] Mainaud Durand H., Alignment requirements for the LHC low beta triplets, EDMS: [344496](#), August 2002.
- [11] Hatch C., Lasseur C., Lissauer D., Alignment of the ATLAS Experiment with the LHC Beam, EDMS: [320043](#), May 2001.
- [12] Duquenne, M. Les collimateurs du LHC, EDMS [1576640](#).
- [13] Baudrenghien, P et al. Functional Specifications of the LHC Prototype Crab Cavity System [CERN-ACC-NOTE-2013-003](#)

Chapter 16

Operation, Commissioning and IT String

16 Operation, Commissioning and IT string

16.1 Operation definitions and parameters

By the time of the commissioning and subsequent operation of the HL-LHC, the LHC itself will have been operational for over 10 years and a wealth of knowledge and experience will have been built up. The key operational procedures and tools will have been well established. The understanding of beam dynamics will be profound and refined by relevant measurement and correction techniques. Key beam-related systems will have been thoroughly optimized and functionality sufficiently enhanced to deal with most challenges up to that point. Availability will have been optimized significantly across all systems. This collected experience will form the initial operational basis following the upgrade.

However, the HL-LHC will pose significant additional challenges. The target integrated luminosity will make considerable demands on machine availability and operational efficiency. The planned beam characteristics will push beam dynamics to new limits. The availability of beam with HL-LHC characteristics following the injector upgrades in LS2 should certainly be used as an opportunity to gain experience with the challenges of high intensity, high brightness beam. In the following discussion the operational cycle is revisited in light of the key HL-LHC challenges. The expectations and issues relating to availability in the HL-LHC are then outlined.

The planned bunch intensity, β^* , and compensation of the geometrical reduction factor lead to a potential bunch luminosity well above the acceptable maximum in terms of pile-up for the experiments. Thus, as discussed in Chapter 2, an obligatory operational principle of the HL-LHC will be luminosity levelling. The aim is to reduce a potential peak or virtual luminosity to a more manageable levelled value by some luminosity reduction technique. As the number of particles in the beam falls with time, appropriate adjustments keep the luminosity at the levelled value. The options include the use of transverse offsets, crab cavities, variation of the crossing angle, and dynamic change of β^* . A combination (e.g. dynamic change of β^* , crossing angle, and crab cavities) will be deployed. This might take the form of, for example, maximum anti-crabbing with the help of crab cavities and dynamic adjustment of β^* and crossing angle so that the maximum crab cavity voltage is only required at the end of a fill where smaller crossing angles can be tolerated. The longitudinal pile-up density is another critical parameter for the experiments, which must be taken into account during the levelling process.

16.1.1 The nominal cycle

The nominal operation cycle provides the framework underpinning luminosity production. Given the higher than ever stored beam energy during the HL-LHC era, the nominal cycle must be fully mastered for effective, safe operation. As of 2016, the nominal operational cycle is well established for operation with 50 ns bunch separation and with bunch population exceeding nominal and for operation with 25 ns bunch separation with nominal bunch population. A brief outline of the phases of the nominal cycle follows.

- Pre-cycle: Following extensive experience during Run 1, it is known that the magnetic state of the machine can be re-established before every fill by rigorous application of either a combined ramp-down/pre-cycle of the main circuits and a de-gaussing of the corrector circuits, or, following an access, by a full pre-cycle of all circuits. In the former, the main circuits are simply ramped down from their

high energy current values to below injection level and not taken through a low-high-low current phase as in the full pre-cycle case. This saves considerable time. Set-up: The machine settings are verified with the injection of a limited number of bunches: first one probe bunch followed by, typically, 12 nominal bunches. A circulating probe bunch is a machine protection prerequisite for the injection of nominal bunch population.

- Injection: The two LHC rings are progressively filled with trains of bunches transferred from the SPS to the LHC. The injection process should be well optimized by the time of the upgrade. However, high bunch intensities will have to be anticipated and all necessary mechanisms to minimize particle loss and emittance blow-up, and to maximize reproducibility, should be deployed.
- Ramp: Once the machine is filled with the required number of bunches, the beams are accelerated to top momentum (7 TeV/c for the nominal LHC configuration with the LHC originally designed for an ultimate beam momentum of ca. 7.5 TeV/c). The ramp should hold no surprises. The characteristics of snap-back and correction of associated parameter swings can be taken as given. The 10 A/s ramp rate for main dipole power converters will still hold. Transverse feedback and tune feedback, and their healthy cohabitation, should be anticipated. Orbit feedback will be mandatory. Controlled longitudinal blow-up will be required.
- Squeeze: The mechanics of the squeeze including feedback will have been fully mastered by the time of the HL-LHC. Issues of beam instabilities should have been resolved and might include squeezing with colliding beams. Again, this should have been made operational before the HL-LHC era. Combining part of the squeeze in the ramp to reduce the time required for the high-energy squeeze process was deployed in 2016.
- Adjust: At the end of the squeeze the beams are brought into collision at the interaction points. There is some flexibility in sequencing the order in which the beams are collided in the different interaction points. The process is relatively fast and will be well established.
- Stable beams: Once all the above procedures are completed and no abnormal conditions are detected, the conditions are met for safely switching on the detectors and the start of data taking. In general, this phase is expected to be stable with sufficient Landau damping from beam-beam, and only small movements of the beam overlap thanks to good orbit stability. Emittance growth and losses to the collimation regions must be anticipated.

The principal challenges during the cycle involve injection, and transmission through the cycle of high bunch and high beam current, while preserving emittance. Given the experience of LHC operations thus far, the following potential issues may be identified:

- electron cloud;
- UFOs;
- localized beam-induced heating of specific hardware or vacuum assembly non-conformities – this can result in outgassing and bad vacuum as a result;
- emittance growth due to Intra Beam Scattering (IBS) – requiring a minimization of the injection time and a controlled longitudinal emittance blowup throughout the whole operation cycle;
- cryogenic heat load;
- excessive beam loss in the cleaning sections. The losses can be triggered by: beam instabilities, halo formation, and fast halo removal during the adjust process.

High bunch population implies the need for very good parameter control and the need to properly control beam loss through the cycle. Hardware systems such as power converters, RF, and transverse dampers have already demonstrated impressive performance. Beam instabilities will have to be fully under control using a variety of measures. Low β^* implies strong non-linearities from the inner triplets and the need for associated

correction. On the positive side, the HL-LHC should, in general, be able to count on excellent magnetic reproducibility and good stability. However, the stability and reproducibility of the new triplet magnets and the D1 and D2 magnets will be the most critical sources of non-linear fields. All these magnets will be new for the HL-LHC and, as yet, there is no experience on the magnet reproducibility of these elements. The triplet magnets, in particular, will be based on a new magnet technology and magnet design.

16.1.2 Availability and operational efficiency

The terms relevant to the year-long operational view are defined below.

- Scheduled proton physics time (SPT) is the time scheduled in a given year for high luminosity proton physics. It does not include initial re-commissioning, special physics runs, ions, machine development (MD), and technical stops. It does include the intensity ramp-up following re-commissioning at the start of the year. Note that high luminosity running involves a number of challenges not present in other modes of operation, and different machine availability can be expected.
- Availability is the SPT minus the time assigned to faults and fault recovery. It is normally expressed as a percentage of the SPT. Edge effects (e.g. recovery from access, the pre-cycle) should be fully included in the assigned fault time.
- The turnaround time is defined as the time taken to go from Stable Beam mode back to Stable Beam mode in the absence of significant interruptions due to fault diagnosis and resolution.
- Physics efficiency is the fraction of the SPT spent in Stable Beams.

16.1.2.1 Standard year of operation

The longer-term operational planning consists of a series of long (~39 weeks) years of operation (see Table 16-1) interspersed with long shutdowns of the order of a year or more. The long shutdowns are foreseen for essential plant maintenance, experiment upgrades, and so forth. It is estimated that the required length of a standard long shutdown in the HL-LHC era will alternate between 16 and 20 months. The approximate breakdown of a generic long year is:

- 13 weeks for the year-end technical stop (YETS), including two weeks for hardware commissioning (this would account for three weeks at the end of a year and for 10 weeks at the start of the following year);
- around 160 days proton-proton operation;
- three technical stops of five days duration during the year;
- a four-week ion run (the current planning is based on the approved ion program which will take place during Run 3 and Run 4 and not beyond);
- around 22 days of machine development (this could be suppressed fully or partially after Run 4);
- time dedicated for special physics – this could include, for example, reference data with protons at ion nucleon-nucleon equivalent energy (again this could be suppressed fully or partially after Run 4).

A more detailed breakdown is shown in Table 16-1

Table 16-1: Potential breakdown of a standard HL-LHC year until end Run 4.

Activity	Time assigned [days]
Christmas technical stop including hardware commissioning	91
Commissioning with beam	21
Machine development	22
Scrubbing	7 (to 14)
Technical stops	15
Technical stop recovery	6
Proton physics including intensity ramp-up	160
Special physics runs	8
Ion run setup	4
Ion physics	24
Contingency	7

16.1.2.2 Availability and operation efficiency

The HL-LHC will place challenging demands on availability and operational efficiency if the ambitious integrated luminosity goals are to be met [1]. Given that the requisite high intensity beam can be injected, ramped, squeezed, collided, and the luminosity levelled, the principle operational challenges will be assuring high availability and maximizing physics efficiency.

16.1.2.3 Faults

Faults cover an enormous range from a simple front-end computer reboot to the loss of a cold compressor with corresponding loss of time to operations ranging from 10 minutes to potentially days. The impact of a typical fault requiring tunnel access shows the following sequence of steps from the occurrence of the original fault through to full recovery.

- Premature beam dump in stable beams.
- Original diagnosis of fault by control room operator – contact expert.
- Remote diagnosis by expert.
- Access required and prepared.
- Travel of expert to site. Travel of radiation protection piquet to site.
- Intervention, on-site diagnosis, and repair by expert.
- Recovery from access.
- Recovery from the impact of the fault (for example, cool-down following quench).
- Re-establish machine state: pre-cycle, injection, etc.

It can be seen that, besides the cost of fixing a fault, there are also significant additional overheads. Faults often dump the beam with the cost of at least a full turnaround to re-establish the state of the machine. The cost in turnaround time and the fault recovery components are examined in more detail below.

16.1.2.4 Turnaround time

A breakdown of the foreseen HL-LHC turnaround time is shown below.

Table 16-2: Breakdown of turnaround and estimated minimum time for each phase.

Phase	Time [minutes]
Ramp-down/pre-cycle	60
Pre-injection set-up	15
Set-up with beam	15
Nominal injection	20
Prepare ramp	5
Ramp	25
Flat-top	5
Squeeze	25
Adjust/collide	10
Total	180

From Table 16-2, one can see that realistically a three-hour minimum turnaround time may be assumed in the HL-LHC era. The main components are the ramp-down from top energy, the injection of beam from the SPS, the ramp to high energy, and the squeeze. The ramp-down, ramp and squeeze duration are given by the current rate limitations of the power converters. Of note is the 10 A/s limit up and down for the main dipoles, the need to respect the natural decay constants of the main quadrupoles, the individually powered quadrupoles, and the triplets during the ramp-down and the squeeze. These quadrupoles are powered by single quadrant power converters, and it takes a considerable time for the current to fall to the required level. Ramp-down times were improved at the start of Run 2 by moving to open loop control. A faster squeeze via upgrades to selected power converters might be anticipated. The triplet magnets of the HL-LHC will be equipped with 2-quadrant power supplies removing them as a potential bottleneck.

In practice, the turnaround has to contend with a number of issues that could involve lengthy beam-based set-up and optimization. Typical beam-based optimization might include the need to re-steer the transfer lines, occasional energy matching between the SPS and LHC, and the need for the SPS to adjust scraping during the injection process. Injector and LHC tuning and optimization are accounted for in the average turnaround time.

16.1.2.5 Lost fills and fill length

Another important consideration directly impacting operational efficiency are the overheads of losing a fill (in the ramp, in the squeeze, in physics). In 2012, for example, 70% of all fills were terminated by a fault with costs ranging from a full turnaround plus fault recovery time to curtailed stable beam time. In 2012, having made it into Stable Beam, operations experienced a lot of short unproductive fills because of premature dumps. The cost of the short fills is a corresponding number of extra turnarounds that directly lead to lost time for physics. All means must be used during Run 2 and Run 3 to target all causes of premature dumps. Some evidence of success in this area was observed in 2016. In the HL-LHC era a choice of robust operating parameters and loss mitigation measures must be made to avoid losing fills to high beam loss and instabilities during the cycle. These measures might include, for example, depleting the beam halo population via tune modulation or hollow electron lens.

16.1.3 Discussion

A number of studies have been made that model the potential integrated luminosity that can be delivered by the HL-LHC at a levelled luminosity of $5 \times 10^{34} \text{ cm}^{-2} \text{ s}^{-1}$. All conclude that it will be challenging to deliver of order 230 to 240 fb^{-1} per year. Every attempt must therefore be made to target high availability, shorter turnaround times, and a low number of premature dumps. Some of the main areas that might be, and have been, targeted in the interest of improved availability and operational efficiency have been identified:

- Reduce the number of faults (hardware and software) – this is the natural target for improved availability. It requires targeted improvements and consolidation across all systems.
- Reduce time to fix faults, reduce intervention times, and reduce the number of tunnel interventions (for example by universal remote reset functionality, improved remote diagnostics, or increased redundancy).
- Reduce the need for tunnel interventions by removing equipment from the tunnel. Indeed this one of the key motivations for the new HL-LHC installations. These will allow access to the new galleries and shafts while beam is in the machine.
- Reduce number of beam-induced faults (radiation to electronics (R2E), beam-induced heating, vacuum issues).
- Reduce the mean turnaround time. Here it is possible to imagine targeting routine optimization, test runs, and the nominal cycle.
- Choose a robust set of beam parameters and implement mitigation measures to avoid unnecessary dumps from beam-related issues.

16.2 Hardware commissioning

16.2.1 Commissioning of the superconducting circuits

16.2.1.1 Testing of the superconducting links in short-circuit configuration

All superconducting links [2] will be individually (cryogenically and electrically) tested in the SM18 magnet test facility prior to installation in the tunnel. As is the case for all superconducting elements installed in the machine, these links will have to be further tested in situ to assess that no degradation occurred during transport and installation.

A test similar to those currently performed on the warm part of all superconducting circuits is suggested, with one extremity in short-circuit configuration: the electrical connections to the power converters are the nominal ones; the conductor at the other extremity of the link is not connected to the magnets, but short-circuited, in a configuration that allows powering up to the nominal current of all busbar pairs. The link will have to be cooled down to its nominal temperature; thus the configuration and the precise place of short-circuit installation will be decided in accordance with the final design of the connection boxes, also taking into account the planning constraints.

Once the short-circuit is installed and the nominal cryogenic conditions established, a high voltage qualification (EIQA) of all lines will be performed in order to validate the galvanic insulation versus ground and the capacity of all lines to withstand the mutual high voltages developed during a fast change of current in the different circuits (typically during a fast abort or quench). The values of voltages to be applied and the maximum acceptable leakage current values will be defined at a later stage.

After the EIQA validation, all lines can be powered. The powering will consist of several phases, each of them to be analyzed and approved by the experts, before progressing to the next phase. At each phase the cryogenics team will have to verify the correct behaviour of the cryogenic system and cooling loop. Each circuit should be powered to increasing current levels (e.g. minimum operational current, 25% of nominal, 50% of nominal, and nominal current). At each current level, the powering, protection, and cryogenic systems will be qualified. The detailed steps and qualification criteria will be identical to those prepared for SM18 and will have to include the simultaneous powering of different circuits, and stress tests such as the fast discharge of a line with all of the others powered at nominal current in order to study the cross-talk between them.

16.2.1.2 Electrical Quality Assurance tests

As stated in [3], the objective of the EIQA tests is to release each individual superconducting circuit for powering, to gather all the necessary electrical parameters for operation, and to track all the data acquired and to manage the related non-conformities.

16.2.1.2.1 EIQA at warm

At the end of the installation and connection of all magnets, resistance measurements and a high voltage qualification of all circuits will be performed: to check whether the circuit is closed, determine a reference resistance value at warm, and to validate the galvanic insulation versus ground. The values of voltages to be applied and the maximum acceptable leakage current values will be defined at a later stage.

16.2.1.2.2 EIQA at cold

Similar tests will be performed at cold, with larger test voltages applied. The circuits and the corresponding link will be cooled down to their nominal temperature. For the high voltage qualification of all lines, this will be performed to validate the galvanic insulation versus ground and the capacity of all lines to withstand the mutual high voltages developed during a fast change of current in the different circuits (typically during a fast abort or quench).

The high voltage qualification also includes testing of all the elements that are electrically connected to the tested circuit. Such elements are:

- the instrumentation and feedthrough systems;
- the magnet protection units;
- the temperature sensors with the related tunnel cabling and electronics;
- the tunnel cabling for routing the voltage taps used for the protection of the superconducting circuits.

In addition, transfer function measurements will be performed, with the aim of determining the impedance as a function of the frequency. The results of these measurements are used to spot possible inter-turn shorts, and by the power converter group to adjust the power converter regulation.

16.2.1.3 Powering tests

The HL-LHC magnets present several peculiarities [4] that have to be kept in mind for their commissioning. The most relevant are: the fact that the vast majority of magnets will be cooled down to 1.9 K (with only a small number of matching section magnets at 4.5 K); that Nb₃Sn will be used extensively for the first time; that the current of the inner triplet will be the highest in the machine (18 kA); and, importantly, that some of the high current magnets will be protected only via energy extraction in a dump resistor without quench heaters. In addition, the powering scheme of the inner triplet will be different from the present one with implications in case of a quench of one of the magnets (see chapter 3). There will be 11 T magnets in the DS where NbTi and Nb₃Sn magnets will be powered in series with powering via a superconducting link.

The powering of all circuits up to nominal current will be done in steps. At the end of each step, online and offline analyses are performed by equipment owners and protection experts to assess the performance of all hardware in the circuit. In particular, for the powering of individual circuits, several cycles at different current levels will be performed to study the performance of the magnets, the efficiency of the protection mechanisms (by provoking fast aborts and even quenches), and to check all functionalities of the powering interlocks and of the power converters (via provoked powering failures).

A typical series of tests includes:

- at minimum operational current, testing of the full interlock chain, with the verification of cryogenic signals, power permit, powering failure, circuit quench transmission, and fast power abort requests;

- at low current, a check of the power converter performance and verification of all protection functionalities, by means of provoked slow and fast power aborts, with energy extraction;
- repetition of a series of power aborts and, possibly, simulation of quenches from progressively higher current levels, with more and more energy stored (e.g. 25%, 50%, and 100% of the nominal current).

Before starting a new powering test, all previous tests must have been validated. The validation includes approval by power converter and powering interlock experts, magnet owners, and protection experts. Cryogenics experts should also confirm the correct operation of their installations and instrumentation. The criteria for approval, the parameters, and the relevant information to be stored will be discussed in due time. The first time that these will be applied is when the test of a full string of magnets (reproducing from Q1 to D1) is foreseen (see 16.5), powered by a superconducting link. All valuable data extracted from the test on the string will be translated in powering procedure steps and criteria.

After the individual test of all circuits up to the design current, the common powering of a set of circuits will be done for magnets that are in the same cryogenic envelope and are powered from the same link (usually referred to as the powering of a group of circuits). The objective of this simultaneous powering is to validate operation of all magnets in nominal conditions; current cycles similar to those applied in normal operation should be used for the powering of a group of circuits. Important at this stage is the behaviour with combined powering in critical conditions, such as the fast power abort of a circuit when the others are at full current. For the inner triplets, in particular, quenching in a triplet quadrupole might induce a quench in a nearby quadrupole or corrector if the current in this related circuit is not extracted fast enough. These tests should be performed on all the magnets and could well trigger the change of detection thresholds and protection configurations. Once more, all tests should be approved by a group of experts and recorded for future reference.

Particular attention also has to be paid to those circuits that are not equipped with heaters and are protected by energy extraction on a dump resistor. For such circuits, a precise estimate of the energy deposited during a quench has to be made, not only in the case of bench tests, but also in the more severe conditions of combined powering in the tunnel. Eventually, the protection threshold should be adapted to reduce energy deposition and improve magnet safety during powering.

16.2.1.4 Magnet training

Operations at 7 TeV should be established during Run 3. In the process extensive experience will be gained with the required dipole training to get to the requisite current level. The effects of a full thermal cycle will also be given by commissioning following LS2. A sound estimate of the number of quenches required following LS3 will thus be possible and well optimized procedures will be in place to assure an effective retraining campaign. Sufficient time should be foreseen in the schedule for this phase.

16.2.2 Hardware commissioning of the HL collimation system

The mechanics and controls of the collimation system should be identical to that of the Run 3 configuration and required tools should be well debugged and validated by the time of the HL-LHC. The collimator settings, controls, and operational sequences should be intensively re-tested during the hardware commissioning phase [5]. A dedicated test to address the reproducibility of collimator movements during critical operational sequences (such as the ramp) will be performed. At this stage the collimators should have been fully installed and the local collimator controls in the tunnel fully validated.

Before beam is injected into the machine, the machine protection (MP) functionality of the collimation system must be guaranteed. Each collimator is connected to the beam interlock system (BIS) and has more than 20 interlocks that will need to be verified. The jaw positions and collimator gaps are monitored via six linear variable differential transformer (LVDT) sensors. These signals are interlocked with inner and outer limit values, making a total of 12 interlocks per collimator. In addition, there are a total of six energy-dependent and β^* -dependent limit functions and an interlock to protect from 'local' mode collimation control. The temperature of the collimators is also monitored and interlocked with minimum and maximum adjustable

thresholds independently for five sensors per collimator. After successful results from these tests, the system will be ready to allow beam into the machine.

The main upgrade of the collimation system for HL-LHC [5] will ensure cleaning of beam halo and will keep losses in high luminosity experimental regions at an appropriate level. For this, the project foresees the installation of local collimation in the dispersion suppressors. The design of a collimator to be installed between two short 11 T dipoles is ongoing. These collimators will feature the latest design improvements, including embedded BPMs for fast alignment. Unlike other hardware commissioning tests (such as the magnets), most of the collimation commissioning can be done parasitically, the main exception being the testing of the interlock system where the BIS needs to be available.

16.2.3 Commissioning of the cryogenic systems

The HL-LHC foresees numerous modifications of the cryogenic system [6]. Among them are:

- The power upgrade for IR1 and IR5;
- the decoupling of the SRF in P4 from the arc magnets;
- the new cooling system for the superconducting links;
- the modifications to cool the elements that previously were at 4.5 K to 1.9 K;
- the cooling loop for the crab cavities, and much more.

The operation of all of them, together with the time needed to qualify and tune the systems, will be detailed once the design is definitive. Provisionally, an approximate time of three weeks is considered to be mandatory to commission the scheme for the superconducting magnets.

16.2.4 Commissioning of the crab cavities

As for all elements in the LHC, the crab cavities will be first tested on the surface to nominal specification prior to installation in the tunnel. In addition, some modules will be installed in the SPS for a complete qualification of the standard two-cavity module with LHC-type beams. This is presently planned for the 2018 run after the year-end technical stop.

The test of the cavities can be differentiated into the commissioning of the RF cavities and associated ancillary systems (cryogenics, vacuum), and RF commissioning with beam. The requirements in terms of time and manpower will be assessed later.

Concerning the commissioning of the cryogenics, the correct operation of the cooling loop and the capacity will be verified, together with the expected behaviour of the instrumentation; proper verification criteria and sequence will be defined at later time with input from the qualification of the cryogenic-module on the surface tests. The vacuum integrity and the vacuum interlocks will be tested as well, which should cut the RF power in case of issues and during cavity conditioning.

The conditioning of the cavities will first be performed on the surface in the nominal configuration, but the commissioning of the low-level RF system (the tuning control, the regulation loop around the amplifier, plus the RF feedback) will have to be validated in the SPS for the first time in its nominal configuration. A detailed procedure for the verification of all functionalities will be prepared well in advance. The information and issues arising from these tests will directly help in the efficient commissioning of the system in the LHC.

All possible RF manipulations foreseen for the LHC operation cycle will first be performed without beam. An important verification concerns the efficiency of the fast feedback of the cavity field. The delay loops in the SPS between the two cavities will be arranged to mimic the cavity setup in the LHC to both ensure the fast and independent control of the cavity set point voltage and phase, and the slower loop to regulate the cavities on either side of the IP. This is essential to ensure machine protection in the event of an abrupt failure of one of the cavities.

16.3 Commissioning with beam

One is fully able to draw on past experience in outlining a commissioning plan for initial operation following LS3. A skeleton plan is shown in Table 16-3.

Table 16-3: Outline of initial commissioning following LS3.

Phase	Key objectives
Injection and first turn	Injection region aperture, injection kicker timing
Circulating beam	RF capture, beam instrumentation, initial parameter checks
450 GeV initial commissioning	Transfer line and injection set-up, orbit,
450 GeV measurements and setup	Beam instrumentation, optics, aperture, collimation, LBDS
450 GeV two-beam operation	Separation bump checks, beam instrumentation
Ramp	Snapback, chromaticity control, orbit and tune feedbacks
Flat-top checks	Collimation, optics, orbit, decay
Squeeze	Optics, collimation set-up
Validation	Loss maps, asynchronous dumps
Collide	First stable beam with a low number of bunches

The initial commissioning phase should evolve through initial set-up, system commissioning through the nominal cycle, standard measurement and correction, set-up of protection devices, and validation. It is a relatively complex phase with necessary interplay between the various teams to allow beam-based commissioning of systems such as tune and orbit feedbacks, transverse dampers, RF, etc. under appropriate conditions at the various phases of the operational cycle.

The aims of the initial commissioning phase are as follows.

- Establish nominal cycle with a robust set of operating parameters. This will include commissioning of the squeeze to an appropriate β^* with measurement and correction of the optics and key beam parameters at each stage. One should not expect to probe the limits of the HL-LHC parameter space at this stage.
- Measure and correct the optics. Measure the aperture.
- Set-up injection, beam dump, and collimation, and validate set-up with beam.
- Commission beam-based systems: transverse feedback, RF, injection, beam dump systems, beam instrumentation, and orbit and tune feedbacks.
- Commission and test machine protection backbone with beam.
- Check the understanding of magnet model and higher order optics.

The initial commissioning phase is performed at low intensity, with a low number of bunches, and a generally safe beam. The output of this phase is taken to be first collisions in stable beams with a small number of bunches. Following this, pilot physics can be delivered with up to 100 widely spaced bunches. Scrubbing will then be required before entering the intensity ramp-up phase. Scrubbing could well follow the two-stage approach deployed following LS1. This approach is outlined below.

- Initial scrubbing with 25 ns beam following initial commissioning opening the way for a period of 25 ns operation with non-nominal batch spacing.
- Initial intensity ramp-up with 25 ns is then foreseen. During this stage, system commissioning with higher intensity continues (instrumentation, RF, injection, beam dumps, machine protection, vacuum, etc.). Variables at this stage include: bunch intensity, batch structure, number of bunches, and emittance. Physics fills can be kept reasonably short. The intensity ramp-up is performed in a number of clearly defined steps with associated machine protection and other checks. This phase will be used to characterize vacuum, heat load, electron cloud, losses, instabilities, UFOs, and impedance.

- Thereafter a further scrubbing period with 25 ns and possibly the doublet beam is foreseen.
- This is followed by an intensity ramp-up with 25 ns dictated by electron cloud conditions, with further scrubbing as required. 2016 experience indicates that a sustained period of physics in the presence of electron cloud will be needed.

Important beam-related characteristics such as lifetime, beam loss through the cycle, stability, quench levels, and UFO rates will only become fully accessible with an increase in bunch intensity and number of bunches during the intensity ramp-up phase.

16.4 Operation with heavy ions

In a typical LHC operating year, one month is reserved for the nuclear collision programme. Operation with ions is planned at least until the end of LHC Run 4, the first HL-LHC run.

16.4.1 Pb–Pb operation

Collisions of fully stripped $^{208}\text{Pb}^{82+}$ nuclei are requested by the ATLAS, ALICE, and CMS experiments. These heavy-ion runs will generally be scheduled following an extended period of p–p operation. The reduced activation of the LHC and injectors will allow interventions to start promptly in the subsequent shutdown periods. The runs will be short, typically of a total of one month, and there is a high premium on rapid commissioning of collision conditions with full luminosity within a few days. The Pb-Pb upgrade, including a major upgrade to the ALICE detector, will take place in LS2 and all procedures and systems should already have been commissioned during Run 3 of the LHC. The only exception are the new insertion magnets, which will have been commissioned during the preceding proton operation of Run 4.

To minimize commissioning time, the heavy-ion magnetic cycle will generally exploit the magnetic reproducibility of the LHC and equal magnetic rigidity of the beams to use as much as possible of the cycle previously established for proton beams. Due care must nevertheless be taken to reproduce the same orbits in the higher-sensitivity mode of the beam position monitors and to adjust the RF frequencies to capture the ion beams [7]. However the collision optics will always be different and a new squeeze process will have to be established to provide a low $\beta^* = 0.5\text{--}0.6\text{ m}$ at the ALICE experiment with similar values (generally not as low as for protons) at ATLAS and CMS. Crossing angles will also be changed, with that of ALICE carefully minimized for the benefit of its zero-degree calorimeter. With the 50 ns bunch spacing, the minimum acceptable separations at parasitic encounters will be established empirically [8][9]. In all cases, the validation of the collimation configuration and machine protection will be an essential step in the set-up of heavy-ion physics conditions. During each run, a reversal of the ALICE spectrometer magnet polarity and flipping of the crossing angle should be foreseen [8].

Controlled blow-up of the longitudinal emittance, using RF noise with a spectrum focussed on the core of the bunch, will play an important role in minimising transverse emittance blow-up due to intra-beam scattering at injection [9] and, very likely, also during stable beams.

Because of the very rapid luminosity burn-off (halving in about two hours with three experiments active), the fills will be short and frequent refilling and recycling of the machine will be required, typically four times per day. Although the experiments will be able to handle the highest peak luminosity foreseen, it may nevertheless be useful to briefly level the luminosity with separation at the start of fills to reduce the intensity burn-off during the initial set-up of collision conditions. This will have negligible impact on average daily luminosity.

Secondary beams created in the collisions [9] [10] will impinge on the beam pipe in the dispersion suppressors on either side of each collision point. The power in these beams is directly proportional to the generated luminosity at the IP and have been shown to be sufficient to quench a superconducting magnet for the ALICE upgrade goals, and counter-measures will have to be applied immediately when the beams are put into collision. The most effective are expected to be the dispersion suppressor collimators [9], which will be

positioned during the squeeze process. Initially these will be installed in IR2 for the ALICE experiment. The attainable peak luminosity for ATLAS and CMS will be maximized using an orbit bump technique that will spread the losses over a larger area. If necessary, similar collimators may be installed in IR1 and IR5 later. In any case, the dump thresholds for the beam-loss monitors in the dispersion suppressors will have to be carefully adjusted.

Because of the more complicated nuclear and electromagnetic processes that can occur when lead ions interact with the material of the collimators, collimation efficiency will be lower than for protons and quite different loss patterns are expected [11]. Here, again, the energy deposition from the losses may approach or exceed quench levels and may necessitate the installation of dispersion suppressor collimators in IR7.

16.4.2 p–Pb operation

Asymmetric collisions of protons with $^{208}\text{Pb}^{82+}$ nuclei are requested by the ATLAS, ALICE, CMS, and LHCb experiments. The smaller forward detectors installed around the ATLAS and CMS interaction points also study these collisions. These runs are scheduled in place of the Pb–Pb runs, to a similar timetable, during a fraction of the operating years.

The feasibility of this complex mode of operation, unforeseen in the original LHC baseline design, was demonstrated by the first runs in 2012 and 2013 [11]. Proton beams will be injected first since the Pb beams suffer more from intra-beam scattering at injection energy. The RF frequencies corresponding to capture of the two beams on their central orbits are significantly different at injection energy, requiring the RF systems of the two rings to operate independently. At collision energy the frequencies will be locked together, displacing the proton orbit outwards and the Pb orbit inwards, by a small fraction of a millimetre, onto off-momentum orbits. A ‘cogging’ procedure, again using RF frequencies, will be used to move the collision points to their proper locations in the experiments [12].

Proton–lead runs place a number of requirements on the filling schemes. The basic bunch spacing must be created by both the heavy-ion and proton pre-injector chains to ensure that the bunch patterns largely match each other. The trains must be distributed to provide an appropriate share of collisions in each experiment. As seen in 2013, this can result in a complicated set of beam–beam encounter classes, bunch parameters, and lifetimes. In general, the proton beam size at the collision points will be smaller than the Pb beam, a circumstance that further reduces the lifetime of the Pb beam.

As in Pb–Pb operation a new squeeze process will have to be commissioned, including all four experiments, with different end-points. This will generally be prepared and corrected first, using on-momentum proton beams. Pre-computed chromatic corrections [12] will be incorporated for the final off-momentum squeeze.

Rapid luminosity burn-off of the Pb beam on the proton beam will determine the length of fills. The luminosity will be essentially proportional to the Pb beam intensity, and the integrated luminosity delivered per fill summed over all experiments will be a fraction of N_{Pb}/σ_b where N_{Pb} is the total number of Pb ions in the beam at the start of collisions and σ_b is the cross-section for luminosity burn-off in p–Pb collisions. The role of the proton bunch intensity is only to determine the lifetime of the Pb beam and the length of the fill. Values a few times less than in proton operation produce fills of reasonable length and satisfy operational constraints related to the functioning of the beam position monitors with unequal beams.

16.4.3 Other species

Collisions of lighter nuclei may eventually be requested by the experiments. The injector chain has operated with argon ions for fixed target operation. The beam quality and intensity data achieved allow performance projections for Ar–Ar and p–Ar collisions in the LHC.

Since most of the performance limitations for ion beams depend on high powers of the nuclear charge as well as beam intensity, their relative importance may shift considerably. First indications are that collimation

losses from lighter ions will be more of a concern than for lead, while losses from collision processes will be less serious.

16.5 HL-LHC IT String

16.5.1 Introduction and goal of the HL-LHC IT String

The HL-LHC IT String (IT String) is a test stand for HL-LHC, which goal is to validate the collective behavior of the IT magnets in their nominal set up and operational condition. Each individual circuit of magnets will be powered through the SC link and its associated current leads up to the nominal operational current while cooled to 1.9 K liquid He. The test stand will be installed in the building 2173 (SM18) and will use magnets, SC link, current leads, power converters and protection equipment designed for the HL-LHC with their final version, usable for the HL-LHC. The test stand may profit from the prototype magnets, but ideally would use the series magnets. The test bench will allow a real size training for the installation and alignment, a study of the protection scheme of the magnets and the superconducting link. At that occasion, all subsystems will be able to fine-tune their set up and to complement and adapt when necessary, before they are finally installed into the HL-LHC. The powering procedures will be written and validated during that test. These tests will improve also our knowledge of every single component and will give us the opportunity to optimize the installation and hardware commissioning procedures.

16.5.2 Description of the IT String

The IT String will be composed by the cryo-magnet assemblies: Q1, Q2a, Q2b, Q3, CP and D1 (Figure 16-1). In total, 21 superconducting magnets using Nb-Ti or Nb₃Sn technology will be required to compose the IT String.

In the IT String, as for the HL-LHC, the magnets will be powered via a SC link (DSH) by standard HL-LHC power converters. The circuit will contain the current leads, the water-cooled cables between the power converter and the leads. The link will be connected to the bus bars of the magnets in a dedicated equipment called DFX and the current leads to the water-cooled cables. The magnets, the SC link and the current leads will be tested separately in a dedicated test stand before their installation in the IT String. The DFX will be tested only in the IT String installations.

The cooling of the magnets will be done via a dedicated cryogenic valve box connected to the DFX and the corrector package (CP) in the same way as planned to be done in the HL-LHC for the liquid He feeding and He pumping. The cryogenic installations will be completed with the cold and warm recovery lines. These lines and the valve box cannot be not re-used in the HL-LHC.

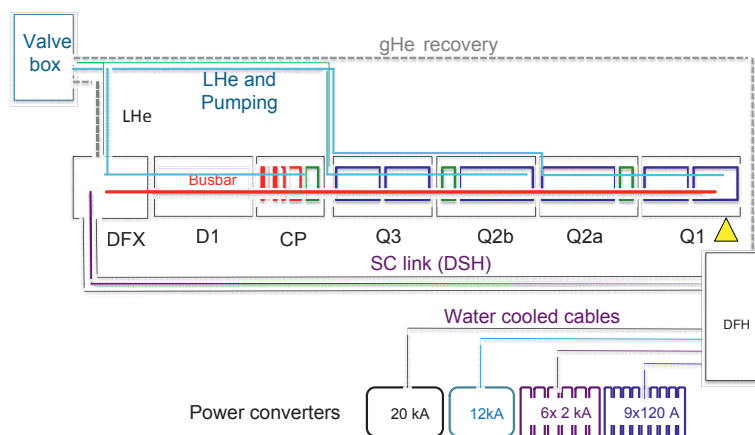


Figure 16-1: Schematic view of the IT String.

16.5.3 Location of the IT String test stand

For practical reasons the IT String will be installed in the building that is housing the cryogenic powering test facility of the RF cavities and SC magnets for both LHC and HL-LHC. The choice of the location is justified by the proximity of the cryogenic installations, the high powering capacity and water cooling capacity already present in the test hall. It should be mentioned that the same building housed the STRING1 (1994-1998) and the STRING2 (2000-2004). These were two test stands for the LHC with similar goals to the IT String. The integration of the test stand in the SM18 is shown in Figure 16-2



Figure 16-2: Integration of the HL-LHC IT String in SM18.

The installation would be along the wall of the building SM18 opposite to the existing magnet test benches of Cluster A and Cluster D. The powering system is centralised on a metallic bridge between the wall and the present structure holding electrical racks of the horizontal magnet test benches. The cryogenic valve box allowing the cooling of the magnets and the SC link will be positioned close to the cryogenic installations and near the cluster G, opposite to the powering part. This configuration would allow preserving the visitor zone for the duration of the IT String test stand.

16.5.4 Time scale of the IT String test stand

One of the main goals of the IT String is to test and confirm the nominal operational conditions and the collective behaviour of the entire IT zone, before the installation of the magnets and main components into the LHC tunnel. The earlier the test can be done the better it is for a feed-forward of the results into the fabrication of the series components. The IT String will use the first magnets of the series production. When this will not be possible, the prototypes will replace them. This could be the case for the D1 and the Q1 cryo-magnet assemblies.

The delivery schedule of the cold masses with other relevant activities of the LHC and of the IT String is shown in Figure 16-3.

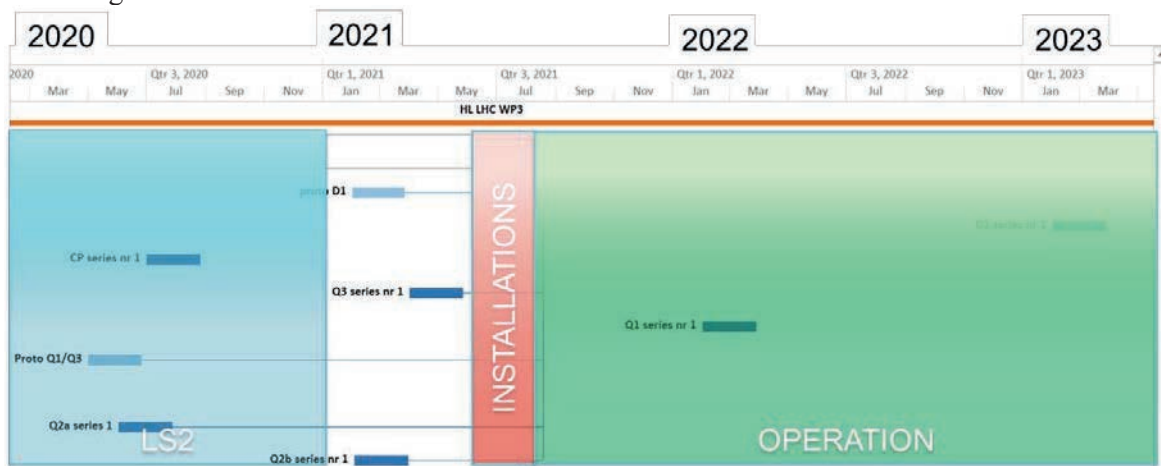


Figure 16-3: Delivery schedule of the cryo-magnet assemblies for the IT String.

The delivery of the needed cryo-magnet assemblies for the completion of the IT string is expected for the end of 2021. Their installation, estimated to 3 months, will start after the end of the LHC long shut down 2 (LS2). The IT String will operate between mid-2021 and mid-2023.

16.5.5 Technical infrastructure for the IT String test stand

The technical infrastructure for the IT String test stand is composed of several systems. The main components are:

- The cryogenic cooling system;
- The water cooling system;
- The electrical powering system.

The SM18 test hall area is equipped with technical infrastructures that allow the IT String test. Its capacity however is not sufficient to be shared between the other activities: the RF cavity and SC magnet test. The HL-LHC SC magnets and links production qualification will require approximately 100 tests for magnets and 20 for SC links in the period between 2019 and 2025. The test stands should also assure the testing of the spare LHC magnets (estimated to 50 tests) during the same period. In view of these activities, the existing infrastructure has to be upgraded.

16.5.5.1 Cryogenic cooling system upgrade

The estimated needs of cryogenic cooling of the IT String are summarized in Table 16-4.

Table 16-4: Cryogenic cooling needs of the IT String.

Characteristics	Units	Value
Cryogenic cooling needs	[g/s]	12
Cryogenic pumping needs	[g/s]	6

The cryogenic powering test of the LHC and HL-LHC magnets is scheduled at the same time, the test facility will therefore have to share the technical infrastructures. The overall needed capacity was estimated using the detailed schedule of tests and the individual needs were summed. It was considered that at the same time, two horizontal test benches and one vertical cryostat will be operational. The RF test needs were also included in the schedule. These considerations implied the need of the upgrade of the liquid He production system from the present 27 g/s to 60 g/s.

The present installations: the warm pumping units 1 (WPU1) and 2 (WPU2) combined will allow to cope with the pumping requirements. By combining the two WPUs the total of 12 g/s capacity can be used for magnet and/or IT String testing. It should be noted that until 2016, the two units each of a pumping capacity of 6 g/s, were use one for the SRF cavities and one for the SC magnet tests. The two units were successfully linked by software in 2016.

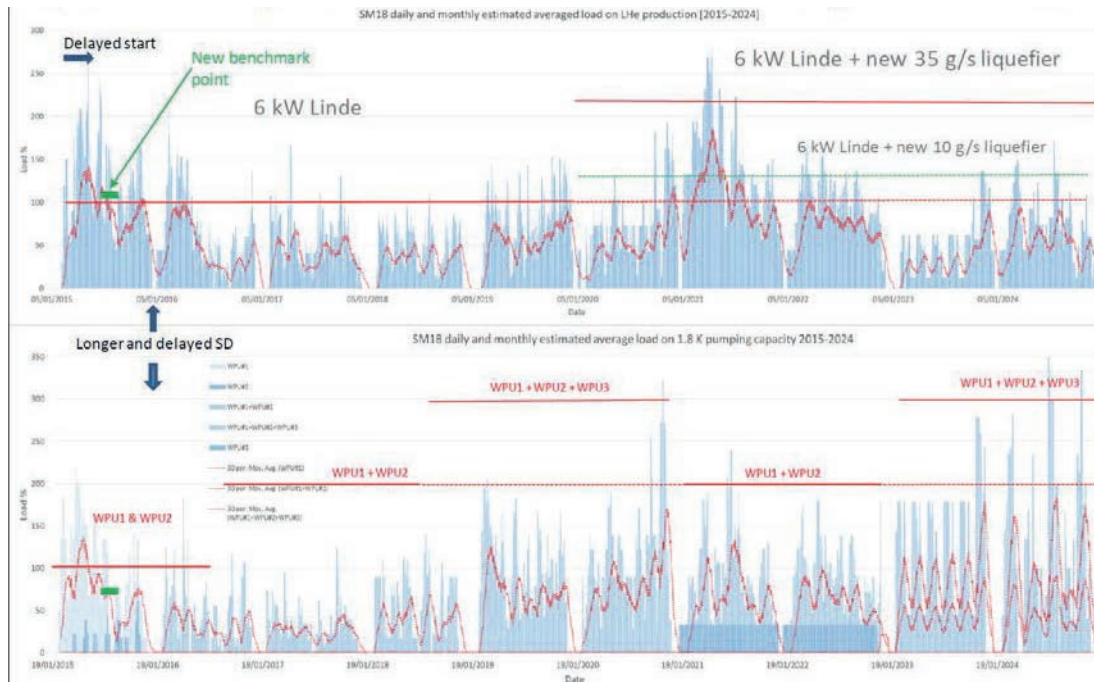


Figure 16-4: Cryogenic cooling system capacity: estimate of consumption. The upper part shows the estimated liquid He production needs. The lower part shows the estimated pumping capacity needs.

16.5.5.2 Water cooling system upgrade

16.5.5.2.1 Demineralised water system

The HL-LHC magnets are powered with currents higher than the LHC magnets. The magnet test benches and the IT String will use, in the case of the quadrupoles of the inner triplets (Q1, Q2a, Q2b and Q3), 70 % higher current than the currently installed LHC type magnets. Therefore, the power converters and associated installations requiring water cooling (water cooled cables and energy extraction systems), will need a higher quantity of demineralised water. The demineralised water production was estimated to increase from the present 48 m³/h to 138 m³/h, considering that the IT String with an estimated consumption of 55 m³/h and the SC Link test stand will not operate at the same time. Figure 16-5 shows the estimated evolution of the demineralised water consumption in SM18.

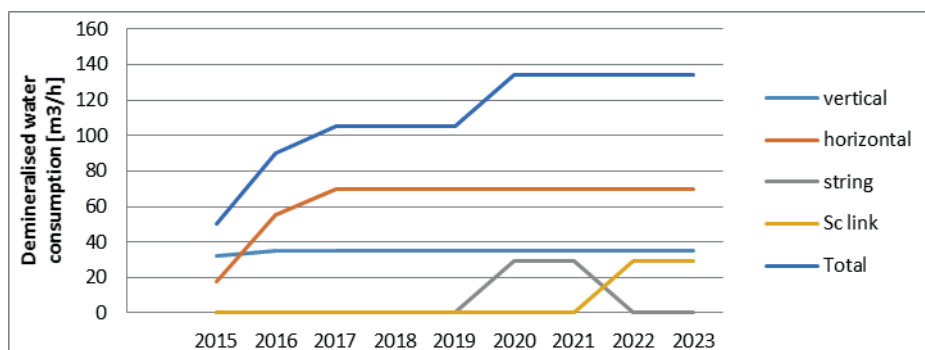


Figure 16-5: Demineralised water consumption in the SM18 from 2016 till 2023.

In 2016, a new cooling station was installed to supply between 55 m³/h and 110 m³/h to the horizontal magnets area.

16.5.5.2 Primary water system

With the increased need of demineralised water and upgraded cryogenic cooling system the needs of primary water also increases. The SRF, the SC magnets and the IT String consumption will be the double of the present 1.6 MW, while the cryogenic upgrade will require an increased capacity from 2.5 MW to 6 MW. The primary water system upgrade, part of a larger upgrade in the SM18 zone, is planned for 2019.

16.5.5.3 Electrical powering system upgrade

The SM18 magnet test facility is served by ERD4, ERD2 and EMT103. EMT103 is powering directly most of the horizontal clusters (B, C, D, E, F) on ERD4. Cluster A, alone is on EMT103.

The powering of the IT String will be made from the power converters listed in Table 16-5.

Table 16-5 Power converters of the HL-LHC IT String.

	CLUSTER	18 [kA]/20 [V]	±2 [kA]/±10 [V]	±0.22 [kA]/±10 [V]	±12 [kA]/±18 [V]
IT String	J	1	1	1	1

The different power converters and their connections to the network are shown in Figure 16-6. The IT String consumption is estimated to 1 MVA and is called Cluster J. It is proposed that the IT string will be connected together with an improved new Cluster F, of a similar consumption to a new transformer with a capacity of 3 MVA, leaving approximately 1 MVA free to power future projects. The installation of the new 3 MVA transformer is scheduled for 2019. Figure 16-6 depicts the different system consumptions in SM18 as a function of their connections to a substation and the proposed connection of the HL-LHC IT String.

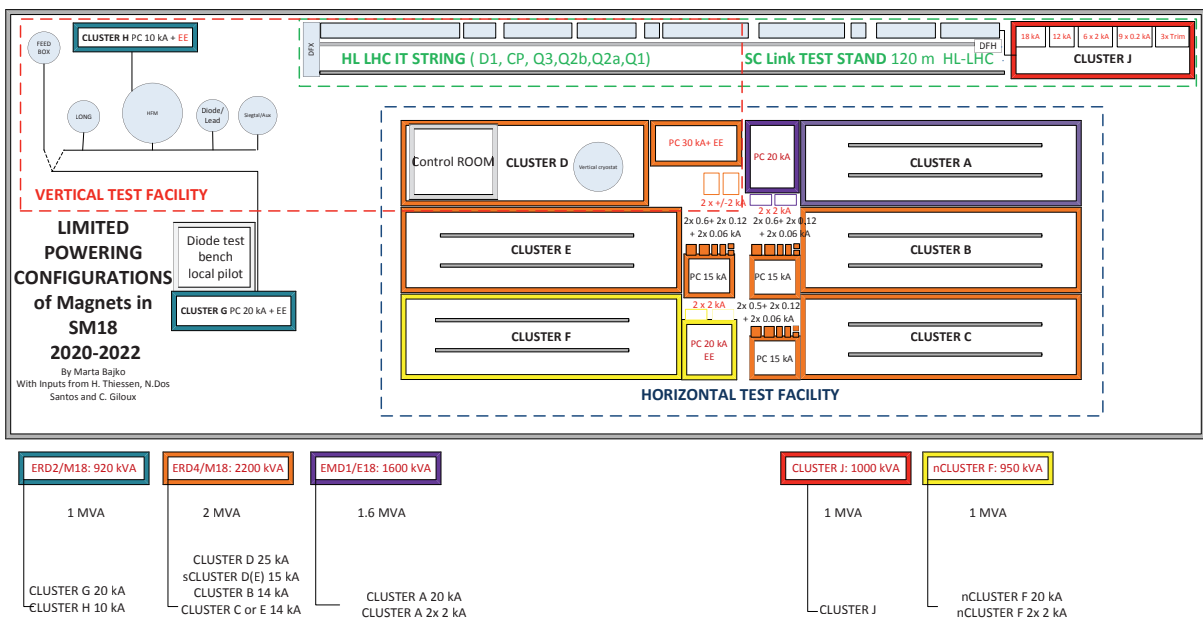


Figure 16-6 SM18 Power converters and their connections to the electrical network.

16.5.5.4 Installation and dismantling of the IT String

The IT String will be installed in the SM18. The heaviest and the largest objects will be installed, positioned and aligned with specific equipment. Table 16-6 is summarizing the length and the weight of the heaviest magnets to be installed to the IT String.

Table 16-6: Length and estimated weight of the heaviest cryo-magnet assemblies to be installed in the IT String.

Q1, Q3		Q2		
Cold mass	Cryostat	Cold mass	MCBXFA	Cryostat
8.6 m	9 m	7 m	1.2 m	9 m
22500 kg	3780 kg	18320 kg	3150 kg	3780 kg
Total	26280 kg	Total	25250 kg	

The present proposal is to handle the cryo-magnet assemblies with the handling tools used for the LHC magnet installations. They will be aligned by expert geometers with laser trackers or similar equipment. A dedicated study is needed to define the slope of the floor to simulate the nominal operational conditions of the LHC tunnel.

16.5.6 Preliminary Test program for the IT String

16.5.6.1 Performance test of components before installation into the IT String

Each individual component will be tested before their installation into the IT String. The responsible institute will test magnets at their premises and/or at CERN at nominal operational condition. The magnets of Q1, Q3, CP components will be subject to an individual test in vertical position before integrating them into the cold mass and tested in the horizontal position. The quadrupole magnets of Q2a and Q2b, since they are longer (7.15 m instead of 4.2m for the Q1 and Q3) will be only tested in horizontal position. The orbit correctors of the Q2a and Q2b will also be subject to vertical powering test. The individual magnets will be powered up to their ultimate current and at each step of the test, their electrical integrity will be checked. High voltage test at max 3 kV will be applied to check the galvanic insulation versus ground. The level of voltage and the leakage current confirming the electrical sanity of the magnet will be defined for each individual magnet and applied at every important step of the testing. The conditions in which the verifications will be done (dry air, He gas or liquid He) will determine the value of the applied test voltage.

16.5.6.2 Electrical circuit integrity test

The typical ELQA test will be performed at the specified level of voltage for each step and each magnet. The continuity of the instrumentations and protection system wiring will be verified. The IT String will allow to test the revised and adapted ELQA procedures for the HL-LHC.

16.5.6.3 Cryogenic system test

The high heat deposition in the 1.9 K bath (13 W/m) and on the beam screen (13 W/m) in the triplet-corrector package-D1 region are one of the major challenges of the HL-LHC project. Specific studies and measurements will be defined to feed back to the design of the cooling systems. The detailed test plan is still to be determined. The cold powering system test is an important step of the cryogenic qualifications. The DFX, the connecting box of the SC link and SC magnets will be exclusively tested in the IT String. Particular attention should be given to the qualification of this component.

16.5.6.4 Vacuum system test

The beam screens of the new inner triplets will be protected by tungsten shielding that will be able to absorb about half of the energy deposited by collision debris escaping the high luminosity detectors. In particular, the validation of the beam screen, not present in the cold masses during their individual test has to be done in the IT String. Those are to be tested during 3 different conditions: when a quench is occurring, when differential thermal contractions occurs and when vibrations are induced due to flow. It is also necessary to measure the heat loads to the cold mass supporting system.

The insulation vacuum will be qualified with leak test and test of different sealing options. The beam vacuum qualification will require:

- Measurements of pump down time before cool down.
- Static vacuum gas analysis.
- He, H₂, CO, CO₂ propagation tests with a-C coating at different beam screen operating temperature in the range 40 - 70 K.
- Study impact of quench and beam screen temperature on vacuum levels along the line and at cold warm transitions (with possibly dedicated vacuum gauges located at interconnects)

16.5.6.5 Powering of the IT magnets

The HL-LHC will require the development of two types of new power converters:

- one-quadrant converter 16.5 kA/20 V, which will be based on an extension of the 13 kA LHC power converter family;
- four-quadrant converter ± 2 kA/ ± 10 V, which will be based on a new topology developed for R2E 600 A power converters.

The electrical powering circuit of the IT magnets will require special attention (see Chapter 6B). Such powering test will be only available in the IT String test.

The cold powering system is composed mainly of the HTS current leads and the SC link which relies on cooling with helium gas. The gas has a temperature range from 4.2 K up to 35 K - 50 K. The use of MgB₂ and HTS materials enables safe operation of the superconducting components, for which a temperature margin of at least 10 K is guaranteed. The components are going to be tested individually on a dedicated test bench. The IT String will use a prototype of 60 m. Although the prototype will go through qualification test, the complete warm and cold powering circuit will be only tested in the IT String configuration before their installation into the LHC tunnel. We should consider among the most critical aspects that the IT String should study the cooling performance of the cold powering part and the electrical cross talk between cables of the SC link. It should be mentioned that in function of the final magnet protection system (quench heaters and/ or CLIQ system) the link behaviour, and its protection system should be studied in detail. The IT String will allow the qualification of the individual splices of the interconnections between magnets and cold powering system.

16.5.6.6 Magnet protection system test

Protection of the magnets is relying on quench heaters and/or Coupling Loss Induced Quench (CLIQ) system. To be fully representative for the tunnel configuration the IT String will not implement for the inner triplets any energy extraction. Eventually only the orbit corrector magnets may have to be equipped with energy extraction systems if quench heaters cannot be integrated. A careful protection system test has to be performed before powering of the magnets at low current. Specifically for Nb₃Sn magnets, it was found that flux jumps appear in the low and medium current range, with amplitudes ranging from 10 mV up to 2 V, and characteristic times of 10 to 20 ms. Their amplitude, characteristic time and event frequency depends very much on the strand lay-out and on the fabrication technology used for the superconductor. New quench protection cards capable of mitigating this feature of the superconducting material are in the design phase. The version available for the IT String will have current dependent, programmable threshold values.

16.5.6.7 Interlock test

The interlock system test will be one of the most critical test. The HL-LHC interlock will integrate and handle, with a given logic, signals from all subsystems. The overall system test will be only possible in the IT String as typically when the cryo-magnet assemblies are tested the interlock system that the test bench uses is a dedicated system, not necessarily working in the same conditions as in the tunnel.

16.5.6.8 DAQ test

As the interlock system, the DAQ of the IT String should be the prototype system of the HL-LHC, very much using the existing tools already implemented in the LHC. Nevertheless, the IT String test will give the first feedback and possibility of validation of the individual systems.

16.5.6.9 Performance test

Under performance test here we understand the different subsystems capability to work together and within the specified conditions.

16.5.6.10 Quality assurance

The IT String will give the opportunity to validate and test all QA steps and installation and test procedures.

16.6 References

- [1] M. Lamont, How to reach the required availability in the HL-LHC era, RLIUP: Review of LHC and Injector Upgrade Plans, Centre de Convention, Archamps, France, 29 - 31 Oct [10.5170/CERN-2014-006.139](https://doi.org/10.5170/CERN-2014-006.139).
- [2] A. Ballarino *et al.*, Chapter 6: Cold Powering, High-Luminosity Large Hadron Collider (HL-LHC) : Preliminary Design Report pp.131-146 [10.5170/CERN-2015-005.131](https://doi.org/10.5170/CERN-2015-005.131)
- [3] M. Bednarek *et al.*, ElQA qualification of the superconducting circuits during hardware commissioning, LHC-DE-TP-0007 rev 2.0, [EDMS 788197](https://cds.cern.ch/record/138197).
- [4] E. Todesco *et al.*, Chapter 3: Insertion Magnets, High-Luminosity Large Hadron Collider (HL-LHC) : Preliminary Design Report pp.61-79 [10.5170/CERN-2015-005.61](https://doi.org/10.5170/CERN-2015-005.61)
- [5] Th. Weiler *et al.*, LHC Collimation system hardware commissioning, 22nd Particle Accelerator Conference, Albuquerque, NM, USA, 25 - 29 Jun 2007, pp.1625 [CERN-LHC-PROJECT-Report-1036](https://arxiv.org/abs/0706.1625)
- [6] S. Claudet *et al.*, Chapter 9: Cryogenics for the HL-LHC, High-Luminosity Large Hadron Collider (HL-LHC) : Preliminary Design Report pp. 161-169 [10.5170/CERN-2015-005.161](https://doi.org/10.5170/CERN-2015-005.161)
- [7] J.M. Jowett, G. Arduini, R.W. Assmann, P. Baudrenghien, C. Carli, *et al.*, First Run of the LHC as a Heavy-ion Collider, 2nd International Particle Accelerator Conference, San Sebastian, Spain, 4 - 9 Sep 2011, pp.TUPZ016. [CERN-ATS-2011-143](https://arxiv.org/abs/1109.143)
- [8] R. Alemany-Fernandez, G.H Hemelsoet, J.M Jowett, M. Lamont, D. Manglunki, S. Redaelli, M. Schaumann, R. Versteegen and J. Wenninger, ALICE spectrometer polarity reversal, [CERN-ATS-Note-2012-039 MD](https://arxiv.org/abs/1203.039) (2012).
- [9] J.M. Jowett *et al.*, Heavy ion operation from run 2 to HL-LHC, RLIUP: Review of LHC and Injector Upgrade Plans, Centre de Convention, Archamps, France, 29 - 31 Oct 2013, pp.167-184 (CERN-2014-006) DOI [10.5170/CERN-2014-006.167](https://doi.org/10.5170/CERN-2014-006.167)
- [10] R. Bruce, D. Bocian, S. Gilardoni and J.M. Jowett, Beam losses from ultraperipheral nuclear collisions between $^{208}\text{Pb}^{82+}$ ions in the large hadron collider and their alleviation, *Phys. Rev.ST Accel. Beams* **12** (2009) 071002. [10.1103/PhysRevSTAB.12.071002](https://arxiv.org/abs/0907.1002)
- [11] J.M. Jowett, R. Alemany-Fernandez, P. Baudrenghien, D. Jacquet, M. Lamont, D. Manglunki, S. Redaelli, M. Sapinski, M. Schaumann, M. Solfaroli Camillocci, R. Tomás, J. Uythoven, D. Valuch, R. Versteegen and J. Wenninger, Proton nucleus collisions in the LHC, 4th International Particle Accelerator Conference, Shanghai, China, 12 - 17 May 2013, pp.49 [CERN-ACC-2013-0057](https://arxiv.org/abs/1305.0057)
- [12] R. Alemany, P. Baudrenghien, D. Jacquet, J. M. Jowett, M. Lamont, D. Manglunki, S. Redaelli, M. Sapinski, M. Schaumann, D. Valuch, R. Versteegen and J. Wenninger, p-Pb feasibility test and modifications of LHC sequence and interlocking, [CERN-ATS-Note-2012-052 MD](https://arxiv.org/abs/1205.052) (2012).

Chapter 17

Technical Infrastructure

17 The HL-LHC Technical Infrastructure

The HL-LHC technical infrastructure includes the civil engineering, the electrical distribution, the cooling & ventilation, the access & alarm system, the technical monitoring, the transport, the logistics, the storage and the operational safety.

17.1 Civil engineering

17.1.1 Introduction

In terms of civil engineering, the needs of the HL-LHC machine are, to a large extent, similar to the LHC machine, which was a considerable extension carried out between 1998 and 2005 of the previous LEP tunnel built in in the 1980's. These needs consist principally of access shafts from the surface to the underground areas together with various underground caverns and galleries¹. Buildings are required on the surface for housing technical infrastructures such as compressors, ventilation equipment, electrical equipment and helium and nitrogen tanks.

The HL-LHC construction work will be split between two existing experimental sites, Point 1 (P1) for the ATLAS experiment, located in Switzerland, and Point 5 (P5) for the CMS experiment, located in France, and will include underground and surface works at both points. Great care has been taken for the connection to re-use the existing civil engineering infrastructure that was created for LHC.

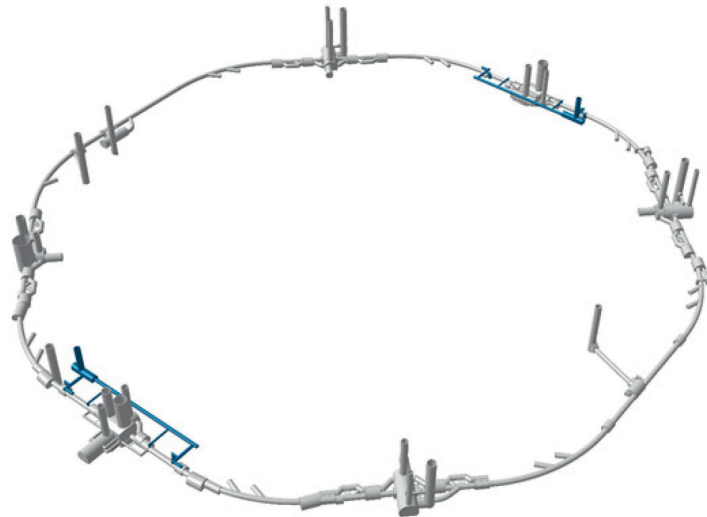


Figure 17-1: Overall indicative axonometry of the underground civil infrastructures (HL-LHC in blue).

The underground works at each point will consist of a shaft, a cavern, a power converter gallery, service galleries, safety galleries and linkage cores to the existing LHC infrastructure. The civil engineering works encompass both the primary concrete and steel structures of the surface and underground structures, and also

¹ Galleries are tunnels where there is not a circulating beam.

the secondary steel structures within the buildings and caverns. At both locations, some of the new works will be located close to existing LHC infrastructure, hence, special protective measures must be taken in order to minimise impact on the operation of the LHC and also on the LHC infrastructure itself.

To fulfil the HL-LHC timeline the majority of the construction will be completed in a 5-year period. Activities will start in 2018 with the excavations of the shafts, the remaining underground excavation work is scheduled for Long shutdown 2 (LS2) (2019-2020), and the concreting and finishing works for the underground works is scheduled during 2021. The surface works are scheduled to take place from late 2019 to the end of 2022 with staged handovers of these buildings. The objective is also to construct the safety galleries that connect the HL-LHC underground structures to the existing LHC tunnel during LS2 and have them operative during infrastructure installation that will take place during the LHC Run 3.

The only construction works that are scheduled outside of this 5-year period is the drilling of the linkage cores from the new HL-LHC infrastructure into the existing LHC tunnel, This work is scheduled for early 2024 at the beginning of the Long shutdown 3 (LS3).

17.1.2 Underground Works

The HL-LHC project requires additional underground space for the installation of its technical services. The possible methods of construction for the underground structures are detailed in section 17.1.4.3, and the dimensions specified for P1 and P5 in Table 17-1 and Table 17-2 respectively.

The underground works consist of the structures described in sections 17.1.2.1 to 17.1.2.6. Figure 17-2 and Figure 17-3 illustrate them.

17.1.2.1 Shaft (PM)

The shaft provides the main connection from surface to underground. A lift in the shaft will provide day-to-day personnel and equipment access; it will be housed into leak tight concrete modules allowing keeping that module over-pressurized with respect to the ambient pressure, a staircase will also be included in these concrete modules. At the bottom and top of the shaft there will be pressurized safe rooms. All cryogenic, power and ventilation connections between the surface and the cavern pass through the shaft.

17.1.2.2 Cavern (US and UW)

The underground cavern is made up of two portions: the US and the UW. It will house the cryogenic equipment and other technical services. A concrete wall will separate the US and UW portions. In the UW and large part of the US, there will be a first floor supported by a steel structure to provide a two storeys facility. Sump pits are required in this cavern at the bottom of the PM shaft to house the collected clear water and sewage in order for it to be pumped up the shaft to the surface.

17.1.2.3 Power converter gallery (UR)

The UR gallery, approximately 400 m long and placed parallel to the LHC tunnel, will mainly house the power converters and the current feed boxes of the superconducting magnets. It is connected to the LHC tunnel via the service galleries.

17.1.2.4 Service galleries (UA, UL)

Four service galleries will provide the connection from the UR gallery to the existing LHC tunnel, via the vertical linkage cores. End-of-zone and ventilation doors will be fitted along the length of each service gallery. The UA galleries will house the RF equipment of the crab-cavities and the UL galleries will house the cryogenic distribution system and the superconducting links.

TECHNICAL INFRASTRUCTURE

17.1.2.5 Vertical linkage cores to existing LHC infrastructure

Vertical cores, of approximately 1 m diameter each, are required to pass services from each of the four service galleries to the existing LHC tunnel. These linkages will allow connecting the newly installed services to the new systems (superconducting magnets, cryogenic distribution lines and RF cavities) that will occupy the LSS in the HL-LHC.

17.1.2.6 Safety galleries (UPR)

A safety gallery for personnel connects each UA gallery directly to the existing LHC infrastructure.

17.1.2.7 Technical data of the underground infrastructures

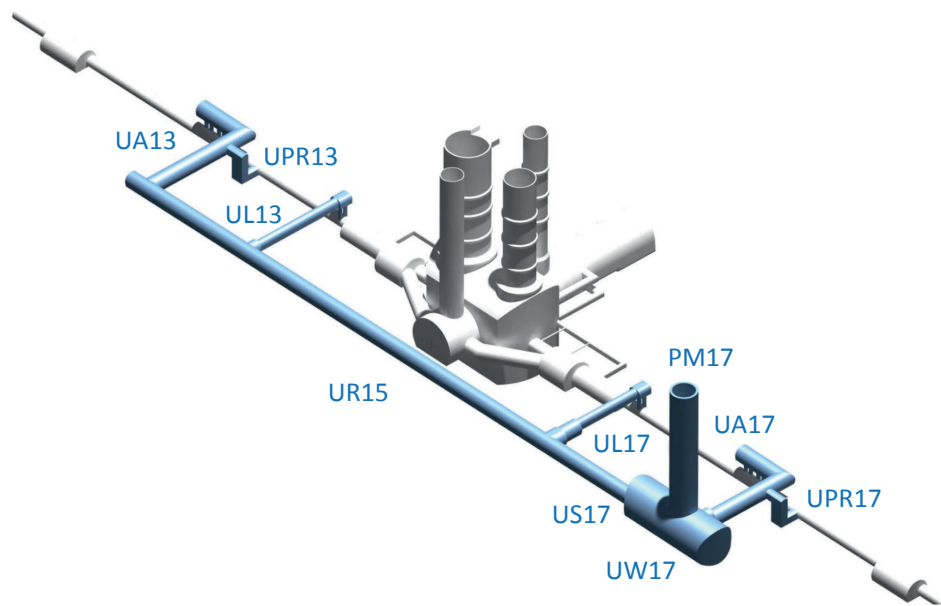


Figure 17-2: P1 indicative underground axonometry.

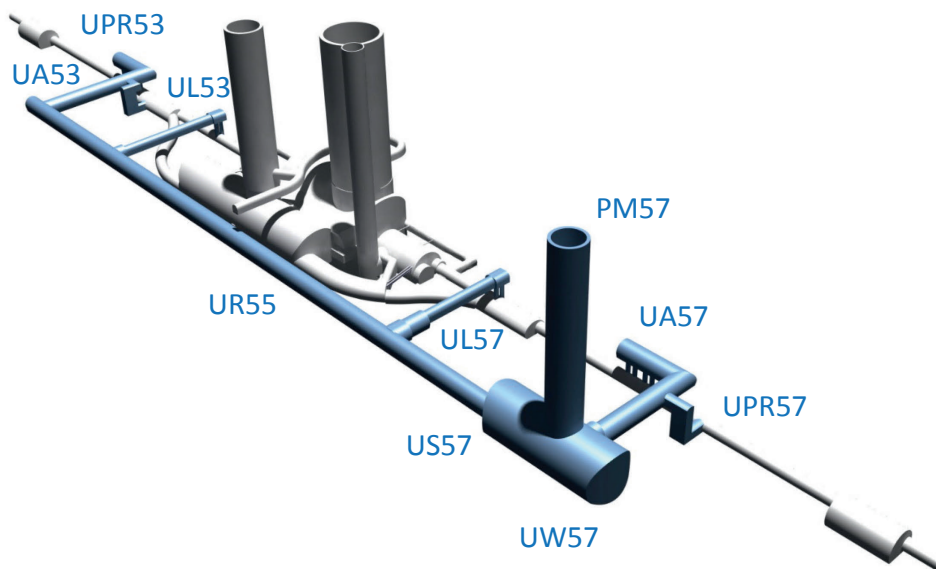


Figure 17-3: P5 indicative underground axonometry.

Table 17-1: P1 underground structures.

Building Code	Building Name	Length [m]	Inside Width (at floor level) [m]	Height [m]	Radius [m]	Floor Area [m ²]	Volume [m ³]
PM17	Shaft	-	-	72.0	5.00	79	5690
US/UW17	Cavern	46.3	14.7	11.2	8.00	681	6924
UR15	Power converter gallery	302.0	5.0	4.7	2.90	1522	7013
UL17, UL13	SC cryo link galleries	53.7	3.7	3.3	1.55	198	618
UA17, UA13,	RF galleries	68.1	5.7	4.4	2.90	389	1579
UPR13, UPR17	Safety galleries	51.1	2.5	2.50	-	128	286

Table 17-2: P5 underground structures.

Building Code	Building Name	Length [m]	Inside Width (at floor level) [m]	Height [m]	Radius [m]	Floor Area [m ²]	Volume [m ³]
PM57	Shaft	-	-	82.2	5.00	79	9 490
US/UW57	Cavern	46.3	14.7	11.2	8.00	681	6 924
UR55	Power converter gallery	302.0	5.0	4.7	2.90	1522	7 013
UL57, UL53	SC cryo link galleries	53.7	3.7	3.3	1.55	198	618
UA57,UA53	RF galleries	68.1	5.7	4.4	2.90	389	1 579
UPR53, UPR57	Safety galleries	54.3	2.5	2.5	-	136	304

17.1.3 Surface Works

All LHC buildings will keep their present functionality during the HL-LHC era; in addition, some new buildings are required at P1 and P5. The surface works at each point will be made up of 5 new buildings, a combination of steel and concrete structures, as well as technical galleries, concrete slabs, roads, drainage and landscaping. At this stage, the buildings represent additional 6 200 m² of floor area. The dimensions for the surface structures at P1 and P5 are specified in Table 17-3 and Table 17-4 respectively.

The surface works consist of the structures described in sections 17.1.3.1 to 17.1.3.11. Figure 17-4, Figure 17-5, Figure 17-6 and Figure 17-7 illustrate them.

17.1.3.1 Head shaft building (SD)

The SD building will cover the PM shaft; a steel frame building with cladding is envisaged. The floor slab of the building will require technical galleries to allow cables, pipes and other services to pass from the PM shaft to the service gallery and other adjacent buildings. A partial false floor on a restricted section around the shaft is envisaged.

17.1.3.2 Ventilation building (SU)

The SU building is required to house the equipment needed for the heating, ventilation and air conditioning of the underground infrastructure. The building will be constructed in reinforced concrete to minimise noise levels outside the building. A reinforced concrete technical gallery running just below ground level is required along one side of the building. This building is partially equipped with a steel mezzanine structure. The building is split into two sections that house compressors and air handling units respectively. Consideration shall be made for acoustic insulation of the building envelope.

TECHNICAL INFRASTRUCTURE

17.1.3.3 Electrical building (SE)

The SE building will be used to house electrical equipment. The building will include a low voltage room and a high voltage room. It will be a steel structure that will be clad in metal sheeting and will include a false floor supported on a steel structure.

17.1.3.4 Cooling towers (SF)

The SF cooling towers are required to extract the heat loads from the equipment, and will be constructed in reinforced concrete. Consideration shall be made for acoustic insulation of the building envelope. The building will be split into two zones, one for the two cooling towers, and one for the pump room. A technical gallery enters the building. This building will be partially equipped with a steel mezzanine structure.

17.1.3.5 Compressor building (SHM)

The SHM building will house the warm compressors of the cryogenic plant. It will be constructed in reinforced concrete. Consideration shall be made for acoustic insulation of the building envelope. This building will be partially equipped with steel mezzanine structures.

17.1.3.6 Technical galleries (SL)

The technical galleries shall run just below ground level between the buildings in order to provide a route for power supplies, cryogenics and cooling pipes. The siting of the new technical galleries will be optimised such that there is no movement or interference to existing services. There will be some openings required in the roof of the galleries to provide access for the installation of services, extraction points and escape points. These additional technical galleries will connect to existing galleries. The galleries will be watertight and are foreseen in reinforced concrete. The maximum loading on the roof of the galleries will be determined by traffic loads.

17.1.3.7 Helium tank platform (SHE)

The SHE platform is a concrete foundation for siting 2 helium tanks on. The support for the tanks will be via a steel frame that will be connected to the foundation using anchor bolts that can transfer seismic loads to the slab. A crash barrier is required around the structure.

17.1.3.8 Nitrogen tank platform (SLN)

The SLN platform is a concrete slab for siting large nitrogen tanks on. The support for the tanks will be via a steel frame that will be connected to the slab using anchor bolts that can transfer seismic loads to the slab. A crash barrier is required around the structure.

17.1.3.9 Harmonic filter & transformer slab

The harmonic filter slab will house the electrical equipment needed for the power quality of the electrical network. A slab for a new electrical sub-station housing a transformer will be required at P5.

17.1.3.10 Roads and landscaping

New roads and car parks are required to provide transport links to the new buildings. At P1, the existing terrain level will be modified to create a platform at approximately the elevation of the ATLAS site. Spoils excavated from the underground structures will be used to construct this platform.

17.1.3.11 External drainage and oil separators

Required drainage for all the new surface and underground structures will be fully integrated into the existing drainage system, this includes requirements for oil separators.

17.1.3.12 Technical data of the surface infrastructures

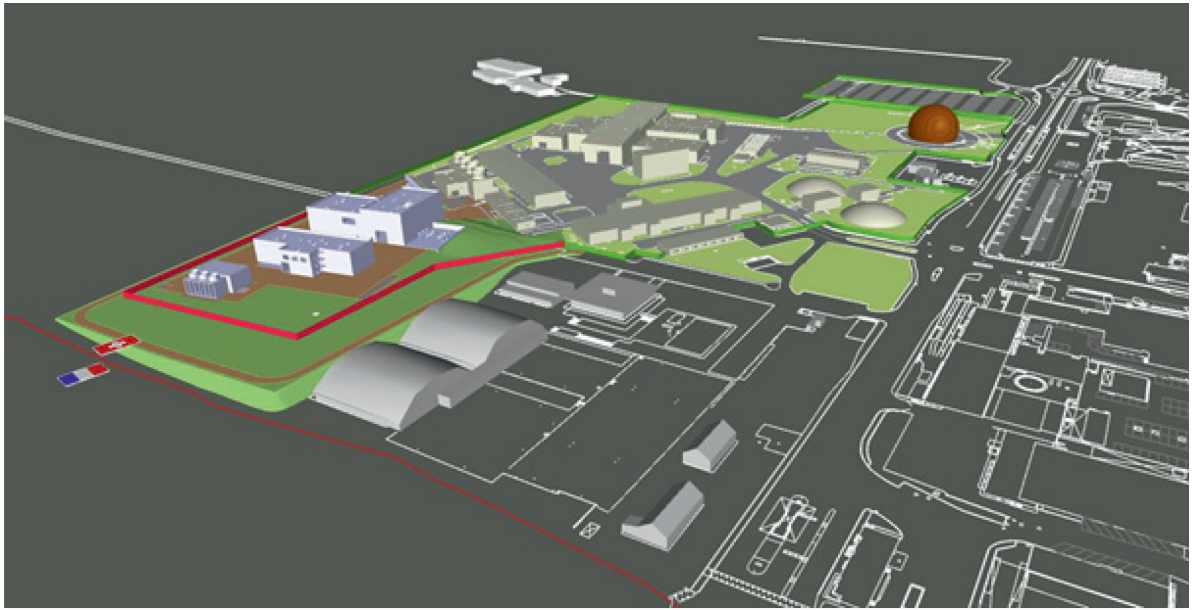


Figure 17-4: P1 indicative surface axonometry.

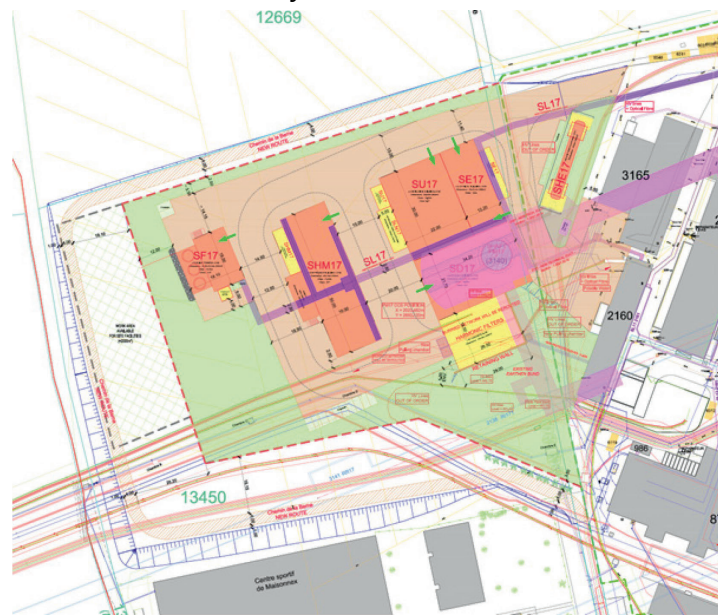


Figure 17-5: P1 surface layout.

Table 17-3: P1 surface buildings.

Building Code	Building Name	Length [m]	Width [m]	Height [m]	Floor Area [m ²]	Volume [m ³]
SD17	Head shaft building	32.0	20.0	16.0	640	10 200
SU17	Ventilation building	30.0	22.0	13.5	660	8 910
SE17	Electrical building	29.5	10.5	7.0	310	2 170
SF17	Cooling towers	19.0	18.1	7.7	344	2 648
SHM17	Compressor building	56.0	16.0	10.9	896	9 770

TECHNICAL INFRASTRUCTURE

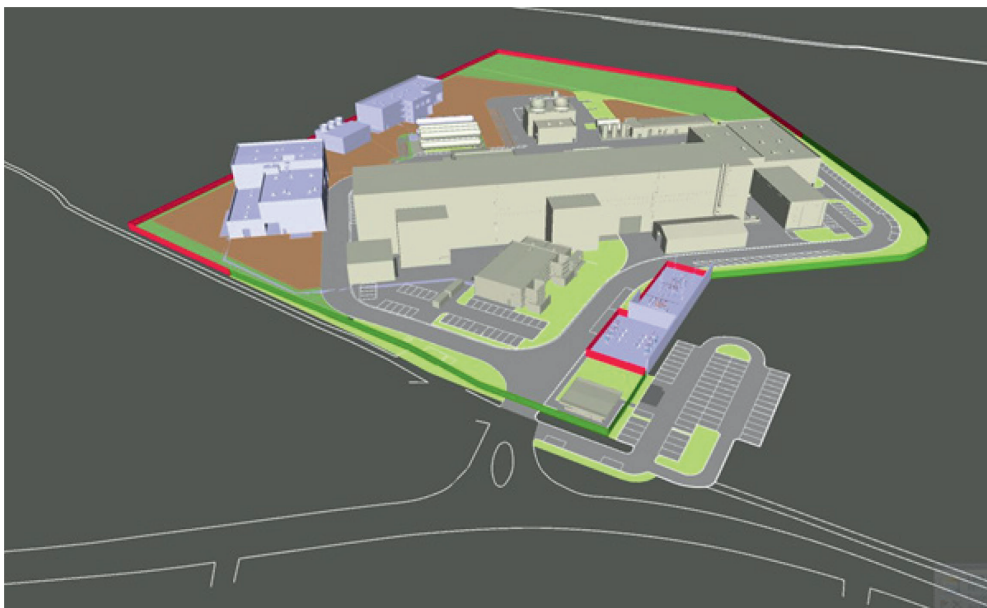


Figure 17-6: P5 indicative surface axonometry.

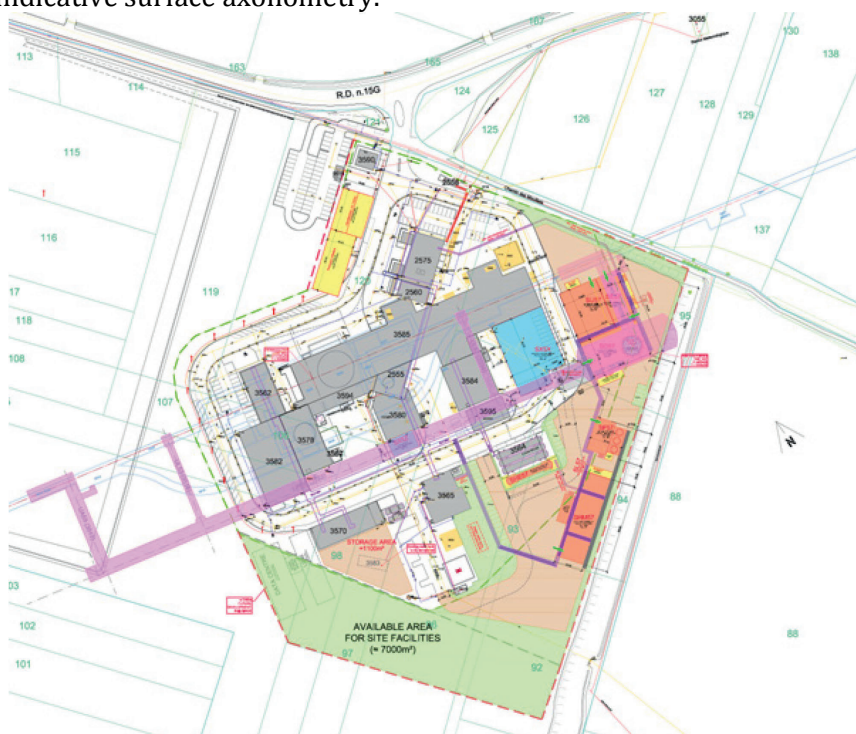


Figure 17-7: P5 surface layout.

Table 17-4: P5 surface buildings.

Building Code	Building Name	Length [m]	Width [m]	Height [m]	Floor Area [m ²]	Volume [m ³]
SD57	Head shaft building	32.0	20.0	16.0	640	10 240
SU57	Ventilation building	30.0	22.0	13.5	660	8 910
SE57	Electrical building	32.0	11.0	7.0	352	2 460
SF57	Cooling towers	19.0	18.1	7.7	344	2 648
SHM57	Compressor building	56.0	16.0	10.9	896	9 770

17.1.4 Requirements and constraints

17.1.4.1 Geology and the Environment

Ground investigations were undertaken in 2015 on the future HL-LHC sites, these investigations have provided information in addition to the existing geotechnical data from the construction of the LHC and LEP.

The initial results for P1 are in agreement with the existing data for the site and indicate that the ground consists of a thin layer of arable land, covering a layer or moraines of a depth of around 3 to 10 m, with molasse below that. However, some traces of natural hydrocarbons were found in some bore holes. Further geotechnical testing is being considered to better quantify the extent of these hydrocarbons.

The preliminary results from the ground investigations for P5 are also in agreement with the existing data for the site. The initial results indicate a layer of arable land over a layer of glacial formations consisting of silty moraines, gravels and ancient alluvium, with a maximum depth of 50 m. However, at the new shaft location the depth of the moraines is only approximately 25 m with molasses below that. This suggests that ground freezing might not be necessary for the construction of the shaft as it was for the construction of all previous shafts at P5.

As with all major construction projects at CERN, environmental considerations are an important constraint. With the assistance of a local architect and some specialist consultants, the necessary requirements for the submissions of building permits will be fulfilled during 2016. This will include an acoustic study to assess the additional noise impact of the new buildings on the surrounding population. It is intended that the new works are integrated into the environment as sensitively as possible.

A significant environmental consideration for the works is the method of disposal of the spoil that will be generated during the underground excavation. It is intended at P1 that some of the spoil is re-used on the site to level the area. For P5, re-use is not a viable solution and disposal in France is likely to be utilized.

A further environmental consideration is the water networks. The existing networks must be assessed. If the capacity of the existing networks cannot accept the new load, additional infrastructure for drainage and treatment must be proposed and constructed. Great attention must be taken to protect any sensitive water aquifers at the sites.

17.1.4.2 Vibration Risk to the LHC during construction

The impact of the HL-LHC construction on the LHC operation is a key constraint of the civil engineering of the HL-LHC project. It has been concluded that excavation of the caverns and galleries cannot take place whilst the accelerator is in operation, hence these activities have been scheduled during LS2. The shaft has been located as far as possible from the interaction region and is located 40 m from the existing infrastructure; its construction has currently been deemed possible whilst the LHC is running and is scheduled during the last year of Run 2 (2018). This is possible with ad-hoc choice of the excavations equipment. Research on the vibration effects of the shaft construction on the operation of the machine is still ongoing. The concreting/finishing phase of the underground construction has been scheduled during the first year of Run 3 (2021), again this has currently been deemed as possible, but research into the vibration effects of the concrete pumps is to be undertaken to confirm if this is acceptable.

17.1.4.3 Construction Methods

Considering the sensitivity of the LHC equipment to vibrations, the shaft excavation in the molasses will possibly have to be done using a hydraulic cutting heads mounted on an excavator. Roadheaders could also be used, but they would probably not be the optimal solution from the technical and economical perspective. The use of explosives can only be envisaged during LS2.



Figure 17-8: Excavator with hydraulic cutting heads.

With regards to the excavation of the underground cavern and galleries, several techniques could be used, mainly, excavator with hydraulic cutting heads or roadheaders. Due to the tunnel's short length, the use of a tunnel boring machine would most certainly be excluded. A "roadheader" type machine as shown in Figure 17-9 has excavation rates will typically vary from 60 to 120 m³/day. In the event of excavation in very hard sandstone layers, the hydraulic rock splitter technique could be used, with rates of circa 15 m³/day, but these solutions would not be compatible with LHC exploitation if the excavation plan would be delayed or anticipated leading to superposition with the physics Run.



Figure 17-9: Roadheader type machine.

The shafts will have to pass through layers of moraines before reaching the molasse rock. The three existing shafts at P5 utilized the ground freezing technique. This involves freezing the ground with a primary cooling circuit using ammonia and a secondary circuit using brine at -23°C, circulating in vertical tubes in pre-drilled holes at 1.5 m intervals around the shaft perimeter. This frozen wall allows excavation of the shafts in dry ground conditions and also acts as a retaining wall. Figure 17-10 shows an example of this method.

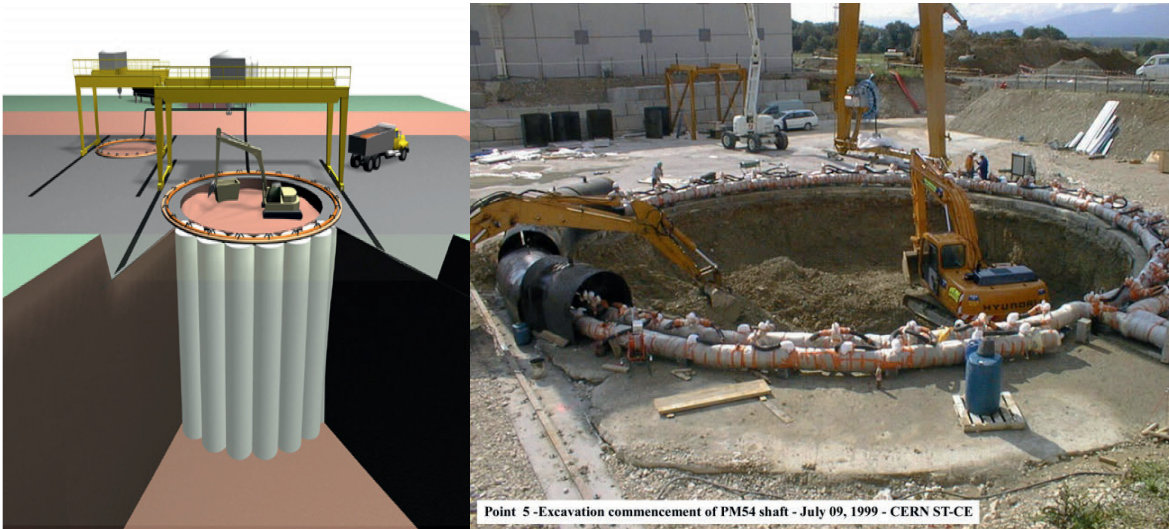


Figure 17-10: Linking up cylinders of ice to construct a temporary wall.

However, initial geotechnical results indicate that the HL-LHC shaft will have to pass through a much thinner layer of moraines, and in relatively dry conditions. This means that an alternative method of excavation may well be adopted. For the shaft excavation itself, the most common method is to use a hydraulic hammer, as shown in Figure 17-11.



Figure 17-11: Hydraulic hammer method of excavation.

This type of machine will most likely create more vibration than other methods, but is the fastest and most efficient technique. The results of the vibration measurements will determine what type of machine will be utilised. Once the shaft is excavated to the top heading of the cavern crown, the permanent lining will be concreted using slip-forming, whereby concrete is poured into a continuously climbing formwork.

It is envisaged that the rock support strategy will consist of a primary shotcrete lining with rock bolts, then an in-situ secondary lining of reinforced concrete, separated by a waterproof lining, this is illustrated in Figure 17-12 below.

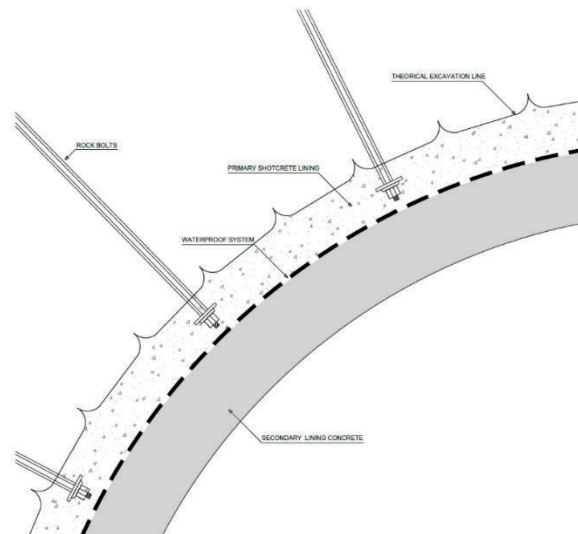


Figure 17-12: Typical rock support strategy detail.

17.2 Electricity

17.2.1 Introduction

This section outlines, from one side, the new infrastructures needed for HL-LHC and, from the other side, the impact of users' requirements on the existing infrastructure, in term of electrical distribution, optical fibre infrastructure and signal cabling. The design principles presented in the document are based on the requirements formulated by the users in 2015; the technical solutions described may change if the user requirements or the forecasted load varies considerably.

17.2.2 Requirements and constraints

17.2.2.1 Environmental and legal

From an environmental point of view, the new electrical infrastructure required for HL-LHC may comport risks in term of noise. The noise level generated by electrical equipment, such as transformers or switchgear, have been provided to an acoustic consultant which will perform studies both for surface and underground installations taking into account also ambient noise level and noise generated by other non-electrical equipment.

It is important to underline that all the distribution transformers that will be installed in the context of HL-LHC will be of dry type and therefore do not create problems in relation to oil pollution.

17.2.2.2 Operational

In terms of electrical distribution, four types of electrical networks will be available for users: general services, machine network, secured network (backed-up by diesel generators) and uninterruptible power supply network (UPS). The 48 V DC will not be distributed to users. High current DC cables will be available for the users as part of the distribution chain connecting the power converters and the accelerator magnets. A resilient, multi-users, optical fibre infrastructure will also be available.

17.2.2.3 Schedule

The schedule for the works outlined in the next sections is strictly related to the hand-over of the surface buildings and underground structures foreseen by the project.

Part of the works related to the transport and distribution infrastructure, such as the pulling of the power cable to LHC5 (section 17.2.3.1.5), and the installation of the infrastructures in the new underground caverns and surface building, can be carried out during the run of the accelerators. A large part especially related to the modifications to existing infrastructure, needs to be executed during a (E)YETS or LS. In P1, the constraints related to the construction of the new buildings require the displacement of power cables and optical fibres. A preliminary study has highlighted that the networks to be displaced supply critical users, such as the LHC cryogenic systems, LHC general services, and the SPS secured network, in the case of the power cables, and TETRA, GSM-MMC, IT network, CSAM, LASS, BIC local permit, timing SPS, timing LHC, BE-BI BST in the case of optical fibres. The displacement of these networks is scheduled for the EYETS 2016. The planning takes in consideration the risks incurred by the users and the unavailability of these systems during the works.

The project for the construction of the new 400 kV electrical substation BE2, which is essential to cope with the increase of loads associated with HL-LHC, is ongoing and its completion is foreseen for the end of 2018 (section 17.2.3.1.1).

17.2.2.4 Radiation protection and other safety requirements

In order to minimize the impact of cumulated dose received during the future maintenance interventions and to adequately select the components to be installed in the radiation areas, the installation requests and systems needs will be communicated in the preparatory phase, so the studies and preparatory actions can be carried out accordingly in collaboration with HSE-RP.

17.2.2.4.1 Radiation to personnel

The installation works in the LHC tunnel will be organized in campaigns according to the correspondent activities and following the ALARA (*As Low As Reasonably Achievable*) principle to minimize the cumulated dose received by the participants [1][2][3].

17.2.2.4.2 Radiation to cabling, fibre optics and electrical equipment

The electrical cables, fibre optics and electrical equipment will be adapted accordingly to the estimated radiation levels expected in the concerned areas and applying the ALARA principle to minimize future maintenance, corrective interventions and upgrades.

17.2.2.5 Other

It is necessary to underline that the technical solutions specified by the users have an important impact on both power requirements and integration in underground facilities. For example, in the case of radio frequency systems, the worst case scenario in terms of power consumption is represented by the use of power amplifiers with IOT technology, while the worst case scenario in terms of integration is represented by the use of Solid State Power Amplifiers (SSAP). The design described in this document is based on the use of SSAP and foreseen to supply 8 crab cavities per point (P1 and P5).

Whenever users' technical solutions cannot be finalized in the short term, it will be necessary to design the electrical infrastructure taking into account the more stringent requirements of all systems. Similar considerations apply to the whole of the optical fibre and cabling requests that are at this stage barely specified by the users.

17.2.3 Technical description of the work

17.2.3.1 Electrical distribution

This section covers the transmission and distribution network, from the 400 kV to low voltage distribution to the users, for loads not backed up by diesel generators nor UPS (described in 17.2.3.2). After a description of the transmission network, are presented the load forecasts, for both P1 and P5, and the consequent impact on the transmission network. Afterwards are presented the design principles related to the distribution network, which covers 18 kV, 3.3 kV and 400 V.

It is important to underline that, while the topology of the transmission network is different in P1 and P5, because of the different amount of power required by the loads in these two sites, the design principles used for the distribution network are the same, allowing an important level of standardization.

17.2.3.1.1 Transmission and distribution network

A detailed description of the existing electrical network is given in [4]. CERN is supplied from two sources: the 400 kV grid, through a connection to the Bois-Tollot substation, located in France near Prévessin, and the 130 kV grid, through a connection to the Verbois substation, located in Switzerland near Geneva. The main source of power for CERN electrical distribution network, used to supply accelerators and experiments, is the 400 kV. The 130 kV connection is used as backup, in case of outages or maintenance. A geographical overview of CERN electrical network is given in Figure 17-13.

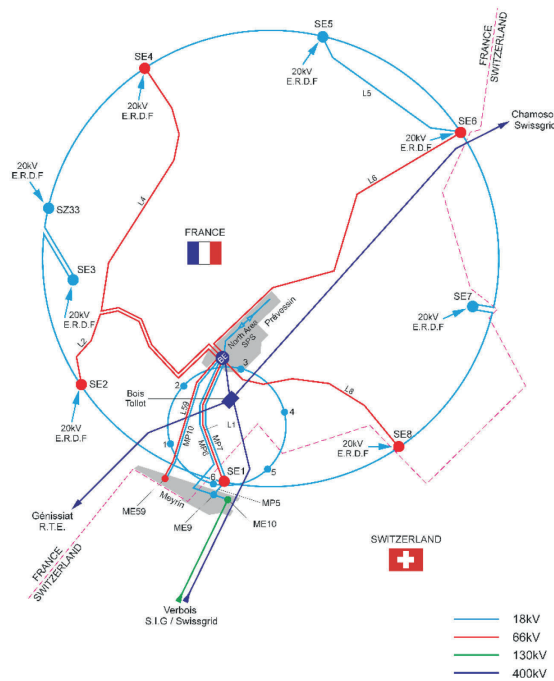


Figure 17-13: Geographical overview of CERN’s existing electrical network.

A 400 kV overhead line connects RTE Bois-Tollot substation to BE substation, where five power transformers are installed (Figure 17-14). Three of them, EHT1-2-3, supply to the SPS, while two of them, EHT4-5, supply the LHC loads and Meyrin site.

The transformers EHT4 and EHT5 reduce the voltage from 400 kV to 66 kV and supply the substation SE9, which is then connected, through underground 66 kV cables to the Meyrin site and to the various LHC points (Point 1, Point 2, Point 4, Point 6 and Point 8).

In these locations the voltage is then reduced from 66 kV to 18 kV for distribution inside each site and finally converted to 3.3 kV or 400 V for distribution to the users.

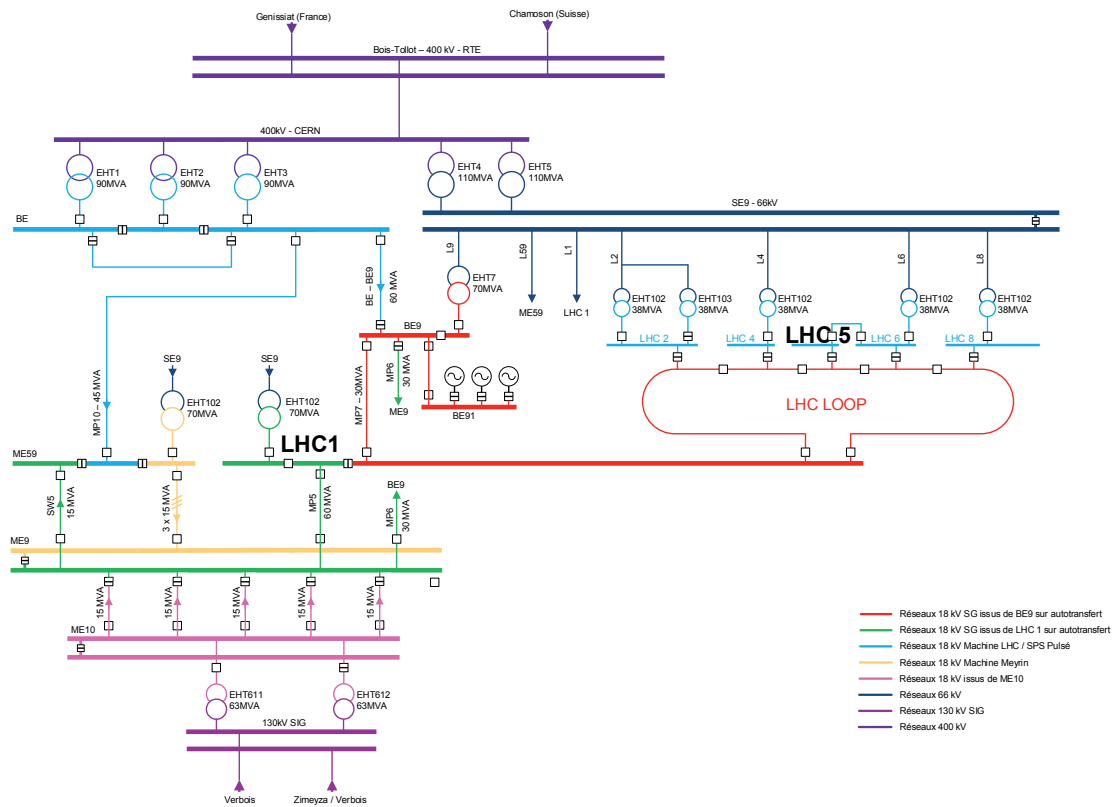


Figure 17-14: Single line diagram of the actual CERN transmission network (LHC1 and LHC5 in bold).

Studies carried out in 2012, in the context of the evolution of the electrical network to the horizon 2025, have highlighted a significant increase of the loads, in particular related to the LHC [5]. Table 17-5 summarizes the load forecast, according to data available in 2012, for the entire CERN electrical network taking into account also the loads associated to HL-LHC.

Table 17-5: Load forecast made in 2012, with the horizon 2025 [5].

Bilan de puissance après à HL-LHC
Unités P [MW], Q [MVar], S [MVA]

POSTE SOURCE	Σ 400kV											
	P			Q ^(*)			S					
	275 MW			57 MVar			281 MVA					
	Σ 66kV : Réseaux Normal + Machine LHC/Meyrin						Σ 18kV : Réseaux Pulsé					
	P		Q ^(*)		S		P	Q ^(*)	S			
	213	43	217	63	14	64						
TOTAL PAR SITE	Σ 18kV LHC			Σ 18kV MEYRIN			Σ 18kV SPS / Zone Nord					
	P	Q ^(*)	S	P	Q ^(*)	S	P	Q ^(*)	S			
	157.4	10.4	157.7	42.2	39.4	57.7	24.2	-4.1	24.5			
REPARTITION PAR SITE	LHC 1 - 1.8			Isolde (sans 513)			SPS (S.G.)			SPS (Pulsé)		
	30.6	17.5	35.2	14.4	14.0	20.1	7.6	5.2	9.2	55.6	153.5	163.2
	Loop LHC			PS			Zone Nord (S.G.)			Zone Nord (Pulsé)		
	15.9	-4.1	16.4	10.6	15.3	18.6	12.8	9.5	15.9	7.3	16.7	18.2
	LHC 2			Zone Administrative			Prévessin (S.G.)/SEO/BE/BE9			Compensateurs		
	25.6	0.2	25.6	7.5	4.8	8.9	3.8	2.2	4.4	0.0	-156.5	156.5
	LHC 4			Zone Ouest			Filtre Stable					
	28.4	-2.1	28.5	3.5	1.9	4.0	0.0	-21.0	21.0			
LHC 5 - 6			Centre de Calcul (513)									
28.8	-0.7	28.8	6.2	3.4	7.1							
LHC 8												
28.1	-0.3	28.1										

(*) : Puissance réactive avec filtres et compensateurs en fonctionnement

As it can be seen in Table 17-5, the transformers EHT4 and EHT5, which supply the LHC, the Meyrin site and part of the SPS, see their load increase to 217 MVA, which is critically close to their 220 MVA rating. For this reasons the consolidation plan of the electrical network [6] included the construction of a new 400 kV substation, called BE2 [7]. This new substation will create various advantages: it will make available the required power for HL-LHC loads, increase the maintainability of the existing 400 kV substation, introduce redundancy on the 66 kV network. The new substation introduces also the possibility of having a new 66 kV Autotransfer System, which will considerably improve the availability of the electrical network in case of outages or faults [8].

The new BE2 substation will be located contiguously to the RTE Bois-Tollot substation, as represented in Figure 17-15, and connected to the 400 kV grid through an underground 400 kV cable.

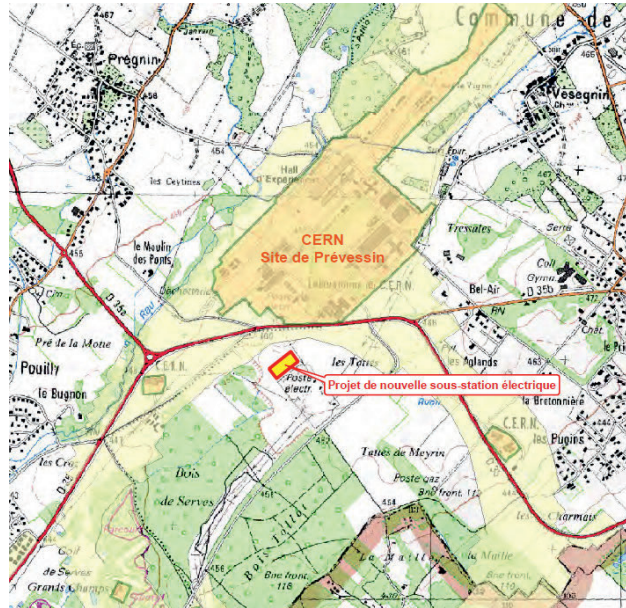


Figure 17-15: Location of the new 400 kV substation BE2.

A 220 MVA power transformer, called EHT8, will reduce the voltage from 400 kV to 66 kV and transmit the power, through an underground 66 kV cable, to the substation SE9 located on the Prévessin site. The loads of the SE9 substation (LHC, Meyrin site and part of the SPS) will be therefore split between the three transformers EHT4, EHT5 and EHT8. The commissioning of the new substation BE2 is foreseen for 2018.

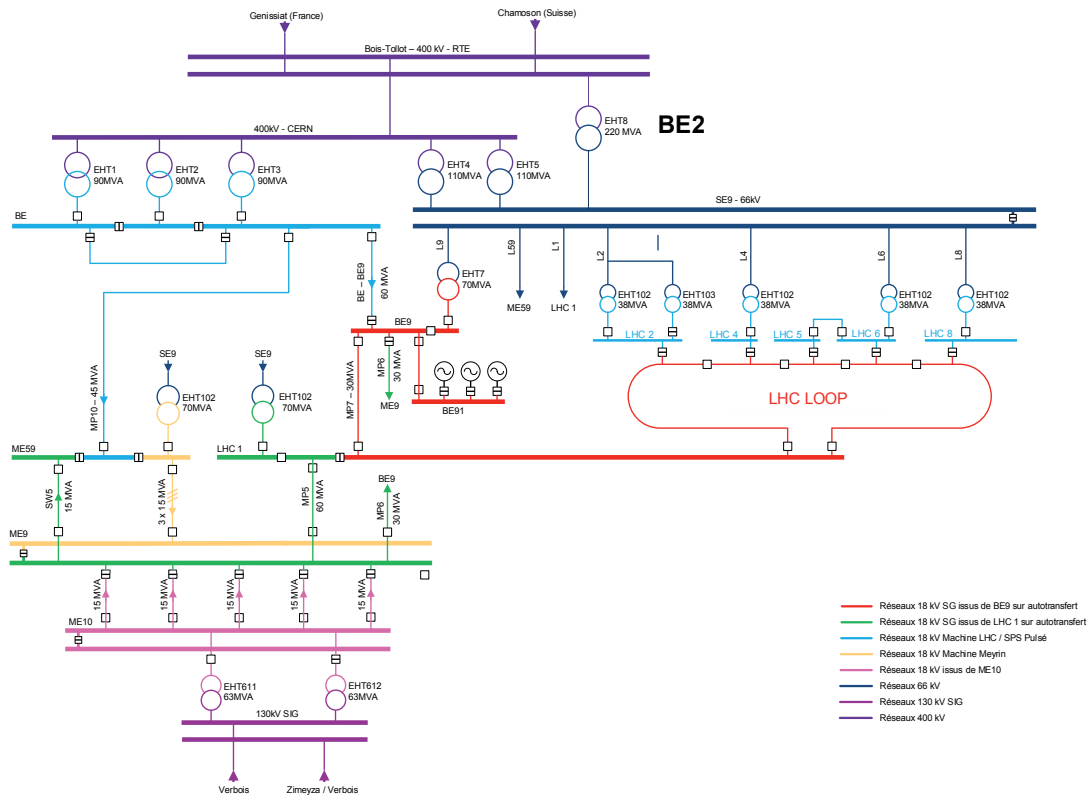


Figure 17-16: Single line diagram of the CERN transmission network at the end of 2018, with BE2.

17.2.3.1.2 P1 load forecast

The load forecast in P1 shall make use of three different sets of data: the values provided by users in the context of the HL-LHC project, the values for ATLAS taken from the study carried out in 2012 [8] and the measurement carried out in September 2016.

The load forecast of HL-LHC project takes in consideration two possible scenarios: one with 4 crab cavities cryomodules per IP, based on IOT technology for the RF power amplifiers (“*1/2 crab cavities*”) and one with 8 crab cavities cryomodules per IP, based on SSPA technology (“*full crab cavities*”). Both scenarios have been evaluated by the main users (cryogenics, radiofrequency, power converters, cooling and ventilation) and are summarized in Table 17-6.

Table 17-6: HL-LHC loads in P1.

USER	LOCATION	SCENARIO WITH 1/2 CRAB CAVITIES				SCENARIO WITH FULL CRAB CAVITIES			
		ELECTRICAL POWER REQUIRED BY USER				ELECTRICAL POWER REQUIRED BY USER			
		[kW]	[kvar]	[kVA]	cos(phi)	[kW]	[kvar]	[kVA]	cos(phi)
TE/CRG	SHM	5000	2967	5814	0.86	5000	2967	5814	0.86
EN/CV ventilation	SE	7.8	4	9	0.9	7.8	4	9	0.9
EN/CV ventilation	SU	32.5	16	36	0.9	32.5	16	36	0.9
EN/CV ventilation	SF	49.4	24	55	0.9	49.4	24	55	0.9
EN/CV ventilation	UW	62.4	30	69	0.9	62.4	30	69	0.9
EN/CV ventilation	SHM	31.2	15	35	0.9	31.2	15	35	0.9
EN/CV cooling	SU	605.8	293.4	673.1	0.9	610	295.3	677.4	0.9
EN/CV cooling	SF	548.6	265.7	609.6	0.9	569	275.8	632.7	0.9
EN/CV cooling	UW	163.8	79.3	182.0	0.9	195	94.4	216.7	0.9
BE/RF	UR	807	265	849	0.95	1614	530	1699	0.95
BE/RF	US	807	265	849	0.95	1614	530	1699	0.95
TE/EPC	UR	900	700	947	0.95	900	700	947	0.95
Various (GS...)	surf+und	1000	800	1281	0.78	1000	800	1281	0.78
TOTAL		10,016	5,725	11,409		11,685	6,282	13,170	

As mentioned in section 17.2.2.5, from an engineering point of view, it’s worth designing the power distribution system for the “full crab cavities” scenario.

The total loads are represented in Table 17-7. It’s important to highlight that the load forecast shown in Table 17-6 takes into account only the existing loads and the HL-LHC loads: a more accurate analysis should take into account also the evolution of loads on the Meyrin site (this requires an update of the document [8]).

Table 17-7: Total power consumption LHC1.

USER	LOCATION	SCENARIO WITH 1/2 CRAB CAVITIES			SCENARIO WITH FULL CRAB CAVITIES		
		ELECTRICAL POWER REQUIRED BY USER			ELECTRICAL POWER REQUIRED BY USER		
		[MW]	[Mvar]	[MVA]	[MW]	[Mvar]	[MVA]
Loads after LS2	LHC1	27.0	31.0	41.1	27.0	31.0	41.1
Additional HL-LHC Loads	LHC1	10.0	5.7	11.4	11.7	6.3	13.2
Additional ATLAS Loads	LHC1	1	0.8	1.3	1	0.8	1.3
Total without filters	LHC1	38.0	37.5	54	39.7	38.1	56

(*) Loads LHC1 + ATLAS + PS Loop + Isolde Loop

17.2.3.1.3 P1 network topology

Considering that the total load in Point1 shown in Table 17-6 (56 MVA) represents 80 % of the rating of the transformer EHT102/1E, it is evident that the network topology does not required to be modified because of the additional HL-LHC loads. It should nevertheless be noted that, in the context of the roadmap of the electrical group, the optimization of the electrical network topology for the Point1 and Meyrin sites is being studied. An updated layout of Point1 network topology might be presented during 2017.

With the actual topology, the substation SEM12 in LHC1 is divided in two functional parts:

- The first part, which supplies the LHC general services loop, is fed by BE9 (EHT7) via the 18 kV power cable MP7.
- The second part, which supplies the loads of LHC, ATLAS, Meyrin site and HL-LHC is fed via the transformer EHT102/1E.

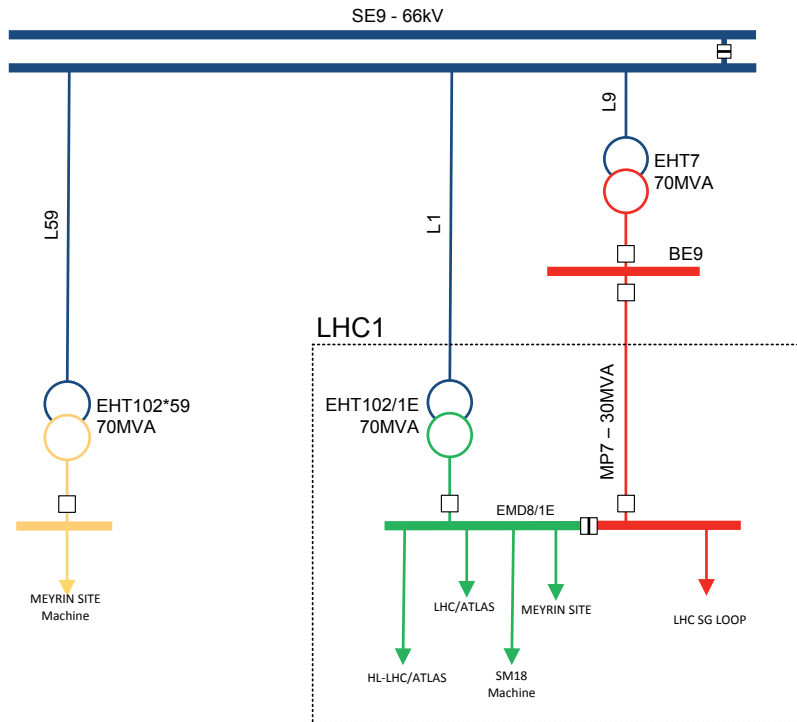


Figure 17-17: Single line diagram of the transmission network supplying LHC1.

17.2.3.1.4 LHC1 power quality

The operation of the HL-LHC accelerator and the Atlas detector imposes the need for excellent power quality. In particular the power converters, controlling DC currents with highest precision of a few ppm are very sensitive to power quality issues. In general terms, assuring a good power quality level comprises the following aspects:

- Generation of the reactive power consumed by the load (reactive power compensation), to assure a low overall reactive power consumption taken by CERN from the 400 kV network.
- Filtering of the harmonic currents generated by the non-linear load, aiming at a clean 50 Hz AC voltage of the 18 kV network with low contents of harmonic frequencies.
- Stabilising voltage fluctuations caused by cycling loads. This requirement does not apply to LHC1, as the loads are not cycling.

The electrical network in LHC1 will be divided in two separate parts, HL-LHC General Services (in red colour, Figure 17-17) and HL-LHC machine network (in green colour, Figure 17-17). HL-LHC general services (in red colour, Figure 17-17): Mixed load which is not cycling. The load during HL-LHC operation will be almost the same as for today for LHC. Harmonic filtering today is assured by the existing harmonic filters in LHC4 and LHC8. These existing harmonic filters are well adapted for HL-LHC operation, they just require consolidation before the start of HL-LHC.

HL-LHC Machine Network (in green colour, Figure 17-17): This network supplies HL-LHC, ATLAS and SM18, while the Meyrin General Services load will not be supplied by the electrical network of LHC1. The mixed-type load in LHC1 is a more or less constant load, not cycling. To compensate for the reactive power consumption of this load, and to filter the higher frequency harmonics, two new high-pass filters of 6 Mvar each will be required. These harmonic filters shall be connected to the 18 kV substation EMD8/1E in LHC1. Each of these two harmonic filters will be switched individually by a dedicated 18 kV circuit breaker, allowing to adapt the reactive power generation. The ratings of the components for these two harmonic filters will be based on CERN's standardised harmonic filter design. The achieved power quality level will be in

conformity with the requirements of the CERN LHC Engineering Specification EDMS113154 and also with the international standard IEC 61000-2-4 class 1.

17.2.3.1.5 LHC4 load forecast

The new loads to be installed in LHC4 site are mentioned in Table 17-8. Taking in account the actual baseline, four new cryogenics compressors and its auxiliaries will be installed in SUH4 building. From the electrical network point of view the actual 18 kV local network in SU4 will need to be updated. Some cooling equipment will be installed in the underground service cavern.

Table 17-8: HL-LHC loads in LHC4.

USER	LOCATION	ELECTRICAL POWER REQUIRED BY USER			
		[kW]	[kvar]	[kVA]	cos(phi)
TE/CRG	SUH4	2500	1483	2907	0.86
EN/CV cooling	US45	60.0	29	67	0.9
TOTAL		2,560	1,512	2,974	

In Table 17-9 is mentioned the LHC4 power consumption with the additional loads of HL-LHC. No major modification is foreseen in the 18 kV network. The actual transformer rated to 38 MVA will be able to supply the additional loads.

Table 17-9: Power consumption LHC4.

USER	LOCATION	ELECTRICAL POWER REQUIRED BY USER		
		[MW]	[Mvar]	[MVA]
Loads after LS2	LHC4	25.0	20	32
Additional HL-LHC Loads	LHC4	2.6	1.5	3.0
Total without filters	LHC4	27.6	21.5	35

(*) Loads without compensation of the SVC

17.2.3.1.6 P5 load forecast

Also in this case the load forecast in P5 shall take into account three different sets of data: the values provided by users in the context of the HL-LHC project, the values for CMS taken from the load forecast carried out in 2012 [8] and the measurement carried out in September 2016.

It's important to underline that users loads have been taken into account using the same scenarios already described in section 17.2.3.1.2 for P1. The differences between the two points are due to the fact that building heating equipment installed in P5 are electric.

Table 17-10: HL-LHC loads in LHC5.

USER	LOCATION	SCENARIO WITH 1/2 CRAB CAVITIES				SCENARIO WITH FULL CRAB CAVITIES			
		ELECTRICAL POWER REQUIRED BY USER				ELECTRICAL POWER REQUIRED BY USER			
		[kW]	[kvar]	[kVA]	cos(phi)	[kW]	[kvar]	[kVA]	cos(phi)
TE/CRG	SHM	5000	2967	5814	0.86	5000	2967	5814	0.86
EN/CV ventilation	SE	27.0	13	30	0.9	27.0	13	30	0.9
EN/CV ventilation	SU	483.5	234	537	0.9	483.5	234	537	0.9
EN/CV ventilation	SF	43.4	21	48	0.9	43.4	21	48	0.9
EN/CV ventilation	UW	62.4	30	69	0.9	62.4	30	69	0.9
EN/CV ventilation	SHM	64.2	31	71	0.9	64.2	31	71	0.9
EN/CV cooling	SU	605.8	293.4	673.1	0.9	610	295.3	677.4	0.9
EN/CV cooling	SF	548.6	265.7	609.6	0.9	569	275.8	632.7	0.9
EN/CV cooling	UW	163.8	79.3	182.0	0.9	195	94.4	216.7	0.9
BE/RF	UR	807	265	849	0.95	1614	530	1699	0.95
BE/RF	US	807	265	849	0.95	1614	530	1699	0.95
TE/EPC	UR	900	700	947	0.95	900	700	947	0.95
Various (GS...)	surf+und	1000	800	1281	0.78	1000	800	1281	
TOTAL		10,513	5,965	11,962		12,183	6,523	13,723	

As mentioned in section 17.2.2.5, from an engineering point of view, it's worth designing the power distribution system for the "full crab cavities" scenario.

As it can be seen in Figure 17-14, the point LHC5 is supplied from Point 6 via an underground 18 kV cable. As a consequence, it's necessary to verify the rating of two possible bottlenecks: the rating of the 18 kV power cable between the two points and the rating of the 66 kV transformer which supplies LHC6 (EHT102/6E).

To verify the ampacity of the cable from P5 to Point6 it is necessary to take into account the total loads represented in Table 17-11.

Table 17-11: Power consumption LHC5.

USER	LOCATION	SCENARIO WITH 1/2 CRAB CAVITIES			SCENARIO WITH FULL CRAB CAVITIES		
		ELECTRICAL POWER REQUIRED BY USER			ELECTRICAL POWER REQUIRED BY USER		
		[MW]	[Mvar]	[MVA]	[MW]	[Mvar]	[MVA]
Loads after LS2 (*)	LHC5	4.0	3	5	4.0	3	5
Additional HL-LHC Loads	LHC5	10.5	6.0	12.0	12.2	6.5	13.7
Additional CMS Loads (**)	LHC5	1	0.8	1.3	1	0.8	1.3
Total (without filters)		15.5	9.8	18.3	17.2	10.3	20.0

(*) Measurements September 2015

(**) from EDMS 1237699 v.2

The 4.4 km long power cable is composed by three single core copper cables of long 4.4 km (Cu 3x1x400mm²) and has a rating of 14.8 MVA. It's clearly seen that the rating of the existing cable is not adequate.

To verify the rating of the 66 kV transformer EHT102/6E it is necessary to take into account also the loads in Point 6, as shown in Table 17-12.

Table 17-12: Power consumption Point 6.

USER	LOCATION	SCENARIO WITH 1/2 CRAB CAVITIES			SCENARIO WITH FULL CRAB CAVITIES		
		ELECTRICAL POWER REQUIRED BY USER			ELECTRICAL POWER REQUIRED BY USER		
		[MW]	[Mvar]	[MVA]	[MW]	[Mvar]	[MVA]
Loads after LS2 for LHC5+LHC6 (*)	LHC5/LHC6	18.0	14	23	18.0	14	23
Additional HL-LHC Loads in LHC5	LHC5	10.9	6.0	12.0	12.2	6.5	13.7
Additional CMS Loads (**)	LHC5	1	0.8	1.3	1	0.8	1.3
Total (without filters)		29.9	20.8	36.1	31.2	21.3	37.8

(*) Measurements September 2015
 (**) from reference [5] EDMS 1237699 v.2

Considering that the transformer EHT102/6E has a rating of 38 MVA, it's evident that the load forecasted is too close to the rated nominal power of the transformer.

17.2.3.1.7 P5 network topology

Considering the values presented, the best technical solution features the installation of a new 38 MVA power transformer in P5, supplied by a new 66 kV cables from the Prévessin site, as represented in Figure 17-18.

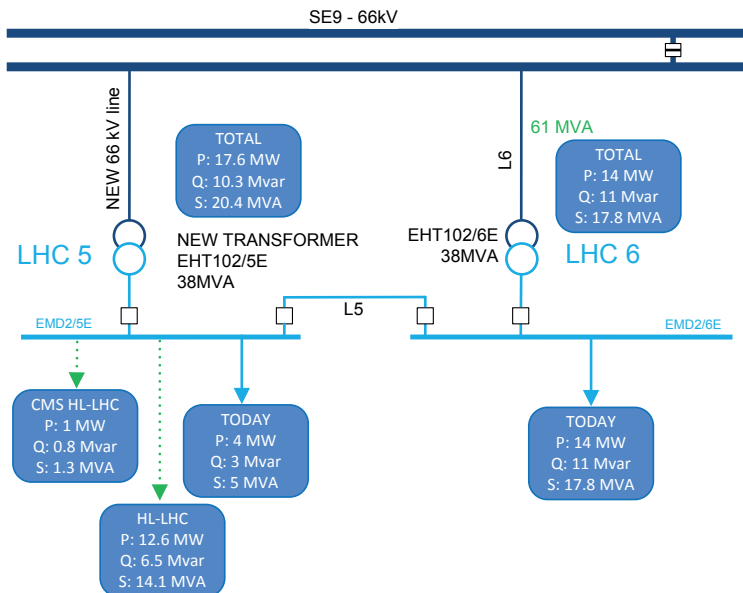


Figure 17-18: Single line diagram of the transmission network supplying LHC6 and LHC5.

17.2.3.1.8 P5 Power quality

For the power quality in LHC5, similar consideration as made for LHC1 (section 1.3.2.4) apply. LHC5 will be supplied via a dedicated 18 kV network supplied via a new 66 kV cable from Preveessin and a new 66/18 kV transformer EHT102/5E. The load is not cycling and consists of systems for HL-LHC and CMS. The total power consumption of the LHC5 load connected to substation EMD2/5E will be 17.6 MW and 10.3 Mvar (see Figure 17-18).

To compensate the reactive power consumed by the load, and to reduce the harmonic distortion of the 18 kV network, two new high-pass filters will be connected to the 18 kV substation EMD2/5E in LHC5. The harmonic filters will have a reactive power rating of 6 Mvar and 4 Mvar respectively, and each of these two harmonic filters will be switched individually by a dedicated 18 kV circuit breaker, allowing to adapt the reactive power generation. The ratings of the components for these two harmonic filters will be based on CERN's standardised harmonic filter design. The achieved power quality level will be in conformity with the requirements of the CERN LHC Engineering Specification EDMS113154 and also with the international standard IEC 61000-2-4 class 1.

17.2.3.1.9 High voltage distribution network

The detailed single line diagram for P1 [9] is shown in Figure 17-19 and the one for P5 is shown in Figure 17-20. As previously mentions the 18 kV and 3.3 kV distribution in P1 and P5 are designed to be as similar as possible.

The main users are the following:

- Cryogenic systems (SHM17-57);
- Cooling and ventilation (SU17-57, SF17-57, UW17-57);
- Radio Frequency (UA13-53, UA17-57); and
- Power converters (UR15-55).

Various options are represented for the RF power amplifiers, as the technology to be used has not been defined yet.

A new 3-rooms building will be constructed in P1 (SE17) and another in P5 (SE57). Inside the first room, called SEH, will host 18 kV and 3.3 kV switchgear. The second room, called SES, will host 18 kV and 3.3 kV protection relays, 400 V main and secondary distribution switchboards (normal and secured network), safety lighting power sources and distribution switchboards, 48 V DC system (chargers and distribution), UPS system units, equipment control/supervision racks and emergency stop rack. The third, smaller room, will host batteries for the 48 V DC system and the UPS.

In the cavern US17 and US57 a fireproof safe room will be created to host all safety-related equipment. The safe room will contain main and secondary secured switchboards, 48 V DC systems (chargers, distribution and batteries) and emergency stop rack.

The equipment to be installed in SE buildings, safe rooms and underground facilities have been defined and integrated in the 3D model on the base of EL known needs, user requirements and affinity with existing LHC installations.

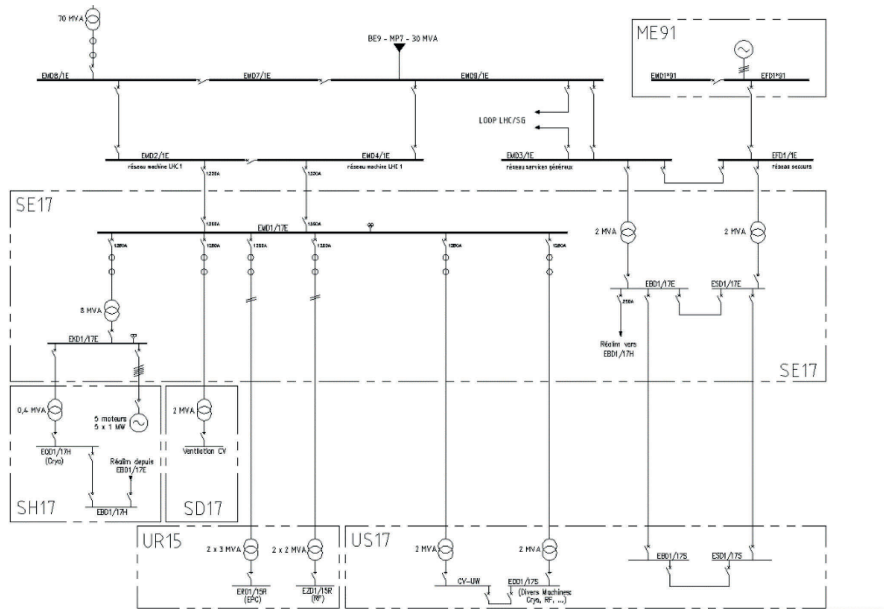


Figure 17-19: Single line diagram of the high voltage distribution network in LHC1.

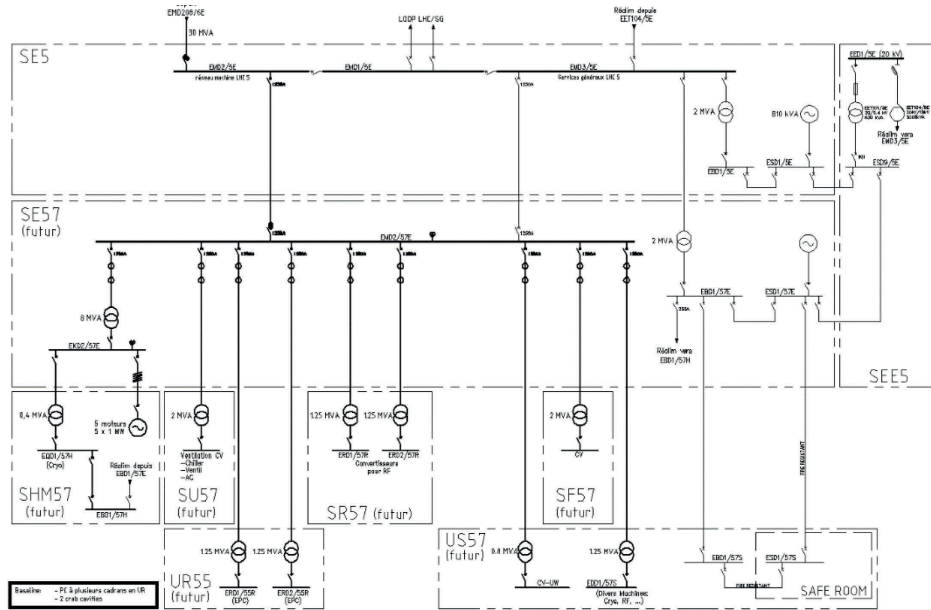


Figure 17-20: Single line diagram of the high voltage distribution network in LHC5.

In LHC 4 site the modifications expected on the 18 kV network will be localised in SU4 for building were the 3.3 kV machine switchboard is installed. This switchboard is foreseen to be replaced and upgraded to allow the new 4 feeders that will supply the new cryogenics compressors in SUH4. In Figure 17-21 is represented the 3.3 kV single line diagram with the two main HV switchboards supplied from the machine network (EKD2/4U) and the general service network (EKD1/4U). The new auxiliaries for the compressors will be fed by a new 400 V switchboard to be installed inside SUH4 building and supplied from the actual main switchboard dedicated to the cryogenics.

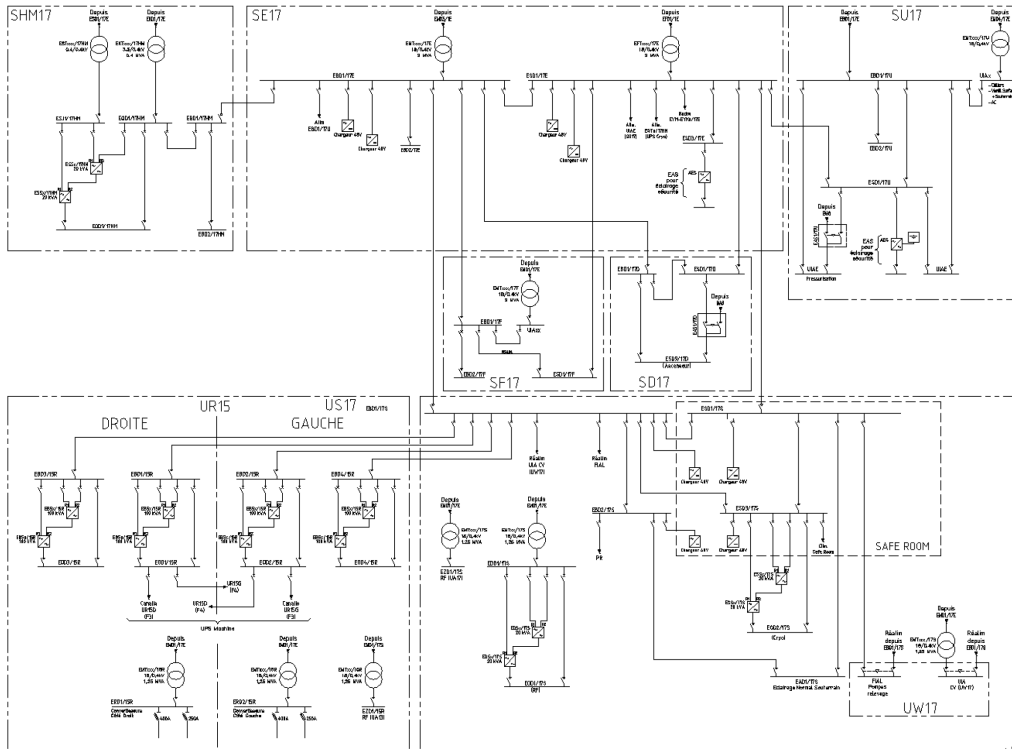


Figure 17-22: Low voltage distribution LHC1.

17.2.3.2 Secured power systems

This section describes the design principles of the low voltage distribution related to the diesel generators, the UPS systems and 48 V DC systems.

17.2.3.2.1 Secured network, supplied by diesel generators

In P1 the load forecast, extrapolated with the data provided by the users at this stage, does not indicate the need of a major modification of the existing infrastructure. The secured network dedicated to HL-LHC loads will be fed by one 18/0.4 kV transformer, located outside SE17 and supplied by the 18 kV switchgear EFD1/1E installed in SE1. The main 400 V distribution switchboard ESD1/17E will feed all secured sub-switchboards installed inside surface buildings and underground facilities.

In P5, in case the estimated loads increase above the values shown in Table 17-13, it will be necessary to replace the existing diesel generator or install a new one (space has been reserved for this scope). The distribution principle will be similar to the one described in the paragraph above for P1.

Table 17-13: Load forecast for the diesel generators in LHC5.

	Location	LHC5	LHC1	Comment	Ref.
		P [kW]	P [kW]		
Handling engineering	PM	-	-		
Cooling and Ventilation		64	64	Pressurisation et extractions	HL-LHC WP17
Access control	US-UR	10	10	5 racks in underg. - 2 kW/rack on secured network	HL-LHC WP17
Other	SD	4	4	2 racks in underg. - 2 kW/rack on secured network	HL-LHC WP17
Total Secured Network		78	78		

17.2.3.2.2 Secured network, supplied by UPS

The UPS network will be constituted by several UPS units (double-conversion AC/DC) associated with batteries and 400 V distribution switchboards. The UPS will have a 10-minute autonomy; underground UPS will be installed with N+1 redundancy.

The UPS and related switchboards will be installed and rated according the users' needs. Depending on this, the UPS can be installed with a centralised configuration, in which a single UPS supplies different functional equipment, or with a single unit dedicated to a specific user.

The load forecast, presented in Table 17-14 highlights the needs of UPS in both P1 and P5.

Table 17-14: Load forecast for the UPS in LHC1 and LHC5.

	Location	LHC5	LHC1	Comment	Ref.
		P [kW]	P [kW]		
Power converters	UR	86	86	1 kW / converter	HL-LHC WP17
	SR	10	10	IOT option	HL-LHC WP17
Radio Frequency	UR	70	70	Tetrode option	HL-LHC WP17
Criogenic systems	SHM	5	5	Extrap. from LHC	
	SDH	5	5	Extrap. from LHC	
	US	10	10	Extrap. from LHC	
Interlock systems and energy extractions	UR	65	65	redundant powering with two UPS lines, 10 mins autonomy	HL-LHC WP7
Cooling and Ventilation		0	0		HL-LHC WP17
Total Réseau UPS		251	251		

17.2.3.2.3 48 V DC network

In addition to the networks described above, there is a 48 V DC network used to supply the auxiliaries of high voltage switchgears and low voltage switchboards, the emergency stop system and Scada-related equipment. The 48 V DC network is constituted by Ni-Cd batteries, distribution switchboards and battery chargers fed by 400 VAC secured network. Only EL equipment will be connected to the 48 V DC network.

17.2.3.3 Safety systems

The safety systems include the emergency lighting and the emergency stop system (AUG).

17.2.3.3.1 Emergency lighting

A dedicated emergency lighting system shall be installed in every surface and underground facilities. The emergency lighting system shall activate in the event of a power failure or a scheduled test. For the underground facilities, it is foreseen to install a full redundant system, with two different and independent sources, separate fireproof cabling and specific luminaires. Surface buildings, more likely, will be equipped with safety luminaires for an emergency evacuation. These luminaires will have their own batteries and will act in the event of a power failure or a scheduled test.

The lighting levels and distribution will be according the last safety norms applicable at CERN.

17.2.3.3.2 Emergency stop (AUG)

The AUG system will be constituted by two racks, one in the surface building SE and one in the safe room inside the US cavern. These racks will host electronics cards, switches to bypass the button loops and cables terminals. Surface buildings and underground facilities will be subject to the action of Emergency Stop Buttons which act on the 18 kV distribution network.

A risk assessment shall be conducted in accordance with IS5 to decide the scope of services affected by an AUG action.

17.2.3.4 Scada System

The electrical equipment of the CERN power distribution network is interfaced with a SCADA system, referred to as Electrical Network Supervision (ENS), which provides the CERN Control Centre (CCC) and the electrical operation personnel with remote monitoring, control facilities, alarm information and historical archiving. The system supervises majority of equipment located in the CERN electrical substations, in surface and underground areas including LHC tunnel and experimental areas, as well as other buildings throughout the site. The equipment supervised in these installations span all voltage levels from 48 VDC battery chargers to 400 kV circuit breakers and transformers. Since the distribution network involves different generations of technology, industrial computers located in the major substations, acting as data concentrator systems (often referred to as RTU), manage from proprietary serial protocol to modern Ethernet based standards such as IEC61850 and exchange information to the SCADA system by the IEC870-5-104 standard protocol.

Altogether the system supervises around 20'000 devices, representing 130'000 digital signals, 90'000 analogue signals and counter, and 21'000 controls spread in 35 areas and 350 substations, interfaced by over 70 RTU. These cover from simple status signals to digital protection relays as well as UPS and battery chargers. Control channels permit remote actions mainly on circuit-breakers, UPS and battery chargers. Majority of devices involved at various levels are synchronised from Time Servers.

Around 90 PLC based systems are installed and the majority are dedicated to automatic network switch-over to secured network in case of main source failure for critical loads. A global architecture of the ENS system is shown in Figure 17-22.

In addition to the conversion of multiple communication protocols from field equipment towards the upstream IEC870-5-104, RTUs allow for a second level of supervision in the major substations through local SCADA software. The implementation is “stand-alone”, remaining fully operational in the event of unavailability of the external informatics infrastructure or main SCADA system.

The main SCADA system, Siemens WinCC OA based (formerly known as PVSS) runs on 2 LINUX servers in a redundant hot-standby configuration. The system is integrated with existing CERN facilities for long term archiving and logging, for alarms and for data exchange with other applications and control systems. Additional software modules have been foreseen to be integrated in the coming years in the main SCADA in support of network operation or network recovery after failure, such as simulation and power flow calculation, event replay and outage management system.

A web based application, open to CERN users, calculates and plots energy consumptions for the main electrical consumers in the accelerator complex and experiments.

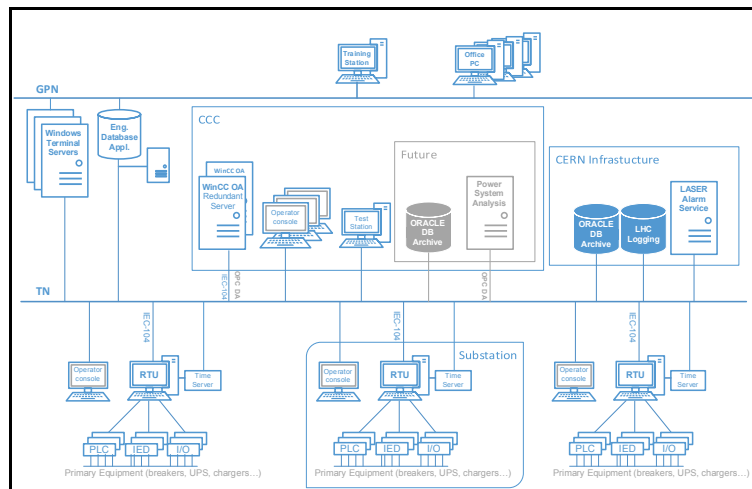


Figure 17-23: ENS System Architecture.

17.2.3.5 High current DC cabling

In the HL-LHC Project, high Direct Current (DC) cables are used between the power converters and the cold powering system (see chapter 6A). Those power cables are either conventional (air-cooled), or water cooled depending on the current requirements. The design of the terminations is adapted to the power converters and to the current leads.

Table 17-15 and Figure 17-24 show the intensity of the current requested and the cross-section of the cables.

	Copper section	Length of the cable above the lug	Minimum bending radius	External diameter
	[mm ²]	h: [mm]	r: [mm]	[mm]
18 kA	2x1300	500	800	2x95
13 kA	2000	500	800	115
6 kA	1000	500	700	95
2 kA	500	500	500	70
600 A	400	300	300	36
200 A	95	200	200	25
120 A	70	150	150	22

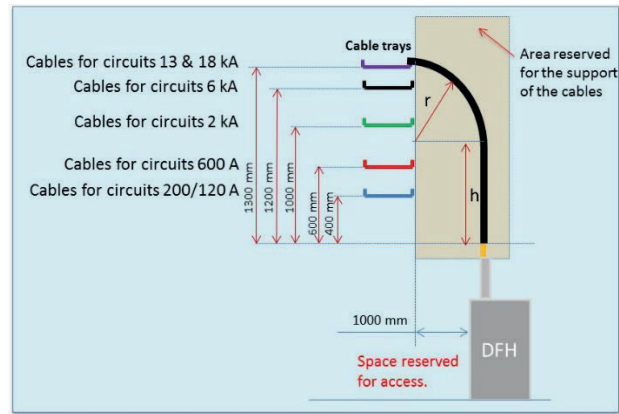


Table 17-15: Intensity requested and cross-section of the cables.

Figure 17-24: Bending radius of the DC cables.

17.2.3.5.1 Conventional DC cabling

The conventional (air-cooled) DC cabling concerns the following intensities: 120, 200 and 600 A and the corresponding cross section of the copper cables are respectively 70, 95 and 400 mm². The cross section of the conventional DC cables is defined in the Reference Database, which contains all information related to the Electrical DC Circuits. Their installation is included in the machine cabling campaigns.

17.2.3.5.2 Water-cooled DC cabling

Water-Cooled Cables (WCCs) will be used for high current DC interconnections between the power converters and the superconducting current leads, part of the DFHs, located in the UR building of the points 1 and 5 of LHC. The WCCs concern the following intensities: 2, 13 and 18 kA and the corresponding cross-section of the cables are respectively 500, 2000 and 2x1300 mm². For the other circuits Q4, Q5 and Q6, the existing water cooled cables installed in the RRs will be reused. Their cross-section is 800 mm² for the transport of an intensity of 6 kA. The cooling of the cables is assured by the circulation of demineralized water inside the cable hose. This technology is well known at CERN and currently used in all the points of the LHC (Figure 17-25).

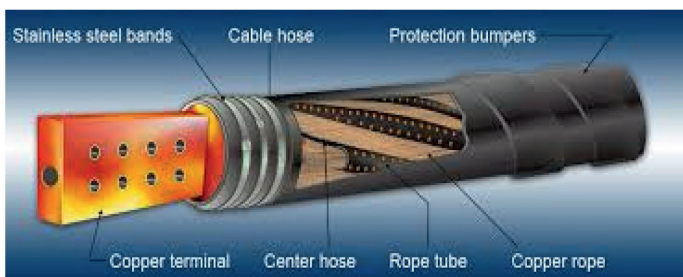


Figure 17-25 – Water cooled cable technology and Water cooled cables used in LHC.

The bending radius of the cables is given in Table 17-15. Due to the configuration of the civil engineering of the UR building, the 18 kA link is composed of 2 cables of 1300 mm² in parallel for each one

TECHNICAL INFRASTRUCTURE

of the polarities to limit the height necessary for the bending radius of the cables. The space required for the links has been reserved in the integration database. The supports of the cables located above the power converters and the LHC DFBs have to be carefully designed in order to avoid stress on the equipment and connectors.

Table 17-16: Estimated length of the DC cables.

	Optic	Location of converters	Magnet Type	L per circuit [mH]	Operating Current [kA]			# of circuits	Cu section [mm ²]	characteristic time [s]	L circuit [m]	R circuit [mΩ]	Time const. [s]	Total cable losses [kW]			Cable type
					Nominal	Ultimate	Rated							Nominal	Ultimate	Rated	
DFHX	Triplet Q1, Q2a, Q2b, Q3	UR	MQXFA / MQXFB	255	16.5	17.8	18.0	1	2600	0.1-0.5	42	0.291	877	79.3	92.5	94.3	WCC
	Trim Q1	UR			2		2.0	1	500		58	2.088		8.4	0	8.4	WCC
	Trim Q3	UR			2		2.0	1	500		60	2.16		8.7	0	8.7	WCC
	Trim Q2a	UR			0.12		2.0	1	70		28	7.2		0.2	0	28.8	ACC
	Corrector	UR	MCBXFVB	59	1.6	1.73	2.00	2	500	0.1-0.5	64	2.304	26	11.8	13.8	18.6	WCC
	Corrector	UR	MCBXFVBH	135	1.47	1.59	2.00	2	500	0.1-0.5	66	2.376	57	10.4	12	19.2	WCC
	Corrector	UR	MCBXFVAV	109	1.6	1.73	2.00	1	500	0.1-0.5	70	2.52	44	6.5	7.6	10.1	WCC
	Corrector	UR	MCBXFVAH	247	1.47	1.59	2.00	1	500	0.1-0.5	72	2.592	96	5.7	6.6	10.4	WCC
	CP	UR	MQSXF	1247	0.182	0.20	0.20	1	95	7.57	28	5.306	236	0.2	0.3	0.3	ACC
	CP	UR	MCSXF / MCSXF	186	0.105	0.11	0.12	2	70	0.41	28	7.2	26	0.2	0.2	0.4	ACC
	CP	UR	MCOXF / MCOSXF	200	0.105	0.11	0.12	2	70	0.41	28	7.2	28	0.2	0.2	0.4	ACC
	CP	UR	MCDXF / MCDXF	187	0.105	0.11	0.12	2	70	0.53	28	7.2	26	0.2	0.2	0.4	ACC
	CP	UR	MCTXF	576	0.105	0.11	0.12	1	70	0.37	28	7.2	80	0.1	0.1	0.2	ACC
	CP	UR	MCTSXF	126	0.105	0.11	0.12	1	70	0.80	28	7.2	18	0.1	0.1	0.2	ACC
D1	UR	MBXF	25	12	13.0	13	1	2000	0.1-0.5	44	0.396	64	57.1	66.6	67	WCC	
DFHM	D2	UR	MBRD	27	12	13.0	13	1	2000	0.1-0.5	36	0.324	84	46.7	54.5	54.8	WCC
DFBL	Correctors D2	UR	MCBRD	600	0.5	0.54	0.6	4	400	10.0	24	1.08	556	1.2	1.6	1.6	ACC
DFBL	Q4	RR	MQY	74.0	4.50	4.9	6.0	2	800	0.1-0.5	28.50	0.642	116	26.2	30.4	46.4	WCC
DFBL	Orbit correctors Q4	tdb	MCBY	5270	0.072	0.08	0.12	8		10.0	tdb	tdb	tdb	tdb	tdb	tdb	ACC
DFBL	Q5	RR	MQY	148.0	4.51	4.9	6.0	2	800	0.1-0.5	26.5	0.597	248	24.4	28.4	43	WCC
DFBL	Orbit correctors present Q4	tdb	MCBY	5270	0.072	0.08	0.12	6		0.4	tdb	tdb	tdb	tdb	tdb	tdb	ACC
DFBL	Q6	RR	MQML	21.0	4.31	4.7	6.0	2	800	0.1-0.5	20.7	0.466	46	17.4	20.2	33.6	WCC
DFBL	Orbit correctors Q6	tdb	MCBC	2840	0.08	0.09	0.12	2		0.2	tdb	tdb	tdb	tdb	tdb	tdb	ACC
11T	11T dipole, MBH		11T dipole, MBH	127.0	11.85	12.798	13			as RB							
	Trim circuit	TZ76			0.25			1	1200		1000	15		1			ACC

According to the actual layout, the total length of the DC cables is shown in Table 17-16. The lengths are identical for the both sides of each P1 and P5. The summary of the cables losses is shown in Table 17-17

Table 17-17: Summary of cable losses.

Location	# of converters	Total cable losses [kW]		
		Nominal	Ultimate	Rated
<i>one side</i>				
UR	25	237	256.3	323.8
RR*	22	68	79	123
<i>Total P1</i>				
UR	50	474	512.6	647.6
RR*	44	136	158	246
TZ76	2	1		

RR*: Orbit correctors not included in the cable losses

17.2.3.6 Optical fibre infrastructure

17.2.3.6.1 Introduction

The optical fibre infrastructure provides optical fibre links across the CERN site, including in between surface and underground buildings. The infrastructure also distributes in each of the LHC service areas and along the LHC arcs. This infrastructure serves a variety of systems (Cryogenics, Beam Interlock, LASS, Evacuation, Power converters, IT Network, GSM, TETRA, and others). The optical fibre infrastructure is designed to cover the upcoming requests and to guarantee a minimum available fibre capacity in the service areas. This capacity is established proportionally to the typical occupancy rate of the optical fibre links for the user systems.

A new portion of the optical fibre infrastructure will be deployed for HL-LHC with the same topology and installation techniques as the existing one, for each of the LHC service areas.

17.2.3.6.2 Installation techniques

Optical fibres for HL-LHC will be installed by air-blowing. This technique consists of laying ducts and microducts where the optical fibre cables can be blown in as required according to the existing and future needs. This installation technique is the same adopted by the past for the existing LHC optical fibre infrastructure, as described in document [12].

The installation of conventional versus special -radiation resistant- optical fibres shall be studied according to the radiation levels estimated for the different areas.

The minimum bending radius of the optical fibre ducts has to be taken into consideration in the design and integration studies for the passages and cable containments, in order to guarantee the minimum requirements for the blowing of the optical fibre cables.

17.2.3.6.3 Topology

The topology of the current optical fibre infrastructure is based on a star-point distribution. For the new distribution, the topology will be mirrored from the existing infrastructure in the LHC service areas. The new distribution will include also main linking paths between the existing and the new star-points. A redundancy path to the surface will also be created over the new pit. This configuration will allow creating redundancy paths for critical systems and serving locally the new systems that could be added later.

17.2.3.6.4 Systems and local distribution

The optical fibre capacity will be dimensioned according to the received requests and calculated spare capacity (in the same proportion as in the existing LHC service areas). The current requests are in phase of study and discussion. The current requests are:

- General optical fibre infrastructure;
- Controls for electrical distribution network;
- IT Network;
- Crab-Cavities monitoring and
- Magnet cold mass monitoring.

17.2.3.7 Signal cabling

Signal cabling includes the installation of electrical cables for data transfer and control for the various user systems. It typically comprises a very large volume of cables to be installed in multiple cabling campaigns.

17.2.3.7.1 *Very first estimation of the volumes*

The quantities of cables shown in Table 17-18 concern only one LHC point. These figures are based on presently available information given by the users and on the past experience during the LHC construction.

Table 17-18: List of systems and sub-systems and estimated cable quantities.

System	Sub-systems	Quantities of signal cables
Access system	Access Control, Access Safety	16
Safety system	Red Phones, Fire Detection, ODH, Evacuation	140
RF (HL)	Input Power, Driver Output, Amplifier Output Signal	132
RF (LL)	Ic/Ig - rev/fwd, TX drive	96
RF (Control)	Interlocks and Monitoring Signal RF	120
MPE (Interl.)	Beam Interl. Signal, WIC, Power Interl Control	59
MPE (Mach. Prot.)	QDS,EE,CLIQ,FMCM,Quench Heaters	255
Survey	Position monitoring and adjustment system	428
CV	Equipment control	20
Cryo	Measurement, control	58
RP	Radiation Monitoring	10
IT	Communication, Ethernet	10
MSC	Control current leads	150
EN-EL	AC distribution Control	50
BE-CO	Remote reset, Worldfip, timing	40
BE-BI	No informations	0
Others	No informations	0
Total		1584

17.2.3.7.2 *Assignment of cable ladders in the UR*

Figure 17-26 shows the assignment of the cable in the UR. The signal cables will be grouped together on the same cable ladder independently of the systems they serve. The great majority of the signal cables are screened, which limits crosstalk and electro-magnetic interference. Cables for those systems that are particularly sensitive to those effects will be pulled on a separated cable ladder.

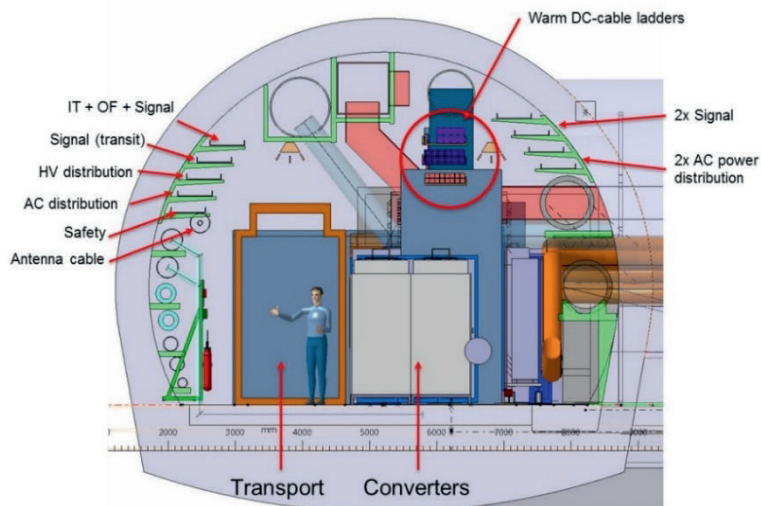


Figure 17-26 – Assignment of cable ladders in UR.

17.2.3.7.3 *Installation principle*

The installation of the signal cables is organized in a series of cabling campaigns in order to optimize the working time and the cost. Cables are installed before the great majority of the equipment. All cables included in a cabling campaign are pulled and fixed in the cable ladders. The requested connectors are mounted at each end and then protected from dust.

Each installed cable is visually checked and tested for insulation and continuity and the wiring convention is verified.

17.3 Cooling

17.3.1 General statements for CV installations

The Cooling and Ventilation installation at P1 and P5 are mostly the same. The section describes the installation in P1 and makes reference to the building names at this location. It is understood that the same installation configuration exists in the equivalent buildings in P5.

The only difference between the two installations consists in the heating solution for the air handling units: at P1 (in Switzerland) the electrical heaters are not allowed. A dedicated extension of the superheated water network will be used. At P5 (in France) there is no superheated water network and the national laws allows electrical heaters and this solution has been used.

The design of the CV installation has been done for the “½ Crab Cavities” configuration (new baseline since August 2016). It has been agreed that all installations that would require large works and or investments to upgrade to the “Full Crab Cavities” configuration will be designed for this last configuration. In particular, pipework and ductwork are sized for full crab cavities flow rates. Volumes for the upgrade of the installations are foreseen in the integration and in the design of the underground facilities.

17.3.2 Primary water cooling

A new 3-cell cooling tower (n+1 redundancy) of 5 MW each will be installed in P1. The total cooling power requirements is listed in Table 17-19. The water supply temperature will vary between 20°C and 25°C. The primary water flowrate is based on 10 K temperature difference between supply and return. Three circuits will distribute the primary water in a duty and standby (1+1) arrangement. The pump heads will be selected to provide approximately 300 kPa at the connexion point of each user equipment. The new plant room will house the three couples of redundant pumps, the sand filtration, water treatment station, and frost protection systems. The pipeline will be made of stainless steel and distributed in the various buildings using technical galleries.

Table 17-19: Overall cooling power requirements at P1.

Location	Final users	Cooling power requirement (MW)
UW17	Power converters, Amplifiers, Cryogenic	1.6
SHM17 and SD17	Cold box, QSCG	5.2
SU17	Water cooled chillers	1.0

17.3.3 UW secondary water cooling

17.3.3.1 Cryo raw water circuit

The cold compressors of the cryogenic system will be cooled by a dedicated water cooling station in UW17. It will include a heat exchanger of 80 kW and a duty and standby pump.

17.3.3.2 Demineralised water cooling

One demineralised water cooling circuit will be installed to service all the underground installation. It will cool the power converters, the machine protection system, the water cooled cables in UR and the IOTs RF system in UA. The station will include one heat exchanger (1.6 MW), a duty and standby pump and a demineraliser. The water conductivity will be maintained below 0.5 µS/cm.

17.3.4 Chilled and cold water

17.3.4.1 Chilled water for fresh air handling unit

The chilled water production plant will be dedicated to the fresh air treatment only because of its dehumidification needs. It will be located in SU17. Two water cooled chillers (n+1 redundancy) of 200 kW each will be installed and connected to a common water buffer tank (3 m³ or more depending on the volume of the circuits). The temperature regime will be 6°C at the supply and 12°C at the return. The chilled water will be distributed to the fresh air handling unit using a duty and standby pumps and an insulated stainless steel pipework DN80.

17.3.4.2 Cold water for air handling units

The cold water production plant will be located in SU17. Three water cooled chillers (n+1 redundancy) of 350 kW each will be installed and connected to a common water buffer tank (5 m³ or more depending on the volume of the circuits). The temperature regime will be 14°C at the supply and 20°C at the return.

The cold water will be distributed to the surface air handling units using a duty and standby pumps and a stainless steel pipework DN80. The chilled water will be distributed to the underground air handling units using a duty and standby pump and an insulated stainless steel pipework DN125.

17.3.4.3 Hot water for air handling units (P1 only)

The CERN Meyrin superheated water network is available close to HL-LHC site. A hot water production station will be installed to distribute hot water to the air handling units located in the surface building of the HL-LHC complex at P1. Electrical heaters will guarantee heating power at P5 instead.

17.3.5 Firefighting network

A firefighting water pipe will be installed in the PM17 for the underground areas. A surface and underground firefighting water network (DN100) will be installed to supply hose reels and firefighting Storz-55 connections. The network will be connected to the existing firefighting network at P1 and P5.

17.3.6 Compressed air

The compressed air needs will be ensured by a dedicated production system. One duty and one standby rotatory air compressor (providing between 90 and 400 Nm³/h at 7 bar each) will be installed in SU17. The air dew point will be maintained below -40°C by an air drier. The system will include a wet and dry air tank of 3 m³ each, 0.5 µm and 0.1 µm filters. The compressed air network will be made of galvanised steel or stainless steel and will distribute compressed air to SHM17, SF17, SE17, US17, UW17 buildings.

17.3.7 Clean and waste water

A clean water sump will be located at the lowest part of the new underground areas (US) in order to collect all the infiltration or accidental water release. A duty and standby pump will lift the clean water to the surface drainage network. A waste water pit and a duty and standby pumps will lift the waste water to the surface waste water network.

17.3.8 Underground air handling units

17.3.8.1 UR15 and UA13

The tunnel temperature will be maintained between 14°C and 25°C. The total dissipated heat load was estimated to be 310 kW (60 kW for each UA). The HVAC system consists of several ventilation units located as close as possible of the equipment generating the heat load.

Six air handling units of 8,500 m³/h will be installed in the UR. They will measure approximately 1.65 m X 1.35 m X 1.65 m. These units will not be equipped with ducts, they will recirculate the air locally taking the warm air from the top part of the tunnel and supplying cold air at the level of the floor.

Two unit of 15,000 m³/h measuring approximately 5.0 m × 2.6 m × 1.65 m will supply air cooling for the two UA tunnels. The units use cold water (14-20°C regime) for cooling and they will not be fitted with any heating battery. The supply and return air duct work will be not insulated and constructed with circular ducts of 900 mm diameter where possible. The air supply and return ducts will have regular spaced duct mounted grids along the UA tunnel.

The UA13 AHU will be installed in UA13. The UA17 AHU will be installed in UW17.

17.3.8.2 US17

The cavern temperature will be maintained between 14°C and 25°C. The total dissipated heat load was estimated to be 47 kW. The HVAC system consists of one ventilation unit of 12,000 m³/h located in UW17. The unit will measure approximately 4.0 m × 1.65 m × 1.65 m.

The unit uses cold water (14-20°C regime) for cooling and it will not be fitted with any heating battery. The supply and return air duct work will be not insulated and constructed with circular ducts of 710 mm diameter. The air supply and return ducts will have regular spaced duct mounted grids.

17.3.8.3 UW17

The cavern temperature will be maintained between 14°C and 25°C. The total dissipated heat load was estimated to be 15 kW.

The HVAC system consists of one ventilation unit of 4,500 m³/h located in UW17. The unit will measure approximately 3.0 m × 1.35 m × 1.2 m.

The unit uses cold water (14-20°C regime) for cooling and it will not be fitted with any heating battery. The supply and return air duct work will be not insulated and it will be constructed with circular ducts of 500 mm diameter where possible. The air supply and return ducts will have regular spaced duct mounted grids.

17.3.8.4 Faraday Cages

Two Faraday cages will be located in US17 and in UR17. Each of them will dissipate about 8 kW and it be ventilated by one duty and one standby air handling units of 3,500 m³/h each. Each unit will measure approximately 1.35 m × 0.85 m × 2.5 m. The room temperature will be maintained between 20°C and 22°C. The supply air temperature will be 15°C. The supply and return air duct work will be constructed with circular ducts of 450 mm diameter where possible. Some fresh air will be directly supplied in the cages for hygienic purpose.

17.3.8.5 Safe room

The safe room will be located in US17 and will be ventilated by one duty and one standby air handling units of 3,500 m³/h each. Each unit will measure approximately 1.35 m × 0.85 m × 2.5 m. The room temperature will be maintained between 18°C and 23°C. The total dissipated heat load was estimated to be 10 kW. The supply air temperature will be 16°C. The supply and return air duct work will be constructed with circular ducts of 450 mm diameter where possible. The safe-room is assumed to be leak tight. A duty and standby extraction units of 1000 m³/h each located in SD17 assures the extraction of the hydrogen potentially produced by the batteries of the safe room. The over pressurisation will be ensured by the fresh air unit.

17.3.9 Fresh air distribution

The fresh air will be provided by one duty and one standby air handling units of 15,000 m³/h each installed in SU17. Each unit will measure approximately 5.0 m × 2.0 m × 1.65 m. The duty air handling unit will ensure the air renewal and the dehumidification of the tunnel. The air dew point will be maintained below 12°C. The moisture load of the tunnel (8600 m²) was considered to be of 5 g/h/m². The quantity of water to be removed by the fresh air supply is estimated to be 80 kg/h.

Each unit uses chilled water (6-12°C regime) for cooling (200 kW) and two hot water (P1) and electrical batteries (P5) (2 X 120 kW) for heating. The supply air duct work will be constructed with circular ducts of 800 mm diameter where possible. The air intake duct and supply ducts will be insulated. The fresh air supply will be either distributed to the underground air handling units or to the rooms directly. The air handling unit will be designed to run on full fresh air only.

17.3.10 Pressurization of staircase and lift shaft

A duty and standby unit of 15,000 m³/h will insure the pressurisation of the staircase, lift shaft to the underground areas and safe area around the lift exit in the US. Both units will be equipped with a hot water battery (P1) or an electrical heater (P5) of 130 kW. Only one of them will be fitted with a cold (14-20°C regime) water battery of 75 kW. The supply air duct work will be constructed with circular ducts of 800 mm where possible. The air intake duct and supply ducts will be insulated.

17.3.11 HVAC for surface buildings

The required hygienic outside fresh air will be provided by the ventilation systems in all the surface buildings.

17.3.11.1 SHM17

The building volume is 7,125 m³. The room temperature will be maintained between 18°C and 26°C in the work area. The total dissipated heat load was estimated to be 200 kW. The HVAC system consists of one ventilation unit of 60,000 m³/h. The unit will measure approximately 9 m × 3 m × 6 m. The unit uses hot water battery (P1) and electrical battery (P5) (200 kW) for heating and it will not include a chilled water battery. The supply and return air duct work will be constructed with circular ducts of 1350 mm where possible. The air intake duct will be insulated. The air return ducts will have regular spaced duct mounted grids. The air supply will be distributed through low velocity displacement units located on ground floor level. The air handling unit will be designed to run on free cooling to save energy. The over-pressure will be released using several roof mounted static exhausts (or louvered penthouse) located on the roof.

17.3.11.2 SE17

The building volume is 1,500 m³. It is divided in two parts for the low voltage (LV) and high voltage (HV) electrical equipment. The room temperature will be maintained between 18°C and 35°C. The total dissipated heat load was estimated to be 11 kW on the LV part and about zero in the HV one.

The HVAC system of the HV part consists of two redundant ventilation unit of 6,000 m³/h. The units will measure approximately 1.2 m × 1.35 m × 3 m. The units are equipped with a hot water battery (P1) or an electrical battery (P5) (10 kW) for heating but will not include a chilled water battery. The supply and return air ductwork will be constructed with circular ducts of 560 mm where possible. The air intake duct will be insulated. The air return ducts will have regular spaced duct mounted grids.

The HVAC system of the LV part consists of two redundant ventilation unit of 3,600 m³/h. The units will measure approximately 1.35 m × 0.85 m × 2.5 m. The units are equipped with a hot water battery (P1) or an electrical battery (P5) (10 kW) for heating, but it will not include a chilled water battery. The supply and return air ductwork will be constructed with circular ducts of 450 mm where possible. The air intake duct will be insulated. The air return ducts will have regular spaced duct mounted grids.

In both HV and LV sides the air supply will be distributed under the false floor, the return air is taken from the top of the room. The air handling unit will be designed to run on free cooling to save energy. The over-pressure will be released using a roof mounted static exhaust (or louvered penthouse) located on the roof.

17.3.11.3 SF17

The building volume is 1,600 m³. The room temperature will be maintained between 18°C and 35°C. The total dissipated heat load was estimated to be 30 kW. The HVAC system consists of one ventilation unit of 15,000 m³/h. The unit will measure approximately 5.0 m × 1.65 m × 2.0 m. The unit a hot water battery (P1) or and electrical battery (P5) (16 kW) for heating, but it will not include a chilled water battery. The supply and return air duct work will be constructed with circular ducts of 800 mm diameter where possible. The air intake duct will be insulated. The air supply ducts will have regular spaced duct mounted grids. The air return will be done in bulk directly in the mixing plenum. The air handling unit will be designed to run on free cooling to save energy. The over-pressure will be released using a roof mounted static exhaust (or louvered penthouse) located on the roof.

17.3.11.4 SU17

The building volume is 6006 m³. The room temperature will be maintained between 18°C and 30°C in the work area. The total dissipated heat load was estimated to be 15 kW. The HVAC system consists of one ventilation unit of 15,000 m³/h. The unit will measure approximately 5.0 m X 1.65 m X 2.0 m. The unit uses cold water (14-20°C regime) for cooling (47 kW) and a hot water battery (P1) or an electrical battery (P5) (28 kW) for heating. The supply and return air duct work will be constructed with circular ducts of 800 mm diameter where possible. The air intake duct and supply ducts will be insulated. The air return ducts will have regular spaced duct mounted grids. The air supply will be distributed through low velocity displacement units located on ground floor level. The air handling unit will be designed to run on free cooling to save energy. The over-pressure will be released using several roof mounted static exhausts (or louvered penthouse) located on the roof.

The building SU17 will house the air handling units for the ventilation of SD17, tunnel's primary fresh air and the pressurisation of staircase and lift shaft.

17.3.11.5 SD17

The building volume is 3328 m³. The room temperature will be maintained between 18°C and 35°C. The total dissipated heat load was estimated to be 10 kW. The HVAC system consists of one ventilation unit of 13,000 m³/h located in SU17. The unit will measure approximately 4.0 m × 1.65 m × 1.65 m. The unit uses hot water battery (P1) or an electrical battery (P5) (26 kW) for heating but will not include a chilled water battery. The supply and return air duct work will be constructed with circular ducts of 710 mm diameter where possible. The air intake duct will be insulated. The air supply and return ducts will have regular spaced duct mounted grids. The air handling unit will be designed to run on free cooling to save energy. The over-pressure will be released using a roof mounted static exhaust (or louvered penthouse) located on the roof.

17.3.11.6 UA and UL pressurisation

Two redundant ventilation systems will assure the pressurisation of the air-lock installed at the end of the UA galleries. In normal operation the units will take air from UA tunnel to pressurise the air-lock zone. In case of alarm in the HL-LHC underground area the units will take the air from LHC tunnel to pressurise the air-lock zone. On the same principle, two redundant ventilation systems will assure the pressurisation of the air-lock installed in the UL galleries.

17.3.12 Smoke extraction

17.3.12.1 Surface buildings

Each of the buildings SHM17, SU17, SD17, SE17 and SF17 will be equipped by a dedicated and independent smoke extraction system. The smoke extraction will be ensured by natural ventilation using dedicated sky domes. The free opening areas will respect 1/200 of the floor area of each building. Mechanical air intake dampers will be installed in addition to the access doors where needed in order to have less than 10 meters without an air intake entry. The static exhaust(s) and air intake damper(s) will be operated using a firemen cubicle located at the entrance of each building.

17.3.12.2 Underground areas

Two smoke extractor fans of 18,000 m³/h each will be installed in SU17. The smoke extractors will be F400 120 (according to EN 12101) and hardwired to a firemen cubicle to be located in front of the building SU17. The fresh air intake will come naturally from the shaft PM17. In addition, motorised fresh air dampers will be installed in SD17 to facilitate the fresh air entry to the shaft. Two galvanised steel ducts of 750 X 750 mm each will be fire-resistant EI120. A fire-resistant door will be installed in the middle of the UR galleries; fire dampers will be installed in the ductwork at the same location. Smoke curtains are installed in different positions on the vault of the gallery to define smoke retention areas. Smoke resistant dampers will be installed in ductwork in the appropriate locations to allow the extraction of the smoke in the targeted area. The two units will be used for the smoke extraction of US that requires 36,000 m³/h. A smaller unit of 5,400 m³/h is installed in parallel to assure the smoke extraction of the UL tunnels.

17.4 Access & alarm systems

17.4.1 Introduction

The HL-LHC project includes many modifications to the current LHC installations. On one hand, large new surface buildings will be constructed and new underground areas excavated for the new equipment, and on the other hand, existing LHC equipment will be upgraded, such as the inner triplet areas of P1 and P5. New types of equipment (e.g., crab cavities) as well as higher prompt and residual radiation levels due to the increased luminosities around interaction points require a re-evaluation of risks around these sections of the LHC tunnel. The new underground areas must be constructed so as to fulfil today's regulations for fire and radiation safety as well as oxygen deficiency hazards.

In this chapter will be enumerated the modifications to the current LHC access and safety systems (LASS/LACS) including integration of the new underground installations at LHC sites 1 and 5. It contains also the modifications and new installations of alarm systems and other associated safety systems, including automatic fire detection system, automatic oxygen deficiency hazard detection system (ODH), red telephones (or emergency telephones), automatic protection system that triggers emergency evacuation (Safety Sound System) and any other safety action required such as closing of fire doors or hot smoke extraction. All alarm systems send level-3 alarms to the fire brigade for immediate interventions via the CERN Safety Alarm Monitoring system (CSAM).

17.4.2 Requirements and constraints

17.4.2.1 Environmental and legal

Installation of safety and access systems poses no particular environmental concerns. However, the LHC is considered as similar to a Basic Nuclear Installation (Installation Nucléaire de Base, INB) under both French and Swiss regulations, and the LHC personnel safety systems are subject to inspections by the competent host state authorities.

Safety document “CERN Safety Code E – Fire protection” specifies that installed equipment shall follow the regulations of the host states on their respective territories. In order to treat LHC and HL-LHC as a whole, a formal derogation will be put in place to treat the HL-LHC as a French installation for this purpose.

17.4.2.2 Operational

Access and safety systems are designed to be operational constantly 24/7, with the exception of clearly defined maintenance windows. During maintenance, the installed equipment may need to be accessed and access control functionality replaced by temporary measures, as applicable. During normal operation, these equipment are for the most part operated remotely, but may require underground access for corrective actions.

17.4.2.3 Radiation and other safety requirements

Access and safety equipment may be sensitive to single event upsets caused by LHC operation. Material degradation due to high radiation fields may also affect certain parts of the equipment, such as cabling. For these reasons, all equipment not required close to high radiation areas, must be located at a safe distance from such areas.

High magnetic fields can cause magnetic locks and electric motors to malfunction. Therefore, all access doors should preferably be located at a safe distance from magnetic fields.

All safety and access equipment are designed to be constantly powered even during electrical cuts by uninterruptible power supplies (UPS) and the CERN secure power grid. That means that standard emergency shut-off (AUG) generally does not cut power of these equipment.

Whenever possible, safety equipment should be located in permanently accessible areas.

17.4.2.3.1 Risk analysis

Safety report [13] defines the precise needs in terms of safety functions and safety systems. This document specifies, among others, fire sectorization, areas with oxygen deficiency hazard (ODH), and emergency access paths in the underground areas, and serves as the design basis for the safety and access systems.

17.4.2.4 Infrastructure requirements

All the systems to be installed require that all infrastructure construction works be finished, such as concreting, painting, final clean-up, and installation of the physical doors and gratings. Electrical infrastructure must be present, meaning CERN regular and secure power grids. All safety and access systems require their own control cabling between the equipment and the control racks. This cabling is to be installed within dedicated safety cables trays, as is the case in the LHC. In addition, the LACS and CSAM require network connectivity via the CERN Technical Network, which must be present close by so as to only require connection via an Ethernet patch cable.

17.4.3 Technical description of the work

17.4.3.1 Access safety system

The LHC Access Safety System (LASS) is the main safety system ensuring personnel safety in the various operational modes of the LHC (e.g., general access, commissioning, powering, beam operations). The LASS consists of two diverse and redundant safety chains for the critical operations. The main safety logic (interlock operation, mode management, supervision) is implemented using Siemens safety PLCs. Interlocking of the exterior envelope is also doubled by a redundant cabled loop using relay-based logic in order to ensure that no intrusion into the controlled areas can go unnoticed even in case of a potential unsafe failure of the PLC equipment.

The HL-LHC will require the following general modifications and additions to the LASS:

- Zoning and sectorization of the LHC is to be modified to accommodate new risks in the existing LHC tunnel:
 - o The new inner triplet areas around the interaction points of sites 1 and 5 will become much more radioactive during beam operations and immediately afterwards. This means that waiting times for entering into these areas after beam shut-off will be considerably longer than currently. For this reason, the intersite doors around sites 1 and 5 in the LHC tunnel, which are presently situated in the middle of the arc sections should ideally be displaced closer to sites 1 and 5 in analogy with the current sites 3 and 7 so as to allow access to a larger portion of the LHC equipment earlier than would otherwise be possible.
 - o The new crab cavities, being radio frequency (RF) equipment, will need similar protections by similar safety elements as the main LHC RF systems on Point 4.
- New important safety elements (EIS) to be installed into the LHC tunnel and the access galleries include access safety elements (EIS-a) as well as machine and optional beam safety elements (EIS-m and EIS-f, respectively). EIS-a consist of access doors and patrol boxes. The total number of elements to be installed at the two sites is:
 - o 12 interlocked end-of-zone doors to isolate the LHC tunnel and service areas from the new HL-LHC underground galleries (UA, UL, UPR). Due to lack of space in the UA galleries, the end-of-zone doors there will also serve as ventilation doors (solid construction), whereas elsewhere they are of grating type. When the zone is in a patrolled state, intrusion by an end-of-zone door will put the LASS into safe mode, which will incur dumping of the beam and possible powering down of various machine elements.
 - o 4 interlocked ventilation doors in the UL galleries.
 - o 4 interlocked overpressure doors in UPR galleries giving towards the LHC tunnel.
 - o 4 non-interlocked ventilation doors in UA galleries. These doors are monitored by the LASS for information.
 - o 12 patrol boxes at suitable locations according to new zoning (UA, UL, UPR).
 - o EIS for the RF of the crab cavities. The exact type and number of these elements will depend on the risk analysis.
- Cabling of the new EIS to the LASS site PLC will be implemented directly via existing pathways in the LHC (EIS-a/m) and possibly via the new HL-LHC service areas (EIS-m) depending on the location of the control racks of the machine elements to be interlocked. If a connection via HL-LHC service areas is eventually required, a LASS rack with remote I/O units connecting to LASS site PLCs will be installed on the surface of the new HL-LHC access pits (PM17 and PM57).
- Review of the existing beam and machine EIS to determine if they remain adequate.

17.4.3.2 Access control system

17.4.3.2.1 Underground areas

The LHC Access Control System (LACS) manages access to the controlled areas according to access modes given by the LASS. The LACS reads the user's badge, checks the access rights, verifies the user's identity via biometric check, and lets the user pass if all access conditions are fulfilled. Access to interlocked areas (i.e., areas, which cannot be accessed during beam) may be possible either in general mode or in restricted mode. Restricted mode is meant for accessing the machine in ready-for-beam conditions, and the user must be in possession of a safety token and the attached restricted mode key. The safety token will ensure that the beam cannot be entered into the machine until the token is returned to its place in the token distributor. The restricted

mode key is used in this mode to activate the access point for passage. In general mode a safety token and key are not required, as other conditions for beam are not supposed to be present.

The new normally accessible underground areas of the HL-LHC (i.e., excepting parts of the UA and UL galleries) will be of non-interlocked type, which means that no safety tokens are necessary, and only general mode will be implemented in the access points. The equipment to be installed in the LACS access points at PM17 (building SD17) and PM57 (building SD57) are:

- Personnel Access Device (PAD) including the iris scanner.
- Material Access Device (MAD) including video surveillance and personnel detection inside the MAD.
- LACS equipment rack at the access point including badge readers, intercoms, and a panel-PC for information display, but without a safety key distributor.
- Video surveillance both on the outside and inside of the access points.
- A supervised but non-interlocked end-of-zone door providing a second emergency evacuation path from the top of the pit.

17.4.3.2.2 Surface areas

Access control in the surface buildings is implemented via the SUSI system, which comprises badge readers and video surveillance both inside and outside of the buildings.

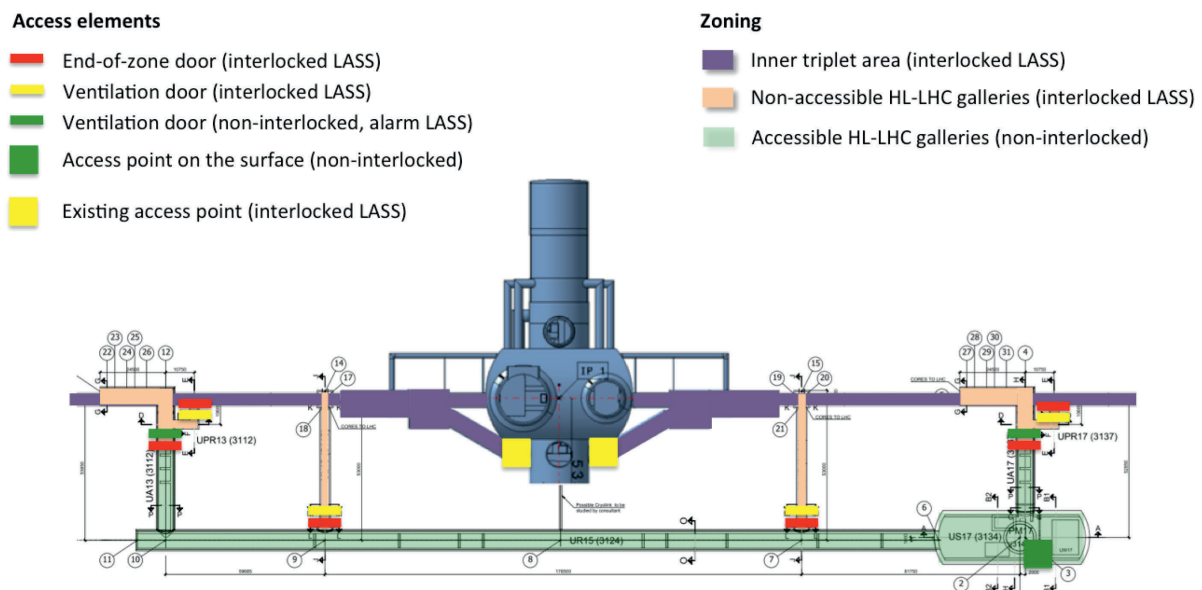


Figure 17-27: Preliminary underground access zoning and access elements of site 1. Zoning of site 5 will be similar as applicable with the exception of existing access point and service tunnel locations.

17.4.3.3 Automatic Fire Detection system

The Automatic Fire Detection (AFD) system consists of detectors of various kinds (point detectors and/or air sampling networks), located in specific areas (i.e., not per equipment) to detect the presence of smoke. These detectors are connected to Control and Indicating Equipment (CIE) located in one of the surface buildings. If a fire or smoke hazard is detected, the CIE generates level-3 alarms and launches automatic safety functions.

17.4.3.3.1 Underground areas

Fire detection is to be installed to all underground areas (US, UW, UR, UA, UL, UPR). The UR gallery will be equipped with smoke curtains designed to divide the gallery into zones that can contain smoke from a

localized fire until smoke extraction can be activated on that zone. The fire detection equipment will be localized so that an accurate determination of the zone with a fire can be made.

17.4.3.3.2 Surface areas

Fire detection is to be installed in all surface buildings (SD, SU, SE, SHM, SF). A reservation is made for an optional installation of fire detection also in the inter-building technical galleries.

17.4.3.4 Red Telephones

The underground areas will be equipped with the red telephones at regular intervals (433 approx. 70m), which provide a direct telephone connection to the fire brigade.

17.4.3.5 CSAM and MMD

The CERN Safety Alarm Monitoring system (CSAM) is the primary safety system for delivering level-3 alarms to CERN fire brigade. The LSAC (Local Safety Alarm Controller) PLC receives all the relevant level-3 alarms within that area and delivers them to the fire brigade via diverse and redundant signal chains. The Multi-purpose Monitoring Device (MMD) is used to deliver alarms directly to the TI operators via TIM. The CSAM system includes the cable infrastructure required to connect all level-3 alarms to CSAM. To accommodate the new alarms, the acquisition capacity of these systems at sites 1 and 5 will need to be increased.

17.4.3.6 TETRA and GSM

The TETRA secure communication system is installed and maintained by IT/CS. However, certain alarms from the TETRA system are transmitted via the CSAM system. As the TETRA uses the same infrastructure as the standard CERN GSM network (leaky feeders), the GSM infrastructure will be installed at the same time.

17.4.3.7 Automatic ODH detection

The Automatic ODH detection system consists of oxygen sensors located in specific areas to detect a gas release. These sensors are connected to a Control and Indicating Equipment (CIE). If an ODH is detected, the CIE generates level-3 alarms and launches automatic safety functions, automatic emergency evacuation, and OFH flashing lights.

17.4.3.7.1 Underground areas

In the new underground areas ODH detection is to be installed to the service caverns (US) as well as to the linear galleries (UR, UA, UL). ODH sensors will be installed approximately at every 50m in a linear gallery and according to need in more complex spaces.

17.4.3.7.2 Surface areas

ODH detection is to be installed in the head shaft building (SD) housing the cold boxes, in the compressor building (SHM) as well as in the inter-building technical galleries.

17.4.3.8 Radiation monitoring

As the accessible non-interlocked areas of the underground HL-LHC galleries are adjacent to some of the most radioactive areas of the future HL-LHC beam line, online monitoring of radiation is required at the end-of-zone doors of the interlocked zones. 4 RAMSES monitors and ionization chambers will be installed in the immediate vicinity of the end-of-zone doors in the UA and the UR next to the UL gallery. During the underground works of both the LS2 and LS3 it will also be necessary to have RP technicians present at the

inner triplet areas supervising the works there as those equipment will have a considerable level of residual radioactivity from the previous LHC runs.

17.4.3.9 Automatic protection system

The automatic protection safety system launches safety functions in case of fire or ODH detection. These functions are compartmentalization, evacuation, and smoke extraction. If necessary, the CERN fire brigade has the possibility of triggering these functions remotely from CCC or SCR and the possibility to sound safety instructions to the HL-LHC area remotely from CCC and SCR.

17.4.3.10 Evacuation system (Safety Sound System)

The emergency evacuation system is a part of the automatic protection system. It consists of audible evacuation signals triggered either automatically by another safety system, such as fire or ODH detection, or manually by pushing one of the evacuation buttons installed within the area in question. The evacuation system is to be installed in all underground areas.

Table 17-20: Synthesis of the principal safety, access, and alarm equipment by system.

Equipment	System	Description	Q
End-of-zone door (grating)	LASS	Interlocked end-of-zone door in the UL and UPR	8
End-of-zone door (solid)	LASS	Interlocked end-of-zone/ventilation door in the UA	4
Overpressure door	LASS	Interlocked ventilation/overpressure door in the UPR	4
Interlocked ventilation door	LASS	Interlocked ventilation door in the UL	4
Non-interlocked ventilation	LASS	Non-interlocked but monitored ventilation door in the UA	4
Patrol box	LASS	Key-operated switch box for arming patrol in a sector	12
Equipment rack	LASS	For cabling, relays, PLC I/O modules	4
RF EIS	LASS	Elements acting on RF powering	4
PAD	LACS	Personnel Access Device, includes iris scanner	2
MAD	LACS	Material Access Device, includes video surveillance	2
Equipment rack	LACS	Includes badge readers, interphonie, panel-PC	2
Access point video camera	LACS	Video surveillance of the access point	4
Non-interlocked door	LACS	Non-interlocked door at top of pit	2
Fire detector	Fire Detection	Fire detector	220
Fire central	Fire Detection	Fire central concentrating several detectors	4
Red telephones	Emergency Com	Direct line to the fire brigade, with alarm	50
TETRA	Emergency Com	Secure communication equipment	2
CSAM rack	CSAM	Secure delivery of level 3 alarms to the fire brigade	2
ODH detector	ODH Detection	Oxygen deficiency hazard detection and warning	74
ODH central	ODH Detection	Oxygen deficiency hazard detection and warning	6
Evacuation siren	Evacuation	Audible evacuation alarm in the underground areas	40
Evacuation central	Evacuation	Audible evacuation alarm in the underground areas	2
RAMSES monitoring station	Radiation Monitor	Detection of ambient radioactivity	8
Ionization chamber	Radiation Monitor	Detection of ambient radioactivity	8
Access controlled door	SUSI	Simple access controlled door	24
Supervised door	SUSI	Non-access controlled but supervised door (emergency exit)	12
Video camera	SUSI	Video surveillance of the buildings and sites	30

17.5 Monitoring and operation of general services

17.5.1 Introduction

All installed equipment are to be monitored for important operational data, events, and alarms. The low-level monitoring of each subsystem depends on the exact equipment and data collection framework used by that

subsystem. Delivery of high-level surveillance and alarm information to CERN TI operators will be realized via the CERN Technical Infrastructure Monitoring system (TIM), which will acquire the required data items and alarms from the local SCADA-systems or directly from the monitored equipment, as applicable.

17.5.2 Technical description of the work

17.5.2.1 TIM infrastructure adaptations

While TIM is capable of connecting to many different equipment and existing SCADA systems to access data of various types, it is always possible that some application-specific development to the core system will be necessary to fully support the control system to be connected to TIM.

17.5.2.2 Subsystem configuration and development

The main bulk of work consists of the owners of various HL-LHC subsystems to set up monitoring of the important parameters of their systems in such a way that they can be read by TIM data acquisition modules. TIM is able to read data reliably from many different sources, including different SCADA-systems and PLCs. The following steps are necessary for setting up TIM monitoring of a device:

- Definition of the device variables to monitor and making them available for readout via network.
- Definition of the tags in the TIM system to correspond to the variable to read. This step consists of defining a hierarchical tag name corresponding to the device in question, defining the data acquisition method and address, and defining the operator action in case of an alarm.
- Building TIM graphical visualization based on the registered tags.

Setting up of monitoring of the devices belonging to the various equipment groups will be carried out in collaboration with the equipment group in question and the TIM team.

17.5.2.3 Networking

Networking will be installed both in the surface buildings and the underground installations. This covers cabled connections to CERN General Purpose Network (GPN) and Technical Network (TN) as well as Wi-fi connections in selected areas:

17.5.2.3.1 Underground areas

Cabled connections will be provided at regular distances in the galleries so that modern network-connected equipment can take advantage of it. Wi-fi coverage will also be provided. This will require installation of a starpoint rack approximately every 70-80 meters.

17.5.2.3.2 Surface areas

All surface buildings will have cabled connections at regular distances. Wi-fi coverage will be limited to the more frequented areas (control rooms, rack areas, etc.).

17.6 Transport

17.6.1 Introduction

The scope of transport covers the surface transport & handling, the transfer to the underground facility and the transport & handling in the tunnels, galleries and caverns.

In this section are enumerated the new transport and handling equipment that will be required in the new facilities for HL LHC installation.

17.6.2 Requirements and constraints

17.6.2.1 Operational

As for the LHC, the tight schedule and the large quantity of items to be transported will require fully integrated logistics for the transport on the surface and even more stringent co-ordination underground. The general means of transport and handling of equipment, together with the organisation necessary to bring the equipment to its final destination will be directly inherited from LHC. A very effective maintenance and consolidation programme will be put in place for the vehicle park and handling equipment. The computer simulation of transport scenarios is very important to identify bottlenecks and resource limitations, as well as to finalize schedules and to compute transport time durations.

17.6.2.1.1 Surface Transport and Handling

Articulated vehicles with hydraulic suspension are used for the road transport. The ROCLA vehicles are used to transport the cold masses and cryo-magnet assemblies in SMS18 and SMA18. Mobile cranes will be used to install big elements such as helium tanks and transformers. Exceptional transport will be rarely used and will be done via one of CERN specialised contractors.

17.6.2.1.2 Storage

Two temporary storage platforms are required in P1 and P5 to allow transit of equipment and for logistic reasons. The use of heavy haulage external company is foreseen with the direct consequence of having to park on site trucks and mobile cranes with high payloads. The pavement in these zone shall withstand a load of 300 kN/axle.

17.6.2.1.3 Installation

Most of the infrastructure equipment in the new HL-LHC underground facilities will be transported using the two new 3-t lift (copy of LHC lift). For the others components, two 25-t electric overhead travelling (EOT) cranes will be installed in the SD17 and SD57 buildings. Most of new surface buildings will be equipped with overhead cranes ranging from 3.2 t to 20 t. The EOT cranes and lifts are described in Table 17-21 and Table 17-22. Upon requirement, CERN or rented mobile cranes will be used. As a general reminder, the existing LHC EOT cranes and lifts will be used to replace all the accelerator components. Drawbridges will be installed in the shafts in order to ease the transport of the ventilation equipment in the second level of the UW caverns.

17.6.2.1.4 Underground Transport and Handling Equipment

No specific requirement for new special transport equipment underground has been identified at this stage (apart from the EOT cranes in the cavern). Preliminary studies show that existing CERN transport equipment will fulfil most requirements for transport underground in tunnels and galleries (electric tractors, trailers, forklifts, etc...). Detailed integration studies to define precise volumes reservation for transport shall be conducted once the layout is finalized to contribute to the optimization process.

17.6.2.2 Radiation and other safety requirements

The new HL-LHC infrastructures are designed in a way that workers involved in transport and handling operations cannot be exposed to the risk of exposure to ionising radiation.

17.6.3 Technical description of the work

17.6.3.1 Infrastructures – Lifts

The specifications are based on LHC 3-t lifts (e.g. PM54, and PM15); the capacity / dimensions of these lifts cover 90% of transport requirements.

TECHNICAL INFRASTRUCTURE

The safety requirement covers LHC specific risks (over pressurized shafts in case of fire or He leak) and they will be fed by UPS and have a safe level-3 communication with the fire brigade so that they will be used as evacuation exits in case of incident in the underground facility. The lifts components will be the same as for LHC lifts (the 6 LHC 3-t lifts will be replaced by 2021) for improving availability (common spare parts, better training/performance of maintenance services). No specific constraints of dimensions or any specific requirement (with respect to LHC lift) have been identified at that stage.

Table 17-21: Main lifts .

Location	Capacity (kg)	Travel Height (m)	Door width (m)	Door height (m)	Speed (m/s)	Cabin dimensions (m)		
						Length	Width	Height
PM17	3000	72.5	1.9	2.7	1.6	2.7	1.9	2.7
PM57	3000	79	1.9	2.7	1.6	2.7	1.9	2.7

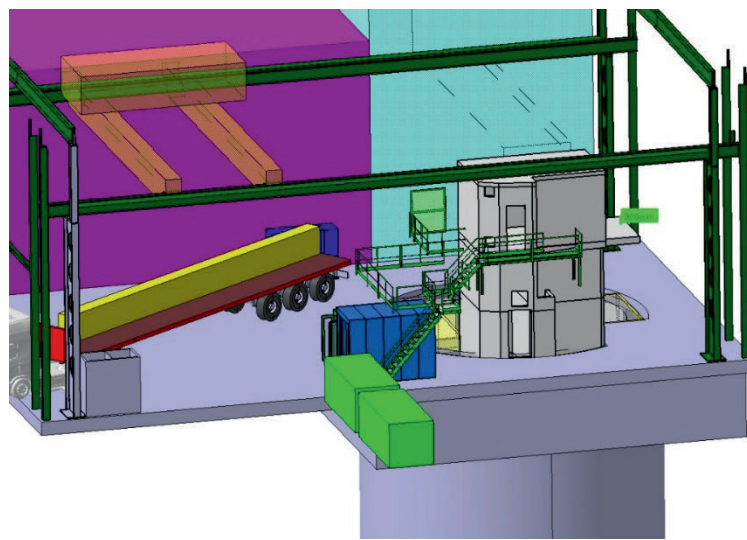


Figure 17-28: SD building lift machinery.

17.6.3.2 Infrastructures –Electric Travelling Cranes

The overhead cranes preliminary design for surface buildings & caverns are based on requirements from users, including size and weight of biggest/heaviest object to be transported to define parameters such as clearance under hook, span and length.

These designs integrate technical and legal requirements for the cranes installation, operation and maintenance, such as the clearance above the cranes and the catwalk to provide access to the rails and to the machinery.

Table 17-22 list the cranes main characteristics. For more detailed information (e.g.: reactions on rails) please refer to the general layout drawing of each building.

Table 17-22: Main overhead travelling cranes.

Location	Capacity (t)	Height Hook (m)	Lifting Height (m)	Hopper (m)		Speed (m/min)	
				Rail length	Spam	Max	Min
SHM17	20	6	6	50	15	5	0.25
SD17	25	10	100	28.4	16.1	20 (without load)	0.5
SF17	3.2	9	9	23	10	5	0.25
SU17	7.5	8	8	16	14	5	0.25
US17	5	7.5	7.5	26	12	5	0.25

UW17 (top)	3.2	3.2	3.2	15	6	5	0.25
UW17 (floor)	3.2	3.2	3.2	15	6	5	0.25
SHM57	20	6	6	50	15	5	0.25
SD57	25	10	100	28.4	16.1	20 (without load)	0.5
SF57	3.2	9	9	23	10	5	0.25
SU57	7.5	8	8	16	14	5	0.25
US57	5	7.5	7.5	26	12	5	0.25
UW17 (top)	3.2	3.2	3.2	15	6	5	0.25
UW17 (floor)	3.2	3.2	3.2	15	6	5	0.25

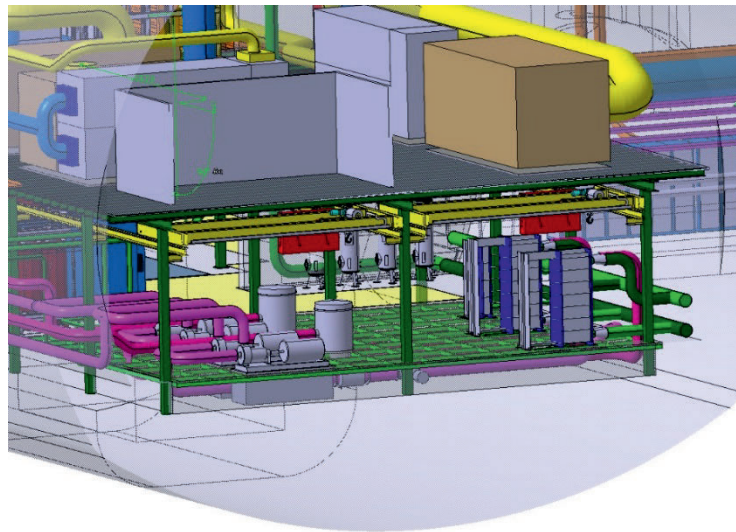


Figure 17-29: UW cavern EOT cranes.

17.6.3.3 Infrastructures – Manual Overhead Travelling Cranes for RF

All UA galleries will be permanently equipped with manual cranes travelling on rails to allow for handling and transport of the RF components.

Table 17-23: Cranes for RF installation in UA galleries.

Location	Capacity (t)	Length (m)	Width (m)
UA53	1	26	5
UA57	1	26	5
UA13	1	26	5
UA17	1	26	5

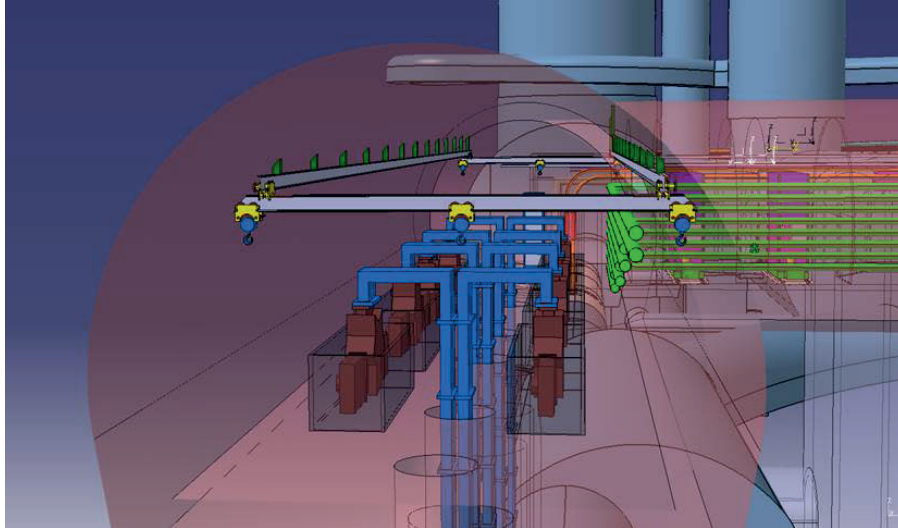


Figure 17-30: MOT crane in UA gallery.

17.6.3.4 Infrastructures – Manual Overhead Travelling Cranes for Cryo

In both P1 and P5, one UL gallery will be permanently equipped with manual cranes travelling on rails to allow for handling and transport during maintenance of cryogenic components.

Table 17-24: Cranes for RF installation in UA galleries.

Location	Capacity (t)	Length (m)	Width (m)
UL17	1	12	2
UL57	1	12	2

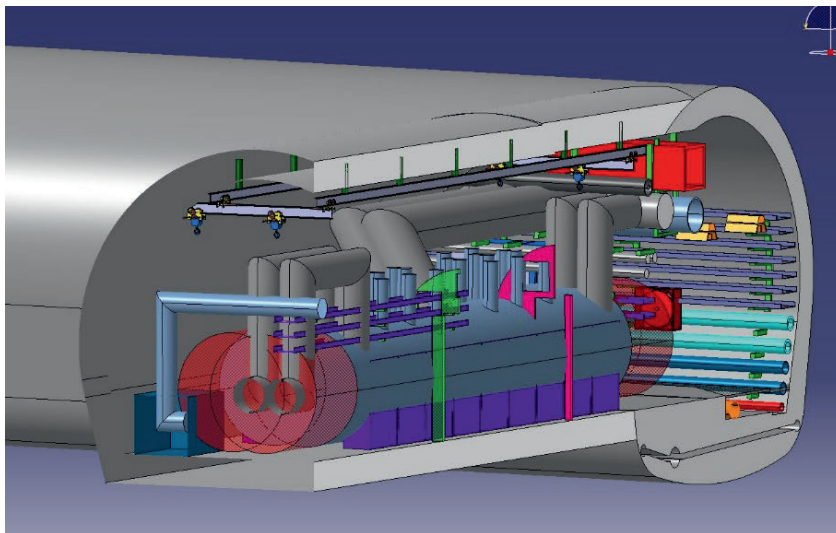


Figure 17-31: MOT crane in UL gallery.

17.6.3.5 Infrastructures – Hoists

17.6.3.5.1 Hoist for the lifting pumps of the water sumps

Water sumps are equipped with heavy lifting pumps that need to be maintained. The support for the hoist will be permanently installed on site. Only one hoist unit is requested, that will be used on demand and moved from one point to another.

Table 17-25: Hoist for the lifting pumps of the water sumps.

Location of supports	Capacity (t)
US17	0.5
US57	0.5

17.6.3.5.2 Hoist for lifting maintenance equipment to the UW top floor (installation on the US side)

The equipment's, tools and materials necessary for the maintenance of the equipment's located in the UW cavern upper floor will be transported from the US side. A small tremie with a dedicated 500 kg hoist will be permanently install to lift the tools and consumables to the US top floor that communicates with the UW top floor through a door in the separation wall.

Table 17-26: Hoist for maintenance of UW cavern equipment's.

Location	Capacity (t)
US17	0.5
US57	0.5

17.6.3.5.3 Hoist for transferring loads in the second bay of the SHM buildings

This equipment is required because of the design of the building that require a hoist on a rail to transfer the load in the second bay of the SHM building.

Table 17-27: Hoist for the SHM buildings.

Location	Capacity (t)
SDH17	1.5
SDH57	1.5

17.6.3.6 Infrastructures – Drawbridges

For installation of the large cooling & ventilation equipment's and all heavy equipment's located in the UW upper floor, two drawbridges will be permanently installed inside the shaft of the US caverns in P1 and 5. (They are kept closed during normal operation. When equipment's need to be transported to the UW upper floor, the drawbridges are open and provide a platform that is accessible with the SD building cranes.)

Table 17-28: Drawbridges.

Location	Capacity (t)
US17	5
US57	5

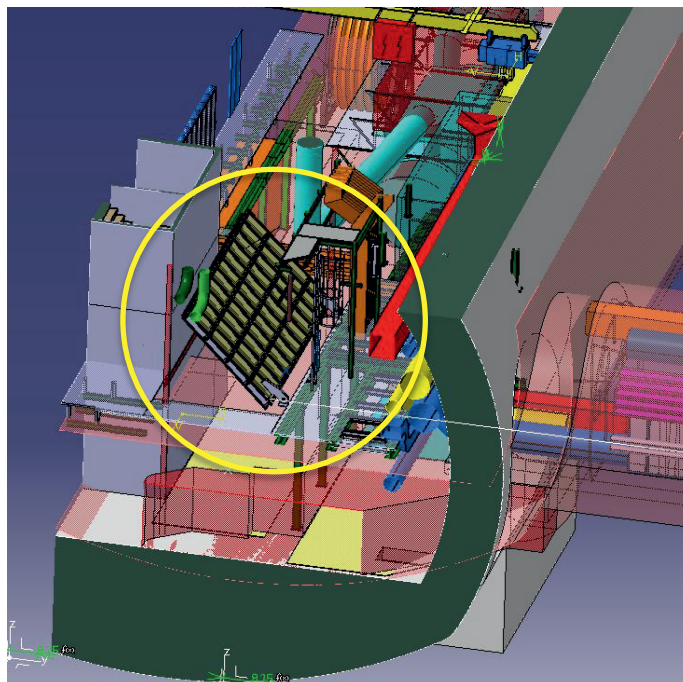


Figure 17-32: Drawbridge in US cavern.

17.6.3.7 Infrastructures – Mobile shielding doors

All UA galleries will be equipped with mobile shielding doors with electrical motors. The dimensions (based on preliminary studies) are: 2m x 0.8m x 2.8m

Table 17-29: Mobile shielding doors.

Location	mass (t)
UA53	12
UA57	12
UA13	12
UA17	12

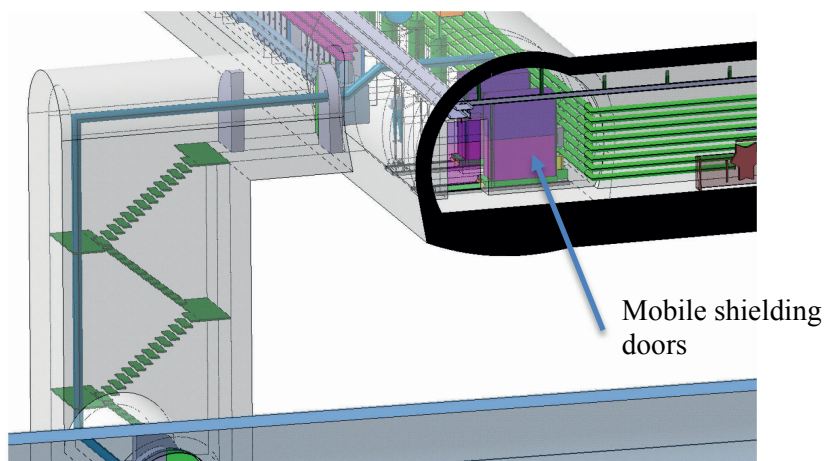


Figure 17-33: Mobile shielding door.

17.6.3.8 Infrastructures – Shielding for UL galleries

102 t of steel and 48 t of concrete blocks will be used in the construction of shielding walls and doors.

17.6.3.9 Infrastructures – Tooling for transport

Special tooling are required for cold box handling, QRL sections, electrical racks, etc...

17.6.3.10 Infrastructures – Special vehicles and trailers

No specific requirement for special transport vehicle has been identified yet at this stage. . The necessity of special vehicles or trailers be for sure appear in the detail design phase.

17.6.3.11 Studies

The following Computer Aided Design (CAD) studies shall be conducted:

- CAD simulation of transport scenarios;
- CAD integration studies to define precise volumes reservation for transport and for feasibility studies;
- Design of new tooling and special equipment's (e.g.: lifting beam, supports, etc...).

17.7 Logistics and storage

17.7.1 Introduction

The HL-LHC project will bring an increase of activity in logistics services. They will have to adapt their capacity to foreseen workload coming during the project period both in term of FTEs and storage space.

17.7.2 Requirements and constraints

17.7.2.1 Risk analysis

The present Logistics industrial support contract will be renewed in April 2019 during the HL-LHC project period. The re-tendering process will integrate HL-LHC requirements. Costs might change depending on the new industrial support contract conditions.

Capacity increase is based on forecasts and LS1 history. In case the activity impact or storage needs exceed significantly the previsions we will end up in a reactive and responsive mode.

17.7.3 Technical description of the work

17.7.3.1 Logistics services

The following services will be impacted by HL-LHC project:

- **Shipping & waste:** Administrative work linked to import activities (transport management from suppliers to CERN, customs clearance, VAT exoneration documentation) and waste traceability requested by the French and Swiss authorities.
- **Goods Reception:** CERN official order matching and registration, quantitative control, packaging control, establishment of eventual reserves and responsibilities in case of damage.
- **Internal distribution:** deliveries of goods and material from goods receptions and Stores to any locations at CERN and vice versa.
- **Stores – Product management:** Supply and demand management for standard items. Price inquiries, replenishment, order follow-up.
- **Stores – Warehousing:** Qualitative reception for standard items, put-away, picking.
- **Storage areas:** Operation of storage areas for radioactive and conventional materials.

The HL-LHC project planning suggested a significant increase in the logistics services from 2017 to S1/2026:

- Wastes will be generated on CERN site at from the beginning of the construction;

TECHNICAL INFRASTRUCTURE

- Increase of official orders and imports foreseen implying extra administrative work and movements in goods receptions;
- Increase of internal distributions from goods reception/Stores to CERN points. Tour re-enforcement might be necessary;
- Increase in volume for strategic standard materials from CERN Stores inducing extra work both for product management and in the warehouses;
- Extra movements foreseen in storage areas.

17.7.3.2 Storage

Both conventional and radioactive storage space is needed in current buildings. A new “flex” building of 10000 m² will be ready during 2018 and will include both conventional and light radioactive storage space. During LS2, the building will be managed by the LS2 team which will also include HL-LHC activities that will take place in that shutdown. SMB will take over the operation of the building after LS2.

17.7.3.2.1 Conventional storage

Existing buildings (897, 917 and 957, 954, SAX area), the temporary storage structures at P1 & 5 (see below) and the new “flex” building will offer enough capacity to cope with HL-LHC project.

17.7.3.2.2 Radioactive storage

It covers only storage of radioactive equipment (ex: spares), not radioactive waste which are managed by HSE-RP. For information, radioactive storage is not possible outside CERN.

Table 17-28: Preliminary study using forecasts collected via HSE-RP in 2015.

Totals	Per period (in m ²)	Integral (in m ²)
End 2016	36	36
LS2	17.1	53.1
LS3	497.86	550.96

Pallet storage is included in the figures for LS3 which will reduce the need of space in m².

The existing radioactive storage buildings (954 and 955) don't have remaining floor areas. To free some space, the new “flex” building will allow storage of light radioactive equipment. A campaign is ongoing to define a threshold for light radioactivity allowing a projection of how much equipment will be eligible for a transfer from buildings 954 and 955. Storage location for HL-LHC cannot be identified yet.

17.7.3.2.3 Temporary storage structure installed at P1 and P5

The actual request space for conventional storage consist of 2 surfaces at P1 & 5, each one will be between 200 to 250 m² (needed between LS2 and LS3). The modalities for implementation and the functional specifications are still to be defined.

“Two temporary storage platforms are required in P1 and P5 to allow transit of equipment and for logistic reasons. The use of heavy haulage external company is foreseen with the direct consequence of having to park on site trucks and mobile cranes with high payloads. The pavement in these zone shall withstand a load of 300 kN/axle.”

17.8 References

- [1] D. R. J.C. Guillaume, “Minimizing collective radiation dose during cabling activities”. EDMS [1111950](#)

- [2] I. M. Martinez, “Compilation des procédures particulières de câblage utilisées dans les zones irradiées”. EDMS [1531482](#).
- [3] S. Meroli, “Monitoring working method: structure and functioning”. EDMS [1516761](#).
- [4] G. Cumer, “Description of the CERN electrical network”. EDMS [559013](#) v.6.
- [5] “Evolution of electrical power requirements for the operation of the CERN Laboratory from March 2011 until the HL-LHC era”. EDMS [1237699](#) v.2.
- [6] “Projet de consolidation et d’extension du réseau Haute Tension du CERN à l’horizon 2025”. EDMS [1153990](#) v.2, 2012.
- [7] C. Richard, “Study for evolution of 400/66 kV network – project CERN2”. EDMS [1407742](#) v1.5.
- [8] C. Bovet, “Analyse de faisabilité du système auto transfert 66 kV”. EDMS [1455160](#) v.2.
- [9] EN-EL, “Drawing “18 kV distribution HL-LHC1 project”. CDD: [LHCEM_1005](#) rev.A.
- [10] EN-EL, “Drawing "18 kV distribution HL-LHC5 project”. CDD: [LHCEM_5003](#) rev.A.
- [11] EN-EL, “Drawing "Low voltage distribution HL-LHC1 project”. CDD: [LHCEB_1208](#) rev.A.
- [12] “LHC design report,” [CERN-2004-003-V-1](#)
- [13] Emergency Preparedness of HL-LHC Underground Service Areas”. EDMS [1610772](#)

Chapter 18

Controls

18 Controls

18.1 Introduction

By the time of the commissioning and subsequent operation of the HL-LHC, many of the physical elements of the control system will have been upgraded due to obsolescence. This applies particularly to the front and back end CPUs and storage. It is not, however, foreseen, that the overall control system strategy and architecture will change in its conceptual structure during this period and many parts of the current controls infrastructure, will still be sufficient for the needs of HL-LHC. Nevertheless, three areas have been identified as having to be addressed so that the control system can respond to the new challenges presented by HL-LHC.

During operation of HL-LHC there will be an increase of radiation in some areas which will trigger re-designs and relocation of electronics (see chapter 10 and 19). There are also new magnets which will raise the need for more diagnostics data (i.e. higher data rates) in subsystems such as QPS. Higher data rates will also be needed during the commissioning of HL-LHC as Equipment Groups will need to fine-tune their systems and will therefore want more diagnostics. In order to assure correct functionality up to the end of the HL-LHC operation period with ultimate performance, it is important to be conservative regarding the design choices and to share proven solutions as much as possible. This approach assures that proven solutions persist and that all design efforts can be concentrated on making a few designs very robust instead of spreading efforts into a large number of sub-optimal designs.

18.2 Control areas requiring new developments for the HL-LHC era

18.2.1 Data Logging

Development of the next generation Accelerator Logging Systems (CALs) has started and the aim is to have a new Logging system in place by mid-2018 with equivalent functionality as today but with significantly faster data extraction and analysis performance.

Following past experience, we are expecting a massive increase in the volume of data to be logged as a direct result of installing, commissioning and then operating HL-LHC. Figure 18-1 shows the massive increase in data logged post LS1 as a result of updates to various LHC systems (most notably the LHC QPS System) and the need to increase data rates to better understand certain behaviours.

Based on user input, and given the extensive hardware and operational changes foreseen for HL-LHC, we must be prepared for similar or even greater increases in the amount of data collected in the Logging System in the HL-LHC era. We foresee the need to install new, properly dimensioned, dedicated database hardware in 2025, to be ready for use in 2026 to support HL-LHC hardware commissioning followed by beam commissioning.

In addition to the need for new database hardware, it is critical to develop and deploy a new software infrastructure to properly support the users of the foreseen data sets. In order to properly validate the behaviour and performance requirements with realistic data and use cases *prior* to the HL-LHC commissioning period - the deployment of this software should take place before the start of Run 3 and will require additional temporary personnel resources.

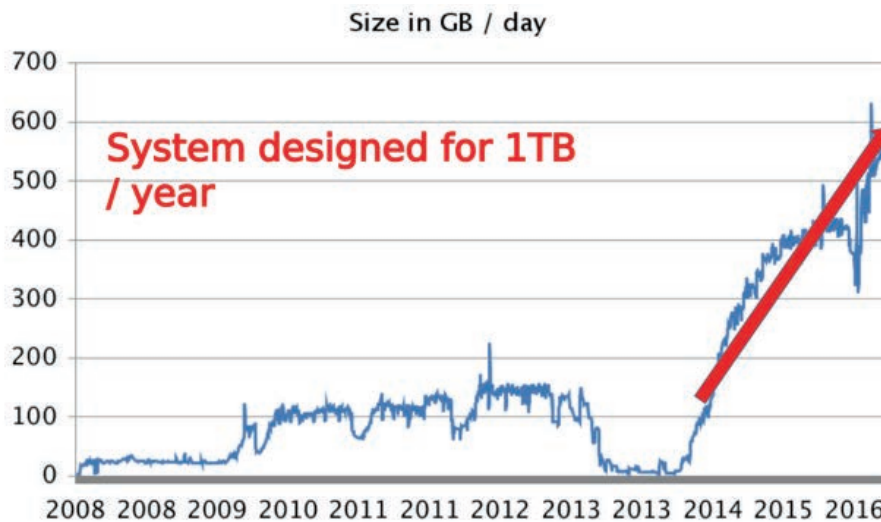


Figure 18-1: Storage evolution.

18.2.2 New Distributed I/O Tier

The HL-LHC will place challenging demands on data acquisition to/from the accelerator components which need to be controlled and diagnosed, such as the new NbSn₃ magnets. The current controls architecture has front-end computer systems (VME or PICMG 1.3) with a large variety of reusable electronic cards to control accelerator components by sending and receiving data and carrying out calculations in real-time.

For HL-LHC, the proposal would be to extend this architecture as shown in Figure 18-2. In this new architecture would be implemented and supported a new I/O layer, which as its name suggests is designed to transmit data, as fast as possible to/from sensors attached to accelerator components. These I/O modules are connected to a fewer number of high-performance front-end computers which process the data and perform the necessary calculations. By collaborating with equipment groups and providing a service in this I/O layer analogous to that of the front-end tier, we will ensure a uniform level of quality and increase overall availability of electronics deployed in this tier, including those subject to radiation.

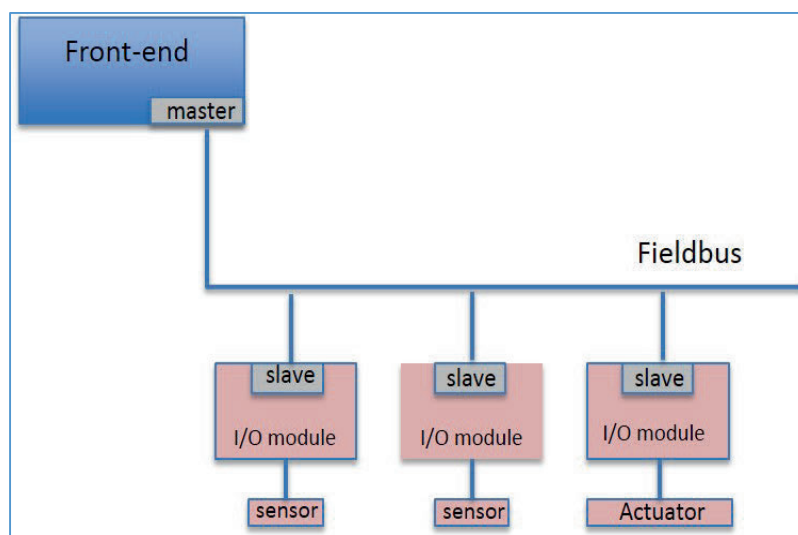


Figure 18-2: Proposed Controls architecture.

CONTROLS

18.2.3 A new High-speed Radiation-tolerant Fieldbus

For HL-LHC the QPS system needs to accommodate the new NbSn₃ magnets in points 1, 5 and 7.

The complexity of the NbSn₃ magnets increases by a factor of 10 the amount of post-mortem data that needs to be transmitted. This makes the current solution based on WorldFIP sub-optimal, due to the very low bandwidth (1Mbps).

The QPS electronics in points 1 and 5 will be installed in radiation-free zones, however the RR alcoves in point 7 may pose some low (<1-2 Gy/year) radiation-tolerance constraints, which should be considered when proposing a new fieldbus for the HL-LHC era.

A re-usable standards-based solution will serve also other users and will help increase overall quality and therefore availability. An industrial, Ethernet-based solution with 100Mbps bandwidth, μ s synchronization, 50 slaves/segment is proposed.

The candidate solutions based on a rigorous market review include: Profinet, EtherCAT and Powerlink.

Each of these technologies will need to be evaluated for use in the HL-LHC era and for use with custom electronics in collaboration with the many equipment groups, especially the Cryogenics and QPS teams, who will need to use this new technology.

Chapter 19

Safety

19 Safety

19.1 Radiation Protection

19.1.1 Design constraints

Design constraints for new or upgraded facilities should ensure that the exposure of persons working on CERN sites, the public, and the environment will remain below the specified dose limits [1] under normal as well as abnormal conditions of operation, and that the optimization principle is implemented [2],[3]. In particular, the following design constraints apply:

- The design of components and equipment must be optimized such that installation, maintenance, repair, and dismantling work does not lead to an effective dose, e.g. as calculated with Monte Carlo simulations, exceeding 2 mSv per person and per intervention. The design is to be revised if the dose estimate exceeds this value for cooling times compatible with operational scenarios.
- The annual effective dose to any member of a reference group outside of the CERN boundaries must not exceed 10 μ Sv. The estimate must include all exposure pathways and all contributing facilities.
- The selection of construction material must consider activation properties to optimize dose to personnel and to minimize the production of radioactive waste. In order to guide the user a web-based code (ActiWiz) is available for CERN accelerators [4].

19.1.2 The As Low As Reasonably Achievable (ALARA) principle

Proton–proton collisions in the LHC experiments produce a secondary radiation field that penetrates into the adjacent accelerator tunnels and can cause severe activation of beam-line elements. Consequently, in such areas the design of components and infrastructure has to be optimized to follow the As Low As Reasonably Achievable (ALARA) principle. The optimization of the design for later interventions is an iterative process: dose equivalent maps per unit time of exposure (called dose rate maps below) of the concerned area(s) are compiled from measurements and/or simulations with Monte Carlo particle transport codes such as FLUKA [5],[6]. Based on these maps, the individual and collective doses of the intervention teams are calculated by using an intervention plan that then allows identification of and optimizing of critical work steps in order to reduce doses. If the latter involves a change in design or work scenario, then doses are re-evaluated by repeating the above steps.

19.1.3 The FLUKA Monte Carlo code for radiation protection studies

The use of general-purpose particle interaction and transport Monte Carlo codes is often the most accurate and efficient choice for assessing radiation protection quantities at accelerators. Due to the vast spread of such codes to all areas of particle physics and the associated extensive benchmarking with experimental data, modelling has reached an unprecedented level of accuracy. Furthermore, most codes allow the user to simulate all aspects of a high energy particle cascade in one and the same run: from the first interaction of a TeV particle to the transport and re-interactions (hadronic and electromagnetic) of the produced secondaries, to detailed nuclear fragmentation, the calculation of radioactive decays, and even the electromagnetic shower caused by the radiation from such decays.

FLUKA is a general-purpose particle interaction and transport code with roots in radiation protection studies at high energy accelerators [5],[6]. It therefore comprises all features needed in this area of application.

Detailed hadronic and nuclear interaction models cover the entire energy range of particle interactions at the LHC, from energies of thermal neutrons to interactions of 7 TeV protons. Moreover, the interface with DPMJET-III [7] also allows the simulation of minimum-bias proton–proton and heavy ion collisions at the experimental interaction points, which enormously facilitates calculations of stray radiation fields and activation.

FLUKA includes unique capabilities for studies of induced radioactivity, especially with regard to nuclide production, their decay and the transport of residual radiation. Particle cascades by prompt and residual radiation are simulated in parallel based on microscopic models for nuclide production and a solution of the Bateman equations for activity build-up and radioactive decay. The decay radiation and its associated electromagnetic cascade are internally flagged as such in order to distinguish them from the prompt cascade. This allows the user to apply different transport thresholds and biasing options to residual and prompt radiation and to score both independently.

Particle fluence can be multiplied with energy-dependent conversion coefficients to effective dose or ambient dose equivalent [8] at scoring time. Prompt and residual dose equivalent can thus be computed in three-dimensional meshes, the latter for arbitrary user-defined irradiation and cooling profiles.

An integral part of the FLUKA code development is benchmarking of new features against experimental data. It includes both the comparison of predictions of individual models to measurement results (e.g. nuclide production cross-sections) as well as benchmarks for actual complex situations as, for example, arising during accelerator operation.

19.1.4 Residual dose rate predictions for the Long Straight Sections in Point 1 and 5

Residual dose rate maps were calculated with FLUKA for the part of Long Straight Sections (LSS) in Point 1 (P1) and 5 (P5) that extend from the Target Absorber Secondary (TAXS) up to cell 4, including crab cavities and quadrupole magnet Q4, according to the latest HL-LHC layout [9]. The results are available for both P1 and P5. The simulations were performed for the high energy secondary radiation field arising from p–p collisions at 14 TeV centre-of-mass energy as it dominates the activation in these areas. The contributions from losses of the beam directed towards the interaction point (IP) and beam–gas interactions are not considered. Results were normalized to two different average luminosity values of $5 \times 10^{34} \text{ cm}^{-2} \text{ s}^{-1}$ (the so-called ‘nominal scenario’) and $7.5 \times 10^{34} \text{ cm}^{-2} \text{ s}^{-1}$ (the so-called ‘ultimate scenario’), respectively, with a 295 μrad half-angle vertical crossing in IP1 and horizontal crossing in IP5, using DPMJET-III as the event generator.

Table 19-1: LHC operational parameters. The third and fourth columns refer to the so-called ‘nominal scenario’, which will lead to a total integrated luminosity of 3060 fb^{-1} . The fifth and sixth columns refer to the so-called ‘ultimate scenario’. This scenario will lead to a total integrated luminosity of 3910 fb^{-1} . These values for the total integrated luminosities include 310 fb^{-1} collected during the operational period before LS3.

Shutdown	Year of LHC operation	Levelled luminosity [$\text{cm}^{-2} \text{ s}^{-1}$]	Integrated luminosity [fb^{-1}]	Levelled luminosity [$\text{cm}^{-2} \text{ s}^{-1}$]	Integrated luminosity [fb^{-1}]
LS3					
	2027	5.00×10^{34}	250	7.50×10^{34}	300
	2028	5.00×10^{34}	250	7.50×10^{34}	300
	2029	5.00×10^{34}	250	7.50×10^{34}	300
LS4					
	2031	5.00×10^{34}	250	7.50×10^{34}	300
	2032	5.00×10^{34}	250	7.50×10^{34}	300
	2033	5.00×10^{34}	250	7.50×10^{34}	300
LS5					
	2035	5.00×10^{34}	250	7.50×10^{34}	300
	2036	5.00×10^{34}	250	7.50×10^{34}	300

	2037	5.00×10^{34}	250	7.50×10^{34}	300
LS6					
	2039	5.00×10^{34}	250	7.50×10^{34}	300
	2040	5.00×10^{34}	250	7.50×10^{34}	300
	2041			7.50×10^{34}	300

The irradiation profiles were based on the operational scenarios reported in Table 19-1. For the inelastic p-p cross-section the value of 85 mb was used on the basis of the extrapolation [10]. Cycles of three years of continuous operation followed by a long shutdown (LS) of a duration of one year were repeated until integrated luminosities of about 3000 fb^{-1} and 4000 fb^{-1} are reached for the nominal and ultimate parameters, respectively.

The studies use the FLUKA implementation of the HL-LHC LSS regions developed for energy deposition studies (See chapter 10) according to the latest design, mechanical layout, and specifications, including a detailed model of the low-beta triplet quadrupoles with new large-aperture Nb_3Sn magnets (150 mm coil aperture), field maps, corrector packages, and segmented tungsten inner absorbers.

As mentioned above, three-dimensional residual dose rate maps have been calculated for the entire area from around 12 m distance from the interaction point up to around 190 m distance (i.e. from TAXS to Q4). Nine different cooling times were considered covering all typical intervention scenarios: 1 second, 1 minute, 1 hour, 8 hours, 1 day, 1 week, 1 month, 4 months, and 1 year after the last HL-LHC operational period, i.e. when 3000 fb^{-1} and 4000 fb^{-1} , respectively, have been reached, for both the nominal and the ultimate scenarios. In order to give examples for the available results, residual dose rates are reported in the following as two-dimensional maps for one month cooling time as well as profile plots for four different cooling times (1 week, 1 month, 4 months, and 1 year). The values correspond to the average over 30 cm around the beam pipe height and between 40–50 cm distances from the outer surface of the cryostat (for the profile plots). Figure 19-1 shows the residual dose rate map for the region from TAXS up to the separation dipole D1 and Figure 19-2 shows the corresponding residual dose rate profiles in the aisle for the nominal scenario, i.e., when a total integrated luminosity of 3060 fb^{-1} has been reached. Results for the ultimate scenario, i.e., a total integrated luminosity of 3910 fb^{-1} , are shown in Figure 19-3 and 19-4. The highest radiation levels will be found next to the magnet interconnections and in front of the TAXS due to the ‘self-shielding’ provided elsewhere by the magnets themselves. Figure 19-5 compares the residual dose rate profiles at one month cooling time for nominal and ultimate scenarios. The average ratio between the two profiles for this cooling time is 1.35. In general, it varies with cooling time and depends solely on the instantaneous luminosity in the case of short cooling times (up to about one week), while for longer cooling times the ratio also depends on the total integrated luminosity.

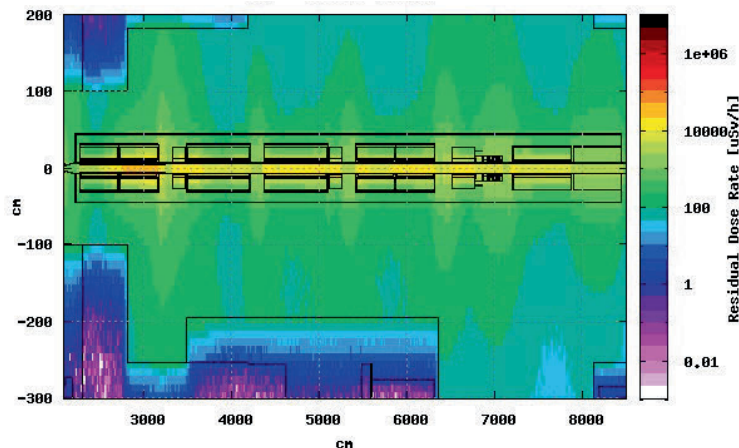


Figure 19-1: Residual dose rates in units of $\mu\text{Sv/h}$ around the low-beta triplet quadrupole and D1 magnets for the nominal scenario after one month of cooling time. Doses are shown for a horizontal section at the level of the beam line. The origin of the coordinate frame is at the interaction point.

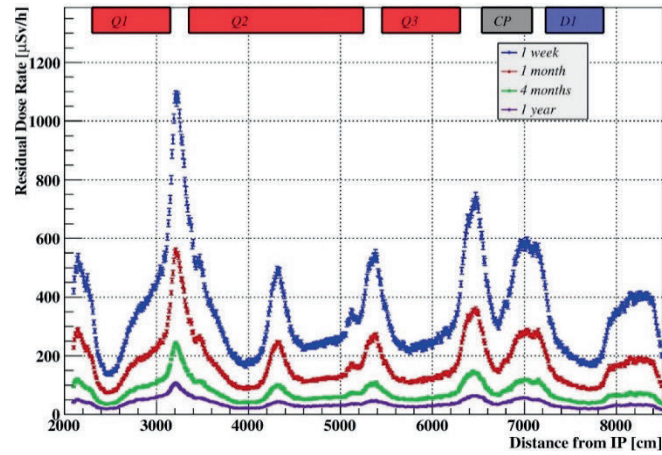


Figure 19-2: Residual dose rate profiles for the nominal scenario in the aisle at 40 cm distance from the cryostat at four different cooling times: 1 week (blue), 1 month (red), 4 months (green) and 1 year (violet).

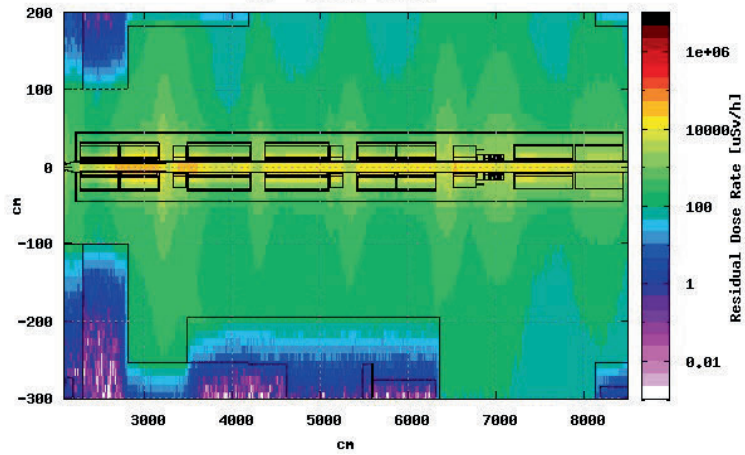


Figure 19-3: Residual dose rates in units of $\mu\text{Sv/h}$ around the low-beta triplet quadrupole and D1 magnets for the ultimate scenario after one month of cooling time. Doses are shown for a horizontal section at the level of the beam line. The origin of the coordinate frame is at the interaction point.

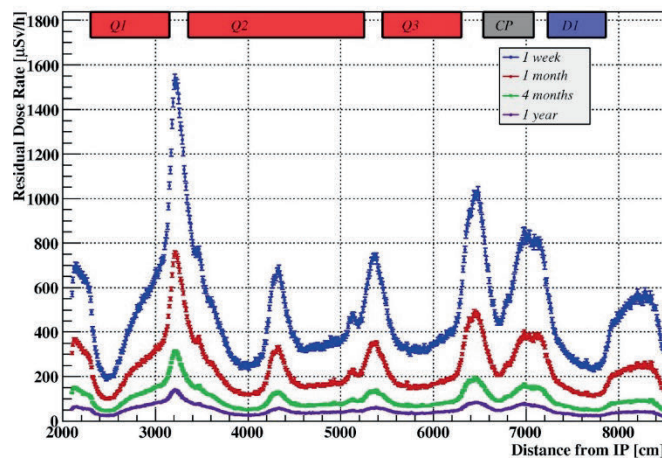


Figure 19-4: Residual dose rate profiles for the ultimate scenario in the aisle at 40 cm from the cryostat at four different cooling times: 1 week (blue), 1 month (red), 4 months (green) and 1 year (violet).

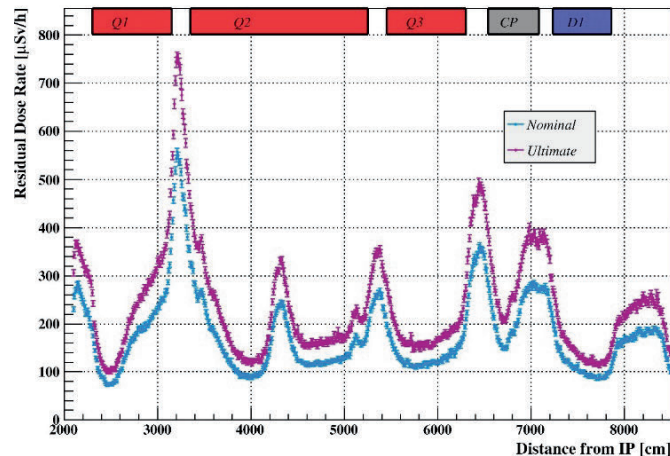


Figure 19-5: Residual dose rate profiles for the nominal (light-blue) and ultimate scenarios (pink) along the aisle at 40 cm distance to the cryostat after one month cooling time.

19.1.5 Radiological risk assessments for the new underground infrastructures in Point 1 and 5

Access to the new US, UR and UA service galleries is foreseen during beam operation (See Chapter 15). For this reason, the radiological impact of the machine operation on the personnel has to be assessed. The UL galleries will be closed during the machine operation, a part from one in which the first 12 m will be accessible. Two radiological risks have been addressed and will be described here after, air activation and stray radiation.

Risks due to activated air can be either due to direct activation of air inside the new infrastructures by stray radiation or due to streaming of activated air from the LHC tunnel into the new service areas. While the former is expected to be negligible the latter is prevented by static and dynamic confinement of the LHC tunnel air with ventilation doors and ventilation schemes that ensure a lower pressure in the LHC tunnel.

Stray radiation levels will impact the radiological classification of the new service areas. It is foreseen to classify them as Supervised Radiation Areas, similar to any other service area of the LHC. Two different scenarios have been studied, stray radiation during normal operation of the machine and an accidental scenario, represented by one full proton beam lost in a bulky object in front of the most exposing connection to the galleries,. The ultimate luminosity and beam intensity are considered ($7.5 \times 10^{34} \text{ cm}^{-2} \text{ s}^{-1}$ and 2808 bunches at $2.2 \cdot 10^{11}$ protons per bunch).

The dose limits follow from the radiological classification as Supervised Radiation Area. During normal operation of the accelerator, in the new service galleries the ambient dose equivalent rate has to be as low as reasonably possible (ALARA principle) and, in any case, it has to be lower than $15 \mu\text{Sv/h}$, the limit for non-permanently occupied work-places. In the accident scenario the effective dose received by personnel must not exceed the legal annual limit for the class B radiation worker, i.e. 6 mSv.

The FLUKA geometry model used for the HL-LHC LSS studies mentioned above does not include the new underground service galleries. Therefore, a standalone geometry model of these galleries was developed and used for the shielding study. The model includes the UR and the UA service galleries, the UA elbow on top of the LHC tunnel with 5 connection cores, and a portion of the LHC tunnel where a beam vacuum pipe and the bulky target to simulate the accidental case are placed (Figure 19-6). The model also includes the UL gallery with the three foreseen connection cores.

In order to reduce the radiation streaming through the cores connecting the UA elbow to the LHC, two concrete shielding walls are placed at the end of the UA gallery next to the UA elbow, as shown in the bottom-right section view in Figure 19-6. These two walls will be 40 cm thick with a sliding door allowing access to the elbow when the accelerator machine is not operating.

Furthermore, it is foreseen to connect the new UA galleries to the LHC tunnel by an emergency escape tunnel for personnel, including a stair-case due to the different height levels of new service galleries and existing LHC tunnel. The entry from the UA gallery is placed next to the first shielding wall. The escape tunnel

also includes two concrete chicane (one close to the UA, 40 cm thick and one close to the LHC tunnel, 80 cm thick). In addition, the 3-flight staircase itself will be made of concrete (20 cm thick) acting as shielding against stray radiation. In this configuration, the accessible part of the UA gallery starts at about 10 m distance from the UA elbow and an access system door, interlocked with the LHC beam, has to be implemented at this location.

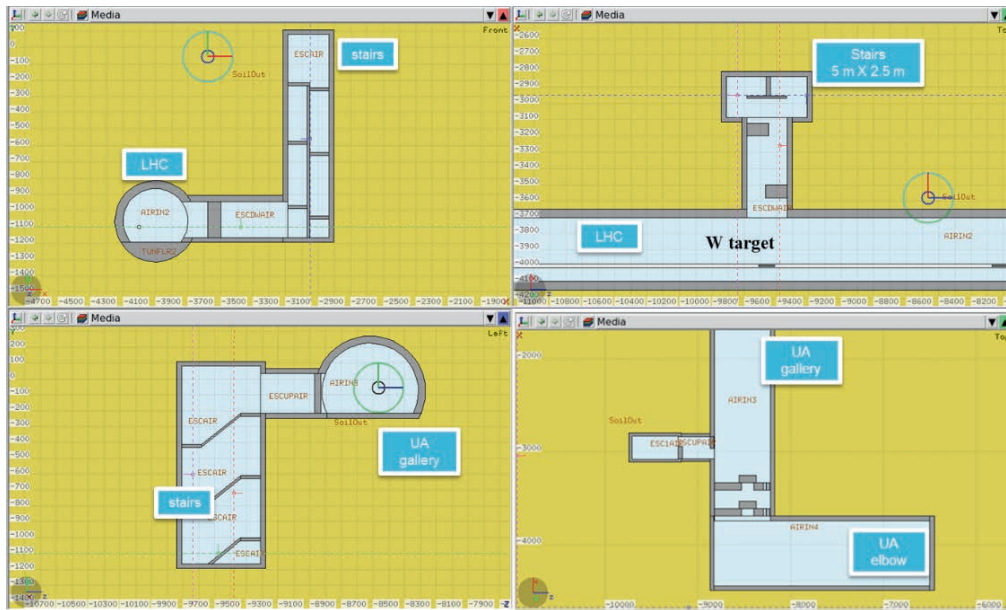


Figure 19-6: Different cross-sectional views of the FLUKA geometry of the UA gallery and elbow including the emergency exit toward LHC tunnel.

The effective dose map, due to accidental loss of a full beam of $6.2 \cdot 10^{14}$ protons in front of the closest connection to the UA gallery, is reported in Figure 19-7. Figure 19-8 shows the effective dose profile along the length of the UA gallery. In this plot the vertical blue lines indicates the location of the access system gate, the grey vertical lines indicate the positions of the shielding walls in the UA gallery and the horizontal green line the 6 mSv limit.

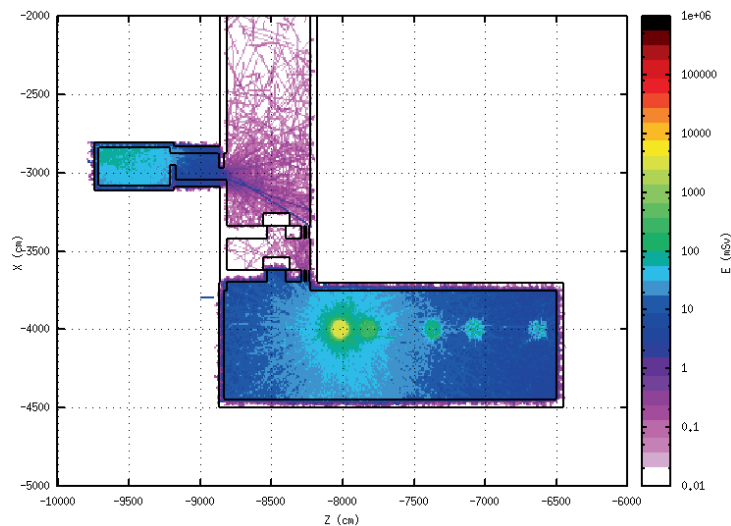


Figure 19-7: Effective dose map in the UA elbow and in the UA gallery, due to the full loss of one beam in front of the emergency exit connection to the LHC tunnel.

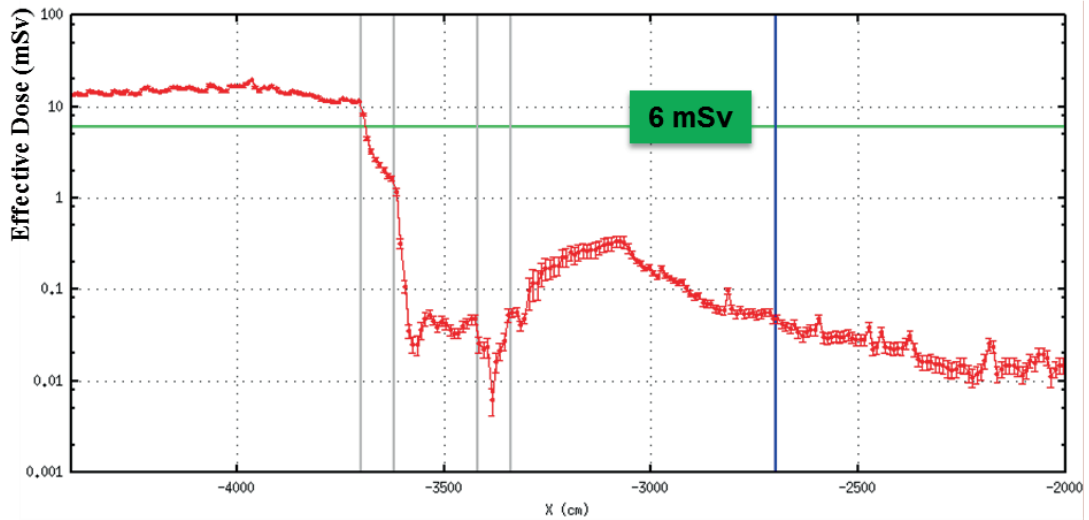


Figure 19-8: Effective dose profile in the UA gallery, due to the full loss of one beam in front of the closest core to the UA.

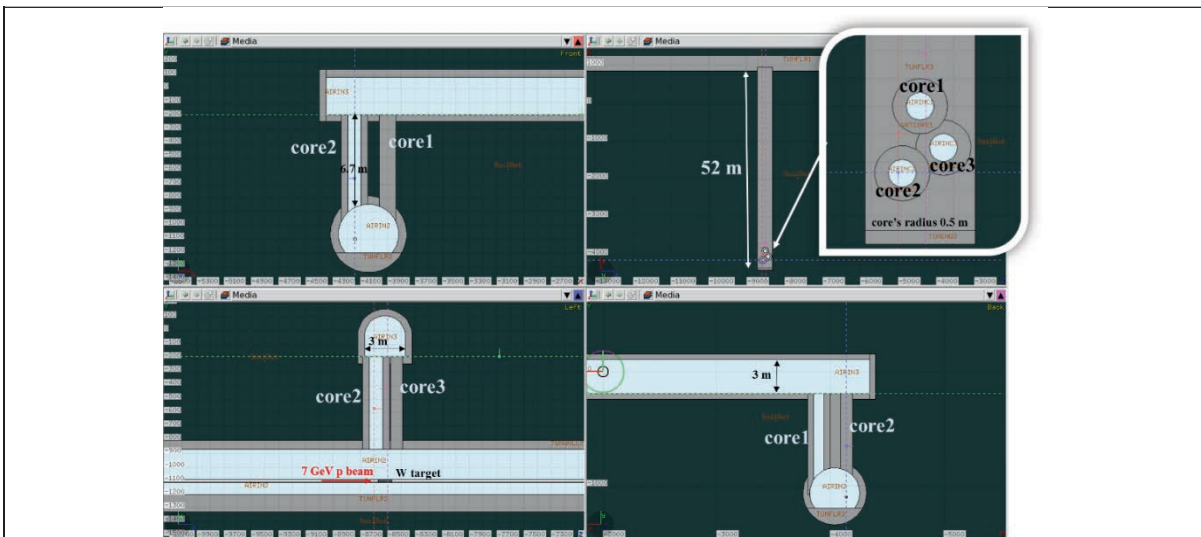


Figure 19-9: Different section views of the UL gallery geometry model.

The geometry model of the UL gallery is shown in Figure 19-9. Also in this case, an accidental full beam loss in a bulky object just in front of the closest core to the LHC beam line is considered. In Figure 19-10 the effective dose map (bottom) and the dose profile (top) along the UL gallery are shown. The 40 m long gallery not accessible is not enough to attenuate the radiation so that the effective dose delivered in the case of an accident, in the most exposed position, is lower than 6 mSv. For this reason it is highly recommended to implement a shielding also in UL gallery, in order to bring the estimated effective dose lower than 6 mSv. In Figure 19-11 the effect of a 40 cm iron wall is shown.

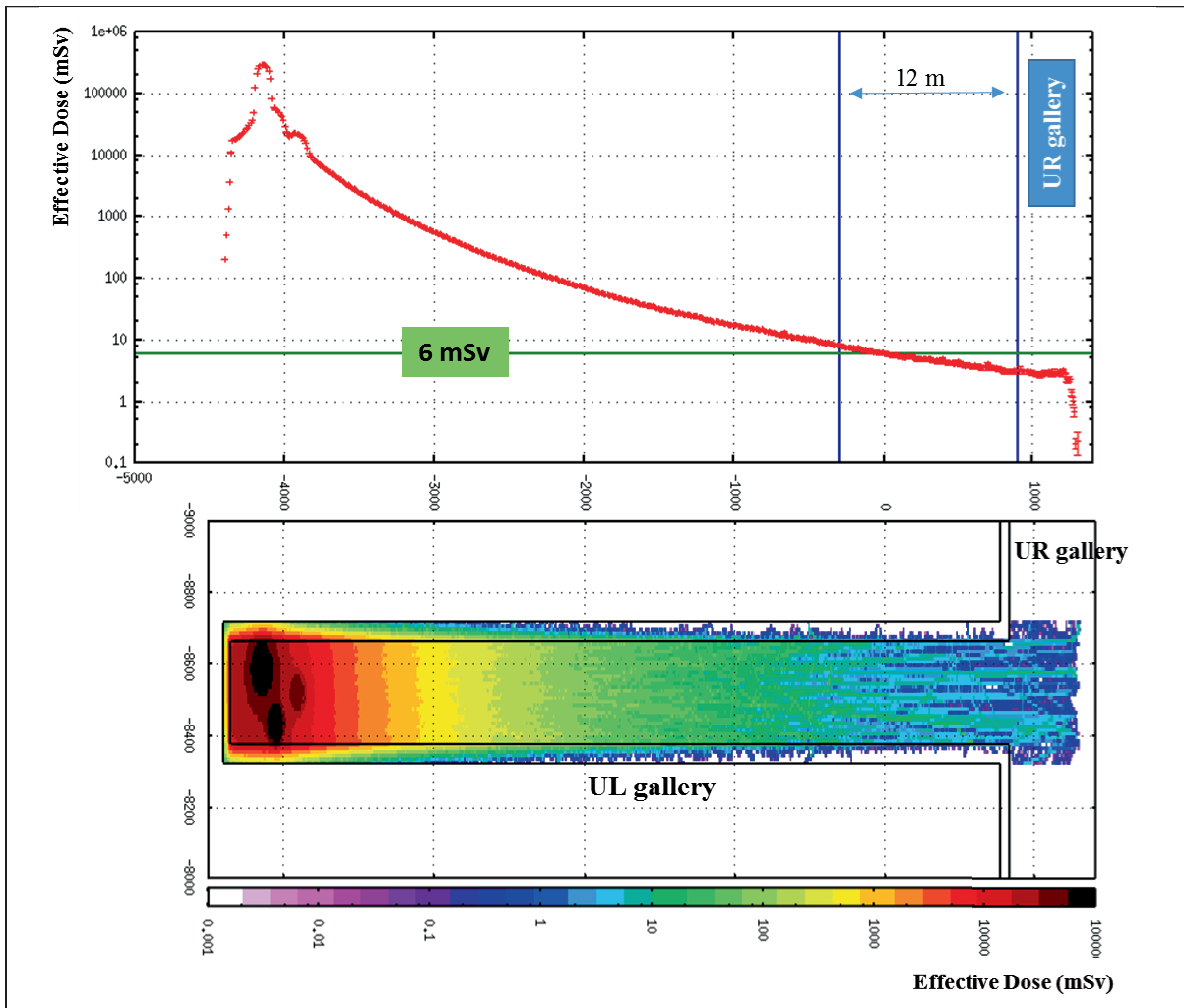


Figure 19-10: Effective dose map (bottom) and the dose profile (top) along the UL gallery, due to the full loss of one beam on a bulky object in front of one of the connections cores to the LHC tunnel.

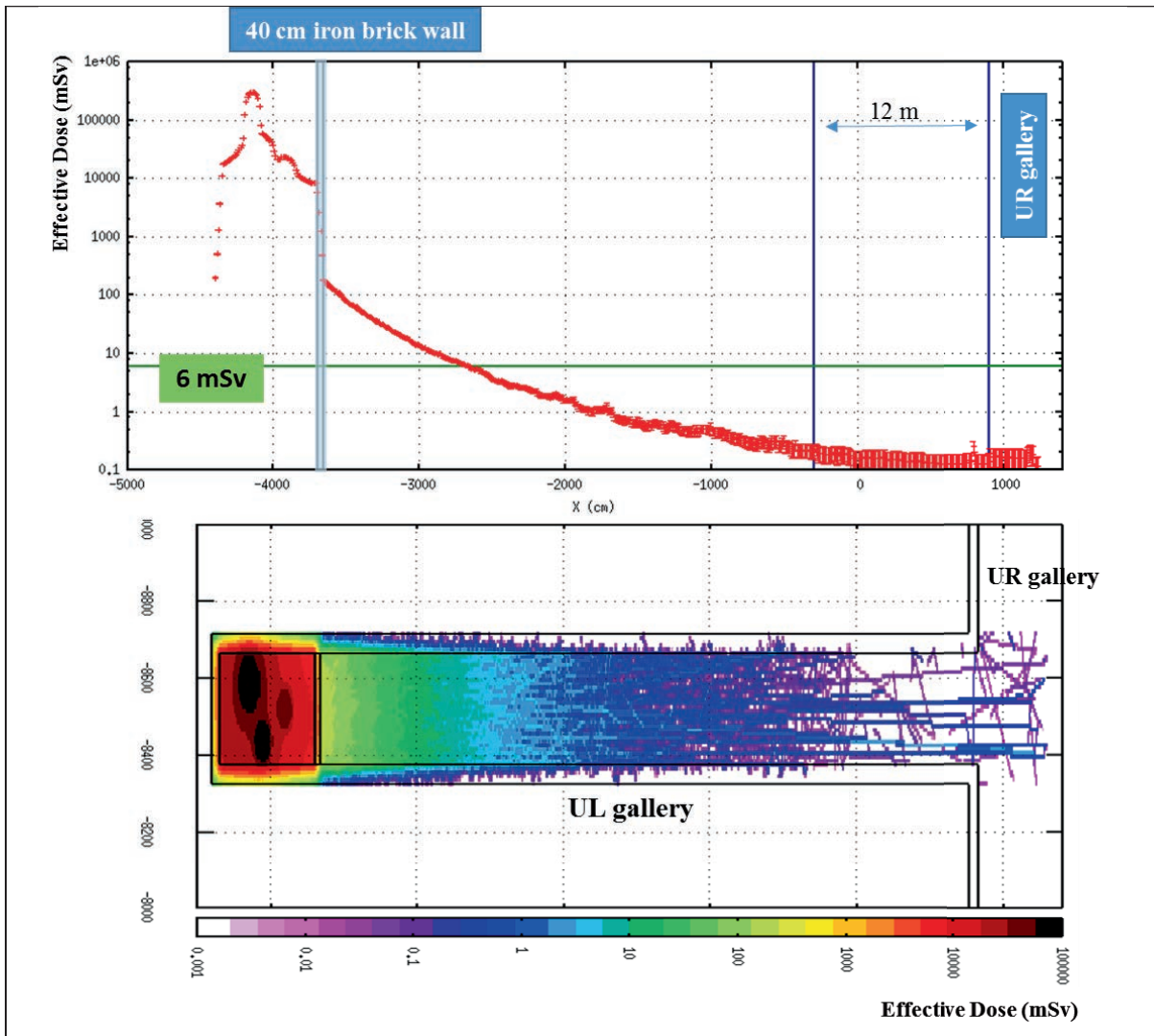


Figure 19-11: Effective dose map (bottom) and the dose profile (top) along the UL gallery with the addition of an iron shielding wall 40 cm thick, due to the full loss of one beam on a bulky object in front of one of the connections cores to the LHC tunnel.

The dose attenuation along the UA and UL galleries obtained in the study of the accidental beam loss can be used to calculate dose rates profiles due to stray radiation during normal machine operation (Figure 19-12). The UL galleries will be connected to the LHC tunnel at the end of D1 magnets, the UA galleries at the location of the crab cavities. The exact location of the connection of the emergency exit is not yet known. Thus, an envelope worst case has been considered where the connection is in the TAXN region. At this location, the ambient dose equivalent rate is about 40 Sv/h at $7.5 \times 10^{34} \text{ cm}^{-2} \text{ s}^{-1}$. This value is scaled using the attenuation factors from the LHC tunnel up to the closest accessible point in the new underground service gallery mentioned above. For the presented configuration, the attenuation factor is at least 10^{-8} to any of the closest accessible points. Applying this factor to the peak dose rate used as envelope case leads to a peak value of ambient dose equivalent rate of about 0.4 $\mu\text{Sv/h}$ due to normal machine operation at ultimate luminosity.

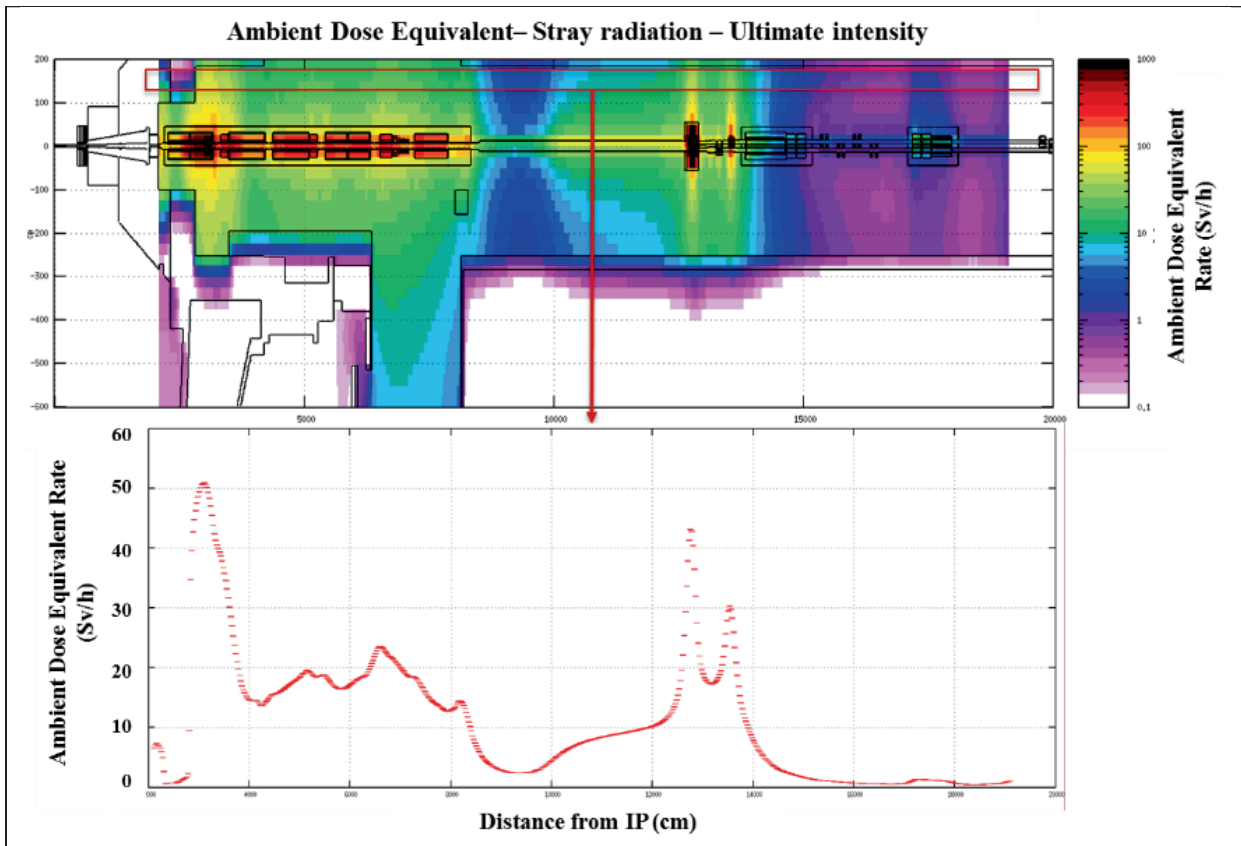


Figure 19-12: On top, ambient dose equivalent rate map due to stray radiation for machine operating at ultimate luminosity ($7.5 \times 10^{34} \text{ cm}^{-2} \text{ s}^{-1}$); on the bottom, ambient dose equivalent rate profile along the machine.

19.2 General safety

19.2.1 Introduction

Safety of a Project can be highlighted from different perspectives: first, there is a temporal distinction between the project phase (further divided in conceptual design, technical design, production and installation phases) and the later operational phase. Second, one can distinguish between the conformity aspect of Safety (the project's realisations shall comply with Safety regulations, standards and recommendations), and the workplace aspect (the prevention of professional accidents and professional illness by instructing, training and protecting workers).

This section highlights the strategies developed to ascertain compliance of HL-LHCs hardware with Safety Standards and regulations, and to make all of CERN's workplaces in the project as safe as reasonably possible. It also gives an outline of the Safety framework between Project Management, the collaborating units (from CERN and from collaborating institutes) and CERN's Health, Safety and Environmental Protection (HSE) Unit.

19.2.2 Project Safety at CERN

The basic model for Safety at CERN is the "Hierarchical Line of Responsibility" [11]. In short, it confers to organisational units at all levels of CERN the responsibility for the Safety of its personnel, equipment and activities. This responsibility is embodied in the Head of the organisational unit, and his executive powers extend to the field of Safety. Implementation of this policy is straightforward for the operation and maintenance of CERN's research and accelerator facilities, conferred to specific organisational units in its sectors and departments, but it needs additional clarification for projects aiming to create new or upgrade existing facilities.

SAFETY

A project pools together resources from numerous, specialised organisational units from all over CERN in a Matrix structure in order to achieve its objectives. A specific organisation is put into place for projects, including the project's Safety aspects [12]. The project leader assumes responsibility for the Safety of the Project, however, neither he, nor the Project organisation substitute the Hierarchical Line of Safety Responsibility. The organisational units participating in the project retain responsibility for results, both technical and in matters of Safety. An example is the timely delivery of accelerator components, meeting applicable safety standards, and best safety practice during their production. The project's responsibility is the provision of the necessary means to meet the technical and safety objectives, in form of manpower, budgets and a common safety organisation.

In a larger project, the project leader is advised to appoint a Project Safety Officer (PSO) [12], [13] to assist him with his Safety responsibilities.

Finally, the HSE unit has the role to establish a regulatory framework for Safety within CERN, to advise organisational units and projects on its implementation, and to monitor the implementation by safety clearances and inspections.

19.2.3 Safety File

The decisions taken on behalf of Safety during the project phase are important knowledge for future operation, maintenance, upgrade and dismantling of the facilities created by the project. They are recorded in a document entitled "Safety File", which is initiated during the conceptual design phase and accompanies the lifetime of the facility, being revised at every major change in the facility's lay-out or operation. The departments in the Accelerator and Technology Sector and the EP department have commonly defined in a management procedure [14] that a Safety File consists of four parts: the Descriptive part contains a Safety-oriented description of the facility's equipment and activities, and the Demonstrative part documents that the facility's equipment meets Safety regulations and standards, and that the activities follow best practice in Safety prevention. The third and fourth part, collecting operational procedures and return of experience are not applicable to a project.

For the HL-LHC project, it has been decided to create one Safety File with a descriptive part and a demonstrative part for each work package delivering hardware to the project. This excludes the work packages of project administration (WP1), accelerator performance (WP2), and energy deposition (WP10) from the process. Some of the remaining work packages may be regrouped into larger contexts, for example machine protection (WP7), experiment-collider interface (WP8), integration (WP15) and IT string and commissioning (WP16).

One of the PSO's tasks is to oversee the edition of the Safety File, in parallel with the project's development. In this function, he collaborates closely with the work package leaders and project engineers, and with members of the HSE unit.

The following two sections explain in detail how Safety conformity and Workplace Safety will be achieved and reflected in the Safety File.

19.2.4 Conformity with Safety Standards

The goal of personal Safety at the workplace is pursued on two complementary paths: the likelihood of equipment failure leading to an accident or occupational illness is reduced by installing only equipment which meets published Safety regulations and standards. These regulatory documents draw on the pooled experience in workplace safety of panels of experts working on behalf of the public authorities. In the European Union, Directives with a Safety focus are published by the European Commission and have to be translated into national law within reasonable delays. They contain so-called "Essential Safety Requirements" (ESR), which must be met to introduce a product on the common market, even for one's own use. The directives are complemented with technical standards in the European Norm (EN) series which give technical solutions for the fulfilment of the ESRs. If an equipment is constructed following the applicable European Norms, it is considered as conforming to the Directive's ESR, but the compliance can also be achieved by other means, CERN's host state France is a member of the EU, whereas Switzerland adopts European Safety directives to

be able to freely trade with its neighbours. At CERN, the ESR of the European Directives are considered as the minimal Safety standards, where they are applicable.

Other sources of Safety regulations and standards may be national regulations of a host state, or specific regulations at CERN, which are published in form of a Safety Regulation (SR) or a General Safety Instruction (GSI) [15].

The project phase is of essential importance for the aspect of conformity with Safety regulations. If a design does not meet a technical safety standard, it is relatively easy to amend, albeit at unavoidable cost of time and manpower, but if the items ready for installation in the accelerator would be found non-conforming, the consequences for the timely success of the project would be much more serious. The process of ascertaining conformity must progress together with the design and development of the equipment produced by the project.

As outlined above, the HSE unit has the mandate of defining the Safety regulations and standards applicable to activities at CERN. It also monitors and verifies the proper implementation of prescriptions standards by inspection and by the process of Safety clearance.

The first step in the conformity process is the establishment of a Hazard Register. The PSO, a HSE correspondent and the WP leader and some engineers participate in this step, where the Safety hazards which may be presented by a certain equipment are identified, following a comprehensive check-list (Hazard Identification Form, HIF) [16]. Based on the Hazard Register and a broad description of the project's planned realisations, the HSE correspondent edits together with topical Safety experts in HSE the so-called "Launch Safety Agreement" (LSA). This document, tailored to the Work Package, contains for each identified hazard the Safety regulations and standards applicable at CERN. An annex to the LSA provides a check-list of the Safety documentation to be made available to HSE inspectors in the course of the project for giving Safety clearance. The LSA and its annex are submitted as a draft for review to the PSO and the WP leader before being officially released by the HSE unit. In this way, it is assured that hazards have been correctly identified and that only the applicable standards and regulations are listed in the annex.

The described process of ascertaining Safety conformity is straightforward to implement as long as equipment is either produced at CERN, contributed by collaborating scientific institutes or purchased from manufacturers, who are established in the European Union or are otherwise familiar with EU Safety regulations (e.g. Swiss or Norwegian contributors or manufacturers).

This is not the case with international collaborators from countries with an existing national framework of Safety conformity, for example from the United States of America or from Japan. Meeting European Safety standards in detail may have high cost in terms of budget, manpower and time for institutions and manufacturers in these countries, while their domestic standards are proven to achieve Safety in a slightly different realisation.

In certain circumstances, where a foreign (i.e. extra-European) manufacturer applies an alternative certification system for Safety compliance, he can make a request for exceptional treatment to the HSE unit at CERN. HSE experts will analyse the case and decide if additional tests, beyond the foreign certification, would be mandatory before declaring the equipment fit for use at CERN.

Once the documentation for demonstrating conformity with Safety regulations and standards is complete, experts in the HSE unit will verify it and then give Safety clearance, either unconditional. Or conditional to some final amendments. At this point, the completed annex to the LSA represents the table of contents for the full safety compliance documentation, and it becomes a part of the Safety File's Demonstrative Part.

19.2.5 HL-LHC Workplace Safety

The hardware construction for HL-LHC will mobilise on the CERN sites hundreds of workers, technicians, engineers and scientists in dozens of workplaces (workshops, laboratories and test areas). To demonstrate that these personnel have a safe workplace and work according to safe procedures is another objective of the Project's Safety File.

In the Hazard Identification Form [16], a distinction is made between hazards which emanate from the finished equipment during operation, and which are collected in form of a check-list, and hazards at the technical workplaces. The workplaces used by a work package are listed in the HIF and reported in the LSA.

The workplaces thus identified become the subject of a Workplace Safety Analysis [17], which is conducted by a Safety Support Officer together with the responsible for the process. The technical work in laboratories and workshops at CERN generates hazards and risks similar to those encountered in industry, and the method for hazard assessment is based on the one proposed by the Swiss professional accident insurance and prevention organism SUVA [18], [19]. The workplace is divided in different perimeters characterised by the activities therein. Then, the activities, the equipment and the substances used or produced in the perimeter are listed and the hazards originating from them are detailed with a checklist [20] oriented to workplace safety. The Hazard Register is compared with workplace Safety rules, regulations and best practice from different sources (CERN, and professional accident prevention organisms in e.g. Switzerland, France and the United Kingdom). The SUVA provides a wide collection of check-lists which allow to identify where a certain process does not meet regulations or the latest recommendations in matter of Safety.

Observations of non-conforming equipment or potentially unsafe behaviour at the workplaces are noted in the assessment and recommendations for improvement are made to the supervisor (usually, a section- or group leader), who can thus exercise his responsibility in matters of Safety.

The documentation of the Workplace Safety Analysis is reviewed by the Supervisors, the Group and Department Head before being published, and it is referenced in the Demonstrative Part of those work packages Safety Files which make use of the analysed workplace.

19.2.6 An example - Superconducting magnets

Two HL-LHC WP will produce superconducting magnets, largely based on the novel Nb₃Sn conductor technology. WP3 will deliver wide-aperture quadrupole magnets for improved focusing of the particle beams in the interaction points 1 and 5, and WP 11 will produce an 11 m long dipole with increased filed-strength (11 T instead of 8 T) which replaces a standard LHC dipole of 15 m length to create space for an additional collimator.

The hazard assessment for WP 3, covering numerous different magnet types, and the resulting Launch Safety Agreement, would have been very repetitive, as the production of these magnets shares large similarities. Instead it was decided to conduct the hazard assessments separately for a generic magnet coil (allowing for the difference in producing coils from Nb-Ti or Nb₃Sn conductors), for a generic cold mass and a generic cryostat. The technologies, equipment and consequently workplaces used for producing the components are very different from each other and it was found that this subdivision of the work was most meaningful for the safety aspects of the work.

WP3 is relying on contributions from partners in Italy, France, Spain, the U.S. and Japan. The extra-European contributors use formal conformity assurance systems with identical goals (protection of workers, environment and equipment) but which differ in details from the assessment rules in the European Directives on Safety. It would be prohibitively expensive in terms of budget and time to assess conformity of their contributions with European Standards, and this assessment would not add significantly to the quality of the equipment received. It has therefore been decided to deviate in this aspect from a strict adherence to the European Safety Directives. The HSE unit will make a judgement if the conformity assurance methods put in place by the U.S. and Japan are suitable to meet the Essential Safety Requirements of the European Directives, and it may decide compensatory measures if necessary.

Superconducting magnets are inserted in so-called cold masses, cooled by superfluid helium to 1.9 K. Under normal circumstances, the helium bath has an operation pressure of not more than 10⁵ Pa above atmosphere, but in case of a quench of the superconductor, the pressure can rise for a short time to 20 * 10⁵ Pa. For this reason, the cold masses must be classified as pressure vessels, and they correspond to the highest classification in the relevant European Directive. For this category, the European legislator foresees in principle an assessment of the conformity involving external experts in form of a “notified body”, i.e. with a formal approval from the public authority to assess pressure devices. Following this route with the European-built

magnets of WP3 would create an asymmetry between the assessment processes for magnets from different continents, and it has been decided that the HSE unit would substitute itself to the “notified body”, which is possible within the special prerogatives on Safety anchored in CERNs constitutive documents.

19.3 References

- [1] CERN, Safety Code F, Radiation Protection, CERN (2006). [EDMS 335729](#)
- [2] CERN, General Safety Instruction, ALARA rule applicable to interventions at CERN, CERN (2017). [EDMS 1751123](#)
- [3] CERN, ALARA Review Working Group, Final report, CERN (2013), [EDMS 1244380](#).
- [4] H. Vincke and C. Theis, ActiWiz – Optimizing your nuclide inventory at proton accelerators with a computer code. Proc. ICRS-12 & RPSD 2012 Conf., Nara, Japan, 2–7 September 2012, [*Prog. Nucl. Sci. Technol.* (2013)]. DOI: [10.15669/pnst.4.228](#)
- [5] T.T. Boehlen, F. Cerutti, M.P.W. Chin, A. Fasso, A. Ferrari, P.G. Ortega, A. Mairani, P.R. Sala, G. Smirnov and V. Vlachoudis, The FLUKA Code: Developments and Challenges for High Energy and Medical Applications, Nuclear Data Sheets 120, 211-214 (2014). DOI: [10.1016/j.nds.2014.07.049](#)
- [6] A. Fassó, A. Ferrari, J. Ranft and P.R. Sala, Fluka: A multi particle transport code. CERN-2005-10, INFN/TC_5/11, SLAC-R-773 (2005). DOI: [10.5170/CERN-2005-010](#)
- [7] S. Roesler, R. Engel and J. Ranft, The Monte Carlo event generator DPMJET-III, Proc. Monte Carlo 2000 Conf., Lisbon, 23–26 October 2000, Eds. A. Kling, F. Barao, M. Nakagawa, L. Tavora and P. Vaz. (Springer-Verlag, Berlin, 2001) pp. 1033–1038. DOI: [10.1007/978-3-642-18211-2_166](#)
- [8] M. Pelliccioni, Overview of fluence-to-effective dose and fluence-to-ambient dose equivalent conversion coefficients for high energy radiation calculated using the FLUKA code, *Radiat. Prot. Dosim.* **88** (2000) 279–297. DOI: [10.1093/oxfordjournals.rpd.a033046](#)
- [9] Layout of HL-LHC insertions, LHCLSXGH0003 and LHCLSXGH0007, [EDMS 1561299](#).
- [10] T. Csörgö *et al.*, Elastic scattering and total cross-section in p+p reactions measured by the LHC Experiment TOTEM at $\sqrt{s} = 7$ TeV, 41st International Symposium of Multiparticle Dynamics, Hiroshima, Japan, 26 - 30 Sep 2011, pp.180-183. [arXiv:1204.5689](#)
- [11] CERN, The CERN Safety Policy, CERN (2014), [EDMS 1416908](#)
- [12] CERN, Safety Regulation SR-SO “Responsibilities and Organisational Structure in Matters of Safety at CERN”, 2016, [EDMS 1389540](#)
- [13] CERN, General Safety Instruction GSI-SO-7, “Project Safety Officer”, CERN (2014), [EDMS 1410233](#)
- [14] P. Bonnal *et al.*, “Quality Management Procedure - Safety Files Management”. [EDMS 1177755](#)
- [15] CERN, Safety Procedure SP-R1 “Establishing, updating and publishing CERN Safety Rules, 2008, [EDMS 872057](#)
- [16] CERN, HL-LHC Hazard Identification Table, 2016, [EDMS 1361970](#)
- [17] F. Viggiano, “Methodological Approach for Safety Analysis in the TE Department”, 2017, [EDMS 1687947](#)
- [18] SUVA Protection de la santé, “Connaissez-vous le potentiel des phénomènes dangereux dans votre entreprise ?”, Lucerne, [4^e édition](#) 2011
- [19] SUVA Protection de la santé, “Méthode Suva d’appréciation des risques à des postes de travail et lors de processus de travail”, Lucerne, [2^e édition](#) 2008
- [20] Th. Otto and F. Viggiano, “Hazard Classification for Technological processes in TE Department, 2016, [EDMS 1586444](#)

List of Machine and Beam Parameters

A. List of machine and beam parameters

A.1. Main machine parameters

Table A-1: HL-LHC nominal machine parameters for proton operation [1].

			Injection	Collision
Geometry				
	Ring circumference	[m]	26658.883	26658.883
	Ring separation in arcs	[mm]	194	194
	Bare inner vacuum screen height in arcs	[mm]	46.5	46.5
	Effective vacuum screen height (incl. tol.)	[mm]	44.04	44.04
	Bare inner vacuum screen width in arcs	[mm]	36.9	36.9
	Effective vacuum screen width (incl. tol.)	[mm]	34.28	34.28
Main magnets				
	Number of main bends		1232	1232
	Length of main bends	[m]	14.3	14.3
	Field of main bends	[T]	0.535	8.33
	Bending radius	[m]	2803.95	2803.95
Lattice				
	Maximum dispersion in arc (H/V)	[m]	2.4/0.27	2.7/0.52
	Minimum dispersion in arc (H/V)	[m]	0.96/-0.27	0.83/-0.48
	Maximum β in arc (H/V)	[m]	178/178	445/445
	Minimum β in arc (H/V)	[m]	31.4/32.1	28.0/28.8
	Minimum β in IP1/2/5/8*	[m]	6/10/6/10	0.2/10/0.2/3
	Horizontal tune		62.27	62.31
	Vertical tune		60.295	60.32
	Momentum compaction	$[10^{-4}]$	3.456	3.46
	Slip factor η	$[10^{-4}]$	3.412	3.46
	Gamma transition γ_{tr}		53.8	53.8
RF System				
	Revolution frequency	[kHz]	11.2455	11.2455
	RF frequency	[MHz]	400.79	400.79
	Harmonic number		35640	35640
	Total RF voltage	[MV]	8	16
	Synchrotron frequency	[Hz]	66.0	23.8
	Bucket area	[eVs]	1.38	7.63
	Bucket half height ($\Delta E/E$)	$[10^{-3}]$	0.965	0.343
Crab Cavities				
	RF frequency	[MHz]	400.79	400.79
	Total RF voltage (per IP side and beam)	[MV]	0	6.8

*The horizontal and vertical β functions are equal at the IP.

Table A-2: HL-LHC nominal machine parameters at the collision points for proton operation. The crossing angle and separation refer to Beam 1 [1].

		Injection	Collision
Interaction data			
Number of collision points		-	4
Half crossing angle at the IP for ATLAS (IP1)	[μ rad]	± 295 (V)	± 255 (V)
Half parallel separation at the IP for ATLAS (IP1)	[mm]	± 2.0 (H)	0.0 (H)
Half external crossing angle at IP for ALICE (IP2) ^{1,2}	[μ rad]	∓ 170 (V)	∓ 170 (V)
Half crossing angle at the IP for ALICE (IP2) ^{1,2}	[μ rad]	∓ 4.5 (H) / ∓ 1259 (V)	∓ 0.3 (H) / ∓ 240 (V)
Half parallel separation at the IP for ALICE (IP2)	[mm]	+2.0 (H)	+0.14 ³ (H)
Half crossing angle at the IP for CMS (IP5)	[μ rad]	+295 (H)	+255 (H)
Half parallel separation at the IP for CMS (IP5)	[mm]	± 2.0 (V)	0.0 (V)
Half external crossing angle at the IP for LHCb (IP8)	[μ rad]	-170 (H)	-250 (H)
Half crossing angle at the IP for LHCb ^{1,2} (IP8)	[μ rad]	-2270/1930 (H) // 12/68 (V)	-385/-115 (H) // ∓ 1.8 (V)
Half parallel angle at the IP for LHCb (IP8) [3]	[μ rad]	± 40 (V)	0
Half parallel separation at IP for LHCb (IP8) [3]	[mm]	± 3.5 (V)	± 0.04 ⁴ (V)
Minimum β at IP1 and IP5 (H/V)	[m]	6/6	0.2/0.2
β at IP2 (H/V)	[m]	10/10	10/10
β at IP8 (H/V)	[m]	10/10	3/3

¹ The crossing angle in IP2 and IP8 is the sum of an external crossing angle bump and an ‘internal’ spectrometer compensation bump and it depends on the spectrometer polarity [2]. The values quoted above correspond to the configuration with the spectrometer ON providing to the minimum long-range beam-beam normalized separation. The external bump extends over the triplet and D1 and D2 magnets. The internal spectrometer compensation bump extends only over the long drift space between the two triplet assemblies left and right from the IP. For IP2 the vertical external crossing angle sign can be changed and therefore the same sign of the internal and external angle can be chosen to be the same. This is not possible for IP8 as the sign of the crossing angle must be compatible with the recombination scheme.

² The first value corresponds to the so-called “positive” polarity of the spectrometers.

³ This corresponds to a full separation of 4.8 σ required to reduce the luminosity down to 10^{31} cm^{-2} s^{-1} for the nominal bunch population

⁴ This corresponds to a full separation of 2.5 σ required to reduce the luminosity down to 2×10^{33} cm^{-2} s^{-1} for the nominal bunch population

A.2. Proton beam parameters in collision

Table A-3: HL-LHC nominal parameters in collision for 25 ns operation for two production modes of the LHC beam in the injectors and for the alternative scenario 8b+4e [1,4-7].

Parameter	HL-LHC (standard)	HL-LHC (BCMS) [#]	HL-LHC (8b+4e) [@]
Beam energy [TeV]	7	7	7
Relativistic gamma	7461	7461	7461
Particles per bunch, N [10^{11}]	2.2	2.2	2.3
Number of bunches per beam	2748	2604	1968
Number of collisions in IP1 and IP5 [*]	2736	2592	1960
N_{tot} [10^{14}]	6.0	5.7	4.5
Beam current [A]	1.09	1.03	0.82
Stored energy per beam [MJ]	678	642	486
Crossing angle in IP1 and IP5 [μrad]	510	510	480
Minimum normalized long-range beam-beam separation [σ]	12.5	12.5	12.5
Minimum β^* [m]	0.2	0.2	0.2
ϵ_n [μm]	2.50	2.50	2.20
ϵ_L [eVs]	2.50	2.50	2.50
R.M.S. energy spread [0.0001]	1.08	1.08	1.08
R.M.S. bunch length [cm]	8.1	8.1	8.1
Minimum R.M.S. beam size at IP1/5 [μm]	7.1	7.1	6.7
IBS horizontal [h]	18.8	18.8	13.6
IBS longitudinal [h]	20.6	20.6	16.9
Longitudinal emittance damping time [h]	13	13	13
Transverse emittance damping time [h]	26	26	26
Power loss due to synchrotron radiation [W/m/beam]	0.41	0.39	0.30
Piwiniski parameter	2.53	2.53	2.53
Total reduction factor R_0 without crab cavities at min. β^*	0.369	0.369	0.369
Total reduction factor R_1 with crab cavities at min. β^*	0.715	0.715	0.740
Beam-beam tune shift/IP	0.010	0.011	0.012
Peak luminosity without crab cavities [$10^{34} \text{ cm}^{-2} \text{ s}^{-1}$]	6.52	6.52	5.8
Peak luminosity with crab cavities $L_{\text{peak}} \times R_1/R_0$ [$10^{34} \text{ cm}^{-2} \text{ s}^{-1}$]	12.6	11.9	11.6
Events/crossing without levelling and without crab cavities	172	172	213
Levelled luminosity [$10^{34} \text{ cm}^{-2} \text{ s}^{-1}$]	5.30 [†]	5.02 [†]	3.81
Events/crossing μ (with levelling and crab cavities) [‡]	140	140	140
Maximum line density of pile-up events during fill [events/mm]	1.3	1.3	1.3
Levelling time [h] (assuming no emittance growth) [‡]	5.14	5.14	6.2
Number of collisions in IP2/IP8	2452/2524 ^{**}	2288/2396 ^{**}	1163/1868 ^{**}

[#]BCMS parameters are only considered for injection and as a backup parameter set in case one encounters larger-than-expected emittance growth in the HL-LHC during injection, ramp and squeeze.

[@]The 8b+4e variant represents a back-up scenario for the baseline 25ns operation in case of electron cloud limitations.

^{*}Assuming one less batch from the PS for machine protection (pilot injection, transfer line steering with 12 nominal bunches) and non-colliding bunches for experiments (background studies, etc.). Note that due to RF beam loading the abort gap length must not exceed the 3 μs design value.

[†]For the design of the HL-LHC systems (collimators, triplet magnets, etc.), a margin of 50% on the peak luminosity (corresponding to the ultimate levelled luminosity of approximately $7.5 \times 10^{34} \text{ cm}^{-2} \text{ s}^{-1}$ and to a pile-up $\mu=200$) has been agreed.

[‡]The total number of events/crossing is calculated with an inelastic cross-section of 81 mb, while the total cross section of 111 mb is pessimistically assumed for calculating the proton burn off and the resulting levelling time [8-9].

**The lower number of collisions in IR2/8 compared to the general-purpose detectors is a result of the agreed filling scheme, aiming as much as possible at an equal sharing of collisions between the experiments.

A.3. Proton beam parameters at LHC Injection (after capture)

Table A-4: HL-LHC nominal parameters at injection (after capture) for 25 ns operation for two production modes of the LHC beam in the injectors and for the alternative scenario 8b+4e [1,5-7].

Parameter	HL-LHC (standard)	HL-LHC (BCMS) [#]	HL-LHC (8b+4e) [@]
Beam energy [TeV]	0.45	0.45	0.45
Relativistic gamma	479.6	479.6	479.6
Particles per bunch, N [10^{11}]	2.30	2.30	2.40
Number of bunches per beam	2748	2604	1968
N_{tot} [10^{14}]	6.3	6.0	4.7
Beam current [A]	1.13	1.08	0.85
Stored energy per beam [MJ]	44	41	31
ϵ_n [μm]	2.00	1.7-2.0 ^{***}	1.7
ϵ_L [eVs]	0.7	0.7	0.7
R.M.S. energy spread [0.0001]	3.7	3.7	3.7
R.M.S. bunch length [cm]	10.4	10.4	10.4
IBS horizontal [h]	4.9	3.5-4.9	3.3
IBS longitudinal [h]	3.9	3.3-3.9	3.1

[#]BCMS parameters are only considered for injection and as a backup parameter set in case one encounters larger-than-expected emittance growth in the HL-LHC during injection, ramp and squeeze.

[@]The 8b+4e variant represents a back-up scenario for the baseline 25ns operation in case of electron cloud limitations.

^{***} For the BCMS scheme, emittances down to 1.7 μm have already been achieved at LHC injection, which might be used to mitigate excessive emittance blow-up in the LHC during injection and ramp.

A.4. Required proton beam parameters at SPS Extraction

Table A-5: Required beam parameters at SPS extraction for 25 ns operation for two production modes of the LHC beam in the injectors and for the alternative scenario 8b+4e [1,5-7].

Parameter	HL-LHC (standard)	HL-LHC (BCMS) [#]	HL-LHC (8b+4e) [@]
Beam energy [TeV]	0.45	0.45	0.45
Particles per bunch, N [10^{11}] ^{††}	2.30	2.30	2.40
Maximum number of bunches per injection	288	288	224
Max N_{tot} /extraction [10^{13}]	6.62	6.62	5.4
ϵ_n [μm] ^{‡‡}	2.00	<2.00 ^{***}	1.7
ϵ_L [eVs]	0.66	0.66	0.66
R.M.S. energy spread [0.0001]	2.7	2.7	2.7
R.M.S. bunch length [cm]	13.7	13.7	13.7

[#]BCMS parameters are only considered for injection and as a backup parameter set in case one encounters larger-than-expected emittance growth in the HL-LHC during injection, ramp and squeeze.

[@]The 8b+4e variant represents a back-up scenario for the baseline 25ns operation in case of electron cloud limitations.

^{††}An intensity loss of 5% distributed along the cycle is assumed from SPS extraction to collisions in the LHC.

^{‡‡}A transverse emittance blow-up of 10–15% on the average H/V emittance in addition to that expected from intra-beam scattering (IBS) is assumed (to reach 2.5 μm of emittance in collision for 25 ns operation).

^{***}For the BCMS scheme, emittances down to 1.7 μm have already been achieved at LHC injection, which might be used to mitigate excessive emittance blow-up in the LHC during injection and ramp.

A.5. Ion beam parameters in collision

Table A-6: Average values of principal beam parameters at the start of Pb-Pb physics [10-12].

Parameter	Nominal LHC (design report)	HL-LHC (projected)	HL-LHC (LIU baseline)	HL-LHC (25 ns option)	HL-LHC (required)
Beam energy in collision [TeV]	574	574	574	574	574
Beam energy per nucleon in collision [TeV]	2.76	2.76	2.76	2.76	2.76
Particles per bunch, N [10^7]	7	10.4	15	15	19
Number of bunches per beam	592	1248	1152	1680	1248
Colliding pairs at IP2	592	1100	1000	1500	1100
N_{tot} [10^9]	41.4	121.7	173	252	222.3
Beam current [mA]	6.12	18.0	25.6	37.2	32.8
Minimum β^* [m]	0.5	0.5	0.5	0.5	0.5
ϵ_n [μm]	1.5	1.6	1.6	1.6	1.5
ϵ_L [eVs/charge]	2.50	2.50	2.50	2.50	2.50
RMS energy spread [0.0001]	1.10	1.10	1.10	1.10	1.10
RMS bunch length [cm]	7.94	7.94	7.94	7.94	7.94
IBS horizontal [h]	7.7	4.5	2.8	2.8	2.2
IBS longitudinal [h]	13	7.5	4.7	4.7	3.7
Half-crossing angle at IP2 [μrad]	60	100	100	100	100
Peak luminosity [$10^{27} \text{ cm}^{-2} \text{ s}^{-1}$]	1.00	4.5	4.5	6.8	8
Levelled luminosity [$10^{27} \text{ cm}^{-2} \text{ s}^{-1}$]	-	-	6-7	6-7	6-7
Levelling time [h]	-	-	-	0.6	1
Maximum number of bunches per injection	54	48	48	56	48

A.6. Main insertion region magnet parameters

Table A-7: New or refurbished quadrupoles for HL-LHC, all operating at 1.9 K, apart from Q6.

Magnet	Inner triplet (single aperture)			Matching section (two-in-one)		
	Q1	Q2	Q3	Q4	Q5	Q6
Number per side per insertion	2			1		
Type	MQXFA	MQXFB	MQXFA	MQY		MQML
Magnetic length [m]	4.2	7.15	4.2	3.4		4.8
Maximum Gradient [T/m]	132.6			200		160
Coil aperture [mm]	150			70		56
Aperture separation [mm]	NA			194		
Beam screen shape	Octagon			Rectellipse		
Beam screen aperture [mm]	95.0(H/V)/ 95.0(45 $^\circ$)	115.0(H/V)/ 106.0(45 $^\circ$)		57.8(d) / 48.0 (g)		45.1(d)/35.3(g)
Alignment tolerances (R/H/V) [mm]	0.6/1.0/1.0			0.84/1.26/0.6		As built

The description of the shapes is made by providing the dimensions corresponding to the horizontal(H)/vertical(V) and 45° cuts for octagons; diameter (d) and gap (g) for rectellipses [10]; radius for circles. The values represent the inner dimensions of the beam screen including mechanical tolerances. This is different to what is done in, e.g., Ref. [13], where the nominal sizes of the beam screens are reported. The orientation of the rectellipse cross section depends on the IP side and beam type and it has been chosen to optimise the beam aperture in collision. The alignment tolerances are represented as a racetrack shape of radius (R), and horizontal (H), vertical (V) extent, respectively. The values provided include ground motion and fiducialization tolerances [14].

Table A-8: Separation and corrector dipole magnets for HL-LHC, all operating at 1.9 K. The orbit correctors can be nested or consecutive as indicated. The order of the correctors refers to IP5 right of Beam 1 starting from the IP5.

Assembly	Separation/recombination dipoles		Orbit correctors				
	D1	D2	Corrector Package	Q2	D2	Q4	Q5
Number per side per insertion	1	1	1	2	2	4	3
Configuration			HV nested	HV nested	HV consecutive	VHVH consecutive	HVH consecutive
Type	MBXF	MBRD	MCBXFA	MCBXFB	MCBRD	MCBY	MCBY
Magnetic length [m]	6.27	7.78	2.2	1.2	1.89	0.9	0.9
Integrated field [Tm]	35	35	4.5	2.5	5.0	2.7	2.7
Coil aperture [mm]	150	105	150	150	100	70	70
Aperture separation [mm]	NA	188	NA	NA	194	194	194
Beam screen shape	Octagon	Octagon	Octagon	Octagon	Octagon	Rectellipse	Rectellipse
Beam screen aperture [mm]	115.0(H/V) 106.0(45°)	83.0(H/V) 74.0(45°)	115.0(H/V) 106.0(45°)	115.0(H/V) 106.0(45°)	83.0(H/V) 74.0(45°)	57.8(d) 48.0 (g)	57.8(d) 48.0 (g)
Alignment tolerances (R/H/V) [mm]	0.6/1.0/1.0	0.84/1.36/0.6	0.6/1.0/1.0	0.6/1.0/1.0	0.84/1.36/0.6		

Table A-9: New multipolar superferric correctors for HL-LHC, all operating at 1.9 K.

Number	1	1	1	1	1	1	1	1	1
Number of poles	4	12	12	10	10	8	8	6	6
Normal/skew	Skew	Normal	Skew	Normal	Skew	Normal	Skew	Normal	Skew
Type	MQSXF	MCTXF	MCTSXF	MCDXF	MCDSXF	MCOXF	MCOSXF	MCSXF	MCSSXF
Magnetic length [m]	0.807	0.43	0.089	0.095	0.095	0.087	0.087	0.111	0.111
Integrated field [mT m] at 50 mm	1000	86	17	25	25	46	46	63	63
Coil aperture [mm]	150								
Beam screen shape	Octagon								
Beam screen aperture (H/V) [mm]	115.0/106.0								
Alignment tolerances (R/H/V) [mm]	0.6/1.0/1.0								

The implementation of the ATS scheme in HLLHCv1.0, and following versions, requires hardware changes in other parts of the LHC ring. In particular, an additional sextupole (MS) magnet should be installed in Q10 in IR1 and IR5. Moreover, Q5 in IR6 should be upgraded for operation at 1.9 K.

A.7. Field error target for the new insertion region magnets

In this section the error tables used in the tracking simulations (as described in Chapter 2, Section 2.3.2) for the various classes of new magnets are collected. Whenever the expected values of the multipoles turned out to cause an unacceptable reduction of the DA, the tables also give the requested values (in red) based on the beam dynamics studies. Note that the expected error tables at injection turned out to be already compatible with the criterion based on DA computation.

Table A-10: Expected field quality errors at injection energy for the new IT ($r_0 = 50$ mm). These values represent IT_errortable_v66_5 in Ref. [15].

Skew	Mean	Uncertainty	Random	Normal	Mean	Uncertainty	Random
a ₂	0.000	0.000	0.000	b ₂	0.000	0.000	10.000
a ₃	0.000	0.650	0.650	b ₃	0.000	0.820	0.820
a ₄	0.000	0.650	0.650	b ₄	0.000	0.570	0.570
a ₅	0.000	0.430	0.430	b ₅	0.000	0.420	0.420
a ₆	0.000	0.310	0.310	b ₆	-15.800	1.100	1.100
a ₇	0.000	0.190	0.190	b ₇	0.000	0.190	0.190
a ₈	0.000	0.110	0.110	b ₈	0.000	0.130	0.130
a ₉	0.000	0.080	0.080	b ₉	0.000	0.070	0.070
a ₁₀	0.000	0.040	0.040	b ₁₀	3.630	0.200	0.200
a ₁₁	0.000	0.026	0.026	b ₁₁	0.000	0.026	0.026
a ₁₂	0.000	0.014	0.014	b ₁₂	0.000	0.018	0.018
a ₁₃	0.000	0.010	0.010	b ₁₃	0.000	0.009	0.009
a ₁₄	0.000	0.005	0.005	b ₁₄	-0.600	0.023	0.023
a ₁₅	0.000	0.000	0.000	b ₁₅	0.000	0.000	0.000

Table A-11: Expected (blue) and target (red) field quality errors at top energy for the new IT ($r_0 = 50$ mm). These values represent IT_errortable_v66_5 in Ref. [15].

Skew	Mean	Uncertainty	Random	Normal	Mean	Uncertainty	Random
a ₂	0.000	0.000	0.000	b ₂	0.000	0.000	10.000
a ₃	0.000	0.650	0.650	b ₃	0.000	0.820	0.820
a ₄	0.000	0.650	0.650	b ₄	0.000	0.570	0.570
a ₅	0.000	0.430	0.430	b ₅	0.000	0.420	0.420
a ₆	0.000	0.310	0.310	b ₆	0.400	1.100 0.550	1.100 0.550
a ₇	0.000	0.190 0.152	0.190 0.095	b ₇	0.000	0.190 0.095	0.190 0.095
a ₈	0.000	0.110 0.088	0.110 0.055	b ₈	0.000	0.130 0.065	0.130 0.065
a ₉	0.000	0.080 0.064	0.080 0.040	b ₉	0.000	0.070 0.035	0.070 0.035
a ₁₀	0.000	0.040	0.040 0.032	b ₁₀	-0.390 -0.156	0.200 0.100	0.200 0.100
a ₁₁	0.000	0.026	0.0260 0.0208	b ₁₁	0.000	0.0260 0.0208	0.0260 0.0208
a ₁₂	0.000	0.014	0.014	b ₁₂	0.000	0.0180 0.0144	0.0180 0.0144
a ₁₃	0.000	0.010	0.010	b ₁₃	0.000	0.0090 0.0072	0.0090 0.0072
a ₁₄	0.000	0.005	0.005	b ₁₄	-0.6700 -0.1675	0.0230 0.0115	0.0230 0.0115
a ₁₅	0.000	0.000	0.000	b ₁₅	0.000	0.000	0.000

Table A-12: Expected field quality at injection energy for the new D1 ($r_0 = 50$ mm). These values represent D1_errortable_v1 in Ref. [15].

Skew	Mean	Uncertainty	Random	Normal	Mean	Uncertainty	Random
a ₂	0.000	0.679	0.679	b ₂	0.000	0.200	0.200
a ₃	0.000	0.282	0.282	b ₃	-16.000	0.727	0.727
a ₄	0.000	0.444	0.444	b ₄	0.000	0.126	0.126
a ₅	0.000	0.152	0.152	b ₅	-0.500	0.365	0.365
a ₆	0.000	0.176	0.176	b ₆	0.000	0.060	0.060
a ₇	0.000	0.057	0.057	b ₇	0.900	0.165	0.165
a ₈	0.000	0.061	0.061	b ₈	0.000	0.027	0.027
a ₉	0.000	0.020	0.020	b ₉	-0.660	0.065	0.065
a ₁₀	0.000	0.025	0.025	b ₁₀	0.000	0.008	0.008
a ₁₁	0.000	0.007	0.007	b ₁₁	0.440	0.019	0.019
a ₁₂	0.000	0.008	0.008	b ₁₂	0.000	0.003	0.003
a ₁₃	0.000	0.002	0.002	b ₁₃	0.000	0.006	0.006
a ₁₄	0.000	0.003	0.003	b ₁₄	0.000	0.001	0.001
a ₁₅	0.000	0.001	0.001	b ₁₅	-0.040	0.002	0.002

Table A-13: Expected (blue) and target (red) field quality at top energy for the new D1 ($r_0 = 50$ mm). These values represent D1_errortable_v1 in Ref. [15].

Skew	Mean	Uncertainty	Random	Normal	Mean	Uncertainty	Random
a ₂	0.000	0.679	0.679	b ₂	0.000	0.200	0.200
a ₃	0.000	0.282	0.282	b ₃	-0.900	0.727	0.727
a ₄	0.000	0.444	0.444	b ₄	0.000	0.126	0.126
a ₅	0.000	0.152	0.152	b ₅	0.000	0.365	0.365
a ₆	0.000	0.176	0.176	b ₆	0.000	0.060	0.060
a ₇	0.000	0.057	0.057	b ₇	0.400 0.200	0.165	0.165
a ₈	0.000	0.061	0.061	b ₈	0.000	0.027	0.027
a ₉	0.000	0.020	0.020	b ₉	-0.590 -0.295	0.065	0.065
a ₁₀	0.000	0.025	0.025	b ₁₀	0.000	0.008	0.008
a ₁₁	0.000	0.007	0.007	b ₁₁	0.470	0.019	0.019
a ₁₂	0.000	0.008	0.008	b ₁₂	0.000	0.003	0.003
a ₁₃	0.000	0.002	0.002	b ₁₃	0.000	0.006	0.006
a ₁₄	0.000	0.003	0.003	b ₁₄	0.000	0.001	0.001
a ₁₅	0.000	0.001	0.001	b ₁₅	-0.040	0.002	0.002

Table A-14: Expected field quality at injection energy for the new D2 ($r_0 = 35$ mm). These values represent D2_errortable_v5 in Ref. [15].

Skew	Mean	Uncertainty	Random	Normal	Mean	Uncertainty	Random
a ₂	0.000	0.679	0.679	b ₂	-5.000	0.200	0.200
a ₃	0.000	0.282	0.282	b ₃	-19.000	0.727	0.727
a ₄	0.000	0.444	0.444	b ₄	2.000	0.126	0.126
a ₅	0.000	0.152	0.152	b ₅	3.000	0.365	0.365
a ₆	0.000	0.176	0.176	b ₆	2.000	0.060	0.060
a ₇	0.000	0.057	0.057	b ₇	1.300	0.165	0.165
a ₈	0.000	0.061	0.061	b ₈	1.000	0.027	0.027
a ₉	0.000	0.020	0.020	b ₉	0.520	0.065	0.065
a ₁₀	0.000	0.025	0.025	b ₁₀	0.000	0.008	0.008
a ₁₁	0.000	0.007	0.007	b ₁₁	0.000	0.019	0.019
a ₁₂	0.000	0.008	0.008	b ₁₂	0.000	0.003	0.003
a ₁₃	0.000	0.002	0.002	b ₁₃	0.000	0.006	0.006
a ₁₄	0.000	0.003	0.003	b ₁₄	0.000	0.001	0.001
a ₁₅	0.000	0.001	0.001	b ₁₅	0.000	0.002	0.002

Table A-15: Expected (blue) field quality at top energy for the new D2 ($r_0 = 35$ mm). These values represent D2_errortable_v5 in Ref. [15]. The value of b_2 requires correction to prevent impact on machine performance due to the large beta-beating induced.

Skew	Mean	Uncertainty	Random	Normal	Mean	Uncertainty	Random
a ₂	0.000	0.679	0.679	b ₂	1.000	1.000	1.000
a ₃	0.000	0.282	0.282	b ₃	1.000	1.667	1.667
a ₄	0.000	0.444	0.444	b ₄	-3.000	0.600	0.600
a ₅	0.000	0.152	0.152	b ₅	-1.000	0.500	0.500
a ₆	0.000	0.176	0.176	b ₆	2.000	0.060	0.060
a ₇	0.000	0.057	0.057	b ₇	2.000	0.165	0.165
a ₈	0.000	0.061	0.061	b ₈	1.000	0.027	0.027
a ₉	0.000	0.020	0.020	b ₉	0.500	0.065	0.065
a ₁₀	0.000	0.025	0.025	b ₁₀	0.000	0.008	0.008
a ₁₁	0.000	0.007	0.007	b ₁₁	0.030	0.019	0.019
a ₁₂	0.000	0.008	0.008	b ₁₂	0.000	0.003	0.003
a ₁₃	0.000	0.002	0.002	b ₁₃	0.000	0.006	0.006
a ₁₄	0.000	0.003	0.003	b ₁₄	0.000	0.001	0.001
a ₁₅	0.000	0.001	0.001	b ₁₅	0.000	0.002	0.002

A.8. References

- [1] E. Métral et al., HL-LHC operational scenarios, [CERN-ACC-NOTE-2015-0009](#) (2015).
- [2] O. Brüning and W. Herr, R. Ostojic, A beam separation and collision scheme for IP2 and IP8 at the LHC for optics version 6.1, [LHC Project Report 367](#).(2000)
- [3] S. Fartoukh, LHCb crossing scheme for Run II & III, LHC Machine Committee Meeting n. 167, 19/6/2013. https://espace.cern.ch/lhc-machine-committee/Presentations/1/lmc_167/LHCb%20crossing%20scheme%20for%20Run%20II%20and%20III_S.Fartoukh.pdf
- [4] HL-LHC Parameter and Layout Committee Parameter table v 4.2 (22/9/2015). <https://espace.cern.ch/HiLumi/PLC/layouts/15/WopiFrame.aspx?sourcedoc=%2FHiLumi%2FPLC%2FSiteAssets%2FParameter%20Table%2Exlsx&action=view>
- [5] G. Arduini, O. Brüning, R. De Maria, R. Garoby, S. Gilardoni, B. Goddard, B. Gorini, M. Meddahi, G. Rumolo and R. Tomás, Beam parameters at LHC injection, [CERN-ACC-2014-0006](#) (2014).
- [6] R. Tomás *et al.*, HL-LHC: Exploring alternative ideas, Proc. Review of LHC and Injector Upgrade Plans Workshop (RLIUP), Archamps, France, 29–31 October 2013, Eds. B. Goddard and F. Zimmermann, [CERN–2014–006](#), pp. 119-126.
- [7] H. Damerau *et al.*, LIU: Exploring Alternative Ideas, Proc. Review of LHC and Injector Upgrade Plans Workshop (RLIUP), Archamps, France, 29–31 October 2013, Eds. B. Goddard and F. Zimmermann, [CERN–2014–006](#), pp. 127-137. DOI: [10.5170/CERN-2014-006.127](https://doi.org/10.5170/CERN-2014-006.127)
- [8] The ATLAS and CMS Collaborations, Expected pile-up values at HL-LHC, [ATL-UPGRADE-PUB-2013-014](#), CERN (30 September 2013).
- [9] D. Contardo, private communication, 3 December 2014.
- [10] O.S. Brüning, P. Collier, P. Lebrun, S. Myers, R. Ostojic, J. Poole and P. Proudlock (Eds.), LHC Design Report , v.1: the LHC Main Ring, CERN-2004-003-V-1 (2012) DOI:[10.5170/CERN-2004-003-V-1](https://doi.org/10.5170/CERN-2004-003-V-1)
- [11] J.M. Jowett *et al.*, Future heavy-ion performance of the LHC, Proc. Review of LHC and Injector Upgrade Plans Workshop (RLIUP), Archamps, France, 29–31 October 2013, Eds. B. Goddard and F. Zimmermann, [CERN–2014–006](#), pp. 167-184.
- [12] J. Jowett, Functional Specification HL-LHC Heavy-Ion Beam Parameters at LHC Injection, [EDMS 1525065](#)
- [13] V. Baglin, N. Kos, Beam screens for the LHC long straight section, LHC-VSS-ES-0002, [EDMS 334961](#)
- [14] J.-B. Jeanneret, Geometrical tolerances for the qualification of LHC magnets, [LHC Project Report 1007](#) (2006)
- [15] <https://espace.cern.ch/HiLumi/WP2/task3/SitePages/Home.aspx> and [/afs/cern.ch/eng/lhc/optics/HLLHCV1.0/errors/](https://afs.cern.ch/eng/lhc/optics/HLLHCV1.0/errors/)

Circuit Layout and Powering

B. Circuit Layout and Powering

B.1 HL-LHC Circuits Upgrade

During LS2 and LS3, the HL-LHC upgrade will impose many changes to the magnet circuits of the LHC at points 1 and 5. **Error! Reference source not found.** and Figure B-2 show the types for magnets in the LHC and the HL-LHC insertion regions at points 1 and 5 respectively. These magnets will be installed in the machine during LS3. In addition to these changes, during LS2, two main dipole magnets (MB) will be replaced by 11T cryo-assemblies in order to add two extra collimators. The two concerned magnets are MBA-B8L7 and MBB-B8R7. Figure B-3 and Figure B-4 show the circuit upgrade for the 11T cryo-assemblies. The next paragraphs will detail each of the circuits concerned.

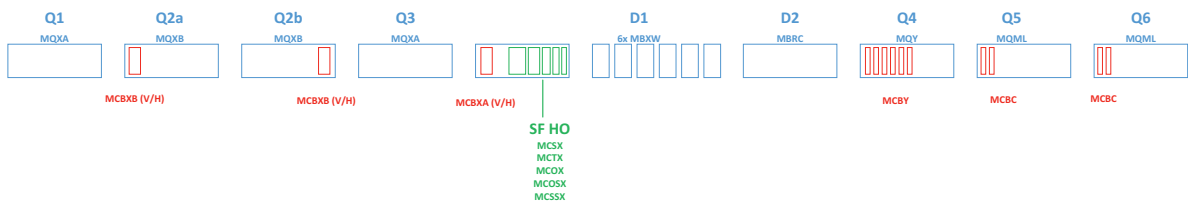


Figure B-1: Magnet representation for the LHC insertion region.

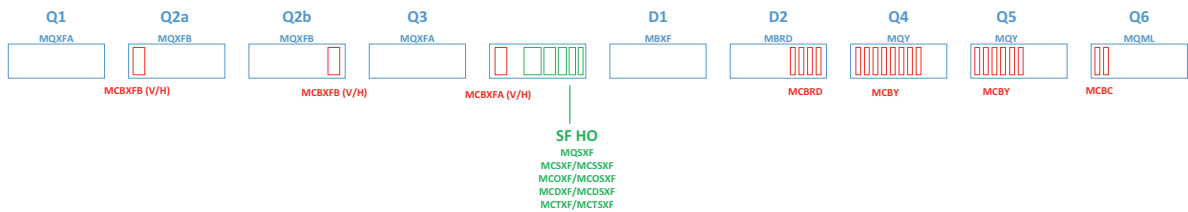


Figure B-2: Magnet representation for the HL-LHC insertion region at point 1 and point 5.

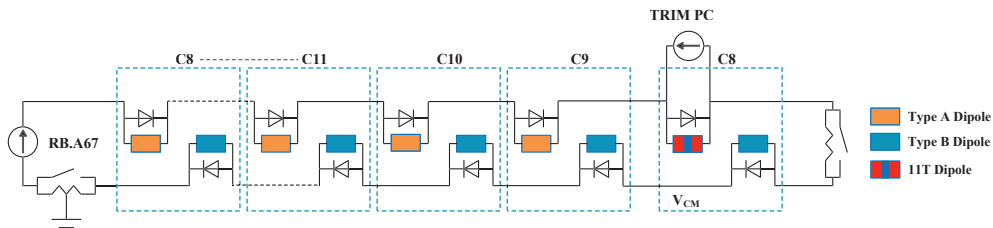


Figure B-3: 11T cryo-assembly replacement of an MB magnet for circuit RB.A67.

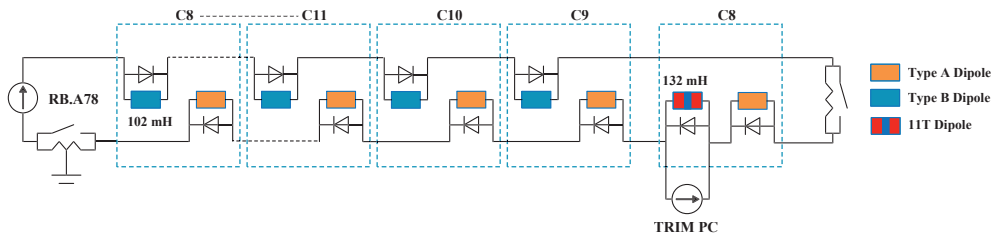


Figure B-4: 11T cryo-assembly replacement of an MB magnet for circuit RB.A78.

B.2 Inner Triplet and Trims

For the HL-LHC, the new MQXFA and MQXFB will replace the MQXA and MQXB magnets as Q1-Q2a/b-Q3 low- β triplet around ATLAS and CMS experiment. In addition, the layout relies on having one main circuit with trim circuits around Q1, Q2a and Q3 as shown on Figure B-5.

- **Power converters:** The main power converter of the Inner Triplet circuit will have a rating of 18 kA. R&D work is being done to develop a new type of 2-quadrant power converter in order to apply positive and negative voltage to the magnets which is mandatory to ramp-down the current in the shadow of the main LHC dipole magnets (refer to paragraph 6B.4.3). Two trim power converters will have a rating of ± 2 kA and the third one will be rated ± 120 A.
- **Quench Protection:** Three technologies are currently investigated to protect the triplet magnet in the case of a quench occurrence: outer layer heaters, inner layer heaters and CLIQ. The outer layers heater technology is well established and validated: it is the primary baseline protection system. As second protection system, useful to reduce the hot spot and necessary to mitigate risk in a multiple fault event, CLIQ and inner quench heaters are both very promising, however their full validation and assessment is still under way. The Quench Protection details are given in paragraph 7.3.
- **DC Cabling and Cold Powering:** Water-cooled cables will be placed between the power converters and the current leads of the DFHX, all placed inside the UR galleries, see Figure 6. The SC Link dedicated for the Inner Triplet will bring the current to the superconducting magnets through the UL galleries. Cable lengths and resistances are shown in Chapter 17.
- **Open Issues:** The main issues to address in the near future are to determine the maximum currents seen by the leads, SC link and bus bars due to the introduction of the CLIQ system, and to complete the study of the soundness of the circuit design in all credible failure scenarios. This study should feed into the choice of the second protection technology. A state-of-the-art study is presented in Chapter 7.

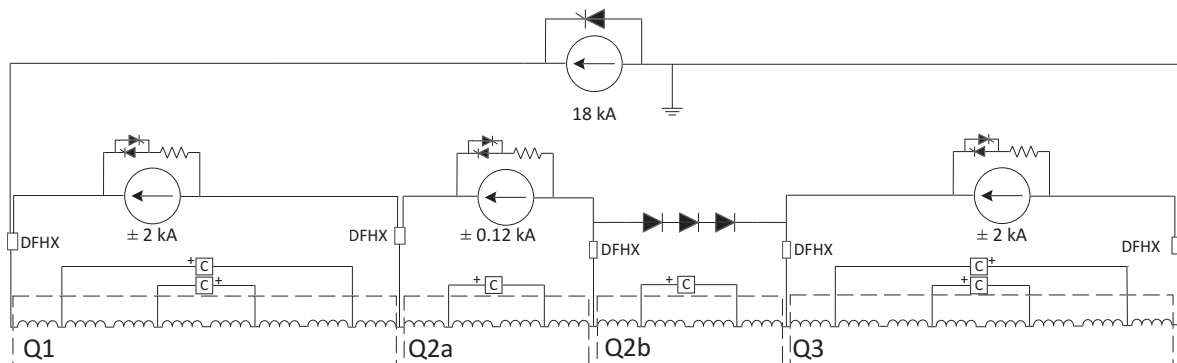


Figure B-5: Circuit layout of the HL-LHC inner triplet.

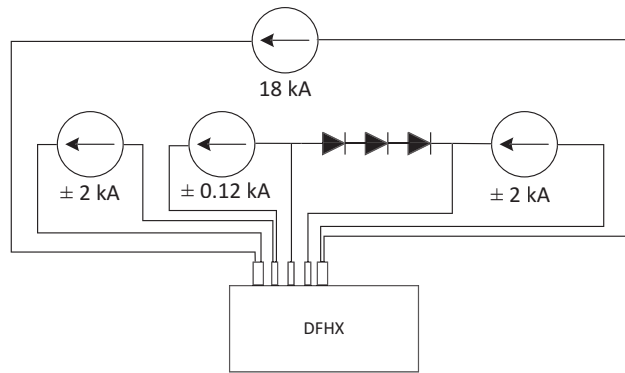


Figure B-6: Connections to cold powering of the inner triplet power converters.

B.3 Triplet Orbit Correctors

For the inner triplet circuit, there will be a total of 6 correctors (1 vertical and 1 horizontal for Q2a, Q2b and Q3 respectively). These new correctors developed for the HL-LHC have a rating of ± 2 kA. The circuit layout of these correctors is shown on Figure B-7.

- **Power converters:** One 4-quadrant power converter per circuit rated at ± 2 kA.
- **Quench Protection:** The baseline for quench protection is quench heaters. Nonetheless, following the recommendation of the International Review of the HL-LHC Circuits ([hyperlink](#)) the use an energy extraction system is being studied. Final decision will be confirmed by end of 2017 when the first tests will be done on the first prototype magnet.
- **DC cabling:** Water-cooled cables will be placed between the power converters and the current leads of the DFHX, all placed inside the UR galleries. The Inner Triplet orbit corrector cables will be placed inside the same SC link feeding the main Inner Triplet circuit. The SC link will bring the current to the superconducting magnets through the UL galleries. Cable lengths and resistances are shown in Chapter 17.
- **Open Issues:** The main issue to address is the quench protection strategy of these corrector magnets (quench heaters versus energy extraction system). The project is oriented in favour of quench heaters for cost and simplicity reasons.

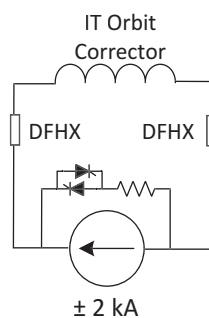


Figure B-7: Circuit layout of each Inner Triplet corrector circuit (MCBXF).

B.4 Inner Triplet high order correctors

Nine high-order correctors (skew quadrupole, normal and skew sextupole, octupole, decapole and dodecapole) are needed for the Inner Triplet magnets. The second order corrector has a rating of ± 200 A whereas all the eight other correctors have a rating of ± 120 A. The circuit layout of these correctors is shown in Figure B-8.

- **Power converters:** 1 power converter per circuit (total of 9 circuits) of rating +/- 200A or +/- 120A will be used.
- **Quench Protection:** The magnets are considered self-protecting. The power converter crowbar resistance (80 mΩ) can help to dissipate the coil's energy in the case of a quench.
- **DC Cabling and Cold Powering:** Copper cables will be placed between the power converters and the current leads of the DFHX, all placed inside the UR galleries. The Triplet high-order corrector conductors will be placed inside the same SC link housing the main Inner Triplet circuit. Cable lengths and resistances are shown in Chapter 17.
- **Open Issues:** No major issues are currently present for these circuits.

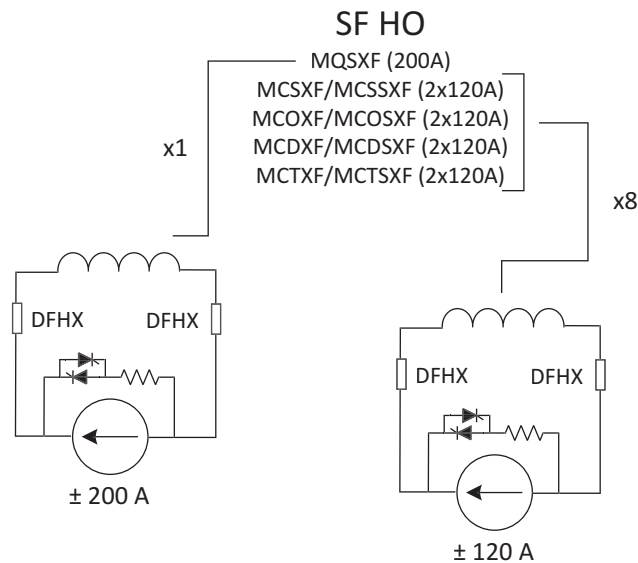


Figure B-8: Superferric, high order correctors' circuit layout.

B.5 Separation Dipole D1

For the HL-LHC, D1 in points 1 and 5 is a cold magnet in contrast with the LHC configuration where D1 is a series of 6 warm magnets (see Figure B-9).

- **Power converters:** One power converter per circuit rated at 13kA. This converter will be 1-quadrant type since no ramp-down issues are foreseen for this circuit. The time constant of the circuit is relatively low, estimated at 93 s.
- **Quench Protection:** The baseline for quench protection is quench heaters.
- **DC Cabling and Cold Powering:** Water-cooled cables will be placed between the power converters and the current leads of the DFHX, all placed inside the UR galleries. The D1 circuit cables will be placed inside the same SC link housing Inner Triplet circuit. Cable lengths and resistances are shown in Chapter 17.
- **Open Issues:** No major issues are currently present for these circuits.

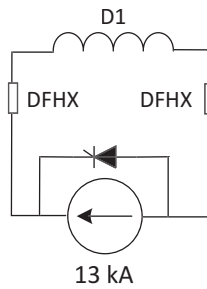


Figure B-9: D1 magnet circuit layout.

B.6 Recombination Dipole D2

The new recombination dipole magnet D2 will be a superconducting magnet with two beam apertures. Each magnet is independently powered, and the two apertures are in series. The circuit layout is shown on Figure B-10.

- **Power converters:** One power converter per circuit rated at 13 kA. This converter will be 1-quadrant type since no ramp-down issues are foreseen for this circuit. The time constant of the circuit is relatively low, estimated at 100 s.
- **Quench Protection:** The baseline for quench protection is quench heaters.
- **DC Cabling and Cold Powering:** Water-cooled cables will be placed between the power converters and the current leads of the DFHM (second electrical feed-box), all placed inside the UR galleries. The D2 circuit will have a dedicated SC Link. Cable lengths and resistances are shown in Chapter 17.
- **Open Issues:** No major issues are currently present for these circuits.

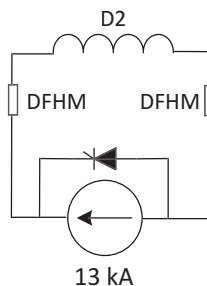


Figure B-10: D2 magnet circuit layout.

B.7 D2 Orbit Correctors

Four orbit correctors are needed for the D2 recombination magnets (one vertical and one horizontal for each aperture). These corrector magnets will have a rating of ± 600 A. The circuit layout of these correctors is shown on Figure B-11.

- **Power converters:** One power converter per circuit rated ± 600 A.
- **Quench Protection:** The magnets are considered self-protecting. The power converter crowbar resistance ($50 \text{ m}\Omega$) can help in the case of a quench.
- **DC Cabling and Cold Powering:** Copper cables will be placed between the power converters and the current leads of the DFHM, all placed inside the UR galleries. The D2 orbit corrector circuits will be included in the D2 dedicated SC Link. Cable lengths and resistances are shown in Chapter 17.

- **Open Issues:** No major issues are currently present for these circuits.

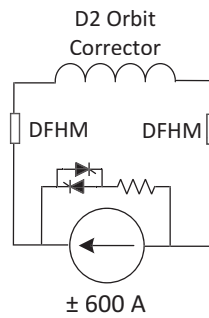


Figure B-11: D2 correctors' circuit layout.

B.8 Individually Powered Quadrupoles Q4, Q5 and Q6

The current Q4 magnet in the LHC will become the Q5 for the HL-LHC. The Q4 magnet in HL-LHC will be of type MQY. However, the Q6 stays the same as in the LHC (MQML). The maximum operation current of the three magnets is 6 kA.

- **Power converters:** 2 power converters magnet will be used as shown on Figure B-12 for Q4, Q5 and Q6. The rating of the power converters is 6kA. The power converters operate in single quadrant. The squeeze time in these circuits can present an issue and will be addressed in the future.
- **Quench Protection:** The protection scheme used for Q4, Q5 and Q6 is quench heaters.
- **DC Cabling and Cold Powering:** The negative polarity DC cables are connected at the current leads of the DFBL. The DSL (low temperature superconducting link as presently in LHC) will be used to connect the DFBL current leads to the magnets.
- **Open Issues:** No major issues are currently present for these circuits.

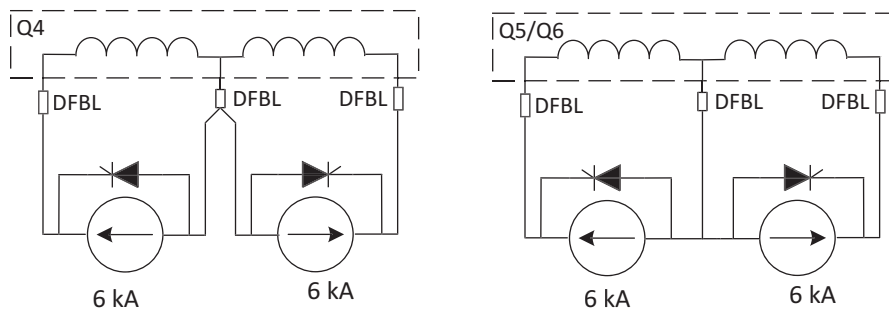


Figure B-12: Q4, Q5 and Q6 circuit layout (no change with respect to the present LHC layout).

B.9 Q4, Q5 and Q6 Orbit Correctors

Sixteen orbit correctors are needed for Q4, Q5 and Q6 magnets (six more than the present scheme). Q4 will have eight corrector circuits, Q5 will have six corrector circuits and Q6 will have two corrector circuits.

- **Power converters:** One power converter per circuit rated at ± 120 A, see Figure B-13.
- **Quench Protection:** The magnets are considered self-protecting. The power converter crowbar resistance (80 m Ω) can help dissipating the energy in the case of a quench.

- **DC Cabling and Cold Powering:** Several solutions are being studied in order to provide cold powering connections for the increasing number of correctors. The solutions proposed are to modify either the DFBL and the DSL, or to provide local powering to the corrector magnets.
- **Open Issues:** The main issue to address is cold powering connections. This issue is under study at present.

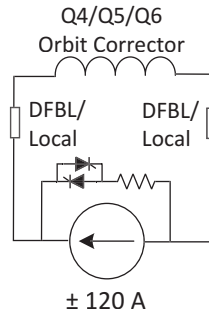


Figure B-13: Circuit layout of each of the 16 corrector circuits for Q4, Q5 and Q6.

B.10 11T

Two main dipole magnets (MB) will be replaced by 11T cryo-assemblies in order to add two extra collimators. The two concerned magnets are MBA-B8L7 and MBB-B8R7 (refer to Figure B-3 and Figure B-4).

- **Power converters:** One power converter per circuit rated at ± 300 A, see Figure B-13.
- **Quench Protection:** The protection scheme used for 11T is quench heaters. The existing RB EE will extract the energy of the RB circuit (11T is in series with the MB magnets in the RB circuit).
- **DC Cabling and Cold Powering:** Copper cables will be placed between the power converters placed in the TZ76 and the local current leads of the 11T (refer to Chapter 11 for details).
- **Open Issues:** The decision to install the leads for a CLIQ system will be made in the future. Some studies and tests will be done on the crowbar resistance value. The tests will start by end of 2016.

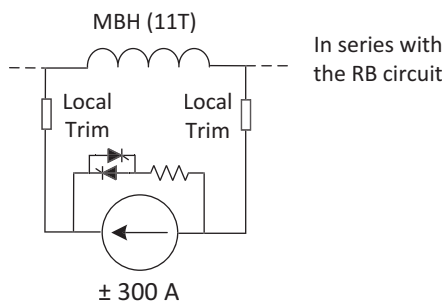


Figure B-14 – Circuit layout of the 11T trim circuit.

C. Voltage Withstand Levels

One of the main aspects for design of superconducting circuits is also the monitoring of the electrical quality of the components during manufacturing, tests and hardware commissioning. All circuit components (magnets, bus bars, link, current leads, instrumentation), including also the warm DC distribution elements, have to be harmonised in this respect. To this aim, the magnet designer has to define already at an early stage the tests and the corresponding voltage levels.

Studies have been conducted through a working group (WG) dealing with aspects related to electrical integrity and quality assurance (the so-called [HL-LHC HVWL Working Group](#)). The main objective of the working group was to find a formal approach in order to obtain high voltage levels from both scaling and safety factors obtained starting from simulated worst case voltages. This formal approach gave either too high voltage values at cold temperature under liquid or superfluid helium, or too low voltage values at room temperature.

The final decision of the WG was to apply the same strategy as the one applied all along the manufacturing, installation and commissioning of LHC magnets, which is as follows: for coil-to-ground voltages, a safety factor of 2 plus 500 V is applied for tests at cold. A factor of 2 is commonly used to scale voltages up to room temperature. For insulation between quench heaters and coil, values are obtained in the same way. The values at cold should be re-confirmed after the first quench at high current.

As an example, the values that are required to be met for the acceptance of a QXF cold mass after manufacturing (at room temperature) and during cold tests are presented in Table C-1.

Table C-1: Test values at warm and cold for a QXF cold mass.

Circuit Element	Expected Vmax [V]	V hi-pot	I hi-pot [μ A]	Minimum time duration [s]
Coil to Ground at RT *	n.a.	3 kV	10	30
Coil to Quench Heater at RT *	n.a.	3 kV	10	30
Coil to Ground at cold **	520	1.5 kV	10	30
Coil to Quench Heater at cold **	900	2.3 kV	10	30

* Room Temperature conditions refer to air at 20 ± 3 °C and relative humidity lower than 60%

** Cold conditions refer to nominal cryogenic conditions

In the particular case of the QXF magnets, and due to limitations given by the geometry, the test voltage between quench heaters and coil are limited to 3 kV at room temperature.

As far as the inter-turn test voltage is concerned, the maximum impulse voltage that can be applied to coils at any intermediate step is 2.5 kV. The expected maximum inter-turn voltage applied is around 70 V. No safety factor is applied to this value. Consequently at least one test at room temperature must be performed after impregnation that proves that the withstand level is correct. The impulse test must include a standard capacitive discharge and proper calibration of the system.

Continuity tests must be applied to guarantee that galvanic separation at low voltage is present between coils and both pole pieces and end shoes.

Acronyms

D. HL-LHC Acronyms

Acronym	Term
a-C	Amorphous carbon
ADT	Transverse damper
AFD	Automatic Fire Detection
ALARA	As low as reasonable achievable
ASIC	Application specific integrated circuit
ATS	Achromatic telescopic squeezing
AUG	Emergency stop buttons
BCAM	Brandeis CCD Angle Monitor
BCMS	Bach compression and beam merging scheme
BCT	Bidirectional Controlled Thyristor
BETS	Beam energy tracking system
BFPP	Bound-free pair production
BGV	Beam gas vertex profile monitor
BIS	Beam interlock system
BLM	LHC beam loss monitoring system
BPM	Beam position monitor
BRAN	TAN luminosity monitor
BS	Beam screen
BSRT	Synchrotron radiation telescope monitor
CALS	CERN accelerator logging system
CC	Crab cavities
CCC	Connection cryostats
CCT	Costheta design
CCB	Cold compressor box
CDD	CERN design directory
CDP	Conductor development programme
CFC	Carbon fibre carbon composites
CLIQ	Coupling loss induced quench
CMOS	Complementary metal-oxide-semiconductor
COTS	Commercial-off-the-shelf
CSAM	CERN Safety Alarm Monitoring system
CTC	Cost to completion
CW	Continuous wave
CVD	Chemical vapour deposition
DA	Dynamic Aperture
DAC	Digital-to-analog converter
DAQ	Data acquisition
DCCT	DC Current Transformer
DF	Distribution feedbox
DFBAM	Distribution feedbox for arc – IR 7/L

DFBAN	Distribution feedbox for arc – IR 7/R
DPA	Displacements-per-atom
DQW	Double quarter wave cavity
DSs	Dispersion suppressors
DVB	Cryogenic distribution valve box
DWR	Extraction resistors
EC	Electron cloud
EE	Energy extraction systems
EIQA	High voltage qualification
EMD	Electromagnetic dissociation
EN	European Norm
EOT	Electric overhead travelling crane
ERA	European Research Area
ESR	Essential Safety Requirements
ESFRI	European Strategy Forum on Research Infrastructure
EUCARD	Enhanced European Coordination for Accelerator Research and Development
EYETS	Extended yearly technical stop
FGC	Function Generator/Controller
FMCM	Fast magnet current change monitors
FNAL	Fermi National Accelerator Laboratory
FPC	Fundamental power coupler
FSI	Frequency Scanning Interferometry
FT	Focusing triplet
GPN	General Purpose Network
GSI	General Safety Instruction
HDR	High dynamic range
HEB	Hollow electron beam
HEP	High Energy Physics
HFM	High-field magnet
HIF	Hazard Identification Form
HL-LHC	High Luminosity Large Hadron Collider
HOM	High-order modes
HTS	High temperature superconductor
HLS	Hydrostatic Levelling Sensor
IBS	Intra-beam scattering
IES	Important safety element
IFS	Instrumentation feed-through system
IOT	Inductive Output Tubes
IP	Interaction point
IR	Interaction region
IT	Inner triplet magnets
LACS	LHC Access Control System
LARP	LHC Accelerator Research Program

LASS	LHC Access Safety System
LBDS	LHC beam dumping system
LCB	Lower cold box
LIU	LHC injector complex upgrade
LLRF	Low level RF
LMBHA/B	Cold mass 11 T
LRBB	Long-range beam-beam
LS[X]	Long shutdown [Id Number]
LSA	Launch Safety Agreement
LSB	Least Significant Bit
LSS	Long Straight Section
LVDT	Linear variable differential transformer
MB	Main LHC dipoles
MBH	11 T dipole
MBU	Multiple bit upsets
MCDO	Magnet corrector decapole/octupole
MCS	Magnet corrector sextupole
MD	Machine development
MFB	Multi-cavity feedback
MIM	Multi-band instability monitor
MIMO	Multiple Input Multiple Output
MKB	Diluter dump kicker
MLI	Multi-Layer Insulation
MKI	Magnet injection kicker
MMD	Multi-purpose Monitoring Device
MP3	Magnet circuits, powering and performance panel
MP	Machine Protection
MPP	Machine protection panel
MPS	Machine protection system
MQY	Insertion region wide aperture quadrupole
MS	Matching section
NEG	Non-evaporable getter
NIEL	Non-ionizing energy losses
NIMS	National Institute of Materials Science
P5	Particle Physics Project Prioritization Panel
PIC	Powering interlock system
PIT	Powder-in-tube process
PLC	Programmable logic controller
PSO	Project Safety Officer
PU	Pile-up
QEN	Bypass cryostat
QPS	Quench protection system
QRL	cryogenic distribution line

QV	Quench buffer
r.m.s.	Root mean square
R2E	Radiation To Electronics
RAMSES	Radiation Monitoring System
RF	Radio frequency
RFD	RF dipole cavity
RHQT	Rapid-heating, quenching transformation
RRP	Restacked rod process
SC	Superconductor
SCL	Superconducting link
SCRF	Superconducting radio frequency
SEE	Single event effects
SEU	Single bit upsets
SEY	Secondary electron yield
SIL	Safety integrity level
SISO	Single Input Single Output
SM	Service module
SPS	Super Proton Synchrotron
SPT	Scheduled proton physics time
SR	Synchrotron radiation
SRF	Superconducting radio frequency
SSAP	Solid State Power Amplifiers
TAXN	Target absorber for insertion region neutrals
TAXS	Target absorber for insertion region secondary
TCAP	Target collimator absorber passive
TCDQ	Collimator for Q4 protection
TCL	Long collimator
TCLA	Target collimator long absorber
TCLD	Auxiliary collimators in DS area
TCP	Primary collimator with BPM
TCSG	Target collimator secondary graphite
TCSMP	Secondary collimator metallic prototype
TCSP	Secondary collimator with pick-up
TCSPM	Secondary collimator with pick-up metallic
TCT	Target collimators tertiary
TCTP	Target collimator tertiary with pick-up
TCTPM	Target collimator tertiary with pick-up metallic
TDE	Target dump for ejected beam
TDI	Beam absorber for injection
TID	Total ionizing dose
TIM	Technical Infrastructure Monitoring system
TMCI	Transverse mode coupling instability
TN	Technical Network

TS[X]	Technical stop [Id number]
UA[X]	Service and access tunnel [point number]
UCB	Upper cold box
UFO	Falling particles
UJ[X]	Service cavern [point number]
UPS	Uninterruptable power supplies
VCT	Vacuum chamber transition
VDWB	Vacuum – dump lines – window
VELO	Vertex locator
WBTN	Wide band time normalizer
WCC	Water Cooled cables
WCS	Warm compressor station
WIC	Warm magnet interlock system
WPS	Wire Positioning Sensors
YETS	Year-end technical stop

Glossary and Definitions

E. Glossary and definitions

Term	Definition
β^*	Optical β -function at the IP.
η	Machine slip factor.
η_D	Normalized dispersion, $\eta D = D/\sqrt{\beta}$, where D is the machine dispersion.
γ	Optic gamma function, $\gamma(s) = (1 + \alpha^2(s))/\beta(s)$ where $\beta(s)$ is the optical betatron function along the machine and $\alpha(s) = -\frac{d\beta}{2 ds}$.
γ_r	The relativistic gamma factor.
Abort gap	Area without any bunches in the bunch train that fits the time required for building up the nominal field of the LHC dump kicker.
Arc	The part of the ring occupied by regular half-cells. Each arc contains 46 half cells. The arc does not contain the dispersion suppressor.
Arc cell	Consists of two arc half-cells and presents the basic period of the optic functions.
Arc half-cell	Periodic part of the LHC arc lattice. Each half-cell consists of a string of three twin aperture main dipole magnets and one short straight section. The cryo magnets of all arc half-cells follow the same orientation with the dipole lead end pointing upstream of Beam 1 (downstream of Beam 2).
Availability	Is the Scheduled proton physics time (SPT) minus the time assigned to faults and fault recovery. It is normally expressed as a percentage of the SPT. Edge effects (e.g. recovery from access, the pre-cycle) should be fully included in the assigned fault time.
Batch	PS batch: train of 72 bunches that is injected into the SPS in one PS to SPS transfer. SPS batch: Train of 4×72 or 3×72 bunches that is injected into the LHC in one SPS to LHC transfer.
Beam 1 and Beam 2	Beam 1 and Beam 2 refer to the two LHC beams. Beam 1 circulates clockwise in Ring 1 and Beam 2 circulates counter clockwise in Ring 2. If colours are used for beams, Beam 1 is marked blue and Beam 2 is marked red.
Beam cleaning	Removal of the large amplitude (larger than 6σ) particles from the beam halo. The LHC has two beam cleaning insertions: one is dedicated to the removal of particles with large transverse oscillation amplitudes (IR7) and one dedicated to the removal of particles with large longitudinal oscillation amplitudes (IR3). These insertions are also referred to as the betatron and momentum cleaning or collimation insertions.
Beam crossing angle	Dedicated orbit bumps separate the two LHC beams at the parasitic beam crossing points of the common beam pipe of Ring 1 and Ring 2. The crossing angle bumps do not separate the beams at the IP, but only at the parasitic crossing points. These orbit bumps generate an angle between the orbit of Beam 1 and Beam 2 at the IP. The full angle between the orbit of Beam 1 and Beam 2 is called the crossing angle. In IR2 and IR8 the crossing angle orbit bumps consist of two separate contributions. One external bump generated for the beam separation at the parasitic beam crossing points and one internal bump generated by the experimental spectrometer and its compensator magnets. The LHC baseline foresees vertical crossing angles in IR1 and IR2 and horizontal crossing angles in IR5 and IR8.

Beam half-life	Time during beam collision after which half the beam intensity is lost.
Beam screen	Perforated tube inserted into the cold bore of the superconducting magnets in order to protect the cold bore from synchrotron radiation and ion bombardment.
Beam types	<p>Pilot beam: consists of a single bunch of 0.5×10^{10} protons. It corresponds to the maximum beam current that can be lost without inducing a magnet quench.</p> <p>Commissioning beam: beam tailored for a maximum luminosity with reduced total beam power (i.e. increased operational margins related to beam losses and magnet quenches) and possibly smaller beam sizes (i.e. increased mechanical acceptance in terms of the transverse beam size and larger tolerances for orbit and β-beat).</p> <p>Intermediate beam: beam tailored for a high accuracy of the beam measurements with reduced total beam power (i.e. increased operational margins related to beam losses and magnet quenches).</p> <p>Nominal beam: beam required to reach the design luminosity of $L = 10^{34} \text{ cm}^{-2} \text{ s}^{-1}$ with $\beta^* = 0.55 \text{ m}$ (\rightarrow normalized emittance $\epsilon_n = 3.75 \text{ } \mu\text{m}$; $N_b = 1.15 \times 10^{11}$; $n_b = 2808$).</p> <p>Ultimate beam: beam consisting of the nominal number of bunches with nominal emittances (normalized emittance of $3.75 \text{ } \mu\text{m}$) and ultimate bunch intensities ($I = 0.86 \text{ A} \rightarrow N_b = 1.7 \times 10^{11}$). Assuming the nominal value of $\beta^* = 0.55 \text{ m}$ and 2808 bunches, the ultimate beam can generate a peak luminosity of $L = 2.3 \times 10^{34} \text{ cm}^{-2} \text{ s}^{-1}$ in the two high luminosity experiments.</p>
BPM	Beam position monitor.
Bunch	Collection of particles captured within one RF bucket.
Bunch duration	<p>The bunch duration is defined as</p> $\sigma_t = \frac{\sigma_s}{v},$ <p>where σ_s is the bunch length and v is the speed of the particles in the storage rings.</p>
Bunch length	The bunch length is defined as the r.m.s. value of the longitudinal particle distribution in one RF bucket. The bunch length is denoted as σ_s .
Busbar	Main cable that carries the current for powering the magnets outside the magnet coil.
Channel	The two apertures of the double bore magnets form two channels through the LHC. Each arc has one outer and one inner channel.
Cold mass	The cold mass refers to the part of a magnet that needs to be cooled by the cryogenic system, i.e. the assembly of magnet coils, collars, iron yoke, and helium vessel.
Crossings	The two machine channels cross at the experimental insertions, i.e. at IP1, IP2, IP5, and IP8.
Cryo-magnet assembly	Complete magnet system integrated into one cryostat, i.e. main magnet coils, collars and cryostat, correction magnets, and powering circuits.
DA	See dynamic aperture
Damper	Transverse or longitudinal feedback system used to damp injection oscillations and/or multi-bunch instabilities of a beam.
Damping time	Time after which an oscillation amplitude has been reduced by a factor $1/e$.

	<p>Longitudinal emittance damping time: Half of the longitudinal amplitude damping time for a Gaussian approximation of the bunch distribution.</p> <p>Transverse emittance damping time: half of the transverse amplitude damping time for a Gaussian approximation of the transverse bunch distribution.</p> <p>If no explicit mentioning of the types of damping times is given the damping times refer to the amplitude damping times.</p>
Decay and snap back	<p>Persistent current decay is a change in the persistent current contribution to the total magnetic field in superconducting magnets powered at constant current (e.g. at injection). This effect varies among magnets and is a function of the powering history (i.e. previous current cycles). When the magnet current is changed (e.g. during the acceleration ramp) the magnetic field comes back to the original value before the decay. This effect is called snap back and occurs for the LHC main dipole magnets within the first 50 A change of the LHC ramp.</p>
Dispersion suppressor	<p>The dispersion suppressor refers to the transition between the LHC arcs and insertions. The dispersion suppressor aims at a reduction of the machine dispersion inside the insertions. Each LHC arc has one dispersion suppressor on each end. The length of the dispersion suppressors is determined by the tunnel geometry. Each LHC dispersion suppressor consists of four individually powered quadrupole magnets that are separated by two dipole magnets. This arrangement of four quadrupole and eight dipole magnets is referred to as two missing dipole cells. For the machine lattice these two missing dipole cells are referred to as one dispersion suppressor. However, reducing the dispersion at the IPs to zero requires a special powering of two more quadrupole magnets on each side of the arc. In terms of the machine optics the dispersion suppressor refers therefore to the two missing dipole cells plus one additional arc cell.</p>
Dogleg magnets	<p>Special dipole magnet used for increasing the separation of the two machine channels from standard arc separation. The dogleg magnets are installed in the cleaning insertions IR3 and IR7 and the RF insertion IR4.</p>
Dynamic aperture	<p>Maximum initial oscillation amplitude that guarantees stable particle motion over a given number of turns. The dynamic aperture is normally expressed in multiples of the RMS beam size (σ) and together with the associated number of turns.</p>
Eddy currents	<p>Eddy currents are screening currents that tend to shield the interior of a conductor or a superconducting cable from external magnetic field changes. In the case of a strand the eddy currents flow along the superconducting filaments in the strand (without loss) and close across the resistive matrix of the strand (copper for the LHC). In the case of a cable the eddy currents flow along the strands (without loss) and close resistively at the contact points among strands in the cable. Eddy currents are also referred to as coupling currents.</p>
Energy spread	<p>The energy spread is defined as the 'RMS' value of the relative energy deviations from the nominal beam energy in a particle distribution. The energy spread is denoted as</p> $\sigma_{\delta E/E0}$
Experimental insertion region	<p>Insertion region that hosts one of the four LHC experiments.</p>
Filament	<p>Superconducting filaments are fine wires of bulk superconducting material with typical dimension in the range of a few microns. The superconducting filaments are embedded in the resistive matrix in a strand.</p>

Hourglass effect H	Luminosity loss due to longitudinal modulation of beta function over the length of the bunch for small β^* .
Insertion region (IR)	Machine region between the dispersion suppressors of two neighboring arcs. The insertion region consists of two matching sections and, in the case of the experimental insertions, of two triplet assemblies and the separation/recombination dipoles.
Interaction point (IP)	Middle of the insertion region (except for IP8). In the insertions where the two LHC beams cross over, the IP indicates the point where the two LHC beams can intersect. In IR8 the experimental detector is shifted by 3/2 RF wavelength and the IP refers to the point where the two LHC beams can intersect and does not coincide with the geometric centre of the insertion.
Ions	The LHC foresees collisions between heavy ions, $^{208}\text{Pb}^{82+}$ (fully stripped) during the first years (208 is the number of nucleons, 82 the number of protons of this particular nucleus).
Ions, nominal scheme	Approximately 600 bunches per beam, with 7×10^7 Pb ions each, are colliding at 2.76 TeV/u to yield an initial luminosity of $L = 1.0 \times 10^{27} \text{ cm}^{-2} \text{ s}^{-1}$ where $\beta^* = 0.5 \text{ m}$.
Ions, early scheme	Approximately 60 bunches per beam, with 7×10^7 Pb ions each, are colliding to yield an initial luminosity of $L = 5.0 \times 10^{25} \text{ cm}^{-2} \text{ s}^{-1}$ with ($\beta^* = 0.5 \text{ m}$).
Lattice correction magnets	Correction magnets that are installed inside the short straight section assembly.
Lattice version	Lattice version refers to a particular hardware installation in the tunnel. It is clearly separated from the optics version and one lattice version can have more than one optics version.
Left, right	See the definition under 'right and left'.
Long-range interactions	Interaction between the two LHC beams in the common part of Ring 1 and Ring 2 where the two beams are separated by the crossing angle orbit bumps.
Long straight section (LSS)	The quasi-straight sections between the upstream and downstream dispersion suppressor of an insertion, including the separation/recombination dipole magnets.
Longitudinal emittance	The longitudinal emittance is defined as: $\epsilon_s = 4\pi\sigma_t\sigma_{\delta E/E_0}E_0,$ where σ_t is the bunch duration in seconds, and $\sigma_{\delta E/E_0}$ the relative energy spread.
Luminosity half-life	Time during beam collision after which the luminosity is halved. The luminosity half-life is generally smaller than the beam half-life.
Luminous region	The 3D distribution of the collision event vertices.
Luminosity reduction	Geometric luminosity reduction factor due to beam offset R: Reduced beam overlap due to transversal offset of collisions, frequently used for reduction of luminosity (levelling) and Van der Meer scans. Luminosity reduction factor due to crossing angle S : reduced beam overlap due to tilted bunch shape due to crossing angle. Total luminosity reduction factor $F = R^*H^*S$ (Strictly speaking here there is no direct multiplication, but provides a reasonable indication of the different contributions, while dominated by the crossing angle contribution).

Machine cycle	The machine cycle refers to one complete operation cycle of a machine, i.e. injection, ramp-up, possible collision flat-top, ejection, and ramp-down. The minimum cycle time refers to the minimum time required for a complete machine cycle.
Machine statistics	<p>Run time: annual time allocated to running with beam [days].</p> <p>Scheduled physics time: annual time allocated to physics (excluding initial beam commissioning, scrubbing, TS, recovery from TS, MDs, special physics) [days].</p> <p>Physics efficiency: time with both beams present and stable beams, versus scheduled physics time [%].</p> <p>Machine availability: time during which the machine is in a state allowing operations to take beam and run through a nominal physics cycle, versus run time [%].</p> <p>Turnaround time: time between the end of one and the start of the next physics run/data taking by the experiments (delimited by the loss of beam presence/beam dump back to declaration of stable beams) [hours].</p> <p>Recovery time: time between the end of one cycle and the readiness for injection of new particles for the next cycle (delimited by the loss of beam presence/beam dump and resumption of the normal operational cycle) [hours].</p>
Magnet quench	Loss of the superconducting state in the coils of a superconducting magnet.
Main lattice magnets	Main magnets of the LHC arcs, i.e. the arc dipole and quadrupole magnets.
Matching section	Arrangement of quadrupole magnets located between the dispersion suppressor and the triplet magnets (or the IP for those insertions without triplet magnets). Each insertion has two matching sections: one upstream and one downstream from the IP.
n_1	The effective mechanical aperture n_1 defines the maximum primary collimator opening in terms of the r.m.s. beam size that still guarantees a protection of the machine aperture against losses from the secondary beam halo. It depends on the magnet aperture and geometry and the local optics perturbations.
N_b	Number of particles per bunch.
n_b	Number of bunches per beam.
Nominal bunch	Bunch parameters required to reach the design luminosity of $L = 1034 \text{ cm}^{-2} \text{ s}^{-1}$ where $\beta^* = 0.55 \text{ m}$. The nominal bunch intensity is $N_b = 1.15 \times 10^{11}$ protons.
Nominal powering	Hardware powering required to reach the design beam energy of 7 TeV.
Normalized transverse emittance	<p>The beam emittance decreases with increasing beam energy during acceleration and a convenient quantity for the operation of a hadron storage rings (and linear accelerators) is the ‘normalized emittance’ defined as</p> $\epsilon_n = \epsilon \gamma_r \beta_r,$ <p>where γ_r and β_r are the relativistic gamma and beta factors</p> $\beta_r = \frac{v}{c}$ $\gamma_r = \frac{1}{\sqrt{1 - \beta_r^2}}$ <p>where v is the particle velocity and c the speed of light in vacuum. The nominal normalized transverse emittance for the LHC is $\epsilon_n = 3.75 \text{ } \mu\text{m}$.</p>

Octant	An octant starts in the center of an arc and goes to the centre of the next downstream arc. An octant consists of an upstream and a downstream half-octant. A half-octant and a half-sector cover the same part of the machine even though they may not have the same number.
Optical configuration	An optical configuration refers to a particular powering of the LHC magnets. Each optics version has several optical configurations corresponding to the different operational modes of the LHC. For example, each optics version has a different optical configuration for injection and luminosity operation, and for luminosity operation the optics features different optical configurations corresponding to different β^* values in the four experimental insertions of the LHC.
Optics version	The optics version refers to a consistent set of optical configurations. There can be several different optics versions for one lattice version.
Pacman bunches	Bunches that do not experience the same number of long-range beam–beam interactions left and right from the IP.
Parallel separation	Dedicated orbit bumps separate the two LHC beams at the IP during injection, ramp, and the optics squeeze. The total beam separation at the IP is called the parallel separation. The LHC baseline foresees horizontal parallel separations in IR1 and IR2 and vertical separations in IR5 and IR8.
Parasitic crossing points	Positions in the common part of the Ring 1 and Ring 2 where the two beams can experience long-range interactions.
Persistent currents	Persistent currents are eddy currents with (ideally) infinitely long time constants that flow in the bulk of the superconducting filaments of a strand and tend to shield the interior of the filament from the external magnetic field changes. These screening currents close inside the superconducting filament, with zero resistance (in steady state). Hence, for practical purposes, they do not decay in time and for this reason they are referred to as ‘persistent’.
Physics efficiency	Is the fraction of the Scheduled proton physics time (SPT) spent in Stable Beams
Physics run	Machine operation at top energy with luminosity optics configuration and beam collisions.
Pile-up	<p>Event pile-up μ: number of visible inelastic proton–proton interactions in a given bunch crossing.</p> <p>Average pile-up: mean value of the pile-up over a fill (averaged over all bunchcrossings).</p> <p>Peak pile-up: maximum pile-up in any bunch crossing at any time (usually at the start of the fill).</p> <p>Peak average pile-up: mean pile-up at the beginning of the fill. It corresponds to the peak luminosity of the fill. In practice, it is determined as the maximum of the pile-up values obtained by averaging over all bunch crossings within time intervals of typically one minute.</p> <p>Average pile-up density: number of inelastic proton–proton interactions in a given bunch-crossing divided by the size of the luminous region in Z.</p>
Pilot bunch	Bunch intensity that assures no magnet quench at injection energy for an abrupt loss of a single bunch but is still large enough provide BPM readings. The pilot bunch intensity of the LHC corresponds to 0.5×10^{10} protons in one bunch.
Piwinski parameter	Parameterization of reduced beam overlap due to finite crossing angle.

Ramp	Change of the magnet current. During the beam acceleration the magnets are ‘ramped up’ and after the end of a physics store the magnets are ‘ramped down’.
Resistive matrix	One of the two main constituents of the strand. The resistive matrix embeds the filaments in the strand and provides a low resistance current shunt in case of quench (transition of superconducting material to the normal state).
RF bucket	The RF system provide a longitudinal focusing that constrains particle motion in the longitudinal phase space to a confined region called the RF bucket.
Right, left	Describes the position in the tunnel relative to an observer inside the ring looking out (same definition as for LEP).
Ring 1 and Ring 2	There are two rings in the LHC, one ring per beam. Ring 1 corresponds to Beam 1, which circulates clockwise, and Ring 2 corresponds to Beam 2, which circulates counter-clockwise in the LHC.
Satellite bunch	Collection of particles inside RF buckets that do not correspond to nominal bunch positions. The nominal bunch spacing for the LHC is 25 ns, while the separation of RF buckets is 2.5 ns. In other words, there are nine RF buckets between two nominal LHC bunch positions that should be empty.
Scheduled proton physics time	Is the time scheduled in a given year for high luminosity proton physics. It does not include initial re-commissioning, special physics runs, ions, machine development (MD), and technical stops. It does include the intensity ramp-up following re-commissioning at the start of the year
Sector	The part of a ring between two successive insertion points (IP) is called a sector. Sector 1-2 is situated between IP1 and IP2.
Separation/recombination magnets	Special dipole magnets left and right from the triplet magnets that generate the beam crossings in the experimental insertions.
Short straight section (SSS)	Assembly of the arc quadrupole and the lattice corrector magnets. Each SSS consists of one quadrupole magnet, one beam position monitor (BPM), one orbit corrector dipole (horizontal deflection for focusing and vertical deflection for defocusing quadrupoles), one lattice correction element (i.e. trim or skew quadrupole elements or octupole magnets). and one lattice sextupole or skew sextupole magnet.
Special straight section (SPSS)	Quadrupole assemblies of the insertion regions. The SPSS features no lattice corrector and sextupole magnets and has only orbit correction dipole magnets and BPMs.
Spool piece correction magnets	Correction magnets directly attached to the main dipole magnets. The spool piece correction magnets are included in the dipole cryostat assembly
Strand	A superconducting strand is a composite wire containing several thousands of superconducting filaments dispersed in a matrix with suitably small electrical resistivity properties. The LHC strands have Nb-Ti as their superconducting material and copper as the resistive matrix.
Superconducting cable	Superconducting cables are formed from several superconducting strands in parallel, geometrically arranged in the cabling process to achieve well-controlled cable geometry and dimensions, while limiting strand deformation in the process. Cabling several strands in parallel results in an increase of the current carrying capability and a decrease of the inductance of the magnet, easing protection. The LHC cables are flat, keystone cables of the so-called Rutherford type.

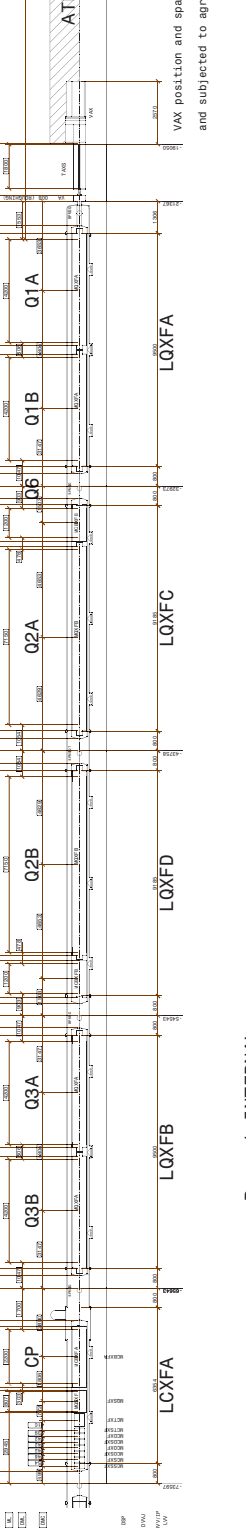
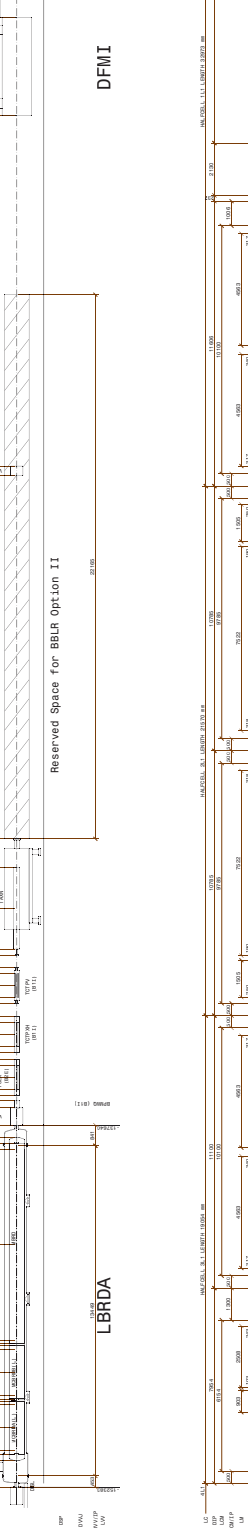
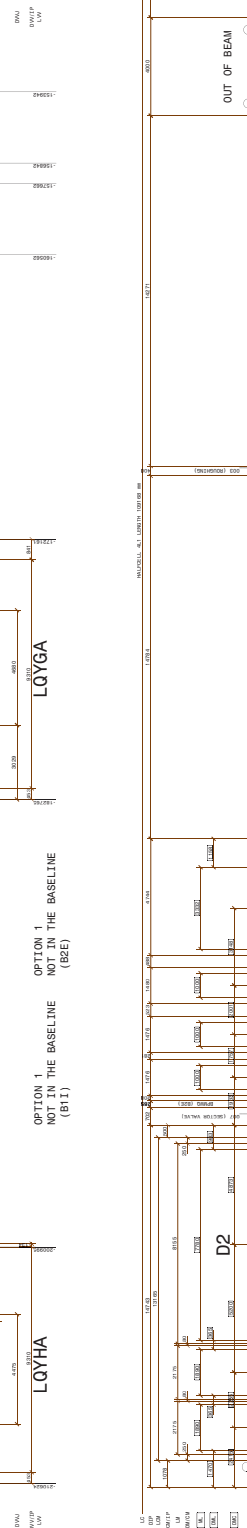
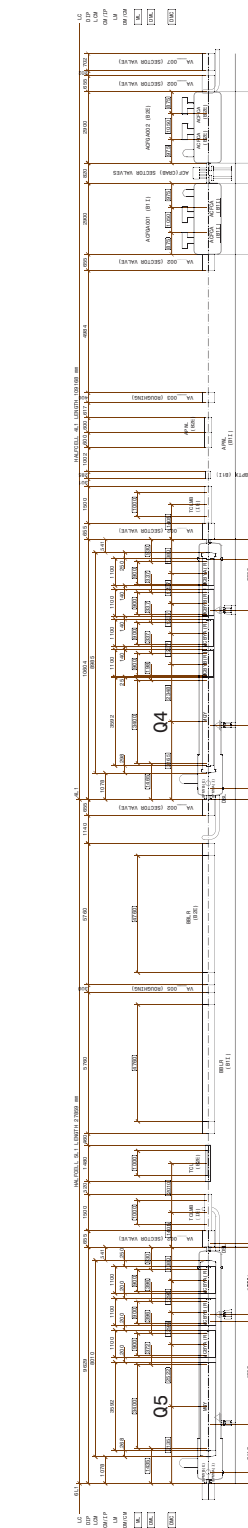
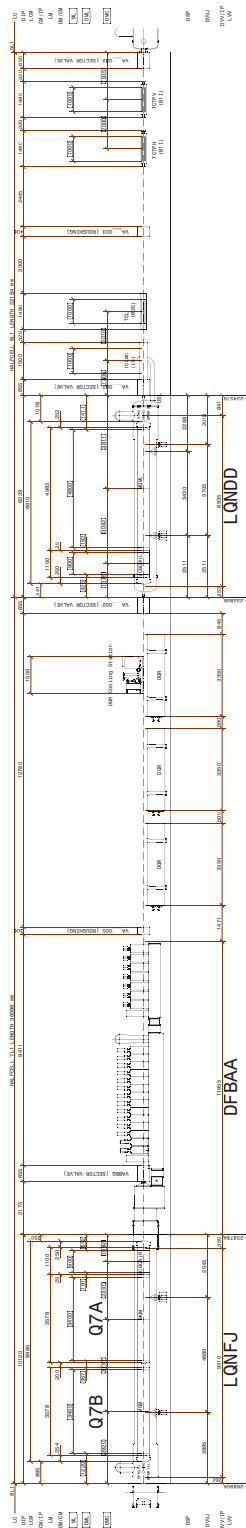
Super pacman bunches	Bunches that do not collide head-on with a bunch of the other beam in one of experimental IPs.
Synchrotron radiation damping times	<p>Longitudinal amplitude damping time: the ratio of the average rate of energy loss (energy lost over one turn divided by the revolution time) and the nominal particle energy.</p> <p>Transverse amplitude damping time: time after which the transverse oscillation amplitude has been reduced by a factor $1/e$ due to the emission of synchrotron radiation. For a proton beam it is just twice the longitudinal amplitude damping time due to the emission of synchrotron radiation.</p> <p>If no explicit mentioning of the types of damping times is given the damping times refer to the amplitude damping times.</p>
TAN	Target absorber neutral: absorber for the neutral particles leaving the IP. It is located just in front of the D1 separation/recombination dipole magnet on the side facing the IP.
TAS	Target absorber secondaries: absorber for particles leaving the IP at large angles. It is located just in front of the Q1 triplet quadrupole magnet on the side facing the IP.
Transverse beam size	The transverse beam size is defined as the r.m.s. value of the transverse particle distribution.
Transverse emittance	<p>The transverse emittance is defined through the invariance of the area enclosed by the single particle phase space ellipse. The single particle invariant under the transformation through the storage ring is given by</p> $A = \gamma x^2 + 2\alpha x x' + \beta x'^2,$ <p>where α, β, and γ are the optical functions. The area enclosed by the single particle phase space ellipse is given by</p> $\text{area of ellipse} = \pi A$ <p>For an ensemble of particles the emittance is defined as the average of all single particle invariants (areas enclosed by the single particle phase space ellipsoids divided by π).</p> <p>The transverse betatron beam size in the storage ring can be written in terms of the beam emittance as</p> $\sigma_{x,y}(s) = \sqrt{\beta_{x,y}(s)\epsilon_{x,y}},$ <p>where $\beta_{x,y}(s)$ is the optical β-function along the storage ring.</p> <p>The transverse emittance is given by the following expression:</p> $\epsilon_z = \sqrt{\langle z^2 \rangle \langle z'^2 \rangle - \langle z z' \rangle^2}; z = x, y,$ <p>where it is assumed that the particle coordinates are taken at a place with vanishing dispersion and where $\langle \rangle$ defines the average value of the coordinates over the distribution. z and z' are the canonical transverse coordinates ($z = x, y$).</p>
Triplet	Assembly of three quadrupole magnets used for a reduction of the optical β -functions at the IPs. The LHC triplet assembly consists in fact of four quadrupole magnets but the central two quadrupole magnets form one functional entity. The LHC has triplet assemblies in IR1, IR2, IR5, and IR8.
Tune	Number of particle trajectory oscillations during one revolution in the storage ring (transverse and longitudinal).

Turnaround time	Is defined as the time taken to go from Stable Beam mode back to Stable Beam mode in the absence of significant interruptions due to fault diagnosis and resolution
Ultimate bunch intensity	Bunch intensity corresponding to the expected maximum acceptable beam–beam tune shift with two operating experimental insertions. Assuming the nominal emittance (normalized emittance of 3.75 μm) the ultimate bunch intensity corresponds to 1.7×10^{11} protons per bunch.
Ultimate powering	Hardware powering required to reach the ultimate beam energy of 7.54 TeV, corresponding to a dipole field of 9 T.
Upstream and downstream	Always related to the direction of one of the two beams. If no beam is specified then Beam 1 is taken as the default. This implies that stating a position as being ‘upstream’ without indicating any beam is equivalent to stating that the position is to the left.

Slope 1.23% Tilt 0.66%

DISPLACEMENTS FROM WARM TO COLD ARE NOT YET COUNTED IN THE FINAL DIMENSIONS AT OPERATIONAL CONDITIONS

BRM6	-208.429 R/1P	AGWAD005 (S)	AGWAD005 (S)	AGWAD005 (S)	-154.817 R/1P
BRM7	-208.429 R/1P	BRM7A	BRM7B (S)	BRM7B (S)	-149.905 R/1P
BRM8	-208.429 R/1P	BRM8A	BRM8B (S)	BRM8B (S)	-147.713 R/1P
BRM9	-208.429 R/1P	BRM9A	BRM9B (S)	BRM9B (S)	-150.206 R/1P
BRM10	-208.429 R/1P	BRM10A	BRM10B (S)	BRM10B (S)	-150.206 R/1P
BRM11	-208.429 R/1P	BRM11A	BRM11B (S)	BRM11B (S)	-150.206 R/1P
BRM12	-208.429 R/1P	BRM12A	BRM12B (S)	BRM12B (S)	-150.206 R/1P
BRM13	-208.429 R/1P	BRM13A	BRM13B (S)	BRM13B (S)	-150.206 R/1P
BRM14	-208.429 R/1P	BRM14A	BRM14B (S)	BRM14B (S)	-150.206 R/1P
BRM15	-208.429 R/1P	BRM15A	BRM15B (S)	BRM15B (S)	-150.206 R/1P
BRM16	-208.429 R/1P	BRM16A	BRM16B (S)	BRM16B (S)	-150.206 R/1P
BRM17	-208.429 R/1P	BRM17A	BRM17B (S)	BRM17B (S)	-150.206 R/1P
BRM18	-208.429 R/1P	BRM18A	BRM18B (S)	BRM18B (S)	-150.206 R/1P
BRM19	-208.429 R/1P	BRM19A	BRM19B (S)	BRM19B (S)	-150.206 R/1P
BRM20	-208.429 R/1P	BRM20A	BRM20B (S)	BRM20B (S)	-150.206 R/1P
BRM21	-208.429 R/1P	BRM21A	BRM21B (S)	BRM21B (S)	-150.206 R/1P
BRM22	-208.429 R/1P	BRM22A	BRM22B (S)	BRM22B (S)	-150.206 R/1P
BRM23	-208.429 R/1P	BRM23A	BRM23B (S)	BRM23B (S)	-150.206 R/1P
BRM24	-208.429 R/1P	BRM24A	BRM24B (S)	BRM24B (S)	-150.206 R/1P
BRM25	-208.429 R/1P	BRM25A	BRM25B (S)	BRM25B (S)	-150.206 R/1P
BRM26	-208.429 R/1P	BRM26A	BRM26B (S)	BRM26B (S)	-150.206 R/1P
BRM27	-208.429 R/1P	BRM27A	BRM27B (S)	BRM27B (S)	-150.206 R/1P
BRM28	-208.429 R/1P	BRM28A	BRM28B (S)	BRM28B (S)	-150.206 R/1P
BRM29	-208.429 R/1P	BRM29A	BRM29B (S)	BRM29B (S)	-150.206 R/1P
BRM30	-208.429 R/1P	BRM30A	BRM30B (S)	BRM30B (S)	-150.206 R/1P
BRM31	-208.429 R/1P	BRM31A	BRM31B (S)	BRM31B (S)	-150.206 R/1P
BRM32	-208.429 R/1P	BRM32A	BRM32B (S)	BRM32B (S)	-150.206 R/1P
BRM33	-208.429 R/1P	BRM33A	BRM33B (S)	BRM33B (S)	-150.206 R/1P
BRM34	-208.429 R/1P	BRM34A	BRM34B (S)	BRM34B (S)	-150.206 R/1P
BRM35	-208.429 R/1P	BRM35A	BRM35B (S)	BRM35B (S)	-150.206 R/1P
BRM36	-208.429 R/1P	BRM36A	BRM36B (S)	BRM36B (S)	-150.206 R/1P
BRM37	-208.429 R/1P	BRM37A	BRM37B (S)	BRM37B (S)	-150.206 R/1P
BRM38	-208.429 R/1P	BRM38A	BRM38B (S)	BRM38B (S)	-150.206 R/1P
BRM39	-208.429 R/1P	BRM39A	BRM39B (S)	BRM39B (S)	-150.206 R/1P
BRM40	-208.429 R/1P	BRM40A	BRM40B (S)	BRM40B (S)	-150.206 R/1P
BRM41	-208.429 R/1P	BRM41A	BRM41B (S)	BRM41B (S)	-150.206 R/1P
BRM42	-208.429 R/1P	BRM42A	BRM42B (S)	BRM42B (S)	-150.206 R/1P
BRM43	-208.429 R/1P	BRM43A	BRM43B (S)	BRM43B (S)	-150.206 R/1P
BRM44	-208.429 R/1P	BRM44A	BRM44B (S)	BRM44B (S)	-150.206 R/1P
BRM45	-208.429 R/1P	BRM45A	BRM45B (S)	BRM45B (S)	-150.206 R/1P
BRM46	-208.429 R/1P	BRM46A	BRM46B (S)	BRM46B (S)	-150.206 R/1P
BRM47	-208.429 R/1P	BRM47A	BRM47B (S)	BRM47B (S)	-150.206 R/1P
BRM48	-208.429 R/1P	BRM48A	BRM48B (S)	BRM48B (S)	-150.206 R/1P
BRM49	-208.429 R/1P	BRM49A	BRM49B (S)	BRM49B (S)	-150.206 R/1P
BRM50	-208.429 R/1P	BRM50A	BRM50B (S)	BRM50B (S)	-150.206 R/1P
BRM51	-208.429 R/1P	BRM51A	BRM51B (S)	BRM51B (S)	-150.206 R/1P
BRM52	-208.429 R/1P	BRM52A	BRM52B (S)	BRM52B (S)	-150.206 R/1P
BRM53	-208.429 R/1P	BRM53A	BRM53B (S)	BRM53B (S)	-150.206 R/1P
BRM54	-208.429 R/1P	BRM54A	BRM54B (S)	BRM54B (S)	-150.206 R/1P
BRM55	-208.429 R/1P	BRM55A	BRM55B (S)	BRM55B (S)	-150.206 R/1P
BRM56	-208.429 R/1P	BRM56A	BRM56B (S)	BRM56B (S)	-150.206 R/1P
BRM57	-208.429 R/1P	BRM57A	BRM57B (S)	BRM57B (S)	-150.206 R/1P
BRM58	-208.429 R/1P	BRM58A	BRM58B (S)	BRM58B (S)	-150.206 R/1P
BRM59	-208.429 R/1P	BRM59A	BRM59B (S)	BRM59B (S)	-150.206 R/1P
BRM60	-208.429 R/1P	BRM60A	BRM60B (S)	BRM60B (S)	-150.206 R/1P
BRM61	-208.429 R/1P	BRM61A	BRM61B (S)	BRM61B (S)	-150.206 R/1P
BRM62	-208.429 R/1P	BRM62A	BRM62B (S)	BRM62B (S)	-150.206 R/1P
BRM63	-208.429 R/1P	BRM63A	BRM63B (S)	BRM63B (S)	-150.206 R/1P
BRM64	-208.429 R/1P	BRM64A	BRM64B (S)	BRM64B (S)	-150.206 R/1P
BRM65	-208.429 R/1P	BRM65A	BRM65B (S)	BRM65B (S)	-150.206 R/1P
BRM66	-208.429 R/1P	BRM66A	BRM66B (S)	BRM66B (S)	-150.206 R/1P
BRM67	-208.429 R/1P	BRM67A	BRM67B (S)	BRM67B (S)	-150.206 R/1P
BRM68	-208.429 R/1P	BRM68A	BRM68B (S)	BRM68B (S)	-150.206 R/1P
BRM69	-208.429 R/1P	BRM69A	BRM69B (S)	BRM69B (S)	-150.206 R/1P
BRM70	-208.429 R/1P	BRM70A	BRM70B (S)	BRM70B (S)	-150.206 R/1P
BRM71	-208.429 R/1P	BRM71A	BRM71B (S)	BRM71B (S)	-150.206 R/1P
BRM72	-208.429 R/1P	BRM72A	BRM72B (S)	BRM72B (S)	-150.206 R/1P
BRM73	-208.429 R/1P	BRM73A	BRM73B (S)	BRM73B (S)	-150.206 R/1P
BRM74	-208.429 R/1P	BRM74A	BRM74B (S)	BRM74B (S)	-150.206 R/1P
BRM75	-208.429 R/1P	BRM75A	BRM75B (S)	BRM75B (S)	-150.206 R/1P
BRM76	-208.429 R/1P	BRM76A	BRM76B (S)	BRM76B (S)	-150.206 R/1P
BRM77	-208.429 R/1P	BRM77A	BRM77B (S)	BRM77B (S)	-150.206 R/1P
BRM78	-208.429 R/1P	BRM78A	BRM78B (S)	BRM78B (S)	-150.206 R/1P
BRM79	-208.429 R/1P	BRM79A	BRM79B (S)	BRM79B (S)	-150.206 R/1P
BRM80	-208.429 R/1P	BRM80A	BRM80B (S)	BRM80B (S)	-150.206 R/1P
BRM81	-208.429 R/1P	BRM81A	BRM81B (S)	BRM81B (S)	-150.206 R/1P
BRM82	-208.429 R/1P	BRM82A	BRM82B (S)	BRM82B (S)	-150.206 R/1P
BRM83	-208.429 R/1P	BRM83A	BRM83B (S)	BRM83B (S)	-150.206 R/1P
BRM84	-208.429 R/1P	BRM84A	BRM84B (S)	BRM84B (S)	-150.206 R/1P
BRM85	-208.429 R/1P	BRM85A	BRM85B (S)	BRM85B (S)	-150.206 R/1P
BRM86	-208.429 R/1P	BRM86A	BRM86B (S)	BRM86B (S)	-150.206 R/1P
BRM87	-208.429 R/1P	BRM87A	BRM87B (S)	BRM87B (S)	-150.206 R/1P
BRM88	-208.429 R/1P	BRM88A	BRM88B (S)	BRM88B (S)	-150.206 R/1P
BRM89	-208.429 R/1P	BRM89A	BRM89B (S)	BRM89B (S)	-150.206 R/1P
BRM90	-208.429 R/1P	BRM90A	BRM90B (S)	BRM90B (S)	-150.206 R/1P
BRM91	-208.429 R/1P	BRM91A	BRM91B (S)	BRM91B (S)	-150.206 R/1P
BRM92	-208.429 R/1P	BRM92A	BRM92B (S)	BRM92B (S)	-150.206 R/1P
BRM93	-208.429 R/1P	BRM93A	BRM93B (S)	BRM93B (S)	-150.206 R/1P
BRM94	-208.429 R/1P	BRM94A	BRM94B (S)	BRM94B (S)	-150.206 R/1P
BRM95	-208.429 R/1P	BRM95A	BRM95B (S)	BRM95B (S)	-150.206 R/1P
BRM96	-208.429 R/1P	BRM96A	BRM96B (S)	BRM96B (S)	-150.206 R/1P
BRM97	-208.429 R/1P	BRM97A	BRM97B (S)	BRM97B (S)	-150.206 R/1P
BRM98	-208.429 R/1P	BRM98A	BRM98B (S)	BRM98B (S)	-150.206 R/1P
BRM99	-208.429 R/1P	BRM99A	BRM99B (S)	BRM99B (S)	-150.206 R/1P
BRM100	-208.429 R/1P	BRM100A	BRM100B (S)	BRM100B (S)	-150.206 R/1P



Beam 1 INTERNAL
Beam 2 EXTERNAL

OPTICS VERSION 1.3

REV	DATE	DESCRIPTION
01	01/01/2011	ISSUE FOR CONSTRUCTION
02	01/01/2011	ISSUE FOR CONSTRUCTION
03	01/01/2011	ISSUE FOR CONSTRUCTION
04	01/01/2011	ISSUE FOR CONSTRUCTION
05	01/01/2011	ISSUE FOR CONSTRUCTION
06	01/01/2011	ISSUE FOR CONSTRUCTION
07	01/01/2011	ISSUE FOR CONSTRUCTION
08	01/01/2011	ISSUE FOR CONSTRUCTION
09	01/01/2011	ISSUE FOR CONSTRUCTION
10	01/01/2011	ISSUE FOR CONSTRUCTION
11	01/01/2011	ISSUE FOR CONSTRUCTION
12	01/01/2011	ISSUE FOR CONSTRUCTION
13	01/01/2011	ISSUE FOR CONSTRUCTION
14	01/01/2011	ISSUE FOR CONSTRUCTION
15	01/01/2011	ISSUE FOR CONSTRUCTION
16	01/01/2011	ISSUE FOR CONSTRUCTION
17	01/01/2011	ISSUE FOR CONSTRUCTION
18	01/01/2011	ISSUE FOR CONSTRUCTION
19	01/01/2011	ISSUE FOR CONSTRUCTION
20	01/01/2011	ISSUE FOR CONSTRUCTION
21	01/01/2011	ISSUE FOR CONSTRUCTION
22	01/01/2011	ISSUE FOR CONSTRUCTION
23	01/01/2011	ISSUE FOR CONSTRUCTION

Index

1

11 T dipole, 283
cold mass, 285
crowbar resistance, 302
cryo heater, 291
cutback, 288
full assembly, 283
installation, 357
instrumentation feed-through system, 291
main parameters, 285
Manufacturing and Inspection Plans, 308
RF-shielded gate valves, 285
trim power converter, 289

A

absorber
TAXS, 237
TCDQ, 350
TCDS, 350
TDE, 349
accuracy Class, 206
Achromatic Telescopic Squeeze, 35
ALARA, 181, 449
alignment, 365
all-digital approach, 204
apodization, 337
Automatic Fire Detection, 432
availability, 375

B

Bardeen-Cooper-Schrieffer resistance, 125
beam
brightness, 9, 27
current, 9
dumping system, 214, 343
energy tracking system, 344
interlock system, 214, 217
loss monitoring, 327
position monitor, 330
size, 117
beam screen, 314, 318
a-C coated, 324
non-shielded, 323
shielded, 320

bound-free pair production, 162
Brandeis CCD Angle Monitor, 133
building
compressor, 397
cooling towers, 397
electrical, 397
head shaft, 396
ventilation, 396
burn-off, 25
bypass cryostat, 283

C

camera
dynamic range, 337
high dynamic range, 337
CARE, 14
cavern
US, 394
UW, 394
cavity
compact, 119
crab, 117
cryomodule, 130
detuning, 125
Double Quarter Wave, 119
full detuning, 137
helium tank, 126
higher order modes, 123
installation, 363
magnetic shield, 131
multipacting, 125
parking, 122
power coupler, 121
quadrature, 120
RF Dipole, 119
tuning, 128
CEA, 20, 110
CERN Safety Alarm Monitoring system, 433
chamber
fast ionization, 338
CIEMAT, 20, 102
cleaning system
betatron, 150
momentum, 150
CLIQ system, 100, 219
coating

- Amorphous carbon (a-C), 319
- cold box, 258, 259
 - installation, 361
- Cold Powering System, 182
- collimation
 - role, 153
- collimator
 - TCAP, 175
 - TCLA, 174
 - TCTP, 176
- commissioning, 378
- connection cryostat, 283, 305
 - full assembly, 306
- continuous wave, 129
- control
 - open loop, 377
 - system, 445
- cores, 395
- corrector
 - D2, 109
- Cost-to-Completion, 14
- Coupling-Loss Induced Quench, 224
- crabbing off, 122
- crane, 436
- cryogenic plant, 257
 - installation, 359
- Crystal collimation, 172
- CSAM, 429
- Current leads, 182
- cycle
 - issues, 374
- cycle
 - adjust, 374
 - injection, 374
 - nominal operational, 373
 - pre-cycle, 373
 - ramp, 374
 - set-up, 374
 - squeeze, 374
 - stable beams, 374

D

- debris, 272
- de-installation, 358
- detector
 - compensated diode, 331
 - CVD diamond, 328
 - liquid helium ionization chambers, 328
 - silicon, 328
- DF, 182
- DFH, 182

- dipole
 - recombination, D2, 107
 - separation, D1, 106
- dose
 - ambient equivalent, 450
 - effective, 450
 - limits personel, 449
 - peak, 266
 - residual, 450
 - total ionizing, 330
- dose limits
 - personel, 449
- double decker, 360
- DPA, 266
- DPMJET-III, 264, 450
- DS magnet
 - quench limit, 159
- DSH, 182
- dump
 - asynchronous beam, 350
- dynamic aperture, 44, 45

E

- EIQA, 378
- energy deposition
 - matching section, 271
- Energy extraction system, 225
- Essential Safety Requirements, 459
- European Norm, 459
- European Research Area, 1

F

- failures
 - fast, 214
 - slow, 214
 - ultra-fast, 214
- fast magnet current change monitors, 217
- fast wire-scanners
 - installation, 357
- fault, 376
- FGClite, 209
- FLUKA, 156, 264, 449
- FNAL, 283
- free-wheeling process, 194, 200
- Frequency Scanning Interferometry, 133, 367
- Function Generator/Controller, 204
- fundamental power coupler, 133

G

- gallery

- power converter, 394
- service UA, 394
- service UL, 394
- General Purpose Network, 435
- General Safety Instruction, 460
- glidcop, 173

H

- halo, 337
 - control, 168
- Hazard Identification Form, 460
- Heat loads, 255, 269
- heavy ions
 - operation, 383
- HEH fluence, 277
- High Field Magnet, 283
- High-order correctors, 103
- HL-LHC AUP, 19
- hollow electron
 - beam, 169
 - lens, 13
- HOM, 123
- hourglass effect, 26
- HTS leads, 181

I

- impedance
 - budget, 164
 - constraints, 150
- important safety elements, 431
- induced background, 234
- Inductive Output Tubes, 118
- inermat, 268
- Inermat 180, 163
- INFN, 20, 107
- injection kicker magnet, 343
- internal metrology
 - fiducialisation, 365
- IT String, 385

K

- KEK, 19, 106
- kicker
 - MKB, 349
 - MSD, 349

L

- LACS, 429, 431
- LARP, 1, 17

- LASA, 103
- LASS, 429
- Launch Safety Agreement, 460
- leaks
 - helium, 315
- LHC Access Safety System, 430
- lifetime
 - HL-LHC, 318
- links, 181, 183
 - installation, 362
 - radiation impact, 274
- loads
 - dynamic heat, 255
 - static heat, 255
- long-range interactions, 338
- Low- β Quadrupoles, 97
- luminosity
 - instantaneous, 5, 26
 - levelling, 6, 373
 - machine peak levelled, 4
 - reduction factor, 117
 - target integrated, 373
 - 'virtual' peak, 25
- Lyot coronagraph, 337

M

- machine protection system, 213
- Manual Overhead Travelling Cranes, 439
- mask
 - TCDD, 345
 - TCDDM, 345
 - TCDDXM, 345
 - TCDQM, 350
 - TCLIM, 346
- maximum possible impact
 - parameter, 344
- MBH, 283
- MCBXFA, 103
- MCBXFB, 103
- MKI
 - heating, 347
- monitor
 - 'head-tail', 336
 - beam gas vertex profile, 333, 334
 - button electrode beam position, 332
 - gas jet, 334
 - streak camera, 336
- MQXF, 97
- multi-cavity feedback, 136
- multipacting, 216

N

neon venting system, 316

O

operation

50 ns space bunching, 7

8b4e, 7

Achromatic Telescopic Squeeze, 9

baseline, 7

BCMS, 7

Pb–Pb, 384

operational efficiency, 377

Orbit correctors, 102

oxygen deficiency hazard detection system, 429

P

passive forward absorber, 236

peak power

density, 266

performance efficiency, 26

physics efficiency, 375

pile-up, 5

density, 373

Piwinski angle, 117

platform

Helium tank, 397

Nitrogen tank, 397

powder-in-tube (PIT), 287

power converter, 192

1-quadrant, 196

2-quadrant, 194, 200

4-quadrant, 201

accuracy, 202

installation, 362

precision, 202

regulation, 202

repeatability, 202

stability, 202

tracking, 202

transfer function, 203

uncertainty, 202

power density

isocontours, 266

powering

Inner Triplets, 193

powering interlock system, 226

Project Safety Officer, 459

Q

Q10, 111

Q4, 110

Q5, 110

Q6, 110

quench

buffer, 259

detection system, 222

R

radiation

stray, 453

streaming, 453

radioactive waste, 449

RadMon, 277

RAMSES, 433

Resistive magnets, 111

restacked rod process (RRP), 287

RF

800 MHz, 357

control system, 136

low level system, 136

transmitter, 137

round optics, 28

S

safety integrity level, 217

Safety Regulation, 460

scenario

nominal, 450

ultimate, 450

scheduled proton physics time, 375

scrubbing, 382

sensor

HLS, 366

Hydrostatic Levelling, 369

WPS, 366

sensors

Wire Positioning, 369

septum magnets, 343

shielding

JTT, 241

shutdown

duration, 375

single event effects, 275

SixTrack, 46

STFC, 20

stored energy, 213

strip-line pick-ups, 332

Supervised Radiation Areas, 453
synchrotron light diagnostics
 installation, 356
synchrotron light monitors
 installation, 356

T

TAXN, 247
TAXS, 237
TCL, 272
TCLD, 156
TCLD collimator, 284
TCLIA, 346
TCLIB, 346
TCLX, 161
TDIS, 344
Technical Infrastructure Monitoring system, 435
TETRA, 433
time
 turnaround, 226, 376
Toohig Fellowship, 19
transverse damper, 144
transverse feedback system
 installation, 357
TSU, 349
turnaround time, 375

U

UFO, 227

ultimate
 current, 100
 performance, 4
underground network, 369
Uppsala, 21

V

vacuum
 buffer, 315
 experiment, 315
 insulation, 314
 layout, 312
 lifetime, 312
vacuum chamber
 alignement, 314
 transitions, 314
vacuum pipe
 experimental, 234

W

wide band
 feedback system, 13
 time normalizer, 330
WorldFIP, 447

Y

year-end technical stop, 375

